CODEN: JASMAN 4966

THE JOURNAL of the Acoustical Society of America

Vol. 104, No. 5 November 1998

SOUNDINGS SECTION

(Continued)

CONTENTS—*Continued from preceding page*

(Continued)

CONTENTS—*Continued from preceding page*

(Continued)

CONTENTS—*Continued from preceding page*

SPEECH PROCESSING AND COMMUNICATION SYSTEMS [72]

BIOACOUSTICS [80]

LETTERS TO THE EDITOR

NOTES CONCERNING ARTICLE ABSTRACTS

1. The number following the abstract copyright notice is a Publisher Item Identifier (PII) code that provides a unique and concise identification of each individual published document. This PII number should be included in all document delivery requests for copies of the article.
2. PACS numbers are for subject classification and indexing. See June and December issues for detailed listing of acoustical classes and subclasses.
3. The initials in brackets following the PACS numbers are the initials of the JASA Associate Editor who accepted the paper for publication.

ACOUSTICAL NEWS—USA

Elaine Moran
Acoustical Society of America, 500 Sunnyside Boulevard, Woodbury, New York 11797

Editor's Note: *Readers of this Journal are asked to submit news items on awards, appointments, and other activities about themselves or their colleagues. Deadline dates for news items and notices are 2 months prior to publication.*

Announcement of the 1999 Election

In accordance with the provisions of the bylaws, the following Nominating Committee was appointed to prepare a slate for the election to take place on 5 March 1999:

Stanley L. Ehrlich, *Chair*
Whitlow W. L. Au
Shira L. Broschat
Dennis McFadden
Winifred Strange
Eric E. Ungar

The bylaws of the Society require that the Executive Director publish in the *Journal* at least 90 days prior to the election date an announcement of the election and the Nominating Committee's nominations for the offices to be filled. Additional candidates for these offices may be provided by any Member or Fellow in good standing by letter received by the Executive Director not less than 60 days prior to the election date and the name of any eligible candidate so proposed by 20 Members or Fellows shall be entered on the ballot.

Biographical information about the candidates and statements of objectives of the candidates for President-Elect and Vice President-Elect will be mailed with the ballots.

CHARLES E. SCHMID
Executive Director

The Nominating Committee has submitted the following slate:

FOR PRESIDENT-ELECT

Katherine S. Harris

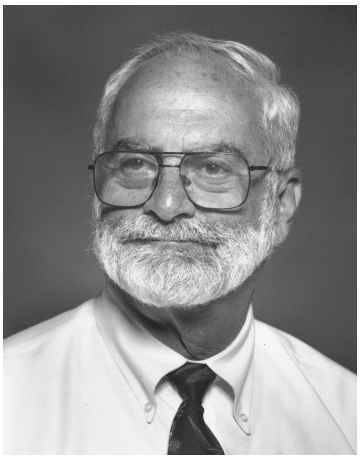

Richard Stern

FOR VICE PRESIDENT-ELECT

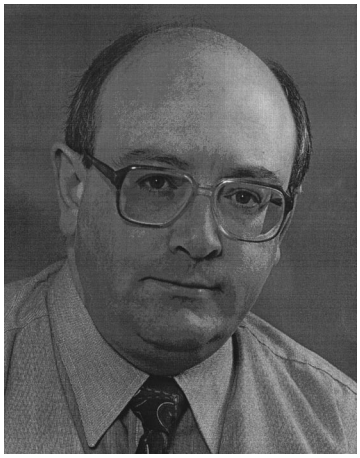

Gilles A. Daigle

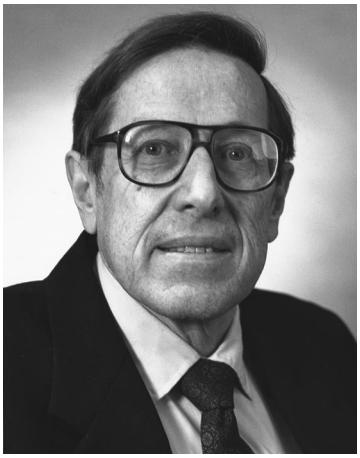

Thomas D. Rossing

 0001-4966/98/104(5)/2537/8/$15.00

John Erdreich

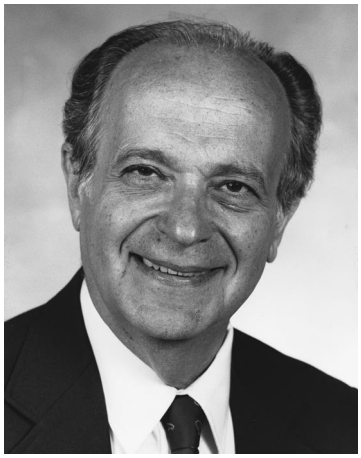

David Feit

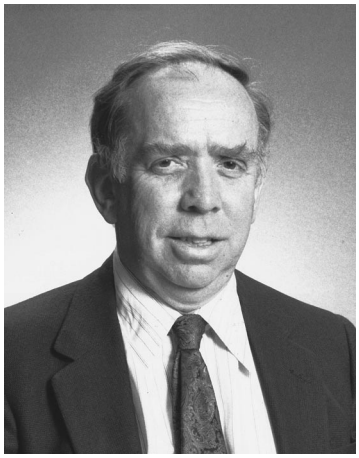

Robert D. Finch

Christy K. Holland

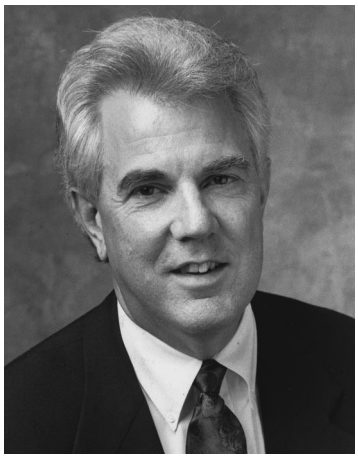

William A. Yost

F. V. Hunt Postdoctoral Research Fellowship awarded to Lily Wang

Lily M. Wang

The 1998–1999 F. V. Hunt Postdoctoral Research Fellowship in Acoustics was awarded to Lily M. Wang. Under the Fellowship Dr. Wang will undertake a research program at the Technical University of Denmark in Lyngby. The subject of her research is on the subjective investigations of spatial impressions.

Dr. Wang holds a BSE degree from Princeton University and the Ph.D. from Pennsylvania State University. Her Ph.D. thesis was on ''Characterization and analysis of the acoustic radiation from bowed violins using multi-planar nearfield acoustic holography.''

The Hunt Fellowship is granted each year to an ASA member who has recently received his or her doctorate or will be receiving the degree in the year in which the fellowship is to be granted. The recipient of the fellowship is that individual who, through personal qualifications and a proposed research topic, is judged to exhibit the highest potential for benefiting any aspect of the science of sound and promoting its usefulness to society. Further information about the Fellowship is available from the Acoustical Society of America, 500 Sunnyside Blvd., Woodbury, NY 11797, Tel.: 516-576-2360; Fax: 516-576-2377; E-mail: asa@aip.org

Whitlow W. L. Au becomes new Associate Editor of the *Journal*

Whitlow W. Au

In June 1998 Dr. Whitlow W. L. Au of the University of Hawaii's Institute of Marine Biology became a new Associate Editor of the *Journal* for papers in Animal Bioacoustics, sharing the PACS 43.80 Bioacoustics responsibility with Professor Floyd Dunn. Gradual expansion of bioacoustics within the *Journal* publication program prompted appointment of an additional associate editor.

Whitlow Au received his B.S. in Electrical Engineering from the University of Hawaii in 1962. He received an M.S. degree in 1964 and a Ph.D. degree in Electrical Science in 1970 from Washington State University.

From 1964 to 1968 Au was a project engineer at the Air Force Weapons Laboratory in New Mexico. From 1970 to 1971 he conducted theoretical research in acoustic propagation at the Naval Ocean Systems Center in San Diego, then transferred to their Hawaii Laboratory where he has conducted research in signal processing, acoustical theory, and dolphin sonar since 1971. Since 1993 he has been Chief Scientist in the Marine Mammal Research Program at Hawaii Institute of Marine Biology.

Au has authored or co-authored 34 articles published in our *Journal*, mostly in animal bioacoustics, and a book *The Sonar of Dolphins* (1993). A Fellow of the ASA and recipient of the Silver Medal in Animal Bioacoustics, Au has also received the Navy Meritorious Civilian Service Award, and several Publication Awards from the Naval Ocean Systems Center. Au is currently Chair of the ASA Animal Bioacoustics Technical Committee.

The Editor-in-Chief and his colleagues welcome Whitlow Au to membership on the Editorial Board.

DANIEL W. MARTIN
Editor-in-Chief

Mark F. Hamilton becomes new Associate Editor of the *Journal*

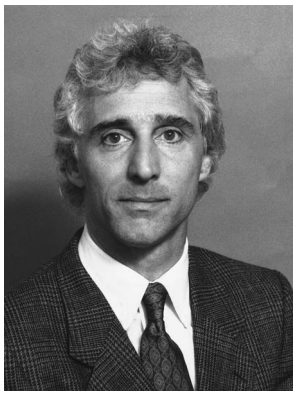

Mark F. Hamilton

In June 1998 Professor Mark Hamilton of the University of Texas at Austin became a new Associate Editor of the *Journal* for papers in Nonlinear Acoustics (PACS 43.25), sharing this responsibility with Professor Mack Breazeale of the University of Mississippi. Gradual expansion of nonlinear acoustics within the *Journal* publication program prompted appointment of an additional associate editor.

Mark Hamilton received a B.S. in Electrical Engineering from Columbia University in 1978. At Pennsylvania State University he was granted an M.S. in 1981 and Ph.D. in 1983, both in Acoustics. He was an F. V. Hunt ASA Postdoctoral Fellow at the University of Bergen Mathematics Institute (1983–84), and at the University of Texas Applied Research Laboratories (1984–85). On the faculty of the University of Texas Department of Mechanical Engineering since 1985, he became a Professor in 1993.

In 1988 Mark Hamilton received the Pi Tau Sigma Gold Medal from the American Society of Mechanical Engineers, and a Packard Fellowship for Science and Engineering. In 1989 he received the R. Bruce Lindsay Award from the Acoustical Society of America.

In ASA he has served on the Executive Council (1993–96), chaired the Committee on Education in Acoustics (1988–91), and has served on the Technical Committees for Physical Acoustics and Engineering Acoustics. He has authored or co-authored 31 articles published in our *Journal* and has been a frequent reviewer.

The Editor-in-Chief and his colleagues welcome Mark Hamilton to membership on the Editorial Board.

DANIEL W. MARTIN
Editor-in-Chief

Reports of Technical Committees

(See October and December issues for reports of other Committees)

Acoustical Oceanography

The meetings for this period were in places with strong representation in Acoustical Oceanography, with the result that there was an unusually large number of papers and special sessions. Planning for the Seattle and Berlin meetings was a major activity for the Technical Committee during this period.

At the Seattle meeting, Jim Lynch, one of the most active AO members, took over as Chair for 1998–2001.

At the Fall meeting in San Diego, Christian de Moustier organized a session on ''Acoustic Observation of Ocean Ridge Processes,'' and Fred Spiess of Scripps Institution of Oceanography presented a special lecture on acoustic geodesy of the seafloor. Terry Ewart organized a special session on ''Stochastic Inverse Methods,'' and John Sahr presented a special lecture on stochastic methods in ionospheric measurements. This was a good example of the kind of cross fertilization that the UW–AO special lectures were designed to promote, and this interdisciplinary spirit was evident in the panel discussion that concluded this session. Another lively panel discussion followed John Potter's special session on the new topic, ''Ambient Noise Inversions,'' Two firsts for AO occurred at San Diego: Bruce Cornuelle's well-attended short course, ''Inverse Methods.'' and the joint UW–AO student reception, ably organized by Aaron Thode. At the San Diego Technical Committee meeting, it was decided to begin a student paper competition beginning with the Norfolk meeting. Barbara Sotirin agreed to chair an ad hoc committee to re-examine the AO policy on special sessions and to establish guidelines that would aid session organizers and encourage participation by younger members.

The Seattle meeting had an unprecedented number of papers, occupying all five days. Joint sessions with UW treated new topics, including Brian Dushaw's session on ''Long-Range Propagation for Measurement of Ocean Processes,'' and the session by Jim Lynch and Grant Deane, ''Surf Zone Oceanography and Acoustics.'' Van Holliday's joint AO–AB session, ''Acoustics of Fisheries and Plankton,'' drew a huge response, requiring that the papers be spread over five sub-sessions. Jim Lynch served as chair at the Technical Committee meeting, where the primary topic was the decline in ONR funding for ocean acoustics.

DARRELL JACKSON
Chair

Animal Bioacoustics

The Animal Bioacoustics Committee had its most successful meeting ever in San Diego. Sessions were conducted over a span of four days with 58 verbal presentations and 10 posters. Whit Au started off the Animal Bioacoustics program by presenting a Tutorial on ''The Dolphin Echolocation System,'' on Monday evening. Approximately 85 people attended the tutorial. The ''C. Scott Johnson session: Whales and Dolphin Acoustics,'' organized by Sam Ridgway and David Helweg was very popular, with two sessions involving 6 invited talks and 10 contributed talks. Ashley Walker and Whit Au organized the two sessions on ''Biologically inspired acoustics models and systems,'' which attracted 3 invited and 13 contributed papers. There was a session on reptile and amphibian bioacoustics, organized by Peter Narins and Ann Bowles, and a session on the effects of noise on animals. Two sessions organized by Charles Greene and Mardi Hastings on Instrumentation in animal bioacoustics wrapped up the animal bioacoustics contribution to the San Diego meeting. Although the final instrumentation session was held on Friday afternoon, the session was surprisingly well attended.

Two student paper awards were granted for the first time in Animal Bioacoustics. Caitlin O'Connell from the School of Veterinary Medicine, University of California, Davis, won the first prize of $300 with her paper on ''Seismic transmission of elephant vocalization and movement.'' Kathleen Stafford of Oregon State University won the 2nd prize of $200 for her paper on ''Low-frequency whale calls recorded on hydrophones moored in the eastern tropical Pacific.''

There were four Animal Bioacoustics sessions at the Seattle meeting, Avian and Insect Acoustics, organized by Timothy Forrest, Temporal Pattern and Rhythm organized by Christopher Clark, Fish Acoustics, and General Animal Bioacoustics. AB and AO co-organized an extremely popular session on the Acoustics of Fisheries and Plankton, that had an overwhelming response with 2 invited papers and 33 contributed papers. Five sessions were devoted to this topic. The AO organizer was Van Holliday and the AB organizer was Whit Au. The first place student award of $300 was presented to Hamilton Farris from Cornell University for his presentation on ''Two-tone suppression of the ultrasound induced startle response of a cricket.'' The runner up student award of $200 was presented to Matthew Mason of the University of Cambridge for his presentation on ''Functional anatomy of the middle ear of insectivores.'' Darlene Ketten representing AB gave an outstanding plenary presentation entitled ''Marine mammal ears: An anatomical perspective on underwater hearing.'' Her presentation was warmly received with many people mobbing her after the talk with numerous discussion topics and questions. Ronald Schusterman was elevated to a Fellow status for his contribution in marine mammal audition and psychoacoustics.

Some of the important issues raised at the Technical Committee meetings included the following:

1. Concern for the high registration fee was voiced by many.
2. There should be a moratorium on joint meetings for the next several

years since joint meetings tend to push registration fee upwards and make for extremely early submission of abstracts. There were also concessions made by the ASA to the ICA in order to organize a joint meeting. The exception to this is the joint meeting with Japan since those meetings have been conducted in the usual ASA format with a minimum of concessions or alteration.

3. Having two locations caused difficulties for those that wanted to attend other sessions in the different locations. The general sense was that the size of the meeting was especially large because of the joint nature of it.

WHITLOW W. L. AU
Chair

Physical Acoustics

This report summarizes the activities of the Physical Acoustics Technical Committee (PATC) over the past year.

The technical program at the Penn State meeting consisted of one special session and eight sessions of contributed papers. These nine sessions contained a total of 5 invited and 90 contributed papers. The special session was ''Time-Reversed Acoustics'' jointly organized with the Underwater and Signal Processing committees and chaired by David Dowling. Sessions of contributed papers (and chairs) were: ''Quantum Acoustics and Thermoacoustics'' (Ralph Muehleisen), ''Radiation, Propagation and Scattering'' (Gregory Kaduchak), ''Drops, Filaments, and Bubbles'' (Felipe Gaitan), ''Nonlinear Acoustics'' (Bruce Denardo), Atmospheric Acoustics (David Gardner), Medical Ultrasound (Christy Holland), Porous Media (Craig Hickey), and ''Ultrasonics'' (L. C. Krysac).

The technical program at the San Diego meeting consisted of five sessions of contributed papers. These five sessions contained a total of 47 contributed papers. Sessions of contributed papers (and chairs) were: ''Nonlinear Acoustics'' (Bart Lipkens), Thermoacoustics (Pat Arnott), ''Radiation, Propagation and Scattering'' (James Chambers), ''Bubbles, Drops, and Particles'' (Robin Cleveland), Inhomogeneous Media (Craig Hickey).

The technical program at the Seattle meeting consisted of seven special sessions and eleven sessions of contributed papers. These eighteen sessions contained a total of 45 invited and 195 contributed papers. The special sessions (and chairs) were: Memorial Session for Isadore Rudnick (Richard Stern and Robert Keolian), Nonlinear Acoustics Part II: 1. Solitons; 2. Biomedical Nonlinearities (Mack A. Breazeale and Lev. A. Ostrovsky), Outdoor Sound Propagation (Henry E. Bass and Daniel Juvé), Sonochemistry and Sonoluminesence: SC I (Kenneth S. Suslick and Jacques L. Reisse), Nonlinear Acoustics I: 1. History; 2. Solids, Rocks; 3. Surface Waves, Part I (Mack Breazeale and Akira Nakamura), Cavitation Dynamics: In Memoriam Hugh Flynn I and II (Charles C. Church, Ronald A. Roy and Werner Lauterborn), Sonochemistry and Sonoluminesence: SL (Thomas J. Matula and R. Glynn Holt). Sessions of contributed papers (and chairs) were: General Topics in Nonlinear Acoustics (Andres Larazza), Cavities and Resonators (Robert M. Keolian), Scattering from Fluid-Loaded Objects (Raymond Lim), Nonlinear Wave Propagation in Fluids (Steve Kargl and Patrick Edson), Ducts and Tubes (James P. Chambers), Topics in Thermoacoustics (Anthony Atchley), Acoustic Characterization and Manipulation of Material Properties (Sameer Madanshetty and D. Keith Wilson), Half-Spaces and Plates (Paul Barbone), Radiation and Diffraction (Andrew A. Piacsek), General Topics in Physical Acoustics, I and II (James Chambers and Michael Bailey), Acousto-Optics and Opto-Acoustics (Harry Simpson).

The TC provided $1500 for travel support for two speakers to attend the San Diego meeting. Willie Moss was the committee's point of contact for this initiative. The TC provided $600 for student receptions at the PSU and Seattle meetings. Steve Garrett organized the student reception at the Penn State meeting. It was held on the patio deck of the ARL research facility and everyone seemed to enjoy themselves. The student reception in Seattle was jointly organized with three other committees, UW, AO, and BV. The TC provided $600 for WEB page construction. John Stroud continues to maintain this page for the committee. He updates member e-mail addresses (thanks to Logan Hargrove) and posts the minutes of the PATC.

President Bob Apfel described an on-line preprint program called *e*-print. The Technical Council announced a dues increase. Various options and benefits are available to members. These include OFFPRINTS, ECHOES, and a new on-line version of JASA. Tom Matula, John Stroud, and Carr Everbach demonstrated the PATC WEB page. Anthony Atchley is the PATC representative to the Long Range Planning Committee. This committee will be evaluating successes of the Seattle and Berlin meetings.

The Chair proposed that the committee spend less time on organizing special sessions and more time on science during the meeting. At the Penn State PATC meeting Bob Apfel showed a video of electro-acoustic generation of charged water drops. At the Seattle meeting Tim Simmons and Bart Lipkens presented shortened versions of their presentations that discussed an Acoustic Radiometer and Physical Effects of Macrosonic Standing Waves, respectively.

The Physical Acoustics Summer School was held 21 June–28 June with a total of 50 participants. Approximately one half the participants were advanced graduate students in physical acoustics. The Physical Acoustics Summer School is sponsored by the Office of Naval Research in cooperation with the Acoustical Society of America and the National Center for Physical Acoustics.

JAMES M. SABATIER
Chair

Phychological and Physiological Acoustics

For Psychological and Physiological Acoustics (P&P), this past year had many cross-disciplinary activities with other Technical Committees (TCs). One such activity deemed particularly important was our participation in the ASA Task Force on Acoustic Barriers in the Classroom to address noise problems in the schools. This group, which sponsored a workshop at the House Ear Institute in December and plans a second meeting in New York this spring, is drafting a formal response to questions from the U.S. Access Board which may lead to future legislation. Peggy Nelson is our representative to the Task Force, and P&P is forming its own interest group to support work in this area. Please contact Dr. Nelson for further information. Other cross-disciplinary activities included three sessions at the San Diego meeting co-sponsored with Signal Processing on Acoustics in Multimedia. Session topics were Perceptual Issues, Head-Related Transfer Functions, and Source Localization. A number of P&P speakers also participated in the Speech workshop at San Diego on the intersection of basic science and clinical issues. The P&P program for San Diego was organized by Robert Shannon.

The Spring meeting remained the main P&P meeting, with a large program at Seattle compared to San Diego. The P&P program at Seattle was organized by Lynne Werner, Donna Neff, Susan Norton, and Edward Burns. P&P co-sponsored two sessions at Seattle. The first, with Speech Communication and Musical Acoustics, was titled''Rhythm in Music and Speech'' and was organized by Robert Port and J. Devin McAuley. The second, with Musical Acoustics, was titled''Purposeful Use of Nonlinear Distortion in Musical Performance: The Eric Dolphy/Jimi Hendrix Celebratory Session'' and organized by Edward Burns. This session was lively, loud, and attracted considerable media interest. The jam session following revealed previously unknown talents of some of our colleagues. Other highlights of the Seattle meeting included plenary lectures by Eric Young and Brian Moore and two special sessions. One, organized by Lynne Werner, was on auditory development. The second, organized by Ervin Hafter, was on auditory attention. Both were well attended and provided broad perspectives on the topics. Multidisciplinary student receptions which included P&P were held at both San Diego and Seattle and were judged to be very successful.

P&P continues to update and develop its WWW site [www.boystown.org/asapp/], thanks to Steven Neely and Brent Edwards. The P&P program for upcoming meetings is posted there as soon as it is available, as well as general information and a number of excellent links. Check them out and contact Steve or Brent to post information there. Another initiative this year was to build a new and improved e-mail list of members with P&P as their primary affiliation. The intent is to maintain this list to pass along news and poll the membership on issues that arise. Please send postings and e-mail address changes or additions to me (neff@boystown.org). The new list was used this spring to encourage attendance at Seattle and voting in the ASA election. Publication in JASA remains strong for both psychological and physiological acoustics, keeping our five editors busy. P&P is strongly supportive of efforts to handle as much of the current publishing process as possible electronically. This past year, two of our members were selected for prestigious awards. P&P congratulates Virginia Richards, who received the Troland Research Award from the National Academy of Sciences in April, and Murray Sachs, who will received the von Békésy Medal at the Norfolk meeting this fall.

Much time this past year was spent planning both the Seattle and upcoming Berlin meetings. Thanks to the efforts of the P&P Technical Committee and our European colleagues, especially Armin Kohlrausch, a series of invited sessions will form the core of what promises to be an excellent P&P program. At Berlin, P&P will also co-sponsor a Workshop on

Auditory Display, which should provide opportunities for exploring broader and more applied topics than usual. Other topics discussed at our meetings this year included reducing registration costs, concern about copyright issues for electronic preprint publishing, and promoting P&P representation within the ASA. A request was made to add a check-off box to the ballot envelope for TC affiliation, so one could learn more about participation in ASA elections. In our own P&P elections this spring, the six members elected to serve on the Committee next year were: Huanping Dai, Ann Clock Eddins, Robert Schlauch, Richard Fay, Stan Sheft, and Peggy Nelson. Our thanks to the outgoing committee members for their work these past three years: Laurel Carney, Mary Ann Cheatham, Craig Formby, Janet Koehnke, Neal Viemeister, and Beverly Wright. Finally, the members elected last spring who begin service this year are: Prudence Allen, Robert Carlyon, David Dolan, Brent Edwards, Nina Kraus, and John Rosowski. Tom Hanna, who was also elected to the Committee last year, died this January and will be greatly missed. In closing, my thanks to the many members who served on committees or helped with various projects in support of P&P.

DONNA L. NEFF
Chair

Speech Communication

The 134th Meeting in San Diego was a busy one for the Speech Communication Technical Committee. On Monday, a workshop (only the second in the history of SCTC) was held, entitled''Basic Science at the Intersection of Speech Science and Communication Disorders.'' This workshop was organized and chaired by Lynne Bernstein and Gary Weismer. The workshop which ran from 11 a.m. to 5 p.m. was attended by scores of interested researchers and there was lively discussion among participants and the audience. Two special sessions were also presented ''Sources of Individual Variability in Speech Production and Perception'' (Tuesday, chaired by Ken Grant) and ''Phonetic Perception and Word Recognition'' (Thursday, chaired by Lynne Bernstein and Edward Auer). Both sessions were well-attended and well-received by participants. In addition, on Wednesday, Thomas Crystal presented the Hot Topics lecture in Speech Communication, entitled ''Conversational Speech Recognition.'' The Speech Communication Poster sessions were even larger and busier than usual. The special effort made by the technical program organizers to reserve a large space for the posters and to allow extra time for their exhibition was viewed as a definite plus. Following long-standing tradition, Speech Communication participated in a graduate student reception. This reception was also jointly sponsored by Architectural, Musical, and Physiological and Psychological Acoustics. Technical initiatives put forward included web site development, Graduate Student Receptions for the Seattle joint ICA/ASA meeting.

TERRANCE M. NEAREY
Chair 1995–1998

USA Meetings Calendar

Listed below is a summary of meetings related to acoustics to be held in the U.S. in the near future. The month/year notation refers to the issue in which a complete meeting announcement appeared.

1999

15–19 March	Joint meeting: 137th meeting of the Acoustical Society of America/Forum Acusticum [Acoustical Society of America, 500 Sunnyside Blvd., Woodbury, NY 11797, Tel.: 516-576-2360; Fax: 516-576-2377; E-mail: asa@aip.org; WWW:asa.aip.org].
10–12 May	AIAA/CEAS Aeroacoustics Conference, Bellevue, WA [Belur Shivashankara, The Boeing Company, P.O. Box 3707, MS 67-ML, Seattle, WA 98124-2207; Tel.: 425-234-9551, Fax: 425-237-5247; E-mail: belun.n.shivashankara@boeing.com].
6–7 June	1999 SEM Spring Conference, Cincinnati, OH [Katherine M. Ramsay, Conference Manager, Society for Experimental Mechanics, Inc., 7 School St., Bethel, CT 06801; Tel.: 203-790-6373; Fax: 203-790-4472; E-mail: meetings@sem1.com].
27–30 June	ASME Mechanics and Materials Conference, Blacksburg, VA [Mrs. Norma Guynn, Dept. of Engineering Science and Mechanics, Virginia Tech, Blacksburg, VA 24061-0219; FAX: 540-231-4574; E-mail: nguynn@vt.edu; WWW:http://www.esm.vt.edu/mmconf/]. Deadline for receipt of abstracts: 15 January 1999.

Revisions to Membership List

New Associates

Afaneh, Abdul-Hafiz A., BAMS/EME, Bosch, 38000 Hills Tech Dr., Farmington Hills, MI 48331-3417 Agnew, Jeremy A., Starkey Laboratories, Inc., Colorado Research Center, 1110 Elkton Dr., Unit E, Colorado—Springs, CO 80907

Alex, Coiret L., 22 rue des Figuiers, Lagord 17140, France

Alter, Harry A., Owens Corning, Insultation Systems Business—Product Development, 2790 Columbus Road, Granville, OH 43023

Ando, Shigeru, Dept. Mathematical Eng. & Information Physics, 7-3-1 Hongo, Bunkyo-ku, Tokyo 113-8656, Japan

Arezes, Pedro M., Lab. Ergonomia, Univ. do Minjo, Guimaraes 4800, Portugal

Auerbach, Richard, 4012 Messina Dr., Plano, TX 75093

Backman, Juha R., Heinjoenpolko 2N 103, Espoo FIN-02140, Finland

Balaban, Evan S., The Neurosciences Institute, 10640 John Jay Hopkins Dr., San Diego, CA 92121

Bates, Kenneth, 15580 SW Barntwood Court, Beaverton, OR 97007

Berndtsson, Gunilla H., Audio & Visual Technology Research, Ericsson Radio Systems AB, Torshamnsgatan 23, Stockholm 16480, Sweden

Bullock, Gary L., RR 11, Box 1340, Bedford, IN 47421

Christoff, James T., 802 West 8th St. Circle, Lynn Haven, FL 32444

Chunchuzov, Igor, Inst. of Atmospheric Physics, Russian Academy of Sciences, 3 Pyzhevskii Per., Moscow 109017, Russia

Cobo, Pedro, Inst. de Acustica, CSIC, ACustica Ambiental, Serrano 144, Madrid 28006, Spain

Crosby, Laurence, Symphonix Devices, 2331 Zanker Rd., San Jose, CA 95131

Day, Robert A., 220 Gates St., San Francisco, CA 94110

Delory, Eric, Acoustics Research Lab., National Univ. of Singapore, Electrical Engineering, Kent Ridge Crescent, Singapore

Didenko, Yuri T., Chemistry, Univ. of Illinois at Urbana-Champaign, 600 South Mathews Avenue, Urbana, IL 61801

Dougherty, Robert P., 10914 Ne 18th St., Bellevue, WA 98004

Dumbrell, Hugh A., DERA Bincleaves, SSMW, Newtons Rd., Weymouth, Doreset DT4 8UR, U.K.

Dykhne, Alexandre M., Ctr. of Theoretical Physics & Applied Mathematics, Federal Science Center ''Triniti'', Troitsky Sity Moscow Region, Troitsk 142092, Russia

Edry, Robert A., 262 Old Mountain Rd., Lyndeborough, NH 03082

Egerev, Sergey V., N. N. Andreyev Acoustics Inst., 4 Shvernik St., Moscow 117036, Russia

Erbe, Christine, Inst. of Ocean Sciences, Acoustical Oceanography, 9860 West Saanich Rd., Sidney, BC V8L 4B2, Canada

Fang, Qiping, Inst. of Acoustics, Chinese Academy of Sciences, 17 Zhongguancun St., Haidian District, Beijing 100080, People's Republic of China

Felgate, Nicholas J., Shepherds Walk 61, Farnborough, Hampshire, GU14 9A, U.K.

Flannery, Colm M., Nanoakustik, Paul-Drude Inst., Havsvogteiplatz 5-7, Berlin 10117, Germany

Fournier, Patrick C., 255 17th Avenue, South, Great Falls, MT 59405

Froelich, Benoit G., Sonics, Schlumberger K. K., 2-2-1 Fuchinobe, Sagamihara, Kanagawa 229 0006, Japan

Furness, Roger K., 333 East 53rd St., Apt. 5N, New York, NY 10022

Gerges, Samir N. Y., Mechanical Engineering, Federal Univ. of Santa Catarina, Campa Universitario—Trindade, Florianopolis SC 88040-900, Brazil

Guo, Jingnan, Occupational Hygiene Program, Dept. of Mechanical Engineering, Univ. of British Columbia, 3rd Floor, 2206 East Mall, Vancouver, BC V6T 1Z3, Canada

Halmrast, Tor, Spangberg Vn. 28A, Oslo N-0853, Norway

Hart, Lynette A., Dept. Population Health & Reproduction, Univ. of California, Center Animals in Society, Davis, CA 95616

Herzel, Hans-Peter, Univ. Hospital & Biology Dept., ITB, Humboldt Univ., Invalidenstr. 43, Berlin D-10115, Germany

Holmes, Gary W., Engineering Systems Company, 7199 South Chase Court, Littleton, CO 80128-4976

Horoshenkov, Kirill V., Civil & Environmental Eng., Univ. of Bradford, Great Morton Rd., Bradford, West Yorkshire, LS2G 6HG, U.K.
Hudson, Scott A., 25445 Doyle Court, Stevenson Ranch, CA 91381
Hutt, Daniel L., DREA, Environmental Acoustics, 9 Grove St., Dartmouth, NS B2Y 3Z7, Canada
Im, Sang H., 959 South Gramercy Place, ♯203, Los Angeles, CA 90019
Isberg, Peter, Acoustics Unit., Ericsson Mobile Communications AB, NVA Vattentornet, Lund 22183, Sweden
Jiang, Dejun, Inst. of Acoustics, Chinese Academy of Sciences, 17 Zhongguancun Rd., Hai Dan District, Beijing 100080, People's Republic of China
Johnson, Paul A., Nonlinear Elasticity Group, Los Alamos National Lab., Mail Stop D443, Los Alamos, NM 87501
Joo, Young-Sang, Korea Atomic Energy Research Inst., Nondestructive Evaluation, Structural Integrity Div., P.O. Box 105, Yusong, Taejon 305-600, Korea
Katsnelson, Boris G., Voronezh Univ., Physics, Universitetskaya Sq. 1, Voronezh 394693, Russia
Kook, Hyungseok, School of Mechanical and Automotive Engineering, Kookmin University, 861-1 Chongnungdong, Songbuk-gu, Seoul 136-702, Korea
Kostarev, Stanislav A., Osenny Blrd. 3-260, Moscow 121609, Russia
Laux, Peter C., 6654 Scenic Shores Dr., Holland, MI 49423
Leamy, Theodore J., Electrotec Productions Inc., 31119 Via Colinas, Westlake Village, CA 91362
Lee, Tom W. C., 7 Oak Hill Dr., Clinton, CT 06413
Lester, Robert A., Paoletti Associates, Inc., 40 Gold St., San Francisco, CA 94133
Locqueteau, Christophe C., 9 Rue Edith Warthon, Hyeres 83400, France
Lu, Jian-Yu, Dept. of Bioengineering, Univ. of Toledo, 5035 Nitschke Hall, 2801 West Bancroft St., Toledo, OH 43606
Lu, Yadong, Inst. of Acoustics, Chinese Academy of Sciences, 9th Division, Zhongguancun Rd. No. 17, Beijing 100080, People's Republic of China
Maksimov, German A., Moscow Engineering Physics InN39 High Energy Density Physics, Kashivskoe Str. 31, Moscow 115409, Russia
Martinez, Michael M., 6415 190th St., SW, Lynnwood, WA 98036-4155
Masanobu, Kumada, Haskins Laboratories, 270 Crown St., New Haven, CT 06511
Matthews, Cathy C., Code 4912, NAWCTSD, 12350 Research Parkway, Orlando, FL 32826
Oakley, Barbara A., Oakland University, Electrical & Systems Eng., Dodge Hall of Engineering, Rochester, MI 48317
Ouis, Djamel, Bogesholmsvagen 19, Kavlinge S-24439, Sweden
Pan, Jian, 21963 Sunflower, Novi, MI 48375
Pavan, Gianni, Centro Interdisciplinare di Bioacustica, Univ. of Pavia, Via Taramelli 24, Pavia PV 27100, Italy
Penrose, Nancy L., 6043 150th Court, NE, Redmond, WA 98052
Piehler, Christian O. M. C., IM Hoverfeld 5, Merzenich NRW 52399, Germany
Rebula, Robertson, Rua Barata Ribeiro, 323/401, Rio de Janeiro 22040-000, Brazil
Ruiz, Robert, L.A.R.A., Maison de la Recherche, Univ. de Toulouse—Le Mirail, 5 Allees Antonio Machado, Toulouse Cedex 1, 31058, France
Saulnier, Louis, 204-291 Christophe-Colomb Est, Quebec, PQ G1K 3T1, Canada
Saunders, Christopher A., Lexmark International Inc., Power Systems Group/d27, 740 New Circle Rd., Bldg. 03213, Lexington, KY 40550
Schell, Stephen F., 3824 Clark Avenue, Long Beach, CA 90808
Schilling-Estes, Natalie, 586 Lagunita Dr., Apt. 22, Stanford, CA 94305-8203
Schmidt, Robert A., 6034 Rothko Lane, Simi Valley, CA 93063
Seeker, Mark R., Miller Henning Associates, 6731 Whittier Avenue, Suite A110, McLean, VA 22101
Shield, Bridget M., 26 Plum Lane, Plumstead SE18 3AE, U.K.
Singh, Dhiraj, 121 Mohalla Chaudharian, Hisar 125001, India
Sonwalkar, Vikas S., Electrical Engineering, University of Alaska, Fairbanks, P.O. Box 755-915, 211 Duckering, Fairbanks, AK 99775
Tanaka, Manabu, Kibougaoka 6-2-6, Toyono-Cho, Toyono-Gun, Osaka 563-0214, Japan
Thomas, Vaughn M., 208 Tillbrook Lane, Harrison City, PA 15636
Tian, Jing, Inst. of Acoustics, Academia Sinica, 17 Zhongguancun St., Beijing 100080 People's Republic of China
Tollin, Daniel J., Dept. Physiology, Univ. of Wisconsin-Madison, 127 SMI, 1300 University Avenue, Madison, WI 53706
Tremblay, Kelly L., Electrophysiology, House Ear Institute, 2100 West Third St., Los Angeles, CA 90057
Vaissiere, Jacqueline, Univ. de Paris III, Phonetique Dept., 19 Ave des Bernardins, Paris 75005, France
Van Biesen, Leo P., Vrije Univ. Brussel, Pleinlaan 2, Brussels B-1050, Belgium
Vovk, Igor V., Hydrodynamical Acoustics, Inst. of Hydromechanics, National Academy of Sciences, 8/4 Zhelyabov Str., Kiev 252057, Ukraine
Waxler, Roger M., 1801 Puddintown Rd., State College, PA 16801
Wu, Qiu, 8110E Speedway Boulevard, #8289, Tucson, AZ 85710
Yang, Weicheng, Research Inst. of Household Electrical Appliance of China, No. 1 Research Lab., No. 6, Yuetan Beixiaojie, Beijing 100037, People's Republic of China
Zaiken, Eliot J., Welch Allyn, 95 Old Shoals Rd., Arden, NC 28704-9739

New Students

Aytar, Pamela K., 10127 Linden, Overland Park, KS 66207
Bazua-Duran, Carmen, Oceanography, Univ. of Hawaii at Manoa, 1000 Pope Rd., MSB, Honolulu, HI 96822
Block, Gareth I., 1605-C Lyndhurst, Savoy, IL 61874
Chang, Steve S., Linguistics, Univ. of California, Berkeley, 1203 Dwinelle Hall, Berkeley, CA 94720-2650
Clinard, Christopher G., 704 Berry Rd., Apt. D3, Nashville, TN 37204
Dapino, Marcelo J., Aerospace Eng. & Eng. Mechanics, Iowa State Univ., 2019 Black Engineering Building, Ames, IA 50011
Farell, Cesar E., 6-43 Hillsboro Ave., Toronto, ON M5R 1S6, Canada
Gulsrud, Timothy E., 2301 Pearl St., #6, Boulder, CO 80302
Guo, Qiushuang, Electrical and Computer Eng., Univ. of Massachusetts–Dartmouth, 285 Old Westport Rd., North Dartmouth, MA 02747
Hopkins, Jonathan K., Box 669, Univ. of Hartford, 200 Bloomfield Ave., West Hartford, CT 06117
Johnston, Todd E., ANP Laboratory–Noise, P.O. Box 3707, MC 1W-03, Seattle, WA 98124-2207
Koperda, Eric F., 2252 Merrymount Dr., Suwance, GA 30024
Kripfgans, Oliver D., Dept. of Radiology, Univ. of Michigan, Zina Pitcher Place, Krege III (R3315), Ann Arbor, MI 48109
Krogseng, Jason J., 71 North Winthrop St., St. Paul, MN 55119-4674
Lentz, Matthew M., 618 Hardin Ave., Aurora, IL 60506
Liu, Chang, Speech and Hearing Sciences, Indiana University, 200 South Jordan St., Bloomington, IN 47405,
Malliopoulos, Christos S. E., 11 Dekelias St., Metamorphosis, Athens 14451, Greece
Mandal, Nirmal K., Inst. of Noise and Vibration, Univ. of Technology Semarak, Kuala-Lumpur 54100, Malaysia
Mason, Matthew J., Dept. of Zoology, Univ. of Cambridge, Downing St., Cambridge CB2 3EJ, U.K.
McCormick, Ryan D., 2341 Chestnut Springs Trail, Marietta, GA 30062-2834
Meglino, Mike P., 353 Hunters Blind Dr., Columbia, SC 29212
Meyer, Jens M., Am. Kirchpfad 34, Weiterstadt 64331, Germany
Neilsen, Tracianne B., 1044 Camino La Costa, #2060, Austin, TX 78752
O'Connell, Caitlin E., 908 Arthur St., Davis, CA 95616
O'Reilly, Thomas P., P.O. Box 12052, Elspark, Johannesburg 1418, South Africa
Prodi, Nicola, Via Gozzi 3/1, Reggio Emilia RE 42100, Italy
Queen, Jennifer S., Psychology, Emory University, Atlanta, GA 30322
Reeder, Davis B., 43 Dexters Mill Dr., Teaticket, MA 02536
Rozelle, Lorna, G., 1244 NE 91st St., Seattle, WA 98115
Sanchez, M. Loreto, Angel Munox 560, Valdivia, Chile
Schenck, Diana L., Cognitive Science, The Johns Hopkins Univ., Krieger Hall, 3400 North Charles St., Baltimore, MD 21218-2686
Sepulveda, Cristian F., C. Colon 3969 Depto. 123, Santiago 6761496, Chile
Sharp, Stephen J., Center for Acoustics and Vibration, Pennsylvania State University, 157 Hammond Building, University Park, PA 16802
Sihn, Danny D. W., 102 Poplar Hall, UNC Charlotte, Charlotte, NC 28223
Slifka, Janet L., Speech Communication Group, RLE, MIT, 55 Vassar St., Room 36-549, Cambridge, MA 02139
Tan, Chin-Tuan, Nanyang Technological Univ., School of Electrical & Electronic Eng., Nanyang Ave., Singapore 639798
Vainikainen, Keijo A., Kylatie 10A11, Helsinki 00320, Finland
Wong, Patrick C. M., Psychology Dept., Univ. of Texas at Austin, Austin, TX 78712
Younghouse, Steven J., Acoustics/Mechanical Engineering, Univ. of Texas, ETC II 6.202, Austin, TX 78712-1063

Zhang, Chao, Physics Dept., Pennsylvania State Univ., 104 Davey Lab., University Park, PA 16802

Members Elected Fellows

J. D. Achenbach, P. G. Cable, R. P. Carlyon, D. E. Chimenti, S. L. Coombs, D. J. Evans, K. W. Ferrara, O: Ghitza, J. F. Greenleaf, F. S. Henyey, D. Juve, A. Kohlrausch, V. A. Krasilnikov, F. L. Lizzi, R. Martinez, J. C. Middlebrooks, E. C. Monahan, K. J. Parker, A. N. Norris, O. V. Rudenko, N. A. Shaw, Y. Tohkura, B. J. Uscinski

Associates Elected Fellows

O. V. Abramov, V. Abramov, K. H. Arehart, R. Aubauer, M. Badiey, R. H. A. Bahr, B. Bajic, S. M. Balabaev, A. C. Balant, L. B. Berry, J. S. Bird, P. Blanc-Benon, R. W. Bland, S. S. Boatright-Horowitz, O.-S. Bohn, R. L. Brill, M. Brussieux, J. M. Burrows, E. Buss, L. H. Carney, V. J. Cerami, K. Chen, R. Cheng, J. P. Christoff, S. Chucheepsakul, Q. Ciao, D. S. Clark, B. D. Cornuelle, M. G. Cote, J. F. Culling, E. A. Cutler, B. B. Djordjevic, D. E. Drommond, K. Eggenschwiler, J. M. Fletcher, E. R. Gerstein, N. J. Giordano, H. S. Gopal, K. W. Grant, H. J. Helimaki, J. M. Hillenbrand, D. Hindl, N. Hiroaki, F. Holmes, D. E. Homa, R. A. Honeycutt, S. S. M. Hussain, T. Imamura, P. Iverson, D. A. Jarinko, S. S. Jarng, P. W. Jusczyk, W. Kainz, C. S. Kaminsky, S.-W. Kang, A. I. Khil'ko, K. S. Kim, J. C. Kingston, A. Lakomyj, K. Lashkari, J.-Y. Lin, S. G. Lindsey, I. Magrin-Chagnolleau, J. W. Malek, D. L. Manger, K. W. Marr, S. E. Marshall, T. J. Mason, T. A. Matthias, T. J. McGraw, J. R. Milet, R. L. Miller, K. N. Milligan, E. C. Mousset, H. Nakasone, R. A. Nobili, P. D. Mourad, J. R. Olson, M. V. Penna, J. A. Porti, M. A. Rodriguez, A. J. Romano, V. Ryaboy, H. Sakai, R. Saliba, M. Salomma, W. D. Shallcross, A. Sharma, M. N. Shipley, I. Shreiber, C. Stamoulis, B. M. Sullivan, V. Summers, A. Y. Supin, F. M. Svinth, M. S. Vlaming, S. Tanner, K. Vokurka, D. C. Walton, P. J. White, D. L. Wieland, D. K. Wilson, Y. Xu, I. Yamada, G. K. Yates, Z. Ye, G. Yuan, N. V. Zacharov

Students to Associates

T. A. Busch, K. Gipson, F. Honarvar, H. Matsuzaki, R. Panneton, B. Rafaely, R. J. Renomeron, G. C. Stecker

Resigned

S. J. Barry, J. M. Ozard, A. J. M. Peters, A. M. Soler-Navarro—*Members*
J. H. Eggen, D. E. Morledge, V. Zhdanov—*Associates*
I. C. Valdebenito—*Student*

Reinstated

S. A. Chapman—*Member*
N. T. Cooley, S. Taherzadeh—*Associates*

Deceased

T. Mariner—*Fellow*
M. D. Fagen—*Member*
H. M. Neustadt, C. Newman—*Associates*

Drops

Fellows

J. F. Brugge, C. R. Fuller, M. P. Haggard, S. K. Numrich, R. R. Rojas, H. L. Saxton

Members

A. Alippi, J. M. Aran, C. R. Arnold, S. E. Auyer, R. C. Baird, D. C. Barber, J. L. Becklehimer, I. A. Beresnev, I. M. Besieris, D. D. Bie, D. Boucher, B. E. Bowers, L. L. Boyer, H. Brandes, C. W. Brokish, C. H. Brown, C. Brunel, M. Burrill, F. J. Canals-Riera, R. F. Carlson, A. S. Chan, W. T. Chan, S-T. Chang, J. L. Christensen, R. J. Christian, J. P. Christopher III, C. J. Dewdney, M. A. Dinno, A. M. K. Edee, F. J. Fahy, T. Y. Fung, F. G. Geil, C. R. Gerke, J. J. Godfrey, M. A. Gonzalez, L. C. Granger, J. J. Grannell, T. A. Graves, L. C. Gray, E. D. Haas, V. Hansen, M. E. Haran, H. W. Hehmann, J. C. Heine, T. L. Henderson, G. R. Hess, R. D. Hilliard, J-M. Ho, J. L. Hook, C-J. Hsu, P. D. Jackins, D. W. Johnson, J. B. Jones-Oliveira, P. K. Kasper, E. L. Kelsey, R. L. Kerlin, F. R. Kern, C-D. Kim, S. Kostek, S. Kishnamurthy, T. E. Landers, M. Lennig, N. D. Lewis, J. L. Locke Head, C. P. Loser, I. R. A. MacKay, P. H. Maedel, Jr., R. P. Maineri, J. B. Malosh, G. Margolis, R. L. Martin, D. J. McCarthy, R. J. McCauley, N. P. McKinney, J. R. Mendez y Suarez, H. L. Merck, C. R. Merz, R. E. Montgomery, K. J. Murphy, R. L. Nasoni, C. H. Norris, W. L. O'Neill, C. C. Oliver, C. W. Olson, E. R. Payne, M. T. Poldino, J. C. Preble, J. R. Prohs, B. Rafine, W. E. Robert, D. Roberti, L. M. Rowe, Jr., S. Ryan, S. Santi, D. J. Snow, A. G. Sotiropoulou, B. S. Spano, H. F. Stewart, J. M. Tattersall, R. Thorne, R. J. Thornhill, D. Thurmond, K. A. Tobin, M. D. Trudeau, K. M. Vandever, A. S. Victor, S. T. Walden, D. N. Washburn, J. M. Whitehead, R. J. Wilkes, J. M. Winey, N. K. Winsor, W. R. Woszczyk, E. A. A. Yaseen, Y. Yong, C. M. Young

Associates

D. C. Anderson, M. A. Armstrong, S. M. Avanesyan, L. M. B. Baart de la Faille, D. G. Baize, S. M. Barlow, A. N. Bart, G. E. Bartuska, N. B. Bea, K. J. Becker, J. K. Bennighof, J. W. Benson, N. Bilaniuk, S. C. Bledsoe, Jr., G. J. Bock, S. M. Bott, J. R. Brazell, J. F. Bridger, R. L. Brill, W. R. Brink, Jr., D. E. Brown, M. L. Brown, B. S. Brubaker, S. K. Bui, R. C. Burkhardt, L. A. Busse, S. Candelaria de Ram, M. R. Cannon, E. Cavanaugh, F. W. Cazier, Jr., M. P. Chamness, H. A. Chandler, C. Chang, F. Charron, F. R. Chen, S-E. Chen, Y. Cho, G. F. Chollet, M. A. Clarkson, G. E. Clunis, E. S. Cole, D. S. Cooper, J-M. Cortambert, E. J. Crouchley, A. T. Culver, I. S. Curthoys, C. M. W. Daft, E. M. Daley, J. A. Daniels, J. de Dios Exparza, X. M. de Gastines, D. T. Derbas, V. R. Desai, Y. Desaubies, M. B. Dev, M. DiPaolo, D. S. Dixon, L. A. Dorney, R. M. Dyas, J. M. Elliott, W. R. Evans, P. A. Ferlino, M. A. Fernandes, H. F. Fjerdingstad, J-F. Fluckinger, R. J. Gaillaard, A. Garcia, R. G. Gibson, D. Goldman, M. D. Good, F. J. Goodman, J. Gorchs, R. L. A. Gorling, G. Green, N. Grenie, M. Greska, C. Griffin, J. A. Gross, Y. Gu, M. Guirao, V. L. Hammen, S. Haran, R. W. Harris, D. R. Hatch, J. A. Henry, J-P. Hermand, R. E. Hillman, M. L. Hilton, A. Hofer, E. S. Holmes, K. D. Holton, S-Y. Hong, S. M. Howard, A. E. Hubbard, P. A. Hwang, K. C. Ireland, R. Jacks, B. M. Jagolinzer, S. K. Jain, P. E. James, R. B. Janisch, S. K. Lee, Z-Y. Jiang, M. S. Johansen, J. R. Johnstone, H. M. Jones, P. X. Joris, Y. Kadman, A. Kahraman, A. J. Kalinowski, K. V. Kamath, E. G. Keate, N. A. Kelly, R. C. Kemerait, R. H. Kemp, Jr., G. B. Kempster, Z. S. Kevanishvili, Issam Kheirallah, C. E. Klayman, K-L. Kong, L. J. J. Kopp, J. D. Krieger, F-M. Kuo, G. M. Kvistad, P. E. LaGasse, J-J. Laissus, R. W. Lally, J. H. LeClere, C. A. Ledoux, H. Y. Lee, S. Lee, S. Lee, T. Lee, K. A. Lenzo, K. D. LePage, T. D. Leroux, E. Lindemann, A. S. Lippa, B. Lisker, Y. Liu, M. F. Lopes, L. Louie, F-L. Lu, M. P. Lyons, C. C. Ma, J. C. Macie, K. K. M. Manabe, T. S. Margulies, J. B. Martinez, Jr., L. J. Marx, M. A. Mastroianni, N. P. McAngus, R. P. Meier, E. Mendez, T. J. Mermagen, J. A. Meyer, L. W. Middleditch, J. A. Miranda, M. A. Moehring, M. Mogilevsky, A. R. Mohanty, K. M. Mok, W. M. L. Morawitz, B. A. Morrongiello, D. C. Mountain, P. D. Mourad, J. W. Mullennix, H. Murakawa, A. Nadim, R. J. Nagem, R. Nici, J. C. Norris, S. Nowicki, B. L. O'Toole, J. F. Olsen, J. A. Ortiz Garcia, J. H. Park, B. J. Parker, S. I. Parks, M. T. Peet, J. J. Phelan, S. P. Pisciotta, R. Pitre, E. Pitts III, T. D. Plemons, M. A. Plummer, D. K. Polican, A. J. Policastro, D. J. Powell, R. Priebe, J. O. Ramsay, K. J. Randolph, P. W. Rappold, M. A. Reed, D. R. Regan, J. A. Resnick, S. A. Rhodes, A. M. Richardson, K. M. Rittenmeyer, R. Robledo, C. A. Rogers, J. Roginsky, R. C. Rose, W. J. Rose, T. H. Rousseau III, D. L. Rowley, E. Sabat Garibaldi, D. A. Sachs, S. Santiago, A. A. Sarkady, S. J. Saunders, A. Sauter, Jr., D. C. Savererbicr, P. R. Saxon, K. P. Scharnhorst, J. C. Schoppe, D. W. F. Schwarz, A. A. S. Sek, X. Serra, C. Sheris, K. A. Shipley, M. Simoni, L. Song, J. E. Spanier, M. W. Sprague, S. L. Staples, J. P. Stec, M. Stevenson, R. E. Sturz, J. A. Sullivan, S. Taherzadeh, T. Takanohashi, A. Tarraf, T. Tateno, A. J. Taylor, T. W. Taylor, S. A. Telenkov, L. F. M. Ten Bosch, R. Todd, S. K. Tomar, R. Torre, B. N. Tran, T. V. Tran, W. K. Trappe, L. Trevino, W. Tsoi, F. M. Tucker, J. S. Uhlman, S. A. Valderrabano, A. M. Vendetti, M. L. Vigilante, J. D. Vrieslander, J. M. Wagner, G. H. Wakefield, K. L. Warner, L. G. Weiss, J. A. Wilder, R. J. Williams, P. A. Wlodkowski, R. L. Woodcock, B. L. Wooley, K-T. Wu, D. D. X. Xiano, J. Yang, J. S. Yaruss, T. J. Yoder, A. Yonovitz, D. A. Zapala, R. L. Zimmerman

Students

V. Aharonson, H. A. Akil, S. K. Alam, G. A. Alderman, M. Arsenault, R. A. Avery, J. Ball, S. R. Bar-Sela, M. G. Brandle, J. L. Brandt, S. R. Brunet, M. P. Bryant, J. C. Bulen, V. G. Burner, A. J. Burnette, J. P. Carneal, M. B. Carroll, C. M. Charlton, M. Chellappa, M. Y. Chen, J. E. Cisneros, K. B. Cohen, D. G. Cole, B. J. Collins, S. M. Cordry, D. L. Cosnowski, R. A. Coury, S. P. Crane, E. L. Da Costa, K. A. Denchfield, D. Distasio, S. S. Dodd, K. B. Doherty, M. Ebel, A. E. Ellis, B. Engers, C-H. Fang, D. L.

Ferguson, B. H. Fitzgerald, E. J. Freeman, M. K. Gangala, L. Gavidia-Ceballos, L. J. Gelin, J. S. Gerber, S. D. Gogate, W. P. Goodwin, M. L. Grabb, R. Hagiwara, F. Hall, C. A. Harsin, H. He, K-A. Hegenwald, K. Heidenreich, M. A. Hennessy, S. R. Hensley, F. J. Herrmann, J. Herro, S. T. Ho, P-L. Hsiao, S. J. Hyun, E-E. Jan, T. K. Kapoor, A. Karali, D. E. Kayala, H-G. Kil, J-H. Kim, T. D. Kite, C. S. Kwiatkowski, Y-K. Kwon, T. Landgren, G. M. Lee, M. D. Lee, L. Levac, Y-F. Li, C. Lorenzi, T. M. J. Loucks, J. F. Madneil, E. S. Martin, C. Mattei, M. R. Mease, W. P. Meres, D. Y. Montoya, W-K. Moon, C. B. Moore, S. T. Myers, H. Nelisse, A. A. Nespor, L. Nguyen, M. N. Novaes, M. L. Oelze, G. W. Oliver, G. A. Owen, N. A. Ozluer, P. S. Palombi, J. A. Pavez Vidal, A. Pelletier, R. A. Peron, D. N. Peterson, H. Pham, M. Popovic, C. S. Post, M. J. Rametta, C. Rathinavelu, C. Remillat, J. Romero, H. H. Rump, T. J. Schwander, D. J. Sebald, M. L. Seltzer, T. M. Shaukat, J. W. Shen, R. K. Sherman, T. Shi, J-H. Shin, J. A. Shore, J. S. Sitter, M. A. Smith, A. B. Spalding, T. D. Sparks, K. J. Staub, W. F. Stewart, R. I. Sujith, J. B. Thoms, R. K. Thorburn, Y. Tian, E. L. Topps, J. D. Travis, S. A. Trent, Q. Wang, S. S. Wang, Z. Wang, T. J. Wardzala, J. M. Winograd, W. B. Wright, J. A. Yahner, L. J. York, J-D. Yu, G. Zhang, Q. Zhang, J. J. Zhou

Fellows	826
Members	2749
Associates	2602
Students	773
	6950

REVIEWS OF ACOUSTICAL PATENTS

Daniel W. Martin
7349 Clough Pike, Cincinnati, Ohio 45244

The purpose of these acoustical patent reviews is to provide enough information for a Journal reader to decide whether to seek more information from the patent itself. Any opinions expressed here are those of reviewers as individuals and are not legal opinions. Printed copies of United States Patents may be ordered at $3.00 each from the Commissioner of Patents and Trademarks, Washington, DC 20231.

Reviewers for this issue:

RONALD B. COLEMAN, *BBN Acoustic Technologies, 70 Fawcett Street, Cambridge, Massachusetts 02138*
SAMUEL F. LYBARGER, *101 Oakwood Road, McMurray, Pennsylvania 15317*
D. LLOYD RICE, *11222 Flatiron Drive, Lafayette, Colorado 80026*
KEVIN P. SHEPHERD, *MS463, NASA Langley Research Center, Hampton, Virginia 23681*
ROBERT C. WAAG, *University of Rochester Medical Center, 601 Elmwood Avenue, Rochester, New York 14642*

5,513,149

43.30.Ky SOUND DAMPING ARRANGEMENT

P. Salmi, J. Pockalén, and A. Järvi, assignors to Kvaerner Masa-Yards OY
30 April 1996 (Class 367/1); filed in Finland 22 November 1993

A system is described for attenuating and diffracting the sound generated by a ship's own propulsion system, via the creation of a zone of appropriately sized gas bubbles in the near neighborhood of the propulsors. In the preferred arrangement the ship's propellers are located forward on the

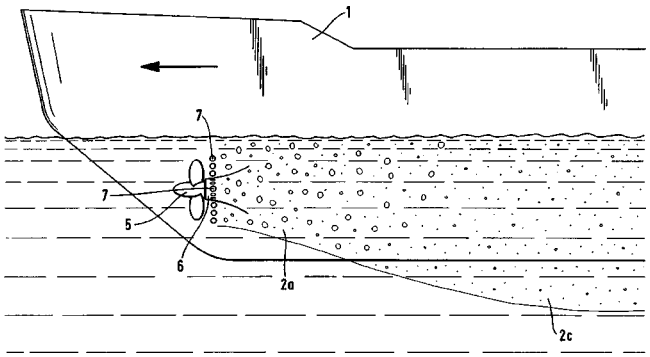

ship, as are the air (or other gas) blowing vents, so that a bubble zone is formed which substantially surrounds the whole hull of the ship. Gas injection rates to produce optimum sized bubbles are quoted—WT

5,515,342

43.30.Yj DUAL FREQUENCY SONAR TRANSDUCER ASSEMBLY

C. M. Stearns *et al.*, assignors to Martin Marietta Corporation
7 May 1996 (Class 367/155); filed 10 July 1989

The headmass of a large low-frequency tonpilz-type transducer is hollowed out so that a number of much smaller high-frequency tonpilz transducers can be mounted within that head. The radiating faces of the single large transducer, and all the small transducers, are coplanar. At the resonance frequency of the large unit, the small transducers simply move in phase with the rest of the large headmass. At the high resonance frequency of the small transducers, the large headmass functions as a rigid support plate.—WT

5,515,343

43.30.Yj ELECTRO ACOUSTIC TRANSDUCERS COMPRISING A FLEXIBLE AND SEALED TRANSMITTING SHELL

D. Boucher and C. Pohlenz, assignors to Etat Francais
7 May 1996 (Class 367/158); filed in France 28 April 1988

The motor section for a flextensional transducer of any class, but particularly Class IV, differs from the conventional stack of piezoceramic disks in that each such stack is terminated at both its ends by counter masses. These two masses are mechanically coupled to the surrounding shell, and the size of the masses is chosen so that the fundamental-length mode resonance frequency of the stack, including the end masses, is slightly higher than that of the fundamental bending mode of the shell. This should result in a broadening of the transmission pass-band of the assembly because of the coupling between these two, close, resonances.—WT

5,736,642

43.35.Zc NONLINEAR ULTRASONIC SCANNING TO DETECT MATERIAL DEFECTS

William T. Yost and John H. Cantrell, assignors to the United States of America
7 April 1998 (Class 73/602); filed 8 January 1997

High-frequency sound waves of different frequency are mixed in an interaction zone in material, generating waves of difference and sum frequencies as a result of a nonlinear property of the material. The nonlinear signal amplitude is an indicator of defects in the interaction zone of the material.—DWM

5,515,341

43.38.Fx PROXIMITY SENSOR UTILIZING POLYMER PIEZOELECTRIC FILM

M. Toda *et al.*, assignors to Whitaker Corporation
7 May 1996 (Class 367/140); filed 14 September 1993

The transducer for a proximity sensing system consists of a curved polyvinylidene fluoride film **16** with rectangular-shaped electroded regions **18** similarly located on both faces of the film. Electrical connection to the film is made via the wires **20**. The PVDF film is supported by backing member **22** with similar shape to the film so that the film bears against the

 0001-4966/98/104(5)/2550/11/$15.00

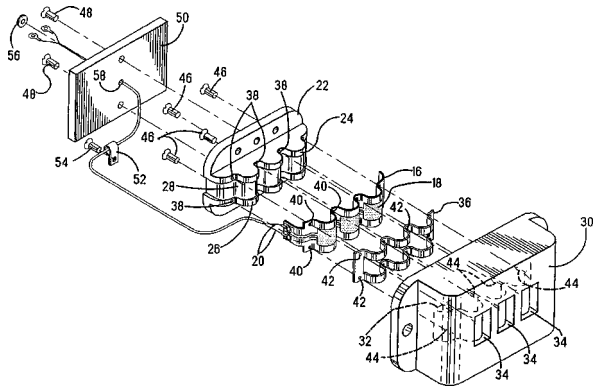

troughs of the backing member, but there is clearance between the crests of the two parts **22** and **16**. The radius of curvature of the arc-shaped regions influences the resonance frequency of the transducer. Gasket **36** and cover plate **30**, with apertures **34**, complete the assembly.—WT

5,519,670

43.38.Pf WATER HAMMER DRIVEN CAVITATION CHAMBER

B. H. Walter, assignor to Industrial Sound Technologies, Incorporated
21 May 1996 (Class 367/142); filed 3 October 1994

A cavitation chamber, useful for degassing liquids, mixing chemicals or slurries, or promoting sonochemical reactions, is energized by repeatedly interrupting the flow of a liquid through a conduit. The acoustic pulse created each time the flow valve is closed propagates directly into the cavitation chamber where it is reflected back and forth by acoustically reflective boundaries creating a large amplitude standing wave.—WT

5,706,251

43.38.Pf SCUBA DIVING VOICE AND COMMUNICATION SYSTEM USING BONE CONDUCTED SOUND

David F. May, assignor to Trigger Scuba, Incorporated
6 January 1998 (Class 367/132); filed 22 November 1996

The patent describes in detail a communication system used for scuba diving and discloses a mouthpiece design that produces bone conducted sound via the teeth. In the figure one form of the mouthpiece is shown. The mouthpiece is made of compliable plastic or rubber. It is provided with bite

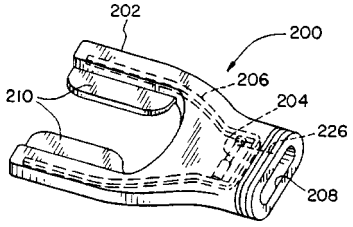

plates **210**, held firmly between the teeth. A magnetostrictive transducer **204** drives two sound conducting members **206** to deliver vibration to the bite plates. Breathing and speaking are through the opening **208**, basically the same as used in regular scuba equipment.—SFL

5,740,257

43.38.Si ACTIVE NOISE CONTROL EARPIECE BEING COMPATIBLE WITH MAGNETIC COUPLED HEARING AIDS

Larry Allen Marcus, assignor to Lucent Technologies, Incorporated
14 April 1998 (Class 381/71.6); filed 19 December 1996

The patent relates to the use of active noise control with handsets that must be compatible with hearing aids having a telephone coil pickup. A true representation of the original input signal is employed to drive a separate

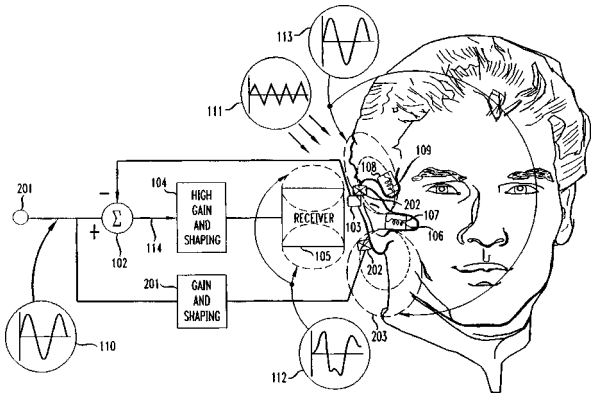

external field coil, positioned between the handset receiver and acoustic output ports located in close proximity to the user's ear cavity, and the magnetically coupled hearing aid.—SFL

5,734,246

43.40.Vn ACTIVE PIEZO-ELECTRIC VIBRATION ISOLATION AND DIRECTIONAL SYSTEMS

Eric T. Falangas, assignor to The Aerospace Corporation
31 March 1998 (Class 318/649); filed 16 May 1995

This patent describes an active control system to provide payload vibration isolation from spacecraft disturbances. Isolation is achieved using activated mounts, where each mount is comprised of a passive plate element **10** formed into the shape of an ''S,'' with piezo-electric actuators **20a–f** and accelerometers (nominally collocated with actuators) mounted to the passive

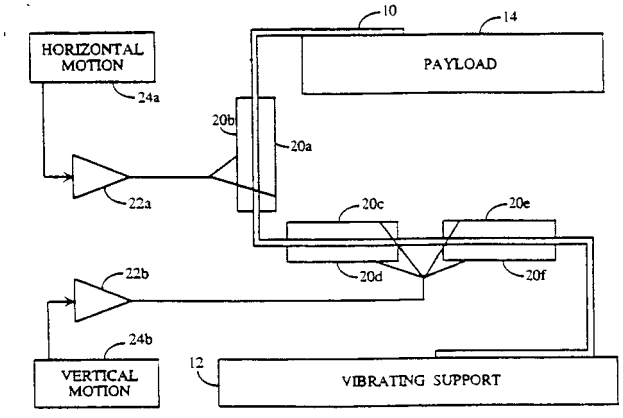

''S'' bracket. The control approach uses accelerometers to measure the low-order modal responses of the system. *H*-infinity control is used to minimize these responses at a few specific resonance frequencies. The approach is said to provide active isolation at low frequencies (i.e., 5–100 Hz), and passive isolation at higher frequencies.—RBC

5,730,510

43.50.Gf SNOWMOBILE DRIVE TRACK WITH NOISE REDUCING TREAD PATTERN

Denis Courtemanche, assignor to Camoplast, Incorporated
24 March 1998 (Class 305/168); filed 9 September 1996

A snowmobile drive track is described in which the frequency of the generated sound is reduced, thus providing increased comfort to the rider, and others. A snowmobile drive track usually consists of a wide belt with evenly spaced, transverse treads which provide traction. It is proposed that one out of every three successive treads have a different physical configuration, and that this pattern is then repeated for all successive threesomes.—KPS

5,734,211

43.50.Gf SPINDLE MOTOR WITH SOUNDPROOFING

Seung Wan Yu, assignor to Samsung Electro-Mechanics Company
31 March 1998 (Class 310/51); filed in Korea 30 November 1995

A spindle motor is described in which noise generated within the cavity formed by the rotor case **5** and the mounting plate **10** escapes through the

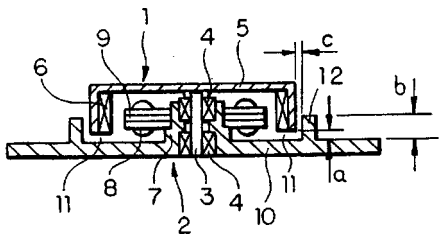

gap **11**. The perimeter wall **12** serves to reflect sound back into the motor. Several variations of the geometry of the wall are described.—KPS

5,735,229

43.50.Gf PERSONAL WATERCRAFT SEAT HAVING AIR INTAKE SILENCER

Ian G. House and Christopher K. Wachowski, assignors to Brunswick Corporation
7 April 1998 (Class 114/363); filed 21 December 1996

This patent relates to personal watercraft which use an internal combustion engine to drive a jet pump which propels the craft. An air intake silencer is described which is integral to the seat base of the watercraft. Numerous examples having combinations of expansion chambers, quarter wavelength resonators, and Helmholtz resonators are given.—KPS

5,736,691

43.50.Gf ACOUSTIC BARRIER FOR MOBILE MACHINERY

Stephen L. Batog and Robert T. Peterson, assignors to Case Corporation
7 April 1998 (Class 181/284); filed 3 July 1995

Machines such as backhoes and front-end loaders frequently have openings in the operator's compartment to allow for movement of control levers. Noise and dust will enter the operator's compartment through such openings. An acoustical barrier is described in which blocks of acoustical material are notched in such a way as to allow movement of the levers and inhibit the passage of dirt and sound. Several barrier configurations are described.—KPS

5,738,061

43.50.Gf ENGINE HAVING SOUND ABSORPTION STRUCTURES ON THE OUTER SIDES OF COMBUSTION CHAMBERS

Hideo Kawamura, assignor to Isuzu Ceramics Research Institute Company
14 April 1998 (Class 123/193.1); filed in Japan 6 July 1995

This patent relates to combustion chambers of internal combustion engines, with particular application to heat insulating engines which contain ceramic components. Arrangements are described in which heat insulating layers and vibration damping layers are combined and applied to the combustion cylinder walls, the cylinder head, the piston head, and the valve guides.—KPS

5,739,483

43.50.Gf AUTOMOBILE EXHAUST NOISE SUPPRESSOR

Haruki Yashiro *et al.*, assignors to Nissan Motor Company
14 April 1998 (Class 181/254); filed in Japan 9 May 1994

A two-mechanism muffler is described. The first mechanism reduces noise in the low engine-speed range and the second reduces noise in the high engine-speed range. A valve **16** is provided that connects the first mecha-

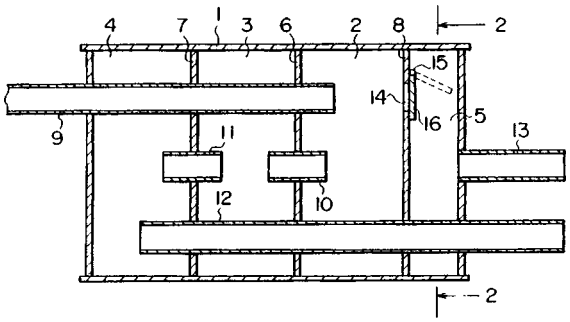

nism to the second, according to the engine exhaust pressure. At low speeds the valve is closed and mainly low-frequency sound is attenuated. At higher speeds the valve opens and higher-frequency sound is attenuated.—KPS

5,739,484

43.50.Gf EXHAUST MUFFLER

Mack L. Jones, Temecula, CA
14 April 1998 (Class 181/264); filed 12 March 1997

An exhaust muffler for an internal combustion engine is described in which a baffle assembly provides two main flowpaths resulting in seven different paths for exhaust gases to follow, and two Helmholtz chambers.

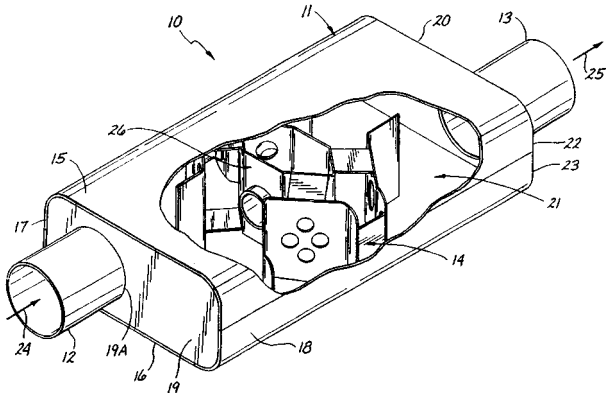

Unequal paths and multiple reflections provided by this assembly improve noise reduction with significantly less backpressure.—KPS

5,732,547

43.50.Ki JET ENGINE FAN NOISE REDUCTION SYSTEM UTILIZING ELECTRO PNEUMATIC TRANSDUCERS

Ronald F. Olsen and Jeffrey M. Orzechowski, assignors to the Boeing Company
31 March 1998 (Class 60/204); filed 24 May 1996

An active noise control system to suppress fan tone noise in jet engines is described. The system proposed is a feedforward approach using fan angular speed or blade passing frequency as the reference signal input. The residual metric to be minimized is the mean-square response of microphones located upstream and downstream of the engine fan and fan exit guide vane stage. The control output signals actuate (modulate) air control valves on each side of the fan stage to direct conditioned (pressure and temperature regulated) high-pressure primary air flow. The active system addresses fan tone noise. Passive treatments are used to reduce fan broadband noise.—RBC

5,734,727

43.50.Ki SUNROOF ASSEMBLY NOISE ATTENUATION SYSTEM

B. Michael Flaherty and William C. Brown, assignors to ASC, Incorporated
31 March 1998 (Class 381/86); filed 7 June 1995

A sunroof noise attenuation system is described to reduce wind-buffeting noise in automobile interiors. The approach uses microphones mounted to the leading and trailing edges of the sunroof opening. Differences in the sound levels at these microphone locations are used to move the location of the sunroof pane for the purpose of reducing wind-buffeting noise. As an alternative to controlling pane position in response to microphone responses, the patent discusses use of vehicle speed to gain-schedule the pane position.—RBC

5,740,984

43.50.Lj LOW SONIC BOOM SHOCK CONTROL/ ALLEVIATION SURFACE

John M. Morgenstern, assignor to McDonnell Douglas Corporation
21 April 1998 (Class 244/1 N); filed 22 September 1994

A sonic boom mitigation device is described which consists of an aerodynamic control surface placed near the nose of a supersonic aircraft. In contrast to the classical *N*-wave sonic boom, the presence of this additional control surface results in a less abrupt nose shock and reduced pressure amplitude. The surface may be retracted when sonic boom control is not required.—KPS

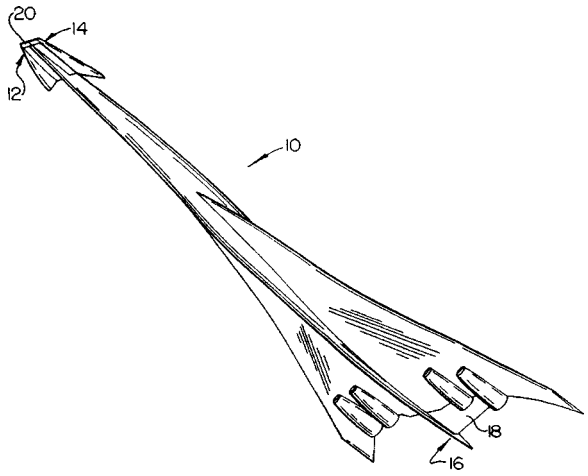

5,728,980

43.55.Dt DUCT SILENCER

Bernard Zarnick, Cleveland, OH
17 March 1998 (Class 181/224); filed 19 February 1997

The patent describes a duct silencer for heating and air conditioning systems. Acoustical panels **12** are mounted parallel to one another and arranged longitudinally in the duct. Each panel consists of a high density, rigid

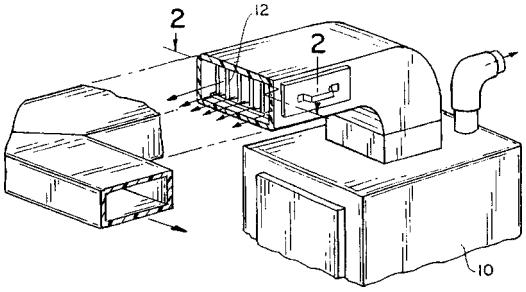

fiberglass core tightly encapsulated in a covering of polyvinylfluoride, 1–5 mils thick.—KPS

5,737,797

43.55.Dt CENTRAL VACUUM WITH ACOUSTICAL DAMPING

Stephen P. Rittmueller *et al.*, assignors to Iowa State University Research Foundation, and White Consolidated Industries
14 April 1998 (Class 15/326); filed 28 November 1995

The patent relates to built-in vacuum systems, consisting of a central vacuum unit and a system of ducts which extend to various rooms of a house. Noise generated in the vicinity of the central vacuum unit is reduced through the application of acoustically absorbent materials to a canister which contains the motor, and to the inlet and exhaust ducts. The ducts are designed to form serpentine pathways which are acoustically treated to reduce emitted noise.—KPS

5,738,098

43.58.Ls MULTI-FOCUS ULTRASOUND LENS

George A. Brock-Fisher and Gregory G. Vogel, assignors to Hewlett-Packard Company
14 April 1998 (Class 128/662.03); filed 21 July 1995

The focal length of an ultrasonic transducer is made variable by the shape of a lens mounted on the transducer. For a linear or curved linear transducer, the curvature of the lens is larger at one end of the array than the other end so that as the area of interest becomes deeper the transducer can be slid or rolled to obtain a focus in elevation at a variable depth. For a phased array, the lens radius of curvature is larger as the distance from the center of the array to the ends of the array increases to provide a focus in elevation at a shallower depth at nearer ranges from the transducer.—RCW

5,710,819

43.66.Ts REMOTELY CONTROLLED, ESPECIALLY REMOTELY PROGRAMMABLE HEARING AID SYSTEM

Jan Topholm and Soren Erik Westermann, assignors to Topholm & Westermann APS
20 January 1998 (Class 381/68.2); filed in Germany 15 March 1993

A remotely controllable hearing aid with an external control device having a keyboard is shown. In the control device there is a signal generator and a data processing section. The control device can be used with the hearing aid to determine the audiometric values for the wearer with more nearly real conditions than obtained with a usual audiometer. The hearing aid may be set to have amplification appropriate for the audiometric measurements. Connection between the control device and the hearing aid may be made by a cable or by a radio frequency channel.—SFL

5,712,917

43.66.Ts SYSTEM AND METHOD FOR CREATING AUDITORY SENSATIONS

George Offutt, Green Lane, PA
27 January 1998 (Class 381/68.6); filed 22 November 1994

The patent describes a hearing aid in which the usual magnetic receiver is replaced by skin contacting electrodes. One electrode **18** is ring-shaped and contacts the skin of the ear canal about halfway toward the eardrum. The other electrode **30** is placed on the skin somewhere on the

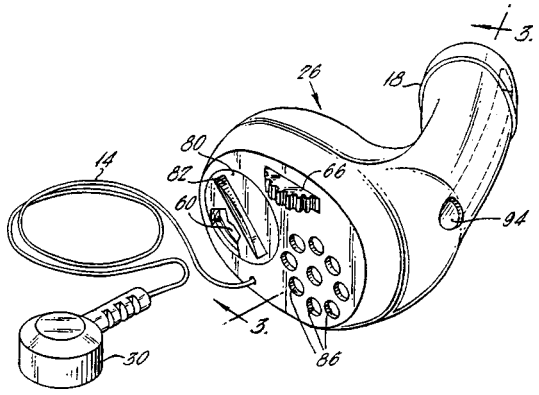

body, for example, below the opposite ear. A microphone in the ear canal unit picks up sound and converts it to an electrical signal that is amplified in the hearing aid and delivered to the electrodes. No data are given as to the gain available from the system.—SFL

5,712,918

43.66.Ts PRESS-FIT EAR WAX BARRIER

Robert S. Yoest, assignor to Beltone Electronics Corporation
27 January 1998 (Class 381/68.6); filed 27 January 1995

A press-fit wax barrier is shown for in-the-ear or in-the-canal type hearing aids that fits into a plastic tubing socket in the aid. The barrier can be readily replaced if wax accumulation is diminishing the hearing aid output. In one construction a mesh element at the outer end of the barrier

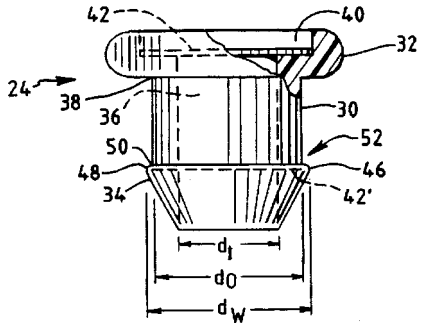

impedes the entrance of ear wax. In another construction, a plurality of undulations extend inwardly in the barrier to occlude wax movement through the acoustical passageway.—SFL

5,712,919

43.66.Ts HEARING AID APPARATUS POWERED BY CAPACITOR

Dale M. Ruhling, assignor to Multi-Line Designs, Incorporated
27 January 1998 (Class 381/69.2); filed 7 June 1995

The patent shows a hearing aid with a built-in power supply consisting of one or more capacitors. Means are provided for recharging the capacitors from an outside recharging unit. According to the patent, recharging can be done very rapidly. It is not mentioned that the voltage delivered to the aid from the capacitors will drop continuously, and that the useful life of a charge will depend on the lowest useful supply voltage suitable for the hearing aid.—SFL

5,715,365

43.72.Ar ESTIMATION OF EXCITATION PARAMETERS

Daniel Wayne Griffin and Jae S. Lim, assignors to Digital Voice Systems, Incorporated
3 February 1998 (Class 395/2.23); filed 4 April 1994

The patent discloses an improved method of estimating voicing and pitch parameters of a speech signal. The input speech is filtered into one or more bands, and a nonlinear operation applied to the band output emphasizes the fundamental frequency component of the band. Nonlinear operations such as absolute value (AV), AV to some power, or log of AV have the desired effect and tend to reduce the broadening of spectral peaks due to frequency changes within the analysis window.—DLR

5,732,188

43.72.Ar METHOD FOR THE MODIFICATION OF LPC COEFFICIENTS OF ACOUSTIC SIGNALS

Takehiro Moriya *et al.*, assignors to Nippon Telegraph and Telephone Corporation
24 March 1998 (Class 395/2.28); filed in Japan 10 March 1995

The patent covers a method of altering linear prediction coefficient values in a way that improves the perceptual characteristics of the encoded speech. The LP coefficients are transformed to the cepstral domain and then

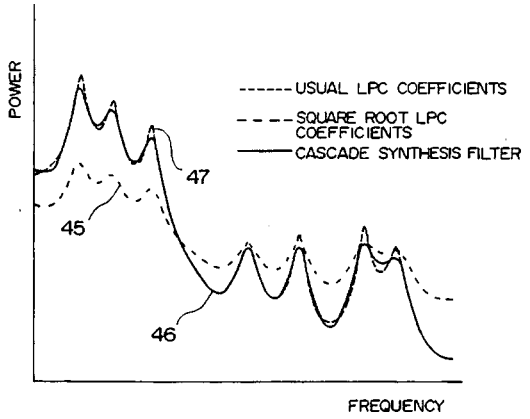

modified according to a perceptual masking function. The result is again transformed back to the LP coefficient domain.—DLR

5,721,807

43.72.Bs METHOD AND NEURAL NETWORK FOR SPEECH RECOGNITION USING A CORRELOGRAM AS INPUT

Wolfgang Tschirk, assignor to Siemens Aktiengesellschaft Oesterreich
24 February 1998 (Class 395/2.64); filed in Austria 25 July 1991

In this isolated-word recognition system, a power spectral density matrix representing the input phrase is first computed. From this matrix a correlogram is generated consisting of the sums of products of the matrix elements. The result is a time-independent feature array which is fed to a neural network analyzer for the word classification.—DLR

5,708,754

43.72.Dv METHOD FOR REAL-TIME REDUCTION OF VOICE TELECOMMUNICATIONS NOISE NOT MEASURABLE AT ITS SOURCE

Woodson Dale Wynn, assignor to AT&T
13 January 1998 (Class 395/2.28); filed 30 November 1993

This is the first patent seen by this reviewer which uses a linear prediction (LPC) model of the ongoing speech signal as a basis for real-time noise reduction. The system uses an LPC-based voice activity detector and updates a noise spectral model during nonspeech. During voicing, the model order is controlled and pole positions are averaged across adjacent frames to minimize the typical LPC analysis problems.—DLR

5,729,657

43.72.Ew TIME COMPRESSION/EXPANSION OF PHONEMES BASED ON THE INFORMATION CARRYING ELEMENTS OF THE PHONEMES

Tomas Svensson, assignor to Telia AB
17 March 1998 (Class 395/2.76); filed in Sweden 25 November 1993

This speech rate changer analyzes the subphonemic structure of the speech signal and adjusts the duration of various parts of each phonemic element according to their information content. The implementation includes what is basically a library of stored rankings of the acoustic elements within each phoneme according to their impact on intelligibility under timescale modification. The highest ranking elements are the most resistant to duration adjustment.—DLR

5,719,993

43.72.Gy LONG-TERM PREDICTOR

Willem Bastiaan Kleijn, assignor to Lucent Technologies, Incorporated
17 February 1998 (Class 395/2.29); filed 28 June 1993

This CELP vocoder includes a long-term (pitch) predictor with improved tracking characteristics, resulting in reduced buzziness and perceptible noise in the speech output. The pitch predictor uses known interpolation methods to allow noninteger pitch periods. A fixed delay greater than an

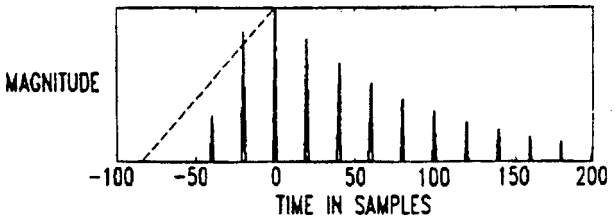

expected period of the codebook excitation allows ''preprocessing'' by a two-tap FIR filter which smooths abrupt transitions from voiceless condition to pitch tracking.—DLR

5,724,480

43.72.Gy SPEECH CODING APPARATUS, SPEECH DECODING APPARATUS, SPEECH CODING AND DECODING METHOD, AND A PHASE AMPLITUDE CHARACTERISTIC EXTRACTING APPARATUS FOR CARRYING OUT THE METHOD

Tadashi Yamaura, assignor to Mitsubishi Denki Kabushiki Kaisha
3 March 1998 (Class 395/2.28); filed in Japan 28 October 1994

The patent describes a variety of linear prediction vocoders, all having in common the use of the extraction of short-term phase information from the LP residual signal. The patent shows various arrangements of the phase

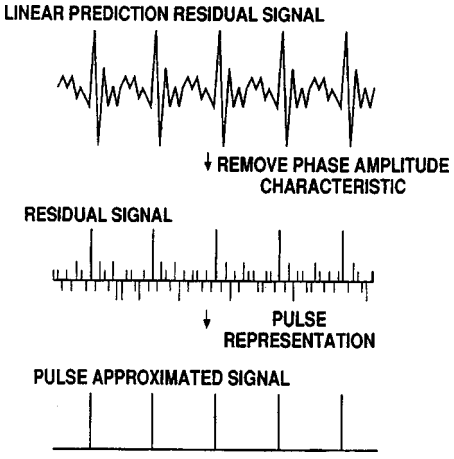

extractor and random, pulse, and/or adaptive vector quantizers, which generate the coded signals for transmission.—DLR

5,727,122

43.72.Gy CODE EXCITATION LINEAR PREDICTIVE (CELP) ENCODER AND DECODER AND CODE EXCITATION LINEAR PREDICTIVE CODING METHOD

Kenichiro Hosoda *et al.*, assignors to Oki Electric Industry Company
10 March 1998 (Class 395/2.32); filed 10 June 1993

This CELP vocoder uses multiple excitation codebooks containing pulselike and stochastic excitations. High quality speech is obtained by summing the two excitation vectors, each with its own gain value. The pulselike codebook is adapted after each search. In a second system the pulselike excitation waveform is shifted by the pitch lag distance, thus removing periodicity effects from that codebook.—DLR

5,727,125

43.72.Gy METHOD AND APPARATUS FOR SYNTHESIS OF SPEECH EXCITATION WAVEFORMS

Chad Scott Bergstrom *et al.*, assignors to Motorola, Incorporated
10 March 1998 (Class 395/12.73); filed 5 December 1994

It has long been recognized that the primary quality limitation of linear prediction vocoders is due to inaccuracies in the representation of the excitation waveform. Many methods have been used to encode a high-quality excitation waveform with a small number of bits. This patent discloses a

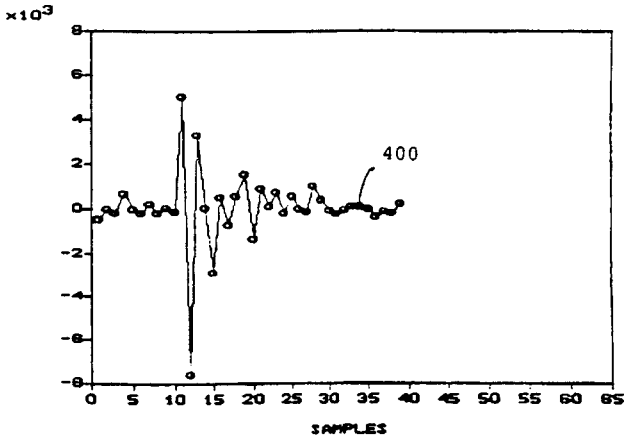

new technique for describing the excitation with a small set of parameter values. The methods used include correlations to improve pitch alignment, improved interpolation, and a waveletlike extraction of common basis functions from the original excitation signal.—DLR

5,729,655

43.72.Gy METHOD AND APPARATUS FOR SPEECH COMPRESSION USING MULTI-MODE CODE EXCITED LINEAR PREDICTIVE CODING

Victor D. Kolesnik *et al.*, assignors to Alaris, Incorporated and G. T. Technology, Incorporated
17 March 1998 (Class 395/2.32); filed 31 May 1994

This patent discloses several strategies for improving the quality and/or reducing the bitrate of a code excited LP (CELP) vocoder. Of several methods described, the most detailed is a system which sequentially applies

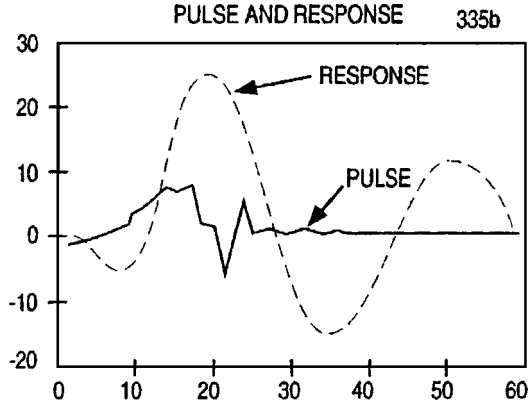

adaptive, ''pulse'' and stochastic codebook searches, using the best-matching excitation of the three searches.—DLR

5,729,658

43.72.Gv EVALUATING INTELLIGIBILITY OF SPEECH REPRODUCTION AND TRANSMISSION ACROSS MULTIPLE LISTENING CONDITIONS

ZeZhang Hou and Aaron R. Thornton, assignors to Massachusetts Eye and Ear Infirmary
17 March 1998 (Class 395/2.79); filed 17 June 1994

The patent describes a procedure for summarizing the performance of a speech processing system under various conditions which would affect the transmission or reproduction of speech. The result is described as an articulation index. The idea is then taken a step further; a loop is set up in which a system is specified, simulated by computer, evaluated to determine its articulation index value, and then refined by a small increment and retested.—DLR

5,732,390

43.72.Gy SPEECH SIGNAL TRANSMITTING AND RECEIVING APPARATUS WITH NOISE SENSITIVE VOLUME CONTROL

Keiichi Katayanagi *et al.*, Sony Corporation
24 March 1998 (Class 704/227); filed in Japan 29 June 1993

This vocoding system contains mechanisms to monitor the background noise level at both transmitting and receiving sites, as well as the transmitted speech signal level. Playback volume at the receiving end is then adjusted to a comfortable loudness level based on these signal and noise level measurements. This reduces the need for the listener to adjust volume levels manually to match changes in the speaker's environment.—DLR

5,734,789

43.72.Gy VOICED, UNVOICED, OR NOISE MODES IN A CELP VOCODER

Kumar Swaminathan *et al.*, assignors to Hughes Electronics
31 March 1998 (Class 395/2.15); filed 1 June 1992

This CELP vocoder uses different coding techniques depending on whether the current frame is classified as voiced and stationary, unvoiced and transient, or background noise. Past and look-ahead frames may alter the initial classification. The final classification affects the subset of line spectral frequency parameters chosen for transmission and various other encoding details.—DLR

5,727,120

43.72.Ja APPARATUS FOR ELECTRONICALLY GENERATING A SPOKEN MESSAGE

Bert Van Coile *et al.*, assignors to Lernout & Hauspie Speech Products N. V.
10 March 1998 (Class 395/2.15); filed 26 January 1995

The usual dilemma for speech synthesis is to produce arbitrary spoken phrases while retaining the quality of a recorded-speech playback system. True text-to-speech of comparable quality is not yet possible. This compromise system extracts certain prosodic information from phrases spoken by arbitrary speakers and applies the extracted patterns to the entire synthesized phrase, so as to minimize changes in the speaker characteristics. It is thus possible to generate arbitrary phrases with near recorded quality.—DLR

5,732,395

43.72.Ja METHODS FOR CONTROLLING THE GENERATION OF SPEECH FROM TEXT REPRESENTING NAMES AND ADDRESSES

Kim Ernest Alexander Silverman, assignor to NYNEX Science & Technology
24 March 1998 (Class 704/260); filed 19 March 1993

This specialized text-to-speech synthesizer operates on text strings representing name and address information such as would comprise a telephone directory entry. Making use of the known structure of the text, the set of rules disclosed in this patent produces a sequence of prosodic markings which allow the synthesis of high-quality output speech.—DLR

5,727,121

43.72.Kb SOUND PROCESSING APPARATUS CAPABLE OF CORRECT AND EFFICIENT EXTRACTION OF SIGNIFICANT SECTION DATA

Takeshi Chiba and Koh Kamizawa, assignors to Fuji Xerox Company
10 March 1998 (Class 395/2.23); filed in Japan 10 February 1994

This voice activity detector divides the speech signal into segments and assigns an initial speech presence estimate to each segment. The initial assignments are then refined by evaluating the segment sequence and durations. The primary detection parameter will typically be a speech power measurement, although several alternative measures are suggested. The patent is primarily concerned with the segment reassignment logic.—DLR

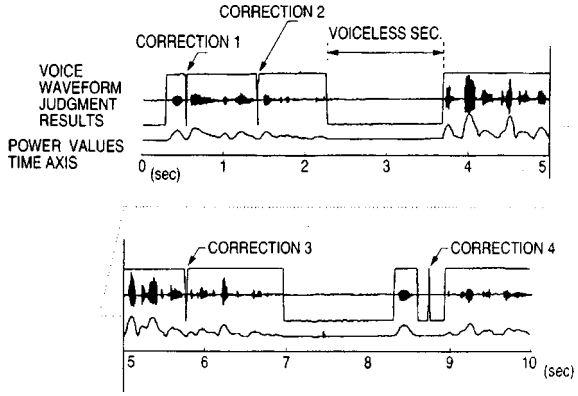

5,732,392

43.72.Kb METHOD FOR SPEECH DETECTION IN A HIGH-NOISE ENVIRONMENT

Osamu Mizuno *et al.*, assignors to Nippon Telegraph and Telephone Corporation
24 March 1998 (Class 704/233); filed in Japan 25 September 1995

This speech presence detector measures the degree and rate of change of the signal spectrum as a means of detecting a speech signal. The rate measure is achieved by counting the number of times a peak of the spectral variation exceeds a threshold.—DLR

5,719,997

43.72.Ne LARGE VOCABULARY CONNECTED SPEECH RECOGNITION SYSTEM AND METHOD OF LANGUAGE REPRESENTATION USING EVOLUTIONAL GRAMMAR TO REPRESENT CONTEXT FREE GRAMMARS

Michael Kenneth Brown and Stephen Charles Glinski, assignors to Lucent Technologies, Incorporated
17 February 1998 (Class 395/2.66); filed 21 January 1994

Many large vocabulary speech recognition systems store the Markov model information in some sort of table structure. The system described here differs in storing that information integrally with the grammar structure. For use with that architecture, this patent presents a symbolic HMM format which allows the HMMs to be constructed as required, saving substantial memory space.—DLR

5,724,481

43.72.Ne METHOD FOR AUTOMATIC SPEECH RECOGNITION OF ARBITRARY SPOKEN WORDS

Roger Borgan Garberg and Michael Allen Yudkovski, assignors to Lucent Technologies, Incorporated
3 March 1998 (Class 395/2.52); filed 30 March 1995

This patent describes an automated telephone operator speech recognition system intended to capture the caller's name for credit card purchases, etc. Since this task is beyond the capability of current recognition technology, the system would have the caller supply a phone number by speech, TouchTone, or callerID, together with a spoken name. The system looks up the number to get the caller's name, then uses a text-to-speech system to generate a speaker-independent template, which is used to verify the spoken name.—DLR

5,727,124

43.72.Ne METHOD AND APPARATUS FOR SIGNAL RECOGNITION THAT COMPENSATES FOR MISMATCHING

Chin-Hui Lee and Ananth Sankar, assignors to Lucent Technologies, Incorporated
10 March 1998 (Class 395/2.42); filed 21 June 1994

Speech recognition systems usually perform poorly under mismatched conditions, such as different microphones being used for training and recognition. One solution is pooled training, in which composite training includes examples of all conditions. This tends to result is less-than-ideal performance for all conditions. This method applies transformations to training and/or unknown signals, making them more similar, thus improving recognition under all conditions.—DLR

5,729,656

43.72.Ne REDUCTION OF SEARCH SPACE IN SPEECH RECOGNITION USING PHONE BOUNDARIES AND PHONE RANKING

David Nahamoo and Mukund Padmanabhan, assignors to International Business Machines Corporation
17 March 1998 (Class 395/2.63); filed 30 November 1994

This speech recognizer isolates segments of speech having similar acoustic characteristics by classifying each centisecond frame, then processing the label string to find the phone boundaries. For each possible boundary position, the enclosed classes are scored and ranked to determine the best boundary position.—DLR

5,729,659

43.72.Ne METHOD AND APPARATUS FOR CONTROLLING A DIGITAL COMPUTER USING ORAL INPUT

Jerry L. Potter, Canton, OH
17 March 1998 (Class 395/2.79); filed 6 June 1995

The patent describes a set of strategies and vocabulary structures to be used in applying a recognizer to the task of operating a computer application, such as a spread-sheet software system. The stated goal is to allow the use of more ''natural language'' constructs than the typical voice-controlled system would.—DLR

5,732,187

43.72.Ne SPEAKER-DEPENDENT SPEECH RECOGNITION USING SPEAKER INDEPENDENT MODELS

Jeffrey L. Scruggs *et al.*, assignors to Texas Instruments, Incorporated
24 March 1998 (Class 395/2.6); filed 27 September 1993

This telephone-based speech recognizer system uses speaker-independent subword models and refers to these using user-specific labels. With this arrangement, only one copy of each word reference pattern is required and yet, the system performance approaches that possible with speaker-dependent stored word models.—DLR

5,732,394

43.72.Ne METHOD AND APPARATUS FOR WORD SPEECH RECOGNITION BY PATTERN MATCHING

Yoshio Nakadai *et al.*, assignors to Nippon Telegraph and Telephone Corporation
24 March 1998 (Class 704/255); filed in Japan 19 June 1995

This isolated word recognizer compares the durations of unknown and matching patterns. If the difference exceeds a threshold, partial matches are

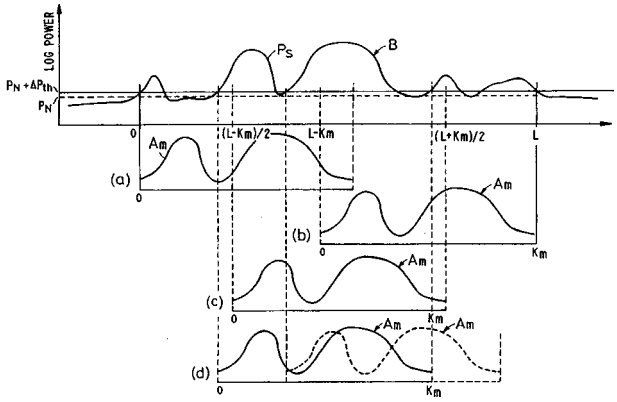

performed by comparing the reference pattern against various short segments of the unknown pattern.—DLR

5,741,992

43.75.Rs MUSICAL APPARATUS CREATING CHORUS SOUND TO ACCOMPANY LIVE VOCAL SOUND

Yuichi Nagata, assignor to Yamaha Corporation
21 April 1998 (Class 84/631); filed in Japan 4 September 1996

A sound wave from a singer is converted into digital form in converter **1**, then after echo **2** is added is reconverted to analog for reproduction from loudspeaker **SPL**. In parallel the digital audio signal passes through filter **6** to one or more frequency converters **PT1–PT4**, with the amount of frequency conversion controlled by central processing unit **7**. The multiple

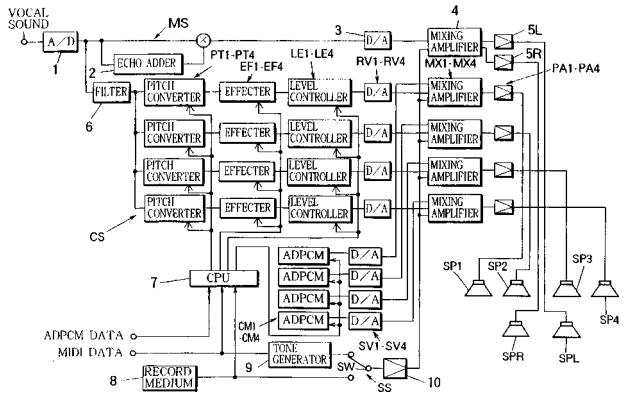

signals of converted frequency, after additional level and effect control and reconversion to analog, are separately radiated from other loudspeakers **SP1–SP4** so that the artificial choral voices are heard from different sound sources.—DWM

5,739,457

43.75.St METHOD AND APPARATUS FOR SIMULATING A JAM SESSION AND INSTRUCTING A USER IN HOW TO PLAY THE DRUMS

John R. Devecka, Clifton, NJ
14 April 1998 (Class 84/743); filed 26 September 1996

After defining ''jamming'' as ''intuitively and naturally playing and reacting to create music as the music proceeds,'' this patent describes a system for helping either a novice or an expert player to simulate a jam session. Room **100**, which may be situated in a coin-operated environment such as an arcade, surrounds the player on seat **40** with loudspeakers **61**, **62**,

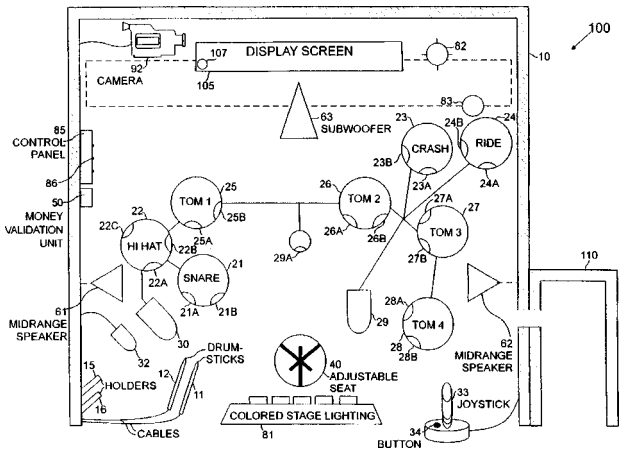

and **63** and electronic drum pads **21–29**, each pad designed to produce electronically the sound of a specific percussion instrument. Drumsticks **11** and **12** may be used in place of manual actuation of the pads to produce the percussion sounds that the player wishes to add in synchronism with prerecorded music reproduced over the loudspeakers.—DWM

5,711,308

43.80.Qf WEARABLE APPARATUS FOR MEASURING DISPLACEMENT OF AN *IN VIVO* TYMPANUM AND METHODS AND SYSTEMS FOR USE THEREWITH

Andrew J. Singer, assignor to Interval Research Corporation
27 January 1998 (Class 128/746); filed 7 June 1995

The primary object is to measure an acoustic pressure wave as sensed by the tympanic membrane. A mirror is attached to the membrane to reflect

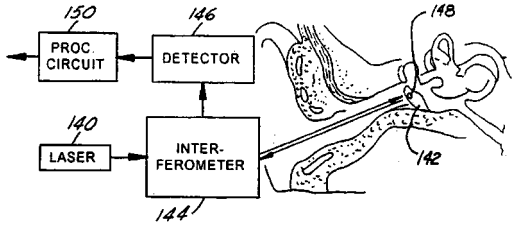

its motion due to sound in the ear canal by means of a laser beam interferometer. Several types of information can be derived from tests described.—SFL

5,737,429

43.80.Qf PORTABLE VIEWABLE AND AUDIBLE STETHOSCOPE

Byung Hoon Lee, Seoul, Korea
7 April 1998 (Class 381/67); filed in Republic of Korea 28 March 1995

The stethoscope shown has two alternate sizes of chestpiece. The sounds picked up are converted to electrical signals by a microphone coupled to both chest pieces. The electrical output signals are transmitted to

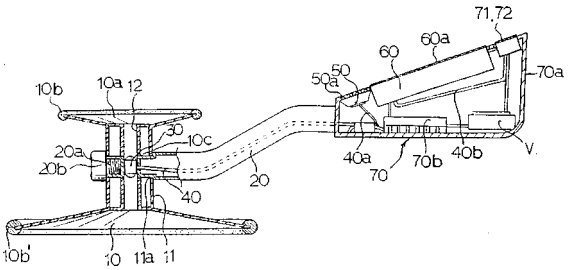

an oscilloscope screen and to a loudspeaker for evaluation by one or more observers.—SFL

5,752,515

43.80.Sh METHODS AND APPARATUS FOR IMAGE-GUIDED ULTRASOUND DELIVERY OF COMPOUNDS THROUGH THE BLOOD-BRAIN BARRIER

Ferenc A. Jolesz and Kullervo Hynynen, assignors to Brigham & Women's Hospital
19 May 1998 (Class 128/653.1); filed 21 August 1996

Ultrasound is used to make an imageable change in tissues or fluids at a selected location in the brain. A vicinity of the selected location is imaged, for example, by magnetic resonance imaging, to confirm the location. A neuropharmaceutical compound in the subject's blood stream is delivered to the confirmed location by applying ultrasound to open the blood-brain barrier at that location and induce uptake of the compound there.—RCW

5,752,924

43.80.Sh ULTRASONIC BONE-THERAPY APPARATUS AND METHOD

Jonathan J. Kaufman and Alessandro E. Chiabrera, assignors to OrthoLogic Corporation
19 May 1998 (Class 601/2); originally filed 25 October 1994

An ultrasonic pulse signal produced by a transducer is applied near the bone that is to be treated. Exposure time is in the range from 5 min to 1 h 1–3 times a day for a period of days. The apparatus includes a special waveform generator and a computer to implement the operations that comprise a treatment.—RCW

5,762,066

43.80.Sh MULTIFACETED ULTRASOUND TRANSDUCER PROBE SYSTEM AND METHODS FOR ITS USE

Wing K. Law *et al.*, assignors to THS International, Incorporated
9 June 1998 (Class 128/660.03); originally filed 21 February 1992

This probe system emits a high-intensity ultrasonic beam for the treatment of localized disease. The probe contains two radiating surfaces, each with a different focus. Selectively energizing the surfaces permits focussing the ultrasonic energy at different distances from the housing.—RCW

5,762,616

43.80.Sh APPARATUS FOR ULTRASONIC TREATMENT OF SITES CORRESPONDING TO THE TORSO

Roger J. Talish, assignor to Exogen, Incorporated
9 June 1998 (Class 601/2); filed 15 March 1996

This apparatus for ultrasonic treatment to aid healing of fractures is comprised of a transducer module and a portable main module. The trans-

ducer module is positioned adjacent to the area of an injury and excited for a predetermined period of time. A means for holding the transducer module on the portion of the body to be treated is included.—RCW

5,732,705

43.80.Vj ULTRASOUND DIAGNOSTIC APPARATUS

Yukinobu Yokoyama and Ryoichi Kanda, assignors to Kabushiki Kaisha Toshiba
31 March 1998 (Class 128/660.07); filed in Japan 12 September 1995

This apparatus processes Doppler signals to obtain levels of color. The maximum of the color level is increased from a first value to a second value to obtain a contrast-enhancement effect by using both brightness and hue gradations.—RCW

5,740,805

43.80.Vj ULTRASOUND BEAM SOFTENING COMPENSATION SYSTEM

Enrico Dolazza and William Wong, assignors to Analogic Corporation
21 April 1998 (Class 128/660.06); filed 19 November 1996

This system contains a controller that decreases the sampling rate of ultrasonic echoes as a function of distance to compensate for the decrease in center frequency of the echo spectrum.—RCW

5,740,806

43.80.Vj DYNAMIC RECEIVE APERTURE TRANSDUCER FOR 1.5D IMAGING

Gregg Miller, assignor to Siemens Medical Systems, Incorporated
21 April 1998 (Class 128/661.01); filed 29 March 1996

This enables 1.5D image information to be obtained from a single firing of a linear transducer array. The transducer is operated to obtain pulses from one row of elements in response to excitation signals and to obtain corresponding echo signals at elements of additional rows. High-voltage and low-voltage multiplexers are used to switch connections to rows of elements. A composite signal to form an image is obtained by summing signals from the array.—RCW

5,743,266

43.80.Vj METHOD FOR PROCESSING REAL-TIME CONTRAST ENHANCED ULTRASONIC IMAGES

Harold Levene and Bob Webster, assignors to Molecular Biosystems, Incorporated
28 April 1998 (Class 128/662.02); filed 25 April 1995

This method produces a colored, contrast-enhanced image in real time from a sequence of gray-scale b-scan images in a video format. The color scheme is varied according to time of arrival, duration of brightening, and absolute brightness.—RCW

5,746,756

43.80.Vj INTERNAL ULTRASONIC TIP AMPLIFIER

George Bromfield and Jeffrey J. Vaitekunas, assignors to Ethicon Endo-Surgery, Incorporated
5 May 1998 (Class 606/169); filed 3 June 1996

This amplifier includes a delivery horn that has a solid proximal portion and a hollow distal portion. The distal portion has a smaller cross-sectional area than the proximal portion. The ultrasonic intensity at the distal portion is increased over that in the proximal portion because of the lower cross-sectional area in the distal portion.—RCW

5,762,067

43.80.Vj ULTRASONIC ENDOSCOPIC PROBE

Paul T. Dunham *et al.*, assignors to Advanced Technology Laboratories, Incorporated
9 June 1998 (Class 128/662.06); filed 30 May 1996

This probe has an articulating tip in which the ultrasonic transducer is located. The articulating section of the probe can be locked in position with a user-variable force. Control of the articulating section is via cable for which tension adjustments are provided. The ultrasonic transducer can be rotated to change the acoustic scan plane during use.—RCW

Acoustic field interaction with a boiling system under terrestrial gravity and microgravity[a)]

J. S. Sitter, T. J. Snyder, and J. N. Chung
School of Mechanical and Materials Engineering, Washington State University, Pullman, Washington 99164-2920

P. L. Marston
Department of Physics, Washington State University, Pullman, Washington 99164-2814

(Received 10 June 1997; revised 1 June 1998; accepted 13 July 1998)

Pool boiling experiments from a platinum wire heater in FC-72 liquid were conducted under terrestrial and microgravity conditions, both with and without the presence of a high-intensity acoustic standing wave within the fluid. The purpose of this research was to study the interaction between an acoustic field and a pool boiling system in normal gravity and microgravity. The absence of buoyancy in microgravity complicates the process of boiling. The acoustic force on a vapor bubble generated from a heated wire in a standing wave was shown to be able to play the role of buoyancy in microgravity. The microgravity environment was achieved with 0.6 and 2.1-s drop towers. The sound was transmitted through the fluid medium by means of a half wavelength sonic transducer driven at 10.18 kHz. At high enough acoustic pressure amplitudes cavitation and streaming began playing an important role in vapor bubble dynamics and heat transfer. Several different fixed heat fluxes were chosen for the microgravity experiment and the effects of acoustics on the surface temperature of the heater were recorded and the vapor bubble movement was filmed. Video images of the pool boiling processes and heat transfer data are presented. [S0001-4966(98)04810-3]

PACS numbers: 43.10.Ln, 43.25.Gf [MAB]

INTRODUCTION

Pool boiling in an acoustic field is very complex due to a myriad of mechanisms occurring simultaneously. To date no research has been found in the open literature on the effects of an acoustic standing wave on pool boiling heat transfer in microgravity. This study examines and elucidates about the effects of using a high-amplitude sound field during pool boiling from a platinum wire heater in FC-72 under terrestrial and microgravity conditions. This is accomplished by measuring the change in the average surface temperature of the heater going from terrestrial condition to microgravity and the effects due to acoustics. The investigation was carried out to explore the ways in which sound may be used to compensate for the lack of buoyancy in microgravity. Video images of vapor bubble dynamics under various heat fluxes, acoustic pressure amplitudes, heater positions within the sound field, and also gravity conditions are presented to aid in the analysis.

The ability of acoustically levitating air bubbles larger than the resonance size in water under both terrestrial and microgravity conditions has been demonstrated.[1,2] Thus the first step in the research involved confirming the ability of levitating air bubbles in water in terrestrial gravity using a modified experimental design based upon Refs. 1 and 2. Once this was accomplished, the acoustic force was then assumed to be strong enough to move vapor bubbles from the vicinity of the heater in microgravity under the proper conditions. A magnitude comparison between the acoustic and buoyancy force is given in Sec. II. Attention is restricted to the standing wave geometry used in the experiment and it is anticipated that excitation of acoustic traveling waves to produce radiation forces of similar magnitude would require significantly greater acoustic power. The other steps of the research involved adding a horizontal wire heater and making other small changes to the acoustic experiment. The newly formed pool boiling-acoustic experiment was then subjected to many different heat fluxes, gravity levels, acoustic pressure amplitudes, and heater positions within the sound field.

The experiment looked specifically at the following pool boiling-acoustics topics in both terrestrial and microgravity conditions:

(1) The effects of changing the acoustic pressure amplitude on pool boiling heat transfer.
(2) The importance of heater position within the acoustic standing wave.
(3) Increases in heat transfer due to acoustic streaming and cavitation.
(4) Vapor bubble movement and levitation caused by acoustic radiation pressure in the absence of gravity.
(5) Erratic dancing of bubbles caused by large acoustic pressure amplitudes.
(6) The breakup of large vapor bubbles into small bubbles on the surface of the heater when using acoustics.
(7) Acoustic streaming of liquid to the heater surface for enhancement of the evaporation and condensation process.

[a)]''Selected research articles'' are ones chosen occasionally by the Editor-in-Chief that are judged (a) to have a subject of wide acoustical interest, and (b) to be written for understanding by broad acoustical readership.

I. LITERATURE REVIEW

A. Relevant effects of acoustics on air bubbles and droplets of oil in water

In an acoustic field, bubbles experience a radiation pressure associated with the average force on the bubble. An approximation for the acoustic radiation force on a gas bubble in a standing wave is derived by Eller.[3] The time-averaged acoustic force on the bubble is approximated as

$$F_a = -\langle V(t)\nabla p_a(\mathbf{r},t)\rangle, \tag{1}$$

where $V(t)$ is the volume of the bubble, and $p_a(\mathbf{r},t)$ is the acoustic pressure evaluated without the bubble present. Eller restricts the derivation to one-dimensional symmetric standing waves in the normal direction (z) relative to the pressure node. The result for the force is

$$F_a = \frac{2\pi^2 R^3 P_a^2}{3P_0\lambda_z\beta(1-\omega^2/\omega_0^2)}\sin\left(\frac{4\pi z}{\lambda_z}\right), \tag{2}$$

where R is the equilibrium radius of the bubble, P_a is the acoustic pressure amplitude, λ_z is the wavelength in the z direction, ω and ω_0 are the frequencies of the sound field and bubble's monopole resonance, respectively, and β is the polytropic constant.

Acoustic levitation of air bubbles larger than resonant size in water is discussed by Asaki *et al.*[2] The relevant results are the design of the acoustic levitator and the ability to levitate bubbles larger than resonance size. The experiment was built to excite quadrupole shape oscillations of air bubbles. The driving frequency of the acoustic-fluid system was 22.5 kHz. The levitation position of air bubbles and their size in a standing wave was measured and discussed in a paper by Asaki and Marston.[4] Observations agreed with calculations of the position based on Eq. (2). They found that, among the three types of monopole oscillation damping mechanisms (radiation, viscous, and thermal), the radiation term is the most significant term for bubbles that are larger than resonance size for the range of sizes explored by them even though the correction to Eq. (2) from that term was small. The apparatus used in their experiment is the same as described in the previous paragraph. Air bubbles were trapped in an acoustic standing wave aboard the space shuttle on USML-1. The experiment and results were discussed by Marston *et al.*[1]

The acoustic force on a liquid droplet in a one-dimensional stationary wave is discussed by Yosioka and Kawasima[5] and Crum.[6] The result is useful for calibration of the pressure amplitude and may be written

$$F_a = \frac{V_0 P_a^2 \sin(2k_z z)}{4\rho_1 c^2}\left[\frac{1}{\delta\sigma_v^2} - \left(\frac{5\delta-2}{2\delta+1}\right)\right], \tag{3}$$

where P_a is the acoustic pressure amplitude, k_z is the wave number in the vertical direction z, ρ_1 is the density of the fluid, σ_v is the velocity ratio, c is the speed of sound in the medium, and δ is the ratio of density of the droplet divided by the density of the fluid medium. Solving for the minimum acoustic pressure amplitude needed to levitate the droplet the equation becomes

$$P_a = \left(\frac{4|1-\delta|g\rho_1^2 c^2}{k_z\left[\frac{1}{\delta\sigma_v^2} - (5\delta-2)/(2\delta+1)\right]}\right)^{1/2}. \tag{4}$$

It was noted that the minimum acoustic pressure needed to levitate a droplet is independent of its volume provided, as assumed here, the drop is small in comparison to $2\pi/k_z$.

In the experiments of Asaki and Marston[4] as well as those of the present authors, the standing wave pressure depended on the transverse coordinates (x,y) as well as on z. The radiation force on compressible particles in water in a standing wave in chambers with rectangular boundaries has been discussed by Whitworth and Nyborg.[7] The generalization to drops and bubbles is discussed by Thiessen and Marston.[8] Even if the drop or bubble is located on a lateral pressure antinode, the z component of radiation force differs from Eqs. (2) and (3) unless ck_z/ω is close to unity. The lateral dimensions of the chambers used in the present study and in Ref. 4 were sufficiently large that errors introduced by neglecting this correction are estimated to be insignificant. An additional approximation used in Eq. (2) is that any dependence on the shape of the bubble is neglected. Measurements of the equilibrium position (and, by inference, the radiation force) by Asaki and Marston[4,9] for bubbles having aspect ratios as large as 1.23 indicate that, for the purposes of the present study, corrections to Eq. (2) associated with the shape of the bubbles observed are negligible.

Erratic motion of bubbles with sizes smaller than resonant size in an acoustic standing wave are discussed by Crum and Eller.[10] The erratic motion of bubbles that are levitated or in motion are thought to be brought about by shape oscillations of the bubbles.[11–13] The amplitude of the acoustic pressure appears to be the controlling mechanism that sets bubbles into erratic motion. Crum and Eller also found that in the presence of an acoustic standing wave, bubbles smaller than resonant size can be propelled through a fluid body several times faster by the acoustic radiation force, Eq. (1), than by the buoyancy.

B. Effects of acoustics on heat transfer

In pool boiling, a heated surface is immersed in a stagnant pool of liquid. For terrestrial pool boiling under a constant pressure, the heat transfer is characterized by the so-called ''boiling curve,'' which is a plot of the heat flux versus the heater surface temperature. The boiling curve is composed of four different regimes. When the heater surface temperature is below that of boiling inception, there is no boiling and the heat transfer is entirely due to natural convection. The next regime is called the nucleate boiling, where the heater surface temperature is higher than the inception requirement and the heat transfer is achieved by the nucleation of vapor bubbles. In the nucleate boiling regime, the heat flux increases with increasing heater surface temperature and this boiling regime ends when a peak heat flux is reached, after that the heat flux decreases with increasing heater surface temperature and this is the transition boiling regime. In transition boiling, the heat transfer is carried out by a mixture of nucleation and broken vapor films on the

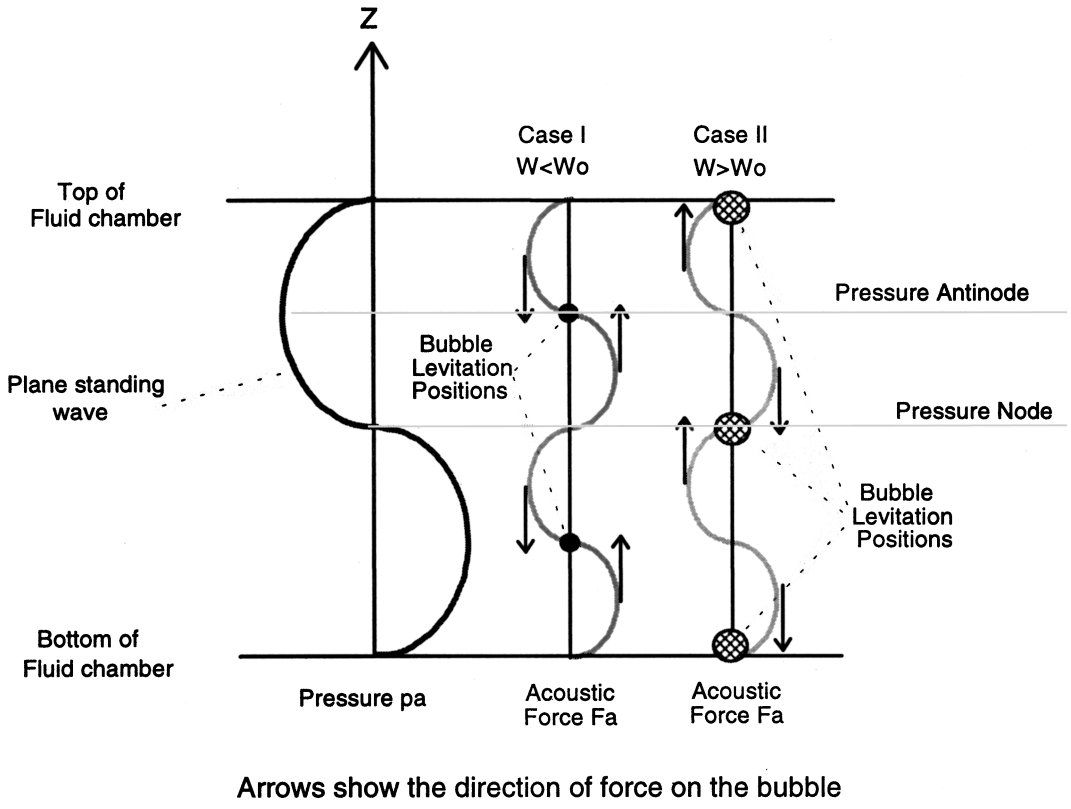

FIG. 1. Bubble levitation positions in an acoustic plane standing wave.

heater surface. The boundary between the transition boiling and the next regime, called film boiling, is characterized by a minimum heat flux. In film boiling, the heat flux increases with increasing heater surface temperature again and the heat transfer is through a stable vapor blanket which covers the entire heater surface. The effects of ultrasonics on pool boiling heat transfer are discussed by Park and Bergles.[14] The experimental setup consisted of a modified ultrasonic cleaning tank with R-113 as the working fluid. The experiments were run with saturated and subcooled fluid. They state that the position of the heater in the acoustic field did not have any noticeable effects on the heat transfer curve under saturated conditions. However, the acoustic pressure amplitude does. It was also noted at moderate heat fluxes that heat transfer decreased. At higher heat fluxes acoustics had minimal effects on the heat transfer curve. These effects are thought to be caused by the development of large amounts of vapor around the heater. As the heat flux is increased, more vapor is produced as with the increase of acoustic pressure. Thus, the highest increase in heat transfer is at low heat fluxes and when the fluid is subcooled.

Wong and Chon[15] found that there is a critical sound pressure (CSP) in which any acoustic pressure below this CSP will have no effect on the heat transfer curve. An 800% increase in heat transfer coefficient was found in the natural convection regime. In the fully developed nucleate boiling regime acoustics had a negligible effect on the heat transfer rate. The reason for the increase in heat transfer was thought to be the erratic motion of bubbles and the radial oscillations of the bubbles in the vicinity of the heater surface. Changing the driving frequency of the system was found to be negligible as long as the same amount of cavitation was maintained.

Iida *et al.*[16] found that acoustics had minimal heat transfer effects on nucleate boiling but did affect the natural convection and film boiling regimes. The peak and minimum heat flux points were raised. The driving mechanism for increasing heat transfer was thought to be mainly acoustic cavitation.

II. THEORETICAL BACKGROUND

In terrestrial gravity, nucleate boiling is one of the most efficient heat transfer mechanisms due to the rapid removal of vapor bubbles by the buoyancy force, which provides the transport of latent heat and turbulent convection of the fluid near the heater surface. In microgravity, acoustic radiation pressure is thought to be able to replace the lost buoyancy force in maintaining nucleate boiling.

For a boiling system, vapor bubbles are generated from the heated surface. They would experience evaporation or condensation depending on the ambient thermodynamic conditions and the applied acoustic field. The interaction of a vapor bubble with a sound field is more complicated than that of a noncondensible gas bubble due to the phase change and associated heat transfer. Vapor bubbles also possess stiffness from an external forcing but the physical process is different from that of a gas bubble. The stiffness of a gas bubble is associated with the compressibility of the gas[17] while that of a vapor bubble can be affected by the phase change and heat transfer between the bubble and its surrounding fluid.[18] For a gas bubble, there is a fundamental

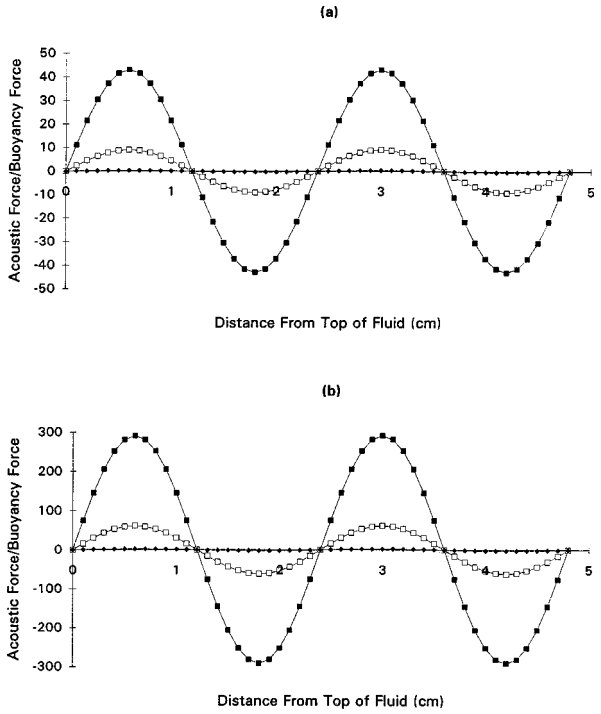

FIG. 2. Ratio of the acoustic radiation force to the buoyancy for different sized bubbles and pressures. Bubble radius is 0.5, 1.0, and 5.0 mm for filled squares, open squares, and diamonds, respectively. (a) Acoustic pressure amplitude is 100 kPa; (b) acoustic pressure amplitude is 260 kPa. The liquid is FC-72 which has a density of 1.692 g/cm^3. For the present purpose of estimating the radiation forces the following approximations were used: (i) the vapor in the bubble was taken to be noncondensable and (ii) the response of the bubble was taken to be radial and sinusoidal.

low-frequency monopole resonance associated with a specific bubble size.[17] For a given acoustic frequency, Finch and Neppiras[18] suggested that there can be two resonance conditions for vapor bubbles. The larger bubble radius resonance condition is generally similar to that of a gas bubble, with a stiffness modified to allow for evaporation and condensation. The smaller bubble resonance condition is more strongly affected by the surface tension.[19] Marston and Greene[20] observed the trapping of small bubbles in liquid helium near the second resonance condition. In the current study of boiling from a wire with an applied acoustic standing wave, it is believed the resonance similar to ordinary gas bubbles is of dominant importance. This is because, for the second condition, the bubble sizes are usually just slightly larger than the critical radius ($\sim$10 μm) for separation from the heater surface; microbubbles adhere to the heater surface and coalesce to form bigger bubbles. Therefore, bubble removal from the heater surface is anticipated to be due to the interaction between the bubbles and the acoustic wave in a size region where the response of the bubble is primarily affected by the ordinary resonance. Our flow visualization also confirmed that bubble departure radii are generally in the range of 0.01–1 cm. Away from the lower resonance condition, the radiation force on a vapor bubble is anticipated to be similar to that on a gas bubble, Eqs. (1) and (2) given previously. These are used as approximations for the boiling vapor bubbles in the present study. It is noted, however, that the vapor bubble's natural frequency is approximated by the Minnaert equation:[17]

$$\omega_0 = \left(\frac{3\beta P_0}{\rho_1 R^2} \right)^{1/2}, \tag{5}$$

which neglects the effects of evaporation and condensation.

The radiation force from Eq. (1) depends on the acoustic pressure amplitude, bubble size, and the driving frequency of the system. The driving frequency, the pressure amplitude, and the bubble size will determine the direction of the radiation force and where the bubble will be levitated.

Looking at Eq. (2) it can been seen that the sign for Fa depends on where the bubble is located in the sound field and the size of the bubble (see Fig. 1). If the bubbles are smaller than resonance size, the bubbles migrate toward the pressure antinodes. If the bubbles are larger than resonance size, the bubbles migrate toward the pressure nodes. Most vapor bubbles observed in the experiment are larger than resonance size.

The two graphs in Fig. 2 show how the acoustic force compares in magnitude to that of the buoyancy force in normal gravity. Both graphs are similar except the acoustic pressure for each graph is different. The parameters that the figures are based on are the same as the actual experiments which correspond to a driving frequency of 10.18 kHz, an atmospheric pressure of 0.92 atm=93 kPa (reduced from standard atmosphere pressure by the elevation of our laboratory), and a liquid bulk temperature equal to approximately 30 °C and $\beta \approx 1.09$ since the contents correspond to the vapor of the liquid used (FC-72). With these parameters the resonant radius is 210 μm in radius and λ_z is 0.048 m. The bubble sizes shown were chosen from within the observed vapor bubble sizes, in the terrestrial and microgravity experiments. For large bubbles the buoyancy force dominates over the acoustic force. This holds true even for large acoustic pressure amplitudes because the ratio of the acoustic force to the buoyancy force is proportional to $1/R^2$:

$$\frac{F_a}{F_b} \propto \frac{1}{R^2}, \tag{6}$$

where the magnitude of the volume pulsations is limited by inertia of the liquid. As the acoustic pressure amplitude is increased, larger and larger bubbles can be trapped near the pressure node. However, in our observation, as the pressure is increased the fluid begins to cavitate and the acoustic pressure is attenuated by the vapor bubbles. The effects of bubble shape are neglected in Eq. (6) as discussed in Sec. I A.

III. EXPERIMENTAL SYSTEM

An apparatus was built for both terrestrial and drop tower experimentation. The system consists of an acoustic resonator, a fluid chamber, a platinum wire heater, a dc power supply, a computer data acquisition hardware, frequency generator, and an acoustic amplifier. The schematic of the experimental system is shown in Fig. 3. FC-72 Fluorinert liquid made by 3M Company was used for the heat transfer experiment. FC-72 is highly dielectric, nontoxic and nonflammable. Under atmospheric condition, FC-72 boils at

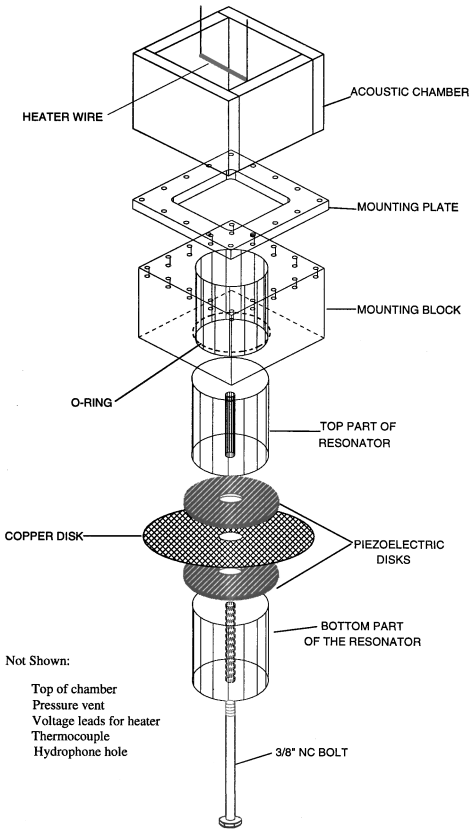

FIG. 3. Exploded view of the experimental setup for pool boiling in an acoustic pressure field under terrestrial and microgravity conditions.

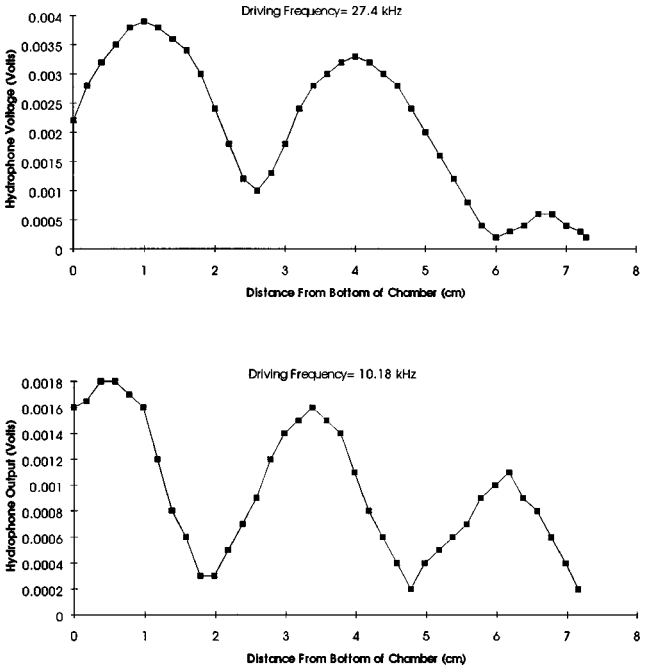

FIG. 4. Pressure distributions in acoustic fluid chambers. (a) Acoustic pressure distribution in water chamber, driving frequency=27.4 kHz; (b) acoustic pressure distribution in FC-72 chamber, driving frequency=10.18 kHz.

56 °C and its sound speed of 528 m/s is about $\frac{1}{3}$ of that in water. Other properties of FC-72 are: kinematic viscosity=0.4 centiStokes, vapor pressure=3×10^4 Pa at 25 °C, latent heat of vaporization=920.9 J/g, and surface tension coefficient=12 dyne/cm. The fluid chamber was designed to have the same natural frequency as the bar resonator. The natural frequency of the chamber was approximated from the solution of the Helmholtz equation for a three-dimensional cavity. The frequencies of vibration for such a chamber are given by

$$\omega_{l,m,n}=c\sqrt{\left(\frac{l\pi}{L_x}\right)^2+\left(\frac{m\pi}{L_y}\right)^2+\left(\frac{n\pi}{L_z}\right)^2}, \tag{7}$$

where c=speed of sound in the fluid, m, n, and l are integers and L_x, L_y, L_z are the outer dimensions of the chamber.[21] The chamber was designed to have three pressure antinodes and two nodes in the vertical direction (z). The material for the chamber was made from acrylic. The base of the chamber was also made from acrylic and the thickness was half the length of the resonator. It should be noted that the side walls of the chamber were approximated as pressure release surfaces in the design.[2]

The bar resonator is driven by a composite piezoelectric transducer. The basic design is well known in the literature and is sometimes called a half-wavelength resonator.[22–24] The half wavelength resonator is composed of a nodal mounting plate, two hollow piezoelectric disks, two quarter wavelength aluminum bars, and a $\frac{3}{8}$-in.-diam bolt. The resonator is usually used for industrial processing in air with only the tip of the resonator touching the point of interest. However, in the current research half the resonator was surrounded by the fluid medium and the other half was exposed to the atmosphere. The tip of the resonator exposed to the fluid body produced high enough acoustic pressure to cavitate the fluid. The piezoelectric disks were purchased from Channel Industries[25] and American Piezoelectric.[26] The piezoelectric elements were made from lead zirconate titanate, Navy type I. A drawing of the resonator is shown in Fig. 4.

Two different resonators were used in the experiment. The basic design of both resonators are the same except they have different diameter and length. The 2- and 3-in. resonators have lengths of 2.188 and 3.798 in., respectively. The 2-in. resonator was used for levitating air bubbles and oil droplets in water for calibrating and hydrophone. The 3-in. resonator was used in the heat transfer experiments.

The total length of each resonator is $\frac{1}{2}\lambda_b$, where the wavelength $\lambda_b=c_b/f$, c_b is the bar velocity of the material, and f is the frequency at which one wishes to run the resonator. Since this basic equation is for a thin rod, the diameter of the resonator should be smaller than $\frac{1}{4}\lambda_b$ so that the transverse modes of vibrations are not pronounced and do not take away from axial vibration.[22] Love's theory comes closer to predicting the true length of the resonator.[23] This equation takes into account lateral inertia effects and the equation is

$$\omega_n=n\pi c_b(L^2+(n\pi\nu_p k_g)^2)^5, \tag{8}$$

where L=length of rod, n=integer, ν_p=Poissons ratio, and k_g=radius of gyration=$D/2$. Using Love's theory the 2-in.-diam resonator length changed only by 1.5%, or 0.130 in. However, the frequency difference was noticeable. The resonators were driven at 27.2 and 10.18 kHz for the 2- and

3-in.-diameters, respectively. Other frequency harmonics could be driven but did not couple as well with the fluid chambers.

The bar resonator has a velocity node at the center and a velocity antinode at the ends. The bar resonator was mounted in the base of the acoustic chamber with an o-ring very close to a velocity node of the bar. The o-ring was used to keep the fluid in the chamber from leaking out. A similar design was demonstrated by Morse *et al.*[27]

The camera used for capturing images was a CCD camera manufactured by Motion Analysis Inc. CV-730 with a $\frac{1}{2}$-in. CCD sensor and a shutter speed that could be varied from $\frac{1}{100}$ to $\frac{1}{10\,000}$ s. The video output went to a Mitsubishi HS-U67 video cassette recorder. The images were then saved on a video tape and viewed on the computer screen, frame by frame using a 24-bit video frame grabber. The images were then imported into an imaging software program and the dimensions of a bubble could then be determined.

The camera was positioned to view through the front of the experiment. Teflon was mounted to the back and one side of the fluid chamber to prevent heating of the fluid from the lighting. The teflon was also used to diffuse the light into the fluid to provide adequate back lighting of the heater and bubble surfaces.

All the heat transfer experiments were performed with a platinum wire heater which had four leads. Two of the leads were used to power the heater, the other two leads were used to measure the voltage drop across the heater. The dimensions of the heater wire are 0.0254 cm in diameter and 6.1 cm in length. This diameter was chosen to be large compared to the capillary length scale to eliminate the edge effects.

The 0.6- and 2.1-s drop towers at Washington State University used in this experiment employ an air bag as a deceleration mechanism. The average microgravity levels are 5×10^{-3} and 5×10^{-4} a/g for the 0.6- and 2.1-s drop towers, respectively.

IV. EXPERIMENTAL PROCEDURE

The first task is to make sure that the acoustic resonator and the fluid chamber are acoustically coupled by adjusting the fluid height in the chamber. The fluid level was adjusted for the highest acoustic pressure amplitude and a roughly sinusoidal pressure spatial distribution in the vertical direction. A hydrophone was built from a piezoelectric material lead zirconate titanante, Navy type II. The hydrophone was calibrated by the technique described by Crum[6] based on Eq. (3) where λ_z was determined by fitting the vertical pressure profile.

The hydrophone was inserted into the FC-72 fluid chamber which uses the 3-in. resonator. The proper fluid height was set according to the highest pressure reading from the hydrophone. A typical vertical pressure profile is also shown in Fig. 4. The hydrophone voltage was found to be proportional to the drive voltage apart from a small offset which does not affect the interpretation of Fig. 4. The driving frequency of the 3-in. resonator was 10.18 kHz, with a fluid height of 7.2 cm.

One drawback of FC-72 is its ability to absorb large amounts of air, therefore degassing before using the fluid for the experiment is very important. The FC-72 was degassed by several different processes: boiling by heating, boiling by drawing a vacuum, and by acoustic cavitation. The most efficient was found by drawing a vacuum. All three worked but drawing a vacuum was the quietest, fastest, and safest. Boiling the fluid by heating introduced the complication that the fluid had to be cooled down before it could be used for the experiment and significant amounts of fluid evaporated during heating.

Once the fluid was in the chamber and degassed, the voltage to the resonator was turned up until heavy cavitation was present. The creation of vapor bubbles at the acoustic pressure antinode was visible as well as the pressure node. Large vapor bubbles were seen levitated at the node until they grew too large. The heaters' position could then be established by visually seeing bubbles at pressure nodes and antinodes. This visual positioning of the antinode and node was double checked with the hydrophone and was determined to be accurate.

The heater surface mean temperature was converted from the resistance reading during the experiment. With the following equation,

$$T=\frac{dT}{dR}R_r+b, \tag{9}$$

dT/dR is the slope from the heater calibration curve and b is from the single point calibration, R_r is the resistance reading taken during the experimental runs. The voltages were measured by the A/D card.

The heat flux from the heater was calculated with the equation

$$q=\frac{VI}{A_s}, \tag{10}$$

where V is the voltage drop across the heater, A_s is the surface area of the heater, and I is the current that is flowing through the heater. The current is determined by a voltage drop across an external fixed resistance. The voltages were measured by the A/D card.

The bulk temperature of the fluid was measured with a Copper–Constantan thermocouple. To ensure that stratifications within the fluid were eliminated before each experimental run, the acoustic pressure field was turned up, producing acoustic streaming. The strong mixing produced by the acoustic streaming brought the fluid body to one temperature. The acoustics were turned off and the fluid was allowed to rest until all signs of fluid motion were subdued.

V. RESULTS AND DISCUSSION

The experiments were conducted under both terrestrial and microgravity conditions. With the acoustics turned on and off, we also examined the effects of sound waves on the boiling system. The boiling chamber was open to the atmosphere, which resulted in a saturation temperature of 54.5 °C for FC-72. The resonator frequency and the acoustic pressure

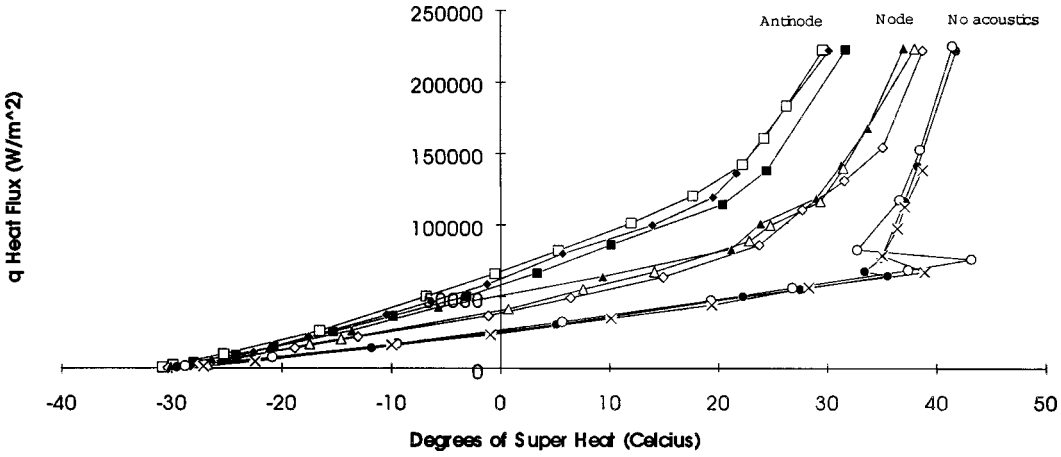

FIG. 5. Heat transfer curve for FC-72 with a platinum wire heater in an acoustic sound field. $T_{\text{bulk}}=24.6\pm1\,^{\circ}\text{C}$.

amplitude were set at 10.18 Hz and 260 kPa gage, respectively. It should be emphasized that the peak acoustic amplitude of 260 kPa is based on a linear extrapolation of the peak acoustic amplitude measured at a lower drive voltage to the transducer. The actual peak voltage will be less than this value. During the heat transfer experiment, the increase in the bulk temperature due to heating, fluid level change due to evaporation, and formation of vapor bubbles all tended to detune the system. As a result, the actual resonance frequency and acoustic pressure amplitude were changing during each experiment. The experimental uncertainties associated with our data are estimated at $\pm5.613\times10^{-4}\ \Omega$ for heat resistance, $\pm1.312\,^{\circ}\text{C}$ for temperature, $\pm0.0269\ \text{W/m}^2$ for heat flux, and $\pm0.04345\ \text{W/m}^2\cdot\text{K}$ for heat transfer coefficient.

A. Boiling heat transfer under terrestrial gravity

The efficiency of a boiling system is measured by the heat transfer coefficient, h, defined as

$$h=\frac{q}{\Delta T_{\text{sup}}},$$

where q is the heat flux and $\Delta T_{\text{sup}}=T_{\text{sur}}-T_{\text{sat}}$ is the degree of superheat which represents the difference between the heater surface temperature, T_{sur}, and the system saturation temperature, T_{sat}. Figure 5 shows the heat transfer coefficient versus the degree of superheat. The curves start from natural convection at $\Delta T_{\text{sup}}\simeq-30\,^{\circ}\text{C}$. The curves shift to different slopes when boiling starts. It is seen that the data are distributed into three distinctive groups. The bottom group is normal pool boiling without the effects of acoustics. The middle group corresponds to pool boiling with acoustics and the heater located at the acoustic pressure node. The top group represents pool boiling with acoustics and the heater located at the acoustic pressure antinode. It is noted that three sets of data are provided for each group to demonstrate the repeatability of data.

It is evident that the location of the heater in the acoustic pressure field is important. We have placed the heater in many positions in the sound field, which included the pressure node, pressure antinode, and halfway between the pressure node and antinode where the acoustic force is the highest according to the simplified theory mentioned previously. It was found that the heat transfer coefficients in a sound field were always higher than those without a sound field. However, the heat transfer coefficient was the highest when the heater was placed at the acoustic pressure antinode and the lowest increase was recorded when the heater was placed at the pressure node. The increase in heat transfer coefficient data for other heater positions are not presented because the plot would become too congested to read. All other heat transfer data fall between those for the heater placed at the antinode and at the node. As a matter of fact, when the heater was placed anywhere in the sound field except close to the pressure node, the heat transfer coefficients approach to that of the heater positioned at the antinode.

It is plausible that the enhancement of heat transfer in a sound field is the result of the following physical mechanisms. The bubbles that are created on the wire would be usually smaller than the resonance size and therefore they tend to stick to the wire and grow in size by liquid vaporization and coalescing with neighboring bubbles. Once they grow larger than the resonance size, then they would be driven off of the wire, provided the heater is displaced from the pressure node. Cavitation was observed to be created by the acoustics and may also enhance the heat transfer as it promotes mixing and turbulence in the fluid.

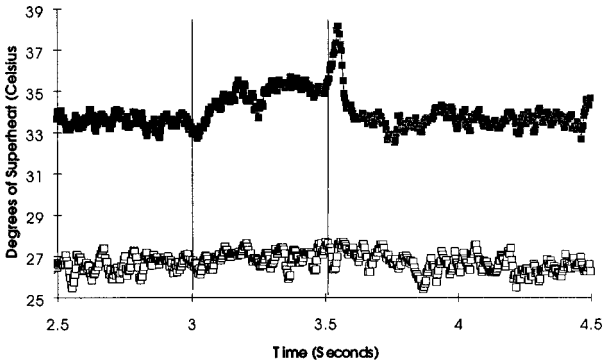

FIG. 6. Pool boiling in terrestrial and microgravity environment at acoustic antinode. Heat flux 24 W/cm^2, $T_{\text{bulk}}=25.9\pm1\,^{\circ}\text{C}$. The apparatus was released at 3.0 s and it freely fell until 3.5 s. The closed and open squares are for no standing wave ($P_a=0$) and a standing wave of $P_a=2.6$ Atm, respectively.

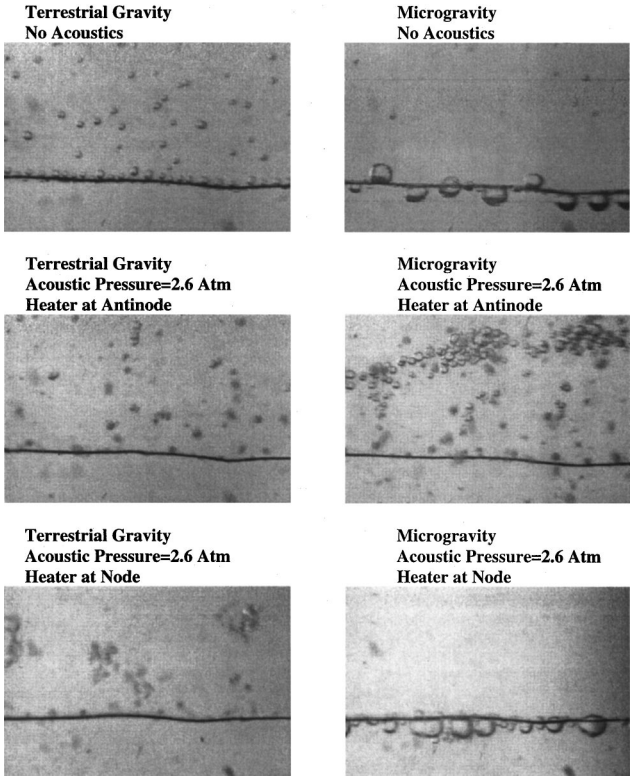

FIG. 7. Pool boiling from a platinum wire heater. Heat flux 24 W/cm^2, $T_{\text{bulk}} = 28.5 \pm 2$ °C.

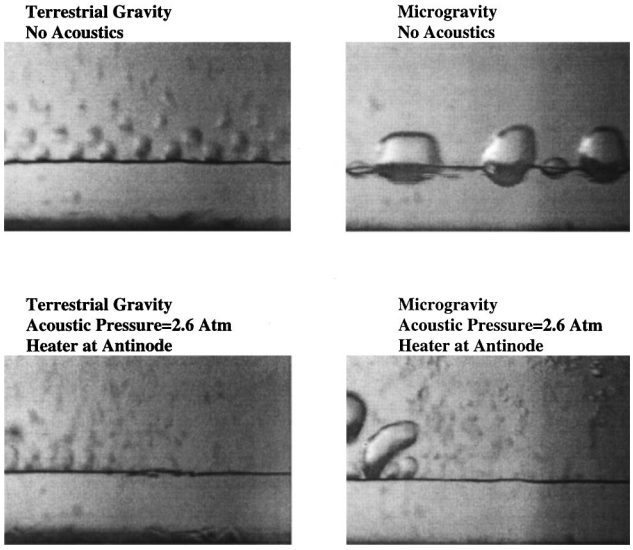

FIG. 8. Pool boiling from a platinum wire heater. Heat flux 36.4 W/cm^2, $T_{\text{bulk}} = 34.7 \pm 0.1$ °C.

Another mechanism for enhanced heat transfer is the acoustic streaming discussed by Rayleigh.[28] For the current case, the acoustic streaming is mainly formed due to the presence of the large amplitude wave in the fluid medium and its interaction with the boundary walls and objects of bubbles in its path. The streaming flow would tend to move the bubbles by drag force and provide convective heat transport, which results in enhanced boiling heat transfer. Some erratic bubble dancing was observed. In summary, boiling heat transfer in the presence of an acoustic field is possibly enhanced by many dynamic mechanisms mentioned above in addition to the primary radiation pressure force. This may explain why the measured maximum heat transfer enhancement does not correspond to the condition where the heater is placed in the middle between a node and an antinode as predicted purely by the radiation force theory.

We also found that acoustics has the largest effects on the boiling heat transfer at the inception of boiling and during film boiling. In general, with the acoustics the temperature of the heater surface dropped by approximately 10 °C at the inception of boiling. The heater surface temperature decreased by several hundred degrees during film boiling.

B. Microgravity boiling heat transfer

The microgravity data were obtained from 0.6- and 2.1-s drop towers at Washington State University. As mentioned previously, we measured both terrestrial and microgravity results in every single run for comparison purposes.

Figure 6 shows a typical result for pool boiling in both terrestrial and microgravity conditions. The effects of sound are also illustrated in Fig. 6. Under a constant heat flux of 24 W/cm^2, the enhancement of heat transfer by the acoustics is represented by the reduction in the degree of superheat. In the absence of acoustics, the degree of superheat increases during microgravity as the removal of bubbles from the heater surface is hindered due to the loss of buoyancy. Once the experiment returned to terrestrial gravity, the heat surface temperature dropped and then went back to its predrop temperature. Both curves in Fig. 6 show fluctuations and oscillations, but the average fluctuation is higher for the case with acoustics, which may be caused by the cavitation and streaming of the fluid. The most significant finding from Fig. 6 is that the acoustic pressure with an amplitude of 260 kPa (determined by extrapolation as previously noted) is dominant over the buoyancy force in maintaining nucleate boiling which is evident by the result that the degree of superheat *is unaffected during microgravity*. This result also suggests that the acoustic standing wave provides a feasible force in maintaining nucleate boiling in space.

Video pictures were taken to provide more physical understanding of the interaction between acoustic pressure waves and a pool boiling system. Figures 7 and 8 show the bubble distribution patterns and sizes in the vicinity of the heater wire for two different heat flux levels of 24 and 36.4 W/m^2, respectively. In the absence of acoustics, the vapor bubbles are removed from the heater surface by buoyancy force in terrestrial gravity. It is apparent that the detachment bubble size is proportional to the heating rate. Under microgravity, bubbles would stick to the wire and coalesce to form larger bubbles without the acoustic radiation force. Some bubbles even hang under the wire, which directly reflects the loss of buoyancy force.

When the acoustics is applied to the system, fewer bubbles are seen on the wire in terrestrial gravity due to the additional force from the sound waves. In microgravity, as shown in Fig. 7, the vapor bubbles are clearly driven off the wire located at the pressure antinode and accumulate about 1.5 cm from the wire where the pressure node is located. In

the lower right picture of Fig. 8, a couple of big bubbles are found near the left-hand-side border, which is caused by the edge effect where the acoustic pressure is substantially weakened and the heating rate is quite high. When the heater wire is located at the acoustic pressure node, the bubbles tended to be levitated around the wire in microgravity. The effect of acoustic cavitation and streaming are also evident from flow visualization. Cavitation breaks up the vapor bubbles formed from the boiling process into smaller bubbles if the heater is not placed at the pressure node. These bubbles dance around in a wild motion and transverse about in the fluid chamber. They eventually coalesce at the pressure node. At higher heat fluxes, the number and size of the vapor bubbles were increased and acoustic cavitation and streaming were not as dominant. The amplitude of the acoustic field was probably attenuated in the vicinity of the wire owing to the presence of bubbles. However, the effects of cavitation and streaming are still noticeable, as shown in Fig. 8. The vapor that normally encapsulates the heater in the absence of acoustics during film boiling was not stable under a sound field. Some of the vapor films were torn off the wire, while others were firmly attached to the wire by surface tension, creating small sections with vapor blanket along the wire. The vapor-blanketed portion was seen rewetted periodically by the acoustic streaming flow. Acoustic streaming also brought colder ambient fluid to the wire, which helped enhance the heat transfer from the wire and prevent drying up on the wire surface. This shows that acoustics is capable of reverting the film boiling process back to at least transition boiling.

VI. CONCLUSIONS

A pool boiling system with a platinum wire heater was designed and built to operate in an acoustic field. The objective of this experimental research is to study the interaction between a pool boiling system and an acoustic standing wave under terrestrial and microgravity conditions.

In terrestrial gravity and a sound field, the boiling heat transfer coefficient was found always higher than that under the same condition but without acoustics. The highest increase in heat transfer was found when the heater wire was placed near the acoustic pressure antinode and the lowest corresponded to placement near the pressure node. Under different heat flux levels, the largest heat transfer enhancements were found at the inception of boiling and during film boiling.

Microgravity experiments have shown that again the acoustic standing waves increased the heat transfer rates. Similar to the results in terrestrial gravity, the highest augmentation of the heat transfer occurred when the heater wire was placed at the acoustic pressure antinode and the heating was at the boiling inception. The most important finding under microgravity is that the acoustic standing waves are capable of playing the role of buoyancy force in maintaining nucleate boiling from a heated wire. In both terrestrial and microgravity conditions, fluid cavitation, acoustic streaming, and erratic bubble motion also contributed to the enhancement of boiling heat transfer.

ACKNOWLEDGMENTS

The research was supported by NASA Grant No. NAG3-1387. Dr. Fran Chiaramonte was the project monitor, who provided constant support.

[1] P. L. Marston, E. H. Trinh, J. Depew, and T. J. Asaki, ''Response of bubbles in ultrasonic radiation pressure: dynamics in low gravity and shape oscillations,'' in *Bubble Dynamics and Interface Phenomena*, edited by J. R. Blake, J. M. Boulton-Stone, and N. H. Thomas (Kluwer, Dordrecht, 1994), pp. 342–353.

[2] T. J. Asaki, P. L. Marston, and E. H. Trinh, ''Shape oscillations of bubbles in water driven by modulated ultrasonic radiation pressure: Observations and detection with scattered laser light,'' J. Acoust. Soc. Am. **93**, 706–713 (1993).

[3] A. Eller, ''Force on a bubble in a standing acoustic wave,'' J. Acoust. Soc. Am. **43**, 170–171 (1967).

[4] T. J. Asaki and P. L. Marston, ''Acoustic radiation force on a bubble driven above resonance,'' J. Acoust. Soc. Am. **96**, 3096–3099 (1994).

[5] K. Yosioka and Y. Kawasima, ''Acoustic radiation pressure on a compressible sphere,'' Acustica **5**, 167–173 (1955).

[6] L. A. Crum, ''Acoustic force on a liquid droplet in an acoustic stationary wave,'' J. Acoust. Soc. Am. **50**, 157–163 (1971).

[7] G. Whitworth and W. L. Nyborg, ''A rotating ultrasonic waveguide for studying acoustic radiation forces on particles,'' J. Acoust. Soc. Am. **90**, 2091–2096 (1991).

[8] D. B. Thiessen and P. L. Marston, ''Principles of some acoustical, electrical, and optical manipulation methods with applications to drops, bubbles, and capillary bridges,'' in Proceedings of FEDSM '98 (American Society of Mechanical Engineering, 1998), paper FEDS98-5298.

[9] T. J. Asaki and P. L. Marston, ''Equilibrium shape of an acoustically levitated bubble driven above resonance,'' J. Acoust. Soc. Am. **97**, 2138–2143 (1995).

[10] L. A. Crum and A. Eller, ''Motion of bubbles in a stationary sound field,'' J. Acoust. Soc. Am. **48**, 181–189 (1970).

[11] A. I. Eller and L. A. Crum, ''Instability of the motion of a pulsating bubble in a sound field,'' J. Acoust. Soc. Am. **47**, 762–767 (1970).

[12] R. G. Holt and D. F. Gaitan, ''The onset of resonance-controlled instability in spherical bubble oscillations,'' in Third Microgravity Fluid Physics Conference (NASA Conference Publications, 1996), pp. 591–597.

[13] R. G. Holt and D. F. Gaitan, ''Observation of stability boundaries in the parameter space of single bubble sonoluminescence,'' Phys. Rev. Lett. **77**, 3791–3794 (1996).

[14] K-A. Park and A. E. Bergles, ''Ultrasonic Enhancement of Saturated and Subcooled Pool Boiling,'' Int. J. Heat Mass Transf. **31**, 664–667 (1988).

[15] S. A. Wong and W. Y. Chon, ''Effects of Ultrasonic Vibrations on Heat Transfer to Liquids by Natural Convection and by Boiling,'' AIChE. J. **15**, 281–288 (1969).

[16] Y. Iida and T. Kentarou, ''Effects of Ultrasonic Waves on Natural Convection, Nucleate Boiling, and Film Boiling Heat Transfer from a Wire to a Saturated Liquid,'' Exp. Therm. Fluid Sci. **5**, 108–115 (1992).

[17] M. Minnaert, ''On musical air-bubble and sounds of running water,'' Philos. Mag. **26**, 235–248 (1933).

[18] R. D. Finch and E. A. Nappiras, ''Vapor bubble dynamics,'' J. Acoust. Soc. Am. **53**, 1402–1410 (1973).

[19] P. L. Marston, ''Evaporation-condensation resonance frequency of oscillating vapor bubbles,'' J. Acoust. Soc. Am. **66**, 1516–1521 (1979); D. Y. Hsieh, ''On oscillation of vapor bubbles,'' *ibid.* **66**, 1514–1515 (1979).

[20] P. L. Marston and D. B. Greene, ''Stable microscopic bubbles in helium I and evaporation–condensation resonance,'' J. Acoust. Soc. Am. **64**, 319–321 (1978).

[21] L. E. Kinsler, A. R. Frey, A. B. Coppens, and J. V. Sanders, *Fundamentals of Acoustics* (Wiley, New York, 1982), 3rd ed.

[22] J. R. Frederick, *Ultrasonic Engineering* (Wiley, New York, 1965).

[23] K. F. Graff, *Wave Motion in Elastic Solids* (Dover, New York, 1975).

[24] E. H. Trinh, ''Compact Acoustic Levitation Device for Studies in Fluid Dynamics and Material Science in the Laboratory and Microgravity,'' Rev. Sci. Instrum. **56**, 2059–2065 (1985).

[25] American Piezo Ceramics, Inc., Duck Run Road, P.O. Box 18, Mackeyville, PA 17750.

[26] Channel Industries, Inc., 839 Ward Drive, Santa Barbara, CA 93111.

[27] S. F. Morse, D. B. Thiessen, and P. L. Marston, ''Capillary bridge modes driven with modulated ultrasonic radiation pressure,'' Phys. Fluids **8**, 3–5 (1996).

[28] Lord Rayleigh, *Theory of Sound* (Dover, New York, 1945).

Effects of amplitude nonlinearity on phoneme recognition by cochlear implant users and normal-hearing listeners[a)]

Qian-Jie Fu[b)] and Robert V. Shannon
Department of Auditory Implants and Perception, House Ear Institute, 2100 West Third Street, Los Angeles, California 90057

(Received 13 October 1997; revised 12 May 1998; accepted 2 July 1998)

It is widely assumed that the proper transformation of acoustic amplitude to electric amplitude is a critical factor affecting speech recognition in cochlear implant users. The goal of this study was to investigate the effects of instantaneous nonlinear amplitude mapping on vowel and consonant recognition in both cochlear implant users and normal-hearing listeners. A four-channel noise-band speech processor was implemented, reducing spectral information to four bands. A power-law transformation was applied to the amplitude mapping stage in the speech processor design, and the exponent of the power function varied from a strongly compressive ($p=0.05$) to a weakly compressive value ($p=0.75$) for implant listeners and from 0.3 to 3.0 for acoustic listeners. Results for implants showed that best performance was achieved with an exponent of about 0.2, and performance gradually deteriorated when either more compressive or less compressive exponents were applied. The loudness growth functions of the four activated electrodes in each subject were measured and those data were well fit by a power function with a mean exponent of 2.72. The results indicated that best performance was achieved when the normal loudness growth was restored. For acoustic listeners, results were similar to those observed with cochlear implant listeners, except that best performance was achieved with no amplitude nonlinearity ($p=1.0$). The similarity of results in both acoustic and electric stimulation indicated that the performance deterioration observed for extreme nonlinearity was due to similar perceptual effects. The function relating amplitude mapping exponent and performance was relatively flat, indicating that phoneme recognition was only mildly affected by amplitude nonlinearity.
[S0001-4966(98)03610-8]

PACS numbers: 43.10.Ln, 43.71.Es, 43.66.Ts, 43.71.Ky, 43.64.Me [WS]

INTRODUCTION

Electric stimulation of the auditory nerve with a cochlear implant can partially restore hearing sensations to deaf listeners. In designing a speech processor for an implant listener, a major concern is in the proper transformation of acoustic amplitude to electric amplitude. Normal acoustic hearing can process sounds over a range of 120 dB, and speech sounds in a normal conversation can range over 40–60 dB. However, implant listeners typically have dynamic ranges of only 6–15 dB in electrical current. This smaller dynamic range can be partly compensated by better sensitivity to intensity changes within the electric range (Nelson *et al.*, 1996). Schroder *et al.* (1994) estimated that the total number of discriminable intensity steps across the dynamic range would be 83 for acoustic stimulation, while Nelson *et al.* (1996) estimated between 6.6 and 45.2 discriminable intensity steps across the dynamic range of electric hearing, with the number of steps varying widely across implant listeners. Thus even though the electric jnd is smaller (in dB) than the acoustic jnd, this difference in size is insufficient to overcome the difference in dynamic range. If the amplitude mapping does not properly maintain loudness relations in both absolute loudness and relative discriminability, critical envelope cues in speech may be lost.

Speech recognition in normal hearing is known to be quite robust with respect to amplitude manipulations. In a dramatic and extreme example, Licklider and Pollack (1948) removed all amplitude variations in the overall speech waveform by ''infinite clipping,'' i.e., converting all amplitude values to either -1 or $+1$. Speech recognition was relatively unaffected by this clipping. More recently, Drullman (1995) applied center clipping and peak clipping to speech that was represented by 24, $\frac{1}{4}$-octave bands of noise. He also found that speech recognition was robust with respect to amplitude peak clipping or center clipping over a 40-dB range. In other words, the level of clipping had to be so extreme as to remove most of the speech amplitude information before intelligibility was reduced.

These two studies measured the effect of clipping, but few studies have systematically measured the effect of altered loudness functions on speech recognition. In recent years digital hearing aids allow individually customizable loudness functions to restore normal loudness growth in each frequency band (Allen *et al.*, 1990). The concept is that the better the loudness function in the aided ear matches a ''normal'' loudness function, the better the speech performance. Different amplitude compression functions in different frequency bands have been evaluated to compensate for loudness recruitment in multiband compression hearing aids

[a)]''Selected research articles'' are ones chosen occasionally by the Editor-in-Chief that are judged (a) to have a subject of wide acoustical interest, and (b) to be written for understanding by broad acoustical readership.
[b)]Electronic mail: qfu@hei.org

(Villchur, 1982; Lippmann *et al.*, 1981; Plomp, 1988; Moore and Glasberg, 1993). Results showed that spectral and temporal contrasts were reduced in multiband compression with detrimental effects on speech recognition. Freyman and colleagues (Freyman and Nerbonne, 1989; Freyman *et al.*, 1991) systematically altered the amplitude ratio between consonants and vowels. They demonstrated that consonant identification was adversely affected by amplitude nonlinearity, particularly in conditions of reduced spectral information.

In normal acoustic hearing, the function relating loudness to acoustic amplitude has a long history. In the most widely accepted model of loudness in acoustic hearing, Steven's Power Law (Stevens, 1955), loudness grows in proportion to the stimulus amplitude (A) raised to a power (p, the exponent of the acoustic power law, is 0.6). With electrical stimulation, however, Stevens and colleagues (Stevens, 1937; Stevens *et al.*, 1959) found that auditory loudness grew as the 3.5 power of electrical amplitude delivered to the tympanic membrane. Müller (1981) also found that the growth of loudness in a cochlear implant could be described by a power function with an exponent of about 3.5.

Eddington *et al.* (1978) used the method of limits to balance loudness between an electrically and an acoustically stimulated ear in one cochlear implant listener. They found a linear relation between acoustic level in dB SPL and electric amplitude in microamperes, i.e., a logarithmic relation between acoustic and electric amplitude. A similar logarithmic relation was also observed in a patient with the Ineraid multichannel cochlear implant (Dorman *et al.*, 1993) and from three auditory brainstem implant patients (Zeng and Shannon, 1992). Zeng and Shannon (1992) argued that this relation follows logically from the loss of the cochlea's normal logarithmic compression, requiring this compression to be implemented externally in a cochlear implant speech processor.

Shannon *et al.* (1992) reported the effect of power-law amplitude mapping on consonant and vowel recognition in one patient with a single-channel auditory brainstem implant (ABI). In their study, a single-channel CIS speech processor was implemented. The envelope of the acoustic signal was obtained by half-wave rectification and low-pass filtering. The resulting acoustic envelope amplitude was mapped to electrical amplitude by a power-law mapping function whose exponent ranged from 0.05 to 2.0. This transformed amplitude was used to modulate the amplitude of a continuous train of charge-balanced, biphasic pulses. The results showed that the percentage correct for consonants and vowels was significantly affected by the value of the exponent, p, of the amplitude mapping function. Best performance was achieved with highly compressive exponents, $p = 0.1$ and 0.2. As the exponent approached 1.0 (which would be linear mapping from acoustic to electrical amplitudes), performance deteriorated.

Boëx *et al.* (1995, 1997) developed mapping functions that preserved normal loudness growth in cochlear implants and investigated whether a speech processor that restores normal growth of loudness would improve speech performance. They fit four subjects with wearable CIS processing systems that implemented normal loudness growth mapping functions on each electrode instead of the standard logarithmic mappings. They reported that two subjects demonstrated a clear preference for, and better performance with, the speech processor with normal loudness growth in most listening conditions.

TABLE I. Subject information for the three Nucleus-22 cochlear implant listeners in the present study.

Subject	Age	Gender	Cause of deafness	Duration of implant use	Performance (CUNY sentence)
N3	55	M	Trauma	6 years	68.2%
N4	39	M	Trauma	4 years	95.1%
N7	54	M	Unknown	4 years	92.6%

However, the importance of the amplitude mapping function for speech recognition is still not clearly understood. The present study describes two experiments designed to investigate the role of the loudness function in speech recognition. Experiment I measured the quantitative effect of acoustic-to-electric amplitude mapping on vowel and consonant recognition in cochlear implant users. In this experiment, a four-channel CIS speech processor was implemented in three Nucleus-22 cochlear implant users. A power-law transformation with varying exponents was used in the nonlinear mapping stage of the CIS processing strategy. Recognition scores for vowels and consonants were measured as a function of the exponent of the power function. The loudness growth functions of the four activated electrodes in all three subjects were also measured. The relation between the loudness growth function of acoustic and electric stimulation and the exponent of the power function with the best performance is discussed. Experiment II collected similar results from normal-hearing subjects listening to a simulation of an implant. The use of normal-hearing listeners addressed the question of whether the performance variations by different mapping functions in experiment I were due to the distorted amplitude caused by the improper restoration of loudness growth or were unique to implant listening. A four-channel noise-band simulation system was implemented in this experiment. The recognition of vowels and consonants was measured in four normal-hearing subjects and recognition as a function of the exponents of the power function were compared with those patterns in electric stimulation. The possible relations between acoustic and implant performance patterns are discussed.

I. EXPERIMENT I: AMPLITUDE NONLINEARITY IN ELECTRICAL STIMULATION

A. Methods

1. Subjects

Three, post-lingually deafened adults with the Nucleus-22 cochlear implant participated in this study. All had at least six months experience utilizing the SPEAK speech processing strategy and all were native speakers of American English. All subjects had 20 active electrodes available for use and all clinical speech processors used the default frequency allocation table 9 (150–10 823 Hz) (Audi-

ologist Handbook, Cochlear Corporation, 1995). Table I contains detailed information for the three subjects.

2. Test materials and procedures

Vowel recognition was measured in a 12-alternative identification paradigm, including 10 monophthongs and 2 diphthongs, presented in a /h/−vowel−/d/ context (heed:h/i/d, hawed: h/ɔ/d, head: h/ɛ/d, who'd: h/ʊ/d, hid h/ɪ/d, hood: h/ʊ/d, hud: h/ʌ/d, had: h/æ/d, heard: h/ɝ/d, hoed: h/o/d, hod: h/ɑ/d, hayed: h/e/d). The tokens for these closed-set tests were digitized natural productions from five men, five women, three boys, and two girls, drawn from the speech samples collected by Hillenbrand *et al.* (1994). Consonant recognition was measured in a 16-alternative identification paradigm, for the consonants /b d g p t k l m n f s ʃ v z j θ/, presented in an /a/-consonant-/a/ context. Two repetitions of each of the 16 consonants were produced by 3 speakers (1 male, 2 female) for a total of 96 tokens (16 consonants *3 talkers *2 repeats). On each trial a stimulus token was chosen randomly, without replacement, from the 180 tokens (12 vowels *15 talkers) in vowel recognition and the 96 tokens in consonant recognition. Following presentation of each token, the subject responded by pressing one of 12 buttons in the vowel test or one of 16 buttons in the consonant test, each marked with one of the possible responses. No feedback was provided, and subjects were instructed to guess if they were not sure, although they were cautioned not to provide the same response for each guess.

All signals were presented at comfortable audible levels based on the CIS speech processing strategy through a custom implant interface system (Shannon *et al.*, 1990). Subjects were well familiarized with the test materials and the test procedure from prior experiments. The subjects started the formal test without training and with no appreciable period of adjustment to each new amplitude-mapping condition. Each data point represents 2 runs by each subject, which represents 30 presentations of each vowel and 12 presentations of each consonant. All conditions (9 mapping index *2 tests *2 runs) were presented in random order and counterbalanced across subjects. Subjects were tested for about 4 h on each test day, with a 15-min break after each two conditions. Subjects were typically tested twice a week and finished all conditions within a two-week period.

3. Signal processing

The four-channel CIS processor was implemented as follows. The signal was first pre-emphasized using a first-order Butterworth high-pass filter with a cutoff frequency of 1200 Hz, and then bandpass filtered into four broad frequency bands using eighth-order Butterworth filters. The corner frequencies of the bands were at 100 Hz, 713 Hz, 1509 Hz, 3043 Hz, and 6000 Hz. The envelope of the signal in each band was extracted by half-wave rectification and low-pass filtering (eighth-order Butterworth) with a 160-Hz cutoff frequency. The amplitude histogram in each band was computed for the test materials presented at 70 dB SPL. The maximum amplitude used ($A_{\max}$) was set to the 99th%-ile of all amplitude levels in all channels and the minimal amplitude ($A_{\min}$) was set to the noise floor in the absence of sound input in all channels. The envelope of each band was modified based on the following function. The current level (E) of electric stimulation in the ith band was determined as follows:

$$E^i=\begin{cases} E^i_{\min}, & A^i<A_{\min} \\ E^i_{\min}+k^i\times(A^i-A_{\min})^p, & A_{\min}<A^i<A_{\max} \\ E^i_{\max}, & A^i>A_{\max}, \end{cases}$$

where $E^i_{\min}$ is the electrical current threshold, $E^i_{\max}$ is the electrical maximum comfortable loudness level, and the value of the constant k^i is chosen so that the output is $E^i_{\max}$ when the acoustic input level is $A_{\max}$. Figure 1 shows the mapping function for several values of p. The exponent of the power function was systematically changed from 0.05, 0.1, 0.15, 0.2, 0.25, 0.3, 0.4, 0.5 to 0.75. Then this transformed amplitude was used to modulate the amplitude of a continuous, 500 pulse/s biphasic pulse train with a 100 μs/phase pulse duration. The stimulus order of the four channels was 1-3-2-4 for electrode pairs (20,22), (15,17), (10,12), and (5,7), respectively.

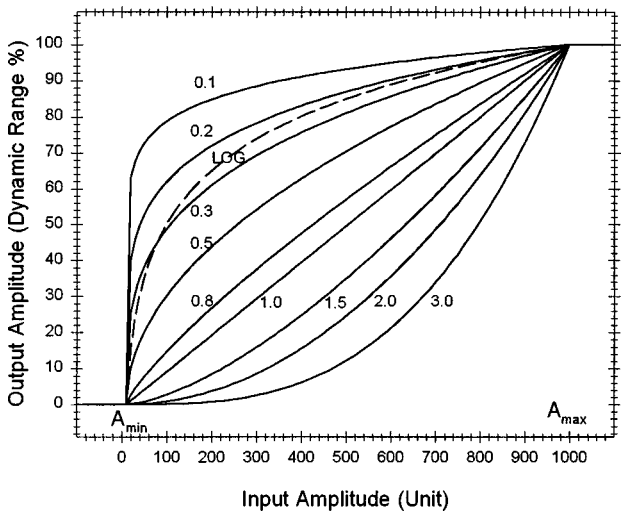

FIG. 1. Examples of the power-law amplitude mapping function for different values of the exponent.

4. Loudness growth function

The growth of loudness as a function of current was measured for each of the four activated electrodes in the three subjects. A 200-ms duration, 100-μs/phase, 500-pulse/s pulse train was used for loudness scaling. A set of 10–15 current values was chosen which spanned the subject's dynamic range from a value just above threshold to the maximum comfortable level (MCL). Subjects were instructed to assign numbers between 0 and 100 to represent the loudness of each sound. No explicit instructions were given in terms of maintaining ratios. An initial training session was conducted for subjects to obtain practice at the task and become comfortable and familiar with their own number system. Stimuli were presented in random order and at least ten estimations were then obtained for each current value. Slope of

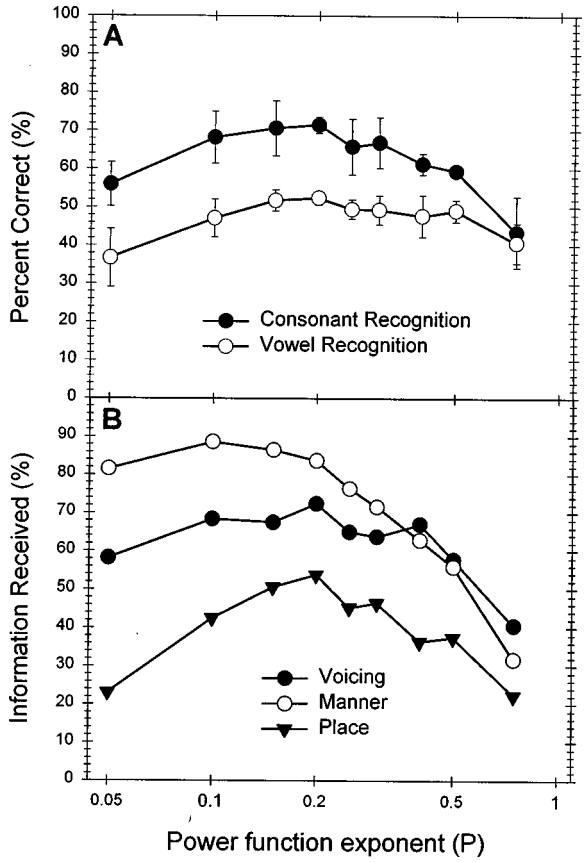

FIG. 2. Phoneme recognition as a function of the exponent of the power function in three cochlear implant users. A: Filled circles show the mean consonant scores, and open circles show the mean vowel scores. B: The received information for consonants on voicing (filled circles), manner (open circles), and place (filled inverted triangles).

loudness growth functions on log–log coordinates for the four different electrodes in each of the three subjects were obtained by linear regression analysis.

B. Results

Figure 2A shows recognition performance for vowels and consonants as a function of the exponent of the power function. The mean vowel score was 36.8% in the most extreme condition ($p=0.05$), was constant at about 50% for values of the exponent from 0.2 to 0.5, and dropped slightly to 40.7% as the exponent of the power function approached

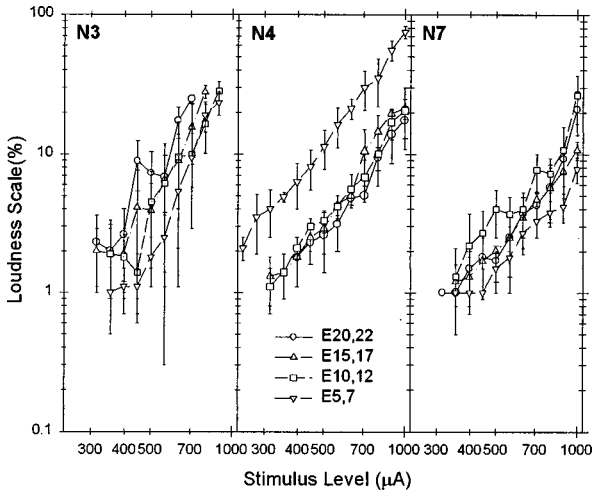

FIG. 3. Loudness growth functions as a function of stimulus level (microamperes) in the four activated electrode pairs of three cochlear implant users. A 200-ms long, 500 pps with 100-μs/phase pulse trains were used to measure the loudness.

0.75. Similarly, the mean consonant score changed from 56.0% when the value of the exponent, p, of the amplitude mapping function was 0.05, to 70.7% when p was 0.20, and dropped to 43.5% when the exponent of the power function was increased to 0.75. A two-way ANOVA showed a significant effect of the exponent of the power function for vowels [$F(8,26)=4.31$, $p<0.01$] as well as for consonants [$F(8,26)=8.92$, $p<0.001$]. The consonant confusion matrices were analyzed further for information received on the production-based features of voicing, manner and place (Miller and Nicely, 1955) and the results are presented in Fig. 2B. Similar to the pattern of performance for vowels, performance on place of articulation showed a peak at $p=0.2$ and performance decreased at higher and lower values. Performance on voicing was relatively flat for values of p between 0.05 and 0.5. Performance on manner was relatively flat for values of p between 0.05 and 0.2, and then dropped dramatically as the exponent was increased to 0.75.

The loudness growth functions of the four electrodes for the three subjects are shown in Fig. 3, where the logarithm of the average loudness estimate for each current tested is plotted against the logarithm of the current in microamperes. All curves could be well fit by a power function with a mean

TABLE II. Slope of loudness growth functions ($L=k*E^p$) for the three subjects and four different electrodes obtained by linear regression analysis [$20\log_{10}$ (estimate)/dB].

Subject	Electrode pair (20,22) loudness growth slope (p)	Electrode pair (15,17) loudness growth slope (p)	Electrode pair (10,12) loudness growth slope (p)	Electrode pair (5,7) loudness growth slope (p)
N3	3.12 ± 0.47 ($r^2=0.88$)	2.96 ± 0.31 ($r^2=0.93$)	3.20 ± 0.35 ($r^2=0.92$)	3.77 ± 0.38 ($r^2=0.93$)
N4	2.48 ± 0.10 ($r^2=0.99$)	2.73 ± 0.17 ($r^2=0.97$)	2.56 ± 0.14 ($r^2=0.98$)	2.50 ± 0.06 ($r^2=0.99$)
N7	2.67 ± 0.29 ($r^2=0.92$)	2.16 ± 0.07 ($r^2=0.99$)	2.38 ± 0.25 ($r^2=0.92$)	2.16 ± 0.22 ($r^2=0.95$)

Mean slope: 2.72 ± 0.47

TABLE III. Slope of loudness growth functions ($L = k*e^{qE}$) for the three subjects and four different electrodes obtained by linear regression analysis [$20 \log_{10}$ (estimate)/mA].

Subject	Electrode pair (20,22) loudness growth slope (q)	Electrode pair (15,17) loudness growth slope (q)	Electrode pair (10,12) loudness growth slope (q)	Electrode pair (5,7) loudness growth slope (q)
N3	55.90±8.32 ($r^2=0.88$)	50.64±3.50 ($r^2=0.97$)	47.94±5.11 ($r^2=0.93$)	57.19±3.98 ($r^2=0.97$)
N4	36.20±1.76 ($r^2=0.98$)	39.94±2.20 ($r^2=0.97$)	34.30±1.55 ($r^2=0.99$)	40.03±1.87 ($r^2=0.98$)
N7	36.39±2.48 ($r^2=0.97$)	30.19±0.89 ($r^2=0.99$)	33.66±2.96 ($r^2=0.94$)	36.70±3.70 ($r^2=0.95$)

exponent of 2.72. Table II lists all regression slopes for a simple power-law function of loudness. The loudness growth functions were also equally well fit by an exponential function (Zeng and Shannon, 1992, 1994). Table III lists all regression slopes for the exponential model of loudness. When comparing a power function mapping and logarithmic mapping, the logarithmic transformation is quite similar to a power function with an exponent value around $p=0.25$ (Fig. 1).

II. EXPERIMENT II: AMPLITUDE NONLINEARITY IN ACOUSTIC HEARING

One question arising from the results of experiment I is whether the pattern of results is generalizable to acoustic hearing or is specific to electrical stimulation. To answer this question we measured consonant and vowel recognition in normal-hearing listeners under conditions of nonlinear amplitude mapping. Previous studies (Licklider and Pollack, 1948; Drullman, 1995) have demonstrated that speech recognition is highly robust to amplitude nonlinearity if full spectral information is available. In this study spectral information was limited to four noise bands to simulate the four electrodes available to the implanted listeners.

A. Methods

1. Subjects

Four subjects, ranging in age from 25 to 35 years old, participated in this study. All subjects had sensitivity thresholds better than 15 dB HL at the audiometric test frequencies from 250 to 8000 Hz and all were native speakers of American English. Subjects were well familiarized with the test materials and the test procedure from prior experiments.

2. Test materials and procedures

Test materials were the same as those for cochlear implant users. All test materials were stored on computer disk and were output via custom software to a 16 bit D/A converter (TDT DD1) at a 16-kHz sampling rate. Speech sounds were presented in a completely randomized test sequence using a Tucker-Davis-Technologies (TDT) AP2 array processor in a host PC connected via an optical interface. All signals were presented at 70 dB SPL through a Sennheiser HDA200 headphone and all subjects were seated in a double-walled sound-attenuating booth (IAC). All conditions (7 mapping index *2 tests *2 runs) were presented in random order and counterbalanced across subjects. Subjects were tested for about 3 h on each test day, with a 15-min break after each three conditions. Subjects were typically tested twice a week and finished all conditions within a two-week period.

3. Signal processing

The noise-band simulation processor was implemented as follows. The temporal envelope extraction and amplitude mapping used the same method described in experiment I. There were two significant differences between acoustic simulation and electric stimulation study. In the electric stimulation study, $E_{\max}$ was set to the maximum comfortable level (MCL) of each electrode, and $E_{\min}$ was set to the threshold level of each electrode. However, in the acoustic study, $E_{\max}$ was set to $A_{\max}$, and $E_{\min}$ was set to $A_{\min}$. The second is that the exponent of the power function ranged from 0.3 to 3.0 instead of from 0.05 to 0.75. In addition, the modified envelope of each band was used to modulate a wideband noise, which was then spectrally limited by the same bandpass filter used for the original analysis band. The output from the four bands were then summed and presented to the listeners diotically through headphones at 70 dB SPL.

B. Results and discussion

Figure 4 shows recognition performance for vowels and consonants as a function of the exponent of the power function. The mean vowel score gradually increased from 48.9% in the most compressive condition ($p=0.3$) to 65.0% in the condition where no mapping was applied ($p=1.0$), and then gradually decreased to 46.3% in the most expansive condition ($p=3.0$). Similarly, the mean consonant score increased from 65.5% in the most compressive condition ($p=0.3$) to 84.0% in the no-mapping condition ($p=1.0$), and then gradually decreased to 50.3% in the most expansive condition ($p=3.0$). A two-way ANOVA showed a significant effect of amplitude mapping for vowels [$F(6,27)=9.77$, $p<0.0001$] as well as for consonants [$F(6,27)=27.64$, $p<0.0001$].

Mean consonant scores were significantly higher (approximately 15%) than the mean vowel scores in all mapping conditions except the most expansive mapping condition ($p=3.0$). Both expansive and compressive mapping had similar effects on vowel recognition. However, consonant recognition was more vulnerable to the expansive mapping, espe-

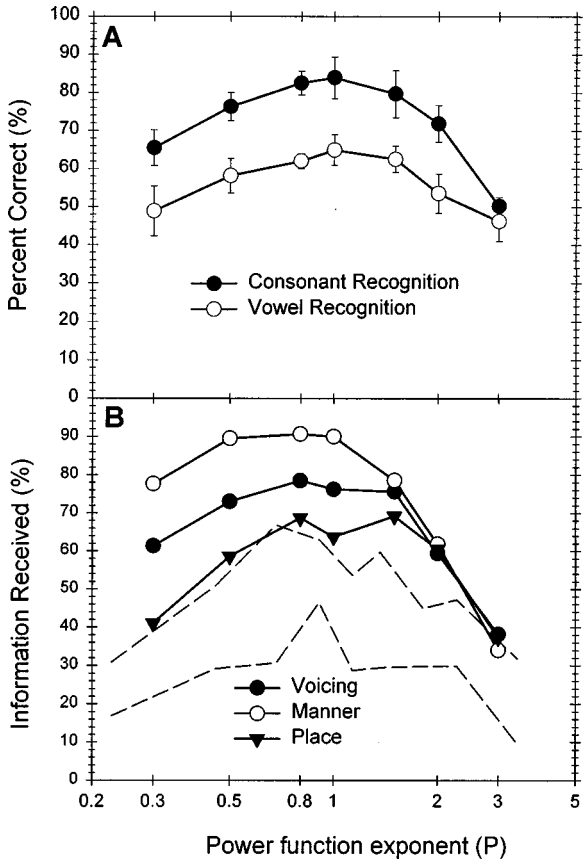

FIG. 4. Phoneme recognition as a function of the exponent of the power function in four normal-hearing subjects. A: Filled circles show the mean consonant scores, and open circles show the mean vowel scores. B: The received information for consonants on voicing (filled circles), manner (open circles), and place (filled inverted triangles). Dashed lines indicate the range of place scores for implant listeners.

cially for the most expansive mapping condition. One possible explanation is that for $p=3$, higher input amplitudes are expanded while lower input amplitudes are compressed, as shown in Fig. 1. This mapping will amplify the vowel information and attenuate the consonant information, resulting in possibly reduced audibility for middle and low-level consonants.

The consonant confusion matrices were analyzed for information received on the production-based features of voicing, manner and place (Miller and Nicely, 1955) and the results are presented in Fig. 4B. Performance on voicing, manner, place increased gradually from the most compressive condition to the linear condition, and then decreased to the most expansive condition. Except for the significant overall performance difference, the recognition patterns of the percent information received on the voicing, manner and place were quite similar when the mapping index changed from the most compressive mapping condition to the linear condition. However, the expansive mapping ($p>1$) had a differential effect on the three categories of information. In the linear four-channel simulation condition, the highest percent of information was received on manner while the lowest percent of information was received on place. However, the difference was much smaller when a small expansive mapping ($p=1.5$) was applied and no difference was observed when the mapping exponent of the power function was 2 or more. The effect of the expansive and compressive condition on the percent information received on the place was quite symmetric around $p=1$ on a log scale, which was similar to the pattern of results for vowels. However, a significant nonsymmetric effect of the expansive and compressive mapping was observed on voicing and manner. Taken together, these results indicate that both compressive and expansive mapping may distort the speech signal, resulting in a significant performance drop with either extreme. However, while both compressive and expansive mapping degraded the spectral (place) information to a comparable extent, the temporal information (voicing and manner cues) was much more sensitive to expansive mapping than compressive mapping.

One factor to note is the minor discrepancy between the overall and received information scores. As shown in Fig. 4, the maximum values of information received on voicing, manner, and place reached maximum with an exponent of 0.8 (Fig. 4B) while overall consonant and vowel recognition scores reached maximum with an exponent of 1 (Fig. 4A). This difference suggests that a slight compression may reduce the difference among individual phonemes, resulting in a small drop in the overall recognition scores in both vowel and consonant recognition. However, this slight compression may enhance the difference across categories, resulting in a small increase in the information received for these categories.

III. GENERAL DISCUSSION

The present results indicate that amplitude mapping does have a significant effect on speech performance in cochlear implant users, consistent with previous results (Boëx *et al.*, 1995, 1997; Shannon *et al.*, 1992; Wilson, 1992).

The pattern of both vowel and consonant recognition as a function of the power-law exponent were remarkably similar between acoustic and electrical simulation except that the mapping exponent with the best performance was shifted from a compressive exponent ($p=0.25$) in electric stimulation to the linear condition ($p=1.0$) in the acoustic simulation study (compare Figs. 2A and 4A). The pattern of information received and the absolute level of information received on voicing and manner were similar between electric and acoustic stimulation. However, acoustic listeners showed better overall performance on both vowels and consonants, primarily because they received more place information. The dashed lines in Fig. 4B show the range of place information received across the three implant listeners. The implant listener with the best overall performance received as much place information as the acoustic listeners, and achieved an overall performance level similar to the acoustic listeners. The poorest performing implant listener received considerably less place information, which limited his overall performance. It is not clear why this implant listener was receiving less place information.

The similarity of patterns of results in acoustic and electric stimulation suggests that the quantitative effect of nonlinear amplitude mapping on phoneme recognition is not specific to cochlear implants. When normal-hearing listeners have limited spectral information similar effects of nonlin-

earity are observed. The primary difference between the results for electric and acoustic stimulation is the value of the exponent that produced the best performance. The acoustic function peaks when $p=1.0$, which is expected because this exponent preserves normal loudness relations. This suggests that the peak in the electrical pattern ($p=0.2$) also occurs at the exponent that provides the best loudness mapping. Let us examine the consistency of the phoneme recognition and loudness estimation data on this point.

The commonly accepted loudness function in acoustic stimulation is a power function in terms of acoustic amplitude with an exponent value 0.6 (Stevens, 1955, 1959). Let us assume that the relation between loudness and sound pressure in acoustic hearing can be described by a power function:

$$L=k_1\times P^{q1}. \tag{1}$$

Let us also assume that the relation between loudness and current level in electric hearing can be described by a power function with a different exponent, $q2$:

$$L=k_2\times E^{q2}. \tag{2}$$

If we could perform a cross-modality match (Stevens, 1959) between acoustic and electric hearing, combining Eqs. (1) and (2) would yield

$$P^{q1}=k_3\times E^{q2}, \tag{3}$$

where E is the current level in electric hearing and P is sound pressure. The relation in Eq. (3) can be rewritten in the form:

$$E=k_4\times P^{q1/q2}=k_4\times P^{q3}, \tag{4}$$

where the exponent $q3$ for cross-modality matching is simply the ratio of the exponents for acoustic and electric hearing. If the exponent of the loudness growth function in acoustic hearing is 0.6 and the exponent of loudness growth function in electric hearing is 2.72, the exponent relating acoustic and electric hearing should be $0.6/2.72=0.22$, which is quite close to the observed exponent value with the best performance. There are two implications of this correspondence: Phoneme recognition is best when loudness is matched, and the effect of amplitude nonlinearity on phoneme recognition is similar for both acoustic and electric hearing. An exponent that is half or twice the optimal will have a similar impact on phoneme recognition in either acoustic or electric hearing.

Although the best phoneme recognition was observed when normal loudness is restored, the effect of nonlinearity was relatively mild. No significant difference in recognition performance for either vowels or consonants was observed over a considerable range: $p=0.5$ to $p=1.5$ for acoustic hearing and $p=0.1$ to $p=0.5$ for electric stimulation. This result indicates that performance does not deteriorate significantly with only moderate amplitude distortion caused by the improper restoration of loudness growth. Consider that the exponent range of the loudness growth functions across all four electrodes in the three implant subjects only ranged from 2.16 to 3.77, which translates to mapping exponents of 0.28 and 0.16, respectively. The similarity of the exponents across electrodes within a subject, combined with the flatness of the recognition function between exponents of 0.1 to 0.5, suggests that the restoration of loudness growth in each electrode may not produce a dramatic performance improvement. In addition, the logarithmic transformation commonly used may work well because the equivalent exponent (around $p=0.25$) is within the tolerable range.

In summary, the effect of nonlinear amplitude mapping on phoneme recognition was significant when an extreme nonlinearity was used. However, within a broad range of the power-law mapping exponent, vowel and consonant recognition was relatively unaffected. The comparison of amplitude nonlinearity in acoustic and electric stimulation indicated that best performance was achieved when normal loudness growth was restored. Normal-hearing listeners and cochlear implant users can tolerate a moderate degree of amplitude distortion caused by an improper loudness growth function even if only limited spectral information is available.

One caveat to these observations is the possible effects of training. Several studies have shown that training can play a major role in evaluating the effects of frequency-shifting (Rosen *et al.*, 1997) in normal-hearing subjects as well as frequency lowering (Posen *et al.*, 1993) in hearing-impaired subjects. Similar training effects might be observed for amplitude nonlinearity, but it is not clear if the asymptotic level of performance would be equal to that of the uncompressed stimulus. An extreme nonlinearity may map discriminable amplitude components onto nondiscriminable amplitudes within a jnd step. This could result in the loss of useful speech information which could not be compensated by training.

IV. CONCLUSIONS

The results of the present study imply that the proper transformation of amplitude from acoustic to electric stimulation is necessary to obtain optimal phoneme recognition performance in cochlear implant users. Nonoptimal amplitude mapping functions cause an improper restoration of normal loudness growth, resulting in a deterioration of phoneme recognition. However, phoneme recognition is only a weak function of the amplitude mapping exponent, so that the exact loudness match may not be as critical a factor affecting speech performance as was previously thought. A simple logarithmic transformation between acoustic and electric amplitude may be accurate enough to provide good recognition performance in most cochlear implant users.

ACKNOWLEDGMENTS

We appreciate the efforts of all subjects, especially the three implant listeners for their tireless and heroic participation in our experiments. We are grateful to Winifred Strange, and an anonymous reviewer for their critical comments on an earlier draft of this paper. We thank Professor James Hillenbrand for allowing us to use the multi-talker vowel test materials.

Allen, J. B., Hall, J. L., and Jeng, P. S. (**1990**). ''Loudness growth in 1/2-octave bands (LGOB)—A procedure for the assessment of loudness,'' J. Acoust. Soc. Am. **88**, 745–753.

Boëx, C. S., Pelizzone, M., Pilloux, V., and Montandon, P. (**1995**). ''Use of loudness scaling measurements to determine compressive mapping in speech processing for cochlear implants,'' Abstracts of 1995 Conference on Implantable Auditory Prostheses, p. 57.

Boëx, C. S., Eddington, D. K., Noel, V. A., Rabinowitz, W. M., Tierney, J., and Whearty, W. E. (**1997**). ''Restoration of normal loudness growth for CIS sound coding strategies,'' Abstracts of 1997 Conference on Implantable Auditory Prostheses, p. 26.

Cochlear Corporation (**1995**). *Audiologist Handbook* (Englewood, CO).

Dorman, M. F., Smith, L., and Parkin, J. (**1993**). ''Loudness balance between acoustic and electric stimulation by a patient with a multichannel cochlear implant,'' Ear and Hearing **14**, 290–292.

Drullman, R. (**1995**). ''Temporal envelope and fine structure cues for speech intelligibility,'' J. Acoust. Soc. Am. **97**, 585–592.

Eddington, D., Dobelle, W., Brackmann, D., Mladejovsky, M., and Parkin, J. (**1978**). ''Auditory prosthesis research with multiple channel intracochlear stimulation in man,'' Ann. Otol. Rhinol. Laryngol. **87**, 1–39.

Freyman, R. L., and Nerbonne, G. P. (**1989**). ''The importance of consonant-vowel intensity ratio in the intelligibility of voiceless consonants,'' J. Speech Hear. Res. **32**, 524–535.

Freyman, R. L., Nerbonne, G. P., and Cote, H. C. (**1991**). ''Effect of consonant-vowel ratio modification on amplitude envelope cues for consonant recognition,'' J. Speech Hear. Res. **34**, 415–426.

Hillenbrand, J., Getty, L., Clark, M., and Wheeler, K. (**1994**). ''Acoustic characteristics of American english vowels,'' J. Acoust. Soc. Am. **97**, 3099–3111.

Licklider, J. C. R., and Pollack, I. (**1948**). ''Effects of differentiation, integration, and infinite peak clipping on the intelligibility of speech,'' J. Acoust. Soc. Am. **20**, 42–51.

Lippmann, R. P., Braida, L. D., and Durlach, N. I. (**1981**). ''Study of multichannel amplitude compression and linear amplification for persons with sensorineural hearing loss,'' J. Acoust. Soc. Am. **69**, 524–534.

Miller, G., and Nicely, P. (**1955**). ''An analysis of perceptual confusions among some English consonant,'' J. Acoust. Soc. Am. **27**, 338–352.

Moore, B. C. J., and Glasberg, B. R. (**1993**). ''Simulation of the effects of loudness recruitment and threshold elevation on the intelligibility of speech in quiet and in a background of speech,'' J. Acoust. Soc. Am. **94**, 2050–2062.

Müller, C. G. (**1981**). ''Survey of cochlear implant work,'' J. Acoust. Soc. Am. Suppl. 1 **70**, S52.

Nelson, D. A., Schmitz, J. L., Donaldson, G. S., Viemeister, N. F., and Javel, E. (**1996**). ''Intensity discrimination as a function of stimulus level with electric stimulation,'' J. Acoust. Soc. Am. **100**, 2393–2414.

Plomp, R. (**1988**). ''The negative effect of amplitude compression in multichannel hearing aids in light of the modulation-transfer function,'' J. Acoust. Soc. Am. **83**, 2322–2327.

Posen, M. P., Reed, C. M., and Braida, L. D. (**1993**). ''Intelligibility of frequency-lowered speech produced by a channel vocoder,'' J. Rehabil. Res. Dev. **30**, 26–38.

Rosen, S., Faulkner, A., and Wilkinson, L. (**1997**). ''Perceptual adaptation by normal listeners to upward shifts of spectral information in speech and its relevance for users of cochlear implants,'' in *Speech, Hearing, and Language: Work in Progress* (Phonetics and Linguistics, University College, London), Vol. 10.

Schroder, A. C., Viemeister, N. F., and Nelson, D. A. (**1994**). ''Intensity discrimination in normal-hearing and hearing-impaired listeners,'' J. Acoust. Soc. Am. **96**, 2683–2693.

Shannon, R. V., Adams, D. D., Ferrel, R. L., Palumbo, R. L., and Grantgenett, M. (**1990**). ''A computer interface for psychophysical and speech research with the Nucleus cochlear implant,'' J. Acoust. Soc. Am. **87**, 905–907.

Shannon, R. V., Zeng, F.-G., and Wygonski, J. (**1992**). ''Speech recognition using only temporal cues,'' in *The Auditory Processing of Speech: From Sounds to Words*, edited by M. E. H. Schouten (Mouton-DeGruyter, New York), pp. 263–274.

Stevens, S. S. (**1937**). ''On hearing by electrical stimulation,'' J. Acoust. Soc. Am. **8**, 191–195.

Stevens, S. S. (**1955**). ''The measurement of loudness,'' J. Acoust. Soc. Am. **27**, 815–829.

Stevens, S. S. (**1959**). ''Cross-modality validation of subjective scales for loudness, vibration, and electric shock,'' J. Exp. Psychol. **57**, 201–209.

Villchur, E. (**1974**). ''Simulation of the effect of recruitment on loudness relationships in speech,'' J. Acoust. Soc. Am. **56**, 1601–1611.

Wilson, B. S., Finley, C. C., Lawson, D. T., Wolford, R. D., Eddington, D. K., and Rabinowitz, W. M. (**1992**). ''New levels of speech recognition with cochlear implants,'' Nature (London) **352**, 236–238.

Zeng, F.-G., and Shannon, R. V. (**1992**). ''Loudness balance between electric and acoustic stimulation,'' Hearing Res. **60**, 231–235.

Zeng, F.-G., and Shannon, R. V. (**1994**). ''Loudness coding mechanisms inferred from electric stimulation of the human auditory system,'' Science **264**, 564–566.

Boundary-variation solutions for bounded-obstacle scattering problems in three dimensions

Oscar P. Bruno[a)]
Applied Mathematics, Caltech, Pasadena, California 91125

Fernando Reitich[b)]
School of Mathematics, University of Minnesota, Minneapolis, Minnesota 55455

(Received 17 December 1997; accepted for publication 6 July 1998)

Rigorous formalisms are presented for the numerical solution of problems of acoustic scattering by bounded obstacles in three dimensions. These methods are based on a perturbative technique recently demonstrated in problems of diffraction by gratings. Like those grating solvers, these new bounded-obstacle algorithms can produce highly accurate solutions for a wide variety of scattering geometries. © *1998 Acoustical Society of America.* [S0001-4966(98)02610-1]

PACS numbers: 43.20.−f, 43.20.Bi, 43.40.At [ANN]

INTRODUCTION

For several decades perturbation methods have been considered inadequate for the treatment of problems of wave scattering, and only few of the many discussions, mainly in the area of diffraction by gratings, are based on perturbative techniques. We have recently shown (Bruno and Reitich, 1992, 1993a, b, c) that grating diffraction can be successfully computed by appropriate uses of perturbation theory and analytic continuation. In this paper we extend our methods to problems of acoustic scattering by bounded-obstacles in three dimensions. Our new algorithms, which incorporate special functions and solutions for exactly solvable geometries, can produce results of high precision for a wide variety of configurations; see Sec. III.

Our methods result from analytic continuation of boundary perturbation expansions *of high order*. Both low- and high-order perturbative methods have been considered before, although the methods of this paper seem to be the first ones in the literature applicable to diffraction by three-dimensional bounded-obstacle scattering. Low-order approaches already occur in the work of Rayleigh (1945); see Wait (1971) for a more recent discussion. Such methods are only appropriate for small departures from exactly solvable geometries, and they cannot be applied to scatterers in the important resonance region, in which wavelengths are comparable to the size of the perturbations (Maystre and Nevière, 1978; Talbot *et al.*, 1990).

As for previous contributions on higher-order methods we mention those of Meecham (1956), Greffet and Maassarani (1990), and Lopez *et al.* (1978). The high-order approach of Meecham produces the scattering by a diffraction grating as a Neumann series whose nth term is given by an n-fold convolution of the Green's function. This method, which Meecham did not implement numerically, was thought to be mathematically incorrect (Uretsky, 1965) and dismissed. Later, Greffet and Maassarani studied these perturbations expansions and proposed that their convergence is tied with the validity of the Rayleigh hypothesis (Greffet and Maassarani, 1990, pp. 1488–1489); we now know (Bruno and Reitich, 1993b) that such a link does not exist. Lopez *et al.*, on the other hand, pointed out certain limitations in convergence in a perturbative approach for diffraction gratings. They proposed these limitations where caused by *poles* of the fields *in the negative real axis of the perturbation parameter plane*. As indicated below, we have proven that poles or other singularities do not occur anywhere in the real parameter axis. And, further, we have established that the observed limitations in convergence can be effectively overcome by use of adequate methods of analytic continuation.

The most comprehensive objection to perturbative approaches in this area is probably that of Uretsky (1965, p. 411), who conjectured that the fields scattered by a grating do not continue analytically to those of a flat interface. As a specific example of his conjecture, he proposed an infinite sinusoidal corrugation of a plane. Uretsky's conjecture was based on a certain integral expression, related to the fields, which appears to become meaningless as the groove depth takes on complex values. He thus suggested that series expansions in powers of the parameters controlling the shape of the scatterers could not be used in the solution of the corresponding scattering problems. As we have proved rigorously and demonstrated numerically, however, the field *does* vary analytically with respect to boundary variations (Bruno and Reitich, 1992).

We are not aware of any high-order treatments of bounded obstacle problems previous to the present work [our two-dimensional bounded-obstacle results were announced in the review (Bruno and Reitich, 1996)]. Unlike their periodic-grating counterparts, the three-dimensional bounded-obstacle algorithms require somewhat subtle numerical uses of special functions for numerical stability and reduced memory use. The results of this paper clearly establish the practicability of a perturbative approach for three-dimensional obstacle scattering, but the present algorithms have not been optimized in terms of computing time and memory use. Such issues will be addressed in forthcoming work. The means for such optimizations are simple: appropriate uses of higher-order integration (to compute Fourier

[a)]Electronic mail: bruno@ama.caltech.edu
[b)]Electronic mail: reitich@math.umn.edu

coefficients) and fast convolutions (to implement our recursive relations). Like our grating solvers, our new bounded obstacle algorithms can produce highly accurate solutions for a wide variety of scattering geometries. In particular, they provide an important source for accurate nontrivial three-dimensional benchmark solutions.

This paper is organized as follows: after setting our notation in the next section, we present, in Sec. II, derivations of the main recursive relations that form the basis of our method; numerical results then follow in Sec. III.

I. THEORETICAL BACKGROUND

We consider the Helmholtz equation

$$\Delta u + k^2 u = 0 \tag{1}$$

in the exterior of a three-dimensional bounded-obstacle Ω; hard and soft acoustic problems lead to boundary conditions of Dirichlet or Neumann type. Our explicit description of the analytic method and the corresponding numerical results below are restricted to the Dirichlet boundary condition

$$u = -u^{in} \quad \text{on} \quad \partial\Omega; \tag{2}$$

extensions to the Neumann and transmission problems are straightforward. Forthcoming numerical implementations for these cases as well as extensions to the full Maxwell system will be presented elsewhere.

Our algorithms are based on a theorem we established recently (Bruno and Reitich, 1992) of analyticity of the acoustic fields with respect to boundary variations. To describe our results let us assume Ω_δ is a family of scatterers, one for each value of the real parameter δ. Further, assume the boundaries Γ_δ of these obstacles admit parameterizations

$$\mathbf{r} = H(s, \delta), \tag{3}$$

where the function H is jointly analytic in the spatial variable s and the perturbation parameter δ. Our theorems state that both the values $v = v(\mathbf{r}, \delta)$ of the fields at a fixed point in space as well as the values at a point *on the varying boundary* depend analytically on the boundary variations. More precisely, if $\mathbf{r}$ is a point in space away from Γ_δ and $\mathbf{r}_\delta \in \Gamma_\delta$ is a point on the interface which varies analytically with δ, then $v(\mathbf{r}, \delta)$ is jointly analytic in $(\mathbf{r}, \delta)$, and $v(\mathbf{r}_\delta, \delta)$ is an analytic function of δ for all real values of δ for which the surface (3) does not self-intersect.

It follows from these theorems that the field can be expanded in a series in powers of δ

$$u(\mathbf{r}, \delta) = \sum_{n=0}^{\infty} u_n(\mathbf{r})\, \delta^n,$$

which converges for δ small enough, and that it can be continued analytically to all values of δ for which the surface (3) does not self-intersect. The fields u_n satisfy the Helmholtz equation as well as conditions of radiation at infinity. They also satisfy boundary conditions on $\Gamma_0 = \Gamma_\delta|_{\delta=0}$ which can be obtained by differentiation as we show in the following section. Such differentiations and use of the chain rule are permissible, as it follows from the analyticity theorems mentioned above and related extension theorems (Bruno and Reitich, 1992). The explicit solutions u_n lead easily to recursive formulae for the Taylor coefficients of the refracted amplitudes B; together with methods for analytic continuation, these formulae provide a numerical algorithm for the calculation of the scattered field.

II. RECURSIVE FORMULAE

In this section we derive the recursive formulas for the Taylor coefficients of the solution u of the Dirichlet problems (1) and (2). As discussed above, we shall view these as (large) perturbations of a sphere of radius a: in spherical coordinates (R, θ, ϕ) (θ = azimuthal angle and ϕ = polar angle) the boundary of the obstacle is given by

$$R = a + \delta f(\theta, \phi),$$

where f is an arbitrary function of (θ, ϕ) and $\delta \in \mathbb{R}$ is the perturbation parameter.

As is well known, the general solution of (1) satisfying the radiation conditions can be written in the form

$$u(R, \theta, \phi) = \sum_{r=0}^{\infty} \sum_{s=-r}^{r} B_{rs} h_r^{(1)}(kR) P_r^s(\cos(\theta)) e^{is\phi},$$

where P_r^s are the Legendre functions of the first kind and $h_r^{(1)}$ is the first spherical Hankel function of order r. As a function of the parameter δ then, we have

$$u(R, \theta, \phi; \delta) = \sum_{r=0}^{\infty} \sum_{s=-r}^{r} B_{rs}(\delta) h_r^{(1)}(kR) P_r^s(\cos(\theta)) e^{is\phi}.$$

It follows from our theory that the coefficients B_{rs} are analytic functions of δ for δ in a neighborhood of the real line. Thus, calling $d_{n,(r,s)}$ the nth Taylor coefficient of B_{rs}

$$B_{rs}(\delta) = \sum_{n=0}^{\infty} d_{n,(r,s)} \delta^n, \tag{4}$$

and denoting

$$u_n(R, \theta, \phi) = \sum_{r=0}^{\infty} \sum_{s=-r}^{r} d_{n,(r,s)} h_r^{(1)}(kR) P_r^s(\cos(\theta)) e^{is\phi} \tag{5}$$

we have, within the (nontrivial) radius of convergence,

$$u(R, \theta, \phi; \delta) = \sum_{n=0}^{\infty} u_n(R, \theta, \phi)\, \delta^n.$$

The Taylor coefficients $d_{n,(r,s)}$ can be computed recursively in n, starting with $d_{0,(r,s)}$ which correspond to the field scattered by an acoustically soft sphere of radius a (Bowman *et al.*, 1987, p. 358). In particular, for an incident wave propagating in the direction of the negative z-axis, we have $\mathbf{k} = (0,0,-k)$ and

$$d_{0,(r,s)} = -\frac{j_r(ka)}{h_r^{(1)}(ka)} A_{rs},$$

where

$$A_{rs} = \delta_{s,0}(2r+1)(-i)^r, \tag{6}$$

$\delta_{p,q}$ denotes the Kronecker delta and j_r is the spherical Bessel function of the first kind and order r.

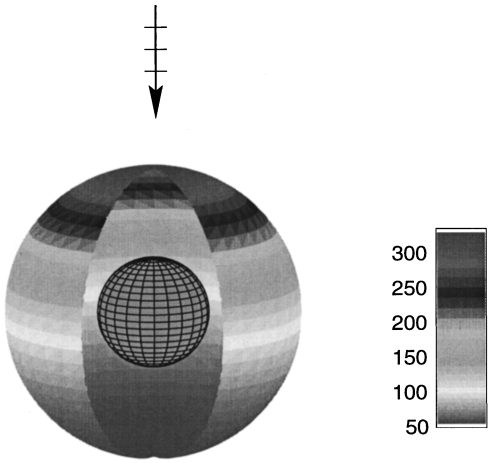

FIG. 1. Far field $4\pi|\Sigma_{r=0}^{\infty}\Sigma_{s=-r}^{r}(-i)^r B_{rs} P_r^s(\cos(\theta))e^{is\phi}|^2$ for the sphere. Parameters: $T=4$, $engytol=10$, $ka=1$.

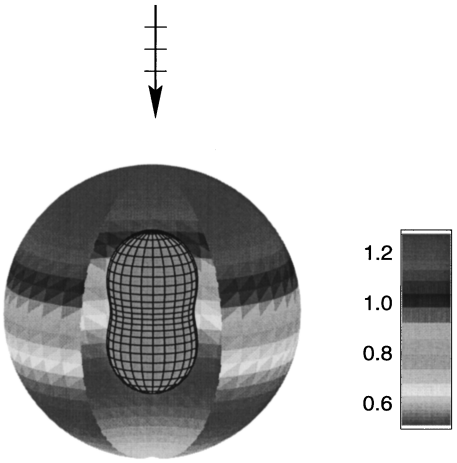

FIG. 2. Scatterer and far field; f defined as in Table I, $\delta=0.5$.

To obtain recursive relations we consider the boundary condition (2) with $u^{in}=e^{i\mathbf{k}\cdot\mathbf{r}}$. In view of the well known expansion (Bowman *et al.*, 1987) of the composite function $e^{-ikR\cos(\theta)}$ in terms of spherical harmonics, this boundary condition can be made to read

$$u(a+\delta f(\theta,\phi),\theta,\phi;\delta) = -\sum_{r=0}^{\infty}(2r+1)(-i)^r j_r(k(a+\delta f(\theta,\phi)))P_r^0(\cos(\theta)).$$

Numerically we will truncate the above expression at some order T

$$u(a+\delta f(\theta,\phi),\theta,\phi;\delta) = -\sum_{r=0}^{T}(2r+1)(-i)^r j_r(k(a+\delta f(\theta,\phi)))P_r^0(\cos(\theta));$$

the exact result is then obtained in the limit as $T\to+\infty$.

Differentiation gives

$$u_n(a,\theta,\phi) = -k^n\frac{f(\theta,\phi)^n}{n!}\sum_{r=0}^{T}(-i)^r(2r+1) \times\frac{d^n j_r}{dz^n}(ka)P_r^0(\cos(\theta)) -\sum_{l=0}^{n-1}\frac{f(\theta,\phi)^{n-l}}{(n-l)!}\frac{\partial^{n-l}u_l}{\partial R^{n-l}}(a,\theta,\phi). \quad (7)$$

We now let $f(\theta,\phi)$ be given by a series of spherical harmonics

$$f(\theta,\phi)=\sum_{p=0}^{F}\sum_{q=-p}^{p}C_{1,(p,q)}P_p^q(\cos(\theta))e^{iq\phi}$$

with either finite or infinite F. Then, substitution in (7) of u_l $(0\leqslant l\leqslant n)$ and their R-derivatives as calculated from (5) permits us to find all the coefficients $d_{n,(r,s)}$ in terms of the coefficients $d_{k,(p,q)}$ with $k<n$ and the Fourier series coefficients $C_{l,(p,q)}$ of the function $f(\theta,\phi)^l/l!$:

$$\frac{f(\theta,\phi)^l}{l!}=\sum_{p=0}^{lF}\sum_{q=-p}^{p}C_{l,(p,q)}P_p^q(\cos(\theta))e^{iq\phi}.$$

Indeed, from (7) we have

$$\begin{aligned}\sum_{r=0}^{\infty}\sum_{s=-r}^{r}d_{n,(r,s)}h_{0,r}P_r^s(\cos(\theta))e^{is\phi} &= -k^n\left(\sum_{p=0}^{nF}\sum_{q=-p}^{p}C_{n,(p,q)}P_p^q(\cos(\theta))e^{iq\phi}\right)\\ &\times\left(\sum_{r=0}^{T}(-i)^r(2r+1)j_{n,r}P_r^0(\cos(\theta))\right)\\ &-\sum_{l=0}^{n-1}\left(\sum_{p=0}^{(n-l)F}\sum_{q=-p}^{p}C_{(n-l),(p,q)}P_p^q(\cos(\theta))e^{iq\phi}\right)\\ &\times\left(\sum_{r=0}^{\infty}\sum_{s=-r}^{r}k^{(n-l)}d_{l,(r,s)}h_{n-l,r}P_r^s(\cos(\theta))e^{is\phi}\right), \quad (8)\end{aligned}$$

where we have put

$$j_{t,r}=\frac{d^t j_r}{dz^t}(ka)$$

and, similarly,

TABLE I. $f(\theta,\phi)=P_2^0(\cos(\theta))=\frac{3}{2}\cos^2(\theta)-\frac{1}{2}$. Parameters: $T=4$, $itol=40$, $ftol=40$, $engytol=10$, $ka=1$.

Padé	δ	$B_{0,0}$	Energy	ϵ (Taylor)	ϵ (Padé)
[5/5]	0.125	−0.681−0.433 i	1.645 368 5	3.3E-11	1.3E-11
[7/7]	0.125	−0.681−0.433 i	1.645 368 5	4.0E-16	6.7E-16
[5/5]	0.25	−0.659−0.407 i	1.633 693 6	3.5E-08	2.1E-08
[7/7]	0.25	−0.659−0.407 i	1.633 693 6	2.7E-10	1.1E-11
[5/5]	0.5	−0.620−0.344 i	1.704 360 1	4.4E-04	2.2E-05
[7/7]	0.5	−0.620−0.344 i	1.704 366 5	1.8E-05	7.4E-08
[5/5]	1.0	−0.514−0.223 i	2.101 361 4	3.9E-01	7.4E-03
[7/7]	1.0	−0.514−0.224 i	2.104 046 3	3.8E-01	2.5E-03

$$h_{t,r}=(d^t h_r^{(1)}/dz^t)\,(ka).$$

Then, upon expanding the products $P_r^s P_p^q$ as linear combinations of Legendre functions

$$P_r^s P_p^q=\sum_{j=0}^{r+p}\alpha_{r,s,p,q}^j P_j^{s+q},$$

we may write, from (8),

$$\sum_{r=0}^{\infty}\sum_{s=-r}^{r} d_{n,(r,s)} h_r^{(1)}(ka)P_r^s(\cos(\theta))e^{is\phi}$$

$$=-k^n\left(\sum_{r=0}^{T}\sum_{p=0}^{nF}\sum_{q=-p}^{p} C_{n,(p,q)}(-i)^r(2r+1)j_{n,r}\left(\sum_{j=0}^{r+p}\alpha_{r,0,p,q}^j P_j^q(\cos(\theta))e^{iq\phi}\right)\right)$$

$$-\sum_{l=0}^{n-1}\left(\sum_{r=0}^{\infty}\sum_{s=-r}^{r}\sum_{p=0}^{(n-l)F}\sum_{q=-p}^{p} C_{(n-l),(p,q)}k^{(n-l)}d_{l,(r,s)}h_{n-l,r}\left(\sum_{j=0}^{r+p}\alpha_{r,s,p,q}^j P_j^{q+s}(\cos(\theta))e^{i(q+s)\phi}\right)\right),$$

from which it follows that

$$\sum_{r=0}^{nF+T}\sum_{s=-r}^{r} d_{n,(r,s)}h_r^{(1)}(ka)P_r^s(\cos(\theta))e^{is\phi}$$

$$=\sum_{j=0}^{nF+T}\sum_{|q|\leqslant j}\left(-k^n\sum_{r=\max(0,j-nF)}^{T}(-i)^r(2r+1)j_{n,r}\sum_{p=\max(0,|q|,j-r)}^{nF}C_{n,(p,q)}\alpha_{r,0,p,q}^j\right)P_j^q(\cos(\theta))e^{iq\phi}$$

$$+\sum_{j=0}^{nF+T}\sum_{|q|\leqslant j}\left(-\sum_{l=0}^{n-1}\sum_{r=\max(0,j-(n-l)F)}^{lF+T}\sum_{s=-r}^{r}k^{(n-l)}d_{l,(r,s)}h_{n-l,r}\sum_{p=\max(0,|q-s|,j-r)}^{(n-l)F}C_{n-l,(p,q-s)}\alpha_{r,s,p,q-s}^j\right)P_j^q(\cos(\theta))e^{iq\phi},$$

where we have used

$$d_{l,(r,s)}=0 \quad \text{for } r>lF+T.$$

By uniqueness of the expansion in terms of spherical harmonics we finally obtain our recursive relations

$$\begin{aligned}h_{0,j}d_{n,(j,q)}=&-k^n\sum_{r=\max(0,j-nF)}^{T}(-i)^r(2r+1)j_{n,r}\\&\times\sum_{p=\max(0,|q|,j-r)}^{nF}C_{n,(p,q)}\alpha_{r,0,p,q}^j\\&-\sum_{l=0}^{n-1}\sum_{r=\max(0,j-(n-l)F)}^{lF+T}\sum_{s=-r}^{r}k^{(n-l)}d_{l,(r,s)}\\&\times h_{n-l,r}\sum_{p=\max(0,|q-s|,j-r)}^{(n-l)F}C_{n-l,(p,q-s)}\alpha_{r,s,p,q-s}^j.\end{aligned}\tag{9}$$

TABLE II. $f(\theta,\phi)=P_4^0(\cos(\theta))=\frac{1}{8}(35\cos^4(\theta)-30\cos^2(\theta)+3)$. Parameters: $T=4$, $itol=40$, $ftol=40$, $engytol=10$, $ka=1$.

Padé	δ	$B_{0,0}$	Energy	ϵ (Taylor)	ϵ (Padé)
[5/5]	0.125	−0.713−0.451 i	1.705 907 4	3.0E-06	2.6E-08
[5/5]	0.25	−0.725−0.439 i	1.750 421 7	7.7E-03	6.8E-06
[5/5]	0.5	−0.757−0.396 i	1.903 955 0	9.4E-01	8.0E-04
[5/5]	1.0	−0.798−0.282 i	2.308 688 7	9.9E-01	3.6E-02

III. NUMERICAL RESULTS

Our numerical method is based on evaluation of the Taylor coefficients (9) and subsequent summation of the Taylor series (4). Complete details on the summation strategies, which actually amount to *analytic continuation of the Taylor series beyond their radii of convergence*, can be found in Bruno and Reitich (1993a, b, c, 1994).

We present numerical results for the configurations of Figs. 2 to 4. The scatterers in these figures were obtained by perturbations from a sphere given by simple combinations of Legendre polynomials and exponentials. These choices of perturbation functions can be handled easily by the test algorithms that are implemented currently. As we said in the introduction, however, algorithms allowing for general perturbations can be obtained by appropriate uses of higher order integration (to compute Fourier coefficients) and fast convolutions (to implement our recursive relations); these extensions are forthcoming.

In Fig. 1 we present the far field scattered by a sphere, which will serve as a pattern of comparison in all of our

TABLE III. $f(\theta,\phi)=\frac{3}{8}\cos(\phi)\sin(\theta)(4-5\sin^2(\theta))$. Parameters: $T=4$, $itol=40$, $ftol=40$, $engytol=10$, $ka=1$.

Padé	δ	$B_{0,0}$	Energy	ϵ (Taylor)	ϵ (Padé)
[5/5]	1.0	−0.776−0.383 i	2.020 891 1	9.0E-01	1.6E-04
[5/5]	0.5	−0.730−0.435 i	1.785 330 5	2.5E-03	5.3E-07

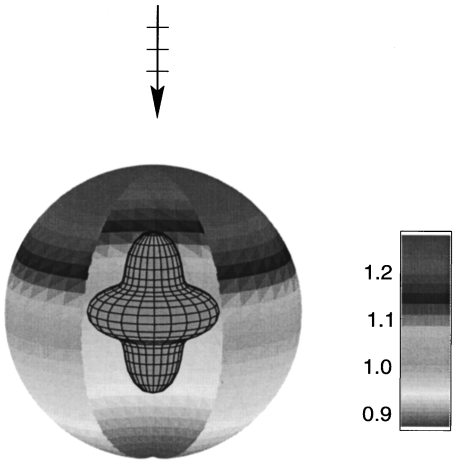

FIG. 3. Scatterer and far field; f defined as in Table II, $\delta=0.5$.

examples; the shading in the subsequent figures represents the far field *normalized* to that of the sphere. In Table I we present calculations and error estimates for the field scattered by the peanut-shaped scatterer of Fig. 2, and related variations of it. The parameter ϵ in this and subsequent tables is a convenient error estimator equal to the defect in the energy balance

$$\epsilon=\left|\sum_{l,q}\ \alpha_{l,q}|B_{l,q}|^2+Re\left(\sum_{l,q}\ \alpha_{l,q}\overline{A_{l,q}}B_{l,q}\right)\right| \Big/ \sum_{l,q}\ \alpha_{l,q}|B_{l,q}|^2, \tag{10}$$

which would vanish for an exact solution. The tabulated ''Energy'' value is $\Sigma_{l,q}\alpha_{l,q}|B_{l,q}|^2$; in these formulae the overbar denotes complex conjugate, $A_{l,q}$ is given by Eq. (6) and

$$\alpha_{l,q}=\frac{2(l+q)!}{(2l+1)(l-q)!}.$$

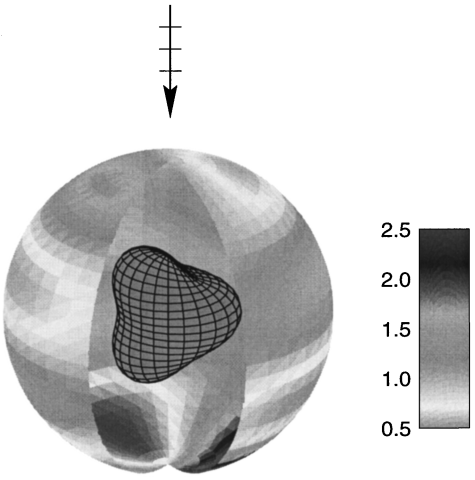

FIG. 4. Scatterer and far field; f defined as in Table III, $\delta=0.5$.

The quantities $itol$, $ftol$, and $engytol$, in turn, are truncation parameters for $d_{n,(p,q)}$, $C_{n,(p,q)}$ and the energy balance relation (10), respectively. That is, coefficients are set to zero for values of p and q beyond these respective tolerances; see Bruno and Reitich (1993a) for details on our truncation strategies. The values of the fields were obtained by means of direct summation of the Taylor series of the fields (Taylor) and by means of Padé approximation (Padé). Very accurate results have been obtained in these cases, as it is apparent from an examination of the error estimates in Table I. Similar considerations apply to the configurations considered in Figs. 3 and 4 and Tables II and III. We do note, however, that in these more complex examples Padé approximations provide substantial improvements over direct summation of the Taylor series.

ACKNOWLEDGMENTS

OB gratefully acknowledges support from NSF (through an NYI award and through Contracts No. DMS-9200002 and DMS-9523292), from the Sloan Foundation (through the fellowships program), from the AFOSR (Contract No. F49620-96-1-0008) and from the Powell Research Foundation. FR gratefully acknowledges support from AFOSR through Contract No. F49620-95-1-0113 and from NSF through Contract No. DMS-9622555.

Bowman, J. J., Senior, T. B. A., and Uslenghi, P. L. E. (**1987**). *Electromagnetic and Acoustic Scattering by Simple Shapes*, revised printing (Hemisphere, New York).

Bruno, O. P., and Reitich, F. (**1992**). ''Solution of a boundary value problem for Helmholtz equation via variation of the boundary into the complex domain,'' Proc. R. Soc. Edinburgh **122A**, 317–340.

Bruno, O. P., and Reitich, F. (**1993a**). ''Numerical solution of diffraction problems: A method of variation of boundaries,'' J. Opt. Soc. Am. A **10**, 1168–1175.

Bruno, O. P., and Reitich, F. (**1993b**). ''Numerical solution of diffraction problems: A method of variation of boundaries II. Dielectric gratings, Padé approximants and singularities,'' J. Opt. Soc. Am. A **10**, 2307–2316.

Bruno, O. P., and Reitich, F. (**1993c**). ''Numerical solution of diffraction problems: A method of variation of boundaries III. Doubly periodic gratings,'' J. Opt. Soc. Am. A **10**, 2551–2562.

Bruno, O. P., and Reitich, F. (**1994**). ''Approximation of analytic functions: A method of enhanced convergence,'' Math. Comput. **63**, 195–213.

Bruno, O. P., and Reitich, F. (**1996**). ''Calculation of electromagnetic scattering via boundary variations and analytic continuation,'' Appl. Comput. Electromagn. Soc. J. **11**, 17–31.

Greffet, J. J., and Maassarani, Z. (**1990**). ''Scattering of electromagnetic waves by a grating: a numerical evaluation of the iterative series solution,'' J. Opt. Soc. Am. A **7**, 1483–1493.

Lopez, C., Yndurain, F. J., and García, N. (**1978**). ''Iterative series for calculating the scattering of waves from a hard corrugated series,'' Phys. Rev. B **18**, 970–972.

Maystre, D., and Nevière, M. (**1978**). ''Electromagnetic theory of crossed gratings,'' J. Opt. **9**, 301–306.

Meecham, W. C. (**1956**). ''On the use of the Kirchoff approximation for the solution of reflection problems,'' J. Rat. Mech. Anal. **5**, 323–334.

Lord Rayleigh (**1945**). *The Theory of Sound*, Vol. 2 (Dover, New York).

Talbot, D., Titchener, J. B., and Willis, J. R. (**1990**). ''The reflection of electromagnetic waves from very rough interfaces,'' Wave Motion **12**, 245–260.

Uretsky, J. L. (**1965**). ''The scattering of plane waves from periodic surfaces,'' Ann. Phys. **33**, 400–427.

Wait, J. R. (**1971**). ''Perturbation analysis for reflection from two-dimensional periodic sea waves,'' Radio Sci. **6**, 387–391.

A spring model for the simulation of the propagation of ultrasonic pulses through imperfect contact interfaces

P. P. Delsanto and M. Scalerandi
INFM, Dipartimento di Fisica, Politecnico di Torino, C.so Duca degli Abruzzi 24, 10129, Torino, Italy

(Received 23 March 1998; accepted for publication 29 July 1998)

A spring model for the simulation of the propagation of ultrasonic pulses in arbitrarily complex heterogeneous media is proposed in the framework of the local interaction simulation approach (LISA). The algorithm used allows us to include heuristically additional local interaction mechanisms. In particular, the problem of propagation of pulses across imperfect contact interfaces is considered. A contact quality tensor, which is expected to be connected, although not necessarily in a trivial way, to the bond quality, is introduced directly into the model in order to treat interface flaws, such as delaminations and/or slipping bonds. To demonstrate the applicability of the technique, which is particularly suitable for parallel processing, a few examples of numerical simulation of pulse propagation in media with various kinds of imperfections are presented. [S0001-4966(98)02411-4]

PACS numbers: 43.20.−f [ANN]

INTRODUCTION

Interfaces play an important role in determining the performance of structural materials on a wide variety of dimension scales, from grain boundaries in metals, to interlaminar bonds in composites and adhesive bonds in a large variety of structures. In all cases, a basic goal of nondestructive evaluation is the determination of the integrity of bonds. In fact, several properties of materials, such as, just to make a couple of examples, the mechanical behavior under stress[1] or the ultrasonic reflection coefficient of the interface,[2] are very sensitive to boundary imperfections.[3]

A major problem in establishing efficient and reliable NDE techniques is the lack of a unique relationship between nondestructively measured parameters and interface mechanical properties. For instance, very different kinds of imperfections may lead to almost identical experimental data, especially as far as the reflectivity of the interface is concerned.[4] Moreover, different theoretical models must be used in order to predict the behavior of the interface, according to the specific kind of defect expected to be present. Combining the experimental information with the experience of previous destructive testings and/or of the processing/fabrication history, it is often possible to gain important information about the microstructure around the interface.

Likewise, other features, such as hysteretic properties of aggregated systems, may be relevant in the determination of the response to external excitations. Simple nonlinear models appear to be insufficient to fully predict the behavior of such materials. Better results have been obtained by combining the nonlinear properties with the hysteretic behavior.[5] However, a simple self-consistent model is still missing, due to the difficulties encountered in modeling the interactions among grains.

Ultrasonic techniques may be extremely valuable tools, e.g., in providing qualitative information on the details of interface flaws and bond quality.[3,6,7] In order to proceed to a more quantitative assessment, it is useful to analyze the experimental results by comparing them with theoretical calculations based on a realistic model. Purely analytical calculations are, however, usually not feasible, due to the extreme complexity of the problem. In fact, in most practical situations, features, such as strong heterogeneities, irregular boundary conditions, nonlinearities, etc., are present. Numerical solutions or, more often, computer simulations are then the tool of choice.

There exists a very extensive body of literature[8] on computer simulation techniques, and in particular on finite difference (FD) methods.[9] They usually yield very satisfactory solutions, except in the case of heterogeneous materials with a large impedance mismatch at the interfaces between different materials. Furthermore, they are generally restricted to the treatment of perfect contact interfaces.

To overcome these difficulties, a method, which is formally similar to FD techniques has been developed. This method, the local interaction simulation approach (LISA),[10–13] aims to a direct introduction of local interactions in the ultrasound propagation mechanism. Thus the problem of discontinuities at interfaces is solved by locally matching the relevant physical quantities, i.e., the particle displacements and stresses in the elementary case of linear media.

The purpose of this article is to describe a novel kind of spring model,[14] which is a spin-off of LISA, designed to extend the treatment to problems of noncontact or flawed interfaces and, after some additional modifications, to attenuative, nonlinear, hysteretic media and even to the plastic regime. The spring model, as the name implies, substitutes the problem of ultrasonic pulse or wave propagation in a medium with the ''analog'' problem of exciting an equivalent set of ''tensorial springs.'' The method is stable and convergent as long as the equivalence between the two problems is justified. It is also easily parallelizable and therefore amenable to parallel processing.[15]

In Sec. I the spring model is introduced (i.e., the equivalence justified) for the 1-D case. The 1-D case is, of course, very elementary. Nevertheless, it is included because it al-

lows us to define in a very natural way the ingredients (external and internal springs, contact quality factor), which can later be extended to 2D in Sec. II. An extension to 3D is straightforward, but omitted here for brevity. In order to illustrate the applicability of the model, three cases of vertical delamination, vertical slippage and rhomboidal slippage are presented in Sec. III, both for a homogeneous medium and for the interface of a bilayer.

I. THE ONE-DIMENSIONAL CASE

A. Propagation along a homogeneous rod

A propagation medium may be considered as one-dimensional if it enjoys transverse symmetry. In our treatment, for simplicity, we start assuming as propagation medium a homogeneous rod of unit cross sectional area and we discretize it as a 1-D grid. Each gridpoint (or node) represents a tiny segment of rod, which we shall call a ''cell,'' of length ϵ and mass $m=\rho\ \epsilon$ centered upon the node. Each node acts on its two neighbors $i\pm1$ with forces $F_i^{\pm}$ given by the elastodynamic equations

$$F_i^{\pm}=\tau_i^{\pm}=S\,\eta_i^{\pm}=S(u_{i\pm1}-u_i)/\epsilon, \tag{1}$$

where $\tau_i^{\pm}$ is the stress on each of the two cell interfaces, S represents the material stiffness and $\eta_i^{\pm}$ the deformation and u_i the node displacement from its equilibrium position.

Thus the grid may be replaced by a system of springs with rest lengths ϵ and elastic constants S/ϵ. From the equation of motion

$$m\ \ddot{u}_i=F_i^{+}+F_i^{-} \tag{2}$$

for each node i, we easily obtain, by discretizing the time and applying the usual FD formalism,[9] the iteration equation

$$u_i^{t+1}=2u_i^t-u_i^{t-1}+c(u_{i+1}^t+u_{i-1}^t-2u_i^t), \tag{3}$$

where

$$c=\frac{\delta^2 S}{\rho\epsilon^2} \tag{4}$$

is the square of the so-called Courant's number and δ is the unit time step. The value of c may be chosen almost at will by varying the ratio δ/ϵ. The problem of convergence and stability of Eq. (3) is discussed in Ref. 10. It turns out that the best choice is $c=1$.

B. Heterogeneous rod. Perfect contact at junctions

Let us now assume that the rod is no longer homogeneous and that, e.g., an interface located at the node i separates two regions of different physical properties S^-,ρ^- and S^+,ρ^+ at the left and at the right side of the node, respectively. If there is perfect (or rigid) contact between the two regions, we split the node i into two infinitely close subnodes $(i)^+$ and $(i)^-$, each representing a half cell, of length ϵ^- and ϵ^+ and mass $m^-=1/2\rho^-\epsilon^-$ and $m^+=1/2\rho^+\epsilon^+$, respectively. We then assume (see Fig. 1) that, besides the ''external'' forces given by Eq. (1), two ''internal'' forces $f_i^{\pm}$ act on the two subnodes in order to keep them together:

$$\ddot{u}^-=\ddot{u}^+=\ddot{u}^{cm}, \tag{5}$$

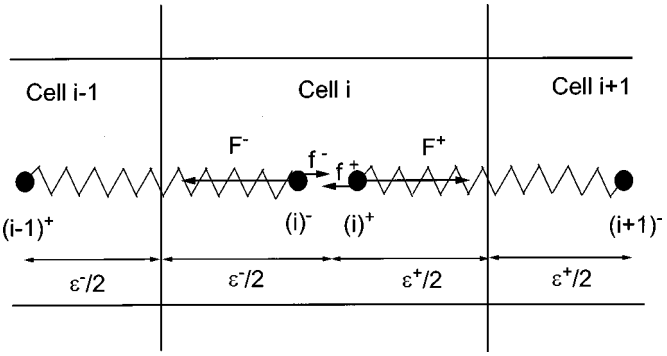

FIG. 1. Splitting of the node i into two subnodes $(i)^+$ and $(i)^-$ and representation of the external and internal forces.

where the center of mass acceleration $\ddot{u}^{cm}$ is given by

$$\ddot{u}^{cm}=\frac{m^-\ddot{u}^-+m^+\ddot{u}^+}{m^++m^-}=\frac{F^++F^-}{m^++m^-}. \tag{6}$$

In Eqs. (5) and following ones we omit the superscript t and subscript i for brevity. Also we assume, in Eq. (6), that the internal forces are equal and opposite: $f^+=-f^-$. From the equations of motion for the two subnodes

$$m^{\pm}\ddot{u}^{\pm}=F^{\pm}+f^{\pm} \tag{7}$$

and from Eqs. (5) and (6) it follows that

$$f^+=-f^-=\frac{m^+F^--m^-F^+}{m^++m^-}. \tag{8}$$

C. Imperfect contact

Let us finally assume that the contact between the two regions at the interface may be imperfect. Then we assume that the internal forces are still equal and opposite, but no longer given by Eq. (8), since the two subnodes may acquire some additional degree of freedom. In this case we introduce a parameter Q in the model, to characterize the contact quality at the interface and write the internal forces as

$$f^{\pm}=Q\ f_{\rm pc}^{\pm}, \tag{9}$$

where $f_{\rm pc}^{\pm}$ represent the internal forces in the case of perfect contact, as given by the right-hand side of Eq. (8). The contact quality parameter Q may vary from the value $Q=0$ (delamination or crack) to the perfect contact value $Q=1$. The bond quality is expected to be connected, although not necessarily in a trivial way, to the contact quality, depending on the physical parameters of the system.

The iteration equations may then be easily obtained:

$$(u^{\pm})^{t+1}=-(u^{\pm})^{t-1}+2u^{\pm}+2c^{\pm}(u_{\pm1}-u^{\pm}) + Q\ t^{\mp}[-c^{\pm}(u_{\pm1}-u^{\pm})+c^{\mp}(u_{\mp1}-u^{\mp})], \tag{10}$$

where

$$c^{\pm}=\frac{\delta^2 S^{\pm}}{(\epsilon^{\pm})^2\rho^{\pm}},\quad t^{\pm}=\frac{2\rho^{\pm}\epsilon^{\pm}}{\rho^+\epsilon^++\rho^-\epsilon^-}, \tag{11}$$

and

$$u_{\pm1}=u_{(i\pm1)}^{\mp}. \tag{12}$$

Equation (10) becomes somewhat simplified if, in order to obtain optimal conditions of convergence and stability, ϵ^+ and ϵ^- are chosen to yield $c^{\pm}=1$. Then we can define the impedance (after and before the interface, respectively) as

$$Z^{\pm}=\sqrt{\rho^{\pm}S^{\pm}}=\frac{1}{\delta}\epsilon^{\pm}\rho^{\pm} \tag{13}$$

and, as a consequence,

$$t^{\pm}=\frac{2Z^{\pm}}{Z^{+}+Z^{-}}=1\pm r, \tag{14}$$

where

$$r=\frac{Z^{+}-Z^{-}}{Z^{+}+Z^{-}}. \tag{15}$$

Equation (10) then becomes

$$\begin{aligned} u^{t+1}&=-u^{t-1}-2rQ\Delta+(1+rQ)u_{+1}+(1-rQ)u_{-1},\\ \Delta^{t+1}&=-\Delta^{t-1}+2Q\Delta+(1-Q)(u_{+1}-u_{-1}), \end{aligned} \tag{16}$$

where $u_{\pm}$ are still defined through Eq. (10) and

$$u=\tfrac{1}{2}(u^{+}+u^{-}),\quad \Delta=\tfrac{1}{2}(u^{+}-u^{-}). \tag{17}$$

In the perfect contact case ($Q=1$), $\Delta=0$ and Eq. (16) becomes

$$u^{t+1}=-u^{t-1}+t^{+}u_{+1}+t^{-}u_{-1}, \tag{18}$$

in agreement with Eq. (2.3) of Ref. 10. Here t^+ and t^- are the transmission coefficients for the displacement in the forward and backward directions, respectively, and r is the reflection coefficient.

D. A model for the internal forces

To conclude the section, it might be useful to attempt a physical interpretation for the internal forces $f^{\pm}$. If we assume that, at the time $t=0$, $u^+=u^-$ and $\dot{u}^+=\dot{u}^-$, from Eqs. (7)–(9) it follows that after a time step δ

$$2\Delta=\frac{1}{2}(\ddot{u}^{+}-\ddot{u}^{-})\delta^2=\frac{(1-Q)f^{-}\delta^2}{2\mu Q}, \tag{19}$$

where

$$\mu=\frac{m^{+}m^{-}}{m^{+}+m^{-}}. \tag{20}$$

We then consider the region (i^-,i^+) as an elastic rod of unit cross section, restlength $\eta\ll\epsilon$ and Young's modulus E. The tiny rod is subject to two concurrent stresses (both in- or outward) f^+ and f^- and to a deformation $2\Delta/\eta$. Then

$$E=\frac{|f^{+}|+|f^{-}|}{2|\Delta|/\eta}=\frac{2\mu Q\eta}{(1-Q)\delta^2}. \tag{21}$$

Since μ, η, and δ are all infinitesimal of the same order, E has a finite value if $0<Q<1$. If $Q\to 1$, $E\to\infty$ and the rod is totally rigid, thus securing a perfect contact at the node i, as expected.

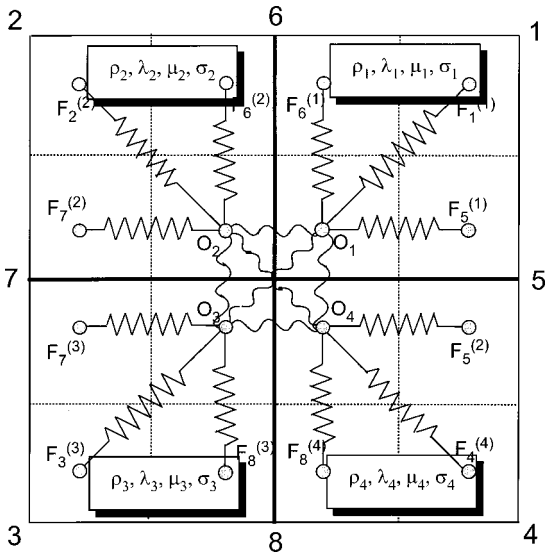

FIG. 2. Representation of the external and internal ''spring'' forces in 2D.

II. THE TWO-DIMENSIONAL CASE

A. Perfect contact

A propagation medium may be considered as two-dimensional if it enjoys translational symmetry with respect to a given direction (e.g., the z axis). As an example we consider a material plate of unit thickness and discretize it as a 2-D grid. To consider the most general heterogeneous case, we assume that the physical properties may vary in the lattice from cell to cell, being constant, however, within each cell. We assume, for simplicity, that the material has cubic symmetry and call ρ_{ij} the density of a generic cell (i,j), σ_{ij}, λ_{ij} and μ_{ij} its elastic constants, corresponding to the cell stiffness components S_{kkkk}, S_{kkll}, S_{klkl} $(k,l=1,3)$, respectively.

In order to simulate the propagation, we consider a crosspoint $O\equiv(i,j)$ at the intersection between two interfaces separating four different materials, whose physical properties we shall label ρ_k, λ_k, μ_k, σ_k, $k=1,4$: see Fig. 2. Following the treatment of the 1-D case in Sec. I, we split the crosspoint (i,j) into four subnodes O_k, each representing a quarter cell in the corresponding quadrant.

For the purpose of simulating the propagation of an ultrasonic wave or pulse, it is possible to prove that the plate is equivalent, in the limit $\epsilon\to 0$, to a system of external and internal springs. The external springs propagate the disturbance of the source pulse throughout the whole grid. Extending to 2D the procedure developed in the Introduction and based on the FD formalism, it is straightforward to obtain an explicit expression for the spring forces $\overline{F}_n^{(k)}$ connecting the subnode O_k to its ''nearest neighbor'' nodes n

$$\overline{F}_n^{(k)}=M_n^{(k)}\Delta w_n, \tag{22}$$

where

$$M_n^{(k)}=\begin{pmatrix} 0 & \psi_k\\ \psi_k & 0\end{pmatrix}\quad (n=k=1,2,3,4),$$

$$M_n^{(k)}=\begin{pmatrix} \frac{1}{2}\sigma_k & -\chi_k \\ \chi_k & \frac{1}{2}\mu_k \end{pmatrix} \quad (n=5,\ k=1,4;\ n=7,\ k=2,3), \tag{23}$$

$$M_n^{(k)}=\begin{pmatrix} \frac{1}{2}\mu_k & \chi_k \\ -\chi_k & \frac{1}{2}\sigma_k \end{pmatrix} \quad (n=6,\ k=1,2;\ n=8,\ k=3,4),$$

and

$$\begin{aligned} &\Delta w_n = w_n - w_0, \\ &\psi_k = (-)^{k+1}(\lambda_k+\mu_k)/4, \\ &\chi_k = (-)^{k+1}(\lambda_k-\mu_k)/4. \end{aligned} \tag{24}$$

Finally

$$w_n=\begin{pmatrix} u_n \\ v_n \end{pmatrix} \tag{25}$$

is the displacement vector of the node n.

If there is perfect contact, the six internal ''springs'' keep the set of four subnodes rigid, as discussed in the next subsection. Calling $\overline{f}_{kl}$ the internal forces connecting the subnodes O_k and O_l, we assume that

$$\overline{f}_{kl}=-\overline{f}_{lk}.$$

Thus from the equation of motion applied to the set of the four subnodes, one obtains, after a time discretization (with time unit δ),

$$w_{t+1}=2w-w_{t-1}+\frac{\delta^2}{\overline{\rho}\,\epsilon^2}\sum_{n,k} M_n^{(k)}\Delta w_n, \tag{26}$$

where

$$\overline{\rho}=\frac{1}{4}\sum_{k=1}^{4}\rho_k.$$

In Eq. (26) we have omitted for brevity the time and/or space subscripts whenever corresponding to the ''current'' time t or to the node O under consideration. We also note that the masses of the four subcells are $\frac{1}{4}\rho_k\epsilon^2$ $(k=1,4)$, since they have the same volume $\frac{1}{4}\epsilon^2$. Equation (26) is equivalent to Eq. (3.18) in Ref. 11.

B. Imperfect contact

In the previous subsection the purpose of splitting the node O into four subnodes was solely due to the need of calculating the spring forces inside a homogeneous region. Thus the forces along the interfaces were split into two separate forces, on either side of the corresponding interface. Following the treatment of the 1-D case in Sec. I, we show here that such a splitting has far more outreaching consequences, since it leads to a natural treatment of imperfect contact interfaces.

In order to maintain the set of four subnodes rigid, as required in the previous subsection, it is necessary that the acceleration of each subnode be equal to the acceleration of their center-of-mass

$$\ddot{w}_k=\ddot{w}_{CM}=\frac{1}{\overline{\rho}\,\epsilon^2}\sum_{l=1}^{4}\overline{F}^l \quad (k=1,4), \tag{27}$$

where $\overline{F}^l$ is the resultant of the three forces $\overline{F}_n^{(l)}$ directly applied to the subnode l: see Fig. 2.

Equations (27) may be easily satisfied if, by a straightforward generalization of Eq. (8), the internal forces are chosen to be given by

$$\overline{f}_{kl}=\frac{\rho_k\overline{F}^l-\rho_l\overline{F}^k}{4\overline{\rho}}. \tag{28}$$

Then, in analogy with the 1-D case [Eq. (9)], we may extend our model to the treatment of imperfect interfaces by defining a contact quality tensor Q_{kl} for each node O through the relationship

$$\overline{f}_{kl}=Q_{kl}\,\overline{f}_{kl}^{(\mathrm{pc})}, \tag{29}$$

where $\overline{f}_{kl}^{(\mathrm{pc})}$ are the internal forces for the perfect contact case, as given by the right-hand side of Eq. (28). Of course in such a case $Q_{kl}=1$, for each k and l.

By varying the values of the various components of the contact quality tensor between 0 and 1, one may model a large variety of interface imperfections. Some of them will be considered in the next section. Furthermore, without any increase of computer time, due to the parallel processing of the simulation, the contact quality tensor may vary arbitrarily from node to node and even be different for the x and y components of the internal forces.

C. The iteration equations

In the case of imperfect contact interfaces the iteration equations must be run independently for all the subnodes, rather than for all the nodes. Their expressions are

$$w_{t+1}^{(k)}=2w^{(k)}-w_{t-1}^{(k)}+\frac{\delta^2}{\overline{\rho}\,\epsilon^2}\left(\overline{F}^k+\sum_{l\neq k}\overline{f}_{kl}\right) \quad (k,l=1,4), \tag{30}$$

where the subscript k denotes the subnode being considered. It should be mentioned, for completeness, that in the expression of the forces $\overline{F}_n^{(k)}$ [see Eq. (22)], included in the forces $\overline{F}^k$, and $\overline{f}_{kl}$, Δw_n must be replaced by the difference between the displacement of the subnode of the node n, closest to the subnode k of O, and the displacement of the latter subnode.

Extending the discussion carried on in Subsection I D to the 2-D case, it is possible to give a more specific physical interpretation to the internal forces. We omit the corresponding discussion for brevity. We limit ourselves to remark here that both the external and internal forces do not represent real springs, in which the force is proportional to the actual distance between subnodes, but rather ''tensorial springs,'' in which the x and y components of the force depend on the corresponding components of their distance.

III. RESULTS AND DISCUSSION

In the case of perfect contact interfaces, the reliability of the spring model has been verified both through a comparison with available analytical results (reflection of a plane

wave from the interface between two different media[11]) and with experimental results (e.g., the scattering of a Gaussian pulse from a circular inclusion[16]). Also, the effects of a delamination, as modeled in the present context, have been compared with the effects of a column of void cells.[17] Provided that the column is sufficiently thin, the two treatments (spring model and LISA) yield very similar results, while differences emerge when the thickness of the column is not negligible.

In this section, we analyze the effects of various kinds of interface flaws, defined as gridpoints in which some of the components of the contact quality tensor Q_{kl} are different from 1. In order to separate them from other reflection or mode-conversion effects, we have considered the propagation of a longitudinal plane wave in a homogeneous Al plate, discretized by means of a 350×300 grid. For the elastic constants we have assumed the values $\lambda=56$ GPa, $\mu=26$ GPa, $\sigma=108$ GPa, and for the density $\rho=2100$ kg/m^3. An imperfection (to be specified later) has been introduced at $i=150$ and $j=148,149,150,151,152$ and the wave has been injected from the left side of the specimen.

In the particular case under consideration, due to the symmetry of the problem, only three kinds of basic flaws are significantly different in the proposed model. An arbitrary flaw may be regarded as a combination thereof:

(a) vertical delamination, affecting one or more cells, for which $Q_{12}=Q_{13}=Q_{24}=Q_{34}=0$. In correspondence with such a region, the two sides of the interface vibrate independently. Kissing bonds may be treated as special instances of vertical delaminations by setting $Q_{12}=Q_{13}=Q_{24}=Q_{34}=0$, when the interface is in tension $Q_{12}=Q_{13}=Q_{24}=Q_{34}=1$ when it is in compression;

(b) vertical slippage, defined, e.g., by $Q_{12}=0$. This interface flaw introduces an element of anisotropy in the contact.[18] The bond retains full strength along the interface, but not across it;[19]

(c) rhomboidal slippage, defined, e.g., by $Q_{13}=0$, describing a different kind of anisotropy.

All the other Q_{kl} are, in the three cases, equal to 1. The three cases are represented, in Figs. 3, 4, and 5, respectively, by three snapshots at different times ($t=180$, 240, and 300 a.u.) of both the amplitude field (left plots) and the y component (v) of the displacement (right plots). In all the plots, lighter tones denote larger displacements. However, regions of zero displacement are represented in black in the left plots, while they are in gray in the right plots, in which darker tones represent regions with negative values of v.

Figure 3 shows the effect of a vertical delamination [case (a)]. Since the defect is small, the incident longitudinal plane wave propagates almost undisturbed (thick white stripe moving to the right in the left plots). However, the effect is quite noticeable in the reflected wave, which reaches an amplitude of almost 20% of the incident wave. In fact, a delamination behaves as a source of almost symmetrical spherical waves, which create a quite conspicuous interference pattern. In addition there is generation, by mode conversion, of shear

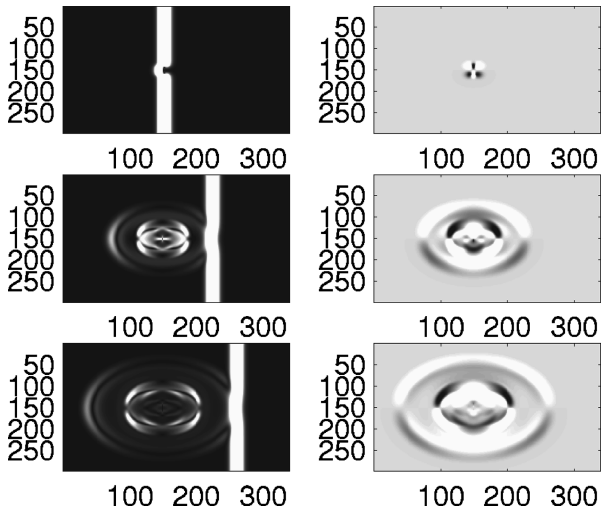

FIG. 3. Snapshots at different times of the wave amplitude (left column) and its y-component (right column) for a longitudinal plane wave propagating in a homogeneous plate with a delamination in its center ($i=150$, $145<j<155$).

waves (v components) of opposite sign between top and bottom (see right plots), accompanied by reconversion to longitudinal modes, since the tips of the defects behave as point sources of shear waves. The behavior of reflected waves is in good qualitative agreement with experimental findings.[20]

Figure 4 shows the effect of a vertical slippage flaw [case (b)]. Again the incident plane wave propagates almost undisturbed, with a noticeable, but much smaller reflected wave (about 4% of the incident wave) and a generation by mode conversion of shear waves. The strong anisotropy of the problem is clearly visible, particularly in the bottom plots, where a vertical shift of the two spherical waves generated by the tips of the flaw is evident, with opposite signs of the amplitude of the mode converted shear waves.

Figure 5 shows the effect of a rhomboidal slippage [case (c)]. The results are similar to those obtained in the previous

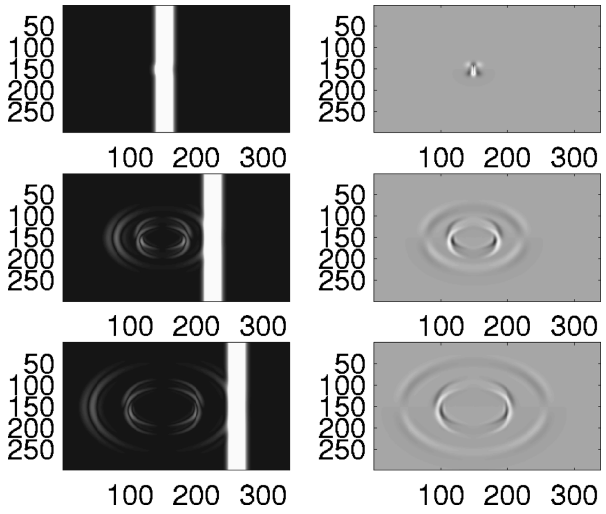

FIG. 4. Snapshots at different times of the wave amplitude (left column) and its y-component (right column) for a longitudinal plane wave propagating in a homogeneous plate with a vertical slippage in its center ($i=150$, $145<j<155$).

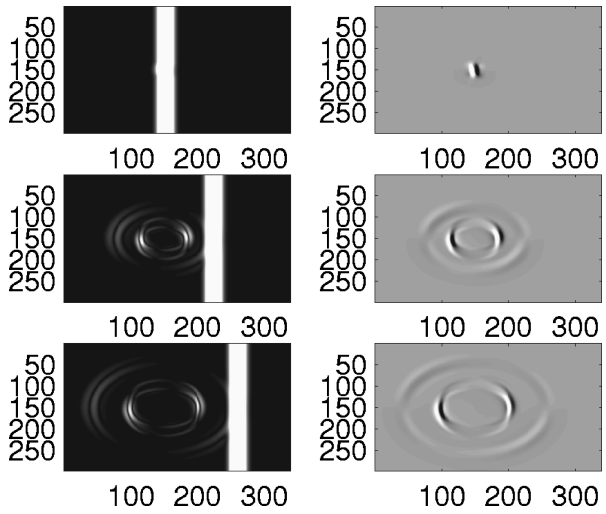

FIG. 5. Snapshots at different times of the wave amplitude (left column) and its y-component (right column) for a longitudinal plane wave propagating in a homogeneous plate with a rhomboidal slippage in its center ($i=150$, $145<j<155$).

case, but with an even stronger anisotropy effect. The wavefront is no longer quasi-spherical and the propagation direction of the generated waves, once they are far enough from the defect, is clearly in a diagonal upward direction. Again the reflected wave has an amplitude of a few per cent of the incident wave.

In order to quantify the effects, we have used a different representation in Fig. 6. We report, for the three cases considered above, the total amount R of reflected wave

$$R=\sum_{i<150}\sum_{j}\sqrt{u_{ij}^2+v_{ij}^2},$$

and the difference A between the wave reflected in the upper and lower quadrant

$$A=\frac{\Sigma_{i<150}(\Sigma_{j<150}\sqrt{u_{ij}^2+v_{ij}^2}-\Sigma_{j>150}\sqrt{u_{ij}^2+v_{ij}^2})}{R},$$

versus time in Fig. 6(a) and (b), respectively. The first quantity provides a quantitative information about the intensity of the effect, while the second defines the anisotropy in the reflection. We see that the reflection effect is very strong and completely isotropic in case (a), much smaller and anisotropic in cases (b) and (c). In the latter cases, the amount of

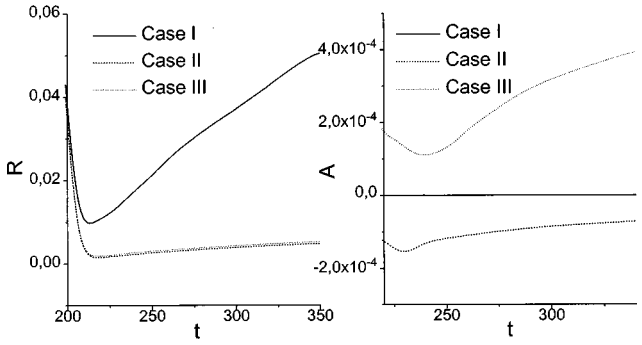

FIG. 6. Amount R of reflected wave (left plot) and anisotropy A (right plot) versus time for the three cases of imperfect contact.

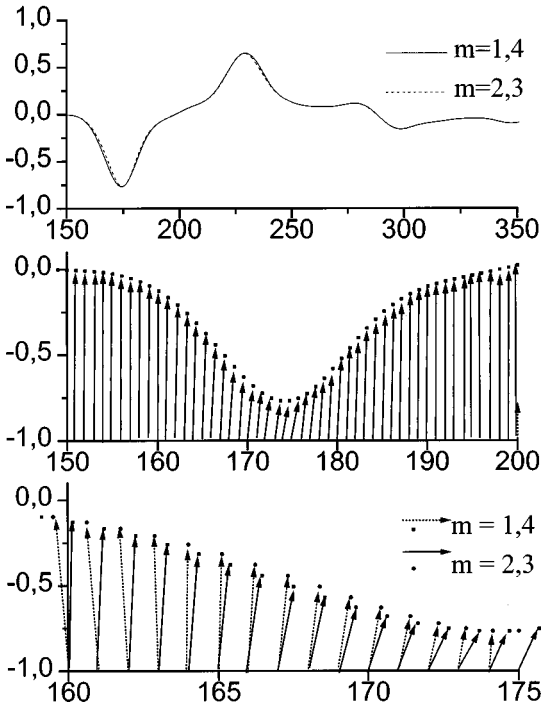

FIG. 7. Vectorial representation versus time of the displacements of the four subnodes m of the node $i=150$, $j=150$ in the case of a rhomboidal delamination.

reflection is virtually the same, but the anisotropy effect is of opposite sign. In case (b), the anisotropy is mainly due to a different generation mechanism at the upper and lower tips of the defect and decreases going farther away from it. Case (c) displays the opposite behavior, since the generated waves seem to have a strong directionality in the propagation direction, with a consequent increment of anisotropy with time.

The main feature of the spring model, as we have described it, is the possibility for the four subnodes to move independently. To show this effect, we have reported in Fig. 7 the vectors representing the displacements in the case (c) of the four subnodes corresponding to the node (150, 150). Due to the symmetry of the defect, the subnodes 1 and 2 behave as the subnodes 4 and 3, respectively. In Fig. 7(a), we have plotted the y components of the displacements vs $t+u$, where t denotes the number of time steps and u the x component of the displacement. The two subnodes oscillate almost completely in-phase, with the small differences rapidly averaging out. In Fig. 7(b), we have zoomed into the region $150<t<200$, and reported the vectors describing the displacements of the subnode 1. In Fig. 7(c), an additional zooming is performed and the motion of the subnodes 1 and 2 compared, showing a large difference in their motion.

In Fig. 8 we have considered the propagation of a longitudinal Gaussian pulse

$$u(0,j)=A\ \exp(-(j-j_{\max}/2)^2/\sigma_j^2)\exp(-(t-t_0)^2/\sigma_t^2),$$

in an Al–Plexiglas bilayer. From top to bottom, the three cases of perfect contact, vertical delamination and rhomboidal slippage have been considered at the interface separating the two materials. In the upper plot the incident, transmitted and reflected waves are visible in the neighborhood of the interface. Also, a mode-converted component, traveling at a

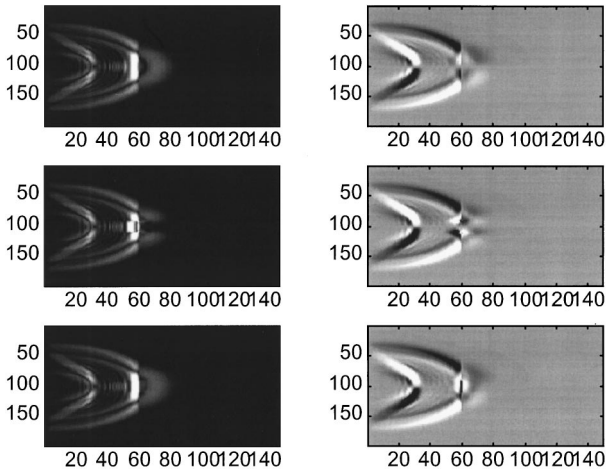

FIG. 8. Snapshots of the wave amplitude (left column) and its y component (right column) for a longitudinal gaussian pulse propagating in an Al–Plexiglas bilayer with perfect contact (upper plots), delamination (middle plots) and rhomboidal slippage (lower plots) at the interface ($i=60$).

lower velocity, is visible and has not yet reached the interface. In the middle and lower plots, superimposed to the usual reflection and transmission patterns, we may observe distortions introduced by the presence of the imperfections at the interface. Such effects are similar to the ones observed in the case of the corresponding flaws in a homogeneous plate. They consist mainly of a shadow effect for the delamination and the generation of anisotropic components for the rhomboidal slippage. Interface waves may be also observed along the delamination, particularly in the upper two snapshots in the left column. However, the incidence angle does not allow the formation of a clear pattern of Stoneley waves along the interface.[11,16]

IV. CONCLUSIONS

We have presented a heuristic derivation, based on a spring model, of the iteration equations for the simulation of the wave propagation in arbitrarily complex media. The method consists in the discretization of the propagation medium into cells represented by gridpoints, each split into four subnodes, connected through ''tensorial springs.'' When the spring constants are properly defined, the spring model represents a good approximation (compared with usual experimental errors) of the propagation medium under study and it ensures convergence.

The model has been applied to the case of both sharp and imperfect contact interfaces. Additional internal ''spring'' forces have been introduced among the subnodes, belonging to the same node, allowing a higher degree of freedom in the description of the interface. In particular, a tensorial parameter Q is introduced to characterize the contact quality. A proper definition of Q as a function of the physical properties of the two materials in contact may be included in order to simulate different bonds. Several numerical results have been presented to illustrate, by varying the Q components, the effects on the pulse propagation of various interface flaws, such as delamination and vertical or rhomboidal slippage.

Due to its local nature, the model can be easily extended to include other physical properties of the propagation medium, such as hysteresis and/or attenuativity[21] or to describe the plastic regime. In fact, both the spring constants and the contact quality tensor may be modified to introduce additional features into the model (e.g., by considering nonlinear springs or including imaginary components).

ACKNOWLEDGMENTS

This work has been partly supported by the EC Program Copernicus No. ERBCIPACT940132 and by the Comitato Nazionale Ricerche through Grant No. 96.01826.CT11. In addition the authors wish to thank Dr. N. K. Batra and Dr. R. B. Mignogna (Materials Branch, Naval Research Laboratory, Washington, DC) for fruitful discussions.

[1] P. P. Delsanto and A. V. Clark, ''Rayleigh wave propagation in deformed orthotropic materials,'' J. Acoust. Soc. Am. **81**, 952–960 (1987).
[2] A. Pilarski and J. L. Rose, ''A transverse-wave ultrasonic oblique-incidence technique for interfacial weakness detection in adhesive bonds,'' J. Appl. Phys. **63**, 300–307 (1987).
[3] P. Nagy, ''Ultrasonic classification of imperfect interfaces,'' J. Nondestruct. Eval. **11**, 127–139 (1992).
[4] F. J. Margetan, R. B. Thompson, J. H. Rose, and T. A. Gray, ''The interaction of ultrasound with imperfect interfaces: Experimental studies of model structures,'' J. Nondestruct. Eval. **11**, 109–126 (1992); A. Bostrom, P. Bovik and P. Olsson, ''A comparison of exact first order and spring boundary conditions from scattering by thin layers,'' J. Nondestruct. Eval. **11**, 175–184 (1992).
[5] K. E-A. Van Den Abeele, P. A. Johnson, R. A. Guyer, and K. R. McCall, ''On the quasi-analytic treatment of hysteretic nonlinear response in elastic wave propagation,'' J. Acoust. Soc. Am. **101**, 1885–1898 (1997).
[6] R. S. Schechter, R. B. Mignogna, and P. P. Delsanto, ''Ultrasonic tomography using curved ray paths obtained by wave propagation simulations on a massively parallel computer,'' J. Acoust. Soc. Am. **100**, 2103–2111 (1996).
[7] P. P. Delsanto, A. Romano, M. Scalerandi, and F. Moldoveanu, ''A genetic algorithm approach to ultrasonic tomography,'' J. Acoust. Soc. Am. **104**, 1374–1381 (1998).
[8] N. Bellomo and L. Preziosi, *Modelling Mathematical Methods and Scientific Computation* (CRC, Boca Raton, FL, 1995).
[9] J. C. Strickwerda, *Finite Difference Schemes and Partial Differential Equations* (Wadsworth-Brooks, New York, 1989).
[10] P. P. Delsanto, T. Whitcombe, H. H. Chaskelis, and R. B. Mignogna, ''Connection machine simulation of ultrasonic wave propagation in materials I: The one dimensional case,'' Wave Motion **15**, 65–80 (1992).
[11] P. P. Delsanto, R. S. Schechter, H. H. Chaskelis, R. B. Mignogna, and R. Kline, ''Connection machine simulation of ultrasonic wave propagation in materials II: The two dimensional case,'' Wave Motion **20**, 297–314 (1994).
[12] P. P. Delsanto, R. S. Schechter, and R. B. Mignogna, ''Connection machine simulation of ultrasonic wave propagation in materials III: The three dimensional case,'' Wave Motion **26**, 329–339 (1997).
[13] P. P. Delsanto, R. B. Mignogna, R. S. Schechter, and M. Scalerandi, ''Simulation of ultrasonic pulse propagation in complex media,'' in *New Perspectives on Problems in Classical and Quantum Physics*, edited by P. P. Delsanto and A. W. Saenz (Gordon Breach, New York, 1998), Vol. 2, pp. 51–74.
[14] J.-M. Baik and R. B. Thompson, ''Ultrasonic scattering from imperfect interfaces: A quasi-static model,'' J. Nondestruct. Eval. **4**, 177–197 (1984).
[15] R. S. Schechter, H. H. Chaskelis, R. B. Mignogna, and P. P. Delsanto, ''Real-time parallel computation and visualization of ultrasonic pulses in solids using the connection machine,'' Science **265**, 1188–1192 (1994).
[16] R. D. Huber, R. B. Mignogna, K. E. Simmonds, R. S. Schechter, and P. P. Delsanto, ''Dynamic full-field visualization of ultrasound interacting with material defects: Experiment and simulation,'' Ultrasonics **35**, 7–16 (1997).
[17] N. K. Batra, R. B. Mignogna, R. S. Schechter, P. P. Delsanto, E. Ruffino, and M. Scalerandi, ''Simulation of ultrasound propagation across inter-

faces with imperfect contact,'' *Review of Progress in Quantitative Nondestructive Evaluation*, edited by D. O. Thompson and D. E. Chimenti (Plenum, New York, 1998), p. 971–977.
[18] L. J. Pyrak-Nolte, L. R. Myer, and N. G. W. Cook, ''Anisotropy in seismic velocities and amplitudes from multiple parallel fractures,'' J. Geophys. Res. **95**, 11345–11358 (1990).
[19] L. B. Felsen and S. Zeroug, ''Ultrasonic beam method from localized weak debonding in a layered Al plate,'' J. Acoust. Soc. Am. **90**, 1527–1538 (1991).
[20] F. J. Margetan, R. B. Thompson, and T. A. Gray, ''Anisotropic Gauss-Hermite beam model applied to through-transmission inspection of delaminations in composite plates,'' in *Review of Progress in Quantitative Non Destructive Evaluation*, edited by D. O. Thompson and D. E. Chimenti (Plenum, New York, 1991), Vol. 10B, pp. 1539–1546.
[21] M. Scalerandi, P. P. Delsanto, and V. Agostini, ''Treatment of attenuation and dispersion in the propagation of ultrasonic pulses,'' Proc. of the the Quantitative Non Destructive Evaluation Conference, held in SnowBird, Utah, 26–30 July 1998, to appear.

Dilatation of *S* waves in smoothly inhomogeneous isotropic elastic media

Aleksei P. Kiselev[a] and Zigmund M. Rogoff[b]
Institute of Mechanical Engineering, 61 Bolshoi Prospekt, Vasilievskii Ostrov, St. Petersburg, 199178, Russia

(Received 4 February 1998; accepted for publication 13 July 1998)

The propagation of high-frequency linear waves in a smoothly inhomogeneous isotropic elastic medium is considered. The dilatation of the *S* wave is found via employment of both the zeroth- and first-order terms of the elastic field by a ray analysis. It is observed that the dilatation is necessarily dependent upon the inhomogeneity of the medium, vanishing in the instance the medium is taken homogeneous. © *1998 Acoustical Society of America.* [S0001-4966(98)04710-9]

PACS numbers: 43.20.Bi, 43.20.Dk, 43.20.Gp, 43.35.Cg [DEC]

INTRODUCTION

We consider body wave propagation in a smoothly inhomogeneous, linear elastic medium subject to high frequency, where it is assumed that the wavelengths are much smaller than any characteristic length scale inherent to the inhomogeneities of the medium.

The primary aim of this paper is to find an explicit asymptotic expression for the dilatation of the high-frequency *S* waves. This may sound initially confusing because the *S* wave of a homogeneous media is just a synonym for the shear or rotational wave (or equivoluminal wave), but this is duely clarified in the instance the media is inhomogeneous where the dilatation is in general not zero.

While the *P* and *S* waves commonly associated with homogeneous media are those of plane wave type, their generalization to inhomogeneous media can only be given in an asymptotic sense when it is assumed that the frequency is large when compared with characteristic scales of the medium. In this way one can obtain asymptotic expressions by a ray approach (Alekseev *et al.*, 1961; Karal and Keller, 1959) where the zeroth-order terms have the local properties of their corresponding plane waves. However, the higher-order terms of the asymptotic expansion demonstrate anomalous features when compared to the plane waves (e.g., Babich and Kiselev, 1989). One of such features is the dilatation of the *S* wave.

In response to the progress made in the field of extensometry (e.g., Amatuni *et al.*, 1989) we are motivated to investigate the effects of inhomogeneities on the dilatation of the *S* wave, which can nowadays be measured directly.

In the following section we give an account of plane and nonplane wave fields and present a revision of the nomenclature of body waves in homogeneous isotropic media. From that foundation we proceed with a ray analysis of the leading-order terms of the elastic field displacement for inhomogeneous medium, and in the following section via consideration of its first-order terms determine the dilatation of the *S* wave. For completeness we present an expression for the rotation of the *P* field. In the final section we discuss the implications of the results.

I. PLANE AND NONPLANE WAVES IN HOMOGENEOUS MEDIUM

We consider a time-harmonic scenario and define the elastic displacement vector by $\Re(\mathbf{U}e^{-i\omega t})$, where $\Re$ refers to the real part, and $\mathbf{U}=\mathbf{U}(\mathbf{r})$ is governed by the equations

$$\frac{\partial \sigma_{ij}}{\partial x_i}+\rho\omega^2 U_j=0, \tag{1}$$

where ω is angular frequency, $\rho(\mathbf{r})$ is volume density, and $\mathbf{r}=(x_1,x_2,x_3)$ is the position vector. For an isotropic medium the stress tensor, σ_{ij}, is given by

$$\sigma_{ij}=\mu\left(\frac{\partial U_i}{\partial x_j}+\frac{\partial U_j}{\partial x_i}\right)+\lambda\,\delta_{ij}\,\frac{\partial U_k}{\partial x_k}, \tag{2}$$

where $\mu(\mathbf{r})$ and $\lambda(\mathbf{r})$, the Lamé parameters, are smooth functions of $\mathbf{r}$.

In the instance the wave motion is taken to be linear the notion of the wave is based [as noted by Babich and Kiselev (1989)] on the properties of plane waves in a homogeneous medium for which μ, λ, and ρ are all constants. For the case of homogeneous medium, (1) may be expressed (e.g., Hudson, 1980) by

$$(\lambda+2\mu)\boldsymbol{\nabla}(\boldsymbol{\nabla}\cdot\mathbf{U})-\mu\boldsymbol{\nabla}\wedge(\boldsymbol{\nabla}\wedge\mathbf{U})+\rho\omega^2\mathbf{U}=\mathbf{0}. \tag{3}$$

Plane wave solutions of this equation are characterized in the form

$$\mathbf{U}=\mathbf{U}_0 e^{i\omega\tau(\mathbf{r})}, \tag{4}$$

where the travel time along the ray, $\tau(\mathbf{r})$, is a linear function of position coordinates x_1, x_2, x_3 and $\mathbf{U}_0$ is a constant, i.e., it is independent of position. Under this assumption, inserting (4) into (3) we immediately obtain that either

$$\mathbf{U}_0\cdot\boldsymbol{\nabla}\tau=0, \tag{5}$$

and then $\tau(\mathbf{r})$ satisfies the eikonal equation

$$(\boldsymbol{\nabla}\tau)^2=\frac{1}{c_S^2},\quad c_S=\sqrt{\frac{\mu}{\rho}}, \tag{6}$$

[a]Electronic mail: aleksei.kiselev@pobox.spbu.ru and kiselev@amath.usr.saai.ru
[b]Now at European Gas Turbines Limited, P.O. Box 1, Thorngate House, Lincoln, LN2 5DF, England.

where c_S is the velocity of the shear wave, or

$$\mathbf{U}_0 \wedge \nabla \tau = \mathbf{0}, \tag{7}$$

and then

$$(\nabla \tau)^2 = \frac{1}{c_P^2}, \quad c_P = \sqrt{\frac{\lambda + 2\mu}{\rho}}, \tag{8}$$

where c_P is the velocity of the longitudinal waves. In both instances the vector $\nabla \tau(\mathbf{r})$ is evidently constant. Further, since this vector is parallel to the direction of wave propagation, the wave displacements obeying Eqs. (5) and (7) are transverse and longitudinal, respectively, and hence bear their established names. It is evident that for the shear plane waves

$$\nabla \cdot \mathbf{U} = 0, \tag{9}$$

and

$$\nabla \wedge \mathbf{U} = 0 \tag{10}$$

for the longitudinal waves. Because $\Re(\nabla \wedge \mathbf{U} e^{-i\omega t})$ is a rotation of a small volume of the medium and $\Re(\nabla \cdot \mathbf{U} e^{-i\omega t})$ is the fractional change of its volume (Hudson, 1980) the waves are sometimes called rotational (or equivoluminal) and dilatational, respectively. Since $c_P > c_S$, seismologists, who are interested in events producing both waves at the same moment call them *P* and *S* waves denoting primary and secondary.

Plane waves in a homogeneous medium can also be represented by either

$$\mathbf{U} = \nabla \wedge \boldsymbol{\Psi}, \tag{11}$$

or

$$\mathbf{U} = \nabla \phi, \tag{12}$$

where the *S* and *P* potentials are given by

$$\boldsymbol{\Psi} = \mathbf{B} e^{i\omega\tau}, \quad \mathbf{U}_0 = i\omega \nabla \tau \wedge \mathbf{B}, \tag{13}$$

with **B** constant;

$$\phi = A e^{i\omega\tau}, \quad \mathbf{U}_0 = i\omega A \nabla \tau, \tag{14}$$

with *A* constant.

Nonplane waves in a homogeneous media are those solutions expressible by (9) and (10) with nonconstant amplitudes where the phase function $\tau = \tau(\mathbf{r})$ is not necessarily linear. Particular, well-known examples are the spherical waves given by

$$\boldsymbol{\Psi} = \mathbf{B} D \frac{e^{i\omega\tau}}{\tau} \quad \text{with} \quad \tau = \frac{R}{c_P} \tag{15}$$

and

$$\phi = D \frac{e^{i\omega\tau}}{\tau} \quad \text{with} \quad \tau = \frac{R}{c_S}, \tag{16}$$

where $R = \sqrt{x_1^2 + x_2^2 + x_3^2}$ and *D* is a constant. More general spherical wave solutions can be obtained if we take *D* to be an arbitrary differential operator with constant coefficients. Several other examples of nonplane wave solutions are described in Fradkin and Kiselev (1997).

For homogeneous media we may express the field in potential form, (11) and (12); demonstrating that the *S* and *P* waves are always rotational and dilatational, respectively. However, such potential representations do not provide a direction of propagation. It is only in an asymptotic sense that the direction of propagation of the wave fields can be understood. Hence, in general, there is no reason to speak of a longitudinal or transverse displacement (i.e., a displacement field perpendicular to the direction of propagation). In general these notions can be introduced only in an asymptotic sense, see, e.g., Babich and Kiselev (1989). Spherical waves are either transverse or longitudinal only in a limit of $k_\alpha R \gg 1$, $k_\alpha = \omega / c_\alpha$, $\alpha = P, S$, apart from the obvious exception of the *P* wave when *D* is taken as a constant in (16), which is valid for all $R > 0$. For any fixed value *R* we consider a frequency that ensures that $k_\alpha R = \omega R / c_\alpha \gg 1$ by taking the frequency sufficiently large.

II. ZEROTH-ORDER RAY THEORY FOR *S* WAVES IN INHOMOGENEOUS MEDIUM

Here we employ a ray analysis (Babich, 1956; Karal and Keller, 1959; Alekseev *et al.*, 1961) which provides a high-frequency asymptotic generalization of plane waves in inhomogeneous medium. The concept of time-harmonic body waves is based on the assumption that the frequency is sufficiently high, $\omega \to \infty$, which means that the following nondimensional quantities:

$$\frac{|\nabla c_S(\mathbf{r})|}{\omega} \ll 1, \quad \frac{|\nabla c_P(\mathbf{r})|}{\omega} \ll 1, \quad \frac{|\nabla \rho(\mathbf{r})| c_S(\mathbf{r})}{\omega \rho(\mathbf{r})} \ll 1 \tag{17}$$

are regarded as small parameters of the same order. We commence by expressing the complex displacement vector by the ansatz

$$\mathbf{U}(\mathbf{r}) = \sum_{n=0}^{\infty} \frac{\mathbf{U}_n(\mathbf{r})}{(-i\omega)^n} e^{i\omega\tau}, \tag{18}$$

where $\tau = \tau(\mathbf{r})$ is no longer assumed to be a linear function of coordinates, and the amplitude vectors $\mathbf{U}_n(\mathbf{r})$ are expected to vary slowly compared to the exponential factor.

Inserting (18) into the equation of motion (1) we immediately obtain the familiar alternative expressions, which correspond to Eqs. (6) and (8), but with $c_S = c_S(\mathbf{r})$, $c_P = c_P(\mathbf{r})$, $\mathbf{U} = \mathbf{U}(\mathbf{r})$, and

$$\mathbf{U}_0(\mathbf{r}) \cdot \nabla \tau(\mathbf{r}) = 0, \tag{19}$$

$$\mathbf{U}_0(\mathbf{r}) \wedge \nabla \tau(\mathbf{r}) = \mathbf{0}, \tag{20}$$

for the *S* and *P* fields, respectively. We do not discuss the case of the *P* wave any further. The first step in the description of the phase function $\tau(\mathbf{r})$ is the construction of the rays, which are in general curvilinear, corresponding to the wave speed $c_S(\mathbf{r})$, which can be presented by the integral

$$\tau(\mathbf{r}) = \int^{\mathbf{r}} \frac{d\sigma}{c_S(\mathbf{r}(\sigma))}. \tag{21}$$

Here σ is the arc length of the ray at point **r**. We note that $\tau(\mathbf{r})$ retains the meaning of the travel time, and $\nabla \tau(\mathbf{r})$, which is tangent to the ray, points in the direction of propagation of

the wave (e.g., Babič and Buldyrev, 1991) At this point we will not continue with the determination of the explicit form of the zeroth-order amplitude $\mathbf{U}_0(\mathbf{r})$ which follows from Babich (1956), Karal and Keller (1959), and Alekseev *et al.* (1961), but just note that it is in agreement with the zeroth-order energy conservation along the rays and that $\mathbf{U}_0(\mathbf{r})$ is orthogonal to the rays, and thus transverse. Henceforth we assume that $\mathbf{U}_0(\mathbf{r})$ is given.

III. FIRST-ORDER RAY THEORY

The first-order amplitude term for the *S* wave is in general not orthogonal to their rays (Karal and Keller, 1959; Alekseev *et al.*, 1961; Kiselev, 1983; Babich and Kiselev, 1989). The presence of this anomalous polarization is due to diffraction, where a small amount of energy diffuses in orthogonal directions while traveling along the ray. We begin by splitting the first-order amplitude displacement $\mathbf{U}_1$ into two parts, given by

$$\mathbf{U}_1 = \mathbf{U}_1^{\perp} + \mathbf{U}_1^{\parallel}, \tag{22}$$

where

$$\mathbf{U}_1^{\perp} \cdot \boldsymbol{\nabla}\tau = 0 \quad \text{and} \quad \mathbf{U}_1^{\parallel} \wedge \boldsymbol{\nabla}\tau = 0. \tag{23}$$

We note that we will not use the expression for $\mathbf{U}_1^{\perp}$. The expression for the so-called additional component $\mathbf{U}_1^{\parallel}$ parallel to the ray can be given in terms of the zeroth-order amplitude by

$$\mathbf{U}_1^{\parallel} = c_S^2\{\mathbf{U}_0 \cdot \mathbf{Q} + \boldsymbol{\nabla} \cdot \mathbf{U}_0\}\boldsymbol{\nabla}\tau, \tag{24}$$

where

$$\mathbf{Q}(\mathbf{r}) = \frac{\gamma^2}{1-\gamma^2}\left(\frac{2\boldsymbol{\nabla} c_S}{c_S} + \frac{\boldsymbol{\nabla}\rho}{\rho} - 2K\mathbf{n}\right), \tag{25}$$

see (e.g., Kiselev, 1983; Kiselev and Roslov, 1991) where $\gamma(\mathbf{r}) = c_S(\mathbf{r})/c_P(\mathbf{r})$, $K(\mathbf{r})$ is curvature of the ray and $\mathbf{n}(\mathbf{r})$ is the unit normal to it. The expression (25) is characterized by the inhomogeneity of the medium, the direction of propagation of the wave field ($\boldsymbol{\nabla}\tau$, which defines K), and by the direction of $\mathbf{U}_0$. We note that $\mathbf{U}_0$ is not defined by $\boldsymbol{\nabla}\tau$ alone since $\mathbf{U}_0$ can be rotated about the direction of propagation, and hence (25) is also dependent upon the polarization of $\mathbf{U}_0$. If we assume the solid homogeneous c_S and ρ are taken as constants, the *S* wave propagates along straight paths (thus $K \equiv 0$), and hence $\mathbf{Q} = \mathbf{0}$. Further, it will be observed that $\mathbf{U}_1^{\parallel}$ (24) is then given by

$$\mathbf{U}_1^{\parallel} = c_S^2(\boldsymbol{\nabla} \cdot \mathbf{U}_0)\boldsymbol{\nabla}\tau. \tag{26}$$

We remark by that in general we do not expect $\boldsymbol{\nabla} \cdot \mathbf{U}_0$ to be zero. Indeed, the numerical modeling by Kiselev and Tsvankin (1989) and Kiselev and Roslov (1991) shows that for nonplane waves it hardly ever assumes small values, and in the instances it does happen to be zero that it occurs only at isolated points. For plane waves, however, $\boldsymbol{\nabla} \cdot \mathbf{U}_0$ is trivially zero because the amplitude of the plane wave is constant.

Taking the divergence of $\mathbf{U}$

$$\mathbf{U} \approx \left(\mathbf{U}_0 + \frac{\mathbf{U}_1}{-i\omega}\right)e^{i\omega\tau}, \tag{27}$$

for the case of the *S* wave it can be easily seen that the leading terms are given by

$$\boldsymbol{\nabla} \cdot \mathbf{U} \approx \{i\omega\boldsymbol{\nabla}\tau \cdot \mathbf{U}_0 - \boldsymbol{\nabla}\tau \cdot \mathbf{U}_1 + \boldsymbol{\nabla} \cdot \mathbf{U}_0\}e^{i\omega\tau}, \tag{28}$$

where we make the obvious note that by (19), the first term is zero. Thereafter, by Eqs. (6), (22), and (23) observing cancellation between the second and third terms, the dilatation is conveniently expressible by

$$\boldsymbol{\nabla} \cdot \mathbf{U} \approx -\mathbf{U}_0 \cdot \mathbf{Q}e^{i\omega\tau}. \tag{29}$$

For simplicity we assume that $\mathbf{U}_0$ is real. Reintroducing the time dependence we show that the dilatation of the *S* wave is given by

$$\Re(\boldsymbol{\nabla} \cdot \mathbf{U}e^{-i\omega t}) \approx -\mathbf{U}_0 \cdot \mathbf{Q}\cos[\omega(\tau - t)]. \tag{30}$$

A comparison with the dilatation of the zeroth-order term of the expansion (18) for the *P* wave, given by

$$\begin{aligned}\Re(\boldsymbol{\nabla} \cdot \mathbf{U}e^{-i\omega t}) &\approx \Re(i\omega\mathbf{U}_0 \cdot \boldsymbol{\nabla}\tau e^{i\omega(\tau - t)}) \\ &= -\omega\mathbf{U}_0 \cdot \boldsymbol{\nabla}\tau \sin[\omega(\tau - t)],\end{aligned} \tag{31}$$

reveals that under a harmonic time dependence, the dilation of the *S* waves is equal to that of the integral over time of that of the *P* waves. The same can also be established for non-time-harmonic waves. Note that the dilatation of the *P* wave is of $O(\omega)$, whereas for the *S* wave is of $O(1)$.

We observe that the divergence of the *S* field is dependent upon the amplitude, polarization, and the direction of propagation of the wave field, as well as upon the inhomogeneity of the elastic medium.

The dual calculation of rotation of *P* waves can be found in a manner very similar to the above analysis, where it can be shown that

$$\Re(\boldsymbol{\nabla} \wedge \mathbf{U}e^{-i\omega t}) \approx c_P^2(\mathbf{U}_0 \cdot \boldsymbol{\nabla}\tau)(\boldsymbol{\nabla}\tau \wedge \mathbf{G})\cos[\omega(\tau - t)], \tag{32}$$

where

$$\mathbf{G}(\mathbf{r}) = \frac{4\gamma^2}{1-\gamma^2}\frac{\boldsymbol{\nabla} c_S}{c_S} + \frac{2\gamma^2 - 1}{1-\gamma^2}\frac{\boldsymbol{\nabla}\rho}{\rho}, \tag{33}$$

and $\mathbf{U}$ is assumed to be of the form (18) but where τ is the travel time of the *P* wave, satisfying (7) and (8). An equivalent form for (33) was found by Gvozdev (1959). The expression for $\mathbf{G}$ is independent of the direction of the wave field and therefore the rotation of the *P* field depends on the angle between $\mathbf{G}$ and the direction of the wave propagation, $\boldsymbol{\nabla}\tau$, as well as upon the inhomogeneity of the medium. In the instance the medium is assumed homogeneous, $\mathbf{G} \equiv 0$.

IV. DISCUSSION

To those who believe that the direct measurement of the dilatation and rotation of seismic waves can be helpful in wave discrimination (e.g., White, 1983), the expressions given by (30) and (32) should prove invaluable.

It is observed that the dilatation of the *S* wave is dependent upon the three parameters of the wave field: the amplitude, direction of propagation, and polarization; and upon the inhomogeneity of the elastic solid. The rotation of the *P* wave, on the other hand, is dependent only upon the two

field parameters: the amplitude of the wave field and its direction of propagation (which is coincident with the zeroth-order polarization); and also upon the inhomogeneity. These additional pieces of information may also be useful. As expected the dilatation of the *S* wave and the rotation of the *P* wave vanish when the inhomogeneity is removed.

We remark that the nomenclature for the *P* and *S* fields, primary and secondary, provides the most adequate description of elastic wave propagation in smoothly inhomogeneous isotropic media.

ACKNOWLEDGMENTS

The first author would like to recognize support of Grant No. 95-0-13.1-66 from the Russian Ministry of Higher Education and 95-0012 from INTAS-RFBR. The second author, holding a Royal Society (UK) One-Year Fellowship in St. Petersburg, gratefully acknowledges their support, as well as the additional financial assistance from the Department of Theoretical Mechanics, University of Nottingham, UK.

Alekseev, A. S., Babich, V. M., and Gel'chinsky, B. Ya. (**1961**). ''Ray method of calculation of intensity of wave fronts,'' in *Voprosy Dynamicheskoi Teorii Rasprostraneniya Seismicheskikh Voln*, edited by G. I. Petrashen (Leningrad U.P., Leningrad), Vol. 5, pp. 5–21.

Amatuni, A. N., Tsotin, V. G., Popov, S. S., and Malygina, T. I. (**1989**). ''Status and prospects for development of high-precision dilatometry,'' Izmer. Tech. **32**(6), 26–18 [English translation: Meas. Tech. **32**(6), 548–550].

Babich, V. M. (**1956**). ''Ray method of calculation of intensity of ray fronts,'' Dokl. Akad. Nauk SSSR **110**(3), 355–367.

Babič, V. M., and Buldyrev, V. S. (**1991**). *Short-Wavelength Diffraction Theory: Asymptotic Methods* (Springer-Verlag, Berlin).

Babhich, V. M., and Kiselev A. P. (**1989**). ''Non-geometrical waves—are there any? An asymptotic description of some 'non-geometrical' phenomena in seismic wave propagation,'' Geophys. J. Int. **99**, 415–420.

Fradkin, L. Ju., and Kiselev, A. P. (**1997**). ''The two-component representation of time-harmonic elastic body waves in the high- and intermediate-frequency regimes,'' J. Acoust. Soc. Am. **101**, 52–65.

Gvozdev, A. A. (**1959**). ''On the conditions at fronts of elastic waves propagating in inhomogeneous medium,'' Prikl. Mat. Mekh. **23**(2), 395–398.

Hudson, J. A. (**1980**). *The Excitation and Propagation of Elastic Waves* (Cambridge U.P., Cambridge).

Karal, F. C., and Keller, J. B. (**1959**). ''Elastic wave propagation in homogeneous and inhomogeneous media,'' J. Acoust. Soc. Am. **31**, 694–705.

Kiselev, A. P. (**1983**). ''Extrinsic components of elastic waves,'' Izv. Acad. Nauk SSSR Fiz. Zem. **19**(9), 51–56 [English translation: Izv., Acad. Sci. USSR, Phys. Solid Earth **19**(9), 707–710].

Kiselev, A. P., and Roslov, Yu. V. (**1991**). ''Use of additional components for numerical modelling of polarization anomalies of elastic body waves,'' Geol. Geofiz. **32**(4), 121–131 [English translation: Sov. Geol. Geophys. **32**(4), 105–114].

Kiselev, A. P., and Tsvankin, I. D. (**1989**). ''A method of comparison of exact and asymptotic wave field computations,'' Geophys. J. **96**(2), 253–258.

White, J. E. (**1983**). *Underground Sound* (Elsevier, Amsterdam).

Velocity shift using the Rytov approximation

Y. Samuelides[a)]
CMAPX, Ecole Polytechnique, 91128 Palaiseau, France

(Received 16 March 1998; accepted for publication 7 July 1998)

The high-frequency propagation of acoustic plane waves in a weakly heterogeneous random stationary 2-D medium is considered. The apparent velocity of the wave is larger than the velocity corresponding to the background homogeneous medium; the difference is called velocity shift. Both this shift and the variance of the apparent velocity are calculated using the Rytov approximation; explicit formulas are given when the covariance of the medium is Gaussian. This enables one to show several properties of the shift and the variance, which are illustrated by some numerical experiments on the wave equation. © *1998 Acoustical Society of America.*
[S0001-4966(98)04210-6]

PACS numbers: 43.20.Bi, 43.20.Hq [ANN]

INTRODUCTION

Heterogeneities of media affect the travel times of acoustic waves. In seismology, the determination of travel times is an important issue. Because surface seismic deterministic methods fail to resolve all the heterogeneities in the Earth, the propagation medium is often described as a random stationary media. Its covariance is either isotropic or anisotropic; the latter is more realistic since the horizontal dimension of heterogeneities is usually much larger than the vertical dimension. Therefore, we are interested in the statistical effects of slowness heterogeneities (of standard deviation ϵ) on travel time, which becomes a random variable. Fluctuations of travel time are a first order effect in ϵ. An effect of slowness heterogeneities of the second order term in ϵ is the velocity shift: the apparent velocity of the wave is larger than the velocity corresponding to the average slowness in the medium. This is intuitively in accordance with Fermat's principle, which states that the wave path minimizes the travel time of the wave.

Numerous studies have investigated acoustic waves in random media.[1–3] The variance of the travel-time fluctuations has been known since 1960.[4] The velocity shift was discovered in the late 1980s.[5–7] Since then, it has been investigated numerically and theoretically. Some numerical studies[8] use finite difference calculations on the wave equation while others[4] use the Huyghens method, which is like an improved eikonal since it takes into account the wavefront healing. Theoretical methods[9,10] are based on small perturbations in geometrical optics and have been developed for a medium with an isotropic covariance. These methods have determined that, if the magnitude of the heterogeneities is sufficiently small, the relative velocity shift increases linearly in the distance of propagation. Of course, the eikonal does not take diffraction into account; thus, its validity range is limited. Recently, Shapiro and his co-workers[11] have deduced from the Bourret and Rytov approximations frequency-dependent formulas for the phase velocity shift in a medium with an isotropic covariance.

The implications of the velocity shift for seismology were first discussed by Nolet and Moser.[12] Some authors have used geometrical optics to investigate the velocity shift in a medium with an anisotropic covariance.[13,14]

In this paper, using the Rytov approximation, we compute the two first moments of the phase velocity of a plane wave in a random media with an anisotropic covariance. The Rytov approximation enables us to obtain for these problems a broader range of results than does geometrical optics. An anisotropic covariance is geologically more relevant than an isotropic covariance for seismic waves and it turns out that, in the former case, the phase velocity becomes itself anisotropic, which is, of course, not true in the latter.

In the first section, we discuss the meaning and the range of validity of our main tool: the Rytov approximation. In the second section, we solve the equations of our model. In the third section, we give explicit solutions for the variance and the shift when the covariance of the medium is Gaussian. We describe how these quantities depend on propagation distance, correlation lengths, and frequency. In the limit of very high frequencies, the solutions collapse to those of geometric optics. We use this fact to answer the following question: if the covariance of the medium is anisotropic, when does geometrical optics hold? In the last section, we describe the propagation of a pulse, and the relation between the travel time of a pulse and the phase velocity.

I. RYTOV APPROXIMATION AND PARABOLIC APPROXIMATION

We start with the Helmholtz equation:

$$\Delta U + k^2 n^2 U = 0, \tag{1}$$

where U is the wave field, k is the wave number which equals $2\pi/\lambda$, and n is the relative fluctuation of slowness. We will consider the wave equation in time domain in the last section when we discuss the propagation of a pulse.

Assume that $n^2 = 1 + \epsilon\eta$, where ϵ is a small parameter, and η is a random field of mean 0, correlation function N. Let l be the smallest correlation length of the medium. We will study only the high-frequency propagation, $kl > 1$. For

a)Electronic mail: yann@cmapx.polytechnique.fr

low-frequency propagation, the apparent velocity of the wave can be investigated using the theory of effective medium.

We consider a plane wave propagating along a direction X; x is the coordinate along X. Let V be such that: $U = \exp(ikx)V$; the equation can be rewritten:

$$2ik\frac{\partial V}{\partial x} + \Delta V + k^2 \epsilon\, \eta = 0. \tag{2}$$

A. Parabolic approximation

The parabolic approximation enables us to neglect the relative variation of $\partial V/\partial x$ on a wavelength. This gives the following equation for V:

$$2ik\frac{\partial V}{\partial x} + \Delta_T V + k^2 \epsilon\, \eta = 0, \tag{3}$$

where Δ_T is the Laplacian transverse to the X direction.

B. The Rytov approximation

Let Φ be such that $V = \exp(\Phi)$. The Rytov approximation assumes that $V-1$ is very small, so Φ can be expressed as a power series in the small perturbation parameter ϵ:

$$\Phi = \epsilon\, \Phi_1 + \epsilon^2 \Phi_2 + O(\epsilon^3). \tag{4}$$

Substituting into the parabolic equation and keeping terms up to second order gives

$$2ik\frac{\partial \Phi_1}{\partial x} + \Delta_T \Phi_1 = -k^2 \eta, \tag{5}$$

$$2ik\frac{\partial \Phi_2}{\partial x} + \Delta_T \Phi_2 = -(\nabla_T \Phi_1)^2. \tag{6}$$

The main goal for these equations is to be explicitly solvable.

C. Meaning of these two approximations

The parabolic approximation[15] neglects the backscattered part of the wave. The Rytov approximation assumes that the wave field U is not very different from the monochromatic wave e^{ikx} which would propagate in the background homogeneous medium. Then the small fluctuations regime holds.

In the Appendix, we give a heuristic argument to show that the Rytov approximation holds when the quantity $\epsilon^2 (kl)^2 (X/l)$ is small (see also Ref. 11), and that the parabolic approximation holds when the same quantity is of the order of 1 or smaller.

Therefore, when we choose to use the Rytov approximation, we can simultaneously use the parabolic approximation. For instance, look at the following situation: $\lambda = 50$ m, $l = 100$ m, and $\epsilon = 0.02$. Then our approximations are valid for propagation distances up to 6 kms. In addition, the phase screen method uses the Rytov approximation beyond its general range of validity.[1,16] Consequently, we will always suppose that the small fluctuations regime holds and when we refer to very large distances of propagation, we will implicitly suppose that the perturbation parameter ϵ is small enough that this regime holds.

II. SOLUTIONS OF THE RYTOV EQUATIONS. VARIANCE AND VELOCITY SHIFT

We will consider a 2-D medium to simplify the notation. Adding a supplementary transverse dimension does not significantly change the problem; in the following section, we give explicit formulas in 2D and in 3D.

We choose a basis (e_x, e_y): e_x is the direction of propagation of the initial plane wave and $\mathbf{r} = (\mathbf{x}, \mathbf{y})$ is the position vector. Rewriting (5) and (6),

$$2ik\frac{\partial \Phi_1}{\partial x} + \frac{\partial^2 \Phi_1}{\partial y^2} = -k^2 \eta, \tag{7}$$

$$2ik\frac{\partial \Phi_2}{\partial x} + \frac{\partial^2 \Phi_2}{\partial y^2} = -\left(\frac{\partial \Phi_1}{\partial y}\right)^2. \tag{8}$$

The initial conditions corresponding to a plane wave are for $x = 0$, $\Phi_1 = \Phi_2 = 0$.

A. Solutions of the Rytov equations

These equations can be solved by using $\hat{\eta}$, the Fourier transform of η in the direction e_y which is transverse to the propagation. Remember that N is the correlation function of the fluctuations η. We will need the following equality:

$$\langle \hat{\eta}(x_1, \kappa)\, \hat{\eta}(x_2, \lambda) \rangle = 2\pi \delta(\kappa + \lambda) \int_{-\infty}^{+\infty} \exp(-i\kappa u) N(x_2 - x_1, u)\, du. \tag{9}$$

The solutions are

$$\Phi_1(x,0) = \frac{ik}{4\pi} \int_{-\infty}^{+\infty} d\kappa \int_0^x \exp\left[\frac{\kappa^2}{2ik}(x - x_1)\right] \hat{\eta}(x_1, \kappa)\, dx_1, \tag{10}$$

$$\langle \Phi_2(x,0) \rangle = \frac{1}{2\pi} \int_{-\infty}^{+\infty} d\kappa \frac{i}{2k} \int_0^x \exp\left(\frac{\kappa^2 (x - z)}{2ik}\right) h(z, \kappa)\, dz, \tag{11}$$

where h is the y Fourier transform of $\partial \Phi_1 / \partial y$.

B. The two first moments of the phase

Recall that in the special case of geometrical optics, the phase ϕ of the wave field U is proportional to the travel time of the wave. We are interested in the phase ϕ of the wave field U. Its first moment is related to the velocity shift, and its second moment is related to the variance of the travel time. Since x is the distance of propagation, we have the following relation:

$$k\phi = kx + \mathrm{Im}(\Phi). \tag{12}$$

Essentially, we want to compute the mean and the variance of the imaginary part of Φ. More precisely:

(1) The variance of the phase is $\mathrm{Var}(\phi) = (1/k^2) \times (\langle \mathrm{Im}(\Phi)^2 \rangle - \langle \mathrm{Im}(\Phi) \rangle^2)$. As $\langle \Phi_1 \rangle = 0$, $\langle \mathrm{Im}(\Phi) \rangle = \epsilon^2 \langle \mathrm{Im}(\Phi_2) \rangle$ so up to second-order terms in ϵ, $\mathrm{Var}(\phi) = \epsilon^2 \langle (\mathrm{Im}\ \Phi_1)^2 \rangle / k^2$.

(2) We define here the velocity shift as the normalized difference between the velocity c_0 corresponding to the average squared slowness $1/c_0^2$ and the velocity $v = (kx/k\langle\phi\rangle)\, c_0$ corresponding to the mean phase. Thus the velocity shift is given by

$$\frac{v-c_0}{c_0} = \frac{kx}{k\langle\phi\rangle} - 1. \tag{13}$$

Let Δv be $v - c_0$. Keeping terms up to second order in ϵ gives

$$\frac{\Delta v}{c_0} = -\epsilon^2 \frac{\langle \mathrm{Im}\,(\Phi_2)\rangle}{kx}. \tag{14}$$

Other authors have based their definition of the shift on the average slowness. In our model, the average slowness is given by

$$\left\langle \frac{1}{c} \right\rangle = \frac{1}{c_0}\left(1 - \frac{\epsilon^2\langle \eta^2\rangle}{8}\right). \tag{15}$$

C. Solutions for the variance of the phase and for the velocity shift

(1) We can deduce from (10) the variance of the phase. Keeping up to second-order terms in ϵ gives

$$\begin{aligned}\mathrm{Var}\,(\phi) = \frac{\epsilon^2}{8\pi}\int_{-\infty}^{+\infty} d\kappa \int_0^x \int_0^x dx_2\, dx_3 \\ \times \cos\left(\frac{\kappa^2}{2k}(x-x_2)\right)\cos\left(\frac{\kappa^2}{2k}(x-x_3)\right) \\ \times \int_{-\infty}^{+\infty} du\, \cos(\kappa u)\, N(x_3-x_2,u).\end{aligned} \tag{16}$$

(2) As for the mean of the phase, it can be easily seen that $\langle\Phi_1\rangle = 0$. This explains why the velocity shift is a second-order term. Therefore, using (11), the velocity shift is given by

$$\begin{aligned}\frac{\Delta v}{c_0} &= -\epsilon^2 \frac{\langle \mathrm{Im}\,(\Phi_2)\rangle}{kx} \\ &= \frac{1}{16\pi x}\int_0^x dx_1 \int_{-\infty}^{+\infty} d\lambda\, \lambda^2 \int_0^{x_1}\int_0^{x_1} dx_2\, dx_3 \\ &\quad \times \cos\left[\frac{\lambda^2}{2k}(2x_1 - (x_2+x_3))\right] \\ &\quad \times \int_{-\infty}^{+\infty} du\, \cos(\lambda u)\, N(x_2-x_3,u).\end{aligned} \tag{17}$$

We see that if N decreases fast enough, the velocity shift is always positive.

III. THE GAUSSIAN COVARIANCE. DISCUSSION

Explicit formulas for the variance and the velocity shift are obtainable provided that the covariance function of the fluctuations, N, is Gaussian. We give these formulas and comment on the results. Figures 1–4 illustrate (20) and (21).

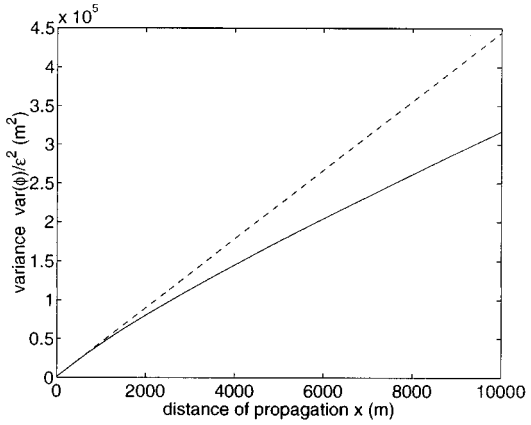

(a)

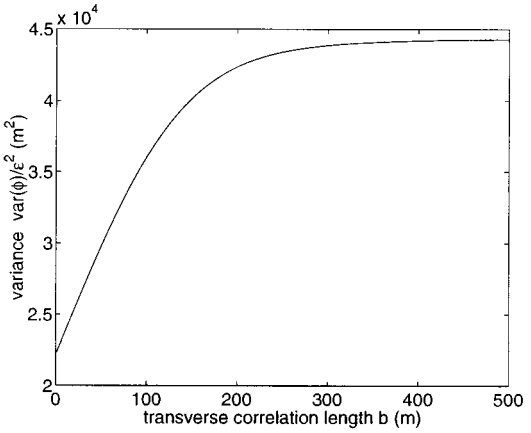

(b)

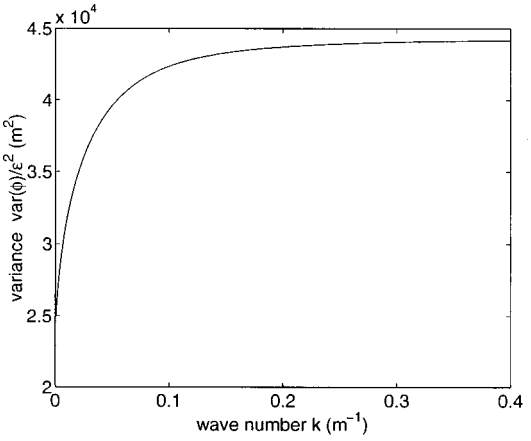

(c)

FIG. 1. (a) The variance var $(\phi)/\epsilon^2$ as a function of the distance of propagation x. The curve on top stands for the variance in geometrical optics, the curve underneath stands for the variance in the Rytov approximation. The parameters are $a = 100$ m, $b = 200$ m, $k = 0.1$ m^{-1}, and $\alpha = 0$ (vertical propagation). (b) The variance var $(\phi)/\epsilon^2$ as a function of the transverse correlation length b. The parameters are: $x = 1000$ m, $a = 100$ m, $k = 0.1$ m^{-1}, and $\alpha = 0$. (c) The variance var $(\phi)/\epsilon^2$ as a function of the wave number k. The parameters are $x = 1000$ m, $a = 100$ m, $b = 200$ m, and $\alpha = 0$.

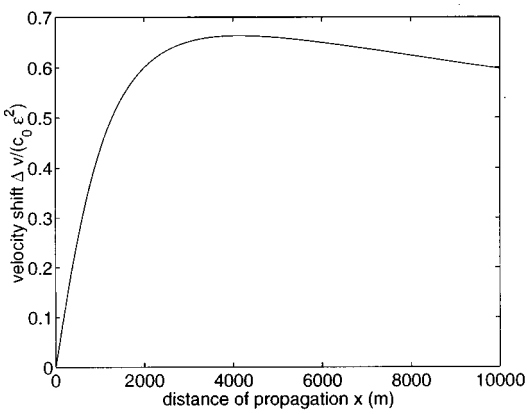

(a)

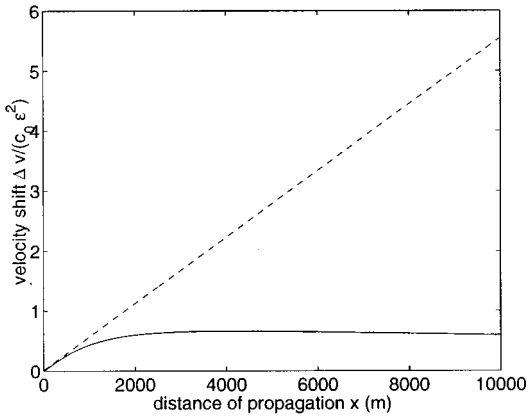

(b)

FIG. 2. The shift $\Delta v/c_0\epsilon^2$ as a function of the distance of propagation x. The parameters are: $a=100$ m, $b=200$ m, $k=0.1$ m^{-1}, and $\alpha=0$; (a) represents the shift using the Rytov approximation and (b) represents both the shift using geometrical optics and the shift using the Rytov approximation at the same scale.

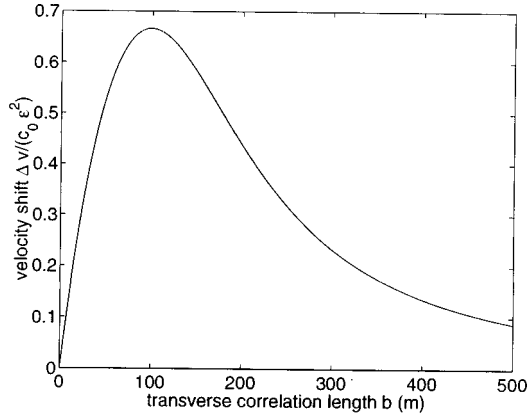

(a)

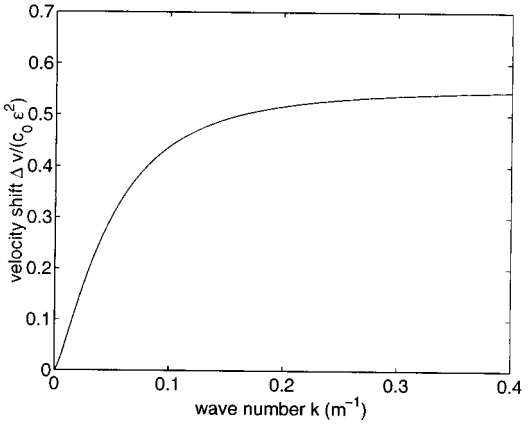

(b)

FIG. 3. (a) The shift $\Delta v/c_0\epsilon^2$ as a function of the transverse correlation length b. The parameters are $x=1000$ m, $a=100$ m, $k=0.1$ m^{-1}, and $\alpha=0$. (b) The shift $\Delta v/c_0\epsilon^2$ as a function of the wave number k. The parameters are $x=1000$ m, $a=100$ m, $b=200$ m, and $\alpha=0$.

Assume that $N(x,y)=\exp[-(x^2/a^2+y^2/b^2)]$ in 2D where a and b are the correlation lengths along x and y axes. The coordinate basis (e_x,e_y) defining $N(\mathbf{r})$ will, in general, be different from the coordinate basis (E_X,E_Y) defined by the direction of wave propagation. The angle between the direction of propagation E_X and the e_x axis of the autocorrelation function will be denoted by α.

We can thus simplify (16) and (17) by using the factorization of the covariance function and new integration variables: x_2+x_3, x_2-x_3. We introduce the quantities

$$\frac{1}{A_\alpha^2}=\frac{\cos^2\alpha}{a^2}+\frac{\sin^2\alpha}{b^2}, \tag{18}$$

$$C_\alpha^2=\sin^2\alpha\, a^2+\cos^2\alpha\, b^2, \tag{19}$$

where A_α is an average correlation length along the direction of propagation; C_α is an average correlation length along the direction perpendicular to the propagation. For instance, for vertical propagation (along e_x), $A_\alpha=a$ and $C_\alpha=b$. The results for the variance of the phase and the velocity shift are

$$\text{Var}\,(\phi)=\frac{\epsilon^2A_\alpha\sqrt{\pi}}{8}\left(x+\int_0^x\left(1+\left(\frac{4x_1}{kC_\alpha^2}\right)^2\right)^{-1/4}\times\cos\left(\frac{1}{2}\arctan\left(\frac{4x_1}{kC_\alpha^2}\right)\right)dx_1\right), \tag{20}$$

$$\frac{\Delta v}{c_0}=\frac{\epsilon^2kA_\alpha\sqrt{\pi}}{8x}\int_0^x\left(1+\left(\frac{4x_1}{kC_\alpha^2}\right)^2\right)^{-1/4}\times\sin\left(\frac{1}{2}\arctan\left(\frac{4x_1}{kC_\alpha^2}\right)\right)dx_1. \tag{21}$$

A. The two limit regimes

We are now able to identify a parameter which plays an important role:

$$D=\frac{4x}{kC_\alpha^2}. \tag{22}$$

(i) If $D\ll 1$, then (20) and (21) become

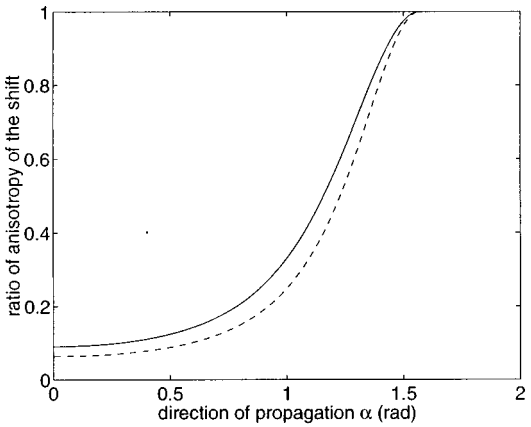

(a)

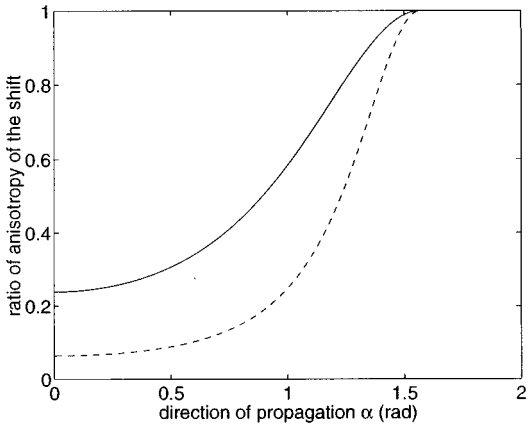

(b)

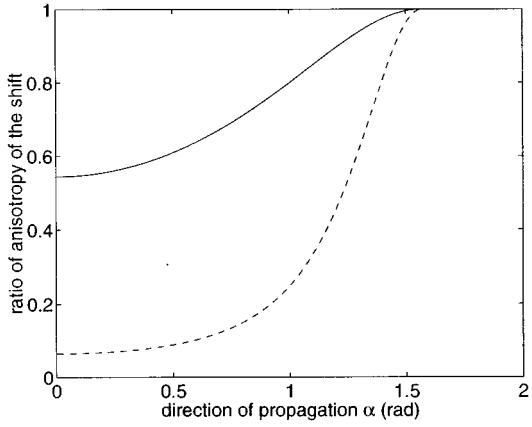

(c)

FIG. 4. The ratio shift (α)/shift $(\pi/2)$ as a function of the angle α. The curve on top stands for this ratio in the Rytov approximation, the curve underneath stands for this ratio in geometrical optics. The parameters are $a=100$ m, $b=250$ m, and $k=0.3$ m^{-1}. (a) The distance of propagation x is 1000 m. (b) $x=4000$ m. (c) $x=16\,000$ m.

$$\mathrm{Var}(\phi)=\frac{\epsilon^2 A_\alpha \sqrt{\pi} x}{4}, \tag{23}$$

$$\frac{\Delta v}{c_0}=\frac{\epsilon^2 A_\alpha \sqrt{\pi} x}{8 C_\alpha^2}. \tag{24}$$

These are the results in the geometrical optics case. They are well known when the correlation function is isotropic[6] and they have been computed recently when it is anisotropic.[14] We can therefore deduce that when the covariance of the medium is anisotropic, ray theory applies to a given direction of propagation α provided that $D \ll 1$. This is the well known condition of the Fresnel zone where the correlation length transverse to the direction of propagation, C_α, plays the role of the unique isotropic correlation length.

(ii) If $D \gg 1$, the Fraunhofer approximation holds and (20) and (21) become

$$\mathrm{var}(\phi)=\frac{\epsilon^2 A_\alpha \sqrt{\pi}}{8}\left(x+\frac{\sqrt{2k}C_\alpha}{2}x^{1/2}\right), \tag{25}$$

$$\frac{\Delta v}{c_0}=\frac{\epsilon^2 k^{3/2} A_\alpha C_\alpha \sqrt{2\pi}}{16}x^{-1/2}. \tag{26}$$

B. The variance

(i) The variance increases as a function of the distance of propagation [Fig. 1(a)]. In the Fraunhofer approximation, the ratio $\mathrm{var}(\phi)/x$ is two times smaller than in geometrical optics. It is important to identify the value of D correctly in order to estimate correctly the variance.

(ii) The variance increases as a linear function of the correlation length along the direction of propagation. It also increases slightly with the correlation length transverse to the direction of propagation [Fig. 1(b)].

(iii) The variance increases as a function of the wave number k in the Fraunhofer region $D \gg 1$. Then it saturates [Fig. 1(c)].

C. The shift

(i) The behavior of the shift as a function of the distance of propagation is one of our main results (Fig. 2). It increases linearly in the geometrical optics region, then saturates. In the Fraunhofer region, it decreases to 0. Therefore, in Rytov approximation, for very large distances of propagation, the velocity corresponding to the mean phase equals the velocity corresponding to the average squared slowness.

(ii) The shift increases as a linear function of the correlation length along the direction of propagation.

(iii) The behavior of the shift as a function of the transverse correlation length is ambiguous [Fig. 3(a)]. It is a decreasing function in the geometrical optics region and an increasing function in the Fraunhofer region.

(iv) The shift increases as a function of the wave number k [Fig. 3(b)].

D. The anisotropy of the shift

We compare the value of the shift for propagation in different directions at the same distance (Fig. 4). The shift is anisotropic: it is a maximum for propagation along the direction of largest correlation length. But the anisotropy itself is a decreasing function of the parameter D. In geometrical optics, the shift is highly anisotropic. On the contrary, in the Fraunhofer zone, there is almost no anisotropy; in fact, the shift is so small that it can hardly be observed.

In geophysical problems, the horizontal correlation length is very often much larger than the vertical correlation length. Therefore, the shift for horizontal propagation is larger than the shift for vertical propagation. However, a given distance of propagation may very well correspond to the geometrical optics for vertical propagation and to the saturated regime for horizontal propagation. If this is true, the anisotropy can be observed, but it is smaller than the anisotropy observed in geometrical optics.

E. The 3D case

The calculations are about the same in 3D. Assume the correlation function is $N(x,y,z)=\exp[-(x^2/a^2+y^2/b^2+z^2/c^2)]$. To simplify the notation, we suppose that the wave propagates along one of the axes of N, for instance, e_x. Then the variance and the velocity shift become

$$\mathrm{Var}(\phi)=\frac{\epsilon^2 a\sqrt{\pi}}{8}\left(x+\int_0^x\left(1+\left(\frac{4x_1}{kb^2}\right)^2\right)^{-1/4}\times\left(1+\left(\frac{4x_1}{kc^2}\right)^2\right)^{-1/4}\cos\left(\frac{1}{2}\left(\arctan\left(\frac{4x_1}{kb^2}\right)+\arctan\left(\frac{4x_1}{kc^2}\right)\right)\right)dx_1\right), \tag{27}$$

$$\frac{\Delta v}{c_0}=\frac{\epsilon^2 ka\sqrt{\pi}}{8x}\int_0^x\left(1+\left(\frac{4x_1}{kb^2}\right)^2\right)^{-1/4}\times\left(1+\left(\frac{4x_1}{kc^2}\right)^2\right)^{-1/4}\sin\left(\frac{1}{2}\left(\arctan\left(\frac{4x_1}{kb^2}\right)+\arctan\left(\frac{4x_1}{kc^2}\right)\right)\right)dx_1. \tag{28}$$

When the transverse correlation lengths are equal ($b=c$), (29) and (30) collapse to

$$\mathrm{var}(\phi)=\frac{\epsilon^2 a\sqrt{\pi}}{8}\left(x+\frac{\arctan(4x/kb^2)}{4/kb^2}\right), \tag{29}$$

$$\frac{\Delta v}{c_0}=\frac{\epsilon^2 ka\sqrt{\pi}\log\left(1+(4x/kb^2)^2\right)}{16\quad 4x/kb^2}. \tag{30}$$

When $a=b$, Rytov and his co-workers calculated (29).[3]

IV. PROPAGATION OF A PULSE

We have studied the propagation of monochromatic waves. However, many applications are concerned with pulses, not monochromatic waves. In the geometrical optics region, the results are identical since this regime is not frequency dependent. More generally, we see now that our formulas enable us to give estimates for the case of a pulse.

We start with the wave equation in the time domain:

$$\Delta U-\frac{n^2}{c_0^2}\frac{\partial^2 U}{\partial t^2}=0. \tag{31}$$

We are looking for plane waves propagating along the X direction. The initial condition for U at $x=0$ is the pulse $f(t)$. We write $f(t)$ as a Fourier integral: $f(t)=\int e^{-i\omega t}\hat{f}(\omega)\,d\omega$. Taking the Fourier transform of the wave equation gives the Helmholtz equation so we can write

$$\hat{U}(\omega)=\hat{f}(\omega)e^{ikx}e^{\Phi_\omega(x)}, \tag{32}$$

where $k=\omega/c_0$ and Φ_ω has been defined previously.

Assume that the Rytov approximation holds for the main range of frequencies $[\omega_m,\omega_M]$ of the pulse. Then Φ_ω is small for each frequency ω of this range and (32) gives

$$U(x,t)=\int\hat{f}(\omega)\,\mathrm{Re}\,(\Phi_\omega(x))e^{i(\omega(x/c_0-t))}\,d\omega+\int\hat{f}(\omega)e^{i(\omega(x/c_0-t)+\mathrm{Im}(\Phi_\omega(x)))}\,d\omega. \tag{33}$$

The first term of the sum is a small pulse propagating at the speed c_0, which is slightly distorted. The second term is the initial pulse propagating with a frequency-dependent shift. Therefore, only the latter is important for the analysis of the travel-time shift. Moreover, we have seen in the previous section that the shift is an increasing function of the wave number k, thus of the frequency ω. Then the travel time shift of the pulse is larger than the value corresponding to ω_m and smaller than the value corresponding to ω_M. An estimate of this shift is given by the integral

$$\int-\frac{c_0\hat{f}(\omega)\langle\mathrm{Im}\,(\Phi_\omega)\rangle}{\omega x}\,d\omega. \tag{34}$$

Using a finite-difference solver in order to solve the full wave equation, we have investigated numerically the propagation of a pulse. The results are shown in Fig. 5. They confirm all the qualitative properties which were stated in the previous sections:

(i) the existence of a positive velocity shift;
(ii) the anisotropic behavior of the shift: it is a maximum for propagation along the direction of the largest correlation length ($sh_2>sh_3$);
(iii) the shift increases as a function of the correlation length along the direction of propagation ($sh_2>sh_1$); and
(iv) the shift saturates for large distances of propagation: sh_3 stops increasing when z is larger than 4000, which is consistent with the result of Fig. 2(a).

Besides, the quantitative results shown in Fig. 5 can be related to (34). For instance, the value of the shift Δv given by sh_3 for $x=2000$ m is $\Delta v=10$ m/s; the main wave number of

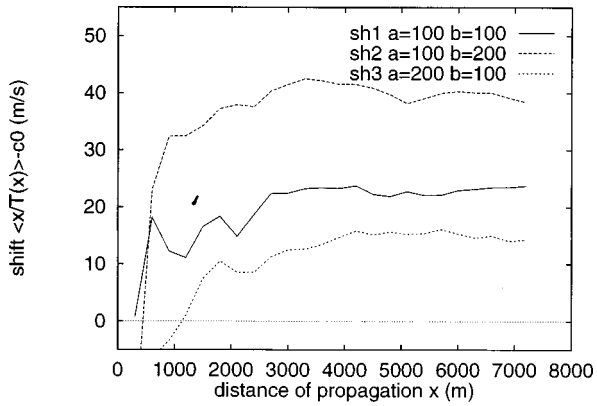

FIG. 5. The velocity shift Δv of a pulse as a function of the distance of propagation x. The velocity is $c_0=3000\ \mathrm{m\,s^{-1}}$. The main wave number of the pulse is $k=0.1\ \mathrm{m^{-1}}$. $\epsilon^2=0.05$. The propagation is vertical ($\alpha=0$): sh_1 stands for the curve $a=100$ m, $b=100$ m, sh_2 stands for the curve $a=200$ m, $b=100$ m, and sh_3 stands for the curve $a=100$ m, $b=200$ m.

the corresponding pulse is $k=0.1\ \mathrm{m^{-1}}$. Now, assume that the pulse is very close to a monochromatic wave whose wave number is $k=0.1\ \mathrm{m^{-1}}$. Then (34) collapses to (21), which gives $\Delta v=9$ m/s (for $x=2000$ m, $a=100$ m, $b=200$ m, $\epsilon^2=0.05$, and $c_0=3000$ m/s).

V. CONCLUSION

When considering the propagation of an acoustic wave in a weakly heterogeneous medium, it is important to determine the difference between the mean of the travel time and the value that the travel time would have in the background heterogeneous medium. For low-frequency propagation, this correction is provided by the effective medium theory.[17,18] In geometrical optics, this correction is the velocity shift. In this paper, we proved that for high frequencies, the velocity shift still exists in the Rytov approximation. This approximation is useful when the propagation distance is too large for diffraction to be neglected, but small enough so that the small fluctuations regime holds. When heterogeneities have a Gaussian covariance, the shift for monochromatic waves is given by (21). It is anisotropic; it is a maximum for propagation along the largest correlation length. Its behavior is governed by the Fresnel parameter D (22). When D is very small, the shift increases linearly as a function of the propagation distance, as in geometrical optics, then saturates, and then decreases to 0. This behavior shows that the geometrical optics result is not sufficient to investigate properly the velocity shift; the Rytov approximation is needed. Additionally, the Rytov approximation allows us to calculate the variance of the phase, given by (20). The propagation of a pulse is very useful for many applications; (34) provides an estimate for the shift. Our experiments show that the shift and its saturation, the latter being a ''typical Rytov effect,'' can actually be observed numerically.

ACKNOWLEDGMENTS

I acknowledge helpful discussions with Joseph Keller, George Papanicolaou, Bertrand Iooss, and Margaret Ebert. This work was done while I was visiting the Department of Mathematics at Stanford University, and was partially supported by Elf Aquitaine.

APPENDIX: VALIDITY CONDITIONS FOR THE RYTOV AND THE PARABOLIC APPROXIMATIONS

We want to find when the Rytov approximation and the parabolic approximation are valid. We start with the wave equation in a 1-D medium:

$$\frac{d^2U}{dx^2}+k^2(1+\epsilon\eta(x))=0. \tag{A1}$$

Recall that l is the correlation length of η: we write $\eta(x)=\eta_0(x/l)$. Let L be the distance of propagation, r be l/L, and t be such that $t/r=x/l$. The equation becomes

$$\frac{d^2U}{dt^2}+\frac{k^2l^2}{r^2}\left(1+\epsilon\eta_0\left(\frac{t}{r}\right)\right)=0 \tag{A2}$$

with $t\in[0,1]$.

We introduce a down-going wave $Ae^{iklt/r}$ and an up-going wave $Be^{-iklt/r}$: $U=Ae^{iklt/r}+Be^{-iklt/r}$. We thus obtain a differential system:

$$\frac{d}{dt}\begin{pmatrix}A\\B\end{pmatrix}=\frac{ikl\epsilon}{2r}\,\eta_0\left(\frac{t}{r}\right)\begin{pmatrix}1 & e^{-2iklt/r}\\ -e^{-2iklt/r} & -1\end{pmatrix}\begin{pmatrix}A\\B\end{pmatrix}.$$

The boundaries conditions are $A(0)=1$, $B(1)=0$: there is no up-going wave coming from $+\infty$.

We know[19] that the scaling of the forward Markov approximation (also called diffusion approximation) is ''$(kl\epsilon/r)^2$ of the same order as $1/r$,'' which is equivalent to ''$\epsilon^2(kl)^2(L/l)$ of the same order as 1.''

(1) When $\epsilon^2(kl)^2(L/l)\ll 1$, the propagation distance is small enough that the random fluctuation is small. It means that the wave U is very close to the down-going wave $e^{iklt/r}$ which would propagate in the homogeneous background medium. Therefore, both the Rytov approximation and the parabolic approximation hold.

(2) When $\epsilon^2(kl)^2(L/l)$ is comparable to 1, the forward Markov approximation can be used. A and B obey two uncoupled first-order stochastic differential equations. Using $B(t=1)=0$, it can be shown that B remains equal to 0. A obeys an equation where the random part is not small, so U is not always close to $e^{iktl/r}$. It means that the perturbation is small enough that we can neglect the up-going wave, but it is large enough so that the down-going wave is significantly perturbed by the heterogeneities of the medium. Therefore, the parabolic approximation is valid but the Rytov approximation is not valid.

(3) When $\epsilon^2(kl)^2(L/l)\gg 1$, the random part is large enough that the up-going wave $Be^{-iklt/r}$ cannot be neglected. Neither the Rytov approximation nor the parabolic approximation are valid.

We conclude that the Rytov approximation is valid when $\epsilon^2(kl)^2(L/l)\ll 1$ and that the parabolic approximation is valid when this same quantity is of the order of 1 or smaller. When adding transverse dimensions (i.e., for a 2-D medium

or a 3-D medium), the mathematical details of the proof become much more complicated[20] but the idea and the results remain the same as in 1D.

[1] A. Ishimaru, *Wave Propagation and Scattering in Random Media* (Academic, New York, 1978).
[2] J. B. Keller, ''Stochastic equations and wave propagation in random media,'' *Proceedings of Symposia in Applied Mathematics*, The American Mathematical Society (McGraw-Hill, New York, 1964), Vol. 16, pp. 145–170.
[3] S. M. Rytov, Y. A. Kravtsov, and V. I. Tatarskii, *Principles of Statistical Radiophysics* (Springer-Verlag, Berlin, 1988), Vol. 4.
[4] L. A. Chernov, *Wave Propagation in Random Media* (McGraw-Hill, New York, 1960).
[5] W. E. Boyse, ''Wave propagation and inversion in slightly inhomogeneous media,'' Ph.D. dissertation, Stanford University, 1986.
[6] M. Roth, G. Müller, and R. Sneider, ''Velocity shift in random media,'' Geophys. J. Int. **115**, 552–563 (1993).
[7] E. Wielandt, ''On the validity of the ray approximation for interpreting delay times,'' in *Seismic Tomography*, edited by G. Nolet (Reidel, Dordrecht, 1987), pp. 85–98.
[8] G. Müller, M. Roth, and M. Korn, ''Seismic-wave travel times in random media,'' Geophys. J. Int. **110**, 29–41 (1992).
[9] R. Snieder and D. F. Aldridge, ''Perturbation theory for travel times,'' J. Acoust. Soc. Am. **98**, 1565–1569 (1995).
[10] W. E. Boyse and J. B. Keller, ''Short acoustic, electromagnetic, and elastic waves in random media,'' J. Opt. Soc. Am. A **12**, 380–389 (1994).
[11] S. A. Shapiro, R. Schwarz, and N. Gold, ''The effect of random isotropic inhomogeneities on the phase velocities of seismic waves,'' Geophys. J. Int. **127**, 783–794 (1996).
[12] G. Nolet and T. J. Moser, ''Teleseismic delay times in a 3-D Earth and a new look at the S discrepancy,'' Geophys. J. Int. **114**, 185–195 (1993).
[13] H. van Avendonk and R. Snieder, ''A new mechanism for shape induced seismic anisotropy,'' Wave Motion **20**, 89–98 (1994).
[14] Y. Samuelides and T. Mukerji, ''Velocity shift in heterogeneous media with anisotropic spatial correlation,'' Geophys. J. Int. **134** (in press 1998).
[15] D. A. Dawson and G. C. Papanicolaou, ''A random wave process,'' Applied Mathematics and Optimization **12**, 97–114 (1984).
[16] *Wave Propagation in Random Media (Scintillation)*, edited by V. I. Tatarskii, A. Ishimaru, and V. U. Zavorotny (SPIE and IOP, 1993).
[17] G. E. Backus, ''Long-wave elastic anisotropy produced by horizontal layering,'' J. Geophys. Res. **67**, 4427–4440 (1962).
[18] J. G. Berryman, ''Long-wave elastic anisotropy in transversely isotropic media,'' Geophysics **44**, 896–917 (1980).
[19] G. C. Papanicolaou, ''Asymptotic analysis of stochastic equations,'' in *Studies in Probability Theory*, edited by M. Rosenblatt (Mathematical Association of America, 1978), Vol. 18, pp. 111–179.
[20] F. Bailly, J. F. Clouet, and J. P. Fouque, ''Parabolic and white noise approximation for waves in random media,'' SIAM (Soc. Ind. Appl. Math.) J. Appl. Math. **56**, 1445–1470 (1996).

The elastodynamic finite integration technique for waves in cylindrical geometries

Frank Schubert,[a] Alexander Peiffer,[b] and Bernd Köhler[c]
Fraunhofer-Institute for Nondestructive Testing, Branch Lab Dresden EADQ, Krügerstrasse 22, D-01326 Dresden, Germany

Terry Sanderson[d]
Lucent Technologies, Inc., 2000 NE Expressway, Norcross, Georgia 30071

(Received 30 December 1997; accepted for publication 28 July 1998)

This paper deals with the elastodynamic finite integration technique for axisymmetric wave propagation in a homogeneous and heterogeneous cylindrical medium (CEFIT). This special variant of a finite difference time domain (FDTD) scheme offers a suitable method to calculate real three-dimensional problems in a two-dimensional staggered grid. In order to test the accuracy of the numerical CEFIT code, problems for which analytical solutions are available are presented. These solutions involve wave propagation in an elastic plate, the scattering of a plane longitudinal wave by a spherical obstacle, and ultrasound generation by a thermoelastic laser source. For the latter problem experimental results are included. The CEFIT code also allows the treatment of more complicated problems. Further possible applications are the investigation of elastic waves generated in an acoustic microscope, the simulation of impact-echo measurements in multi-layer systems, axisymmetric wave propagation in arbitrary bodies of revolution, the calculation of elastic wave fields of longitudinal wave transducers with a circular aperture, and the investigation of multi-layer models for particulates. [S0001-4966(98)01911-0]

PACS numbers: 43.20.Bi, 43.20.Fn, 43.35.Ud [DEC]

INTRODUCTION

The propagation of transient elastic waves in solids is known to be a very complex problem. The mode conversions between pressure, shear, and Rayleigh waves at inner and outer boundaries of the specimen make it difficult, and in most cases nearly impossible, to find closed analytical solutions even for simple geometries. For such problems, only numerical modeling techniques can be used.

The elastodynamic finite integration technique (EFIT), originally developed by Fellinger *et al.*,[1] represents a very stable and efficient numerical scheme to investigate wave propagation in homogeneous and heterogeneous, isotropic, and anisotropic linear elastic media.[2,3] Liu *et al.*[4] presented a Cartesian finite difference formulation with a staggered grid resulting in exactly the same equations. The difference between Liu's FD and Fellinger's FIT discretization is only a technical one. While the staggered grid is a direct consequence of the finite integration technique, it is not imperative for the FD scheme. It is introduced ''ad hoc'' in the FD scheme to get a higher accuracy.

In earlier works, EFIT was exclusively used with a Cartesian cubic grid formulation. Because of the large amount of computer capacity required, in most cases only plane strain simulations were performed in a two-dimensional quadratic grid. For problems involving cylindrical geometry, it is more convenient to use cylindrical instead of Cartesian coordinates. By searching for axisymmetric solutions, real three-dimensional problems can be treated in a two-dimensional rectangular grid in the (r,z) half-plane.

In the following paper we present this cylindrical extension of the elastodynamic finite integration technique, abbreviated CEFIT in accordance with the acoustic version of this code for fluid media, CAFIT.[5] In contrast to comparable FD formulations based on the wave equation,[6] the CEFIT procedure discretizes a system of first order equations in time, Hooke's law, and the equation of motion. This technique proves superior in the treatment of boundary conditions (especially in heterogeneous media) and in questions concerning numerical stability.

The accuracy of the CEFIT scheme for homogeneous media is shown by a comparison between simulation results and the Green's functions of an infinite plate. The heterogeneous version of CEFIT is also presented and compared with analytical near-field solutions for the scattering of a plane longitudinal wave by an isotropically elastic sphere and by a spherical cavity.

One example of application deals with the laser generation of ultrasound, modeling a thermoelastic source. In this case the simulation results are compared with experimental measurements and with theoretical solutions based on integral transformations.

I. BASIC EQUATIONS

The starting point of the following considerations are the basic equations of linear elasticity in a cylindrical (r,φ,z) coordinate system,[7] the equations of motion,

[a]Electronic mail: schubert@eadq.izfp.fhg.de
[b]Electronic mail: peiffer@bigfoot;de
[c]Electronic mail: koehler@eadq.izfp.fhg.de
[d]Electronic mail: tmss@mindspring.com

$$\rho\dot{v}_r=\frac{\partial T_{rr}}{\partial r}+\frac{1}{r}\frac{\partial T_{r\varphi}}{\partial\varphi}+\frac{\partial T_{rz}}{\partial z}+\frac{T_{rr}-T_{\varphi\varphi}}{r}+f_r, \tag{1}$$

$$\rho\dot{v}_\varphi=\frac{\partial T_{r\varphi}}{\partial r}+\frac{1}{r}\frac{\partial T_{\varphi\varphi}}{\partial\varphi}+\frac{\partial T_{\varphi z}}{\partial z}+\frac{2}{r}T_{r\varphi}+f_\varphi, \tag{2}$$

$$\rho\dot{v}_z=\frac{\partial T_{rz}}{\partial r}+\frac{1}{r}\frac{\partial T_{\varphi z}}{\partial\varphi}+\frac{\partial T_{zz}}{\partial z}+\frac{1}{r}T_{rz}+f_z, \tag{3}$$

and Hooke's law for an isotropically elastic medium,

$$\dot{T}_{ij}=\lambda\dot{\epsilon}_{kk}\delta_{ij}+2\mu\dot{\epsilon}_{ij}, \tag{4}$$

with

$$\dot{\epsilon}_{rr}=\frac{\partial v_r}{\partial r},\quad \dot{\epsilon}_{\varphi\varphi}=\frac{1}{r}\frac{\partial v_\varphi}{\partial\varphi}+\frac{v_r}{r},\quad \dot{\epsilon}_{zz}=\frac{\partial v_z}{\partial z},$$

$$\dot{\epsilon}_{rz}=\frac{1}{2}\left(\frac{\partial v_z}{\partial r}+\frac{\partial v_r}{\partial z}\right),\quad \dot{\epsilon}_{\varphi z}=\frac{1}{2}\left(\frac{\partial v_\varphi}{\partial z}+\frac{1}{r}\frac{\partial v_z}{\partial\varphi}\right),$$

$$\dot{\epsilon}_{r\varphi}=\frac{1}{2}\left(\frac{1}{r}\frac{\partial v_r}{\partial\varphi}+\frac{\partial v_\varphi}{\partial r}-\frac{v_\varphi}{r}\right).$$

Here, v_i, T_{ij}, and ϵ_{ij} with $i,j=r,\varphi,z$ are the components of the particle displacement velocity vector and that of the stress and strain tensor, respectively. f_i denotes a volume force density. The properties of the elastic medium are given by the two Lamé constants λ and μ and the mass density ρ.

We search for axisymmetric solutions. Therefore all derivations with respect to φ in Eqs. (1)–(4) vanish. This leads to a decoupling of the field components into two independent systems of equations, one system with the six field components v_r, v_z, T_{rr}, $T_{\varphi\varphi}$, T_{zz}, and T_{rz}, and another system with the remaining three field components v_φ, $T_{r\varphi}$, and $T_{\varphi z}$. The latter components are only necessary to describe rotationally invariant torsion waves, which are rather of minor interest. Therefore the following discussion focuses on the first system of equations which is given as follows:

$$\rho\dot{v}_r=\frac{\partial T_{rr}}{\partial r}+\frac{\partial T_{rz}}{\partial z}+\frac{T_{rr}-T_{\varphi\varphi}}{r}+f_r, \tag{5}$$

$$\rho\dot{v}_z=\frac{\partial T_{rz}}{\partial r}+\frac{\partial T_{zz}}{\partial z}+\frac{T_{rz}}{r}+f_z, \tag{6}$$

and

$$\dot{T}_{rr}=(\lambda+2\mu)\frac{\partial v_r}{\partial r}+\lambda\left[\frac{v_r}{r}+\frac{\partial v_z}{\partial z}\right], \tag{7}$$

$$\dot{T}_{\varphi\varphi}=(\lambda+2\mu)\frac{v_r}{r}+\lambda\left[\frac{\partial v_r}{\partial r}+\frac{\partial v_z}{\partial z}\right], \tag{8}$$

$$\dot{T}_{zz}=(\lambda+2\mu)\frac{\partial v_z}{\partial z}+\lambda\left[\frac{\partial v_r}{\partial r}+\frac{v_r}{r}\right], \tag{9}$$

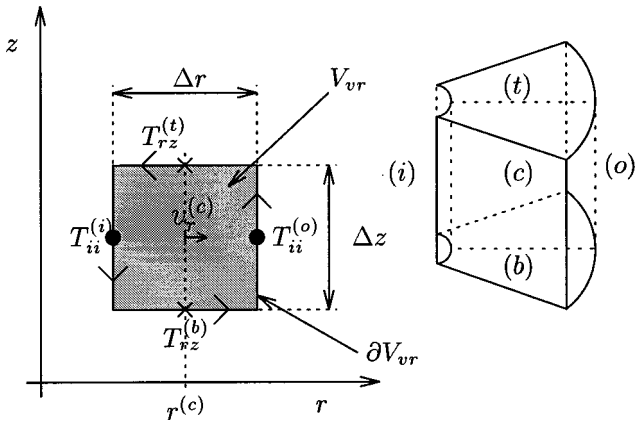

FIG. 1. Naming conventions in the v_r integration cell.

$$\dot{T}_{rz}=\mu\left[\frac{\partial v_r}{\partial z}+\frac{\partial v_z}{\partial r}\right]. \tag{10}$$

These equations need to be discretized by the FIT procedure as described in the next section.

II. DISCRETE EQUATIONS

The idea of the finite integration technique (FIT) or finite volume method (FVM) is to perform an integration of differential equations like Eqs. (5)–(10) over a certain control volume or integration cell.

Note that it is also possible to discretize the three-dimensional Eqs. (1)–(4) allowing nonaxisymmetric solutions (see, for example, Refs. 8 and 9). But in the case of an elastic medium, the finite integration over curvilinear three-dimensional control volumes bears some problems which deteriorate the accuracy of the resulting numerical code (these problems are beyond the scope of this work). Besides, a 3-D code is not efficient at present due to the large amount of computer memory required. On standard workstations available today only very coarse grids can be realized, leading to severe numerical dispersion and an inadequate discretization of curved surfaces.

For these reasons we will here only perform the area integration of Eqs. (5)–(10) over the axial (z) and radial component (r), focusing on the problem of axisymmetric wave propagation.

A. Conventions

In Fig. 1 the three-dimensional control volume for the v_r component is shown together with the corresponding two-dimensional area cell. The superscripts (o) and (i) denote the outer and inner gridpoints relative to the center point (c). (t) and (b) represent the top and bottom gridpoint. Δr and Δz are the edge lengths of the area cell.

B. FIT procedure

The area integration of Eq. (5) according to Green's law gives

$$\int\int_{V_{vr}} \rho \dot{v}_r \, dr \, dz$$

$$= \int\int_{V_{vr}} \left[\frac{\partial T_{rr}}{\partial r} + \frac{\partial T_{rz}}{\partial z} + \frac{T_{rr} - T_{\varphi\varphi}}{r} + f_r \right] dr \, dz$$

$$= \oint_{\partial V_{vr}} [T_{rr} \, dz - T_{rz} \, dr]$$

$$+ \int\int_{V_{vr}} \left[\frac{T_{rr} - T_{\varphi\varphi}}{r} + f_r \right] dr \, dz. \tag{11}$$

These integrals can be approximated by multiplying the mean value of the integrand (averaged over the area cell and over the edge, respectively) by the corresponding area or edge length. This yields the following discrete approximation of Eq. (11):

$$\rho \dot{v}_r^{(c)} \Delta r \Delta z = [T_{rr}^{(o)} - T_{rr}^{(i)}] \Delta z + [T_{rz}^{(t)} - T_{rz}^{(b)}] \Delta r + \left[\frac{T_{rr}^{(c)} - T_{\varphi\varphi}^{(c)}}{r^{(c)}} + f_r^{(c)} \right] \Delta r \Delta z. \tag{12}$$

In contrast to the Cartesian EFIT equations,[1] some stress components (T_{rr} and $T_{\varphi\varphi}$) are located on the edges and additionally at the center of the v_r integration cell. For the central components we use a linear interpolation,

$$T_{rr}^{(c)} = \frac{T_{rr}^{(o)} + T_{rr}^{(i)}}{2}, \quad T_{\varphi\varphi}^{(c)} = \frac{T_{\varphi\varphi}^{(o)} + T_{\varphi\varphi}^{(i)}}{2}. \tag{13}$$

Using this interpolation and dividing by $\Delta r \Delta z$ results in the discrete equation of motion for v_r:

$$\rho \dot{v}_r^{(c)} = \frac{T_{rr}^{(o)} - T_{rr}^{(i)}}{\Delta r} + \frac{T_{rz}^{(t)} - T_{rz}^{(b)}}{\Delta z} + \frac{T_{rr}^{(o)} + T_{rr}^{(i)} - T_{\varphi\varphi}^{(o)} - T_{\varphi\varphi}^{(i)}}{2r^{(c)}} + f_r^{(c)}. \tag{14}$$

The derivation of the discrete versions of Eqs. (6)–(10) is similar to the procedure described before, resulting in

$$\rho \dot{v}_z^{(c)} = \frac{T_{rz}^{(o)} - T_{rz}^{(i)}}{\Delta r} + \frac{T_{zz}^{(t)} - T_{zz}^{(b)}}{\Delta z} + \frac{T_{rz}^{(o)} + T_{rz}^{(i)}}{2r^{(c)}} + f_z^{(c)}, \tag{15}$$

$$\dot{T}_{rr}^{(c)} = (\lambda + 2\mu) \frac{v_r^{(o)} - v_r^{(i)}}{\Delta r} + \lambda \left[\frac{v_z^{(t)} - v_z^{(b)}}{\Delta z} + \frac{v_r^{(o)} + v_r^{(i)}}{2r^{(c)}} \right], \tag{16}$$

$$\dot{T}_{\varphi\varphi}^{(c)} = (\lambda + 2\mu) \frac{v_r^{(o)} + v_r^{(i)}}{2r^{(c)}} + \lambda \left[\frac{v_r^{(o)} - v_r^{(i)}}{\Delta r} + \frac{v_z^{(t)} - v_z^{(b)}}{\Delta z} \right], \tag{17}$$

$$\dot{T}_{zz}^{(c)} = (\lambda + 2\mu) \frac{v_z^{(t)} - v_z^{(b)}}{\Delta z} + \lambda \left[\frac{v_r^{(o)} - v_r^{(i)}}{\Delta r} + \frac{v_r^{(o)} + v_r^{(i)}}{2r^{(c)}} \right], \tag{18}$$

$$\dot{T}_{rz}^{(c)} = \mu \left[\frac{v_r^{(t)} - v_r^{(b)}}{\Delta z} + \frac{v_z^{(o)} - v_z^{(i)}}{\Delta r} \right]. \tag{19}$$

In the following the volume force density components f_r and f_z are excluded from consideration because we will only present examples of application where the elastic wave generation takes place at the surface and not inside the specimen.

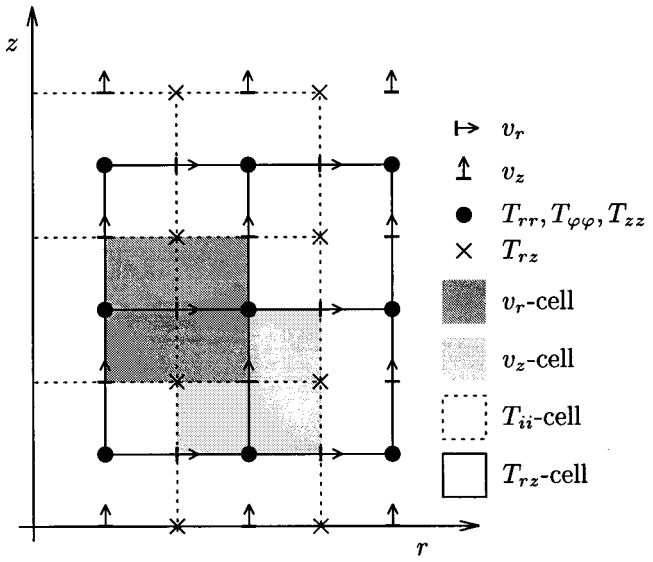

FIG. 2. CEFIT grid arrangement.

Note that the concept of FIT given above leads to a staggered grid automatically. The arrangement of all control cells is shown in Fig. 2, representing the CEFIT grid in the (r,z) half-plane. CEFIT is an explicit scheme. Each new time step is calculated by using the time derivatives of Eqs. (14)–(19) and a central difference operator in time:

$$v_i^{(l)} = v_i^{(l-1)} + \dot{v}_i^{(l-1/2)} \Delta t, \tag{20}$$

$$T_{ij}^{(l+1/2)} = T_{ij}^{(l-1/2)} + \dot{T}_{ij}^{(l)} \Delta t, \tag{21}$$

where the index (l) denotes full and half time steps of Δt. Thus the time steps with regard to T_{ij} and v_i are also staggered. This fact follows directly from the staggered arrangement of the spatial grid.

C. Stability and spatial discretization

As stability criterion for the CEFIT scheme we used a similar condition as derived by Fellinger *et al.* for the two-dimensional Cartesian EFIT code.[1] No difficulties were encountered. The temporal discretization is related to the highest wave speed according to

$$\Delta t \leqslant \frac{1}{c_{\max} \sqrt{1/\Delta r^2 + 1/\Delta z^2}}, \tag{22}$$

where $c_{\max}$ represents the highest (longitudinal) wave speed of the elastic medium. If a quadratic grid is used ($\Delta r = \Delta z$), Eq. (22) reduces to

$$\Delta t \leqslant \frac{\Delta z}{c_{\max} \sqrt{2}}. \tag{23}$$

It should be noted that this stability condition is less restrictive than that of Ilan and Weight's FD scheme,[6] but more advanced FD schemes using a staggered grid (for example Refs. 8 and 9) give the same condition.

While the criterion for the temporal discretization must be satisfied strictly in order to guarantee the stability of

CEFIT, the criterion for the spatial discretization is a ''soft'' condition that should (but not must) be fulfilled.

It seems reasonable that the shortest wavelength in the signal should be discretized by eight grid points at least. This condition leads to

$$\Delta z \leqslant \frac{1}{8}\lambda_{\min} = \frac{1}{8}\frac{c_{\min}}{f_{\max}}, \tag{24}$$

where $f_{\max}$ denotes the highest frequency in the signal. $c_{\min}$ is the lowest wave speed of the medium and this is a Rayleigh wave speed in general. Since Rayleigh waves are between 4.5% and 12.6% slower than the shear waves, we can replace Eq. (24) by the following approximation which is somewhat easier to handle:

$$\Delta z \leqslant \frac{1}{8}\frac{c_{R,\min}}{f_{\max}} \approx \frac{1}{10}\frac{c_{S,\min}}{f_{\max}}, \tag{25}$$

where $c_{R,\min}$ and $c_{S,\min}$ denote the (lowest) Rayleigh and the (lowest) shear wave speed, respectively. Of course the condition for Δr is equivalent.

In Sec. III A the effect of an insufficient discretization of the shortest wavelengths is shown.

D. Boundary conditions

The simple treatment of different boundary conditions will show one advantage of the finite integration technique compared to classical FD schemes using a nonstaggered grid. For the applications presented here, boundary conditions at the axis, at the outer surface of the specimens and, in the case of heterogeneous media, at inner boundaries must be implemented.

1. Axial boundary conditions

Boundary conditions need to be applied at the axis for $r=0$. For reasons of stability it is more convenient to locate T_{rz} and v_r instead of T_{ii} and v_z at the axis. Because of the cylindrical geometry, both v_r $(r=0)$ and T_{rz} $(r=0)$ vanish. Therefore, no field component has to be calculated at the axis. Naming the grid points immediately *beside* the axis by the superscript (a) we get the following equations:

$$\rho \dot{v}_z^{(a)} = 2\frac{T_{rz}^{(o)}}{\Delta r} + \frac{T_{zz}^{(t)} - T_{zz}^{(b)}}{\Delta z}, \tag{26}$$

$$\dot{T}_{rr}^{(a)} = (2\lambda + 2\mu)\frac{v_r^{(o)}}{\Delta r} + \lambda\frac{v_z^{(t)} - v_z^{(b)}}{\Delta z}, \tag{27}$$

$$\dot{T}_{\varphi\varphi}^{(a)} = (2\lambda + 2\mu)\frac{v_r^{(o)}}{\Delta r} + \lambda\frac{v_z^{(t)} - v_z^{(b)}}{\Delta z}, \tag{28}$$

$$\dot{T}_{zz}^{(a)} = (\lambda + 2\mu)\frac{v_z^{(t)} - v_z^{(b)}}{\Delta z} + 2\lambda\frac{v_r^{(o)}}{\Delta r}. \tag{29}$$

2. Stress-free boundary conditions

In the simulations described in Secs. III and IV, we applied stress-free boundary conditions at the outer boundaries of the synthetic specimen, resulting in $\mathbf{n}\cdot\mathbf{T}=\mathbf{0}$, where $\mathbf{n}$ denotes the outward unit normal vector on the grid edges. That leads to explicit conditions at the following boundaries:

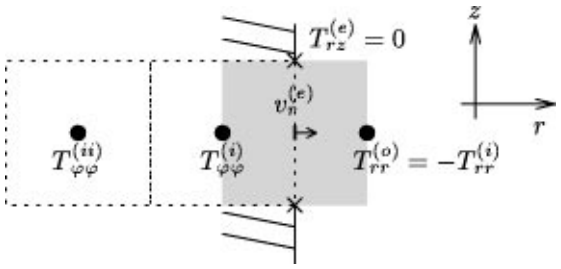

FIG. 3. v_r integration cell at the lateral surface.

(1) Front and rear surface of cylinder:

$$T_{zz}(z=0,r) = T_{rz}(z=0,r) = 0, \tag{30}$$

$$T_{zz}(z=z_0,r) = T_{rz}(z=z_0,r) = 0. \tag{31}$$

(2) Lateral surface:

$$T_{rr}(z,r=r_0) = T_{rz}(z,r=r_0) = 0. \tag{32}$$

Because of the staggered grid formulation, the stress-free boundary conditions can be realized by placing either the T_{ii} or the T_{rz} components at the boundary. To demonstrate the procedure at the lateral surface, we consider Fig. 3 where a v_r integration cell is shown. In this case, we placed the v_r and the T_{rz} components at the stress-free boundary, denoted by the superscript (e).

Because of Eq. (32), $T_{rz}^{(t)}$ and $T_{rz}^{(b)}$ vanish at the boundary. To guarantee that $T_{rr}^{(e)}$ is also zero there, we have to use a pseudo-component outside the specimen: $T_{rr}^{(o)} = -T_{rr}^{(i)}$. The stress component $T_{\varphi\varphi}^{(o)}$ is approximated by a linear extrapolation using the two $T_{\varphi\varphi}$ values from the neighboring grid cells on the left side of the central cell, $T_{\varphi\varphi}^{(i)}$ and say $T_{\varphi\varphi}^{(ii)}$, where the superscript (ii) denotes a grid position to the left of position (i). By that we obtain $T_{\varphi\varphi}^{(o)} = 2T_{\varphi\varphi}^{(i)} - T_{\varphi\varphi}^{(ii)}$. Considering these facts, we get as a discrete equation for the lateral boundary:

$$\rho \dot{v}_r^{(e)} = -\frac{2T_{rr}^{(i)}}{\Delta r} - \frac{3T_{\varphi\varphi}^{(i)} - T_{\varphi\varphi}^{(ii)}}{2r^{(e)}}. \tag{33}$$

The treatment of the front and rear boundary is similar, except that the problem with the $T_{\varphi\varphi}$ component does not appear. The discrete equations for $v_z^{(e)}$ are:

(1) Front boundary:

$$\rho \dot{v}_z^{(e)} = \frac{2T_{zz}^{(t)}}{\Delta z}. \tag{34}$$

(2) Rear boundary:

$$\rho \dot{v}_z^{(e)} = -\frac{2T_{zz}^{(b)}}{\Delta z}. \tag{35}$$

Note that this implementation of the boundary is very simple. In standard FD schemes using a nonstaggered grid, more effort is required to derive the equations for the field components at the boundary.[10]

As mentioned above, it is also possible to place the T_{ii} instead of the T_{rz} components at the stress-free boundary. This problem can also be solved in a straightforward way. This alternative treatment becomes important if the genera-

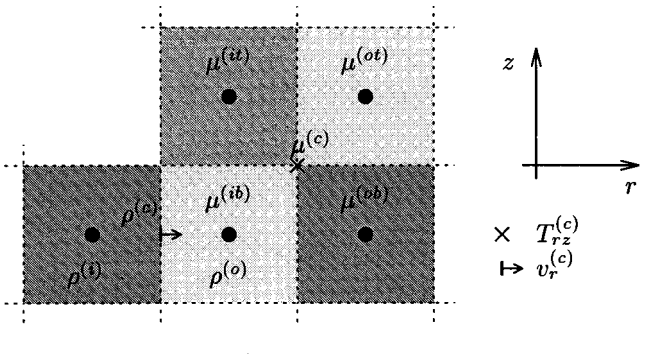

FIG. 4. Control volumes of different material properties.

tion of the elastic waves at the surface of the specimen is realized by using the stress components instead of the velocity components as ''elastic sources.''

3. Plane wave boundary conditions

In order to realize a plane longitudinal wave propagating in the positive z direction, plane wave boundary conditions must be implemented at the lateral boundary. If v_r and T_{rz} are placed there, these conditions require $T_{rr}^{(o)}=T_{rr}^{(i)}$, $T_{\varphi\varphi}^{(o)}=T_{\varphi\varphi}^{(i)}$, and $v_z^{(o)}=v_z^{(i)}$, resulting in

$$\rho\dot{v}_r^{(e)}=\frac{T_{rz}^{(t)}-T_{rz}^{(b)}}{\Delta z}+\frac{T_{rr}^{(i)}-T_{\varphi\varphi}^{(i)}}{r^{(e)}} \tag{36}$$

and

$$\dot{T}_{rz}^{(e)}=\mu\,\frac{v_r^{(t)}-v_r^{(b)}}{\Delta z}. \tag{37}$$

Note that the plane wave boundary conditions should only be valid for the incoming wave, but in fact they are also active for secondary waves, e.g., scattered waves from inside the specimen. This leads to some conflicts of interests which can only (partly) be solved by using absorbing boundary conditions. But for the applications presented in Sec. III, the formulation of Eqs. (36) and (37) is sufficient.

4. Inhomogenous materials

In isotropic heterogeneous media, a suitable discretization of the material parameters $\rho(r,z)$, $\lambda(r,z)$, and $\mu(r,z)$ has to be realized. On the surface of these material cells, appropriate boundary conditions must be fulfilled resulting in the continuity of $\mathbf{n}\cdot\mathbf{T}$ and $\mathbf{v}$.

It can be shown that the only consistent way to obtain stable results is to choose the material parameter grid to coincide with the T_{ii} integration cells. That means the T_{rz} components are placed at the corners of the material cells while v_r and v_z are located on the edges.

To give an example, we consider $v_r^{(c)}$ lying on the vertical edge between two different material cells (o) and (i) (see Fig. 4). Using an averaging procedure we propose a definition for the left hand side of Eq. (14):

$$\rho\dot{v}_r^{(c)}\rightarrow\rho^{(c)}\dot{v}_r^{(c)}:=\lim_{\delta r\rightarrow 0}\tfrac{1}{2}\left[\rho^{(o)}\dot{v}_r^{(c+\delta r)}+\rho^{(i)}\dot{v}_r^{(c-\delta r)}\right], \tag{38}$$

with $\delta r>0$. In Eq. (38), $\dot{v}_r^{(r\pm\delta r)}$ represents two (imaginary) velocity positions *inside* the two neighboring material cells (δr should not be mixed up with Δr, which denotes the spatial discretization in r-direction). The continuity of $\dot{v}_r$ requires $\dot{v}_r^{(c+\delta r)}=\dot{v}_r^{(c-\delta r)}=\dot{v}_r^{(c)}$ for $\delta r\rightarrow 0$. We obtain for the resulting density:

$$\rho^{(c)}=\frac{\rho^{(o)}+\rho^{(i)}}{2}. \tag{39}$$

Consequently for heterogeneous media, the density ρ on the left hand side of Eq. (14) must be replaced by $\rho^{(c)}$ as given by Eq. (39).

In analogy to the procedure above we obtain for the v_z component and the LHS of Eq. (15):

$$\rho^{(c)}=\frac{\rho^{(t)}+\rho^{(b)}}{2}. \tag{40}$$

As described before, the T_{rz} components are placed at the corners where four different material cells meet. After dividing by μ we can therefore write for the LHS of Eq. (19):

$$\frac{T_{rz}^{(c)}}{\mu}\rightarrow\frac{T_{rz}^{(c)}}{\mu^{(c)}}:=\lim_{\substack{\delta r\rightarrow 0\\ \delta z\rightarrow 0}}\frac{1}{4}\left[\frac{T_{rz}^{(c-\delta r-\delta z)}}{\mu^{(ib)}}+\frac{T_{rz}^{(c-\delta r+\delta z)}}{\mu^{(it)}}+\frac{T_{rz}^{(c+\delta r-\delta z)}}{\mu^{(ob)}}+\frac{T_{rz}^{(c+\delta r+\delta z)}}{\mu^{(ot)}}\right], \tag{41}$$

where (ib), (it), (ob), and (ot) denote the inner bottom, inner top, outer bottom, and outer top material cells (see Fig. 4). The continuity of $\dot{T}_{rz}$ for $\delta r\rightarrow 0$ and $\delta z\rightarrow 0$ leads to

$$\mu^{(c)}=\frac{4}{1/\mu^{(ib)}+1/\mu^{(it)}+1/\mu^{(ob)}+1/\mu^{(ot)}}, \tag{42}$$

which has to be used instead of μ in Eq. (19).

Since the T_{ii} integration cells coincide with the material parameter grid Eqs. (16)–(18) remain unchanged, taking into account that the values of λ and μ depend on the properties of the corresponding material cell.

III. TEST CASES

In order to prove the accuracy of the CEFIT code for homogeneous and inhomogeneous media, the numerical results were compared with analytical solutions, i.e., wave propagation in an elastic plate and the scattering of plane compressional waves by spherical obstacles.

A. Homogeneous media

To verify the discretization scheme of Eqs. (14)–(21), the wave propagation in a homogeneous elastic plate caused by a normal force impact acting on one surface of the plate in the positive z direction was calculated numerically.

The elastic parameters of the plate were chosen to be $c_L=5900$ m/s, $c_S=3200$ m/s, and $\rho=7820$ kg/m^3, which

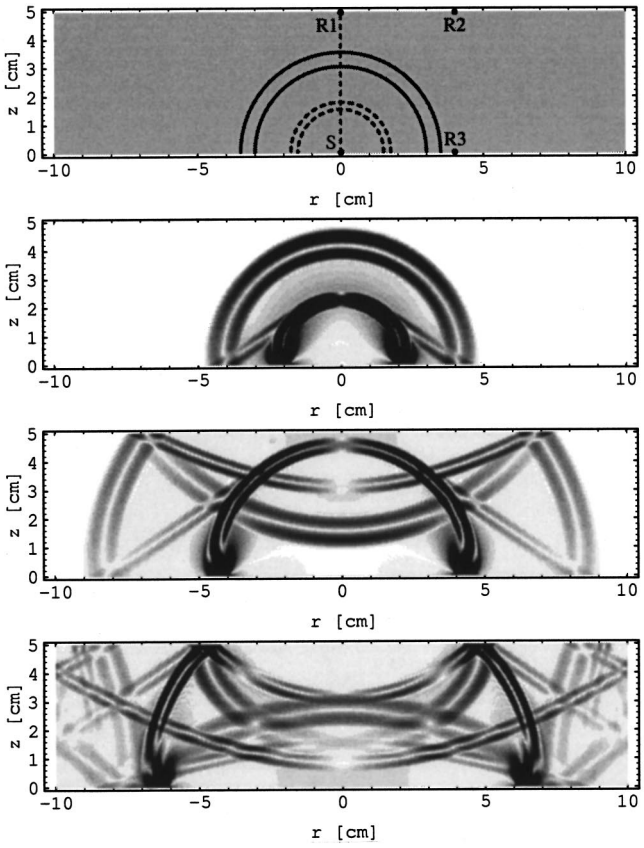

FIG. 5. Snapshots of wave propagation in an elastic plate. The gray scale images represent the absolute value of the particle velocity vector. The points denote the different receiver positions where the (calculated) time signals were detected.

are typical values for steel. The thickness of the (cylindrical) plate was $d=5$ cm, while its radius amounted to $r_0=10$ cm. The impact excitation was modeled as a half-cycle sine^2 wave with a duration of 2 μs, using the T_{zz} component of the grid point $P(r=0, z=0)$ at the bottom surface of the plate as ''elastic source'' *S*.

Since the maximum frequency of the impact spectrum can approximately be chosen as $f_{\max}=2$ MHz, conditions (23) and (25) lead to $\Delta r \leqslant 160$ μm and $\Delta t \leqslant 19.175$ ns. In order to fulfill these conditions we used a quadratic grid with the discretization parameters $\Delta r=\Delta z=80$ μm and $\Delta t=9.587$ ns, resulting in 1250×625 grid cells and 2608 time steps (total observation time $t\approx 25$ μs).

Figure 5 shows the test setup and the calculated CEFIT snapshots of the elastic wave field at three different times, $t_1=8.15$ μs, $t_2=15.34$ μs, and $t_3=22.53$ μs. The wavefronts are displayed as gray scale images representing the absolute value of the particle velocity vector, $|\mathbf{v}|=\sqrt{v_r^2+v_z^2}$. For reasons of a better presentation, the calculated wave field on the right side of the (r,z) half-plane (positive r values) was mirrored at the cylinder axis so that the wave field on the left side (denoted by negative r values) simply represents the reflected image of the right side.

TABLE I. Arrival times at receiver positions (in μs).

	P wave	*S* wave	*R* wave	*P*-*P* reflex
R1	8.4678	15.6125	···	···
R2	10.8517	20.0078	···	···
R3	6.7864	12.5125	13.5110	18.2447

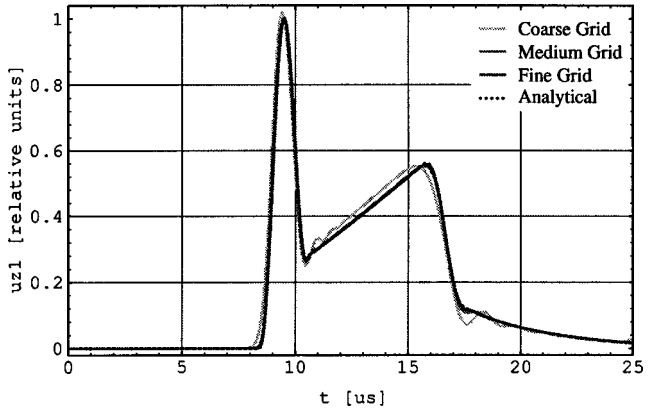

FIG. 6. Displacement u_z at receiver position R1.

To verify the accuracy of the homogeneous CEFIT code, the plate response was detected at three different receiver positions, namely at position R1 ($r=0$, $z=5$ cm) to check the wave propagation along the cylinder axis, at position R2 ($r=4$, $z=5$ cm) to get a strong shear wave, and at position R3 ($r=4$, $z=0$ cm) to look at the Rayleigh wave and first longitudinal backwall reflection. The results are compared with analytical Green's functions of an infinite plate. For the Green's functions we used a program developed by Hsu,[11] based on a ray-theory solution by Ceranoglu and Pao.[12] Table I shows the arrival times of the different modes at the three receiver positions representing results of the analytical solutions.

Using the discretization grid from above ($\Delta r=80$ μm) and therefore fulfilling the criterion $\Delta r \leqslant 160$ μm leads to a nearly perfect agreement between the analytical solutions and the simulation results.

Nevertheless, in order to show the effect of insufficient discretization of the shortest wavelengths, we also used discretization parameters of $\Delta r=200$, 400, and 800 μm, which do not fulfill the Δr criterion from above. Figures 6–8 show the detected displacements at the three receiver positions. The different discretization grids are denoted as coarse, medium, and fine grid.

As it can be seen from Figs. 6–8, an inadequate spatial

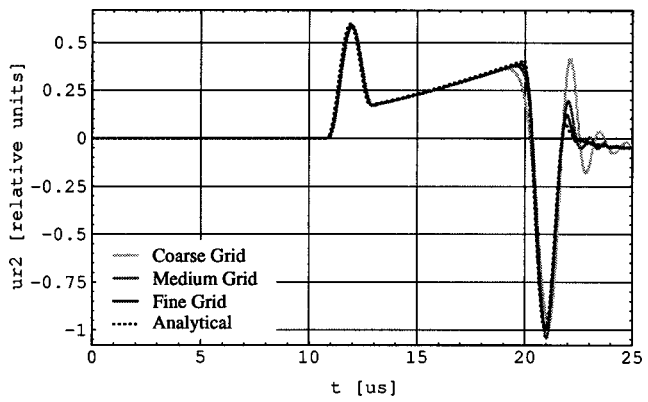

FIG. 7. Displacement u_r at receiver position R2.

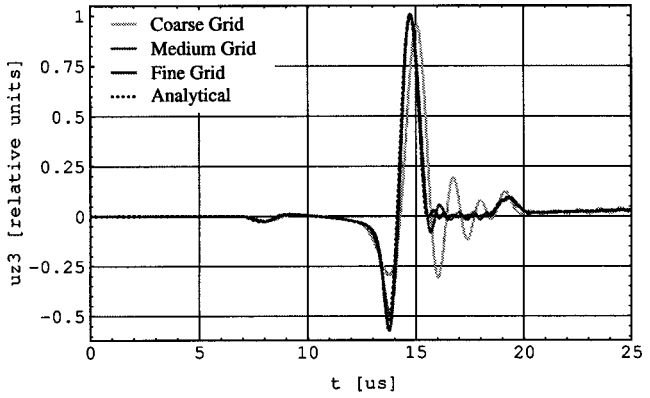

FIG. 8. Displacement u_z at receiver position R3.

discretization leads to numerical ringing in the signals. For the shear and the Rayleigh wave, dominating in Fig. 7 and 8, respectively, this effect is much stronger than for the longitudinal wave, due to the lower wave speeds. As the grid becomes finer, the numerical ringing decreases. Here the 200-μm grid (the ''fine'' grid) leads to only small deviations from the analytical solutions. These deviations become negligible if the Δr criterion is fulfilled.

It should be pointed out that in CEFIT there are no numerical problems involving the wave propagation along the cylinder axis. This fact demonstrates the consistency of the axial boundary conditions given in Sec. II D, placing the staggered grid in such a way that no field component has to be calculated immediately at the axis.

B. Heterogeneous media

To test the accuracy of CEFIT for heterogeneous media, we considered the scattering of a plane longitudinal wave by a spherical cavity and by an isotropically elastic sphere, using the material properties from Table II.

The spherical obstacle of radius $R=1$ cm was placed at the cylinder axis so that the center of the sphere was located at $r=0$ and $z=50$ mm (see Fig. 9 top). The cavity surface was discretized by using the stress-free boundary conditions described in Sec. II D. For the elastic sphere the averaged material parameters (39)–(42) were used.

A plane longitudinal wave was sent into the synthetic specimen by using each of the discrete T_{zz} components along the front surface of the cylinder as elastic sources. For the incoming wave, the plane wave boundary conditions from Sec. II D were realized at the lateral boundary. The time history of the input pulse was modeled as an RC2 signal,

$$T_{zz}^{(z=0)}=\begin{cases}(1-\cos(\pi f_c t))\cos(2\pi f_c t), & 0\leqslant t\leqslant 2/f_c\\ 0, & t>2/f_c\end{cases},$$

with a center frequency of $f_c=500$ kHz. By choosing $f_{\max}\approx 1$ MHz, conditions (23) and (25) lead to $\Delta r\leqslant 225$ μm and $\Delta t\leqslant 25.537$ ns. For the simulations we used three different quadratic discretization grids, namely $\Delta r=\Delta z=168.75$, 112.5, and 56.25 μm, with appropriate time steps.

TABLE II. Material parameters.

	c_L [m/s]	c_S [m/s]	ρ [kg/m^3]
Cement matrix	3950	2250	2050
Basalt inclusion	6230	3330	2950

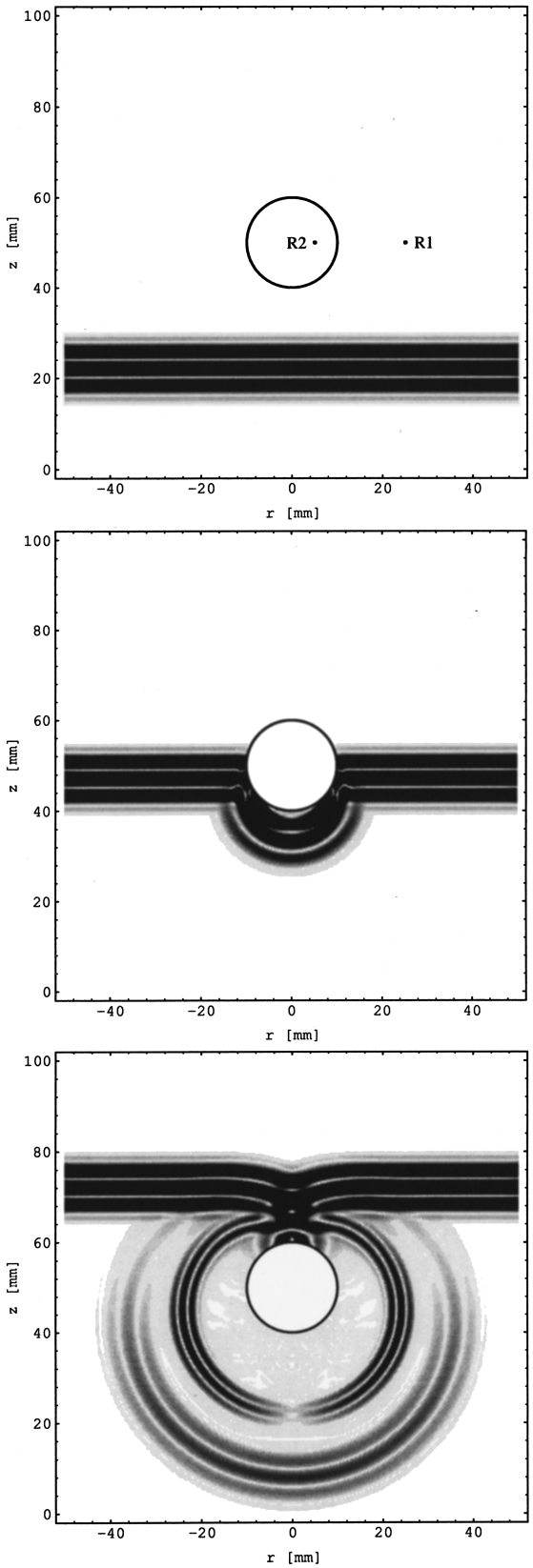

FIG. 9. Gray scale images of scattering by a spherical cavity representing the absolute value of particle velocity.

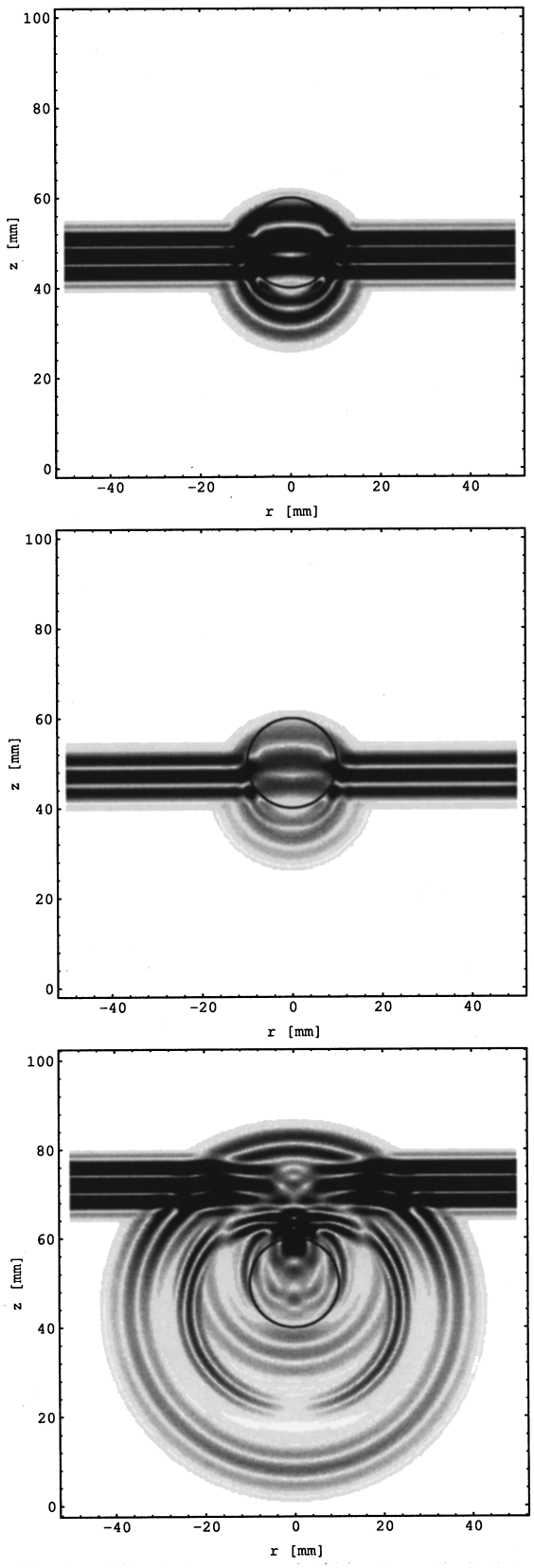

FIG. 10. Gray scale images of scattering by an isotropically elastic sphere representing the absolute value of particle velocity.

The particle velocity was detected outside the obstacle at position R1 ($r=25$, $z=50$ mm) and, in the case of the elastic sphere, additionally at position R2 ($r=5$, $z=50$ mm) inside

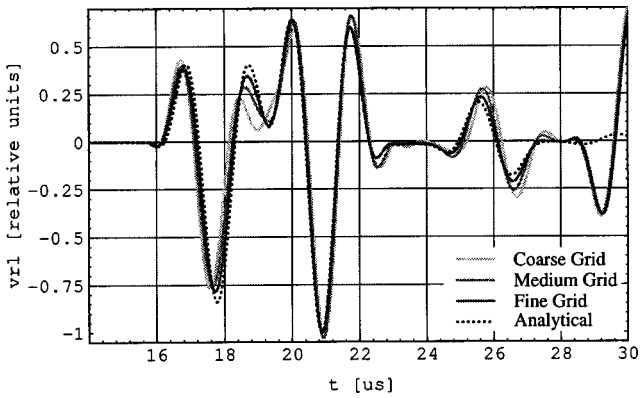

FIG. 11. Velocity v_r at receiver position R1 (cavity).

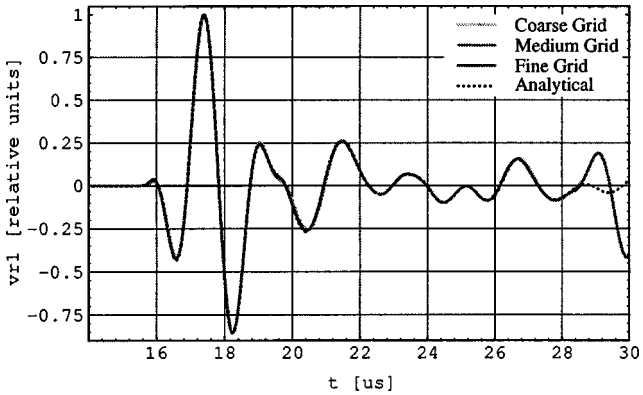

FIG. 12. Velocity v_r at position R1 (elastic sphere).

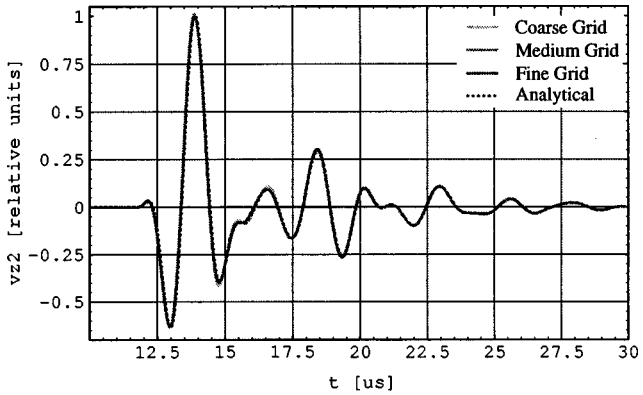

FIG. 13. Velocity v_z at position R2 (elastic sphere).

the obstacle. The simulation results were compared with analytical solutions based on the theory of Ying and Truell,[13] using the matrix formulation of Pao and Mow.[14] For the evaluation Bessel and Hankel functions up to orders of $m=50$ were taken into account in order to guarantee the convergence of the infinite sums for frequencies up to $f_{\max}=1$ MHz.

Figures 9 and 10 show snapshots of the scattering process at the cavity and at the elastic sphere for three different times, $t_1=7.59\ \mu$s, $t_2=13.92\ \mu$s, and $t_3=20.25\ \mu$s. In the case of the elastic sphere the snapshot at $t_2=13.92\ \mu$s is repeated with a different gray scale in order to show more details of the wave inside the scatterer.

In Figs. 11 and 12 the detected velocity signal v_r is given at receiver position R1 in the near field of the cavity

and the elastic sphere. It can be seen that the roughness of the discretized cavity surface has a significant effect on the signal. But the finer the spatial grid, the better the agreement with the analytical curve.

In the case of the elastic sphere the agreement between the simulation and the analytical results is much better, even for the coarse discretization. This is possibly due to the fact that here the main part of the detected signal is caused by a transmission process through the sphere of higher wave speed, and not only by a reflection from the surface as in the case of the cavity. This explanation is confirmed by the fact that the first velocity signal from the elastic sphere arrives a little bit earlier than that from the cavity.

Moreover, because of the longer wavelength of the wave inside the scatterer, the surface discretization of the obstacle is much better for this transmitted wave than for the incoming (and reflected) wave. Therefore the agreement with the analytical curve is significantly better for the same spatial discretization grid.

In both cases (cavity and elastic sphere) at $t \approx 28\ \mu$m, a reflection from the lateral boundary appears in the simulation signals due to the imperfect boundary conditions at the lateral surface of the specimen. The plane wave boundary conditions are only optimum for the incoming wave but not for the scattered waves (compare Sec. II D).

In Fig. 13 the velocity signal v_z inside the obstacle is shown. Again we can see a nearly perfect agreement between the simulation results and the solution obtained by the theory of Ying and Truell.

To the knowledge of the authors, this is the first published test of a heterogeneous EFIT version against analytical solutions. Note that for $r \to \infty$ (and neglecting $T_{\varphi\varphi}$) the CEFIT equations (14)–(19) are transformed into the Cartesian 2D-EFIT equations *including* the boundary conditions. Therefore the investigations of this section can also be taken as an indirect test of the heterogeneous 2D-EFIT in a Cartesian grid.

IV. EXAMPLE OF APPLICATION—LASER SOURCE

An application of practical interest is the calculation of laser generated ultrasound. References dealing with this problem[15–17] give integral transformed solutions, which have to be evaluated by numerical methods. However, most solutions require certain simplifications concerning source and specimen. In the CEFIT scheme we are free to model different kinds of laser sources and solids.

The correct treatment of thermoelastic sources at the surface requires the consideration of heat transfer. For very short laser pulses in the range of picoseconds, it is even necessary to take hyperbolic heat equations. Here, we only deal with the thermoelastic generation mechanism, neglecting thermal diffusion.

The thermoelastic source in locally isotropic media gives only contributions to the symmetric components of the stress tensor in Eqs. (1)–(3).[18,16] But for optically opaque media, the local heating takes place at the irradiated surface. Therefore, there is an instant mode conversion that is the reason for the generation of shear waves.

To further validate CEFIT, we compare the results of CEFIT to the analytical results[17] including thermal diffusion, and to measurements performed at the Fraunhofer Branchlab (EADQ) in Dresden.[19] As thermal diffusion is not included in CEFIT, there are some differences between the waveforms along the axis.

A. Implementation of source and material

A cylindrical disk with free surfaces is taken as specimen. The implementation of the thermoelastic source is performed in a very simple way. The volume expansion due to local heating leads to an additional source term T^+ on the RHS of Eqs. (7)–(9):[18]

$$\dot{T}^+(z,r,t) = -\beta_0 \dot{q}(z,r,t), \quad \beta_0 = \Gamma \frac{c_L^2}{c_p}\left(3 - 4\frac{c_S^2}{c_L^2}\right). \tag{43}$$

β_0 is the thermoelastic coupling constant, c_p the specific heat at constant pressure, Γ the linear thermal expansion coefficient, and q the energy per volume (c_p should not be mixed up with the longitudinal wave speed c_L). The penetration depth of lasers into steel is in the range of some nanometers, but we are not able to use such fine grids. The number of grid points would be to high. Thus we apply source term (43) for the stress components T_{rr}, $T_{\varphi\varphi}$, and T_{zz} of the first layer of gridpoints at the surface. The thickness of the heated region is therefore determined by Δz and not by the physical parameters of penetration depth and thermal diffusion. The cross section of the laser beam is assumed to be Gaussian:

$$\Psi(r) = \frac{1}{2\pi\sigma^2} e^{-r^2/(2\sigma^2)}. \tag{44}$$

Using the normalized temporal profile given in Ref. 17 we get

$$\dot{q}(z = \Delta z/2, r, t) = -\frac{E_0}{\Delta z}\Psi(r)\frac{8t^3}{\tau^4}\exp\frac{-2t^2}{\tau^2}. \tag{45}$$

E_0 is the absorbed energy and τ the rise time.

The smallest wavelength in the z direction is determined by the spectrum of $T^+(r,t)$ and the lowest wave speed. At the frequency of $f_{\max} \approx 90$ MHz the magnitude is below 10% of the maximum. Taking c_S as $c_{\min}$ in Eq. (24) we get $\Delta z \approx 5\ \mu$m (see Table III).

The shortest wavelength in the radial direction is determined by the laser profile and is estimated by $\lambda_{r,\,\min} \approx \sigma$. Using Eq. (25) we get $\Delta r \approx 80\ \mu$m.

This grid is extremely noncubic. If we would take a cubic grid using $\Delta r = \Delta z = 5\ \mu$m, the specimen of $2 \times 5\ \text{cm}^2$ must be represented by a grid of $4000 \times 10\,000$ points. Assuming a memory usage of 8 bytes per component

TABLE III. Source and material parameters.

σ	571.0 μm	τ	15.5 ns
E_0	0.928 mJ	ρ	7700 kg m^{-3}
c_L	6040.2 m/s	c_S	3391.5 m/s
Γ	12.2×10^{-6} K^{-1}	c_p	465 J kg^{-1} K^{-1}
R	5.0 cm	D	2.0 cm
Δr	80 μm	Δz	5 μm

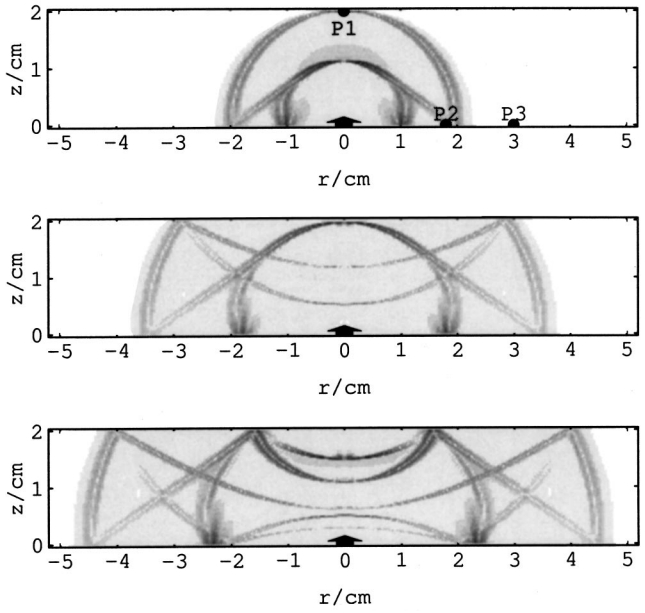

FIG. 14. Snaphots of laser generated wave propagation. The gray scale corresponds to the absolute value of the displacement velocity. The points denote the position of the calcuated and measured time signals.

we would require about 2 GB of RAM. This is currently impractical. Taking the different grid distances shown above, we only need 120 Megabyte RAM. But this noncubic grid demands a very small time step Δt, in comparison with the radial discretization Δr. As shown by Fellinger,[1] this leads to numerical dispersion in the r direction.

B. Results and comparison

The calculations were performed, using the parameters given in Table III. Most parameters were taken from literature. Some were measured. The shear wave speed is calculated from the arrival times of the wave modes in the experimental data.

In Fig. 14 the gray scale images of the absolute value of the displacement velocity at three different time steps are shown. The positions of the calculated time signals are shown in the first figure by P1: $z=20$ mm, $r=0$ mm, P2: $z=0$ mm; $r=18$ mm; and P3: $z=0$ mm, $r=30$ mm.

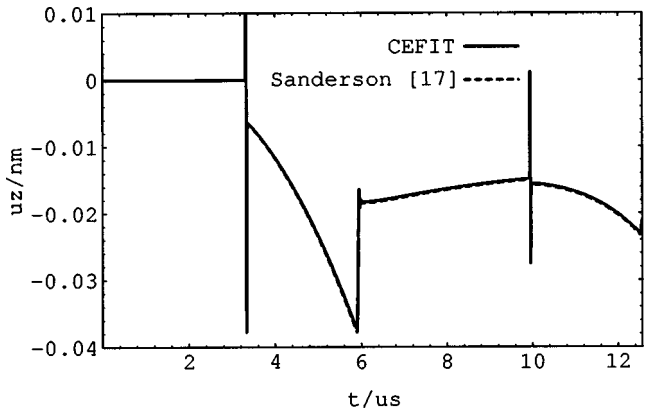

FIG. 15. Displacement u_z at receiver position P1.

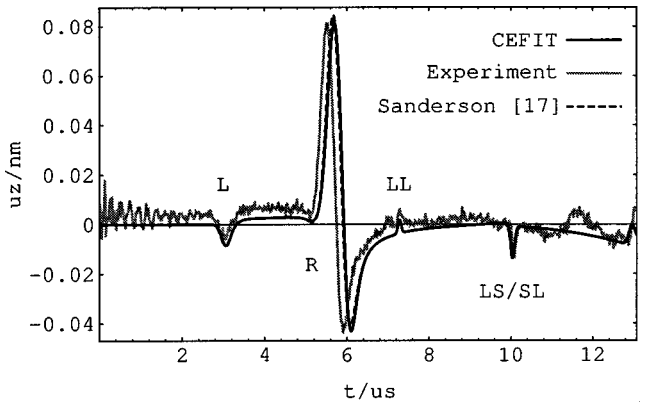

FIG. 16. Displacement u_z at receiver position P2.

The typical waveform of the u_z displacement at the opposite surface (P1) can be seen in Fig. 15. There occurs a small peak at the arrival time in the analytical solution. The shape of this so-called precursor is determined by thermal diffusion and hidden by the uncorrect precursor of the CEFIT solutions in this figure. As mentioned before, the precursor of the CEFIT solutions is too high, because the thickness of the heated region is determined by Δz and not by the process of thermal diffusion that increases the thickness of the heated layer. Nevertheless, the following envelope fits well. There is only some slight numerical ringing after the arrival of the shear wavefront.

Figures 16 and 17 show two waveforms at the irradiated surface, dominated by the Rayleigh wave. The small peaks are caused by the direct or multiple reflected waves. The wave type is denoted by capital letters. One letter means a direct path, for example ''R'' for Rayleigh wave, two letters denote a combination. ''LS'' denotes a longitudinal wave, reflected and mode converted into a shear wave. The arrival time of the ''SL'' path is the same.

The agreement to the theoretical results is very good, there is only some slight numerical dispersion visible in the shape of the Rayleigh wave in Fig. 17. Even the agreement with the experimental curve is very well, especially the modes of multiple reflections. In Fig. 16 there is a certain time offset, but the shape and the amplitude is nearly the same. In Fig. 17 the agreement between theoretical and experimental results is better.

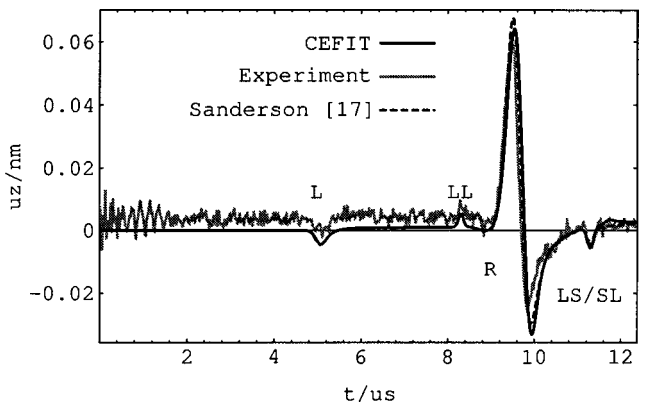

FIG. 17. Displacement u_z at receiver position P3.

This agreement is a further proof for the applicability of the CEFIT scheme. Note that with CEFIT, calculations for arbitrarily shaped sources and specimen are possible, e.g., multi-layers of different materials, inclusions, or gradients of material properties. The only restriction is that the source must be axisymmetric. Furthermore, other kinds of source mechanisms like ablation may be calculated by modeling of pressure forces. Further investigation shall deal with the implementation of heat transfer, by solving on-line the heat equation in a further grid.

V. CONCLUSIONS

In the present paper a new version of the elastodynamic finite integration technique for axisymmetric wave propagation in homogeneous and inhomogeneous linear elastic media was presented. By using the CEFIT code, real three-dimensional problems can be treated in a two-dimensional rectangular grid in the (r,z) half-plane.

The spatial and temporal staggered grid formulation as a direct consequence of the FIT discretization produces a very stable and efficient numerical code. The implementation of boundary conditions at inner and outer boundaries of the synthetic specimen is much easier than in standard FD schemes using a nonstaggered grid. The choice of examples of application presented here was limited by the need to compare the simulation results with analytical solutions first. Good agreement between theory and numerical calculations shows the accuracy of the discrete CEFIT equations and the corresponding boundary conditions.

Nevertheless, the CEFIT code can be used in a wide field of more complicated problems, e.g., the investigation of multi-layer systems, sound radiation from ultrasonic probes with a circular aperture, axisymmetric wave propagation in arbitrary bodies of revolution, and the investigation of matrix-inclusion interphases.

ACKNOWLEDGMENTS

We are indebted to Dr. Eric Landis from the University of Maine, Orono for the programm ''gplate'' allowing us to calculate the Green's functions. We would like to thank Niels Hoppe and Volker Liebig for the experimental Laser results. This paper was supported in part by the society of heavy ion research (GSI) in Darmstadt, Germany, and the German Science Foundation (DFG).

[1] P. Fellinger, R. Marklein, K. J. Langenberg, and S. Klaholz, ''Numerical modelling of elastic wave propagation and scattering with EFIT—Elastodynamic finite integration technique,'' Wave Motion **21**, 47–66 (1995).

[2] R. Marklein, R. Bärmann, and K. J. Langenberg, ''The ultrasonic modeling code EFIT as applied to inhomogeneous dissipative isotropic and anisotropic media,'' Rev. Prog. Quant. Nondestr. Eval. **14**, 251–258 (1995).

[3] F. Schubert and B. Köhler, ''Numerical modeling of elastic wave propagation in random particulate composites,'' in *Nondestructive Characterization of Materials VIII* (Plenum, New York, 1998), pp. 567–574.

[4] Q.-H. Liu, E. Schoen, F. Daube, C. Randall, H.-L. Liu, and P. Lee, ''A three-dimensional finite difference simulation of sonic logging,'' J. Acoust. Soc. Am. **100**, 72–79 (1996).

[5] A. Peiffer, B. Köhler, and S. Petzold, ''The acoustic finite integration technique for waves of cylindrical geometry (CAFIT),'' J. Acoust. Soc. Am. **102**, 697–706 (1997).

[6] A. Ilan and J. P. Weight, ''The propagation of short pulses of ultrasound from a circular source coupled to an isotropic solid,'' J. Acoust. Soc. Am. **88**, 1142–1151 (1990).

[7] K. F. Graff, *Wave Motion in Elastic Solids* (Clarendon, Oxford, 1975).

[8] C. J. Randall, D. J. Scheibner, and P. T. Wu, ''Multipole borehole acoustic waveforms: Synthetic logs with beds and borehole washouts,'' Geophysics **56**, 1757–1769 (1991).

[9] Y.-H. Chen, W. C. Chew, and Q.-H. Liu, ''A three-dimensional finite difference code for the modeling of sonic logging tools,'' J. Acoust. Soc. Am. **103**, 702–712 (1998).

[10] A. P. Cherukuri and T. G. Shawki, ''A finite-difference scheme for elastic wave propagation in a circular disk,'' J. Acoust. Soc. Am. **100**, 2139–2155 (1996).

[11] N. N. Hsu, ''Dynamic Green's functions of an infinite plate—A computer program,'' Report NBSIR 85-3234, National Bureau of Standards, Gaithersburg, MD, 1985.

[12] A. N. Ceranoglu and Y. H. Pao, ''Propagation of elastic pulses and acoustic emission in a plate: Part I. Theory; Part II. Epicentral response; Part III. General response,'' J. Appl. Mech. **48**, 125–147 (1981).

[13] C. F. Ying and R. Truell, ''Scattering of a plane longitudinal wave by a spherical obstacle in an isotropically elastic solid,'' J. Appl. Phys. **27**, 1086–1097 (1956).

[14] Y. H. Pao and C. C. Mow, ''Scattering of plane compressional waves by a spherical obstacle,'' J. Appl. Phys. **43**, 493–499 (1963).

[15] F. A. McDonald, ''On the calculation of laser-generated ultrasound pulse,'' J. Nondestruct. Eval. **9**, 223–228 (1990).

[16] L. R. F. Rose, ''Point-source representation for laser generated ultrasound,'' J. Acoust. Soc. Am. **78**, 723–732 (1984).

[17] T. Sanderson, C. Ume, and J. Jarzynski, ''Laser generated ultrasound: A thermoelastic analysis of the source,'' Ultrasonics **35**, 115–124 (1997).

[18] G. E. Sieger and H. W. Lefevre, ''Time-resolved measurement of acoustic pulses generated by MeV protons stopping in aluminum,'' Phys. Rev. A **31**, 3929–3936 (1985).

[19] N. Hoppe, ''Charakterisierung thermoelastischer Quellen,'' Diplomarbeit TU-Dresden, Fakultät Elektrotechnik (1997).

Inverse Neumann obstacle problem

L. S. Couchman
Naval Research Laboratory, Code 7130, 4555 Overlook Avenue, Washington, DC 20375-5350

D. N. Ghosh Roy and J. Warner
SFA, Inc., 1401 McCormick Drive, Landover, Maryland 20785

(Received 24 August 1997; accepted for publication 19 August 1998)

Results are reported for direct and inverse scattering of plane acoustic waves from sound-hard scatterers of arbitrary shapes in an infinite, homogeneous ambience. The direct problem is solved via a shape deformation technique which is valid for finite deformations. The resulting solution requires solving only a set of algebraic recursion relations, but neither integral equations nor Green's function. The methodology has three essential features: all calculations refer exclusively to a known simple boundary Γ_s instead of the iteratively updated scatterer shapes; the Jacobian of the scattered field is evaluated by solving a series of Helmholtz's equations (with different boundary data) in the region exterior to the simple shape Γ_s; and no ambiguity in the solution arises due to the interior eigenvalues. The inverse problem of recovering the scatterer boundary shape is solved by least square minimization using the Levenberg–Marquardt algorithm. Inversions of several two-dimensional shapes with varying degrees of complexity are reported. The procedures described generalize straightforwardly to transmission and three-dimensional problems. © *1998 Acoustical Society of America.* [S0001-4966(98)06111-6]

PACS numbers: 43.20.Fn, 43.60.Pt, 43.30.Pc, 43.40.Le [DEC]

INTRODUCTION

The recovery of the boundary shape of a sound-hard (Neumann) scatterer from the knowledge of the scattered field (near or far) is an important problem and much attention has been focused on its solution during the last decade. An exhaustive account can be found in Colton and Kress (1992). Almost all known approaches (including the one presented here) for solving this inverse problem require that the corresponding forward problem be solved. In an overwhelming majority of applications, the forward problem is solved by the integral equation method (Colton and Kress, 1992). However, there are approaches that do not use integral equations directly. The most important of these are the techniques that invoke Rayleigh's hypothesis (Angel *et al.*, 1989; Scotti and Wirgin, 1996) or its variant (Jones and Mao, 1989).

The solution technique for the forward problem in this paper is different from either of these approaches. It is a combination of the shape differentiation of the scattered field and Padé extrapolation. This is an extension of a closely related method of Bruno and Reitich (1992, 1995) to the solution of the Neumann obstacle problem.

Some preliminary results regarding the inverse solution of the Neumann problem using this boundary variation technique were reported in an earlier paper (Ghosh Roy *et al.*, 1997). In the current work we expand on those results including consideration of the case of less than 360° of input data.

The approach is summarized briefly as follows. It is assumed that the boundary, Γ_{sc}, of the scatterer consists of a deformation $\delta\Gamma$ (not necessary infinitesimal) superimposed on an underlying simple geometry (such as a canonical shape) Γ_s. It is also assumed that $\delta\Gamma$ is of the form $\lambda f(\hat{\theta})$, $\hat{\theta} \in$ unit sphere $\hat{S}^2$, and the real parameter $\lambda \in [0,\lambda_0)$ is a measure of the amount of the deformation. In other words, the actual shape of the scatterer is given by

$$\Gamma_{sc} := \{x_\lambda \in R^3;\ \ x_\lambda(\hat{\theta}) = x(\hat{\theta}) + \lambda f(\hat{\theta}),\ \ \forall x \in \Gamma_s\}.$$

For sufficiently small values of λ, the scattered field ψ_{sc} is expanded in a Taylor series around $\lambda = 0$. Thus

$$\psi_{sc}(x;\lambda, f(\hat{\theta})) = \sum_{m=0}^{\infty} \frac{1}{m!}\, \psi^{(m)}(x; f(\hat{\theta}))\lambda^m, \tag{1}$$

where $\psi^{(m)} = (\partial^m \psi_{sc}/\partial\lambda^m)|_{\lambda=0}$. The coefficients $\psi^{(m)}$ can be determined (Ghosh Roy *et al.*, 1997) by solving appropriate Neumann problems (with inhomogeneous boundary data) in a domain exterior to the simple shape Γ_s instead of Γ_{sc}. Once the coefficients in the Taylor expansion are obtained, the Padé approximation (Baker and Graves-Morris, 1984) is then invoked in order to extrapolate the boundary perturbation (small λ) to the actual boundary variation which may be finite. It is well known (Baker and Graves-Morris, 1984) that the Padé approximation of a function can provide a representation of a function beyond the radius of convergence of its Taylor expansion.

The solution of the forward problem thus reduces essentially to that of determining the functions $\psi^{(m)}$. These are obtained by solving a set of algebraic recursion relations that result from the solutions of a sequence of Neumann problems exterior to the simple shape Γ_s and involve neither Green's functions nor integral representations of the field. Two advantages follow from this. First, since no integral representation is involved, the problem of nonuniqueness associated with the eigenvalues of the corresponding interior Dirichlet problem (Colton and Kress, 1992) is avoided. Second, it leads to simplifications in the implementation of a Gauss–Newton-type iteration scheme which was used here

for solving the inverse problem. A Gauss–Newton procedure, it may be recalled, requires the knowledge of the Jacobian of the scattered field, that is, the derivatives of ψ_{sc} with respect to the parameters that characterize the boundary Γ_{sc}. Since in the approach used in this work, all calculations refer only to Γ_s and not to Γ_{sc} (which is different in different stages of iteration), the evaluation of the full Jacobian essentially involves solving a series of Helmholtz's equations with different boundary data, but in the same domain. The important point is that this exterior domain in which Helmholtz's scattering problems are solved remains fixed over the entire iteration process. This is discussed further in Sec. II.

This formalism can be easily extended to include transmission boundary conditions. In this case two Taylor expansions (one for the interior and one for the exterior domain) must be used instead of a single one as in the Neumann problem. This result will be described in a future article. Finally, we would like to point out that although much of the detailed computations reported here are for scattering in two dimensions, analogous results can be obtained for three-dimensional obstacles also, but with added computational complexities.

I. THE FORWARD PROBLEM

The methodology is described only briefly, the details appearing in Ghosh Roy *et al.* (1997). In the domain Ω_e exterior to an obstacle occupying a region of space $\Omega \subset R^3$, the Neumann problem is given by

$$(\Delta + k_0^2)\psi(x,k_0) = 0 \quad \text{in} \quad \Omega_e = R^3 \backslash \overline{\Omega},$$
$$\left.\frac{\partial \psi}{\partial n}\right|_{\Gamma_{sc}} = 0. \tag{2}$$

$k_0 > 0$ is a fixed wave number and $\hat{n}$ is the unit normal to the scatterer surface Γ_{sc} pointing into Ω_e. $\psi = \psi^{inc} + \psi^{sc}$ is the total field. The incident field ψ^{inc} is assumed to be a plane wave $\exp(ik_0 \hat{k}_0 \cdot x)$ and the scattered field ψ_{sc} satisfies the radiation condition of infinity, namely

$$\frac{\partial \psi_{sc}}{\partial |x|} - ik_0 \psi_{sc} = O(|x|^{-1})$$

uniformly in $\hat{x} = x/|x|$ as $|x| \to \infty$.

As discussed in the Introduction, the scatterer surface Γ_{sc} is parametrized as

$$x_\lambda(\hat{\theta}) = x(\hat{\theta}) + \lambda f(\hat{\theta}) = T_\lambda(f(\hat{\theta}), x(\hat{\theta})), \tag{3}$$

where $x_\lambda \in \Gamma_{sc}$, $x \in \Gamma_s$ and T_λ is the perturbation of the identity. $f(\hat{\theta})$ is a deforming function and the real parameter λ determines the magnitude of the deformation. Moreover, Γ_s is taken to be a simple shape for which Rayleigh's hypothesis holds. That is, the scattered field can be expanded in terms of the outgoing wave functions alone in all of $R^3 \backslash \Omega$. For a fixed point x away from the scatterer the ''partial'' derivative of ψ^{sc} is defined as

$$\psi_{sc}^{(1)}(x) = \lim_{\lambda \to 0} \frac{1}{\lambda} \{\psi_{sc}^{\lambda}(x) - \psi_{sc}(x)\},$$

whereas for x on the boundary, Γ_{sc} as in (3) the Eulerian derivative $\psi^{[1]}$ is given by

$$\psi^{[1]}(x) = \lim_{\lambda \to 0} \frac{1}{\lambda} \{\psi_{sc}^{\lambda}(x_\lambda(\theta)) - \psi_{sc}(x)\}$$
$$= \frac{d}{d\lambda} (\psi_{sc}^{\lambda} \circ T_\lambda)\Big|_{\lambda = 0}.$$

The mth Eulerian and partial derivatives are denoted by $\psi^{[m]}$ and $\psi^{(m)}$, respectively.

The Neumann boundary data (2) can be written as

$$N_\lambda \cdot \nabla_\lambda \psi^\lambda = 0, \tag{4}$$

where the unitary normal $\hat{n}_\lambda = N_\lambda / |N_\lambda|$, N_λ being the normal vector. Differentiating Eq. (4) m-times with respect to λ, that is, applying the operator $d/d\lambda := \partial/\partial\lambda + f\hat{n} \cdot \nabla$ m-times in succession and then setting $\lambda = 0$, yields the Neumann boundary data for $\psi^{(m)}$, namely

$$\left.\frac{\partial \psi^{(m)}}{\partial n}\right|_{\Gamma_s} = -\sum_{r=1}^{m} \sum_{s=0}^{m-r} \binom{m}{r} \binom{m-r}{s} f^s \left(\frac{d^r N_\lambda}{d\lambda^r}\right)_{\lambda=0}$$
$$\times \frac{\partial^s}{\partial n^s} \{\nabla \psi^{(m-r-s)}\}$$
$$- \sum_{r=1}^{m} \binom{m}{r} f^r \frac{\partial^{r+1}}{\partial n^{r+1}} \psi^{(m-r)}. \tag{5}$$

Now the scattered field is given by the Taylor series (1). Then each $\psi^{(m)}$ is a radiating solution of Helmholtz's equation and is given by the same exterior Neumann problem as (2).

In what follows we apply this result to the case of scattering in two space dimensions only (Γ_s is a circle, Γ_c, of radius r_0). $f(\theta)$ [Eq. (3)] is parameterized in terms of a finite Fourier series

$$f(\theta) = \sum_{l=-L}^{L} \alpha_l e^{il\theta}, \tag{6}$$

$\alpha_{-l} = \alpha_l^*$,* being the complex conjugate. Assuming a harmonic time dependence of $\exp(-i\omega t)$, the total field $\psi^{(0)}$ corresponding to the circular boundary Γ_c is given by

$$\psi^{(0)}(x) = \sum_{s=-\infty}^{\infty} (-i)^s J_s(k_0|x|) e^{is\theta}$$
$$+ \sum_{s=-\infty}^{\infty} (-i)^s \beta_{0,s} H_s^{(1)}(k_0|x|) e^{is\theta}, \tag{7}$$

where $\beta_{0,s} = -\{(d/d\xi) J_s(\xi)/(d/d\xi) H_x^{(1)}(\xi)\}$, $\xi = k_0|x|$, J_s and $H_s^{(1)}$ being the Bessel and the Hankel function (of the first kind) of integer order s, respectively. Finally $\psi^{(m)}$ is expanded as

$$\psi^{(m)}(x) = \sum_{n=-\infty}^{\infty} \beta_{m,n} (-i)^n H_n^{(1)}(k_0|x|) e^{in\theta}. \tag{8}$$

Substituting (6)–(8) into (5) and equating the coefficients of the exponentials on both sides of the resulting equation then yields the following recursion relation for $\beta_{m,n}$, namely:

$$\beta_{m,n} = -\frac{k_0^m}{H_n^{(1)\prime}(\xi)} \sum_{i=1}^{4} T_i, \tag{9}$$

where

$$T_1 = \left(\frac{1}{m!}\right) \sum_{l=-Lm}^{Lm} (-i)^{-l} \alpha_{m,l} J_{n-l}^{(m+1)}(\xi),$$

$$T_2 = \left(\frac{1}{m}\right) \sum_{j=0}^{m-1} \sum_{l=-Lm}^{Lm} (-i)^{-l} (-1)^j \{(m-j-l)!\}^{-1} \times (1+j) l (n-l) (k_0 r_0)^{-(2+j)} \alpha_{m,l} J_{n-l}^{(m-j-1)}(\xi),$$

$$T_3 = \sum_{j=0}^{m-1} \sum_{l=-(m-j)L}^{(m-j)L} (-i)^{-l} \{(m-j)!\}^{-1} k_0^{-j} \alpha_{m-j,l} \times \beta_{j,n-l} (H_{n-l}^{(1)})^{(m-j+1)}(\xi),$$

and

$$T_4 = \sum_{j=0}^{m-1} \sum_{k=0}^{m-j-1} \sum_{l=-(m-j)L}^{(m-j)L} (-i)^{-l} (-1)^k \times (1+k) l (n-l) k_0^{-j} (k_0 r_0)^{-(2+k)} \times [(m-j)\{(m-j-k-1)!\}^{-1}] \times \alpha_{m-j,l} \beta_{j,n-l} (H_{n-l}^{(1)})^{(m-j-k-1)}(\xi).$$

In summary, then, the forward problem is solved (for small λ) by Taylor expanding the scattered field [Eq. (1)]. The coefficients $\psi^{(m)}$ in this expansion are given by Eq. (8); the constants $\beta_{m,n}$ in which are evaluated by the recursion relations (9).

The final stage in the solution of the forward problem for the actual boundary $\Gamma_{sc} = \Gamma_c + \delta\Gamma$ consists of extrapolating the boundary perturbations (λ small) to the actual boundary variations $\partial\Gamma$ (which may be finite) via the Padé approximation. Toward this, we note that the scattered field ψ_{sc} from Γ_{sc} can be written as

$$\psi^{sc}(x) = \sum_{m=-\infty}^{\infty} \left[\sum_{n=-\infty}^{\infty} \beta_{m,n} \lambda^m \right] (-i)^m H_m^{(1)}(k_0|x|) e^{in\theta}, \tag{10}$$

where $|x| > r_0 + \max|\lambda f(\theta)|$.

The Padé approximation is then applied to the power series over m in (10). The Padé approximated series (10) is then the final solution of the forward problem for finite $\partial\Gamma$. The details of the Padé approximation appear in our previous paper.

II. THE CALCULATION OF THE JACOBIAN

The most vital element in the implementation of a Gauss–Newton inversion procedure is the calculation of a Jacobian of a scattered field which is responsible for most of the CPU time. Its calculation thus deserves special attention and is discussed in detail in this section. The Jacobian is a column vector (for a fixed point of observation), the elements of which are the derivatives of the scattered field ψ^{sc} with respect to the Fourier coefficients, $\alpha_l, l = -L, -L+1, \ldots, -1, 0, 1, \ldots, L-1, L$, of Eq. (6). Now α_l is complex and the function $f(\theta)$ is real. Hence $\alpha_l = \alpha_{-l}^*$. If α_{lR} and α_{lI} are the real and the imaginary parts of α_l, respectively, then the Jacobian of ψ^{sc} is a $(2L+1)$ column vector. Therefore, $\mathbf{J}_{\psi^{sc}} = \{\psi_0', \psi_{jR}', \psi_{jI}'\}^T$, $j = 1,2,\ldots,L$, and $\psi_{jR(I)}' = \partial\psi^{sc}/\partial\alpha_{jR(I)}$. The total number of the Fourier coefficients is $(2L+1)$.

Let $\boldsymbol{\alpha}$ be the Fourier vector for the unperturbed domain. Then $\boldsymbol{\alpha} \in R^{2L+1}$, is a vector in a $(2L+1)$ dimensional Euclidean space. Denoting the unit basis vectors in R^{2L+1} by $\hat{e}_i$, we have $\boldsymbol{\alpha} = \Sigma_{i=1}^{2L+1} \alpha_{i-L-1} \hat{e}_i$. Now let $\boldsymbol{\alpha}$ be changed along the j-th basis vector $\hat{e}_j$ by an infinitesimal amount $\delta\alpha_j$ and let ${}^j\boldsymbol{\alpha}$ denote the new Fourier vector. That is, ${}^j\boldsymbol{\alpha} = \boldsymbol{\alpha} + \hat{e}_j \delta\alpha_j$. Then $\psi_{jR(I)}'$ is defined by

$$\psi_{jR(I)}'(x) \approx \{\psi_{R(I)}^{sc}(x; {}^j\boldsymbol{\alpha}) - \psi_{R(I)}^{sc}(x; \boldsymbol{\alpha})\} / |\partial\alpha_j|. \tag{11}$$

Now $\psi^{sc}(x; {}^j\boldsymbol{\alpha})$ is calculated exactly as $\psi^{sc}(x; \boldsymbol{\alpha})$ described in Sec. I, but with $\boldsymbol{\alpha}$ replaced by ${}^j\boldsymbol{\alpha}$. The calculation is repeated for all $(2L+1)$ basis vector $\hat{e}_j$. However, the form of the recursion relation (9) simplifies the determination of the Jacobian $\mathbf{J}_{\psi^{sc}}$ significantly. It allows us to calculate the entire Jacobian by solving $(2L+1)$ exterior Helmholtz equations in the same domain (which, in our case, is the region exterior to the canonical surface Γ_c) as opposed to solving $(2L+1)$ distinctly different boundary value problems on $(2L+1)$ distinctly different surfaces Γ_j, one for each ${}^j\boldsymbol{\alpha}$. This follows from the fact that the numerical coefficients in (9) multiplying the product terms such as $(\alpha_{m-j,l}\beta_{j,m-l})$ are independent of the index j of the derivatives $\beta_{m,n}^{(j)}$. These coefficients, therefore, need to be calculated only once in the determination of all $(2L+1)$ derivatives comprising the Jacobian $\mathbf{J}_{\psi^{sc}}$. This is equivalent to solving $(2L+1)$ Helmholtz's equations in the same domain (the region exterior to Γ_c), but with a $(2L+1)$ dimensional vector $\boldsymbol{\alpha}$ or $(2L+1)$ different boundary data. This is how the Jacobian $\mathbf{J}_{\psi^{sc}}$ was evaluated in our numerical computations.

At this point it is interesting to point out that this method of calculating the Jacobian is closely related to the domain derivative of Kirsch (1994). As a matter of fact, the form of recursion relation (9) is such that the domain derivatives can be obtained from it with only very minor algebraic manipulations. In order to see this explicitly, let us rearrange the terms in recursion relation (9) and rewrite it as

$$\beta_{m,n} + \frac{k_0^m}{H_n^{(1)\prime}(\xi)} \{T_3(\beta_{m,p}) + T_4(\beta_{m,p})\} = -\frac{k_0^m}{H_n^{(1)\prime}(\xi)} (T_1 + T_2), \quad p < n. \tag{12}$$

The arguments $\beta_{m,p}$, $p < n$, in T_3 and T_4 in (12) indicate the existence of a recursion relation. Let us now replace $\boldsymbol{\alpha}$ by ${}^j\boldsymbol{\alpha}$ in (9) and calculate the right-hand side of (11) in the limit $\delta\alpha_j \to 0$. This leads to the following result:

$$\beta_{m,n}^{(j)} + \frac{k_0^m}{H_n^{(1)\prime}(\xi)} \{T_3(\beta_{m,p}^{(j)}) + T_4(\beta_{m,p}^{(j)})\} = -\frac{k_0^m}{H_n^{(1)\prime}(\xi)} \sum_{i=1}^{4} \tilde{T}_i. \tag{13}$$

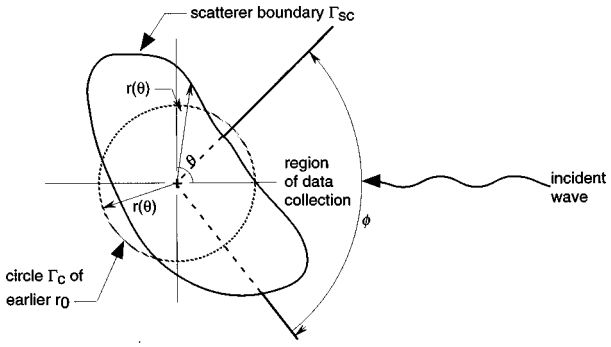

FIG. 1. The geometry of scattering. The scatterer shape is given by $r(\theta) = r_0 + \lambda f(\theta)$, $0 \leq \theta \leq 2\pi$. $\Phi_0 \leq \Phi \leq 2\pi$, $\Phi_0 > 0$.

In Eq. (13), $\beta^{(j)}_{m,q} = \partial \beta_{m,q} / \partial \alpha_j$, and $p < n$, as before. The terms $\tilde{T}_i$, $i = 1,2,3,4$, are exactly the same as T_i, $i = 1,2,3,4$, of Eq. (9) except that m in the summations over the index l and in the powers of α_l appearing inside the summations is replaced by $(m-1)$ and the index l in the summands is replaced by $(l+j)$. Equation (13) has the same form as Eq. (12), but with a modified right-hand side and indicates that the Jacobian $\mathbf{J}_{\psi^{sc}}$ is evaluated by solving $(2L+1)$ exterior boundary value problems for the same Helmholtz equation in the same domain (again the exterior of the circle Γ_c), but with different boundary data. This is exactly analogous to the domain derivative calculation of the Jacobian discussed by Kirsch (1994) for the Dirichlet problem with one exception. The present computations always refer to the circle Γ_c as opposed to the actual updated boundary surfaces in Kirsch's paper. In other words, in our case, the domain in which the scattering problems are solved remains fixed irrespective of the stage of iteration. However, the method by which $\mathbf{J}_{\psi^{sc}}$ was actually calculated here is numerically more convenient than using Eq. (13) directly.

Finally, the inversions of some Neumann obstacles are presented below using the above formalism.

III. RESULTS

A number of sound-hard obstacles of various boundary shapes were considered for inversions. These included a ''sausage'' shape given by $r(\theta) = 1 + 0.30\cos 2\theta + 0.03\cos 4\theta$; a clover-leaf for which $r(\theta) = 1 + 0.30\cos 4\theta$; ellipses with eccentricities 1.2:1.0, 1.6:1.0, 2.0:1.0, and 2.5:1.0, the parametric equation being $r(\theta) = ab(b^2\cos^2\theta + a^2\sin^2\theta)^{-1/2}$, the ratio $(a:b)$ representing the eccentricity; and finally, an ''airplane'' shape the parametrization of which was given by $r(\theta) = 1 + 0.20\cos 3\theta + 0.20\cos 4\theta + 0.10\cos 6\theta + 0.10\cos 8\theta$.

The scattering geometry is shown in Fig. 1. The inversions were performed with a fixed direction of incidence of single and multiple frequency and for both full-circle (360°) as well as limited-angle (less than 360°) data collection. All obstacles except the ellipses were oriented with one of the axes of symmetry making an angle of 30° to the direction of the incident wave. The ellipses were oriented with their major axes inclined at an angle of 45° to the incident wave. The inversions reported here all used the far-field pattern which was obtained by solving Helmholtz's equation in the domain

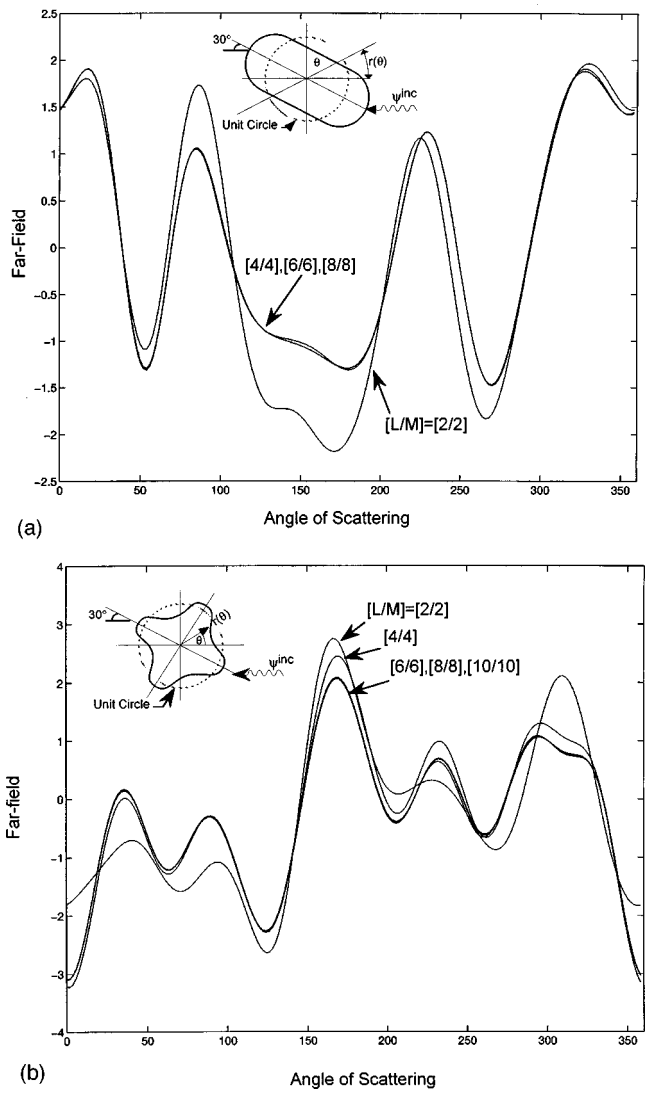

FIG. 2. The angular distribution of the far-field pattern demonstrating the convergence of the Padé approximations. (a) The real part of the field for the sausage shape: $r(\theta) = 1 + 0.30\cos(2\theta) + 0.03\cos(4\theta)$, (b) The imaginary part of the field for the cloverleaf shape: $r(\theta) = 1 + 0.30\cos(4\theta)$.

exterior to Γ_{sc} by the finite element method (FEM). All numerical computations were done on an SGI Indy machine.

Data inversions for recovering the Fourier coefficients α_l were done by minimizing an objective function defined by

$$Q = \sum_{i=1}^{I} |\rho_i|^2,$$

where I is the number of observation points, and the residual ρ_i at the i-th observation point x_i is given by

$$\rho_i = \psi_p^{sc}(x_i; \boldsymbol{\alpha}) - \psi_m^{sc}(x_i; \boldsymbol{\alpha}_0).$$

Subscripts p and m refer to predicted (i.e., calculated) and ''measured'' (that is, FEM solution) respectively. $\boldsymbol{\alpha}$ and $\boldsymbol{\alpha}_0$ represent the calculated and the true boundary parametrization, respectively. Q was minimized for the Fourier vector $\boldsymbol{\alpha}$ via the Levenberg–Marquardt nonlinear parameter fitting scheme. The Levenberg–Marquardt algorithm requires the knowledge of the Jacobian $\mathbf{J}_{\psi^{sc}}$ the determination of which

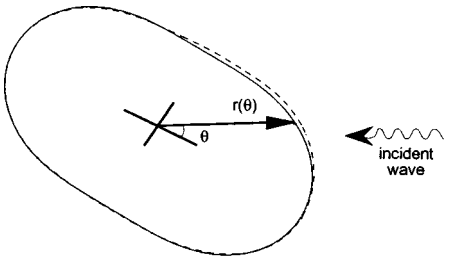

a

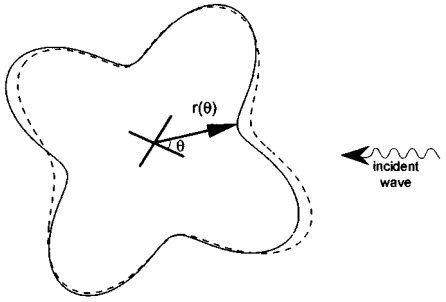

b

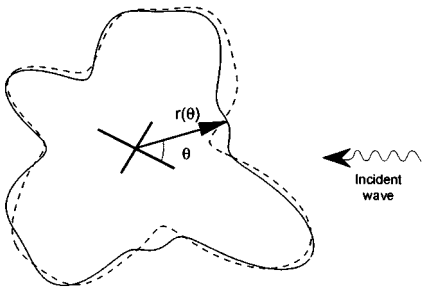

c

FIG. 3. The reconstruction of several shapes from the full-circle, far-field data. In all cases 60 receivers were used, the shapes were rotated 30° relative to the incident wave, and 8% random noise was added to the data. (a) The sausage shape, using a single frequency ($k_0=5$) plane incident wave. The number of unknown Fourier coefficients recovered was 17. (b) The clover-leaf shape, using two frequencies ($k_0=1,5$). The number of unknown Fourier coefficients recovered was 17. (c) The ''airplane'' shape: $r(\theta)=1+0.20\cos(3\theta)+0.20\cos(4\theta)+0.10\cos(6\theta)+0.10\cos(8\theta)$ using three frequencies ($k_0=1,2,5$). The number of unknown Fourier coefficients recovered was 25.

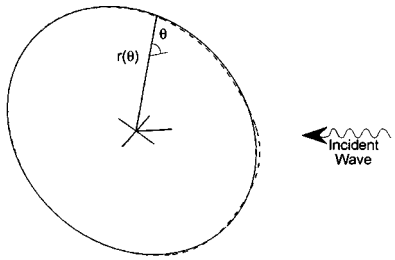

a

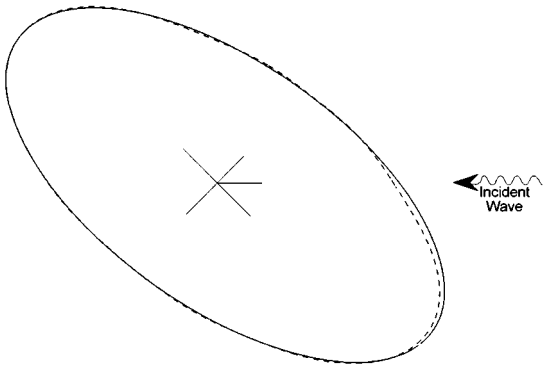

b

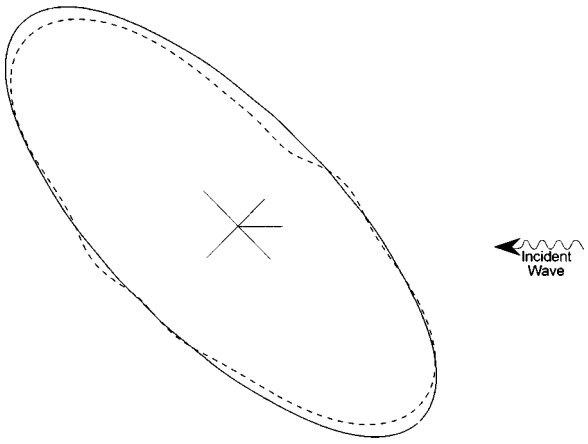

c

FIG. 4. The reconstruction of ellipses from the full-circle, far-field data with 8% random noise added. The ellipses are parameterized by $r(\theta)=ab[(b\cos\theta)^2+(a\sin\theta)^2]^{-1/2}$; a,b being the semi-major and the semi-minor axis, respectively. For all ellipses the number of detectors was 60 and the number of unknown Fourier coefficients recovered was 17. All ellipses are rotated 45° to the direction of the incident wave. (a) $a:b=1.2:1.0$. Only one frequency ($k_0=5$) was used. (b) $a:b=2.0:1.0$. Two frequencies ($k_0=1,5$) were used. (c) $a:b=2.5:1.0$. Two frequencies ($k_0=1,5$) were used.

was already discussed in Sec. II. Also 8% random noise was added to the data.

Figure 2(a) shows the angular variation of the real part of the scattered field for the sausage shape. It is clear that the scattered fields given by the Padé approximants agree extremely well with the corresponding FEM solutions. The Taylor series result was not plotted since the deformation $\delta\Gamma$ for this scatterer is far beyond the radius of convergence of the Taylor expansion. Explicit demonstrations of the breakdown of the Taylor expansion with increasing λ and the validity of the Padé calculations of the scattered field well beyond the range of the Taylor expansion in close agreement with the FEM solutions were given in our previous paper (Ghosh Roy *et al.*, 1997). The plots in Fig. 2(b) are for the imaginary part of the scattering data for the clover-leaf and again demonstrate how well the Padé approximation agrees with the FEM solution. This is typical of all the scatterers reported here.

Next we present the results of inversions for full 360° data collections. The number of the full-circle data points

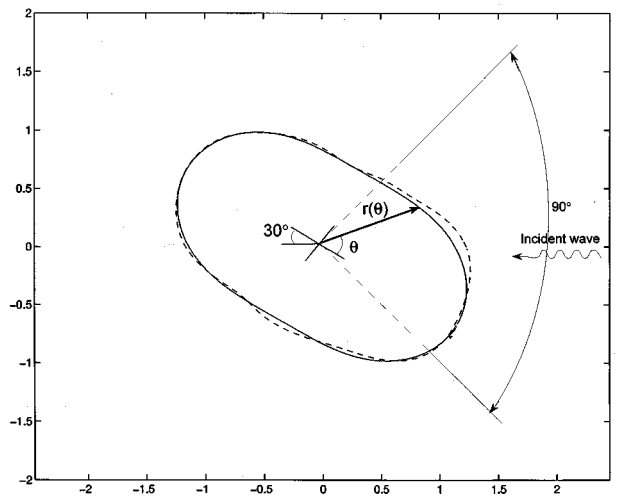

FIG. 5. The reconstruction of the sausage shape from the far-field data collected over a 90° wedge around the direction of incidence; that is, Φ of Fig. 1 is 90°. Number of frequencies used is three ($k_0=1,2,5$). Total number of receivers is 45 and 17 Fourier coefficients were recovered. 8% random noise was added to the data.

were 60 and 8% noise was added to the FEM solutions. Figure 3(a) shows the reconstruction of the sausage shape using a single frequency ($k_0=5$) and 17 unknown Fourier coefficients. The recovery of the clover-leaf is shown in Fig. 3(b) with two frequencies ($k_0=1$ and 5) and again with 17 unknown Fourier coefficients. In Fig. 3(c) is shown the reconstruction of the ''airplane.'' Three frequencies $k_0=1$, 2, and 5 were used and the number of the unknown Fourier coefficients was 25. A [4/4] Padé approximant was used. Figure 4 shows the reconstructions of ellipses for which the number of unknown Fourier coefficients was taken to be 17. Figure 4(a) shows the inversion of an ellipse with eccentricity (1.2:1.0) using only one frequency of $k_0=5$. The reconstruction for eccentricity 2.0:1.0 and 17 unknown Fourier coefficients is shown in Fig. 4(b). Two frequencies of $k_0=1$ and 5 were used. Finally, Fig. 4(c) shows the recovery of an ellipse with eccentricity 2.5:1.0, again with 17 Fourier coefficients. Three frequencies $k_0=1$, 2, and 5 were used in its reconstruction.

Finally, in Figs. 5–7, inversions with limited-angle data collections are reported. Figure 5 shows the recovery of the sausage shape from the far-field data collected over a 90° aperture. The data were collected in the backscattering mode with detectors placed symmetrically about the direction of incidence. This was done for all the limited-angle inversions reported here. In the inversion shown in Fig. 5, three frequencies ($k_0=1,2,5$) were used along with a total number of 45 receivers. The number of Fourier coefficients was 17. The reconstruction of the clover-leaf from 90° data is shown in Fig. 6(a), all parameters being as in Fig. 5. Figure 6(b) and (c) shows the same clover-leaf reconstructions, but for 45° and 15° region of data collection, respectively. The number of frequencies used were 41 ($k_0=1$ through 5) and the number of detectors was 23 in the 45° and 7 in the 15° data collection. Finally, the recovery of the ''airplane'' from the far field, 90° aperture data is shown in Fig. 7 for three frequencies ($k_0=1,2,5$) and 45 detectors, the number of unknown Fourier coefficients being 25.

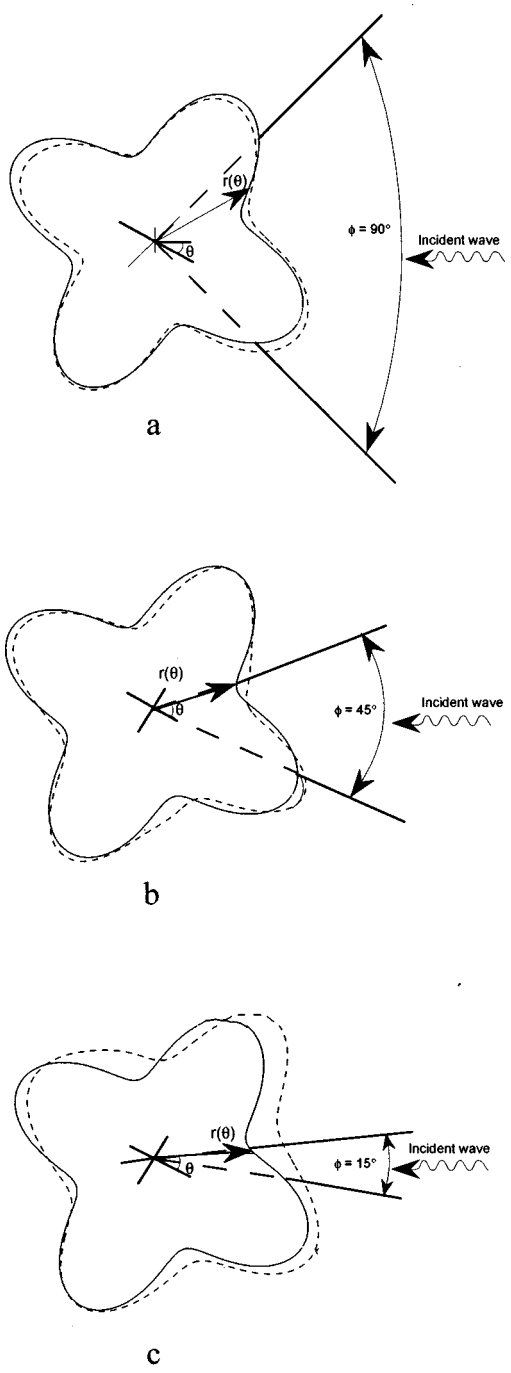

FIG. 6. The reconstruction of the cloverleaf from the far-field data collected over limited angles. 17 Fourier coefficients were recovered in all cases. No noise was added to this data. (a) 90° wedge ($\Phi=90°$), with a total of 45 receivers. Three frequencies were used ($k_0=1,2,5$). (b) 45° wedge ($\Phi=45°$), with a total of 23 receivers. 41 frequencies were used ($k_0=1$–5). (c) 15° wedge ($\Phi=15°$), with a total of 7 receivers. 41 frequencies were used ($k_0=1-5$).

Before concluding, some comments are due as to the selection of the initial, starting guesses. The Gauss–Newton procedures are known to be sensitive to the choice of the initial conditions. However, the technique of the Padé approximation proves to be useful here. Before doing a full-scale inversion which may require Padé approximants of

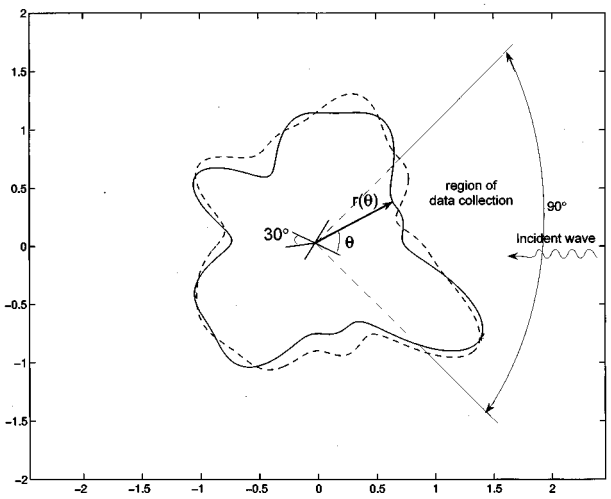

FIG. 7. The reconstruction of the ''airplane'' from the far-field data collected over a 90° wedge ($\Phi = 90°$) using three frequencies ($k_0 = 1,2,5$) and with no noise added to the data. The total number of receivers was 45, and 25 unknown Fourier coefficients were recovered.

higher orders, a low-order (such as [2/2]) Padé inversion can lead to a fast, yet a reasonably accurate guess of the starting point (especially, the initial radius r_0) for the Gauss–Newton iterations. Our numerical experiments show that this was the case for all of the objects reported here. For inversion with single frequency data, the initial selection of r_0 was made exclusively in this manner. For the inversions using multiple frequency, advantage was taken of both low-order Padé approximation as well as the lowest k_0 reconstruction results. For inversions requiring more than one frequency, the results obtained after inverting the far-field data for the lowest k_0 were used as the initial starting point for the Gauss–Newton iterations for the next higher k_0 and so on. We must also mention in passing that although the inversions reported here involve only the far-field patterns, comparable reconstructions can be obtained with the near-field data also.

Finally, the inversion of the transmission boundary value problem is in progress and will soon be reported elsewhere.

IV. SUMMARY

In summary, the inverse problem of recovering the boundary shapes of sound-hard obstacles in a homogeneous, infinite acoustic medium from full-circle and/or limited-angle far-field patterns is discussed. The associated forward problem is solved via boundary variation and Padé extrapolation. The method uses neither Green's functions nor the integral representations of the scattered field. It is thus free of the nonuniqueness of the solutions associated with the interior eigenvalues of the corresponding adjoint Dirichlet problem. The technique used here has further advantages. First, all calculations are performed essentially with respect to a known, simple boundary shape. Therefore, the domain over which all exterior Helmholtz problems are solved remains independent of the stages of iteration which is a critical point. It is demonstrated that this leads to a substantial simplification in the computation of the Jacobian of the scattered field.

ACKNOWLEDGMENTS

This work supported by the Naval Research Laboratory and the Office of Naval Research. The authors gratefully acknowledge the help of J. Shirron, Physical Acoustics Division, Naval Research Laboratory, in obtaining the FEM solutions used in this paper.

Angell, T. S., Kleinmann, R. E., Kok, B., and Roach, G. F. (**1989**). ''A constructive method for identification of an impenetrable scatterer,'' Wave Motion **II**, 185–200.

Baker, G. A., and Graves-Morris, P. (**1981**). *Padé Approximants. Part I: Basic Theory; Part II: Extensions and Applications* (Addison-Wesley, Reading, MA).

Bruno, O. P., and Reitich, F. (**1992**). ''Solution of a boundary value problem for the Helmholtz equation via variation of the boundary into the complex domain,'' Proc. R. Soc. Edinburgh **122A**, 317–340.

Bruno, O. P., and Reitich, F. (**1995**). ''A new approach to the solution of problems of scattering by bounded obstacles,'' Proc. SPIE **2192**, 20–28.

Colton, D., and Kress, R. (**1992**). *Inverse Acoustic and Electromagnetic Scattering Theory* (Springer-Verlag, New York).

Ghosh-Roy, D. N., Couchman, L. S., and Warner, J. A. (**1997**). ''Scattering and inverse scattering of sound-hard obstacle via shape deformation,'' Inverse Probl. **13**, 585–606.

Jones, D. S., and Mao, X. Q. (**1989**). ''The inverse problem in hard acoustic scattering,'' Inverse Probl. **5**, 731–748.

Kirsch, A. (**1993**). ''The domain derivative and two application in inverse scattering theory,'' Inverse Probl. **9**, 81–96.

Scotti, T., and Wirgin, A. (**1996**). ''Shape reconstructions of an impenetrable scattering body via the Rayleigh hypothesis,'' Inverse Probl. **12**, 1027–1055.

Acoustical and mechanical characterization of anisotropic open-cell foams

M. Melon,[a] E. Mariez, C. Ayrault, and S. Sahraoui
Laboratoire d'Acoustique de l'Université du Maine, Institut d'Acoustique et de Mécanique (UMR 6613), Av. Olivier Messiaen, 72085 Le Mans Cedex 9, France

(Received 24 November 1997; accepted for publication 29 July 1998)

Acoustical (viscous static permeability, tortuosity, and viscous characteristic length) and mechanical (skeleton viscoelasticity tensor) parameters which characterize the behavior of porous media are provided from measurements along three perpendicular axes. The measurements are performed on cubic samples of open-cell foams. The longitudinal direction is chosen to be parallel to the growth direction of the foam. The results show that the samples tested here exhibit a quasi-axisymmetrical geometry. It appears that a precise description of this type of reticulated polymeric foam must include its anisotropy, especially for vibroacoustic behavior prediction. © *1998 Acoustical Society of America.* [S0001-4966(98)02311-X]

PACS numbers: 43.20.Jr, 43.40.Yq, 43.35.Mr, 43.55.Ev [ANN]

INTRODUCTION

Polymeric foams are frequently used for the damping of sound in the automotive and aeronautics industries or in the building trade. During the last ten years, many improvements have been made in both experimental and theoretical characterization of these materials. Two cases must be distinguished; the first one, when the skeleton remains motionless, is called the rigid frame case. This assumption is valid when the density of the saturating fluid is much lower than the density of the structure or/and when the viscous permeability of the porous media is high. Consequently, the skeleton of the foam is not excited by the energy of the soundwave. Thus the only wave traveling in the material is a fluid-borne wave. However, the existence of a motionless skeleton requires modifying accordingly the mass density and the compressibility of the saturating fluid, these two quantities becoming complex and frequency dependent. Several models have been published for many years to characterize the propagation of sound in rigid frame porous materials.[1,2] In this paper, the model used has first been developed by Johnson[3] in 1987 for porous rocks saturated with water. It has been chosen for the interesting physical meaning of input parameters. This theory takes into account the inertial and the viscous couplings between the saturating fluid and the solid structure. A good agreement has been obtained between this theory and measurements of the speed of the slow wave by Nagy[4] and Gist.[5] On the other hand, an excessive attenuation has been observed for the slow mode at high frequencies, which has been attributed to viscous losses[6] or to scattering effects.[7] This discrepancy is less important when dealing with high porosity materials such as glass wools or open-cell polymeric foams. However, these media are generally saturated by air where thermal losses cannot be neglected. Allard[8] and Lafarge[9] have extended Johnson's model to take into account thermal exchanges between the fluid and the structure. Thus six parameters (i.e., porosity, viscous and thermal permeabilities, tortuosity, viscous, and thermal characteristic lengths) are needed to describe the acoustic behavior of an isotropic porous medium. The second case, when the energy of the soundwave is sufficient to make the structure of the foam vibrate, requires the use of the Biot theory.[10] Therefore, the mass density and the compressibility modulus of the polymer that forms the structure in addition to the mechanical properties of the viscoelastic skeleton (i.e., Young's modulus and Poisson's ratio) are needed to describe the acoustics of porous media. Adding these four parameters to the six required by the rigid frame model fully characterizes an ideal isotropic plastic foam in the frame of the Biot theory. Due to the fabrication process, polymeric foams are often anisotropic. Cells are usually longer in the growth direction than in the plane normal to it. In many cases, such anisotropy can be reduced to hexagonal symmetry.[11] The aim of this paper is to verify this hypothesis and to evaluate the amount of anisotropy on the acoustical and mechanical parameters that physically describe the reticulated polymeric foam behavior. Experimental investigations are done by using precise measurement techniques which have been previously published.[12–15] The first part reviews the acoustical parameter characterization whereas the second one presents some mechanical measurements.

I. PARAMETERS OF THE RIGID FRAME MODEL—MEASUREMENT PRINCIPLE

This section describes the measurement methods of the parameters required by the rigid frame model for a foam having hexagonal symmetry. The porosity ϕ, the thermal characteristic length Λ', and the thermal permeability k_0' which are scalar parameters remain isotropic. Thus they will not be studied any further in this paper. On the other hand, the tortuosity α_∞, the viscous characteristic length Λ, and the viscous static permeability k_0 which are defined from vectorial fields are different along the transversal and normal directions of the plastic foam.

[a]Present address: Laboratoire d'acoustique, CNAM, 292 rue St. Martin, 75141 Paris Cedex 3, France.

The viscous static permeability is measured by a classical method described by Bies *et al.*[16] This method consists in measuring the pressure drop ΔP between two opposite faces of a porous sample when a steady air flow of known value is crossing it. The viscous static permeability k_0 is then given by

$$k_0 = \frac{\eta D e}{\Delta P}, \tag{1}$$

where e is the thickness of the sample, η the viscosity of the saturating fluid, and D is the mean air flow by unit surface area. We prefer to use the parameter k_0 instead of the air flow resistivity σ ($\sigma = \eta/k_0$), which depends also on the saturating fluid and not only on the microgeometry of the foam.

Tortuosity and the viscous characteristic length are measured using low-frequency ultrasonics. These techniques have proven to be a valuable tool for the evaluation of these parameters,[17,12] especially for materials having high porosity (i.e., more than 0.95). The viscous skin depth is given by

$$\delta = \sqrt{\frac{2\eta}{\rho_0 \omega}}, \tag{2}$$

where ρ_0 is the mass density of the saturating fluid, whereas ω is the angular frequency. At such frequencies, the viscous skin depth is small enough compared to the characteristic lengths, thus the real part of the squared propagation index takes the following form at the first order[13]

$$n_r^2(\omega) = \left(\frac{c(\omega)}{c_0}\right)^2 = \alpha_\infty \left[1 + \delta\left(\frac{1}{\Lambda} + \frac{\gamma - 1}{B\Lambda'}\right)\right], \tag{3}$$

where $c(\omega)$ and c_0, respectively, are the wave speed in the saturating fluid and in the free air at rest. The squared root of the Prandtl's number is equal to B while γ is the ratio of the specific heats. An ultrasonic method based on the measurement of the dispersion curve of the wave speed in the porous media has been recently proposed to recover the tortuosity.[13] This technique is convenient for impulsive signals having high signal-to-noise ratio. In our case, the large thickness of the samples creates a strong attenuation of the ultrasonic signal and the computation of the dispersion curve cannot be done with the appropriate precision. To overcome this problem, measurements are performed with sine bursts of 83 kHz. This frequency is chosen to be high enough to work in the asymptotic regime [i.e., Eq. (3)] and low enough to avoid scattering effects in the foam.[14] Johnson *et al.*[3] have proposed a method for the measurement of the viscous characteristic length with the help of the quality factor Q which is given by

$$Q = \frac{\omega}{2\alpha c(\omega)}, \tag{4}$$

where α is the attenuation (in neper) of the ultrasonic signal. For porous media saturated by a fluid having a negligible thermal expansion coefficient, the product $Q\delta$, in the high-frequency domain tends to

$$\lim_{\omega \to \infty} Q\delta = \Lambda. \tag{5}$$

For porous materials saturated with gases, thermal effects cannot be generally neglected. Thus the $Q\delta$ product tends to the length l (Ref. 17)

$$\lim_{\omega \to \infty} Q\delta = l = \left(\frac{1}{\Lambda} + \frac{\gamma - 1}{B\Lambda'}\right)^{-1}. \tag{6}$$

According to Eqs. (3) and (6), the value of the tortuosity is obtained from the measurement of the ultrasonic phase velocity $c(\omega)$ and of the quality factor Q

$$\alpha_\infty = \frac{c^2(\omega)}{c_0^2(1 + 1/Q)}. \tag{7}$$

When considering a homogeneous anisotropic material, the quantities k_0, α_∞, and Λ become second rank tensors, respectively, noted as $k_{0_{ij}}$, $\alpha_{\infty_{ij}}$, and Λ_{ij}. These tensors diagonalize in a system of three orthogonal axes—the so-called principal axes. In the case of axisymmetrical porous materials, the previous tensors take the following form

$$k_{0_{ij}} = \begin{pmatrix} k_{0L} & 0 \\ 0 & k_{0T} \end{pmatrix}, \quad \alpha_{\infty_{ij}} = \begin{pmatrix} \alpha_{\infty L} & 0 \\ 0 & \alpha_{\infty T} \end{pmatrix},$$

and (8)

$$\Lambda_{ij} = \begin{pmatrix} \Lambda_L & 0 \\ 0 & \Lambda_T \end{pmatrix},$$

where L and T, respectively, stand for the values along the longitudinal direction and in the plane normal to it. Because there is no shear wave in the saturating fluid, the measurement methods described above for the isotropic media can be used along the principal axes to determine the components of the different tensors.

II. MECHANICAL PARAMETERS—MEASUREMENT PRINCIPLE

In the case of vibrating foams, the Biot model needs the identification of mechanical skeleton properties to be done. In recent papers,[18,19] a quasistatic (1–100 Hz) experimental technique was proposed to measure the whole components of the stress–strain viscoelastic tensor C_{ijkl} of polyurethane foams skeleton which exhibit axisymmetrical behavior. These components are supposed to be complex values depending on frequency. The experimental method, designed for cubic sample compressed between two plates, needs the specimen axes to be supposed principal. One of these principal directions is called the longitudinal (noted L) and must correspond as close as possible to the observed rise direction of the foam. Both perpendicular directions to L are noted T and T'. According to the axisymmetric behavior assumption, the plane $(T - T')$ is supposed to be isotropic. Mechanical measurements consist in applying successively a small sinusoidal axial compression into the three directions L, T, and T' normal to the sample faces. For each direction, the ratio of the axial force response F_i and the axial displacement response D_i between plates provides a complex stiffness function

$$K_i=\frac{F_i}{D_i} \quad (i\in\{L,T,T'\}). \tag{9}$$

On the other hand, measurement of both perpendicular displacements D_j of lateral faces centers provide two further biaxial complex transfer functions between directions j and i

$$T_{ji}=\frac{D_j}{D_i} \quad (j\in\{L,T,T'\} \text{ and } j\neq i), \tag{10}$$

where j denotes the directions perpendicular to the loading direction. The nine complex and frequency dependent transfer functions of Eqs. (9) and (10) are put together in a vector of ''experimentally measured'' quantities

$$V_m=[K_L,T_{LT},T_{LT'},K_T,T_{TL},T_{TT'},K_{T'},T_{T'L},T_{T'T}]. \tag{11}$$

Due to the supposed sample symmetry, redundancy may occur in vector V_m. Since isotropy of plane $(T-T')$ can be expressed by the relationships

$$\begin{aligned} &K_T=K_{T'}, \quad T_{LT}=T_{LT'},\\ &T_{TL}=T_{T'L}, \quad T_{TT'}=T_{T'T}, \end{aligned} \tag{12}$$

only five functions in V_m are independent. Thus in order to investigate how much axisymmetrical foams are, we use the redundancy of the measurements. Two vectors are provided for each sample from Eqs. (11) and (12)

$$V_m^{LT}=[K_L,T_{LT},K_T,T_{TL},T_{TT'}] \tag{13}$$

and

$$V_m^{LT'}=[K_L,T_{LT'},K_{T'},T_{T'L},T_{T'T}]. \tag{14}$$

The first one [Eq. (13)] takes preferentially account of directions L and T, whereas the second one [Eq. (14)] emphasizes directions L and T'. Vectors V_m^{LT} and $V_m^{LT'}$ are able to characterize a difference between the measured behavior and the supposed axisymmetric one. They are obviously identical if the material is exactly axisymmetrical.

The measurements only depend on the skeleton viscoelasticity tensor if the viscous static permeability of foam is high enough. At low frequencies, this assumption is justified for the present material and viscous damping between the air and the skeleton can be neglected compared to the intrinsic mechanical dissipation. If permeability is too high, its effects on mechanical responses can be eliminated using Biot modeling, as shown in Fig. 1. Then viscoelasticity tensor components can be achieved from vector V_p containing the (yet unknown) material parameters:

$$V_p[E_L,E_T,G_{LT},\nu_{LT},\nu_{TT}], \tag{15}$$

where the Young's moduli in the longitudinal direction and in the transverse plane $(T-T')$ are respectively noted E_L and E_T. Scalar G_{LT} is the shear modulus in the plane $(L-T)$, whereas ν_{LT} and ν_{TT} denote Poisson's ratios in planes $(L-T)$ and $(T-T')$, respectively. Although these parameters are complex value and frequency dependent as well as the measurements, relations between vectors V_p and V_m^{LT} are obtained by using a static finite element model of an axially loaded cube made of axisymmetric elastic solid. Taking into account the correspondence principle between elastic problems and viscoelasticy, the real part of vector V_m^{LT} is predicted from the real part of the mechanical properties contained in V_p. In addition, an inversion numerical scheme has been developed[15] in order to estimate the unknown vector V_p versus a given vector V_m^{LT}. Of course, if the vector $V_m^{LT'}$ is different from V_m^{LT}, its inversion provides a second set of material parameters, which can be compared to the first one, as done in the next section.

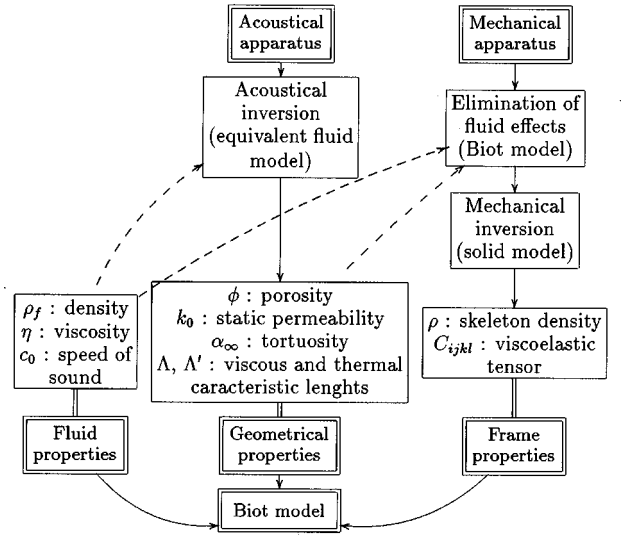

FIG. 1. Schematic diagram of experimental determination of the Biot parameters for acoustic materials. -----: Needed parameters for successive acoustic and mechanical identifications.

III. EXPERIMENTAL RESULTS AND ANALYSIS

In order to evaluate each of the previous parameters along the three perpendicular directions, the experiments (see Fig. 2) are carried out on five neighboring cubes of plastic foams cut out of the same slab. The length of the edge of the cube is 5 cm. The longitudinal direction (as shown in Fig. 3) is chosen to be parallel to the direction of the foaming process. The manufacturer has given this information. The other directions form a plane which is perpendicular to the

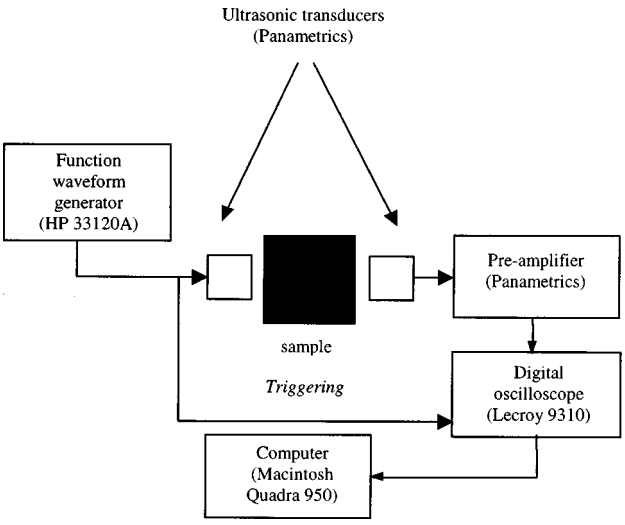

FIG. 2. Experimental setup of the ultrasonic measurements.

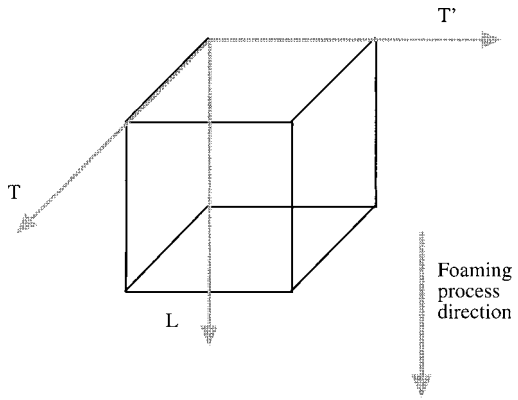

FIG. 3. Measurement directions of the cubic sample.

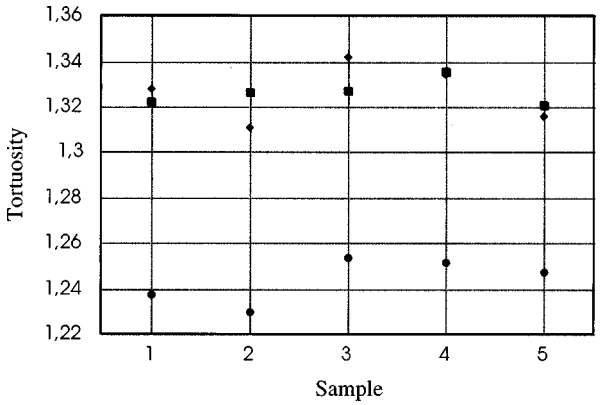

FIG. 5. Tortuosity along the three perpendicular directions of five cubic samples of PU foam. ●: L; ■: T; and ◆: T'.

normal direction. Due to the axisymmetry of the material, the orientation of the two transversal axes in this plane is not fundamental. This hypothesis should be verified by measuring the magnitude of discrepancy between parameters versus angle. This is rather difficult to realize with cubes of small size. Nevertheless, this assumption has already been checked for identical types of foams.[12] A simple look at the ultrasonics sine bursts transmitted along the three directions of the foam (Fig. 4) justifies fairly well the assumption of hexagonal symmetry. The wave, which has propagated along the normal direction, has higher amplitude and a faster arrival time than the two other signals. These last ones are very similar in both magnitude and time delay. The wave speed $c(\omega)$ in the porous media is calculated from an intercorrelation algorithm between the signals with and without sample, whereas the quality factor is obtained from the amplitude ratio of the two sine bursts. The values of the tortuosity along the three perpendicular axes have been computed from Eq. (7) and are shown in Fig. 5. The reproducibility of the results between the different samples is fairly good (relative variation lower than 2.5%) meaning that the heterogeneity of this slab of foam is small. Some 2-D scans of acoustical porous materials slabs have already pointed out that the heterogeneity of the tortuosity (measured in the same direction) is generally in order of 5%.[20] The important outcome is that the tortuosity is smaller in the foaming process direction than in the transversal directions. This result outlines the axisymmetry of the samples tested here. Due to the small differences between the principal directions, one can notice that such results would have been difficult to obtain with the electrical method for the tortuosity measurements.[21] Figure 6 shows the measurements of the length ℓ along the three directions for the five cubic samples. As the thermal characteristic length is isotropic, the differences observed among the three axes are only due to the viscous characteristic length. The expected hexagonal symmetry on Λ is less convincing than on tortuosity. However, with the exception of sample no. 2, the values computed along the transversal directions are more similar than the values along the longitudinal direction. Measurements of the viscous static permeability are shown in Fig. 7. Surprisingly, the values are nearly equal along the direction L and T', whereas values along direction T are 10% lower. This fact could be partially explained by taking into account some remaining thin membrane effects across the faces of the foam cells, although this remains a simple assumption which will be explored further later. Among these results, steady flow measurements seem to be more affected by walls than ultrasonic measurements. The reproducibility between the five samples is not so clear as for tortuosity measurements. Relative variation can reach 10% whereas measurement incertitudes are estimated at about 5%, which traduces a weak heterogeneity of permeability tensor.

As far as mechanical behavior is concerned, previous

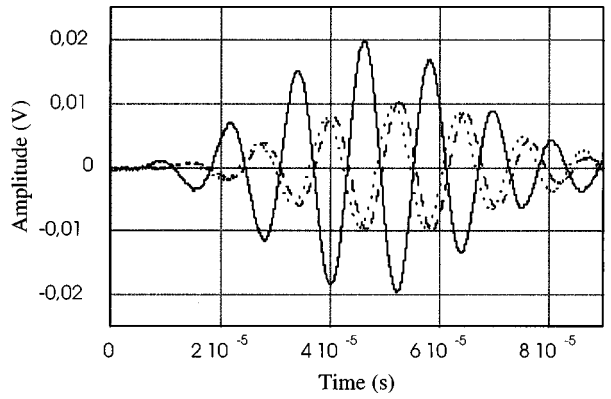

FIG. 4. Transmitted signals along the three directions of a cubic sample of PU foam; ———: L; --- : T; ⋯: T'.

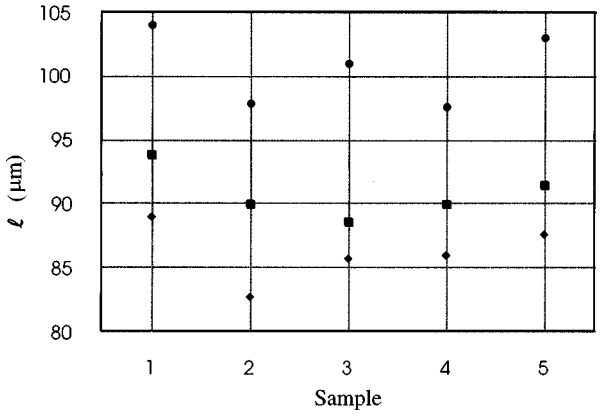

FIG. 6. Length ℓ along the three perpendicular directions of five cubic samples of PU foam. ●: L; ■: T; and ◆: T'.

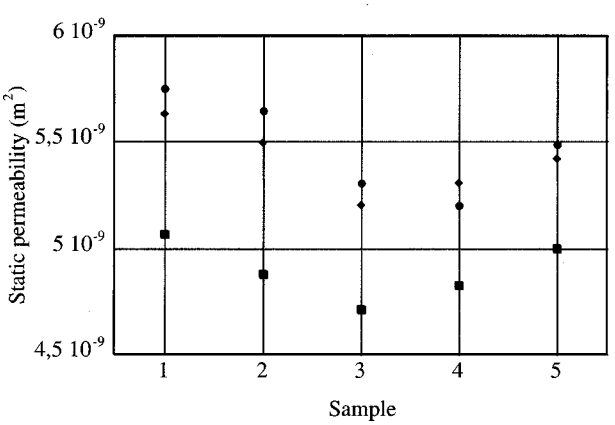

FIG. 7. Viscous static permeability along the three perpendicular directions of five cubic samples of PU foam. ●: L; ■: T; and ◆: T'.

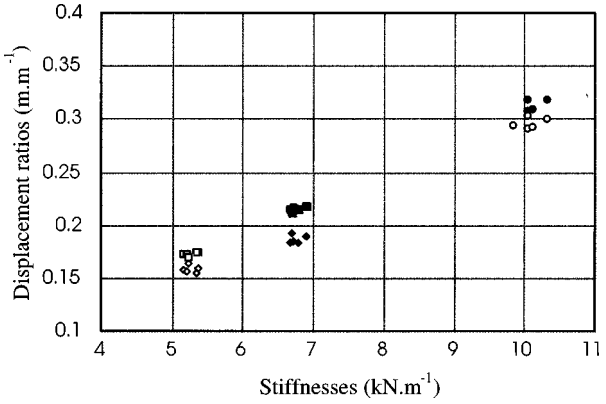

FIG. 8. Quasistatic measurements (at 60 Hz) on five neighboring cubes made of PU foam. Actual displacement ratios against stiffnesses real part are plotted. Black symbols denote V_m^{LT} components. ●: T_{LT} vs K_L; ■: T_{TL} vs K_T; and ◆: $T_{TT'}$ vs K_T. Blank symbols denote $V_m^{LT'}$ components. ○: $T_{LT'}$ vs K_L; □: $T_{T'L}$ vs $K_{T'}$; and ◇: $T_{T'T}$ vs $K_{T'}$.

samples were also investigated. The present results have been achieved at fixed temperature (23 °C) versus frequency. The frequency dependence is not discussed here and emphasis is given to the real part of measurements V_m at a single frequency of 60 Hz. As for out of phase measurements, all stiffnesses [Eq. (9)] have the same loss factor and displacement ratios [Eq. (10)] are merely real values.

In Fig. 8, we have plotted the actual displacement ratios versus the real parts of stiffnesses transfer function, directly obtained after measurement and calibration. Since the measured foam is not exactly axisymmetric, transfer function does not respect relationships (12) and inversion cannot be safely carried out with the single vector V_m^{LT} of Eq. (13). On the first hand, using both measured vectors V_m^{LT} and $V_m^{LT'}$, we can observe that behavior versus loading direction is not exactly axisymmetric since axes T and T' seem to be quite different (as for squares and diamonds markers, black and blank ones do not fit together). Nevertheless comparison of measurement between longitudinal direction and both so-called transversal directions even so justifies the transverse isotropy assumption. On the other hand, results are not very affected by measurements on different samples. Thus the material tested is quite homogeneous and main variations of results only come from the anisotropic mechanical behavior. Let us notice that the error on the measured magnitude of all transfer functions presented is estimated to around 3%.

From vectors V_m^{LT} and $V_m^{LT'}$, two inversions per sample provide two sets of stress–strain tensor components. Measurements of the three moduli are complex values exhibiting an identical complex dependence (the single complex dependence in stiffnesses measurements) whereas Poisson's ratios are real values. As for real parts, Poisson's ratios versus moduli are plotted in Fig. 9 for the different samples. As shown, Young's moduli (E_L, E_T) and Poisson's ratio ν_{LT} are achieved with a fairly good approximation. Their values' variations are mainly due to the gap between the axisymmetric model chosen for inversion and the actual behavior of the foam. On the other hand, the sensitivity of the shear modulus G_{LT} and the Poisson's ratio ν_{TT} to variations in the measurements is large during inversion. This fact is not so surprising since compression loading applied during measurements includes very few shear strains whereas components G_{LT} and ν_{TT} describe only shear behavior. So, differences between foam behavior and axisymmetric ones cannot be observed with these components because their errors can reach 100% by estimating the measurement errors to be close to 3%. In spite of these limitations, mean values of each stress–strain tensor components can provide better modeling in comparison with an isotropic model.

IV. CONCLUSION

Anisotropy of cubic samples of an open-cell foam has been investigated by acoustical and mechanical experimental methods. The results show that this material exhibits a quasi-axisymmetrical behavior. With the exception of the static viscous permeability, the samples tested seem to be described with a better accuracy in the case of transverse isotropy for both acoustical and mechanical parameters. The discrepancy observed between the measurements and the hexagonal symmetry could be explained by considering the noteworthy conveyor direction during the manufacturing process. Such improvement of the model would not lead to notable changes of physical properties compared to their re-

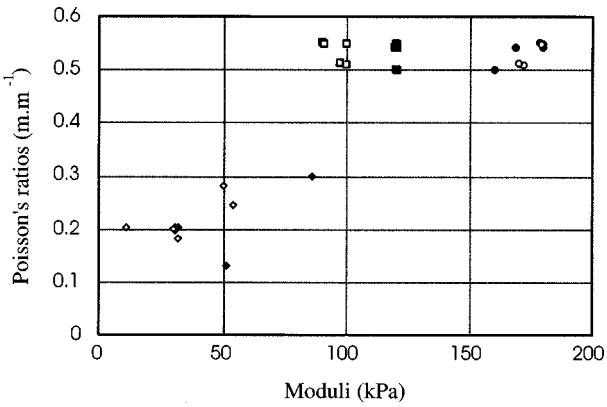

FIG. 9. Amplitude of the stress–strain tensor components of PU foam at 60 Hz. Poisson's ratios versus different moduli. ●, ○: ν_{lt} vs E_l; ■, □: ν_{lt} vs E_t; and ◆, ◇: ν_{tt} vs G_{lt}. Black symbols denote inversion results from V_m^{LT}. Blank symbols denote inversion results from $V_m^{LT'}$.

spective gradient in the foam block (in terms of heterogeneity). For example, the foam density is higher in the bottom and near the sidewalls, respectively, due to gravity and frictional drags. One can also notice that the amount of anisotropy is lower on the rigid frame model parameters (10%) compared to the component of the viscoelasticity tensor (70% on moduli, 200% on Poisson's ratios). This first report of mechanical and acoustical anisotropic characterization on reticulated foams allows better vibroacoustic prediction of multi-layered damping materials behavior.

ACKNOWLEDGMENT

The authors would like to thank M. P. Moreau from Recticel Inc. for supplying samples of plastic foams having indicated rising direction.

[1] C. Zwikker and C. W. Kosten, *Sound Absorbing Materials* (Elsevier, New York, 1949).
[2] K. Attenborough, ''Acoustical characteristics of porous materials,'' Phys. Rep. **82**, 179–227 (1982).
[3] D. L. Johnson, J. Koplik, and R. Dashen, ''Theory of dynamic permeability and tortuosity in fluid-saturated porous media,'' J. Fluid Mech. **176**, 379–402 (1987).
[4] P. B. Nagy, ''Slow wave propagation in air filled permeable solids,'' J. Acoust. Soc. Am. **93**, 3224–3234 (1993).
[5] G. A. Gist, ''Fluid effects on velocity and attenuation in sandstones,'' J. Acoust. Soc. Am. **96**, 1158–1173 (1994).
[6] P. B. Nagy, ''Local variations of slow wave attenuation in air-filled permeable materials,'' J. Acoust. Soc. Am. **99**, 914–919 (1996).
[7] P. B. Nagy and D. L. Johnson, ''Improved materials characterization by pressure-dependent ultrasonic attenuation in air-filled permeable solids,'' Appl. Phys. Lett. **68**, 3707–3709 (1996).
[8] J. F. Allard, *Propagation of Sound in Porous Media: Modelling Sound Absorbing Materials* (Chapman and Hall, London, 1993).
[9] D. Lafarge, ''Propagation du son dans les matériaux poreux à structure rigide saturés par un fluide viscothermique,'' Ph. D. dissertation, Université du Maine, 1993.
[10] M. A. Biot, *Acoustics, Elasticity, and Thermodynamics of Porous Media, Twenty One Papers by M. A. Biot*, edited by I. Tolstoy (American Institute of Physics, Woodbury, NY, 1992).
[11] L. J. Gibson and M. F. Ashby, *Cellular Solids: Structure and Properties* (Pergamon, Oxford, 1988).
[12] M. Melon, ''Caractérisation de matériaux poreux par ultrasons basse-fréquence,'' Ph. D. dissertation, Université du Maine 1996.
[13] N. Brown, M. Melon, V. Montembault, B. Castagnède, W. Lauriks, and Ph. Leclaire, ''Evaluation of the viscous characteristic length of air-saturated porous materials from the ultrasonic dispersion curve,'' C. R. Acad. Sci. Paris **322**, 121–127 (1996).
[14] Ph. Leclaire, L. Kelders, W. Lauriks, J. F. Allard, and W. Glorieux, ''Ultrasonic wave propagation in reticulated foams saturated by different gases—High frequency limit of the classical models,'' Appl. Phys. Lett. **69**, 2641–2643 (1996).
[15] E. Mariez and S. Sahraoui, ''Transfer function method for investigating the viscoelasticity tensor of acoustical materials: Cubic specimen'' Exp. Mech. (unpublished).
[16] D. A. Bies and C. H. Hansen, ''Flow resistance information on acoustical design,'' Appl. Acoust. **13**, 357–391 (1980).
[17] Ph. Leclaire, L. Kelders, W. Lauriks, M. Melon, N. Brown, and B. Castagnède, ''Determination of the viscous and thermal characteristic lengths of plastic foams by ultrasonic measurements in helium and air,'' J. Appl. Phys. **80**, 2009–2012 (1996).
[18] E. Mariez and S. Sahraoui, ''Elastic constants of polyurethane foam's skeleton for Biot model,'' Internoise Congress Proceedings, Liverpool, 951–954 (1996).
[19] E. Mariez and S. Sahraoui, ''Measurement of mechanical anisotropic properties of acoustic foams for the Biot model,'' Internoise Congress Proceedings, Budapest, 1683–1686 (1997).
[20] M. Melon and B. Castagnède, ''Correlation between tortuosity and transmission coefficient of porous media at high frequency,'' J. Acoust. Soc. Am. **98**, 1228–1230 (1995).
[21] R. J. S. Brown, ''Connection between formation factor of electrical resistivity and fluid-solid coupling factor in Biot's equation for acoustic waves in fluid-filled porous media,'' Geophysics **45**, 1269–1275 (1980).

Noise control of a master harmonic oscillator coupled to a set of satellite harmonic oscillators

G. Maidanik and K. J. Becker
Carderock Division, Naval Surface Warfare Center (DTMB), 9500 MacArthur Boulevard, West Bethesda, Maryland 20817-5000

(Received 4 February 1998; accepted for publication 3 August 1998)

The overall gain is defined as the ratio of the stored energy in the isolated master harmonic oscillator to that in the coupled one. This gain is composed of two distinct factors: The first factor, the external input power gain, relates to the ratio of the external input power into the isolated master harmonic oscillator to that into the coupled one. The second factor, the loss factor gain, relates to the ratio of the loss factor of the coupled master harmonic oscillator to that of the isolated master harmonic oscillator. Both loss factors are in reference to the stored energy in the master harmonic oscillator only. It has been customary to assume the first factor to be unity and, thus the overall gain and the loss factor gain have been assumed to be identical. It is argued here that often this assumption is not valid. Therefore, noise control measures that are based on this assumption may have been wrongly evaluated. A few examples that illustrate the disparity between the overall gain and the loss factor gain are cited in this paper. [S0001-4966(98)03111-7]

PACS numbers: 43.20.Ks, 43.40.Tm [DEC]

INTRODUCTION

In a recent paper the authors discussed the definition of the loss factors of a master harmonic oscillator (HO) that is an integral element in a complex. The complex is composed of the master HO, the satellite harmonic oscillators (HOs), and their couplings to the master HO. Two distinct steady state loss factors are defined, both in reference to the master HO which is the only driven HO in the complex. The difference between these loss factors is that the first, the *U* loss factor $\eta_{b1}(\omega)$, is defined in reference to the stored energy $E_1(\omega)$ in the master HO while the second, the effective loss factor $\eta_{e1}(\omega)$, is defined in reference to the stored energy $E(\omega)$ in the complex as a whole; namely

$$\eta_{b1}(\omega)=\Pi_{e1}(\omega)/\omega E_1(\omega)$$

and (1)

$$\eta_{e1}(\omega)=\Pi_{e1}(\omega)/\omega E(\omega);$$

$$E(\omega)=E_1(\omega)+E_s(\omega), \quad \zeta_1^s(\omega)=[E_s(\omega)/E_1(\omega)], \quad (2)$$

where $\Pi_{e1}(\omega)$ is the external input power into the master HO, $E_s(\omega)$ is the energy stored in the coupled set of satellite HOs, and (ω) is the frequency variable; this variable is the Fourier conjugate of the temporal variable (t). It is to be noted that the energy stored in the couplings is assigned, in part, to $E_1(\omega)$ and, in part, to $E_s(\omega)$. The quantity $\zeta_1^s(\omega)$ is then the ratio of the energy stored in the satellite HOs (together with that stored in the couplings that are assigned to them) to the energy stored in the master HO (together with that stored in the couplings that is assigned to it).[1] Clearly

$$\eta_{b1}(\omega)\gtrsim\eta_{e1}(\omega), \quad (3)$$

and in particular

$$\eta_{b1}(\omega)=\eta_1(\omega)+\eta_s(\omega)\zeta_1^s(\omega), \quad \zeta_1^s(\omega)\geqslant 0, \quad (4a)$$

$$\eta_{e1}(\omega)=\eta_{b1}(\omega)[1+\zeta_1^s(\omega)]^{-1}$$

$$=[\eta_1(\omega)+\eta_s(\omega)\zeta_1^s(\omega)][1+\zeta_1^s(\omega)]^{-1}. \quad (4b)$$

In Eqs. (4) $\eta_1(\omega)$ is the inherent loss factor in the master HO

$$\eta_1(\omega)=[\Pi_{e1}^o(\omega)/(\omega)E_1^o(\omega)], \quad (5)$$

where $\Pi_{e1}^o(\omega)$ is the external input power and $E_1^o(\omega)$ is the stored energy in the ''isolated'' master HO.[1] The loss factor $\eta_1(\omega)$ accounts for losses in the master HO and in the couplings that are assigned to the master HO. The stored energy ratio $\zeta_1^s(\omega)$ in Eq. (4) is as stated in Eq. (2). On the other hand, in Eq. (4) $\eta_s(\omega)$ is the averaged loss factor associated with the satellite HOs; namely,

$$\eta_s(\omega)=\left[\sum_{n=2}^{N}\eta_n(\omega)E_n(\omega)\right]\left[\sum_{n=2}^{N}E_n(\omega)\right]^{-1}. \quad (6)$$

In Eq. (6) $\eta_n(\omega)$ is the inherent loss factor and $E_n(\omega)$ is the stored energy in the (n)th satellite HO. Again, $\eta_n(\omega)$ and $E_n(\omega)$, respectively, account also for the losses and stored energies in the couplings that are assigned to the (n)th satellite HO. In Ref. 1, $\eta_{b1}(\omega)$ and $\eta_{e1}(\omega)$ were investigated for a number of complexes composed of a master HO and several different sets of satellite HOs. It was stated in these investigations that although the loss factors do indicate the manner in which the external input powers are dissipated, they do not necessarily indicate the noise control gain achievable for a master HO in coupling it to a set of satellite HOs. Situations arise in which the overall gain in a noise control goal is more central than ensuring efficient dissipation of the stored energies. Thus in these situations the loss factors may play only partial roles. To quantify such situations, one may use Eqs. (1) and (5) to derive an overall (stored energy) gain $\Gamma_{o1}(\omega)$ which is the ratio of the stored energy $E_1^o(\omega)$ in the isolated master HO to the stored energy

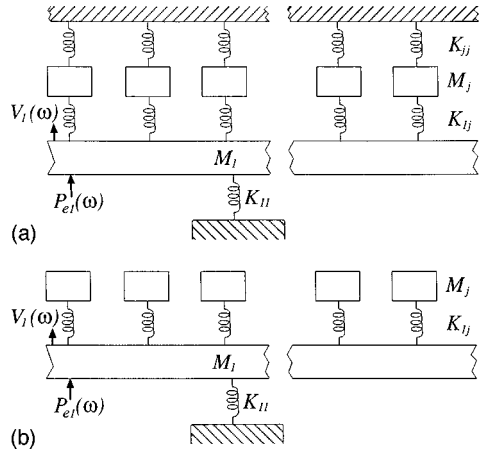

FIG. 1. (a) A complex composed of a master harmonic oscillator coupled to a set of satellite harmonic oscillators. The satellite harmonic oscillators are uncoupled to each other and the couplings to the master harmonic oscillator are restricted to stiffness controlled elements only. (b) The set of satellite harmonic oscillators are replaced, in (a), by a mere set of satellite masses.

$E_1(\omega)$ of the coupled master HO. This overall gain is

$$\Gamma_{o1}(\omega)=[E_1^o(\omega)/E_1(\omega)]=[\bar{\bar{\Pi}}_{e1}(\omega)]^{-1}[\overline{\eta}_{b1}(\omega)],$$
$$[\bar{\bar{\Pi}}_{e1}(\omega)]^{-1}=[\Pi_{e1}^o(\omega)/\Pi_{e1}(\omega)], \tag{7}$$
$$\overline{\eta}_{b1}(\omega)=[\eta_{b1}(\omega)/\eta_1(\omega)].$$

Consequently, the overall gain $\Gamma_{o1}(\omega)$ is the product of two factors. The first factor $[\bar{\bar{\Pi}}_{e1}(\omega)]^{-1}$—the external input power gain—is the ratio of the external input power into the isolated master HO to that into the coupled one. The second factor, $[\overline{\eta}_{b1}(\omega)]$, the loss factor gain is the ratio of the U loss factor of the coupled master HO to that of the isolated one.[1] An overall gain $\Gamma_{o1}(\omega)$ that substantially exceeds unity in a wider frequency bandwidth may be a credible noise control goal. This may be achieved by manipulating the external input power gain and/or the loss factor gain. In this paper rendering $\Gamma_{o1}(\omega)$ with these attributes is considered to be a desired noise control achievement. The prevailing wisdom has been to assume *a priori* that the external input power gain $[\bar{\bar{\Pi}}_{e1}(\omega)]^{-1}$, on the right of Eq. (7), is substantially equal to unity so that the loss factor gain $[\overline{\eta}_{b1}(\omega)]$ becomes the determining factor for the overall gain; notwithstanding that, often it is the external drive and not the external input power that is specified as the agent responsible for the excitation of the complex. The examination of this prevailing wisdom for a complex composed of a number of coupled HOs is, in large part, the focus of this paper.[2,3]

I. EQUATION OF MOTION FOR THE COMPLEX

A sketch of the complex investigated in this paper is shown in Fig. 1(a). Since the complex is similar to that specialized in Ref. 1, the derivation of the relevant equations is detailed in this reference. Familiarity with this derivation is assumed in this paper. Moreover, the notational procedure in Ref. 1 is adopted herein. In particular, the equation of motion for the isolated master HO, in response to an external *force* drive $P_{e1}(\omega)$, is

$$Z_{11}^-(\omega)V_1^o(\omega)=P_{e1}(\omega),$$
$$\Pi_{e1}^o(\omega)=\mathrm{Re}\{[(\omega M_1)/Z_1^-(\omega)]\}\Pi_{o1}(\omega), \tag{8}$$

and that for the coupled master HO, in response to the same external force drive, is

$$Z_1(\omega)V_1(\omega)=P_{e1}(\omega),$$
$$\Pi_{e1}(\omega)=\mathrm{Re}\{[(\omega M_1)/Z_1(\omega)]\}\Pi_{o1}(\omega), \tag{9}$$

where $Z_{11}^-(\omega)$ and $V_1^o(\omega)$ are, respectively, the impedance and response of the isolated master HO, $Z_1(\omega)$ and $V_1(\omega)$ are, respectively, the impedance and response of the coupled HO and

$$\Pi_{e1}^o(\omega)=\mathrm{Re}\{V_1^0(\omega)P_{e1}^*(\omega)\},$$
$$\Pi_{e1}(\omega)=\mathrm{Re}\{V_1(\omega)P_{e1}^*(\omega)\}, \tag{10}$$
$$\Pi_{o1}(\omega)=(\omega M_1)^{-1}|P_{e1}(\omega)|^2.$$

The impedance $Z_{11}^-(\omega)$ of the isolated master HO may be expressed in the form

$$Z_{11}^-(\omega)=(i\omega M_1)[1-(\omega_{11}/\omega)^2(1+i\eta_{11})], \tag{11a}$$

where

$$\omega_{11}^2=(K_{o1}/M_1), \quad K_1=K_{o1}(1+i\eta_{11}). \tag{11b}$$

The impedance $Z_1(\omega)$ of the coupled master HO may be similarly expressed in the form

$$Z_1(\omega)=[Z_{11}^-(\omega)+Z_{c1}(\omega)], \quad Z_{c1}(\omega)=\sum_{j=2}^{N} Z_{cj}(\omega), \tag{12a}$$

where

$$Z_{cj}(\omega)=[|Z_{jj}^-(\omega)|^2Z_{1j}(\omega)+|Z_{1j}(\omega)|^2Z_{jj}^-(\omega)]|Z_{jj}(\omega)|^{-2},$$
$$Z_{jj}(\omega)=Z_{jj}^-(\omega)+Z_{1j}(\omega),$$
$$Z_{jj}^-(\omega)=(i\omega M_j)[1-(\omega_{jj}/\omega)^2(1+i\eta_{jj})],$$
$$Z_{1j}(\omega)=(K_{1j}/i\omega)=Z_{j1}(\omega), \tag{12b}$$
$$K_{jj}=K_{ojj}(1+i\eta_{1j}), \quad (\omega_{jj})^2=(K_{ojj}/M_j),$$
$$K_{1j}=K_{o1j}(1+i\eta_{1j}), \quad (\omega_{1j})^2=(K_{o1j}/M_j), \quad j\geqslant 2.$$

In Eq. (11), M_1, K_1, and η_{11} are, respectively, the mass, the complex stiffness, and the loss factor of the master HO. In Eqs. (12), M_j, K_{jj}, and η_{jj} are, respectively, the mass, the complex stiffness, and the loss factor of the (j)th satellite HO and K_{1j} and η_{1j} are, respectively, the complex stiffness and the loss factor of the coupling of the (j)th satellite HO to the master HO.[1] Moreover, the equation of motion for the isolated master HO, in response to an external *velocity* drive $V_1(\omega)$, is

$$Z_{11}^-(\omega)V_1(\omega)=P_{e1}^o(\omega),$$
$$\Pi_{e1}^o(\omega)=\mathrm{Re}\{[Z_{11}^-(\omega)/(\omega M_1)]\}\Pi_{o1}(\omega), \tag{13}$$

and for the coupled master HO, in response to the same external velocity drive, is

$$Z_1(\omega)V_1(\omega)=P_{e1}(\omega),$$
$$\Pi_{e1}(\omega)=\mathrm{Re}\{[Z_1(\omega)(\omega M_1)]\}\Pi_{o1}(\omega), \tag{14}$$

where $P^o_{e1}(\omega)$ and $P_{e1}(\omega)$ are, respectively, the external force drives that maintain equal the response $V_1(\omega)$ for the isolated as well as for the coupled master HO and

$$\Pi^o_{e1}(\omega)=\mathrm{Re}\{V^*_1(\omega)P^o_{e1}(\omega)\},$$
$$\Pi_{e1}(\omega)=\mathrm{Re}\{V^*_1(\omega)P_{e1}(\omega)\}, \tag{15}$$
$$\Pi_{o1}(\omega)=(\omega M_1)|V_1(\omega)|^2.$$

From Eqs. (8) to (10) one may conveniently normalize the external input powers $\Pi^o_{e1}(\omega)$ and $\Pi_{e1}(\omega)$, generated by an external *force* drive in the forms

$$\overline{\Pi}^o_{e1}(\omega)=[\Pi^o_{e1}(\omega)/\Pi_{o1}(\omega)]$$
$$=\mathrm{Re}\{(\omega M_1)Z^-_{11}(\omega)\}|Z^-_{11}(\omega)|^{-2}, \tag{16a}$$
$$\overline{\Pi}_{e1}(\omega)=[\Pi_{e1}(\omega)/\Pi_{o1}(\omega)]$$
$$=\mathrm{Re}\{(\omega M_1)Z_1(\omega)\}|Z_1(\omega)|^{-2}. \tag{16b}$$

Again, from Eqs. (8) to (10) one may derive the external input power gain, pertaining to an external *force* drive, to be

$$[\bar{\bar{\Pi}}_{e1}(\omega)]^{-1}=[\Pi^o_{e1}(\omega)/\Pi_{e1}(\omega)]$$
$$=[\mathrm{Re}\{Z^-_{11}(\omega)\}/\mathrm{Re}\{Z_1(\omega)\}]|Z_1(\omega)/Z^-_{11}(\omega)|^2. \tag{16c}$$

Similarly, from Eqs. (13) to (15) one may conveniently normalize the external input powers into an isolated and a coupled master HO generated by an external *velocity* drive, in the forms

$$\overline{\Pi}^o_{e1}(\omega)=[\Pi^o_{e1}(\omega)/\Pi_{o1}(\omega)]=\mathrm{Re}\{Z^-_{11}(\omega)/(\omega M_1)\}, \tag{17a}$$
$$\overline{\Pi}_{e1}(\omega)=[\overline{\Pi}_{e1}(\omega)/\Pi_{o1}(\omega)]=\mathrm{Re}\{Z_1(\omega)/(\omega M_1)\}. \tag{17b}$$

Again, from Eqs. (13) to (15) one may derive the external input power gain, pertaining to an external *velocity* drive, to be

$$[\bar{\bar{\Pi}}_{e1}(\omega)]^{-1}=[\Pi^o_{e1}(\omega)/\Pi_{e1}(\omega)]$$
$$=[\mathrm{Re}\{Z^-_{11}(\omega)\}/\mathrm{Re}\{Z_1(\omega)\}]. \tag{17c}$$

In passing, it is recognized that the ratio of the loss factors that constitutes the loss factor gain $[\overline{\eta}_{b1}(\omega)]$, may be substantially equated to the ratio of the real parts of the impedances $Z_1(\omega)$ and $Z^-_{11}(\omega)$ of the coupled and isolated master HO, respectively. Therefore, and independently of the type of the external drive, the loss factor gain is

$$\overline{\eta}_{b1}(\omega)=[\eta_{b1}(\omega)/\eta_1(\omega)]\simeq[\mathrm{Re}\{Z_1(\omega)\}/\mathrm{Re}\{Z^-_{11}(\omega)\}]. \tag{18}$$

In addition, it is observed that both gain factors; the external input power gain $[\bar{\bar{\Pi}}_{e1}(\omega)]^{-1}$ and the loss factor gain $[\overline{\eta}_{b1}(\omega)]$, are proper functionals of the complex; i.e., these gains are functionals of parameters and quantities that specify the complex only; they are independent of the measures of the response and the external drive.[1] Moreover, the gains $[\bar{\bar{\Pi}}_{e1}(\omega)]^{-1}$ and $[\overline{\eta}_{b1}(\omega)]$ are not only proper functionals, but these functionals may harbor common parametric factors. Thus Eq. (7) does not only ensure that the overall gain is also a proper functional of the complex, but in the overall gain $\Gamma_{o1}(\omega)$ some of these common parametric factors may be reduced. Indeed, for a master HO that is subjected to an external force drive, the overall gain $\Gamma_{o1}(\omega)$ can be expressed, from Eqs. (7), (16), and (18), in the form

$$\Gamma_{o1}(\omega)=|Z_1(\omega)/Z^-_{11}(\omega)|^2. \tag{19}$$

On the other hand, and naturally, there can be no overall gain when the velocity $V_1(\omega)$ of the master HO is maintained fixed. A fixed velocity is commensurate with an infinite impedance being assigned to the master HO. In this situation Eq. (19) would suggest that $\Gamma_{o1}(\omega)=1$. Indeed, from Eqs. (7), (17), and (18) one obtains

$$\Gamma_{o1}(\omega)=1, \tag{20}$$

for the overall gain of a master HO that is subjected to an external velocity drive. The reduction in the overall gain due to common factors, in the external input power gain and in the loss factor gain, are clearly demonstrated in Eqs. (19) and (20). It transpires then that manipulation of parameters that specify the complex intended to benefit one gain factor may be detrimental in the other and vice versa. This delineates a category of dangers in which one gain factor is fixed *a priori* without examining the influence that such fixing may induce in the other gain factor. In particular, setting to unity the value of the external input power gain, thereby equating the loss factor gain to the overall gain lies in this category. The noise control temptation for identifying the loss factor gain as the overall gain is demonstrated, in this paper, on complexes composed of a master HO that is coupled to various sets of satellite HOs. The purpose of coupling the master HO to a set of satellite HOs, as already mentioned, is intended to achieve a noise control goal that result in a value for the overall gain that substantially exceeds unity and maintains this value over a wide frequency band.

Finally, ever since structural fuzzies began reverberating within the noise control community, sprung masses, as vibration control devices, have become hot commodities.[4–10] In consequence, there exists in the literature a number of papers and many discussions in which the master structure is merely a mass and the coupled HOs are merely sprung masses.[1,8–10] Therefore, it may be useful to render the essence of this paper relevant to this *reduced complex*. This is made available in a brief Appendix.

II. COMPUTATIONS AND DISPLAYS OF THE GAIN FACTORS IN RESPONSE OF A MASTER HO SUBJECTED TO AN EXTERNAL FORCE DRIVE

A ''standard complex'' is defined in terms of a standard master HO, standard satellite HOs, and standard couplings. These standard constituents in the standard complex are defined in Eq. (32) of Ref. 1 and are adopted in this paper. It is recognized that the normalized external input power $\Pi^o_{e1}(\omega)$, generated by an external force drive, is identical for all the complexes that commonly incorporate the standard

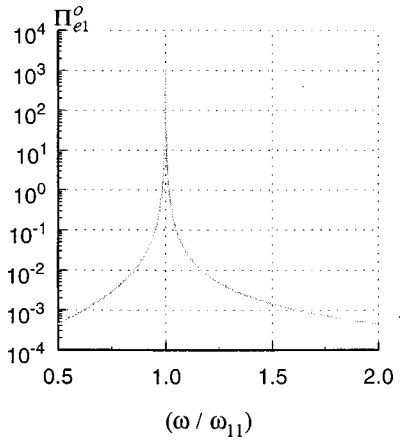

FIG. 2. The normalized external input power $\Pi^o_{e1}(\omega)$ into the isolated master harmonic oscillator as a function of the normalized frequency (ω/ω_{11}).

master HO. This external input power is computed and displayed as a function of the normalized frequency (ω/ω_{11}) in Fig. 2. Correspondingly, computations are performed on the gains $[\bar{\bar{\Pi}}_{e1}(\omega)]^{-1}$, $[\overline{\eta}_{b1}(\omega)]$, and $\Gamma_{o1}(\omega)$, as functions of the normalized frequency (ω/ω_{11}), in the frequency range $0.5 \leqslant (\omega/\omega_{11}) \leqslant 2.0$.[1] Initially, computations and displays pertaining to two distinct coupled sets of satellite HOs are offered; the first set, depicted in Fig. 3, involves a single satellite HO and the second set, depicted in Fig. 4, involves nine satellite HOs. Finally, computations and displays of the gains $[\overline{\eta}_{b1}(\omega)]$ and $\Gamma_{o1}(\omega)$ pertaining to four additional distinct coupled sets of satellite HOs are offered in Figs. 5–8. The displays in these figures are in support of the arguments and comments made with respect to Figs. 3 and 4. In each of Figs. 3–8, three shades of curves are displayed: The light curves pertain to the standard loss factor for either the satellite HOs or the couplings, the dark and the darkest curves pertain to changes in the relevant loss factor from the standard value of 10^{-3} to 10^{-2} to 10^{-1}, respectively.

In Fig. 3 the complex incorporates a single satellite HO with a resonance frequency that matches that of the isolated master HO. From Figs. 2 and 3(a), the latter depicting the external input power gain $[\bar{\bar{\Pi}}_{e1}(\omega)]^{-1}$, it emerges that the coupling to the satellite HO profoundly influences the normalized external input power $\overline{\Pi}_{e1}(\omega)$ that is received by the master HO; notwithstanding that the mass of the standard satellite HO is one-tenth of that of the standard master HO.[1] However, this influence is largely limited to the frequency range spanning the resonance frequency at $(\omega/\omega_{11})=1$. In particular, the degeneracy, in the identical resonance frequencies of the two HOs in the complex, is resolved into two distinct resonance frequencies that straddle the original resonance frequency of the master HO.[11–13] At these distinct resonance frequencies, $[\bar{\bar{\Pi}}_{e1}(\omega)]^{-1}$ exhibits gain deficiencies; i.e., a frequency region in which the referenced gain is less than unity. A gain deficiency in the external input power gain, one recalls, indicates that the coupled master HO receives more external input power than does the corresponding isolated one. A response rule has it that between two distinct resonances an anti-resonance must exist.[11–13] This anti-resonance, with an anti-resonance frequency (ω/ω_{11}), yields a peak at this frequency in the external input power gain. This anti-resonance peak, moreover, is reinforced by the peak in $\bar{\bar{\Pi}}^o_{e1}(\omega)$ exhibited in Fig. 2. The peak in $\overline{\Pi}^o_{e1}(\omega)$ lies, by definition, at (ω/ω_{11}), which matches that of the anti-resonance frequency. Thus the prominent features in Fig. 3(a) consist of an enhanced peak at (ω/ω_{11}) and two distinct nadirs on either side of the peak. Beyond the nadirs, on the lower and upper frequency ranges, the external input power gain $[\bar{\bar{\Pi}}_{e1}(\omega)]^{-1}$ is substantially unity. Also shown in Fig. 3(a) is the influence, on $[\bar{\bar{\Pi}}_{e1}(\omega)]^{-1}$, of variations in the loss factor η_{jj} of the satellite HOs; the light curve pertains to the standard value of 10^{-3} for (η_{jj}) and the dark and darkest curves are for $\eta_{jj}=10^{-2}$ and $\eta_{jj}=10^{-1}$, respectively.[1] These variations again influence the external input power that is received by the coupled master HO. However, this influence is largely and naturally confined to the frequency ranges spanning the anti-resonance frequency at $(\omega/\omega_{11})=1$ and the resolved resonance frequencies on either side of the anti-resonance frequency.[11]

Figure 3(b) depicts the loss factor gain $[\overline{\eta}_{b1}(\omega)]$. The

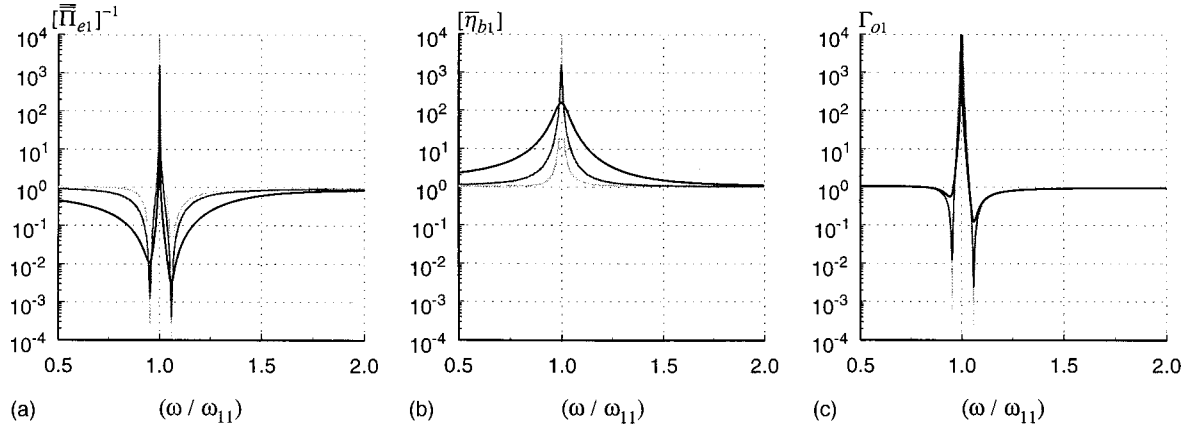

FIG. 3. Energetics pertaining to a standard master harmonic oscillator that is coupled to a single satellite harmonic oscillator and is subjected to an external force drive [cf. Eq. (32) and Fig. 4 of Ref. 1]. (a) The external input power gain $[\bar{\bar{\Pi}}_{e1}(\omega)]^{-1}$ of the master harmonic oscillator as a function of the normalized frequency (ω/ω_{11}). (b) The loss factor gain $[\overline{\eta}_{b1}(\omega)]$ of the master harmonic oscillator as a function of the normalized frequency (ω/ω_{11}). (c) The overall gain $\Gamma_{o1}(\omega)$ of the master harmonic oscillator as a function of the normalized frequency (ω/ω_{11}).

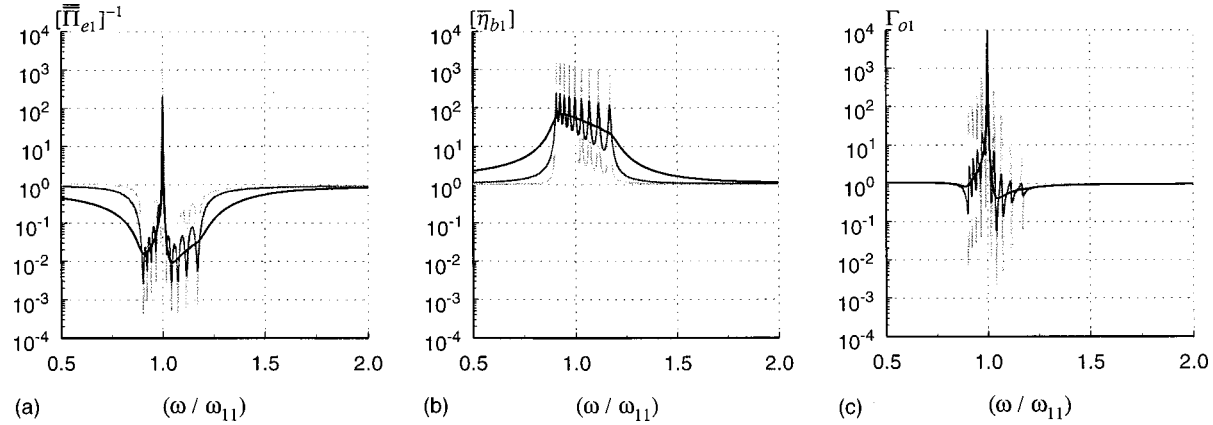

FIG. 4. Energetics of a standard master harmonic oscillator that is coupled to a set of nine satellite harmonic oscillators and is subjected to an external force drive [cf. Eq. (36) and Fig. 10 of Ref. 1]. (a) The external input power gain $[\bar{\bar{\Pi}}_{e1}(\omega)]^{-1}$ of the master harmonic oscillator as a function of the normalized frequency (ω/ω_{11}). (b) The loss factor gain $[\bar{\eta}_{b1}(\omega)]$ of the master harmonic oscillator as a function of the normalized frequency (ω/ω_{11}). (c) The overall gain $\Gamma_{o1}(\omega)$ of the master harmonic oscillator as a function of the normalized frequency (ω/ω_{11}).

loss factor gain is observed to peak at the anti-resonance frequency at $(\omega/\omega_{11}) \simeq 1$ and to fall-off sharply to unity on either side of this frequency. The height of the peak and the bandwidth of the associated ridge are sensitive, in a recognized manner, to the values of the loss factor (η_{jj}) that are assigned to the single satellite HO. Were the loss factor gain $[\bar{\eta}_{b1}(\omega)]$, exhibited in Fig. 3(b), the overall gain, the noise control achievement rendered by the single satellite HO may be deemed desirable, especially for the higher value of the loss factor (η_{jj}) for the satellite HO; e.g., when $\eta_{jj} = 10^{-1}$. The actual overall gain $\Gamma_{o1}(\omega)$, stated in Eq. (7), is depicted in Fig. 3(c); this figure is based on computations depicted in Fig. 3(a) and (b). Comparing Fig. 3(b) and (c) exposes the temptation to declare, *a priori*, the external input power gain $[\bar{\bar{\Pi}}_{e1}(\omega)]^{-1}$ to be unity. An overall gain corresponding to Fig. 3(b) includes features that are preferred to

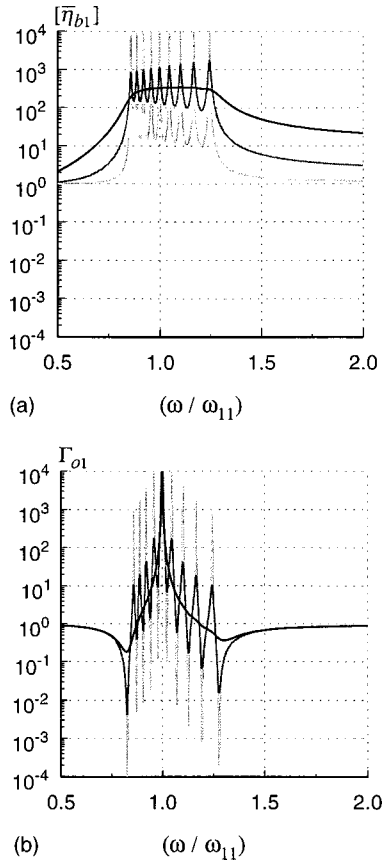

FIG. 5. Energetics of a standard master harmonic oscillator subjected to an external force drive and is coupled to a set of nine satellite masses, thus $N=10$ and the numerical increment Δ is chosen equal to 0.8 [cf. Eq. (37) and Fig. 13(a) and (b) of Ref. 1]. (a) The loss factor gain $[\bar{\eta}_{b1}(\omega)]$ of the master harmonic oscillator as a function of the normalized frequency (ω/ω_{11}). (b) The overall gain $\Gamma_{o1}(\omega)$ of the master harmonic oscillator as a function of the normalized frequency (ω/ω_{11}).

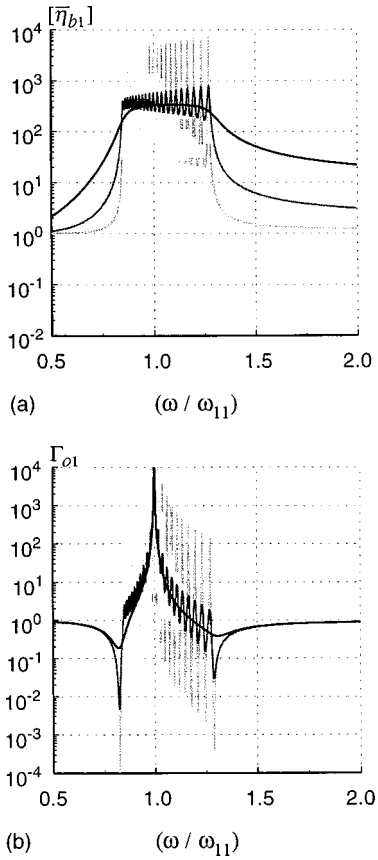

FIG. 6. As Fig. 5 except that $N=22$ and $\Delta=0.8$ [cf. Eq. (37) and Fig. 13(c) and (d) of Ref. 1].

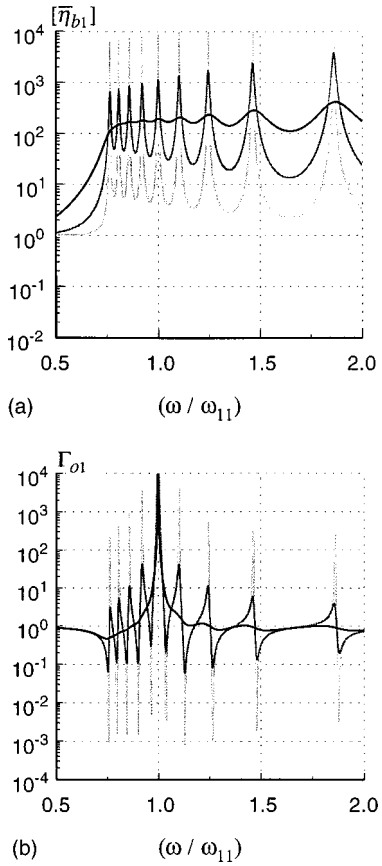

FIG. 7. As Fig. 5 except that $N=10$ and $\Delta=1.6$ [cf. Eq. (37) and Fig. 14(a) and (b) of Ref. 1].

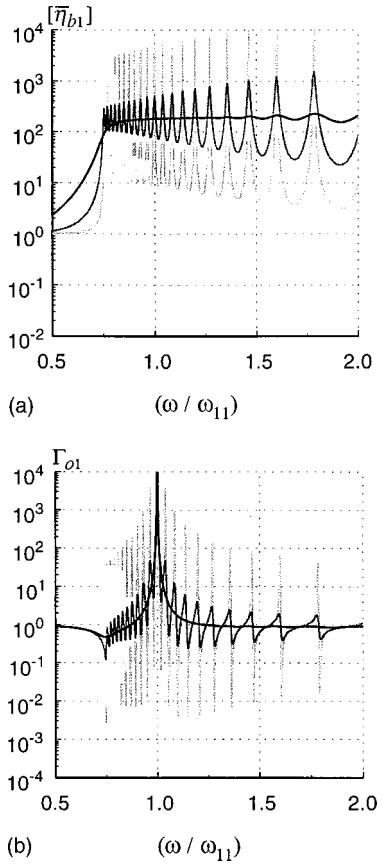

FIG. 8. As Fig. 5 except that $N=22$ and $\Delta=1.6$ [cf. Eq. (37) and Fig. 14(c) and (d) of Ref. 1].

those in Fig. 3(c), again, especially for the higher value of (η_{jj}). It is observed, in Fig. 3(c), that a major gain is accrued at and in the immediate vicinity of the anti-resonance frequency at $(\omega/\omega_{11})=1$. This major gain is accompanied by deficiencies in gain at and in the immediate vicinity of the resolved resonance frequencies on either side of the anti-resonance frequency. Beyond these resonance frequencies, on the lower and upper frequency ranges, the overall gain $\Gamma_{o1}(\omega)$ remains quiescent. From a noise control point of view, placing an anti-resonance at the resonance frequency of an isolated master HO by coupling it to a satellite HO is a device of considerable significance provided the reversal in overall gain, at and in the vicinity of the resolved resonance frequencies, is not a problem of concern.[10]

The experience of Fig. 3 is extended to a complex of nine satellite HOs that are not coupled to each other, but are coupled to the master HO [cf. Fig. 1(a)]. This complex is defined in Eq. (36) and is depicted in Fig. 10 of Ref. 1. Again, the computations are performed on $[\bar{\bar{\Pi}}_{e1}(\omega)]^{-1}$, $[\overline{\eta}_{b1}(\omega)]$, and $\Gamma_{o1}(\omega)$, as functions of the normalized frequency (ω/ω_{11}), in the frequency range $0.5\leqslant(\omega/\omega_{11})\leqslant 2.0$. These computations are displayed in Fig. 4(a)–(c), respectively. As in Fig. 3, the displays for the standard complex are depicted by the light curves in Fig. 4; the dark and the darkest curves reflect changes in the standard value of 10^{-3} for the loss factor (η_{jj}) of the satellite HOs to 10^{-2} and 10^{-1}, respectively. In all the complexes here considered, the resonance frequencies of the satellite HOs are, directly or indirectly, incremented evenly, by a square root, on either side of the resonance frequency of the isolated master HO, but with one coincidence. The coincidence is resolved by the coupling of the master HO to that coincident satellite HO. This rule of determining the resonance frequencies of the satellite HOs renders the separations, between adjacent resonance frequencies, frequency dependent.[1] The skew that the frequency dependent separations introduces in the distribution of the resonance frequencies is discernible in Fig. 4. It is observed that Figs. 3(a) and 4(a) are grossly similar; notwithstanding that the total mass of the satellite HOs remains unchanged. (In all the complexes considered herein this total mass is one-tenth of the mass of the master HO.[1]) The standard curve, the light curve in Fig. 3(a) exhibits in the external input power gain $[\bar{\bar{\Pi}}_{e1}(\omega)]^{-1}$ two nadirs and one peak, extending over a bandwidth that is determined by the strength of the coupling in the complex.[14,15] On the other hand, in Fig. 4(a) this gain exhibits ten nadirs and nine peaks, extending over a bandwidth that is determined by the difference in the resonance frequencies of the two satellite HOs that span all the others. Note that the bandwidth in Fig. 4(a) is wider than that in Fig. 3(a). In both Fig. 3(a) and Fig. 4(a) the peak in $[\bar{\bar{\Pi}}_{e1}(\omega)]^{-1}$ at $(\omega/\omega_{11})=1$ is reinforced by the peak in $\Pi^{o}_{e1}(\omega)$ exhibited in Fig. 2. The undulations, a series of successive nadirs and peaks on either side of the peak at $(\omega/\omega_{11})=1$, are confined, in Fig. 4(a), to within the frequency band just prescribed. As the nadirs in Fig. 3(a), these undulations lie in gain deficient regions; i.e., frequency

regions in which the referenced gain is less than unity. (One recalls that a gain deficiency in $[\bar{\bar{\Pi}}_{e1}(\omega)]^{-1}$, indicates that the coupled master HO receives more external input power than does the corresponding isolated one.) As in Fig. 3(a), the influence of changing the loss factor (η_{jj}) in the satellite HOs, from the standard value of 10^{-3} to 10^{-2} and 10^{-1}, is revealed in Fig. 4(a) by comparing the light curve with the dark and darkest curves, respectively. In Fig. 4(a) the phenomenon of a ''modal overlap'' emerges.[1,12,13] The phenomenon of modal overlap suitably defines a condition of modal overlap: Given a loss factor $\eta(\omega)$ and a normalized frequency separation $[\delta\omega/\omega]$, between adjacent resonance frequencies of HOs, the *condition* of modal overlap is met if $\eta(\omega) \geqslant 2[\delta\omega/\omega]$. When the condition of modal overlap is not met, individual peaks and nadirs in the undulated response of the HOs are distinguishable. When the condition of modal overlap is met, the undulations in the response are substantially suppressed. The undulations are suppressed into a sort of a mean value.[16] The *average* condition of modal overlap of concern here may be expressed in the form $\eta_{e1}(\omega) \gtrsim 2[\delta\omega/\omega]$, where on the *average* $[\delta\omega/\omega] = 10^{-1}(\Delta/N)^{1/2}$, with ($N$) the number of HOs in the complex and (Δ) is a numerical increment that is defined in Eq. (37c) of Ref. 1 and the effective loss factor $\eta_{e1}(\omega)$ tends to match, in this context, ($\eta_{1j}+\eta_{jj}$). Correspondingly, on the *average* the overall normalized bandwidth ($\Delta\omega$) may be equated in the form $(\Delta\omega) \simeq N(\delta\omega)$ and, therefore, on the *average* $[\Delta\omega/\omega] \simeq 10^{-1}(N\Delta)^{1/2}$. For the complex in Fig. 4, $N=10$ and $\Delta \simeq 0.4$ so that $(\Delta/N)^{1/2} \simeq 2\times 10^{-1}$ and $(N\Delta)^{1/2} \simeq 2$. Figure 4(a) clearly demonstrates the phenomenon of modal overlap under the condition just stated. The suppression of the undulations in the external input power gain $[\bar{\bar{\Pi}}_{e1}(\omega)]^{-1}$, as the loss factor ($\eta_{jj}$) of the satellite HOs increases, on the *average* obeys the stated modal overlap condition. The skew in the suppression, on the right and the left of the resonance frequency at $(\omega/\omega_{11})=1$, is the result of choosing the separations between adjacent resonance frequencies to be specifically frequency dependent.[1] Finally, just as in Fig. 3(a), Fig. 4(a) shows that in the lower and upper frequency ranges, beyond the frequency band defined by the smallest and highest resonance frequencies, the external input power gain $[\bar{\bar{\Pi}}_{e1}(\omega)]^{-1}$ asymptotically converges to unity.

The loss factor gain $[\bar{\eta}_{b1}(\omega)]$ for the complex depicted in Fig. 4 is displayed in Fig. 4(b) as a function of the normalized frequency (ω/ω_{11}). One observes that the bandwidth over which this gain is high, in excess of unity, is as wide as that of the external input power gain $[\bar{\bar{\Pi}}_{e1}(\omega)]^{-1}$ shown in Fig. 4(a). Moreover, the undulations in the value of the loss factor gain $[\bar{\eta}_{b1}(\omega)]$ are present when the condition of modal overlap is not met. When the condition of modal overlap is met, the undulations are suppressed and the value assumes a sort of a mean value.[16] Again, were one to assume that the external input power gain factor $[\bar{\bar{\Pi}}_{e1}(\omega)]^{-1}$ is unity, the loss factor gain $[\bar{\eta}_{b1}(\omega)]$ becomes the overall gain. An overall gain with characteristics exhibited in Fig. 4(b) is potentially an attractive noise control proposition, especially for the higher value of (η_{jj}). The actual overall gain $\Gamma_{o1}(\omega)$ for the complex depicted in Fig. 4 is displayed as a function of the normalized frequency (ω/ω_{11}) in Fig. 4(c). Much of the attractiveness in the loss factor gain, as an overall gain, evaporates in Fig. 4(c). Indeed, comparison of Fig. 4(c) with Fig. 3(c) clearly demonstrates that, in the gross, the overall gain is substantially the same in these figures. From a noise control point of view, if at all, the overall gain in Fig. 3(c) may be preferred to that in Fig. 4(c).

To further explore the noise control attractiveness of the loss factor gain $[\bar{\eta}_{b1}(\omega)]$, as a potential overall gain, and the actual gain $\Gamma_{o1}(\omega)$, several variations on the complex are investigated. For brevity sake, in these investigations only the loss factor gains $[\bar{\eta}_{b1}(\omega)]$ and the overall gain $\Gamma_{o1}(\omega)$ are displayed. These displays are cast in the format of Fig. 4(b) and (c), respectively. In the context of Ref. 1, these are A3 complexes in which the master mass is restored to a master HO. The impedance of $Z_{11}^{-}(\omega)$ of this restored master HO is as stated in Eq. (11). A typical construction of these complexes is sketched in Fig. 1(b) [cf. Fig. A1 of the Appendix]. Four complexes are investigated and the results are displayed in Figs. 5–8. Specifically, in Fig. 5: $N=10$ and $\Delta=0.8$; in Fig. 6: $N=22$ and $\Delta=0.8$; in Fig. 7: $N=10$ and $\Delta=1.6$; and in Fig. 8: $N=22$ and $\Delta=1.6$. The characteristics and frequency bandwidths in Figs. 5(a), 6(a), 7(a), and 8(a) are commensurate with those argued with respect to Fig. 4(b); these arguments include those pertaining to the condition of modal overlap. In particular, were the external input power gain to be set, in every case, *a priori* to unity, so that the loss factor gain assumes the role of the overall gain, these figures show definite noise control advantages; i.e., overall gains that are in excess of unity over wide frequency bandwidths. These advantages are clearly decipherable when the condition of modal overlap is reasonably satisfied. Figures 5(b), 6(b), 7(b), and 8(b), which display the actual overall gain $\Gamma_{o1}(\omega)$ in the format of Fig. 4(c), conform and thus support, the discussion advanced with respect to Figs. 3(c) and 4(c). In particular, the efficient gains with wider frequency bandwidths in the likes of Figs. 4(b), 5(a), 6(a), 7(a), and 8(a), again, all but evaporate in the overall gains $\Gamma_{o1}(\omega)$ that are exhibited in Figs. 4(c), 5(b), 6(b), 7(b), and 8(b), respectively.

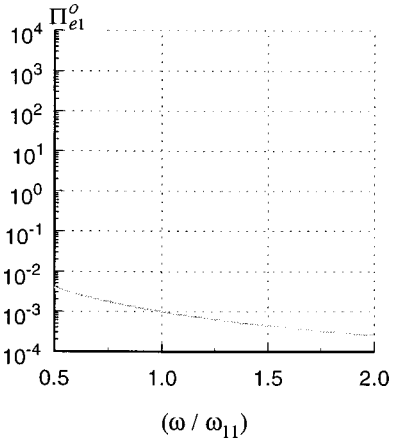

FIG. 9. As in Fig. 2 except that the isolated master harmonic oscillator is subjected to an external velocity drive instead of an external force drive.

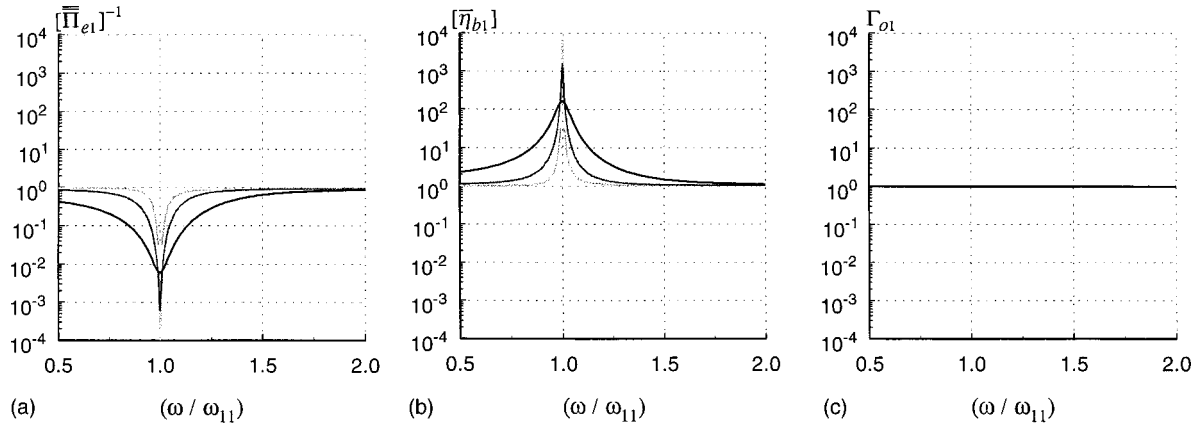

FIG. 10. As in Fig. 4 except that the master harmonic oscillator is subjected to an external velocity drive instead of an external force drive.

III. COMPUTATIONS AND DISPLAYS OF THE GAIN FACTORS IN THE RESPONSE OF A MASTER HO SUBJECTED TO AN EXTERNAL VELOCITY DRIVE

Figures 2–4 depict the energetic characteristics of a standard isolated master HO and a standard master HO that is coupled to a set of a single and nine satellite HOs, respectively. In these figures, the master HO is excited by an external *force* drive, as described in Eqs. (8)–(10). In this section Figs. 2–4 are repeated in Figs. 9–11, respectively, except that the external *force* drive is replaced by an external *velocity* drive. This replacement is accounted for in the description of the external input power quantities $\bar{\Pi}^o_{e1}(\omega)$ and $[\bar{\bar{\Pi}}_{e1}(\omega)]^{-1}$. For the external velocity drive the quantities are stated in Eqs. (17a) and (17c), respectively. In this replacement, however, the loss factor gain $[\bar{\eta}_{b1}(\omega)]$, stated in Eq. (18), remains unchanged. The computations under this replacement result in displays that replace Fig. 2 with Fig. 9, Fig. 3(a)–(c) with Fig. 10(a)–(c) and Fig. 4(a)–(c) with Fig. 11(a)–(c).

The purpose for the investigations in this section is to decipher whether the overall gain in the case of an external *velocity* drive may be more or less dominantly governed by the loss factor gain than in the case of an external *force* drive. The normalized external input power $\bar{\Pi}^o_{e1}(\omega)$ of the isolated master HO is shown in Fig. 9. From Eqs. (11) and (17a) one obtains

$$\bar{\Pi}^o_{e1}(\omega) = \mathrm{Re}\{Z^-_{11}(\omega)/(\omega M_1)\} = (\omega/\omega_{11})^2 \eta_{11}. \tag{21}$$

Thus $\bar{\Pi}^o_{e1}(\omega)$ is an asymptotically decreasing function of (ω/ω_{11}) if η_{11} is a weak function of (ω/ω_{11}). The standard value of η_{11} is fixed at 10^{-3}. For a coupled master HO that is excited by an external velocity drive, the external input power gain $[\bar{\bar{\Pi}}_{e1}(\omega)]^{-1}$ is given in Eq. (17c) and is shown in Fig. 10(a) for a single satellite HO and in Fig. 11(a) for a set of nine satellite HOs. It is observed from Figs. 9, 10(a), and 11(a) that even in this case of an external velocity drive the influence of the coupling, on the normalized external input powet, is profound. Although Figs. 10(a) and 11(a) do not closely resemble Figs. 3(a) and 4(a) respectively, the former figures are at least as intricate as are the latter. The loss factor gain $[\bar{\eta}_{b1}(\omega)]$, stated in Eq. (18) is computed and displayed in Fig. 10(b) for the single satellite HO and in Fig. 11(b) for the set of nine satellite HOs. Since the loss factor gain $[\bar{\eta}_{b1}(\omega)]$ remains unchanged, and in view of Eqs. (7) and (20), one finds that

$$[\bar{\eta}_{b1}(\omega)] = \Pi_{e1}(\omega), \tag{22}$$

which means that Figs. 10(b) and 11(b) are, respectively, the mirror images of Figs. 10(a) and 11(a) in the horizontal axis. It follows then that Figs. 10(b) and 11(b) are as intricate as Figs. 10(a) and 11(a), respectively. Again, were the external input power gain $[\bar{\bar{\Pi}}_{e1}(\omega)]^{-1}$ to be assumed equal to unity, the loss factor gain $[\bar{\eta}_{b1}(\omega)]$ becomes the overall gain

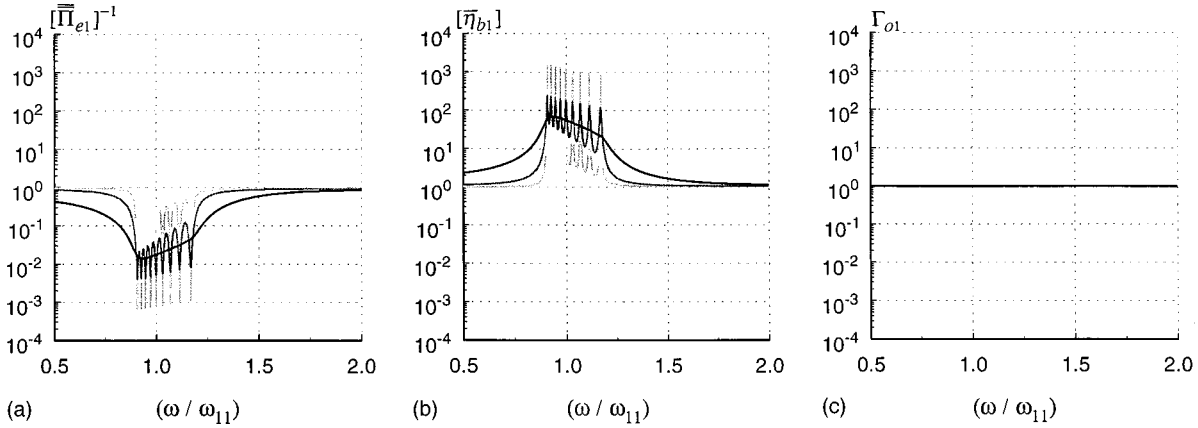

FIG. 11. As in Fig. 5 except that the master harmonic oscillator is subjected to an external velocity drive instead of an external force drive.

$\Pi_{o1}(\omega)$ of the coupled master HO. All the ramifications that such identities imply are included; e.g., with respect to the bandwidths over which beneficial noise control achievements may be extended. When the master HO is excited by an external velocity drive and the assumption that be external input power gain is equal to unity is retracted, the overall gain $\Gamma_{o1}(\omega)$ substantially simplifies. As Eq. (20) attests and Figs. 10(c) and 11(c) show, the overall gain becomes unity, which is vastly different from the loss factor gain $[\overline{\eta}_{b1}(\omega)]$ shown in Figs. 10(b) and 11(b), respectively; an overall gain of unity is a zero gain device.

IV. CONCLUSION AND REMARKS

Noise control benefits accrued by a simple master structure coupled to a single neutralizer, dynamic absorber, and structural fuzzy appear to be well understood.[10,12,13] The simple master structure is often simulated by a master HO and the single neutralizer, dynamic absorber, and structural fuzzy by a satellite HO. Noise control engineers, however, find irresistible the wider frequency bandwidths with little sacrifice in levels that are exhibited by the loss factor gain of a master HO when coupled to a multiplicity of satellite HOs; notwithstanding that the total mass of this elaborated set of satellite HOs is fixed to that of the single satellite HO. (This fixing is devised to dismiss consideration of weight *a priori*.) Often, therefore, noise control practitioners are persuaded to purport that the elaborated complexes, with still high levels, but wider frequency bandwidths in their loss factor gains, may achieve wide bands vibration (noise) control.[10,12,13] It is argued here, in terms of Figs. 4(c), 5(b), 7(b), and 9(b) that mother nature is not ready to be fooled by elaborations alone. Cavalier analytical pursuit to account for the noise control achievements of efficient wideband vibration neutralizers, dynamic absorbers, and structural fuzzies will not do. Accounting for these noise control devices require careful analytical consideration. Here, analytical consideration of this kind for mundane complexes is presented. Extensions to less mundane complexes may now be cautiously pursued.

APPENDIX: A REDUCED COMPLEX

There exists, in the literature, a number of papers in which the master structure is even simpler than a HO is; namely, the master structure is merely a mass.[1,8–10] Moreover, the satellite structure is also composed of a mere set of individual masses.[1,8–10] The couplings between the master structure and the satellite structure constitute unto the master structure sprung masses. This is constructed by assigning to each of the satellite masses a stiffness element. The satellite masses are not directly coupled to each other. This reduced complex, designated an A3 complex in Ref. 1, is sketched in Fig. A1 (cf. Fig. 1). To accommodate this model for the complex, the expressions for the impedances $Z_{11}^{-}(\omega)$ and $Z_1(\omega)$ require adaptation. In this vein it is recognized that Eqs. (11a) and (12a) remain valid, but the elements in these equations assume reduced forms

$$Z_{11}^{-}(\omega)=(i\omega M_1), \quad \omega_{11}^2=(\omega_{1(N+2)/2})^2[M_1/M_{(N+2)/2}], \tag{A1}$$

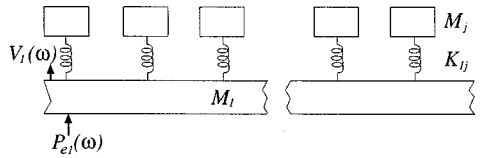

FIG. A1. The master harmonic oscillator is replaced, in Fig. 1(b), by a mere master mass.

$$Z_{jj}^{-}(\omega)=(i\omega M_j), \quad (\omega_{jj})^2=0;$$
$$Z_{1j}(\omega)=(K_{1j}/i\omega)=Z_{j1}(\omega); \tag{A2}$$
$$K_{1j}=K_{o1j}(1+\eta_{1j}), \quad (\omega_{1j})^2=(K_{o1j}/M_j), \quad j\geqslant 2$$

[cf. Eqs. (11b) and (12b)]. Assuming that the master mass is subject to an external force drive, the normalized external input power $\overline{\Pi}_{e1}^{o}(\omega)$ received by the isolated master mass is as stated in Eq. (16a). Substituting Eq. (A1) in Eq. (16a), a difficulty arises in the evaluation of $\overline{\Pi}_{e1}^{o}(\omega)$ since a mere mass is usually expressed in terms of a purely imaginary quantity. In this usual setting

$$\mathrm{Re}\{Z_{11}^{-}(\omega)\}\rightarrow 0. \tag{A3}$$

The corresponding external input power gain $[\bar{\bar{\Pi}}_{e1}(\omega)]^{-1}$ is as stated in Eq. (16c). Noting that the attachment of a sprung mass or sprung masses to the master mass enables the resulting A3 complex to accept external input power; as measured by $\overline{\Pi}_{el}(\omega)$ expressed in Eq. (16b), by providing resonant constituents to the A3 complex. One may then conclude that $[\bar{\bar{\Pi}}_{e1}(\omega)]^{-1}$ exhibits a highly deficient gain; in fact,

$$[\bar{\bar{\Pi}}_{e1}(\omega)]^{-1}=[\overline{\Pi}_{e1}^{o}(\omega)/\overline{\Pi}_{e1}(\omega)]\rightarrow 0, \tag{A4}$$

at least in the frequency band that spans the resonance frequencies of the sprung masses [cf. Eq. (A3)]. The corresponding loss factor gain $[\overline{\eta}_{b1}(\omega)]$ is as stated in Eq. (18). Substituting Eqs. (A1) and (A2) in Eq. (18) one finds that this quantity is singular for the same reasons and substantially in the same frequency band that the external input power gain is negligible. Indeed, as deduced from Eqs. (A1), (A2), and (19), even in this extreme example the overall gain is properly defined and is meaningful.[1,8–10] The danger of assuming that the external input power remains unchanged, by the couplings, is made amply transparent in this example. Setting the external input power gain $[\bar{\bar{\Pi}}_{e1}(\omega)]^{-1}$ to unity would imply a singular overall gain, which is physically unacceptable. The importance of appropriately evaluating the external input power gain could not be emphasized more strongly than by this example. In closure, the computations of the overall gain $\Gamma_{o1}(\omega)$, for the complex sketched in Fig. A1, are displayed in Fig. A2(a)–(d). In Fig. A2(a) the satellite is a single mass; in Fig. A2(b) the satellite is a set of 9 masses; in Fig. A2(c) the satellite is a set of 21 masses; and in Fig. A2(d) the satellite is a set of 9 masses, but with a (Δ) that is twice the value in Fig. A2(b) (cf. Figs. 3, 4, and 5, respectively). The total mass of the satellite structure is fixed, as in the text, to one-tenth of the mass of the master structure in the complex and the resonance frequencies of the satellite masses, when the master mass is blocked, are chosen to be distributed about the frequency (ω_{11}).[8,10] That center fre-

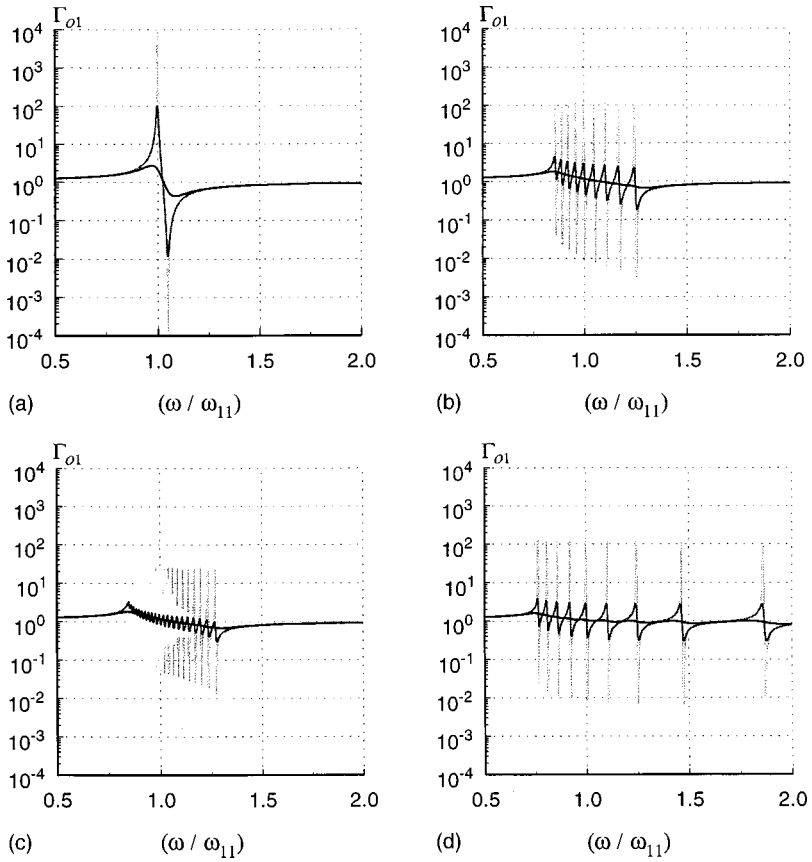

FIG. A2. The overall gain $\Gamma_{o1}(\omega)$, as a function of the normalized frequency (ω/ω_{11}), for a master mass coupled to a set of sprung masses. (a) A single sprung mass (cf. Fig. 3). (b) A set of nine sprung masses (cf. Figs. 4 and 5). (c) The set of 21 sprung masses (cf. Fig. 6). (d) As in (b) except that (Δ) is doubled (cf. Fig. 7).

quency (ω_{11}) is defined in Eq. (A1). The overall gain $\Gamma_{o1}(\omega)$ in Fig. A2 clearly show undulations in curves pertaining to the lower loss factors. Undulations of the kind exhibited in Fig. A2 can hardly be relied upon to yield an efficient overall gain over a wide frequency band; notwithstanding that, when the loss factor (η_{1j}) is higher, so that the conditions of modal overlap is satisfied, the overall gain $\Gamma_{o1}(\omega)$ assumes a sort of mean-value that lies on a neutral curve that is substantially unity.[16]

[1] G. Maidanik and K. J. Becker, ''Various loss factors of a master harmonic oscillator that is coupled to a number of satellite harmonic oscillators,'' J. Acoust. Soc. Am. **103**, 3184–3195 (1998).

[2] G. Maidanik and J. Dickey, ''Design criteria for the damping effectiveness of structural fuzzies,'' J. Acoust. Soc. Am. **100**, 2029–2033 (1996).

[3] G. Maidanik and J. Dickey, ''On the external input power into coupled structures,'' Proceedings of the Symposium on Statistical Energy Analysis, IUTAM, Southampton, England (1997).

[4] C. Soize, ''Probabilistic structural modeling in linear dynamic analysis of complex mechanical systems,'' Rech. Aerosp. **1986-3**, 23–48 (1986); C. Soize, ''A model and numerical method in the medium frequency range for vibroacoustic predictions using the theory of structural fuzzy,'' J. Acoust. Soc. Am. **94**, 849–865 (1993).

[5] A. D. Pierce, V. W. Sparrow, and D. A. Russell, ''Fundamental structural acoustics idealizations for structures with fuzzy internals,'' Am. Soc. Mech. Eng. J. Vib. Acoust. **117**, 1–10 (1995).

[6] M. Strasberg, ''Continuous structures as 'fuzzy' substructures,'' J. Acoust. Soc. Am. **100**, 3456–3459 (1996).

[7] R. H. Lyon, ''Statistical energy analysis and structural fuzzy,'' J. Acoust. Soc. Am. **97**, 2878–2881 (1995).

[8] G. Maidanik, ''Power dissipation in a sprung mass attached to a master structure,'' J. Acoust. Soc. Am. **98**, 3527–3533 (1995).

[9] M. Strasberg and D. Feit, ''Vibration damping of large structures induced by attached small resonant structures,'' J. Acoust. Soc. Am. **99**, 335–344 (1996).

[10] M. J. Brennan, ''Characteristics of a wideband vibration neutralizer,'' Noise Control Eng. J. **45**, 201–207 (1997).

[11] D. M. Morse, *Vibration and Sound*, 2nd ed. (McGraw-Hill, New York, 1948).

[12] R. H. Lyon, *Statistical Energy Analysis of Dynamic Systems: Theory and Applications* (MIT, Cambridge, 1975).

[13] R. H. Lyon and R. G. Dejung, *Theory and Application of Statistical and Energy Analysis* (Butterworth-Heinemann, Boston, 1995), 2nd ed.

[14] S. H. Crandall and R. Lotz, ''On the coupling loss factor in statistical energy analysis,'' J. Acoust. Soc. Am. **49**, 352–356 (1971).

[15] G. Maidanik, ''Response of coupled dynamic systems,'' J. Sound Vib. **46**, 561–583 (1976).

[16] E. Skudrzyk, ''The mean-value method of predicting the dynamic response of complex vibrators,'' J. Acoust. Soc. Am. **67**, 1105–1135 (1980).

Guided waves in layered cubic media: Convergence study of a polynomial expansion approach

Vito Lancellotti and Renato Orta[a)]
Dipartimento di Elettronica, Politecnico di Torino, C.so Duca degli Abruzzi 24, 10129 Torino, Italy

(Received 5 November 1997; accepted for publication 6 July 1998)

A new numerical method to compute propagation constants and mode functions of a planar layered acoustic waveguide is described. The basic feature is the expansion of velocity and stress fields in each layer on different Legendre polynomial bases, which ensures an exponential convergence rate of the method. No transcendental equation has to be solved and also modes that have very close propagation constants (e.g., coupled Rayleigh waves) are computed with great accuracy. Convergence of the method is studied and a way to estimate and control the error on the solutions is discussed. © *1998 Acoustical Society of America.* [S0001-4966(98)03710-2]

PACS numbers: 43.20.Mv, 43.20.Ks, 43.35.Pt [DEC]

INTRODUCTION AND MOTIVATION

Multilayered media support the propagation of various types of elastic waves and the determination of the field functions and propagation constants is a classical problem. The eigenmodes can be utilized to express the relevant Green's function, which is necessary to formulate scattering and junction problems by the integral equation technique.[1,2]

Planar stratified media are typically analyzed along the direction normal to the interfaces: the T-matrix,[3,4] the propagator matrix,[5] coupled transmission lines and lumped circuits[6] are commonly employed in describing the layers. The propagation constants of guided modes can then be found by imposing the transverse resonance condition and solving the resulting transcendental dispersion equation. Though complex-function theory can be invoked, automated search for the roots is however a hard task and some of them may be missed.

To overcome these drawbacks we propose a numerical method that allows to compute mode functions and propagation constants without solving any transcendental equation. The basic concept is the expansion of the unknowns on a set of functions. The differential problem turns into an algebraic eigenvalue one, where the eigenvalues are the propagation constants; the field configurations are readily obtained as linear combinations of the expansion functions, weights of which are the eigenvector elements. In principle, an entire domain basis might be chosen (see, for example, Refs. 7, 8, where Laguerre polynomials were used to investigate acoustic surface waves in semi-infinite layered media), but this would cause a slow (power-law) convergence, owing to the fact that $\underline{v}$ and $\underline{\underline{T}}$ are infinitely differentiable everywhere in space but at an interface. Hence, separate bases in each layer are required to ensure a correct modeling of the discontinuities. An exponential convergence ensues adopting Legendre polynomials as expansion functions; a similar technique was employed in Ref. 9 to study optical gratings comprising isotropic dielectric layers.

The convergence properties of the method have been studied and, by means of extensive numerical experiments, we have developed a criterion to relate the eigenvalue relative error to the number of polynomials used in representing the fields in each layer.

I. FORMULATION

An acoustic planar waveguide, comprising N isotropic or cubic media, is sketched in Fig. 1; we assume that the crystal principal axes coincide with the structure ones. Clamped, stress-free and phase-shift boundaries are considered, but also more general boundary conditions can be taken into account by the present method. The ith layer has thickness h_i and is characterized by the stiffness constants c_{11}^i, c_{44}^i, c_{12}^i and density ρ^i. For computational purposes, that will be explained in the section of convergence analysis, these quantities are intended as relative to convenient reference stiffness c_a and density ρ_a, which may be interpreted as the relevant physical constants of an ideal fluid. The wave number $k_a=\omega(\rho_a/c_a)^{1/2}$ and acoustic impedance $Z_a=(\rho_a c_a)^{1/2}$ are also introduced.

We are concerned with y-independent solutions of the velocity wave equation that in this case splits into two distinct differential problems involving v_2 (*shear horizontal* waves) and the pair v_1, v_3 (*pressural-shear vertical* waves). These equations must be supplemented with continuity conditions at the internal interfaces and boundary conditions at the terminal ones for v_l^i, $l=1,2,3$, and T_L^i, $L=1,5,6$ (the abbreviated subscripts notation is used).

We solve the resulting differential eigenvalue problems by the Lanczos method,[10] i.e., by representing the unknowns in a set of Legendre polynomials $\{P_m(\xi)\}_{m=0}^{M_i}$ defined in each layer, $\xi\in[-1,1]$ being a normalized variable:

$$\xi=\alpha_i x-(x_{i+1}+x_i)/h_i, \quad \alpha_i=2/h_i. \tag{1}$$

Hence $v_l^i(\xi)$, the first and second derivatives of $v_l^i(\xi)$ and $T_L^i(\xi)$ are written as

$$v_l^i=\sum_{m=0}^{M_i} p_{m,l}^i P_m(\xi), \quad \partial_\xi v_l^i=\sum_{m=0}^{M_i-1} a_{m,l}^i P_m(\xi), \tag{2}$$

a)Electronic mail: orta@polito.it

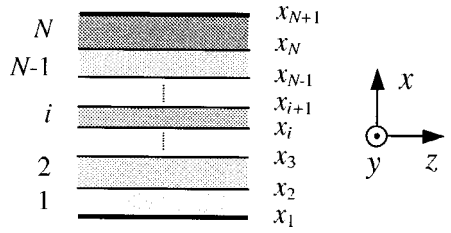

FIG. 1. Geometry and coordinate system.

$$\partial_\xi^2 v_l^i = \sum_{m=0}^{M_i-2} b_{m,l}^i P_m(\xi), \quad T_L^i = \sum_{m=0}^{M_i} q_{m,L}^i P_m(\xi), \tag{3}$$

with $a_{m,l}^i$ and $b_{m,l}^i$ related to $p_{m,l}^i$ by[10]

$$a_{m,l}^i = (2m+1) \sum_{n=m+1,m+3}^{M_i} p_{n,l}^i, \tag{4}$$

$$b_{m,l}^i = \left(m+\frac{1}{2}\right) \sum_{n=m+2,m+4}^{M_i} (n+m+1)(n-m) p_{n,l}^i, \tag{5}$$

or more succinctly $\underline{a}_l^i = \underline{\underline{A}}^i \underline{p}_l^i$ and $\underline{b}_l^i = \underline{\underline{B}}^i \underline{p}_l^i$, where $\underline{p}_l^i = [p_{0,l}^i \cdots p_{M_i,l}^i]^T$ and $\underline{\underline{A}}^i$ and $\underline{\underline{B}}^i$ have size $M_i \times (M_i+1)$ and $(M_i-1)\times(M_i+1)$, respectively.

A. Shear horizontal (*SH*) modes

The relevant differential equation, holding in each layer i, takes the simple form:

$$(\partial_x^2/k_a^2 + \rho^i/c_{44}^i) v_2^i = \beta_n^2 v_2^i, \tag{6}$$

while the related stress tensor elements are

$$T_4^i = -\beta_n c_{44}^i Z_a v_2^i, \quad T_6^i = -jc_{44}^i Z_a \partial_x v_2^i / k_a. \tag{7}$$

The eigenvalue β_n is the propagation constant normalized to k_a. Now the first of Eqs. (2)–(3) with $l=2$ are substituted into Eqs. (6) and then inner products on the bases $\{P_m(\xi)\}_{m=0}^{M_i-2}$ are taken, in order to reduce the differential problem to a linear homogeneous algebraic system consisting of $\Sigma_{i=1}^N (M_i-1)$ equations in $\Sigma_{i=1}^N (M_i+1)$ unknowns. After partitioning $\underline{\underline{B}}^i$ in the form $[\underline{\underline{B}}_1^i \ \underline{\underline{B}}_2^i]$, where $\underline{\underline{B}}_2^i$ contains the last two columns, the contribution of the ith layer to the complete system of equations can be written

$$\alpha_i^2 (\underline{\underline{B}}_1^i \underline{p}'^i_2 + \underline{\underline{B}}_2^i \underline{\tilde{p}}^i_2)/k_a^2 + \rho^i \underline{p}'^i_2 / c_{44}^i = \beta_n^2 \underline{p}'^i_2, \tag{8}$$

with $\underline{p}'^i_2 = [p_{0,2}^i \cdots p_{M_i-2,2}^i]^T$ and $\underline{\tilde{p}}^i_2 = [p_{M_i-1,2}^i \ p_{M_i,2}^i]^T$. Then Eqs. (8) can be arranged in a compact form:

$$\underline{\underline{W}} \underline{\Psi}' + \underline{\underline{Z}} \underline{\tilde{\Psi}} + \underline{\underline{K}} \underline{\Psi}' = \beta_n^2 \underline{\Psi}', \tag{9}$$

where $\underline{\underline{W}}$, $\underline{\underline{Z}}$, and $\underline{\underline{K}}$ are block diagonal matrices with elements $\alpha_i^2 \underline{\underline{B}}_1^i / k_a^2$, $\alpha_i^2 \underline{\underline{B}}_2^i / k_a^2$, and $\rho^i \underline{\underline{I}}^i / c_{44}^i$, respectively, with $\underline{\underline{I}}^i$ the identity matrix of size $M_i - 1$, and $\underline{\tilde{\Psi}} = [\underline{\tilde{p}}^1_2 \cdots \underline{\tilde{p}}^N_2]^T$, $\underline{\Psi}' = [\underline{p}'^1_2 \cdots \underline{p}'^N_2]^T$.

The boundary conditions and continuity at interfaces provide $2N$ equations that are utilized to express $p_{M_i-1,2}^i$ and $p_{M_i,2}^i$ in terms of the other coefficients, so they can be eliminated from Eqs. (8). More precisely, $N-1$ constraints result from the continuity of v_2^i at the interfaces of coordinates x_{i+1}, $i=1,...,N-1$, and are directly stated as

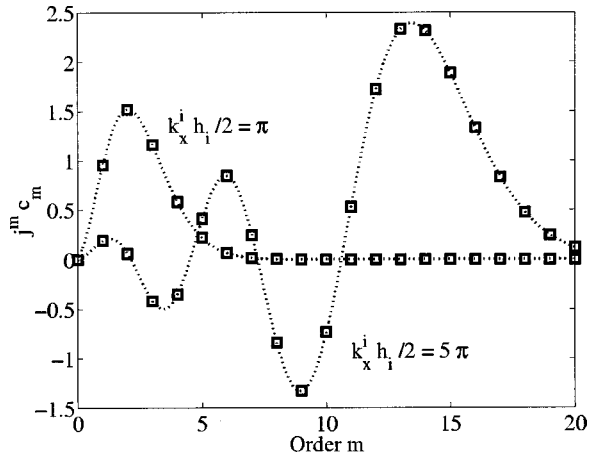

FIG. 2. Expansion coefficients of complex exponentials on a Legendre basis, see Eqs. (30); □ indicate integer m values.

$$\sum_{m=0}^{M_i} p_{m,2}^i = \sum_{m=0}^{M_{i+1}} (-1)^m p_{m,2}^{i+1}, \tag{10}$$

while further $N-1$ relationships enforce the continuity of T_6^i [see Eqs. (7)]:

$$\frac{\alpha_i}{k_a} c_{44}^i \sum_{m=0}^{M_i} \frac{m(m+1)}{2} p_{m,2}^i = \frac{\alpha_{i+1}}{k_a} c_{44}^{i+1} \sum_{m=0}^{M_{i+1}} (-1)^{m+1} \frac{m(m+1)}{2} p_{m,2}^{i+1}. \tag{11}$$

Finally, the boundary conditions at x_1, x_{N+1} give rise to the last two equations, which have the same structure as Eqs. (10)–(11). In writing them, account has been taken of the values of Legendre polynomials and their first derivatives at the ends of the orthogonality interval:

$$P_m(\pm 1) = (\pm 1)^m, \quad \left.\frac{dP_m}{d\xi}\right|_{\pm 1} = (\pm 1)^{m+1} \frac{m(m+1)}{2}. \tag{12}$$

Equations (10)–(11) can be collected in the form

$$\underline{\underline{Q}} \underline{\tilde{\Psi}} = -\underline{\underline{R}} \underline{\Psi}', \tag{13}$$

where $\underline{\underline{Q}}$ and $\underline{\underline{R}}$ have size $2N \times 2N$ and $2N \times \Sigma_{i=1}^N (M_i-1)$, respectively. At last $\underline{\tilde{\Psi}}$ is eliminated from Eq. (9) by means of Eq. (13):

$$(\underline{\underline{W}} - \underline{\underline{Z}} \underline{\underline{Q}}^{-1} \underline{\underline{R}} + \underline{\underline{K}}) \underline{\Psi}' = \beta_n^2 \underline{\Psi}'. \tag{14}$$

The original problem has been reduced to finding eigenvalues and eigenvectors of a matrix with size $\Sigma_{i=1}^N (M_i-1)$.

The expansion coefficients of T_4^i and T_6^i are easily related to the velocity ones by

$$\underline{q}_4^i = -\beta_n c_{44}^i Z_a \underline{p}_2^i, \quad \underline{q}_6^i = -jc_{44}^i Z_a \alpha_i \underline{\underline{\tilde{A}}}^i \underline{p}_2^i / k_a, \tag{15}$$

where $\underline{\underline{\tilde{A}}}^i$ is obtained from $\underline{\underline{A}}^i$ adding an M_i+1th null row.

B. Pressural-shear vertical (*PSV*) modes

The differential equation for the modal field in this case is

$$(\mathscr{L}^i_0 - j\beta_n \mathscr{L}^i_1 - \beta_n^2 \mathscr{L}^i_2)\phi^i(x) = 0, \tag{16}$$

where $\phi^i(x) = [v^i_1 \; v^i_3]^T$ and $\mathscr{L}^i_r$ are dimensionless 2×2 matrix differential operators, whose nonnull elements are

$$\mathscr{L}^i_{0,11} = c^i_{11}\partial_x^2/k_a^2 + \rho^i, \quad \mathscr{L}^i_{0,22} = c^i_{44}\partial_x^2/k_a^2 + \rho^i, \tag{17}$$

$$\mathscr{L}^i_{1,12} = \mathscr{L}^i_{1,21} = (c^i_{12} + c^i_{44})\partial_x/k_a, \tag{18}$$

$$\mathscr{L}^i_{2,11} = c^i_{44}, \quad \mathscr{L}^i_{2,22} = c^i_{11}, \tag{19}$$

and the stress tensor components follow from:

$$\begin{bmatrix} T^i_1 \\ T^i_2 \\ T^i_3 \\ T^i_5 \end{bmatrix} = -Z_a \begin{bmatrix} jc^i_{11}\partial_x/k_a & \beta_n c^i_{12} \\ jc^i_{12}\partial_x/k_a & \beta_n c^i_{12} \\ jc^i_{12}\partial_x/k_a & \beta_n c^i_{11} \\ \beta_n c^i_{44} & jc^i_{44}\partial_x/k_a \end{bmatrix} \phi^i(x). \tag{20}$$

After substituting Eqs. (2) and the first of Eqs. (3) with $l = 1,3$ into Eqs. (16) and taking inner products on the bases $\{P_m(\xi)\}_{m=0}^{M_i-2}$, the differential problem turns into a linear homogeneous algebraic system consisting of $2\Sigma_{i=1}^N (M_i - 1)$ equations in $2\Sigma_{i=1}^N (M_i + 1)$ unknowns. The contribution of the ith layer can be given the form:

$$(c^i_{11}\alpha_i^2 \underline{\underline{B}}^i/k_a^2 + \rho^i \underline{\underline{G}}^i)\underline{p}^i_1 - j\beta_n (c^i_{12} + c^i_{44})\alpha_i \underline{\underline{A}}^i \underline{p}^i_3/k_a - \beta_n^2 c^i_{44}\underline{\underline{G}}^i \underline{p}^i_1 = 0, \tag{21}$$

$$(c^i_{44}\alpha_i^2 \underline{\underline{B}}^i/k_a^2 + \rho^i \underline{\underline{G}}^i)\underline{p}^i_3 - j\beta_n (c^i_{12} + c^i_{44})\alpha_i \underline{\underline{A}}^i \underline{p}^i_1/k_a - \beta_n^2 c^i_{11}\underline{\underline{G}}^i \underline{p}^i_3 = 0, \tag{22}$$

where $\underline{\underline{G}}^i = [\underline{\underline{I}}^i \; 0 \; 0]$.

In this case the continuity and the boundary conditions for v^i_1, v^i_3, T^i_1, and T^i_5 provide $4N$ constraints. However, the elimination scheme applied previously in the *SH* case is not convenient, because it would lead to a nonpolynomial eigenvalue problem. Therefore the above mentioned $4N$ equations are simply added to those deriving from the differential system. If all the relevant equations are gathered and the unknowns are arranged in the column vector $\underline{\Phi} = [\underline{p}^1_1 \cdots \underline{p}^N_1 \; \underline{p}^1_3 \cdots \underline{p}^N_3]^T$, a quadratic eigenvalue problem is obtained:

$$(\underline{\underline{L}}_0 - j\beta_n \underline{\underline{L}}_1 - \beta_n^2 \underline{\underline{L}}_2)\underline{\Phi} = 0. \tag{23}$$

$\underline{\underline{L}}_0$ is always nonsingular, while $\underline{\underline{L}}_1$ and $\underline{\underline{L}}_2$ are rank deficient due to the fact that boundary and continuity conditions do not involve β_n^2 in general and β_n in some cases. As a consequence, some eigenvalues may be infinite[11] and, of course, do not correspond to any physical solution. On the other hand, as the waveguide has reflection symmetry, if β_n is a complex eigenvalue, in the case of lossless media, then $-\beta_n$, β_n^* and $-\beta_n^*$ solve (23) too.

Equation (23) can be solved by introducing the auxiliary unknown $\underline{\Theta} = -j\beta_n \underline{\underline{L}}_2 \underline{\Phi}$ and getting an equivalent system:

$$\begin{bmatrix} -\underline{\underline{L}}_1 & -\underline{\underline{I}} \\ \underline{\underline{L}}_2 & \underline{\underline{0}} \end{bmatrix} \begin{bmatrix} \underline{\Phi} \\ \underline{\Theta} \end{bmatrix} = \frac{j}{\beta_n} \begin{bmatrix} \underline{\underline{L}}_0 & \underline{\underline{0}} \\ \underline{\underline{0}} & \underline{\underline{I}} \end{bmatrix} \begin{bmatrix} \underline{\Phi} \\ \underline{\Theta} \end{bmatrix}, \tag{24}$$

whose form, under the assumption that β_n never vanishes, allows to handle infinite eigenvalues, since $1/\beta_n$ approaches zero in that case and can thus be detected and neglected.

Finally, the stress expansion coefficients in each layer derive from Eq. (20) after using Eqs. (2) and the second of Eqs. (3):

$$\underline{q}^i_1 = -Z_a(jc^i_{11}\alpha_i \underline{\underline{\tilde{A}}}^i \underline{p}^i_1/k_a + \beta_n c^i_{12}\underline{p}^i_3), \tag{25}$$

$$\underline{q}^i_2 = -Z_a(jc^i_{12}\alpha_i \underline{\underline{\tilde{A}}}^i \underline{p}^i_1/k_a + \beta_n c^i_{12}\underline{p}^i_3), \tag{26}$$

$$\underline{q}^i_3 = -Z_a(jc^i_{11}\alpha_i \underline{\underline{\tilde{A}}}^i \underline{p}^i_1/k_a + \beta_n c^i_{11}\underline{p}^i_3), \tag{27}$$

$$\underline{q}^i_5 = -Z_a(\beta_n c^i_{44}\underline{p}^i_1 + jc^i_{44}\alpha_i \underline{\underline{\tilde{A}}}^i \underline{p}^i_3/k_a). \tag{28}$$

II. CONVERGENCE ANALYSIS

When computing the modes of a layered waveguide by the method described above, a part of the eigenvalues are approximations (with varying accuracy) of the true propagation constants, while the others are so far away that they are to be discarded. Besides, the propagation constant of a certain eigenmode becomes more and more closely approximated by an eigenvalue as soon as the number of polynomials exceeds a threshold value, which in turn increases with the mode order. Hence, it is important in practice to derive the relationship between the accuracy of each eigenvalue and the number of polynomials used in the analysis.

On the basis of extensive numerical experiments, we have observed that the accuracy of an eigenvalue is uniquely related to the accuracy with which combinations (2)–(3) approximate the corresponding mode eigenfunction. It is well known that in the ith layer a mode eigenfunction consists of a suitable superposition of either two (*SH* case) or four (*PSV* case) exponentials that can be written as $\exp(-jk^i_x h_i \xi/2)$, in terms of the normalized variable introduced in (1), where k^i_x depends on β_n. Therefore, it is useful to expand a complex exponential on a Legendre basis:

$$\exp(-jk^i_x h_i \xi/2) = \sum_{m=0}^{\infty} c_m P_m(\xi), \tag{29}$$

where

$$c_m = (-j)^m (2m+1)\sqrt{\pi/(k^i_x h_i)}\, J_{m+1/2}(k^i_x h_i/2). \tag{30}$$

Figure 2 shows a plot of $j^m c_m$ for two different values of $k^i_x h_i/2$. For clarity of representation, the integer variable m has been extended to real values. The coefficients reach a maximum depending on the value of $k^i_x h_i$, after which they decrease exponentially, owing to the properties of Bessel functions of fixed argument and varying order. In particular, the decay has already started when the order of the Bessel function $m + 1/2$ equals the argument. We can conclude that the mode function expansion coefficients show the same behavior and in the case of an eigenfunction that has P complete oscillations over the thickness h_i, the onset of convergence corresponds to $M_i \simeq P\pi$. To determine the relationship between the eigenvalue accuracy and the number of polynomials to be used, we studied the simple problem of an isotropic plate with stress-free boundary conditions by the present method. In Fig. 3 the logarithm of the relative error ϵ

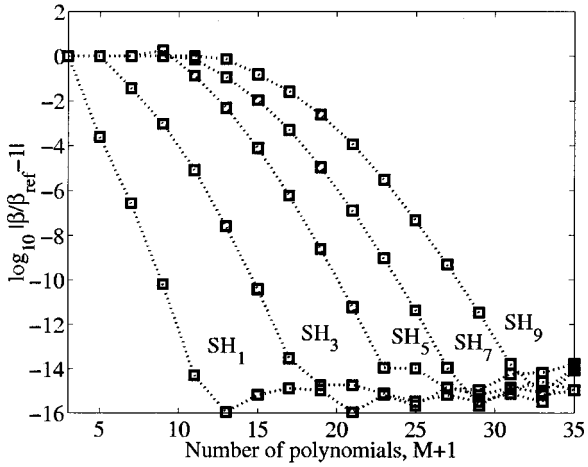

FIG. 3. Eigenvalue relative error versus the number of polynomials for a plate with stress-free walls, $h=0.1$ mm, $c_{44}=3.12\times10^{10}$ N/m^2, $\rho=2200$ kg/m^3, $f=100$ MHz.

of the propagation constant is reported for some *SH* modes versus the number of polynomials $M+1$. Since after a threshold typical of each mode the curves approach a straight line, an exponential decay of the eigenvalue relative error with $M+1$ ensues. In order to produce a normalized curve, the number of polynomials $M+1$ has been specified indirectly by the logarithm r of the ratio of the largest element of the eigenvector to the last one. All the curves in Fig. 3 collapse into a straight line (see Fig. 4), limited in the lower part of the graph by double precision arithmetic. We have numerically experimented that the eigenvalue relative error can be described by a single curve only if $k_a\Sigma_{i=1}^{N}h_i\leqslant 0.1$, which can be achieved by a convenient choice of the normalizing constants c_a and ρ_a. If this condition were not satisfied, the plot of Fig. 4 would contain many lines (one for each mode) not perfectly overlapped, but slightly dispersed.

The universal character of the plot of Fig. 4 has then been verified by analyzing several layered structures, with various types of boundary conditions. In each layer i a number M_i+1 of Legendre polynomials has been introduced and

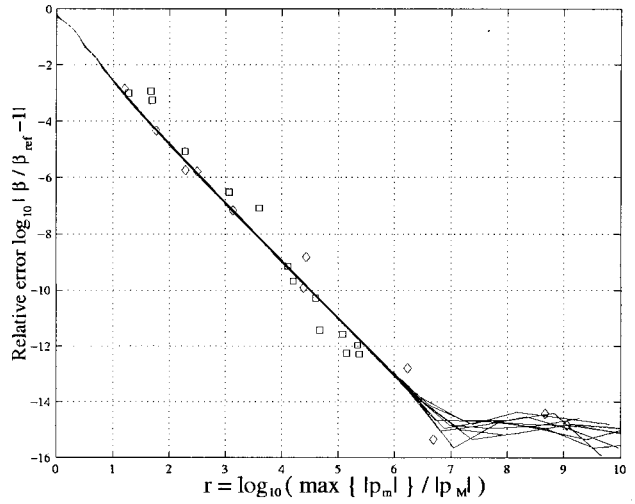

FIG. 4. Universal error plot (solid line) and actual data points: □, *PSV* modes; ◇, *SH* modes.

TABLE I. Parameters of the waveguide under study.

Medium	c_{11} (10^{10} N m^{-2})	c_{44} (10^{10} N m^{-2})	ρ (kg m^{-3})	h (mm)
1 and 3	6.13	2.18	3879	0.4
2	5.82	1.81	2243	0.2

a number of eigenvalues both of *SH* and *PSV* kind has been computed, as well as their relative error. The reference values were calculated by the transverse resonance technique after describing each layer by a scattering matrix. Then the corresponding eigenvector has been examined and the ratios $r_{i,l}=\log_{10}(\max|p^i_{m,l}|/|p^i_{M_i,l}|)$ have been determined. Finally, the smallest one has been used to enter a data point (□, *PSV* modes and ◇, *SH* modes) in the plot of Fig. 4. Since the points corresponding to different frequencies, modes and structures fall almost on this curve, its universal character is confirmed. It is to be remarked that this behavior applies to all modes, i.e., even if the propagation constants are imaginary or complex and is maintained also when lossy media are present.

For an efficient application of this algorithm, the number of polynomials in each layer has to be chosen conveniently, so that all the resulting $r_{i,l}$ turn out to be almost the same, as it is the smallest one that determines the eigenvalue accuracy. On the other hand, an optimal choice of M_i could be carried out provided that the transverse propagation constants k^i_x for *SH* and *PSV* polarizations were approximately known *a priori*. In practice one can estimate the form of the mode functions only for the strongly cutoff modes: in fact, in that case a mode function with P transverse complete oscillations, $P\gg1$, is fairly independent of the number and the type of layers and the quantities $z_i=k^i_x h_i/2$ are approximately given by $P\pi h_i/\Sigma_{i=1}^{N}h_i$. Once the z_i have been estimated, the $r_{i,l}$ can be computed and the number of polynomials in each layer M_i+1, needed to achieve a specified accuracy ϵ, can be derived by means of the plot in Fig. 4. For convenience, the function $M_i(\epsilon,z_i)$ has been obtained by numerical fitting in the form:

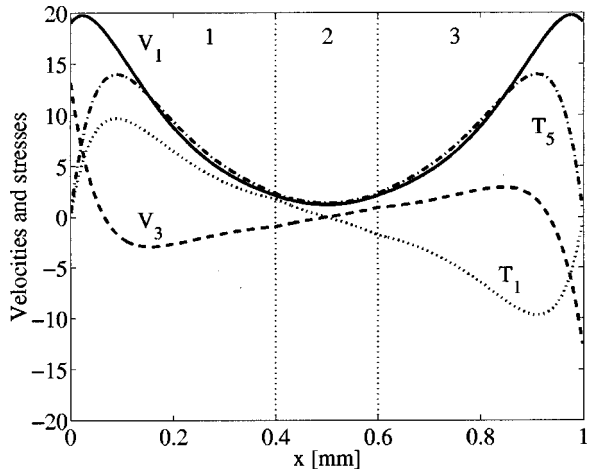

FIG. 5. Velocity [mm/s] and stress [10^4 N/m^2] profiles of the mode PSV_1 for a multilayered waveguide (see Table I); at the frequency 6.5 MHz the propagation constant is 18.828 409 5 mm^{-1}.

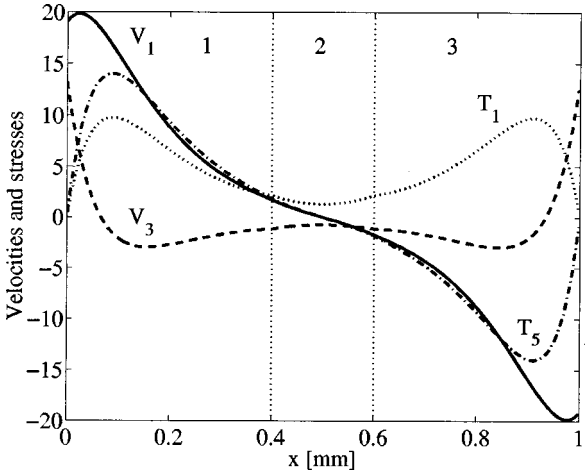

FIG. 6. Velocity [mm/s] and stress [10^4 N/m^2] profiles of the mode SH_1 for the same waveguide as in Fig. 5; at the frequency 6.5 MHz the propagation constant is 17.006 050 1 mm^{-1}.

$$M_i \approx 4.79\, z_i^{7/24} \sqrt{\left(\frac{\log\,\epsilon + 0.69}{14.52}\right)^2} + 1 + 0.96\, z_i - 1.14. \tag{31}$$

This expression turns out to be quite accurate in the range of interest of the parameters.

III. RESULTS AND DISCUSSIONS

As an example of application, the present method was used to determine the mode functions of an acoustic waveguide comprising three isotropic layers (see Table I) and with stress-free boundary conditions, at the frequency $f = 6.5$ MHz. By inspection of the field distributions, it is found that the two lowest order modes of this structure are symmetric and antisymmetric *surface acoustic waves* (SAWs), which result from coupling of two single Rayleigh waves propagating at each terminal interface (see Figs. 5 and 6). At this frequency the propagation constants, computed with a relative error of about 10^{-9} using 30 polynomials globally, are 18.828 409 5 and 18.822 390 5 mm^{-1}. Though these two values are very close, thus denoting a weak coupling between the Rayleigh waves, they are found without any difficulty. The next mode of the waveguide is *SH* polarized and is shown in Fig. 7: the propagation constant is 17.006 050 1 mm^{-1}, computed with a relative error of about 10^{-9} by means of 20 polynomials globally. Note that T_4 is discontinuous and T_6 has discontinuous first derivative. To confirm the ability of the method to determine even strongly cutoff modes, in Figs. 8–9 the field profile of the mode PSV_{12} is reported; the propagation constant is 0.926 877 $-j10.5879$ mm^{-1}, computed with a relative error of about 10^{-6}, still by means of 30 polynomials.

Dispersion curves can be easily obtained solving Eqs. (14) and (24) for different frequency values. It is to be noted that only some matrices depend on frequency and need to be recomputed. Figures 10 and 11 show the dispersion curves (real and imaginary parts or the propagation constants, respectively) for the five lowest order *PSV* modes in the waveguide under study. Mode labeling is made according to Auld.[12] As a well known consequence of the reflection symmetry of the waveguide with respect to the *xy* plane, modes

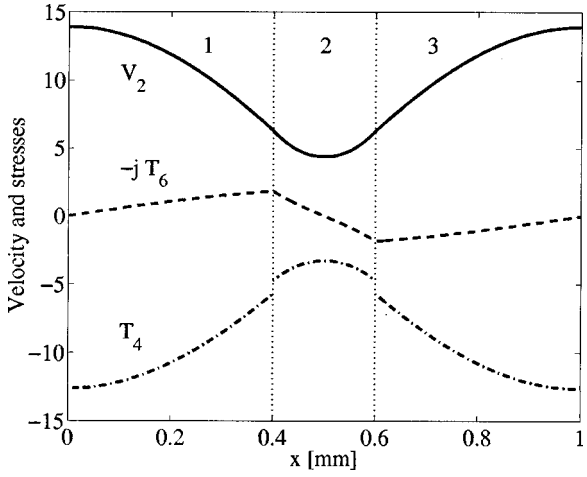

FIG. 7. Velocity [mm/s] and stress [10^4 N/m^2] profiles of the mode SH_1 for the same waveguide as in Fig. 5; at the frequency 6.5 MHz the propagation constant is 17.006 050 1 mm^{-1}.

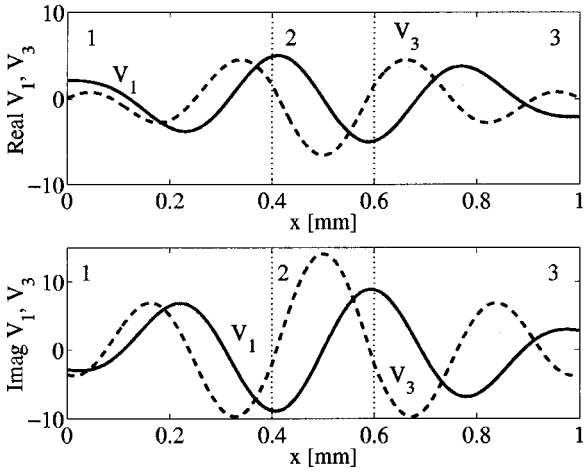

FIG. 8. Velocity [mm/s] profiles of the mode PSV_{12} for the same waveguide as in Fig. 5; at the frequency 6.5 MHz this mode has a complex propagation constant 0.926 877 $-j10.5879$ mm^{-1} and no active power flow is associated with it.

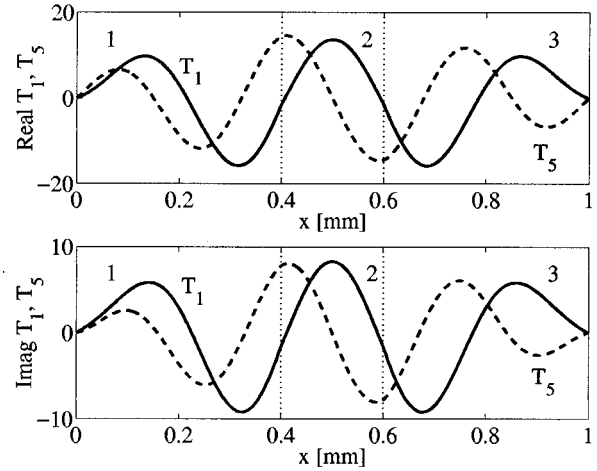

FIG. 9. Stress [10^4 N/m^2] profiles of the mode PSV_{12} (see caption of Fig. 8).

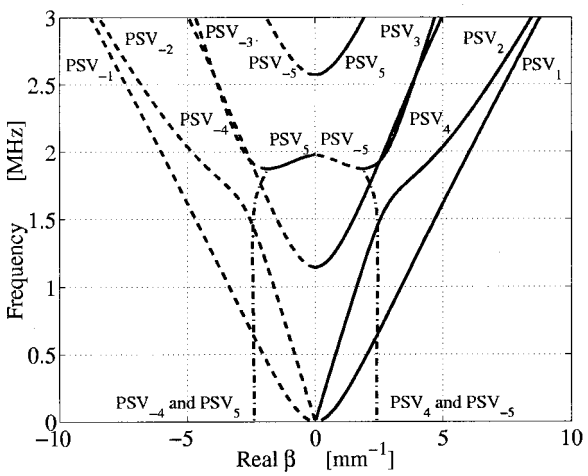

FIG. 10. Dispersion curves (f vs Real β) for the five lowest order *PSV* modes of the waveguide described in Table I. Positive (negative) indexes and solid (dashed) lines correspond to progressive (regressive) modes. The two dash–dotted branches are relative to four complex modes with propagation constants $\pm\beta$, $\pm\beta^*$.

come in pairs with opposite propagation constants. Progressive (regressive) modes, i.e., carrying energy or decaying in the $+z$ ($-z$) direction, are labeled with positive (negative) integers. From Fig. 10 it can be noted that the two SAWs (PSV_1 and PSV_2) have no cutoff and tend to be degenerate for high frequency, since the media 1 and 3 are identical. In fact they can be interpreted as resulting from the coupling of two Rayleigh waves on the two extreme surfaces $x=x_1$ and $x=x_4$. Their coupling increases at low frequency and reaches its maximum at about 1.5 MHz, in correspondence with the largest separation between the curves. Also note the presence of four complex modes ($PSV_{\pm 4}$ and $PSV_{\pm 5}$), if the frequency is lower than 1.88 MHz. The PSV_5 mode behaves as a *backward wave* in the range $1.88 \div 1.98$ MHz, in the sense that it carries power in the $+z$ direction but its phase velocity is negative.

As discussed in Sec. II, the number of modes that can be found by this method is only limited by the size of the matrix

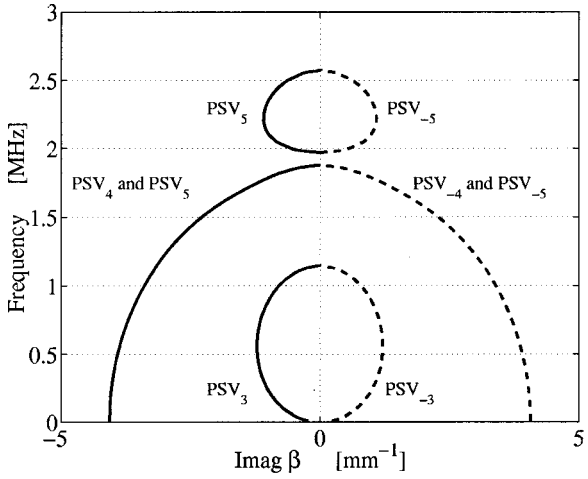

FIG. 11. Dispersion curves (f vs Imag β) for the five lowest order *PSV* modes of the waveguide described in Table I. Modes PSV_1 and PSV_2 have Imag $\beta=0$ identically. See caption of Fig. 10 for mode labeling.

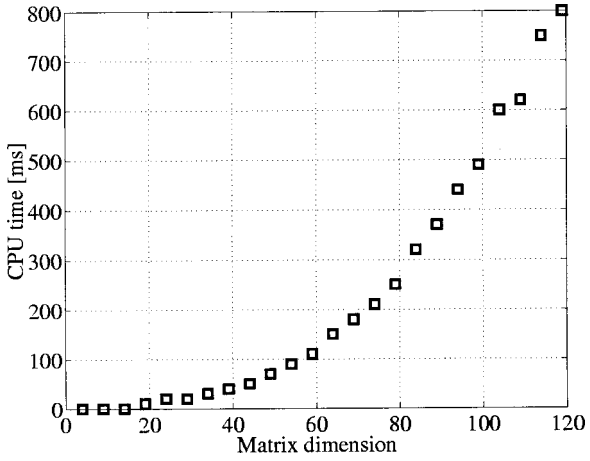

FIG. 12. CPU time needed to solve a standard eigenvalue problem as a function of the matrix dimension. See the text for software and hardware data.

that can be diagonalized by the available computer. In order to give an indication of the CPU time requirements of this method, the *SH* modes of a plate have been computed with an increasing number of polynomials. The `eig.m` routine of MATLAB[13] has been used on a PC (200 MHz Pentium-Pro with 64 MB RAM) and the results are shown in Fig. 12. Figure 13 shows plots of the CPU time needed to compute the propagation constants of certain higher order *SH* plate modes versus their accuracy.

IV. CONCLUSIONS

A matrix method has been presented to compute the propagation constants and the mode eigenfunctions in layered planar waveguides and it has been shown to be a valid alternative to the classical solution of a transcendental equation. Work is in progress in order to extend this technique to the case of waveguides consisting of anisotropic layered media.

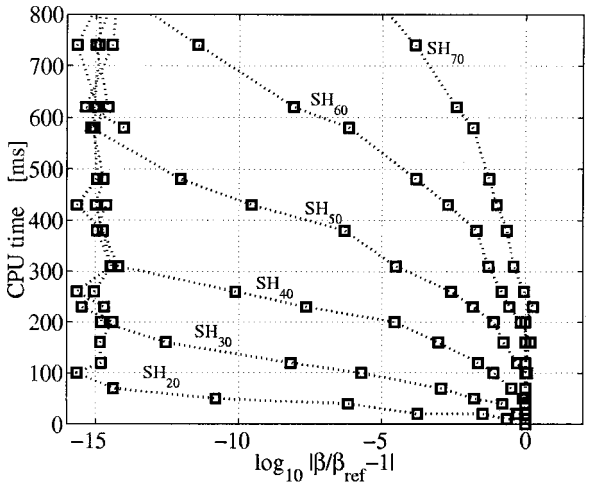

FIG. 13. CPU time versus the relative error on the propagation constants of a single isotropic layer for various higher order modes.

ACKNOWLEDGMENTS

The authors are indebted to the reviewers for their useful suggestions.

[1] J. J. Ditri, ''Some results on the scattering of guided elastic *SH* waves from material and geometric waveguide discontinuities,'' J. Acoust. Soc. Am. **100**, 3078–3087 (1996).
[2] W. Karunasena and A. H. Shah, ''Guided waves in a jointed composite plate,'' J. Acoust. Soc. Am. **95**, 1206–1212 (1994).
[3] P. J. Shull, D. E. Chimenti, and S. K. Datta, ''Elastic guided waves and the Floquet concept in periodically layered plates,'' J. Acoust. Soc. Am. **95**, 99–108 (1994).
[4] C. Potel and J. de Belleval, ''Propagation in an anisotropic periodically multilayered medium,'' J. Acoust. Soc. Am. **93**, 2669–2677 (1993).
[5] B. Zhang, M. Yu, C. Q. Lan, and W. Xiong, ''Elastic wave and excitation mechanism of surface waves in multilayered media,'' J. Acoust. Soc. Am. **100**, 3527–3538 (1996).
[6] A. J. Rudgers, ''Equivalent networks for representing the two-dimensional propagation of dilatational and shear waves in infinite elastic plates and in stratified elastic media,'' J. Acoust. Soc. Am. **91**, 28–38 (1992).
[7] S. Datta and B. J. Hunsinger, ''Analysis of surface waves using orthogonal functions,'' J. Appl. Phys. **49**, 475–479 (1978).
[8] Y. Kim and W. D. Hunt, ''Acoustic fields and velocities for surface-acoustic-wave propagation in multilayered structures: An extension of the Laguerre polynomial approach,'' J. Appl. Phys. **68**, 4993–4997 (1990).
[9] R. H. Morf, ''Exponentially convergent and numerically efficient solution of Maxwell's equations for lamellar gratings,'' J. Opt. Soc. Am. **12**, 1043–1056 (1995).
[10] S. A. Orszag and D. Gottlieb, *Numerical Analysis Of Spectral Methods: Theory And Applications* (SIAM, Philadelphia, 1977), pp. 37–42.
[11] C. B. Moler and G. W. Stewart, ''An algorithm for generalized matrix eigenvalue problem,'' SIAM (Soc. Ind. Appl. Math.) J. Numer. Anal. **10**, 241–256 (1973).
[12] B. A. Auld, *Acoustic Fields and Waves in Solids* (Wiley–Interscience, New York, 1973), pp. 155–160.
[13] MATLAB, The Language of Technical Computing, Version 5.0, The MathWorks, Inc. (1996).

The second-harmonic generation of a conical sound source

Desheng Ding
National Laboratory of Molecular and Biomolecular Electronics, Department of Biomedical Engineering, Southeast University, Nanjing 210096, People's Republic of China

Xiaojun Liu
Institute of Acoustics, Nanjing University, Nanjing 210093, People's Republic of China

(Received 16 May 1996; revised 14 May 1998; accepted 13 July 1998)

The second-harmonic sound beam nonlinearly generated by a conical source is analytically described. It is shown that the radial second-harmonic beam is distributed as the Bessel function and independent of the propagation distance. Another important feature is that the beamwidth of the second-harmonic component is just equal to 1/2 times that of the fundamental, not $1/\sqrt{2}$ times in the general cases. A potential application of this beam in the acoustic nonlinearity parameter B/A imaging or measurement is also discussed. © *1998 Acoustical Society of America.* [S0001-4966(98)05010-3]

PACS numbers: 43.25.Cb [MAB]

INTRODUCTION

In application of medical ultrasonic imaging and ultrasonic testing, it is often desired that the field have a narrow beamwidth to gain higher lateral resolution. For a fixed depth in tissue, the use of focused transducers or acoustic lenses can achieve this effect. However, there is a loss of depth of field. A simple and significant way to overcome this problem is to employ special transducers, such as a conical transducer (ultrasonic axicon)[1,2] or a Bessel ultrasonic beam transducer,[3–5] which radiate the ultrasonic field with both narrow beamwidth and long depth. The field of a conical transducer has a defined beamwidth without spreading and a zero-order Bessel function distribution in the radial direction. The axial pressure amplitude is proportional to the square root of the propagation distance. This beam is also considered as a kind of nondiffracting beam. Owing to these properties, it has potential applications in medical ultrasonic imaging and shows some advantages over other types of transducers.[6,7] In recent years, an attempt has been made to image the acoustic nonlinear parameter B/A of biological samples.[8,9] In this system, the possession of both narrow beamwidth and large field depth is required not only for the fundamental sound beam but also for the nonlinearly generated second-harmonic component.

This paper presents the properties of the second-harmonic component nonlinearly generated by a conical transducer. It is found that the second harmonic in this beam, like the fundamental component, is also distributed as a Bessel function and in independent of the axial distance in the radial direction, and that the beamwidth of the second harmonic is just equal to 1/2 times that of the fundamental. Furthermore, some advantages of this beam and a potential application in B/A imaging are also pointed out.

I. THEORY

The KZK equation with the parabolic approximation is a convenient form for describing the propagation of a finite amplitude sound wave in a fluid. It takes into account, simultaneously, diffraction, nonlinear distortion, and absorption. Suppose that an axially symmetric source, with an angular frequency ω and a characteristic radius a, oscillates harmonically in time and that the sound absorption of the medium can be neglected. A simplified form of the KZK equation can be expressed in terms of nondimensional variables,[10,11]

$$\left[\frac{1}{\xi}\frac{\partial}{\partial\xi}\left(\xi\frac{\partial}{\partial\xi}\right)-4\frac{\partial^2}{\partial\tau\,\partial\eta}\right]\overline{p}=-\frac{\beta\omega^2u_0a^2}{c^3}\frac{\partial^2}{\partial\tau^2}\overline{p}^2, \tag{1}$$

where $\xi=r/a$ and $\eta=2z/ka^2$ are the radially and axially nondimensional coordinates, $k=\omega/c$ is the wave number at the fundamental frequency and $\tau=\omega t-kz$. Correspondingly, the notations r and z denote the radial and axial coordinates. For a real transducer, a may be taken as its radius. Furthermore, $\overline{p}=p/p_0$, where p is the pressure and $p_0=\rho u_0c$, and u_0 is a characteristic vibration amplitude on the source. The quantities ρ, c, and β are the static density, sound speed at small amplitude, and the acoustic nonlinearity coefficient of the medium, respectively. We assume that depletion of the fundamental wave can be ignored, as can the generation of harmonics higher than the second. Under this quasilinear approximation, the linearized solution to Eq. (1) for the fundamental pressure field is[10]

$$p_1(\xi,\eta,\tau)=\mathrm{Re}[p_0e^{-i\tau}\overline{q}_1(\xi,\eta)], \tag{2a}$$

where

$$\overline{q}_1(\xi,\eta)=\frac{2}{i\eta}\int_0^\infty\exp\left(i\frac{\xi^2+\xi'^2}{\eta}\right)J_0\left(\frac{2\xi\xi'}{\eta}\right)\overline{q}_1(\xi')\xi'\,d\xi' \tag{2b}$$

and the quasilinear solution for the second-harmonic component is

$$p_2(\xi,\eta,\tau)=\mathrm{Re}\left\{-2p_0^2\left[\frac{\beta(ka)^2}{\rho c^2}\right]e^{-i2\tau}\overline{q}_2(\xi,\eta)\right\}, \tag{3a}$$

where

$$\overline{q_2}(\xi,\eta)=\frac{1}{2}\int_{\eta'=0}^{\eta}\int_{\xi'=0}^{\infty}\frac{\xi'}{\eta-\eta'}\exp\left(\frac{i2(\xi^2+\xi'^2)}{\eta-\eta'}\right)\times J_0\left(\frac{4\xi\xi'}{\eta-\eta'}\right)\overline{q_1^2}(\xi',\eta')\,d\xi'\,d\eta'. \tag{3b}$$

In Eq. (2b), $\overline{q_1}(\xi')$ is the distribution function of the sound beam on the plane $\eta=0$. The solution (2) satisfies the boundary condition $p_1(\xi,0,\tau)=\mathrm{Re}[p_0\overline{q_1}(\xi)e^{-i\tau}]$ at $\eta=0$, i.e., $\overline{q_1}(\xi,0)=\overline{q_1}(\xi)$ for the fundamental field. For the second-harmonic component, the solution (3) satisfies the boundary condition $\overline{q_2}(\xi,0)=0$. This means that the second harmonic is not generated at the source plane. Equations (2b) and (3b) are the complex-valued pressure amplitudes in nondimensional form for the fundamental and second-harmonic components, respectively.

We now consider the fundamental field radiation and the second-harmonic generation of the conical sound source. The apex of a conical source is located at the origin of the cylindrical coordinate, and the axis of the cone with an angle θ coincides with the η axis. The vibration velocity is assumed to be uniformly distributed with an amplitude u_0 on the conical surface. The fundamental pressure field of such a system then can be equivalent to the radiation of a sound source

$$\overline{q_1}(\xi')=e^{-i\alpha\xi'}. \tag{4}$$

Here $\alpha=ka\sin\theta$. With the substitution of Eq. (4) into Eq. (2b), we write the fundamental component of the conical source in the form

$$\overline{q_1}(\xi,\eta)=\frac{2}{i\eta}\int_0^{\infty}\exp\left(i\,\frac{\xi^2+\xi'^2}{\eta}\right)J_0\left(\frac{2\xi\xi'}{\eta}\right)e^{-i\alpha\xi'}\xi'\,d\xi'. \tag{5}$$

By the method of stationary phase,[2,12,13] the above expression is finally reduced to

$$\overline{q_1}(\xi,\eta)=-i\sqrt{\pi}\alpha J_0(\alpha\xi)\,\eta^{1/2}e^{-i\alpha^2\eta/4+i\pi/4}. \tag{6}$$

For the fundamental pressure of the conical source, Patterson *et al.*[1] presented a similar description as follows:

$$p(r,z,t)=2\pi A\sin\theta\sqrt{\frac{2\pi z\cos\theta}{k}}\times J_0(kr\sin\theta)e^{i(kz\cos\theta+\pi/4)} \tag{7a}$$

with $A=-ik\rho u_0 c e^{-i\omega t}/2\pi$. Rewriting Eq. (7a) in nondimensional variables

$$p(\xi,\eta,\tau)=-\rho u_0 c(ka\sin\theta)\sqrt{\pi}\eta^{1/2}e^{i\pi/4}\times\sqrt{\cos\theta}J_0(\alpha\xi)\exp[-ikz(1-\cos\theta)]e^{-i\tau} \tag{7b}$$

and noting that for small θ (for example, $\sin\theta<0.2$), $\sqrt{\cos\theta}\approx 1$ and $-i[kz(1-\cos\theta)]$ in the exponential term is approximated to $-i\alpha^2\eta/4$, it is seen that Eq. (6) is identical to Eq. (7) for small θ. As indicated by Patterson *et al.*, this is a very good approximate description for the field of a real conical transducer. In the following, we will evaluate, from Eq. (6), the second-harmonic generation of the conical source.

Substitution of Eq. (6) into (3b) leads to the second-harmonic component in the conical beam

$$\overline{q_2}(\xi,\eta)=\frac{-i\pi\alpha^2}{2}\int_{\eta'=0}^{\eta}\int_{\xi'=0}^{\infty}\frac{\xi'}{\eta-\eta'}\times\exp\left(\frac{i2(\xi^2+\xi'^2)}{\eta-\eta'}\right)J_0\left(\frac{4\xi\xi'}{\eta-\eta'}\right)\eta' J_0^2(\alpha\xi')\times\exp\left(-\frac{i\alpha^2}{2}\,\eta'\right)d\xi'\,d\eta'. \tag{8}$$

By using the relation

$$J_0^2(z)=\frac{2}{\pi}\int_0^{\pi/2}J_0(2z\sin t)\,dt \tag{9}$$

Eq. (8) is then transformed to a triple integral

$$\overline{q_2}(\xi,\eta)=-i\alpha^2\int_{\eta'=0}^{\eta}\int_{\xi'=0}^{\infty}\int_{t=0}^{\pi/2}\frac{\xi'}{\eta-\eta'}\times\exp\left(\frac{i2(\xi^2+\xi'^2)}{\eta-\eta'}\right)J_0\left(\frac{4\xi\xi'}{\eta-\eta'}\right)J_0(2\alpha\xi'\sin t)\times\exp\left(-\frac{i\alpha^2}{2}\,\eta'\right)\eta'\,d\xi'\,d\eta'\,dt. \tag{10}$$

From formula (A1) in Appendix A, the integral over ξ' in Eq. (10) can be integrated to yield

$$\overline{q_2}(\xi,\eta)=\frac{\alpha^2}{4}\int_{\eta'=0}^{\eta}\int_{t=0}^{\pi/2}\exp\left(\frac{\alpha^2}{i2}\,\eta\sin^2 t\right)\times J_0(2\alpha\xi\sin t)\times\exp\left[\left(-\frac{i\alpha^2}{2}\cos^2 t\right)\eta'\right]\eta'\,d\eta'\,dt. \tag{11}$$

Integrating over η' and simplifying,

$$\overline{q_2}(\xi,\eta)=\frac{i}{2}\exp\left(-\frac{i\alpha^2}{2}\,\eta\right)\times\int_{t=0}^{\pi/2}J_0(2\alpha\xi\sin t)\left\{\left[\left(\eta-\frac{2i}{\alpha^2\cos^2 t}\right)+\frac{2i}{\alpha^2\cos^2 t}\exp\left(\frac{i\alpha^2}{2}\,\eta\cos^2 t\right)\right]\frac{1}{\cos^2 t}\right\}dt \tag{12}$$

which is an exact solution for the second-harmonic component in the conical sound beam under the quasilinear approximation. It is difficult from Eq. (12) to find the features of the second-harmonic pressure of the conical beam. In the original study, we observe that the real and the imaginary parts of the function

$$f(t)=\left[\left(\eta-\frac{2i}{\alpha^2\cos^2 t}\right)+\frac{2i}{\alpha^2\cos^2 t}\exp\left(\frac{i\alpha^2}{2}\,\eta\cos^2 t\right)\right]\frac{1}{\cos^2 t} \tag{13}$$

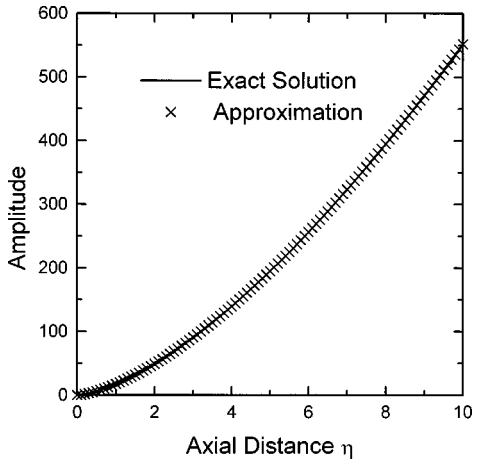

FIG. 1. A comparison of exact and approximate solutions along the acoustic axis. In all the figures, the parameter $\alpha=41.8$.

are extremely similar to the delta function. On the basis of this fact, and with the help of numerical evaluation, we obtain intuitively a semianalytical description for the second-harmonic beam. Another approximate expression

$$\overline{q_2}(\xi,\eta)=\frac{\alpha}{3}\sqrt{\frac{\pi}{2}}\,e^{i\pi/4}J_0(2\alpha\xi)\,\eta^{3/2}\exp\left(-\frac{i\alpha^2}{2}\,\eta\right) \tag{14}$$

is derived through an elegant treatment. A detailed derivation and a comparison of these two approximations are presented in Appendix D.

II. DISCUSSION

Equation (14) is a remarkably good approximation to Eq. (12). To verify this, we draw the second-harmonic pressure amplitude at the acoustic axis, as shown in Fig. 1, where the crosses denote Eq. (14) and the solid line the exact expression (12). Numerical integration of Eq. (12) indicates that in the region extremely close to the source (η about less than 0.05) the radial beam distribution is slightly different from the J_0 Bessel function but for greater distances the function is basically the Bessel function $J_0(2\alpha\xi)$. Figure 2 shows the pressure amplitudes at various transverse planes from near to far zones ($\eta=0.05$, 1.0, and 5.0), for comparison, the curves of $J_0(2\alpha\xi)$ and $J_0(\alpha\xi)$ are also plotted in Fig. 2. The second harmonic field of a conical source is almost radially nondiffracting.

The conical beam at the fundamental frequency has potential application in ultrasonic medical imaging due to its very large depth of field, sharply lateral beamwidth without spreading, and negligible diffraction.[1–5] These would simplify the system of emitting ultrasound in an imaging instrument.[6,7] Similarly, the second-harmonic component of this beam would have these advantages in some situations where it is used for imaging or measurement. For instance, in imaging or measuring the acoustic nonlinearity parameter B/A of tissues, the correction of the influence of diffraction in the conventional system might be omitted in this system.[9]

Another important feature is the relationship between the beamwidths of the second-harmonic and fundamental components in the conical beam. For most ultrasonic beams

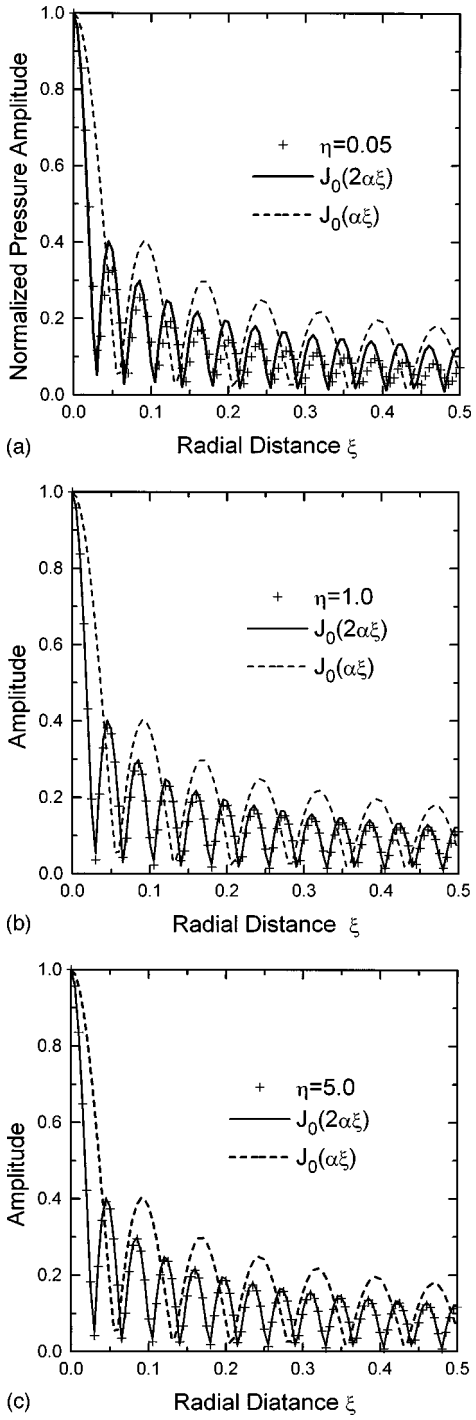

FIG. 2. The radial pressure amplitudes (normalized to the values at the center $\xi=0$) of a second harmonic in the conical beam, at transverse planes, calculated from Eq. (12).

(focused or not), the beamwidth of the nonlinearly generated second harmonic is generally $1/\sqrt{2}$ times that of the fundamental component, this has been experimentally verified and theoretically predicted.[14,15] However, from (14) and (6), or more clearly from Fig. 2, the beamwidth of the second harmonic is just 1/2 times that of the fundamental component in the conical beam. This indicates that in ultrasonic imaging due to the nonlinearity of materials, higher resolution will be obtained by using the conical beam instead of the ultrasonic beams of other types when their resolution powers at the fundamental frequency are the same.

Finally, it must be emphasized that Eqs. (12) and (14) are derived under the quasilinear approximation. From the perturbation theory, these solutions are valid when the following inequality is satisfied:

$$\frac{\sqrt{2}}{3}\,\beta(ka)^2\left(\frac{u_0}{c}\right)\eta<C. \tag{15}$$

Here the constant $C\sim O(1)$. Also, the present analysis is based on the ''ideal'' case under which the aperture of the sound source is assumed to be infinite. In practical use, the size of the transducers is always finite. For the conical source with a finite aperture, the fundamental radiation and second-harmonic generation may be simulated by using numerical integration, from Eqs. (2) and (3). Further theoretical and experimental investigations are needed to develop a complete understanding of the conical source.

III. CONCLUSION

In summary, we have presented the solution for the second-harmonic component of a conical source, showing that this beam profile in the radial direction is nearly nondiffracting and the pressure amplitude on the beam axis has a simple relation with the propagation range. Other features and possible applications for the second harmonic of a conical beam also are pointed out.

APPENDIX A: SOME FORMULAS

Some formulas are collected below for the convenience of the reader. The notation is, for the most part, that of the original authors and the symbols do not have the same meanings as in the text of this paper.

(1) From Gradshteyn and Ryzhik's *Table of Integrals, Series, and Products*,[16] p. 758, formulas 6.728.3-4:

$$\int_0^\infty xJ_0(\beta x)\sin(\alpha x^2)dx=\frac{1}{2\alpha}\cos\left(\frac{\beta^2}{4\alpha}\right)$$

and

$$\int_0^\infty xJ_0(\beta x)\cos(\alpha x^2)dx=\frac{1}{2\alpha}\sin\left(\frac{\beta^2}{4\alpha}\right),$$

$\alpha>0$, $\beta>0$.

Page 758, 6.729.1-2:

$$\int_0^\infty x\,\sin(ax^2)J_\nu(bx)J_\nu(cx)dx$$

$$=\frac{1}{2a}\cos\left(\frac{b^2+c^2}{4a}-\frac{\nu\pi}{2}\right)J_\nu\left(\frac{bc}{2a}\right),$$

$a>0$, $b>0$, $c>0$, $\mathrm{Re}(\nu)>-2$ and

$$\int_0^\infty x\,\cos(ax^2)J_\nu(bx)J_\nu(cx)dx$$

$$=\frac{1}{2a}\sin\left(\frac{b^2+c^2}{4a}-\frac{\nu\pi}{2}\right)J_\nu\left(\frac{bc}{2a}\right),$$

$a>0$, $b>0$, $c>0$, $\mathrm{Re}(\nu)>-1$. Noting that $J_0(0)=1$ and formulas 6.728.3-4 can be viewed, respectively, as a special case of formulas 6.729.1-2 for $\nu=0$ and $c=0$, we write compactly

$$\int_0^\infty J_0(\alpha t)J_0(\beta t)e^{\pm i\gamma^2t^2}t\,dt$$

$$=\pm\frac{i}{2}\,\gamma^{-2}\exp\left[\mp\frac{i}{4}\,\gamma^{-2}(\alpha^2+\beta^2)\right]J_0\left(\frac{1}{2}\,\alpha\beta\gamma^{-2}\right). \tag{A1}$$

Page 979, formula 8.513.3:

$$J_0(z\,\sin\,t)=\sum_{m=0}^{\infty}\epsilon_mJ_m^2\left(\frac{z}{2}\right)\cos 2mt. \tag{A2}$$

Here $\epsilon_0=1$; the other ϵ is equal to 2.

(2) From Watson's *Bessel Functions*.[17]

Page 358, Eq. (1):

$$J_0(\omega)=\sum_{m=0}^{\infty}\epsilon_mJ_m(Z)J_m(z)\cos\,m\phi, \tag{A3}$$

where ϵ has the same meaning as Eq. (A2), and for brevity, we write

$$\omega=(Z^2+z^2-2Zz\,\cos\,\phi)^{1/2}.$$

Multiplying both sides by $d\phi$ and integrating from 0 to π, we obtain

$$\int_0^\pi J_0(\omega)d\phi=\pi J_0(Z)J_0(z). \tag{A4}$$

(3) Function ${}_2F_2$ and its asymptotic expansion.

The function ${}_2F_2(\alpha,\beta;\gamma,\theta;z)$, as a kind of the generalized hypergeometric function, is defined by a series of the form[16,18]

$${}_2F_2(\alpha,\beta;\gamma,\theta;z)=\sum_{k=0}^{\infty}\frac{(\alpha)_k(\beta)_k}{(\gamma)_k(\theta)_k}\frac{z^k}{k!}, \tag{A5}$$

where $(\alpha)_k=\alpha(\alpha+1)(\alpha+2)\cdots(\alpha+k-1)$, $(\alpha)_0=1$, and so on.

This function has an integral representation, known as Barnes' integral or Mellin–Barnes type integral, as follows[16,18]

$$\frac{\Gamma(\alpha)\Gamma(\beta)}{\Gamma(\gamma)\Gamma(\theta)}\,{}_2F_2(\alpha,\beta;\gamma,\theta;z)$$

$$=\frac{1}{2\pi i}\int_{-i\infty}^{+i\infty}\frac{\Gamma(\alpha+s)\Gamma(\beta+s)}{\Gamma(\gamma+s)\Gamma(\theta+s)}\,\Gamma(-s)(-z)^{+s}ds.$$

Here $-\pi<\arg(-z)<\pi$ and the path of integration is chosen such that the poles of $\Gamma(\alpha+s)$ and $\Gamma(\beta+s)$, i.e., the points $s=-\alpha-n$ and $s=-\beta-m(n,m=0,1,2,...)$, are at its left side and the poles of $\Gamma(-s)$, i.e., $s=0,1,2,...$, are at its right side. The case in which $-\alpha$, $-\beta$, $-\gamma$, or $-\theta$ are nonnegative integers or $\alpha-\beta$ is equal to an integer are excluded. From the residue formula, this integral can be evaluated to be

$$\frac{\Gamma(\alpha)\Gamma(\beta)}{\Gamma(\gamma)\Gamma(\theta)}\,{}_2F_2(\alpha,\beta;\gamma,\theta;z)$$

$$=(-z)^{-\alpha}\sum_{k=0}^{\infty}\frac{\Gamma(\beta-\alpha-k)\Gamma(\alpha+k)}{\Gamma(\gamma-\alpha-k)\Gamma(\theta-\alpha-k)k!}\,z^{-k}$$

$$+(-z)^{-\beta}\sum_{k=0}^{\infty}\frac{\Gamma(\alpha-\beta-k)\Gamma(\beta+k)}{\Gamma(\gamma-\beta-k)\Gamma(\theta-\beta-k)k!}\,z^{-k} \tag{A6}$$

which can be seen as the asymptotic expansion of ${}_2F_2$ for large $|z|$.

(4) Kummer's function.

In the special case of $\alpha=\gamma$ or $\alpha=\theta$, the function ${}_2F_2$ becomes Kummer's function. From formula 13.5.1 on p. 508 of Ref. 18 it has an asymptotic expansion for large $|z|$ in the form

$$\frac{M(a,b,z)}{\Gamma(b)}$$

$$=\frac{e^{\pm i\pi a}z^{-a}}{\Gamma(b-a)}\left\{\sum_{n=0}^{R-1}\frac{(a)_n(1+a-b)_n}{n!}\,(-z)^{-n}+O(|z|^{-R})\right\}$$

$$+\frac{e^{z}z^{a-b}}{\Gamma(a)}\left\{\sum_{n=0}^{S-1}\frac{(b-a)_n(1-a)_n}{n!}\,z^{-n}+O(|z|^{-S})\right\} \tag{A7}$$

the upper sign being taken if $-\frac{1}{2}\pi<\arg z<\frac{3}{2}\pi$, the lower sign if $-\frac{3}{2}\pi<\arg z\leqslant-\frac{1}{2}\pi$.

APPENDIX B

In this Appendix we present a detailed derivation of Eqs. (2) and (3), the linearized and quasilinear solutions for the fundamental and second-harmonic components. More generally, we begin with an original form of the KZK equation that contains the absorption term for the medium and is expressed as[10]

$$\left[\frac{1}{\xi}\frac{\partial}{\partial\xi}\left(\xi\frac{\partial}{\partial\xi}\right)-4\frac{\partial^2}{\partial\tau\partial\eta}+4\bar{\alpha}\frac{\partial^3}{\partial\tau^3}\right]\bar{p}=-\frac{\beta(ka)^2u_0}{c}\frac{\partial^2}{\partial\tau^2}\bar{p}^2, \tag{B1}$$

where $\bar{\alpha}=ka^2\alpha/2$ with the absorption coefficient α at the fundamental frequency, and the other notations are the same as in Eq. (1) [$\bar{\alpha}$ corresponds to αr_0 of Eq. (17) in Ref. 10]. We use the perturbation method to solve this equation and write the solution to Eq. (B1) as

$$\bar{p}=\bar{p}_1+\bar{p}_2+\cdots, \tag{B2}$$

where

$$\bar{p}=\tfrac{1}{2}[\bar{q}_1(\xi,\eta)e^{-i\tau}+\bar{q}_1^{*}(\xi,\eta)e^{i\tau}]=\mathrm{Re}[\bar{q}_1(\xi,\eta)e^{-i\tau}] \tag{B3}$$

and

$$\bar{p}_2=\frac{\epsilon'}{2}[\bar{q}_2(\xi,\eta)e^{-i2\tau}+\bar{q}_2^{*}(\xi,\eta)e^{i2\tau}]$$

$$=\mathrm{Re}[\epsilon'\bar{q}_2(\xi,\eta)e^{-i2\tau}]. \tag{B4}$$

The asterisk represents complex conjugation and $\epsilon'=-2\beta(ka)^2u_0/c$. The expressions (B3) and (B4) are the approximate solutions of the first and second order of the equation, respectively. Substituting these into Eq. (B1), we obtain, in consideration of the quasilinear assumption, the following two equations:

$$\left[\frac{1}{\xi}\frac{\partial}{\partial\xi}\left(\xi\frac{\partial}{\partial\xi}\right)+i4\frac{\partial}{\partial\eta}+i4\bar{\alpha}\right]\bar{q}_1(\xi,\eta)=0 \tag{B5}$$

and

$$\left[\frac{1}{\xi}\frac{\partial}{\partial\xi}\left(\xi\frac{\partial}{\partial\xi}\right)+i8\frac{\partial}{\partial\eta}+i32\bar{\alpha}\right]\bar{q}_2(\xi,\eta)=-\bar{q}_1^{2}(\xi,\eta). \tag{B6}$$

Making the Hankel transform of the Eq. (B5) with respect to ξ yields[11]

$$\left(-s^2+i4\frac{\partial}{\partial\eta}+i4\bar{\alpha}\right)\tilde{q}_1(s,\eta)=0. \tag{B7}$$

In this paper, the Hankel transform of a function $f(\xi)$ is defined by

$$\tilde{f}(s)=\int_0^{\infty}f(\xi)J_0(s\xi)\xi\,d\xi$$

and its inverse transform by

$$f(\xi)=\int_0^{\infty}\tilde{f}(s)J_0(\xi s)s\,ds.$$

The solution of Eq. (B7) which satisfies the boundary condition $\bar{q}_1(\xi,0)=\bar{q}_1(\xi)$ is

$$\tilde{q}_1(s,\eta)=\tilde{q}_1(s,0)\exp\left[\left(\frac{s^2}{i4}-\bar{\alpha}\right)\eta\right]. \tag{B8}$$

By the inverse Hankel transform, we obtain

$$\bar{q}_1(\xi,\eta)=\int_{s=0}^{\infty}\tilde{q}_1(s,0)\exp\left[\left(\frac{s^2}{i4}-\bar{\alpha}\right)\eta\right]J_0(\xi s)s\,ds$$

$$=\int_{s=0}^{\infty}\int_{\xi'=0}^{\infty}\bar{q}_1(\xi')J_0(\xi's)J_0(\xi s)\times\exp\left[\left(\frac{s^2}{i4}-\bar{\alpha}\right)\eta\right]s\xi'\,d\xi'. \tag{B9}$$

Using formula (A1) and making some adjustments, Eq. (B9) may be reduced to

$$\bar{q}_1(\xi,\eta)=\frac{2}{i\eta}e^{-\bar{\alpha}\eta}\int_0^{\infty}\exp\left(i\frac{\xi^2+\xi'^2}{\eta}\right)\times J_0\left(\frac{2\xi\xi'}{\eta}\right)\bar{q}_1(\xi')\xi'\,d\xi'. \tag{B10}$$

In the absence of the absorption term in Eq. (B10), i.e., at $\bar{\alpha}=0$, the above expression is just Eq. (2b) in the text.

A similar but slightly complicated procedure is also applicable to solve Eq. (B6). The solution of this equation, after the Hankel transform, consists of two parts

$$\tilde{q}_2(s,\eta)=\tilde{q}_2(s,0)\exp\left[-\left(\frac{-s^2}{i8}+4\bar{\alpha}\right)\eta\right]-\int_{\eta'=0}^{\eta}\frac{1}{i8}\exp\left[\left(\frac{-s^2}{i8}+4\bar{\alpha}\right)(\eta'-\eta)\right]\times\tilde{Q}_2(s,\eta')d\eta', \tag{B11}$$

where $\tilde{Q}_2(s,\eta)=\int_0^\infty J_0(s\xi)\bar{q}_1^2(\xi,\eta)\xi\, d\xi$ and $\tilde{q}_2(s,0)$ is the Hankel transform of the boundary condition $\bar{q}_2(\xi,0)$ for the second-harmonic generation. Under the assumption $\bar{q}_2(\xi,0)=0$, that is to say, the second-harmonic component does not generate at the source, we then have $\tilde{q}_2(s,0)=0$. Using the inverse Hankel transform to Eq. (B11), we express the quasilinear solution for the second-harmonic field as

$$\begin{aligned}\bar{q}_2(\xi,\eta)&=-\int_{s=0}^{\infty}\int_{\eta'=0}^{\eta}\frac{1}{i8}\exp\left[\left(\frac{-s^2}{i8}+4\bar{\alpha}\right)\times(\eta'-\eta)\right]\tilde{Q}_2(s,\eta')J_0(\xi s)s\, ds\, d\eta'\\&=-\frac{1}{i8}e^{-4\bar{\alpha}\eta}\int_{\xi'=0}^{\infty}\int_{\eta'=0}^{\eta}\int_{s=0}^{\infty}e^{4\bar{\alpha}\eta'}J_0(s\xi)J_0(s\xi')\times\exp\left[\frac{s^2}{i8}(\eta-\eta')\right]\bar{q}_1^2(\xi',\eta')\xi' s\, ds\, d\xi' d\eta'.\end{aligned} \tag{B12}$$

The integration over s can be performed, in consideration of formula (A1), to yield

$$\bar{q}_2(\xi,\eta)=\frac{1}{2}e^{-4\bar{\alpha}\eta}\int_{\eta'=0}^{\eta}\int_{\xi'=0}^{\infty}e^{4\bar{\alpha}\eta}\frac{\xi'}{\eta-\eta'}\times\exp\left(\frac{i2(\xi^2+\xi'^2)}{\eta-\eta'}\right)J_0\left(\frac{4\xi\xi'}{\eta-\eta'}\right)\times\bar{q}_1^2(\xi',\eta')d\xi'\, d\eta'. \tag{B13}$$

When $\bar{\alpha}=0$, this expression changes to Eq. (3b).

APPENDIX C

In Ref. 10 Aanonsen *et al.* developed another form of the linearized and quasilinear solutions to Eq. (1). For the fundamental pressure field, the imaginary unit i appears before $\bar{q}_1(\xi,\sigma)$ of their solution (σ there corresponding to η here), but it does not appear in the present equations (2a) and (2b). This difference is mainly due to the different assumption of the time variation of the on-source pressure distribution. According to their equations (31) and (32), and with the notation in this paper, the pressure distribution on the source is taken as $p_1(\xi,0,\tau)=\mathrm{Re}[ip_0\bar{q}_1(\xi)e^{-i\tau}]$, varying sinusoidally in time, while we assume in this paper that the time dependence of the pressure has the form with $\cos\tau$. Noting this fact, these two equations are indeed identical. For the second-harmonic generation, however, the form of Eq. (3) is not fully the same as that of Eq. (34) there. We show below that in fact, they are completely equivalent.

With substitution of Eq. (B10) into Eq. (B13) and with use of formula (A4), we have

$$\begin{aligned}\bar{q}_2(\xi,\eta)&=\frac{1}{2}e^{-4\bar{\alpha}\eta}\int_{\eta'=0}^{\eta}\int_{\xi'=0}^{\infty}e^{2\bar{\alpha}\eta'}\frac{\xi'}{\eta-\eta'}\exp\left(\frac{i2(\xi^2+\xi'^2)}{\eta-\eta'}\right)J_0\left(\frac{4\xi\xi'}{\eta-\eta'}\right)\\&\times\left[\frac{2}{i\eta'}\right]^2\left[\int_{\xi_1=0}^{\infty}\exp\left(i\frac{\xi'^2+\xi_1^2}{\eta'}\right)J_0\left(\frac{2\xi'\xi_1}{\eta'}\right)\bar{q}_1(\xi_1)\xi_1\, d\xi_1\right]\\&\times\left[\int_{\xi_2=0}^{\infty}\exp\left(i\frac{\xi'^2+\xi_2^2}{\eta'}\right)J_0\left(\frac{2\xi'\xi_2}{\eta'}\right)\bar{q}_1(\xi_2)\xi_2\, d\xi_2\right]d\xi'\, d\eta'\\&=\frac{1}{2\pi}e^{-4\bar{\alpha}\eta}\int_{\eta'=0}^{\eta}\int_{\xi'=0}^{\infty}\int_{\xi_1=0}^{\infty}\int_{\xi_2=0}^{\infty}\int_{\phi=0}^{\pi}e^{2\bar{\alpha}\eta'}\frac{\xi'}{\eta-\eta'}\exp\left(\frac{i2(\xi^2+\xi'^2)}{\eta-\eta'}\right)J_0\left(\frac{4\xi\xi'}{\eta-\eta'}\right)\\&\times\left[\frac{2}{i\eta'}\right]^2\exp\left[\frac{i(2\xi'^2+\xi_1^2+\xi_2^2)}{\eta'}\right]J_0\left(\frac{2\xi'}{\eta'}\sqrt{F_+}\right)\bar{q}_1(\xi_1)\bar{q}_1(\xi_2)\xi_1\xi_2\, d\xi_1\, d\xi_2\, d\xi'\, d\eta'\, d\phi,\end{aligned} \tag{C1}$$

where $F_{\pm}=\xi_1^2+\xi_2^2\pm 2\xi_1\xi_2\cos\phi$. Using formula (A1) to perform the integral about ξ' in the above expression and making some arrangements, we then obtain

$$\overline{q_2}(\xi,\eta)=-\frac{i}{2\pi\eta}e^{-4\overline{\alpha}\eta}\int_{\xi_1=0}^{\infty}\int_{\xi_2=0}^{\infty}\int_{\phi=0}^{\pi}G(\xi_1,\xi_2,\eta)\times\exp\left(i\frac{4\xi^2+F_+}{2\eta}\right)J_0\left(\frac{2\xi}{\eta}\sqrt{F_+}\right)\times\overline{q_1}(\xi_1)\overline{q_1}(\xi_2)\xi_1\xi_2\,d\xi_1\,d\xi_2\,d\phi \tag{C2}$$

and the function G with the form

$$G(\xi_1,\xi_2,\eta)=\int_{\eta'=0}^{\infty}\exp\left(\frac{iF_-}{2\eta'}+2\overline{\alpha}\eta'\right)\eta'^{-1}d\eta'. \tag{C3}$$

By combining the present representations (C2) and (C3), it can be seen that the solution (3) for the second-harmonic field is identical to the result in Ref. 10 and it seems simpler in form.

APPENDIX D

The following step is to evaluate the integral defined by

$$X(\xi,\eta)=\int_{t=0}^{\pi/2}J_0(2\alpha\xi\sin t)\left\{\left[1+\frac{1}{z\cos^2 t}-\frac{1}{z\cos^2 t}\exp(z\cos^2 t)\right]\frac{1}{\cos^2 t}\right\}dt \tag{D1}$$

with $z=i\alpha^2\eta/2$.

Using formula (A3) and expanding the exponential term in Eq. (D1), we rewrite

$$X(\xi,\eta)=(-1)\sum_{m=0}^{\infty}\epsilon_m J_m^2(\alpha\xi)F_m(z), \tag{D2}$$

where

$$F_m(z)=\int_{t=0}^{\pi/2}\left(\sum_{n=2}^{\infty}\frac{z^{n-1}}{n!}[\cos t]^{2(n-2)}\right)\cos 2mt\,dt. \tag{D3}$$

From

$$\cos^{2n}t=\frac{1}{2^{2n}}\sum_{k=0}^{2n}\binom{2n}{k}\cos[(2n-2k)t]$$

and

$$\int_0^{\pi/2}\cos 2mt\cos 2nt\,dt=\begin{cases}\pi/4, & |m|=|n|\\ 0, & |m|\neq|n|.\end{cases}$$

Equation (D3) can be thus expressed in terms of the generalized hypergeometric function,

$$\begin{aligned}F_m(z)&=\frac{\pi}{2}\sum_{n=2}^{\infty}\frac{z^{n-1}}{n!}\frac{1}{2^{2n-4}}\binom{2n-4}{n-m-2}\\&=\frac{\pi z^{m+1}}{2^{2m+1}\Gamma(m+3)}\sum_{k=0}^{\infty}\frac{z^k}{k!}\frac{(m+\frac{1}{2})_k(m+1)_k}{(m+3)_k(2m+1)_k}\\&=\frac{\pi z^{m+1}}{2^{2m+1}\Gamma(m+3)}\,{}_2F_2\left(m+\frac{1}{2},m+1;m+3,2m+1;z\right).\end{aligned} \tag{D4}$$

In the special case $m=0$, $F_0(z)=(\pi z/4)M(\frac{1}{2},3,z)$.

From formulas (A6) and (A7) we have an asymptotic expression of $F_m(z)$ for large $|z|$ (taking its leading term of its expansion),

$$F_m(z)=\frac{2i}{3}\pi^{1/2}z^{1/2}(-1)^m. \tag{D5}$$

Then the integral (D1) is approximated by

$$X(\xi,\eta)=(-i)\frac{2}{3}\pi^{1/2}z^{1/2}\sum_{m=0}^{\infty}\epsilon_m J_m^2(\alpha\xi)(-1)^m \tag{D6}$$

in which the summation can be evaluated, from formula (A2), to be $J_0(2\alpha\xi)$. Finally we have

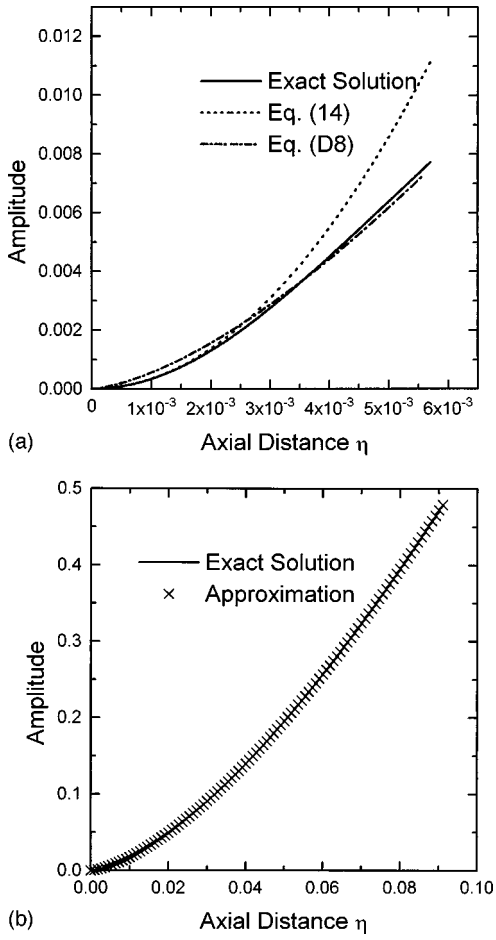

FIG. D1. Same as Fig. 1. A comparison of Eqs. (12) and (D8) in the very small region close to the source plane $\eta=0$. Here Eq. (14) is also plotted. (a) is a part of (b).

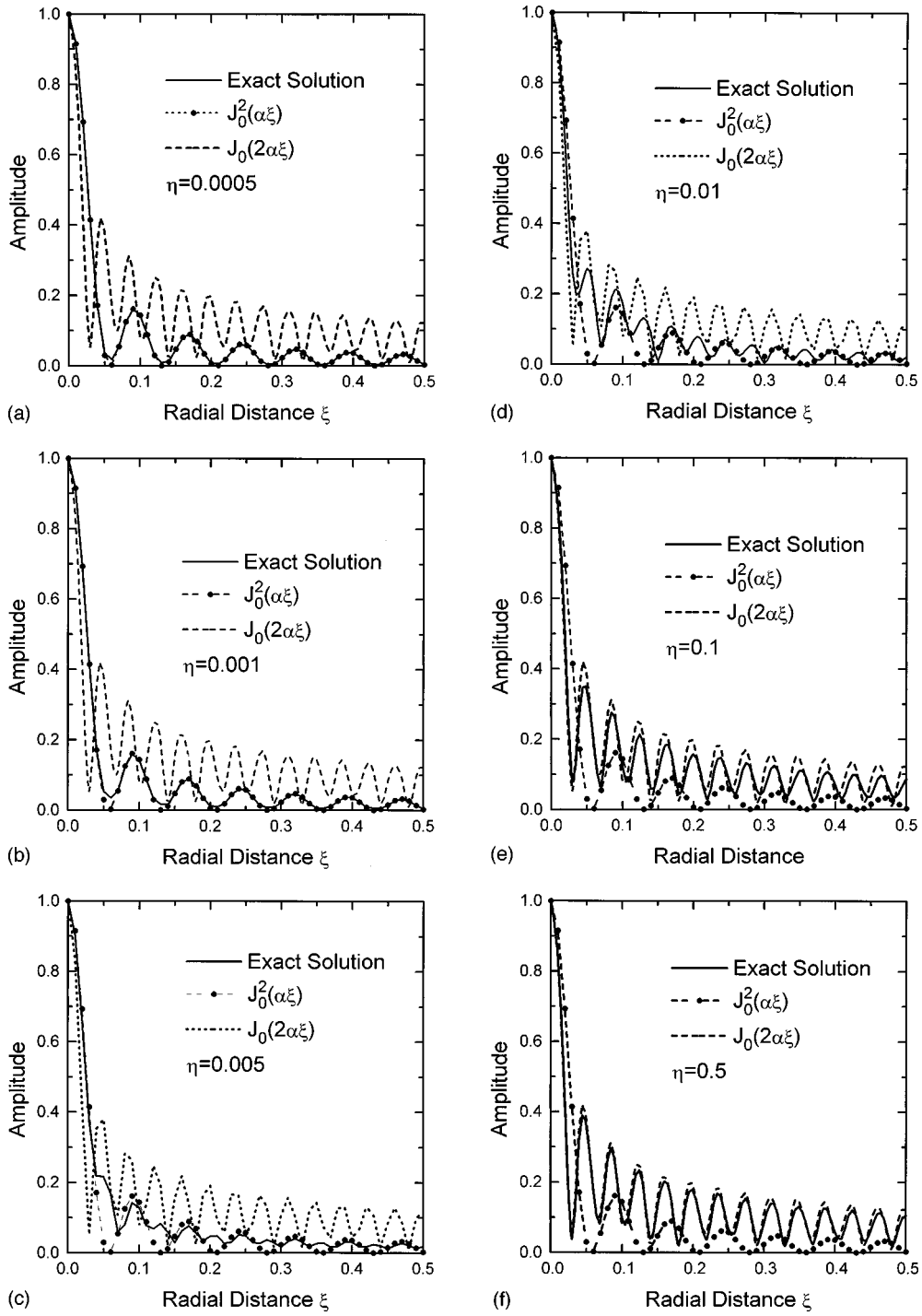

FIG. D2. Same as Fig. 2. (a)–(f) correspond to the axial distances $\eta = 0.0005$, 0.001, 0.005, 0.01, 0.1, and 0.5.

$$X(\xi,\eta) = (-i)^{\frac{2}{3}}\pi^{1/2}z^{1/2}J_0(2\alpha\xi) \tag{D7}$$

and Eq. (14) for the second-harmonic field.

The above analysis is made under the condition that $|z|$ is relatively large. In reality, for very small values of $|z|$ (less than 1), a more accurate evaluation of Eq. (D1) can be derived by taking the first expansion term of Eq. (D2). Therefore we have

$$\begin{aligned}\overline{q}_2(\xi,\eta) &= \frac{i\eta}{2}\exp\left(-\frac{i\alpha^2}{2}\eta\right)X(\xi,\eta)\\ &\approx \frac{\pi\alpha^2}{16}J_0^2(\alpha\xi)\eta^2 M\left(\frac{1}{2},3;\frac{i\alpha^2}{2}\eta\right)\exp\left(-\frac{i\alpha^2}{2}\eta\right)\\ &\approx \frac{\pi\alpha^2}{16}J_0^2(\alpha\xi)\eta^2\exp\left(-\frac{i\alpha^2}{2}\eta\right).\end{aligned} \tag{D8}$$

The calculated results from Eqs. (D8) and (D1) [or (12)] are plotted in Figs. D1 and D2. It can be seen from these figures

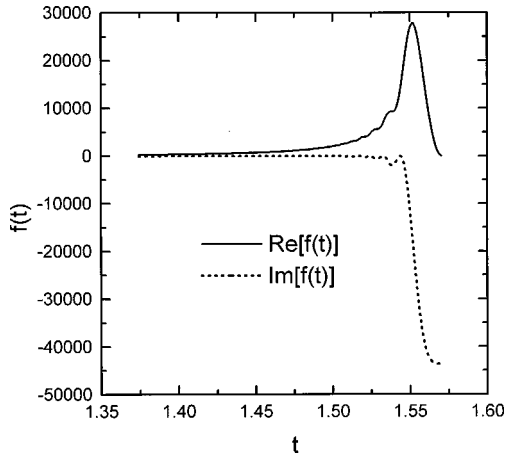

FIG. D3. The real and imaginary parts of the function $f(t)$ in the range $[7\pi/16,\pi/2]$. The amplitudes in other ranges, far smaller than in this range, are not drawn. Here $\eta=10$.

that in this region the radial profile of the second-harmonic field takes $J_0^2(\alpha\xi)$ rather than $J_0(2\alpha\xi)$ function distribution. However, it should be noted that this discrepancy occurs only at extremely small distances from the source.

Between these two extremes for small and large values of $|z|$, we are unable to get a simple description, as done in the above, through an analytical approach. But Figs. 1 and 2 show that Eq. (14) is a fairly good approximation to the second-harmonic field of a conical source.

From the above analysis, Eq. (14) may reasonably reveal the characteristics of the second-harmonic generation in the total region of field.

Some are supplemented as follows. In our original manuscript, we guess from the numerical computation of Eq. (12) that the second-harmonic pressure field has an expression

$$\overline{q_2}(\xi,\eta)=\frac{\alpha}{\pi}\sqrt{\frac{\pi}{2}}\,e^{i\pi/4}J_0(2\alpha\xi)\,\eta^{3/2}\left(1+\frac{2\pi}{\alpha\eta^{1/2}}\right)\times\exp\left(-\frac{i\alpha^2}{2}\,\eta\right). \tag{D9}$$

The derivation of this result is based on the similarity between $f(t)$ [Eq. (13)] and the delta function. The real and imaginary parts of the function $f(t)$, as shown in Fig. D3, are extremely similar to the delta function. Therefore the dominant contribution to the integral (12) is the part in a very small range around $t=\pi/2$. The integration of Eq. (13) about t can be verified numerically to be

$$\int_{t=0}^{\pi/2}f(t)dt=\frac{2}{\pi}\sqrt{\frac{\pi}{2}}\left(\frac{\alpha^2\eta}{2}\right)^{1/2}\eta(1-i)\left(1+\frac{2\pi}{\alpha\eta^{1/2}}\right). \tag{D10}$$

From the feature of the delta function, one can obtain the result of Eq. (D9). Of course, this is empirical.

[1] M. S. Patterson and F. S. Foster, ''Acoustic fields of conical radiators,'' IEEE Trans. Sonics Ultrason. **SU-29**, 83–92 (1982).
[2] D. R. Dietz, ''Apodized conical focusing for ultrasound imaging,'' IEEE Trans. Sonics Ultrason. **SU-29**, 128–138 (1982).
[3] J. Durnin and J. J. Miceli, Jr., ''Diffraction-free beams,'' Phys. Rev. Lett. **58**, 1499–1501 (1987).
[4] D. K. Hsu, F. J. Margetan, and D. O. Thompson, ''Bessel beam ultrasonic transducer: Fabrication method and experimental results,'' Appl. Phys. Lett. **55**, 2066–2068 (1989).
[5] J. A. Compbell and S. Soloway, ''Generation of a nondiffracting beam with frequency-independent beamwidth,'' J. Acoust. Soc. Am. **88**, 2467–2477 (1990).
[6] J. Y. Lu and J. F. Greenleaf, ''Ultrasonic nondiffracting transducer for medical imaging,'' IEEE Trans. Ultrason. Ferroelectr. Freq. Control **39**, 438–447 (1990).
[7] J. Y. Lu and J. F. Greenleaf, ''Pulse-echo imaging using a nondiffracting beam transducer,'' Ultrasound Med. Biol. **17**, 265–281 (1991).
[8] T. Sato, A. Fakusima, N. Ichida, H. Ishkawa, Y. Igarashi, T. Shimura, and K. Mwrakami, ''Nonlinear parameter tomography system using counter-propagation probe and pump wave,'' Ultrason. Imaging **7**, 49–50 (1985).
[9] A. Cai, J. Sun, and G. Wade, ''Imaging the acoustic nonlinear parameter with diffraction tomography,'' IEEE Trans. Ultrason. Ferroelectr. Freq. Control **39**, 708–715 (1992).
[10] S. Aanonsen, T. Barkve, J. N. Tjøtta, and S. Tjøtta, ''Distortion and harmonic generation in the nearfield of a finite amplitude sound beam,'' J. Acoust. Soc. Am. **75**, 749–768 (1984).
[11] B. G. Lucas and T. G. Muir, ''Field of a finite-amplitude focusing source,'' J. Acoust. Soc. Am. **74**, 1522–1528 (1983).
[12] A. Vasara, J. Turunen, and A. T. Friberg, ''Realization of general nondiffracting beams with computer-generated holograms,'' J. Opt. Soc. Am. A **6**, 1748–1754 (1989).
[13] C. Paterson and R. Smith, ''Higher-order Bessel waves produced by axicon-type computer-generated holograms,'' Opt. Commun. **124**, 121–130 (1996).
[14] L. Germain and J. D. N. Cheeke, ''Generation and detection of high-order harmonics in liquid using scanning acoustic microscope,'' J. Acoust. Soc. Am. **83**, 942–949 (1988).
[15] D. Rugar, ''Resolution beyond the diffraction limit in the acoustic microscope: A nonlinear effect,'' J. Appl. Phys. **56**, 1338–1346 (1984).
[16] I. S. Gradsthteyn and I. M. Ryzhik, *Table of Integrals, Series, and Products* (Academic, New York, 1980).
[17] G. N. Watson, *A Treatise on the Theory of Bessel Functions* (Cambridge U.P., Cambridge, England, 1958), 2nd ed.
[18] M. Abramowitz and I. A. Stegun, *Handbook of Mathematical Functions with Formulas, Graphs and Mathematical Tables* (Dover, New York, 1964).

Conservation of energy and absorption in acoustic fields for linear and nonlinear propagation

Janusz Wójcik
Department of Ultrasound, Institute of Fundamental Technological Research, Polish Academy of Science, 00-049 Swietokrzyska 21 Warsaw, Poland

(Received 10 December 1996; revised 31 July 1998; accepted 3 August 1998)

In the present paper, the energy effects accompanying a strong sound disturbance of a medium are analyzed. The waves may be, in time, periodic — continuous or pulsed — or have the form of single pulses. The description is based on equations which are commonly applied in nonlinear acoustics. The Fourier analysis, elements of the theory of linear operators, and analytical functions are applied. A general method is given for the construction of the absorption operator in the domain of space–time coordinates $(\mathbf{x},t)$, to which the small-signal absorption coefficient corresponds. By analogy to linear equations and the corresponding dispersions equations, the quasi-dispersion equations in the case of nonlinear description are introduced. Simplification of the ''classical'' equation of nonlinear acoustics was performed. The relations between absorption operators in the space and time domains are shown. It is demonstrated that in nonlinear interactions, where terms of such type — nonlinear function of pressure — dominate, the power (energy) of the disturbance is conserved. Just as in the linear notation, the only reason why the total power (energy) changes is linear absorption, but that one which occurs under the conditions of nonlinear propagation. In consequence, the equations of power (and energy) balancing the disturbance have the same formal shape in nonlinear and linear descriptions. The equations provide a theoretical basis for different, easier, and more accurate methods than those used previously for determination (numerical and experimental) of, e.g., the power density of heat sources generated by sound. The function of the nonlinear gain of absorption and the function of effective absorption were also introduced. On the basis of quasi-dispersion equations the phenomenon of overtone generation (not harmonics) is shortly discussed. [S0001-4966(98)02911-7]

PACS numbers: 43.25.Ed [MAB]

INTRODUCTION

This study emerged as a result of considerations of the energy processes occurring in a medium subjected to a strong acoustic disturbance. Given their medical applications, the present theoretical studies focused on the phenomena of absorption and generation of heat sources in a variety of media. Periodic — continuous or pulsed — waves or single pulses were applied, with powers used in ultrasonography and lithotripsy. The main purpose was to understand the generation of Fourier spectrum components of the disturbance and the exchange of energy between these components, and to consider absorption, in particular, so as to arrive at a general formal description of this phenomenon. In the equations which describe the propagation of strong sound disturbances, the dominating term which describes the generation of harmonics (the extension of the spectrum) is of the second order with respect to the disturbance (pressure). In turn, in these equations, absorption is represented by a term which is linear with respect to the disturbance.[1] In general, it is well-known that nonlinearity enhances the absorption of sound energy by the medium. It seems logical to conclude that, for nonlinear propagation, the equation which describes the conservation of energy taking into account absorption losses (i.e., considering the heat energy generated by the disturbance) should be different from the equation of transport of power or energy (the equation of conservation) for linear propagation. After all, the nonlinear equations include an additional term. In specific equations of transport (conservation), i.e., those that describe separately the power or energy of each spectral component, it produces an additional element of the third order with respect to the disturbance. This term describes the exchange of energy between the *n*-th component and all the others; see Refs. 1, 2. It seems that, for this reason, further progress in the analysis of the problem of energy transport of the potential disturbance with finite amplitude cannot be achieved. The knowledge in this domain and its adaptation for acoustics is presented in Refs. 1–6, and all the other studies on this issue are referred to in Ref. 1.

It turns out — and it will be demonstrated below — that the equations of transport (conservation) of power or energy have the same formal shape for linear and nonlinear descriptions of acoustic disturbances! They are different, however, in their specific physical interpretations and numerical results for the solutions of the same boundary problems (initial or boundary value) in cases of linear and nonlinear propagation. It follows from the fact that in the aforementioned nonlinear interactions the principle of conservation of energy is intact.

A consequence of the equations derived here is a radical change in the method of determination, above all, the opportunity of measuring almost directly, of the absorption, or the power density of sources of heat generated by even very complex acoustic fields (therefore, the ones that are difficult to model numerically). In particular cases, these methods were already applied earlier.[7] Intuitively understandable as

they might be, they were, however, not justified mathematically beyond the applicability range of the linear theory of sound propagation.

The problem of description of energy transport, or more generally, the conservation laws, are important not only for the reasons mentioned earlier. In the situation when the exact (analytical) solutions of the nonlinear equations of acoustics are not known [with the exception of formally important, although trivial, or one-dimensional asymptotical cases (Burgers equation)], every exact result describing the properties of equations and their solutions is valuable. It concerns especially the description of a very important quantity, like energy or power of the propagating disturbance.

Analysis of conservation laws makes it possible to complete the physical interpretation of acoustical phenomena. They may also be helpful in the situation, when the proof of the existence of the solution of propagation equations is needed. In the description of a continuous medium, usually the transport equations of particular kinds of energy (kinetic, internal, thermal) are included in the equations of conservation of momentum and of mass.[4] The density of acoustical energy and the density of the current of acoustical energy are composed of the quantities mentioned above.[5] The transport equation of these quantities for an ideal medium can be easily derived from the above mentioned system of equations for a continuous medium (hydrodynamic system of equations). Nevertheless the supposition of the nonideal continuous medium (not only fluid) makes it necessary to additionally consider the entropy transport equation and the additional thermodynamic relations. In such a case the situation, generally speaking, becomes more complex. Nevertheless it can be shown[8] that the adequate approximations lead to the transport equations of energy of sound presented in this paper and obtained on the bas of propagation equations. This problem, for fluids, was also discussed in Ref. 9.

The main results of our work are presented in Secs. III and IV. Sections I and II have a preliminary character with respect to the next sections. However, the same problems in Sec. II deserve comments as well as an analytical presentation, buy from the point of view of the main purpose of this paper, we had to confine our considerations to an indispensable minimum.

I. BASIC EQUATIONS. ASSUMPTIONS

In a dimensionless system of variables, the ''classical'' equation of nonlinear acoustics,[1] as given by Kuznetsov,[10] which describes potential disturbances in a lossy medium as follows:

$$\Delta\Phi-\partial_{tt}\Phi-2\partial_t\mathscr{A}\Phi=q\beta\partial_t(\partial_t\Phi)^2+2q\partial_t L[\Phi],$$

$$L[\Phi]\equiv\tfrac{1}{2}[(\nabla\Phi)^2-(\partial_t\Phi)^2],\quad \mathbf{v}=\boldsymbol{\nabla}\Phi,\quad \beta\equiv\frac{\gamma+1}{2}, \tag{1}$$

where $\boldsymbol{\nabla}$ is the gradient operator, $\Delta\equiv\boldsymbol{\nabla}\cdot\boldsymbol{\nabla}$ is the Laplace operator and $\boldsymbol{\nabla}\cdot$ is the divergence operation. The following normalizations were applied in Eq. (1):

$$t\equiv\omega_0 t',\quad \mathbf{x}\equiv k_0\mathbf{x}',\quad \partial_t\equiv\frac{1}{\omega_0}\partial_{t'},\quad \boldsymbol{\nabla}\equiv\frac{1}{k_0}\boldsymbol{\nabla}',$$

$$k_0\equiv\frac{\omega_0}{c_0},\quad q\equiv\frac{P_0}{\rho_0 c_0^2},\quad \mathbf{v}\equiv\frac{\mathbf{v}'}{v_0}, \tag{2}$$

$$v_0\equiv\frac{P_0}{\rho_0 c_0^2}=qc_0,\quad \Phi\equiv\frac{\Phi'}{\Phi'_{\mathrm{nor}}},\quad \Phi'_{\mathrm{nor}}\equiv\frac{P_0}{\rho_0\omega_0},$$

where $\Phi'(\mathbf{x}',t')$ is the acoustic potential; $\mathbf{v}'(\mathbf{x}',t')$ is the vector of the velocity field of the medium; $(\mathbf{x}',t')$ are the space and time coordinates [in Cartesian coordinates $\mathbf{x}\equiv(x,y,z)$; and $\mathbf{x}\equiv(\mathbf{r},z)$ in cylindrical ones, where $\mathbf{r}$ is the radial coordinate]; $\omega_0\equiv 2\pi/T_0$, T_0 is the characteristic time interval, or $\omega_0\equiv 2\pi f_0$, f_0 is the characteristic frequency; P_0 is the characteristic pressure (e.g., the pressure amplitude of the disturbance source, or the maximum pressure for a given disturbance); ρ_0, c_0 are the equilibrium density and velocity of sound; $\gamma=c_p/c_v$ is the exponent of the adiabate; and c_p, c_v are the specific heats at constant pressure and volume, respectively. For γ determined empirically[3,11] $\gamma=B/A+1$, B/A being the nonlinearity parameter. From our point of view, due to the characteristic order of approximation of Eq. (1), γ is a quantity obtained from experiment or from the equation of state. In this context, differences between γ determined theoretically or empirically have no influence on the general form of propagation equations. The relations between γ determined in these different ways are discussed in Ref. 3 and 11. For classic viscous media $\mathscr{A}\equiv-\alpha_2\Delta$, $\alpha_2\equiv[4\eta_s'/3+\eta_b'+(\gamma-1)c_h/c_p]\omega_0/2c_0^2$ is the dimensionless hybrid viscosity; η_s', η_b', c_h are, respectively, the kinematic coefficients of shear and bulk viscosity and that of heat conduction.

Equation (1) and its approximation (e.g., the KZK equation[1,12,13]) describes well the sound propagation in a number of media, where the mechanism of absorption is different from that in the classical viscous liquids (numerical simulations). Apart from a few singular cases,[14] references give no general analytical form of the operator $\mathscr{A}$ which would lead to the absorption described in the frequency domain by the absorption coefficient $a(\omega)$ ($\omega\equiv\omega'/\omega_0$ is the dimensionless frequency). This restricts the application of methods for numerical solution of Eq. (1) other than the method of harmonics balance.

When the Fourier representation of medium disturbances is adopted, the effect of operator $\mathscr{A}$ can be described in the following way:

$$\mathscr{A}\Phi\equiv A(\mathbf{x})\underset{\mathbf{x}}{\otimes}\Phi(\mathbf{x},t), \tag{3}$$

$$A(\mathbf{x})=\hat{F}^{-1}[a(\mathbf{e}\cdot\mathbf{K})], \tag{4}$$

where $A(\mathbf{x})$ is the kernel of the integral operation of the convolution $\underset{\mathbf{x}}{\otimes}$ with respect to the space variables; $\mathbf{e}$ is the unit vector in the direction of the real component of the complex wave vector $\mathbf{K}=\mathbf{k}_R-i\mathbf{k}_I$. Apart from the fact that definition [Eqs. (3), (4)] of operator $\mathscr{A}$ agrees in particular with the description of absorption in classical viscous liquids, it results also from the spectral operator theory in relevant function spaces; specifically, from the spectral theorem

for these operators[15–17] and the Fourier representation of operators adopted here. Operator $\mathscr{A}$ can be represented in terms of a complete, orthogonal set of functions other than the Fourier set, e.g., the Hermitian polynomials. Here, the set of Fourier functions $\{\exp(\pm i\mathbf{K}\cdot\mathbf{x})\}$, $\{\exp(\pm i\omega t)\}$, is distinguished by the properties of measuring and generating devices. The measured value of the absorption coefficient $a(\omega)$, $(a(\mathbf{e}\cdot\mathbf{K}))$ is the eigenvalue of operator $\mathscr{A}$ corresponding to a disturbance in the form of eigenfunction, a Fourier function with the frequency ω (the wave vector $\mathbf{K}$). Transition $a(\mathbf{e}\cdot\mathbf{K})\Leftrightarrow a(\omega)$ results from the dispersion relation for the disturbance $\exp[i(\omega t\pm\mathbf{K}\cdot\mathbf{x})]$. In Appendix A the form of the kernel $A(\mathbf{x})$ is determined for the case $a(\omega)=\alpha_1|\omega|$, i.e., $a(\mathbf{e}\cdot\mathbf{K})=\alpha_1\mathbf{e}\cdot\mathbf{K}$. $\hat{F}^{-1}[\,\cdot\,]$ as a generalized Fourier transform. Out of several equivalent ways of determining it, the formula $\hat{F}[\,\cdot\,]\equiv L_B[\,\cdot\,;i\mathbf{K}]$ is chosen, where L_B is the superposition of three one-dimensional two-sided Laplace transforms.[17] The components $i\mathbf{K}=i\mathbf{k}_{R;x,y,z}+\mathbf{k}_{I;x,y,z}$ correspond subsequently to the Laplace variable. In formal representation,

$$
\begin{aligned}
&\hat{F}[\,\cdot\,]\equiv\int_{-\infty}^{\infty}\int_{-\infty}^{\infty}\int_{-\infty}^{\infty}(\,\cdot\,)e^{-i\mathbf{K}\cdot\mathbf{x}}\,d^3\mathbf{x},\\
&F[\,\cdot\,]\equiv\int_{-\infty}^{\infty}(\,\cdot\,)e^{i\omega t}\,dt,\\
&\hat{F}^{-1}[\,\cdot\,]\equiv L_B^{-1}[\,\cdot\,;\mathbf{x}]\\
&\qquad=\frac{1}{(2\cdot\pi)^3}\int_{-\infty-i\kappa_1}^{\infty-i\kappa_1}\int_{-\infty-i\kappa_1}^{\infty-i\kappa_1}\int_{-\infty-i\kappa_1}^{\infty-i\kappa_1}(\,\cdot\,)e^{i\mathbf{K}\cdot x}\,d^3\mathbf{K},\\
&F^{-1}[\,\cdot\,]\equiv\frac{1}{2\pi}\int_{-\infty}^{\infty}(\,\cdot\,)e^{-i\omega t}\,d\omega,
\end{aligned}
\tag{5}
$$

where κ_1, κ_2, κ_3 are the coordinates of the absolute convergence (see, e.g., Ref. 17). Application of the generalized Fourier transform with respect to the variables $(\mathbf{x})$ is a natural result of the use of complex wave vectors in describing the propagation under the conditions of absorption. Analogous results can be obtained using the ''ordinary'' transforms of appropriately modified functions $[g(\mathbf{x})\rightarrow g(\mathbf{x})\exp(-k_I|\mathbf{x}|)]$, but this involves formal and calculation complications. The theory and analysis of the properties of generalized transforms can be found, e.g., in Refs. 17–19. The nonlinearity coefficient q is a small quantity, even when $P_0\sim 100$[MPa]. Dimensionless parameters which characterize the absorption (e.g., α_1, α_2) are similar. This makes it possible to estimate the operator $\mathscr{A}$ as a quantity of the order α (a strict definition of α was given in Chap. V). In the order of approximation under which Eq. (1) was obtained, the pressure and energy density of a potential disturbance are given by $P=-\partial_t\Phi$. When Φ is a periodic function, P is also peridic, and $P_a(\mathbf{x})=\langle P\rangle_{T_0}=0$, where $\langle\,\cdot\,\rangle_{T_0}$ is a time average over 2π (T_0). It does not follow from the fact that P is a periodic function that Φ is also periodic. Moreover, P_a may be different from zero. It follows, however, from the equations of liquid motion in potential approximation that $P_a(\mathbf{x})\sim o(q+\alpha)$ (it can be shown that $P_a\sim q\langle(\Phi_t)^2\rangle_{T_0}$); $o(\,\cdot\,)$ is a small quantity compared with the quantity in the brackets, the order of which is equal to the number of the factors of the product of the expressions in the brackets. The adoption of $P=P_a-\partial_t\Phi$, albeit a more general one, exceeds, however, the order of approximation characteristic of Eq. (1). Two types of disturbances will be considered: *periodic* $\Phi(\mathbf{x},t)=\Phi(\mathbf{x},t+2\pi)$ and in the form of *single pulses* $\Phi(\mathbf{x},t)=\Phi_{St}(\mathbf{x})$ for $t\notin(t_0,t_0+2\pi)$ $[t'\notin(t_0',t_0'+T_0)]$, where T_0 denotes here the duration of the pulse for dimensional variables, and T_0 may be arbitrarily large. In the case of pulsed disturbances, the symbol $\langle\,\cdot\,\rangle_s$ will be used to denote integration with respect to the time t, including the interval $(t_0,t_0+2\pi)$. Since the distinction between periodic disturbances and those in the form of single pulses is of no significance for the initial considerations $\langle\,\cdot\,\rangle$ given here, it is convenient to introduce a uniform symbol so as to avoid the need for repeating the relations already obtained.

II. DISPERSION AND QUASI-DISPERSION RELATIONS

In this section, applying the Fourier analysis, we consider basic relations between the wave parameters and Fouriers spectra of the disturbances described by Eq. (1). The results of the performed analysis, utilized in the next parts of this work are: simplification of Eq. (1) in the description of the nonlinear phenomenon, however, with preservation of accuracy; description of the transition from the absorption operator acting in the domain of space to the operator acting in the time domain.

A. General relations

For an isotropic medium, the complex wave vector $\mathbf{K}$ can be represented by means of the real vector $\mathbf{k}$ and the phase factor $\exp(i\varphi)$,

$$
\mathbf{K}=\mathbf{k}e^{i\varphi}=\mathbf{e}ke^{i\varphi}=\mathbf{e}_K K=\zeta\mathbf{e},\quad K=(\mathbf{K}\cdot\mathbf{K}^*)^{1/2}=(\mathbf{k}\cdot\mathbf{k})^{1/2}=k,
\tag{6}
$$

$$
\zeta\equiv\mathbf{e}\cdot\mathbf{K},\quad \zeta^2=\mathbf{K}\cdot\mathbf{K}=(\mathbf{e}\cdot\mathbf{K})^2=k^2e^{i2\varphi},\quad \mathbf{e}_K=\mathbf{e}e^{i\varphi},
\tag{7}
$$

where $\mathbf{e}_K\equiv\mathbf{K}/k$ is the complex unit vector in the direction of $\mathbf{K}$; $\mathbf{e}\equiv\mathbf{k}/k$; and ζ is the complex wave number. Applying the Fourier transforms $\hat{F}F$ to Eq. (1) we have

$$
\mathrm{Dsp}[\zeta,\omega;a(\zeta)]\hat{\Phi}=qi\omega\hat{U}[\hat{\Phi}]+qi\omega 2\hat{L}[\hat{\Phi}].
\tag{8}
$$

Here $\hat{\Phi}(\mathbf{K},\omega)=\hat{F}F[\Phi(\mathbf{x},t)]$, $\hat{\Phi}(\mathbf{K},-\omega)=\hat{\Phi}^*(\mathbf{K},\omega)=\hat{\Phi}(-\mathbf{K},\omega)$,

$$
\begin{aligned}
\mathrm{Dsp}[\zeta,\omega;a(\zeta)]&\equiv\zeta^2-\omega^2\left(1+i\,\frac{2a(\zeta)}{\omega}\right)\\
&=\mathrm{Dsp}[\zeta,\omega;0]+o(\alpha),
\end{aligned}
\tag{9}
$$

$$
\begin{aligned}
2\hat{L}[\hat{\Phi}]\equiv\hat{F}F[2L[\Phi]]&=-\tfrac{1}{2}\mathrm{Dsp}[\zeta,\omega;0][\hat{\Phi}\otimes\hat{\Phi}]\\
&\quad+\hat{\Phi}\otimes[\mathrm{Dsp}[\zeta,\omega;0]\hat{\Phi}],
\end{aligned}
\tag{10}
$$

$$
\hat{U}[\hat{\Phi}]\equiv\hat{F}F[\beta(\partial_t\Phi)^2]=-\beta(\omega\hat{\Phi})\otimes(\omega\hat{\Phi}),
\tag{11}
$$

$\otimes$ is the convolution operator with respect to $\mathbf{K}$ and ω. Using Eqs. (8) and (9) we may rewrite (10) in the form

$$2\hat{L}[\hat{\Phi}]\equiv\hat{F}F[2L[\Phi]]=-\tfrac{1}{2}\mathrm{Dsp}[\zeta,\omega;a(\zeta)][\hat{\Phi}\otimes\hat{\Phi}]+o(q+\alpha), \tag{12}$$

which, according to Ref. 1, is equivalent to

$$2L[\Phi]=\tfrac{1}{2}\Box\Phi^2-\Phi\Box\Phi=\tfrac{1}{2}\Box\Phi^2+o(q+\alpha),\qquad \Box\equiv\Delta-\partial_{tt}, \tag{13}$$

for the solutions of Eq. (1) and Eq. (8).

B. Dispersion relations

The linear part of Eq. (8) gives the dispersion equation

$$\mathrm{Dsp}[\zeta,\omega;a(\zeta)]=0=\zeta^2-\omega^2\left(1+i\,\frac{2a(\zeta)}{\omega}\right). \tag{14}$$

If $a(\zeta)=\alpha_l(\mathbf{e}\cdot\mathbf{K})^l=\alpha_l\zeta^l$, this equation can be solved strictly, e.g., for $l=1/2,2/3,1,4/3,3/2,2,8/3,3,4,6,8$. For $l=2$ ($\mathscr{A}=-\alpha_2\Delta$) the well-known result is obtained: $K=|\omega|/(1+2\alpha_2\omega^2)^{1/2}$, $\sin(2\varphi)=2\alpha_2\omega/(1+(2\alpha_2\omega)^2)$, i.e., $\mathbf{K}=\mathbf{e}(|\omega|+i\alpha_2|\omega|\omega)+o(\alpha_2^2)=\mathbf{e}(|\omega|+i\ \mathrm{sgn}(\omega)\alpha_2|\omega|^2)+o(\alpha_2^2)$; $\mathrm{sgn}(\omega)\equiv\omega/|\omega|$. For $l=1$, $\mathbf{K}=\mathbf{e}|\omega|(1+i\ \mathrm{sgn}(\omega)\alpha_1)+o(\alpha_1^2)$. The form of $a(\zeta)=\alpha_1\zeta^1$ can be determined in positional representation; see Appendix A. In general, out of different approximate methods, that of successive approximations gives very good results in the range $|2a(\omega)/\omega|<1$. When applied to the equation

$$\zeta=|\omega|\left(1+i\,\frac{2a(\zeta)}{\omega}\right)^{1/2}. \tag{15}$$

Even the first iteration gives a very good result,

$$\zeta=|\omega|\left(1+i\,\frac{2a(\omega)}{\omega}\right)=|\omega|+i\ \mathrm{sgn}(\omega)a(|\omega|)+o(\alpha^2),\quad \mathbf{K}=\mathbf{e}\zeta. \tag{16}$$

It can be noticed that a consequence of the dispersion equation is

$$a(\mathbf{e}\cdot\mathbf{K})=a(\zeta)=a(|\omega|)+o(\alpha^2). \tag{17}$$

C. Quasi-dispersion equations

At the beginning of this part of our considerations, it can be noticed that, if $\hat{\Phi}$ ($\hat{\Phi}\neq 0$) is the solution of Eq. (8), then the dispersion function given by definition of Eq. (9) must be a quantity of the $o(q)$ range.

Equation (8) can be represented in the following way:

$$[\mathrm{QDsp}[\zeta,\omega;a(\zeta),\hat{\Phi}]]\hat{\Phi}=0,$$

$$\mathrm{QDsp}[\zeta,\omega;a(\zeta),\hat{\Phi}]\equiv\mathrm{Dsp}[\zeta,\omega;a(\zeta)]-qi\omega NL[\hat{\Phi}], \tag{18}$$

$$NL[\hat{\Phi}]\equiv(\hat{U}[\hat{\Phi}]+2\hat{L}[\hat{\Phi}])/\hat{\Phi}=(\hat{U}[\hat{\Phi}]+2\hat{L}[\hat{\Phi}])(\hat{\Phi}^*/|\Phi|^2), \tag{19}$$

where, from this moment on, we suppose that $2\hat{L}$ is given by Eq. (12). The term ''dispersion equation'' has a well-defined meaning for linear equations, e.g., Eq. (14). Its solutions, i.e., the relation (relations) between $\mathbf{K}$ (ζ) and ω, are valid for all the solutions of these equations irrespectively of their form. The equation $\mathrm{QDsp}[\zeta,\omega,a(\zeta),\Phi]=0$, which may be rewritten in the form

$$\mathrm{Dsp}[\zeta,\omega;a(\zeta)]=qi\omega\,\frac{\hat{U}[\hat{\Phi}]}{\hat{\Phi}}-\mathrm{Dsp}[\zeta,\omega;a(\zeta)]\times\frac{qi\omega}{2}\,\frac{[\hat{\Phi}\otimes\hat{\Phi}]}{\hat{\Phi}}+o(q(q+\alpha)), \tag{20}$$

can be defined as a ''quasi-dispersion'' one. For, in contrast to Eq. (14), Eq. (20) and the expression in brackets in Eq. (18) depend on $\hat{\Phi}(\mathbf{K},\omega)$, i.e., on the form of the solution. Nevertheless, it can be used to determine the relation between $\mathbf{K}$ (ζ) and ω. It can be noticed that, if $\hat{\varphi}(\mathbf{K},\omega)(\varphi(\mathbf{x},t))$, is a given function but not a solution of Eq. (8), then Eq. (20) is no dispersion equation. However, it may have solutions $\zeta=\zeta(\omega,\varphi)$ (if they exist), but that is not a dispersion relation.

The iteration process applied to the Eq. (20) or Eq. (8), with respect to the linear dispersion function $\mathrm{Dsp}[\cdot]$ or $\mathrm{Dsp}[\cdot]\hat{\Phi}$, shows that the term $\hat{L}$ produces equivalent series which starts from the term of higher $o(q(q+\alpha))$ order approximation than $o(q)$, i.e., of the order of the $\hat{U}$ term. Equation (20) my be solved for $\mathrm{Dsp}[\cdot]$, so it is the equivalent of the infinite sequence of iterations. The result is

$$\mathrm{Dsp}[\zeta,\omega;a(\zeta)]=\frac{qi\omega\hat{U}[\hat{\Phi}]}{(1+qi\omega X)\hat{\Phi}}+o(q(q+\alpha)),\qquad X\equiv\frac{\hat{\Phi}\otimes\hat{\Phi}}{2\hat{\Phi}}, \tag{21}$$

and

$$2\hat{L}=-\frac{1}{2}\,\mathrm{Dsp}[\cdot]\hat{\Phi}\otimes\hat{\Phi}=-\frac{qi\omega X}{1+qi\omega X}\,\hat{U}[\hat{\Phi}]+o(q(q+\alpha)), \tag{22}$$

$$\hat{U}+2\hat{L}=\frac{\hat{U}}{1+qi\omega X}=\hat{U}+o(q). \tag{23}$$

Comparing Eq. (22) with Eq. (23) we see that the term $2\hat{L}$ is of higher order of approximation than the full term in Eq. (23). Because both formulas on the right-hand side have the same denominator (analytical properties), then their other forms (in other coordinates or function spaces, for example, connected by integro-differentials operations, inverse Fourier transforms, etc.) keep this near terms ordering relations. In the study of Ref. 1 it was suggested that the term $q\partial_t L$ does not cause cumulative effects (of the same range as $\hat{U}$; see also Ref. 12). The present considerations yield a similar conclusion.

The results presented above allow to neglect the $\hat{L}$ term in Eq. (18) and also L in Eq. (1). Therefore we may rewrite Eq. (1) in the form

$$\Delta\Phi-\partial_{tt}\Phi-2\partial_t\mathscr{A}\Phi=q\beta\partial_t(\partial_t\Phi)^2+o(q(q+\alpha)). \tag{24}$$

We would like also to stress that, if (in the quasi-dispersion relations) for a certain frequency $\omega=\omega_r$ or $\mathbf{K}=\mathbf{K}_r$ ($\zeta=\zeta_r$)

$\hat{\Phi}=0$ (if it is possible), then from Eq. (8) it must follow $\hat{U}+2\hat{L}|_{\omega=\omega_r}=0$ too. This means that the spectral components with these wave parameters do not appear in the disturbance and are not produced in nonlinear interactions. So they may be used to demonstrate that $NL[\hat{\Phi}]$ exists in the usually sense for $\hat{\Phi}\to 0$, i.e., $qNL[\hat{\Phi}]$ is still a *small* quantity of the order $o(q)$ or higher (in the quasi-dispersion relations). Substituting $\hat{\Phi}(\mathbf{K},\omega)=S(\mathbf{K},\omega)/i\omega$, where S corresponds, by relations $P=-\partial_t\Phi$, to the Fourier spectrum of pressure, we have analogous results as above. Equation (18) assumes the form

$$\left[\zeta^2-\omega^2\left(1+i\,\frac{2a(\zeta)}{\omega}-qNL[S]\right)\right]S=0,$$
$$NL[S]=\beta[S(K,\omega)\otimes S(K,\omega)]/S(K,\omega)+o(q(q+\alpha)). \tag{25}$$

If, in keeping with the form of Eq. (25), the impact of $S(\mathbf{K},\omega)$ $(\hat{\Phi}(\mathbf{K},\omega))$ on the form of this relation is considered, in the category of solutions for which the quantity $qNL[S]$ $(qNL[\hat{\Phi}])$ is small, of the order of $o(q)$ then, using, e.g., the method which was previously applied in Eq. (15), the following result is obtained:

$$\zeta=\mathbf{e}\cdot\mathbf{K}=|\omega|\left(1+i\,\frac{2a(|\omega|)}{\omega}-qNL[S(\mathbf{e}|\omega|,\omega)]\right)^{1/2}$$
$$=|\omega|+o(\alpha+q). \tag{26}$$

Analogous to Eq. (17),

$$a(\zeta)=a(\mathbf{e}\cdot\mathbf{K})=a(|\omega|)+o(\alpha(q+\alpha)), \tag{27}$$

for each $S(\mathbf{K},\omega)(\hat{\Phi}(\mathbf{K},\omega))$ which satisfies Eq. (25) [Eq. (18)] and for which $qNL[S]\sim o(q)$. Hence, for all disturbances satisfying Eq. (24), with the spectrum $S(\mathbf{K},\omega)(\hat{\Phi}(\mathbf{K},\omega))$,

$$a(\zeta)S(\mathbf{K},\omega)=a(|\omega|)S(\mathbf{K},\omega)+o(\alpha(q+\alpha)). \tag{28}$$

Calculating the inverse Fourier transform $\hat{F}^{-1}$ on both sides of Eq. (28) and taking Eqs. (3) and (4) into account, we obtain

$$A(\mathbf{x})\underset{\mathbf{x}}{\otimes}S(\mathbf{x},\omega)=a(\omega)S(\mathbf{x},\omega)+o(\alpha(q+\alpha)). \tag{29}$$

Therefore the operator of absorption, defined as acting on the disturbance by space variables, may be changed [for the solutions of the Eq. (24), as acting by time t variable]

$$\mathscr{A}^t\Phi\equiv A(t)\underset{t}{\otimes}\Phi(\mathbf{x},t),$$
$$A(t)=F^{-1}[a(\omega)]+o(\alpha(q+\alpha)), \tag{30}$$
$$\mathscr{A}=\mathscr{A}^t+o(\alpha(q+\alpha)).$$

We should remember that

$$\mathscr{A}^t e^{\pm i\omega t}=a(\omega)e^{\pm i\omega t},\quad a(-\omega)=a(\omega), \tag{31}$$

which means that $a(\omega)$ is the eigenvalue of the absorption operator corresponding to the eigenfunction $\exp(i\omega t)$.

III. DERIVATION OF EQUATIONS

Both sides of Eq. (24) may be multiplied by $\partial_t\Phi$ and the identity

$$(\partial_t\Phi)\Delta\Phi=\boldsymbol{\nabla}\cdot(\boldsymbol{\nabla}\Phi\ \partial_t\Phi)-\tfrac{1}{2}\partial_t(\boldsymbol{\nabla}\Phi)^2 \tag{32}$$

may be used. The averaging operations $\langle\cdot\rangle_{T_0}$, or integration over the time $\langle\cdot\rangle_S$ may be applied to the equation derived. If u is a periodic function or a pulse, then for many function spaces (or sets), from which function $g(\cdot)$ and $b(\cdot)$ originate,

$$\langle g(u)\partial_t b(u)\rangle=0. \tag{33}$$

Especially Eq. (32) is true if $g(\cdot)$ and $b(\cdot)$ are polynomials. Considering Eq. (32),

$$\langle\nabla\cdot((\partial_t\Phi)\nabla\Phi)-2(\partial_t\Phi).\mathscr{A}\partial_t\Phi\rangle=0+o(q(q+\alpha)). \tag{34}$$

After the aforementioned operations are performed, the nonlinear term $q\beta\partial_t(\partial_t\Phi)^2$ in Eq. (24) does not contribute to Eq. (34). As a result, in formal terms Eq. (34) has the same form as in the linear description!

The quantity

$$\tilde{\mathbf{I}}\equiv-(\partial_t\Phi)\boldsymbol{\nabla}\Phi=P\mathbf{v} \tag{35}$$

is the energy current density vector (the instantaneous value of the power intensity vector, in dimensions units, $[|\mathbf{I}'|]=\mathrm{W/m^2}$). For periodic disturbances the mean value

$$\mathbf{I}\equiv\langle\tilde{\mathbf{I}}\rangle_{T_0}=\langle P\mathbf{v}\rangle_{T_0}=-\langle\Phi_t\boldsymbol{\nabla}\Phi\rangle_{T_0} \tag{36}$$

is the sound intensity vector. For disturbances in the form of single pulses it is impossible to use the concept of mean value but only the operation $\langle\cdot\rangle_s$. It becomes necessary to introduce the pulse energy intensity vector

$$\mathbf{E}\equiv\langle\tilde{\mathbf{I}}\rangle_S\equiv\langle P\mathbf{v}\rangle_S. \tag{37}$$

It is a vector of direction of $\mathbf{v}$ and length equal to the pulse energy which penetrates, in the course of its propagation, a unit surface perpendicular to $\mathbf{v}$ (in dimensions units $[|\mathbf{E}'|]=\mathrm{J/m^2}$). Putting Eq. (36) and Eq. (37) into Eq. (34), we obtain

$$\boldsymbol{\nabla}\cdot\mathbf{I}+2\langle P.\mathscr{A}P\rangle_{T_0}=0+o(q(q+\alpha)) \tag{38}$$

for periodic (continuous or pulsed) disturbances, and

$$\boldsymbol{\nabla}\cdot\mathbf{E}+2\langle P.\mathscr{A}P\rangle_S=0+o(q(q+\alpha)) \tag{39}$$

for pulsed disturbances.

IV. FACTORIZATION

The forms of Eqs. (38) and (39) are general in such a meaning that they are independent of the way of description of the disturbances Φ $(P,\mathbf{v})$, which means of the representation, although the decomposition of the absorption operator with respect to the Fourier function was presented. It was carried out because of the reasons presented already in Sec. I, and because of the general notation and formal properties of the Fourier analysis. It easily allows interpretation and comparison of the results of mathematical analysis with experimental results. Nevertheless, such an option, being natural,

does not formally arise from the derived equations and it is also not necessary for their obtaining. Leaving Eqs. (38) and (39) in general (abstract) forms, that means, in the form independent of the representation of disturbance, with respect to the chosen and complete set of functions, one limits the possibilities of proper interpretation of the equations and their terms.

Application of the concrete, complete set of functions with respect to that the decomposition of the disturbance is performed, yields the particular form of the terms of Eqs. (24), (38), and (39), which depends on this choice. Such a procedure is called ''factorization.'' As above, we consider the Fourier representation of disturbances. The set of Fourier functions is complete, orthogonal, and represents the set of eigenfunctions of the absorption operator. Although the two last properties radically simplify the factorization and the form of the obtained expressions, they are not necessary for their execution. It should be stressed that the advantages of the Fourier analysis mentioned above may be of secondary importance in numerical simulations of the problem under consideration. In such cases, the effectiveness of the numerical code is decisive for the choice of the functional basis.

Adopting the Fourier representation of disturbances,

$$\Phi(\mathbf{x},t)=\frac{1}{2\pi}\int_{-\infty}^{\infty}\frac{S(\mathbf{x},\omega)}{i\omega}\,e^{-i\omega t}\,d\omega+\Phi_{St}(\mathbf{x}),$$

$$P(\mathbf{x},t)=\frac{1}{2\pi}\int_{-\infty}^{\infty}S(\mathbf{x},\omega)e^{-i\omega t}\,d\omega, \tag{40}$$

$$S(\mathbf{x},-\omega)=S^{*}(\mathbf{x},\omega),$$

and for periodic disturbances,

$$\Phi(\mathbf{x},t)=\Phi_0(\mathbf{x})+\frac{1}{2}\sum_{n=1}^{N}\frac{C_n(\mathbf{x})}{in}\,e^{-int}+\text{c.c.},$$

$$P(\mathbf{x},t)=\sum_{n=-N}^{N}P_n=\frac{1}{2}\sum_{n=1}^{N}C_n(\mathbf{x})e^{-int}+\text{c.c.}, \tag{41}$$

$$C_{-n}(\mathbf{x})=C_n^{*}(\mathbf{x}),\quad N=1,2,...,\infty.$$

The case $N=1$ is trivial, as it is applicable only in linear description. In linear problems the number of functions C_n different from zero does not change and it is equal to the number of components used to describe the boundary conditions. In this case, we assume that $N<\infty$ is justified. In nonlinear problems the spectral composition of a disturbance varies and it is only for the description of boundary conditions that $N<\infty$; otherwise, theoretically, $N=\infty$. In permitting N to be a finite number, the properties of computers are taken into account, among other things. For it should be stressed that property Eq. (33) for the nonlinear term in Eq. (24) when multiplied by $\partial_t\Phi$ is independent of the representation of the disturbance; in particular, it does not depend on N. This means that in nonlinear interactions described by $q\beta\partial_t P^2$, energy is also conserved when the infinite system of balance equations $C_n(\mathbf{x})$ is replaced by one cut-down to N equations. Therefore, Eqs. (38) and (39) remain valid for $N<\infty$. It can be noted that the use of Eq. (33) makes it readily possible to demonstrate that the sum N of Eqs. (29), given in Ref. 1, produces an equation with its right-hand side equal to zero, i.e., a special case of Eq. (38) obtained here (for $\mathscr{A}=-\alpha_2\Delta$).

Using Eq. (40) and Eq. (41) in $\langle P.\mathscr{A}P\rangle$, we obtain

$$\langle P.\mathscr{A}P\rangle_S=\frac{1}{2\pi}\int_{-\infty}^{\infty}d\omega\;S^{*}(\mathbf{x},\omega)\int_{-\infty}^{\infty}\int_{-\infty}^{\infty}\int_{-\infty}^{\infty}A(\mathbf{x}-\mathbf{x}')\times S(\mathbf{x}',\omega)d^3\mathbf{x}'. \tag{42}$$

Adopting the results of analysis of the dispersion and quasi-dispersion equations performed in Sec. II, Eqs. (27), (28), (29), we may replace the convolution integral in Eq. (42) by the term on the right-hand side of Eq. (29). Substituting Eq. (29) into Eq. (42), and Eq. (42) into Eq. (39), we obtain for pulsed disturbances,

$$\nabla\cdot\mathbf{E}+\frac{2}{\pi}\int_0^{\infty}\alpha(\omega)|S(\mathbf{x},\omega)|^2d\omega=0+o((q+\alpha)^2). \tag{43}$$

To simplify the calculations for the periodic disturbances we applied an equivalent form of the absorption operator, where Eq. (30) and Eq. (31) may be used. Since, in this case

$$\mathscr{A}^tP(\mathbf{x},t)=\frac{1}{2}\sum_{n=-N}^{N}C_n(\mathbf{x})a(n)e^{-int}, \tag{44}$$

$$\langle P_mP_n\rangle_{T_0}=C_mC_n\langle e^{-imt}e^{-int}\rangle_{T_0}=C_mC_n\delta_{m,-n}, \tag{45}$$

where $\delta_{l,j}$ is the Kronecker delta function, and

$$\langle P.\mathscr{A}^tP\rangle_{T_0}=\frac{1}{4}\sum_{n=-N}^{N}\sum_{m=-N}^{N}C_n(\mathbf{x})C_m(\mathbf{x})a(m)\delta_{m,-n}, \tag{46}$$

then we have

$$\langle P.\mathscr{A}P\rangle=\sum_{n=1}^{N}a(n)\,\frac{|C_n(\mathbf{x})|^2}{2}+o(\alpha(q+\alpha)). \tag{47}$$

Substituting Eq. (47) into Eq. (38), for periodic disturbances

$$\nabla\cdot\mathbf{I}+2\sum_{n=1}^{N}a(n)\,\frac{|C_n(\mathbf{x})|^2}{2}=0+o((q+\alpha)^2),\qquad N=1,2,...,\infty, \tag{48}$$

where

$$\mathbf{I}=\sum_{n=1}^{N}\mathbf{I}_n=\sum_{n=1}^{N}\frac{C_n^{*}\nabla C_n-C_n\nabla C_n^{*}}{i4n}=\sum_{n=-N}^{N}\frac{1}{4}\,C_n^{*}\nabla\,\frac{C_n}{in}, \tag{49}$$

$$\mathbf{E}=\int_{-\infty}^{\infty}P(\mathbf{x},t)\mathbf{v}(\mathbf{x},t)dt=\frac{1}{2\pi}\int_{-\infty}^{\infty}S^{*}(\mathbf{x},\omega)\mathbf{v}(\mathbf{x},\omega)d\omega$$

$$=\frac{1}{2\pi}\int_{-\infty}^{\infty}\Xi(\mathbf{x},\omega)d\omega$$

$$=\frac{1}{2\pi}\int_{-\infty}^{\infty}S^{*}(\mathbf{x},\omega)\boldsymbol{\nabla}\frac{S(\mathbf{x},\omega)}{i\omega}\,d\omega$$

$$=\frac{1}{2\pi}\int_{0}^{\infty}\frac{S^{*}\boldsymbol{\nabla}S-S\boldsymbol{\nabla}S^{*}}{i\omega}\,d\omega, \tag{50}$$

where Ξ is the spectral density of $\mathbf{E}$.

Equations (38) and (39) remain true also after a nonsingular transformation of independent and dependent variables [in the case of Eqs. (43) and (48), as well as in the case of the change of the basis of the function space]. However, in such a case particular forms of terms composing those equations can be varied. Due to the reasons given in Appendix B we show an example demonstrating the influence of the transformation of independent variables on the shape of Eqs. (38) and (43) and Eqs. (39) and (48).

V. ABSORPTION FUNCTIONS

Dividing both sides of Eq. (48) by $2I$, $I=|\mathbf{I}|$, we have

$$\mathrm{a}_{ef}^{I}(\mathbf{x})=\mathrm{a}_{r.ef}^{I}(\mathbf{x}), \tag{51}$$

$$\mathrm{a}_{ef}^{I}(\mathbf{x})\equiv\sum_{n=1}^{N}a(n)\frac{|C_n|^2}{2}\Big/I,\quad \mathrm{a}_{r.ef}^{I}(\mathbf{x})\equiv-\boldsymbol{\nabla}\cdot\mathbf{I}/2I, \tag{52}$$

where $\mathrm{a}_{r.ef}^{I}(\mathbf{x})$ is a well-known[20] differential coefficient (function) of effective absorption; $\mathrm{a}_{ef}(\mathbf{x})$ is the coefficient of effective absorption introduced by the present author. Analogously, over the continuous spectrum range, with $E=|\mathbf{E}|$,

$$\mathrm{a}_{ef}^{E}(\mathbf{x})=\mathrm{a}_{r.ef}^{E}(\mathbf{x}), \tag{53}$$

$$\mathrm{a}_{ef}^{E}(\mathbf{x})\equiv\frac{1}{\pi}\int_{0}^{\infty}a(\omega)|S(\mathbf{x},\omega)|^2\,d\omega\Big/E,$$

$$\mathrm{a}_{r.ef}^{E}(\mathbf{x})\equiv-\boldsymbol{\nabla}\cdot\mathbf{E}/2E. \tag{54}$$

In the case of the power law dependence of the small-signal absorption coefficient on ω, $a(\omega)=\alpha_l\omega^l$, it is convenient to introduce the functions $W_l(\mathbf{x})$,

$$\mathrm{a}_{ef}(\mathbf{x})=\alpha_l W_l(\mathbf{x}),\quad W_l(\mathbf{x})\equiv\sum_{n=1}^{N}n^l\frac{|C_n|^2}{2}\Big/I(\mathbf{x}). \tag{55}$$

If in dimensional units the absorption coefficient has the form $a'(\omega')=\alpha_l'(\omega')^l$, $[\alpha_l']=\mathrm{Np}/(\mathrm{Hz}^l\,\mathrm{m})$, the following relation occurs between the dimensionless parameter α_l and the dimensional one α_l': $\alpha_l=\alpha_l'\omega_0^l/k_0=a'(\omega_0)/k_0$. Given this, $\mathrm{a}_{ef}'(\mathbf{x}')=k_0\mathrm{a}_{ef}(\mathbf{x})=a'(\omega_0)W(\mathbf{x})$. Using the coefficient of effective absorption, it is possible to specify the concept of the parameter α which was introduced in Sec. I to characterize the magnitude of the operator $\mathscr{A}$, $\alpha\equiv\max_{\mathbf{x}}[\mathrm{a}_{ef}^{I,E}(\mathbf{x})]$.

VI. DISCUSSION AND CONCLUSIONS

In general, Eqs. (43) and (48) indicate that the doubled mean value (cumulated $\langle\cdot\rangle_s$) of the absorption operator is equal to the power density of losses (energy of losses). A factor of 2 follows from the conventional definition of $a(\omega)$. Of course, if $a(\omega)\geqslant 0$ for all ω then,

$$\langle P\mathscr{A}P\rangle\geqslant 0.$$

It means that $\mathscr{A}$ is a positive definite operator. However, the above inequality may be also true if for certain ω, $a(\omega)\leqslant 0$. Equations (38) and (39) are true for other linear operators which describe more general types of dispersion, caused not only by absorption.

Although, in formal terms, Eqs. (43) and (48) have the same form in linear and nonlinear descriptions, their specific interpretations are different. In the linear description of sound propagation the nth spectral component of disturbance does not interact with other components; in addition to Eqs. (43) and (48), the following relations are also true:

$$\boldsymbol{\nabla}\cdot\mathbf{I}_n+2a(n)|C_n|^2/2=0,\quad n=1,2...N,\quad N=1,2,...,\infty,$$
$$\nabla\cdot\Xi(\mathbf{x},\omega)+2a(|\omega|)|S(\mathbf{x},\omega)|^2=0,\quad \omega\in(-\infty,\infty), \tag{56}$$

they describe the transport of energy and power of each of the spectral components. In nonlinear theory, the spectral components C_n, $S(\mathbf{x},\omega)$ of the disturbance are not independent of each other. Equations (56) have their right-hand sides,

$$\boldsymbol{\nabla}\cdot\mathbf{I}_n+2a(n)|C_n|^2/2=q\beta\langle P_n\partial_t P^2\rangle_{T_0},$$
$$n=1,2,...,N,\quad N=1,2,...,\infty. \tag{57}$$

In contradistinction to the linear case, in nonlinear description the intensity (energy, power) of the nth spectral component may additionally vary, due to an exchange of energy with the other ones. Nevertheless,

$$\sum_{n=1}^{N}\langle P_n\partial_t P^2\rangle_{T_0}=0. \tag{58}$$

This follows from Eqs. (33) and (41) and expresses the principle of conservation of the total energy in nonlinear interactions. Therefore, after summarize by sides, all spectral Eqs. (56) and, respectively, in nonlinear case, Eqs. (57), we become the equations which have the same formal shapes, Eq. (48). Although, for the nonlinear, P^{NL}, and linear, P^{L}, solutions the same boundary problems,

$$\langle P^{Nl}\mathscr{A}P^{Nl}\rangle\neq\langle P^{L}\mathscr{A}P^{L}\rangle,$$

because the spectral shape of the disturbances (for instance Fourier spectra) are differ in both cases. The absorption of power from a periodic disturbance produces in the medium a stationary spatial power density distribution of heat sources $\dot{Q}(\mathbf{x})=-\boldsymbol{\nabla}\cdot\mathbf{I}$.[21] As a result of the equations introduced here [Eqs. (38), (48)], we have

$$\dot{Q}(\mathbf{x})=\sum_{n=1}^{N}a(n)|C_n(\mathbf{x})|^2. \tag{59}$$

The quantity $\dot{Q}(\mathbf{x})$ plays an important role in the study on heat effects caused by acoustic fields. It follows from Eq. (60) that, irrespective of the geometry of the disturbance, the determination of $\dot{Q}(\mathbf{x})$ at point $\mathbf{x}$ requires only one measurement, of the time profile of pressure, and its Fourier analysis at this point (of course, if for the given medium, the small-signal coefficient of absorption is known). Even if it is possible (for disturbances with a large degree of symmetry), the experimental determination of $-\boldsymbol{\nabla}\cdot\mathbf{I}$ involves large error and requires at least two measurements (for a plane wave). Since in the course of propagation in real media, absorption is accompanied by scattering, the experimentally determined quantity $-\boldsymbol{\nabla}\cdot\mathbf{I}$ will describe damping rather than absorption. The approximation of the measurement points aimed at reducing the share of scattering imposes, however, greater and greater requirements on the sensitivity and accuracy of the measuring devices. An analogous situation occurs in the range of numerical calculations of $\dot{Q}(\mathbf{x})$. Equation (59) directly provides the value of $\dot{Q}(\mathbf{x})$ at point $\mathbf{x}$ [or, if the result is $P(\mathbf{x},t)$, after an additional Fourier analysis]. The calculation of $\dot{Q}(\mathbf{x})=-\boldsymbol{\nabla}\cdot\mathbf{I}$ requires at least one additional operation of numerical differentiation which introduces, in addition, considerable error if the calculations of P or C_n were not accurate. Equation (59) ensures sufficient accuracy, even for not very accurate disturbance calculations. As the accuracy improves,

$$-\boldsymbol{\nabla}\cdot\mathbf{I}\rightarrow\sum_{n=1}^{N} a(n)|C_n(\mathbf{x})|^2. \tag{60}$$

Comparison of quantity $\dot{Q}(\mathbf{x})$ calculated by means of these two methods is a very good ''energy test'' of the accuracy of numerical calculations. Similar conclusions can be drawn about the disturbances with a continuous spectrum. However, it impossible to speak here of stationary heat effects. The quantity

$$Q(\mathbf{x})=\frac{2}{\pi}\int_0^{\infty} a(\omega)|S(\mathbf{x},\omega)|^2\,d\omega \tag{61}$$

is the density distribution of the energy absorbed by the medium as the pulse crosses it, and emitted as heat. It can readily be shown that $\mathrm{a}_{ef}^{I}(\mathbf{x})$ does not depend on the proportion between the duration of the pulse and the repetition time, but only on the time profile of a single pulse in a periodic wave. If the discrete spectrum C_n was obtained by sampling the continuous spectrum $S(\mathbf{x},\omega)$, then for the same media $\mathrm{a}_{ef}^{I}(\mathbf{x})=\mathrm{a}_{ef}^{E}(\mathbf{x})$. It can be shown that in the limits $T_0\rightarrow\infty$ $(T_d/T_0\rightarrow 0)$, where T_d is the duration, Eq. (51) transforms into Eq. (53). It can be noted that for media with $a(\omega)=\alpha_1|\omega|$, the dimensionless parameter $\alpha_1\equiv\alpha_1' c_0$, which is present in Eq. (24), does not depend on ω_0. Hence, all the solutions of boundary problems (which differ only by the parameter ω_0) for these equations, and also all the functions defined on the basis of them, e.g., $W_1, \mathrm{a}_{ef}^{I,E}$, have the same form in a dimensionless system of coordinates. The following functions of nonlinear gain of absorption can be used to characterize the ''force'' of nonlinear interactions and to define the regions of space where they are significant:

$$G_a(\mathbf{x})\equiv \mathrm{a}_{ef}^{NL}(\mathbf{x})/\mathrm{a}_{ef}^{L}(\mathbf{x}). \tag{62}$$

Here a_{ef}^{NL} and a_{ef}^{L} are calculated from Eq. (52) or Eq. (54) for the nonlinear and linear solutions, respectively, of the same boundary problem. It can be noted that, within the linear description of propagation, $\mathrm{a}_{ef}^{L}(\mathbf{x})$ does not depend on the amplitude of the boundary disturbance. An essential advantage of the equations obtained here is that they enable more accurate and easier measurements or calculations of physical quantities which are important for the description of the effects accompanying the sound propagation. Due to the property expressed by Eq. (33), the applied methods are sufficiently general to be used in other equations of nonlinear acoustics, for example, for Eq. (9) referred to in Ref. 22. The formal results are the same.

We would like to discuss here the additional results, obtained as an effect of the quasidispersion equations introduced in Sec. II C, for describing the generation of harmonics. In the linear theory, due to dispersion (in our case absorption), independently of the shape of the solution, there occurs the frequency shift of spectral components of the propagating disturbance with respect to the corresponding frequency components of the disturbance source. The introduced quasi-dispersion equation and its solution [Eq. (26)] demonstrate an additional effect — the nonlinear shift of frequency. It occurs for the fundamental and for secondary components of the spectrum, generated in nonlinear interactions. This frequency shift is proportional to the $q\omega NL[S]$ nonlinear term in Eqs. (25) and (26); this means that its value depends on the solution and is a significant factor in the formation of the spectrum. The expression $q\omega NL[S]$ depends on the term describing the generation of spectral components, called harmonics generation. Also the same term in the quasi-dispersion relation causes their shift in the space of wave parameters (ζ,ω). This phenomenon may be described as deformation of the spectrum acting along the frequency axis (only). Therefore, this phenomenon may be examined in mixed coordinates $(\mathbf{x},\omega)$, which corresponds to the case, when the representation $S(\mathbf{x},\omega)$ or given by Eq. (41) is applied. The distinctly visible effect caused by this deformation is the shift of main components in the spectrum. So the frequencies of the secondary main components are not harmonic frequencies of the first main component. Generally speaking, the frequency relations between the main (principal) components of the spectrum vary in the propagation space. Special results of the experiments performed and numerical simulations with theoretical analysis based on the results obtained in Sec. II C, will be presented in a separate paper [J. Wójcik, ''Overtone generation—Theory and Experiment'' (in preparation)]. Nevertheless, let us call our attention, for example, to Figs. 3, 4, and 5 in Ref. 23, where the mentioned phenomenon was observed by the author of this paper. In the above context, the term ''overtone generation'' is more precise than ''harmonic generation,'' for the abbreviated characterisation of the processes occurring in nonlinear sound wave propagation.

ACKNOWLEDGMENTS

The author is grateful to Professor Leszek Filipczynski and Professor Henryk Zorski for their critical reviews and comments. This work was supported by the KBN Grant No. 7T07B02808.

APPENDIX A

The form of $a(\zeta)=\alpha_1\zeta$ [$a(\mathbf{e}\cdot\mathbf{K})=\alpha_1\mathbf{e}\cdot\mathbf{K}$] [corresponding to $a(\omega)=\alpha_1\omega$] can be determined in positional representation. It follows from the dispersion relation that $\varphi\sim\alpha_1$. From Eq. (A1) it can be found that

$$\alpha_1\mathbf{e}\cdot\mathbf{K}=\alpha_1\frac{\mathbf{K}\cdot\mathbf{K}}{K}+o(\alpha_1{}^2)=\alpha_1\frac{\mathbf{k}\cdot\mathbf{k}}{K}+o(\alpha_1{}^2)$$
$$=\alpha_1K+o(\alpha_1{}^2). \tag{A1}$$

Equation (4) becomes

$$A(\mathbf{x})=\hat{F}^{-1}[\alpha_1K]+o(\alpha_1{}^2)=\alpha_1\hat{F}^{-1}\left[\frac{\mathbf{K}\cdot\mathbf{K}}{K}\right]+o(\alpha_1{}^2). \tag{A2}$$

Since

$$\hat{F}^{-1}\left[\frac{1}{K}\right]=\frac{1}{2\pi^2|\mathbf{x}|^2},\quad \hat{F}^{-1}[\mathbf{K}]=-i\nabla\delta(\mathbf{x}), \tag{A3}$$

where $\delta(\mathbf{x})$ is the Dirac distribution (analytical representation), we obtain

$$A(\mathbf{x})=-\alpha_1\left((\nabla\cdot)\delta(\mathbf{x})\otimes\nabla\delta(\mathbf{x})\otimes\frac{1}{2\pi|\mathbf{x}^2|}\right)$$
$$=\frac{\alpha_1}{\pi^2}\nabla\cdot\delta(\mathbf{x})\otimes\left(\frac{\mathbf{x}}{|\mathbf{x}|^4}\right), \tag{A4}$$

$$\mathscr{A}\Phi=\alpha_1\frac{1}{\pi^2}\nabla\cdot\left(\frac{\mathbf{x}}{|\mathbf{x}|^4}\otimes\Phi(\mathbf{x},t)\right). \tag{A5}$$

In cylindrical coordinates and for axially symmetric disturbances

$$\mathscr{A}\Phi=\alpha_1\frac{1}{\pi}\nabla\cdot\int_0^\infty\int_0^\infty\hat{\mathbf{H}}(z-s,r,\rho)\Phi(\rho,s,t)d\rho^2\,ds, \tag{A6}$$

where $\hat{\mathbf{H}}(z-\zeta,r,\rho)$ is the vector kernel

$$\hat{\mathbf{H}}=\begin{bmatrix}H^z\\H^r\end{bmatrix}=\begin{bmatrix}(z-s)((z-s)^2+r^2+\rho^2)\\r((z-s)^2+r^2-\rho^2)\end{bmatrix}$$
$$\times\frac{1}{(((z-s)^2+r^2+\rho^2)^2-4r^2\rho^2)^{3/2}}. \tag{A7}$$

For a one-dimensional disturbance $\Phi(z.t)$, Eq. (A6) can be reduced to

$$\mathscr{A}\Phi=-\alpha_1\frac{1}{\pi}\partial_z\int_{-\infty}^{\infty}\frac{\Phi(s,t)}{s-z}\,ds=-\alpha_1\partial_z\hat{H}[\Phi], \tag{A8}$$

where $\hat{H}$ is Hilbert's transform. These formulae suggest that the integral operation on the convolution with the kernel $\mathbf{x}/|\mathbf{x}|^4$ can be considered as a three-dimensional generalization of Hilbert's transform. Substitution of Eq. (A8) into the one-dimensional linear equation of propagation and the assumption that $\Phi\sim\exp(-i(\omega t-K_zz))$ leads to the one-dimensional equation Eq. (A4),

$$K_z{}^2-\omega^2-i2\omega\alpha_1K_z\ \mathrm{sgn}(k_z)=0,\quad K_z{}^2=(\mathrm{sgn}(k_z)K_z)^2; \tag{A9}$$

here, the function $\mathrm{sgn}(k_z)$ is a counterpart to the unit vector $\mathbf{e}$.

APPENDIX B

Let us consider the following transformation of coordinates (independent variables) and of the accompanying dependent variables.

$$t\to\tau=t-z,\quad \mathbf{x}\to\overline{\mathbf{x}}=\mathbf{x},$$
$$\partial_t\to\partial_\tau=\partial_t,\quad \nabla\to\overline{\nabla}=\nabla_{\overline{\mathbf{x}}}-\mathbf{e}_z\partial_\tau=\nabla-\mathbf{e}_z\partial_t,$$
$$\Phi(\mathbf{x},t)\to\overline{\Phi}(\overline{\mathbf{x}},\tau)=\Phi(\mathbf{x},t-z), \tag{B1}$$
$$P(\mathbf{x},t)\to\overline{P}(\overline{\mathbf{x}},\tau)=P(\mathbf{x},t-z),$$
$$\mathbf{v}(\mathbf{x},t)\to\overline{\mathbf{v}}(\overline{\mathbf{x}},\tau)=\nabla\overline{\Phi}(\overline{\mathbf{x}},\tau)+\mathbf{e}_z\overline{P}=\mathbf{v}(\mathbf{x},t-z),$$

where $\mathbf{e}_z$ is a unit vector in a chosen direction z. We introduce here the retarded time. It makes it possible to compensate the fast alternating components of disturbances that occur in the original coordinates $(\mathbf{x},t)$ in systems with a distinguished direction of propagation (with a distinguished symmetry). So it is possible to use many asymptotic approximations (near axis or parabolic). As is known, the KZK equation is of this type of description of nonlinear propagation, based on transformation Eq. (B1). Transformation Eq. (B1), when used in numerical calculations, significantly decreases the time of computations. Moreover, many of important characteristics of disturbances (i.e., intensity) and relations between the quantities describing disturbances assume a very simple form. Therefore in those variables many estimations important for the experiments are carried out.

Since $\langle\overline{\nabla}\cdot(\overline{P\mathbf{v}})\rangle=\nabla\cdot\langle(\overline{P\mathbf{v}})\rangle$, then for variables with retarded time,

$$\overline{\nabla}\cdot\overline{\mathbf{I}}+2\langle\overline{P}.\overline{\mathscr{A}P}\rangle_{T_0}=0+o((q+\alpha)^2), \tag{B2}$$

$$\overline{\nabla}\cdot\overline{\mathbf{E}}+2\langle\overline{P}.\overline{\mathscr{A}P}\rangle_{S}=0+o((q+\alpha)^2) \tag{B3}$$

where

$$\overline{\mathbf{I}}=\sum_{n=1}^{N}\overline{\mathbf{I}}_n=\sum_{n=1}^{N}\begin{bmatrix}I_n^z\\I_n^\perp\end{bmatrix}$$
$$=\sum_{n=1}^{N}\frac{1}{2}\begin{bmatrix}|\overline{C}_n|^2+\dfrac{\overline{C}_n^*\partial_z\overline{C}_n-\text{c.c.}}{i2n}\\[2ex]\dfrac{\overline{C}_n^*\nabla_\perp\overline{C}_n-\text{c.c.}}{i2n}\end{bmatrix}, \tag{B4}$$

$$\overline{\mathbf{E}}=\int_{-\infty}^{\infty}\overline{P(\mathbf{x},t)\mathbf{v}}(\mathbf{x},\tau)d\tau=\int_{-\infty}^{\infty}\overline{P}\begin{bmatrix}\overline{P}-\partial_z\overline{\Phi}\\ \nabla_\perp\overline{\Phi}\end{bmatrix}d\tau$$

$$=\frac{1}{2\pi}\int_{-\infty}^{\infty}\overline{\Xi}\,d\omega$$

$$=\frac{1}{2\pi}\int_{-\infty}^{\infty}\overline{S}^*(\mathbf{x},\omega)\overline{\mathbf{v}}(\mathbf{x},\omega)d\omega,$$

$$=\frac{1}{2\pi}\int_{-\infty}^{\infty}\overline{S}^*\begin{bmatrix}\overline{S}+\dfrac{\partial_z\overline{S}}{i\omega}\\ \dfrac{\nabla_\perp\overline{S}}{i\omega}\end{bmatrix}d\omega$$

$$=\frac{1}{\pi}\int_{0}^{\infty}\begin{bmatrix}|\overline{S}|^2+\dfrac{\overline{S}^*\partial_z\overline{S}-\text{c.c.}}{i2\omega}\\ \dfrac{\overline{S}^*\nabla_\perp\overline{S}-\text{c.c.}}{i2\omega}\end{bmatrix}d\omega. \tag{B5}$$

The symbol $\perp$ denotes the components perpendicular to z. Space coordinates transform, described in Eq. (B1), is orthogonal (however trivial) and $|\partial\tau/\partial t|=1$. Therefore $\nabla\cdot\mathbf{I}=\nabla_{\overline{x}}\cdot\mathbf{I}=\nabla\cdot\mathbf{I}$, and from Eqs. (B2) and (B3), the expected (average) value of the absorption operator does not change, $\langle P.\mathscr{A}P\rangle=\langle P.\mathscr{A}P\rangle$. Equations (B1) lead to the following relations between the Fourier spectra of disturbances in an ordinary system of variables $S(\mathbf{x},\omega)$ and those in a system with retarded time $S(\mathbf{x},\omega)(C_n(\mathbf{x}),C_n(\mathbf{x}))$,

$$S(\mathbf{x},\omega)=\overline{S}(\mathbf{x},\omega)e^{i\omega z},\quad C_n(\mathbf{x})=\overline{C}_n(\mathbf{x})e^{inz};$$
$$|S|=|\overline{S}|,\quad |C_n|=|\overline{C}_n|, \tag{B6}$$

$$\mathbf{v}(\mathbf{x},\omega)=\nabla\Phi(\mathbf{x},\omega)=\mathbf{v}_{St}\delta(\omega)+\nabla\frac{S}{i\omega}$$
$$=\mathbf{v}_{St}\delta(\omega)+\left(\nabla\frac{\overline{S}}{i\omega}+\mathbf{e}_z\overline{S}\right)e^{i\omega z}$$
$$=\overline{\mathbf{v}}(\mathbf{x},\omega)e^{i\omega z},$$
$$\mathbf{v}_n(\mathbf{x})=\nabla\frac{C_n(\mathbf{x})}{in}=\left(\nabla\frac{\overline{C}_n}{in}+\mathbf{e}_z\overline{C}_n\right)e^{inz}=\overline{\mathbf{v}}_n(\mathbf{x},\omega)e^{inz}. \tag{B7}$$

$\delta(\omega)$ is the Dirac delta function, and $\mathbf{v}_{St}=\nabla\Phi_{St}(\mathbf{x})$ is the flow field constant in time. Substituting Eq. (B6) in Eqs. (50) and (51) and considering Eqs. (B7), Eqs. (B4) and (B5) are obtained, and conversely. Thus $\mathbf{I}=\mathbf{I}$, $\mathbf{E}=\mathbf{E}$. It can be noted that the forms of average value $\langle\cdot\rangle_{S,T_0}$ of the operator of absorption do not change.

In parabolic approximation, Eqs. (1) and (24) transform into a modified KZK equation, after calculating ∂_τ on both sides. In this case, the terms $o(\cdot)$ are absent. For $\mathscr{A}=-\alpha_2\Delta$ ($\mathscr{A}\cong-\alpha_2\partial_{\tau\tau}$) the KZK equation is obtained. The z-th spectral component $I_n^z=|\overline{C}_n|^2/2$, in parabolic approximation. In general, the relation between I_n and $|\overline{C}_n|^2$ is given by

$$\overline{I}_n=|\overline{\mathbf{I}}_n|=\frac{|\overline{C}_n|^2}{2}\left(\left(1+\frac{\overline{\psi}_{nz}}{n}\right)^2+\left(\frac{\nabla_\perp\overline{\psi}}{n}\right)^2\right)^{1/2}$$
$$=((I_n^z)^2+(I_n^\perp)^2)^{1/2}, \tag{B8}$$

where $\overline{C}_n=|\overline{C}_n|\exp(i\overline{\psi}_n)$. In the approximation of a slowly variable phase (close to the propagation axis),

$$\overline{I}_n=I_n^z\cong|\overline{C}_n|^2/2. \tag{B9}$$

[1] S. I. Aanonsen, T. Barkve, J. N. Tjøtta, and S. Tjøtta, ''Distortion and harmonic generation in the near field of a finite amplitude sound beam,'' J. Acoust. Soc. Am. **75**, 749–768 (1984).

[2] P. J. Westervelt, ''Self-scattering of high intensity sound,'' in *Proceedings of the 3rd International Congress on Acoustics*, Stuttgart, 1959 (Elsevier, Amsterdam, 1961), Vol. I, pp. 316–321.

[3] S. Makarov and D. Ochman, ''Nonlinear and thermoviscous phenomena in acoustics, Part I,'' Acustica **82**, 579–606 (1996).

[4] J. F. Clark and M. McChesney, *The Dynamics of Real Gases* (Butterworths, London, 1964).

[5] L. K. Zarembo and B. A. Krasilnikow, *Introduction to Nonlinear Acoustics* (Nauka, Moscow, 1966).

[6] L. D. Landau and E. M. Lifshitz, *Fluid Mechanics* (Pergamon, Oxford, 1963).

[7] L. Filipczynski and M. Piechocki, ''Estimation of the temperature increase in the focus of lithotriptor for the case of high-rate administration,'' Ultrasound Med. Biol. **16**, 149–156 (1990).

[8] J. Wójcik, ''Energy transport of potential disturbances with finite amplitude in lossy media'' (in Polish), Habilitations thesis, IPPT PAN (1998), in print.

[9] J. N. Tjøtta and S. Tjøtta, ''Nonlinear equations of acoustics,'' in *Frontiers of Nonlinear Acoustics: Proceedings of 12th ISNA*, edited by M. F. Hamilton and D. T. Blackstock (Elsevier Science, London, 1990).

[10] V. P. Kuznetsov, ''Equations of nonlinear acoustics,'' Akust. Zh. **16**, 548–553 (1970).

[11] R. T. Beyer, *Nonlinear Acoustics in Fluids* (Van Nostrand Reinhold, New York, 1984), pp. 302–304.

[12] E. A. Zabolotskaya and R. V. Khokhlov, ''Quasi-plane waves in nonlinear acoustics of bounded beams,'' Sov. Phys. Acoust. **15**, 35–40 (1969).

[13] J. N. Tjøtta and S. Tjøtta, ''Nonlinear equations of acoustics, with application to parametric arrays,'' J. Acoust. Soc. Am. **69**, 1644–1652 (1981).

[14] D. T. Blackstock, ''Generalized Burgers equation for plane waves,'' J. Acoust. Soc. Am. **77**, 2050–2053 (1985).

[15] F. W. Byron and R. W. Fuller, *Mathematics of Classical and Quantum Physics* (Addison-Wesley, Reading, MA), Chap. 9.

[16] L. D. Landau and E. M. Lifshyc, *Quantum Mechanics Nonrelativistics Theory* (Nauka, Moskva, 1974), 3rd ed., Chap. 1.

[17] G. A. Korn and T. M. Korn, *Mathematical Handbook for Scientists and Engineers* (Mc-Graw-Hill, New York, 1961), Chaps. 8, 15.

[18] H. Bremerman, *Distributions, Complex Variables and Fourier Transforms* (Addison-Wesley, Reading, MA, 1965), Chaps. 7, 8.

[19] A. H. Zemanian, *Generalized Integral Transformations* (Wiley, New York, 1968), Chap. 3, p. 64.

[20] E. L. Carstensen, N. D. McKay, D. Dalecki, and T. G. Muir, ''Absorption of finite amplitude focused ultrasound in tissues,'' Acustica **51**, 116–123 (1982).

[21] W. L. Nyborg, ''Heat generation by ultrasound in a relaxing medium,'' J. Acoust. Soc. Am. **70**, 310–312 (1981).

[22] J. N. Tjøtta and S. Tjøtta, ''Finite amplitude ultrasound beams,'' IEEE Ultrasonic Symposium, 709–714 (1994).

[23] A. C. Baker and V. F. Humphrey, ''Distortion and high-frequency generation due to nonlinear propagation of short ultrasonic pulses from a plane circular piston,'' J. Acoust. Soc. Am. **92**, 1699–1705 (1992).

Nonlinear standing waves in an acoustical resonator

Yurii A. Ilinskii, Bart Lipkens, Timothy S. Lucas, Thomas W. Van Doren,
and Evgenia A. Zabolotskaya
MacroSonix Corporation, 1570 East Parham Road, Richmond, Virginia 23228

(Received 6 November 1997; revised 31 July 1998; accepted 3 August 1998)

A one-dimensional model is developed to analyze nonlinear standing waves in an acoustical resonator. The time domain model equation is derived from the fundamental gasdynamics equations for an ideal gas. Attenuation associated with viscosity is included. The resonator is assumed to be of an axisymmetric, but otherwise arbitrary shape. In the model the entire resonator is driven harmonically with an acceleration of constant amplitude. The nonlinear spectral equations are integrated numerically. Results are presented for three geometries: a cylinder, a cone, and a bulb. Theoretical predictions describe the amplitude related resonance frequency shift, hysteresis effects, and waveform distortion. Both resonance hardening and softening behavior are observed and reveal dependence on resonator geometry. Waveform distortion depends on the amplitude of oscillation and the resonator shape. A comparison of measured and calculated wave shapes shows good agreement. © *1998 Acoustical Society of America.* [S0001-4966(98)02711-8]

PACS numbers: 43.25.Gf [MAB]

INTRODUCTION

The resonant macrosonic synthesis technology developed at MacroSonix Corp. involves acoustic standing waves of very high amplitude with peak acoustic pressures that exceed the ambient pressure 3–4 times.[1] When the acoustic pressure is so high, the standing waves are strongly nonlinear, and phenomena such as resonance frequency shift, hysteresis effects, and harmonic generation take place and can be observed. Power is delivered to the resonator by a motor that shakes the entire cavity.

Most of the experimental and theoretical studies reported in the literature are limited to finite-amplitude standing waves in tubes of constant cross section with a piston excitation at one end and a rigid cap at the other. Saenger and Hudson,[2] Weiner,[3] and Temkin[4] assumed in their analysis that the wavefront consists of discontinuous shock fronts connected by a continuous section. Chester[5] introduced a second order theoretical analysis that included the effects of boundary layer and volume absorption. Cruikshank[6] compared measurements in a tube with Chester's predictions and found good qualitative agreement. Coppens and Sanders[7] presented a perturbation expansion for a one-dimensional second order nonlinear wave equation, which they extended later to a three-dimensional model for lossy cavities.[8] A single nonlinear equation was used to describe the finite-amplitude standing waves in a cavity. Linear resonance frequencies and quality factors are used to predict the amplitude of the higher harmonics of the finite-amplitude wave. Gaitan and Atchley[9] used the model of Coppens and Sanders to study finite-amplitude standing waves in so-called harmonic and anharmonic tubes. The harmonic tube was a cylinder, while the anharmonic tube consisted of a cylindrical tube with a midsection that had an expansion or a contraction. The measurements showed good agreement with the model. It was also found that the tubes with nonequidistant modal spectra effectively suppressed the energy transfer from the fundamental to the higher harmonics.

Gaitan and Atchley use the term ''harmonic tubes'' to describe resonators for which the harmonics of the fundamental resonance coincide with the higher resonance frequencies. The term ''anharmonic tube'' is used to describe a resonator for which the harmonics of the fundamental do not coincide with the higher resonance frequencies. This terminology is essentially based on linear parameters. However, confusion can arise, since the term ''anharmonic'' has been used in literature to describe a nonlinear oscillator (see, for example, the book by Goldstein).[10] Therefore we introduce the following terminology: (1) a resonator with an equidistant spectrum, i.e., higher resonances are integer multiples of the fundamental resonance, is called a consonant resonator; and (2) a resonator with a nonequidistant spectrum is called a dissonant resonator. The term ''consonance'' is also used by Coppens and Atchley[11] in their review article on nonlinear standing waves in cavities.

In this paper we introduce a one-dimensional mathematical model that has been developed at MacroSonix to analyze standing waves of high amplitude. The model is based on the nonlinear gas dynamics equations for an ideal gas inside a resonator that is axisymmetric, but otherwise has an arbitrary shape. An external harmonic force shakes the entire resonator cavity and excites the gas oscillation. Losses are introduced through bulk viscosity. The model provides insight into the physics of nonlinear standing waves in resonators of different shape and gives a tool to design resonators that have characteristics suitable for specific applications.

First, in order to study the strongly nonlinear 1D standing waves in the resonator, the time domain basic equation for the velocity potential is derived from the fundamental gasdynamic equations for potential motion of a perfect gas. The equation includes the total nonlinearity of gas and gas dynamic equations, the effects of volume absorption, the external force that shakes the entire resonator, and the resonator radius that varies along the resonator axis. Then the basic equation is prepared for numerical calculations: dimension-

less variables are introduced, the single equation is replaced by the set of two lower order equations, and the set of equations in the time domain is transformed into the spectral equations. N harmonics and the dc component are considered. The equations for the complex amplitudes of spectral components are integrated numerically. In the numerical calculations up to 20 harmonics are taken into account. Several acoustic variables are calculated. First, the harmonic amplitudes of the velocity potential wave are obtained directly from the solution of the frequency domain equations. Second, the shape of the pressure wave is calculated for different coordinates along the resonator axis. Last, a Fourier transform is performed to find the harmonic amplitudes of the pressure wave and the harmonic amplitude distributions along the resonator axis. Three resonator geometries are chosen to demonstrate the results: a cylinder, a cone, and a bulb.

I. BASIC EQUATIONS

Let us consider the one-dimensional acoustic wave field in a resonator of arbitrary axisymmetric shape. The entire resonator is oscillated along its axis by an external force supplied by a motor.

Three equations are required to describe the motion of a viscous gas in the acoustical resonator: (1) the mass conservation equation, (2) the momentum conservation equation, and (3) the state equation.

The mass conservation equation for the resonator with the radius that is variable with the coordinate along the resonator axis may be written in the form

$$\frac{\partial M}{\partial t}+\frac{\partial F}{\partial x}=0. \tag{1}$$

Here the following notations are introduced: M is a mass per unit length, F is a mass flux through the resonator cross section of the radius r, t is time, and x is a coordinate along the resonator. The radius is a function of x

$$r=r(x). \tag{2}$$

The resonator oscillates in the x direction.

In this case, the mass of gas per length unit and its flow through the cross section of radius r are equal to

$$M=\rho\pi r^2, \tag{3}$$

$$F=\rho u\pi r^2, \tag{4}$$

where ρ is the mass density and u is a particle velocity in the x direction.

After substituting Eqs. (3) and (4) into Eq. (1) we obtain the continuity equation for the gas in the resonator of the axisymmetric, but otherwise arbitrary shape:

$$\frac{\partial\rho}{\partial t}+\frac{1}{r^2}\frac{\partial}{\partial x}(r^2\rho u)=0. \tag{5}$$

The momentum equation for one-dimensional motion is

$$\frac{\partial u}{\partial t}+u\frac{\partial u}{\partial x}=-\frac{1}{\rho}\frac{\partial p}{\partial x}-a(t)+\frac{(\zeta+4\eta/3)}{\rho}\frac{\partial}{\partial x}\left(\frac{1}{r^2}\frac{\partial}{\partial x}(r^2u)\right). \tag{6}$$

Here, p is the pressure, $a(t)$ is the acceleration of the resonator, and ζ and η are coefficients of viscosity. All of these equations are written in the coordinate system that is moving with the resonator body.

A few words should be said about the dissipative term [the last term on the right-hand side of Eq. (6)]. In general, the dissipative term in the equation for the i velocity component can be presented in the three-dimensional form (see, for example, Landau and Lifshitz[12])

$$\eta\frac{\partial^2 u_i}{\partial x_k\,\partial x_k}+\left(\zeta+\frac{1}{3}\eta\right)\frac{\partial^2 u_k}{\partial x_i\,\partial x_k}. \tag{7}$$

For the velocity potential φ introduced as

$$u_i=\frac{\partial\varphi}{\partial x_i}, \tag{8}$$

Eq. (7) takes the form

$$\eta\frac{\partial^3\varphi}{\partial x_i\,\partial x_k\,\partial x_k}+\left(\zeta+\frac{1}{3}\eta\right)\frac{\partial^3\varphi}{\partial x_i\,\partial x_k\,\partial x_k}=\left(\zeta+\frac{4}{3}\eta\right)\frac{\partial^3\varphi}{\partial x_i\,\partial x_k\,\partial x_k}. \tag{9}$$

After integrating Eq. (9) over x_i and equating the arbitrary function to 0 we obtain

$$\left(\zeta+\frac{4}{3}\eta\right)\frac{\partial^2\varphi}{\partial x_k\,\partial x_k}=\left(\zeta+\frac{4}{3}\eta\right)\frac{\partial u_k}{\partial x_k}=\left(\zeta+\frac{4}{3}\eta\right)\nabla\cdot u. \tag{10}$$

The term $\nabla\cdot u$ should be written in the one-dimensional form of Eq. (5)

$$\nabla\cdot u=\frac{1}{r^2}\frac{\partial}{\partial x}(r^2u). \tag{11}$$

Combination of Eqs. (10) and (11) yields the dissipative term as written in Eq. (6).

The state equation is taken for an ideal gas

$$p=p_0\left(\frac{\rho}{\rho_0}\right)^{\gamma}, \tag{12}$$

where p_0, ρ_0 are ambient values of the pressure and density and γ is the ratio of specific heats.

Equation (6) written through the velocity potential φ takes the form

$$\frac{\partial^2\varphi}{\partial t\,\partial x}+\frac{1}{2}\frac{\partial}{\partial x}\left(\frac{\partial\varphi}{\partial x}\right)^2=-\frac{1}{\rho}\frac{\partial p}{\partial x}-a(t)+\frac{(\zeta+4\eta/3)}{\rho}\frac{\partial}{\partial x}\left(\frac{1}{r^2}\frac{\partial}{\partial x}\left(r^2\frac{\partial\varphi}{\partial x}\right)\right). \tag{13}$$

After substituting p from Eq. (12) into Eq. (13) and integrating over x we obtain

$$\frac{\partial\varphi}{\partial t}+\frac{1}{2}\left(\frac{\partial\varphi}{\partial x}\right)^2=-\frac{\gamma p_0}{(\gamma-1)\rho_0^{\gamma}}\,\rho^{(\gamma-1)}-a(t)x+\frac{\delta}{r^2}\frac{\partial}{\partial x}\left(r^2\frac{\partial\varphi}{\partial x}\right)+\phi(t). \tag{14}$$

Here, $\phi(t)$ is an arbitrary function of time and δ is

$$\delta=\frac{(\zeta+4\eta/3)}{\rho_0}. \tag{15}$$

The replacement of ρ by ρ_0 in the dissipative term means that the nonlinear terms that include absorption are ignored. This assumption states that the energy dissipation is small.

It is worth noting that the propagation speed c is equal to

$$c^2=\frac{dp}{d\rho}=\frac{\gamma p_0}{\rho_0^{\gamma}}\,\rho^{(\gamma-1)}. \tag{16}$$

The arbitrary function $\phi(t)$ in Eq. (14) is chosen as

$$\phi(t)=\text{const}. \tag{17}$$

Since the velocity potential φ is determined with the precision up to an arbitrary function of time, and we are interested in solutions that are periodic in time, we can add any periodic function to the potential to choose the proper solution; the only thing that cannot be compensated in this way is the dc component of the function ϕ. That's why we put ϕ as written by Eq. (17) where const is chosen to have the linear case in the limit when ρ approaches ρ_0,

$$\text{const}=\frac{c_0^2}{\gamma-1}. \tag{18}$$

Here c_0 is the small signal propagation speed. Equation (14) then takes the form

$$\frac{\partial\varphi}{\partial t}+\frac{1}{2}\left(\frac{\partial\varphi}{\partial x}\right)^2=-\frac{c^2-c_0^2}{\gamma-1}-a(t)x+\frac{\delta}{r^2}\frac{\partial}{\partial x}\left(r^2\frac{\partial\varphi}{\partial x}\right). \tag{19}$$

Differentiation of Eq. (14) with respect to t gives

$$\frac{\partial^2\varphi}{\partial t^2}+\frac{1}{2}\frac{\partial}{\partial t}\left(\frac{\partial\varphi}{\partial x}\right)^2=-\frac{\gamma p_0}{\rho_0^{\gamma}}\,\rho^{(\gamma-2)}\frac{\partial\rho}{\partial t}-\frac{da}{dt}\,x+\frac{\delta}{r^2}\frac{\partial^2}{\partial t\,\partial x}\left(r^2\frac{\partial\varphi}{\partial x}\right). \tag{20}$$

The derivative $\partial\rho/\partial t$ can be eliminated from Eq. (20) by using Eq. (5) in the form

$$\frac{\partial\rho}{\partial t}=-\frac{1}{r^2}\frac{\partial}{\partial x}\left(r^2\rho\frac{\partial\varphi}{\partial x}\right)=-\frac{\partial\rho}{\partial x}\frac{\partial\varphi}{\partial x}-\frac{\rho}{r^2}\frac{\partial}{\partial x}\left(r^2\frac{\partial\varphi}{\partial x}\right). \tag{21}$$

Substitution of $\partial\rho/\partial t$ into Eq. (20) yields

$$\frac{\partial^2\varphi}{\partial t^2}+\frac{1}{2}\frac{\partial}{\partial t}\left(\frac{\partial\varphi}{\partial x}\right)^2=\frac{\gamma p_0}{\rho_0^{\gamma}}\,\rho^{(\gamma-2)}\left[\frac{\partial\rho}{\partial x}\frac{\partial\varphi}{\partial x}+\frac{\rho}{r^2}\frac{\partial}{\partial x}\left(r^2\frac{\partial\varphi}{\partial x}\right)\right]-\frac{da}{dt}\,x+\frac{\delta}{r^2}\frac{\partial^2}{\partial t\,\partial x}\left(r^2\frac{\partial\varphi}{\partial x}\right). \tag{22}$$

The derivative $\partial\rho/\partial x$ is eliminated from Eq. (22) by differentiation of Eq. (14) with respect to x

$$\frac{\partial^2\varphi}{\partial x\partial t}+\frac{1}{2}\frac{\partial}{\partial x}\left(\frac{\partial\varphi}{\partial x}\right)^2=-\frac{\gamma p_0}{\rho_0^{\gamma}}\,\rho^{(\gamma-2)}\frac{\partial\rho}{\partial x}-a(t). \tag{23}$$

The dissipative term is dropped because $\partial\rho/\partial x$ appears only in the nonlinear term in Eq. (22). According to Eq. (23) $\partial\rho/\partial x$ is

$$\frac{\partial\rho}{\partial x}=-\left(\frac{\gamma p_0}{\rho_0^{\gamma}}\,\rho^{(\gamma-2)}\right)^{-1}\left[\frac{\partial^2\varphi}{\partial x\,\partial t}+\frac{1}{2}\frac{\partial}{\partial x}\left(\frac{\partial\varphi}{\partial x}\right)^2+a(t)\right]. \tag{24}$$

Substituting Eq. (24) into Eq. (22) we obtain

$$\frac{\partial^2\varphi}{\partial t^2}+\frac{1}{2}\frac{\partial}{\partial t}\left(\frac{\partial\varphi}{\partial x}\right)^2=-\left[\frac{\partial^2\varphi}{\partial x\,\partial t}+\frac{1}{2}\frac{\partial}{\partial x}\left(\frac{\partial\varphi}{\partial x}\right)^2+a(t)\right]\frac{\partial\varphi}{\partial x}+\frac{\gamma p_0}{\rho_0^{\gamma}r^2}\,\rho^{(\gamma-1)}\frac{\partial}{\partial x}\left(r^2\frac{\partial\varphi}{\partial x}\right)-\frac{da}{dt}\,x+\frac{\delta}{r^2}\frac{\partial^2}{\partial t\,\partial x}\left(r^2\frac{\partial\varphi}{\partial x}\right). \tag{25}$$

Using Eq. (16) we present Eq. (25) in the form

$$\frac{\partial^2\varphi}{\partial t^2}+\frac{1}{2}\frac{\partial}{\partial t}\left(\frac{\partial\varphi}{\partial x}\right)^2=-\left[\frac{\partial^2\varphi}{\partial x\,\partial t}+\frac{1}{2}\frac{\partial}{\partial x}\left(\frac{\partial\varphi}{\partial x}\right)^2+a(t)\right]\frac{\partial\varphi}{\partial x}+\frac{c^2}{r^2}\frac{\partial}{\partial x}\left(r^2\frac{\partial\varphi}{\partial x}\right)-\frac{da}{dt}\,x+\frac{\delta}{r^2}\frac{\partial^2}{\partial t\,\partial x}\left(r^2\frac{\partial\varphi}{\partial x}\right). \tag{26}$$

Propagation speed c^2 is eliminated from Eq. (26) by Eq. (19) to yield

$$c^2=c_0^2-(\gamma-1)\left[\frac{\partial\varphi}{\partial t}+\frac{1}{2}\left(\frac{\partial\varphi}{\partial x}\right)^2+a(t)x\right]. \tag{27}$$

Again, the dissipative term is dropped. After substituting Eq. (27) into Eq. (26) we obtain

$$\frac{c_0^2}{r^2}\frac{\partial}{\partial x}\left(r^2\frac{\partial\varphi}{\partial x}\right)-\frac{\partial^2\varphi}{\partial t^2}+\frac{\delta}{r^2}\frac{\partial^2}{\partial t\,\partial x}\left(r^2\frac{\partial\varphi}{\partial x}\right)=\frac{da}{dt}\,x+a(t)\,\frac{\partial\varphi}{\partial x}+\frac{\gamma-1}{r^2}\,a(t)x\,\frac{\partial}{\partial x}\left(r^2\frac{\partial\varphi}{\partial x}\right)+2\frac{\partial^2\varphi}{\partial x\,\partial t}\frac{\partial\varphi}{\partial x}+\frac{\gamma-1}{r^2}\frac{\partial\varphi}{\partial t}\frac{\partial}{\partial x}\left(r^2\frac{\partial\varphi}{\partial x}\right)+\frac{1}{3}\frac{\partial}{\partial x}\left(\frac{\partial\varphi}{\partial x}\right)^3+\frac{\gamma-1}{2r^2}\left(\frac{\partial\varphi}{\partial x}\right)^2\frac{\partial}{\partial x}\left(r^2\frac{\partial\varphi}{\partial x}\right). \tag{28}$$

Equation (28) describes the nonlinear standing waves in the resonator of axisymmetric, but otherwise arbitrary shape. The resonator shape is given by the function $r=r(x)$. Oscillation of the entire resonator is characterized by the acceleration $a(t)$. The approximations used in the derivation are that the acoustic attenuation is small so that the nonlinear terms with dissipation are dropped, and that the coefficients of viscosity are constant. During the derivation, energy dissipation in the volume is taken into account. Although the energy losses in the boundary layer are not considered here, they are taken into account by an effective absorption coefficient whose value is greater than the volume dissipation. It is interesting to note that for a perfect gas the dynamic equations are reduced to the single equation for the velocity potential. The equation includes only quadratic and cubic nonlinear terms in spite of the fact that one of the original equations, Eq. (12), has the nonlinearity as ρ^{γ}.

For $a(t)=0$ and for an ideal gas without losses, $\delta=0$, Eq. (28) takes the form

$$\frac{c_0^2}{r^2}\frac{\partial}{\partial x}\left(r^2\frac{\partial\varphi}{\partial x}\right)-\frac{\partial^2\varphi}{\partial t^2}=2\frac{\partial^2\varphi}{\partial x\,\partial t}\frac{\partial\varphi}{\partial x}+\frac{\gamma-1}{r^2}\frac{\partial\varphi}{\partial t}\frac{\partial}{\partial x}\left(r^2\frac{\partial\varphi}{\partial x}\right)+\frac{1}{3}\frac{\partial}{\partial x}\left(\frac{\partial\varphi}{\partial x}\right)^3+\frac{\gamma-1}{2r^2}\left(\frac{\partial\varphi}{\partial x}\right)^2\frac{\partial}{\partial x}\left(r^2\frac{\partial\varphi}{\partial x}\right). \tag{29}$$

Equation (29) is the exact equation for the axisymmetric resonator of an arbitrary shape filled with a lossless perfect gas.

For the resonator of constant radius Eq. (29) is reduced to

$$c_0^2\frac{\partial^2\varphi}{\partial x^2}-\frac{\partial^2\varphi}{\partial t^2}=2\frac{\partial^2\varphi}{\partial x\,\partial t}\frac{\partial\varphi}{\partial x}+(\gamma-1)\frac{\partial\varphi}{\partial t}\frac{\partial^2\varphi}{\partial x^2}+\frac{1}{3}\frac{\partial}{\partial x}\left(\frac{\partial\varphi}{\partial x}\right)^3+\frac{\gamma-1}{2}\left(\frac{\partial\varphi}{\partial x}\right)^2\frac{\partial^2\varphi}{\partial x^2}. \tag{30}$$

Equation (30) coincides with Eq. (26) in Chapter 3 of *Model Equations* by Hamilton and Morfey.[13]

II. PREPARATION FOR NUMERICAL CALCULATIONS

Since the problem is solved numerically, some transformations are required to introduce dimensionless variables, to reduce the order of Eq. (28), and to replace the time domain equations with spectral ones.

A. Dimensionless variables

For numerical purposes it is better to write Eq. (28) in dimensionless form. The dimensionless variables are

$$X=\frac{x}{l},\quad T=\omega t,\quad R=\frac{r}{l},\quad A=\frac{a}{l\omega_0^2},\quad \Phi=\frac{\varphi}{l^2\omega_0}, \tag{31}$$

where l is the length of the resonator, ω is the angular frequency of the periodic force that shakes the resonator, and ω_0 is the frequency of the lowest mode of a cylindrical resonator of length l. The frequency ω_0 is equal to

$$\omega_0=\frac{\pi c_0}{l}. \tag{32}$$

In the dimensionless variables Eq. (28) takes the form

$$\frac{1}{\pi^2R^2}\frac{\partial}{\partial X}\left(R^2\frac{\partial\Phi}{\partial X}\right)-\Omega^2\frac{\partial^2\Phi}{\partial T^2}+\frac{G\Omega}{\pi^3R^2}\frac{\partial^2}{\partial T\,\partial X}\left(R^2\frac{\partial\Phi}{\partial X}\right)=\Omega\frac{dA}{dT}X+A(T)\frac{\partial\Phi}{\partial X}+\frac{\gamma-1}{R^2}A(T)X\frac{\partial}{\partial X}\left(R^2\frac{\partial\Phi}{\partial X}\right)+2\Omega\frac{\partial^2\Phi}{\partial X\,\partial T}\frac{\partial\Phi}{\partial X}+\frac{(\gamma-1)\Omega}{R^2}\frac{\partial\Phi}{\partial T}\frac{\partial}{\partial X}\left(R^2\frac{\partial\Phi}{\partial X}\right)+\frac{1}{3}\frac{\partial}{\partial X}\left(\frac{\partial\Phi}{\partial X}\right)^3+\frac{\gamma-1}{2R^2}\left(\frac{\partial\Phi}{\partial X}\right)^2\frac{\partial}{\partial X}\left(R^2\frac{\partial\Phi}{\partial X}\right). \tag{33}$$

Here the new notations, Ω and G, are introduced

$$\Omega=\frac{\omega}{\omega_0},\quad G=\frac{\pi\delta\omega_0}{c_0^2}. \tag{34}$$

In numerical calculations the different dimensionless attenuation coefficient G_1 has been taken

$$G_1=G\Omega_0. \tag{35}$$

Here, Ω_0 is a frequency in the middle of the narrow frequency interval we work with. As a rule, it is a resonance frequency. The value G_1 makes physical sense, it is equal to

$$G_1=\frac{\lambda}{L}, \tag{36}$$

where λ is the wavelength that corresponds to the resonance frequency, and L is the attenuation length which is reciprocal to the attenuation coefficient α for the same frequency

$$L=\frac{1}{\alpha},\quad \alpha=\frac{\delta\omega^2}{2c_0^3}. \tag{37}$$

B. New variables

To reduce Eq. (33) to a set of differential equations that would contain only the first derivatives with respect to X, a new variable is introduced

$$V=R^2\frac{\partial\Phi}{\partial X}. \tag{38}$$

Multiplying all terms of Eq. (33) by R^2 and performing some transformations we obtain the set of two equations

$$\frac{1}{\pi^2}\frac{\partial V}{\partial X}-\Omega^2R^2\frac{\partial^2\Phi}{\partial T^2}+\frac{G\Omega}{\pi^3}\frac{\partial^2V}{\partial T\,\partial X}=\Omega\frac{dA}{dT}XR^2+AV+(\gamma-1)AX\frac{\partial V}{\partial X}+\frac{\Omega}{R^2}\frac{\partial V^2}{\partial T}+(\gamma-1)\Omega\frac{\partial\Phi}{\partial T}\frac{\partial V}{\partial X}+\frac{\gamma+1}{2R^4}V^2\frac{\partial V}{\partial X}-\frac{2}{R^5}\frac{dR}{dX}V^3, \tag{39}$$

and

$$\frac{\partial \Phi}{\partial X} = \frac{V}{R^2}. \tag{40}$$

Equations (39) and (40) should be transformed to frequency domain.

C. Frequency domain equations

The acceleration is assumed to be periodic and can be presented in the form

$$A = \sum_{k=-N}^{N} A_k e^{ikT}. \tag{41}$$

Here A_k are the complex amplitudes of harmonic components of the acceleration, and $A_{-k} = A_k^*$, where A_k^* are complex conjugates to A_k.

The periodic solutions of Eqs. (39) and (40) are

$$V = \sum_{k=-N}^{N} V_k e^{ikT}, \tag{42}$$

$$\Phi = \sum_{k=-N}^{N} \Phi_k e^{ikT}. \tag{43}$$

Here, V_k are the complex amplitudes of the harmonic components of the function V, $V_{-k} = V_k^*$, where the functions V_k^* are complex conjugates, and $V_0 = V_{\mathrm{dc}}$ is the dc component of the function V. The functions Φ_k are the complex amplitudes of the harmonic components of the velocity potential wave. The functions Φ_{-k} are equal to Φ_k^* where the functions Φ_k^* are complex conjugates. The function $\Phi_0 = \Phi_{\mathrm{dc}}$ is the dc component of the velocity potential. N is the number of harmonics included. Both functions V_{dc} and Φ_{dc} are real. All of the complex amplitudes V_k and Φ_k as well as real functions V_{dc} and Φ_{dc} depend only on X. So Eqs. (39) and (40) are replaced by ordinary differential equations for the complex amplitudes of the harmonic components. The equations for the k component are

$$\begin{aligned}
&\frac{1}{\pi^2}\frac{dV_k}{dX} + k^2\Omega^2 R^2 \Phi_k + \frac{ikG\Omega}{\pi^3}\frac{dV_k}{dX} \\
&\quad = ik\Omega R^2 X A_k + \frac{ik\Omega}{R^2}[V^2]_k \\
&\qquad + \sum_{l=-N+k}^{N} \left\{ A_{k-l} V_l + (\gamma-1) X A_{k-l} \frac{dV_l}{dX} \right. \\
&\qquad \left. + i(k-l)(\gamma-1)\Omega \Phi_{k-l} \frac{dV_l}{dX} \right\} \\
&\qquad + \sum_{l=-N}^{N} \left\{ \frac{\gamma+1}{2R^4}[V^2]_{k-l} \frac{dV_l}{dX} - \frac{2}{R^5}\frac{dR}{dX}[V^2]_{k-l} V_l \right\},
\end{aligned} \tag{44}$$

$$\frac{d\Phi_k}{dX} = \frac{V_k}{R^2}. \tag{45}$$

The index k varies from 0 to N, and the term $[V^2]_k$ is

$$[V^2]_k = \sum_{l=-N+k}^{N} V_{k-l} V_l, \tag{46}$$

where the index k takes values from 0 to $2N$. Equation (44) in matrix form is

$$D_{kl} \frac{dV_l}{dX} = F_k. \tag{47}$$

As follows from Eq. (44), the matrix D_{kl} and the function F_k are equal

$$D_{kl} = \left(\frac{1}{\pi^2} + \frac{ikG\Omega}{\pi^3} \right) \delta_{kl} + D'_{k-l}, \tag{48}$$

$$\begin{aligned}
F_k = &-k^2\Omega^2 R^2 \Phi_k + ik\Omega R^2 X A_k + \frac{ik\Omega}{R^2}[V^2]_k \\
&+ \sum_{l=-N+k}^{N} \{A_{k-l} V_l\} - \frac{2}{R^5}\frac{dR}{dX} \sum_{l=-N}^{N} \{[V^2]_{k-l} V_l\},
\end{aligned} \tag{49}$$

where δ_{kl} is the Kronecker delta function, and D'_m is

$$D'_m = -(\gamma-1) X A_m - im(\gamma-1)\Omega \Phi_m - \frac{\gamma+1}{2R^4}[V^2]_m. \tag{50}$$

Note that

$$D'_{-m} = (D'_m)^*, \quad F_{-k} = F_k^*. \tag{51}$$

Equations (47) and (45) are integrated numerically.

D. Algorithm for numerical calculation

First the derivatives dV/dX are expressed from Eq. (47) as

$$\frac{dV_l}{dX} = S_l(V_k, \Phi_k, X). \tag{52}$$

Here, S_l are functions that are obtained from the solution of Eqs. (47). The functions S_l can be calculated analytically because Eqs. (47) are the linear equations with respect to dV/dX, but we calculate them numerically.

Putting together Eqs. (52) and (45) we have a set of $(4N+1)$ coupled first order ordinary differential equations in real variables. These equations can be solved with a Runge–Kutta method. The boundary conditions are given at $X=0$ and $X=1$ (i.e., on the ends of the resonator). There are $(4N+1)$ equations for the boundary conditions. They are

$$V_k = 0, \quad V_{\mathrm{dc}} = 0, \quad \text{at} \quad X = 0, \tag{53}$$

$$V_k = 0, \quad \text{at} \quad X = 1. \tag{54}$$

The condition $V_{\mathrm{dc}} = 0$ at $X=1$ is satisfied automatically if Eqs. (53) are true, and the mass conservation law is satisfied.

In this particular case the fifth-order Runge–Kutta formulas with adaptive stepsize control[14] are applied to the two-point boundary value problem with $(2N+1)$ known functions at $X=0$ and $2N$ given functions at $X=1$.

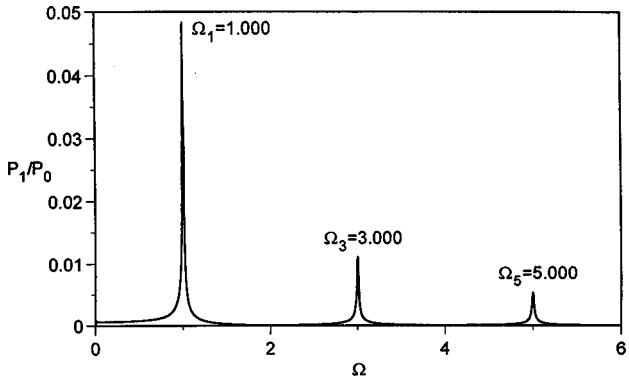

FIG. 1. Response of the cylindrical resonator to the periodic external force that drives the entire resonator with the acceleration amplitude $\tilde{A}=1\times10^{-4}$. Here $N=3$, $G_1=1\times10^{-2}$, and $\gamma=1.2$.

When the functions V_k and Φ_k are obtained, any acoustical variable of interest may be calculated. In particular, the pressure and density in the resonator are evaluated with the following equations:

$$\frac{P}{P_0}=\left[1-(\gamma-1)\pi^2\left(\Omega\,\frac{\partial\Phi}{\partial T}+\frac{1}{2R^4}\,V^2+AX-\frac{G}{\pi^3R^2}\,\frac{\partial V}{\partial X}\right)\right]^{\gamma/(\gamma-1)}, \tag{55}$$

$$\frac{\rho}{\rho_0}=\left[1-(\gamma-1)\pi^2\left(\Omega\,\frac{\partial\Phi}{\partial T}+\frac{1}{2R^4}\,V^2+AX-\frac{G}{\pi^3R^2}\,\frac{\partial V}{\partial X}\right)\right]^{1/(\gamma-1)}. \tag{56}$$

A Fourier transform of the function $P(T,X)$ given by Eq. (55) yields the amplitudes of the harmonic components of the pressure for a certain fixed value X.

III. NUMERICAL RESULTS

Numerical results are presented for three resonators: a cylinder, a cone, and a bulb. The acceleration is assumed to be harmonic. So there is only one harmonic component in the acceleration that is given by the following equation:

$$A(T)=\tilde{A}\cos T. \tag{57}$$

The coefficients A_k in Eq. (41) are

$$A_1=\tilde{A}/2,\quad A_k=0\ \text{ for }\ k>1. \tag{58}$$

In calculations, different values of γ have been taken: $\gamma=1.4$, $\gamma=1.2$, $\gamma=1.15$, and $\gamma=1.1$.

A. Cylindrical resonator

The frequency response of the cylindrical resonator to the periodic acceleration is shown in Fig. 1. The acceleration of the resonator is relatively small, $\tilde{A}=1\times10^{-4}$, so that we operate in the linear region. The cylindrical resonator is a consonant resonator: all the resonance frequencies are integer multiples of the fundamental frequency; i.e., the modes of a cylindrical resonator are equidistant. Note that only odd modes are excited while the even modes are not. For a cylinder, the entire resonator drive can only deliver power when the dynamic pressures at the two opposite ends are out of phase.

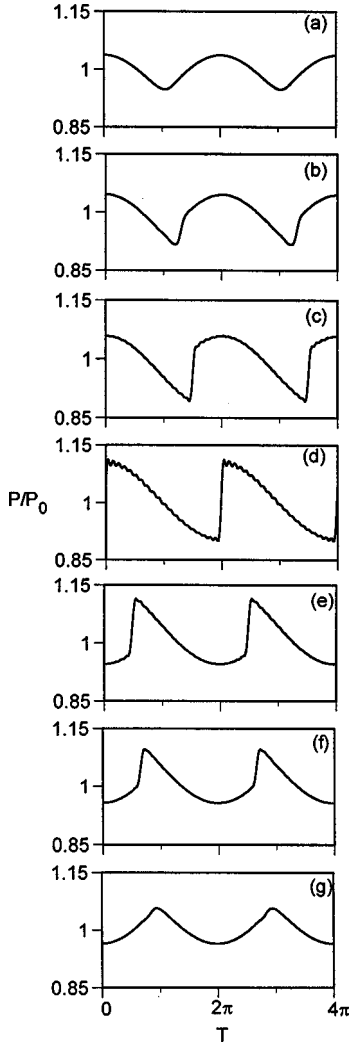

FIG. 2. The wave shapes of the pressure wave near the resonance frequency in the cylindrical resonator: the top three shapes are before resonance: $\Omega=0.970$ (a), $\Omega=0.975$ (b), and $\Omega=0.980$ (c), the fourth waveform corresponds to the resonance frequency $\Omega=1.0$ (d), and the lower three shapes are after resonance: $\Omega=1.020$ (e), $\Omega=1.025$ (f), and $\Omega=1.030$ (g). Here $\tilde{A}=5\times10^{-4}$, $N=20$, $G_1=1\cdot10^{-2}$, $\gamma=1.2$.

Changes of the shape of the pressure wave in a cylindrical resonator are very strong near the resonance frequency ($\Omega=1$). Several waveforms calculated at $X=0$ for $\tilde{A}=5\times10^{-4}$ are shown in Fig. 2. The upper three plots (a), (b), and (c) display pressure wave shapes below resonance. The fourth plot (d) corresponds to the resonance frequency $\Omega=1$. The lower three plots (e), (f), and (g) demonstrate the waveform above resonance. The dimensionless attenuation coefficient is $G_1=1\times10^{-2}$. This value of the attenuation coefficient is chosen in order to obtain a Q-factor that is close to the value of the Q-factor of the cylindrical resonator measured by experiment.[1] The Q-factor is expressed through the attenuation coefficient as

$$Q=\frac{\pi}{G_1}. \tag{59}$$

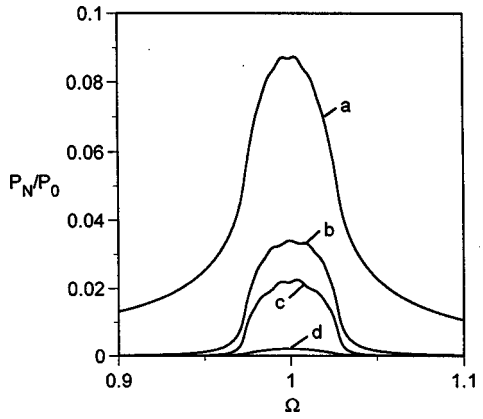

FIG. 3. Frequency response of the pressure amplitudes of the fundamental (curve a), second (curve b), and third (curve c) harmonic components, as well as the dc component (curve d) in the cylindrical resonator. Here $\tilde{A}=5\times10^{-4}$, $N=10$, $G_1=1\times10^{-2}$, $\gamma=1.2$.

The evolution of the waveform shapes agree well with the prediction by Chester[5] and the measurements by Cruikshank[6] and MacroSonix.[1] At low frequencies the cusps appear at the bottom part of the waveform, while for high frequencies cusps appear at the top. In the calculation 20 harmonics are taken into account.

Figure 3 shows the dependence of the amplitudes of the first three harmonics [curves (a), (b), and (c)] and dc component [curve (d)] on the external force frequency. Here the acceleration is $\tilde{A}=5\times10^{-4}$, and the amplitudes are calculated at $X=0$. The dc component is very small.

When the acceleration is increased, the amplitudes of all harmonic components are getting larger, but the resonance curves are getting broader. The intense harmonic generation at the high amplitude introduces additional attenuation that results in a decreasing ''*Q*-factor.'' This can be seen in Fig. 4, where the resonance curve of the fundamental pressure wave is shown for different amplitudes of the acceleration: $\tilde{A}=5\times10^{-4}$ [curve (a)], $\tilde{A}=2.5\times10^{-4}$ [curve (b)], and $\tilde{A}=1\times10^{-4}$ [curve (c)]. From the calculations it is also obvious that there is no significant resonance frequency shift (softening or hardening behavior) noticeable with increasing

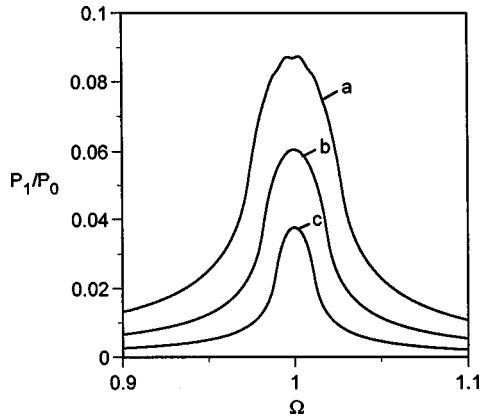

FIG. 4. Frequency response of the fundamental pressure wave in the cylindrical resonator for different acceleration amplitudes: $\tilde{A}=5\times10^{-4}$ (curve a), $\tilde{A}=2.5\times10^{-4}$ (curve b), and $\tilde{A}=1\times10^{-4}$ (curve c). Here $N=10$, $G_1=1\times10^{-2}$, $\gamma=1.2$.

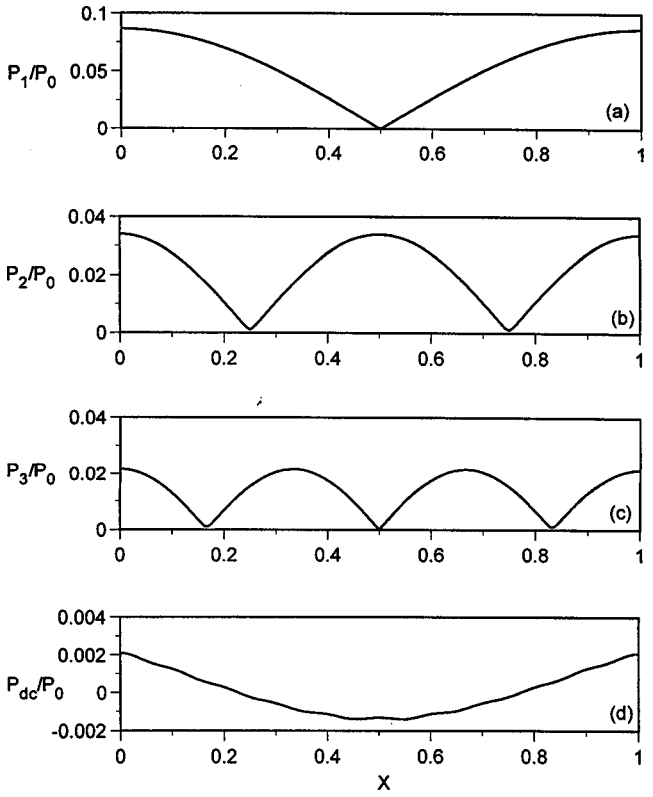

FIG. 5. Amplitude distributions of the fundamental pressure wave (a), the second (b), and third harmonics (c), as well as the dc component (d) along the cylindrical resonator axis. Here $\tilde{A}=5\times10^{-4}$, $N=10$, $G_1=1\times10^{-2}$, $\gamma=1.2$.

amplitude: the resonance curve is not skewed; it remains symmetric, and the maximum response is always obtained at $\Omega=1$. A similar behavior is obtained for the second and third harmonic, where no hardening or softening is observed. Cruikshank[6] presents evidence of a fairly small hard spring behavior for oscillations in a tube excited by a piston. Coppens and Sanders show that the response of the second and third harmonic increases slightly (on the order of 0.2%) with amplitude. In both cases, it is possible that this is caused by the difference in excitation mechanism, i.e., single piston motion in Cruikshank's and Coppens and Sanders' experiment versus entire resonator driving in this model. However, the small increase in resonance frequency observed by Cruikshank and Coppens and Sanders could also be explained by an increase in ambient temperature of the gas inside the tube caused by a higher energy dissipation at higher drive amplitudes. The increase in ambient temperature inside the tube raises the speed of sound at the rate of 0.17% per deg Celsius increase for a 20 deg Celsius tube. In the experiments performed by MacroSonix,[1] no significant hardening or softening is observed, in agreement with the results reported here.

Pressure distributions along the cylindrical resonator axis for $\tilde{A}=5\times10^{-4}$ and $\Omega=1$ are plotted in Fig. 5 for the fundamental component (a), the second harmonic (b), and third harmonic amplitudes (c), as well as for the dc component (d).

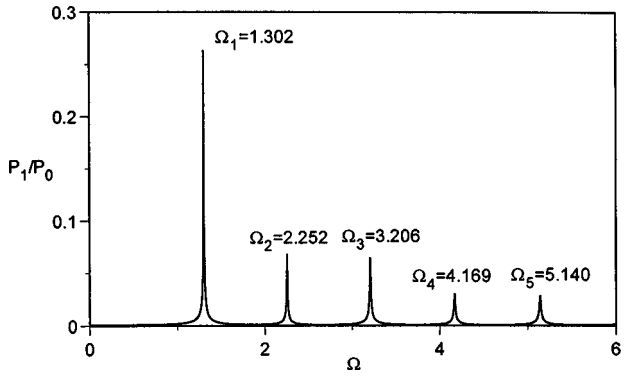

FIG. 6. Response of the conical resonator to the periodical external force that drives the entire resonator with the acceleration amplitude $\tilde{A}=1\times10^{-4}$. Here $N=3$, $G_1=1\times10^{-2}$, $\gamma=1.2$.

B. Conical resonator

The geometry of the conical resonator is

$$r(x)=0.0056+0.2680\cdot x, \quad \text{for} \quad 0\leqslant x\leqslant 0.17 \text{ m}, \quad (60)$$

where r is the radius in meters and x is the coordinate along the resonator axis.

The frequency response of the conical resonator to the periodic acceleration is shown in Fig. 6. Again, the acceleration of the resonator is small, $\tilde{A}=1\times10^{-4}$, so that this closely approximates the linear case. The conical resonator is an example of a dissonant resonator. As seen in Fig. 6, the higher resonance frequencies are not integer multiples of the fundamental frequency.

For high amplitudes of oscillation, for example, when $\tilde{A}=5\times10^{-4}$, hysteresis takes place in the conical resonator. Figure 7 displays the dependence of the fundamental pressure wave amplitude [curves (a)] and the second harmonic [curves (b)] on the frequency: the upper branches are obtained when frequency increases (sweep up), and lower curves correspond to decreasing frequency (sweep down). There are some frequencies where P_1 and P_2 are double valued. The conical resonator behaves as a hard spring, the resonance frequency increases with increasing amplitude. The hardening behavior is very pronounced, and it is very different from that of the cylindrical resonator.

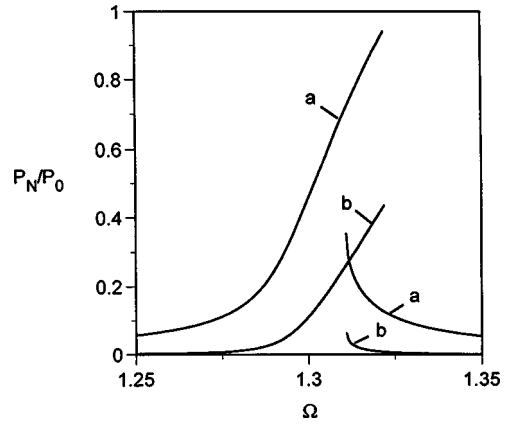

FIG. 7. Frequency responses of the pressure amplitudes of the fundamental (curves a) and second (curves b) harmonic components in the conical resonator. Here $\tilde{A}=5\times10^{-4}$, $N=10$, $G_1=1\times10^{-2}$, $\gamma=1.2$.

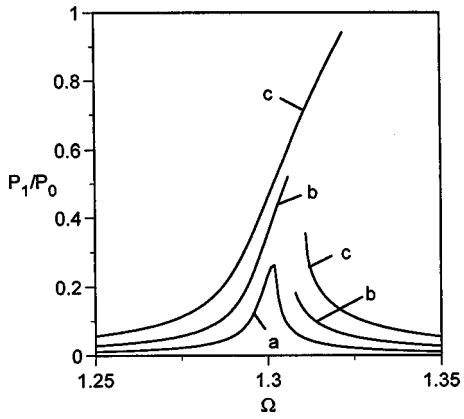

FIG. 8. Frequency responses of the fundamental pressure wave in the conical resonator for different acceleration amplitudes: $\tilde{A}=1\times10^{-4}$ (curve a), $\tilde{A}=2.5\times10^{-4}$ (curves b), and $\tilde{A}=5\times10^{-4}$ (curves c). Here $N=10$, $G_1=1\times10^{-2}$, $\gamma=1.2$.

In Fig. 8 the dependence of the fundamental wave amplitude on frequency is shown for three different amplitudes of the acceleration of the conical resonator. There is no hysteresis for $\tilde{A}=1\times10^{-4}$ [curve (a)]. When $\tilde{A}=2.5\times10^{-4}$ the resonance curve is skewed to the right but the upper and the lower branches are not overlapped [curves (b)]. For $\tilde{A}=5\times10^{-4}$, a multi-valued function is obtained [curves (c)].

Figure 9 shows the pressure waveform at $X=0$ for $\tilde{A}=5\times10^{-4}$ and for the frequency $\Omega=1.325$, at which the maximum pressure response is obtained for the sweep up calculation. The waveform does not resemble a sawtooth shape at all, and has a smooth signal that does not contain any shocks. The waveform has a broad bottom part and a peaked top. The peak pressure is about 3.2 and the minimum pressure is about 0.5, so that a pressure ratio of 6.4 is achieved. This is more than five times the pressure ratio obtained in the cylindrical resonator (see Fig. 2), where the peak pressure is 1.1, the minimum pressure is 0.9, and the pressure ratio is 1.22.

The pressure distributions along the conical resonator are shown in Fig. 10 for the amplitudes of the first three harmonic components [(a), (b), (c)] and the dc pressure (d). The parameters are $\tilde{A}=5\times10^{-4}$, $\Omega=1.325$.

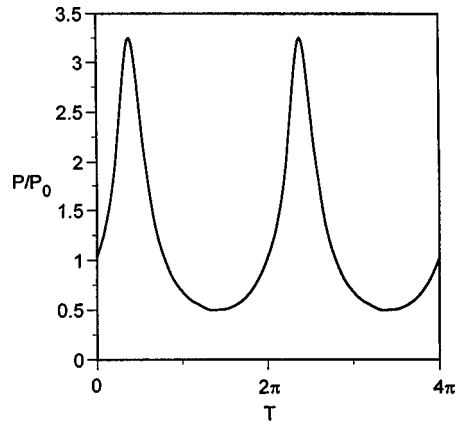

FIG. 9. The wave shape of the pressure wave at frequency $\Omega=1.325$ in the conical resonator. Here $\tilde{A}=5\times10^{-4}$, $N=10$, $G_1=1\times10^{-2}$, $\gamma=1.2$.

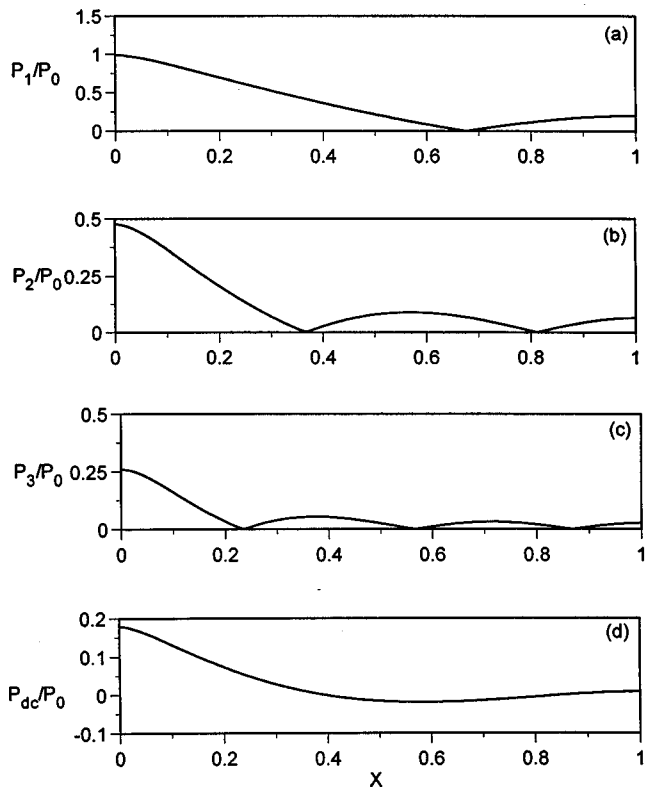

FIG. 10. Amplitude distributions of the fundamental pressure wave (a), the second (b), and third harmonic (c), as well as the dc component (d) along the conical resonator axis. Here $\tilde{A}=5\times10^{-4}$, $\Omega=1.325$, $N=10$, $G_1=1\times10^{-2}$, $\gamma=1.2$.

For the calculation of the conical resonator ten harmonics are taken into account, and the attenuation coefficient is $G_1=1\times10^{-2}$ which gives the ''Q-factor'' that is close to the value measured by experiment.

From Fig. 10 it is seen that the pressure amplitude of the fundamental component at the throat, the narrow end of the resonator at $X=0$, is about five times higher than the pressure at the mouth, the wide end at $X=1$. For the conical resonator the dc pressure amplitude at the throat is much bigger than for the cylinder, a dc pressure value of 0.18 versus 0.002.

From Fig. 10, one sees that at the narrow end the amplitude of the fundamental wave is $P_1/P_0=0.99$, the second harmonic is $P_2/P_0=0.48$, and the third is $P_3/P_0=0.26$. It is interesting to note that high amplitudes of the fundamental wave and harmonics can be achieved without the presence of a shock in the waveform.

C. Bulb resonator

In this section, the strong influence of the resonator shape on the acoustical field inside the resonator is demonstrated. As shown in Fig. 11, two very similar resonators are considered: both of them are bulbs, one has a flare at the narrow end, as seen in Fig. 11(a), and the second one in Fig. 11(b) has no flare. Frequency responses of both resonators are shown in Fig. 12, where (a) corresponds to the bulb with a flare, and (b) to the bulb without a flare. The resonator with a flare has a slightly lower fundamental resonance frequency, but a significantly lower second and third resonance frequency. The hysteresis effects are different for the resonators. Both of these resonators display a softening behavior, i.e., the fundamental resonance frequency decreases with increasing amplitude, but for the bulb with the flare a very pronounced hysteresis is apparent, while for the resonator without a flare no hysteresis is present. The softening behavior for the resonator with a flare is shown in Fig. 13 for three values of the acceleration: there is no hysteresis for $\tilde{A}$

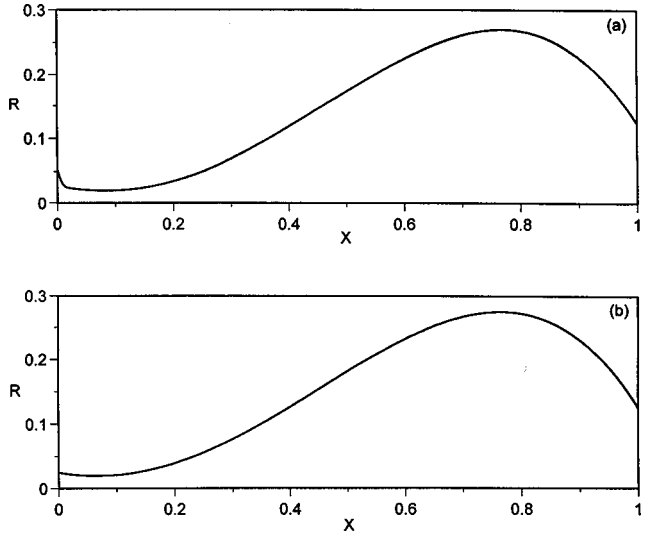

FIG. 11. Two bulb resonators: the bulb with a flare (a) and the bulb without a flare (b).

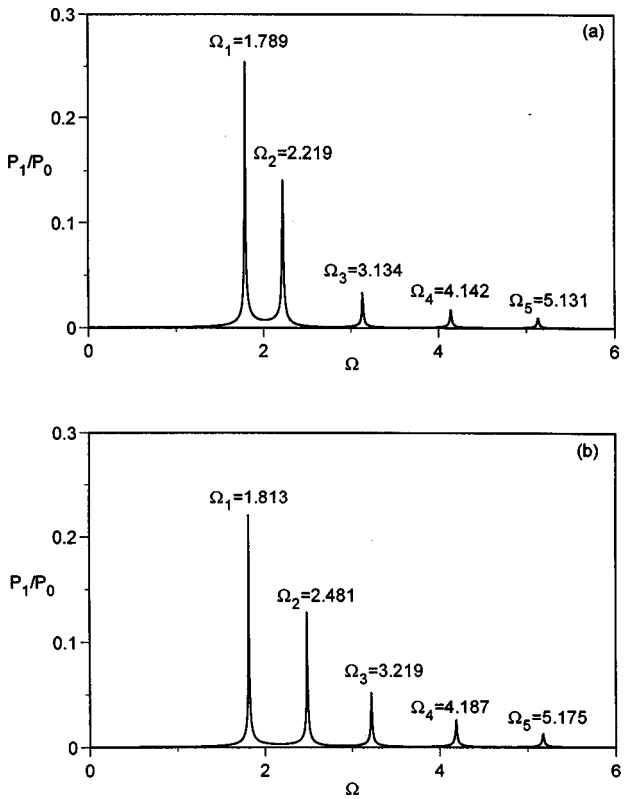

FIG. 12. Responses of two bulb resonators with the flare (a) and without flare (b) to the periodical external force that drives each of them with the acceleration amplitude $\tilde{A}=0.5\times10^{-4}$. Here $N=3$, $G_1=0.5\times10^{-2}$, $\gamma=1.2$.

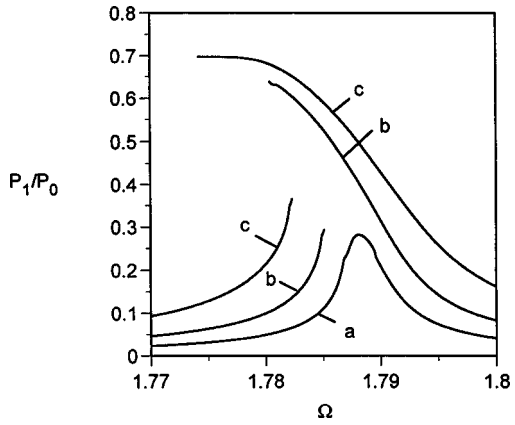

FIG. 13. Frequency responses of the fundamental pressure wave in the bulb with a flare for different acceleration amplitudes: $\tilde{A}=0.25\times10^{-4}$ (curve a), $\tilde{A}=0.5\times10^{-4}$ (curves b), and $\tilde{A}=1\times10^{-4}$ (curves c). Here $N=10$, $G_1=0.5\times10^{-2}$, $\gamma=1.2$.

$=0.25\times10^{-4}$ [curve (a)], but the swept up and swept down branches are overlapped for $\tilde{A}=0.5\times10^{-4}$ [curves (b)] and for $\tilde{A}=1\times10^{-4}$ [curves (c)].

It is necessary to emphasize that any axisymmetric geometry can be considered in this model. Besides a cylinder, a cone, and two bulbs we have modeled a horn, a horn cone, and another bulb. Dissonance characterizes all resonators we considered except the cylinder, and results in a phase mismatching between the harmonic components that prevents shock formation.

D. Comparison with experiment

The numerical results obtained with the model are in good agreement with measurements done at MacroSonix[1] and with results known from the literature.[6,7] A detailed quantitative comparison of experimental results with theoretical predictions is beyond the scope of this paper. Qualitatively, the model describes all phenomena observed in the experiments: resonance frequency shift, hysteresis, and waveform distortion.

As measurements and calculations show, the resonance frequency shift depends not only on the amplitude of oscillations but very strongly on the resonator shape. The resonator shape determines the sign of the frequency shift which results in a hardening (increase of the resonance frequency) or softening (decrease of the resonance frequency) behavior. Measurements conducted at MacroSonix[1] showed the same hardening behavior for the conical resonator and the softening behavior for the bulb resonator. For the cylinder, the calculations showed no significant hardening or softening and again this is confirmed by measurements.

The waveform distortion calculated with the model is very similar to that measured. As an example, Fig. 14 demonstrates a measured wave shape (solid line) and a calculated wave shape (dashed line) for the conical resonator. The waveform predicted by the model is in very good agreement with the measurement. In Table I the values of the fundamental, second, and third harmonic amplitudes are shown for the predicted and the measured waveforms.

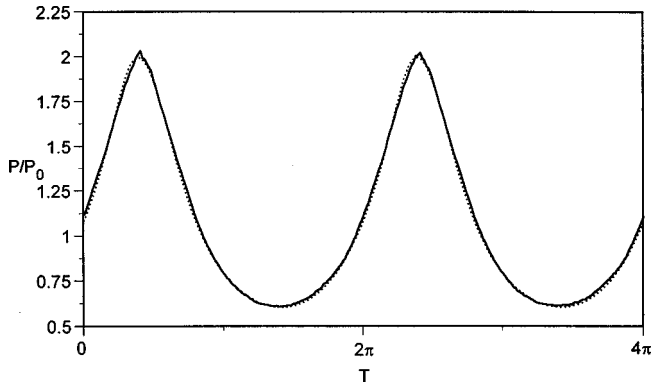

FIG. 14. Comparison of the measured wave shape (the solid line) with the theoretical prediction (the dash line) for the conical resonator. The parameters are $\tilde{A}=2.85\times10^{-4}$, $\Omega=1.31$, $N=10$, $G_1=1\times10^{-2}$, $\gamma=1.1$.

IV. CONCLUSIONS

A one-dimensional mathematical model and a numerical code have been developed for the analysis of nonlinear standing waves in axisymmetric resonators. The model equation is derived from the fundamental gas dynamics equations for an ideal gas. Total nonlinearity of the gas and gasdynamic equations, volume attenuation due to viscosity, entire resonator driving, and dependence of the radius on the coordinate along the resonator are included in the model equation. The model equation is solved numerically in the frequency domain.

Results are presented for a cylindrical, a conical, and a bulb resonator. For the cylinder the results agree well with measurements done at MacroSonix and with predictions and measurements reported in the literature. For moderate to high shaking amplitudes, a shock is formed in the cylinder, and the pressure ratio, ratio of peak pressure to minimum pressure, that can be obtained is very limited. No significant hardening or softening behavior of the cylindrical resonator is observed.

The conical and bulb resonators reveal a different behavior compared to the cylinder. Because of dissonance, harmonic generation is inefficient. Therefore, shock waves are not formed and significant pressure ratios can be achieved. The high pressure ratios and shock-free waveforms create the potential for new applications such as acoustic compressors, pumps, and others. The results of the conical resonator also indicate a very strong hardening behavior while the bulb demonstrates a softening one. At high shaking amplitudes the resonance curves of both cavities are characterized by hysteresis.

Finally, the one-dimensional model presented here can be used as a tool in the design of resonators to create high

TABLE I. Comparison between predicted and measured values of fundamental, second, and third harmonic component amplitudes in a conical resonator.

	P_1/P_0	P_2/P_1	P_3/P_1
Model	0.62	0.31	0.11
Experiment	0.62	0.30	0.09

amplitude standing waves of a given shape and given pressure ratio.

[1] C. Lawrenson, B. Lipkens, T. S. Lucas, D. K. Perkins, and T. W. Van Doren, ''Measurements of macrosonic standing waves in oscillating closed cavities,'' J. Acoust. Soc. Am. **104**, 623–636 (1998).

[2] R. Saenger and G. Hudson, ''Periodic shock waves in resonating gas columns,'' J. Acoust. Soc. Am. **32**, 961–970 (1960).

[3] S. Weiner, ''Standing sound waves of finite amplitude,'' J. Acoust. Soc. Am. **40**, 240–243 (1966).

[4] S. Temkin, ''Propagating and standing sawtooth waves,'' J. Acoust. Soc. Am. **45**, 224–227 (1969).

[5] W. Chester, ''Resonant oscillations in closed tubes,'' J. Fluid Mech. **18**, 44–64 (1964).

[6] D. B. Cruikshank, Jr., ''Experimental investigation of finite-amplitude acoustic oscillations in a closed tube,'' J. Acoust. Soc. Am. **52**, 1024–1036 (1972).

[7] A. B. Coppens and J. V. Sanders, ''Finite-amplitude standing waves in rigid-walled tubes,'' J. Acoust. Soc. Am. **43**, 516–529 (1968).

[8] A. B. Coppens and J. V. Sanders, ''Finite-amplitude standing waves within real cavities,'' J. Acoust. Soc. Am. **58**, 1133–1140 (1975).

[9] D. F. Gaitan and A. A. Atchley, ''Finite amplitude standing waves in harmonic and anharmonic tubes,'' J. Acoust. Soc. Am. **93**, 2489–2495 (1993).

[10] H. Goldstein, *Classical Mechanics* (Addison-Wesley, London, 1981).

[11] A. B. Coppens and A. A. Atchley, ''Nonlinear standing waves in cavities,'' in *Encyclopedia of Acoustics*, edited by M. J. Crocker (Wiley, New York, 1997).

[12] L. D. Landau and E. M. Lifshitz, *Fluid Mechanics* (Pergamon, Oxford, 1987).

[13] M. F. Hamilton and C. L. Morfey, ''Model equations,'' in *Nonlinear Acoustics*, edited by M. F. Hamilton and D. T. Blackstock (Academic, New York, 1997).

[14] W. H. Press, S. A. Teukovsky, W. T. Vetterling, and B. P. Flannery, *Numerical recipes in FORTRAN* (Cambridge U.P., New York, 1992).

Ultrasound induced cavitation and sonochemical yields

Cuiling Gong and Douglas P. Hart
Massachusetts Institute of Technology, Department of Mechanical Engineering, Cambridge, Massachusetts 02139-4307

(Received 6 August 1997; revised 13 August 1998; accepted 18 August 1998)

The introduction of a strong acoustic field to an aqueous solution results in the generation of cavitation microbubbles. The growth and collapse of these microbubbles focuses and transfers energy from the macroscale (acoustic wave) to the microscale (vapor inside the bubbles) producing extremely high localized pressures and temperatures. This unique energy focusing process generates highly reactive free radicals that have been observed to significantly enhance chemical processing. This paper presents a model that combines the dynamics of bubble collapse with the chemical kinetics of a single cavitation event. The effects on sonochemical yields and bubble dynamics of gas composition and heat transfer are assessed and compared with previous theoretical and experimental studies. Results from this model are used to explain unusual experimentally observed sonochemical phenomena. © *1998 Acoustical Society of America.* [S0001-4966(98)06611-9]

PACS numbers: 43.25.Yw [MAB]

LIST OF SYMBOLS

C_k	molar concentration
h_k	enthalpy of species k per unit mass
$k(T)$	$=AT^{\beta}\exp(E/\Re T)$ reaction-rate constant
K	thermal conductivity
P_b	pressure within the bubble
P_∞	pressure at the infinity
R	bubble radius
T	temperature
v	velocity of the bubble wall
V	volume of a bubble
W	mean molecular weight of all species
Y_k	species mass fraction
δr	thermal boundary layer thickness
μ	fluid viscosity
ρ	mean density of all species
ρ_1	fluid density
$\Re$	universal gas constant
σ	coefficient of surface tension
$\dot{\omega}_k$	molar rate of formation due to chemical reaction, in mole/(volume time)
ν_κ	stoichiometric coefficient in reactions
R_r	chemical reaction rate in moles/(volume time)

INTRODUCTION

Ultrasound enhances chemical reactions in a solution through the generation of cavitation microbubbles. The growth and collapse of these microbubbles results in the transfer and focusing of energy from the macroscale motion of the acoustic transducer to the microscale vapor inside the bubbles. During collapse, extremely high pressures on the order of hundreds of atmospheres and extremely high temperatures on the order of thousands of degrees Kelvin are locally generated. Consequently, highly reactive free radicals are produced. This unique energy focusing mechanism provides a means of reacting compounds in an aqueous solution. The applications of this technology range from degradation of environmental pollutants to drug synthesis for medical treatment.

Sonochemistry, the chemistry associated with ultrasound, is governed by parameters that include amplitude and frequency of an applied sound field, temperature, surface tension, vapor pressure, gas content, and nuclei density of the solution, as well as vessel and probe geometry.[1] The close coupling of these parameters as well as the small size and high oscillation frequency of the microbubbles, and the low species concentration inside any single bubble make experimental and theoretical investigations of sonochemistry extremely difficult. Nonetheless, there have been a number of investigations from various perspectives each providing useful insight into this fascinating phenomenon.

The dynamics of cavitation bubbles in the absence of chemical reactions has been extensively investigated largely because of its importance to ship propulsion and hydraulic pumping. Rayleigh and later Plesset studied the dynamics of a single cavitation bubble leading to the well-known Rayleigh–Plesset equation.[2,3] Gaitan *et al.*, using a unique laser scattering technique, experimentally investigated the behavior of single bubbles pulsating in a 23.3-kHz, ± 1.22-atm acoustic field.[4] Matsumoto and Takemura studied thermal conduction, vapor condensation, and diffusion of noncondensable gas on bubble motion.[5]

Except for a few pioneering researchers, the chemical kinetics of cavitating bubbles, until recently, has received little attention. Anbar and Pecht investigated the location of the sonochemical formation of hydrogen peroxide and found that H_2O_2 is produced in the bubble vapor phase and not in the liquid phase.[6] Hart and Henglein conducted extensive experiments of the production rate of H_2O_2 when water is sonicated under various gas mixtures.[7,8] Suslick *et al.* investigated the application of sonochemistry in numerous commercial processes and found that either better quality of the

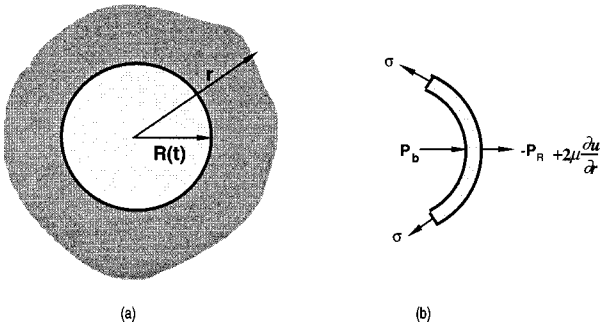

FIG. 1. (a) Sketch for bubble modeling. (b) Boundary conditions at the bubble wall.

products was achieved or simpler experimental conditions were required when ultrasound was introduced.[9–11] In addition, Suslick, along with Flint, analyzed the sonoluminescence spectrum from silicone oil and estimated the effective cavitation temperature to be approximately 5000 K.[12]

Several recent studies have attempted to explain the interactions between bubble motion and chemical kinetics. Arguably, the most insightful and certainly the most extensive of these studies is the one by Kamath *et al.*[13] Using a comprehensive thermal model, they estimate the production of radicals resulting from the dissociation of water vapor in an oscillating argon bubble. They conclude that the bubble radius and heat transfer between the bubble and the liquid are critical parameters for sonochemical yields. Despite the detail of this model, it does not directly couple the dynamics of the bubble with the chemical reactions that take place in the vapor phase. Consequently, the effects of chemical reactions on the temperature field of the bubble are not taken into account. More significant is the assumption of constant gas properties made in this model. The enthalpy, entropy, and specific heat of bubble gas contents vary significantly with temperature and must be accurately modeled to predict sonochemical behavior.

This paper presents a model that directly couples chemical kinetics occurring in a cavitation bubble with the bubble dynamics. By combining the extensive chemical kinetics program CHEMKIN-II, developed at Sandia National Laboratory, with a detailed bubble dynamic model, the effect of parameters such as dissolved gas content, initial bubble radius, acoustic pressure, and acoustic frequency on bubble vapor chemistry can be systematically investigated. Results from this model are compared with results from the model of Kamath *et al.* and experimental results obtained by Hart and Henglein. Such a model provides a means of investigating the chemical kinetics that takes place at each stage of the bubble collapse process elucidating the mechanics of unusual sonochemical phenomena and helping to resolve fundamental scaling relationships.

I. MODEL

The model presented herein is derived from the conservation of species, momentum, and energy. It assumes a single spherical bubble immersed in an unbound liquid, as shown in Fig. 1(a). The dynamic behavior of the bubble wall can be obtained from the equations for the conservation of mass,

$$4\pi R^2 u(R,t) = 4\pi r^2 u(r,t), \tag{1}$$

and the conservation of momentum,

$$\frac{\partial u}{\partial t} + u\,\frac{\partial u}{\partial r} = -\frac{1}{\rho_l}\frac{\partial P}{\partial r} + \frac{\mu}{\rho_l}\left(\frac{1}{r^2}\frac{1}{\partial r}\left(r^2\,\frac{\partial u}{\partial r}\right) - \frac{2u}{r^2}\right). \tag{2}$$

Substituting Eq. (1) into Eq. (2) and applying the relation $v = u(R,t) = dR/dt$ before integrating in the r direction from R to infinity, the equation

$$R\,\frac{dv}{dt} + \frac{3}{2}\,v^2 = \frac{1}{\rho_l}\,(P_R - P_\infty) \tag{3}$$

is obtained. At the bubble wall, as shown in Fig. 1(b), the force balance provides a connection between the internal bubble pressure and the pressure immediately outside the bubble,

$$P_R = P_b - \frac{2\sigma}{R} - \frac{4\mu v}{R}. \tag{4}$$

Substituting this expression for P_R into Eq. (3), the well-known Rayleigh–Plesset equation that describes the dynamics of bubble motion is obtained,[2,3]

$$R\,\frac{dv}{dt} = \frac{1}{\rho_l}\left(P_b - \frac{2\sigma}{R} - \frac{4\mu v}{R} - P_\infty\right) - \frac{3}{2}\,v^2. \tag{5}$$

The coupling of the Rayleigh–Plesset equation with chemical kinetics is accomplished by accounting for the conservation of energy and chemical species in the vapor phase of the bubble. The equation governing the conservation of species is

$$\frac{dY_k}{dt} = \frac{\dot{\omega}_k \cdot W_k}{\rho} \tag{6}$$

and the energy equation, allowing heat conduction between the bubble and the solution neglecting viscous dissipation of gases inside the bubble, can be written as

$$\rho\,\frac{dh}{dt} - \frac{dP_b}{dt} = \nabla(K \cdot \nabla T). \tag{7}$$

Note that $h = \Sigma Y_k h_k$ and the enthalpy of each component $h_k = \Delta h^0_{f,k} + \int_{T_0}^{T} C_{p,k}\,dT$. Carrying out the derivatives of each component of h with respect to time, Eq. (7) becomes

$$\frac{dP_b}{dt} = \rho\left(\sum_k h_k\,\frac{dY_k}{dt} + \overline{c_p}\,\frac{dT}{dt}\right) - K\,\frac{\Delta T}{(\delta r)^2}, \tag{8}$$

where $\overline{c_p} = \Sigma Y_k C_{p,k}$ and ΔT is the temperature difference between the bulk solution and the bubble. The important feature of Eq. (8) is that the bulk temperature and pressure of the bubble as well as properties of each individual species inside the bubble are present in the same equation. Since the bulk bubble temperature and pressure are directly related to the bubble dynamic behavior, and the production of species is directly related to the chemical kinetics, Eq. (8) provides a direct coupling between bubble dynamics and chemical kinetics. Note that the heat conduction term in Eq. (7) has been linearized in Eq. (8) based on a thermal boundary layer of

thickness δr. This linearization greatly simplifies calculations, eliminating the need to accurately model species transport within the bubble. The thermal boundary layer thickness, δr, is based on results from the model of Kamath *et al.* and is typically 20% of the bubble radius.

The gas inside the bubble is treated as an ideal gas as the partial pressure of vapor, in general, is very small. Thus the corresponding state equation is

$$P_b V = m\Re T/W. \tag{9}$$

Differentiation of the state equation with respect to time provides yet another coupling relation between bubble dynamics and the chemical kinetics occurring in the vapor phase,

$$\frac{dT}{dt} = -WT\left(\sum_k \frac{1}{W_k}\frac{dY_k}{dt}\right) + \frac{4\pi R^2 W}{m\Re}\left(\frac{R}{3}\frac{dP_b}{dt} + P_b\frac{dR}{dt}\right). \tag{10}$$

The time derivative of temperature can be obtained by eliminating the time derivative of pressure term from Eq. (8) and Eq. (10),

$$\frac{dT}{dt} = \left(-WT\sum_k \frac{1}{W_k}\frac{dY_k}{dt} + \frac{W}{\Re}\sum_k h_k\frac{dY_k}{dt} + \frac{3T}{R}\frac{dR}{dt}\right) \Big/ \left(1 - \frac{W}{\Re}\overline{c_p}\right). \tag{11}$$

Detailed chemical kinetics is required to model the variation of the mass fraction of each species. Even for the simplest sonochemical system, sonication of a pure water solution under argon gas, the kinetics are exceedingly complicated. A total of 21 elementary, independent, reversible reactions and 8 species are necessary to accurately compute the reaction rates and the rate of formation of all species under a wide range of temperature and pressure variation. All 21 reaction mechanisms are taken into account in the present model. The species involved in each or the reactions are stable species: H_2, O_2, H_2O; radicals: O, H, OH; and metastable species: HO_2, H_2O_2. Five chain reactions of radicals among the 21 mechanisms are listed here as examples:

$$H_2O + M \Leftrightarrow H^{\cdot} + OH^{\cdot} + M, \tag{12}$$

$$H^{\cdot} + H^{\cdot} + M \Leftrightarrow H_2 + M, \tag{13}$$

$$OH^{\cdot} + OH^{\cdot} + M \Leftrightarrow H_2O_2 + M, \tag{14}$$

$$H_2O_2 + O^{\cdot} \Leftrightarrow OH^{\cdot} + HO_2^{\cdot}, \tag{15}$$

$$H_2O + OH^{\cdot} \Leftrightarrow H_2O_2 + H^{\cdot}, \tag{16}$$

where M is the third body which plays an important role in the reactions supplying the energy required for dissociation or absorbing the energy released by recombination. For a general reaction with A and B being the reactants and C and D the products,

$$\nu_A A + \nu_B B \rightarrow \nu_C C + \nu_D D, \tag{17}$$

the reaction rate is

$$R_r = k(T) C_A^{\nu_A} C_B^{\nu_B}, \tag{18}$$

where C_A and C_B are the molar concentrations of reactants A and B. The reaction rate constant $k(T)$ in the temperature dependent Arrhenius form is

$$k(T) = AT^{\beta}\exp\left(-\frac{E}{\Re T}\right), \tag{19}$$

where A is the frequency factor which accounts for the fraction of colliding molecules having the necessary orientation for the reaction to proceed, β is a generalized temperature exponent, and E is the activation energy required for the reaction to proceed. The relation between $\dot{\omega}_k$ in Eq. (6) and R_r is $\dot{\omega}_k = \nu_k R_r$. The rate coefficients A, β, and E for the hydrogen–oxygen reactions, developed by Konnov,[14] are used in the present model.

The dynamics of a collapsing bubble in pure water and the resulting sonochemical yields were predicted by solving Eqs. (5), (6), (8), (11), and $v = dR/dt$ simultaneously. The system constitutes $K+4$ ordinary differential equations and the $K+4$ unknowns are bubble radius R, bubble wall velocity v, bubble temperature T_b, pressure P_b, and K mass fractions of species Y_k. CHEMKIN-II, a FORTRAN chemical kinetics package developed at Sandia National Laboratories,[15] was incorporated with the bubble dynamic model for the analysis of gas-phase chemical kinetics. CHEMKIN-II, interacting with its Thermodynamic Database,[16] provides the thermodynamic properties and chemical production rates for all the species and reaction schemes. A variable-coefficient ordinary differential equation (ODE) solver based on EPISODE and EPISODEB[17,18] package, which can handle both stiff or nonstiff systems of first order ODEs, was used to solve the governing equations.

Several approximations are made in the current model:

(1) **Bubbles remain spherically symmetric.** The assumption of spherical bubble collapse is widely used because of its simplicity. This assumption breaks down when the bubble collapse becomes unstable from excessive driving pressure or from an asymmetry in the surrounding region such as a wall or another bubble in close proximity. It is believed that surface tension forces on small bubbles maintain their sphericity at moderate driving pressures. At high driving pressures such as typically used when sonoluminescence is observed, the spherical collapse assumption is under contention. Sonochemistry has been observed at driving pressures far below that of sonoluminescence, and thus the assumption of spherical bubble collapse is believed to be generally applicable as far as it accurately represents the condition in which vapor chemistry occurs.

(2) **The thermodynamic properties of species vary with temperature following polynomial fits of data available between 300 K and 5000 K.** The thermodynamic database provided by Sandia National Laboratory is between 300 K and 5000 K and polynomial fitting curves for thermodynamic properties are made within this temperature range. When the bubble temperature is above 5000 K, the same polynomial fitting relations are extended as an approximation. Although temperatures can reach above 5000 K in some applications, almost all reactions take place at lower temperatures due to the nonlinearity of bubble collapse. Conse-

quently, inaccuracies resulting from errors in data interpolation are expected to be small.

(3) **No mass transfer between the bubble and the surrounding fluid.** As shown by Matsumoto and Takemura evaporation/condensation of vapor and diffusion of noncondensable gas have significant effects on bubble motion.[5] Undoubtedly, it will also have a significant effect on bubble chemistry. These effects, however, occur over multiple cycles of oscillation altering the size of the bubble and changing the internal composition of the vapor. Little is known about the accuracy of existing mass transfer models. To separate the physics of mass transfer from the fundamental physics of bubble chemistry occurring in a few oscillation cycles, the current model takes, as input, bubble vapor composition and neglects mass transfer during bubble expansion and collapse. Deviations from initial vapor composition are assumed to be small within a few bubble oscillation cycles. This is consistent with Matsumoto and Takemura's analysis.

(4) **Uniform pressure inside the bubble.** The assumption of spatial uniform pressure inside the bubble is valid as long as the velocity of the bubble wall is below the speed of sound in the vapor–gas mixture.

(5) **Thermal conduction occurs through a thin thermal boundary layer between the bubble and the solution.** The assumption that the thermal boundary layer within an oscillating bubble is localized to a thin layer is justified by Fujikawa and Akamatzu.[19] Studies done by Kamath *et al.*[13] also show that the temperature profile in the vapor phase of the bubble is roughly uniform except for a strong thermal boundary layer at the wall. Such an assumption has a minimal effect on the results. In order to reduce computational intensity, the current model predicts heat transfer through the bubble wall based on a linear approximation of the shape of the temperature profile predicted by Kamath *et al.* This approximation greatly simplifies the chemical kinetics calculations and eliminates the need to account for species convection and diffusion within the bubble.

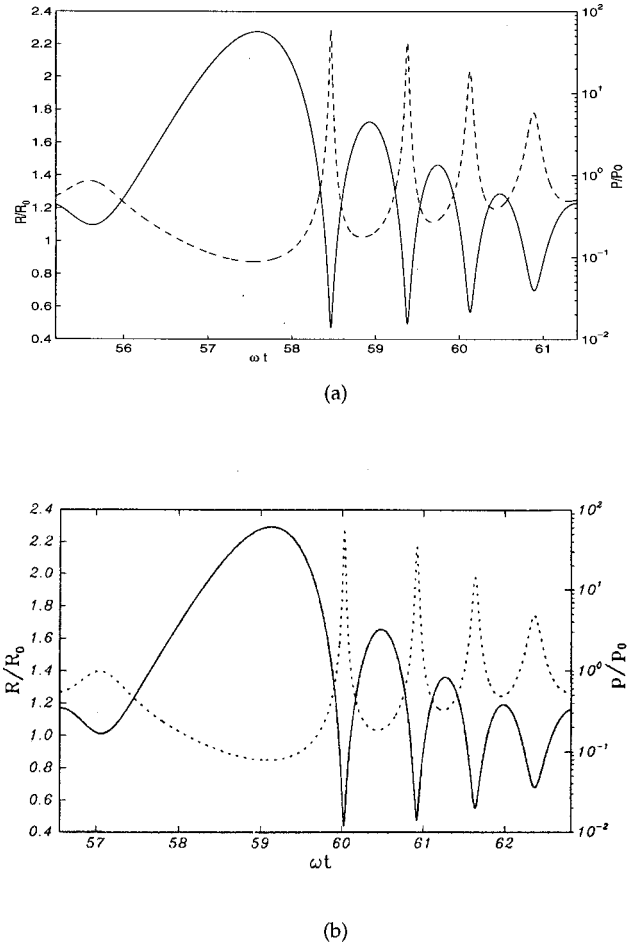

FIG. 2. The normalized radius (solid line, left scale) and internal pressure (dotted line, right scale) predicted numerically in one cycle of driving pressure for an argon bubble at $P_A=0.93$ atm, $R_0=26$ μm, $f=21$ kHz. The bubble expands slowly and collapse violently followed by three rebounds. The maximum pressure occurs at the first collapse of the bubble and peak pressures at each rebound decrease significantly. (a) Results from the current model; (b) results from the study by Kamath *et al.*

II. RESULTS

A. Bubble dynamics

The current model was used to predict the bubble dynamic behavior of a single bubble in water sonicated at a frequency of 21 kHz and magnitude of 0.93 atm. The bubble has an initial radius of 26 μm. The viscosity of the surrounding liquid is 0.001 kg/(s·m) and the surface tension coefficient is 0.073 N/m. An argon bubble was chosen as the focus of this study because of the simple chemical reactions that occur during sonication. In addition, it allows comparison between the current model and that of Kamath *et al.*

Figure 2(a) shows the normalized radius (solid line, left scale) and internal pressure (dotted line, right scale) as a function of time calculated using the current model in one cycle of the driving acoustic field. Typical features of bubbles oscillating in a sound field are illustrated in this figure. The bubble expands slowly when the pressure inside the bubble is higher than the ambient pressure. It continues expanding even when the inside pressure is lower than the ambient pressure due to the inertia of the water until a maximum radius of $2.3R_0$ is reached. The bubble then collapses violently and reaches a minimum radius of $0.47R_0$. The time scale of the first collapse is roughly one-third that of expansion with the final stage of collapse in which temperatures are sufficiently high to disassociate water vapor occurring in a few microseconds. The maximum pressure, on the order of 100 bar, and maximum temperature, on the order of 2000 K, occur during the first collapse of the bubble. There are three rebounds following the initial collapse. With each rebound, the collapse becomes weaker resulting in significant decrease in rebound temperature and pressure.

Figure 2(b) shows the results obtained from the Kamath *et al.*'s model under the same conditions. In general, the bubble behavior predicted by these two models is very similar especially the bubble radius and pressure as a function of time. Slight differences in the peak temperature at collapse are due, in part, to the difference in the way in which thermal distributions are modeled. In addition, detailed modeling of variation of gas properties as a function of temperature and the coupling of chemical kinetics and bubble dynamics in the current model contribute to these differences. These additions, while having minimal effect on the bubble radius as a

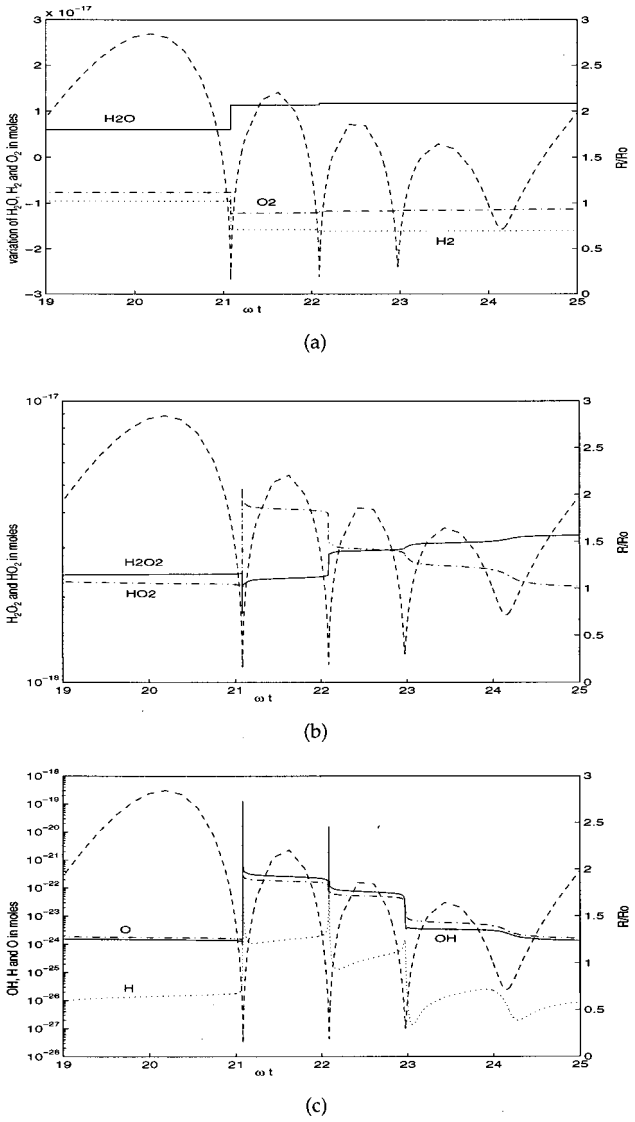

FIG. 3. The production of radicals and molecules inside the bubble as a function of time as water is sonicated under a mixture of 60% H_2 and 40% O_2 at $P_A=1.34$ atm, $R_0=2$ μm, $f=300$ kHz. Normalized bubble radius is plotted in the background as a reference. There is an increase in the concentration of H_2O and decrease in H_2 and O_2 at the first collapse shown in (a). Variations in HO_2 (dash-dot line) and H_2O_2 (solid line) are shown in (b). Due to their reactive natures, variations in O, H, and OH shown in (c) are more sensitive to the bubble oscillations.

function of time, effect vapor temperature during the final stages of bubble collapse and are, consequently, critical in predicting sonochemical yields.

B. Predicted sonochemical yields

The coupling of bubble dynamics and chemical kinetics makes it possible to study the sonochemical yields at different stages of bubble collapse. In this study, the driving pressure has an amplitude of 1.34 atm at 300 kHz and the gas contents in volume percentage are 60% H_2 and 40% O_2. The initial bubble radius of 2 μm is assumed. The productions of radicals, OH, O, H, HO_2, and H_2O_2, and the corresponding changes in H_2, O_2, and H_2O, in one cycle of driving pressure are presented in Fig. 3.

Figure 3(a) shows the changes of the stable species H_2, O_2, and H_2O as a bubble oscillates. Hydrogen and oxygen contents both decrease during the first violent collapse while the water vapor content increases correspondingly. The overall chemical reaction is similar to the process of burning hydrogen in an oxygen environment with water vapor being the byproducts. The changes of metastable species HO_2 and H_2O_2 at different stages of bubble collapses are shown in Fig. 3(b). HO_2 first increases as the bubble collapses violently and decreases gradually as the bubble oscillation becomes weaker. H_2O_2 decreases at the first bubble collapse due to its instability at high temperature. During rebound, H_2O_2 increases from the recombination of radicals as the bubble vapor expands and the temperature drops.

The reaction rates of the unstable radicals H, O, and OH, as shown in Fig. 3(c), are very sensitive to dynamic changes in the bubble volume. When the bubble first collapses, the internal bubble temperature and species concentrations are both high resulting in a very high production rate of OH. As the bubble expands, recombination of unstable radicals that occur at low temperatures tend to reduce the OH composition. At the same time, the low species concentrations slow the OH recombination mechanisms. Therefore, at the early stage of rebound following the first collapse, an initial decrease in OH content is primarily due to the drop in temperature resulting from the expanding vapor. As bubble volume increases further, the OH content does not significantly change as the species concentrations drop. At the early stage of the second collapse, the increased concentration of species accelerates the recombination mechanisms of radicals and causes a decrease in OH concentration. As the bubble collapses further, the temperature increases and the reaction generating OH dominates over the contribution from the recombination mechanisms resulting in an overall increase in OH content. Similarly, at the rebound stage of the second collapse, OH content decreases due to temperature drop while the species concentration is still relatively high. At the third and fourth collapse, the temperature increase is not significant; consequently, recombination rates of OH dominate and there is a net decrease in OH content. O and H radicals

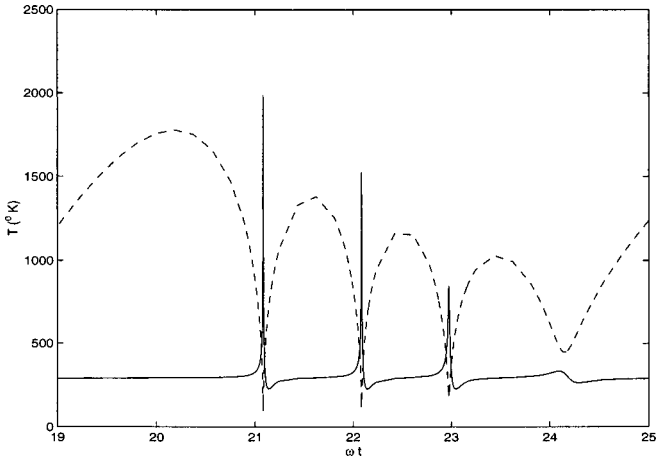

FIG. 4. Bubble temperature variation as a 2-μm bubble oscillates in the sound field under the condition described in Fig. 3. Temperature at first collapse is much higher than that at the second and the third, which results in the most intense chemical reactions.

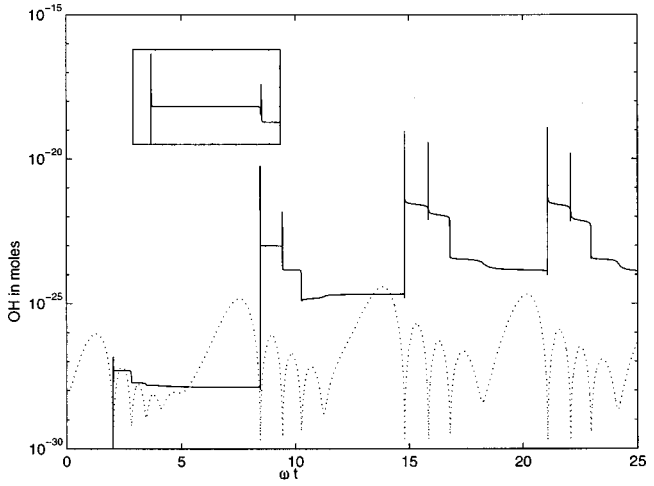

FIG. 5. Production of OH radicals over the first a few cycles of driving pressure under the condition described in Fig. 3. Each step increase in OH radicals corresponds to the most violent collapse of the bubble in each cycle of the driving pressure. The accumulation of OH radicals is due to a sudden drop in vapor density as the bubble expands. The blowup window shows the detail variation in OH production during the first and second collapses. Bubble oscillation in dotted line is shown in the background.

show similar behaviors but exist in much lower concentrations than OH radicals.

An important phenomena illustrated in Fig. 3 is that chemical kinetics is more significant in the first collapse than the second. The reason is that the chemical reactions are very strongly dependent on temperature and molar concentration of species, as shown in Eqs. (18) and (19). When bubble radius is large, the temperature and species concentrations are low. Few reactions take place in the vapor phase under these conditions. When the bubble collapses to a small fraction of its original volume, the increase of species concentration and temperature inside the bubble results in a dramatic increase in chemical reaction rate. Since the reaction rate of each species is an exponential function of the temperature as shown in Eq. (19), it is far more sensitive to the change in temperature than it is to variations in species concentrations. Figure 4 shows the bubble temperature variation as a bubble oscillates. The peak temperature reached during the first collapse is much higher than the second and the third. Thus most of the reactions that take place occur during the first bubble collapse.

An interesting phenomenon in Fig. 3(c) is the accumulation of OH over the first few bubble oscillations. This accumulation is shown in detail in Fig. 5, in which the bubble oscillations are plotted in dot line as a reference. Each significant step increase in OH radicals corresponds to the most violent collapse of the bubble in each cycle of the driving pressure. In each bubble oscillation cycle, the expansion process causes an extremely rapid cooling. The formation of OH that was established at the peak collapse temperature is *frozen* by the expansion process because the rate of other reactions fall too rapidly for there to be time for the chemical equilibrium to adjust to the new temperature. Consequently, there is a net increase in OH concentration inside the bubble for the first few oscillation cycles. The net increase in OH concentration with each oscillation decreases over multiple

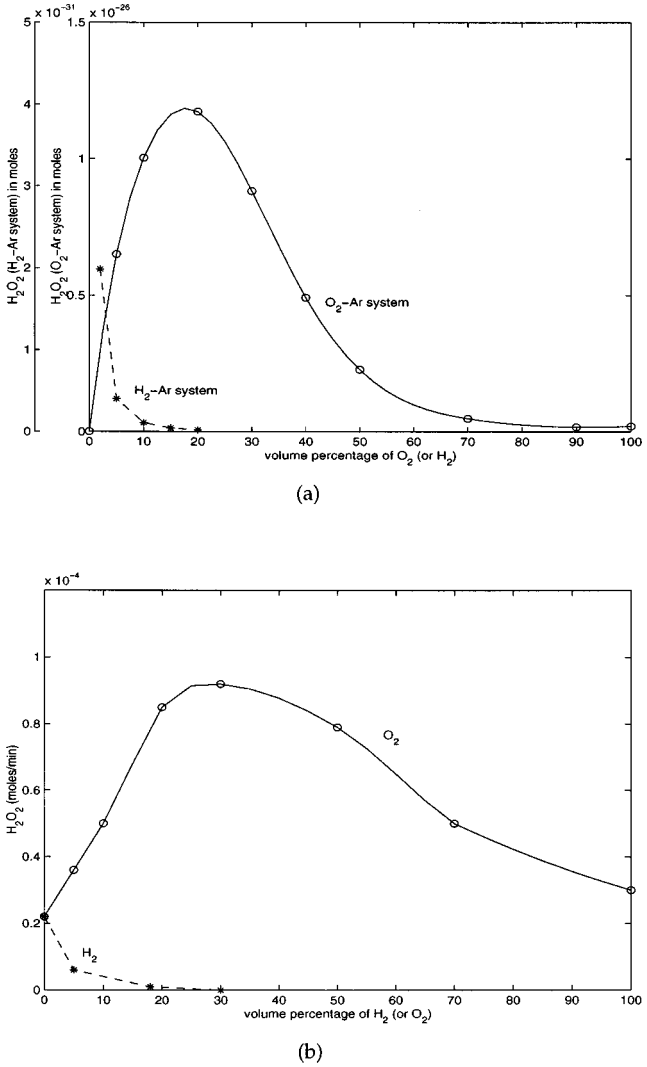

FIG. 6. Comparison of the production of hydrogen peroxide in water sonicated under a mixture of H_2/Ar and O_2/Ar at $P_A = 1.32$ atm, $f = 300$ kHz between (a) numerical predictions and (b) experimental results from Henglein. Though an exact comparison is not possible, the plot indicates that the trends of the sonochemical yields in a single bubble (numerical predictions) and those in bulk production (measurements) are very similar. As illustrated, the production rate of H_2O_2 decreases rapidly as H_2 concentration increases; the production rate of H_2O_2 first increases as O_2 concentration increases and then decreases with a further increase in O_2 concentration.

cycles and eventually reaches zero as the bubble obtains a steady oscillation. This effect is amplified somewhat in the results shown in Fig. 6 as species transport to the bulk solution is not taken into account. It is likely that with a species transport mechanism a stable cavitation bubble in an acoustic field will accumulate OH asymptotically, achieving a steady state concentration that is somewhat lower than the level indicated. Nonetheless, it illustrates the significance of coupling the kinetics of the bubble vapor chemistry with the bubble dynamics. The time scale of the bubble collapse phenomena is not insignificant relative to the rate of reactions occurring in the bubble vapor.

C. Effects of gas composition on sonochemical yields

Using the current model, the effects of gas compositions on sonochemical yields were investigated. To simplify the

chemical kinetics modeling, only three gas combinations H_2–Ar, O_2–Ar, and O_2–H_2 were assessed. The acoustic frequency of the sound field in this study is 300 kHz, which is the same as that used in Henglein's experiments. The viscosity of the surrounding liquid is 0.001 kg/(s·m), and the amplitude of the sound is 1.32 atm. The variations in thermal conductivity as a function of gas composition changes are not considered in this study in order to separate gas composition effects from the effects due to heat conduction.

1. O_2–Ar *and* H_2–Ar *gas mixtures*

Figure 6(a) shows the predicted formation of H_2O_2 in water sonicated under gas mixtures of H_2–Ar and O_2–Ar. The initial bubble radius of 2 μm is used in the simulations. The solid line represents the result for an O_2–Ar gas mixture. The production rate of H_2O_2 first increases as O_2 concentration increases until the volume percentage of the oxygen reaches roughly 20%. It then decreases as the volume percentage of O_2 increases further. The related mechanism corresponding to the increase of H_2O_2 at low oxygen concentration is

$$O_2 + H^{\cdot} \rightarrow HO_2^{\cdot}.$$

More HO_2 is produced when the oxygen concentration increases. Consequently, more H_2O_2 is produced according to the mechanism

$$HO_2^{\cdot} + HO_2^{\cdot} \rightarrow H_2O_2 + O_2.$$

When the O_2 concentration rises, the final collapse temperature becomes lower because the specific heat at constant pressure of O_2 is about 1.8 times that of argon at 1500 K. Thus the dissociation mechanisms become less effective and consequently less reactive radicals are produced during bubble collapse and consequently less H_2O_2 is produced at higher oxygen concentration.

For the H_2–Ar gas mixture, the production of H_2O_2 decreases rapidly as the volume percentage of H_2 increases as shown by the dashed line in Fig. 6(a). The dominant reaction mechanism for this case is $OH^{\cdot} + H_2 \rightarrow H_2O + H^{\cdot}$. As H_2 concentration increases, the formation of H_2O_2 from the combination of OH radicals is less effective.

2. O2–H2 gas mixture

When the gas composition is H_2–O_2, the predicted yield of H_2O_2 at the early rebound of the first collapse in the fifteenth cycle is shown in Fig. 7(a). The initial bubble radius is 2.2 μm in this case. The production of H_2O_2 shows a double peak feature as the volume percentage of H_2 changes from 0 to 100% with the valley occurring at the volume percentage of the hydrogen is around 65%.

From the simulations, three major factors that affect the final production of hydrogen peroxide in the H_2–O_2 gas mixtures are identified. The first important factor is the collapse temperature. As hydrogen content increases in the mixture, the collapse temperature becomes higher since the hydrogen has lower specific heat and enthalpy compared to oxygen. The overall chemical reactions become more effective resulting in an increase in H_2O_2 production. The second factor is

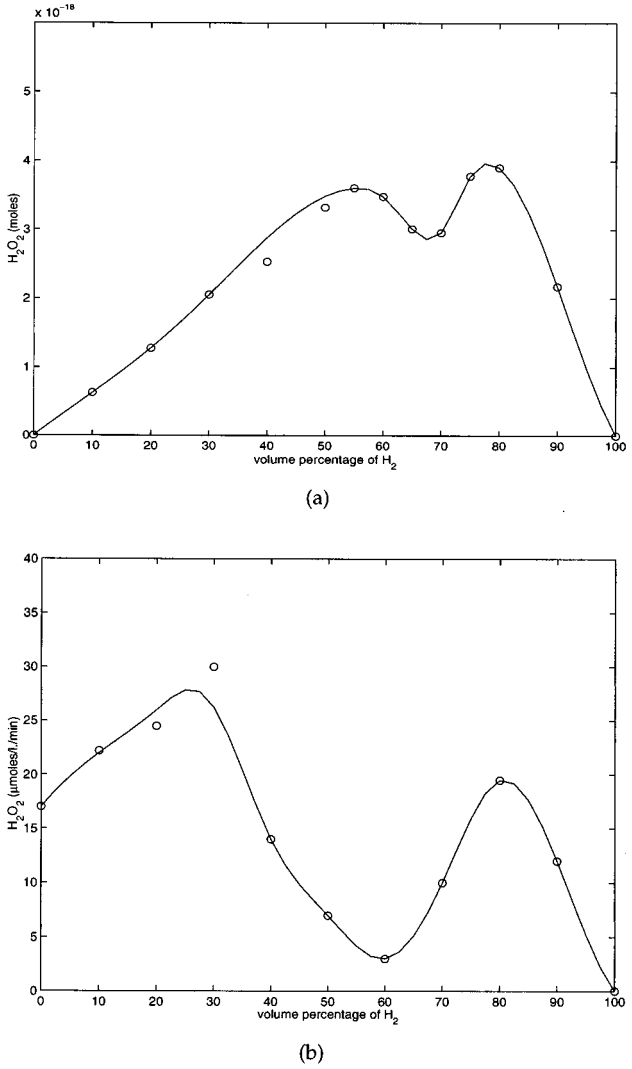

FIG. 7. Comparison of the production of hydrogen peroxide in water sonicated under mixture of H_2/O_2 at $P_A = 1.32$ atm, $f = 300$ kHz between (a) numerical predictions and (b) experimental results from Henglein. Double peak formation of H_2O_2 is observed in both numerical prediction and experimental measurement.

the chemical composition in the system. Since hydrogen prevents the production of H_2O_2, the overall production of H_2O_2 decreases when hydrogen content is over 90%, even when the collapse temperature is higher than the cases with low hydrogen content. The third factor is related to stoichiometric combustion. Maximum combustion occurs when the mixture of hydrogen and oxygen is close to stoichiometric: two moles of hydrogen and one mole of oxygen, which is equivalent to 66% H_2 and 34% O_2. The early stage of bubble collapse provides the initial conditions for combustion to proceed. Consequently, water vapor and other radicals form and reaction heat due to hydrogen combustion is released in the bubble. Compared to other gas compositions, the stoichiometric mixture releases the highest amount of reaction heat at combustion, which induces a higher final collapse temperature. Since H_2O_2 is unstable at high temperatures, a low production of H_2O_2 results at mixtures around stoichiometric ratios. Therefore, the production of H_2O_2 is the result of the competition between these three major factors.

Note that the induction of the chemical reactions is very sensitive to the bubble dynamic behavior. The stronger the bubble collapses, the more significant the hydrogen combustion effects are. When the collapse becomes weaker, which could result from a lower magnitude of the driving pressure or a larger initial bubble radius, the effect of hydrogen combustion is not significant. The double peak feature of H_2O_2 production is not observed from the simulation in these situations.

Figures 6(b) and 7(b) show the experimental results obtained by Henglein under similar sonication conditions. Even though an direct comparison between the simulation and experimental results is not possible as the present model focuses a single bubble while Henglein's data were based on the bulk production, the overall trends of sonochemical yields appear similar.

III. SUMMARY AND CONCLUSIONS

Presented is a model that directly couples the dynamics and the chemical kinetics of a single cavitation bubble in a sound field. Comparisons with theoretical studies by Kamath *et al.* and experimental studies by Henglein *et al.* show that this model not only captures the main characteristics of the dynamics of bubble collapse but also qualitatively predicts the unusual observed behavior of sonochemical yields produced under varying dissolved gas content and composition. It illustrates the importance of kinetically modeling the bubble vapor properties, demonstrating that the extremely short time scale associated with bubble collapse is on the same order as the reaction time scales within the vapor. The model predicts a relatively weak effect of the kinetic change in vapor properties on bubble radius but a fairly strong effect on the temperature profile during collapse. Consequently, kinetic changes in vapor properties have a strong effect on the sonochemical phenomena. As the model presented accounts only for the chemistry occurring in the vapor phase of a single cavitation bubble and does not account for the transport of species into solution, the overall sonochemical reaction rates cannot be predicted quantitatively. Despite this, it provides a means of resolving fundamental parametric relationships and investigating effects of gas properties on chemical kinetics and bubble dynamics in sonochemical processes.

[1] T. J. Mason and J. P. Lorimer, *Sonochemistry: Theory, Applications And Uses Of Ultrasound In Chemistry* (Ellis Horwood, London, 1988).
[2] M. S. Plesset, J. Appl. Mech. **16**, 277–282 (1949).
[3] L. Rayleigh, Philos. Mag. **34**, 94–98 (1917).
[4] D. F. Gaitan, L. A. Crum, C. C. Church, and R. A. Roy, J. Acoust. Soc. Am. **91**, 3166–3183 (1992).
[5] Y. Matsumoto and F. Takemura, JSME International Journal, Series B, Fluids and Thermal Engineering **37**, 288–296 (1994).
[6] M. Anbar and I. Pecht, J. Phys. Chem. **68**, 352–355 (1964).
[7] E. H. Hart and A. Henglein, J. Phys. Chem. **91**, 3654–3656 (1987).
[8] A. Henglein, Advances in Sonochemistry **3**, 17–83 (1993).
[9] K. S. Suslick, Mingming Fang, and T. Hyeon, J. Am. Chem. Soc. **118**, 119–160 (1996).
[10] K. S. Suslick, S. B. Choe, A. A. Cichowlas, and M. W. Grinstaff, Nature (London) **353**, 414–416 (1991).
[11] K. S. Suslick, S. J. Doktycz, and E. B. Flint, Ultrasonics **28**, 280–290 (1990).
[12] E. B. Flint and K. S. Suslick, Science **253**, 248–249 (1991).
[13] V. A. Kamath, A. Prosperetti, and F. N. Egolfopoulos, J. Acoust. Soc. Am. **94**, 248–260 (1993).
[14] A. A. Konnov, Detailed reaction mechanism for small hydrocarbons combustion, Release 0.3, *http://homepages.vub.ac.be/~akonnov* (1997).
[15] R. J. Kee, F. M. Rupley, and J. A. Miller, ''CHEMKIN, a FORTRAN chemical kinetics package for the analysis of gas-phase chemical kinetics'' (Sandia National Laboratories, Albuquerque, 1994).
[16] R. J. Kee, F. M. Rupley, and J. A. Miller, ''The Chemkin Thermodynamic Database,'' Sandia National Laboratories Reports, SAND87-8215, 1987.
[17] A. C. Hindmarsh and G. D. Byrne, ''EPISODE: An Effective Package for the Integration of Systems of Ordinary Differential Equations,'' LLNL Report UCID-30112, Rev. 1, April 1977.
[18] G. D. Byrne and A. C. Hindmarsh, ''EPISODEB: An Experimental Package for the Integration of Systems of Ordinary Differential Equations with Banded Jacobians,'' LLNL Report UCID-30132, April 1976.
[19] S. Fujikawa and T. Akamatsu, J. Fluid Mech. **97**, 481–512 (1980).

Sound propagation over convex impedance surfaces

Kai Ming Li[a)]
Department of Mechanical Engineering, Hong Kong Polytechnic University, Hung Hom, Kowloon, Hong Kong

Qiang Wang and Keith Attenborough
Engineering Mechanics Discipline, Faculty of Technology, The Open University, Milton Keynes MK7 6AA, United Kingdom

(Received 20 June 1997; revised 14 July 1998; accepted 11 August 1998)

Theoretical calculations for the diffraction of sound by large spheres and cylinders with finite impedance surfaces are reported. The differences between existing two-dimensional and new three-dimensional results are made explicit and are shown to involve a simple correction factor in the case of a large sphere. The results for propagation over an infinitely long cylinder have a bearing on the widely used analogy between sound propagation over a curved surface and sound propagation in a refracting atmosphere above an impedance plane. Specifically, it is found that there is a rigorous analogy between sound propagation above a large circular cylinder and propagation in a medium where the sound speed varies exponentially with height. This differs from the bilinear profile that is often used when exploiting the analogy [see, for example, J. Acoust. Soc. Am. **83**, 2047–2058 (1988)]. Predictions for both profiles are found to agree well with each other and with the published data in the shadow zone, but considerable discrepancies are found in the penumbra region. © *1998 Acoustical Society of America.* [S0001-4966(98)05311-9]

PACS numbers: 43.28.Fp, 43.20.Fn [LCS]

INTRODUCTION

Analytical approximations for the scattering and diffraction of sound by smooth convex surfaces are considered together with their relevance to predictions of outdoor sound propagation. The present investigation is primarily concerned with the problem where the radius of curvature of the curved surface is much larger than the wavelength of interest. Ignoring the scattering effects of atmospheric turbulence, the diffraction of sound by irregular terrain remains an interesting problem in predicting outdoor sound propagation. However, through analogy, the approximations presented here are relevant to effects of temperature and wind gradients also.

There has been extensive research into the scattering and diffraction of electromagnetic waves by convex surfaces.[1] The analogy with propagation over flat ground under an appropriate wave speed profile was identified and most of the theoretical formulas were derived during this period.[2] Although most of these analyses were developed in the context of electromagnetic wave theory, the underlying principle has been applied to underwater acoustics,[3] and in the context of general linear acoustics.[4,5]

There has been considerable progress in constructing asymptotic solutions for propagation over arbitrarily curved but sufficiently smooth convex curves;[6] however, the theory involves a tedious and complicated analysis that rapidly becomes intractable. Not only are simpler problems more tractable analytically, but also they help with understanding the intriguing physical phenomenon of sound diffraction by curved surfaces. Here we shall consider two types of convex surfaces; a sphere and an infinitely long circular cylinder.

Based on previous analyses (see, for example, pp. 469–478 of Ref. 7), Berry and Daigle[8] have proposed that the sound field above a large cylinder with no refraction is analogous to the sound field above a flat ground with the sound speed gradient varying according to the so-called bilinear profile [see Fig. 1(a) and (b)]. Hereafter, we shall refer to this version of the analogy as the bilinear analogy. By interpreting R_c as the radius of the cylinder, z as the height transverse to the cylinder, and r as the arc length along the surface, Berry and Daigle derive a residue series solution that enables the prediction of the sound field in the penumbra and shadow zone. The theoretical results agree well with their experimental measurements deep in the shadow zone but the agreement is less satisfactory in the penumbra region. In a recent study,[9] Berthelot has introduced a heuristic modification such that the arc length along the curved surface is replaced by the shortest distance between the source and receiver in the bilinear analogy. This heuristic modification has led to better agreement between theory and experimental measurements in the penumbra region. In this paper, we wish to investigate rigorously the validity of the bilinear analogy, but the theoretical justification of Berthelot's modification is beyond the scope of our current study.

Almgren[10] has suggested that a spherically curved surface should be used in a scale model experiment if the sound speed gradient is induced by a temperature gradient, but a cylindrically curved surface should be used if the refraction is caused by a linear wind velocity gradient. We examine this hypothesis in detail for the purpose of devising associated experimental studies. These experiments and their results have been reported elsewhere.[11]

Di and Gilbert[12] have considered conformal transformation by mapping a series of cylindrical surfaces in order to model the propagation of sound over irregular terrain. They

a)Corresponding author. Electronic mail: mmkmli@polyu.edu.hk

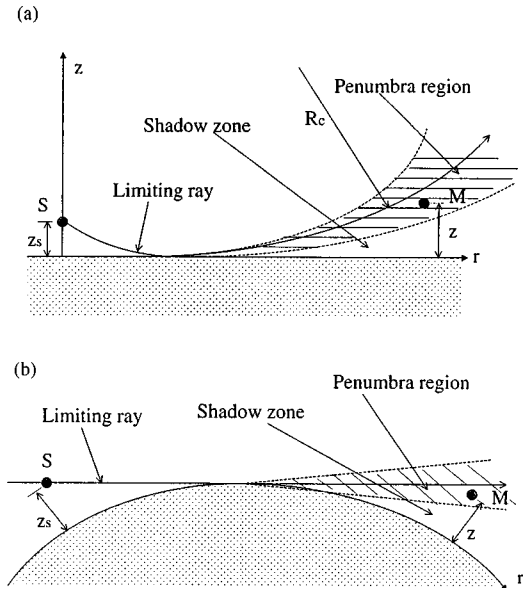

FIG. 1. Schematic diagrams to show (a) a curved ray path above a plane boundary and (b) line-of-sight propagation above a convex surface. In the diagrams, S is a point source, z_s indicates the source height, M is a measurement point with z indicating the receiver height, and R_c is the radius of curvature of the limiting ray.

pointed out that there is a stricter analogy between propagation over a cylindrical surface and propagation over flat ground under an exponential sound speed profile. Recent numerical calculations using a fast field formulation together with the exponential profile have confirmed this result.[13] Also we note that the use of matched asymptotic expansions (MAE) has proved useful in predicting the sound field in the penumbra region,[14–16] but the MAE theory is restricted to the propagation of plane waves. Further modifications are needed to compute the sound field due to a point source or a line source. Moreover, it appears difficult to extend the current MAE theory to allow for the prediction of sound field due to a directional source. Therefore, we shall follow the approach of the residue series solution together with the conformal transformation[17] from a cylindrical surface to an equivalent flat ground. In the current study, we extend the analogy to three dimensions for sound propagation over an infinitely long cylinder and investigate the corresponding analogy for sound propagation over a large sphere.

This paper is confined to theoretical studies of the sound field behind these two types of curved surfaces and numerical comparisons with the bilinear analogy. The paper is organized as follows. First we recall the standard residue series solution for a monopole in an upward-refracting medium above a finite impedance ground and the previous basis for the analogy between refraction and surface curvature. In Sec. II, we derive residue series solutions for three-dimensional propagation above a large sphere. In Sec. III we concentrate on the derivation of an analytic formula for sound propagation over a large infinitely long cylinder. Finally we discuss the various numerical results and their comparisons with published experimental data in Sec. IV.

I. THE REFRACTING MEDIUM ANALOGY TO PROPAGATION OVER A CURVED SURFACE

Based on Pierce's analysis,[7] Berry and Daigle[8] postulated that the sound field above a curved surface with a circular cross section in an otherwise homogeneous medium is equivalent to that in an upward refracting medium in which the adiabatic sound speed, $c(z)$, varies according to a bilinear profile such that

$$c(z)=c(0)/\sqrt{1+z/R_c}. \tag{1}$$

As remarked earlier, we refer it as the bilinear analogy for convenience. In the above equation, R_c is the radius of curvature of the curved surface and z is the height above an impedance plane with a normalized specific admittance of β. It is worth noting that $1/R_c$ corresponds to the inverse of the normalized sound velocity gradient for large R_c. If the wavelength of interest is much smaller than R_c, then the sound field due to a monopole can be expressed in an integral form as

$$\begin{aligned} p^{(b)}(r,z)\approx S_0 l e^{i\pi/6}\int_0^\infty H_0^{(1)}(\kappa r) \\ \times \mathrm{Ai}\left[\left(\tau-\frac{z_>}{l}\right)e^{i2\pi/3}\right]\left\{\mathrm{Ai}\left[\tau-\frac{z_>}{l}\right]\right. \\ \left. -\frac{\mathrm{Ai}'(\tau)-q\,\mathrm{Ai}(\tau)}{e^{i2\pi/3}\mathrm{Ai}'(\tau e^{i2\pi/3})-q\,\mathrm{Ai}(\tau e^{i2\pi/3})}\right. \\ \left. \times \mathrm{Ai}\left[\left(\tau-\frac{z_<}{l}\right)e^{i2\pi/3}\right]\right\}\kappa\, d\kappa, \end{aligned} \tag{2}$$

where S_0 is the monopole source strength, the time dependence $\exp(-i\omega t)$ is understood and suppressed throughout, r is the horizontal separation between the source and receiver, z and z_s are, respectively, the source and receiver heights, $z_>$ is the greater of z and z_s, and $z_<$ is the lesser of z and z_s. The Hankel function, the Airy function, and the derivative with respect to its argument are denoted by $H_0^{(1)}$, Ai, and Ai$'$, respectively. In Eq. (2), we use the superscript (b) to denote the corresponding sound field for a stratified medium with a bilinear sound speed profile. The creeping wave layer thickness l, the nondimensionalized scaled admittance q, and the dimensionless scale factor τ are given, respectively, by

$$l=(R_c/2k_0^2)^{1/3}, \tag{3}$$

$$q=ik_0\beta l, \tag{4}$$

and

$$\tau=(\kappa^2-k_0^2)l^2, \tag{5}$$

where $k_0=2\pi f/c(0)$ and f is frequency. The sound field can then be expressed by[8,18]

$$p^{(b)}(r,z)\approx S_0\,\frac{\pi e^{i\pi/6}}{l}\sum_n\ \frac{\mathrm{Ai}[(\tau_n-z_s/l)e^{i2\pi/3}]\mathrm{Ai}[(\tau_n-z/l)e^{i2\pi/3}]H_0^{(1)}(K_nr)}{(q^2-\tau_n)[\mathrm{Ai}(\tau_ne^{i2\pi/3})]^2}, \tag{6}$$

where

$$\tau_n=(K_n^2-k_0^2)l^2. \tag{7}$$

The horizontal wave number, $\kappa=K_n$, is the solution of the eigenvalue equation

$$e^{i2\pi/3}\mathrm{Ai}'(\tau e^{i2\pi/3})-q\,\mathrm{Ai}(\tau e^{i2\pi/3})=0. \tag{8}$$

The total sound field is the sum of all contributions due to these eigenvalues (or poles). The expression given in Eq. (6) is analogous to that given in Ref. 8 [their Eq. (6)].

In the limit of high frequency and large range such that K_nr is large, the Hankel function in Eq. (6) can be approximated by its asymptotic form. In this situation, the sound pressure can be simplified to

$$p^{(b)}(r,z)\approx S_0\,\frac{e^{i\pi/12}}{l}\left(\frac{2\pi}{r}\right)^{1/2}\times\sum_n\ \frac{\mathrm{Ai}[(\tau_n-z_s/l_s)e^{i2\pi/3}]\mathrm{Ai}[(\tau_n-z/l_s)e^{i2\pi/3}]e^{iK_nr}}{\sqrt{K_n}(q^2-\tau_n)[\mathrm{Ai}(\tau_ne^{i2\pi/3})]^2} \tag{9}$$

which corresponds to the relevant expression in Ref. 19 [their Eq. (15)]. Furthermore, it is noteworthy that the residue series analysis has been extended to other profiles with a monotonically decreasing sound speed gradient in a recent study.[20]

II. THE SOUND FIELD NEAR A LARGE SPHERE

In this section, we study the diffraction of sound in a homogeneous medium near a spherical surface of large radius. It is convenient to use a spherical polar coordinate system, (R,θ,ψ), in this problem. A point source is located at (R_s,θ_s,ψ_s). The sound field can be determined by solving the Helmholtz equation with a constant wave number, k_0 say, for a homogeneous medium. Again, we treat the sphere as a locally reacting surface. Let the radius and specific normalized admittance of the sphere be R_c and β, respectively. The boundary condition at the surface of sphere is

$$\frac{\partial p}{\partial R}+ik_0\beta p=0. \tag{10}$$

The solution for the scattering of sound by a spherical surface is well known[2,21] and the details of the analysis will be omitted here. In the high-frequency limit, the sound field can be expressed in an integral form as

$$p^{(s)}(R,\theta,\psi)\approx\frac{iS_0}{4\pi}\,\frac{\exp[i(\Theta/2-\pi/4)]}{\sqrt{\tfrac{1}{2}\pi\,\sin\Theta}}\times\int_D\frac{\nu!}{(\nu-\tfrac{1}{2})!}\exp(i\nu\Theta)\times\left\{j_\nu(k_0R)-\frac{j_\nu'(k_0R_c)+i\beta j_\nu(k_0R_c)}{h_\nu'^{(1)}(k_0R_c)+i\beta h_\nu^{(1)}(k_0R_c)}\times h_\nu^{(1)}(k_0R)\right\}h_\nu^{(1)}(k_0R_s)\,d\nu, \tag{11}$$

where the functions $h_\nu^{(1)}(\ )$ and $j_\nu(\ )$ are νth-order spherical Bessel functions and Θ is the total angle subtended between the source and receiver (see Fig. 2). It can be determined according to

$$\cos\Theta=\sin\theta\,\sin\theta_s\,\cos(\psi-\psi_s)+\cos\theta\,\cos\theta_s. \tag{12}$$

The primes denote the derivative of the spherical Bessel functions with respect to their arguments and the superscript (s) is used to denote the sound field above a large sphere. The path of integration D is shown in Fig. 3. Note that the integral expression given in Eq. (11) is valid only when $R_s\geqslant R$, but there is no loss of generality when it is used because the reciprocity theorem allows one to exchange the source and receiver position if $R_s<R$.

Assuming that the source and receiver are, respectively, z_s and z above the large sphere, we can write

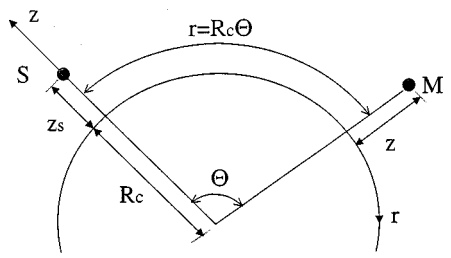

FIG. 2. A schematic diagram for the source and receiver above a large sphere (not to scale).

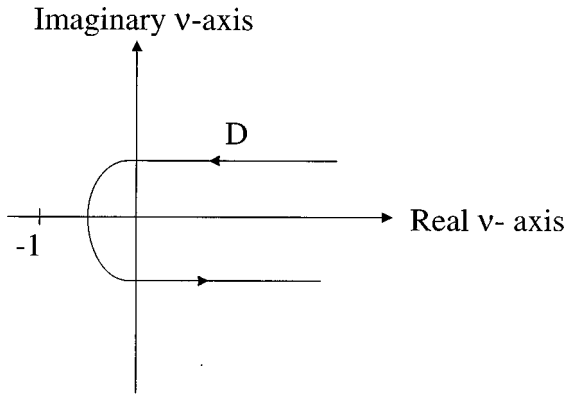

FIG. 3. Diagram to show the contour of integration, D, for the integral given in Eq. (11).

$$R_s = R_c + z_s \quad \text{and} \quad R = R_c + z, \tag{13}$$

where $R_c \gg z_s > z$. A close examination of Eq. (11) suggests that the main contribution to $p_m^{(s)}$ comes from the neighbourhood of $\nu = k_0 R_c$ because R_s and R are both nearly equal to R_c. To proceed with the evaluation of the integral of Eq. (11), it is worth noting that the spherical Bessel functions can be written in terms of the Bessel functions $J_n(\ )$ and $H_n^{(1)} \times(\ )$ as follows:

$$j_\nu(Z) = \left(\frac{\pi}{2Z}\right)^{1/2} J_{\nu+1/2}(Z) \tag{14a}$$

and

$$h_\nu^{(1)}(Z) = \left(\frac{\pi}{2Z}\right)^{1/2} H_{\nu+1/2}^{(1)}(Z), \tag{14b}$$

where Z is the complex argument of the functions. Furthermore, for $|Z|$ close to but greater than 1, the Bessel functions can be expanded asymptotically according to

$$J_\nu(\nu Z) \approx 2^{1/3}\nu^{-1/3}\mathrm{Ai}[-2^{1/3}\nu^{2/3}(Z-1)], \tag{15a}$$

$$J_\nu'(\nu Z) \approx -\frac{2^{2/3}}{Z}\,\nu^{-2/3}\mathrm{Ai}'[-2^{1/3}\nu^{2/3}(Z-1)], \tag{15b}$$

$$H_\nu^{(1)}(\nu Z) \approx 2^{4/3}\nu^{-1/3}e^{-i\pi/3}\mathrm{Ai}[-2^{1/3}\nu^{2/3}(Z-1)e^{i2\pi/3}], \tag{15c}$$

and

$$H_\nu^{(1)\prime}(\nu Z) \approx \frac{2^{5/3}}{Z}\,\nu^{-2/3}e^{i4\pi/3} \times \mathrm{Ai}'[-2^{1/3}\nu^{2/3}(Z-1)e^{i2\pi/3}], \tag{15d}$$

where the primes denote the derivatives with respect to their arguments. We remark that Eqs. (9.3.35), (9.3.37), (9.3.39), (9.3.43), and (9.3.45) of Ref. 22 have been used to obtain Eqs. (15a)–(15d). In addition, the factorials in Eq. (11) can be approximated by means of the Stirling formula [see Eq. (6.1.37) of Ref. 22] and it is straightforward to show that $\nu!/(\nu-\frac{1}{2})! \approx \sqrt{\nu}$. Substituting Eqs. (14a) and (14b) into Eq. (11), invoking the asymptotic expressions for the Bessel functions [Eqs. (15a)–(15d)], putting

$$\nu + \tfrac{1}{2} = k_0 R_c(1 + \tfrac{1}{2}\mu), \tag{16}$$

and neglecting higher powers of μ, we can rewrite Eq. (11) as

$$p^{(s)} \approx \frac{k_0 S_0}{4\pi}\,\frac{\exp[i(k_0 R_c\Theta - \pi/12)]}{\sqrt{k_0 l}} \times \sqrt{\frac{\pi}{\sin\Theta}}\int_{-\infty}^{\infty}\mathrm{Ai}\left[-k_0^2 l^2\left(\frac{2z_0}{R_c}-\mu\right)e^{i2\pi/3}\right] \times\left\{\mathrm{Ai}\left[-k_0^2 l^2\left(\frac{2z}{R_c}-\mu\right)\right] + \Gamma(\mu)\mathrm{Ai}\left[-k_0^2 l^2\left(\frac{2z}{R_c}-\mu\right)e^{i2\pi/3}\right]\right\} \times \exp[i(k_0 l)^3\mu\Theta]\,d\mu, \tag{17}$$

where the creeping wave layer thickness l is given by Eq. (3), the reflection coefficient $\Gamma(\mu)$ is given by

$$\Gamma(\mu) = \frac{\mathrm{Ai}'(k_0^2 l^2\mu) - q\,\mathrm{Ai}(k_0^2 l^2\mu)}{e^{i2\pi/3}\mathrm{Ai}'(k_0^2 l^2\mu e^{i2\pi/3}) - q\,\mathrm{Ai}(k_0^2 l^2\mu e^{i2\pi/3})}, \tag{18}$$

and the nondimensionalized scaled admittance q is given by Eq. (4).

Comparison of Eqs. (2) and (17) reveals the similarity of these two equations. Figure 2 illustrates the connection between the parameters for a spherical surface and those for a stratified medium over a flat ground. We put

$$r = R_c\Theta \tag{19a}$$

and

$$\kappa^2 = k_0^2(1+\mu). \tag{19b}$$

Hence, we can write

$$d\mu = 2\kappa\,d\kappa/k_0^2. \tag{19c}$$

Since the main contribution comes from the region close to $\mu \approx 0$ (or $\kappa \approx k_0$), we can approximate μ by

$$\mu \approx 2(\kappa/k_0 - 1). \tag{19d}$$

Substitution of Eqs. (19a)–(19d) into Eq. (17) leads to

$$p^{(s)}(r,z) \approx \left(\frac{\Theta}{\sin\Theta}\right)^{1/2}\sqrt{\frac{2}{\pi}}\,S_0 l e^{-i\pi/12} \times \int_{-\infty}^{\infty}\mathrm{Ai}\left[\left(\tau - \frac{z_>}{l}\right)e^{i2\pi/3}\right]\left\{\mathrm{Ai}\left[\tau - \frac{z_>}{l}\right] - \frac{\mathrm{Ai}'(\tau) - q\,\mathrm{Ai}(\tau)}{e^{i2\pi/3}\mathrm{Ai}'(\tau e^{i2\pi/3}) - q\,\mathrm{Ai}(\tau e^{i2\pi/3})} \times \mathrm{Ai}\left[\left(\tau - \frac{z_<}{l}\right)e^{i2\pi/3}\right]\right\}\frac{d\kappa}{\sqrt{\kappa r}}. \tag{20}$$

Replacing the Hankel function with its asymptotic expression in Eq. (2), we can demonstrate that $p^{(b)}(r,z)$ differs from $p^{(s)}(r,z)$ by a factor of $\sqrt{\Theta/\sin\Theta}$. Using the theoretical result from the bilinear analogy, the sound field near a large sphere is simply

$$p^{(s)} \approx (\sqrt{\Theta/\sin\Theta})\,p^{(b)}, \tag{21}$$

where $p^{(b)}$ is given by Eq. (9).

Consequently, the amplitude of the sound field above a large sphere is different from the bilinear analogy by a factor of $\sqrt{\Theta/\sin\Theta}$, where Θ is the total angle between the source and receiver. As shown in Fig. 4, the correction factor has a relatively small influence on the total sound field and it is only noticeable at large Θ, i.e., for the receiver deep in the shadow zone. Equation (21) justifies the suggestion that a spherically curved surface serves as an indoor model for studying the situation where the sound speed gradient is induced by a temperature gradient.[10]

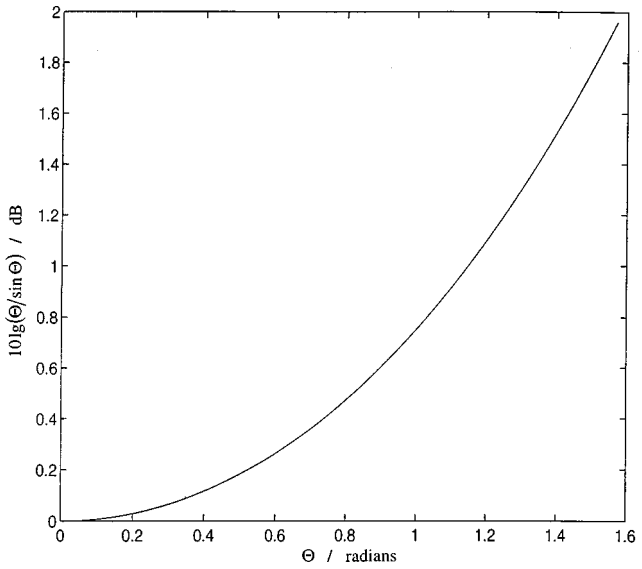

FIG. 4. The correction factor $10\lg(\Theta/\sin\Theta)$ versus the total angle between the source and receiver Θ.

III. THE SOUND FIELD ABOVE AN INFINITELY LONG CIRCULAR CYLINDER

In this section, we consider a two-dimensional cylinder with the longitudinal axis aligned with the v-axis where Cartesian co-ordinates (u,v,w) are used. Suppose that the source and receiver are close to the large circular cylinder with R_c as the radius of the cylinder. The Helmholtz equation for the acoustic pressure due to a source located at (u_s,v_s,w_s) can be written in a simple form as

$$\frac{\partial^2 p^{(c)}}{\partial u^2}+\frac{\partial^2 p^{(c)}}{\partial v^2}+\frac{\partial^2 p^{(c)}}{\partial w^2}+k_0^2 p^{(c)} = -\delta(u-u_s)\,\delta(v-v_s)\,\delta(w-w_s) \tag{22}$$

subject to the impedance boundary condition of

$$\frac{\partial p^{(c)}}{\partial R}+ik_0\beta p^{(c)}=0 \quad \text{at } R=R_c, \tag{23a}$$

where

$$R=\sqrt{u^2+w^2}, \tag{23b}$$

and k_0 is the wave number of the homogeneous atmosphere. The superscript (c) denotes the sound field above a long cylinder. Again, we are interested in the case where the radius of the cylinder is much greater than the wavelength of interest.

There are numerous investigations into the scattering of sound by an infinitely long cylinder in which the solutions are usually constructed by means of a Fourier series expansion of the incident and reflected waves [see Ref. 21, Chap. 8]. On the other hand, Di and Gilbert[12] considered a two-dimensional problem in connection with the formulation of the parabolic equation (PE) for the prediction of sound propagation over irregular terrain. In their study, they use the method of conformal transformation[17] in which the sound field above an irregular terrain in an otherwise homogeneous atmosphere is mapped to the corresponding situation of the sound field above a flat ground but the speed of sound varies

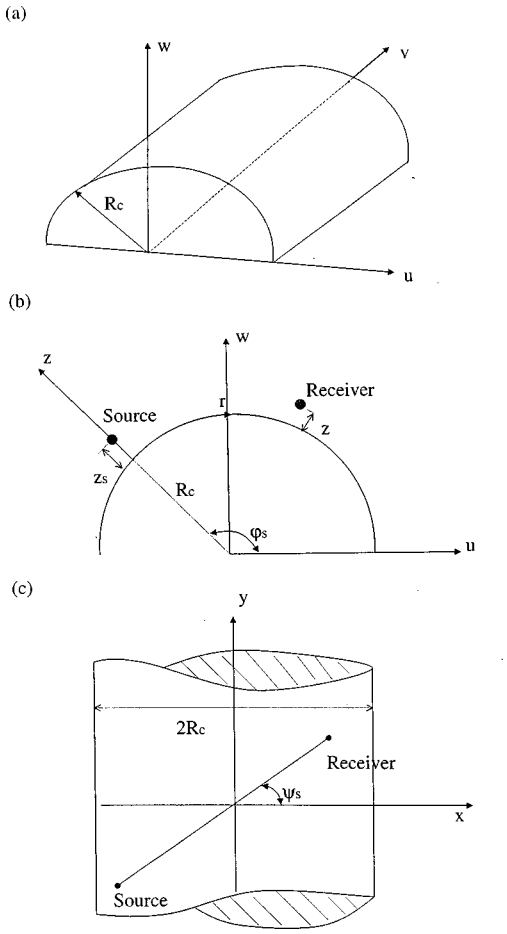

FIG. 5. An illustration of the coordinate systems used in the analysis of sound field above an infinitely long cylinder.

exponentially with height. In this paper, we endeavor to extend the conformal transformation approach to three dimensions. Rather than using the PE approach, we demonstrate that the total sound field can be expressed as an inverse Fourier integral through the use of the method of Fourier transformation. Analytic evaluation of the inverse Fourier integral allows the sound field to be expressed as a sum of a residue series. Following the suggestion of Di and Gilbert,[12] we set

$$\begin{aligned} u&=R_c\,\exp(z/R_c)\cos(x/R_c+\varphi_s),\\ v&=y,\\ w&=R_c\,\exp(z/R_c)\sin(x/R_c+\varphi_s), \end{aligned} \tag{24}$$

where φ_s is a constant angle specified in Fig. 5. It is then possible to show that

$$\begin{aligned} \frac{\partial^2 p^{(c)}}{\partial u^2}&=\frac{1}{\Lambda}\frac{\partial^2 p^{(c)}}{\partial x^2},\\ \frac{\partial^2 p^{(c)}}{\partial v^2}&=\frac{\partial^2 p^{(c)}}{\partial y^2},\\ \frac{\partial^2 p^{(c)}}{\partial w^2}&=\frac{1}{\Lambda}\frac{\partial^2 p^{(c)}}{\partial z^2}, \end{aligned} \tag{25}$$

and

$$\delta(u-u_s)\,\delta(v-v_s)\,\delta(w-w_s)$$

$$=\frac{1}{\Lambda}\,\delta(x-x_s)\,\delta(y-y_s)\,\delta(z-z_s), \tag{26}$$

where Λ is the Jacobian of the transformation given by

$$\Lambda=\frac{\partial(u,w)}{\partial(x,z)}=\exp(2z/R_c), \tag{27}$$

and (x_s,y_s,z_s) are the source position in the transformed space. It is tedious but straightforward to show that the inverse transformations of x, y, and z can be determined according to

$$\begin{aligned} x&=R_c[\tan^{-1}(w/u)-\varphi_s],\\ y&=v,\\ z&=R_c\,\ln(R/R_c). \end{aligned} \tag{28}$$

Hence the source and receiver locations can be expressed in terms of the original Cartesian coordinates (u,v,w) by means of Eq. (28).

By virtue of the conformal transformation [Eqs. (25) and (26)], the Helmholtz equation and the boundary condition become

$$\frac{\partial^2 p^{(c)}}{\partial x^2}+\Lambda\,\frac{\partial^2 p^{(c)}}{\partial y^2}+\frac{\partial^2 p^{(c)}}{\partial z^2}+k_0^2\Lambda p^{(c)}$$

$$=-4\pi S_0\,\delta(x-x_s)\,\delta(y-y_s)\,\delta(z-z_s) \tag{29}$$

and

$$\frac{\partial p_m^{(c)}}{\partial z}+ik_0\beta p^{(c)}=0 \quad \text{at } z=0, \tag{30}$$

respectively. Hence, the problem of predicting the sound field above a two-dimensional cylinder can be interpreted as analogous to that of predicting the propagation of sound in an upward refracting medium above an impedance ground. The transformed wave equation differs from the Helmholtz equation by the Jacobian factor Λ in the second term of the left side of Eq. (29), i.e., $\partial^2 p^{(c)}/\partial y^2$. Nevertheless, this extra term does not pose any analytical difficulty in solving the transformed wave equation for the acoustic pressure above a large cylinder.

Using the method of Fourier transformation on Eqs. (29) and (30), it is possible to show that the acoustic pressure can be expressed in terms of $P(\kappa,\psi,z)$, which is the z-dependent part of the Green's function, to give[20]

$$p^{(c)}(x,y,z)=\int_{-\pi}^{\pi}\int_0^{\infty}\kappa P\,\exp[i\kappa r\,\cos(\psi-\psi_s)]\,d\kappa d\psi. \tag{31}$$

The z-dependent part Green's function, $P(\kappa,\psi,z)$, satisfies the following equation:

$$\frac{d^2P}{dz^2}+k_z^2(z;\kappa)P=-4\pi S_0\,\delta(z-z_s), \tag{32}$$

where

$$k_z(z;\kappa)=+\sqrt{(k_0^2-\kappa^2\sin^2\psi)\exp(2z/R_c)-\kappa^2\cos^2\psi}, \tag{33}$$

and the horizontal wave number is expressed in terms of the polar coordinates (κ,ψ), with magnitude κ, and ψ is the azimuthal angle in the plane of constant z. In addition, k_z can be interpreted as the vertical wave number, which is a function of z. It follows, from Eqs. (32) and (33), that P no longer has azimuthal symmetry as in the previous cases (such as sound propagation over a large sphere), but depends on azimuthal angle. The integral over ψ in Eq. (31) can be estimated straightforwardly by the method of stationary phase provided that P is a slowly varying function of ψ. This condition is satisfied if ψ_r is small as it would be if the propagation of sound is approximately perpendicular to the longitudinal axis of the cylinder. In other words, the theory will be less satisfactory if the straight line joining the source and receiver is almost parallel to the longitudinal axis of the cylinder.

It is straightforward to show that the inverse Fourier integral of Eq. (31) can be approximated by a sum of a residue series as[20]

$$p^{(s)}(r,\psi_r,z)$$

$$\approx\frac{S_0e^{i\pi/4}}{\sqrt{2\pi r}}\sum_n\left\{\frac{\bar{\xi}_s\bar{\xi}}{[k_z(z_s)k_z(z)]^2}\right\}^{1/4}$$

$$\times\frac{\sqrt{K_n}\,\mathrm{Ai}(-\bar{\xi}_s e^{i2\pi/3})\mathrm{Ai}(-\bar{\xi}e^{i2\pi/3})e^{iK_nr}}{[(\xi_0+q_n^2)(\partial\bar{\xi}_0/\partial K_n)-(\partial q_n/\partial K_n)][\mathrm{Ai}(-\xi_0e^{i2\pi/3})]^2}, \tag{34}$$

where

$$q_n=ik_0\beta\sqrt{\bar{\xi}_0/(k_0^2-K_n^2)}, \tag{35a}$$

$$\frac{\partial q_n}{\partial K_n}=\left(\frac{1}{2\bar{\xi}_0}\,\frac{\partial\bar{\xi}_0}{\partial K_n}+\frac{K_n}{k_0^2-K_n^2}\right)q_n, \tag{35b}$$

$$\frac{\partial\bar{\xi}_0}{\partial K_n}=-\left(\frac{R_c}{\sqrt{\bar{\xi}_0}}\right)\left[\frac{K_n\sqrt{k_0^2-K_n^2}\,\sin^2\psi_r}{k_0^2-K_n^2\sin^2\psi_r}+\cos\psi_r\,\tan^{-1}\left(\frac{\sqrt{k_0^2-K_n^2}}{K_n\cos\psi_r}\right)\right], \tag{35c}$$

if $z\leqslant\mathrm{Re}[z_r]$, then

$$\bar{\xi}(z)=\left[\frac{3}{2}\int_{z_t}^{z}\bar{k_z}\,dz\right]^{2/3}$$

$$=\left\{\frac{3}{2}K_nR_c\,\cos\psi_r\left[\frac{\bar{k_z}(z)}{K_n\cos\psi_r}-\tan^{-1}\left(\frac{\bar{k_z}(z)}{K_n\cos\psi_r}\right)\right]\right\}^{2/3}, \tag{35d}$$

and if $\mathrm{Re}(z)>\mathrm{Re}[z_t]$, then

$$\overline{\xi}(z) = -\left[\frac{3}{2}\int_z^{z_t}\sqrt{-k_z^2(z)}\,dz\right]^{2/3}$$
$$= -\left\{\frac{3}{2}K_n R_c\cos\psi_r\left[-\frac{\sqrt{-k_z^2(z)}}{K_n\cos\psi_r} + \tanh^{-1}\left(\frac{\sqrt{-k_z^2(z)}}{K_n\cos\psi_r}\right)\right]\right\}^{2/3}, \quad (35e)$$

In Eqs. (34) and (35a)–(35e), we set $\overline{\xi}\equiv\overline{\xi}(z)$, $\overline{\xi}_0\equiv\overline{\xi}(0)$, $\xi_s\equiv\xi(z_s)$, and $k_z(z)\equiv k_z(z;K_n)$. The horizontal wave number K_n is the solution of the eigenvalue equation

$$e^{i2\pi/3}\mathrm{Ai}'(-\overline{\xi}_0 e^{i2\pi/3}) - q_n\,\mathrm{Ai}(-\overline{\xi}_0 e^{i2\pi/3}) = 0. \quad (36)$$

The turning point z_r, which is determined by setting $\overline{k_z}=0$,[20] is given by

$$z_t = R_c\,\ln\left(\frac{K_n\cos\psi_r}{\sqrt{k_0^2 - K_n^2\sin\psi_r}}\right). \quad (37)$$

Using the methods detailed in Refs. 18 and 20, we can solve the eigenvalues equation numerically and, hence, the sound field can be computed through the use of Eq. (34). Details of the numerical results will be presented in the next sections. The solution given in Eq. (34) is the principal result of the present paper and, to the best of our knowledge, it has not been published elsewhere. It should be noted that the analogy to propagation over a cylindrical surface is refraction in an exponential sound speed profile over a plane. On the other hand, the bilinear profile should be used for the corresponding analogy to propagation over a spherical surface.

We remark that the differences between Eq. (28) of Ref. 20 and Eq. (34) do not support the statement[10] that the sound field behind a cylindrically curved surface is analogous to the sound field over a flat ground in the presence of a wind-induced linear sound speed gradient.

IV. COMPARISONS BETWEEN THEORETICAL PREDICTIONS

In this section, we present numerical results that (a) compare the prediction for an exponential sound speed profile and the prediction for a bilinear profile in the shadow zone above an impedance plane and (b) compare the predictions for both profiles with the published data in the penumbra region.

A. Exponential and bilinear profile predictions in the shadow zone

According to Secs. II and III, it is apparent that the bilinear analogy is generally valid when predicting the sound field behind a large sphere. On the other hand, we can examine the analogy that the sound field above an infinitely long circular cylinder is equivalent to that in the exponential sound speed profile [see Eq. (34)] rather than the bilinear sound speed profile [see Eq. (9)] over a flat ground by comparing predictions in the shadow zone and in the penumbra region.

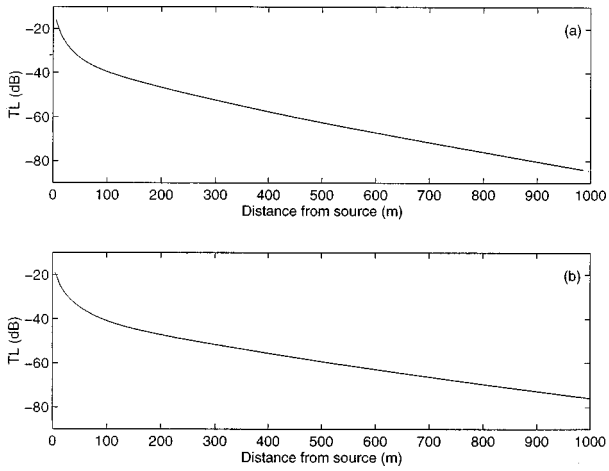

FIG. 6. The predictions of transmission loss at 100 Hz above an impedance ground ($\beta=0.0428-0.0388$i), with $z_s=1.5$ m and $z=1.0$ m. The solid line is the prediction for a bilinear profile ($dc/dz=-0.1\ \mathrm{s}^{-1}$) and the dash–dot line is that for an exponential profile with the same sound speed gradient. Two lines coincide as predictions for both profiles agree to within less than 0.5 dB. (a) $\psi_r=0$ and (b) $\psi_r=\pi/4$.

Figure 6 shows the predictions calculated from these two solutions in the shadow zone. The sound pressure is presented in terms of transmission loss defined by

$$\mathrm{TL} = 20\,\lg\left|\frac{p}{p_1}\right|, \quad (38)$$

where p_1 is the acoustic pressure at a distance of 1 m from the source in the absence of the reflected wave. The angle of the horizontal wave number r axis with an angle, is ψ_r in Eq. (31); for the bilinear analogy, the radius R_c will be replaced by an effective radius

$$R_{\mathrm{eff}} = R_c/\cos^2\psi_r. \quad (39)$$

Figure 6 shows the transmission loss predicted by these two solutions deep in the shadow zone with $\psi_r=0$ and $\pi/4$. Here, when $\psi_r=0$, the line linking the source and receiver is perpendicular to the cylinder axis (see Fig. 5). The sound speed gradient of $-0.1\ \mathrm{s}^{-1}$ (which corresponds to the cylinder radius of 3430 m), the source frequency of 1 kHz, the source and receiver heights of 1.5 and 1 m, respectively, and the specific normalized admittance of (0.0428,0.0388) (which is a typical value for outdoor ground surfaces) are used in the plots. Such a large cylinder is chosen to illustrate a representative atmospheric refraction. We have also compared the sound fields for cylinder with smaller radii of curvature, i.e., stronger sound speed gradients, other source/receiver geometries, and other ground admittance. However, these numerical results show a rather similar trend to that shown in Fig. 6 and, for brevity, they are not plotted here. As shown in Fig. 6, the two solutions show nearly identical results in the shadow zone and the predictions agree to within 0.5 dB. They are valid for both the sound fields behind a large sphere and behind an infinitely long circular cylinder.

B. Predictions in the penumbra region

The agreement between the two models, the bilinear and exponential sound speed profiles, is excellent in the shadow

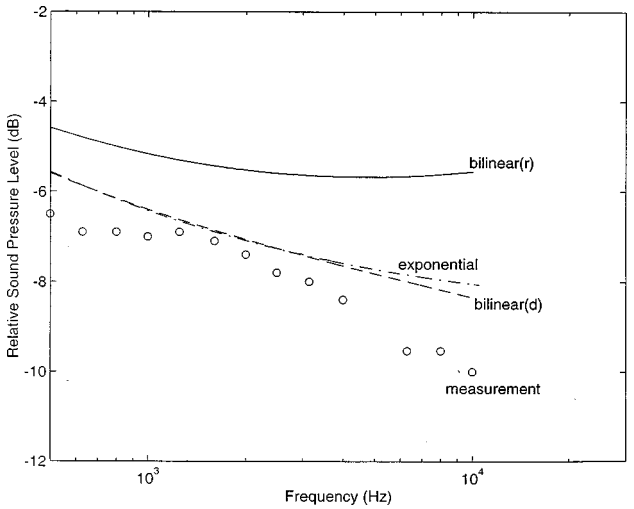

FIG. 7. Relative sound pressure level as a function of frequency for a receiver placed on the limiting ray in the penumbra region behind a rigid curved surface. The circles are the measured results [their Fig. 6(b)] in Ref. 8 with $R_c=5.0$ m, $r=3.85$ m, $z_s=0.43$ m, and $z=0.38$ m. The solid line is the theoretical predictions with the use of the bilinear profile. The dash–dot line is the predictions with the use of the exponential profile and the dashed line is that due to Berthelot's modification on the bilinear profile.

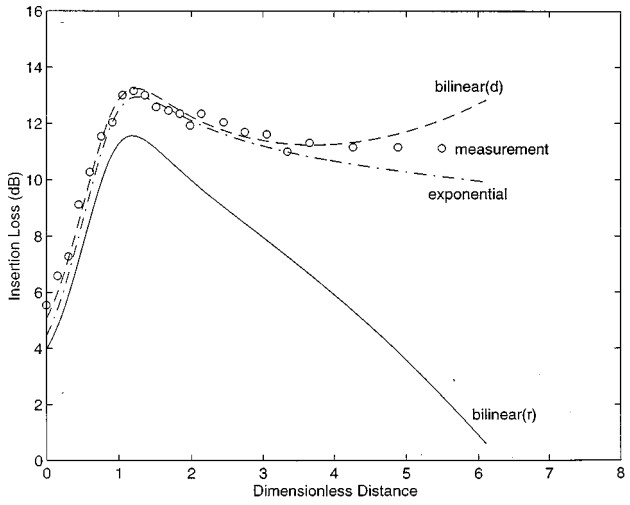

FIG. 8. Insertion loss at 10 kHz as a function of dimensionless distance above an impedance surface ($\sigma=16$ kPa s m^{-1}). The circles are the measured results taken from Fig. 4(b) of Ref. 10, with $R_c=2.5$ m and $z_s=0.24$ m. The solid line is the theoretical predictions with the use of the bilinear profile. The dash–dot line is the predictions with the use of the exponential profile and the dashed line is that due to Berthelot's modification on the bilinear profile.

zone. However, this is not the case along the line of sight in the penumbra region. In this region, the predictions for these two profiles fail to accord with each other. In Fig. 7, we compare these predictions with Berry and Daigle's experimental results when the receiver was moved along the limiting ray [see Fig. 1(b)] above a rigid cylinder with a radius of curvature of 5.0 m in the penumbra region. Experimental results were obtained with the source height of 0.43 m, receiver height of 0.38 m, and a separation of 3.85 m measured along the rigid cylinder. The prediction (dash–dot line) calculated from Eq. (34) shows much better agreement with the experimental results [Fig. 6(b) of Ref. 8] than that (solid line) from Eq. (9). The two residue series converge quite rapidly up to a frequency of 10 kHz with no more than ten terms. The relative sound pressure considered by Berry and Diagle[8] is used in the plot. This is the sound-pressure level relative to free field plus pressure doubling (i.e., 6 dB). Berthelot[9] suggested that interpreting the source–receiver distance r in Eq. (9) as the shortest path d between the source and receiver improves the predictions of the residue series solution for the bilinear profile. However, no rigorous proof is offered for this proposed modification in the definition of r.[9] The improved prediction using d instead of r is shown by the dash line in Fig. 7. In this figure, we demonstrate that this improvement may be achieved also by the more rigorous prediction for the exponential sound speed profile (dash–dot line) in the penumbra region of an infinitely long cylinder.

To investigate the problem in the penumbra region of a cylindrically curved surface further, these three versions of theory are compared to the experimental data obtained by Berthelot and Zhou [Fig. 4(b) of Ref. 16] along the line of sight over an absorbing cylinder. Figure 8 shows these results expressed in terms of the insertion loss, which is defined as

$$\mathrm{IL}=20\ \lg\left|\frac{p_d}{p}\right|, \tag{40}$$

where p_d is the sound pressure at an identical field point in the absence of the cylinder according to Berthelot and Zhou's notation.[16] The dimensionless distance is $X=(k_0R_c)^{1/3}x/R_c$, where x is the distance along the limiting ray from the apex of the cylinder, and $R_c=2.5$ m. The impedance was calculated from the Delany–Bazley model[23] with a flow resistivity of 1.6 MPa s m^{-1} and frequency of 10 kHz. The solid line is the prediction based on Eq. (9), the dashed line is the calculated result of Berthelot[9] using d instead of r, the dash–dot line is predicted by Eq. (34), and the circles are the measured data.[16] A source height of 0.24 m is used[24] in the residue series for the prediction of sound fields. Again, it is obvious that the prediction for the exponential profile shows much better agreement with the experimental data than that for the bilinear profile in the penumbra region over the absorbing cylinder. Moreover, it can be seen that there is again a close agreement between the prediction for the exponential profile (dash–dot line) and Berthelot's improved prediction (dashed line) up to a dimensionless distance of 3 from the apex. Beyond this distance, the discrepancies between the predictions and the measurements are almost equal for the dash–dot line and the dashed line.

V. CONCLUDING REMARKS

We have examined the diffraction of sound by spherical and cylindrical surfaces of finite impedance. An analytical expression has been derived for the sound field scattered by a large sphere. It has been shown that the bilinear analogy is adequate in predicting the sound field over a sphere, but a correction factor is needed for those receivers deep in the shadow zone. Furthermore, an analytical expression has been derived for the sound field diffracted by a cylindrical surface

of a large radius of curvature. It is analogous to the sound field above a flat ground in the presence of an exponential sound speed gradient.

The residue solution for the exponential sound speed profile has been compared to the residue series solution for a bilinear profile, to Berry and Daigle's experimental data, and to Berthelot and Zhou's experimental data. It has been found that the predictions for both profiles agree well with the experimental results within the shadow zone. In the penumbra region, however, there are considerable discrepancies between the prediction for the bilinear profile and the experiments, while the prediction for the exponential profile shows much better agreement with the experiments. For the predictions of the sound field above an infinitely long cylinder, it has been demonstrated that the exponential profiles are very close to those resulting from Berthelot's modification to predictions based on the bilinear profile which involves using the shortest distance instead of an arc length measured from the source to receiver.

The theoretical results reported in this paper justify the use of a spherically curved surface for laboratory measurements of the influence of outdoor temperature gradients on sound propagation. On the other hand, they suggest that it would be rather misleading to use a cylindrically curved surface for indoor measurements as a valid model to study the influence of wind speed gradients on sound propagation outdoors.

ACKNOWLEDGMENTS

We thank the Research Committee of the Open University for support. One of the authors (QW) was supported by an Open University Competitive Studentship. The project was supported in part by the Engineering and Physical Science Research Council (UK) through Grant ref. GR/L 15326.

[1] R. E. Langer (ed.), *Electromagnetic Waves* (Univ. of Wisconsin, Madison, 1962).
[2] N. A. Logan and K. S. Yee, ''A mathematical model for diffraction by convex surfaces,'' in Ref. 1, pp. 139–180.
[3] C. L. Perkeris, ''Theory of propagation of sound in a half-space of variable sound velocity under conditions of formation of a shadow zone,'' J. Acoust. Soc. Am. **18**, 295–315 (1946).
[4] B. D. Seckler and J. B. Keller, ''Geometrical theory of diffraction in inhomogeneous media,'' J. Acoust. Soc. Am. **31**, 192–205 (1959).
[5] B. D. Seckler and J. B. Keller, ''Asymptotic theory of diffraction in inhomogeneous media,'' J. Acoust. Soc. Am. **31**, 206–216 (1959).
[6] V. M. Babic and V. S. Buldyrev, *Short-Wavelength Diffraction Theory* (Springer-Verlag, Berlin, 1991).
[7] A. D. Pierce, *Acoustics. An Introduction to Its Physical Principles and Applications* (Acoustical Society of America, Woodbury, NY, 1991).
[8] A. Berry and G. A. Daigle, ''Controlled experiments of the diffraction of sound by a curved surface,'' J. Acoust. Soc. Am. **83**, 2047–2058 (1988).
[9] Y. H. Berthelot, ''A note on the acoustic penumbra behind a curved surface,'' J. Acoust. Soc. Am. **99**, 2428–2429 (1996).
[10] M. Almgren, ''Simulation by using a curved ground scale model of outdoor sound propagation under the influence of a constant sound speed gradient,'' J. Sound Vib. **118**, 353–370 (1987).
[11] Q. Wang, ''Atmospheric refraction and propagation over curved surfaces,'' Ph.D. thesis, The Open University, 1997.
[12] X. Di and K. E. Gilbert, ''The effect of turbulence and irregular terrain on outdoor sound propagation,'' in Proceedings of 6th International Symposium on Long Range Sound Propagation (1994), pp. 315–333.
[13] J. P. Chambers, R. Raspet, Y. H. Berthelot, and M. J. White, ''Use of the fast field program for predicting diffraction of sound by curved surfaces,'' J. Acoust. Soc. Am. **102**, 646–649 (1997).
[14] A. D. Pierce and G. L. Main, ''Computational algorithms for the matched asymptotic expansion solution of high frequency acoustic wave diffraction by curved surface of finite impedance,'' in *Advances in Computer Methods for Partial Differential Equations-6* (IMACS, Rutgers Univ., New Brunswick, NJ, 1987), pp. 187–194.
[15] Y. H. Berthelot, A. D. Pierce, J. X. Zhou, and J. A. Kearns, ''Outdoor Sound propagation of sources of noise behind a ridge,'' Proc. InterNoise 88, **3**, 1511–1515 (1988).
[16] Y. H. Berthelot and J. X. Zhou, ''Scale model experiments on the validity of the matched asymptotic expansions theory for sound diffraction by curved surfaces of finite impedance,'' J. Acoust. Soc. Am. **93**, 605–608 (1993).
[17] P. M. Morse and H. Feshbach, *Methods of Theoretical Physics, Part I* (McGraw–Hill, New York, 1953), pp. 502–504.
[18] R. Raspet, G. E. Baird, and W. Wu, ''The relationship between upward refraction above a complex impedance plane and the spherical wave evaluation for a homogeneous medium,'' J. Acoust. Soc. Am. **89**, 107–114 (1991).
[19] M. West, F. Walden, and R. A. Sack, ''The acoustic shadow produced by wind speed and temperature gradients close to the ground,'' Appl. Acoust. **27**, 239–260 (1989).
[20] K. M. Li and Q. Wang, ''Analytical solutions for outdoor sound propagation in the presence of wind,'' J. Acoust. Soc. Am. **102**, 2040–2049 (1997).
[21] D. S. Jones. *Acoustics and Electromagnetic Waves* (Claredon, Oxford, 1986), Chap. 8, pp. 411–524.
[22] M. Abramowitz and I. Stegun, *Handbook of Mathematical Functions* (Dover, New York, 1970).
[23] M. E. Delany and E. N. Bazley, ''Acoustical properties of fibrous absorbent materials,'' Appl. Acoust. **3**, 105–116 (1970).
[24] J. P. Chambers, ''Scale model experiments on the diffraction and scattering of sound by geometrical step discontinuities and curved rough surfaces,'' Ph.D. thesis, Georgia Institute of Technology, 1994.

The insertion loss of screens under the influence of wind

Karsten B. Rasmussen and Marta Galindo Arranz[a)]
Department of Acoustic Technology, Building 352, Technical University of Denmark, DK-2800 Lyngby, Denmark

(Received 21 September 1997; revised 5 August 1998; accepted 19 August 1998)

Point source propagation over a screen located on a finite impedance surface representative of grass-covered ground is investigated under upwind and downwind conditions. The theoretical part of the investigation involves extended use of parabolic equation methods (PE) allowing for the changes in the vertical wind speed profile when the wind field passes the screen. The influence of turbulence is also implemented. The experimental part of the investigation relies on a scale model technique based upon a 1:25 scaling ratio and a triggered spark source. The main results relate to the size of the insertion loss of a screen under windy conditions and to the acoustic importance of the redirection of the flow before and after the screen. © *1998 Acoustical Society of America.* [S0001-4966(98)06511-4]

PACS numbers: 43.28.Fp, 43.20.Bi [LCS]

INTRODUCTION

The attenuation obtained by means of outdoor sound barriers has been studied in detail for homogeneous and still air.[1–3] The influence of wind and temperature gradients and turbulence has been investigated considerably for the case of sound propagation over plane unobstructed ground,[4–14] but not for screens. In practice the insertion loss will often be influenced by temperature gradients and wind, including turbulence effects, but it appears that only few studies of this exist.[15–19]

In the present work a screen on a finite impedance surface representative of grass-covered ground is investigated experimentally and theoretically under the influence of wind. Upwind as well as downwind conditions are investigated. The experimental data are the result of model experiments in a 1:25 scale model within a boundary layer wind tunnel. The experiments simulate the effect of noise screens located on porous outdoor surfaces for monopole point source propagation. The sound field is measured using a triggered spark source and averaging on a power basis in the frequency domain. The approximate wind field is determined by means of hot-wire anemometry in positions on both sides of the screen, as well as directly over the screen. While the wind tunnel has been improved, the technique of acoustic measurement and flow measurement is as previously described.[19]

The measured data are compared with calculated results obtained by means of parabolic equation methods. Most of the calculations are based upon assumptions of laminar flow while gradual changes of the wind speed profile along the propagation path are taken into account. To some extent the measurements will be influenced by turbulence generated near the ground and additional turbulence generated by the screen. Additional calculations estimating the influence of turbulence when a screen is present are included and the influence of turbulence is discussed and interpreted.

[a)]Present affiliation: CTBTO, IMS, Hydroacoustics, Vienna International Centre, P.O. Box 1250, A-1400 Vienna, Austria.

I. ACOUSTIC PARABOLIC EQUATIONS THEORY

A. Theory for laminar flow

Starting from the Helmholtz equation the family of parabolic differential equations may be derived. For the case of atmospheric propagation this was first done by Gilbert and White.[4] The main stages of the derivation are repeated here for the sake of clarity.

In a constant density medium with symmetry around a vertical axis through the source location we may write the homogeneous Helmholtz equation in cylindrical coordinates,

$$\frac{\partial^2 p}{\partial r^2}+\frac{1}{r}\frac{\partial p}{\partial r}+\frac{\partial^2 p}{\partial z^2}+k_0^2 n^2 p=0, \tag{1}$$

where the refraction index $n(r,z)$ is equal to $c_0/c(r,z)$ and where the pressure is specified as a function of range and height, $p(r,z)$. k_0 is a reference wave number.

Using the $e^{-i\omega t}$ time convention the solution may be written as a product of two functions, one of which is the Hankel function,

$$p(r,z)=H_0^1(k_0 r)\phi(r,z), \tag{2}$$

where ϕ represents the envelope of the outgoing cylindrical wave given by the Hankel function. The envelope is assumed to be slowly varying in range, r.

Under far field conditions this leads to a simplified elliptic equation,

$$\frac{\partial^2 \phi}{\partial r^2}+2ik_0\frac{\partial \phi}{\partial r}+\frac{\partial^2 \phi}{\partial z^2}+k_0^2(n^2-1)\phi=0. \tag{3}$$

The elliptic wave equation may be further transformed. Considering the outgoing part of the field only and exploiting the assumption that the medium is slowly varying with range, the following equation may be obtained:[13]

$$\frac{\partial \phi}{\partial r}=ik_0\left(\sqrt{n^2+\frac{1}{k_0^2}\frac{\partial^2}{\partial z^2}}-1\right)\phi. \tag{4}$$

This equation is an exact one-way equation in the far field for a range independent medium. However, the presence of

the square root, which is a pseudo-differential operator, necessitates further approximation. Different approximate solution methods exist and these are denoted parabolic equation (PE) methods. The approach used in this work is the standard Crank–Nicolson[13,20] wide angle approximation which employs implicit finite difference for marching the solution in range. This approach is slow in comparison with the fast-PE methods[21,22] but it is well suited for treating range dependent effects. The starter used for source representation is a Greene starter.[13,23,24]

The screen was included in the calculations by means of setting the field to zero on the screen surface as originally suggested by Salomons.[17]

B. Theory for turbulent flow

For the sake of the present investigation an approach estimating the influence of turbulence on the acoustic propagation is needed. The approach used in this work was developed by Galindo[13] which in turn follows the ideas from Gilbert *et al.*[8] but with a different implementation.

From Eq. (4), our standard parabolic equation, the refraction index $n(r,z)$ may be rewritten as $n_d+\mu(r,z)$, where n_d is the deterministic component and μ is the stochastic component, and the pseudo-differential operator, Q, may be expressed as

$$Q=\sqrt{1+q}, \quad q=(n_d+\mu)^2+\frac{1}{k_0}\frac{\partial^2}{\partial z^2}-1. \tag{5}$$

q may be written as

$$q=q_d+\mu^2+2\mu n_d, \quad q_d=n_d^2+\frac{1}{k_0}\frac{\partial^2}{\partial z^2}-1, \tag{6}$$

where the right hand equation defines q_d. As a result the parabolic equation may be written as

$$\frac{\partial \phi}{dr}=ik_0(\sqrt{1+q_d+2n_d\mu}-1)\phi, \tag{7}$$

where weak turbulence ($\mu^2 \ll 1$) has been assumed. Expanding the square root for small argument one obtains

$$\sqrt{1+q_d+2n_d\mu}=1+\tfrac{1}{2}(q_d+2n_d\mu)-\tfrac{1}{8}(q_d+2n_d\mu)^2+\cdots. \tag{8}$$

Ignoring small terms one obtains the result

$$\sqrt{1+q_d+2n_d\mu}\approx 1+\tfrac{1}{2}q_d-\tfrac{1}{8}q_d^2+n_d\mu. \tag{9}$$

In this equation the first three terms represent the Taylor expansion of $(1+q_d)^{1/2}$. This means that the pseudo-differential operator, Q, may be written as

$$Q\approx Q_d+n_d\mu, \quad Q_d=\sqrt{1+q_d}. \tag{10}$$

The Crank–Nicolson implicit difference scheme is applied for marching the equation in range. This is a relatively slow approach. This may perhaps be improved by means of the split-step algorithm as proposed in Gilbert *et al.*[8]

In order to introduce the stochastic fluctuations into the calculations it is necessary to introduce the assumption that the two-dimensional autocorrelation function $B_n(s)$ is Gaussian:

$$B_n(s)=\mu_0^2 e^{-|s|^2/L^2}. \tag{11}$$

L is the correlation length (turbulence scale), s is the separation distance in the r-z plane, and μ_0^2 is the variance of μ (turbulence strength).

The wave number spectrum $W(k_r,k_z)$ is defined as the Fourier transform of the autocorrelation function,

$$W(k_r,k_z)=\int\int B_n(s_r,s_z)e^{i(k_r s_r+k_z s_z)}\,ds_r\,ds_z, \tag{12}$$

where k_r and k_z are the radial and the vertical components of the wave number vector, and s_r and s_z are the radial and vertical components of the spatial separation.

From integration of Eq. (12) one obtains the wave number magnitude spectrum,

$$\sqrt{W(k_r,k_z)}=\mu_0 L\sqrt{\pi}e^{-(1/8)(k_r^2+k_z^2)L^2}. \tag{13}$$

$\mu(r,z)$ may be found from inverse Fourier transformation of $(W)^{1/2}$ multiplied by a uniformly distributed random phase function, ψ,

$$\mu(r,z)=\frac{N}{(2\pi)^2}\int\int\sqrt{W(k_r,k_z)}e^{-i(k_r r+k_z z)} \times e^{-i\psi(k_r,k_z)}\,dk_r\,dk_z, \tag{14}$$

where N is a normalization factor given by the square root of the area over which μ is defined. Different randomizations of ψ represent different realizations of the turbulence.[8]

C. Implementation

Fluid mechanics research on flow over obstacles seems to imply that while the velocity profile takes more than 50 screen heights after the screen to recover to the condition before the screen, some sort of logarithmic profile is found again as early as 6 step heights after the screen.[25] Numerical simulations may be carried out based on Navier–Stokes equations taking viscosity into account. No analytical representation of the development of the flow over a vertical screen on a horizontal surface exists[26] except for the approach based on Laplace's equation valid for irrotational flow only.[27] This simplification leads to a flow which is symmetric with respect to the screen. Such a symmetry is by no means present in experimental data as may be inferred from the above statement concerning flow recovery reported by fluid mechanics specialists.

In the present work, the flow is described by logarithmic profiles all the way over the screen. The expression for the sound speed profile is

$$c(z)=c_0+v_0\ln\left(\frac{z}{z_0}\right), \tag{15}$$

where c_0 is the sound speed in the absence of wind and $c(z)$ expresses the effective sound speed profile used in simulations. Two different screens are considered, one 2.5 m high, the other 1.25 m high.

An interpolation of the flow parameters v_0 and z_0 determining the sound speed profile is initiated 5 m before the flow arrives at the screen. The vertical profile is gradually modified so that the roughness length, z_0, is equal to the

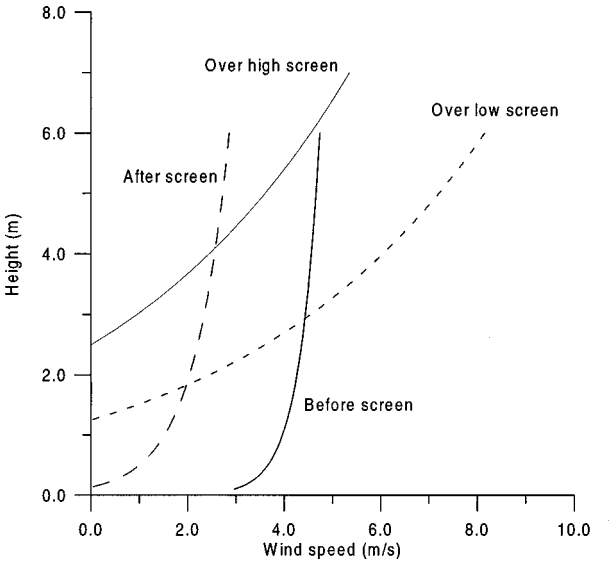

FIG. 1. Analytical approximations for wind speed profiles.

screen height at the screen position. The transition is based on simple linear interpolation of the values of (v_0, z_0). The interpolation is determined by $(v_0, z_0) = (0.4341, 0.000\,108\,3)$ at 5 m before screen, $(v_0, z_0) = (5.2, 2.5)$ at high screen or $(v_0, z_0) = (5.2, 1.25)$ at low screen. The values for the parameters (v_0, z_0) are determined from flow measurements and $(0.4341, 0.000\,108\,3)$ represents flow for unobstructed terrain, whereas the values given at the screen position represent the flow at this position for the two screen heights.

After the flow has passed the screen, a similar transition is used but the interpolation is carried out in a zone extending to 15 m after the screen. Hence, the rate of change of the profile is taken to be three times slower after the screen than before the screen. At 15 m $(v_0, z_0) = (0.7498, 0.1321)$. These parameter values lead to the curves in Fig. 1.

It should be stressed that the transition of flow close to the screen is only modeled in a very simplified way by these considerations but a more accurate description is not easily found.

The ground was characterized by flow resistivity and layer thickness (full scale values) in the impedance model described by Attenborough[28] as the 2PA model. In the present notation $(e^{-i\omega t})$ it reads thus:

$$Z(\sigma,\beta) = \sqrt{\frac{\sigma}{f}}\,0.4342(1+i) + i\,\frac{\beta}{f}\,9.6485, \tag{16}$$

where convenient values have been inserted for sound speed (340 m/s), density (1.204 13 kg/m^3), and ratio of specific heats (1.4021). The parameter Z denotes the relative characteristic impedance and β denotes the rate of exponential decrease of porosity with depth. Alternatively β may be interpreted as $2/d_e$, where d_e is the effective thickness of a porous layer of constant porosity on a hard backing. σ is the flow resistivity.

The PE calculations are based upon the use of 8 points per wavelength horizontally as well as vertically and a total of 4000 vertical discretization points.

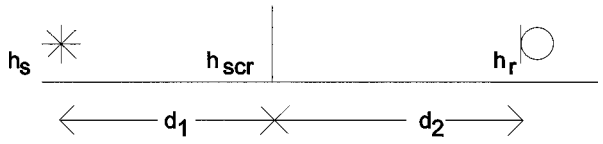

FIG. 2. Full scale geometrical parameters. $h_s = 1.5$ m in all cases.

II. RESULTS

A. Meteorological data from scale model

The meteorological data are obtained from Dantec Streamline hot-wire anemometry equipment (using a type 55p11 single wire probe). The wind speed is found as an average over 54 s. A meteorological sampling rate of 300 Hz was used; this rate was found to be more than sufficient. The anemometer probes were positioned with a vertical wire to obtain measured data that was insensitive to vertical flow.

The wind speed profile was measured in positions (converted to full scale) 12.5 m before the flow reaches the screen; another profile measurement was made just above the screen and in positions 12.5 m after the screen. The logarithmic wind speed profiles obtained by curve fitting are shown in Fig. 1. Note that the speed above the screen is higher than before and after the screen as a consequence of the redirection of the flow caused by the screen.

B. Comparison with acoustical data from scale model

The acoustic measurements are based on energy averaging in the frequency domain of 12 pulses, each of which has been edited in the time domain so that reflections from tunnel walls, etc. are removed. Energy averaging is necessary because of the stochastic process involved in propagation under the influence of wind. The frequency range of the measured data is limited to between 125- and 3000-Hz full scale—the frequency range where the signal-to-noise ratio was satisfactory. The basic setup involving the screen is shown in Fig. 2. The thickness of the model screen was 9 mm corresponding to 22.5 cm in full scale. Equation (16) was used to describe the acoustic impedance of the ground surface (which was a layer of very open synthetic material on top of a thin cotton material on hard backing) with $\sigma = 7$ kNsm^{-4} and $\beta = 125$ m^{-1} for full scale frequencies. The value of β corresponds to a homogeneous porous layer of thickness $d_e = 2/\beta = 0.0160$ m on a hard backing. This full scale thickness is approximately 25 times the physical thickness of the material used in the scale model. The choice of parameter values in the 2PA model is the result of curve-fitting sound pressure level results as a function of full scale frequency for the case without wind and for unobstructed terrain.

The measured results shown in the figures are all scale model data which are shown in a full scale context. Hence, all frequencies and heights and distances refer to full scale conditions. The source height is 1.5 m in all cases. Figure 3 shows relative sound pressure levels for an unscreened case with a wind speed profile as shown in Fig. 1 (curve labeled ''before screen''). The agreement between measured data and calculated values is seen to be quite good except for

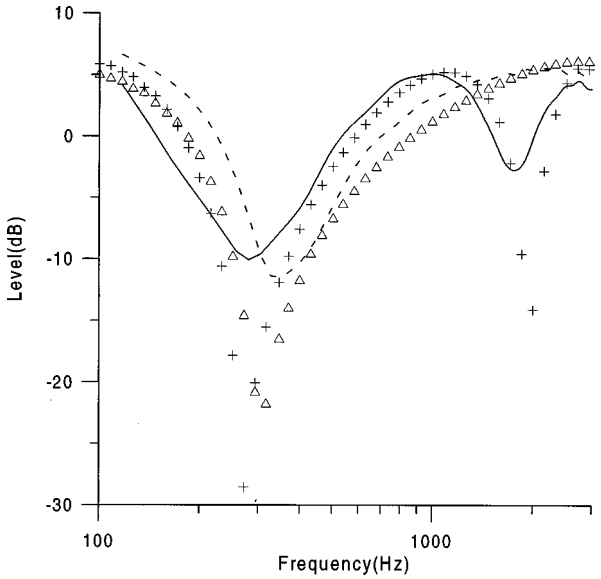

FIG. 3. Sound pressure level relative to free field. $h_{scr}=0$, $h_r=2.5$ m, $d_1+d_2=60$ m. Full line, measured for downwind; +, calculated for downwind; dashed line, measured for upwind; △, calculated for upwind.

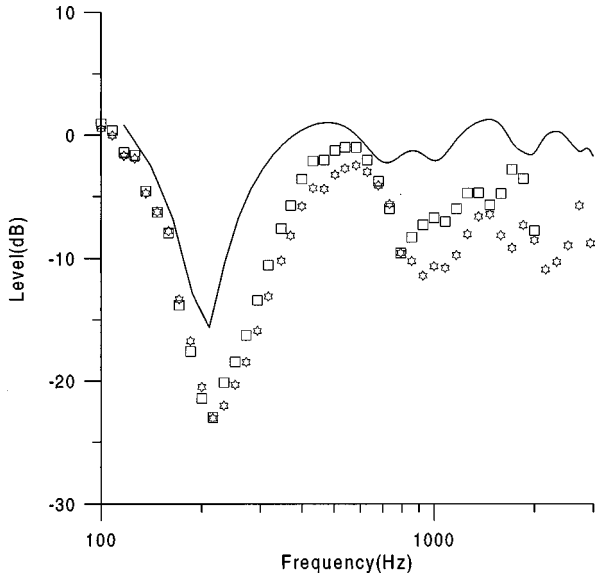

FIG. 5. Sound pressure level relative to free field. $h_{scr}=2.5$, $h_r=2.5$ m, $d_1=25$ m, $d_2=35$ m. Full line, measured for downwind; calculated for downwind (□) based on 5-m flow transition zone upstream of screen and 15-m transition zone downstream of screen. Additional calculations (☆) for discontinuous wind speed profile (no transition zone).

frequencies where the level has a sharp minimum. (Results without wind and measured over a similar acoustic surface may be found in previous work[3] and they also agree well with calculated data from the 2PA model.)

In Fig. 4 the distance from source to screen is 25 m and from screen to receiver 35 m. The screen height is 1.25 m and the receiver height is 0.5 m. The calculations are for laminar wind flow. The agreement between measured and calculated data is good, especially for no wind.

In Figs. 5 and 6 the distances and heights are the same as in Fig. 4 except for the screen height which is now increased to 2.5 m and the receiver height which is increased to 2.5 m. It should be noted that Figs. 5 and 6 show results of two slightly different calculations. Either a transition zone of 5 m before and 15 m after the flow passes the screen is included in the simulations taking the wind into account, or the wind profile is considered to change abruptly at the screen location. The former approach is a simulation of the actual flow conditions near the screen, whereas the latter approach treats the wind speed profiles as constant from source to screen and again from screen to receiver. The results indicate that the simple discontinuous approach is insufficient for higher frequencies, and also that better agreement is obtained for upwind than for downwind. This is a general trend and is re-

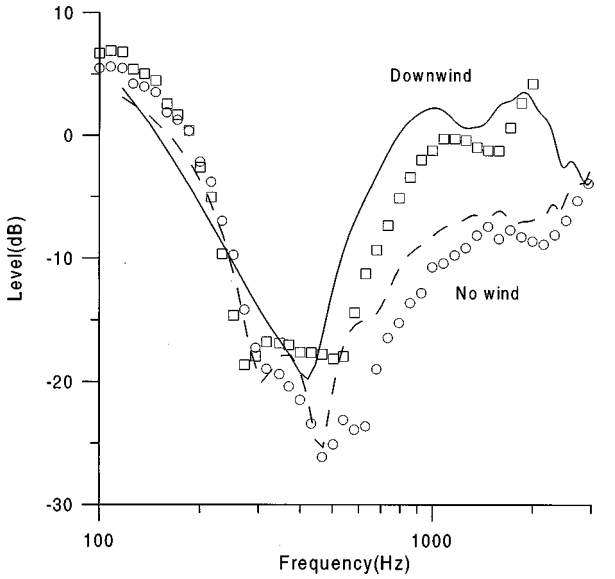

FIG. 4. Sound pressure level relative to free field. $h_{scr}=1.25$, $h_r=0.5$ m, $d_1=25$ m, $d_2=35$ m. Full line, measured for downwind; □, calculated for downwind; dashed line, measured for nowind; ○, calculated for nowind. Calculations for wind based on 5-m flow transition zone upstream of screen and 15-m transition zone downstream of screen.

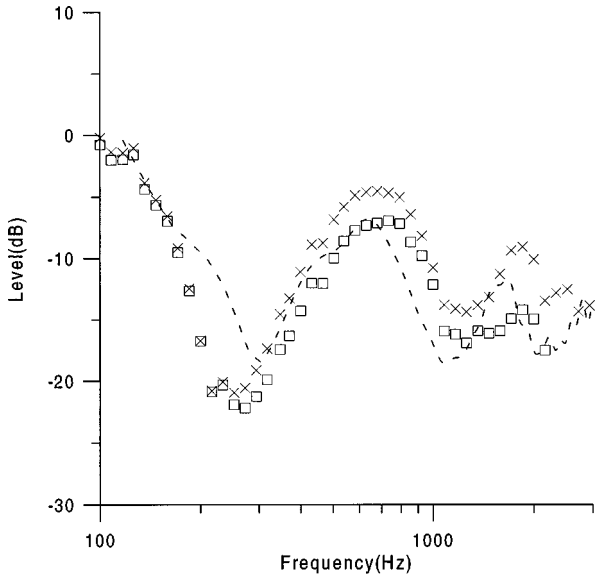

FIG. 6. Sound pressure level relative to free field. $h_{scr}=2.5$, $h_r=2.5$ m, $d_1=25$ m, $d_2=35$ m. Interrupted line, measured for upwind; calculated for upwind (□) based on 5-m flow transition zone upstream of screen and 15-m transition zone downstream of screen. Additional calculations (×) for discontinuous wind speed profile (no transition zone).

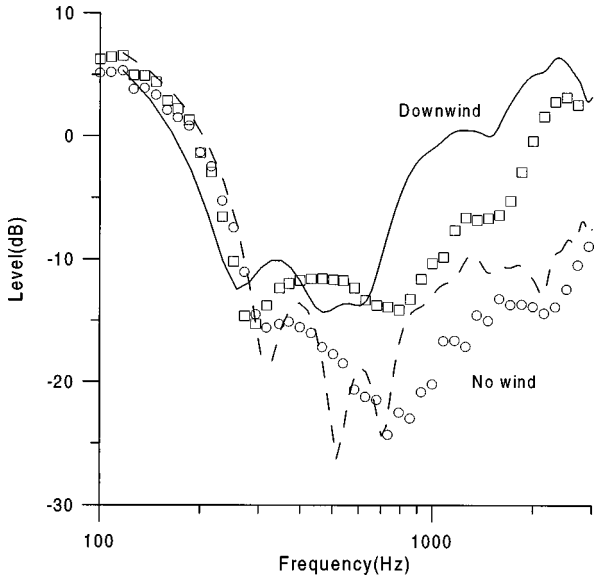

FIG. 7. Sound pressure level relative to free field. $h_{scr}=1.25$, $h_r=0.25$ m, $d_1=25$ m, $d_2=25$ m. Full line, measured for downwind; □, calculated for downwind. Calculations for wind based on 5-m flow transition zone upstream of screen and 15-m transition zone downstream of screen. Interrupted curve, measured for no wind; ○, calculated for no wind.

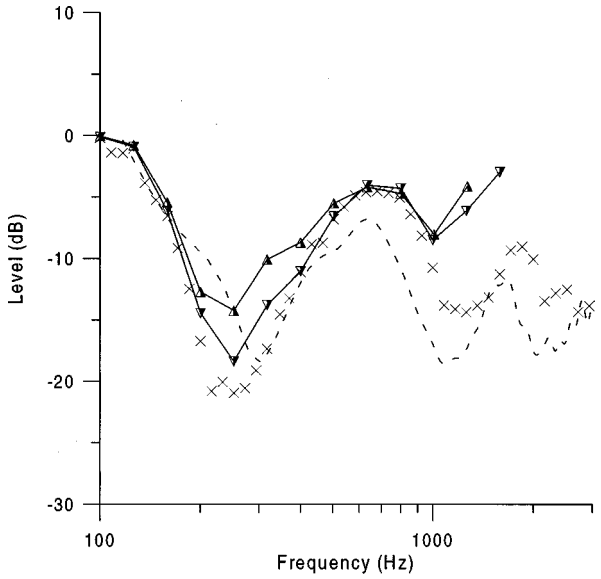

FIG. 8. Sound pressure level relative to free field. $h_{scr}=2.5$, $h_r=2.5$ m, $d_1=25$ m, $d_2=35$ m. Interrupted line, measured for upwind; ×, calculations for discontinuous wind speed profile (no transition zone). Triangles denote calculations including turbulence effect for ten realizations. Turbulence is assumed to originate from the screen and is taken into account until 10 m after the flow has passed the screen. $\mu_0^2=0.0002$. Triangles base down: correlation length $L=1.1$; base up: $L=0.4$.

lated to the asymmetry of the flow pattern close to the screen. When the extended transition region is on the receiver side (i.e., for downwind) the acoustic results become sensitive to the lack of a precise flow representation in the region.

An additional example is shown in Fig. 7 representing the case where the distance from screen to receiver is reduced to 25 m. The low screen height of 1.25 m is used and the receiver height is only 0.25 m. The distance from source to screen is still 25 m.

Experimental evidence obtained using the anemometer equipment and correlation analysis as suggested by Daigle *et al.*[6] shows that the full scale correlation length, L, is approximately 0.4 m, and that μ_0^2 is of the order 3×10^{-6} measured as the variance of the wind speed divided by the sound speed squared. Strictly speaking, the scale modeling technique is not applicable when turbulence is considered, since turbulence effects do not scale. The primary reason for this is that the viscous properties of the fluid are not scaled.[27] It must be added, however, that the correlation length usually found in outdoor experiments without screens is around 1.1 m, and μ_0^2 is usually close to 2×10^{-6}, values that are close to those obtained from the scale model experiment. Numerical simulations according to the method described in Sec. I B have shown negligible influence from turbulence using the abovementioned values. The turbulence calculation example included as Fig. 8 is made for exaggerated turbulence values in order to show the qualitative influence. It is seen that the interference minima are affected as could be expected.

The measured and calculated insertion loss of the screens are displayed directly in Figs. 9 and 10 valid for downwind and upwind, respectively, for a 2.5-m screen. The agreement between measured and calculated results is quite good, especially for upwind. For downwind the results show that the insertion loss fluctuates around zero. This is in agreement with findings of Scholes *et al.*[16] who measured the influence of screens (full scale measurements) and who found that in a downwind situation the insertion loss was not always positive.

III. CONCLUSIONS

The primary conclusion of the present work is that the experiments infer that the applied PE method is applicable to the combined effect of screens and wind provided that sufficient information about the wind field is present. This result is not trivial since a number of approximations are inherent

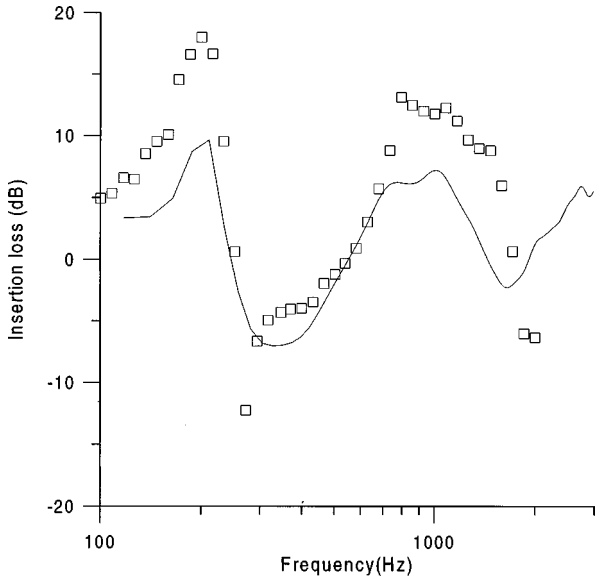

FIG. 9. Insertion loss for downwind based upon data from Figs. 3 and 5. Full line, measured; □, calculations for wind based on 5-m flow transition zone upstream of screen and 15-m transition zone downstream of screen.

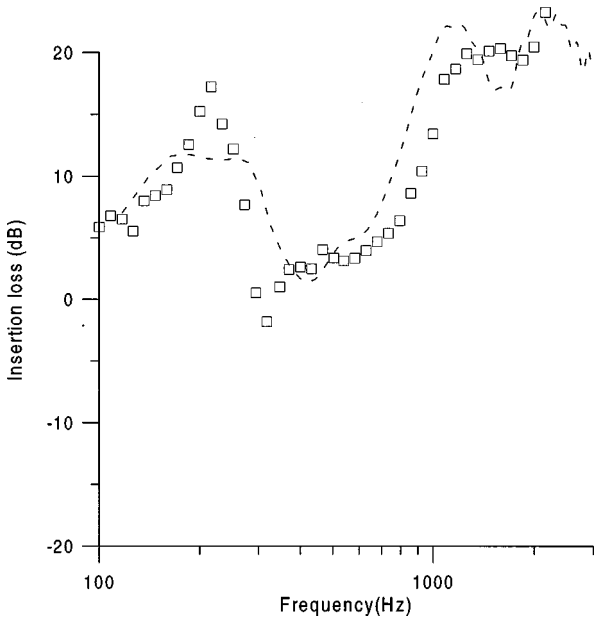

FIG. 10. Insertion loss for upwind based upon data from Figs. 3 and 6. Interrupted line, measured; □, calculations for wind based on 5-m flow transition zone upstream of screen and 15-m transition zone downstream of screen.

in the numerical approach used, namely one-way propagation only, decreasing accuracy as the acoustic emission angle reaches around 40 degrees measured from horizontal (this is a combination of the PE approach and the choice of starter representing the source field). These are the fundamental PE limitations. In addition to that the screen is included in the calculations in a nonrigorous manner and the mere presence of the screen is in conflict with the assumption included in the PE approach that the topography must only change slowly.

Additional problems are related to the wind field. It is very difficult to make an accurate implementation of a wind speed profile which develops with distance in a realistic manner. And lastly the turbulence is taken into account in (some of) the calculations but based on assumptions of Gaussian distributions and of weak turbulence only.

The most important problem is believed to be the problems related to the wind field. Results in other publications[1–3] have shown that when no wind is present, very satisfactory results for the sound pressure level behind screens may be obtained. Trying to understand the details of that limitation, it may be said that the complicated flow pattern (laminar flow) was more important to the results than hitherto supposed, and for the results presented here the turbulence seems to play a less significant role than previously believed.[18]

The experiments presented in this work are meant to be representative of full scale noise barriers. Such a transformation of results is likely to cause inaccuracies, and for the case of turbulence it is in fact known to be inaccurate since the viscous properties of the fluid are not scaled. It is unlikely, however, that the deviations related to the incomplete scaling will affect the overall tendencies in the results obtained for flow. On the basis of the results obtained in this work it therefore is reasonable to expect the exact flow pattern close to a noise screen to be important for the insertion loss. This means that the flow pattern associated with a specific noise screen design could be an important parameter. Previous studies of the influence of the screen shape in a still and homogeneous atmosphere[1] should in the future be supplemented by studies taking the wind flow over the screen into account.

[1] D. C. Hothersall, S. N. Chandler-Wilde, and M. N. Hajmirzae, ''Efficiency of single noise barriers,'' J. Sound Vib. **146**, 303–322 (1991).
[2] D. J. Saunders and R. D. Ford, ''A study of the reduction of explosive impulses by finite sized barriers,'' J. Acoust. Soc. Am. **94**, 2859–2875 (1993).
[3] K. B. Rasmussen, ''Model experiments related to outdoor sound propagation over an earth berm,'' J. Acoust. Soc. Am. **96**, 3617–3620 (1994).
[4] K. E. Gilbert and M. J. White, ''Application of the parabolic equation to sound propagation in a refracting atmosphere,'' J. Acoust. Soc. Am. **85**, 630–637 (1989).
[5] K. B. Rasmussen, ''Computer simulation of sound propagation over ground under the influence of atmospheric effects. Letter to the editor,'' J. Sound Vib. **141**, 347–354 (1990).
[6] G. A. Daigle, J. E. Piercy, and T. F. W. Embleton, ''Effects of atmospheric turbulence on the interference of sound waves near a hard boundary,'' J. Acoust. Soc. Am. **64**, 622–630 (1978).
[7] G. A. Daigle, ''Effects of atmospheric turbulence on the interference of sound waves above a finite impedance boundary,'' J. Acoust. Soc. Am. **65**, 45–49 (1979).
[8] K. E. Gilbert, R. Raspet, and X. Di, ''Calculation of turbulence effects in an upward-refracting atmosphere,'' J. Acoust. Soc. Am. **87**, 2428–2437 (1990).
[9] M. R. Stinson, D. I. Havelock, and G. A. Daigle, ''Comparison of predicted and measured sound pressure levels within a refractive shadow in the presence of turbulence,'' Proceedings of Inter-Noise 95, July 10–12, 1995 (Newport Beach, CA, 1995), pp. 327–330.
[10] A. L'Espérance, Y. Gabillet, and G. A. Daigle, ''Outdoor sound propagation in the presence of atmospheric turbulence: Experiments and theoretical analysis with the fast field program algorithm,'' J. Acoust. Soc. Am. **98**, 570–579 (1995).
[11] R. Raspet and Wenliang Wu, ''Calculation of average turbulence effects on sound propagation based on the fast field program formulation,'' J. Acoust. Soc. Am. **97**, 147–153 (1995).
[12] P. Chevret, Ph. Blanc-Benon, and D. Juvé, ''A numerical model for sound propagation through a turbulent atmosphere near the ground,'' J. Acoust. Soc. Am. **100**, 3587–3599 (1996).
[13] Galindo Arranz, ''The parabolic equation method for outdoor sound propagation,'' Department of Acoustic Technology, DTU, Report No. 68 (1996).
[14] V. E. Ostashev, G. Goedeke, F. Gerdes, R. Wandelt, and J. Noble, ''Line-of-sight sound propagation in the turbulent atmosphere with Gaussian correlation functions of temperature and wind velocity fluctuations,'' *Proceedings of Seventh Int. Symp. on Long Range Sound propagation*, Ecole Centrale de Lyon, 24–26 July 1996, Lyon, France, pp. 339–357.
[15] R. DeJong and E. Stusnick, ''Scale model studies of the effects of wind on acoustic barrier performance,'' J. Noise Control Eng. **6**, 101–109 (1976).
[16] W. E. Scholes, A. C. Salvidge, and J. W. Sargent, ''Field performance of a noise barrier,'' J. Sound Vib. **16**, 627–642 (1971).
[17] E. M. Salomons, ''Diffraction by a screen in downwind sound propagation: A parabolic-equation approach,'' J. Acoust. Soc. Am. **95**, 3109–3117 (1994).
[18] K. B. Rasmussen and M. Galindo Arranz, ''Scale model investigations into the insertion loss of screens under the influence of wind,'' J. Acoust. Soc. Am. **100**, 2589(A) (1996).
[19] K. B. Rasmussen, ''Sound propagation over screened ground under upwind conditions,'' J. Acoust. Soc. Am. **100**, 3581–3586 (1996).
[20] D. Lee and S. T. McDaniel, *Ocean Acoustic Propagation by Finite Difference Methods* (Pergamon, New York, 1988).
[21] K. E. Gilbert and Xiao Di, ''A fast Green's function method for one-way sound propagation in the atmosphere,'' J. Acoust. Soc. Am. **94**, 2343–2352 (1993).
[22] M. Galindo, M. R. Stinson, and G. Daigle, ''Comparison of some methods

used for prediction of atmospheric sound propagation,'' Canadian Acoustics **25**, 3–12 (1997).
[23] R. R. Greene, ''The rational approximation to the acoustic wave equation with bottom interaction,'' J. Acoust. Soc. Am. **76**, 1764–1773 (1984).
[24] F. B. Jensen, W. A. Kuperman, M. B. Porter, and H. Schmidt, *Computational Ocean Acoustics* (AIP Press, New York, 1994).
[25] H. Le, P. Moin, and J. Kim, ''Direct numerical simulation of turbulent flow over a backward-facing step,'' J. Fluid Mech. **330**, 349–374 (1997).
[26] N. O. Jensen, Risø National Laboratory, Risø, Denmark, Personal communication (1997).
[27] B. S. Massey, *Mechanics of Fluids* (Van Nostrand Reinhold, U.K., 1983), 5th ed.
[28] Equation (12) in K. Attenborough, ''Ground parameter information for propagation modeling,'' J. Acoust. Soc. Am. **92**, 418–427 (1992).

Bubble counting using an inverse acoustic scattering method

Ramani Duraiswami,[a] Sankar Prabhukumar, and Georges L. Chahine
Dynaflow, Inc., 7210 Pindell School Road Fulton, Maryland 20759

(Received 19 February 1997; revised 30 April 1998; accepted 19 August 1998)

A nuclei size measurement technique is developed, based on a dispersion relation for propagation of sound waves through a bubbly liquid. This is used to relate the attenuation and phase velocity of a sound wave to the bubble population, leading to two integral equations. These equations are ill posed, and require special treatment for solution. Algorithms based on a minimization method that imposes a number of physical constraints on the solution, rendering the equation well posed, are developed. The procedure is first tested on analytical data with varying artificial noise added, and found to be successful in recovering the bubble density function, and to perform much better than other published solution techniques. Then, bubbles were generated using electrolysis and air injection through porous tubes, and bubble populations measured. Short monochromatic bursts of sound at different frequencies were emitted and received using hydrophones. The received signals were then processed and analyzed to obtain the attenuation and phase velocity. The void fraction and known experimental errors were also obtained and were fed as constraints to the inverse problem solution procedure. This resulted in bubble populations which compare favorably to those obtained by microphotography. [S0001-4966(98)05811-1]

PACS numbers: 43.30.Es, 43.30.Pc, 43.20.Ye, 43.25.Yw [SAC-B]

INTRODUCTION

Determination of the bubble population in a sample of liquid is an important problem in many fields. A significant amount of experimental work has been performed to determine the bubble size distribution in given samples of water (e.g., Refs. 1–11). These experiments can be divided into optical studies (including scattering, photographic, and holographic), acoustical studies (including scattering, attenuation, and dispersion), and others (including electrical impedance[12] and cavitation susceptibility[13]).

Acoustical methods are inverse methods, relying on the fact that bubbles have a strong effect on the propagation of acoustic waves. The acoustical cross section of a bubble is three to four orders of magnitude greater than its geometrical cross section.[2] Acoustical techniques are relatively simple, and applicable to much larger liquid samples. Additionally, the ocean is much more transparent to the passage of acoustic waves than it is to light.

The predictions of existing acoustical and optical techniques differ widely;[14] for instance, the acoustical method of Wildt[15] overpredicts the bubble population density by as much as two orders of magnitude at small radii, and underpredicts it significantly at larger radii. The error lies in the procedures used to infer the bubble population from the measurements. In this paper we present a consistent method for obtaining the bubble population from measurements.

Using a set of effective equations, derived by taking the limit of the complete equations of motion to small bubble volume fractions,[16] a dispersion relation for bubbly fluids was developed by Commander and Prosperetti.[17] This relationship was used to obtain the attenuation and phase velocity for *given bubble populations* and was compared very favorably with measurements. They also found that the computed attenuation and phase velocity were quite sensitive to the bubble population distribution. Here, we use the inverse procedure and obtain two integral equations for the bubble population density in terms of the phase velocity and attenuation. Solution of these equations using *measured* values of the attenuation and change in phase velocity will allow computation of the bubble population. The problem faced in the solution of these equations is that the equations are ill posed. We considered in Refs. 18 and 19 several approaches for solving this ill-posed problem, and found that among the approaches tested one based on constrained minimization worked best.

In Sec. I we describe the governing equations of the problem and their characteristics. In Sec. II we present the details of our algorithm. In Sec. III we apply the algorithm to synthetic data obtained from assumed bubble populations and show that the algorithm is successful in recovering the bubble population. In Sec. IV, we describe experiments conducted to validate the method for measurement of the bubble population. The signal processing procedures used to analyze the signals are described in Sec. V. The method is applied to obtaining bubble populations from experiments in Sec. VI, and the resulting bubble populations validated against photographic data in Sec. VII. Conclusions are presented in Sec. VIII.

I. GOVERNING EQUATIONS

Consider a bubbly medium consisting of a pure liquid of sound speed c_l containing spherical bubbles of different radii. The bubble size distribution in the liquid is characterized by the bubble population density, $N(a)$, defined such that

[a]Electronic mail: ramani@dynaflow-inc.com

$$\int_{a_1}^{a_2} N(a)\, da = \text{number of bubbles with radii in } [a_1, a_2] \text{ per unit volume.} \tag{1}$$

Here a denotes the equilibrium radius of the bubbles. N thus is a *density* and has SI units: number/m^{-4}.

When sound of frequency ω propagates through the bubbly medium, the bubbles oscillate, and extract and reradiate energy into the medium, thereby making it dispersive. Each bubble may be treated as an oscillator with a characteristic natural frequency ω_0 and a damping constant b that depend upon the frequency of the insonifying wave and the radius of the bubble. The effect of this dispersive behavior is to make the sound speed in the mixture, C_m, complex.

A dispersion relation relating the complex sound speed in the mixture to the sound speed in the pure medium, as a function of the bubble density function, was derived by Commander and Prosperetti,[17] on the basis of effective equations for sound propagation in bubbly liquids (valid at low bubble void fractions) obtained by Caflisch *et al.*[16] This equation is the starting point of our work, and is

$$\frac{c_l^2}{C_m^2} = 1 + 4\pi c_l^2 \int_{a_{\text{lo}}}^{a_{\text{hi}}} \frac{aN(a)}{\omega_0^2 - \omega^2 + 2ib\omega}\, da, \tag{2}$$

where i represents the imaginary unit.

Equation (2) enables computation of the complex speed of sound in the bubbly mixture, C_m, for a monochromatic wave of frequency $\omega/2\pi$ for known bubble population distribution and known bubble natural frequencies and damping. We use the expressions obtained in Ref. 20 for the bubble natural frequency and the damping. These are obtained on the basis of a linearized study of the oscillation of a single gas bubble in response to a monochromatic wave, and are

$$\omega_0^2 = \frac{p_\infty - p_v + 2\sigma/a}{\rho a^2}\left(\Re(\Phi) - \frac{2\sigma}{a p_0}\right), \tag{3}$$

$$b = \frac{2\mu}{\rho a^2} + \frac{p_0}{2\rho a^2}\,\Im(\Phi) + \frac{\omega^2 a}{2c} = b_v + b_{th} + b_{ac}. \tag{4}$$

Here, p_∞ refers to the liquid equilibrium pressure, p_v the liquid vapor pressure in the bubble, σ is the surface tension, and the quantity p_0 is the gas pressure in the bubble at equilibrium and is given by

$$p_0 = p_{g0} + p_v = p_\infty + \frac{2\sigma}{a}. \tag{5}$$

Here p_{g0} is the pressure due to noncondensible gases in the bubble; $\Re$ and $\Im$, respectively, refer to the functions that yield the real and imaginary parts of a complex quantity. The three parts making up the expression for b are the damping due to viscosity, thermal effects, and acoustic reradiation. The quantity Φ is given by

$$\Phi = \frac{3\gamma}{1 - 3(\gamma-1) i\chi[(i/\chi)^{1/2}\coth(i/\chi)^{1/2} - 1]}, \tag{6}$$

where γ is the ratio of specific heats for the gas in the bubble, and where

$$\chi = \frac{D}{\omega a^2}, \tag{7}$$

with D the gas thermal diffusivity.

The dispersion relation (2) can be separated into its real and imaginary parts to obtain two new equations for $N(a)$, as

$$\frac{c_l}{C_M} = u - iv. \tag{8}$$

Doing so, one obtains

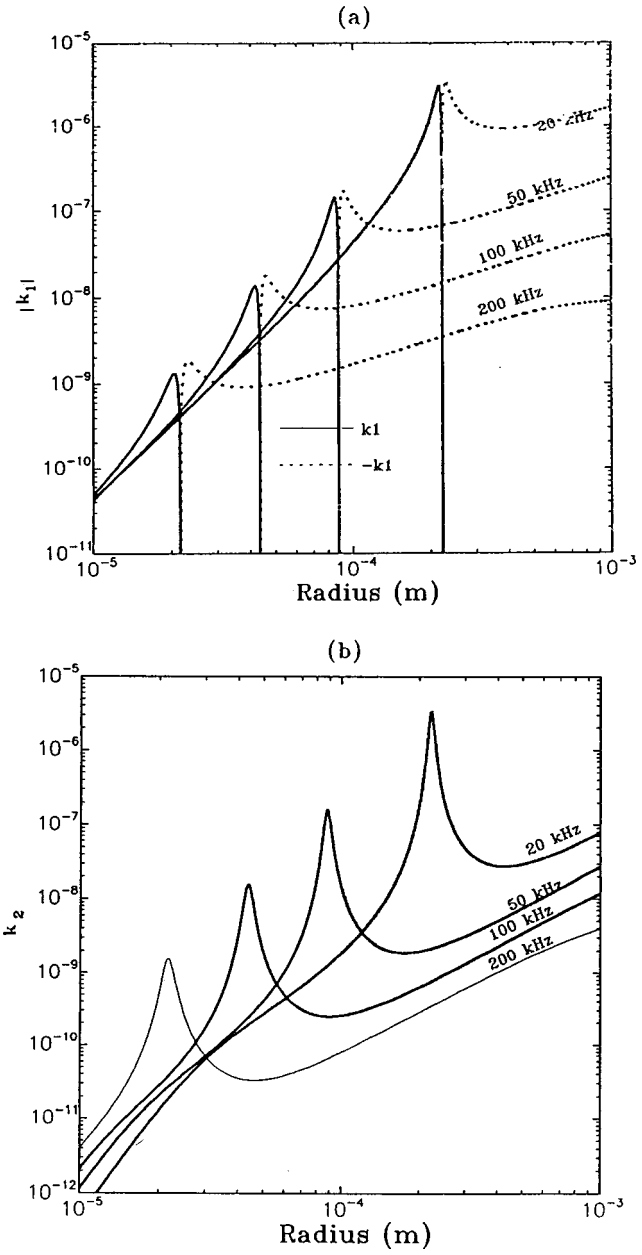

FIG. 1. The kernel functions $|k_1|$ and k_2 are plotted against the bubble radius for different insonification frequencies. The function k_2 is peaked at the radius corresponding to resonance at the insonification frequency, but has a strongly growing tail which can be of the same order of magnitude as the peak. Since the function k_1 is zero at the resonant radius and negative for larger radii these values are shown with a dotted line.

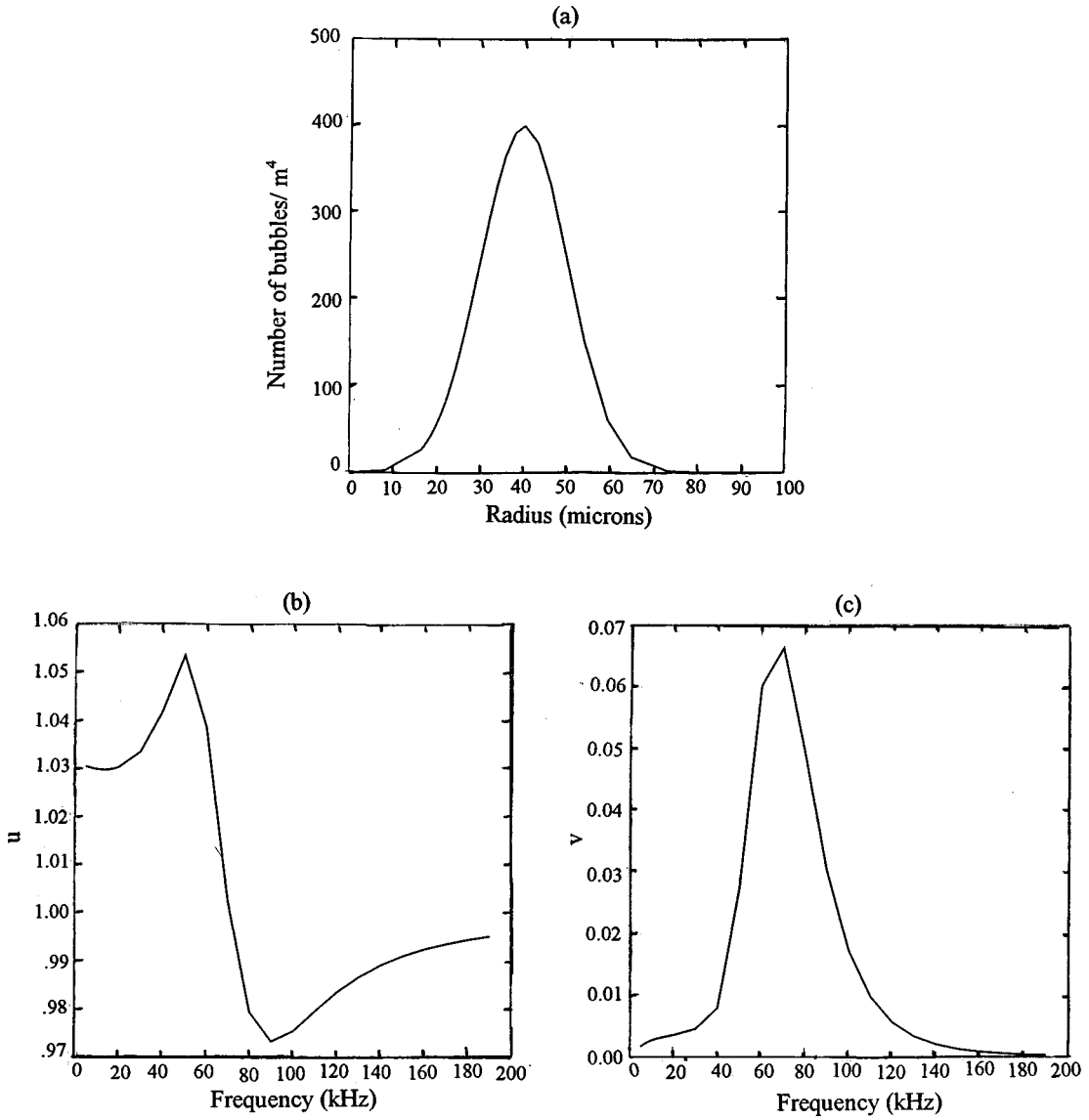

FIG. 2. (a) Assumed bubble density function, (b) corresponding u and (c) corresponding v curves produced by using the dispersion relation.

$$4\pi c_l^2 \int_{a_{\rm lo}}^{a_{\rm hi}} \left[\frac{(\omega_0^2-\omega^2)a}{(\omega_0^2-\omega^2)^2+4b^2\omega^2} \right] N(a)\ da = \int_{a_{\rm lo}}^{a_{\rm hi}} k_1(a,\omega)N(a)\ da = u^2-v^2-1, \tag{9}$$

$$4\pi c_l^2 \int_{a_{\rm lo}}^{a_{\rm hi}} \left[\frac{b\omega a}{(\omega_0^2-\omega^2)^2+4b^2\omega^2} \right] N(a)\ da = \int_{a_{\rm lo}}^{a_{\rm hi}} k_2(a,\omega)N(a)\ da = uv, \tag{10}$$

where we have introduced the notation k_1 and k_2 to denote the kernels of the two integral equations. These kernels are the crucial input of this model to the computations. These in turn depend upon accurate evaluation of the bubble resonance frequency, ω_0, and the damping, b. As a check on the procedure for evaluating the resonance frequency and the damping we have reproduced all the results presented for them in Ref. 20. Figure 1 shows the two kernel functions.

The quantities u and v may be obtained by measuring the phase velocity c_m and the attenuation A of the wave in the bubbly liquid. We note that for a wave propagating with the mixture speed C_m, quantities are proportional to

$$\exp i\omega\left(t-\frac{x}{C_M}\right) = \exp i\omega\left(t-\frac{x}{c_l}(u-iv)\right) = \exp\left(-\frac{\omega v x}{c_l}\right)\exp i\omega\left(t-\frac{x}{c_l/u}\right). \tag{11}$$

The phase velocity c_m of the sound wave is given by

$$c_m = c_l/u, \tag{12}$$

while the attenuation A, in dB per unit length, is given by

$$A = 20\log_{10} e\left(\frac{\omega v}{c_l}\right), \tag{13}$$

where $e=2.71828$ is the base of the natural logarithms.

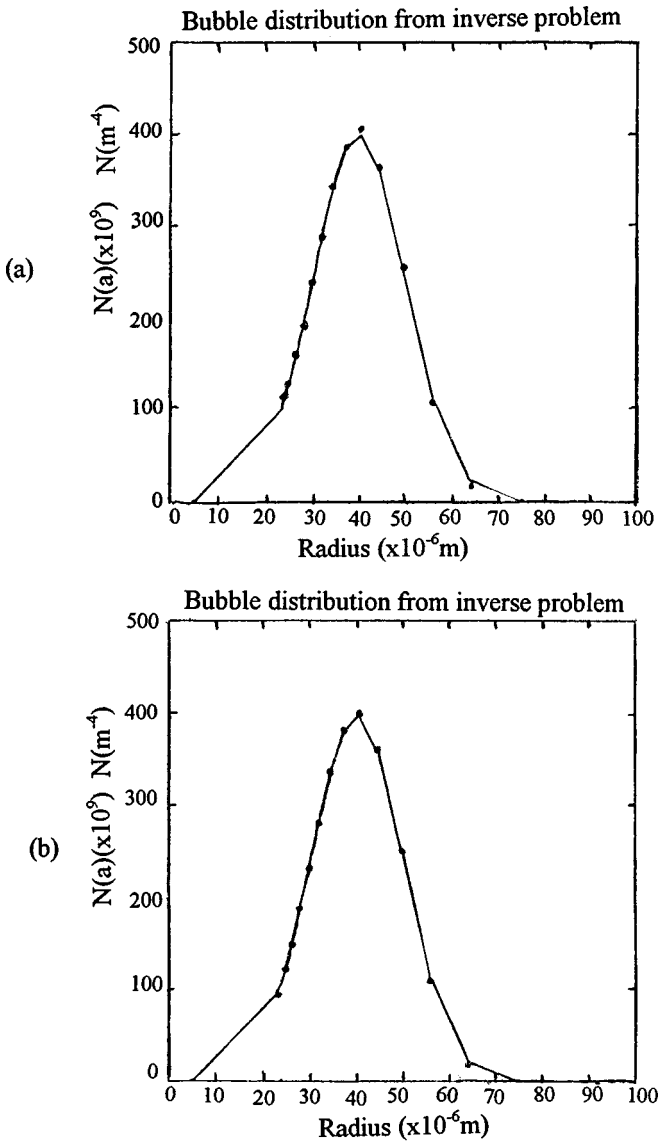

FIG. 3. Inverse problem solution for the bubble density $N(a)$ using the non-negativity and noninfinity constraints and (a) K_1 terms alone as objective functions and (b) K_2 terms alone as objective functions.

In our experiments, where we emit short bursts of monochromatic waves. These quantities are calculated as follows:

$$u(f)=\frac{c_l \Delta t}{d_{\mathrm{ER}}}, \quad v(f)=-\frac{c_l \log[\overline{p^2}(f)/\overline{p^2_{\mathrm{ref}}}(f)]}{4\pi f d_{\mathrm{ER}}}, \tag{14}$$

where

$$\overline{p^2}(f)=\frac{1}{T}\int_0^T p^2\, dt, \tag{15}$$

where $p(t)$ is the raw pressure signal at the measurement location. This quantity is referred to as the mean square amplitude (MSA) of the pressure signal. The other quantities are described below:

$f=\omega/2\pi$	frequency of the insonifying wave
d_{ER}	distance between emitter and receiver
c_l	speed of sound in the pure liquid (water)
Δt	time for signal to travel between hydrophones
$\overline{p^2_{\mathrm{ref}}}(f)$	MSA of the pressure signal at a distance d_{ER} in pure water
$\overline{p^2}(f)$	MSA of a pressure signal at a distance d_{ER} in the bubbly medium

A. Comments on the equations

Integral equations relating the bubble population to attenuation, or to backscattering, were presented in Ref. 15 in 1945, and have been used by several investigators. Sarkar and Prosperetti[21] showed that the earlier equations can be obtained from the dispersion relation (2) by making a binomial expansion valid at low void fraction. In this case the phase velocity can be taken to be that in the pure liquid, and the integral equation with k_1 kernel becomes of higher order, while that with the k_2 kernel survives. The present equations thus must be considered to hold at higher void fractions than these earlier equations.

It should be noted that the present procedure for obtaining the bubble density *requires* simultaneous knowledge of the attenuation and phase velocity. However, if these are known, each equation, (9) or (10), can be used independently to solve for the bubble population. In the method developed below we find a population that satisfies best both equations simultaneously.

It is useful to restate the assumptions inherent in these equations before designing an experiment that uses them. The theory of Caflisch *et al.*[16] is valid at low void fraction, and the bubbles are assumed to oscillate spherically. The analysis used to obtain the natural frequencies and attenuation also assumes spherical oscillations, with small deviations of the bubble instantaneous radius from the mean value. This requires that the pressure fields experienced by the bubbles be of small amplitude. Further, the bubbles are assumed to oscillate in a linear fashion (without exciting subharmonics or higher harmonics). The derivation of the expression for Φ also requires the insonifying waves to be monochromatic. Thus in the experiments, we must make sure that these criteria are satisfied.

II. INVERSE PROBLEM SOLUTION

Equations (9) and (10) obtained for the bubble distribution are *Fredholm integral equations* of the first kind (IFK) with analytic, compact kernels, and are consequently ill posed.[22] The ill posedness exhibits itself by making solutions to the equations discontinuous with respect to the problem data. Continuity of the solution of a mathematical model with respect to data is important for practical reasons, since experiments are prone to measurement errors and numerical computations are subject to round-off and other errors. For an ill-posed problem this may result in the error in the solution oscillating wildly when refining discretization until finally the ''solution'' has little relation to the original data. It is then necessary to look for the solution of a stable approximate problem, which in some sense is the closest to the exact solution, and is achieved by constraining the possible solutions of the problem. This process is termed *regularizing* the problem.

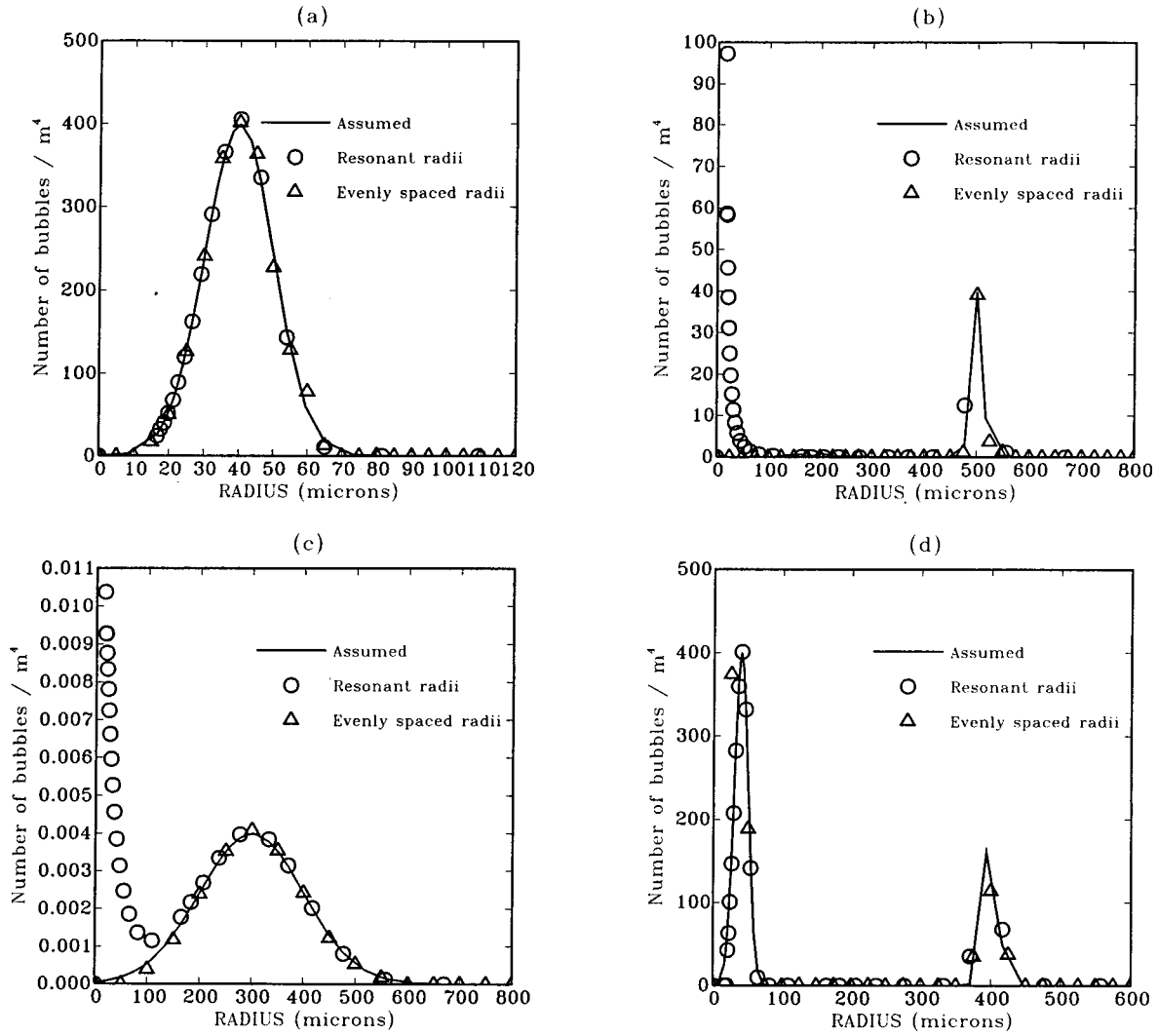

FIG. 4. Inverse problem solution checkout on four assumed bubble distributions using two methods of distributing collocation points: radii based on the peaks of k_2, and evenly spaced radii. (a) Single peak distribution with the peak at 40 μm and standard deviation=10 μm. (b) Single peak distribution with the peak at 500 μm and standard deviation=10 μm. (c) Single peak distribution with the peak at 300 μm and standard deviation=100 μm. (d) Double peak distribution with peaks at 40 and 400 μm and standard deviation=10 μm for both peaks. The method based on evenly spaced radii is able to capture the correct solution in all cases. Twenty-eight frequencies between 5 and 190 kHz were used for interrogation.

A. Constraints on the bubble density function

An ill-posed problem can be regularized by imposing *a priori* constraints on the solution. Imposition of these constraints explicitly restricts the solution set, and can restore uniqueness and/or well posedness to the solution. Two techniques for accomplishing this task have been suggested in Ref. 23. These are based on the concepts of ''prior knowledge'' and ''parsimony.'' The first requires that all prior physical knowledge about the solution be included in the modeling, while the second requires that of all solutions not eliminated by the first principle, the one that adds the least amount of ''new information,'' be selected. The second condition prevents the introduction of nonphysical phenomena, which are artifacts of the solution technique.

For the bubble-counting problem the following information about the expected solution is known:

(1) The function $N(a)$ is strictly positive or equal to zero.
(2) The function is expected to be a piecewise smooth continuous function of a.
(3) The limits of integration, and discretization, for the radius can be set to some expected minimum and maximum radius, say a_{lo}, a_{hi}.
(4) The solution should depend continuously on the data, e.g., small changes in the measured attenuation should be associated with small changes in the bubble density.
(5) The distributions obtained from the solution of one of the equations (9) and (10) should satisfy the other equation.
(6) The volume fraction and surface area per unit volume of bubbles is bounded.

While these conditions might seem ''obvious,'' in the case of an ill-posed problem *a priori* imposition of such conditions during the solution process is essential to restore well posedness.

B. Discretization of the integral equation

Numerical solution of the integral equations involves discretization, interpolation of the unknown function $N(a)$

using a parametric interpolant, numerical quadrature to perform the integrals, and solution of the systems of linear equations and inequality constraints thus obtained. The method we found to be most robust for the present problem[17] was to divide the range over which the integral was done, $[a_{\rm lo}, a_{\rm hi}]$ into M subdomains, with the unknown function interpolated linearly as follows:

$$N(a) = N_i \frac{a - a_{i+1}}{a_i - a_{i+1}} + N_{i+1} \frac{a - a_i}{a_{i+1} - a_i} = N_i A(a) + N_{i+1} B(a), \tag{16}$$

where $A(a)$ and $B(a)$ represent the linear spline basis functions. The discretized equations then are

$$\sum_{i=1}^{M} \left[\int_{a_i}^{a_{i+1}} k(\omega, a) A(a)\, da + \int_{a_{i-1}}^{a_i} k(\omega, a) B(a) da \right] N = \alpha(\omega).$$

The integrations over the subdomains are performed using a 12-point Gauss–Legendre scheme. The equations are then written in linear system form by using collocation at the breakpoints between the subdomains. The data obtained at each frequency ω_j results in a new equation, and these equations can be combined in a standard linear system as

$$KN = \alpha. \tag{17}$$

In all our computations we scale the matrices and the intervals of integration by the corresponding leading term to ensure that $O(1)$ quantities are dealt with throughout.

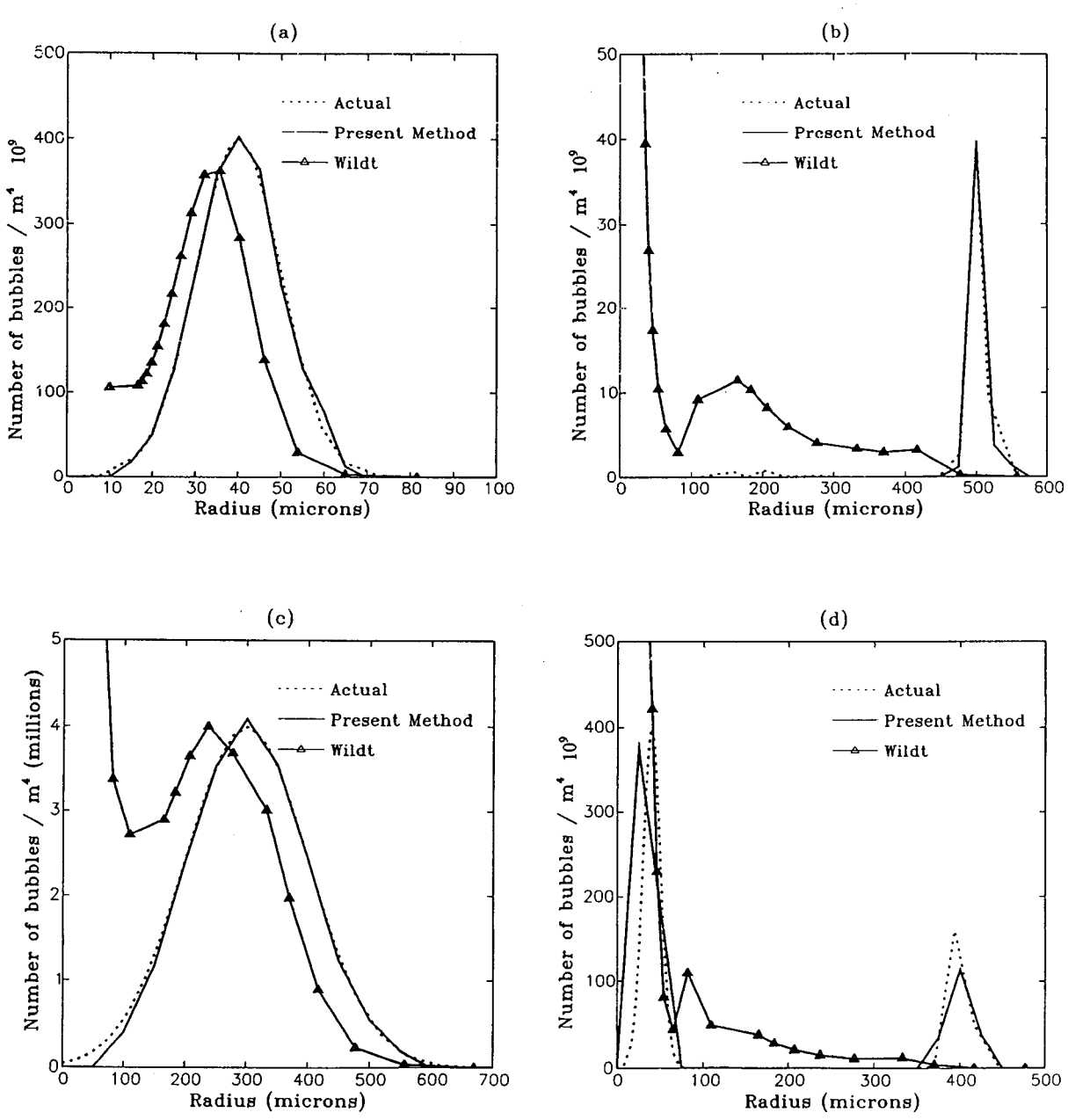

FIG. 5. Comparison of the present technique with the Wildt technique for four assumed bubble distributions.

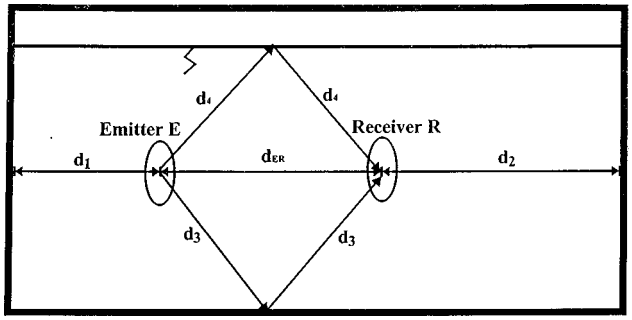

FIG. 6. Sketch of signal paths in a finite size tank.

C. Solution via constrained minimization

Several techniques for achieving well-posed solutions to the inverse problem were considered in Ref. 18. Of these, the following method based on linear optimization was found to be most successful.

The motivation for using this technique was that classical techniques such as the Tikhonov regularization method[22,24] do not allow imposition of all available physical constraints. Rather, they only impose some mathematical constraints such as smoothness or bound on the norm of the solution. Here, since we have two sets of equations for the bubble population (9) and (10), in the Tikhonov method the equations have to be solved separately, and the error in the residue of the second equation can only be checked *a posteriori*.

The methods used in the field of *constrained optimization* seem particularly appropriate for this problem. In Refs. 18 and 19 we cast the integral equations as a linear optimization problem by using a simplex method.[25] This method seems very useful for the present problem because

(1) The solution is guaranteed to be positive, without having to impose non-negativity as an explicit constraint.
(2) Upon solution, constraint errors are immediately available.
(3) The solution is minimized in the L_1 norm.
(4) Imposition of additional constraints does not require reformulation of the problem.
(5) Additional regularization techniques such as Tikhonov regularization, which provide further linear equations, can be easily introduced in the framework.

In this approach our objective function for minimization is $|K_2 N - \alpha_2|$, subject to the constraints

$$K_1 N = \alpha_1, \quad N(a) \geqslant 0, \qquad \int_{a_{\rm lo}}^{a_{\rm hi}} N(a) a^2 \, da < C_1, \quad \int_{a_{\rm lo}}^{a_{\rm hi}} N(a) a^3 \, da < C_2. \tag{18}$$

Here, the objective function comes from Eq. (10), and the first constraint comes from the fact that Eqs. (9) and (10) must be simultaneously satisfied. Also, C_1 and C_2 are constants which are larger than the expected surface area per unit volume and the volume fraction of bubbles. If information about these parameters is not available, they can be set to very large numbers. Incorporation of further experimental constraint information in the solution procedure can be made.

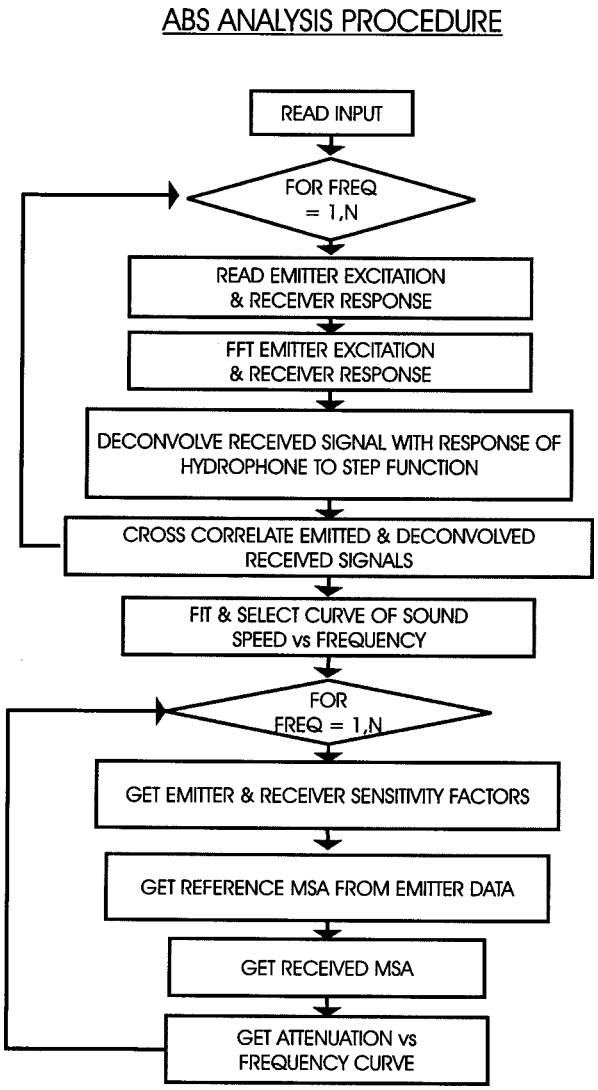

FIG. 7. Signal analysis procedure used in the acoustic bubble spectrometer (ABS).

If the data is available for M frequencies, we usually compute the matrices on the right-hand side at up to $1.5M$ different radii, to reduce the quadrature errors in the representation of the K_{ij}. The use of the constrained optimization formulation lets us accurately calculate the bubble density function at more points than insonification frequencies.

III. ANALYSIS OF THE SOLUTION PROCEDURE

Direct solution of an ill-posed inverse problem can give large errors if the input data contains small errors. The accuracy of a regularization scheme will depend upon the constraints used in the procedure, as well as numerical errors in the solution. In the following we performed a series of calculations to study the effect of these constraints on the accuracy of the obtained bubble distribution by using synthetic input data corresponding to a known bubble distribution. Input dispersion u and v data were generated using a given bubble distribution and the inverse problem solved using this data. This data was also used with the conventional method

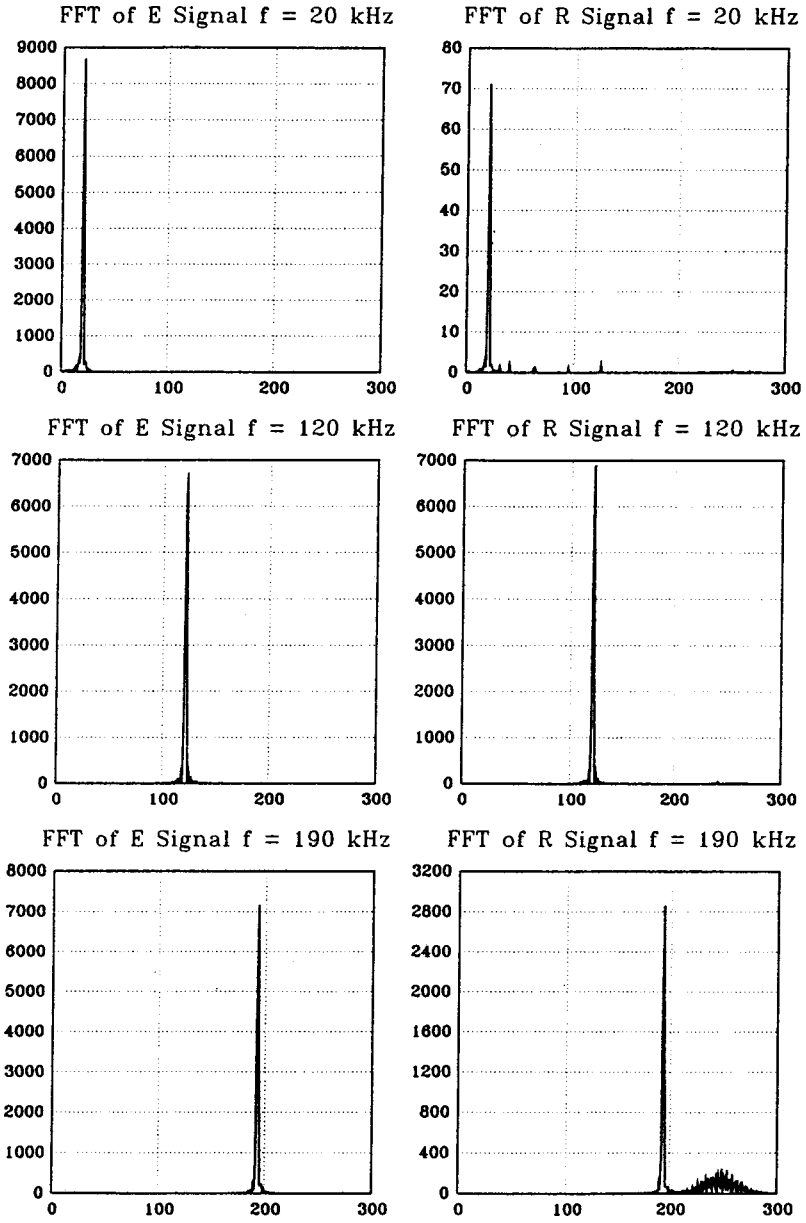

FIG. 8. Example emitter excitation and receiver response signals at three frequencies recorded during experiments performed with bubbles being generated using electrolysis with stainless steel wires of diameter 0.4 mm. Amplitude scale is arbitrary.

of solving the bubble counting problem, and a systematic comparison performed.

A. Effect of imposing different constraints on the solution

A bubble distribution was assumed, and used with the dispersion relation to obtain corresponding u and v curves. Figure 2(a) shows the distribution and Fig. 2(b) and (c) shows the corresponding u and v curves.

Figure 3(a) and (b) shows the results of solving the problem using equations corresponding to either K_1 and K_2 as objective functions separately and imposing the nonnegativity of $N(a)$ and noninfinity constraints on the void fraction and surface area free unit volume. The figure shows that in this case the inverse problem solution procedure is able to obtain the assumed solution with either of the kernels K_1 or K_2.

However, on some data with input errors of the order of 1%, we found that use of the K_1 equations resulted in impossibility of satisfaction of the system of equations and constraints. For such problems we substantially relax the K_1 constraints and effectively only use the equations involving K_2 and the remaining constraints.

B. Effect of the selection of the collocation points

The accuracy of the inverse problem solution depends upon the accuracy of the discretization—since the kernel functions at a particular frequency of insonification have peaks near the resonant radius corresponding to that frequency (see Fig. 1). More points near that radius are needed to adequately resolve the integral. Resonant radii not being the same for different frequencies one would need very many points for adequate resolution of the integral for all kernels. Thus there is a tradeoff in choosing more points to resolve the integral and ending up with too large and unstable a

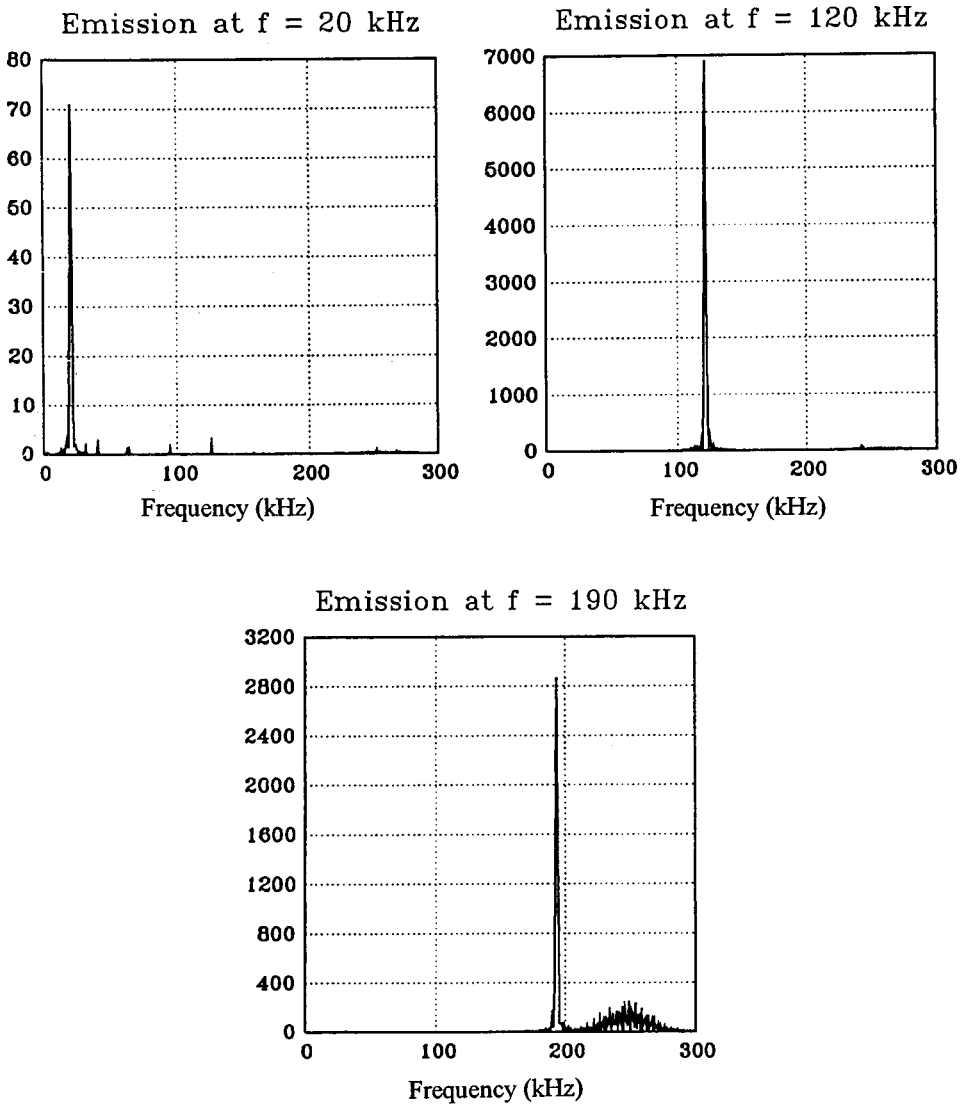

FIG. 9. Example fast Fourier transform results for received signals at three typical frequencies with generation of bubbles by electrolysis. Note that the signal remains monochromatic despite the presence of bubbles and indicates that we are operating in the linear acoustic regime of theory. Amplitude scale is arbitrary.

linear system. To decide on an optimal strategy the solution quality was studied on three sample bubble populations, constructed from an exponential distribution:

A. a single peak distribution with the peak at 40 μm, and a standard deviation of 10 μm,

B. a single peak distribution with the peak at 500 μm, and a standard deviation of 10 μm,

C. a single peak distribution with the peak at 300 μm, and a standard deviation of 100 μm, and

D. a bimodal distribution with one peak at 40 μm and the other at 400 μm, with a standard deviation of 10 μm for each peak.

The inverse problem in each case was solved using two different ways to choose the discretization radii:

(1) using the radii corresponding to the peaks of the kernel $k_2(a,\omega_i)$ curve at each insonification frequency, ω_i, and
(2) using radii evenly distributed in the range $(a_{\rm lo},a_{\rm hi})$.

Figure 4 shows the results obtained on solving the inverse problem using the two methods. On distributions A and D both methods achieved satisfactory reconstructions. However, on distributions B and C the method with evenly spaced radii was remarkably better. We suspect this is due to the fact that the collocation points become very far apart in the region of large radii, unless the frequencies of insonification are chosen to be very close to each other (fractions of a kilohertz), and consequently the integrals cannot be resolved accurately. Through the matrix formulation this error is propagated to all radii and causes the whole method to become inaccurate.

Based upon these results we chose distributions of radii that were relatively even, and with the insonification frequencies that yield resonant radii corresponding to the collocation points, subject to a minimum separation in frequencies of 1 kHz.

C. Comparison of the results of the present method with previous solution methods

The present results were compared with the solution procedure of Wildt.[15,26] In this approach a low volume frac-

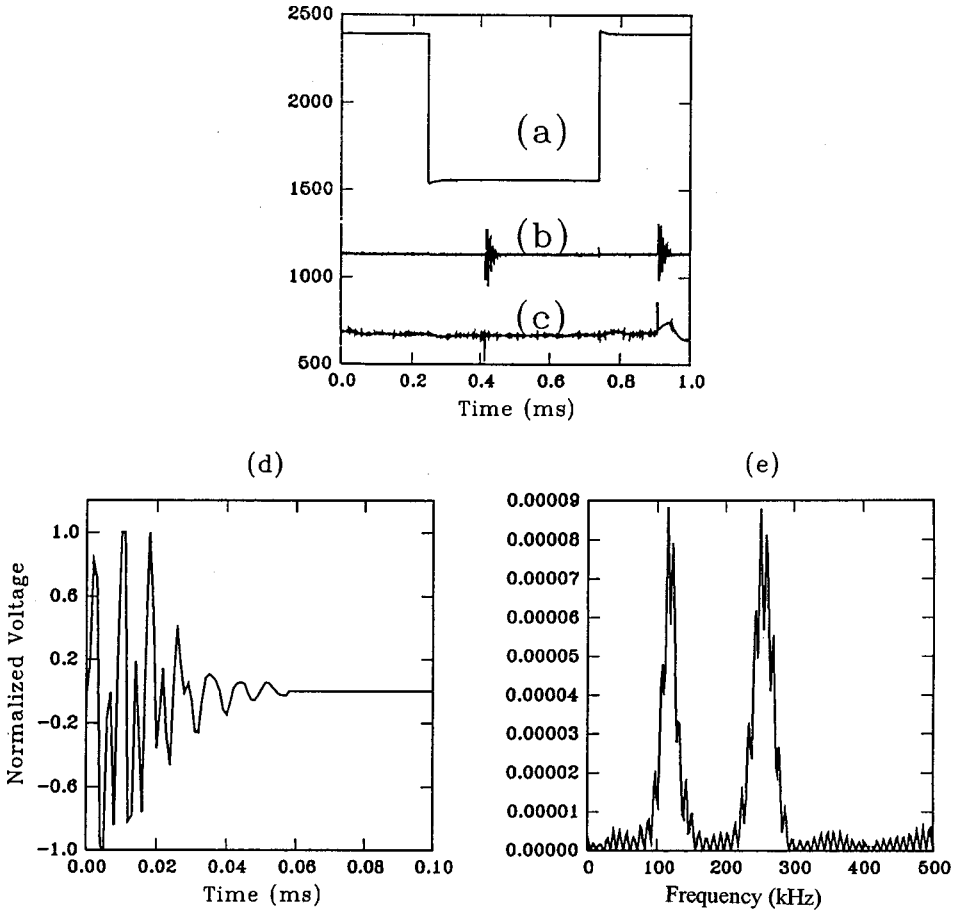

FIG. 10. (a) Input square wave used to excite the emitting hydrophone. (b) Signal received in response to the square wave. (c) Signal deconvolved with the response to a square wave of the system to a square wave. (d) Response function of emitter-receiver hydrophone system [a blow up of (b)]. (e) The FFT of the response to a square wave. Amplitude scale is arbitrary.

tion argument is used to set u to unity, and only the integral equation with kernel k_2 is considered. This equation is solved by using the argument that the primary contribution to the integral arises from bubbles that are close to the frequency of insonification, and allows replacement of many components in the kernel by their values at resonance.[21] The final formula obtained for the bubble size distribution $N(a)$ is

$$N(a_R) = \frac{4f^2 v}{c_l^2 a_R^2}, \tag{19}$$

where a_R is the resonant radius corresponding to the insonification frequency, f. Thus this formula predicts a bubble population that is essentially a scaled version of the attenuation curve. This formula has been used by several researchers over the last five decades.[1–6,8] Deficiencies in its ability to capture the solution were pointed out in Ref. 26.

The solutions obtained by this method and by the method developed were compared for the four bubble population distributions of Fig. 4. Figure 5(a)–(d) shows that for case (a) the Wildt method show bubble distributions that follow the general trend of the assumed curve, and produce bubble populations which have the same order of magnitude. However, for the other three distributions a wide departure from the assumed solution is seen especially for very small radii where the predicted populations are several orders of magnitude higher. In each case the present constrained optimization solution is able to capture the correct solution.

The variance of the results of these methods from the current one can be explained by observing the nature of the kernel function k_2 (see Fig. 1). At a given frequency this function is characterized by a sharp peak at the resonant radius with decay in each direction away from the radius. However, at larger radii the function grows, and the ''tail'' of the function corresponding to these larger radii approaches the values at the peak. Comparing the functions corresponding to different frequencies of insonification we see that the magnitude of the function for larger frequencies is much smaller than that for smaller frequencies. In the conventional methods the attenuation in the signal at the higher frequency is wrongly attributed to small bubbles. Further, many more small bubbles are needed to achieve the same attenuation in the signal. The cumulative result of the presence of bubbles of several sizes is the overestimation of bubbles of smaller sizes. We speculate that the widespread adoption of power law profiles for bubble population densities can, at least in part, be attributed to this feature of the solution, as has also been noted in Refs. 14 and 26.

IV. EXPERIMENTAL SETUP

The basic experimental procedure consists of emitting signals of various frequencies using a hydrophone located in

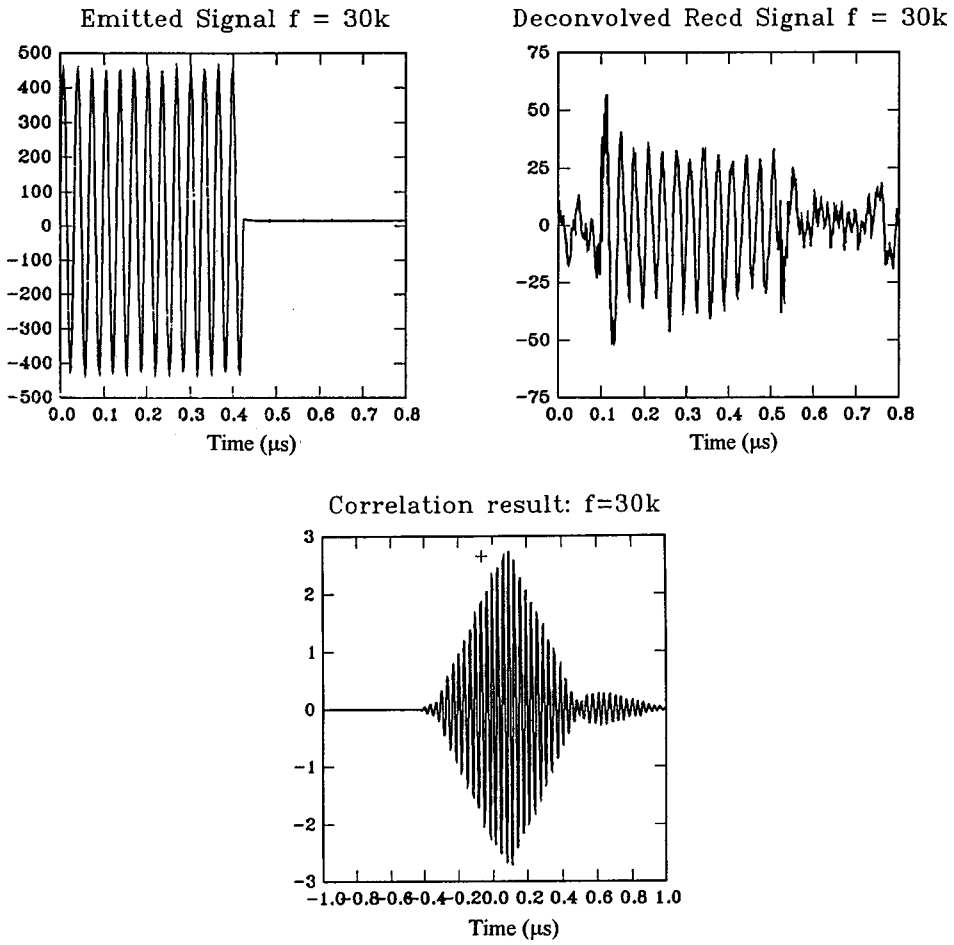

FIG. 11. Example results from cross correlating the emitter excitation signal with the received signal deconvolved with the response of the hydrophone to a square wave. Amplitude scale is arbitrary.

a bubbly medium and receiving the signal with a second hydrophone. The emitted and received signals are acquired and stored. They are then analyzed to obtain the attenuation and sound speed as a function of frequency, and the bubble distribution is deduced. The objective of the experiments is to use these measurements and obtain the sound speed ratio $u(f)$ and the attenuation $v(f)$ which form the right-hand sides of Eqs. (9) and (10) in the inverse problem.

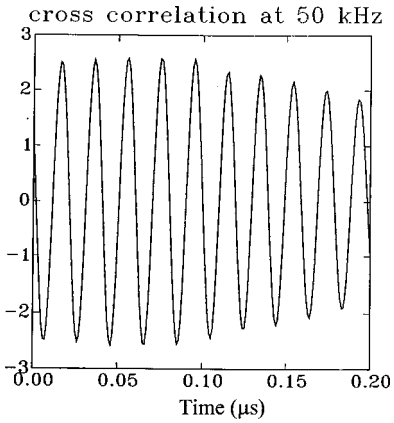

FIG. 12. Example where it is hard to distinguish the highest peak in the result of cross correlating an emitter excitation signal of frequency 50 kHz with the corresponding received response deconvolved with the response of the hydrophone system to a square function. Amplitude scale is arbitrary.

In order to achieve the above purpose, we use two hydrophones, an IBM-compatible PC, a data acquisition board, a signal generator, a digital delay generator, and bubble generators. The experiments were performed in a cubic plexiglass tank of side 1.83 m.

Two model 8103 Brüel & Kjaer hydrophones were used in the experiments. The hydrophones can be operated over a

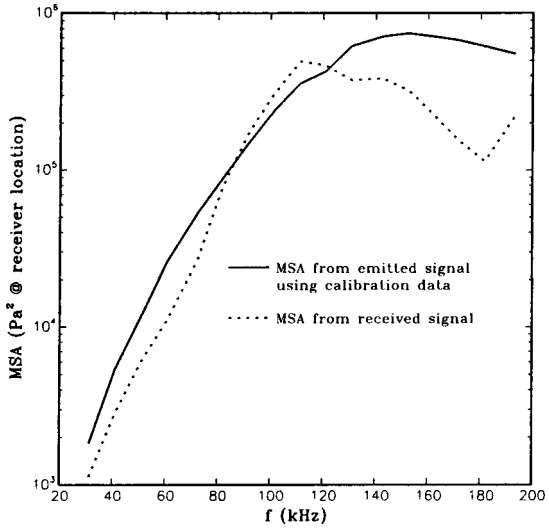

FIG. 13.

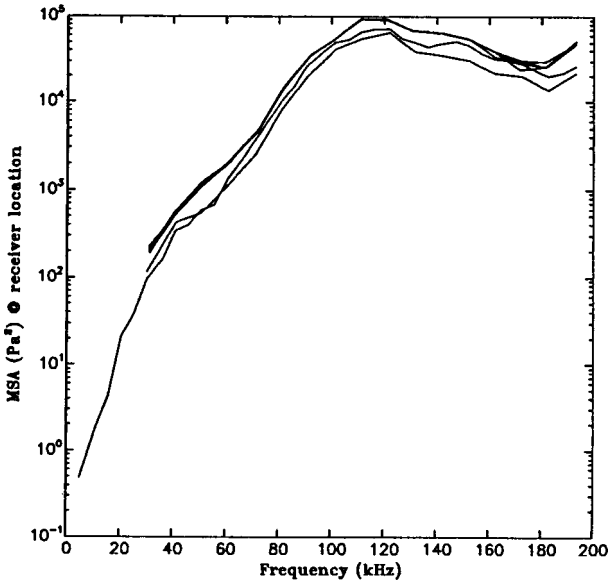

FIG. 14. The MSA power in received signals for experiments performed on different days with no bubbles generated.

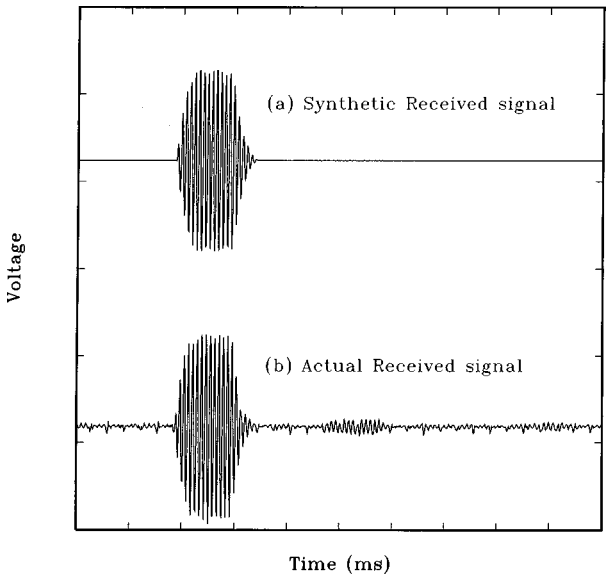

FIG. 15. (a) Synthetically generated received signals assuming a bubble population density and a given emitter frequency. (b) Actual received signal recorded during an experiment for the same conditions and at the same distance.

range of frequencies from 15 to 190 kHz. The hydrophones are calibrated for sensitivity in both emission and reception, and have a maximum sensitivity at around 120 kHz, which corresponds to their resonant frequency. The frequency of the signal generated was precisely controlled using a voltage-controlled signal generator.

Two types of bubble generators were manufactured and used. Electrolysis at stainless steel wires generated bubbles between 10 and 80 μm. A second technique was based on injecting compressed air through pores in microporous tubes (DYNAPERM®). This produces bubbles of size larger than those generated using electrolysis (10–300 μm).

The finite size of the tank prohibits the use of continuous signals in the experimental procedure (see Fig. 6). If the duration of emission is too long, reflections from the walls of the tank interfere with the signals emitted, thereby producing composite signals which make data analysis complicated. In order to avoid reflections, the time during which a signal is emitted needs to be shorter than the return time of the first reflected signal. The duration of the emission τ_e is given by

$$\tau_e < (d_m - d_{\mathrm{ER}})/c_l, \tag{20}$$

where d_m is the distance to the closest reflecting boundary. For example, in our experiments $d_{\mathrm{ER}}=0.3048$ m, $d_m=0.9144$ m, and for $c_l=1450$ m/s, $\tau_e<0.42$ ms. This requirement imposes a certain amount of low frequency content in the signal. However (as shown by the spectrum of the received signal in Fig. 9 below), this contamination is low. In any case, this defect would be eliminated in the case of measurements in natural waters using this technique, where longer signals could be used.

The signal is received by the other hydrophone and is acquired using the A/D channel 1 of the board. This whole process is repeated successively, thus spanning the interesting range of frequencies (usually 38 values). We experimentally determined that signals generated in one emission die down sufficiently quickly, and that the whole frequency range could be covered in less than 1 s. Our observations showed that the repeated signals received at any particular frequency changed very little between experiments performed within that interval.

Since the hydrophones have different emitting and receiving sensitivities at different frequencies, an automatic procedure for determining the necessary gain factor for a particular measurement was developed. A preliminary measurement is made at the desired frequencies prior to each experiment, and from the magnitude of the received signal the gain is determined. This procedure was automated and coded, and ensured that the best value of the gain was used for each measurement.

V. SIGNAL PROCESSING PROCEDURES

Signal processing software was developed to analyze the data acquired and stored during the experiments. The flow chart for the analysis procedure is depicted in Fig. 7.

For each frequency, the received signals are read, and any constant dc components removed using

$$s_i = s_i' - \frac{\sum_{i=1}^{i=N} s_i'}{N}. \tag{21}$$

More sophisticated methods for removing the background noise could be incorporated in acoustically noisy environments. Example emitted and received signals for three different frequencies are shown in Fig. 8 with bubbles generated using electrolysis.

A fast Fourier transform (FFT) of the signal is then performed. Example FFT results using emitter excitation and receiver response signals at three typical frequencies (20, 120, and 190 kHz) are shown in Fig. 9 with bubbles being generated. These results show that the received signals are quite pure.

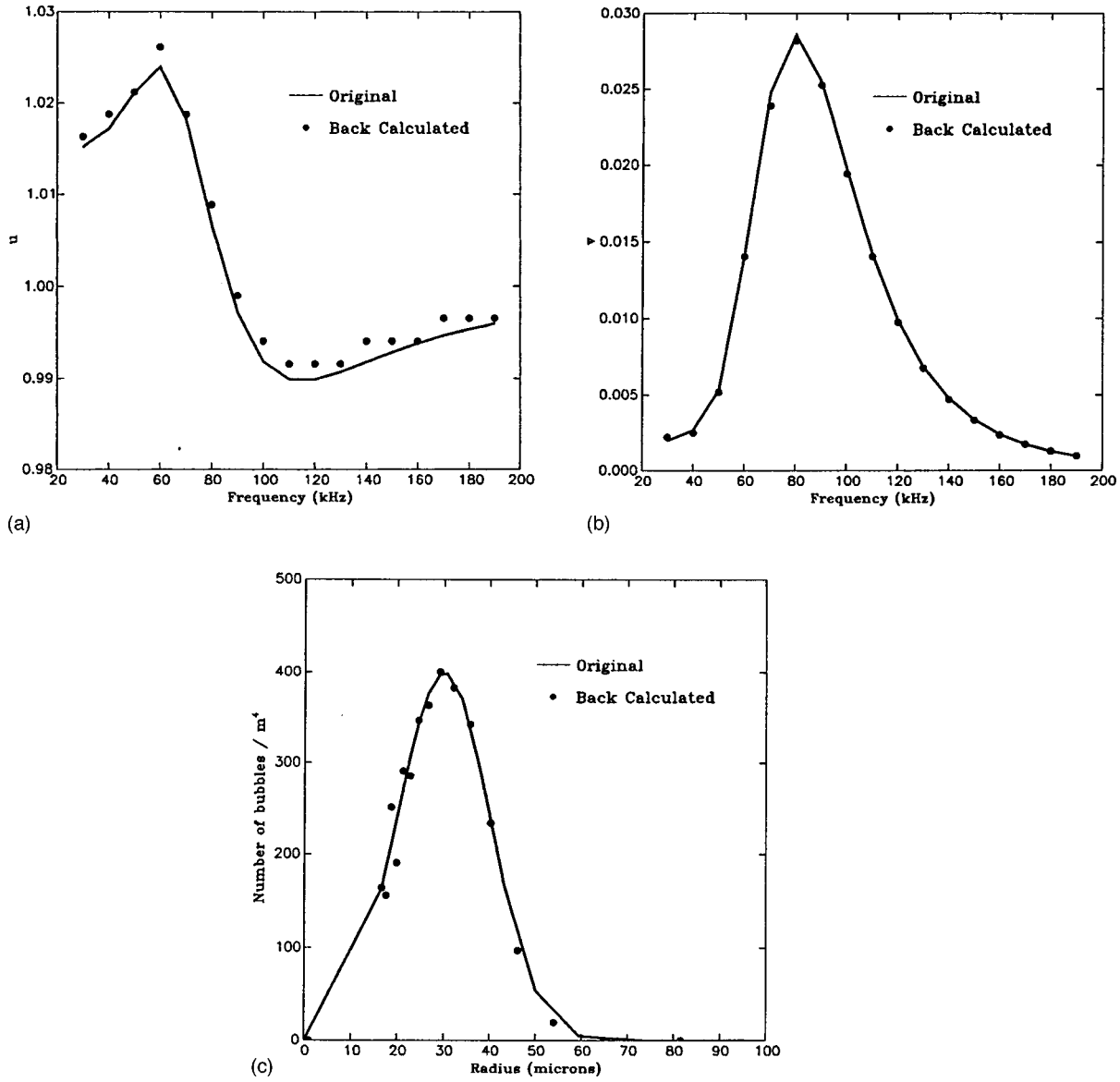

FIG. 16. (a) Original and back-calculated u curves. (b) Original and back-calculated v curves. (c) Original and back-calculated bubble distributions.

A. Processing for phase speed determination

In order to compute the wave speeds a cross correlation is performed between the emitted and received signals. The peak of the cross correlation provides the time, Δt, required for the signal to travel between the emitter and the receiver. The phase speed can then be obtained using the known distance between the emitter and receiver d_{ER},

$$c_m = d_{\mathrm{ER}}/\Delta t. \tag{22}$$

Nominally the accuracy of the cross correlation is given by the sampling time, equal to 1 μs for our experiments. However, in the presence of real effects such as ringing of the hydrophone or background noise, this estimate may be substantially in error. These errors are removed following the procedure described below.

A sudden change in voltage is rich in high frequencies and leads to a ''ringing'' of the hydrophone and a finite amount of time to respond. This time affects the results of the cross correlation, and could result in large errors in the speed of sound calculated unless accounted for. This is done using a deconvolution procedure with the response of the hydrophone to a step function.

Figure 10(a) shows a square wave generated using a function generator that was used to excite the hydrophone. Figure 10(b) shows the signals received by the other hydrophone. The resulting signal after deconvolving the received signal with the response function of the hydrophone is shown in Fig. 10(c). Figure 10(c) shows two impulse functions which are the derivatives of the square wave that was sent. Figure 10(d) shows a blow-up of the initial part of the received signal and is the response of the hydrophone system (emitter and receiver pair) to a step function. The figures illustrate the fact that the hydrophones are not perfect. Figure 10(e) shows the FFT of the response curve and exhibits two dominant frequencies, i.e., around 120 and 240 kHz, which correspond to the resonant frequency of the hydrophone system and the first harmonic.

A typical result of cross-correlating an emitter excitation

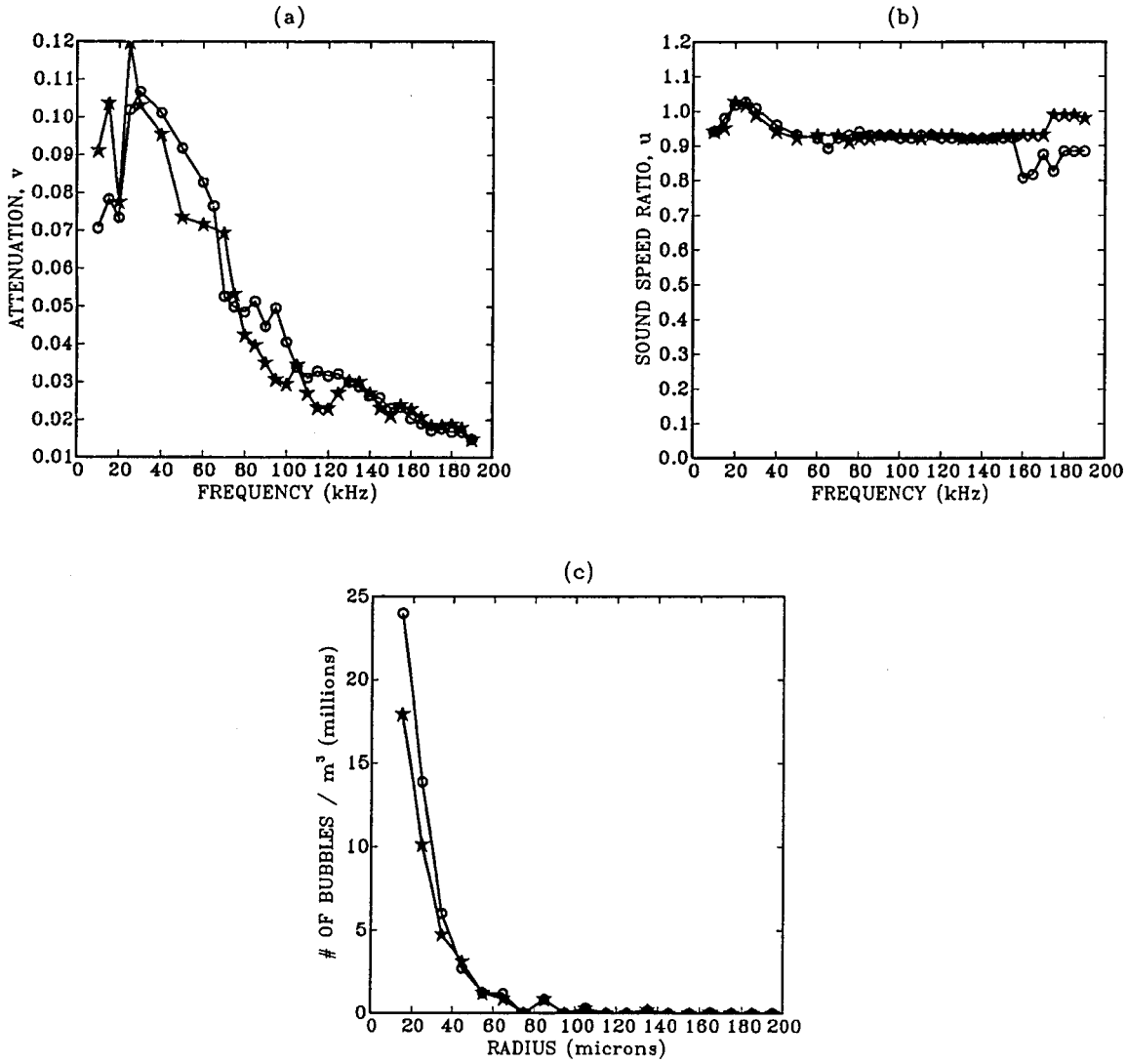

FIG. 17. Results from experiments performed at two different times (2 h apart). (a) v calculated using emitter sensitivity data and assumption of sphericity to get reference power. (b) u calculated using deconvolution and curve-fitting. (c) Bubble distribution curves.

and deconvolved received signal pair is shown in Fig. 11.

Figure 12 illustrates that the difference in correlation amplitudes between the highest and second highest peaks could be rather small. If a neighboring peak is chosen, an error of order $1/f$ will be made in the time estimate. For the smaller frequencies (15 kHz) this *peak uncertainty* can introduce significant errors (66 μs), while the possible uncertainty error is lower at higher frequencies (5 μs at 190 kHz). Considering the very small times and distances involved in the problem, this choice of peaks could result in substantial errors in sound speed evaluation. As a result, the computed/measured curve of sound speed as a function of frequency may not be smooth. To overcome this problem and minimize the probability for error, a condition for smooth curve of sound speed as a function of frequency is used.

The following *a priori* conditions are imposed:

(a) Values of the speed c_m obtained using signals that have the lowest signal/noise ratio are given minimum weight.

(b) Speeds cannot be higher than 1.25 times the speed in pure water.

(c) Speeds cannot be less than 0.5 times a value based on a low-frequency estimate based on the void fraction.

This procedure enables use of information at all frequencies to select a correct value for the correlation peak at a given frequency, and eliminates the peak uncertainty error.

B. Processing for *v*

For a given frequency, the mean square amplitude of the pressure wave is estimated using the hydrophone sensitivity calibration data digitized from the charts provided by the manufacturer.

The start and end of emission/reception are determined using the time Δt calculated above. A certain percentage ($\simeq$5%) of the signal near the start and end is removed to eliminate the influence of the unwanted transients due to the hydrophone response. The remaining portion which has an approximately constant amplitude is used to compute the MSA in the bubbly liquid.

To obtain the quantity v we need to obtain the MSA under conditions of transmission through pure water. Two

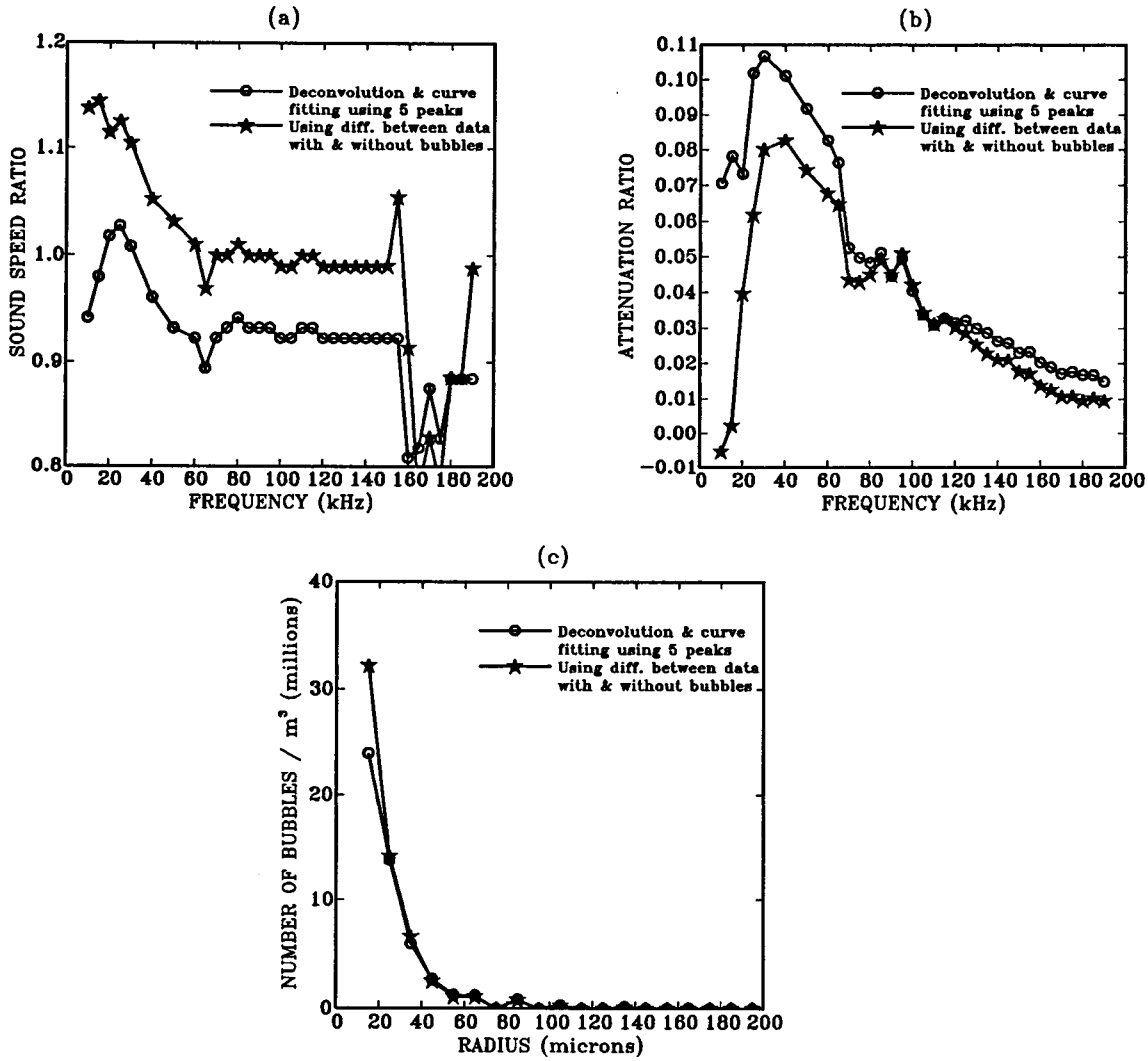

FIG. 18. Comparison of results analyzed using two different methods to get u and v curves: a deconvolution method, and comparison with no injected bubble test.

methods to obtain the reference MSA were used.

In the first method, using the manufacturer's calibration for the hydrophone along with the assumption that the waves are emitted spherically enabled calculation of the reference MSA. This method was tested by performing experiments in the tank with no bubbles being generated. The comparison of the expected and measured MSA is shown in Fig. 13. While the two curves are relatively close, the difference in the quantity could result in substantial amounts of spurious bubbles being predicted.

In the second technique a calibration phase of the experiments is performed in ''pure'' water (i.e., with no bubbles being injected). The reference MSA is calculated using the recorded received signal data. This approach has the advantage of eliminating sources of error that are common to the two measurements. Experiments with no bubbles generated were performed on different days and the MSA of the different received signals computed as a function of frequency is shown in Fig. 14. The fact that the different experiments without bubbles are repeatable indicates that the already existing bubble nuclei population in the tank water is very stable. Based on the repeatability of these experiments we decided to use a comparison method for the calculation of the attenuation factor v. It was felt that such a procedure would not cause a large error in the measurements when bubble populations were being generated, as the microscopic population already in the tank was likely to be much smaller than the bubble population being generated, and have negligible influence on the attenuation and phase velocities at the frequencies considered.

C. Verification of solution procedure with synthetic data

The various steps used to extract the u and v data from the various digitized signals and the possible errors introduced could have a bearing on the inverse problem accuracy. We thus performed using synthetic data an end-to-end checkout of the developed algorithms for consistency. The synthetic data were generated by assuming a bubble distribution (shown earlier in Fig. 2). Then the various numerical steps were calculated as follows.

(1) u and v were obtained as functions of frequency by solving the forward problem.

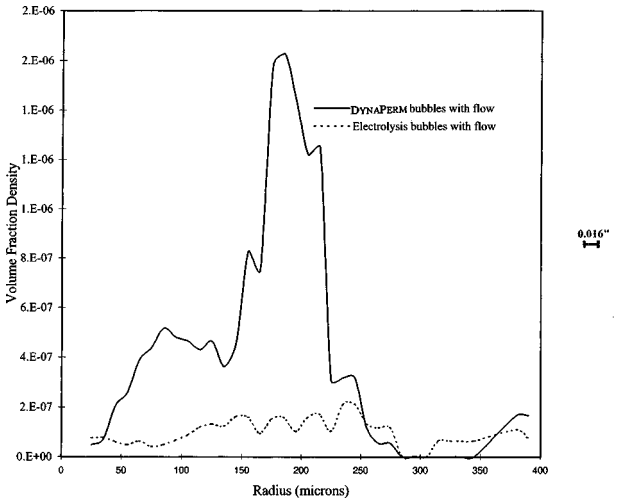

FIG. 19. The volume fraction density of bubbles at a given radius versus the radius of bubbles is shown for the electrolysis and porous tube bubblers with flow. The density was computed by integrating the bubble density function over bins of size 10 μm.

(2) The excitation signal was convolved with the response of the hydrophone system to a step function.
(3) The resulting convolved voltage signal was converted to pressure using the emitter sensitivity curve at the given frequency.
(4) Using u, the time elapsed ΔT between the emitter excitation and synthetic receiver response signals was obtained.
(5) The attenuation due to the bubbles was obtained using the v value at the given frequency.
(6) The emitter excitation signals and the synthetically generated received signals were used by the signal analysis program to yield back u and v curves as functions of frequency. These u and v curves are used by the inverse problem program to obtain back the desired bubble distribution curve.

Figure 15 compares a synthetically generated received signal with a frequency of 120 kHz for the emission with an actual received signal recorded during an experiment. The figure clearly illustrates the closeness of the synthetically generated received signals to the actual received signals. Figure 16(a) and (b) compare the u and v curves obtained after performing signal analysis using the synthetic data with the corresponding original curves that were used to generate the data. Figure 16(c) compares the back calculated bubble distributions with the original assumed distributions.

These figures show that the back calculated u curve follows the original u curve. The small discrepancy between the two can be related to the inaccuracy resulting from the limited sampling frequency of the data acquisition board which results in a margin of error on u of ± 0.005. For the particular experimental setup, u is better estimated at large distances between the emitting and receiving hydrophones. However, the larger the distance, the greater is the attenuation and the smaller the amplitude of the signals. The resolution in v decreases with decrease in amplitude of the signal if the voltage gain factor of the data acquisition board is kept unchanged. As discussed before, the distance between the hydrophones is also limited by the finite size of the tank and the reflections which could combine with the direct signal.

VI. BUBBLE SIZE MEASUREMENT EXPERIMENTS

The two hydrophones were placed at the same vertical level at the center of the tank, with a separation distance between them of 0.152 m. In order to minimize noise, the same emission frequency was repeated many times, the signals were stored, and an average generated. Experiments were first performed with no artificial bubbles injection.

Bubbles were generated using electrolysis on stainless steel wires of diameter 0.4 mm. Figure 17 shows typical analysis results corresponding to data obtained in this case. The duration of emission of the sinusoidal signals was chosen to be 0.4 ms based on Eq. (20). Figure 17(a) shows the v curves computed at two different times about 2 h apart and Fig. 17(b) shows the corresponding u curves. The v data were computed using the calibration curves and the u data were computed using the combination of deconvolution and curve fitting procedures described earlier. Figure 17(c) shows the corresponding bubble distribution curves. The bubble distribution curves from the inverse problem were grouped by dividing the guesses for minimum and maximum radii a_{lo} and a_{hi} into 100 bins. In this case the size of a bin was about 10 μm. It can be seen from the figures that the data are repeatable, but that the experimental and analysis procedure limits the measurements to bubble sizes larger than 15 μm. This can be improved with better instrumentation.

Figure 18(a) and (b) compares the u and v curves obtained using two different methods. The solid lines with circles show results obtained using a method similar to that of Fig. 17. The lines with stars represent results obtained by using the difference between data with and without bubbles to compute u and v as described earlier. The bubble size distributions obtained in each case are shown in Fig. 18(c), and appear to be very close except at the low bubble radii where the experimental errors are the largest.

VII. VALIDATION OF RESULTS

Some of the results obtained using the acoustic technique were attempted to be validated using microphotography. Results are presented here for one case using the electrolysis bubble generator and one case using the DYNAPERM bubble generator. Figure 19 shows the void fraction distribution corresponding to these two types of generators.

The image processing technique we used to obtain the bubble population from the photographs is as follows: A photograph of the generated bubbles with a reference scale was taken while the experiments were performed. The photograph was then scanned at 150 dots per inch (dpi). A threshold level for the gray-scale image was determined based on the closeness of comparison between the thresholded image and the gray-scale image. The width and height in pixels, the dpi, and the threshold level for the image were noted. From the resulting raw image the area in pixels for each bubble detected was obtained using developed image processing software, and converted to an equivalent radius. The resulting radii were then grouped into a number of bins

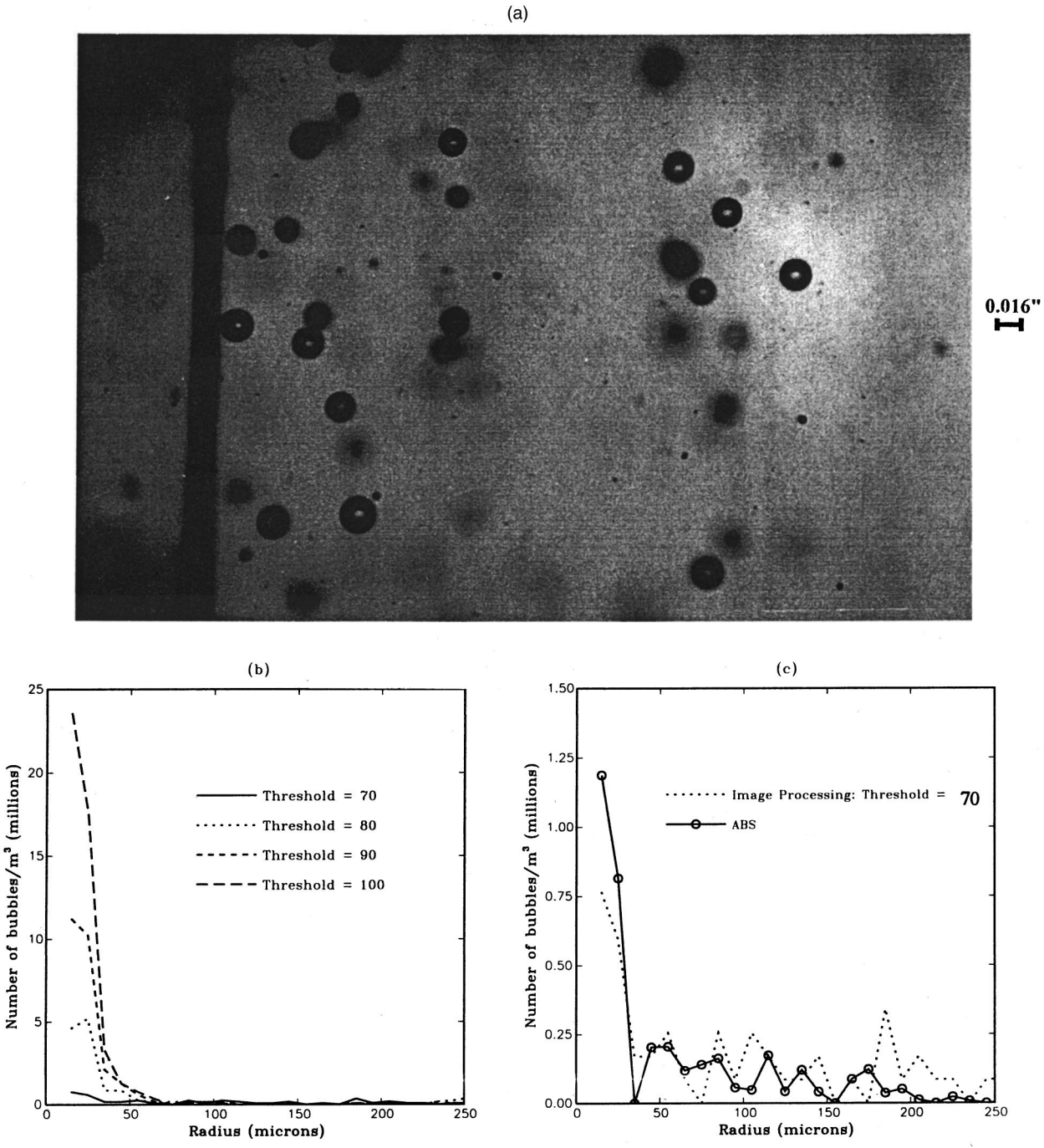

FIG. 20. (a) Example photograph of bubbles generated using the DYNAPERM tubes with no shear flow. (b) Results of analyzing the photo using image processing software with threshold levels of 70, 80, 90, and 100. (c) Comparison of bubble distribution from photography with that from the present procedure.

obtained by subdividing the range spanned between the maximum and minimum radius of the bubbles, and using the area of the scanned image were converted to numbers per square meter. The data was extrapolated to numbers per cubic meter by using the depth of field of the photograph.

Figure 20(a) shows an example photograph taken of the bubbles generated using DYNAPERM tubes without shear flow. Figure 20(b) shows the result of image analysis of the photograph using different threshold levels and a depth of field of 7.5 cm. As can be seen from the figure, the number of bubbles detected is very sensitive to the threshold level selected. However, the shape of the bubble distribution curve remains the same. A threshold level of 70 was selected on the basis that it yielded a binary image that compared best with the original grayscale image.

Figure 20(c) compares the bubble distribution curve obtained from processing the photograph at a threshold level of 70 with that from the present solution. The figure illustrates a reasonable comparison between the two methods. One drawback of the photograph shown is that it sampled a very small area ($\simeq$2 cm^2) relative to the size of the bubbles involved and as a result is prone to substantial variance in the bubble population estimates.

Figures 21(a) shows an example photograph taken dur-

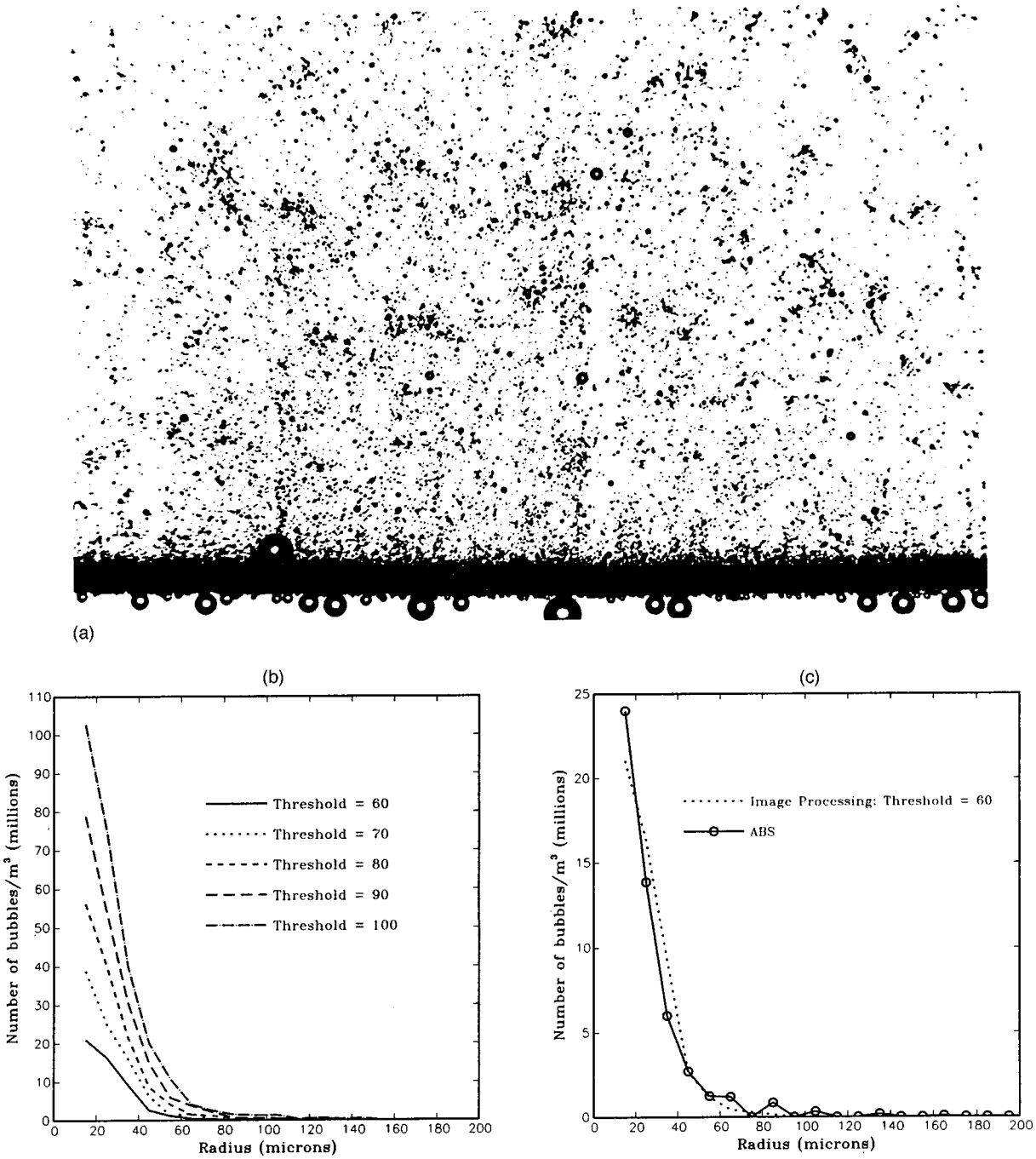

FIG. 21. (a) Example photograph of bubbles generated with the electrolysis bubbler. (b) Results of analyzing the photo using image processing software with threshold levels of 60, 70, 80, 90, and 100. (c) Comparison of bubble distribution from photography with that from the present procedure.

ing experiments performed with bubbles being generated using electrolysis. Figure 21(b) shows the result of analyzing the photo using different threshold levels to convert the gray scale to a binary image. A threshold level of 60 was selected on the basis that it yielded a binary image that compared best with the original gray scale image. Figure 21(c) compares the bubble distribution curve obtained from processing the photograph at a threshold level of 60 with that from the present solution. The figure illustrates again a very good comparison between the two techniques.

Because of the subjectivity in the choice of the threshold, these results only validate the fact that the shapes of the bubble populations are similar. Because of the difficulties associated with different methods, the absolute validation of any technique for measuring microscopic bubbles remains an unsolved experimental problem.

VIII. SUMMARY AND CONCLUSIONS

The dispersion relation for propagation of monochromatic waves in bubbly liquids was used to obtain two equations for the bubble population density. These equations,

which are ill posed, were regularized by imposing different constraints on the solutions, including the fact that the equations must be satisfied simultaneously, that the bubble number density has to be positive, and that the volume fraction is bounded. A constrained minimization procedure based on the simplex method was used to solve these equations.

The accuracy of the solution for different problem discretizations was studied and a discretization that resulted in uniform accuracy of the solution for different test problems developed. The effect of choices of different objective functions and constraints was also studied. Based on these results a procedure for the solution of the ill-posed equations of bubble counting was developed. This procedure was compared with conventional formulas for estimating bubble and was found to be much more accurate. While the developed procedure for the solution of the inverse problem is more intensive computationally than the conventional formula, the algorithms we have developed are efficient and can achieve solution relatively quickly.

Experimental procedures were developed to measure the phase velocity and attenuation simultaneously for monochromatic acoustic waves in bubbly liquids. A signal analysis procedure was developed that enabled deduction of these quantities from the measurements, and that accounted for the effect of the ringing of the transducers by using deconvolution. The analysis procedure was also verified on synthetic signals.

Several experiments were performed with artificially generated bubbles, and the resulting bubble populations obtained. For some of the experiments simultaneous microphotography was performed. A procedure to obtain bubble size distributions from the photographs was also developed. Comparisons of the populations indicate that the bubble size distribution obtained by the two techniques are similar.

In ongoing work, the developed method is being packaged into a user friendly Windows-based application that integrates the different components of the system, and produces near real-time estimates of bubble distributions. Efforts are underway to produce instrumentation for bubble detection, void-fraction measurement, and bubble population measurement using the developed techniques. This instrument—the *Acoustic Bubble Spectrometer*—is being commercialized.

ACKNOWLEDGMENTS

This work was supported by the National Science Foundation under Grant Nos. III-9160484 and III-9301379. We would like to thank the associate editor and an anonymous referee for several suggestions for improvement of the manuscript.

[1] H. Medwin, ''In situ acoustic measurements of bubble populations in coastal ocean waters,'' J. Geophys. Res. **75**, 599–611 (1970).
[2] H. Medwin, ''Counting bubbles acoustically: a review,'' Ultrasonics **15**, 7–13 (1977).
[3] H. Medwin, ''Acoustical determination of bubble-size spectra,'' J. Acoust. Soc. Am. **62**, 1041–1044 (1977).
[4] N. Breitz and H. Medwin, ''Instrumentation for *in situ* acoustical measurements of bubble spectra under breaking waves,'' J. Acoust. Soc. Am. **86**, 739–743 (1989).
[5] H. Medwin and N. D. Breitz, ''Ambient and transient bubble spectral densities in quiescent seas and under spilling breakers,'' J. Geophys. Res. **94**, 12 751–12 759 (1989).
[6] A. Lovik, ''Acoustic Measurements of the Gas Bubble Spectrum in Water,'' in *Cavitation and Inhomogeneities in Underwater Acoustics*, edited by W. Lauterborn (Springer-Verlag, Berlin, 1980), pp. 211–218.
[7] I. P. Schippers, ''Density of Air-Bubbles Below the Sea Surface, Theory and Experiments,'' in *Cavitation and Inhomogeneities in Underwater Acoustics*, edited by W. Lauterborn (Springer-Verlag, Berlin, 1980), pp. 205–210.
[8] P. A. Crowther, ''Acoustical Scattering from near-surface bubble layers,'' in *Cavitation and Inhomogeneities in Underwater Acoustics*, edited by W. Lauterborn (Springer-Verlag, Berlin, 1980), pp. 187–193.
[9] T. J. O'Hearn, ''Cavitation inception scale effects,'' Ph.D. thesis, California Institute of Technology, 1987.
[10] S. Prabhukumar, R. Duraiswami, and G. L. Chahine, ''Bubble size measurement using inverse acoustic scattering: Theory & Experiments,'' ASME Cavitation & Multiphase Flow Forum, 1996.
[11] S. Vagle and D. M. Farmer, ''The measurement of Bubble-Size Distributions by Acoustical Backscatter,'' J. Atmos. Ocean. Technol. **9**, 630–644 (1992).
[12] T. Ohern, J. Torczynski, S. Tassin, S. Ceccio, G. Chahine, R. Duraiswami, and K. Sarkar, ''Development of an Electrical Impedance Tomography System for an Air-Water Vertical Bubble Column,'' Proceedings, Forum on Measurement Techniques in Multiphase Flows, ASME IMEC&E (1995).
[13] D. M. Oldenziel, ''A new instrument in cavitation research: the cavitation susceptibility meter,'' J. Fluids Eng. **104**, 136–142 (1982).
[14] F. MacIntyre, ''On reconciling optical and acoustical bubble spectra in the mixed layer,'' in *Oceanic Whitecaps*, edited by E. C. Monahan and G. Macniocaill (Reidel, New York, 1986), pp. 75–94.
[15] R. Wildt, editor, *Physics of Sound in the Sea, Part IV* (National Research Council, Dept. of Defense, Washington, DC, 1949).
[16] R. E. Caflisch, M. J. Miksis, G. C. Papanicolau, and L. Ting, ''Effective Equations for wave propagation in bubbly liquids,'' J. Fluid Mech. **153**, 259–273 (1985).
[17] K. W. Commander and A. Prosperetti, ''Linear pressure waves in bubbly liquids: Comparison between theory and experiments,'' J. Acoust. Soc. Am. **85**, 732–746 (1989).
[18] R. Duraiswami and G. L. Chahine, ''Bubble density measurement using an inverse acoustic scattering technique,'' NSF SBIR Phase I project report, also Dynaflow Technical Report 92004-1 (1992).
[19] R. Duraiswami, ''Bubble Density Measurement Using an Inverse Acoustic Scattering Technique,'' ASME Cavitation and Multiphase Flow Forum, Washington, DC, June 1993, edited by O. Furuya (ASME, New York, 1993), FED Vol. 153, pp. 67–74.
[20] A. Prosperetti, ''Physics of Acoustic Cavitation,'' in *Frontiers in Physical Acoustics* **XCIII** Corso, (Soc. Italiana di Fisica, Bologna, Italy, 1986), pp. 145–188.
[21] K. Sarkar and A. Prosperetti, ''Coherent and incoherent scattering by oceanic bubbles,'' J. Acoust. Soc. Am. **96**, 332–341 (1994).
[22] R. Kress, *Linear Integral Equations* (Springer-Verlag, Berlin, 1989), particularly Chaps. 15–17.
[23] S. W. Provencher and R. H. Vogel, ''Regularization techniques for inverse problems in molecular biology,'' in *Numerical Treatment of Inverse Problems in Differential and Integral Equations*, edited by P. Deuflhard and E. Hairer (Birkhauser, Boston, 1983).
[24] K. W. Commander and R. J. McDonald, ''Finite-element solution of the inverse problem in bubble swarm acoustics,'' J. Acoust. Soc. Am. **89**, 592–597 (1991).
[25] I. Barrodale and F. D. K. Roberts, ''Solution of an overdetermined system of equations in the l_1 norm,'' Commun. ACM **17**, 319–320 (1974).
[26] K. W. Commander and E. Moritz, ''Off resonance contributions to acoustical bubble spectra,'' J. Acoust. Soc. Am. **89**, 592–597 (1989).

Thin-sediment shear-induced effects on low-frequency broadband acoustic propagation in a shallow continental sea

Dag Tollefsen
Forsvarets Forskningsinstitutt, Box 115, N-3191 Horten, Norway

(Received 10 October 1997; accepted for publication 6 August 1998)

Low-frequency (6.3–630 Hz) acoustic broadband propagation loss data collected in areas of a shallow continental sea where the seabed is composed of hard substrates covered by thin (less than 40 m) deposits of unconsolidated sediment are presented. Data are shown to exhibit characteristics consistent with loss due to coupling to interface waves at the sediment–substrate interface [K. E. Hawker, J. Acoust. Soc. Am. **65**, 682–686 (1979)]. In instances of a physically thin sediment cover, loss is also attributed to coupling to guided elastic waves in the sediment [S. J. Hughes *et al.*, J. Acoust. Soc. Am. **88**, 283–397 (1990)]. Interpretations are supported by numerical modeling of propagation loss using a recently developed wave number integration code for horizontally layered fluid–solid media, and geoacoustic models consistent with geophysical data from the sites of acoustic experiments. © *1998 Acoustical Society of America.* [S0001-4966(98)05211-4]

PACS numbers: 43.30.Ma, 43.30.Bp [DCB]

INTRODUCTION

Low-frequency acoustic propagation in shallow waters may be strongly affected by interaction with the bottom. Over a homogeneous solid bottom, conversion to shear waves may be an important effect,[1] especially for sediments with small degree of consolidation. In many coastal and continental shelf areas, the seabed consists of several layers of sediment of varying degrees of consolidation. Additional loss effects may then come into play and trap energy away from propagation in the water column. Vidmar[2] showed that in a thin sediment layer between the water column and bedrock, high loss may be experienced due to the excitation of guided shear waves in the sediment. This mechanism was proposed by Hughes *et al.*[3] as an explanation to observed high loss in field data from several sites at the Canadian continental shelves. Hawker[4] and later Hovem and Kristensen[5] studied loss due to an interface wave propagating at the boundary between a fluid sediment layer and a solid substrate. High propagation loss has been reported in broadband field data in shallow water by several investigators,[6–10] but the identification of the principal loss mechanisms in such data is not always straightforward. Subsequent studies[11–15] have further addressed the issue of shear-wave-induced loss, but to date little new broadband field data from shallow water exhibiting high loss have been presented.

This continued interest in low-frequency shallow water propagation has inspired our consideration of field data collected by the Norwegian Defence Research Establishment. High loss is reported in data below 1–200 Hz, so in this respect we address an expectation that thin-sediment continental shelf areas other than those surveyed by Hughes *et al.* should have propagation characteristics similar to what was reported in Ref. 3.

This paper is organized as follows. Shallow water acoustic data are presented in Sec. I, with geoacoustic models for the sites of acoustic experiments developed in Sec. II. In Sec. III some characteristic features associated with two shear-dependent loss mechanisms in thin-sediment seabed environments are elucidated. In Sec. IV results from numerical modeling of propagation loss using a wave number integration code are presented. In Sec. V we finish with some concluding remarks.

I. PROPAGATION LOSS DATA

The shallow water region considered extends from the continental shelf of the eastern Norwegian Sea to the western part of the Barents Sea, north to the Svalbard archipelago. The seabed of this region (mean water depth 230 m) is of varying composition, ranging from basins with up to several kilometers of layered consolidated sediment above bedrock to shallow banks and coastal areas with exposed bedrock or hard substrate covered by thin (less than 40 m) layers of unconsolidated sediment.[16] Acoustic data from the region has previously been presented by Hug,[9] who observed high loss associated with basement outcrop at a basin site, and by Jensen[10] who considered high loss in data obtained at a shallow bank.

Our data were collected using 0.86 kg explosive (SUS) charges detonated at standard depths (18 or 91 m), received on a single hydrophone suspended approximately at midwater depth from a deployed sonobuoy. Source levels were obtained from a compilation of tabulated depth-dependent values,[17] with the shot depth estimated from the bubble pulse period. Data were processed for propagation loss in $\frac{1}{3}$-octave

TABLE I. Water depth, source–receiver depths (nominal), and source–receiver range at four shallow water sites.

Site	Water depth (m)	Source–receiver depths (m)	Range (km)
I	200	91–91	8.4
II	175	91–91	5.1
III	50	18–18	8.1
IV	190	91–91	26.5

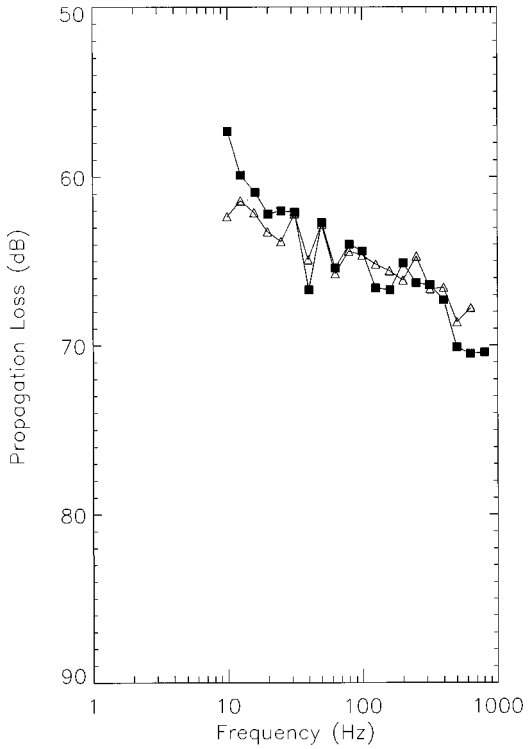

FIG. 1. Propagation loss versus $\frac{1}{3}$ octave center frequency at site I. Data (filled squares) and modeled propagation loss with fluid sediment–fluid substrate seabed model (open triangles). Source-to-receiver range is 8.4 km; water depth is 200 m.

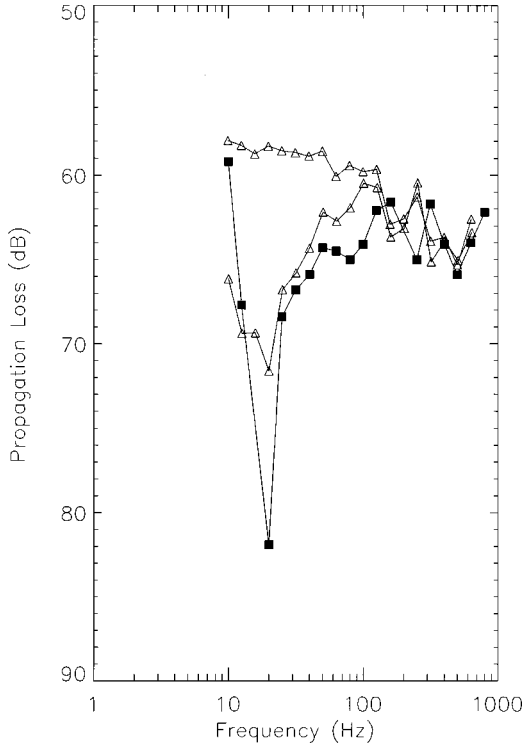

FIG. 2. Propagation loss versus $\frac{1}{3}$ octave center frequency at site II. Data (filled squares), and modeled propagation loss with fluid sediment–fluid substrate seabed model (upward pointing triangles; upper) and solid sediment–solid substrate seabed model (upward pointing triangles; lower). Source-to-receiver range is 5.1 km; water depth is 175 m.

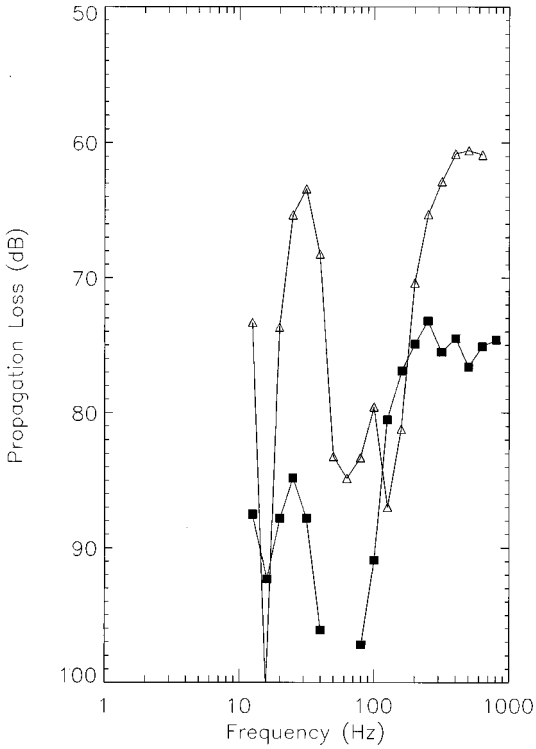

FIG. 3. Propagation loss versus $\frac{1}{3}$ octave center frequency at site III. Data (filled squares) and modeled propagation loss with solid sediment–solid substrate seabed model (open triangles). Source-to-receiver range is 8.1 km; water depth is 50 m.

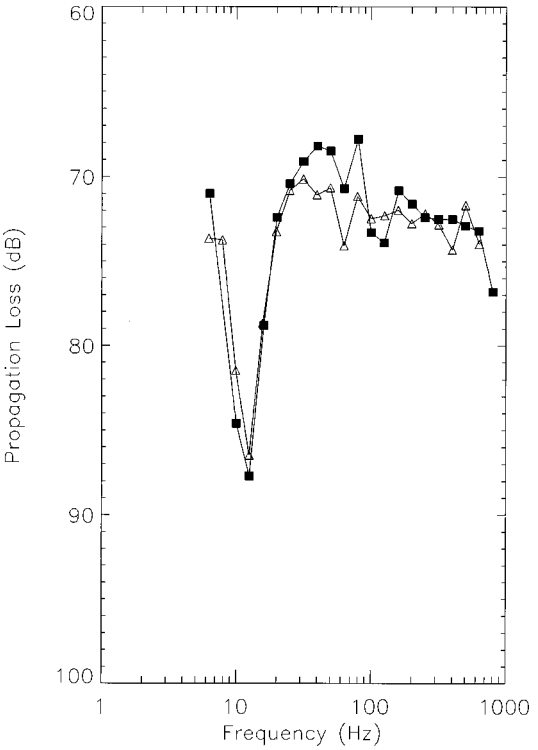

FIG. 4. Propagation loss versus $\frac{1}{3}$ octave center frequency at site IV. Data (filled squares) and modeled propagation loss with solid sediment–solid substrate seabed model (open triangles). Source-to-receiver range is 26.5 km; water depth is 190 m.

TABLE II. Geoacoustic model for site I. Values are given for compressional (*p*) and shear waves (*s*).

Layer	Thickness (m)	Sound speed (m/s)	Attenuation (dB/m/kHz)	Density (g/cm^3)
Water	200	*p* 1470	⋯	1.00
Sediment	20	*p* 1600	*p* 0.30	1.50
(sandy clay)		*s* ⋯	*s* ⋯	
Substrate		*p* 3100	*p* 0.02	2.45
(claystone)		*s* 1800	*s* 0.06	

TABLE III. Geoacoustic model for site II. Values are given for compressional (*p*) and shear waves (*s*).

Layer	Thickness (m)	Sound speed (m/s)	Attenuation (dB/m/kHz)	Density (g/cm^3)
Water	175	*p* 1470	⋯	1.00
Sediment	18	*p* 1600	*p* 0.63	1.65
(clayey sand)		*s* 170	*s* 11.7	
Substrate		*p* 5300	*p* 0.01	2.60
(limestone)		*s* 3074	*s* 0.03	

TABLE IV. Geoacoustic model for site III. Values are given for compressional (*p*) and shear waves (*s*).

Layer	Thickness (m)	Sound speed (m/s)	Attenuation (dB/m/kHz)	Density (g/cm^3)
Water	50	*p* 1450	⋯	1.00
Sediment	3	*p* 1700	*p* 0.59	1.80
(sand)		*s* 200	*s* 5.0	
Substrate		*p* 3850	*p* 0.01	2.48
(sandstone)		*s* 2250	*s* 0.04	

frequency bands centered at 6.3 Hz to 1 kHz for deep sources (nominal detonation depth 91 m) and from 12.5 Hz for shallow sources (nominal detonation depth 18 m).

Data from four sites are presented in this paper. Water depths, source–receiver depths, and ranges for the sites and shots presented are summarized in Table I. By a delineation proposed by Weston,[18] the signals at sites I and II would be ''raylike'' whereas at sites III and IV signals are ''modelike'' at the respective ranges and frequencies of interest. Processed data from these shots are presented in Figs. 1–4. The figures show $\frac{1}{3}$-octave frequency band-averaged propagation loss (in dB *re*: 1 μPa at 1 m) versus frequency, and data are plotted with filled squares.

Figure 1 shows data from a deep shot (91 m) received at a range of 8.4 km at a basin site (site I) at water depth of 200 m. Loss is seen to increase with frequency, and no abnormally high loss is reported. This contrasts to data collected at a site (site II) approximately 100 km from site I. In Fig. 2 results from a deep shot detonated at 86-m depth and received at 91 m at a range of 5.1 km are presented. Loss increases from a value of 65 dB at 100 Hz to a maximum of 82 dB at 20 Hz, with a sharp decrease in loss in the 10- and 12.5-Hz bands. Signal-to-noise ratios were less than 3 dB in the 16-Hz band and below the 10-Hz bands, where data are not plotted. Water depth at the site was 175 m. Data at site II were collected in two subsequent years in early and late summer season, respectively, with the loss pattern consistent between the years.

Further observations of high loss were made at a shallow bank site (site III, Fig. 3) and an Arctic site (site IV, Fig. 4). At the shallow bank site (water depth 50 m) there is a sharp increase in loss from a level of 73 dB above 200 Hz to a maximum of 97 dB at 80 Hz, with data in lower frequency bands indicating a resonant structure with nulls in the 40–80-Hz bands and in the 16-Hz band, and a peak in the 20–40 Hz bands. The shot presented in Fig. 3 is for source–receiver depths of 18 m. Two runs were performed in perpendicular directions, and a resonant structure was observed in several shots from this site.

Data in Fig. 4 (site IV) are from a deep shot received at a hydrophone at similar depth at a distance of 26.5 km. Good data were here obtained from 6.3 Hz. There is a pronounced high loss ''dip'' centered at 12.5 Hz, with loss increasing by 15 dB from a level of 70 dB above 40 Hz to a maximum of 83 dB at 12.5 Hz, then decreasing to 67 dB at 6.3 Hz. A similar loss versus frequency pattern was observed over the range of the experiment, from 5 to 30 km. Water depth at the site was 200 m.

II. GEOACOUSTIC MODELS

Geoacoustic models (Tables II–V) for the sites of acoustic experiments were compiled using Hamilton's methods[19] based on regional and site geophysical data[16,20–25] and, where collected, our own geophysical data. Substrate rock type was taken from a geological map,[20] with compressional speed estimates based on a sonobuoy refraction velocity technique by Houtz[21] and data from Refs. 16 and 21. Substrate shear speeds were assigned using a shear speed (c_s) to compressional speed (c_p) ratio of $\beta=0.58$. Sediment thickness was based on data from our own seismic profiling equipment (a sparker, and a TOPAS PS 018 Parametric Subbottom Profiler from Kongsberg Simrad AS) where in use. Compressional and shear speeds and density of sediment were based on mean values for categories of sediment in a regional analysis of shallow cores in the Barents Sea,[22] the sediment category taken from regional geophysical maps.[23,24] Sediment shear and compressional speed variations with depth were introduced using the relations

$$c_s(D)=c_s^{(1)}D^{0.28}, \tag{1a}$$

$$c_p(D)=c_p^{(1)}D^{0.015}, \tag{1b}$$

with $c_{s,p}^{(1)}$ the surficial speeds in m/s from Ref. 22 and D the sediment layer thickness in meters, the relations adapted from Ref. 19. In the models, a homogeneous sediment layer was assumed, with the speeds set to the maximums as obtained from Eqs. (1). Attenuations were assigned within a range of values suggested by Hamilton.[19] No reported measurements of sediment attenuation from the region were found. Details of the site-specific models are outlined below.

At the basin site (site I), located at water depth of 200 m, a refraction measurement yielded a substrate com-

pressional velocity of 3.1 km/s. Seismic profiling showed a sediment layer of thickness 20–40 m, assumed to be of a sandy clay type with negligible shear speed.

In the area of site II bedrock emerges as a strong seismic reflector close to the seabed. Compressional speed is typically 4.5–5.8 km/s for the type of rock (limestone) in this area, and a value of 5.3 km/s is used in the model (Table III). A seismic profile showed a sediment layer of thickness between 12 and 20 m along the experiment track, a more precise determination prevented by the finite penetration length of the sonar signal and the resolution of the sparker signal. In the model, a homogeneous layer of 18-m thickness is assumed. Refraction velocity measurements gave values of 1.65–1.75 km/s for the sediment layer. The sediment is assumed to be of a ''clayey'' sand composition, with an estimated surficial shear speed of 75 m/s. From Eq. (1a), for a depth D of 18 m a value of 170 m/s at the bottom of the layer is obtained. A water depth of 175 m is used along the experiment track. The sound speed in water was 1.47 km/s.

The shallow bank at site III consists of consolidated sediment of sandstone or siltstone type. Refraction measurements from the area[21] give velocities of 3.35–4.3 km/s, and in the model (Table IV) a value of 3.85 km/s is used. A thin sediment layer of 1–3 m thickness covers this bank.[23] A core sample in the vicinity of the site reported sediment to be of high sand and gravel content. A compressional wave speed of 1.70 km/s is used. Assuming a surficial shear speed of 150 m/s, using Eq. (1a) a shear speed of 200 m/s is obtained at a depth D of 3 m. Water depth varied from 48 to 52 m. The sound speed in water was 1.45 km/s.

A general model for the area of site IV[24] reports a thin ''soft muddy'' sediment layer over a layer of consolidated glaciomarine sediment of thickness less than 15 m. Compressional speeds of up to 2.4 km/s are reported for the upper 1–3 m of consolidated sediment. In the geoacoustic model (Table V) a value of 2.0 km/s is used and the soft top layer is ignored. Sediment is reported to be of high shear strength, thus a shear speed of 600 m/s is not unrealistic. Sediment thickness was taken from a detailed map based on an interpretation of sparker profiles, with 12 m the average over the track. The bedrock is probably silicified limestone,[20] with a compressional speed set at 5.3 km/s. Mean water depth was 190 m. The sound speed in water was 1.45 km/s.

In the geoacoustic models of Tables II–V, range independence is assumed in environments which are moderately range dependent even at the ranges for which we have presented acoustic data. The control of sediment thickness was best at sites I and II where our own seismic profiling equipment was carried. In the models and in the subsequent discussion, oceanographic effects are neglected and a constant sound speed in water is used.

TABLE V. Geoacoustic model for site IV. Values are given for compressional (p) and shear waves (s).

Layer	Thickness (m)	Sound speed (m/s)	Attenuation (dB/m/kHz)	Density (g/cm^3)
Water	190	p 1450	⋯	1.00
Sediment	12	p 2000	p 0.50	2.00
(glaciomarine)		s 600	s 2.5	
Substrate		p 5300	p 0.01	2.60
(limestone)		s 3074	s 0.03	

III. BOTTOM LOSS

The influence of the seabed on the acoustic pressure field in an ocean waveguide [e.g., Ref. 26, Eq. (5.2.4)] is specified by the reflection coefficient for plane waves incident on the water–sediment interface at a given grazing angle. A qualitative assessment of the influence of the seabed on broadband propagation loss is thus facilitated by plots of the plane-wave reflection loss $\mathrm{RL}=-20\log_{10}|V(\theta,f)|$, with $V(\theta,f)$ (the reflection coefficient) a function of frequency f and grazing angle θ, as easily computed, e.g., by the SAFARI code.[27]

In Figs. 5 and 6, the plane wave reflection loss is plotted versus grazing angle and frequency for the geoacoustic models of Tables III and IV, respectively. In Figs. 5(a) and 6(a) the shear parameters of the sediment have been omitted, in Figs. 5(a) and 6(b) the full set of parameters has been included. The plots exhibit regions of high loss for grazing angles *below* the critical angles associated with conversion to compressional and shear waves in the bottom. As seen from Fig. 5(a), loss is dominated by a region of high loss at grazing angles less than critical over a broad span of frequencies from less than 10 Hz to above 100 Hz. In Fig. 6(a), a similar high-loss region is seen to extend from about 100 Hz to a few hundred Hz.

A. The sediment–substrate interface wave

The mechanism causing these regions of high loss at grazing angles below critical was proposed by Hawker,[4] and attributed to the excitation of an interface wave (of the Stoneley type, the sediment treated as a fluid) propagating along the boundary between a fluid sediment and a solid substrate. In a more recent paper, Hovem and Kristensen[5] extended the discussion to a three-layer medium. They analyzed the dispersion equation of the interface wave to derive the combinations of seabed parameters required to support the loss mechanism. In the large argument limit ($fD\rightarrow\infty$, with f the frequency and D the sediment layer thickness) this analysis condenses nicely into a single curve. In Fig. 7 this curve is reproduced for two values of substrate shear-to-compressional speed ratio β. The curves give, for a given relative sediment compressional speed (to the sound speed in water), the minimum relative substrate shear speed (to the sound speed in water) required to excite an interface wave.[28]

An additional environmental condition arises from the requirement that the compressional wave field in the sediment must have a nonvanishing amplitude at the sediment–substrate interface. In Ref. 5, it was argued that this condition effectively restricts the thickness of the sediment layer to less than one wavelength of the sediment compressional wave, corresponding to frequencies

$$f<c_P/D, \tag{2}$$

with c_P the sediment compressional speed. Thus a simple tool for predicting the *high-frequency* limit for onset of high

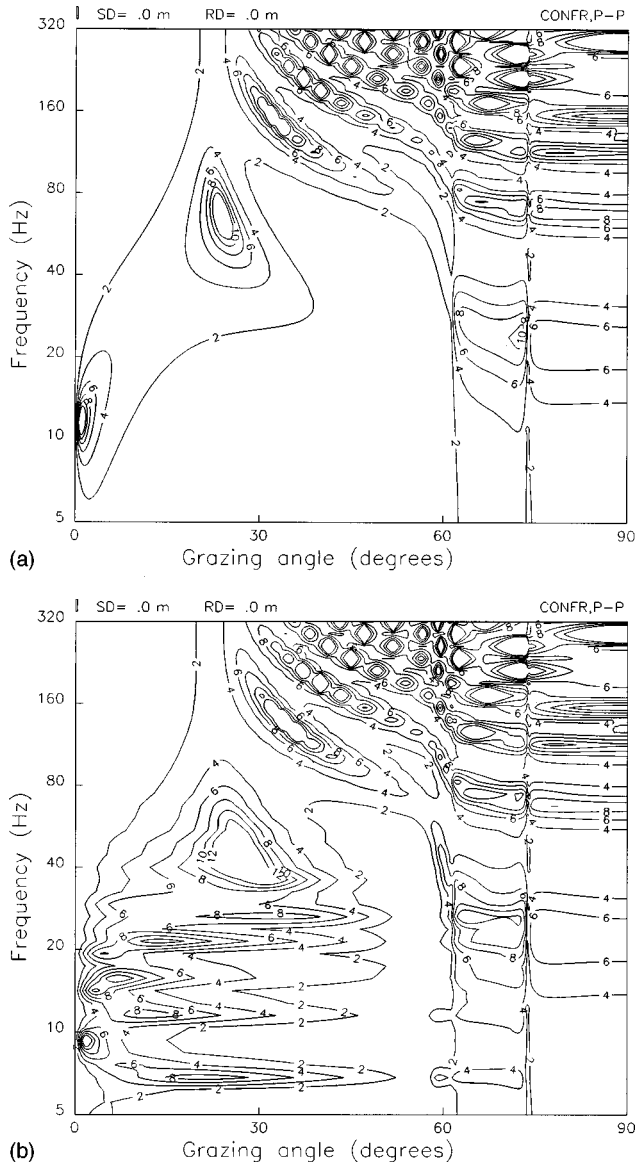

FIG. 5. Plane wave reflection loss at the water–sediment interface (in dB) versus grazing angle and frequency for a thin fluid sediment over solid substrate seabed model. Geoacoustic parameters as in Table III, elastic parameters of sediment omitted. (b) Plane wave reflection loss at the water–sediment interface (in dB) versus grazing angle and frequency for a thin elastic sediment over solid substrate seabed model. Geoacoustic parameters as in Table III.

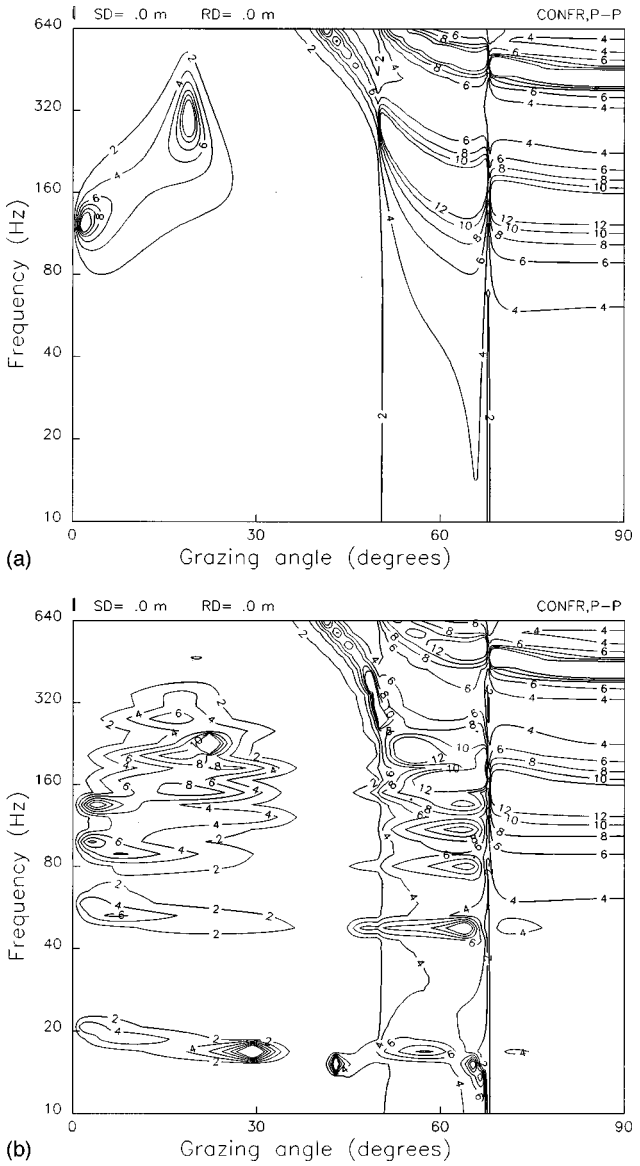

FIG. 6. Plane wave reflection loss at the water–sediment interface (in dB) versus grazing angle and frequency for a fluid sediment over solid substrate seabed model. Geoacoustic parameters as in Table IV, elastic parameters of sediment omitted. (b) Plane wave reflection loss at the water–sediment interface (in dB) versus grazing angle and frequency for a solid sediment over solid substrate seabed model. Geoacoustic parameters as in Table IV.

bottom loss is provided by Eq. (2), for combinations of seabed parameters to the right of the appropriate curve in Fig. 7.

By application of this prediction tool to the geoacoustic models of Tables II–V, we find that, for the model of Table II, high loss is not predicted due to a low substrate shear speed, while for the models of Tables III and V, high loss is predicted due to a high relative substrate shear speed. For the model of Table IV, high loss is predicted when a shear-to-compressional speed ratio $\beta=0.58$ is assumed. However, with a lower ratio of $\beta=0.50$, the transition curve now represented by the dashed line in Fig. 7, high loss is *not* predicted. In this sensitive regime, high loss is also strongly dependent on the relative sediment compressional speed.

Additional properties of the interface wave loss mechanism were derived and discussed in Ref. 5. It was pointed out that for a sediment layer of finite thickness, there are actually two types of interface waves. Each of these arises as a propagating solution of its respective dispersion equation when certain constraints on the horizontal phase velocity [Eq. (15) of Ref. 5] are met. These constraints also define a *low-frequency* limit (one for each of the interface waves) below which the interface wave cannot exist and the loss mechanism vanishes.

These solutions were exhibited in Fig. 4(a) and (b) of Ref. 5 for a particular choice of sediment parameters. In Fig. 8 the low-frequency limit is plotted versus relative substrate shear speed (to the sound speed in water) for one of the interface waves, for four values of sediment compressional wave speed in the interval 1600–2000 m/s, in the limit where the interface wave velocity reaches the sound speed in water.[29] The curves give a low-frequency limit, with high

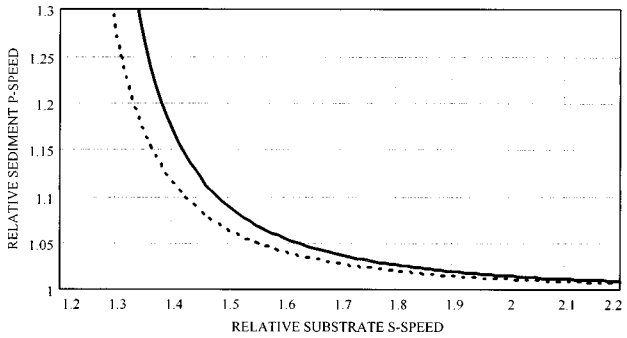

FIG. 7. Combinations of seabed geoacoustic parameters that may result in high propagation loss due to the sediment–substrate interface wave loss mechanism. High loss is predicted for combinations of parameters to the right of the curves. Based on an analysis from Ref. 5. Speeds are relative to sound speed in water. The curves correspond to two ratios (0.50 dashed curve; 0.58 solid curve) of substrate shear-to-compressional speed.

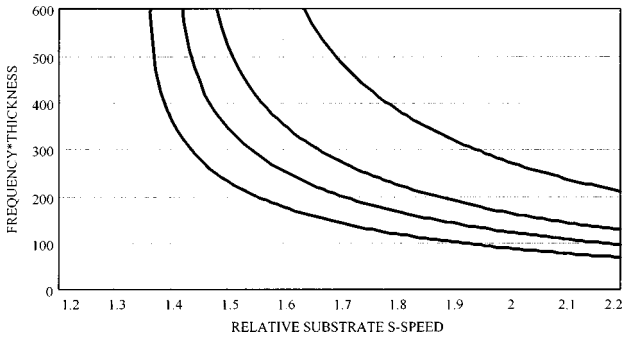

FIG. 8. Minimum fD product as a function of relative substrate shear speed (to sound speed in water) for solutions to the dispersion equation for a sediment–substrate interface wave. High loss is predicted for combinations of parameters to the right of the curves. Interface wave velocity equal to the sound speed in water (1470 m/s). Sediment compressional wave speeds of 1600 m/s, upper curve; 1700 m/s, second curve; 1800 m/s, third curve; and 2000 m/s, lower curve.

loss predicted for parameter combinations to the right of the respective curve (also restricted by the high-frequency limit discussed above). It is noted that this limit decreases with increasing sediment compressional speed, and also decreases with a decreasing sound speed in water. In Ref. 5, the low-frequency limits for both of the interface waves were discussed in more detail.

Combining the high- and low-frequency limits, a frequency regime

$$f_b < f < c_p/D \tag{3}$$

(with f_b a *low-frequency* limit), where high loss due to the sediment-substrate interface wave loss mechanism is predicted, has been delineated. Using Eq. (3) with f_b taken from Fig. 8, we find that for the geoacoustic model of Table III, high loss is predicted for frequencies of about 10–100 Hz, while for the model of Table IV, high loss is predicted for a span of frequencies 100–550 Hz. This is in good agreement with the high-loss regions as observed in Figs. 5(a) and 6(a).

The low-frequency limit of the interface wave loss mechanism could imply a ''reopened acoustic window'' at low frequencies where the acoustic field could be expected to propagate without significant bottom loss [cf. also Fig. 2(c) of Ref. 14 in this respect]. However, this treatment does not account for elastic properties of the sediment.

B. Sediment shear waves

For an elastic sediment, additional bottom loss can be induced by conversion to sediment shear waves at the sediment–substrate interface,[2] which introduces a second important loss mechanism. An illustration of additional bottom loss induced by sediment shear is seen in Figs. 5(b) and 6(b), where sediment shear parameters have been reintroduced in the seabed models.

High loss due to sediment shear waves is most distinct at regularly spaced resonance frequencies centered at

$$f_n = (2n+1)c_s/4D \tag{4}$$

with $n = 0,1,2,...,c_s$ the sediment shear speed, and D the sediment layer thickness. At these resonance frequencies, energy converted to sediment shear waves is eventually lost due to absorption, and high propagation loss is predicted. This loss mechanism was studied by Vidmar[2] and later by Hughes *et al.*[3] in interpretation and modeling of data exhibiting a resonant loss structure.

For the geoacoustic model of Table III, loss due to sediment shear waves is by Eq. (4) predicted to be centered at 7, 11.8, 16.5, 21.2 Hz and higher. As seen from Fig. 5(b), all but the lowest-order resonances are blended into and masked by the high-loss region associated with the interface wave loss mechanism. For the geoacoustic model of Table IV, high loss is predicted by Eq. (4) to be centered at 16, 50, 83, 116 Hz and higher. By inspection of Fig. 6(b) the two lowest-order resonances are distinct, while higher-order resonances are blended into the high-loss region associated with interface waves. This provides an opportunity to probe the existence of high loss due to sediment shear waves when propagation loss data in frequency bands below 100 Hz are considered. The sediment shear speed of the geoacoustic model in Table V of 600 m/s cannot be considered low, and Eq. (4) may not be directly applicable.

C. Propagation loss

Observation of high propagation loss in a seabed environment of predicted high bottom loss is further dependent on the properties of the water column, and the distribution of acoustic energy over angles of propagation (grazing angles) as dependent on the source–receiver geometry. In the high-frequency limit, the interface wave loss mechanism is confined to a small interval of grazing angles, thus high loss can be expected to be sensitive to source–receiver depths. In the low-frequency limit, high bottom loss extends over a wider span of grazing angles, and high propagation loss can be expected to be less dependent on source–receiver depths. The bands of high loss associated with sediment shear wave resonances extend over a wide span of grazing angles, thus high propagation loss from this effect is less sensitive to source–receiver depths, at least for low sediment shear speed.

In this section, a few characteristic features associated with two known loss mechanisms in seabed environments consisting of a homogeneous thin sediment layer over a hard solid substrate have been elucidated. For theoretical develop-

ments of bottom loss, reference is made to Refs. 2–5, with recent investigations found in Refs. 11–15. In treatments by Chapman and Chapman[12] and Ainslie,[15] approximate expressions [e.g., Eq. (12) of Ref. 12] for reflection coefficients in the case of an elastic sediment have been derived and analyzed. These expressions are valid for low sediment shear speed, and in the limit of a fluid sediment reduce to the expression analyzed in detail in Ref. 5.

IV. MODELING OF PROPAGATION LOSS

Propagation loss has been modeled using the recently developed wave number integration model XFEM[30,31] for laterally homogeneous, range-independent fluid–solid media. The code models wide-angle propagation at short ranges, and accounts for the wave types discussed in Sec. III. Compared to the fast-field model SAFARI,[27] also of the wave number integration type, XFEM has some potentially advantageous features (a higher-order adaptive integration technique and use of exact Hankel functions in range). A version of the XFEM model employing a normal mode solution including branch cut contributions[32] is also available.

The XFEM model takes as input a horizontally stratified medium with homogeneous layers of fluid or solid properties. For bottom parameters, the geoacoustic models of Tables II–V were used. As in these models, and for simplicity, we have assumed iso-density and iso-velocity layers, that is, although the numerical model allows a stair-step approximation to vertical parameter gradients, none were introduced. The estimated source depths were used, while around the nominal receiver position a small range-depth matrix was averaged over. Model runs were performed at 1596 frequencies spaced equidistant on a logarithmic scale from 5.55 to 710 Hz. Then an unweighted incoherent average was applied to the pressure magnitudes in each $\frac{1}{3}$ octave band from 6.3 to 630 Hz. Stability of the frequency sampling against frequency spacing and the averaging method was checked.

The $\frac{1}{3}$ octave band averaged propagation loss values $\mathrm{TL}=20\log_{10}|P(f,R)|$ [with $|P(f,R)|$ the pressure magnitude at range R, averaged over a frequency band f, normalized with respect to the pressure field at $R=1$ m in an unbounded medium] are plotted with open triangles in Figs. 1–4 for sites I–IV, respectively.

A. Site I

Modeling of loss at site I (Fig. 1) is accurate to within 2 dB for all frequency bands, except for the 10-Hz band. In this case using a fully fluid seabed model (fluid sediment over fluid substrate) is adequate, as no shear-dependent loss is predicted for the frequencies considered.

B. Site II

At site II (Fig. 2), model predictions using a fully fluid seabed model (upper row of triangles) clearly misses shear-induced loss below 100 Hz. Including sediment and substrate elasticity in the model (lower row of triangles), propagation loss is modeled to within 3 dB at all frequencies above 20 Hz (except for the 250-Hz band). The deep null at 16–20 Hz and lower loss in the 10–12.5-Hz bands has been modeled well. At 20 Hz, a modeled loss value of 72 dB is to be compared with a data value of 82 dB. It is noted that low loss in the 10–12.5-Hz bands can be associated with the low-frequency limit of the sediment–substrate interface wave loss mechanism.

A variation of sediment and substrate parameters from the nominal values in Table III showed that loss above 40 Hz was affected only marginally, while loss at 16–20 Hz was highly sensitive to the sediment and the substrate shear parameters. For example, by increasing the substrate shear speed to 3.8 km/s, the highest loss band was shifted to 16 Hz at a value of 71 dB. High loss in the 16–20-Hz bands increased further with increasing sediment attenuation. The sediment was also modeled as a fluid, with a highest loss of 65 dB in the 20-Hz band and little effect above the 40-Hz band.

C. Site III

At site III (Fig. 3) high loss below 200 Hz has been modeled with moderate success. Loss values are off by as much as 15 dB, but, more importantly, a resonant structure with nulls at 16 Hz and 40–80 Hz is seen. A source of mismatch may here be the assumed range independence in the geoacoustic model. In modeling of this data, a homogeneous solid bottom (no sediment cover) was also tried. Only by lowering the substrate shear speed to 800 m/s could a reasonably good model fit to data be obtained. This model, however, is discarded as being unrealistic, given the geoacoustic data quoted in Sec. II. Moreover, such a model does not produce a resonant structure below the null at 80 Hz. A similar data point from this shallow bank was considered by Jensen.[10] Due to lack of data below the first deep propagation null, he would not conclude which loss mechanism, a homogeneous low shear speed bottom or sediment shear waves, was the principal cause of observed loss in his data. In our case we conclude that data is consistent with characteristics of the sediment shear wave loss mechanism.

D. Site IV

At site IV (Fig. 4), model loss predictions agree with data to within 3 dB for all frequencies from 6.3 to 630 Hz. In particular, the ''dip'' centered at 12.5 Hz, corresponding to a predicted fundamental shear wave resonance frequency, and evidence of the third predicted resonance at 62.5 Hz have been modeled in excellent agreement with the data. For this relatively thick sediment layer (as compared to site III), signatures of second- and higher-order resonances are diminished due to a relatively higher attenuation suffered by energy traversing the sediment layer. An interpretation of the observed null in the 12.5-Hz band and the indicated weaker null in the 63-Hz band as a shear wave resonance effect seems reasonable.

V. SUMMARY

In this paper low-frequency broadband propagation loss data collected at four sites of a shallow water region has been presented, with high loss reported for frequencies below 1–200 Hz at three of these sites. The data as such are not

unique, but augment a sparse amount of data of this kind reported from this and other shallow-water continental shelf regions.

Geoacoustic models for the sites of experiment suggest a thin layer of unconsolidated sediment over a hard solid substrate at the high-loss sites. Within the framework of such two-layer seabed models, two known bottom loss mechanisms, both requiring a hard solid substrate close to the water–bottom interface, have been shown to explain characteristic features of high propagation loss as observed.

High loss at one site exhibits characteristics consistent with the predictions of the sediment–substrate interface wave loss mechanism. A critical parameter for predicting high loss due to this effect is the substrate shear speed which needs to be in excess of a certain limit, secondarily dependent on the properties of the sediment layer. The physical thickness of the sediment layer determines a high-frequency limit for onset of high propagation loss. A low-frequency limit below which loss due to this effect diminishes, for the case of fluid sediment, has also been commented on.

High loss attributed to the excitation of shear waves in the sediment is most distinctly exhibited in a resonant loss structure at frequencies below the low-frequency limit of the interface wave. This has been observed in data at a site of a physically thin sediment cover of low shear speed, and at a site of a sediment cover of higher shear speed. In the intermediate region between the low- and high-frequency limits of the interface wave loss mechanism, loss exclusively attributable to sediment shear waves is not exhibited distinctly. One conclusion from the present work is that excitation of guided shear waves in the sediment does not *exclusively* explain the principal features of propagation loss in broadband field data acquired from the shallow waters as considered in this paper.

Propagation loss data from all sites have been modeled well using a recently developed wave number integration code for laterally homogeneous fluid–solid media, accounting for shear-induced loss mechanisms. The results of this paper may aid in locating areas of similar acoustic propagation characteristics, and in establishing an improved acoustic prediction capability in this and possibly other complex shallow water environments of similar kind.

ACKNOWLEDGMENTS

This work was inspired by a visit to the National Defence Research Establishment (FOA), Stockholm, Sweden, in 1994 as sponsored by the Nordic Academy for Scientific Education, and hosted by Professor Ilkka Karasalo of FOA. The field data were collected by the Norwegian Defence Research Establishment.

[1] T. Akal and F. B. Jensen, ''Effects of the sea-bed on acoustic propagation,'' in *Acoustics and the Sea-Bed*, edited by N. G. Pace (Bath U. P., Bath, UK, 1983), pp. 225–232.

[2] P. J. Vidmar, ''The effect of sediment rigidity on bottom reflection loss in typical deep sea sediments,'' J. Acoust. Soc. Am. **68**, 634–638 (1980).

[3] S. J. Hughes, D. D. Ellis, D. F. M. Chapman, and P. R. Staal, ''Low-frequency acoustic propagation loss in shallow water over hard-rock seabeds covered by a thin layer of elastic-solid sediment,'' J. Acoust. Soc. Am. **88**, 283–297 (1990).

[4] K. E. Hawker, ''The existence of Stoneley waves as a loss mechanism in plane-wave reflection problems,'' J. Acoust. Soc. Am. **65**, 682–686 (1979).

[5] J. M. Hovem and Å. Kristensen, ''Reflection loss at a bottom with a fluid sediment layer over a hard solid half-space,'' J. Acoust. Soc. Am. **92**, 335–340 (1992).

[6] R. D. Worley and R. A. Walker, ''Low-frequency ambient ocean noise and sound transmission over a thinly sedimented rock bottom,'' J. Acoust. Soc. Am. **71**, 863–870 (1982).

[7] J. H. Beebe and C. W. Holland, ''Shallow-water propagation effects over a complex, high-velocity bottom,'' J. Acoust. Soc. Am. **80**, 244–250 (1986).

[8] P. R. Staal, D. M. F. Chapman, and P. Zakarauskas, ''The effect of variable roughness of a granite seabed on low-frequency shallow-water acoustic propagation,'' in *Progress in Underwater Acoustics*, edited by H. M. Merklinger (Plenum, New York, 1986), pp. 485–492.

[9] E. Hug, ''A propagation anomaly observed in the Barents Sea,'' in *Ocean Seismo-Acoustics*, edited by T. Akal and J. M. Berkson (Plenum, New York, 1986), pp. 217–222.

[10] F. B. Jensen, ''Excess attenuation in low-frequency shallow-water acoustics: a shear wave effect?'' in *Shear Waves in Marine Sediments*, edited by J. M. Hovem, M. D. Richardson, and R. D. Stoll (Kluwer, Amsterdam, 1991), pp. 421–430.

[11] S. J. Hughes, D. F. M. Chapman, and N. R. Chapman, ''The effect of shear wave attenuation on acoustic bottom loss resonance in marine sediments,'' in *Shear Waves in Marine Sediments*, edited by J. M. Hovem, M. D. Richardson, and R. D. Stoll (Kluwer, Amsterdam, 1991), pp. 439–446.

[12] N. R. Chapman and D. F. M. Chapman, ''A coherent ray model of plane-wave reflection from a thin sediment layer,'' J. Acoust. Soc. Am. **94**, 2731–2738 (1993).

[13] S. A. L. Glegg, ''The effective depth approximation for sound propagation in shallow water over a sediment layer and a hard rock basement,'' J. Acoust. Soc. Am. **94**, 3302–3311 (1993).

[14] S. Ivansson, ''Shear-wave induced transmission loss in a fluid-solid medium,'' J. Acoust. Soc. Am. **96**, 2870–2875 (1994).

[15] M. A. Ainslie, ''Plane-wave reflection and transmission coefficients for a three-layered elastic medium,'' J. Acoust. Soc. Am. **97**, 954–961 (1995).

[16] O. Eldholm and M. Talwani, ''The sediment distribution and structural framework of the Barents Sea,'' Bull. Geol. Soc. Am. **88**, 1015–1029 (1977).

[17] N. R. Chapman, ''Source levels of shallow explosive charges,'' J. Acoust. Soc. Am. **84**, 697–702 (1988).

[18] D. Weston, ''Intensity-range relations in oceanographic acoustics,'' J. Sound Vib. **18**, 271–287 (1971).

[19] E. L. Hamilton, ''Geoacoustic modeling of the sea floor,'' J. Acoust. Soc. Am. **68**, 1313–1340 (1980).

[20] E. M. O. Sigmond, ''Bedrock, Norway and adjacent Seas,'' Norwegian Geological Mapping Agency, 1992.

[21] R. E. Houtz, ''Seafloor and Near-Surface Sound Velocities From Barents Sea Sonobuoy Data,'' J. Geophys. Res. **85**, 4838–4844 (1980).

[22] S. K. Breeding, D. A. Dunn, and T. H. Orsi, ''Shear wave velocities of glacio-marine sediments: Barents Sea,'' in *Shear Waves in Marine Sediments*, edited by J. M. Hovem, M. D. Richardson, and R. D. Stoll (Kluwer, Amsterdam, 1991), pp. 149–156.

[23] A. Elverhøi and A. Solheim, ''The Barents Sea ice sheet—a sedimentological discussion,'' Polar Res. **1**, 23–42 (1983).

[24] A. Solheim, ''The depositional environment of surging sub-polar tidewater glaciers,'' Norsk Polarinst. Skrifter **194**, (1991).

[25] A. Solheim and Y. Kristoffersen, ''The physical environment, Western Barents Sea, 1:1500000, sheet *B*; sediments above the upper regional unconformity: thickness, seismic stratigraphy and outline of the glacial history,'' Norw. Pol. Inst. Rept Ser. 179B (1983).

[26] L. Brekhovskikh and Yu. Lysanov, *Fundamentals of Ocean Acoustics* (Springer-Verlag, Berlin, 1982).

[27] H. Schmidt, ''SAFARI: Seismo-acoustic fast-field algorithm for range-independent environments,'' Rep. SR-113, SACLANT Undersea Research Centre, La Spezia, Italy, 1988.

[28] A relative sediment compressional speed above unity is required, and sediment elasticity is not assumed. In Fig. 7, substrate shear-to-compressional speed ratios of 0.50 (dashed curve) and 0.58 (solid curve) are used. The dependence on density ratio (here set to 1.80/2.50) is negligible. Attenuation in the substrate, and compressional attenuation in the sediment layer is required for nonzero bottom loss.

[29] The curves in Fig. 8 are based on an expansion of the trigonometric function in the dispersion equation for the interface wave [Eq. (8) of Ref. 5], in the limit when the horizontal phase velocity reaches its lowest limit, the sound velocity in water. The expansion is valid to within 10% for frequency-thickness products $fD \leqslant 600$ for the range of sediment compressional speeds (<2000 m/s) considered here. A sound speed in water of 1470 m/s and a substrate shear-to-compressional speed ratio of 0.58 has been used.

[30] I. Karasalo, ''Exact finite elements for wave propagation in range-independent fluid-solid media,'' J. Sound Vib. **172**, 671–688 (1994).

[31] S. Ivansson and I. Karasalo, ''A high-order adaptive integration method for wave propagation in range-independent fluid-solid media,'' J. Acoust. Soc. Am. **92**, 1569–1577 (1992).

[32] S. Ivansson and I. Karasalo, ''Computation of modal wavenumbers using an adaptive winding-number integral method with error control,'' J. Sound Vib. **161**, 173–180 (1993).

Experimental demonstration of the pseudo-Rayleigh (A_0) wave

A. C. Ahyi, P. Pernod, and O. Gatti
IEMN-DOAE, Groupe Electronique Acoustique, Ecole Centrale de Lille, B.P. 48, F-59651 Villeneuve d'Ascq Cédex, France

V. Latard and A. Merlen
Laboratoire de Mécanique de Lille, USTL1, Cité Scientifique, F-59655 Villeneuve d'Ascq Cédex, France

H. Überall
IEMN-DOAE, Groupe Electronique Acoustique, Ecole Centrale de Lille, B. P. 48, F-59651 Villeneuve d'Ascq Cédex, France and Department of Physics, Catholic University of America, Washington, DC 20064

(Received 29 August 1997; accepted for publication 29 June 1998)

It is well known that the circumferential waves supported by thin cylindrical, water-loaded shells correspond closely to those on a water-loaded plate, i.e., to the Scholte–Stoneley wave A and to the Lamb waves $A_0, A_1, A_2, \ldots$, and $S_0, S_1, S_2 \ldots$. Until now, however, it had not been possible to definitely observe the acoustic excitation of the A_0 wave on a shell using steady-state or long-pulse incident sound waves (while excitation of the A and S_0 waves was clearly evident). The reason for this is the rapid decay of the propagating A_0 waves, whose high attenuation also rendered their multicircuit resonances too broad to be individually observable. In the present experiment, carried out with ultrashort, spark-generated acoustic pulses whose diffraction by a steel shell is visualized by the shadowgraph method, the A_0 (''pseudo-Rayleigh'') wave could be observed immediately after its excitation, before it had any time to decay. Spectral analysis of its observed re-radiation permitted the extraction of its phase-velocity dispersion curve, which by comparison with previously calculated dispersion curves uniquely characterized it as being the A_0 wave. [S0001-4966(98)01910-9]

PACS numbers: 43.35.Bf, 43.35.Cg, 43.20.Tb [DEC]

INTRODUCTION

A number of experiments on the scattering of acoustic waves normally incident on empty, water-immersed thin cylindrical metal shells have been performed, some[1–3] as early as 1969, and have been continuing to the present. Typical targets were duraluminum, stainless steel, or copper shells. After the advent of the resonance scattering theory (RST),[4,5] subsequent shell scattering experiments have been analyzed in terms of resonating circumferential waves.[6] Of these experiments, some were carried out essentially using steady-state incident signals,[7–14] and were analyzed by the MIIR method;[7] others used acoustic pulses and their Fourier analysis.[15–19] Theoretical analysis, always based on the circumferential-wave concept, was carried out for the process of thin-shell scattering over the same period.[15,17,20–27]

The circumferential waves on water-loaded, thin cylindrical shells have been shown,[15,16,25] by comparing their calculated dispersion and attenuation curves versus frequency with those of the Scholte–Stoneley wave and the Lamb waves on a fluid-loaded plate of the same material (duraluminum or stainless steel), to be extremely close to each other (except for ultra-low frequencies), so that the plate could be used for a model description of shell scattering. The lowest circumferential waves obtained theoretically on a shell have been labeled[17,23] $l=0,...,3$, and were found to correspond to the fluid-borne Scholte–Stoneley wave A ($l=0$), the lowest antisymmetric Lamb wave A_0 ($l=1$ or pseudo-Rayleigh wave), the lowest symmetric Lamb wave S_0 ($l=2$) and the higher Lamb waves A_1 ($l=3$), etc. All of these waves have been identified by observing their excitation in the mentioned acoustic shell scattering experiments, with the exception of the A_0 wave which was not observed. In a recent resonance analysis[28] of calculated scattering amplitudes from a cylindrical shell with an internal rib attached to the shell wall,[29] it was likewise found that the circumferential waves that manifested themselves in the resonances of the scattering amplitudes were S_0 and A only, excluding the excitation of the A_0 wave even in this case.

The reason for the nonobservability of the A_0 wave was recognized by Talmant and Quentin[15,25] to lie in the fact that the attenuation (caused by re-radiation) of the A_0 wave is at small frequencies, especially for frequency-thickness values $fe \leqslant 1$ MHz mm (e=plate thickness), an order of magnitude higher than, e.g., that of the S_0 wave, due to the transverse (flexural) nature of the A_0 wave which causes higher re-radiation, as shown in Fig. 1 for a duraluminum shell as taken from Ref. 15 (see also Ref. 23). This figure presents the attenuation coefficient of these waves (in Np/rd) for a cylindrical duraluminum shell as modeled by plate waves (on the plate, the A wave has zero attenuation[15] and cannot be used to model the A wave attenuation on the shell). Incidentally, it was also shown[15] that the attenuation coefficient is inversely proportional to $(1-b/a)$, where a and b are outer and inner radius of the shell, respectively, so that the thinner the shell, the larger are the attenuation and re-radiation of the wave. To quote Ref. 16: ''When the velocity of the A_0 wave approaches the velocity of sound in the fluid medium, the imaginary part of its wave vector becomes exceedingly large and this wave cannot be propagative any more.'' However, Talmant[15] notes that the attenuation for the

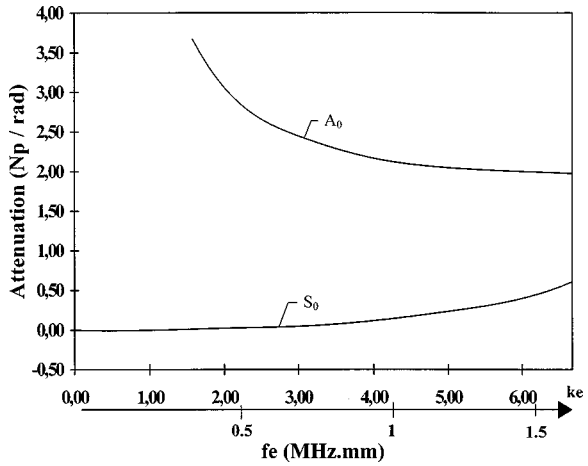

FIG. 1. Attenuation coefficients (in Np/rad) of Lamb waves A_0 and S_0 in a duraluminum plate water loaded from one side, plotted vs ke (k =propagation constant in water, e=plate thickness). From Ref. 15 (with permission).

A_0 wave on a steel shell is lower by a factor of 3 than on a duraluminum shell, so that on steel shells there might be a chance to observe the propagating A_0 wave in conventional experiments. In fact, in the experiments of Talmant and Quentin[15,16] which were done observing the radiation from multiply circumnavigating pulses on the shells, one singly circumnavigating pulse was seen on the steel shell (but not on the duraluminum shells) in addition to those of the A and S_0 waves. This might have been an example of the A_0 wave, but it could not be identified as such in their experiment. In our ultra-short-pulse experiments, to be described below, where only the initial portion of just the first circumnavigation is observed, the propagation of the A_0 wave on steel shells (and also on plates) has been positively identified. This was achieved by extracting its phase-velocity dispersion curve from its observed re-radiation into the fluid using spectral analysis and noting that it agreed closely with calculated A_0 wave dispersion curves.

In the following section, we describe the spark source employed here and the generation by it of the ultra-short (essentially δ-function) acoustic pulses used in our experiment. We also discuss the Shadowgraph visualization system that was used in order to observe the re-radiation into the ambient fluid of the shell waves excited by the incident pulses. Section II shows visualization results of the experiment and, in particular, it describes the spectral analysis of the observed re-radiated waves which was employed here in order to extract the dispersion curves of the shell waves. In Sec. III, these dispersion curves (obtained for the propagating waves observed on stainless-steel shells, and also on stainless-steel plates) were compared with previously calculated dispersion curves of the A_0 wave on steel shells; the close agreement that was found here demonstrates uniquely that in our experiment, the A_0 wave has been excited, and that its propagation has been directly observed over the relatively short distance before it got attenuated. This is the first unequivocal experimental demonstration of the acoustic generation of the A_0 wave on thin cylindrical shells, and the observation of its propagation.[30] The S_0 wave, which has been seen in earlier conventional shell scattering experiments, is also observed by us. The A wave, which has zero attenuation in plates, and very small attenuation (and hence, small re-radiation) in shells,[15] has not been observed in our present experiment (although it has been seen in related experiments of ours using different shell targets, to be published separately). All of these points will be considered further in our summary and discussion, Sec. IV.

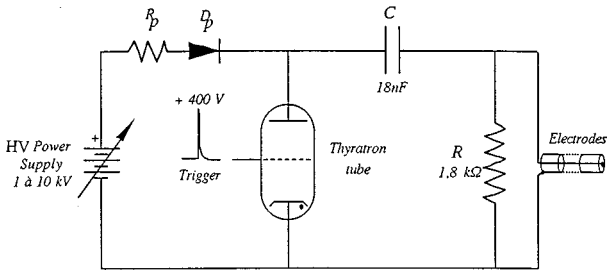

FIG. 2. Diagram of mini-sparker sound source.

I. DESCRIPTION OF SOUND SOURCE AND OF THE VISUALIZATION SYSTEM

A. Mini-sparker sound source

The schematic diagram of the mini-sparker is presented Fig. 2. A coaxial oil field capacitor of 18 nF, designed for rapid discharges (low inductance 10–40 nH), is charged through resistance and diode protections (R_p,D_p) by a high voltage power supply adjustable from 1 to 10 kV. The discharge of this capacitor is triggered by means of a rapid switching device (thyratron tube): a half-period sinusoid of several hundred nanoseconds typical duration, and several hundred amperes maximum, is therefore delivered to the circuit. A spark is then created between the electrode tips immersed in water (discharge gap=0.5 mm). As a result of the strong local perturbation created by this electric arc, an intense acoustic impulse is generated.

B. Cinematographic shadowgraph

The visualization system used the Cranz–Schardin visualization principle[31] presented in Fig. 3. It employs 24 light flashes triggered successively with an adjustable Δt time in-

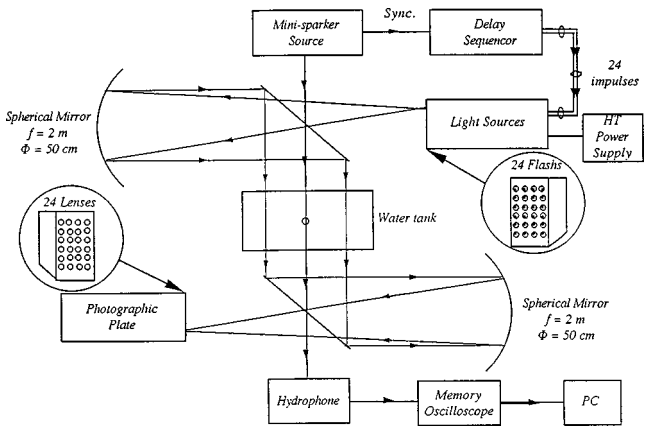

FIG. 3. Shadowgraph visualization system based on Cranz–Schardin visualization principle.

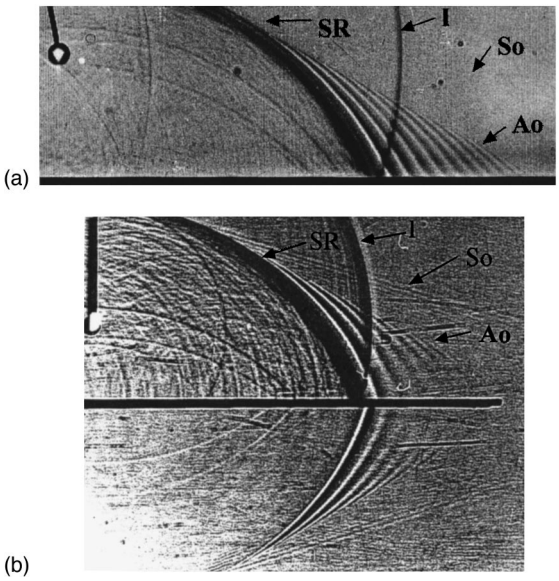

FIG. 4. Visualization of steel plate diffraction of thickness $e=1$ mm at $t=59$ μs (a) water loaded on one side, (b) water loaded on both sides.

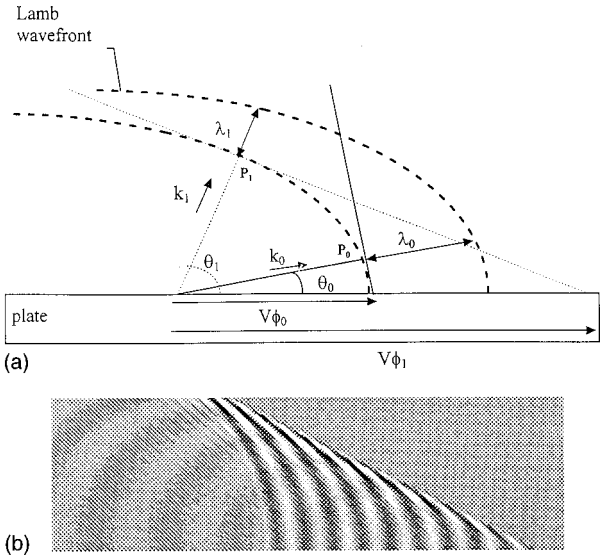

FIG. 5. (a) Method of extraction of the dispersion curves from the photographs; (b) calculation of an interaction between a spherical wave and a plate.

terval ranging from 100 ns to 1 s. A delay between synchronization and the beginning of the sequence can be introduced when necessary. Each light flash of 300-ns duration is transformed in a parallel beam by a spherical mirror of 50 cm diameter and 4 m radius of curvature. The beam is then reflected by a plane mirror before crossing the field interest where the mini-sparker is placed, and is focalized by a series of two mirrors identical to the first ones on a receiving photographic plate. As a result 24 images of 26×32 mm^2 size representing a cinematography of the phenomena are obtained on an 18×24 cm^2 film. All of the experiments presented in this paper were made in a water tank of $40\times30\times30$ cm^3.

II. VISUALIZATION AND SPECTRAL ANALYSIS OF RESULTS

A first series of experiments has been carried out on plates. Two kinds of plates, aluminum and stainless steel, and two kinds of loads (fluid on both sides of the plate, or fluid only on one side and air on the other side) were considered. High quality photographs showing the interaction of the pulse with a steel plate when the acoustic source was placed 3 cm above the plate are presented in Fig. 4, with (a) water loading on one side of the plate, and (b) water loading on both sides.

In addition to the incident wave (I) and the specular reflection (SR), the photographs clearly show the re-radiation in water (''head waves'') of two kinds of waves. The first one, its re-radiation appearing with a rather slight tilt and being scarcely visible, has a high velocity of 5300 m/s and is interpreted as the S_0 wave in the plate. The second one, with lower velocity, demonstrates a large broadening of its temporal behavior with alternating black and white streaks typical of a dispersion phenomenon. When the plate is loaded by water on both sides, one can observe the antisymmetric pattern of these alternating black and white areas. It indicates an antisymmetric pressure field in the water as it is the case for antisymmetric Lamb waves. Actually the shadowgraph reveals second derivatives of pressure field which is obviously in phase with the pressure field itself.

In order to better analyze the real nature of this (second) wave, we have developed a method of extracting from the photographs the dispersion curves of this type of wave. The pattern of alternating areas is considered as the result of the interference of plane harmonic waves re-radiated from the plate in various directions defined by the geometrical construction of Fig. 5(a).

For each position of the point P moving from P_0 to P_1 along an equiphase line of the photograph of Fig. 4, the value of the angle θ_0, θ_1 furnishes the phase velocity of the corresponding spectral component, whose frequency is obtained by measurement of its wavelength in water, determined by the length in the direction of propagation of one complete period of alternated equiphase lines [Fig. 5(a)]. Details of this analysis can be found in the doctoral dissertation of the first author.[32]

The results of this specific processing are presented and compared to theoretical calculations in the next section. As will be shown the analyzed wave corresponds to an A_0 wave.

In order to verify our interpretation regarding the nature of this alternating pattern, a model calculation of the interference pattern of plane harmonic waves radiated from the plate, employing the geometrical construction presented above, was carried out, also using the dispersion curve obtained as indicated. The result presented in Fig. 5(b) shows a spatial behavior of the pattern very similar to those in the photographs [Fig. 4(a),(b)], thereby justifying our method of geometrically extracting the dispersion curve from the photographs.

A second series of experiments was carried out on cylindrical shells under normal isonification by the spark acoustic source. The results are presented in Fig. 6 for a shell of thickness ratio $b/a=0.94$, a being the outer and b the

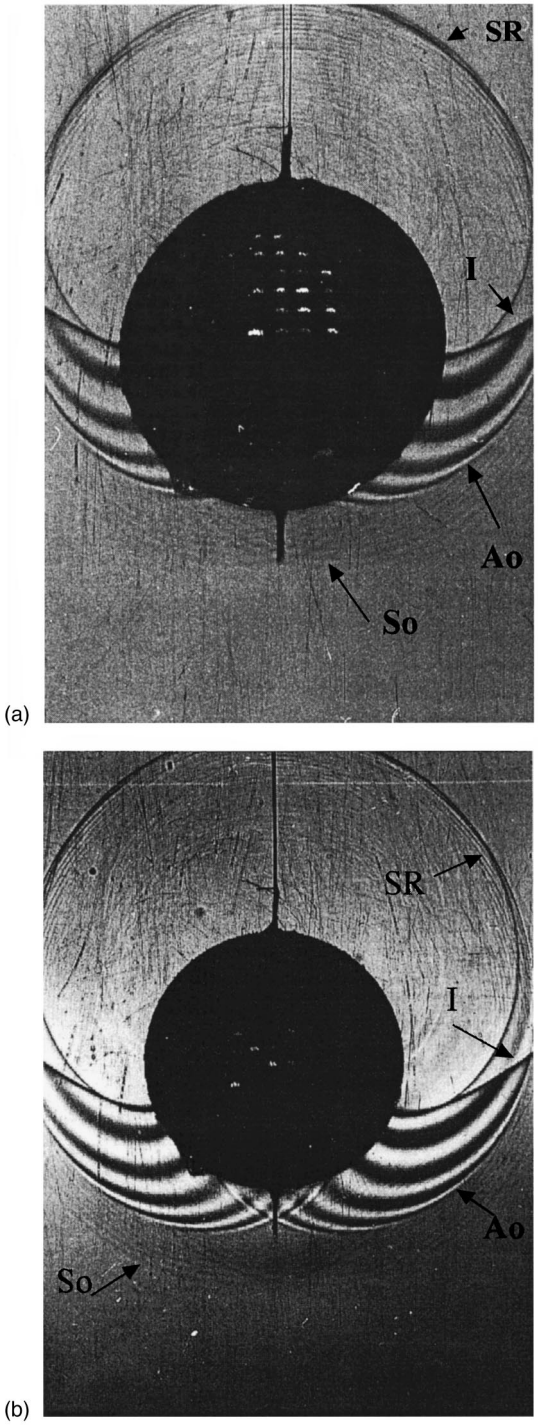

FIG. 6. Visualization of cylindrical shells under normal isonification by the spark acoustic source, for a shell of thickness ratio $b/a=0.94$, a being the outer and b the inner shell radius. One can observe in the photographs the incident acoustic pulse, the specular reflection, the diffracted ''Franz wave'' (which is the prolongation of the incident wave observed in the shadow zone of the object), and the re-radiation in water of two kinds of shell waves which have traveled ahead of the incident pulse: (a) $t=52\ \mu$s; (b) $t=58\ \mu$s.

inner shell radius. One can observe in the photographs the incident acoustic pulse (I), the specular reflection (SR), the diffracted ''Franz wave'' observed in the shadow zone of the object, and the re-radiation in water of two kinds of shell waves which have traveled ahead of the incident pulse. Identification of these waves was performed by the processing described above for the plate with improvement for curved surfaces (extraction of dispersion curves).

III. A_0 WAVE DISPERSION CURVES

Theoretical calculations of dispersion curves of the A_0 and other circumferential waves on water-loaded cylindrical steel shells (material parameters: $c_L=5790$ m/s, $c_T=3100$ m/s, $\rho=7900$ kg/m^3, $c_w=1470$ m/s, and $\rho_w=1000$ kg/m^3) have previously been carried out by Talman,[15] and by Subrahmanyam[22] (see Talmant *et al.*[17]) and Maze *et al.*;[26] the first reference (Talmant[15]) also contains theoretical results for a water-loaded plate. As shown in that reference (see above), there exists a very close similarity between the circumferential waves on thin shells and the corresponding plate waves, this being the reason for our use of the plate wave nomenclature $A,A_0,S_0,\ldots$ also for the shell. In addition, this will enable us to refer all the dispersion curves that were calculated for shells of various thicknesses, to one standard representation (that of the equivalent plate), since the curves vary sensitively with shell thickness while the plate curves are independent of plate thickness if the scale is taken proportional to it. The conversion formula between the ka variable for the cylindrical shell (of outer radius a and inner radius b, with k being the wave number in the ambient fluid), and the usual plate variable fe (f =frequency, e=plate thickness), is[19]

$$fe=(c_w/2\pi)(1-b/a)ka, \tag{1}$$

but here fe is dimensional (usually MHz mm), and it is preferable to introduce a nondimensional variable ke even for the plate. In this case, Eq. (1) becomes simply:

$$ke=(1-b/a)ka, \tag{2}$$

which allows us to refer the cylindrical shell curves for various b/a values to a common scale, ke, thereby rendering them directly comparable to the plate values (as well as to each other regardless of the value of b/a).

Comparisons of calculated A_0 wave dispersion curves on thin cylindrical shells with those obtained from the spectral analysis of our ultra-short-pulse experimental results on steel shells or plates as described in the preceding section, will here be carried out using this common frequency scale ke. We first show in Fig. 7 our experimental results, for the phase velocity of the wave observed on a water immersed steel plate (crosses) as compared to the calculated[26] A_0 wave phase velocity on a steel shell with $b/a=0.80$ (asterisks). Note that calculated shell curves[15,17,22,26] reach at most up to $ke=4$, while our plate wave curve when extended reaches to $ke=45$; we shall thus present in Fig. 8 a blow-up of the low-frequency region of Fig. 7 in which we shall also enter additional shell results. It may, however, be pointed out already with reference to Fig. 7 that the measured plate wave curve for high frequency asymptotes from below to the transverse wave speed (3100 m/s), or rather[33] to the nearby Rayleigh wave speed c_R, and thus generally satisfies all the characteristics of the A_0 wave on a plate, indicating the correctness of our procedure of analysis of our experimental results.

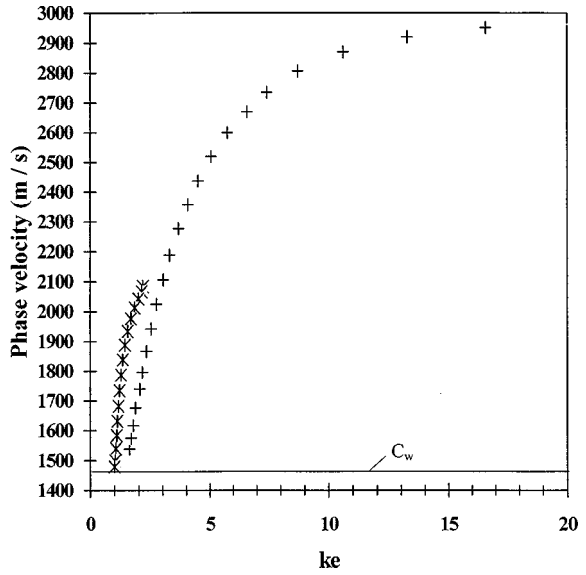

FIG. 7. Phase velocity of the experimentally observed plate wave water loaded on both sides (crosses), compared with calculated (Ref. 26) A_0 wave phase velocity on water-loaded, air-filled steel shell of thickness $b/a = 0.80$ (asterisks), its ka scale having been transferred to the ke plate scale. (Note that the A_0 wave phase velocity dispersion curves are closely the same for plates water loaded on one side or on both sides, while the A_0 attenuation coefficient for a semi-immersed plate is only half that of the fully immersed plate[15]).

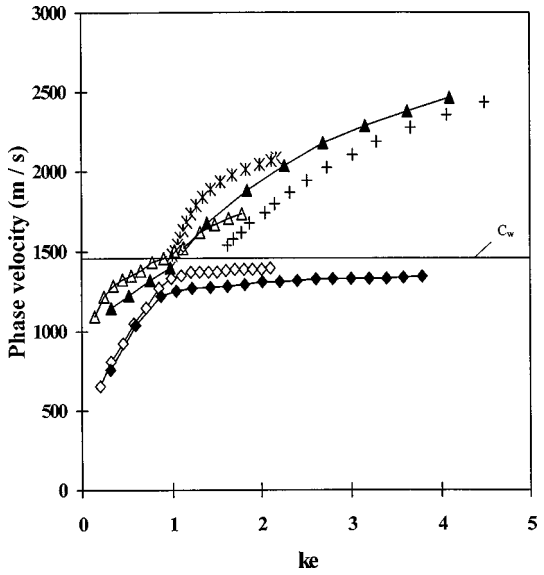

FIG. 8. Phase velocities of experimentally observed wave on $b/a = 0.94$ steel shell (asterisks), together with experimental plate wave water loaded on both sides (crosses) of Fig. 7, as compared with those of A_0 (triangles) and A (diamonds) waves on steel shells of various thicknesses: $b/a = 0.80$ (black symbol), and $b/a = 0.90$ (white symbol) (Ref. 26).

In Fig. 8 we have entered the following calculated results for water-loaded steel shells, for both the A_0 and the A waves:

(a) shell with $b/a = 0.80$ (black symbols); A_0 wave (triangles), A wave (diamonds);

(b) shell with $b/a = 0.90$ (white symbols): A_0 wave (triangles) A wave (diamonds), all from Ref. 26.

The close similarity of these curves shows the small influence of the value of b/a on the phase velocities (except for the shift in ka scale), the only noticeable difference being a small systematic shift with increasing b/a toward higher frequencies for the A_0 wave, and toward lower frequencies for the A wave. The experimental A_0 wave phase velocity for our plate is here shown by crosses.

Finally, the phase velocity extracted from our experimental observations on a $b/a = 0.94$ steel shell by the method outlined in Sec. II is shown by asterisks in the region up to $ke = 2$. Disregarding small differences with the calculated A_0 phase velocities, it is clear that the wave observed by us has all the characteristics of the A_0 (pseudo-Rayleigh) wave on a cylindrical shell, namely its phase velocity showing a rapid rise with frequency which later begins to diminish, and most of all, its exceeding the sound speed c_w in the ambient water over the entire range of observation. Under no circumstances can it be identified with the A-wave curves shown in Fig. 8 which asymptote from below to c_w, so that from the mentioned facts alone the observed wave has to be identified with the A_0 wave. Note that a full comparison with the A_0 curve calculated by Maze *et al.*[26] for $b/a = 0.95$ would not be possible here, since this curve extends over frequencies below those covered by our experimental curve, except for the last calculated point at $ka = 23.3$, or $ke = 1.16$, which corresponds to a phase velocity of 1,583 m/s, in near perfect agreement with one of our first measured points (asterisks) in Fig. 8.

The reason for the slight discrepancy of our experimental curve with the calculated curves may lie in the fact that our method of analysis of the experimental data is a rather indirect procedure, being also based on data of inherently limited precision in view of their optical (shadowgraph) nature. The calculations, however, are based on the results of linear elasticity theory, whose computational evaluation of truncated normal-mode series also admits limited accuracy only. We thus believe that the approximate agreement between calculated and experimental curves in Fig. 8 is as good as can be expected under the circumstances; in any case, it is sufficient by far to clearly verify the observation of the A_0 wave in our experiment.

Regarding the calculated A and A_0 dispersion curves of Fig. 8, a little side remark could be made with respect to nomenclature. When following these curves coming down from high frequencies, one observes them approaching each other, but then diverging again. This phenomenon has been referred to as a ''repulsion'' of dispersion curves, which in the absence of coupling caused by the fluid loading would have crossed over.[17] The question then arises how to label the curves (which conventionally are referred to as A_0 for the curve that asymptotes to c_R at high frequencies, and as A for the curve that asymptotes to c_w), in the region to the left of the near-crossover point. (This question is not imminent in the case of our experimental values that are only obtained to the right of the near-crossover point.) One way to answer this question is to label the entire upper continuous curve, from $ka = 0$ through ∞, by A_{0+} and the entire lower curve by A_{0-} as done in Ref. 26. It was shown, however,[33] that the nature of the wave A_{0+} is of the usual A_0 type, i.e., flexural, only to the right of the near-crossover point, and that of A_{0-} of the usual A type, i.e., water borne, while to the left of the near-

crossover point this physical property gets exchanged between the two waves. It is thus suggested to assign the label A_0 on the basis of this physical (flexural-wave) property, and that of A on the water-borne property. If this nomenclature is observed, then A_0 would be the upper curve and A the lower curve to the right of the near-crossover point, while to the left of the near-crossover point, A would be the upper curve and A_0 the lower curve. This new nomenclature preserves the physical nature of the A_0 and A wave curves through all frequencies, but with the curves each possessing a discontinuous gap at the near-crossover point for each curve; it would be the natural nomenclature for the case of no coupling, where the two curves simply cross over. For very strong coupling where the gap would become too large, the new nomenclature would become less appropriate, however.

IV. SUMMARY AND DISCUSSION

Circumferentially propagating waves, acoustically excited on water-immersed, air-filled cylindrical metal shells under normal incidence, have been studied experimentally using three different methods:

(a) Incident wave trains, with the observation of resonances in the frequency domain[7–14] which are caused by the phase matching of the waves upon their multiple circumnavigations of the shells;

(b) Incident acoustic pulses, with the observation of successive pulses radiated off by the circumferential waves during their multiple circumnavigations;[15–19]

(c) Direct observation of the propagating circumferential waves, as excited by ultra-short incident pulses, and visualized by the shadowgraph method,[30] as done in the present experiment. The present experiment has also applied these methods to the observation of propagating waves on plates which were water-loaded either on one side only, or on both sides.

For thin shells, it is possible to label the shell waves by the labels used for plate waves (A,A_0,S_0,A_1,…), due to their close coincidence.[15,25] The results of experiments (a) and (b) were the clear observation of A, S_0, and A_1 waves on duraluminum, stainless steel, and copper shells, while the A_0 wave has not been observed there to any identifiable degree. This is explained by the large attenuation (imaginary part of the propagation constant) of this wave,[15,23,25] especially for the case of duraluminum (that for steel being three times smaller[15]), while the attenuations of the A or S_0 waves are very much less.[15,17,25] Since experiments (a) and (b) are based on multiple circumnavigations of the circumferential waves, the A_0 wave had been much attenuated over these distances and was no longer observable.

In our experiment, the A_0 wave could be directly seen since (i) it was observed during the initial part of its first circuit before it could get attenuated too much, and (ii) its strong radiation into the surrounding water (large attenuation corresponding to strong radiation) made it highly visible by the shadowgraph visualization of this radiation.

After having thus directly observed the propagation of the A_0 wave on a thin steel shell, we have proceeded to actually identify this wave with the A_0 wave as it has been theoretically obtained on thin shells.[15,17,22,23,25,26] Comparison of the dispersion curve of the observed wave with those of the A_0 wave as calculated from theory[17,22,26] led to very reasonable agreement (the principal point being the experimental dispersion curve largely exceeding the sound speed in water), thus proving without any doubt that in our experiment, the propagation of the A_0 wave had been observed.

ACKNOWLEDGMENTS

The authors thank Professor G. Maze and Professor D. Décultot from Laboratoire d'Acoustique Ultrasonore et d'Electronique, University of Le Havre, for their help and the loan of the tubes.

[1] R. E. Bunney, R. R. Goodman, and S. W. Marshall, J. Acoust. Soc. Am. **46**, 1223 (1969).
[2] W. G. Neubauer and L. R. Dragonette, J. Acoust. Soc. Am. **48**, 1135 (1970).
[3] C. W. Horton, Sr. and M. V. Mechler, J. Acoust. Soc. Am. **51**, 295 (1971).
[4] L. Flax, L. R. Dragonette, and H. Überall, J. Acoust. Soc. Am. **63**, 723 (1978).
[5] See also A. Derem, Rev. Cethedec **58**, 43 (1979).
[6] H. Überall, L. R. Dragonette, and L. Flax, J. Acoust. Soc. Am. **61**, 711 (1977).
[7] G. Maze and J. Ripoche, Rev. Phys. Appl. **18**, 319 (1983).
[8] G. Maze, Dissertation, University of Rouen (1984).
[9] G. Maze, J. Ripoche, A. Derem, and J. L. Rousselot, Acustica **55**, 69 (1984).
[10] J. L. Izbicki, G. Maze, and J. Ripoche, J. Acoust. Soc. Am. **80**, 1215 (1986).
[11] J. L. Izbicki, G. Maze, and J. Ripoche, Acustica **61**, 137 (1986).
[12] A. Gérard, J. L. Rousselot, J. L. Izbicki, G. Maze, and J. Ripoche, Rev. Phys. Appl. **23**, 289 (1988).
[13] M. Talmant, J. L. Izbicki, G. Maze, G. Quentin, and J. Ripoche, J. Acoust. **9**, 509 (1991).
[14] J. L. Izbicki, J. L. Rousselot, A. Gérard, G. Maze, and J. Ripoche, J. Acoust. Soc. Am. **90**, 2602 (1991).
[15] M. Talmant, dissertation, University of Paris VII, 1987.
[16] M. Talmant and G. Quentin, J. Appl. Phys. **63**, 1857 (1988).
[17] M. Talmant, G. Quentin, J. L. Rousselot, J. V. Subrahmanyam, and H. Überall, J. Acoust. Soc. Am. **84**, 681 (1988).
[18] M. Talmant, J. M. Conoir, and J. L. Rousselot, Acust. Acta Acust. **3**, 509 (1995).
[19] J. P. Sessarego, J. Sagéloli, C. Gazanhes, and H. Überall, J. Acoust. Soc. Am. **101**, 135 (1997).
[20] E. D. Murphy, E. D. Breitenbach, and H. Überall, J. Acoust. Soc. Am. **64**, 677 (1978).
[21] E. D. Breitenbach, H. Überall, and K. B. Yoo, J. Acoust. Soc. Am. **74**, 1267 (1983).
[22] J. V. Subrahmanyam, Ph.D. thesis, Catholic University, Washington, DC, 1983.
[23] J. L. Rousselot, Acustica **58**, 291 (1985).
[24] N. D. Veksler, Wave Motion **8**, 525 (1986).
[25] G. Quentin and M. Talmant, in *Elastic Wave Propagation*, Proceedings of the 2nd IUTAM-IUPAP Symposium on Elastic Wave Propagation, Galway, Ireland, 20–25 March 1988, edited by M. F. McCarthy and M. A. Hayes (Elsevier Science, North Holland, Amsterdam, 1989).
[26] G. Maze, F. Léon, J. Ripoche, A. Klauson, J. Metsaveer, and H. Überall, Acustica **81**, 201 (1995).
[27] F. Magand and P. Chevret, Acust. Acta Acust. **82**, 707 (1996).
[28] O. Poncelet, A. Gérard, M. Deschamps, A. Guran, B. Belinskiy, A. Dauer, and H. Überall, preprint.
[29] A. Klauson and J. Metsaveer, J. Acoust. Soc. Am. **91**, 1834 (1992).
[30] See also A. Ahyi, P. Pernod, V. Latard, and A. Merlen, in Proceedings of the 4th Congress on Acoustics, Société Française d'Acoustique, Marseille, France, 14–18 April 1997.
[31] C. Cranz and H. Schardin, Z. Phys. **56**, 147 (1929).
[32] A. C. Ahyi, dissertation, University of Sciences and Technologies of Lille I, France, 1997; and Acust. Acta Acust. (to be published).
[33] H. Überall, B. Hosten, M. Deschamps, and A. Gérard, J. Acoust. Soc. Am. **96**, 908 (1994).

Direct and continuous measurement of depth-dependent reflection coefficients of Rayleigh waves for surface discontinuity: Normal slot

Byoung-Geuk Kim[a] and Sekyung Lee
NDE Group, Failure Prevention Research Center, Korea Research Institute of Standards and Science, P.O. Box 102, Yusong, Taejon 305-600, Republic of Korea

Manabu Enoki and Teruo Kishi
Research Center for Advanced Science and Technology, The University of Tokyo, Komaba 4-6-1, Meguro-ku, Tokyo 153, Japan

(Received 3 September 1997; accepted for publication 21 July 1998)

A new method and principle were presented for the continuous measurement of the depth-dependent reflection coefficient of Rayleigh waves or their pulse interacting with various surface discontinuities. The method was to record the reflection echo amplitudes for varying depth during scanning the Rayleigh wave pulse with a small lateral beam width along a surface discontinuity with a small slope in depth. In the experiments using a declined slot and intensively focused Rayleigh waves, the coefficients were continuously measured with quite good reproducibility in the range of $0.05<d/\lambda$ (slot-depth/Rayleigh wave wavelength) <2.57. In $0.05<d/\lambda<1.4$, the results showed good agreement with other experimental results that had been determined by conventional method [L. J. Bond, Ultrasonics **71**, 71–77 (1979); M. Hirao *et al.*, J. Acoust. Soc. Am. **72**, 602–606 (1982); H. M. Frost *et al.*, Proc. Ultrason. Symp. IEEE (**1975**), 604–607] as intermittent point-to-point data and several numerical results [L. J. Bond, Ultrasonics **71**, 71–77 (1979); R. J. Blake and L. J. Bond, *ibid.* **28**, 214–228 (1990); M. Munasinhe, Ph.D. thesis, McGill University, Canada 1973; A. K. Mal and L. Knopoff, Bull. Seismol. Soc. Am. **55**, 319–334 (1965)]. Especially, in the extremely shallow range of $0.05<d/\lambda<0.3$, the reflection coefficients, showing quite good agreement with the numerical estimation, were measured while any other experimental data for slots or down steps have not been reported in $0.05<d/\lambda<0.25$. It was shown that the new method could be used to evaluate more conveniently and quantitatively the depth or depth profile of various surface features in the long-wavelength or shallow-depth region of about $0.05<d/\lambda<0.5$. © *1998 Acoustical Society of America.* [S0001-4966(98)01311-3]

PACS numbers: 43.35.Cg [HEB]

INTRODUCTION

The interaction of surface acoustic waves, in particular Rayleigh waves, with surface features is of interest to workers in many different fields of study such as physics, geophysics, seismology, civil engineering, nondestructive testing, and electronics.[1,2] When Rayleigh waves encounter surface discontinuities, a part of the incident energy is reflected and transmitted as Rayleigh waves, while the other part is converted into the bulk modes. It has been expected that depth- or wavelength-dependent reflection coefficients or transmission coefficients of Rayleigh waves should provide a good means of determining important parameters like crack depth, especially in nondestructive testing. Many theoretical and experimental studies have been related with the problem of determining more accurately the reflection and transmission coefficients of Rayleigh waves interacting with surface discontinuities having different sizes and features.[1–21] Integral equation formulation[6,7] and theoretical analyses with exact solution[4,16,22] as analytic solutions for edge or wedge crack, numerical modeling of wave–defect interaction[9] and irregularly shaped boundary,[10] numerical analysis for normal discontinuities,[11,12] up step,[13] and crack distribution,[5] and numerical or experimental studies for wedge problems[3,17] and for down steps[1,2,15,18–21] have been reported.

However, so far, despite such an interest, no experimental results measuring continuously the depth-dependent coefficients of Rayleigh waves have been reported. Only intermittently determined point-to-point data have been shown in the results. Moreover, in the extremely shallow depth range of slots or down steps, in the range of d/λ (slot-depth/Rayleigh wave wavelength) <0.25, no experimental coefficients have been reported, probably owing to low signal-to-noise ratio. This implies that the analytical and numerical results[1,2,18,19] estimating the coefficients have not been strictly confirmed by experimental evidence. The purpose of the present study is to continuously measure the depth-dependent coefficients of Rayleigh waves. Here, we concentrated on measuring the reflection coefficients for normal slot. Slots or down steps are the fundamental surface features that many investigators have studied in order to understand scattering phenomena of Rayleigh waves.

In this paper, we present a new experimental principle and method to measure continuously the depth dependence of reflection coefficients of Rayleigh waves. Recently, a new ultrasonic transducer to focus Rayleigh waves intensively

[a]Electronic mail: busykim@kriss.re.kr

was developed.[23–25] It showed the characteristics[25] of the narrow lateral beam width of about 0.6 mm at the focal distance, high signal-to-noise ratio and energy, and the narrow frequency bandwidth of 26%. We describe the experiments performed by using the scan system that was composed of the steel block with the long normal slot having a small slope in the depth and the ultrasonic transducer focusing Rayleigh waves. Strictly speaking, we observed the reflected peak amplitudes of the Rayleigh wave pulse having a frequency bandwidth (not having only a single frequency) from the slot having the varying depth.

If the direct relation between the reflected echo amplitude of a Rayleigh wave pulse and the depth can be continuously determined in the wide range of the depth of surface discontinuities without any secondary spectral analysis, it will be possible to estimate the depth by simply measuring echo amplitudes like the conventional pulse-echo testing method to estimate the size of a flaw. So far, the direct relation has not been continuously measured. Under conventional experimental setup using conventional angle transducers, it would be impossible to perform the experiments to determine the direct relation because, in principle, an infinite series of specimens, having different depths, would be required. Even if asymptotic measuring was performed with a small step in depth instead of continuous measuring, it should be boring because a number of specimens and tests would be requested.

The reflection coefficients of the Rayleigh wave pulse that were continuously measured in the wide range of $0.05 < d/\lambda < 2.54$ under the present experimental setup were compared with other numerical and experimental results for normal down steps. We showed that, based on the fact that the results showed good agreement with other results, the depth-dependent results of the Rayleigh wave pulse could replace those wavelength-dependent reflection coefficients obtained by the conventional technology such as spectral analysis. The results were compared with those measured using a conventional angle transducer instead of the focusing transducer under the same experimental setup. Also, we described how to estimate the depth of discontinuities in the shallow depth range of $d/\lambda < 0.5$ utilizing the present method and results.

I. THEORY AND PRINCIPLE

A. Fundamental principle to measure depth-dependent reflection coefficients

A reflection coefficient, R, is defined as the ratio of the amplitude of the reflected signal from a discontinuity, A_R, to the amplitude of incident signal,[26] A_I, that is, as $R = A_R/A_I$. So far, in the experiments and numerical calculations for measuring and estimating the depth dependence of reflection coefficients of Rayleigh waves, the depth dependence has been induced from the frequency or wavelength dependence of the reflection coefficients obtained by spectral analysis of an incidence signal and reflected signals from discontinuities.[1–3,8–22] When the frequency component obtained by Fourier transform of an incidence pulse at frequency f is $S_I(f)$ and the frequency component of a reflected pulse is $S_R(f)$, the frequency-dependent reflection coefficients[3] becomes $R(f) = S_R(f)/S_I(f)$. Then if the depth, d, of a tested discontinuity is known, the depth-dependent relations of the reflection coefficients are represented as function of d/λ with the relation of $\lambda = c/f$ where c is constant, the velocity of Rayleigh waves. That is, the depth dependence of reflection coefficients is given by

$$R(d/\lambda) = S_R(d/\lambda)/S_I(d/\lambda). \tag{1}$$

In principle, the depth-dependent reflection coefficient should be identical to wavelength-dependent reflection coefficient given by Eq. (1) based on fundamental wave theory.

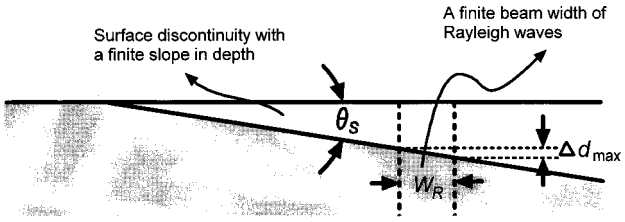

FIG. 1. The schematic diagram showing the interaction of Rayleigh waves having a finite lateral beam width, W_R, with a surface discontinuity having a finite slope, θ_S, in depth.

B. Principle for direct and continuous measurement of depth-dependent reflection coefficients

Now, in order to develop the principle to measure directly and continuously the depth dependence of the reflection coefficients of a Rayleigh wave pulse, first suppose that Rayleigh waves have an infinitesimal lateral beam width and only a single frequency component and those are scattered by a long slot or wedge having a finite slope in the depth on the surface of a specimen. Then, if the Rayleigh waves were scanned along the discontinuity and the amplitudes of reflected signals were recorded during the scanning, the depth dependence of reflection coefficients in the wide range of d/λ would be accurately measured with only an infinitesimal average effect for depth. Or, if the slope of the discontinuity was infinitesimal while Rayleigh waves had a finite lateral beam width, then, in principle, the depth dependence of reflection coefficients could be obtained by the same scanning, too, with only an infinitesimal average effect for depth although it would be impossible to perform an actual experiment because infinite distance should be scanned to obtain the depth dependence.

Second, as shown in Fig. 1, let us consider a real situation where Rayleigh waves having a finite lateral beam width, W_R, interact with a surface discontinuity having a finite slope θ_S. Then, the maximum variation $\Delta d_{\max}$ in depth of the discontinuity corresponding to the beam width is given by

$$\Delta d_{\max} = W_R \tan(\theta_S). \tag{2}$$

The smaller W_R and θ_S are, the smaller $\Delta d_{\max}$ is. This implies that everywhere the Rayleigh waves are scanned along the surface discontinuity, the depth of a surface discontinuity interacting with Rayleigh waves can be regarded as being uniform within an error limit of the negligible variation, $\Delta d_{\max}$, if the beam width of Rayleigh waves or the slope of

a surface discontinuity is sufficiently small. That is, this implies that it is possible to measure directly and continuously the depth dependence of reflection coefficients by only scanning the focused Rayleigh waves with a small lateral beam width along a surface discontinuity with a small slope in depth.

In the present study, actually, we tried to measure directly and continuously the depth dependence of reflection coefficients with a scan using both a focused Rayleigh wave pulse and a steel block with the slot having a small slope of which the depth varies in a wide range of d/λ. The employed Rayleigh wave pulse was a wave flux having a frequency bandwidth. The peak echo amplitudes $A_{RP}(d)$ of reflected signals were measured corresponding to the varying depth of the slot. Now, let us define the depth-dependent reflection coefficients, $R(d)$, of a Rayleigh wave pulse as the ratio of $A_{RP}(d)$ to the peak amplitude of the incidence pulse A_{IP}. That is,

$$R(d)=A_{RP}(d)/A_{IP}. \tag{3}$$

Equation (3) can be represented again as a function of the ratio of depth to the wavelength, λ_0, corresponding to the peak frequency of the incidence pulse by

$$R(d/\lambda_0)=A_{RP}(d/\lambda_0)/A_{IP}. \tag{4}$$

The depth-dependent reflection coefficients represented by Eq. (4) would be equivalent to the wavelength-dependent reflection coefficients by Eq. (1) if the frequency spectrum of the Rayleigh wave pulse had a sufficiently narrow frequency bandwidth, the peak frequency component dominating the energy of the pulse, and thus the pulse could be approximately regarded as having only a single frequency component.

Moreover, it would be possible to obtain data in the shallow region of small d/λ if a focusing transducer showing a good signal-to-noise ratio for smaller discontinuity than wavelength would be used.

II. EXPERIMENTS

A. Preparation of test specimens having a declined normal slot and a flat slot

A test block having a slot was fabricated using stainless steel (SUS420J2), as shown in Fig. 2. The slot was normal to the top surface of the block, its depth had a slope in length-direction. It is called a declined normal slot. Rayleigh wave velocity measured on the block was 3.10 km/s. The declined angle θ_S was 0.76 degrees. The total horizontal length of the slot was 150 mm and its maximum depth at the edge of the block was 2 mm. That is, $\tan(\theta_S)=2/150$. Also, in order to determine absolutely the reflection coefficients, a calibration block with a flat slot was fabricated using stainless steel (SUS420J2) and the depth of the flat slot was 0.35 mm.

The surfaces of the blocks were carefully polished, and then the slots were fabricated to have the sharp edges within the error limit of $+5$ and -0 μm in depth by the electric discharge method. The width of the slot was 1.0 mm, and the thickness of the block was 20.0 mm. The Poisson's ratio, σ, of stainless steel 420J2[27] was 3.0.

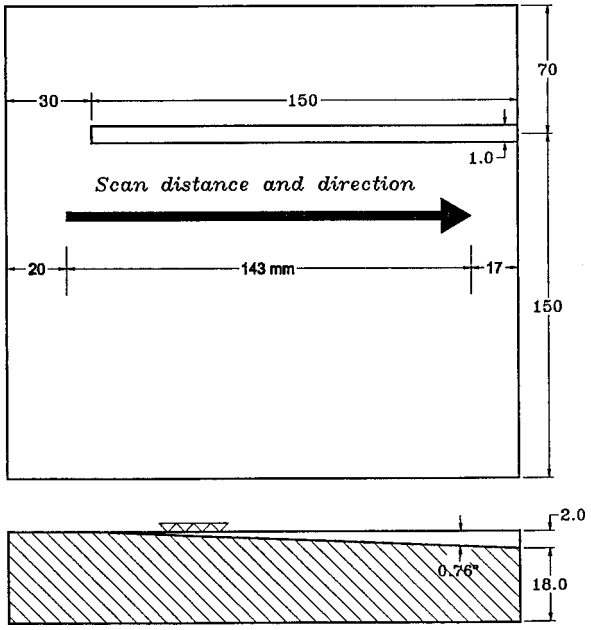

FIG. 2. Showing the drawing of a test block with the slot having a finite slope in depth and the scan distance and direction on the block.

B. Preparation of ultrasonic transducer for intensive focusing of Rayleigh waves

For the present experimental setup, an ultrasonic transducer to focus Rayleigh waves intensively was used. The focusing transducer, called the PZT PFUTOS[25] (point-focusing transducer of surface waves), was recently developed using a curved PZT $[Pb(Zr, Ti)O_3]$ ceramic element having a new shape and a specially designed acoustic lens. Hereafter, it will be simply called the PFUTOS. Figure 3(a) and (b) shows, respectively, the waveform and its frequency spectrum obtained by the test using the PFUTOS of the surface flat-bottom-hole whose diameter and depth were 1 mm, respectively. A number of ringing cycles in the waveform implies the narrow bandwidth characteristic of the PFUTOS. As shown in the frequency spectrum, both peak and center frequencies were 4.49 MHz, and the frequency bandwidth was about 26% (1.17 MHz). The signal-to-noise ratio was about 39 dB when the surface flat-bottom-hole having the size of 1 mm was tested using the PFUTOS.

Figure 4(a) shows the two-dimensional beam profile of the PFUTOS. The amplitudes represented by the black and white contrast in the beam profile image correspond to the peaks of pulse-echo signals measured during the scanning of the area of 6 mm (± 3 mm lateral distance from the center of the flat-bottom-hole)$\times$16 mm (axial distance from the center of the flat-bottom-hole) around the flat-bottom-hole having the size of 1 mm using the PFUTOS. Figure 4(b) shows the normalized lateral beam profiles at focal distances obtained by scanning around the flat-bottom-holes whose each size were 0.1, 0.5, and 0.2 mm. The results demonstrate that Rayleigh waves generated by the PFUTOS were effectively focused with the small lateral half-width of about 0.6 mm at the focal distance of about 8 mm, and the -6-dB region for the peak echo-amplitude was narrow ellipsoidal within the axial half-width of about 5.5 mm ranging from 5.3–10.8 mm

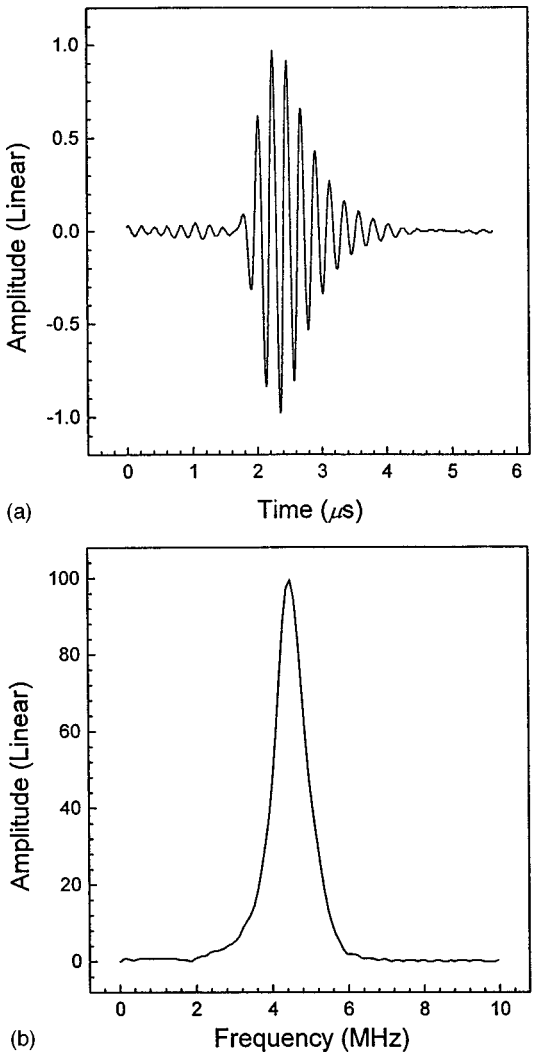

FIG. 3. (a) The waveform obtaied by testing the flat-bottom-hole with the size of 1 mm using the PFUTOS and (b) its frequency spectrum.

and the lateral half-width. The wavelength λ_0 corresponding to the peak frequency was 0.69 mm. The ratio of the detected smallest flaw size to the wavelength was about 0.29 smaller than the wavelength.

C. Experimental setup and procedure

Figure 5 shows the schematic diagram of the experimental setup to investigate continuously the depth-dependent reflection coefficients of a Rayleigh wave pulse. The system was composed of the steel block having the declined normal slot, the PFUTOS, a scanning system, a PC, and a printer. The scanning system was composed of a five-axis manipulator, a pulser and receiver, and a control box. The PC was used for system control, and AD/DA converting, signal processing, and analysis. The steel block was mounted on the large acrylic board that played the role of a spring to make good acoustical contact between the PFUTOS and the steel block. SAE-20 oil was used as a coupling.

A single time contact scan, passing only once, was performed along the declined normal slot using the PFUTOS which was placed at the focal distance of 8 mm from the slot. The PFUTOS was moved laterally and slowly at the speed of

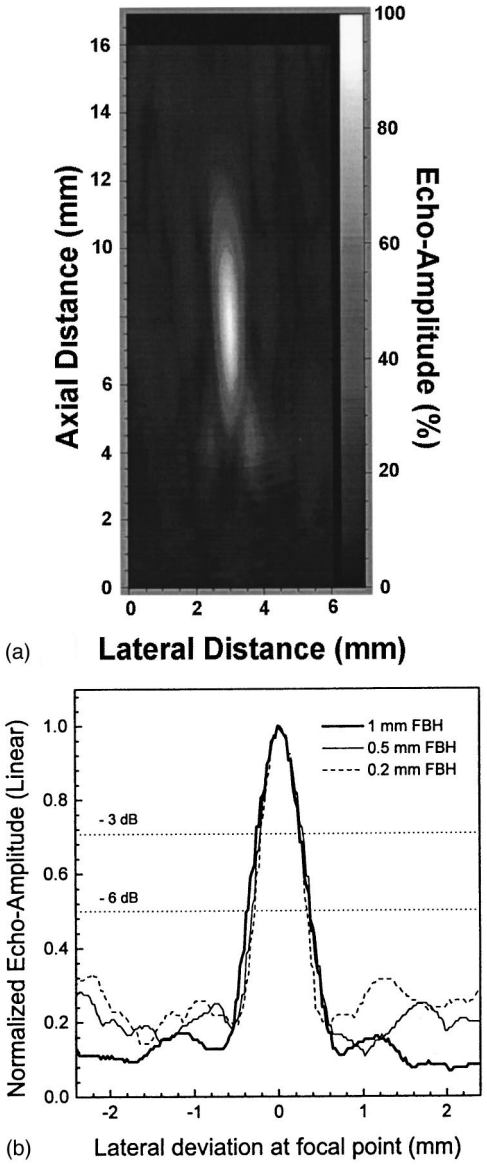

FIG. 4. (a) The two-dimensional beam profiles of the PFUTOS obtained by scanning around the flat-bottom-hole (FBH) with the size of 1 mm and (b) the lateral beam profiles at the focal distance obtained by scanning around the flat-bottom-holes with the sizes of 1.0, 0.5, and 0.2 mm.

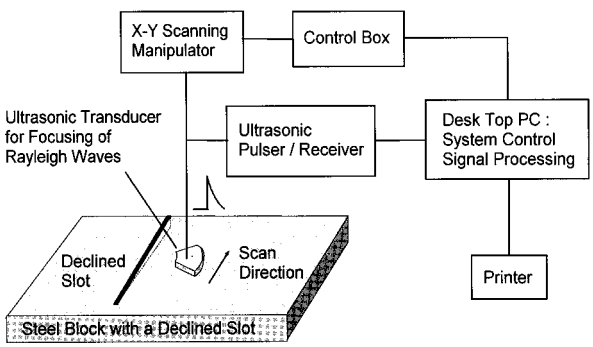

FIG. 5. The schematic diagram of the experimental setup for continuously measuring the depth-dependent reflection coefficients of Rayleigh waves for the slot.

0.0254 mm/s, and the total scan distance was 143 mm from 10 mm ahead of the slot to 17 mm ahead of the end of the block as shown in Figs. 2 and 5. The peak amplitudes of pulse-echo signals within a gate were recorded during scanning with the scan step of 0.0254 mm. The position of the PFUTOS during scanning was measured within the error limit of ± 0.002 mm.

For the comparison, a scan using a conventional-type angle transducer instead of the PFUTOS under the same test setup was performed along the slot at a distance of 8 mm. The frequency characteristics of the conventional-type angle transducer were almost the same as those of the PFUTOS because it was fabricated by using a piezoelectric element with the same piezoelectric property and thickness as those for the PFUTOS and the conventional-type acoustic wedge (shoe) made of the same material as that for the acoustic lens in the PFUTOS. The lateral beam width of the transducer was about 20.0 mm.

In order to give the reference level of the reflection coefficients, the calibration block with the flat slot was tested by the conventional technique, two-transducer (pitch-catch) technique,[1,3] and the amplitude of input pulse and reflection signal from the slot could be measured while the amplitude of input pulse could not be measured by pulse-echo technique. The source transducer generating Rayleigh waves was located at the rear of the receiving transducer to detect echo signals from the flat slot by pitch-catch technique. The amplitude of the input signal was measured at a part on the calibration block which had no discontinuities and the distance between two transducers was the same as the total path length of Rayleigh waves in the case of the system setup for measuring the echo signal from the flat slot. Also, the acoustic lens having the same dimension as the receiving transducer was put between two transducers when measuring the amplitude of input pulse and thus the damping effect of Rayleigh waves arising when Rayleigh waves passed under the acoustic wedge of the receiving transducer could be eliminated.

In the experimental setup for scan, the ratio of the scan step to λ_0 (0.69 mm) was 0.000 491, the total number of data points of reflection coefficients was about 5234 in the full range of $0<d<1.77$ mm ($0<d/\lambda_0<2.57$), and thus the reflection coefficients were measured approximately continuously when considering the small step interval in d/λ_0.

D. Validity and benefit of the experimental setup

As mentioned, when describing the principle to measure the depth-dependent reflection coefficients in Sec. I, Rayleigh waves, having a finite lateral beam width, W_R, interact with the slot having the small finite slope θ_S of 0.76 degrees in depth under the experimental setup composed of the PFUTOS and the steel block having the declined normal slot. Suppose that the intensity of focused Rayleigh waves generated by the PFUTOS is dominant within the lateral half-width of 0.6 mm near the focal distance and thus the scattering intensity by interaction of the slot with the Rayleigh waves of the outside of the lateral half-width is negligible. Then, the maximum variation $\Delta d_{\max}$ in depth corresponding to the width of 0.6 mm becomes 8.0 μm by Eq. (2), and $\Delta d_{\max}/\lambda_0=0.012$. This means that, under the assumption, a single time scan for the slot at the focal distance of the PFUTOS is equivalent to the experiments using infinite series of specimens having the slots of which the depths are in the range of $0<d/\lambda_0<2.57$ and each depth is uniform within the small error limit of 8.0 μm in depth or within 1.2% in d/λ_0. That is, it means that the error in depth in the present experimental setup is negligible and the depth-dependent reflection coefficients of a Rayleigh wave pulse can be continuously determined in the wide range of d/λ_0 and in a short period of time. If the depth-dependent reflection coefficients of a Rayleigh wave pulse were measured by using a conventional angle transducer and a number of specimens having different depths, it might induce considerable errors by the problem such as different coupling condition and should be boring.

On the other hand, in the case of using the conventional transducer having the lateral half-width of 20 mm instead of the PFUTOS in the present experimental setup, the corresponding $\Delta d_{\max}$ and $\Delta d_{\max}/\lambda_0$ become about 266 μm and 0.39, respectively. This implies that when the conventional angle transducer is used, the complex scattering of Rayleigh waves can be caused by the interaction with the slot having large variation up to 39% of the wavelength, and the resultant depth-dependent reflection coefficients may involve large errors.

III. RESULTS AND DISCUSSION

A. Reproducibility of continuously measured reflection coefficients

We repeatedly performed contact scanning to confirm reproducibility of the experiments using the PFUTOS and the steel block having the declined normal slot. The measured depth-dependent reflection coefficients of the Rayleigh wave pulse are shown in Fig. 6. The three curves of ''A,'' ''B,'' and ''C,'' called the CMDDRC (continuously measured depth-dependent reflection coefficient) curves, were the results successively measured under almost the same test condition. The top one, ''D,'' was measured under a slightly different testing condition in contact pressure, cleaning of the slot, and amount of coupling oil, etc. The lowest one, ''AVE,'' is the average of ''A,'' ''B,'' and ''C'' curves. The lower four curves are almost the same, and it is difficult to differentiate those. The curve ''D'' shows almost the same feature as the other four, too, but it shows the relatively slightly lower amplitudes in the range of $d/\lambda_0>1$. It is shown that even the large fluctuation in reflection coefficients, frequently varying for the small variation of the depth of the slot, especially as shown in the range of $d/\lambda_0>1$, was measured with quite good reproducibility. It implies that the fluctuated data are significant. Thus, the results demonstrate that the depth-dependent reflection coefficients of the Rayleigh wave pulse have measured with quite good reproducibility in the whole range of $d/\lambda_0<2.57$ under the present system setup.

The reflection coefficients were calibrated by the reference values obtained by the two-transducer technique under the experimental setup using the calibration block and the

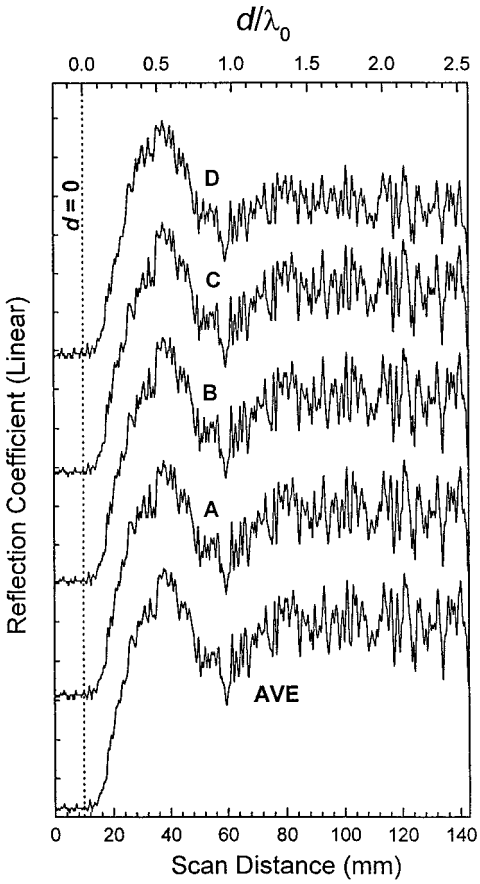

FIG. 6. The depth-dependent reflection coefficients of Rayleigh waves were continuously measured for the slot. ''A,'' ''B,'' and ''C'' were successively measured under almost the same test condition, and the top one, ''D,'' was measured under a slightly different condition, and the lowest one. ''AVE'' is the average of ''A,'' ''B,'' and ''C.''

fabricated conventional-type angle transducers. The reflection coefficient for the flat slot with the depth of 0.35 mm ($d/\lambda_0=0.5$) was about 0.435.

B. Comparison with other experimental and numerical results

It has been expected that reflection coefficients of Rayleigh waves for a normal down step may be equivalent to those for a normal slot since scattering from the down step dominates scattering from a slot.[2] As shown in Fig. 7, the CMDDRC curve, ''AVE'' in Fig. 6, for the steel block of $\sigma=0.3$ was compared with other experimental and numerical results for the normal down steps which have been reported by other investigators. In the results, we did not distinguish λ_0 as constant from λ as a varying parameter because there were good agreements between the CMDDRC curve and other experimental and numerical results obtained by spectral analysis.

First, let us concentrate on the experimental results.[1,21] It is shown in the results that intermittent point-to-point data have been measured in the range of $0.27<d/\lambda<1.5$ by other investigators. The fluctuation existing in the CMDDRC curve is shown in the other experimental results, too. In the results obtained by Bond[1] for aluminum blocks ($\sigma=0.34$) in $0.27<d/\lambda<1.4$, such a fluctuation is shown well and those

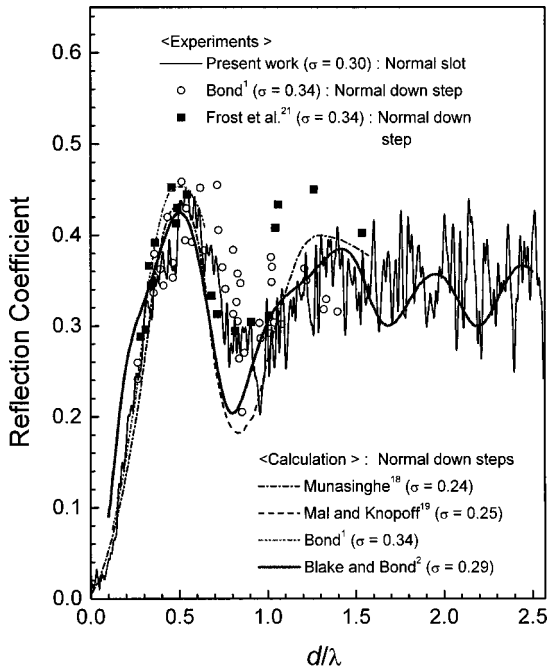

FIG. 7. The CMDDRC curve is compared with other experimental and numerical results for the normal down steps.

show good agreements with the CMDDRC curve. Especially, in the range $0.27<d/\lambda<0.5$, the results by Bond show quite good agreements with the CMDDRC curve including the range having the fluctuated reflection coefficients. This means that the fluctuated reflection coefficients shown in the CMDDRC curve are significant in $0.27<d/\lambda<1.4$. Also, the fact that the fluctuated data in the range of $0.27<d/\lambda<1.4$ is meaningful implies that even the large fluctuated reflection coefficients obtained in the whole range of $1<d/\lambda<2.57$ may be significant and may not result from experimental errors such as unstable contact problem which may usually arise in contact scan. Thus, the results demonstrate that the depth-dependent reflection coefficients, the CMDDRC curve, were continuously and effectively measured having significance in the wide range of $0.05<d/\lambda<2.57$ by using the present experimental setup while, so far, only intermittent point-to-point data of reflection coefficients have been reported in the range $0.27<d/\lambda<1.5$, as a part of our work.

Now, let us turn our attention to numerical results[1,2,18,19] compared with the CMDDRC curve. In the range of $0.05<d/\lambda<1.5$, the CMDDRC curve shows good agreement with the numerical results in overall trend. However, in $1.5<d/\lambda<2.57$, it is difficult to find a similar trend between the CMDDRC curve and the numerical result obtained by Blake and Bond which is only the numerical result in the range. The correlation between the CMDDRC curve and numerical results in the range of $d/\lambda<0.55$ is more clearly shown in Fig. 8, which is plotted in the short range. In the range of $0.05<d/\lambda<0.15$, the CMDDRC curve shows good agreement with the numerical result for $\sigma=0.24$ obtained by Munasinghe[18] which is only the numerical result in the range. In $0.15<d/\lambda<0.3$, the numerical results for both $\sigma=0.34$ obtained by Bond[1] and $\sigma=0.24$ by Munasinghe show

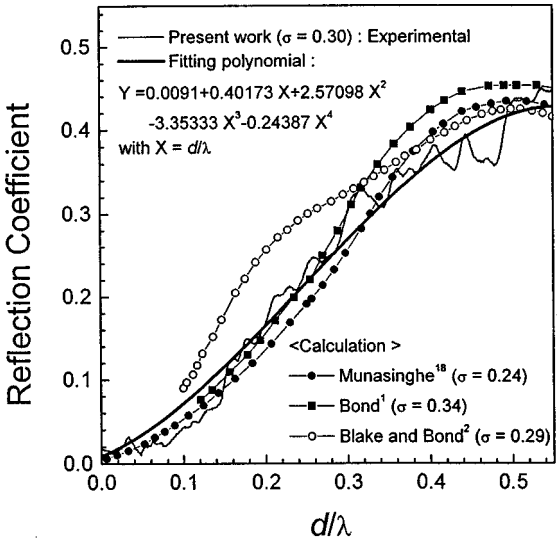

FIG. 8. The CMDDRC curve is compared with numerical results in the range of $d/\lambda<0.55$ and its fitting polynomial is shown.

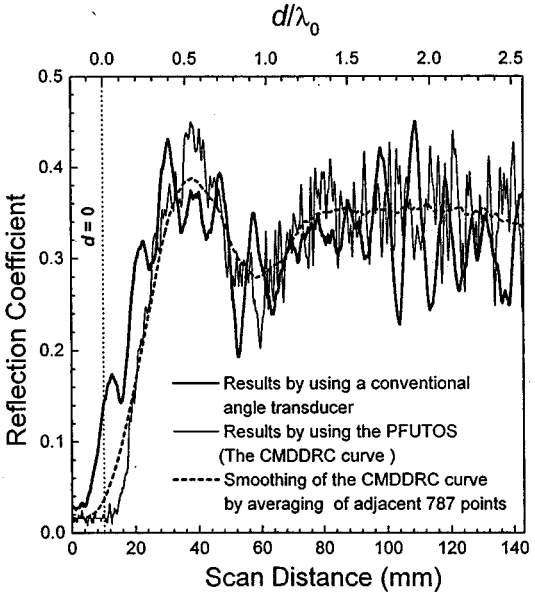

FIG. 9. The results obtained by using the conventional angle transducer are compared with the CMDDRC curve and smoothing of the CMDDRC curve obtained by averaging of adjacent 787 points which correspond to the width of 20 mm.

quite good agreement with the CMDDRC curve, although the result by Bond is closer to it.

In $0.3<d/\lambda<0.5$, up to about the maxima of the numerical results, the CMDDRC curve is closer to the numerical result for $\sigma=0.29$, obtained by Blake and Bond, having a relatively smaller slope than the other numerical results. But, in the range, the fluctuation of the reflection coefficients shown in the CMDDRC curve is not interpreted by all the smooth numerical curves. In $0.5<d/\lambda<0.96$, up to the sharp deep dip of the CMDDRC curve, the CMDDRC curve shows a trend similar to the numerical results by Blake and Bond, Munasinghe, and Mal and Knopoff,[19] but the CMDDRC curve is rightward shifted about 0.16 in d/λ from the numerical results and the fluctuation is shown in only the CMDDRC curve. Also, in $0.96<d/\lambda<1.5$, the similar trend is shown between numerical results and the CMDDRC curve although the large fluctuation is shown only in the CMDDRC curve, too.

Thus, in the range of $d/\lambda<1.5$, the depth-dependent reflection coefficients, the CMDDRC curve, showed good agreement in overall trend with other experimental and numerical results, the wavelength-dependent reflection coefficients. The fact induces a conclusion as follows: the Rayleigh wave pulse having the narrow frequency bandwidth of 26% showed behavior as if having only a single frequency component of the peak frequency of 4.49 MHz and the CMDDRC curve can take the place of the other wavelength-dependent reflection coefficients obtained by spectral analysis. Also, the results demonstrate that, in an extremely shallow range of $0.05<d/\lambda<0.25$, while any other experimental data for slots or down steps have not been reported,[1,21] the reflection coefficients showing good agreement with the numerical estimation[1,2,18–20] were measured. That reflection signals could be precisely measured in the shallow range seems to be attributed to intensively focused Rayleigh waves having the high signal-to-noise ratio. It is interesting that in $0.05<d/\lambda<0.3$ the CMDDRC curve for $\sigma=0.3$ is much closer to the numerical results for $\sigma=0.34$ and 0.24 than the numerical result for $\sigma=0.29$ by Blake and Bond.[2] This implies that reflection coefficients of Rayleigh waves in the range of $0.05<d/\lambda<0.3$ could be interpreted better by the numerical model of Bond or Munasinghe than that of Blake and Bond. In the range of $0<d/\lambda<0.05$ ($0<d<34\ \mu$m), at present, we cannot confirm whether the small peak is meaningful or not. That is because no other data to compare are available and the small peak may arise from unexpected small defects near the part where the slot begins on the steel block. It is expected that it can be confirmed in the further study using other specimens having the same surface feature.

C. Scan using the conventional angle transducer

In Fig. 9, the results obtained by using the conventional angle transducer were compared with the CMDDRC curve. The lateral beam width of Rayleigh waves generated by the transducer was 20 mm at the distance of 8 mm. Also, the results were compared with the smoothing of the CMDDRC curve obtained by the averaging of adjacent 787 points that correspond to the width of 20 mm. In the plots, the scan distances of the conventional angle transducer and the PFUTOS correspond to the positions of the center line of the acoustic wedge in the conventional angle transducer and the axial symmetry axis of the PFUTOS, respectively. It is shown that the results for the conventional angle transducer are considerably different from the CMDDRC curve in that as d/λ_0 increases in $d/\lambda_0<0.5$, the reflection coefficients in the results increase in an oscillating manner showing several round subpeaks, the fluctuation in the reflection coefficients corresponds to relatively large variation of d/λ_0, and the peak and the deep were relatively shifted. Also, the results are showing a considerably different trend from the smoothing of the CMDDRC curve, too. This implies that the results from the conventional angle transducer did not result from a

simple averaging of scattering amplitudes of Rayleigh waves for the variation in the depth ranging from 0% to 39%. Those are attributed to complex backscattered Rayleigh waves corresponding to the varying depths in which the displacement and stress components are different from one another. Thus, the results demonstrate that for measuring continuously and precisely depth-dependent reflection coefficients by employing a declined discontinuity, it is essential to use an ultrasonic transducer generating Rayleigh waves having a narrow lateral beam width such as the PFUTOS.

D. Depth profiling of a surface slot in the long-wavelength region

As shown in Fig. 8, in the region of $d/\lambda < 0.55$ of the CMDDRC curve, about up to the peak, the reflection coefficients show approximately one-to-one correspondence to d/λ. It is expected that the CMDDRC curve or the present experimental setup could be utilized to determine the depth or depth profile of surface discontinuities in the long-wavelength region that d/λ is small ($d/\lambda \ll 1$). The reflection coefficients or echo amplitudes depend on a kind of material.[1,5] If it is known that the depth of a surface discontinuity in a specimen is in the long-wavelength region and a CMDDRC curve has been investigated once for the same material as the specimen, the depth of the discontinuity can be determined by only measuring echo amplitudes from the discontinuity using the PFUTOS without any secondary spectral analysis. Also, it will be possible to obtain the depth profile of a surface discontinuity if a scan using the PFUTOS is performed along the discontinuity. Instead of the CMDDRC curve, as shown in Fig. 8, the fitting polynomial of the reflection coefficients can be used for easy evaluation. In the short-wavelength region for edge crack, it was reported that time-of-flight measurement[3,28] in $d/\lambda > 1$ and ray-theory analysis[16,29] in $d/\lambda > 2$ allowed an accurate evaluation of the actual crack depth. The present method can be used complementarily with the other methods for the purpose of estimating the depth of various surface features such as wedges and angled down steps as well as a slot.

IV. SUMMARY AND CONCLUSION

We have shown that the depth-dependent reflection coefficients of Rayleigh waves interacting with surface discontinuities are measured continuously for varying depth by a new method. In the experiments for the declined slot, the depth-dependent reflection coefficients were precisely measured with quite good reproducibility in the wide range of $0.05 < d/\lambda < 2.57$. The results also showed good agreement with other experimental point-to-point data and numerical results in overall trend in the range of $0.05 < d/\lambda < 1.4$. Especially, in the extremely shallow range of $0.05 < d/\lambda < 0.3$ the reflection coefficients (showing quite good agreement with the numerical estimations) were measured while any other experimental data for slots or down steps have not been reported in $0.05 < d/\lambda < 0.25$. However, in $1.5 < d/\lambda < 2.57$ the results showed a different trend from the numerical result obtained by Blake and Bond. It was demonstrated that, when Rayleigh waves had a sufficiently narrow frequency bandwidth, the depth-dependent reflection coefficients could take the place of the frequency-dependent reflection coefficients determined by a conventional method such as spectral analysis. It was shown that even the fluctuation existing in the measured reflection coefficients, frequently varying for the small variation of the depth of the slot, was significant. Also, it was shown that in the long-wavelength region of about $0.05 < d/\lambda < 0.5$, the method could be applied to evaluate the depth or depth profile of surface discontinuity by measuring only reflection echo amplitudes without secondary spectral analysis.

It is expected that the new method will be applied to the continuous measurement of the depth-dependent scattering amplitudes of Rayleigh waves for various surface features such as wedge and angled down step as well as a slot, and thus more accurate experimental evidence will be presented for numerous analytical and numerical results. Also, the method is expected to be used to evaluate more effectively and quantitatively the depth or depth profile of actual cracks in the long-wavelength region.

[1] L. J. Bond, Ultrasonics **71**, 71–77 (1979).
[2] R. J. Blake and L. J. Bond, Ultrasonics **28**, 214–228 (1990).
[3] M. Hirao, H. Fukuoka, and Y. Miura, J. Acoust. Soc. Am. **72**, 602–606 (1982).
[4] A. S. Cheng and M. T. Resch, Ultrasonics **33**, 31–35 (1995).
[5] M. T. Resch, D. V. Nelson, H. H. Yuce, and G. F. Ramusat, J. Nondestruct. Eval. **5**(1), 1–7 (1982).
[6] A. K. Gautesen, Wave Motion **9**, 51–59 (1987).
[7] M. Ostoja-Starzewski, Mech. Res. Commum. **13**, 53–58 (1986).
[8] L. J. Bond, ''Methods for the computer modeling of ultrasonic wave in solids,'' in *Research Techniques in Nondestructive Testing*, edited by R. S. Sharpe (Academic, New York, 1982), Vol. 6, pp. 107–150.
[9] G. A. Georgiu and L. J. Bond, Ultrasonics **25**, 328–334 (1987).
[10] L. E. Alsop and A. S. Goodman, IBM J. Res. Dev. **16**, 367–398 (1972).
[11] F. C. Cuozzo, E. L. Cambiaggio, J.-P. Damiono, and E. Rivier, IEEE Trans. Sonics Ultrason. **SU-24**, 280–289 (1977).
[12] M. Munasinghe and G. W. Farnell, J. Geophys. Res. **78**, 2454–2466 (1973).
[13] M. Fuyuki and M. Nakano, Bull. Seismol. Soc. Am. **74**, 893–991 (1984).
[14] B. T. Khuri-Yakub, S. G. Kino, and A. G. Evans, J. Am. Ceram. Soc. **63**, 65–71 (1980).
[15] L. Martel, M. Munasinghe, and G. W. Farnell, Bull. Seismol. Soc. Am. **67**, 1277–1290 (1977).
[16] J. D. Achenbach, A. K. Gautesen, and D. A. Mendelsohn, IEEE Trans. Sonics Ultrason. **SU-27**, 124–129 (1980).
[17] Y. C. Angle and J. D. Achenbach, J. Acoust. Soc. Am. **75**, 313 (1984).
[18] M. Munasinhe, ''Numerical solutions for acoustic Rayleigh wave scattering in discontinuous media,'' Ph.D. thesis, McGill University, Canada, 1973.
[19] A. K. Mal and L. Knopoff, Bull. Seismol. Soc. Am. **55**, 319–334 (1965).
[20] A. McGarr and L. E. Alsop, J. Geophys. Res. **72**, 1269–2180 (1967).
[21] H. M. Frost, J. Setares, and T. L. Szabo, ''Applications for new electromagnetic SAW transducers,'' Proc. Ultrasonics Symp. IEEE (**1975**), 604–607.
[22] D. A. Mendelsohn, J. D. Achenbach, and L. M. Keer, Wave Motion **2**, 277–292 (1980).
[23] B. G. Kim, S. K. Lee, and J. O. Lee, U.S. Patent No. 5094108 (1992).
[24] B. G. Kim, J. O. Lee, and S. Lee, IEEE Trans. Ultrason. Ferroelectr. Freq. Control **40**(2), 162 (1993).
[25] B.-G. Kim, S. Lee, M. Enoki, and T. Kishi, ''Development and Application of Ultrasonic Transducer for Intensive Focusing of Rayleigh Waves,'' Ultrasonics **36**, 825–836 (1998).
[26] H. F. Pollard, *Sound Waves in Solids* (Pion, London, 1977), pp. 201–202.
[27] S. S. Lee, U.-S. Min, and B. Y. Ahn, Rev. Prog. Quant. Nondestr. Eval. **15**, 1423–1429 (1996).
[28] M. G. Silk, in *Research Techniques in Non-Destructive Testing*, edited by R. S. Sharpe (Academic, London, 1977), Vol. 3, pp. 51–99.
[29] T. Kundu and A. K. Mal, J. Appl. Mech. **48**, 570–576 (1981).

Hill-type ultrasonic relaxation spectra of liquids

K. Menzel, A. Rupprecht, and U. Kaatze[a)]
Drittes Physikalisches Institut, Georg-August-Universität, Bürgerstr. 42-44, D-37073 Göttingen, Germany

(Received 4 June 1997; accepted for publication 27 June 1998)

The Hill relaxation spectral function, originally designed for the description of dielectric relaxation spectra, has been applied to a variety of sonic attenuation spectra. Both theoretical models and measured broadband spectra have been considered. It was found that the Hill function can be favorably used to represent the acoustic relaxation properties of critically demixing liquids but also of such liquid systems that show precritical behavior. The Hill spectral function also complies with the thermal and viscoelastic boundary effects in suspensions and emulsions, with the special absorption characteristics of surfactant solutions with high critical micelle concentration, and with effects of cluster formation in solutions of transition metal halides. Empirical relations between the relaxation time distribution parameters of the Hill function and characteristics of theoretical models are displayed. © *1998 Acoustical Society of America.* [S0001-4966(98)01511-2]

PACS numbers: 43.35.Fj, 43.35.Bf [HEB]

INTRODUCTION

During the second half of this century acoustic spectrometry has developed into a powerful tool for the study of fast elementary chemical reactions in liquids. Much interest is currently directed toward the ultrasonic properties of liquid systems, not only for many fascinating fundamental aspects but also in view of a variety of applications such as noninvasive *in situ* sample characterization in industrial monitoring and control procedures.

Many acoustic relaxation measurements so far have focussed on the study of stoichiometrically well-defined chemical equilibria, equivalent to discrete relaxation times in the sonic spectra. Examples are the wide fields of proton transfer reactions and ion complex equilibria as well as the formation of large micelles.[1] In Fig. 1, two relevant sonic excess absorption spectra are shown. One reflects a single Debye-type relaxation[2] with discrete relaxation time τ_D, the other one exhibits a superposition of two Debye relaxation terms. More generally such spectra may be represented by a sum of discrete relaxation terms:

$$(\alpha\lambda)_{\mathrm{ex}}=\sum_{n=1}^{N}\frac{A_{Dn}\omega\tau_{Dn}}{1+(\omega\tau_{Dn})^2}. \tag{1}$$

Here, α is the sonic attenuation coefficient, λ is the wavelength within the sample at frequency ν, and $\omega=2\pi\nu$ denotes the angular frequency. The relaxation amplitudes A_{Dn}, $n=1,\ldots,N$, are related to the reaction volumes and enthalpies and the relaxation times τ_{Dn} are related to the velocity constants of the chemical equilibria under consideration.[1,8–12] The excess absorption per wavelength, $(\alpha\lambda)_{\mathrm{ex}}$, is considered since the so-called classical contribution[13]

$$(\alpha\lambda)_{cl}=B\nu=\alpha\lambda-(\alpha\lambda)_{\mathrm{ex}} \tag{2}$$

to the total sonic absorption per wavelength, $\alpha\lambda$, is of no interest here. In the examples shown in Fig. 1, a Debye relaxation term corresponds with a particular step in the Eigen mechanism[7] of stepwise dissociation/association of salts in solution.

Recent advances in broadband acoustic measurement techniques for liquids[14] resulted in spectra exhibiting significant deviations from Debye-type relaxation behavior as expressed by Eq. (1). Aqueous solutions of zinc chloride, for instance, yield sonic excess absorption that, on the one hand, clearly extends over a broader frequency band than a Debye term (Fig. 2) but, on the other hand, does not show indications for a superposition of a few discrete terms. Aqueous solutions of symmetric tetraalkylammonium bromides offer another example.[16] Their sonic excess absorption spectra may be alternatively discussed. They may be either due to a superposition of some few Debye-type contributions with relaxation times so close together that a clear dissolution into individual terms is impossible. They may, however, also reflect an underlying continuous distribution of relaxation times. A similar situation exists with the aqueous $ZnCl_2$ solutions.[17,18] Hence, so far we are left with the eventuality of basically different molecular mechanisms which might be reflected by the sonic spectra of these salt solutions, namely either the formation of stoichiometrically defined ionic species or the existence of thermally driven (local) fluctuations in the ion concentration.

Concentration fluctuations are currently discussed with respect to the special properties of critical and precritical binary mixtures. Theoretical models of thermal fluctuations in concentration[16,19–28] predict more or less unsymmetric sonic absorption spectra (Fig. 2). However, the predictions made by different theoretical models differ from one another in various interesting details. Unfortunately, a generally accepted formulation of the acoustic properties of binary liquids has not been achieved so far. At the present it is even unclear on which conditions the sonic absorption spectra may, at least in parts, be also due to visco-inertial and thermal conductivity effects at internal interfaces of acoustically microheterogeneous liquid systems.[29–39] It has been shown

a)Electronic mail: uka@physik3.gwdg.de

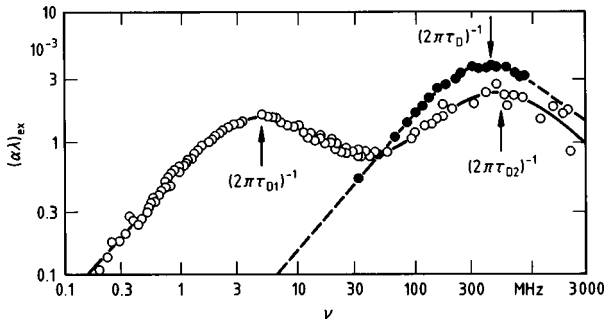

FIG. 1. Ultrasonic excess absorption spectra for 0.5 molar aqueous solutions of $MnSO_4$ at 20 °C (○)[4–6] and of $CuCl_2$ at 25 °C (●).[3] The former spectrum reflects two steps in the Eigen–Tamm mechanism[7] of stepwise dissociation of salts (τ_{D1},$[Mn^{2+}(H_2O)SO_4^{2-}]_{aq} \rightleftharpoons [Mn^{2+}(H_2O_2SO_4^{2-}]_{aq}$; τ_{D2}, $[Mn^{2+}(H_2O)_2SO_4^{2-}]_{aq} \rightleftharpoons Mn_{aq}^{2+} + SO_{4aq}^{2-}$). The latter spectrum is assumed to be due to the equilibrium between outer-sphere complexes and the completely dissociated ions (τ_D,$[Cu^{2+}(H_2O)Cl^-]_{aq} \rightleftharpoons Cu_{aq}^{2+} + Cl_{aq}^-$).

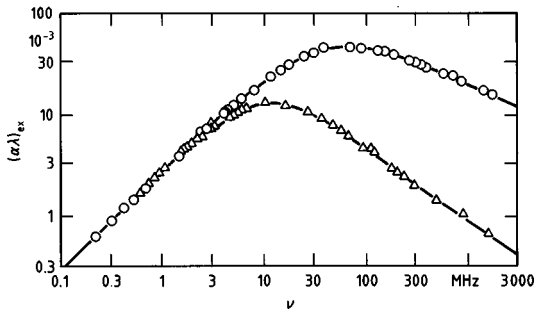

FIG. 2. Sonic excess absorption spectra for an aqueous solution of 2-(2-butoxyethoxy)-ethanol at 25 °C (○, [15], C_4E_2) and an aqueous solution of zinc chloride at 25 °C (△, [3,18]$ZnCl_2$). In the former example the full curve is the graph of the restricted version of the Hill function [Eq. (12)], in the latter it represents the Dissado–Hill spectral function [Eq. (38)].

that such effects play a dominant role in the acoustic spectrometry of suspensions[40,41] and emulsions.[42]

In this situation, an almost universal formulation of measured sonic attenuation spectra is most desired for various reasons. A uniform representation of experimental findings clearly facilitates the numerical treatment of the multitude of measured data and it also simplifies the exchange of results between different laboratories, a subject of considerable importance in practical applications. Moreover, the direct intercomparison of parameter values for different liquid systems is enabled by a quasi-universal description of spectra. There is also a guarded hope that fundamental trends in the spectra of different systems may become obvious from a simple and uniform representation of a variety of measured facts.

We found the relaxation spectral function, originally introduced by Hill,[43,44] discussing non-exponential decay in the polarization of dielectrics,[45] to be favorably utilized in physical acoustics. In this paper special properties of the Hill function are shown and comparison is made with existing theoretical models of sonic relaxation. Experimental results for different aqueous systems are also briefly discussed in the light of a semi-empirical Hill relaxation spectral function.

I. CHARACTERISTICS OF THE HILL FUNCTION, COMPARISON TO OTHER EMPIRICAL RELAXATION MODELS

Applied to acoustic spectra, the Hill function $R_H(\nu)$ is given by the relation

$$R_H(\nu) = (\alpha\lambda)_{ex} = \frac{A_H(\omega\tau_H)^{m_H}}{(1+(\omega\tau_H)^{2s_H})^{(m_H+n_H)/(2s_H)}}. \tag{3}$$

Here, A_H and τ_H denote the relaxation amplitude and principle relaxation time, respectively, and m_H,n_H as well as s_H ($0<m_H,n_H,s_H\leqslant 1$) are parameters that determine the shape and width of the underlying continuous relaxation time distribution function G_H. This distribution function is defined by

$$R_H(\nu) = A_H \int_0^\infty G_H(r_H) \frac{\omega\tau}{1+\omega^2\tau^2}\, dr_H \tag{4}$$

with

$$\int_0^\infty G_H(r_H)\, dr_H = 1. \tag{5}$$

Here,

$$r_H = \ln(\tau/\tau_H). \tag{6}$$

If $m_H = n_H = s_H = 1$, then

$$G_H(r_H) = \delta(r_H), \tag{7}$$

hence the Hill spectral function changes into a Debye term.[2] In Fig. 3, $G_H(r_H)$ is displayed for some sets of m_H, n_H, s_H values different from 1, in order to indicate how these quantities are related to the distribution of relaxation times. According to

$$G_H(r_H) = \frac{2}{\pi\tilde{A}} \mathrm{Re}\left\{ \frac{(-ie^{-r_H})^{m_H}}{(1+(-ie^{r_H})^{2s_H})^{(m_H+n_H)/(2s_H)}} \right\}, \tag{8}$$

the distribution functions shown in the figure have been calculated by analytical continuation[46] of the Hill spectral function $R_H(\nu)$. For example, in (8), parameter $\tilde{A}$ follows from normalization [Eq. (5)].

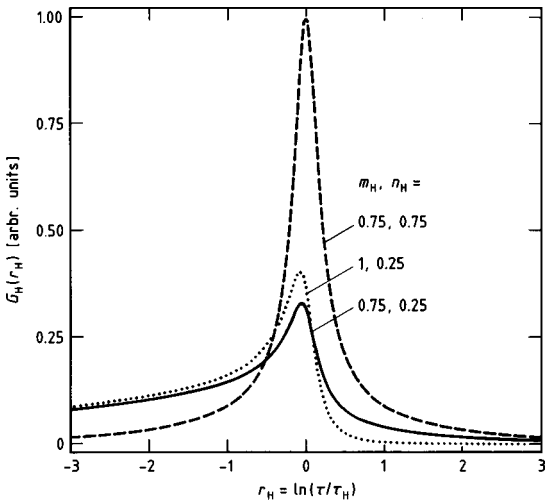

FIG. 3. Relaxation time distribution function $G_H(r_H)$ [Eq. (8)] for three sets of Hill parameters m_H, n_H, s_H. Here $s_H=0.9$ throughout. The dashed curve resembles the symmetric Cole–Cole relaxation time distribution,[50] the dotted curve models the unsymmetric Davidson–Cole relaxation time distribution function.[51]

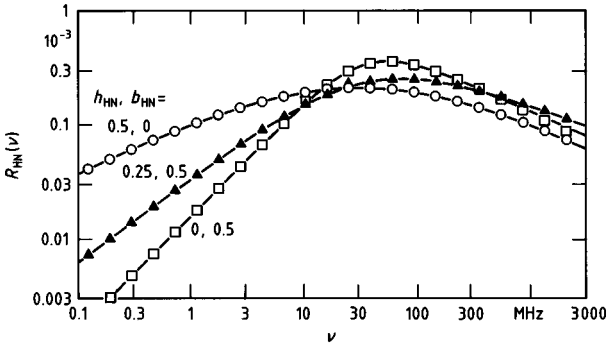

FIG. 4. Plot of the Havriliak–Negami relaxation spectral function for three sets of relaxation time distribution parameters h_{HN}, b_{HN}. The curves are graphs of the Hill function $R_H(\nu)$ [Eq. (3); ○, $m_H=0.49$, $n_H=0.5$, $s_H=0.29$; ▲, $m_H=0.74$, $n_H=0.36$, $s_H=0.52$; □, $m_H=1$, $n_H=0.44$, $s_H=0.95$].

A favorable characteristic of the Hill spectral function is the clear relation between the relaxation time distribution parameters m_H, n_H, and s_H and attributes of the shape of $R_H(\nu)$,

$$\lim_{\nu\to 0}\{d\log(R_H(\nu))/d\log(\nu)\}=m_H, \tag{9}$$

$$\lim_{\nu\to\infty}\{d\log(R_H(\nu))/d\log(\nu)\}=-n_H, \tag{10}$$

$$R_H(\nu_H)=A_H 2^{-(m_H+n_H)/(2s_H)}. \tag{11}$$

Here, $\nu_H=(2\pi\tau_H)^{-1}$ is the principal relaxation frequency. Using the Hill function it was found that many acoustic excess absorption spectra of liquids can be well represented assuming $m_H=1$ and $n_H=1/2$ [corresponding with an exponential decay function (Debye-type behavior) at low frequencies and a diffusion law behavior at high frequencies]. With a reduced number of adjustable parameters the restricted Hill function

$$R_H^*(\nu)=\frac{A_H\omega\tau_H}{(1+(\omega\tau_H)^{2s_H})^{3/(4s_H)}} \tag{12}$$

is then appropriate. An example for the suitability of this spectral function is presented in Fig. 2.

Another empirical relaxation function, the Havriliak–Negami function $R_{HN}(\nu)$,[47] is controlled by two relaxation time distribution parameters, h_{HN} and b_{HN}, respectively. $R_{HN}(\nu)$ has been favorably used, for instance, to characterize ultrasonic properties of polymeric systems.[48,49] In a compact form the Havriliak–Negami function applies to the sonic attenuation per wavelength as

$$R_{HN}(\nu)=(\alpha\lambda)_{\mathrm{ex}}=\mathrm{Im}\left\{\frac{A_{HN}}{(1+(i\omega\tau_{HN})^{(1-h_{HN})})^{(1-b_{HN})}}\right\}, \tag{13}$$

where $i=(-1)^{1/2}$. Again, A_{HN} denotes the relaxation amplitude and τ_{HN} the principal relaxation time. The Havriliak–Negami function obviously includes the well-known Cole–Cole[50] ($b_{HN}=0$, $h_{CC}=h_{HN}$) and Davidson–Cole[51] ($h_{HN}=0$, $b_{DC}=b_{HN}$) relaxation spectral functions and also the Debye function ($b_{HN}=h_{HN}=0$) as limiting forms. The examples shown in Fig. 4 may be taken to indicate that, over a significant frequency range, $R_{HN}(\nu)$ can be well represented by the Hill function [Eq. (3)].

In Fig. 4, the spectra are shown for the frequency range of measurements covered by our laboratory. Systematic comparison of the spectral functions has been made for a multitude of values for the relaxation time distribution parameters. In doing so, $R_{HN}(\nu)$ has been calculated at a series of frequencies ν_i, $i=1,\ldots,N$, for numerous pairs of h_{HN}, b_{HN} values. In these model calculations the frequencies ν_i have been distributed equidistantly on a logarithmic scale, covering the range of six decades [$10^{-3}\nu_{HN}\leqslant\nu_i\leqslant 10^3\nu_{HN}$, $\nu_{HN}=(2\pi\tau_{HN})^{-1}$]. The $R_H(\nu)$ function has been fitted to the numerically generated spectra afterwards. The following relations between the relaxation time distribution parameters of the two different functions have been found thereby: $m_H=1-h_{HN}$, $n_H=(1-b_{HN})(1-h_{HN})$, $s_H<1$. Hence $m_H=1-h_{HN}$, $n_H=m_H$ has to be used to represent the Cole–Cole function whereas $m_H=1$, $n_H=(1-b_{HN})$ is suited to simulate the Davidson–Cole function within the frequency range of measurements mentioned before.

In his evaluation of susceptibility functions,[44] Hill also treated the Fuoss-Kirkwood and the Kohlrausch–Williams–Watts spectral functions. He has already discussed the behavior of these particular semi-empirical functions in light of the Hill function. We thus shall focus in the following on theoretical relaxation models for sonic spectra.

Frequently it is desirable to consider, instead of the principal relaxation time of a spectral function, the relaxation time τ_m that corresponds with the frequency ν_m at which the sonic excess absorption per wavelength adopts its relative maximum $(\alpha\lambda)_{\mathrm{ex},m}$. For the Hill function, with ν_m defined by

$$dR_H(\nu)/d\nu|_{\nu_m}=0,\quad d^2R_H(\nu)/d\nu^2|_{\nu_m}<0, \tag{14}$$

the relation[52]

$$\tau_m=(2\pi\nu_m)^{-1}=\tau_H(n_H/m_H)^{(2s_H)^{-1}} \tag{15}$$

holds. The maximum value $(\alpha\lambda)_{\mathrm{ex},m}$ is related to the relaxation amplitude according to

$$(\alpha\lambda)_{\mathrm{ex},m}=R_H(\nu_m)=A_H\frac{(m_H/n_H)^{m_H/(2s_H)}}{(1+m_H/n_H)^{(m_H+n_H)/(2s_H)}}. \tag{16}$$

Equations (15) and (16) are particularly useful when results for unsymmetric relaxation time distribution functions are discussed. In the case of symmetric relaxation time distributions, like the Cole–Cole distribution function, $\tau_m=\tau_H$, in correspondence with the Debye relaxation spectral function.

II. MODELING THEORETICAL FUNCTIONS, COMPARISON WITH MEASURED SPECTRA

A. Concentration fluctuations including critical behavior

Sonic excess absorption of mixtures may result from the coupling of the sound field to long-ranging fluctuations in the concentration that are accompanied by fluctuations in thermodynamic parameters like the local density and tempera-

ture. Application of a sound field leads to a new equilibrium in the fluctuation amplitudes which is adopted by diffusion. In contrast to chemical relaxation spectra, sonic absorption due to concentration fluctuations is characterized by a continuous relaxation time distribution, corresponding with the continuous decay of the individual spatial Fourier components of the thermal fluctuations. Theoretical formulations of concentration fluctuations usually involve a Debye density of state and a van Hove exponential decay of fluctuations. The sonic excess absorption per wavelength can then be expressed as

$$(\alpha\lambda)_{\mathrm{ex}}=A(T)\int_0^\infty k^2 g(k)\frac{\omega k^2/h(k)}{(k^2/h(k))^2+(\omega/(2D))^2}\,dk, \tag{17}$$

where $A(T)$ is an amplitude that only weakly depends on the frequency, $k=2\pi/\lambda$, $g(k)$ is the Laplace transform of the spatial correlation function $\hat{g}(r)$, $h(k)$ considers specific molecular interactions and D is the diffusion coefficient representing the exponential decay of fluctuations. Fixman[19] and Kawasaki[22] described the molecular interactions by a long-ranging correlation function according to the Ornstein–Zernike ansatz[53,54]

$$\hat{\phi}_{OZ}(r,0)=r^{-1}\exp(-r/\xi), \tag{18}$$

$$\phi_{OZ}(k,0)=(1+k^2\xi^2)^{-1} \tag{19}$$

with ξ denoting the correlation length of the order parameter. They used $g(k)=\phi_{OZ}^2$ and $h(k)=\phi_{OZ}$ and obtained

$$(\alpha\lambda)_{\mathrm{ex}}=R_{F/K}(\nu)=A_{FK}(T)S_{F/K}(\nu) \tag{20}$$

with the scaling function

$$S_{F/K}(\nu)=\int_0^\infty \frac{x^2}{(1+x^2)^2}\cdot\frac{K_{F/K}(x)\Omega}{K_{F/K}^2(x)+\Omega^2}\,dx. \tag{21}$$

Herein,

$$\Omega=\omega\xi^2/(2D)=\omega\tau_\xi,\quad \tau_\xi=\xi^2/(2D) \tag{22}$$

is a reduced frequency and $x=k\xi$. In the Fixman theory

$$K_F(x)=x^2(1+x^2), \tag{23}$$

while in the Kawasaki model

$$K_K(x)=\tfrac{3}{4}(1+x^2+(x^3-1/x)\arctan(x)). \tag{24}$$

In the limit of small correlation lengths ($\xi\ll\lambda, x\ll 1$) both theories predict the same excess absorption per wavelength [$K_K(x)=K_F(x)$, $S_K(\nu)=S_F(\nu)$]. Extending the original Kawasaki mode-coupling theory Shiwa and Kawasaki[25] led to a rather complicated relation. For this reason, preference has mostly been given to the Bhattacharjee–Ferrell model which offers an easier to handle spectral function.

Bhattacharjee and Ferrell[26] using $g(k)=k\phi_{OZ}^2$ and $h(k)=\phi_{OZ}^p$ with $p\in[0,1]$ found

$$(\alpha\lambda)_{\mathrm{ex}}=R_{BF}(\nu)=(\alpha\lambda)_{\mathrm{ex,cr}}S_{BF}(\nu), \tag{25}$$

where $(\alpha\lambda)_{\mathrm{ex,cr}}$ denotes the excess absorption per wavelength at the critical point and where the scaling function is given by

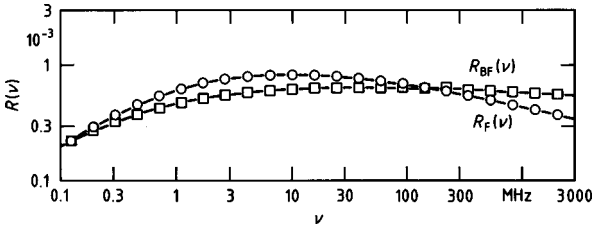

FIG. 5. The Fixman [$R_F(\nu)$, Eq. (20)] and the Bhattacharjee–Ferrell [$R_{BF}(\nu)$, Eq. (25)] spectral function. The curves represent best fits of the Hill function [Eq. (3)] with $s_H\equiv 0.25$ to these models [○, $m_H=1$, $n_H=0.25$, corresponding with Eq. (29) and $n_H=0.25$; □, $m_H=0.94$, $n_H=0.06$].

$$S_{BF}(\nu)=\int_0^\infty \frac{x^3}{(1+x^2)^2}\cdot\frac{K_{BF}(x)\Omega}{K_{BF}^2(x)+\Omega^2}\,dx \tag{26}$$

with

$$K_{BF}(x)=x^2(1+x^2)^p. \tag{27}$$

The scaling functions $S_F(\nu)$, $S_K(\nu)$, and $S_{BF}(\nu)$ reveal a rather complex dependence upon frequency. To facilitate applications of their model, Bhattacharjee and Ferrell presented the empirical scaling function

$$\tilde{S}_{BF}(\nu)=\Omega(1+\Omega^{1/2})^{-2}=\omega\tau_\xi(1+\sqrt{\omega\tau_\xi})^{-2} \tag{28}$$

as a reasonable approximation of $S_{BF}(\nu)$.

The Hill function enables a simple representation of both the Fixman–type spectrum (Fig. 5) and the spectral form of the Bhattacharjee–Ferrell theory. We again simulated the Fixman model for various sets of parameter values and fitted the Hill relaxation function to the resulting spectra. We found $m_H\approx 1$, $s_H\approx 0.25$ and $n_H\approx 0.25$. An example for the excellent representation of a Fixman spectrum by the Hill relaxation function is shown in Fig. 5. For the Bhattacharjee–Ferrell model $m_H=0.94$, $s_H=0.25$, and $n_H=0.06$ follows analytically if $\tilde{S}_{BF}$ is used in Eq. (25) and if the relevant expression for $(\alpha\lambda)_{\mathrm{ex,cr}}$ is inserted. Over a rather broad frequency band the sonic spectra resulting from the models of concentration fluctuations discussed before may thus be approximated by the special form

$$\tilde{R}_H(\nu)=A_H\frac{\omega\tau_H}{(1+\sqrt{\omega\tau_H})^{2(1+n_H)}} \tag{29}$$

of the Hill function. This form contains only one relaxation time distribution parameter. The value of this parameter depends on the particular theory under consideration.

B. Noncritical concentration fluctuations

A model describing fluctuations in the concentration of binary liquids far from a critical demixing point has been developed by Romanov and Solov'ev.[20] In their original model no specific molecular interactions are considered at small molecular distances. Hence $g(k)=h(k)=1$ has been used in Eq. (17). Since the integral on the right-hand side of Eq. (17) does not exist on such conditions, Romanov and

Solov'ev introduced a maximum wave number $k_{\max}$, corresponding with a minimum interaction length $\ell_{\min}=2\pi k_{\max}^{-1}$ of regions of different concentration. Then

$$(\alpha\lambda)_{\mathrm{ex}}=R_{RS}(\nu)=A_{RS}(T)S_{RS}(\nu) \tag{30}$$

with $A_{RS}(T)=Q/(3\ell_m^3)$ and

$$S_{RS}(\nu)=\int_0^{k_{\max}}\frac{\omega k^4}{k^4+(\omega/(2D))^2}\,dk. \tag{31}$$

Here, Q is given by thermodynamic parameters of the binary system.[20]

The Romanov–Solov'ev model has been extended recently[16] in order to also take into account long-ranging correlations according to the Ornstein–Zernike ansatz [Eq. (18)]. That model of correlated (precritical) concentration fluctuations can be expressed as

$$(\alpha\lambda)_{\mathrm{ex}}=R_{\mathrm{ccf}}(\nu)=3\omega\tau_{RS}x_m^{-2}A_{RS}(T)I_{\mathrm{ccf}}(\omega,x_m) \tag{32}$$

with

$$\tau_{RS}=\ell_m^2/D,\quad x_m=\xi/\ell_m, \tag{33}$$

and with the scaling function

$$\begin{aligned}I_{ccf}(\omega,x_m)&=(x_m^{-4}+(\omega\tau_{RS})^2)^{-1}\Bigg\{x_m^{-3}\arctan(x_m)\\&+\sqrt{\frac{\omega\tau_{RS}}{8}}(\omega\tau_{RS}-x_m^{-2})\Bigg[\arctan\left(\sqrt{\frac{2}{\omega\tau_{RS}}}+1\right)\\&+\arctan\left(\sqrt{\frac{2}{\omega\tau_{RS}}}-1\right)\Bigg]\\&+\sqrt{\frac{\omega\tau_{RS}}{32}}(\omega\tau_{RS}+x_m^{-2})\ln\left[\frac{\omega\tau_{RS}-\sqrt{2\omega\tau_{RS}}+1}{\omega\tau_{RS}+\sqrt{2\omega\tau_{RS}}+1}\right]\Bigg\}.\end{aligned} \tag{34}$$

In the limit of vanishing correlation length ($x_m\ll 1$), Eq. (34) turns into the explicit form of the Romanov–Solov'ev function $S_{RS}(\nu)$ which is here defined by the integral given in Eq. (31).

It turns out that the Hill function can be less favorably used to represent the Romanov–Solov'ev function $R_{RS}(\nu)$ [Eq. (30)] or the extended version $R_{ccf}(\nu)$ [Eq. (32)]. As an example, deviations between the $R_{RS}(\nu)$ function, with a given set of parameters, and its best fit to a Hill function is displayed in Fig. 6. In some frequency bands noticeable deviations result and these appear to be adversely systematic rather than statistically distributed. By the way of contrast, measured sonic absorption spectra, for systems that are assumed to be precritical, may be advantageously represented using the Hill spectral function. This finding is illustrated by Fig. 7 where the spectra for a n-pentanol/water mixture with and without LiCl added are displayed. In the most part of the frequency range of measurement the sonic absorption per wavelength seems to be dominated by a Hill-type relaxation term.

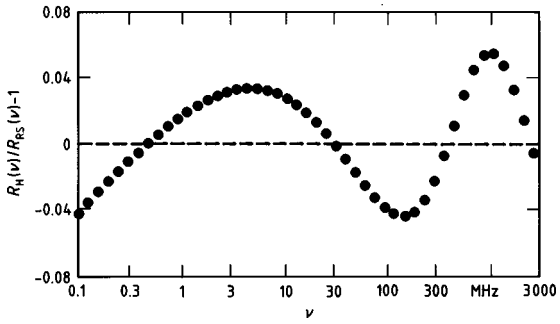

FIG. 6. Relative deviation of the best fit of the Hill relaxation spectral function R_H [Eq. (3)] from the Romanov–Solov'ev model R_{RS} [Eq. (30)] displayed as a function of frequency ν ($m_H=0.96$, $n_H=1$, $s_H=0.64$).

The reason for the discrepancy in the representation of the theoretical spectral functions and the measured spectra may be as follows. First of all, the theoretical models may still inadequately predict the details of the sonic absorption over a broad frequency range. On the other hand, as in the examples displayed in Fig. 7, existing measured broadband spectra mostly do not allow for a clear-cut conclusion on the shape of the relaxation term that results from the precritical behavior of the mixtures. The reason for this situation is the finding of significant parts of the spectrum to be masked by contributions from one or even two additional relaxation processes. Hence, as far as no definite conclusions can be drawn on the underlying relaxation model, the Hill function allows for a suitable interpolation of the measured data and a useful evaluation of trends in the relaxation parameters.

C. Visco-inertial and thermal boundary effects

In the examples shown in Fig. 7 the restricted version of the Hill function, $R_H^*(\nu)$ [Eq. (12)], was applied. Under many conditions this function is also suitable to model the visco-inertial and thermal boundary effects that have been reported for suspensions and emulsions.[29–39,55–57] A spectrum exhibiting such effects is presented in Fig. 8. The different contributions indicated in this diagram represent the relevant terms of a series expansion

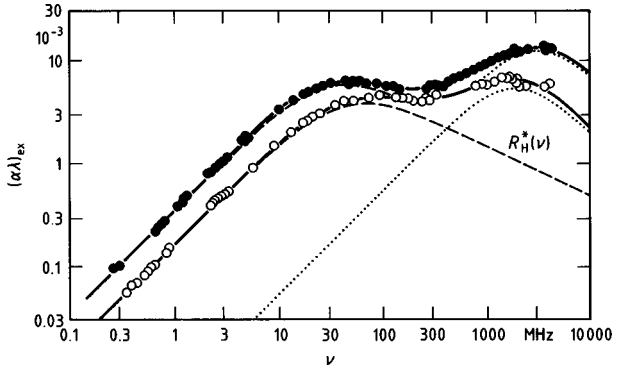

FIG. 7. Sonic excess absorption spectra for a *n*-pentanol/water mixture (mole fraction of alcohol $x=0.02$, 25 °C) without (○) and with (●) lithium chloride (0.3 mol/L) added.[72] The dashed curves show the Hill-type contributions [Eq. (12), $m_H\equiv 1$, $n_H\equiv 0.5$] to the spectra (○, $s_H=0.77$; ●, $s_H=0.81$). Dotted curves indicate an additional Debye contribution at high frequencies.

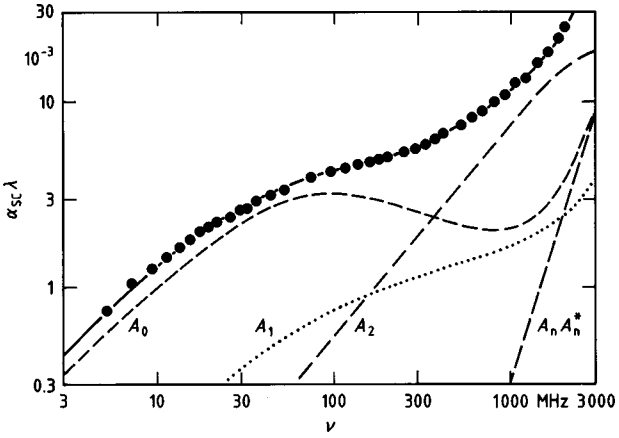

FIG. 8. The part $\alpha_{sc}\lambda$ due to ''scattering'' to the sonic attenuation per wavelength plotted versus frequency ν for an aqueous suspension of polysterene-latex globules[41] (●, mean radius of particles = 41 nm, volume fraction of solute=0.2, 25 °C). Dashed and dotted curves indicate the relevant terms in the series expansion [Eq. (35)] of $\alpha_{sc}(\nu)$. The full curve represents the sum of these terms. $A_0=A_{01}+A_{02}$. A_{01} represents the monotonous increase of $\alpha_{sc}\lambda$ at $\nu>1000$ MHz, A_{02} the relaxation behavior around 100 MHz.

$$\alpha_{\mathrm{sc}}(\nu)=-\frac{3}{2}\frac{\varphi_V}{R^3\mathrm{Re}(k_c^2)}\sum_{n=0}^{\infty}(2n+1)[\mathrm{Re}(A_n)-A_nA_n^*] \tag{35}$$

of part α_{sc} in the sound attenuation coefficient α that is due to scattering of the sonic wave from spherically shaped particles in a suspending phase. In Eq. (35) φ_V denotes the volume fraction of the particles, R the particle radius, and $k_c=\omega/c_{/\!/}+i\alpha_{/\!/}$ the wave number of the compressional wave reflected from the particles. Here $c_{/\!/}$ and $\alpha_{/\!/}$ are the sound velocity and attenuation coefficient, respectively, of the suspending liquid. The scattering coefficients A_n, $n=1,2,3,\ldots$, are given by the boundary conditions at the particle/suspending liquid interface.[41] The above relation [Eq. (35)] is based on the assumption that the particle size is much smaller than the wavelength of the incident compressional wave and that the distance between the particles is smaller than the wavelengths

$$\lambda_s=2\pi(2\eta_s/(\omega\rho))^{1/2} \quad \text{and} \quad \lambda_T=2\pi(2\Lambda/(\omega\rho C_P))^{1/2} \tag{36}$$

of a viscosity wave and a thermal wave, respectively. In this equation η_s denotes the shear viscosity, ρ the density, Λ the thermal conductivity, and C_P the specific heat capacity at constant pressure of the suspending liquid.

Term A_0, the graph of which is shown in Fig. 8, may be additionally subdivided into two parts, A_{01} and A_{02}. The former describes the resulting classical absorption of a binary mixture of constituents with different sonic attenuation coefficient, sound velocity, and density. The latter corresponds

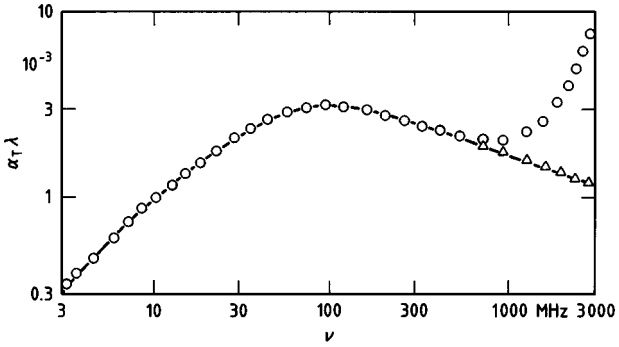

FIG. 9. The thermal part to the attenuation coefficient per wavelength plotted as a function of frequency ν for the example shown in Fig. 8. Circles represent the exact formulation[41] of the thermal boundary effect (contribution A_0 in Fig. 8). Triangles represent the explicit relation[58,59] which is inappropriate at high frequencies. The curve is the graph of the Hill relaxation spectral function.

with the so-called thermal part $\alpha_T(\nu)$ in the sound attenuation coefficient. This part is related to the monopole field distribution around a particle. It results from a difference in the heat capacity and thermal conductivity, respectively, between both subphases of the liquid leading to an irreversible heat transport within the sound field, accompanied by pulsation of the particles. Term A_1 corresponds with the so-called visco-inertial contribution $\alpha_\eta(\nu)$ to the total attenuation coefficient. It is related to transversal viscosity waves that are accompanied by dipole-type oscillations of the particles. These oscillations result if, due to different densities of the particle and the continuous phase, an inertial force acts on the suspended particles. Term $A_nA_n^*$ is due to Rayleigh scattering into different directions.

In the ultrasonic absorption spectra of emulsions the quadrupole oscillations are of minor importance since in liquid/liquid mixtures their contribution to the attenuation coefficient is significantly shifted up to higher frequencies. Normally, acoustic spectra are considered up to some hundred MHz only, particularly if the studies aim at applications in monitoring and control systems. For this reason, explicit formulations of both the thermal part $\alpha_s(\nu)$ and the viscosity part $\alpha_\eta(\nu)$ of the attenuation coefficient have been given in the literature.[31,58,59] Due to the specific assumptions made when deriving these explicit expressions, the $\alpha_T(\nu)$ and $\alpha_\eta(\nu)$ values at high frequencies substantially deviate from those predicted by the exact formulation of the theory (Fig. 9). At lower frequencies, however, both approaches yield nearly the same result. The explicit expressions for the scattering coefficients A_0 and A_1 are given by[31,41,58,59]

$$A_0=\left[-i\frac{a_c}{3}(a_c^2-\delta a_c'^2)\right]+\left[ia_c\frac{b_c}{b_T}\left(1-\delta\frac{b_c'}{b_c}\right)\frac{H_1}{H_2}\right]$$
$$:=A_{01}+A_{02}, \tag{37}$$

$$A_1=-\frac{i}{3}\frac{a_c^3(\delta-1)[h_2(a_s)Q(a_s')-\epsilon a_s h_1(a_s)j_2(a_s')]}{[3\delta h_2(a_s)+2(\delta-1)h_0(a_s)]Q(a_s')-\epsilon a_s h_1(a_s)j_2(a_s')(\delta+2)}, \tag{38}$$

where

$$\delta=\rho/\rho', \quad \varepsilon=\eta_s/\eta_s', \tag{39}$$

$$H_1=a_T h_1(a_T)\left(1-\frac{\Lambda b_T}{\Lambda' b_T'}\right),$$

$$H_2=h_0(a_T)-\frac{\Lambda a_T h_1(a_T)}{\Lambda' a_T' j_1(a_T')} j_0(a_T'), \tag{40}$$

$$Q(a_s')=a_s' j_1(a_s')-2(1-\varepsilon) j_2(a_s'), \tag{41}$$

$$a_c=Rk_c, \quad a_T=Rk_T, \quad a_s=Rk_s, \quad c_1^2=\left(\frac{\zeta+\frac{2}{3}\mu}{\rho}\right)^{1/2}, \tag{42}$$

$$b_c=-\frac{\kappa}{c_1^2\beta}\left[\omega^2-\left(\frac{c_1^2}{\kappa}+\frac{4\mu}{3\rho}\right)k_c^2\right],$$

$$b_T=-\frac{\kappa}{c_1^2\beta}\left[\omega^2-\left(\frac{c_1^2}{\kappa}+\frac{4\mu}{3\rho}\right)k_T^2\right], \tag{43}$$

and $k_s=2\pi/\lambda_s$, $k_T=2\pi/\lambda_T$. In these equations the primed quantities refer to the particles and unprimed quantities to the suspending face. Here j_n and h_n $(n=0,1,2)$ denote the spherical Bessel functions of the first and third kind, respectively, μ and ζ are Lamé constants, β is the coefficient of cubic expansion and κ is the ratio of specific heat at constant pressure and constant volume.

The contributions to the sonic absorption coefficient are related to the scattering coefficients according to

$$\alpha_{01}=-\frac{3}{2}\varphi_V\frac{\mathrm{Re}(A_{01})}{\mathrm{Re}(k_c^2)R^3},$$

$$\alpha_T=\alpha_{02}=-\frac{3}{2}\varphi_V\frac{\mathrm{Re}(A_{02})}{\mathrm{Re}(k_c^2)R^3}, \tag{44}$$

$$\alpha_\eta=\alpha_1=-\frac{9}{2}\varphi_V\frac{\mathrm{Re}(A_1)}{\mathrm{Re}(k_c^2)R^3}.$$

It is also found that the explicit form of the α_η spectra can be well represented by the restricted Hill function [Eq. (12)] with only three adjustable parameters. The distribution parameter s_H adopts values between about 0.3 and 0.8 in this model. The Hill function [Eq. (3)] does not as adequately apply to the explicit form of the α_T term. Nevertheless, a fairly good representation of the thermal part in the sound attenuation (Fig. 9) is possible if the distribution parameters are allowed to adopt the following values: $m_H\equiv 1$, $n_H=0.5,\ldots,1$, and $s_H=0.5,\ldots,1$. Representation of the $\alpha_T(\nu)$ and $\alpha_\eta(\nu)$ spectra by the Hill function is of considerable practical interest since the need for more complicated functions like the spherical Bessel functions of different kinds can thereby be avoided.

D. Kinetics of micelle formation

In the discussion of micelle kinetics the Aniansson–Wall scheme of coupled reactions[60,61]

$$A_1+A_{i-1}\underset{k_i^b}{\overset{k_i^f}{\rightleftharpoons}}A_i, \quad i=2,\ldots,\mathcal{N}, \tag{45}$$

is now generally accepted. It basically considers the equilibrium between monomers A_1 and all supramolecular structures (oligomers, micelles) with aggregation numbers i up to $\mathcal{N}$, assuming a Gaussian distribution of the equilibrium concentrations of the micellar species ($i\geqslant 10$). The Aniansson–Wall model predicts two relaxation processes, the slower one with a relaxation time τ_s in the order of milliseconds or seconds, the faster one with a relaxation time τ_f in the order of nanoseconds or microseconds. Based on these ideas, Debye-type relaxation terms have been predicted theoretically and the dependence of the relaxation parameters upon the total amphiphile concentration has been derived.[62,63] For solutions of long-chain amphiphiles these predictions have been verified. However, it has been shown recently[64] that for systems with high critical micelle concentration cmc, that is for solutions of short-chain amphiphiles, only one relaxation term exists in the time domain down to 1 ns. This term obviously is subject to a continuous relaxation time distribution (Fig. 10). Its principal relaxation time and relaxation amplitude differ in a characteristic manner from the theoretical predictions. An extended model of stepwise association shows indeed the measured trends in the relaxation parameters.[64] However, the width of the relaxation time distribution as calculated according to this model is substantially smaller than resulting from the measurements (Fig. 10). Since even the extended model does not completely comply with the experimental findings, it is an obvious attempt to describe the spectra measured for systems with high cmc utilizing the Hill spectral function. As illustrated by the example shown in Fig. 10, this function can again be favorably used. Rather small values for the relaxation time distribution parameters are found for amphiphile solutions near the cmc (e.g., $m_H=0.5$, $n_H=0.2$, $s_H=0.9$ for the spectrum displayed in Fig. 10).

It is only briefly mentioned here that the extended model of micelle formation evidences the existence of an additional ultrafast Debye-type relaxation term (with relaxation time τ_{uf}, Fig. 10) which is due to the exchange of monomers between oligomers and the suspending liquid.[64]

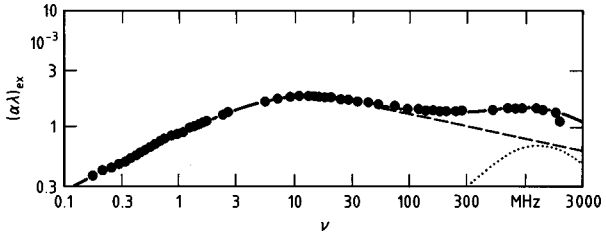

FIG. 10. Ultrasonic excess absorption spectrum of an aqueous solution of *n*-heptylammonium chloride ($c=0.45$ mol/L, 25 °C) near the critical micelle concentration[64] (cmc=0.4 mol/L). The dashed curve is the graph of the Hill function [Eq. (3)] with the following parameters: $m_H=0.5$, $n_H=0.2$, $s_H=0.9$. The dotted curve indicates an additional Debye-type contribution to the spectrum with a relaxation time τ_{uf}.

TABLE I. Relation of the Hill relaxation time distribution parameters to characteristics of semi-empirical and theoretical models as well as to experimental spectra.

Model, function	Ref.	m_H	n_H	s_H
Debye	2	1	1	1
Cole–Cole	50	$1-h_{CC}$	$1-h_{CC}$	<1
Davidson–Cole	51	1	$1-b_{DC}$	<1
Havriliak–Negami	47	$1-h_{HN}$	$(1-b_{HN})(1-h_{HN})$	<1
Dissado–Hill	72	m_{DH}	$1-m_{DH}$	$\leqslant 1$
Fixman	19	≈ 1	≈ 0.25	≈ 0.25
Bhattacharjee–Ferrell	26	0.94	0.06	0.25
Precritical conc. fluct.	16	≈ 1	1	0,...,0.8
Thermal boundary effects	31	1	0.5,...,1	0.5,...,1
Viscous boundary effects	58	1	0.5	0.3,...,0.8
Micellar systems near cmc	64	0.5,...,1	0.2,...,0.7	$\leqslant 1$

E. Formation of ion complexes

In Fig. 2, a spectrum is shown for an aqueous solution of zinc chloride ($ZnCl_2$) that differs in a characteristic manner from the spectra usually found for electrolyte solutions in which ion complexes are present (Fig. 1). The reason for the special behavior of various salts of transition metal ions is the ability of the cations to form a great variety of ion complex structures.[18,65–67] For aqueous solutions of zinc chloride, for instance, evidence has been obtained for the existence of the differently charged inner sphere complexes $[ZnCl]^+$, $[ZnCl_2]$, $[ZnCl_3]^-$, and $[ZnCl_4]^{2-}$. In addition, outer sphere complexes like $[Zn(H_2O)Cl]^+$, $[Zn(H_2O)_2Cl_2]$, $[Zn(H_2O)_3Cl_3]^-$, and $[Zn(H_2O)_4Cl_4]^{2-}$ are also assumed to exist.[68,69] For this reason the sonic absorption spectra of the aqueous solutions of such salts may be discussed in terms of a superposition of a series of Debye-type relaxation terms, each representing one step in the complex scheme of coupled equilibria between the different species.[18] Alternatively, a continuous distribution of ion clusters might be assumed rather than stoichiometrically well-defined species.[17] The spectra of zinc chloride aqueous solutions at various concentrations between 0.1 and 0.8 mol/L have thus also been treated[17] in terms of the Dissado–Hill function, given by[70,71]

$$(\alpha\lambda)_{\mathrm{ex}} = R_{DH}(\nu) = A_{DH}\,\mathrm{Im}\left\{ \frac{\lim\limits_{\epsilon\to 0}\int_{\epsilon}^{1} \frac{t^{-n_{DH}}}{(1-t(1-i\omega\tau_{DH})^{-1})^{1-m_{DH}}}\,dt}{(1+i\omega\tau_{DH})^{1-n_{DH}}} \right\}. \tag{46}$$

In the Dissado–Hill relaxation model, parameter n_{DH} characterizes the growth of the suggested ion clusters and parameter m_{DH} considers correlations between different clusters. A_{DH} and τ_{DH} again denote a relaxation amplitude and characteristic relaxation time, respectively.

The $R_{DH}(\nu)$ function can also be represented by the much easier applicable Hill function. The parameters controlling the shape and width of the underlying relaxation time distribution are related as $s_H \approx 1$, $m_H = m_{DH}$, and $n_H = 1 - m_{DH}$.

III. CONCLUSIONS

The Hill relaxation spectral function offers a quasi-universal analytical description of broadband ultrasonic absorption spectra of a variety of liquids. It is capable to empirically represent the sonic attenuation due to critical or precritical effects in liquid mixtures and due to thermal or visco-inertial boundary effects in emulsions and suspensions as well. It also complies with the uncommon spectra accompanied with the kinetics of micelle formation in surfactant solutions near the cmc and with those resulting from the dynamics of ion clusters which are suggested to exist in aqueous solutions of some transition metal ions. The simple structured Hill function enables a lucid representation of many theoretical models and, therefore, allows for an obvious classification of measured spectra in terms of possibly underlying molecular mechanisms. A rough classification is possible on grounds of the Hill relaxation time distribution parameters found in the regression analysis of measured spectra. The data displayed in Table I indicate how these parameters are related to specific relaxation models. Further hints may be obtained from the dependence of the Hill relaxation amplitude and characteristic relaxation time upon relevant parameters like the mixture composition. Favorable use is particularly made of the Hill function in the description of spectra for which theoretical models are currently not available.

ACKNOWLEDGMENTS

We thank R. Behrends, V. Kühnel, and T. Telgmann for helpful discussions. Financial support by the Deutsche Forschungsgemeinschaft is gratefully acknowledged.

[1] H. Strehlow, *Rapid Reactions in Solution* (VCH, Weinheim, 1992).
[2] P. Debye, *Polare Molekeln* (Hirzel, Leipzig, 1929).
[3] B. Wehrmann, Dissertation, Georg-August-Universität Göttingen, 1991.
[4] K. Lautscham, Dissertation, Georg-August-Universität Göttingen, 1986.
[5] B. Wehrmann, Diplom-Thesis, Georg-August-Universität Göttingen, 1985.
[6] M. Brai, Diplom-Thesis, Georg-August-Universität Göttingen, 1988.
[7] M. Eigen and K. Tamm, Ber. Bunsenges. Phys. Chem. **66**, 93–121 (1962).
[8] K. Tamm, in *Handbuch der Physik*, edited by S. Flügge (Springer-Verlag, Berlin, 1961), Vol. 11/1, pp. 202–274.
[9] M. Eigen and L. De Maeyer, in *Technique of Organic Chemistry*, edited by A. Weissberger (Interscience, New York, 1963), Vol. 8/2, pp. 895–1054.

[10] J. Stuehr and E. Yeager, in *Physical Acoustics*, edited by W. P. Mason (Academic, New York, 1965), Vol. 2/A, pp. 351–462.
[11] M. J. Blandamer, *Introduction to Chemical Ultrasonics* (Academic, London, 1973).
[12] R. A. Pethrick, in *Molecular Interactions*, edited by H. Ratajczak and W. J. Orville-Thomas (Wiley, New York, 1982), Vol. 3, pp. 489–532.
[13] P. D. Edmonds, *Ultrasonics* (Academic, New York, 1981), p. 186.
[14] F. Eggers and U. Kaatze, Meas. Sci. Technol. **7**, 1–19 (1996).
[15] K. Menzel, A. Rupprecht, and U. Kaatze, J. Phys. Chem. B **101**, 1255–1263 (1997).
[16] V. Kühnel and U. Kaatze, J. Phys. Chem. **100**, 19 747–19 757 (1996).
[17] U. Kaatze, K. Menzel, and D. Wehrmann, Z. Phys. Chem. (Munich) **177**, 27–36 (1992).
[18] U. Kaatze and B. Wehrmann, Z. Phys. Chem. (Munich) **177**, 9–26 (1992).
[19] M. Fixman, Adv. Chem. Phys. **4**, 175–228 (1964).
[20] V. P. Romanov and V. A. Solov'ev, Sov. Phys. Acoust. **11**, 68–71, 219–220 (1965).
[21] M. A. Isakovic and I. A. Chaban, Sov. Phys. JETP **23**, 893–905 (1966).
[22] K. Kawasaki, Ann. Phys. **61**, 1–56 (1970).
[23] M. J. Blandamer and D. Waddington, Adv. Mol. Relax. Processes **2**, 1–40 (1970).
[24] D. M. Kroll and J. M. Ruhland, Phys. Rev. A **23**, 371–374 (1981).
[25] Y. Shiwa and K. Kawasaki, Prog. Theor. Phys. **66**, 406–420 (1981).
[26] R. A. Ferrell and J. K. Battacharjee, Phys. Rev. A **31**, 1788–1809 (1985).
[27] H. Endo, J. Chem. Phys. **92**, 1986–1993 (1990).
[28] M. A. Anisimov, *Critical Phenomena in Liquids and Liquid Crystals* (Gordon and Breach, Amsterdam, 1991), pp. 229–234.
[29] I. A. Ratinskya, Sov. Phys. Acoust. **8**, 160–164 (1962).
[30] J. C. F. Chow, J. Acoust. Soc. Am. **36**, 2395–2401 (1964).
[31] J. R. Allegra and S. A. Hawley, J. Acoust. Soc. Am. **51**, 1545–1564 (1972).
[32] A. S. Ahuja, J. Acoust. Soc. Am. **66**, 801–805 (1979).
[33] M. C. Davis, J. Acoust. Soc. Am. **65**, 387–390 (1979).
[34] A. H. Hay and R. W. Burling, J. Acoust. Soc. Am. **72**, 950–959 (1982).
[35] I. S. Kol'tsova, Sov. Phys. Acoust. **33**, 297–298 (1987).
[36] A. H. Harker and J. A. G. Temple, J. Phys. D **21**, 1575–1588 (1988).
[37] M. J. McClements and M. J. Povey, J. Phys. D **22**, 38–47 (1989).
[38] D. J. McClements, J. Acoust. Soc. Am. **91**, 849–853 (1992).
[39] L. W. Anson and R. C. Chivers, J. Acoust. Soc. Am. **93**, 1687–1699 (1993).
[40] C. A. Farrow, L. W. Anson, and R. C. Chivers, Acustica **81**, 402–411 (1995).
[41] U. Kaatze, C. Trachimow, R. Pottel, and M. Brai, Ann. Phys. (Heidelberg) **5**, 13–33 (1996).
[42] A. Schröder and E. Raphael, Europhys. Lett. **17**, 365–370 (1992).
[43] R. M. Hill, Nature (London) **275**, 96–99 (1978).
[44] R. M. Hill, Phys. Status Solidi B **103**, 319–328 (1981).
[45] L. A. Dissado and R. M. Hill, Nature (London) **279**, 685–689 (1979).
[46] K. Giese, Adv. Mol. Relax. Processes **5**, 363–373 (1973).
[47] S. Havriliak and S. Negami, J. Polym. Sci., Part C: Polym. Symp. **14**, 99–117 (1966).
[48] I. Alig, D. Lellinger, K. Nancke, A. Rizos, and G. Fytas, J. Appl. Polym. Sci. **44**, 829–835 (1992).
[49] M. Matsukawa and I. Nagai, J. Acoust. Soc. Am. **99**, 2110–2115 (1996).
[50] K. S. Cole and R. H. Cole, J. Chem. Phys. **9**, 341–351 (1941).
[51] D. W. Davidson and R. H. Cole, J. Chem. Phys. **18**, 1417 (1950).
[52] V. Kühnel, Dissertation, Georg-August-Universität Göttingen, 1995.
[53] L. Z. Ornstein and F. Zernike, Proc. Acad. Sci. Amsterdam **17**, 793 (1914).
[54] L. Z. Ornstein and F. Zernike, Phys. Z. **19**, 134 (1918).
[55] D. J. McClements, P. Fairly, and M. J. W. Povey, J. Acoust. Soc. Am. **87**, 2244–2248 (1990).
[56] R. A. Roy and R. A. Apfel, J. Acoust. Soc. Am. **87**, 2332–2341 (1990).
[57] P. V. Zinin, Ultrasonics **30**, 26–34 (1992).
[58] P. S. Epstein and R. R. Carhart, J. Acoust. Soc. Am. **25**, 553–565 (1953).
[59] A. Ahuja and W. R. Hendee, J. Acoust. Soc. Am. **63**, 1074–1080 (1978).
[60] E. A. G. Aniansson and S. N. Wall, J. Phys. Chem. **78**, 1024–1030 (1974).
[61] E. A. G. Aniansson, Prog. Colloid Polym. Sci. **70**, 2–5 (1985).
[62] M. Teubner, J. Phys. Chem. **83**, 2917–2929 (1979).
[63] M. Kahlweit and M. Teubner, Adv. Colloid Interface Sci. **13**, 1–64 (1980).
[64] T. Telgmann and U. Kaatze, J. Phys. Chem. B **101**, 7758–7765, 7766–7772 (1997).
[65] D. F. C. Morris, E. L. Short, and D. N. Waters, J. Inorg. Nucl. Chem. **25**, 975–983 (1963).
[66] K. Tamura, J. Phys. Chem. **81**, 820–826 (1977).
[67] H. Weingärtner, K. J. Müller, H. G. Hertz, A. V. J. Edge, and R. Mills, J. Phys. Chem. **88**, 2173–2178 (1984).
[68] C. O. Quicksall and T. G. Spiro, Inorg. Chem. **5**, 2232–2233 (1966).
[69] G. S. Darbari, M. R. Richelson, and S. Petrucci, J. Chem. Phys. **53**, 859–866 (1970).
[70] L. A. Dissado and R. M. Hill, Proc. R. Soc. London, Ser. A **390**, 131–180 (1983).
[71] L. A. Dissado and R. H. Hill, J. Appl. Phys. **66**, 2511–2524 (1989).
[72] C. Hoeschen, Diploma-Thesis, Georg-August-Universität Göttingen, 1996.

The contrast mechanism of bond defects with the scanning acoustic microscopy

Lugen Wang[a)]
Edison Joining Technology Center, Welding Engineering, The Ohio State University, Columbus, Ohio 43210

(Received 30 April 1998; accepted for publication 7 August 1998)

This paper discusses the theoretical aspects of the scanning acoustic microscopy response when used to inspect layered solids with bond defects. By using the transfer matrix method and spring boundary conditions, the solution of elastic wave scattering by an interface weakness in a layered solid has been presented in the wave number domain. The microscopy response has been calculated by combining this scattering solution with the scanning acoustic microscopy model. The results show that the acoustic microscopy response is sensitive to normal bond compliance in all defocus range. However, the shear bond compliance has influence on the response only at large defocus. The relations between the microscopy response and bond compliances significantly depend on the defect width, shape, and the material properties of the layer and substrate. © *1998 Acoustical Society of America.* [S0001-4966(98)04011-9]

PACS numbers: 43.35.Sx [ANN]

INTRODUCTION

The scanning acoustic microscopy (SAM) has been widely used to inspect the quality of bond between the thin layer and substrate.[1,2] Experimental results show that SAM response [$V(z)$ curve], at least, can qualitatively evaluate the bond quality between the layer and substrate. The reflection amplitude images obtained by SAM at different defocus show the contrast variation in bond and debond area. This contrast variation has been explained by comparing the $V(z)$ curve of completely debond with that of perfect bond between the layer and substrate.[1] Addison *et al.*[2] have tried to inverse the bond quality by measuring the surface wave velocity variation from the $V(z)$ curve. However, it is still not clear to what aspect of adhesion quality the $V(z)$ curve is sensitive. There is still no quantitative analysis of the $V(z)$ curve for specimens with bond defects.

A widely used model to calculate the $V(z)$ curve expresses the incident focus wave as plane waves, and then solves the plane-wave scattering problem.[3] For layered materials without bond defects, the solution of this plane-wave scattering problem is the reflection coefficient, which can be obtained by the transfer matrix method.[4] The plane-wave scattering by an interface debond has been solved by the boundary element method in spatial domain, and the bond defect has been modeled by the spring-boundary conditions.[5] For an infinite uniform bond defect, the reflection coefficient can be calculated easily by including this spring-boundary condition in the assembly of the transfer matrix.[6] In this paper, the solution of plane-wave scattering by a bond defect with arbitrary shapes will be presented in the wave number domain. This solution can be easily combined with the SAM model. By using this model, the effects of shear and normal bond stiffness on the acoustic microscopy response have been analyzed.

a)Electronic mail: wang.422@osu.edu

I. MODEL FOR THE SAM RESPONSE WITH BOND DEFECTS

A. Output from SAM

Figure 1 shows the configuration of an SAM and a specimen with a thin layer. The acoustic probe consists of a transducer and a cylindrical lens. The coupling fluid between the lens and specimen is water. The output voltage at different z_0 (defocus) has been analyzed by the ray or wave method. A widely used model can be written as[3]

$$V_{\text{out}}(z,\omega)=\int_{-\infty}^{+\infty}\int_{-\infty}^{+\infty}L_1(k_{x1})L_2(k_{x2}) \times\exp(i(k_{z1}z_0+k_{z2}z_0))G(k_{x1},k_{x2})dk_{x1}\,dk_{x2}, \tag{1}$$

where $L_1(k_{x1})$ is the angular spectrum of the incident wave at the focal plane and $L_2(k_{x2})$ is the response function. They are characteristic functions of the acoustic lens. $G(k_{x1},k_{x2})$ is the Green function in the wavenumber domain. It corresponds to the plane-wave scattering by the fluid–solid interface.

B. Scattering by a bond defect

As shown in Eq. (1), the difficulty in calculating the SAM output is solving the scattering problem. We consider a layered solid composed of an isotropic elastic layer of thickness d bonded at its face $z=0$ to an isotropic elastic halfspace and in contact at its face $z=d$ with an inviscid fluid (see Fig. 1). There is a bond defect between $x=a$ to $x=b$; therefore, the boundary conditions for this structure in terms of the stress t_x,t_z and particle velocity ν_x,ν_z are

$$\begin{aligned}&t_x^f(d)=0,\quad t_z^f(d)=t_z^l(d),\quad \nu_z^f(d)=\nu_z^l(d)\\ &\text{at } z=d \text{ and } -\infty<x<\infty,\\ &t_x^l(0)=t_x^s(0),\quad t_z^l(0)=t_z^s(0),\quad \nu_x^l(0)=\nu_x^s(0),\\ &\nu_z^l(0)=\nu_z^s(0) \text{ at } z=0 \text{ and } x<a \text{ or } x>b.\end{aligned} \tag{1a}$$

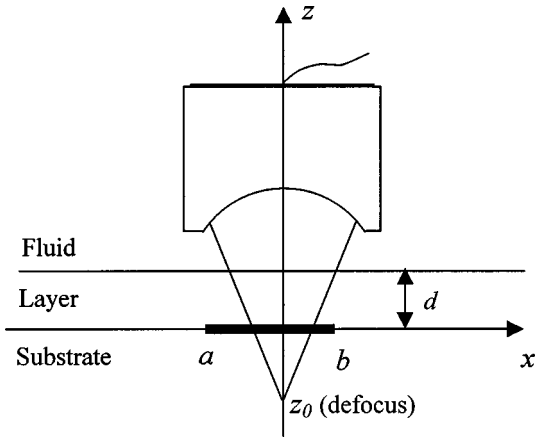

FIG. 1. The schematic diagram of the layered solid and acoustic microscopy. There is a bond defect between $x=a$ and b in the interface.

The bond defect can be modeled by the spring model[5,6] and the boundary conditions can be written as

$$t_x^l(0)=t_x^s(0), \quad \nu_x^l(0)-\nu_x^s(0)=-i\omega s(x)t_x^s(0),$$
$$t_z^l(0)=t_z^s(0), \quad \nu_z^l(0)-\nu_z^s(0)=-i\omega n(x)t_z^s(0), \qquad (1b)$$
$$\text{at } z=0 \text{ and } a<x<b.$$

$s(x)$ and $n(x)$ represent the shear and normal bond compliance. The total debond corresponds to $s=n=\infty$ and $s=n=0$ represents a perfect bond. The boundary relations (1a) and (1b) are written in the spatial domain. They can be transferred to wave number domain by applying Fourier transfer with respect to the x coordinate. Equation (1a) will have the same form and (1b) will be

$$\begin{aligned} V_x^l(k_x)-V_x^s(k_x)&=-i\omega\int_{-\infty}^{+\infty}T_x^s(k_x')S(k_x-k_x')dk_x' \\ &=-i\omega S(k_x)\otimes T_x^s(k_x), \\ V_z^l(k_x)-V_z^s(k_x)&=-i\omega\int_{-\infty}^{+\infty}T_z^s(k_x')N(k_x-k_x')dk_x' \\ &=-i\omega N(k_x)\otimes T_z^s(k_x). \end{aligned} \qquad (2)$$

We use the capital T, V, S, and N to represent the wave number domain. $\otimes$ represents convolution. The superscript f, l, and s represent fluid, layer, and substrate, respectively.

A plane wave with wave potential $\varphi_2^f\delta(k_x-k_{x0})$ in the fluid propagates to the fluid–layer interface at an angle θ. Then, the wave potentials in the fluid, layer, and substrate can be represented as follows: in the fluid:

$$\phi^f(k_x,z,\omega)=(\phi_1^f e^{i\alpha_f z}+\phi_2^f e^{-i\alpha_f z}\delta(k_x-k_{x0}))e^{-i\omega t};$$

in the layer:

$$\phi^l(k_x,z,\omega)=(\phi_1^l e^{i\alpha_L z}+\phi_2^l e^{-i\alpha_L z})e^{-i\omega t},$$
$$\psi^l(k_x,z,\omega)=(\psi_1^l e^{i\alpha_S z}+\psi_2^l e^{-i\alpha_S z})e^{-i\omega t};$$

and in the substrate:

$$\phi^s(k_x,z,\omega)=\phi_2^s e^{-i\beta_L z}e^{-i\omega t},$$
$$\psi^s(k_x,z,\omega)=\psi_2^s e^{-i\beta_S z}e^{-i\omega t},$$

where

$$k_{x0}=k_f\sin(\theta), \quad \alpha_f^2=k_f^2-k_x^2, \quad \alpha_L^2=k_{lL}^2-k_x^2,$$
$$\alpha_S^2=k_{lS}^2-k_x^2, \quad \beta_L^2=k_{sL}^2-k_x^2 \quad \text{and} \quad \beta_S^2=k_{sS}^2-k_x^2.$$

$k_f=\omega/\nu_f$ and ν_f is the wave speed in the fluid. k_{li} ($i=L$ or S) are the longitudinal ($i=L$) and shear ($i=S$) wave numbers in the layer, and k_{si} are the wave numbers in the substrate. The subscript 1 and 2 represent wave propagation along positive or negative z direction. The velocity and traction at $z=0$ and $z=d$ are related by the transfer matrix,[7]

$$\begin{aligned} \mathbf{f}(d)&=\begin{bmatrix} V_x^l(d) \\ V_z^l(d) \\ T_z^l(d) \\ T_x^l(d) \end{bmatrix}=\mathbf{A}\begin{bmatrix} V_x^l(0) \\ V_z^l(0) \\ T_z^l(0) \\ T_x^l(0) \end{bmatrix} \\ &=\mathbf{A}\left(\mathbf{f}^s(0)-i\omega\begin{bmatrix} T_x^s\otimes S \\ T_z^s\otimes N \\ 0 \\ 0 \end{bmatrix}\right). \end{aligned} \qquad (3)$$

The velocity and traction $\mathbf{f}^s(0)$ at boundary $z=0$ in the substrate side can be written in terms of the transmitted wave potential ϕ_2^s and ψ_2^s

$$\mathbf{f}^s(0)=\begin{bmatrix} V_x^s(0) \\ V_z^s(0) \\ T_z^s(0) \\ T_x^s(0) \end{bmatrix}=\mathbf{B}\begin{bmatrix} \phi_2^s \\ \psi_2^s \end{bmatrix}. \qquad (4)$$

The velocity and traction on the layer top can be represented by the incident wave potential $\phi_2^f\delta(k_x-k_{x0})$ and reflected wave potential ϕ_1^f.

$$\begin{bmatrix} V_z^l(d) \\ T_z^l(d) \\ T_x^l(d) \end{bmatrix}=\begin{pmatrix} i\alpha_f e^{i\alpha_f d} & -i\alpha_f e^{-i\alpha_f d} \\ -i\rho_f\omega e^{i\alpha_f d} & -i\rho_f\omega e^{-i\alpha_f d} \\ 0 & 0 \end{pmatrix} \times\begin{bmatrix} \phi_1^f \\ \phi_2^f\delta(k_x-k_{x0}) \end{bmatrix}, \qquad (5)$$

where ρ_f is the density of the fluid. By substituting Eqs. (4) and (5) into (3), the reflected wave potential ϕ_1^f, transmitted longitudinal wave potential ϕ_2^s, and shear-wave potential ψ_2^s can be obtained as

$$\begin{bmatrix} \phi_1^f \\ \phi_2^s \\ \psi_2^s \end{bmatrix} + i\omega \mathbf{D} \begin{bmatrix} \int_{-\infty}^{+\infty} (b_{41}(k_x')\phi_2^s(k_x') + b_{42}(k_x')\psi_2^s(k_x'))S(k_x - k_x')dk_x' \\ \int_{-\infty}^{+\infty} (b_{31}(k_x')\phi_2^s(k_x') + b_{32}(k_x')\psi_2^s(k_x'))N(k_x - k_x')dk_x' \\ 0 \\ 0 \end{bmatrix} = \begin{bmatrix} R_0 \\ T_{L0} \\ T_{S0} \end{bmatrix} \delta(k_x - k_{x0}), \tag{6}$$

where $\mathbf{D}=\mathbf{M}^{-1}\mathbf{A}'$ and

$$\mathbf{M}=\begin{pmatrix} -i\alpha_f e^{i\alpha_f d} & c_{21} & c_{22} \\ i\rho_f \omega e^{i\alpha_f d} & c_{31} & c_{32} \\ 0 & c_{41} & c_{42} \end{pmatrix}.$$

$\mathbf{A}'$ is the matrix of $\mathbf{A}$ without the first row, c_{ij} is the element in matrix $\mathbf{C}=\mathbf{AB}$. R_0, T_{L0} and T_{S0} are the reflection coefficient, longitudinal, and shear-wave transmission coefficients without the bond defect. The expressions for matrix $\mathbf{A}$ and $\mathbf{B}$ can be found in Ref. 7.

Now, three coupled equations (Eq. 6) for the reflected wave ϕ_1^f, longitudinal, and shear transmission waves ϕ_2^s, ψ_2^s have been obtained. In the coupled integral equations, $b_{41}(k_x)$, $b_{42}(k_x)$, $b_{31}(k_x)$, and $b_{32}(k_x)$ are all continuous functions. In numerical calculation, the infinite integration has to be truncated into a finite integration. The truncation position is determined by the behaviors of $S(k_x)$ and $N(k_x)$. For bond defects with small widths or sharp edges, the bandwidth of $S(k_x)$ and $N(k_x)$ will be large; therefore the truncation position also has to be large. Equation (6) can be discretized to obtain a set of algebraic equations. The Green function $G(k_{x1},k_{x2})$ in Eq. (1) corresponds to the reflection coefficient $\phi_1^f(k_x,k_{x0})$, which can be obtained by solving this algebraic equation using the Gaussian elimination method.

When the bond compliances S and N are small, then the iterative solution of this integral equation is more efficient. By assuming S and N are small and neglecting the second term in the right side of Eq. (6) in the zeroth approximation, we get

$$\begin{bmatrix} \phi_1^f \\ \phi_2^s \\ \psi_2^s \end{bmatrix}^0 = \begin{bmatrix} R_0 \\ T_{L0} \\ T_{S0} \end{bmatrix} \delta(k_x - k_{x0}).$$

The higher-order approximation can be obtained by iterative sequence

$$\begin{bmatrix} \phi_1^f \\ \phi_2^s \\ \psi_2^s \end{bmatrix}^n = \begin{bmatrix} R_0 \\ T_{L0} \\ T_{S0} \end{bmatrix} \delta(k_x - k_{x0}) - i\omega \mathbf{D} \begin{bmatrix} (b_{41}\phi_2^{s(n-1)} + b_{42}\psi_2^{s(n-1)}) \otimes S \\ (b_{31}\phi_2^{s(n-1)} + b_{32}\psi_2^{s(n-1)}) \otimes N \\ 0 \\ 0 \end{bmatrix}.$$

The first order, i.e., the Born approximation, can be obtained as:

$$\begin{aligned} G(k_{x1},k_{x2}) = \phi_1^f(k_{x1},k_{x0}) &= R_0(k_{x2})\,\delta(k_{x2}-k_{x1}) \\ &- i\omega(d_{l1}(b_{41}T_{L0}(k_{x1})S(k_{x2}-k_{x1}) \\ &+ b_{42}T_{S0}(k_{x1})S(k_{x2}-k_{x1})) \\ &+ d_{l2}(b_{31}T_{L0}(k_{x1})N(k_{x2}-k_{x1}) \\ &+ b_{32}T_{S0}(k_{x1})N(k_{x2}-k_{x1})) \end{aligned}$$

where the b_{ij} and d_{ij} are elements in matrix $\mathbf{B}$ and $\mathbf{D}$.

If the width of the bond defect becomes infinite and the bond compliance $n(x)$ and $s(x)$ are invariable with respect to x, then $S(k_x)$ and $N(k_x)$ will be delta functions in the wave number domain, $S=S_0\delta(k_x)$ and $N=N_0\delta(k_x)$. In this case, the convolution in Eq. (6) becomes simple multiplication and Eq. (6) becomes a simple linear equation which can be solved analytically. Equations (1) and (6) are formulated for line-focus transducers; for spherical-focus transducers (axial symmetry problems), similar equations can be obtained by using the polar coordination system.

II. NUMERICAL RESULTS AND DISCUSSION

In order to solve the coupled Eq. (6) and calculate the integration of Eq. (1), the wave number k_x should be truncated and discretized. $G(k_{x1},k_{x2})$ is obtained by solving Eq. (6), which has been discretized to a set of linear equations; then the amplitude V_{out} is calculated by numerical integration of Eq. (1). In our calculation, a lens with semiaperture angle 60 deg has been used, and the characteristic functions $L_1(k_x)$ and $L_2(k_x)$ are calculated by the method described in Ref. 8. The operation frequency is 225 MHz. The coupling fluid (water) has density 9.98 g/cm^3 and wave speed 1.48 km/s. Two kinds of specimens are used, and the properties are shown in Table I.

Material one corresponds to fused quartz with gold coating, and the velocities of layer are smaller than that of the substrate. Material two is aluminum with silicon-nitride coating, and the velocities of layer are larger than that of the substrate. Therefore, for material one, more than one surface

TABLE I. Properties for the layer and substrate.

	Material 1		Material 2	
	Layer	Substrate	Layer	Substrate
Longitudinal velocity (mm/μs)	3.24	5.97	10.61	6.37
Shear velocity (mm/μs)	1.2	3.76	6.20	3.11
Density (g/cm^3)	19.3	2.2	3.18	2.69

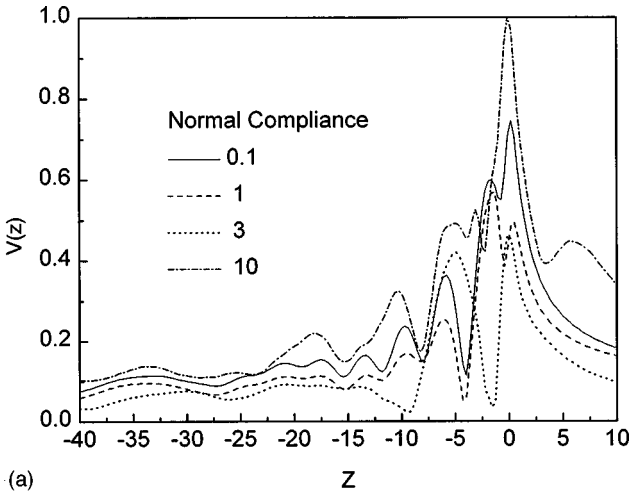

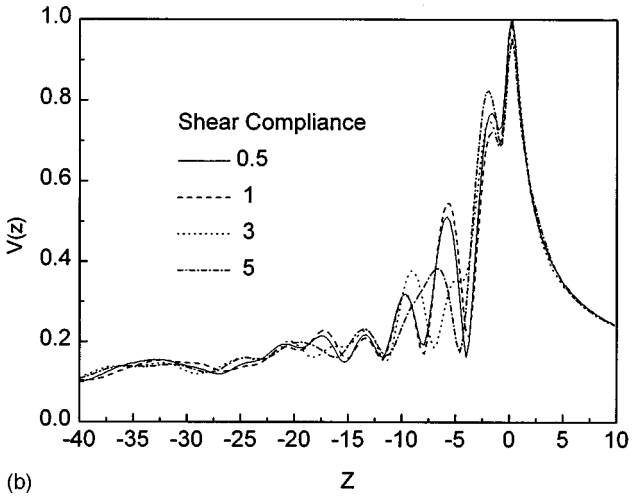

FIG. 2. (a) $V(z)$ curves for material one with different normal bond compliance. (b) $V(z)$ curves for material one with different shear bond compliance.

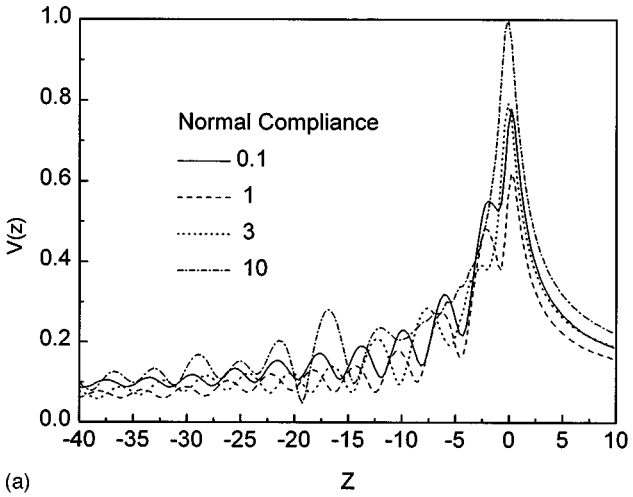

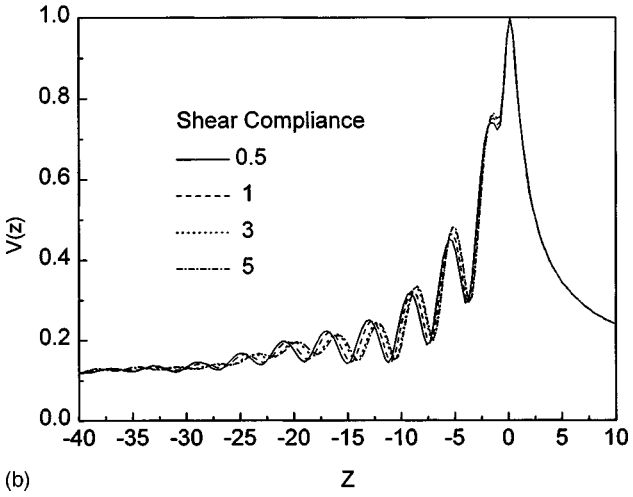

FIG. 3. (a) $V(z)$ curves for material two with different normal bond compliance. (b) $V(z)$ curves for material two with different shear bond compliance.

wave can exist when the frequency and layer thickness increase.[9] However, for material two, only one surface wave exists.

In all of the following figures, the defocus is normalized by the wavelength in the fluid, i.e., $Z=z_0/\lambda_f$. The nondimensional bond compliance has been used, i.e., $N=N_0/N_l$ and $S=S_0/S_l$. N_l and S_l may be written as: $N_l=\lambda_{lL}/\rho_l\nu_{lL}^2$ and $S_l=\lambda_{lS}/\rho_l\nu_{lS}^2$. λ_{lL} and λ_{lS} are the longitudinal and shear wavelengths of the layer. N_l and S_l correspond to the layer compliance with thickness of λ_{lL} and λ_{lS}, respectively. The thickness of the layer is $0.01\lambda_{lL}$ in the calculations.

Figures 2(a) and (b) and 3(a) and (b) show the $V(z)$ curves for difference bond compliances. The bond defect width is $0.5\lambda_{lL}$. For material one, there are two surface waves (Sezawa wave and Rayleigh wave) at this thickness and frequency.[10] The Sezawa wave has higher velocity than the Rayleigh wave. As shown in Fig. 2, for small bond compliance, the $V(z)$ curve is dominated by the Rayleigh wave at small defocus ($Z>-15$), and at large defocus ($Z<-15$), the Sezawa wave becomes more important. It is well known that the oscillation in the $V(z)$ curve is due to the interference between the specular reflection and the leaky surface wave. The specular reflection corresponds to the small incident angle, i.e., normal incident wave. The leaky surface wave corresponds to the ray incident at the critical angle. For the normal incident wave, the shear stress on the interface approaches zero; therefore, the shear bond compliance has little influence on the specular reflection wave. However, the normal incidence reflection coefficient greatly depends on the normal bond compliance. As shown in Figs. 2(a) and 3(a) the $V(z)$ curve is sensitive to normal bond compliance in the whole defocus range. For different shear bond compliances, the $V(z)$ curve has variation only after some defocus. At a small defocus, the main attribution to the $V(z)$ curve is the specular reflection due to the focus position around the specimen surface. This explains why the $V(z)$ curve is insensitive to shear bond compliance at a small defocus. Comparing $V(z)$ curves for normal and shear bond compliance, the shear bond compliance mainly changes the phase difference between the specular reflection and the leaky surface wave, and therefore shifts the maximum and minimum position in the $V(z)$ curve. For the normal compliance, the whole $V(z)$ curve can move up and down for difference bond compliances due to the change of specular reflection coefficient amplitude. For material two, the behaviors for shear and normal bond compliance are similar to

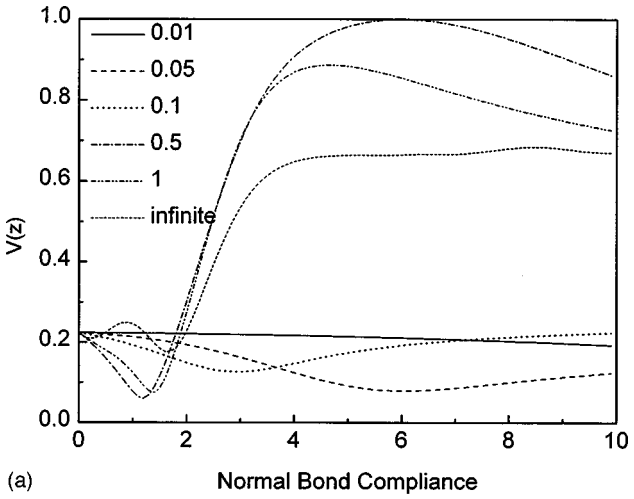

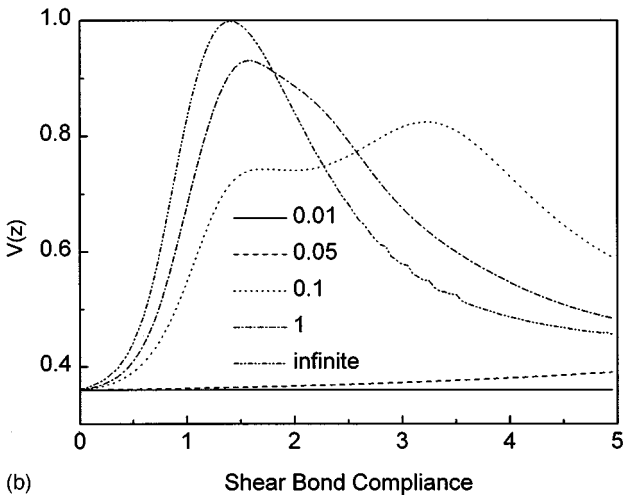

FIG. 4. (a) Response amplitude vs normal bond compliance for material one. (b) Response amplitude vs shear bond compliance for material one.

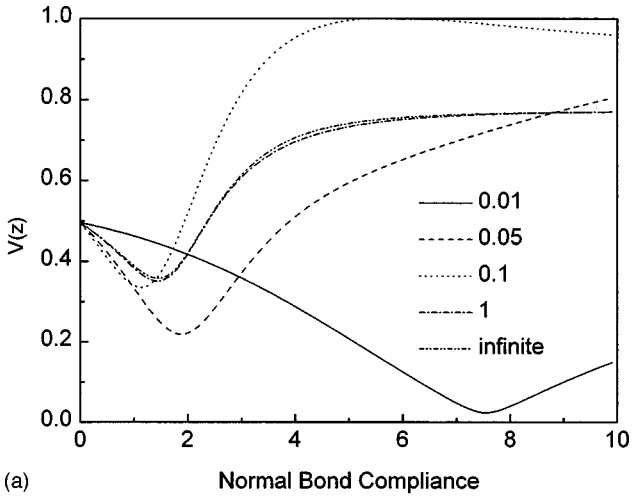

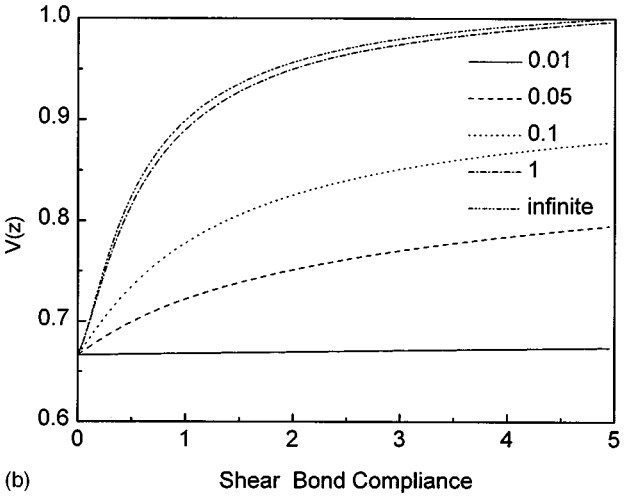

FIG. 5. (a) Response amplitude vs normal bond compliance for material two. (b) Response amplitude vs shear bond compliance for material two.

material one. Comparing Figs. 2(b) and 3(b), the response of material one is more sensitive to shear bond compliance than that of material two. Because there are two surface waves in material one, the phase difference between the two surface waves and specular reflection makes the response have more complicated features.

Figures 4(a) and (b) and 5(a) and (b) show the relation between SAM response and bond compliance for different bond defect widths. The defect width is normalized by the longitudinal wavelength in the layer. The defocus is chosen to be the first minimum defocus position in the $V(z)$ curve of perfect bond. The results show that the amplitude does not simply increase when the bond compliance increases; there are maximum and minimum positions as the bond compliance increases. For normal bond compliance, as shown in Figs. 4(a) and 5(a), the two materials have similar behaviors. The amplitude decreases at small normal bond compliance and reaches the minimum value at a certain compliance value. The compliance value corresponding to this minimum position is significantly influenced by the bond defect width. The smaller bond defect width generally has a larger decreasing range. For material one, there is a small oscillation in small bond compliance range for infinite bondwidth. These behaviors are almost the same for all defocus positions as shown in Figs. 2(a) and 3(a); the $V(z)$ curve will decrease at small bond compliance and then increase at high compliance in all defocus positions. This is due to the specular reflection coefficient amplitude, which decreases at small bond compliance and increases at high bond compliance. As the bond compliance increases from zero, the specimen surface becomes ''effectively soft'' due to the spring-boundary condition between the layer and substrate, and the acoustic impedance of stiff surface matches that of the water; therefore, reflection amplitude decreases. But when the normal bond compliance becomes too high, the surface becomes ''too soft,'' the acoustic impedance becomes mismatched again, and the reflection amplitude increases as the normal bond compliance increases. For shear bond compliance, the behaviors of the two materials are different. For material two, the response amplitude only increases as compliance increases. For material one, the response amplitude has a maximum point. The relations also depend on the defocus for material two, as shown in Fig. 3(b). If the defocus is within the range where the amplitude increases as defocus decreases in Fig. 3(b), the amplitude will increase as the bond compliance increases. However, at defocus in the amplitude decreasing range in Fig. 3(b), the amplitude will decrease as the bond compliance increases. The sensitivity

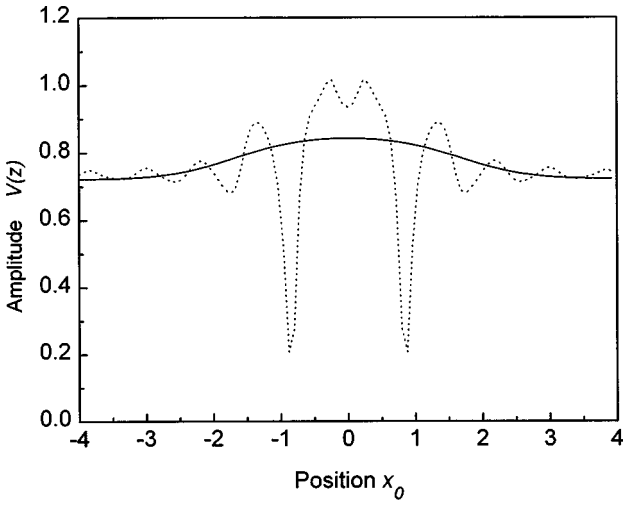

FIG. 6. Amplitude changes when scanning over defects with different bond compliance shapes. The solid line corresponds to a Gaussian shape and the dashed line corresponds to a step-function shape. The defect width is λ_{lL} and the position is normalized by λ_{lL}.

seems to be higher at defocus between the maximum and minimum positions in Fig. 3(b). However, for material one, due to the existence of Sezawa and Rayleigh waves, the behaviors become more complicated. As shown in these figures, the defect width has significant influence on the responses. The response amplitude approaches that with infinite bond defect when the defect width becomes larger than the longitudinal wavelength of the layer λ_{lL}. The amplitude variation may still be detectable as the bond compliance increases when the defect width is smaller than $0.05\lambda_{lL}$.

Figure 6 shows the response when the SAM scans over an area with a bond defect of different shapes. The normalized normal bond compliance is 6, and shear bond compliance is 3. The solid line corresponds to the bond defect with Gaussian shape and the dashed line corresponds to the bond defect with a step-function shape. For smooth bond defect, the responses are also smooth and without oscillation. For a step-function bond defect, there is oscillation in the response; this oscillation is similar to that for the specimen with a surface crack.[11] In Eq. (6), the behaviors of the $N(k_x)$ and $S(k_x)$ depend on the shape of the defects. For bond defects with sharp edges, $N(k_x)$ and $S(k_x)$ will be functions with oscillation. This leads to the output amplitude oscillation at the sharp edges as shown in Fig. 6.

III. CONCLUSION

The results show that the SAM response is sensitive to bond compliance between layer and substrate. The contrast mechanism is due to the variation of specular reflection coefficient amplitude and phase difference between the specular and leaky surface wave. The reflection coefficient amplitude is significantly affected by the normal bond compliance. Shear bond compliance has influence on the phase difference between the specular and leaky surface wave by changing the surface wave velocity. The contrast also depends on the defocus, defect width, and material properties. Quantitative evaluation of the bond quality may be possible by minimizing the difference between the measured $V(z)$ curve and the simulated $V(z)$ curve.

[1] R. C. Bray, C. F. Quate, and R. Koch, Thin Solid Films **74**, 295–301 (1980).
[2] R. C. Addison, M. G. Somekh, and G. A. D. Briggs, *IEEE Ultrasonics Symposium* (IEEE, New York, 1986), pp. 775–795.
[3] M. G. Somekh, H. L. Bertoni, G. A. D. Briggs, and N. J. Burton, Proc. R. Soc. London, Ser. A **401**, 29–51 (1985).
[4] L. M. Brekhovskikh, *Waves in Layered Media* (Academic, New York, 1960), Chap. 2, pp. 65–80.
[5] S. Hirose and M. Kitahara, *Review of Progress in Quantitative Nondestructive Evaluation*, edited by D. O. Thompson and D. E. Chimenti (Plenum, New York, 1989), Vol. 8A, pp. 47–56.
[6] A. Pilarski, Mater. Eval. **43**, 765–764 (1985).
[7] D. B. Bogy and S. M. Graceski, J. Appl. Mech. **50**, 405–412 (1983).
[8] Y. C. Lee, J. O. Kim, and J. D. Achenbach, J. Acoust. Soc. Am. **94**, 923–925 (1993).
[9] G. W. Farnell and E. L. Adler, *Physical Acoustic*, edited by W. P. Mason and R. N. Thurston (Academic, New York, 1972), Vol. 9, Chap. 2, pp. 110–213.
[10] J. Kushibiki, T. Ishikaua, and N. Chubachi, Appl. Phys. Lett. **57**, 1967–1971 (1990).
[11] G. A. D. Briggs, *Acoustic Microscopy* (Clarendon, Oxford, 1992), Chap. 12, pp. 260–288.

A technique for measuring the ellipticity and rotation of the polarization plane of ultrasound

V. V. Gudkov[a] and B. V. Tarasov
Institute for Metal Physics, Ural Department of Russian Academy of Sciences, Ekaterinburg 620219, Russia

(Received 16 April 1996; accepted for publication 24 July 1998)

A technique for investigating magnetoacoustic phenomena such as the ultrasonic analogs of the Faraday, Cotton–Mouton, and Kerr effects is reported. This technique makes it possible to measure the ellipticity and the angle of rotation of the polarization plane of ultrasound. Measurements were made using data on amplitude and phase variations of the voltage on a receiving piezoelectric transducer as a function of the magnetic induction. © *1998 Acoustical Society of America.* [S0001-4966(98)01411-8]

PACS numbers: 43.35.Yb [HEB]

INTRODUCTION

The need to obtain quantitative data on the ellipticity ε and the angle of rotation of the polarization plane ϕ (or the major ellipse axis, when $\varepsilon \neq 0$) arises during investigation of magnetoacoustic polarization phenomena (MPP) which are ultrasonic analogs of the well-known magnetooptic Faraday, Cotton–Mouton, and Kerr effects. The first two effects refer to the bulk phenomena and the third to the surface phenomena since an alteration of the polarization takes place at the interface of two media which have different magnetoelastic properties.

Ultrasonic analogs of the Faraday and Cotton–Mouton effects have been discovered in single crystals of yttrium-iron garnet under magnon-phonon resonance.[1,2] The magnitudes of ε and ϕ obtained in these experiments were rather large and it was possible to evaluate them by distorting the exponential decay for the ultrasonic echo pulses in the oscilloscope screen. Rotation of the polarization was later found in metals due to an interaction of ultrasound with conduction electrons at low temperatures.[3] The values of ϕ obtained in metals were fairly small; therefore a technique for precise investigation of rotation of the polarization was developed.[4] It was based on the measurements of amplitude versus a magnetic field for two cases: (i) a field parallel and (ii) antiparallel to the wave vector **k**, while the receiving piezoelectric transducer (receiver) was rotated through the angle $\psi \neq 0$ or $\pm\pi/2$ with respect to the generating transducer (generator) (see Fig. 1). This technique might be applied to investigation of the Faraday effect. The effect is odd with respect to the inversion of magnetic induction **B**:

$$\phi(B) = -\phi(-B), \quad \varepsilon(B) = -\varepsilon(-B). \tag{1}$$

To improve the technique and to make it applicable for measuring not only ϕ but ε as well, the phase measurements were included[5] in the above scheme. This also gave rise to the measurement of phase velocities $s^{\pm}$ and absorption $\Gamma^{\pm}$ of circularly polarized modes when MPP are due to both circular magnetic birefringence and circular magnetic dichroism (i.e., due to differences in the magnetic field dependences of phase velocities and of absorption for two circularly polarized normal modes).

A further advance[6] in the technique of ultrasonic polarimetry introduced the acoustic analog of the Cotton–Mouton effect. Originally, it was thought that the measurements should be taken with the direction of **B** defined. However, there were two different values of ψ, namely, $\psi_1 = \pi/4$ and $\psi_2 = -\pi/4$. Such a variant made possible the study of MPP which are neither characterized by properties of symmetry with respect to **B** inversion nor described by Eq. (1) nor by any other. A generalization of this technique for arbitrary values of ψ_1 and ψ_2 was presented in Ref. 7. Unfortunately, the method described in the above two references required existence of a state characterized by $\varepsilon = 0$ and $\phi = 0$ at a definite **B**. This requirement proved to be a sufficient restriction when applied to magneto-ordered materials.

This paper describes a new technique with no such a restriction. Moreover, the possibility of using this technique to investigate a recently discovered[8] ultrasonic analog of the Kerr effect is discussed. The method[5] often used for measuring ε and ϕ for the Faraday effect (see, for example, Refs. 9–11) is briefly given in Sec. II.

I. GENERAL EXPRESSIONS

As in the previous papers,[5–7] a technique is used to measure the amplitude and phase of the voltage on the receiver. A traveling wave regime is arranged in a specimen or other actions are undertaken to eliminate the effect from numerical reflections of ultrasound from the specimen's boundaries.

Let us consider propagation of a shear ultrasonic wave along the positive direction of the z axis. Elastic shifts **A** at a moment t are given by $\mathbf{A}(z,t) = A_1\mathbf{u}_1 + A_2\mathbf{u}_2$, where $\mathbf{u}_1$ and $\mathbf{u}_2$ are the unit vectors of the x and y axes, respectively. On a complex plane (x, iy) the vector **A** corresponds to a complex number $A(z,t) = A_1 + iA_2$, which may be represented as the sum of two circular components $A^+(z,t)$ and $A^-(z,t)$. Figure 2 shows the rotation direction of these components; the directions of the polarization of the generator and receiver (the directions are defined by the unit vectors $\mathbf{u}_g$ and $\mathbf{u}_r$, respectively); and the positive directions for estimating the angles ϕ, ψ, and Ψ (the angle between $\mathbf{u}_1$ and $\mathbf{u}_g$).

[a]Electronic mail: gudkov@imp.uran.ru

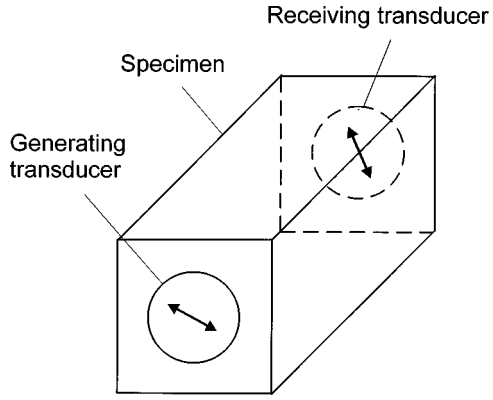

FIG. 1. Location of piezoelectric transducers on a specimen. The arrows indicate the polarization of the transducers.

Elastic vibrations excited by the generator, which is located at $z=0$, are spread by shear bulk modes. They are assumed to be of an elliptical polarization (the most general case). It should be noted that circular and linear polarizations are particular variants of an elliptical one (when $|\varepsilon|=1$ or $\varepsilon=0$, respectively). Each mode, indicated by an index l, is characterized by the absorption coefficient Γ_l, ellipticity ε_l, wave vector $\mathbf{k}_l$, and the direction of the major ellipse axis, defined by φ_l^+ and φ_l^- phases, which are independent of z and t. The modulus of ε_l is the ratio of the minor and major ellipse axes. Its sign indicates the direction of the $\mathbf{u}$ movement over the elliptical trajectory: minus corresponds to the movement similar to the rotation when the $(-)$-polarized mode propagates (i.e., counter-clockwise motion if we look along the positive direction of the z axis) and plus corresponds to the $(+)$-polarized mode (clockwise rotation).

Elastic shifts, defined at the complex plane, are due to propagation of the lth normal mode. These are given as a sum of two circular components:

$$A_l(z,t)=A_l^+(z,t)+A_l^-(z,t), \tag{2}$$

where

$$A_l^{\pm}(z,t)=a_l^{\pm}\exp\{-\Gamma_l z\}\exp\{\pm i(\omega t-k_l z\mp\varphi_l^{\pm}\pm\Psi)\}, \tag{3}$$

$a_l^{\pm}$ are real and determine the amplitudes of circular components, k_l are z components of $\mathbf{k}_l=(0,0,k_l)$, and ω is the cyclic frequency of ultrasound. Using these definitions we can write

$$A^{\pm}(z,t)=\exp\{\pm i\omega t\}a^{\pm}\exp\{i(\Psi\mp\varphi^{\pm})\}, \tag{4}$$

where

$$a^{\pm}\exp\{i(\Psi\mp\varphi^{\pm})\}\equiv\sum_l a_l^{\pm}\exp\{-\Gamma_l z\}\times\exp\{\mp i(k_l z\pm\varphi_l^{\pm}\mp\Psi)\}. \tag{5}$$

Note that $a^+(z=0)=a^-(z=0)$ and $\varphi^+(z=0)=\varphi^-(z=0)$. These relations are due to the linear polarization of ultrasonic vibrations called forth by a piezoelectric transducer in a $\mathbf{u}_g$ direction.

Ellipticity and the angle of rotation of the polarization are presented in terms of $a^{\pm}$ and $\varphi^{\pm}$ as

$$\varepsilon=\frac{a^+-a^-}{a^++a^-},\quad \phi=-\frac{1}{2}(\varphi^--\varphi^+). \tag{6}$$

For this study it is convenient to introduce a parameter,

$$p=\frac{a^-\exp(i\varphi^-)}{a^+\exp(i\varphi^+)}, \tag{7}$$

and to transform Eq. (6) as follows:

$$\varepsilon=\frac{1-|p|}{1+|p|},\quad \phi=-\frac{1}{2}\mathrm{Im}[\ln(p)]. \tag{8}$$

Thus, in order to estimate ε and ϕ the amplitudes and phases of two circular components of ultrasonic vibrations or, more accurately, the ratio of the amplitudes and the difference in phases of the components should be measured.

Since the receiver is sensitive to vibrations which are parallel to the direction $\mathbf{u}_r$, we should write an expression for the projection of $\mathbf{A}(z,t)$ on $\mathbf{u}_r$ as

$$\begin{aligned}A_r(z,t)=\mathbf{A}\cdot\mathbf{u}_r&=\mathrm{Re}[(A^++A^-)u_r^*]\\&=\mathrm{Re}\{a^+\exp[i(\omega t-\varphi^+-\psi_1)]\\&\quad+a^-\exp[-i(\omega t-\varphi^-+\psi_1)]\},\end{aligned} \tag{9}$$

where $*$ denotes the operation of complex conjugation and the complex number $u_r=\exp[i(\psi_1+\Psi)]$ corresponds to the $\mathbf{u}_r$ vector.

Ultrasonic vibrations A_r initiate the ac voltage

$$\eta A_r=U\cos(\omega t-\vartheta) \tag{10}$$

on the receiver, η^2 is the transformation coefficient of the energy of elastic vibrations into the energy of the electric field, U is the amplitude of the voltage, and ϑ is the phase.

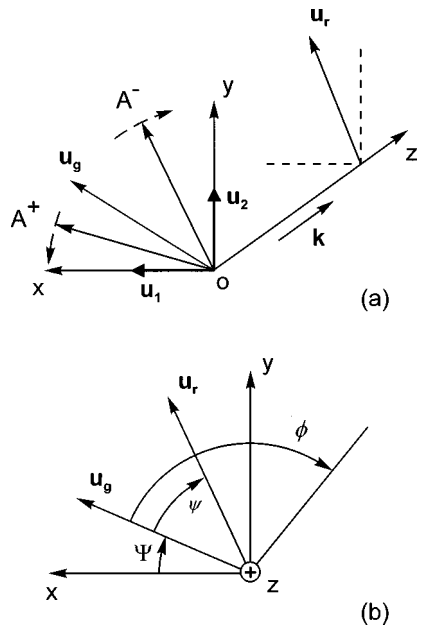

FIG. 2. (a) Directions of the polarization of the generating piezoelectric transducer ($\mathbf{u}_g$) and the receiving one ($\mathbf{u}_r$) and directions of rotation of circular components $A^{\pm}$; (b) the positive direction for estimating the angles introduced in the text.

Using A_r from Eq. (9), Eq. (10) can be written in the following form:

$$[a^+\cos(\varphi^+ + \psi_1) + a^-\cos(\varphi^- - \psi_1)]\cos\omega t + [a^+\sin(\varphi^+ + \psi_1) + a^-\sin(\varphi^- - \psi_1)]\sin\omega t = \frac{U}{\eta}[\cos\omega t\cos\vartheta + \sin\omega t\sin\vartheta]. \tag{11}$$

Since Eq. (11) is valid for an arbitrary t, it can be transformed into two equations:

$$a^+\cos(\varphi^+ + \psi_1) + a^-\cos(\varphi^- - \psi_1) = \frac{U}{\eta}\cos\vartheta, \tag{12}$$

$$a^+\sin(\varphi^+ + \psi_1) + a^-\sin(\varphi^- - \psi_1) = \frac{U}{\eta}\sin\vartheta. \tag{13}$$

Multiplying the left- and right-hand sides of Eq. (13) by i and adding the result to Eq. (12) we obtain

$$a^+\exp[i(\varphi^+ + \psi_1)] + a^-\exp[i(\varphi^- - \psi_1)] = \frac{U}{\eta}\exp i\vartheta. \tag{14}$$

II. THE FARADAY EFFECT

It should be noted that this effect relates to odd phenomena and is observed when the direction of the waves' propagation is parallel to the vector of magnetic induction and to a rotational symmetry axis of the nth order ($n \geqslant 3$): $\mathbf{k}_l \| C_n \| \mathbf{B} = (0,0,B)$.

From Eq. (1), when $\varepsilon = 0$ and $\phi = 0$ at $B = 0$, it follows that $a^+ = a^-$ and $\varphi^+ = \varphi^-$ and Eq. (14) for $B = 0$ assumes the form

$$2a_0\exp i\varphi_0\cos\psi_1 = \frac{U_0}{\eta}\exp i\vartheta_0, \tag{15}$$

where a_0 and φ_0 are the values of $a^\pm$ and $\varphi^\pm$ at $B = 0$, respectively, as well as any other equation with 0 index.

Equation (14) is written for an arbitrary $B = B_1 \neq 0$, denoting $U(B_1)$ as U_1 and $\vartheta(B_1)$ as ϑ_1:

$$a^+(B_1)\exp[i(\varphi^+(B_1) + \psi_1)] + a^-(B_1) \times \exp[i(\varphi^-(B_1) - \psi_1)] = \frac{U_1}{\eta}\exp i\vartheta_1. \tag{16}$$

From the Onsager relations for hydrotropic media,[12]

$$a^+(B) = a^-(-B) \quad \text{and} \quad \varphi^+(B) = \varphi^-(-B). \tag{17}$$

Denoting $U(-B_1)$ as U_2 and $\vartheta(-B_1)$ as ϑ_2 we can rewrite Eq. (16) in which $B_2 = -B_1$. In accordance with Eq. (17), substituting $a^\pm(-B_1)$ and $\varphi^\pm(-B_1)$ by $a^\mp(B_1)$ and $\varphi^\mp(B_1)$, respectively, it follows that

$$a^+(B_1)\exp[i(\varphi^+(B_1) - \psi_1)] + a^-(B_1) \times \exp[i(\varphi^-(B_1) + \psi_1)] = \frac{U_2}{\eta}\exp i\vartheta_2. \tag{18}$$

After dividing the left- and right-hand sides of Eqs. (16) and (18) by the corresponding sides of Eq. (15), the following system may be obtained:

$$\begin{aligned} &\frac{a^+(B_1)}{a_0}\exp[i(\varphi^+(B_1) - \varphi_0 + \psi_1)] + \frac{a^-(B_1)}{a_0}\exp[i(\varphi^-(B_1) - \varphi_0 - \psi_1)] = 2\cos\psi_1\frac{U_1}{U_0}\exp[i(\vartheta_1 - \vartheta_0)], \\ &\frac{a^+(B_1)}{a_0}\exp[i(\varphi^+(B_1) - \varphi_0 - \psi_1)] + \frac{a^-(B_1)}{a_0}\exp[i(\varphi^-(B_1) - \varphi_0 + \psi_1)] = 2\cos\psi_1\frac{U_2}{U_0}\exp[i(\vartheta_2 - \vartheta_0)]. \end{aligned} \tag{19}$$

The solution of this system is

$$\frac{a^\pm(B_1)}{a_0}\exp[i(\varphi^\pm(B_1) - \varphi_0)] = \frac{(U_2/U_0)\exp[i(\vartheta_2 - \vartheta_0 \mp \psi_1)] - (U_1/U_0)\exp[i(\vartheta_1 - \vartheta_0 \pm \psi_1)]}{2i\sin(\mp\psi_1)}. \tag{20}$$

Let us introduce

$$\Delta\vartheta_i = \vartheta_i - \vartheta_0 \quad \text{and} \quad N_i = -20\lg\frac{U_i}{U_0}, \tag{21}$$

which are the variations of the phase and attenuation of the signal (dB) caused by the alteration of B from 0 to B_1. It should be noted that $\Delta\vartheta_i$ and N_i are the only parameters that are measured experimentally. Now we can obtain p, according to Eq. (7):

$$p = \frac{10^{-N_1/20}\exp[i(\Delta\vartheta_1 - \psi_1)] - 10^{-N_2/20}\exp[i(\Delta\vartheta_2 + \psi_1)]}{10^{-N_2/20}\exp[i(\Delta\vartheta_2 - \psi_1)] - 10^{-N_1/20}\exp[i(\Delta\vartheta_1 + \psi_1)]}, \tag{22}$$

ε and ϕ can be also obtained using Eq. (8). After completing some operations we establish:

$$|p|^2=\frac{10^{-N_1/10}+10^{-N_2/10}-2\times10^{-(N_1+N_2)/20}\cos(\Delta\vartheta_1-\Delta\vartheta_2-2\psi_1)}{10^{-N_1/10}+10^{-N_2/10}-2\times10^{-(N_1+N_2)/2o}\cos(\Delta\vartheta_1-\Delta\vartheta_2+2\psi_1)}, \tag{23}$$

and

$$\phi=\frac{1}{2}\arctan\frac{[10^{-N_1/10}-10^{-N_2/10}]\sin 2\psi_1}{[10^{-N_1/10}+10^{-N_2/10}]\cos 2\psi_1-2\times10^{-(N_1+N_2)/20}\cos(\Delta\vartheta_1-\Delta\vartheta_2)}. \tag{24}$$

If MPP are due to circular magnetic dichroism and birefringence, it is possible to determine the magnetic-state-dependent components of the absorption $[\Delta\Gamma^{\pm}=\Gamma^{\pm}(B)-\Gamma_0]$ and those for phase velocity $[\Delta s^{\pm}=s^{\pm}(B)-s_0]$ of two circularly polarized normal modes:

$$\Delta\Gamma^{\pm}=-\frac{1}{z_0}\ln\frac{a^{\pm}}{a_0} \quad \text{and} \quad \Delta s^{\pm}=-\frac{s_0^2}{\omega z_0}(\varphi^{\pm}-\varphi_0),$$

where z_0 is the distance, covered by ultrasound in the specimen. According to Eq. (20),

$$\Delta\Gamma^{\pm}=-\frac{1}{2z_0}\ln\frac{10^{-N_1/10}+10^{-N_2/10}-2\times10^{-(N_1+N_2)/20}\cos(\Delta\vartheta_2-\Delta\vartheta_1\mp2\psi_1)}{4\sin^2\psi_1}, \tag{25}$$

and

$$\Delta s^{\pm}=-\frac{s_0^2}{\omega z_0}\arctan\frac{10^{-N_1/20}\cos(\Delta\vartheta_1\pm\psi_1)-10^{-N_2/20}\cos(\Delta\vartheta_2\mp\psi_1)}{10^{-N_1/20}\sin[(\Delta\vartheta_1\pm\psi_1)-10^{-N_2/20}\sin(\Delta\vartheta_2\mp\psi_1)}. \tag{26}$$

III. THE COTTON–MOUTON EFFECT

The second well-known type of MMP, namely, the acoustic analog of the Cotton–Mouton effect, is observed under $\mathbf{k}\perp\mathbf{B}$. It refers to even phenomena and conforms to the following relations:

$$\phi(B)=\phi(-B) \quad \text{and} \quad \varepsilon(B)=\varepsilon(-B). \tag{27}$$

The method of measuring ε and ϕ in this case consists of evaluating the amplitude and phase variation of the signal at no less than two different B (B_1 and B_2) with respect to a specific initial $B=B_0$ using three different angles ψ: ψ_1, ψ_2, and ψ_3.

The relevant equations may be obtained on the basis of Eq. (16), while performing appropriate substitutions,

$$a^+(B_0)\exp[i(\varphi^+(B_0)+\psi_1)]+a^-(B_0)\times\exp[i(\varphi^-(B_0)-\psi_1)]=\frac{U_0}{\eta}\exp i\vartheta_0, \tag{28}$$

$$a^+(B_1)\exp[i(\varphi^+(B_1)+\psi_1)]+a^-(B_1)\times\exp[i(\varphi^-(B_1)-\psi_1)]=\frac{U_1}{\eta}\exp i\vartheta_1, \tag{29}$$

and

$$a^+(B_2)\exp[i(\varphi^+(B_2)+\psi_1)]+a^-(B_2)\times\exp[i(\varphi^-(B_2)-\psi_1)]=\frac{U_2}{\eta}\exp i\vartheta_2. \tag{30}$$

Denoting the left-hand side of Eq. (28) as a complex number A_0, and dividing Eqs. (29) and (30) by (28), we establish

$$\frac{a^+(B_1)}{A_0}\exp[i(\varphi^+(B_1)+\psi_1)]+\frac{a^-(B_1)}{A_0}\times\exp[i(\varphi^-(B_1)-\psi_1)]=10^{-N_1(B_1)/20}\exp[i\Delta\vartheta_1(B_1)], \tag{31}$$

and

$$\frac{a^+(B_2)}{A_0}\exp[i(\varphi^+(B_2)+\psi_1)]+\frac{a^-(B_2)}{A_0}\times\exp[i(\varphi^-(B_2)-\psi_1)]=10^{-N_1(B_2)/20}\exp[i\Delta\vartheta_1(B_2)]. \tag{32}$$

Similar equations for $\psi=\psi_2$ follow:

$$\frac{a^+(B_1)}{A_0}\exp[i(\varphi^+(B_1)+\psi_2)]+\frac{a^-(B_1)}{A_0}\times\exp[i(\varphi^-(B_1)-\psi_2)]=10^{-N_2(B_1)/20}\{\exp[i\Delta\vartheta_2(B_1)]\}10^{-L_2/20}\exp i\lambda_2, \tag{33}$$

and

$$\frac{a^+(B_2)}{A_0}\exp[i(\varphi^+(B_2)+\psi_2)]+\frac{a^-(B_2)}{A_0}\times\exp[i(\varphi^-B_2)-\psi_2)]=10^{-N_2(B_2)/20}\{\exp[i\Delta\vartheta_2(B_2)]\}10^{-L_2/20}\exp i\lambda_2, \tag{34}$$

where L_2 and λ_2 describe variations in amplitude (dB) and phase of the signal, respectively, due to the differences in linkage of the transducers with the specimen while ψ is being changed from ψ_1 to ψ_2. Note, that N_2 and $\Delta\vartheta_2$ are defined with respect to the values determined when $B=B_0$

and $\psi=\psi_1$. One more change in ψ produces the following equations in addition to Eqs. (31)–(34):

$$\frac{a^+(B_1)}{A_0}\exp[i(\varphi^+(B_1)+\psi_3)]+\frac{a^-(B_1)}{A_0}\times\exp[i(\varphi^-(B_1)-\psi_3)]=10^{-N_3(B_1)/20}\{\exp[i\Delta\vartheta_3(B_1)]\}10^{-L_3/20}\times[\exp i\lambda_3]10^{-L_2/20}\exp i\lambda_2, \tag{35}$$

and

$$\frac{a^+(B_2)}{A_0}\exp[i(\varphi^+(B_2)+\psi_3)]+\frac{a^-(B_2)}{A_0}\times\exp[i(\varphi^-B_2)-\psi_3)]=10^{-N_3(B_2)/20}\{\exp[i\Delta\vartheta_3(B_2)]\}10^{-L_3/20}\times[\exp i\lambda_3]10^{-L_2/20}\exp i\lambda_2. \tag{36}$$

Here L_3 and λ_3 have the same origin as L_2 and λ_2 but correspond to the variation of ψ from ψ_2 to ψ_3. Dividing Eq. (35) by (36) and introducing

$$\frac{a^\pm(B_j)}{A_0}\exp[i\varphi^\pm(B_j)]=F_j^\pm,\quad N_k(B_j)=N_{kj},\quad L=10^{-L_2/20}\exp i\lambda_2, \tag{37}$$

and

$$\Delta\vartheta_k(B_j)=\Delta\vartheta_{kj},$$

we establish that

$$F_1^+\exp[i\psi_3]+F_1^-\exp[-i\psi_3]=10^{-(N_{31}-N_{32})/20}\exp[i(\Delta\vartheta_{31}-\Delta\vartheta_{32})]\times\{F_2^+\exp[i\psi_3]+F_2^-\exp[-i\psi_3]\}. \tag{38}$$

The solution of Eqs. (31)–(34) may be written as follows:

$$F_j^\pm=\frac{10^{-N_{1j}/20}\exp[i\Delta\vartheta_{1j}]\exp[\mp i\psi_2]-L\times10^{-N_{2j}/20}\exp[i\Delta\vartheta_{2j}]\exp[\mp i\psi_1]}{2(\mp i)\sin(\psi_2-\psi_1)}. \tag{39}$$

After substituting Eq. (39) into Eq. (38) we determine L:

$$L=\frac{\sin(\psi_3-\psi_2)}{\sin(\psi_3-\psi_1)}\,\frac{10^{-(N_{11}-N_{31})/20}\exp i(\Delta\vartheta_{11}-\Delta\vartheta_{31})-10^{-(N_{12}-N_{32})/20}\exp i(\Delta\vartheta_{12}-\Delta\vartheta_{32})}{10^{-(N_{21}-N_{31})/20}\exp i(\Delta\vartheta_{21}-\Delta\vartheta_{31})-10^{-(N_{22}-N_{32})/20}\exp i(\Delta\vartheta_{22}-\Delta\vartheta_{32})}, \tag{40}$$

where

$$10^{-L_2/10}=\frac{\sin^2(\psi_3-\psi_2)}{\sin^2(\psi_3-\psi_1)}\{10^{-[N_{11}-N_{31}]/10}+10^{-[N_{12}-N_{32}]/10}-2\times10^{-[N_{11}-N_{31}+N_{12}-N_{32}]/20}\cos(\Delta\vartheta_{11}+\Delta\vartheta_{32}-\Delta\vartheta_{31}-\Delta\vartheta_{12})\}\times\{10^{-[N_{21}-N_{31}]/10}+10^{-[N_{22}-N_{32}]/10}-2\times10^{-[N_{21}-N_{31}+N_{22}-N_{32}]/20}\cos(\Delta\vartheta_{21}+\Delta\vartheta_{32}-\Delta\vartheta_{31}-\Delta\vartheta_{22})\}^{-1}, \tag{41}$$

and

$$\lambda_2=\arctan\{10^{-[N_{11}+N_{21}-2N_{31}]/20}\sin(\Delta\vartheta_{11}-\Delta\vartheta_{21})-10^{-[N_{11}+N_{22}-N_{32}-N_{31}]/20}\sin(\Delta\vartheta_{11}+\Delta\vartheta_{32}-\Delta\vartheta_{22}-\Delta\vartheta_{31})-10^{-[N_{12}+N_{21}-N_{31}-N_{32}]/20}\sin(\Delta\vartheta_{12}+\Delta\vartheta_{31}-\Delta\vartheta_{32}-\Delta\vartheta_{21})+10^{-[N_{12}+N_{22}-2N_{32}]/20}\sin(\Delta\vartheta_{12}-\Delta\vartheta_{22})\}\times\{10^{-[N_{11}+N_{21}-2N_{31}]/20}\cos(\Delta\vartheta_{11}-\Delta\vartheta_{21})-10^{-[N_{11}+N_{22}-N_{32}-N_{31}]/20}\cos(\Delta\vartheta_{11}+\Delta\vartheta_{32}-\Delta\vartheta_{22}-\Delta\vartheta_{31})-10^{-[N_{12}+N_{21}-N_{31}-N_{32}]/20}\cos(\Delta\vartheta_{12}+\Delta\vartheta_{31}-\Delta\vartheta_{32}-\Delta\vartheta_{21})+10^{-[N_{12}+N_{22}-2N_{32}]/20}\cos(\Delta\vartheta_{12}-\Delta\vartheta_{22})\}^{-1}. \tag{42}$$

Now the parameter p, which is present in Eq. (8), may be obtained at an arbitrary B in the following form:

$$p(B)=\frac{F^-(B)}{F^+(B)}=\frac{L\times10^{-N_2(B)/20}\exp\{i[\Delta\vartheta_2(B)+\psi_1]\}-10^{-N_1(B)/20}\exp\{i[\Delta\vartheta_1(B)+\psi_2]\}}{10^{-N_1(B)/20}\exp\{i[\Delta\vartheta_1(B)-\psi_2]\}-L\times10^{-N_2(B)/20}\exp\{i[\Delta\vartheta_2(B)-\psi_1]\}}, \tag{43}$$

where $N_1(B)$ and $\Delta\vartheta_1(B)$ are variations of the amplitude (dB) and phase of the signal due to the change in the magnetic induction from B_0 to B measured at $\psi=\psi_1$; $N_2(B)$ and $\Delta\vartheta_2(B)$ are variations for $\psi=\psi_2$, but the variations are defined with reference to the initial state at $B=B_0$ and $\psi=\psi_1$. L is determined by Eq. (40).

Finally,

$$|p|^2=\{10^{-[L_2+N_2(B)]/10}+10^{-N_1(B)/10}-2\times10^{-[L_2+N_2(B)+N_1(B)]/20}\cos[\Delta\vartheta_2(B)-\Delta\vartheta_1(B)-\psi_2+\psi_1+\lambda_2]\}\times\{10^{-[L_2+N_2(B)]/10}+10^{-N_1(B)/10}-2\times10^{-[L_2+N_2(B)+N_1(B)]/20}\cos[\Delta\vartheta_2(B)-\Delta\vartheta_1(B)+\psi_2-\psi_1+\lambda_2]\}^{-1}, \tag{44}$$

and

$$\phi(B)=\tfrac{1}{2}\arctan\{10^{-[L_2+N_2(B)]/10}\sin 2\psi_1+10^{-N_1(B)/10}\sin\psi_2-2\times10^{-[L_2+N_2(B)+N_1(B)]/20}\sin 2(\psi_1+\psi_2)$$
$$\times\cos[\Delta\vartheta_2(B)-\Delta\vartheta_1(B)+\lambda_2]\}\{10^{-[L_2+N_2(B)]/10}\cos 2\psi_1+10^{-N_1(B)/10}$$
$$\times\cos 2\psi_2-2\times10^{-[L_2+N_2(B)+N_1(B)]/20}\cos 2(\psi_1+\psi_2)\cos[\Delta\vartheta_2(B)-\Delta\vartheta_1(B)+\lambda_2]\}^{-1}. \quad (45)$$

If the values of ϕ and ε are known at a certain B_0 (according to our designations they are ϕ_0 and ε_0), the measurements at the two angles ψ_1 and ψ_2 are enough to determine L. As a result of Eqs. (6) and (7) for this case,

$$p_0=\frac{1-\varepsilon_0}{1+\varepsilon_0}\exp(-i2\phi_0). \quad (46)$$

Using Eq. (43) it is possible to obtain the following:

$$L=10^{-(N_1-N_2)/20}\exp[i(\Delta\vartheta_1-\Delta\vartheta_2)]$$
$$\times\frac{\exp(i\psi_2)+p_0\exp(-i\psi_2)}{\exp(i\psi_1)+p_0\exp(-i\psi_1)}. \quad (47)$$

To summarize, it should be mentioned that as far as Eq. (27) was not used in an explicit form, the formulas obtained for this case may be applied to determine ε and ϕ even for investigating phenomena which are not characterized by any property of symmetry involving an inversion of **B**.

IV. KERR EFFECT

A typical diagram for such an experiment is presented in Fig. 3. Medium I is isotropic as expected, while elastic properties of medium II depend on **B**. In such a case a change of polarization occurs only at the interface of the media. A description of the polarization at point 3 may be obtained with the use of Eqs. (2)–(8). We must take into account, however, that there are two circularly polarized normal modes and their contribution to the right part of Eq. (4) should be multiplied by factors $R^{\pm}\exp i\rho^{\pm}$ as soon as the ultrasound passes through point 2. These factors describe the ellipticity and rotation of the polarization which appear due to reflection of ultrasound from the interface of the media. Probably, after reflection, the (+)-polarized mode should change the polarization and become a (−)-polarized mode (if the polarizations in the system K'' were defined in which the z-axis is parallel to the wave vectors of the reflected waves) and vice versa for (−) polarization. However, this circumstance is not significant since the absorption and phase velocities are equal for these two modes in the medium I. Thus,

$$A^{\pm}(z,t)=\exp\{\pm i\omega t\}(R^{\pm}\exp i\rho^{\pm})^{\theta(z_2-z)}a_0^{\pm}$$
$$\times\exp\{-\Gamma^{\pm}(z-z_1)\}$$
$$\times\exp\{\mp i[k^{\pm}(z-z_1)\pm\varphi_o^{\pm}\mp\Psi]\}$$
$$\equiv\exp\{\pm i\omega t\}a^{\pm}\exp\{i(\Psi\mp\varphi^{\pm})\}, \quad (48)$$

where $a_0^{\pm}=a_0$ are amplitudes of the modes at $z=z_1$, $\varphi_0^{\pm}$ are initial phases, and $\theta(z)$ is the step-function. Such a transformation leads to a new definition of $a^{\pm}$ and $\varphi^{\pm}$, but does not change the meaning. As a result, the procedure of ε and ϕ evaluation presented in Sec. III is quite applicable and Eqs. (41)–(47) may also be used in the case in question.

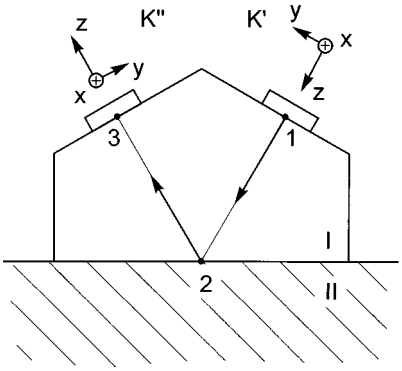

FIG. 3. An experimental setup to investigate the ultrasonic analog of the Kerr effect.

V. CONCLUSION

While investigating magnetic crystals it is not necessary to use a precise method for measuring ε and ϕ since the values obtained in the experiment are rather large and can be evaluated with a less complicated technique.[1,2]

Quite a different situation arises when the bulk MPP are studied in normal metals[10,11] and magnetic poly-crystals.[13] The values of ε and ϕ may be quite small. Thus, the described method is the only one applicable. The same may be said concerning the Kerr effect even when considering magnetic single crystals. In Ref. 8 it was reported that ε and ϕ were less than 1% and 1 degree, respectively, and were obtained in an experiment dealing with reflection of ultrasound from the interface between a yttrium–iron garnet and quartz. Such small variations of polarization are not important in relation to any practical application. However, they are important for science since they provide information about physical characteristics of the object studied.

Indirect confirmation of this statement can be seen in Ref. 14, where the amplitude on the receiver as a function of magnetic field $A(H)$ is compared with $\Delta\Gamma^{-}(H)$ calculated with the use of Eq. (25). In fact, these two types of curves are the results of direct measurement of ultrasonic absorption in tungsten and one was obtained while taking into account variations of the polarization. The data were applied to determine nonlocal conductivity of the metal using the position in the H-scale of the peak caused by resonant interaction of ultrasound with a circularly polarized electromagnetic wave. It can be seen that the data of the direct measurement have to be corrected by a few kOe in keeping with a proper experimental approach.

ACKNOWLEDGMENTS

We would like to acknowledge the financial support by the International Science Foundation (Grant No. RGD000).

[1] H. Matthews and R. C. Le Craw, ''Acoustic wave rotation by magnon-phonon interaction,'' Phys. Rev. Lett. **8**(10), 397–399 (1962).
[2] B. Luthi, ''Ferro-acoustic resonance in yttrium iron garnet,'' Phys. Lett. **3**(6), 285–287 (1963).
[3] B. K. Jones, ''The attenuation of ultrasound by electrons in aluminum,'' Philos. Mag. **9**(98–99), 217–230 (1964).
[4] J. R. Boyd and J. D. Gavenda, ''Attenuation and rotation of plane-polarized ultrasound in copper on longitudinal magnetic field,'' Phys. Rev. **152**(2), 645–658 (1966).
[5] V. V. Gudkov and K. B. Vlasov, ''Measurements of rotation of the polarization plane and the ellipticity of ultrasonic waves in magnetically polarized media,'' Fiz. Met. Metalloved. **46**(2), 254–261 (1978) (in Russian).
[6] A. B. Rinkevich, ''Determination of parameters of an ultrasonic wave in a magnetically polarized medium,'' Metrologia **8**, 36–40 (1982) (in Russian).
[7] V. V. Gudkov, ''Some additions to the technique for measuring the ellipticity and rotation of the polarization plane of ultrasound,'' Deposited article No. 5348-B90 (21.09.1990), All-Union Institute for Science and Technological Information (in Russian).
[8] A. M. Burkhanov, B. V. Tarasov, K. B. Vlasov, and V. V. Gudkov, ''Ultrasonic analogue of Kerr effect,'' Ultrasonics World Congress, Berlin 1995, Proceedings, Part 1 of 2 (1996), pp. 233–236.
[9] V. V. Gudkov, ''Rotation of polarization and ellipticity of ultrasound in helicon-phonon resonance conditions in indium,'' Solid State Commun. **44**(2), 229–231 (1982).
[10] V. V. Gudkov and K. B. Vlasov, ''Quantum oscillations of rotation of the polarization and ellipticity of ultrasound,'' Phys. Lett. A **102**(3), 129–132 (1984).
[11] V. V. Gudkov and A. V. Tkach, ''Magnetoacoustic oscillations of ellipticity in indium,'' Philos. Mag. Lett. **65**(50), 267–271 (1992).
[12] L. Onsager, ''Reciprocal relations in irreversible processes,'' Phys. Rev. **38**(12), 2265–2279 (1931).
[13] A. M. Burkhanov, K. B. Vlasov, V. V. Gudkov, and I. V. Zhevstovskikh, ''Ellipticity and rotation of the polarization plane of ultrasound nickel ferrite in experiment, corresponding to geometry of Cotton-Mouton effect,'' Akust. Zh. **34**(6), 991–997 (1988) [English translation: Sov. Phys. Acoust. **34**(6), 569–572 (1988)].
[14] V. V. Gudkov and I. V. Zhevstovskikh, ''Specificity of electromagnetic absorption of circularly polarized ultrasound in tungsten in the Doppler-shifted cyclotron resonance region,'' Zh. Eksper. i Teor Fiz. **92**(1), 208–220 (1987) [English translation: Sov. Phys. JETP **65**(1), 150–158 (1987)].

Generalized material model for lead magnesium niobate (PMN) and an associated electromechanical equivalent circuit

Jean C. Piquette and Stephen E. Forsythe
Naval Undersea Warfare Center, 1176 Howell Street, Newport, Rhode Island 02841-1708

(Received 25 July 1997; revised 2 February 1998; accepted 24 July 1998)

An existing one-dimensional nonlinear material model of lead magnesium niobate [J. C. Piquette and S. E. Forsythe, ''A nonlinear model of lead magnesium niobate (PMN),'' J Acoust. Soc. Am. **101**, 289–296 (1997)] is generalized to three dimensions. The resulting theory is applied to two practical systems: the ''thickness expander plate'' and the ''length expander bar.'' Linearizing the theory results in an electromechanical equivalent circuit that is applicable to predicting the first-order behavior of transducers based on either of these practical systems. The methods used are sufficiently general that the circuit is also appropriate for piezoelectric, and even for electrostatic, transducers. Preliminary experimental data that confirm the validity of the circuit are presented. Connections between the constants of the theory and those of piezoelectricity are derived, and a general expression for the coupling coefficient is obtained. Known theoretical coupling coefficients for piezoelectric and electrostatic transducers are recovered as special cases. The coupling coefficient of the PMN bar at zero prestress and zero remanent polarization is examined in some detail. For this case it is found that, to a good approximation, the bias voltage of the optimal (i.e., maximum) coupling coefficient is $\sqrt{2}$ times the bias voltage which produces the maximum effective piezoelectric d_{33}. A simple formula for estimating second harmonic distortion at zero stress and remanent polarization is given. The D field for the bar is obtained in terms of a Maclaurin series in stress. This series is asymptotic in the electric field, and is useful for estimating harmonic distortion when the stress or remanent polarization are nonzero. [S0001-4966(98)00911-4]

PACS numbers: 43.38.Ar, 43.20.Px, 43.30.Yj, 43.58.Vb [SLE]

INTRODUCTION

Recently, a one-dimensional material model for the behavior of lead magnesium niobate (PMN) was described.[1] The model is a generalization of a theory of electrostriction by Mason.[2] In order to broaden its applicability, the model is generalized here to three dimensions. The theory is solved for two practical cases: the ''thickness expander plate'' and the ''length expander bar,'' as considered in Ref. 3. The first-order behavior resulting from these nonlinear solutions is summarized in a lumped-parameter equivalent circuit. The methods used to derive the circuit are sufficiently general that it is equally applicable to transducers which incorporate a piezoelectric, electrostatic, or electrostrictive actuator. In this sense, the equivalent circuit may be considered to be ''universal'' (i.e., it is not restricted to any one of these three transducer types).

In Sec. I the material model is generalized to three dimensions, and the two practical applications are derived. The equivalent circuit is presented in Sec. II. Circuit elements are expressed in such a way that both the thickness expander plate and the length expander bar are subsumed. Special cases of this equivalent circuit are the piezoelectric[3] transducer and the Hunt[4] electrostatic transducer. The coupling coefficient for the general case, as well as for several particular cases, is discussed in Sec. III. Experimental data are presented in Sec. IV. A summary and conclusion are given in Sec. V. Appendix A presents connections between the constants of the theory and those of piezoelectricity. Appendix B furnishes approximate analytical solutions of the theory for the D field in the case of the bar, and discusses the problem of estimating harmonic distortion for nonzero stress or remanent polarization.

I. PMN THEORY GENERALIZED TO THREE DIMENSIONS

In Ref. 1 it is postulated that the strain at zero stress of PMN is exactly quadratic in the displacement field D. This postulate is continued here, and extended to three dimensions. (It is worthwhile noting here that numerous data sets have been analyzed since the appearance of Ref. 1, and these data sets have been found to be consistent with this postulate in the sense that agreement between theory and experiment is similar to that seen in Fig. 3 of Ref. 1. The postulate also has been found to continue to hold to a similar degree of accuracy under conditions of prestress as high as 83 MPa.) In analogy to Ref. 2, constants Q are introduced to represent the strength of electrostriction, but a somewhat more complex material model is considered here than was considered there. Although the underlying electrostrictive material is symmetric, suggesting the viability of a two-elastic-constant model as used in Ref. 2, the imposition of a bias or a remanent polarization breaks the symmetry, with the result that a greater number of material constants must be retained. [As can be seen by examining Table VIII, pp. 202–204 of Ref. 3, even $BaTiO_3$, for which the theory of Ref. 2 was developed, exhibits unique values for more than two elastic constants, owing to the broken symmetry arising from the remanent polarization. Thus more elastic constants must be retained if

the piezoelectric crystal resulting from the polarization (or biasing) of an electrostrictive material is to be fully described. Here, it is desired to retain a sufficient number of matrix elements to describe the behavior of the usual piezoelectric ceramics,[3] as well as the behavior[5] of PMN. See p. 177 of Ref. 3 for a useful representation of the required nonzero parameters, and the symmetries these parameters must exhibit, for this case.] Five elastic constants are retained for consistency with the materials of interest. The retained elastic constants are s_{11}^D, s_{12}^D, s_{13}^D, s_{33}^D, and s_{44}^D. (Alternatively, the corresponding elastic *c*-constants could be used.) Here, and in what follows, it is to be understood that the notations for the active and passive material constants, and variables, are the standard ones.[2,3] (Of course, in the absence of a bias, the underlying PMN material is isotropic. Nonetheless, the imposition of a bias breaks this simple symmetry. In the case of PMN, the specific numerical values of the material constants are herein assumed to be experimentally determined at each bias of interest.) The elements retained in, and the symmetries imposed upon, the *Q*-matrix are also those necessary for a proper description of the behavior of PMN. (Cf. Ref. 5, the ''*m*-matrix'' described on p. 127. The required symmetries of the *Q*-matrix are the same.) The retained elements of the *Q*-matrix are Q_{13}, Q_{33}, and Q_{44}.

The equations which result from generalizing the model of Ref. 1 to three dimensions by imposing the assumed properties[6–8] are

$$E_1=\frac{D_1-P_0^{(1)}}{\sqrt{(\epsilon_0\epsilon_{11}^T)^2-a(\epsilon_{11}^T)^2W}}-2Q_{33}T_1D_1-2Q_{13}T_2D_1 -2Q_{13}T_3D_1-4Q_{44}T_6D_2-4Q_{44}T_5D_3, \tag{1}$$

$$E_2=\frac{D_2-P_0^{(2)}}{\sqrt{(\epsilon_0\epsilon_{22}^T)^2-a(\epsilon_{22}^T)^2W}}-4Q_{44}T_6D_1-2Q_{33}T_2D_2 -2Q_{13}T_3D_2-2Q_{13}T_1D_2-4Q_{44}T_4D_3, \tag{2}$$

$$E_3=\frac{D_3-P_0^{(3)}}{\sqrt{(\epsilon_0\epsilon_{33}^T)^2-a(\epsilon_{33}^T)^2W}}-4Q_{44}T_5D_1-4Q_{44}T_4D_2 -2Q_{33}T_3D_3-2Q_{13}T_1D_3-2Q_{13}T_2D_3, \tag{3}$$

$$S_1=s_{11}^DT_1+s_{12}^DT_2+s_{13}^DT_3+Q_{33}D_1^2+Q_{13}D_2^2+Q_{13}D_3^2, \tag{4}$$

$$S_2=s_{12}^DT_1+s_{11}^DT_2+s_{13}^DT_3+Q_{13}D_1^2+Q_{33}D_2^2+Q_{13}D_3^2, \tag{5}$$

$$S_3=s_{13}^DT_1+s_{13}^DT_2+s_{33}^DT_3+Q_{13}D_1^2+Q_{13}D_2^2+Q_{33}D_3^2, \tag{6}$$

$$S_4=s_{44}^DT_4+4Q_{44}D_2D_3, \tag{7}$$

$$S_5=s_{44}^DT_5+4Q_{44}D_1D_3, \tag{8}$$

and

$$S_6=s_{66}^DT_6+4Q_{44}D_1D_2. \tag{9}$$

In Eqs. (1)–(3) $P_0^{(1)}$, $P_0^{(2)}$, and $P_0^{(3)}$ are the components of the remanent polarization vector $\mathbf{P}_0$, and $W\equiv\Sigma_{j=1}^3[(D_j-P_0^{(j)})/\epsilon_{jj}^T]^2$. For permanently poled ferroelectrics, only two physically independent dielectric permittivities (conventionally ϵ_{11}^T and ϵ_{33}^T) exist, and (usually) $P_0^{(1)}=P_0^{(2)}=0$; $P_0^{(3)}\equiv P_0$; thus

$$\epsilon_{11}^T=\epsilon_{22}^T. \tag{10}$$

(For unbiased PMN, we have $\epsilon_{11}^T=\epsilon_{22}^T=\epsilon_{33}^T$.) However, the equations have been written to allow for some generality. [If *all* components of $\mathbf{P}_0$ are negligible *and* no bias voltage V_0 is applied (i.e., if the symmetry is not broken), then $\epsilon_{11}=\epsilon_{22}=\epsilon_{33}\equiv\epsilon$ and the five passive constants considered would reduce to two, in conformity with the approach of Ref. 2.] Continuing the notation and terminology of Ref. 1, the product $\epsilon_0\,\epsilon$ denotes the *low-field* dielectric permittivity (at constant stress), and *a* is the ''saturation parameter'' (which is a measure of the rate at which saturation occurs in both the *P* vs *E* and *S* vs *E* curves). See Ref. 1 for more details. (It is of course an assumption that only a single saturation parameter is required for three dimensions.)

For the materials of interest, s_{66}^D of Eq. (9) is not an independent elastic constant. It is related to the other elastic constants according to

$$s_{66}^D=\begin{cases}2(s_{11}^D-s_{12}^D) & \text{(piezoelectric ceramics, biased PMN)}\\ s_{44}^D & \text{(unbiased PMN).}\end{cases} \tag{11}$$

It will be noted that Eqs. (1)–(11) embody a *preferred* set of axes. This was done to avoid a proliferation of elastic *s*-constants[9] (as would be required for complete generality).

It should also be understood that Eqs. (1)–(3) are each subject to a limitation of field strength similar to that noted in Ref. 1. In particular, a restriction of the form

$$\sum_{j=1}^{3}\sqrt{[(D_j-P_0^{(j)})/\epsilon_{jj}^T]^2}<0.99\epsilon_0/\sqrt{a} \tag{12}$$

applies to these equations. [This restriction on field strength can be relaxed, if desired, but more complicated expressions than those of Eqs. (1)–(3) would result, cf. Ref. 1.]

Next, following Ref. 3, two simple applications of the three-dimensional theory will be considered, viz., the ''thickness expander plate'' and the ''length expander bar.'' Only the nonlinear versions of these practical cases will be developed at this point. Consideration of the linearized versions of the equations will be postponed until the equivalent circuit is addressed in Sec. II.

A. Thickness expander plate

Applying the equations of the three-dimensional theory to the problem of a laterally constrained plate (i.e., $S_1=S_2=0$) polarized through its thickness (taken to be the ''3'' direction), assuming that *D* and *E* fields exist only in the ''3'' direction, and solving for E_3 and S_3 gives

$$E_3=\frac{D_3-P_0}{\sqrt{(\epsilon_0\epsilon_{33}^T)^2-a(D_3-P_0)^2}}-2\beta_2T_3D_3 +\beta_3(D_3^3-P_0^2D_3), \tag{13}$$

and

$$S_3=\beta_1 T_3+\beta_2 D_3^2, \tag{14}$$

where

$$\beta_1=s_{33}^D-\frac{2(s_{13}^D)^2}{s_{11}^D+s_{12}^D}=\frac{1}{c_{33}^D}, \tag{15}$$

$$\beta_2=Q_{33}-\frac{2s_{13}^D Q_{13}}{s_{11}^D+s_{12}^D}, \tag{16}$$

and

$$\beta_3=\frac{4Q_{13}^2}{s_{11}^D+s_{12}^D}. \tag{17}$$

[In order to derive Eq. (13), the zero of strain for S_1 and S_2 has been redefined so that Eq. (13) might satisfy a boundary condition which imposes $E_3=0$ when $T_3=0$ and $D_3=P_0$.] It will be noted that Eq. (13) and Eq. (14) are equivalent to Eq. (9) and Eq. (10), respectively, of Ref. 1 except that Eq. (13) contains an extra term in β_3. Only terms less than the cubic power in D were retained in the approximation considered in Ref. 1. Here, however, the perspective is taken that Eqs. (1)–(9) are ''exact,'' in the sense that these equations are not considered to arise from series expansions. Thus *all* terms have been retained in producing Eq. (13) and Eq. (14). [However, Eq. (13) also contains an extra term in D.] It is worthwhile remarking that the β_3 term of Eq. (13) is necessary in order for the linear form of the theory to give good agreement with piezoelectricity. These matters are considered further in Appendix A.

B. Length expander bar, end electroded

Next, consider the problem of a bar lying in the ''3'' direction with electrodes on its ends and poled along its length. Solving the three-dimensional equations for E_3 and S_3 subject to appropriate conditions ($T_1=T_2=T_4=T_5=T_6=0$; $D_1=D_2=0$) gives essentially the same solution as for the thickness expander plate, i.e., Eq. (13) and Eq. (14), except that the definitions of the ''β'' constants change to

$$\beta_1=s_{33}^D, \tag{18}$$

$$\beta_2=Q_{33}, \tag{19}$$

and

$$\beta_3=0. \tag{20}$$

In what follows, the reader should bear in mind the fact that Eq. (13) and Eq. (14) can be made to represent the solutions of either the thickness expander plate or the length expander bar by switching between the two sets of expressions for the parameters β_1, β_2, and β_3; viz., Eqs. (15)–(17) and Eqs. (18)–(20), respectively.

II. ''UNIVERSAL'' EQUIVALENT CIRCUIT

An equivalent circuit can be derived by linearizing the theory either for the length expander bar or the thickness expander plate. The linearization is achieved by writing the D field as $D=Q_0/A+q/A$, where q is the first-order charge and Q_0 is a fixed charge on the electrodes (each of area A), arising either from a fixed polarization P_0, a bias voltage V_0, or a combination of these. The strain is written in the form $S=S^{(0)}+S^{(1)}$, where $S^{(0)}$ is a fixed strain whose definition is at our disposal, and $S^{(1)}$ is the first-order strain. Similarly, the electric field is expressed as $E=E^{(0)}+E^{(1)}$. By substituting these expressions into either the theory for the plate or the bar, expanding the functional dependence about Q_0, and retaining only first-order terms, a first-order theory is deduced from which an equivalent circuit can be derived. (Boundary conditions are imposed in the manner of Ref. 3. A sufficiently narrow frequency range is assumed that frequency-independent circuit components may be used.) The resulting circuit is presented in Fig. 1. The circuit element values are given by

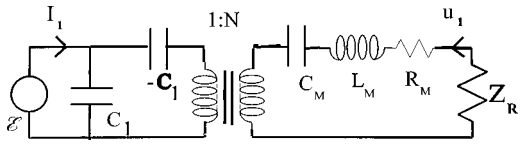

FIG. 1. ''Universal'' equivalent circuit based on the linearized version of the three-dimensional theory. $\mathscr{E}$ = first-order signal, or drive, voltage; I_1 = first-order current supplied by power amplifier; u_1 = first-order velocity of transducer radiating face; N = electromechanical transformer turns ratio $=(C_1/C_0)(Q_0/d)$; C_1 = total blocked capacitance $=m_s n_e/(Gd)$;

$$G=\frac{(\epsilon_0\epsilon_{33}^T)^2}{A[(\epsilon_0\epsilon_{33}^T)^2-a(Q_0/A-P_0)^2]^{3/2}}+4(\beta_2^2/\beta_1)Q_0^2/A^3$$
$$+\beta_3(3Q_0^2/A^3-P_0^2/A)-2\beta_2 T_3^{(0)}/A;$$

$C_0=-n_e Q_0\div(2\beta_2 Q_0 d/\beta_1 A-V_0)$; $T_3^{(0)}$ = constant stress (such as a prestress); P_0 = remanent polarization; V_0 = bias voltage; Q_0 = bias (or remanent) charge is a root of the equation;

$$V_0/d=\frac{Q_0/A-P_0}{\sqrt{(\epsilon_0\epsilon_{33}^T)^2-a(Q_0/A-P_0)^2}}+\beta_3(Q_0^2/A^2-P_0^2)Q_0/A$$
$$-2\beta_2(Q_0/A)T_3^{(0)};$$

C_M = total motional capacitance $=n_e\beta_1 d/(m_s A)$; L_M = total motional inductance $=M$ (''effective mass'' including loading mass; see Ref. 11); R_M = total motional resistance $=m_s r_M/n_e$; r_M = motional resistance (single element); Z_R = radiation impedance (see, e.g., Ref. 12); n_e = number of elements in each stack (elements are *electrically* in parallel, *mechanically* in series); m_s = number of stacks (applied mechanically in parallel to the transducer radiating face); d = plate separation (single element); A = surface area of active material (single element).

$$N=(C_1/C_0)(Q_0/d) \tag{21}$$

(N is the electromechanical transformer turns ratio),

$$C_1=m_s n_e/(Gd) \tag{22}$$

(C_1 is the ''blocked'' capacitance), where

$$G=\frac{(\epsilon_0\epsilon_{33}^T)^2}{A[(\epsilon_0\epsilon_{33}^T)^2-a(Q_0/A-P_0)^2]^{3/2}}+4(\beta_2^2/\beta_1)Q_0^2/A^3$$
$$+\beta_3(3Q_0^2/A^3-P_0^2/A)-2\beta_2 T_3^{(0)}/A, \tag{23}$$

and Q_0 is a root of the equation

$$V_0/d=\frac{Q_0/A-P_0}{\sqrt{(\epsilon_0\epsilon_{33}^T)^2-a(Q_0/A-P_0)^2}}+\beta_3(Q_0^2/A^2-P_0^2)$$
$$\times Q_0/A-2\beta_2(Q_0/A)T_3^{(0)} \tag{24}$$

(Q_0 is the bias charge, or remanent charge, on a single element). In the above equations, $T_3^{(0)}$ represents a constant stress (such as a prestress). For the case of the length-expander bar ($\beta_3=0$), Eq. (24) reduces to a fourth-degree polynomial; in the case of the plate it reduces to an eighth-degree polynomial.

In Eqs. (21)–(24) and in what follows, the actuator of the transducer is assumed to consist of ''stacks'' of active material, where each element of each stack acts electrically in parallel but mechanically in series. Each such stack contains n_e elements. Moreover, it is assumed that several such stacks act mechanically in parallel to drive the transducer face. There are m_s such *mechanically* parallel stacks; all such stacks are also wired *electrically* in parallel with each other. A is the area of one of the plates of a single element; d is the equilibrium separation between the plates of one element in the presence of the bias voltage V_0 and remanent polarization P_0; and $\mathscr{E}$ of Fig. 1 is the first-order driving voltage. (The circuit parameters are summarized in the caption to Fig. 1.) The second term in the quantity G, given by Eq. (23), multiplied by the area A, is the difference between the ''dielectric impermeability'' *at constant stress* (usually denoted as β_{33}^T) and that *at constant strain* (usually denoted by β_{33}^S) predicted by the theory. (The *entire* quantity GA is equal to β_{33}^S. See Appendix A for further consideration of this parameter.)

In Eq. (21) C_0 is a capacitive term (not explicitly appearing in the circuit) given by

$$C_0=\frac{-n_eQ_0}{2\beta_2Q_0d/\beta_1A-V_0}. \tag{25}$$

When the (rather unusual) circumstance arises in which the denominator of Eq. (25) is zero, the electrostrictive and electrostatic forces are in balance. In this situation, the electromechanical turns ratio N is zero, and no first harmonic output occurs.

The motional impedance of the circuit Z_m is given by

$$\begin{aligned}Z_m&=j\omega L_M+R_M+\frac{1}{j\omega C_M}\\&=j\omega M+\frac{m_s}{n_e}r_M+\frac{m_sA}{j\omega n_e\beta_1d}\end{aligned} \tag{26}$$

(with M the total ''effective'' motional mass[10,11] including ''loading'' mass, r_M the motional resistance of a single element, and ω the angular frequency). The quantity Z_R is the radiation impedance. (See, e.g., Ref. 12.)

In deriving the expressions for the circuit elements, an additional stress has been added to the equations of the theory to account for the presence of the electrostatic force F_e (i.e., the force which each electrode exerts on the other owing to the presence of charge). The purpose of including such a term is to permit the recovery of the electrostatic transducer, and the calculations are only approximately valid in the limits of vanishingly small values of β_2, β_3, and $T_3^{(0)}$. This force, presumed to exist only in the ''3'' direction, is given approximately by

$$F_e\approx-\tfrac{1}{2}(D_3-P_0)E_3A. \tag{27}$$

(The first harmonic contribution arising from this force is approximately $-qV_0/d$, with q the signal charge.) The equivalent circuit of Fig. 1, with element values as given, will recover both the length-expander bar and the thickness expander plate piezoelectric equivalent circuits. [Cf. Ref. 3, p. 237, Fig. 24; and p. 239, Fig. 26, respectively.] To do so, make the replacements $V_0=0$ (since the ceramic is assumed to be unbiased); $T_3^{(0)}=0$ (since the influence of zeroth-order stress is not taken explicitly into account); $m_s=n_e=1$ (since these circuits involve single elements only); and either the ''plate'' or ''bar'' prescriptions for the parameters β_1, β_2, and β_3, given in Sec. I A and Sec. I B, respectively, are substituted as appropriate. [Account must also be taken of the fact that the circuit of Fig. 1 represents single-sided operation (i.e., one side of the ceramic is assumed stationary). In addition, the explicit V_0 term in Eq. (25) is set to zero because the electrostatic force is ignored in these circuits. Expressions which relate the parameters of the present theory to those of piezoelectric theory, given in Appendix A, must also be used. An unimportant minus sign arises from a negative surface velocity boundary condition imposed at the right side of the ceramic by Berlincourt *et al.* See Ref. 3, p. 235, Eq. (111). Finally, the fact that $\epsilon_0\epsilon_{33}^T$ of the theory is equivalent to ϵ_{33}^T of Ref. 3 should be kept in mind.]

In a similar way, the equivalent circuit for the single-sided electrostatic transducer of Ref. 4 is recovered with the replacements $P_0=0$; $T_3^{(0)}=0$; $a=0$; $\beta_2=\beta_3=0$; and $m_s=n_e=1$. In order to recover Hunt's equations for the equilibrium charge and displacement [Ref. 4, p. 179, Eq. (6.9a) and Eq. (6.9b)], generally the ''zeroth-order'' version of Eq. (14) is required viz.,

$$S_3^{(0)}=\beta_1T_3^{(0)}+\beta_2(Q_0/A)^2. \tag{28}$$

However, for the case of the electrostatic transducer the contribution from the zeroth-order electrostatic force must (obviously) also be included. Using the zeroth-order electrostatic force deducible from Eq. (27), with β_2 and β_3 presumed small, we get

$$\begin{aligned}S_3^{(0)}&=\beta_1T_3^{(0)}+\beta_2(Q_0/A)^2\\&\quad+\frac{1}{2}\frac{\beta_1(Q_0/A-P_0)^2}{\sqrt{(\epsilon_0\epsilon_{33}^T)^2-a(Q_0/A-P_0)^2}}.\end{aligned} \tag{29}$$

In deriving Hunt's equations, it is also important to note that $T_3^{(0)}=0$, and again β_2, P_0, and a are to be set to zero as well. Hunt's zeroth-order electric field follows from Eq. (24).

Since the theory underlying the equivalent circuit is nonlinear, it is important to estimate harmonic distortion. Such an estimate is provided by solving the theory (prior to linearization) for the second-to-first harmonic ratio in the surface velocity of the transducer. When the electrostatic force, pre-stress, and remanent polarization are negligible, the approximate result is

$$\left|\frac{u_2}{u_1}\right| \approx \left|\frac{(Z_m+Z_R)_{1\omega}}{(Z_m+Z_R)_{2\omega}} \frac{E_1[-1+a(E_0^2+E_1^2)+5a^2(E_0^4-2E_0^2E_1^2)+a^3(3E_0^6+5E_0^4E_1^2)]}{2E_0(1+aE_0^2)(2+4aE_0^2+2a^2E_0^4-3aE_1^2+3a^2E_0^2E_1^2)}\right|, \tag{30}$$

where the subscripts on the impedance sum Z_m+Z_R indicate the harmonic for which the sum should be evaluated; $E_0 = V_0/d$ denotes the bias electric field; and $E_1=\mathscr{E}/d$ denotes the first harmonic driving electric field. This equation accurately predicts harmonic distortion for peak drive voltages as high as the bias voltage. For that case, the error between the harmonic ratio predicted by Eq. (30) and the exact harmonic ratio is less than 1.25 dB. For drives up to 75% of the bias, the error is less than 0.5 dB. For higher-level drives, or nonzero values of prestress and/or remanent polarization P_0, the calculation of harmonic distortion is more difficult. This matter is considered in Appendix B.

As with most equivalent circuits, the present one is an approximation to the underlying theory. Thus its application is more restricted than the theory. The present circuit yields an accurate prediction for the first harmonic output of the transducer if driving voltages are not extremely high. In particular, for peak ac drives up to 75% of the bias voltage, the first harmonic amplitude is predicted by the circuit to within approximately 1 dB of the exact value.

III. THE COUPLING COEFFICIENT

A. The general case

The coupling coefficient associated with a circuit having the topology of Fig. 1 is simply calculated in terms of the circuit capacitances[13] (once the usual technique of removing the transformer from the circuit to produce an all-electric representation is carried out). After simplification, the result for the square of the coupling coefficient in the general case is

$$k^2=\frac{\beta_1}{d^2GA}\left(\frac{2\beta_2 Q_0 d}{\beta_1 A}-V_0\right)^2, \tag{31}$$

where G and Q_0 are given by Eq. (23) and Eq. (24), respectively.

B. Piezoelectric thickness expander plate

Interesting special case solutions can be obtained for unbiased ($V_0=0$) and unstressed ($T_3^{(0)}=0$) piezoelectric ceramics. As a first example, consider the piezoelectric thickness expander plate. Applying the results given in Appendix A to the definition of G given by Eq. (23) [the expression for G which results is the right-hand side of Eq. (A10), multiplied by an extra factor of A; i.e., $GA=\beta_{33}^S$]; imposing the special case values of β_1, β_2, and β_3 for the thickness expander plate given in Sec. I A; and substituting into Eq. (31) (with $V_0=0$) yields

$$k^2=h_{33}^2/(\beta_{33}^S c_{33}^D). \tag{32}$$

This result is equivalent to the coupling coefficient of Berlincourt *et al.*[3] [Cf. Ref. 3, p. 191, Eq. (34).] Similar methods of calculation show that Eq. (31) also gives the correct coupling coefficient for the case of the length-expander bar [cf. Ref. 3, p. 191, Eq. (35)], accounting, of course, for the proper values of β_1, β_2, and β_3 which apply to that case.

C. Single-sided electrostatic transducer

In the case of the electrostatic transducer all terms that make the material between the plates ''active'' are set to zero, as is the remanent pole P_0, the prestress $T_3^{(0)}$, and the saturation parameter a. Hence, $\beta_2=\beta_3=0$; $P_0=0$; and $a=0$. With these substitutions, the equations for G and Q_0 simplify to

$$G=1/(\epsilon_0\epsilon_{33}^T A), \tag{33}$$

and

$$Q_0=\epsilon_0\epsilon_{33}^T A V_0/d. \tag{34}$$

Substituting Eq. (33) and Eq. (34), together with the assumed values of the other parameters, into Eq. (31) produces

$$k^2=\beta_1 V_0^2\epsilon_0\epsilon_{33}^T/d^2. \tag{35}$$

This expression for the coupling coefficient of the electrostatic transducer is seen to be equivalent to that of Hunt [Ref. 4, p. 181, Eq. (6.15)] with the identification that the definition of zero strain used here leads to the equivalence of the plate-separation parameter d of the present theory to the combination $d+x_0$ in Hunt's theory; that is, the definition of zero strain used here includes the strain induced by the bias voltage, which Hunt's definition does not. The remainder of Hunt's parameters ''go over'' to the parameters of the present theory according to $c_m\rightarrow\beta_1 d/A$ (cf. the definition of C_M in Fig. 1, with $m_s=n_e=1$); $C_0\rightarrow\epsilon_0\epsilon_{33}^T A/d$; and $E_0\rightarrow V_0$. (Of course, $\epsilon_{33}^T=1$ for the vacuum case studied by Hunt.)

D. PMN: The zero prestress length-expander bar

While the general case for PMN requires the use of Eq. (31), a special case can be considered in order to see the explicit dependence of the coupling coefficient on bias in a relatively simple way. For PMN the electrostatic force is negligible, so the explicit V_0 term of Eq. (31) can be omitted. It is also assumed that P_0 can be ignored (although this is not always an accurate assumption). Moreover, zero prestress is assumed here, and we consider only the case of the bar (i.e., $\beta_3=0$). Under these conditions, the coupling coefficient[14] for PMN resulting from Eq. (31) simplifies to

$$(k_{\mathrm{PMN}}^2) = \frac{4\beta_2^2(\epsilon_0\epsilon_{33}^T)^3(V_0/d)^2}{\beta_1\{[1+a(V_0/d)^2]^{5/2}+(4\beta_2^2/\beta_1)(\epsilon_0\epsilon_{33}^T)^3(V_0/d)^2\}}. \tag{36}$$

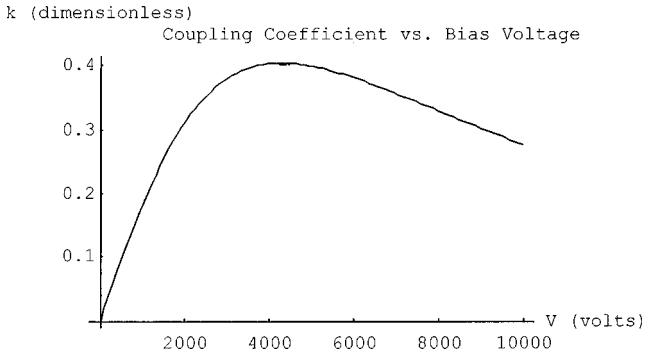

FIG. 2. Coupling coefficient k vs bias voltage V_0 for a typical PMN material. The thickness through which the bias is applied is $d=0.5$ cm. The case considered is a length expander bar at zero prestress.

The coupling coefficient k_{PMN} is plotted as a function of bias voltage in Fig. 2 using some *typical* numerical values for the parameters. [Strictly speaking, Fig. 2 is an approximation since the elastic ''constant'' s_{33}^D used to derive the plot has been held fixed, whereas it must generally vary at least somewhat with bias, as is suggested by the fact that $s_{11}^D \neq s_{33}^D$ for piezoceramics. While permittivity also varies with bias, this effect is already included in the theory (with the bias-variable permittivity being given, for the present case, by the reciprocal of the first term of Eq. (23) with the area A removed). Recall that ϵ_{33}^T denotes the *low-field* permittivity in these equations.] The peak value of k_{PMN}, approaching approximately 0.4 in Fig. 2, is fairly typical. In the *best* cases, such as for the material considered in Ref. 7, the peak value of k_{PMN} is closer to 0.5.

The ''optimal'' bias, i.e., the bias which causes the maximum value of (k_{PMN}^2), is

$$V_0^{(\mathrm{opt})} = d\sqrt{\frac{2}{3a}}, \tag{37}$$

and the value of (k_{PMN}^2) at $V_0^{(\mathrm{opt})}$ is

$$(k_{\mathrm{PMN}}^2)^{\mathrm{opt}} = \frac{1}{1+(25/24)\sqrt{5/3}a\beta_1/[\beta_2^2(\epsilon_0\epsilon_{33}^T)^3]}, \tag{38}$$

where, again, the variation of the elastic constant with bias has been ignored.

The maximum value of the effective d_{33} constant does not occur at the same bias as the maximum coupling coefficient. By computing $d_{33}=(\partial S_3/\partial E_3)_T$ using Eq. (6) (the general equation for S_3) subject to the conditions satisfied by the length-expander bar (i.e., $D_1=D_2=0$; $T_1=T_2=T_4=T_5=T_6=0$), it is found that

$$d_{33}^{(\mathrm{effective})} = \frac{2Q_{33}(\epsilon_0\epsilon_{33}^T)^2E_3}{(1+aE_3^2)^2} = 2Q_{33}D_3/[\beta_{33}^T]^{\mathrm{bias}}. \tag{39}$$

The second equality in Eq. (39) is presented to show the similarity of $d_{33}^{(\mathrm{effective})}$ to the equation for d_{33} that arises in deriving piezoelectricity, as given by Eq. (A3) in Appendix A. Notice that the role played in Eq. (A3) by the remanent polarization P_0 is played in Eq. (39) by the value of D_3 *at bias* [i.e., the zero-stress solution of Eq. (3) for D_3 evaluated at $E_3=V_0/d$, with $P_0=0$]. The quantity $[\beta_{33}^T]^{\mathrm{bias}}$ is the dielectric impermeability at constant stress, also evaluated at bias [i.e., the first term of Eq. (23), multiplied by A]. Computing the maximum value of $d_{33}^{(\mathrm{effective})}$ through differentiation with respect to E_3; substituting the bias field $E_3=V_0/d$; and thus solving for the ''optimal'' bias (with respect to maximizing d_{33}), one finds

$$V_0^{(\mathrm{opt})} = d\sqrt{\frac{1}{3a}}. \tag{40}$$

Comparing Eq. (37) with Eq. (40), it is seen that the bias voltage of the maximum coupling coefficient is $\sqrt{2}$ times the bias voltage of the maximum effective d_{33} at zero stress.

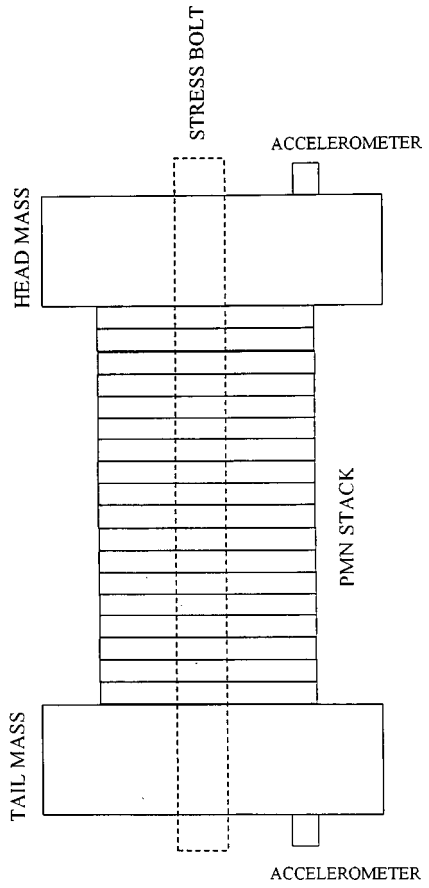

FIG. 3. The experimental setup.

IV. PRELIMINARY EXPERIMENT

A preliminary experiment was undertaken to attempt to verify the equivalent circuit. The experimental setup is shown in Fig. 3. The experiment was carried out on a sample that comprises an unloaded 18-element stack of 0.5-cm-thickness PMN circular rings, with each ring having an effective area of 0.00266 m^2. Such an unloaded stack may be considered to be two single-sided 9-element stacks mounted back to back along the zero-velocity plane which must be present owing to symmetry. The low-field relative dielectric permittivity of the sample material was first determined to be 18 200 using zero-bias measurements. (The D field is simply related to the first harmonic drive current, and the E field to the first harmonic drive voltage, with low-level drives assumed. The ratio of D to E gives the zero-bias permittivity.)

TABLE I. Comparison of experiment and theory for a single-sided PMN transducer.

			Experiment			Theory		
Freq. (Hz)	Bias (V)	Drive (V)	I_1 (A)	a_1 (m/s^2)	a_2/a_1	I_1 (A)	a_1 (m/s^2)	a_2/a_1
300	351.5	72.1	0.103	0.175	0.199	0.103	0.176	0.205
300	355.3	144.0	0.207	0.352	0.399	0.205	0.357	0.407
300	357.1	215.9	0.312	0.532	0.601	0.307	0.539	0.609
300	240.6	75.0	0.107	0.123	0.285	0.107	0.127	0.309
300	242.5	149.2	0.214	0.247	0.573	0.214	0.254	0.614
300	244.4	224.5	0.321	0.371	0.864	0.321	0.385	0.917
400	335.4	72.6	0.142	0.303	0.212	0.138	0.303	0.221
400	345.8	144.8	0.284	0.610	0.426	0.275	0.622	0.430
400	350.5	217.4	0.426	0.936	0.626	0.413	0.946	0.636
400	239.7	71.2	0.141	0.214	0.300	0.135	0.212	0.308
400	242.5	142.0	0.282	0.431	0.596	0.270	0.430	0.609
400	244.4	212.9	0.424	0.651	0.895	0.405	0.648	0.909
500	351.5	74.0	0.172	0.498	0.212	0.176	0.505	0.205
500	356.2	147.6	0.345	1.01	0.422	0.350	1.02	0.406
500	358.1	221.4	0.519	1.52	0.635	0.525	1.54	0.607
500	239.7	72.4	0.171	0.341	0.308	0.172	0.338	0.299
500	242.5	144.6	0.343	0.687	0.616	0.344	0.684	0.592
500	244.4	216.4	0.516	1.04	0.926	0.515	1.03	0.884

The Q_{33} electrostriction constant was determined to be 0.021 m^4/C^2 at zero bias. [Equation (14), evaluated for the case of the length-expander bar and zero stress, shows that second harmonic strain is simply related to first harmonic D field through Q_{33}.] Bias and drive voltages were then applied simultaneously. Axial acceleration was monitored by the use of accelerometers. Experimental limitations permitted only low-frequency, low-bias measurements. The results are summarized in Table I. The symbols a_1 and a_2 denote the first and second harmonic axial accelerations, respectively. The first six columns of the table are experimental data, and the last three columns are theory, based on the length-expander bar. Columns seven and eight are based on the equivalent circuit while column nine is based on Eq. (30). (The ratio $a_2/a_1=2u_2/u_1$, assuming harmonic excitation. Also, at low bias the saturation parameter a can be taken to be zero.) The equivalent circuit element values were evaluated using the results of the zero-bias measurements. (Although the parameter β_1 was not determined, the low-frequency limit of the circuit output is independent of that parameter.) Experimental results from columns four through six should be compared with corresponding theoretical results in columns seven through nine. As can be seen agreement is quite good, with most results differing by a few percent or less. The worst agreement is for the a_2/a_1 calculation for the fourth entry given for 300 Hz. The error in this case is approximately 8.4%.

V. SUMMARY AND CONCLUSION

A theory of PMN has been generalized to three dimensions. The two classic problems of the length-expander bar and the thickness expander plate were solved. A ''universal'' equivalent circuit that is applicable to electrostrictive, piezoelectric, and electrostatic transducers was given. The circuit is useful for approximately predicting first harmonic transducer output. The results of a preliminary experiment which investigated the correctness of the circuit were described. Second harmonic distortion can be estimated using a simple formula that was presented. A general formula for the coupling coefficient was obtained, and several special cases were considered. Future work will focus on applications including the effects of prestress.

ACKNOWLEDGMENTS

The PMN stack used in the experiment was designed and fabricated by Kim Benjamin. Special equipment for use in stack fabrication was provided by Raytheon, Portsmouth, RI. This work was supported by the Office of Naval Research.

APPENDIX A: RELATIONS TO PIEZOELECTRIC PARAMETERS

Derivations of the connections between the parameters of the present theory and those of the theory of piezoelectricity are given here. The first attempt to derive piezoelectricity from electrostriction was made by Mason. (See Ref. 2, pp. 301–303.) Such derivations were also carried out by Berlincourt and Jaffe.[15]

The definition of the piezoelectric g constant is[3]

$$g=(\partial S/\partial D)_T. \tag{A1}$$

This definition is straightforward to apply directly to the model equations. For the materials under consideration, the piezoelectric d constant is simply related to the g constant through the equation $d_{33}\beta_{33}^T=g_{33}$. The piezoelectric e and h constants are also related in a relatively simple manner to g [see Ref. 3, p. 189, Eq. (27)]. Thus it is a straightforward matter to relate all the piezoelectric constants to the constants of the present theory. (It is assumed that $P_0^{(3)}\equiv P_0$ is the only nonzero component of remanent polarization, and that the material is unbiased, i.e., $V_0=0$, and unstressed, i.e., $T_3^{(0)}=0$.) The results are

$$<\beta_{33}^T d_{31} = g_{31} = 2Q_{13}P_0, \tag{A2}$$

$$\beta_{33}^T d_{33} = g_{33} = 2Q_{33}P_0, \tag{A3}$$

$$\beta_{33}^S e_{33} = h_{33} = 2g_{31}c_{13}^D + g_{33}c_{33}^D = 2\beta_2^{\text{plate}} P_0 c_{33}^D, \tag{A4}$$

$$\beta_{11}^T d_{15} = g_{15} = 4Q_{44}P_0, \tag{A5}$$

$$\beta_{11}^s e_{15} = h_{15} = g_{15}c_{44}^D, \tag{A6}$$

and

$$\beta_{33}^S e_{31} = h_{31} = g_{31}(c_{11}^D + c_{12}^D) + g_{33}c_{13}^D, \tag{A7}$$

where in Eq. (A4) β_2^{plate} denotes the value of β_2 for the case of the plate, Eq. (16). In Eq. (A5) $\beta_{11}^T = 1/(\epsilon_0 \epsilon_{11}^T)$, where ϵ_{11}^T is the permittivity of Eq. (1). In Eq. (A6), β_{11}^S is given by

$$\beta_{11}^S = \beta_{11}^T + g_{15}h_{15}. \tag{A8}$$

The expression given for d_{31} in Eq. (A2) is equivalent to that found by Mason [Ref. 2, p. 301, Eq. (12.28)], once account is taken of notational differences. However, the expression for d_{33} given in Eq. (A3) differs from his expression [cf. Ref. 2, p. 303, Eq. (12.32)], but agrees with that of Ref. 15, p. 147, Eq. (30). The term in square brackets in Mason's Eq. (12.32) is equivalent to β_2 for the case of the plate, Eq. (16), whereas Eq. (A3), the equation for d_{33}, involves β_2 for the case of the bar, Eq. (19). Mason's equation is actually analogous to Eq. (A4), since his derivation is based on the behavior of a plate, which is controlled by h_{33}. (See Ref. 3, pp. 238–239.) Hence, Mason's equation actually calculates h_{33} (to within a factor of c_{33}^D), and not d_{33}.

In Eq. (A2) and Eq. (A3), the quantity β_{33}^T is the dielectric impermeability *at constant stress*, and is related to the dielectric permittivity ϵ_{33}^T of Eq. (3) of the theory through the equation $\beta_{33}^T = 1/(\epsilon_0 \epsilon_{33}^T)$. The quantity β_{33}^S of Eq. (A4) is the dielectric impermeability *at constant strain.* Its value can be determined from the calculations presented for the thickness expander plate, and is obtained by comparing the plate results to the relevant results from piezoelectric theory. [Compare C_1 of Eqs. (22)–(24) with C_0 of Fig. 26, p. 239 of Ref. 3, imposing $V_0 = 0$ and $T_3^{(0)} = 0$, assuming an unbiased piezoceramic at zero prestress, noting that $Q_0 = P_0 A$ is a root of Eq. (24) for these conditions, and using for β_1, β_2, and β_3 the plate expressions given by Eqs. (15)–(17), respectively.] The outcome of this comparison is

$$\beta_{33}^S = \frac{1}{(\epsilon_0 \epsilon_{33}^T)} + 4\beta_2^2 P_0^2 c_{33}^D + \frac{8Q_{13}^2 P_0^2}{s_{11}^D + s_{12}^D} \tag{A9}$$

(where β_2 has been explicitly retained for convenience, and denotes the plate value), or,

$$\beta_{33}^S = \beta_{33}^T + \frac{h_{33}^2}{c_{33}^D} + \frac{2g_{31}^2}{s_{11}^D + s_{12}^D}. \tag{A10}$$

Equation (A10) results from replacing the electrostrictive parameters of Eq. (A9) with the relevant piezoelectric parameters using the equations given above. [It is worthwhile pointing out that Eq. (A8) also follows from the theory by methods similar to those used to derive Eq. (A9).] The ''exact'' relationship between β_{33}^S and β_{33}^T based on piezoelectric theory can be deduced from Table XXXII of Ref. 2, p. 452. In SI units this relationship is

$$\beta_{33}^S = \beta_{33}^T + 2g_{31}h_{31} + g_{33}h_{33}. \tag{A11}$$

The right-hand-side of Eq. (A11) can be shown to be formally equivalent to the right-hand side of Eq. (A10), using the interconnections between the piezoelectric constants.

TABLE AI. Computed values of dielectric impermeability β_{33}^S for various materials compared with measured. Column 3 expression and results are based on present theory; expression and results of column 4 are based on ''exact'' piezoelectric theory. Numerical values are from Ref. 3, p. 202, Table VIII. (All numerical values are expressed in SI units.)

Material	β_{33}^S	$\beta_{33}^T + h_{33}^2/c_{33}^D + 2g_{31}^2/(s_{11}^D + s_{12}^D)$	$\beta_{33}^T + 2\,g_{31}\,h_{31} + g_{33}\,h_{33}$
PZT-4	1.78×10^8	1.77×10^8	1.77×10^8
PZT-5	1.36×10^8	1.37×10^8	1.36×10^8
$PbZr_{0.54}Ti_{0.46}O_3$	4.35×10^8	4.26×10^8	4.25×10^8
$BaTiO_3$	8.97×10^7	9.02×10^7	9.03×10^7
95-wt % $BaTiO_3$, 5-wt % $CaTiO_3$	1.24×10^8	1.14×10^8	1.12×10^8

Numerical values of the expressions of Eq. (A10) and Eq. (A11) are examined in Table AI. Here, values for the constants listed in Table VIII of Ref. 3, pp. 202–203, have been substituted. The value given for β_{33}^S has been computed by taking the reciprocal of the value listed for the dielectric permittivity at constant strain. It is noted here that if the β_3 term of Eq. (13) had been omitted, as was done in Ref. 1, the last two terms on the right-hand side of Eq. (A10) would be different, and the present theory would then not agree very well with piezoelectric theory.

An expression for the difference between the dielectric permittivity at constant stress and that at constant strain given in Ref. 15 [p. 145, Eq. (21)] yields results with generally the same accuracies for the computed values of β_{33}^S compared with those of Table AI, with the exception of the entry for 95%-wt $BaTiO_3$, 5%-wt $CaTiO_3$. In this case the expression of Ref. 15 gives a result with much better accuracy than Eq. (A10). This is likely due to the fact that the piezoelectric *d*-constants (required in the cited equation of Ref. 15) have been measured to better accuracy than the *g*- and *h*-constants [required in Eq. (A10)] as reported in the table of Ref. 3. The computed entries in Table AI for 95%-wt $BaTiO_3$, 5%-wt $CaTiO_3$, which exhibit errors approaching 10%, can be brought into agreement (to within the accuracy of the numerical values) by using *computed* values of *g* and *h* instead of the directly measured values. First, the two required *g*-constants are computed from the measured *d*-constants and β_{33}^T using Eq. (A2) and Eq. (A3). Next, the two *h*-constants are computed by substituting the resulting values of *g* into Eq. (A4) and Eq. (A7), along with the required *c*-constants. When evaluated in this manner, the value of h_{33} computed for 95%-wt $BaTiO_3$, 5%-wt $CaTiO_3$ is 1.80×10^8 V/m, a value that is over 7% greater than the measured value for h_{33} for this material as listed in the table of Ref. 3. The computed values for g_{31}, g_{33}, and h_{31} all come out to within less than 1% of the listed values. Thus, the relatively large error in h_{33} is sufficient to explain most of the discrepancy in the computed values of β_{33}^S in Table AI.

Good agreement between theory and data was reported in Ref. 1, despite the absence of the β_3 term in the equation used there to fit the data [i.e., the β_3 term of Eq. (13) was ignored there]. This is not inconsistent with the statement made here that this term is needed for good agreement with piezoelectric theory. Since $\beta_3=0$ in the theory for the length-expander bar, the agreement between theory and data noted in Ref. 1 almost certainly indicates that in the experiments considered the samples were acting more like length-expander bars than like thickness expander plates. No lateral motion occurs in the case of the thickness expander plate. This condition could not have obtained in the experiments considered since no lateral constraints were applied to the samples. On the other hand, in predicting piezoelectric properties from electrostriction the β_3 term was found to contribute to the *first-order* expression for β_{33}^S, owing to the influence of the strong remanent pole that is present in such materials.

APPENDIX B: APPROXIMATE SOLUTIONS AND HARMONIC DISTORTION

For the general case, calculation of harmonic distortion is difficult. One approach is entirely numerical: That is, a monofrequency driving electric field (with bias) can be input into Eq. (13), which can be solved numerically for *D*, and the result substituted into Eq. (14). A discrete Fourier transform (DFT) can then be then performed to determine harmonics. Another approach is to find an approximate analytical solution to the model equations and to use a power series expansion of the result to determine harmonics. Although tedious, this latter approach is viable if a modern symbolic manipulation computer program (such as Mathematica™, Maple™, or Macsyma™) is available.[16]

Since high drive voltages produce the greatest harmonic distortions, an asymptotic solution of the equations in electric field, parameterized by prestress, is useful in this regard. Such a solution of Eq. (13), for the case of the length-expander bar, can be written in the form

$$D=f_0+f_1T_3+f_2T_3^2+f_3T_3^3+f_4T_3^4, \tag{B1}$$

where f_0 through f_4 are functions of E given by

$$f_0=P_0+\frac{\epsilon_0\epsilon_{33}^T E}{\sqrt{1+aE^2}}, \tag{B2}$$

$$f_1=\frac{2\beta_2\epsilon_0\epsilon_{33}^T(\epsilon_0\epsilon_{33}^T E+P_0\sqrt{1+aE^2})}{(1+aE^2)^2}, \tag{B3}$$

$$\begin{aligned} f_2=&\frac{-2\beta_2^2\epsilon_0\epsilon_{33}^T}{(1+aE^2)^{7/2}}[-2\epsilon_0\epsilon_{33}^T P_0\sqrt{1+aE^2}\\ &+6a\epsilon_0\epsilon_{33}^T P_0E^2\sqrt{1+aE^2}+3aE^3((\epsilon_0\epsilon_{33}^T)^2+aP_0^2)\\ &+(-2(\epsilon_0\epsilon_{33}^T)^2+3aP_0^2)E], \end{aligned} \tag{B4}$$

$$\begin{aligned} f_3=&\frac{4\beta_2^3\epsilon_0\epsilon_{33}^T}{(1+aE^2)^5}[-10aE^3(\epsilon_0\epsilon_{33}^T)^3\\ &+\sqrt{1+aE^2}P_0(2(\epsilon_0\epsilon_{33}^T)^2-aP_0^2)\\ &+3aE^2\sqrt{1+aE^2}P_0(-7(\epsilon_0\epsilon_{33}^T)^2+aP_0^2)\\ &+4a^2E^4\sqrt{1+aE^2}P_0(3(\epsilon_0\epsilon_{33}^T)^2+aP_0^2)\\ &+4a^2E^5\epsilon_0\epsilon_{33}^T((\epsilon_0\epsilon_{33}^T)^2+3aP_0^2)+2E((\epsilon_0\epsilon_{33}^T)^3\\ &-6a\epsilon_0\epsilon_{33}^T P_0^2)], \end{aligned} \tag{B5}$$

and

$$\begin{aligned} f_4=&\frac{2\beta_2^4\epsilon_0\epsilon_{33}^T}{(1+aE^2)^{13/2}}[80a^3E^6\sqrt{1+aE^2}\epsilon_0\epsilon_{33}^T P_0((\epsilon_0\epsilon_{33}^T)^2+aP_0^2)+8\sqrt{1+aE^2}\epsilon_0\epsilon_{33}^T P_0(-(\epsilon_0\epsilon_{33}^T)^2+2aP_0^2)\\ &-40a^2E^4\sqrt{1+aE^2}\epsilon_0\epsilon_{33}^T P_0(9(\epsilon_0\epsilon_{33}^T)^2+2aP_0^2)-48aE^2\sqrt{1+aE^2}\epsilon_0\epsilon_{33}^T P_0(-4(\epsilon_0\epsilon_{33}^T)^2+3aP_0^2)+E(-8(\epsilon_0\epsilon_{33}^T)^4\\ &+120a(\epsilon_0\epsilon_{33}^T)^2P_0^2-15a^2P_0^4)+20a^3E^7((\epsilon_0\epsilon_{33}^T)^4+6a(\epsilon_0\epsilon_{33}^T)^2P_0^2+a^2P_0^4)+5a^2E^5(-23(\epsilon_0\epsilon_{33}^T)^4-54a(\epsilon_0\epsilon_{33}^T)^2P_0^2\\ &+5a^2P_0^4)-2aE^3(-44(\epsilon_0\epsilon_{33}^T)^4+135a(\epsilon_0\epsilon_{33}^T)^2P_0^2+5a^2P_0^4)]. \end{aligned} \tag{B6}$$

[It should come as no surprise that Eq. (B2), the zeroth-order stress solution, is equivalent to the result obtained when Eq. (13) is solved with T_3 set equal to zero. The method used to derive these formulas is described elsewhere.[17]] Since Eq. (B1) is an asymptotic expansion in E, it becomes increasingly accurate as drive levels are increased, and is less accurate for low-level drives. Numerical tests show that for a peak ac drive equal to 35% of the bias or greater, the error in the first harmonic strain based on the *D*-field determined from Eq. (B1) is about 0.2 dB or less. The error in the second harmonic is about 0.7 dB, and in the third harmonic is about 3 dB. (But the third harmonic amplitude is less than 1% of the first harmonic amplitude for this case.) For very high drive levels, the error can be very small. For example, in one numerical test using a bias of 0.9 MV/m, a peak ac drive equal to three times the bias, and a prestress of 12 ksi (82.7 Mpa), the errors in the harmonics of the strain determined using the value of the *D*-field calculated from Eq. (B1) are as follows: first harmonic, 0.017 dB; second harmonic, 0.021 dB; third harmonic, 0.006 dB; fourth harmonic, 0.213 dB; fifth harmonic, 0.250 dB; and sixth harmonic, 2.07 dB. In this case, the second harmonic amplitude is about twice the first harmonic amplitude; and the third harmonic amplitude is approximately equal to the first harmonic amplitude. The

sixth harmonic amplitude is about 2.5% of the first harmonic amplitude. Hence, Eq. (B1) results in accurate approximations for those harmonics which are most significant.

Upon substitution of Eq. (B1) into Eq. (14), and expansion of the resulting expression for S_3 into a power series in E, an expression for the harmonic components can be derived assuming $E=E_0+E_1\sin(\omega t)$, with E_0 the bias field. By collecting contributions to the first and second harmonics from each term of the power series, the second-to-first harmonic strain ratio can be computed using the approximation

$$\frac{S_2}{S_1}\approx-\frac{(1/2)c_2+(1/2)c_4+(15/32)c_6+(7/16)c_8}{c_1+(3/4)c_3+(5/8)c_5+(35/64)c_7}. \quad \text{(B7)}$$

Here, $c_1, c_2, \ldots$ are the coefficients of $\sin(\omega t), \sin^2(\omega t), \ldots$, respectively, in the power series expansion for D^2 and the numerical values in the numerator (denominator) are the contributions to the second harmonic (first harmonic) arising from each power of $\sin(\omega t)$. [Equation (B7) applies only to an unloaded sample, including prestress, and not to a full transducer. Generalization to a full transducer, however, is straightforward.]

[1] J. C. Piquette and S. E. Forsythe, ''A nonlinear material model of lead magnesium niobate (PMN),'' J. Acoust. Soc. Am. **101**, 289–296 (1997).

[2] W. P. Mason, *Piezoelectric Crystals and Their Application to Ultrasonics* (Van Nostrand, New York, 1950), pp. 296–304.

[3] D. A. Berlincourt, D. R. Curran, and H. Jaffe, ''Piezoelectric and piezomagnetic materials and their function in transducers,'' in *Physical Acoustics 1 (Part A)*, edited by W. P. Mason (Academic, New York, 1964), pp. 169–270.

[4] F. V. Hunt, *Electroacoustics* (Harvard U.P., Cambridge, 1954).

[5] G. H. Blackwood and M. A. Ealey, ''Electrostrictive behavior in lead magnesium niobate (PMN) actuators,'' Smart Mater. Struct. **2**, 124–133 (1993).

[6] X. D. Zhang and C. A. Rogers, ''A macroscopic phenomenological formulation for coupled electromechanical effects in piezoelectricity,'' J. Intell. Mater. Syst. Struct. **4**, 307–316 (1993).

[7] C. L. Hom, S. M. Pilgram, N. Shankar, K. Bridger, M. Massuda, and S. R. Winzer, ''Calculation of quasi-static electromechanical coupling coefficients for electrostrictive ceramic materials,'' IEEE Trans. Ultrason. Ferroelectr. Freq. Control **41**, 542–551 (1994).

[8] Reference 7 describes a three-dimensional theory of PMN that incorporates a phenomenological polarization model from Ref. 6. As discussed in Ref. 1, however, the hyperbolic tangent polarization model of Ref. 6 does not fit the available PMN data as accurately as the square root polarization model of Ref. 1. A three-dimensional generalization of the polarization model of Ref. 1 is incorporated within the present theory. Also, Eqs. (1)–(9) have been written out in full, following the practice of Ref. 2, rather than in the compact tensor notation of Ref. 7, in order that all the material symmetries imposed here are explicitly seen.

[9] It is assumed that a biased specimen of PMN behaves in a manner similar to a permanently polarized piezoelectric ceramic. Advantage is taken of this assumed behavior in orienting the preferred set of axes in such a way as to reduce the number of elastic constants required to represent material behavior. Thus it is assumed that if a remanent pole $\mathbf{P}_0$ exists (in the absence of a bias voltage), its direction is taken to be the ''3'' direction. This is the convention generally used in piezoelectricity, resulting in the reduction of the number of *s*-constants to the five retained here. Similarly, if no remnant exists but bias voltage is applied, the ''3'' direction is taken to be the direction of the corresponding *D*-field (denoted $\mathbf{D}_0$). Finally, should both a remanent pole $\mathbf{P}_0$ and a bias which produces field $\mathbf{D}_0$ exist, the ''3'' direction is taken to be the direction of the vector resultant $\mathbf{D}_0+\mathbf{P}_0$. Only in this latter case would remanent components $P_0^{(1)}$, $P_0^{(2)}$, $P_0^{(3)}$ all likely have unique values. The unique values would arise from the rotation of axes (such as that considered in Ref. 2, pp. 455–461) required to orient the ''3'' direction along the resultant $\mathbf{D}_0+\mathbf{P}_0$. Nonetheless, it is assumed that the rotation restricts the number of *s*-constants to five, and the number of permittivities to two.

[10] Since the equivalent circuit of interest represents a *single-sided* system, i.e., one end of the active material is assumed stationary, the effective mass may be considered to be a single lumped inductance, as depicted in Fig. 1. For a *double-sided* system, such as considered in Ref. 3, p. 237, Fig. 24; and p. 239, Fig. 26, *two* separate impedances are required in general, as shown there.

[11] Since frequency-independent circuit elements have been used in Fig. 1, the effective mass required depends on the frequency range, and loading mass, of interest. Consider first the case of *zero* loading mass. Owing to the behavior of the functions which arise in solving the wave equation, at frequencies well below resonance the effective mass is $\frac{1}{2}$ the ceramic mass, a result which is fairly obvious from the low-frequency behavior of the trigonometric-function circuit elements depicted in Ref. 3, p. 237, Fig. 24; and p. 239, Fig. 26, evaluated for the single-sided case. Near the frequency at which the total impedance of the trigonometric-function circuit elements vanishes in the circuits of Ref. 3 (which is not the true resonance frequency owing to the influence of the negative blocked capacitance), the effective mass is $4/\pi^2$ times the ceramic mass. This follows from solving for the frequency which causes the total impedance of the trigonometric-function circuit elements to vanish, and then determining what effective mass causes the total impedance of L_M and C_M of Fig. 1 to vanish at the same frequency. Consider next the case in which the loading mass is much greater than the ceramic mass. Here, the well-known result in which the effective mass is equal to the loading mass plus 1/3 the ceramic mass applies. Thus, it is not possible to represent the behavior of the system over the entire low-frequency-to-resonance interval with the simple frequency-independent circuit elements shown in Fig. 1. For *broadband* representation it is necessary to resort to the frequency-dependent circuit elements used in Ref. 3. The circuit of Fig. 1 can be generalized to the broadband case in a fairly obvious way, producing a circuit with the same topology as the circuits of Ref. 3.

[12] L. L. Beranek, *Acoustics* (McGraw-Hill, New York, 1954), p. 121, Fig. 5.5(a), for the case of a piston in an infinite baffle.

[13] D. Stansfield, *Underwater Electroacoustic Transducers* (Bath U.P., Bath, U.K., 1991), p. 82, Eq. (4.12).

[14] An expression for a PMN coupling coefficient is given in Ref. 7. However, that coupling coefficient differs in a fundamental way from the one presented here, since the Ref. 7 result yields nonzero values of k for zero bias voltage V_0. When $V_0=0$ (and $P_0=0$, as is assumed there), the output at the *fundamental* frequency must be zero, so the present coupling coefficient (which is a predictor of behavior at the fundamental) necessarily vanishes. The fact that nonzero coupling coefficients are predicted for zero bias from the theory of Ref. 7 means that *second harmonic output* is related to *first harmonic input* by that coefficient.

[15] D. Berlincourt and H. Jaffe, ''Elastic and piezoelectric coefficients of single-crystal barium titanate,'' Phys. Rev. **111**, 143–148 (1958).

[16] Equation (13) can also be solved exactly for the case of the bar, since in that case it is simply a fourth degree polynomial. However, that approach is not helpful for determining analytical expressions for the harmonics, owing to the complexity of the expressions. In fact, an attempt to obtain the first-order Maclaurin-series expansion in stress of the exact solution using Mathematica failed on a PC with 65 megabytes of physical memory. Hence, an approximate solution, such as the asymptotic solution given here, is more useful in deducing analytical expressions for harmonic components than is the exact solution.

[17] J. C. Piquette, ''Method for obtaining analytical corrective Maclaurin-series solutions to algebraic and transcendental systems,'' SIAM (Soc. Ind. Appl. Math.) J. Appl. Math. (in review).

A Fourier series solution for the radiation impedance of a finite cylinder

John L. Butler and Alexander L. Butler
Image Acoustics, Inc., 97 Elm Street, Cohasset, Massachusetts 02025

(Received 22 May 1998; accepted for publication 1 August 1998)

A mathematical model for the radiation impedance of a finite cylinder with extended rigid ends is developed using a Fourier series approach. This series approach is shown to be possible by modeling the cylinder as a widely separated periodic replica representation. Radiation impedance results are obtained for the cylinder operating in uniform, dipole, and cardioid radial modes of vibration. The cardioid mode is then used as a radiation impedance model for the underwater sound slotted cylinder transducer. © *1998 Acoustical Society of America.* [S0001-4966(98)02611-3]

PACS numbers: 43.38.Fx, 43.40.Rj, 43.20.Rz [SLE]

INTRODUCTION

The finite cylinder transducer shape is commonly used in underwater sound applications. In particular, the slotted finite cylinder transducer[1] has been found to be a useful source for low-frequency applications because of its small size. A modified equivalent sphere model with an area equal to two-thirds the actual radiating area of the cylinder has been used as an approximate radiation impedance model with some success.[2] However, the validity of this model may be questioned for large cylinder aspect ratios or large size parameters where the size is large compared to the wavelength of sound. Accordingly, we have developed a model based on a more rigorous mathematical foundation. The model is based on Robey's radiation impedance model[3] for a finite cylinder with uniform motion and rigid cylindrical extensions on the ends of the cylinder. His mathematical foundation is based on a Fourier integral approach which yields a solution in the form of an integral. Greenspon[4] developed a procedure for evaluating the remainder of the reactive part of Robey's integral. We shall develop a mathematical model with a simpler series solution which may be readily applied to nonuniform angular motion and used to model the radiation load on a slotted cylinder.

I. MATHEMATICAL MODEL

Consider the cylinder of height h and radius a with center located at $z=0$ and $r=0$, illustrated in cylindrical coordinates in Fig. 1 with rigid extensions along the z axis. These rigid cylindrical extensions provide significant simplification by allowing the velocity boundary conditions along the entire z direction to be applied at the radial distance $r=a$. This model is an approximation to the model of a finite cylinder with rigid end caps and approaches this case as the radius ''a'' decreases in size compared to the wavelength of sound in the adjacent medium. The rigid extension model was originally proposed by Laird and Cohen[5] to determine the far-field beam pattern response from a cylinder of finite extent.

The differential Helmholtz version of the wave equation may be written in cylindrical coordinates as

$$\frac{1}{r}\frac{\partial(r\partial p/\partial r)}{\partial r}+\frac{1}{r^2}\frac{\partial^2 p}{\partial \phi^2}+\frac{\partial^2 p}{\partial z^2}+k^2 p=0, \tag{1}$$

where p is the acoustic pressure, the wave number $k=\omega/c=2\pi/\lambda$, ω is the angular frequency, c is the sound speed, and λ is the wavelength. The cylindrical coordinates are the radius r, azimuth angle ϕ, and axial distance z.

The pressure is periodic in the ϕ angular direction with period 2π and because the pressure is also an even function, we may expand it in a Fourier cosine series as

$$p(r,\phi,z)=\sum_{n=0}^{\infty} p_n(r,z)\cos(n\phi), \tag{2}$$

where

$$p_n(r,z)=\frac{\epsilon_n}{\pi}\int_0^{\pi} p(r,\phi,z)\cos(n\phi)\,d\phi, \tag{3}$$

with $\epsilon_0=1$ and $\epsilon_n=2$ otherwise. If we now substitute Eq. (2) into Eq. (1), we obtain the Helmholtz differential equation for each nth angular mode as

$$\frac{1}{r}\frac{\partial(r\partial p_n/\partial r)}{\partial r}-\frac{n^2}{r^2}p_n+\frac{\partial^2 p_n}{\partial z^2}+k^2 p_n=0 \tag{4}$$

and have, accordingly, eliminated the second order differential in ϕ.

The second order differential in z could be eliminated, as Robey[3] did, by means of a Fourier integral transform along the z direction. However, since the velocity distribution has a finite value only on the surface of the active cylinder and is zero beyond $z=\pm h/2$, we would expect, as a result of spreading, the pressure to decrease to some small value as z increases along the surface $r=a$. Accordingly, we may consider this acoustic system to be analogous to an electrical band limited system; thus allowing the use of a periodic replicated model as illustrated in Fig. 2. In this model the active cylinder system is replicated to $\pm\infty$ in the $\pm z$ direction with period d. Because the model is now periodic, we may use a Fourier series rather than integral to obtain our solution if the period d is chosen large enough so that the pressure on one band, caused by all the other bands, has decreased to some small value on the surface $r=a$. We

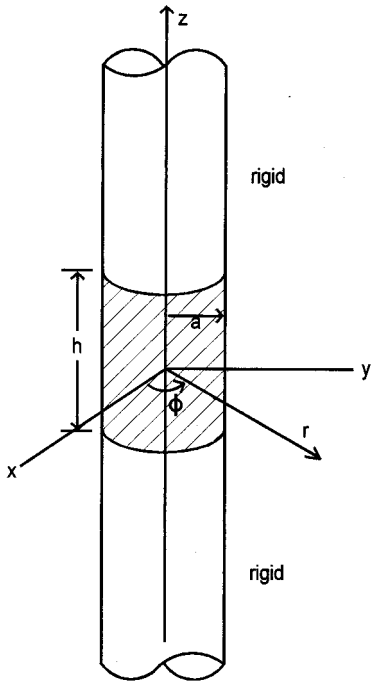

FIG. 1. Single cylinder of radius *a* and length *h* with rigid extensions.

should point out that this method is not applicable to far-field solutions (see, e.g., Ref. 5) since the pressure from the replicas can add to the solution as a result of nearly equal distances to a far-field point.

Within this model we may now write the even function modal solution for p_n as

$$p_n(r,z)=\sum_{m=0}^{\infty} p_{nm}(r)\cos\left(\frac{m2\pi z}{d}\right), \tag{5}$$

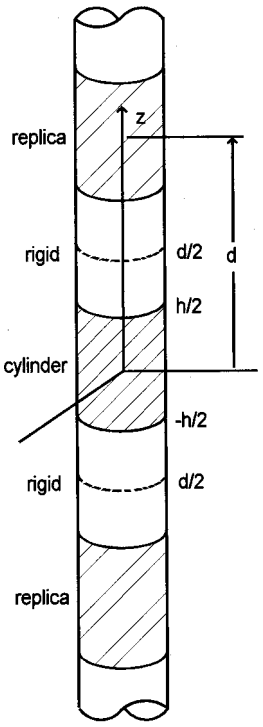

FIG. 2. Actual cylinder and replicated cylinders with period *d*.

where the Fourier series expansion coefficients are given by

$$p_{nm}(r)=\frac{2\epsilon_m}{d}\int_0^{d/2} p_n(r,z)\cos\left(\frac{m2\pi z}{d}\right)dz, \tag{6}$$

with $\epsilon_0=1$ and $\epsilon_m=2$ otherwise. If we now substitute Eq. (5) into Eq. (4), we get

$$\frac{1}{r}\frac{\partial(r\partial p_{nm}/\partial r)}{\partial r}-\frac{n^2}{r^2}p_{nm}-\alpha_m^2 p_{nm}+k^2 p_{nm}=0, \tag{7}$$

where $\alpha_m\equiv m2\pi/d$.

Equation (7) may be rewritten in the form of Bessel's equation as

$$r\frac{\partial(r\partial p_{nm}/\partial r)}{\partial r}+(\beta_m^2 r^2-n^2)p_{nm}=0, \quad \beta_m^2\equiv k^2-\alpha_m^2, \tag{8}$$

with the *n*th modal radiation solution from Eq. (8) written as

$$p_{nm}=A_{nm}H_n(\beta_m r), \tag{9}$$

where the coefficients A_{nm} are to be determined from the boundary conditions. The Hankel function of order *n* is given by $H_n(x)=J_n(x)+iY_n(x)$, where $J_n(x)$ and $Y_n(x)$ are the Bessel and Neumann functions of order *n*. This Hankel function with a + sign between the Bessel and Neumann functions is the Hankel function of the first kind which yields a negative reactive impedance. We will display these results with a positive sign to comply with normal convention.

The value of the radial velocity is presumed to be the known boundary condition along the surface of the cylinder from which we can determine the coefficients A_{nm}. In general the radial velocity $u=(1/i\omega\rho)\partial p/\partial r$, where ρ is the density of the medium. Thus the modal velocity from Eq. (9) is

$$u_{nm}(r)=\beta_n A_{nm}H_n'(\beta_m r)/i\omega\rho, \tag{10}$$

where $H_n'(x)=\partial H_n(x)/\partial x$. Solving the above equation for A_{nm} at $r=a$, and then substituting into Eq. (9) yields

$$p_{nm}=i\omega\rho u_{nm}(a)H_n(\beta_m a)/[\beta_m H_n'(\beta_m a)]. \tag{11}$$

Then on substitution into Eq. (5) we get the modal solution

$$p_n(a,z)=i\omega\rho\sum_{m=0}^{\infty} u_{nm}(a)\frac{H_n(\beta_m a)}{[\beta_m H_n'(\beta_m a)]}\cos\left(\frac{m2\pi z}{d}\right), \tag{12}$$

where [from Eq. (6) and using $u=(1/i\omega\rho)\partial p/\partial r$,]

$$u_{nm}(a)=\frac{2\epsilon_m}{d}\int_0^{d/2} u_n(a,z)\cos\left(\frac{m2\pi z}{d}\right)dz. \tag{13}$$

Consider now the specific case where the cylinder motion is a constant, v_n, along the *z* direction and zero along the rigid surface extension which was originally constructed for this velocity boundary condition. In this case Eq. (13) becomes

$$u_{nm}=\frac{2\epsilon_m}{d}v_n\int_0^{h/2}\cos(\alpha_m z)dz=\frac{\epsilon_m h v_n}{d}\,\mathrm{Sinc}\left(\frac{\alpha_m h}{2}\right), \tag{14}$$

where $\mathrm{Sinc}(x)=\sin(x)/x$ and $\alpha_m=m2\pi/d$ as before. Substitution of Eq. (14) into Eq. (12) then yields the modal solution for the pressure on the surface as

$$p_n(a,z)=i\omega\rho v_n h\sum_{m=0}^{\infty}\epsilon_m\ \mathrm{Sinc}\left(\frac{\alpha_m h}{2}\right)\times\frac{H_n(\beta_m a)}{[\beta_m dH_n'(\beta_m a)]}\cos(\alpha_m z). \tag{15}$$

The total solution for the pressure on the surface is then given through Eq. (2) at $r=a$ as

$$p(a,\phi,z)=\sum_{n=0}^{\infty}p_n(a,z)\cos(n\phi) \tag{16}$$

with the modal velocities determined by

$$v_n=\frac{\epsilon_n}{\pi}\int_0^{\pi}v(\phi)\cos(n\phi)d\phi, \tag{17}$$

where $\epsilon_0=1$, $\epsilon_n=2$ otherwise, and $v(\phi)$ is the given velocity distribution around the circumference of the cylinder given by

$$v(\phi)=\sum_{n=0}^{\infty}v_n\cos(n\phi). \tag{18}$$

We can now determine the force and radiation impedance load on the cylinder from the above pressure distribution. Since the angular velocity distribution *may not necessarily be uniform*, the impedance will be derived from the real and reactive power radiated[6] from the cylinder. Here the radiation impedance is defined as $Z=W/v_r^2$, where v_r is a reference velocity. The power radiated is given by $W=\int\int pv^*\,dA$, where $dA=a\,d\phi\,dz$ is an incremental area on the cylinder; and thus

$$W=v_r^2Z=a\int_0^{2\pi}\int_{-h/2}^{h/2}pv^*\,d\phi\,dz. \tag{19}$$

The surface intensity is arrived at from Eqs. (16) and (18) and may be written as

$$I=pv^*=\sum_{n=0}^{\infty}\sum_{n'=0}^{\infty}p_n v_{n'}^*\cos(n\phi)\cos(n'\phi). \tag{20}$$

Substitution of Eq. (20) into Eq. (19) yields

$$W=Zv_r^2=\sum_{n=0}^{\infty}\left(2\pi a\,\delta_n\int_0^{h/2}p_n\,dz\right)v_n^*=\sum F_n v_n^*=\sum W_n, \tag{21}$$

with $\delta_0=2$ and $\delta_n=1$ otherwise, and where the force

$$F_n=2\pi a\,\delta_n\int_0^{h/2}p_n\,dz. \tag{22}$$

With $W_n=Z_n v_r^2$ the impedance for each mode is then $Z_n=F_n v_n^*/v_r^2$. In the cases where we chose $v_r=v_n$ the modal impedance $Z_n=F_n/v_n$.

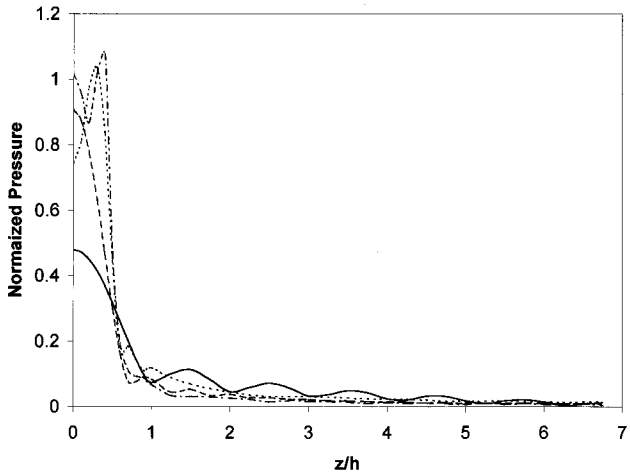

FIG. 3. Normalized pressure distribution for $ka=0.25$ (———), 0.5 (– – –), 1.0 (...), and 2 (–·–·–·).

If we now use the modal pressure solution, Eq. (15), in Eq. (22), and perform the indicated integration we get, finally, the solution for the impedance for each mode as

$$Z_n=i\pi a h^2\rho\omega\delta_n\sum_{m=0}^{\infty}\epsilon_m\ \mathrm{Sinc}^2\left(\frac{\alpha_m h}{2}\right)\frac{H_n(\beta_m a)}{[\beta_m dH_n'(\beta_m a)]}, \tag{23}$$

where, as before, $\alpha_m=m2\pi/d$, $\beta_m^2=k^2-\alpha_m^2$, $k=\omega/c=2\pi/\lambda$, and d is the replication period.

Consider β_m written as

$$\beta_m=(k^2-\alpha_m^2)^{1/2}=k[1-(m\lambda/d)^2]^{1/2}=k[1-(m/M)^2]^{1/2}, \tag{24}$$

where $M\equiv d/\lambda$. We wish the replicating distance d to be much greater than h and more importantly much greater than λ so that the mutual radiation coupling between the cylinder and its replicates is negligible. For point sources the normalized radiation resistance mutual coupling function is $R_{\mathrm{mc}}=[\sin(kd)]/kd=[\sin(2\pi M)]/(2\pi M)$ which decreases in value as $1/2\pi M$. Thus for $M=40.5$, $R_{\mathrm{mc}}=0.004$ compared to a perfect coupling value of 1.00. The parameter β_m becomes imaginary for $m>M$ and has little effect on the radiation resistance in this range. However, there is a significant contribution to the reactive portion in this range and a considerable number of terms (500–1000) beyond $m=40$ must accordingly be carried. With β_m given by Eq. (24) we can then write

$$\beta_m a=ka[1-(m/M)^2]^{1/2},\quad \beta_m d=2\pi M[1-(m/M)^2]^{1/2},\quad \alpha_m h=kh(m/M) \tag{25}$$

for use in the computation of Eq. (23).

II. RESULTS

Consider now the modal pressure given by Eq. (15) evaluated for the zero order mode. These results are presented in Fig. 3 for the pressure magnitude per ρc unit velocity as a function of the axial distance relative to the cyl-

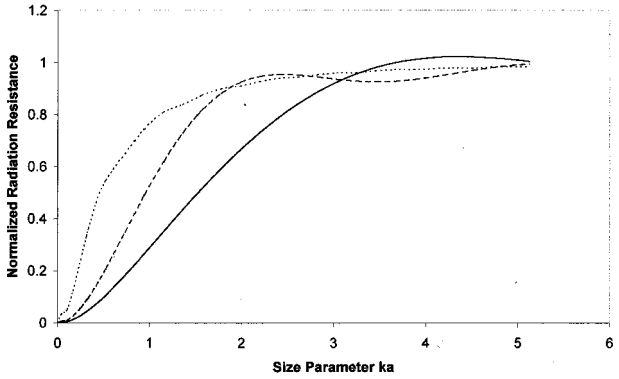

FIG. 4. Normalized radiation resistance for uniform motion, mode $n=0$, for $h/2a=0.5$ (———), 1.0 (– – –), and 5.0 (···).

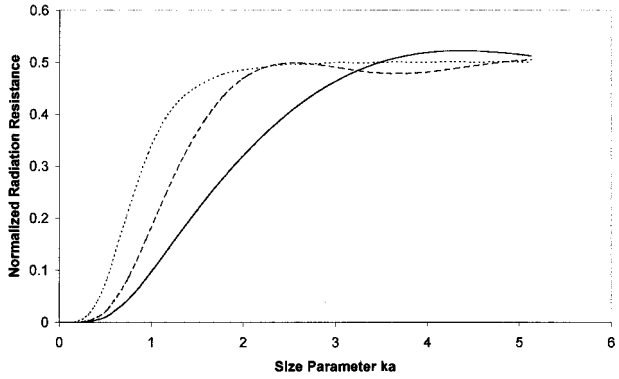

FIG. 6. Normalized radiation resistance for dipole motion, mode $n=1$, for $h/2a=0.5$ (———), 1.0 (– – –), and 5.0 (···).

inder height, h. The edge of the cylinder is at $z/h=\pm 1/2$ where the relative pressure is approximately 0.5 for the larger ka values. Beyond this distance the relative pressure decreases, as expected. The zero order mode radiation resistance and reactance [calculated from Eq. (23) and normalized to $\rho c 2\pi a h$] are shown in Figs. 4 and 5, respectively. The zero order (''omni'') mode represents a cylinder uniformly oscillating in a radial direction. These results are presented here as a function of ka for height to diameter ratios from 0.5, 1.0, and 5. As seen, the resistive results approach unity more rapidly for higher values of $h/2a$. The case of $h/2a=5$ approaches the case of an infinitely long cylinder as would be expected. The initial slope of the reactance curve is proportional to the radiation mass and the curves of Fig. 5 indicate a greater mass loading for greater cylinder lengths at small values of ka. The $h/2a=1$ small ka results have been found[7] to compare favorably with results based on Robey's complete integral and the CHIEF boundary element[8] computer program.

The normalized radiation resistance and reactance curves for the dipole mode ($n=1$) are displayed in Figs. 6 and 7 for the same height to diameter ratios. The radiation resistance for this dipole case is very small for small ka. For large ka the resistive results approach a normalized limiting value of 0.5 since the radial motion over the surface is not uniform and follows a cosine function. The reference velocity was chosen to be at the maximum value of the cosine function.

We have also computed the normalized radiation resistance and reactance for a cardioid mode. As a result of comparisons with finite element modal analysis,[2,7] we believe that the cardioid mode represents a good approximation to the radial motion of a slotted cylinder. Moreover, it has also been shown[7] using the CHIEF model[8] that the rigid cylinder extension model,[3,5] on which our theory is based, provides impedance results that approximate the results for a finite cylinder with end caps. The cardioid function may be written as $C(\phi)=[1+\cos(\phi)]/2$, where $\phi=0$ is located at the gap of the slotted cylinder and $\phi=180°$ is opposite the gap and at the back of the cylinder. It can be seen that $C(0)=1$, $C(90)=1/2$, and $C(180)=0$. It can also be seen that the function $C(\phi)$ is composed of a uniform motion $n=0$ mode of value 1/2 and a dipole motion $n=1$ mode also of maximum value 1/2. Because of this and with $v_0=v_1$, the cardioid impedance is given by $Z_c=(Z_0+Z_1)/2$. We have calculated the impedance of this combination ''cardioid'' mode through Eq. (23) evaluated with $n=0$ and $n=1$. The radiation resistance and reactance results normalized relative to $\rho c 2\pi a h$ are shown in Figs. 8 and 9 and may be compared with the mode 0 results of Figs. 4 and 5. As seen, the general structure of the curves appears similar; however, the magnitude of the reactance is somewhat less and the magnitude of the resistance is significantly less. The resistance is approximately one-half the uniform $n=0$ mode for very small ka values since here the dipole $n=1$ mode contributed values

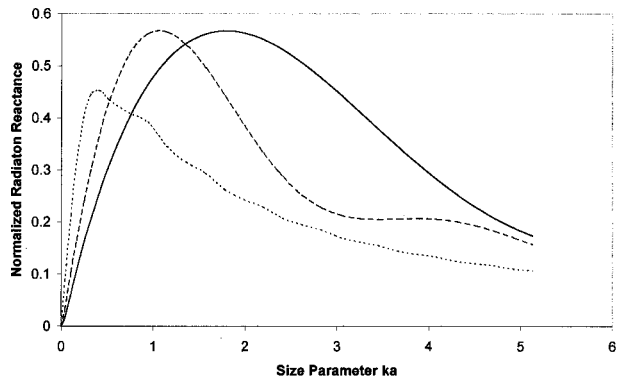

FIG. 5. Normalized radiation reactance for uniform motion, mode $n=0$, for $h/2a=0.5$ (———), 1.0 (– – –), and 5.0 (···).

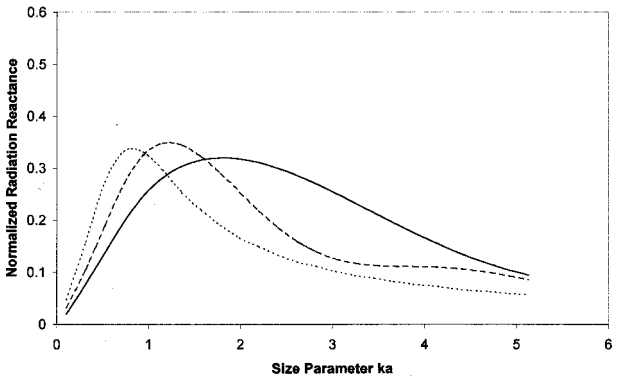

FIG. 7. Normalized radiation reactance for dipole motion, mode $n=1$, for $h/2a=0.5$ (———), 1.0 (– – –), and 5.0 (···).

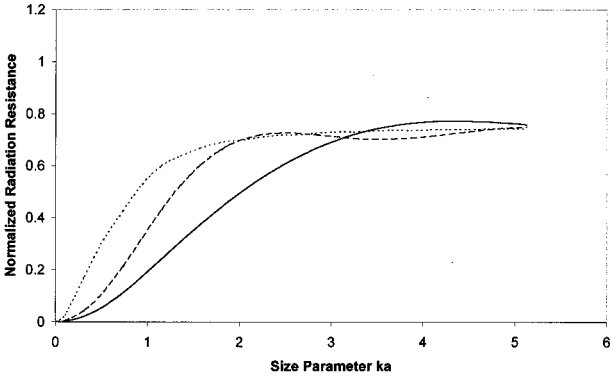

FIG. 8. Normalized radiation resistance for cardioid motion, modes $n=0$ and 1, for $h/2a=0.5$ (———), 1.0 (– – –), and 5.0 (···).

are negligible. The 25% reduction in the limiting resistive value is due to the inclusion of the dipole mode which results in a reduction in the effective radiating area because of the cosine distribution.

The cardioid impedance function was incorporated as an option in the program TSCAT.[2] A sketch of the sample slotted cylinder transducer design is shown in Fig. 10. The piezoelectric shell drives the cylinder into a bending mode producing low-frequency vibrations as in the tines of a tuning fork. The inner shell is composed of two Navy type I piezoelectric cylinders operated in the 31 drive each with height 3.175 cm (1.25 in.), outside diameter 1.27 cm (0.5 in.), wall thickness 0.0762 cm (0.03 in.), and gap width 0.127 cm (0.05 in.). The outer shell was chosen to be steel with height 12.7 cm (5 in.), outside diameter 0.1422 cm (0.56 in.), wall thickness 0.0762 cm (0.03 in.), and gap width 0.127 cm (0.05 in.). A mechanical efficiency of 75%, which reduces the ideal radiation loaded Q by the factor 0.75, was assumed for this example. The resulting transmitting voltage response for 1 volt drive with pressure at 1 m in dB *re*: 1 μPa is shown in Fig. 11 for the modified equivalent sphere radiation loading (equivalent sphere for cylinder area reduced by two-thirds) and the cylindrical radiation loading using the cardioid mode. As seen, in this particular case, the cylinder results are very similar to the results using the modified equivalent sphere. This close agreement is probably a result of the transducer operating resonance in the region of ka

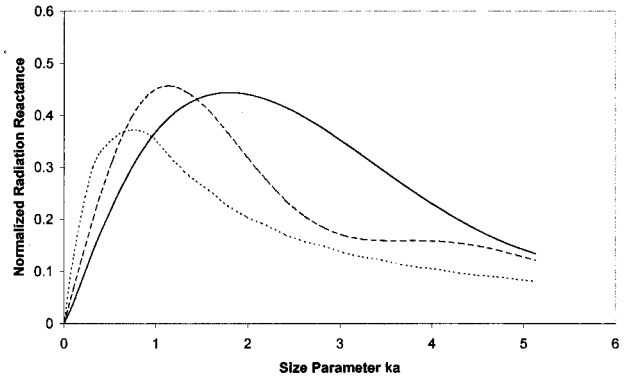

FIG. 9. Normalized radiation reactance for cardioid motion, modes $n=0$ and 1, for $h/2a=0.5$ (———), 1.0 (– – –), and 5.0 (···).

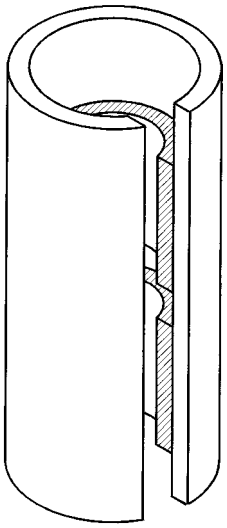

FIG. 10. Sketch of sample slotted cylinder with inner piezoelectric slotted shell and outer slotted steel shell.

$\ll 1$. The levels at resonance are nearly the same with mechanical Q's 9.0 and 10.7 for cylindrical and spherical loading, respectively, indicating slightly greater cylindrical resistive loading. On the other hand, the cylindrical loading yields slightly less radiation mass loading exhibiting a slightly higher resonance frequency.

III. CONCLUSIONS

We have presented a model for the radiation impedance of a finite length cylinder with nonuniform angular vibration. The model is based on Robey's original model with rigid extension along the axial direction which approximates the model of a finite cylinder with rigid end caps. Our approach to this problem is to consider the cylinder to be replicated along the axis with large enough spacing between the replicates for negligible mutual radiation loading. This allows a simpler series solution rather than an integral solution to the problem. This model also allowed the simple inclusion of multiple angular modes which lead to the development of a cardioid vibration distribution function and its corresponding radiation impedance. We believe that this distribution is a

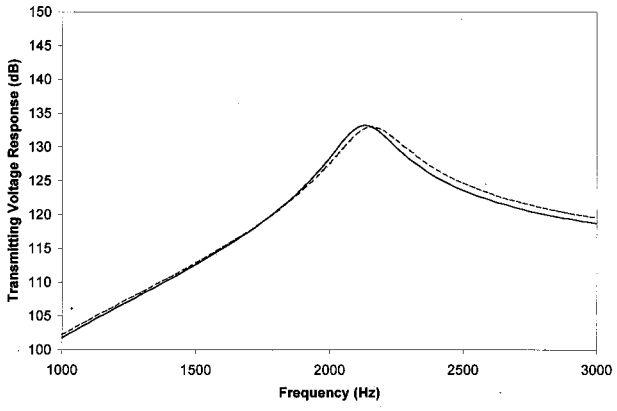

FIG. 11. Transmitting voltage response of slotted cylinder transducer with cylindrical (···) and modified equivalent sphere (———) radiation loading.

good approximation to the radial motion of a slotted cylinder. The results showed that the cardioid function achieves 75% of the uniform vibration radiation resistance loading under large size parameter conditions. The calculated results for a particular sample slotted cylinder transducer design were nearly the same for both modified equivalent sphere loading and the cylindrical loading model developed here. The replicating scheme appears to be successful and should be useful for casting other radiation impedance problems in the form of a Fourier series solution.

ACKNOWLEDGMENTS

We would like to thank Jan F. Lindberg of the Office of Naval Research, Arlington, VA 22217 for his encouragement and support. We would also like to thank George W. Benthien of SPAWAR System Center, San Diego, CA for providing comparative calculated mode $n=0$ radiation impedance results based on the CHIEF boundary element program and Robey's complete integral.

[1] W. T. Harris, U.S. Patent 2,812,452 (1957).
[2] J. L. Butler, ''The Computer Program TSCAT for a Tapered Slotted Cylinder,'' Image Acoustics, Inc., Cohasset, MA 02025, 1994.
[3] D. H. Robey, ''On the radiation impedance of an array of finite cylinders,'' J. Acoust. Soc. Am. **27**, 706–710 (1995); see also J. Acoust. Soc. Am. **27**, 1227 (1955).
[4] J. G. Greenspon, ''An approximation to the remainder of Robey's reactive impedance integral,'' J. Acoust. Soc. Am. **33**, 1428–1429 (1961).
[5] D. T. Laird and H. Cohen, ''Directionality patterns for acoustic radiation from a source on a right cylinder,'' J. Acoust. Soc. Am. **24**, 46–49 (1952).
[6] C. H. Sherman, ''Analysis of acoustic interactions in transducer arrays,'' IEEE Trans. Sonics Ultrason. **SU-13**, 9–15 (1966).
[7] Private communication with G. W. Benthien, SPAWAR Systems Center, San Diego, CA, March, 1998.
[8] H. Schenck, ''Improved integral formulation for acoustic radiation problems,'' J. Acoust. Soc. Am. **44**, 41–58 (1968).

Coupled finite-element wave number decomposition method for the modeling of piezoelectric transducers radiating in fluid-filled boreholes

Didace Ekeom, Bertrand Dubus, and Christian Granger
Institut d'Electronique et de Microélectronique du Nord, U.M.R. C.N.R.S. 9929, Département ISEN, 41 boulevard Vauban, 59046 Lille Cedex, France

(Received 19 November 1997; revised 7 May 1998; accepted 5 August 1998)

A numerical model is proposed to describe in the frequency domain the radiation of a piezoelectric transducer in a fluid-filled borehole surrounded by a formation of infinite extent. Finite elements are used to model the transducer, the borehole fluid, and the fluid–formation interface. The unbounded character of the domain is accounted for by using a wave number decomposition on the borehole surface and dampers on the top and bottom surfaces of the borehole mesh. The method is validated by studying three configurations with analytical solutions: (i) normal stress acting on an empty borehole; (ii) normal stress acting on a fluid-filled borehole; and (iii) point source acting on the fluid-filled borehole axis. The radiation of a piezoelectric ring transducer in an oil-filled tube surrounded by water is also studied experimentally and numerically. © *1998 Acoustical Society of America.* [S0001-4966(98)03311-6]

PACS numbers: 43.38.Fx, 43.20.Rz, 43.20.Mv, 43.40.Ph [SLE]

LIST OF SYMBOLS

c_f or c_{f1}	sound velocity of the internal fluid
c_p	real part of the longitudinal wave velocity in the elastic formation
c_s	real part of the shear wave velocity in the elastic formation
$[D]$	radiation damping matrix
d_{ij}	piezoelectric strain constants
e	symbol restricted to element e
$\mathbf{F}$	vector of the nodal values of the external force
$[H]$	fluid stiffness matrix
$H_n^{(2)}$	cylindrical Hankel function of second kind and order n
$H_n'^{(2)}$	derivative with respect to argument of cylindrical Hankel function of second kind and order n
h	half-height of the borehole mesh
J_0	cylindrical Bessel function of zero order
J_0'	derivative with respect to argument of cylindrical Bessel function of zero order
$[K_{uu}]$	solid stiffness matrix
$[K_{u\varphi}]$	piezoelectric matrix
$[K_{\varphi\varphi}]$	dielectric matrix
$k_f=\omega/c_f$ or $k_{f1}=\omega/c_{f1}$	acoustic wave number in the internal fluid
$k_{f2}=\omega/c_{f2}$	acoustic wave number in the external fluid
$k_p=\omega/c_p$	compressional wave number in the elastic formation
$k_s=\omega/c_s$	shear wave number in the elastic formation
k_T (resp. k_T', k_T'')	modulus (resp. real part, imaginary part) of the wave number of the tube wave
k_z	wave number along z axis
$[L]$	solid–fluid coupling matrix
L	length of finite elements on borehole surface
l	height of the borehole surface with nonzero applied normal stress
$[M]$	solid mass matrix
$[M_1]$	fluid mass matrix
N	number of nodes on the borehole surface (or number of computation points in the formation)
$\mathbf{N}_p$	vector of interpolation functions of pressure
$\mathbf{N}_T$	vector of interpolation functions of stress normal to borehole surface
N_z	number of roots of $g(k_z)$ inside γ
$\mathbf{P}$	vector of the nodal values of the pressure
p	pressure in the (r,z) domain
$\overline{p}$	pressure in the (r,k_z) domain
$\mathbf{Q}_0$	vector of the nodal values of the applied electrical charge
$\ddot{Q}_0$	volume acceleration of point source
s_{ij}^E	elastic compliance constants at constant electric field
r	distance from the borehole axis
r_1	borehole radius
$\mathrm{sgn}(z)$	function equal to 1 if $z>0$ and to -1 if $z<0$
$\mathbf{T}_n$	vector of nodal values of stress normal to borehole surface
t	time
t_n	stress component normal to borehole surface in the (r,z) domain
$\overline{t_n}$	stress component normal to borehole surface in the (r,k_z) domain
$\mathbf{U}$	vector of the nodal values of the displacement

$\mathbf{U}_r$	vector of the nodal values of the radial displacement on the borehole surface
$\underline{\mathbf{u}}$	displacement in the (r,z) domain
$\overline{\mathbf{u}}$	displacement in the (r,k_z) domain
U_i	analytically computed (longitudinal or transverse) displacement at ith node of borehole surface (or ith computation point in the formation)
u_i	numerically computed (longitudinal or transverse) displacement at ith node of borehole surface (or ith computation point in the formation)
$\overline{u_p}$	compressional displacement component in the (r,k_z) domain
$\underline{u_r}$	radial displacement in the (r,z) domain
$\overline{u_s}$	shear displacement component in the (r,k_z) domain
u_z	axial displacement in the (r,z) domain
$[Z]$	global fluid–formation impedance matrix
$[Z_2]$	global fluid–fluid impedance matrix
z	coordinate along borehole axis
z_i	coordinate along z of the ith node of the borehole surface
Γ	borehole surface
Γ_∞	cover surface
γ	regular close contour around k_T in the complex wave number plane
α_i	normalization constants for figures
ϵ	computational error
ϵ_p	imaginary part of the normalized compressional wave velocity in the formation
ϵ_s	imaginary part of the normalized shear wave velocity in the formation
ϵ_{ij}^T	dielectric permittivity constants at constant stress
λ,μ	Lamé constants
ρ	density of the elastic formation
ρ_c	density of PZT5A ceramic
ρ_f or ρ_{f1}	density of the internal fluid
ρ_{f2}	density of the external fluid
$\mathbf{\Phi}_0$	vector of the nodal values of the applied electrical potential
Φ_0	voltage applied on the transducer
$\mathbf{\Psi}$	vector of the nodal values of the flux of pressure gradient through the mesh boundary (borehole surface or covers)
ψ	flux of pressure gradient through the borehole surface or the covers in the (r,z) domain
$\overline{\psi}$	flux of pressure gradient through the borehole surface in the (r,k_z) domain
Ω_e	elastic formation
Ω_f or Ω_{f1}	internal fluid domain (inside the borehole)
Ω_{f2}	external fluid domain
Ω_p	piezoelectric domain
ω	circular frequency

INTRODUCTION

In petroleum acoustics, piezoelectric transducers are used as acoustic sources in boreholes for different applications, depending upon the frequency. This work is mainly concerned with the low-to-medium frequency range for which the wavelengths of interest are larger or comparable to the borehole radius. Typical applications are crosswell seismic imaging and sonic logging.[1]

Most of the theoretical works on acoustic sources in boreholes have dealt with ideal sources. Considering a low frequency point source in a borehole, Lee and Balch[2] proposed an analytical model describing the far-field radiation into the formation and the propagation of the tube waves along the borehole. Kurkjian and Chang[3] presented a frequency wave number formulation for ideal monopole, dipole, and quadrupole sources and displayed synthetic array waveforms for both slow and fast formations using source excitations in several frequency bands. In all of these cases, the effects relative to the source geometry, the physical mechanism of energy transduction, and the effect of the radiation medium on the source were not included.

More recently, Kostek and Randall[4] proposed a numerical method based on a velocity-stress finite-difference scheme to model a piezoelectric ring transducer in a fluid-filled borehole in the time domain. They provided numerically computed waveforms and analyzed the deviation of some transducer characteristics from free-field to borehole radiation conditions. The choices made for the numerical model in the present work differs from those of Kostek and Randall for two reasons. Our work focuses on the characterization of narrow-band resonant piezoelectric transducers (resonance frequency, impedance, radiation patterns) in a borehole environment. Such a problem is more naturally analyzed in the frequency domain. In addition, the finite-element method is used instead of the finite-difference method in order to avoid any limitation on the geometry of the transducer.

A numerical model based on the finite-element method (ATILA code) is proposed here to model the radiation of piezoelectric transducers in boreholes. The problem is assumed to be axisymmetrical. No other simplifying assumption is made on the source geometry or the transduction mechanism. The unbounded character of the domain is accounted for by using a wave number decomposition on the borehole surface and dampers on the top and bottom surfaces of the borehole mesh. The theoretical formulation is presented in Sec. I. Validation and comparison with measurements are displayed in Sec. II.

I. THEORETICAL FORMULATION

The axisymmetrical geometry of the problem is described using (r,z) cylindrical coordinates (Fig. 1). It consists of a piezoelectric domain Ω_p (the transducer) immersed in an infinite cylindrical borehole, filled with an ideal fluid

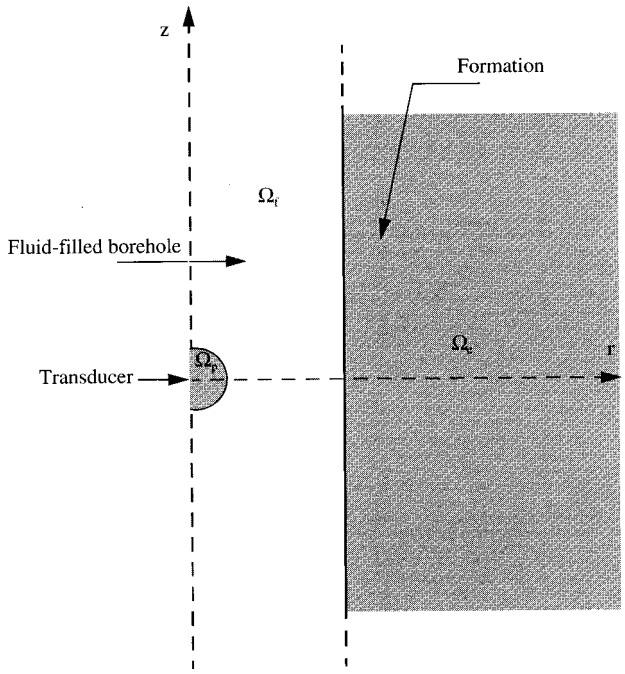

FIG. 1. Geometry of the problem.

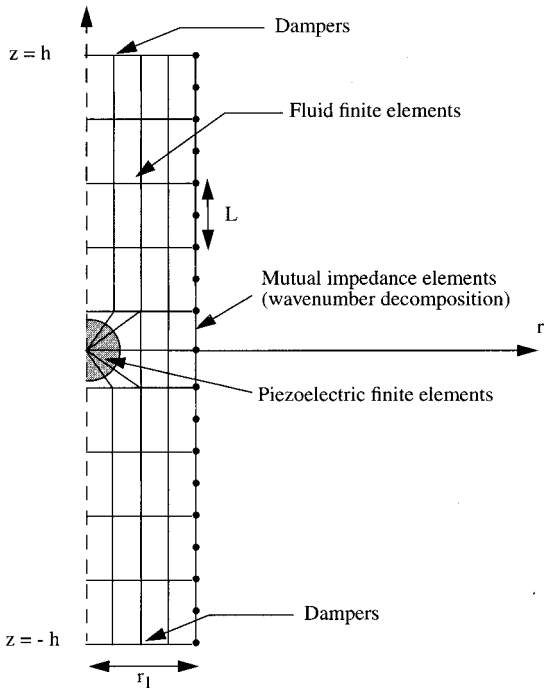

FIG. 2. Spatial discretization of the geometry used in the numerical analysis.

Ω_f and surrounded by an homogeneous, isotropic, elastic formation Ω_e of infinite extent. The steady-state problem is considered. The time dependence is $e^{+j\omega t}$. The finite-element modeling of a piezoelectric domain immersed in an ideal fluid of infinite extent has already been dealt with by many authors[5–7] and is just briefly summarized in Sec. I A. Specific developments taking into account the infinite extent of the formation and the borehole are described in Secs. I B and I C, respectively. Computation of radiation in the formation is carried out in Sec. I D.

A. Piezoelectric transducer and solid–fluid coupling

The finite-element modeling of a piezoelectric transducer radiating in a fluid of infinite extent starts with a variational formulation which enforces the constitutive equations of piezoelectricity, Newton's law and Gauss's law in Ω_p, Helmholtz equation in Ω_f, and kinematic and dynamic continuity conditions at the solid–fluid interface. The spatial discretization of the physical variables (displacement, electric potential, and pressure field) and the application of the variational principle lead to a linear set of equations

$$\begin{bmatrix} [K_{uu}]-\omega^2[M] & [K_{u\varphi}] & -[L] \\ [K_{u\varphi}]^t & [K_{\varphi\varphi}] & [0] \\ -\rho_f^2 c_f^2 \omega^2 [L]^t & [0] & [H]-\omega^2[M_1] \end{bmatrix} \begin{bmatrix} \mathbf{U} \\ \mathbf{\Phi}_0 \\ \mathbf{P} \end{bmatrix} = \begin{bmatrix} \mathbf{F} \\ -\mathbf{Q}_0 \\ \rho_f c_f^2 \mathbf{\Psi} \end{bmatrix}. \tag{1}$$

where ^{t} means transposed.

B. Elastic formation

For problems of cylindrical geometry in borehole acoustics, the displacement vector $\overline{\mathbf{u}}$ is usually expressed in the (r,k_z) domain[2,3]

$$\overline{\mathbf{u}}(r,k_z)=\int_{-\infty}^{\infty}\mathbf{u}(r,z)e^{jk_z z}\,dz. \tag{2}$$

At given k_z, the compressional and shear displacement components, associated to the displacements along r and z, are[8]

$$\overline{u_p}(r,k_z)=\overline{u}_{0p}(k_z)H_1^{(2)}(\hat{k}_p r), \tag{3}$$

$$\overline{u_s}(r,k_z)=\overline{u}_{0s}(k_z)H_0^{(2)}(\hat{k}_s r), \tag{4}$$

where

$$\hat{k}_p^2=k_p^2-k_z^2, \tag{5}$$

$$\hat{k}_s^2=k_s^2-k_z^2. \tag{6}$$

Here, $\overline{u}_{0p}$ and $\overline{u}_{0s}$ are complex constants determined by the boundary conditions and given in Appendix A. The square roots of $\hat{k}_p^2$ and $\hat{k}_s^2$ are chosen in order to verify Sommerfeld's conditions at infinity.

A spatial discretization of the borehole surface is performed using a three-noded isoparametric finite element as shown in Fig. 2. In element e, the stress component normal

to the surface is related to the vector of the nodal values of normal stress using Lagrange interpolation functions[9] as

$$t_n^e(r_1,z)=\mathbf{N}_T^{et}\mathbf{T}_n^e. \tag{7}$$

The Fourier transform of Eq. (7) is written

$$\overline{t_n^e}(r_1,k_z)=\left(\int_{-\infty}^{\infty}\mathbf{N}_T^{et}e^{jk_z z}\,dz\right)\mathbf{T}_n^e=\overline{\mathbf{N}}_T^{et}\mathbf{T}_n^e. \tag{8}$$

$\mathbf{N}_T^e$ and $\overline{\mathbf{N}}_T^e$ are evaluated analytically, as shown in Appendix B. The vector of the nodal values of the radial displacement of the borehole surface due to the normal stress on element e is obtained by combining Eqs. (3), (8), and (A1)–(A3)

$$\begin{aligned}\mathbf{U}_r^e=&\left(\frac{1}{2\pi}\int_{-\infty}^{\infty}\frac{-\hat{k}_s H_0'^{(2)}(\hat{k}_s r_1)H_1^{(2)}(\hat{k}_p r_1)\overline{\mathbf{N}}_T^{et}}{\Delta}\right.\\&\left.\times\begin{bmatrix}e^{-jk_z z_1}\\ \cdot\\ e^{-jk_z z_N}\end{bmatrix}dk_z\right)\mathbf{T}_n^e\\=&[Y^e]\mathbf{T}_n^e.\end{aligned} \tag{9}$$

Δ is given in Appendix A. The quantity in integral (9) is not formally defined at $k_z=\pm k_p$ and $\pm k_s$, but can be prolonged by continuity. A global impedance relation between normal stresses and normal displacements at nodes of the borehole surface is obtained by a classical assembling process

$$[Y]\mathbf{T}_n=\mathbf{U}_r,\quad [Y]=\sum_e [Y^e]. \tag{10}$$

To couple the wave number decomposition with finite elements, it appears from Eq. (1) that it is necessary to obtain a matrix relation between nodal displacements and nodal forces rather than nodal stresses. The nodal elementary force vector on surface Γ^e is given by

$$\mathbf{F}^e=\int_{\Gamma^e}\mathbf{N}_T^e t_n(r_1,z)\,d\Gamma^e=\left(\int_{\Gamma^e}\mathbf{N}_T^e\mathbf{N}_T^{et}\,d\Gamma^e\right)\mathbf{T}_n^e=[P^e]\mathbf{T}_n^e, \tag{11}$$

or after assembling

$$[P]\mathbf{T}_n=\mathbf{F}. \tag{12}$$

After combining Eqs. (10) and (12), the final relation is obtained

$$\mathbf{F}=[P][Y]^{-1}\mathbf{U}_r=[Z]\mathbf{U}_r. \tag{13}$$

The global impedance matrix $[Z]$ is full, complex, nonsymmetrical, and frequency-dependent.

C. Fluid-filled borehole

The propagation of acoustic waves in the borehole is described by the Helmholtz equation. The pressure field $\overline{p}$ is expressed in the (r,k_z) domain

$$\overline{p}(r,k_z)=\int_{-\infty}^{\infty}p(r,z)e^{jk_z z}\,dz. \tag{14}$$

The solution is the cylindrical Bessel function[10]

$$\overline{p}(r,k_z)=\overline{p}_0 J_0(\hat{k}_f r), \tag{15}$$

where $\overline{p}_0$ is a complex constant determined by the boundary conditions and

$$\hat{k}_f^2=k_f^2-k_z^2. \tag{16}$$

The boundary conditions on the borehole surface are the continuity of normal stress, the continuity of the normal displacement, and the cancellation of the tangential stress. The wave numbers of the waves propagating along the borehole are the roots of the determinant of the resulting matrix equation

$$\begin{aligned}g(k_z)=&\frac{\hat{k}_f J_0'(\hat{k}_f r_1)}{\omega^2\rho_f}\left[(\lambda+2\mu)\hat{k}_p H_1'^{(2)}(\hat{k}_p r_1)+\frac{\lambda}{r_1}\right.\\&\left.\times H_1^{(2)}(\hat{k}_p r_1)\right]\hat{k}_s H_0'^{(2)}(\hat{k}_s r_1)+\frac{\hat{k}_f J_0'(\hat{k}_f r_1)}{\omega^2\rho_f}\lambda k_z^2\\&\times H_0^{(2)}(\hat{k}_s r_1)H_1^{(2)}(\hat{k}_p r_1)+\hat{k}_s H_0'^{(2)}(\hat{k}_s r_1)\\&\times H_1^{(2)}(\hat{k}_p r_1)J_0(\hat{k}_f r_1)=0.\end{aligned} \tag{17}$$

At low frequency Eq. (17) has only one root which is generally associated with the tube wave.[11] To get the wave number k_T of the tube wave, a Newton–Raphson algorithm is used. The initial value is taken equal to the approximate wave number given by Lee *et al.*[2] which is valid when the formation is fast $(c_p>c_s>c_f)$ and when the diameter of the borehole is very small compared with the wavelengths

$$k_0=\left(k_f^2+\frac{\rho_f k_s^2}{\rho}\right)^{1/2}. \tag{18}$$

At low frequency for a borehole of any diameter, k_T is computed as the limit of the series

$$k_{n+1}=k_n-\frac{g(k_n)}{g'(k_n)}, \tag{19}$$

where the prime denotes derivative with respect to k_z. For a computation at a higher frequency denoted f, the domain $[0,+f]$ is divided into m subdomains of width $\Delta f=f/m$. Δf

must be small enough to enable the computation with the previous method of wave numbers $k_T^{(1)}$ and $k_T^{(2)}$, associated to tube waves at frequencies $f_1=\Delta f$ and $f_2=2\Delta f$. For $i>1$, the initial value $k_0^{(i)}$ is obtained from $k_T^{(i-1)}$ and $k_T^{(i-2)}$ using linear extrapolation

$$k_0^{(i)}=2k_T^{(i-1)}-k_T^{(i-2)}. \tag{20}$$

To verify that only one tube wave exists at the frequency of interest, a regular closed contour γ around k_T in the complex plane is considered. The number of roots N_z inside γ is given by[12]

$$\frac{1}{2j\pi}\oint_\gamma\left(\frac{g'(k)}{g(k)}+g(k)\right)d\gamma=N_z. \tag{21}$$

The computation of this integral is carried out numerically.

To take into account the radiation condition through the surfaces limiting the mesh along the z axis (these surfaces are called covers in the following), classical finite-element dampers[7] are used. For the covers situated far enough from the acoustic source, the pressure field at the cover is given by

$$p(r,z)=p_0(r)e^{-jk_T|z|}. \tag{22}$$

The pressure gradient normal to the cover is written as

$$\frac{\partial p}{\partial z}=-j\ \mathrm{sgn}(z)k_T p. \tag{23}$$

The covers are spatially discretized using three-noded line elements. In each element, the vectors of the nodal values of the pressure and of the pressure gradient are

$$\mathbf{P}^e=\int_{\Gamma_\infty^e}\mathbf{N}_p^e p\ d\Gamma_\infty^e, \tag{24}$$

$$\mathbf{\Psi}^e=\int_{\Gamma_\infty^e}\mathbf{N}_p^e \psi\ d\Gamma_\infty^e. \tag{25}$$

Using Eqs. (23)–(25), it can be shown that[7]

$$\mathbf{\Psi}^e=-jk_T[D^e]\mathbf{P}^e, \tag{26}$$

with

$$[D^e]=\int_{\Gamma_\infty^e}\mathbf{N}_p^{e^t}\ \mathrm{sgn}(z)\mathbf{N}_p^e\ d\Gamma_\infty^e. \tag{27}$$

D. Final set of equations and radiation in the formation

The final set of equations is obtained by combining Eqs. (1), (13), and (26) as

$$\begin{bmatrix}[K_{uu}]+[Z]-\omega^2[M] & [K_{u\varphi}] & -[L]\\ [K_{u\varphi}]^t & [K_{\varphi\varphi}] & [0]\\ -\rho_f^2c_f^2\omega^2[L]^t & [0] & [H]-\omega^2[M_1]-j\rho_f c_f^2 k_T[D]\end{bmatrix}\begin{bmatrix}\mathbf{U}\\ \mathbf{\Phi}_0\\ \mathbf{P}\end{bmatrix}=\begin{bmatrix}\mathbf{F}\\ \mathbf{Q}_0\\ \mathbf{0}\end{bmatrix}. \tag{28}$$

The components of the displacement field in the formation $\mathbf{u}(r,z)$ can be computed using Eqs. (3), (4), and (A1)–(A3), if $t_n(r_1,k_z)$ is known. On the borehole surface meshed using finite elements, $t_n(r_1,k_z)$ is obtained by combining Eqs. (8)–(10). For the part of the borehole surface located outside the mesh, the normal stresses are extrapolated using the tube wave propagation hypothesis:

$$t_n(r_1,z)=\begin{cases}t_n(r_1,-h)e^{jk_T(z-h)}, & \text{for } z<-h\\ t_n(r_1,h)e^{-jk_T(z-h)}, & \text{for } z>h\end{cases}. \tag{29}$$

If k_T is not on the real axis, the corresponding spectrum is given by

$$\overline{t_n}(r_1,k_z)=-j\ \frac{t_n(r_1,-h)e^{-jk_zh}}{k_z-k_T}+j\ \frac{t_n(r_1,h)e^{jk_zh}}{k_z+k_T}. \tag{30}$$

When k_T lies on the real axis, a particular computation is needed to take into account the singularity at $k_z=k_T$.[13]

II. VALIDATION TESTS

The materials used in the computation have the following properties

$$\begin{aligned}&\text{fluid (oil):} && c_f=1425\ \text{m/s}, && \rho_f=856.5\ \text{kg/m}^3,\\ &\text{fast formation:} && c_p=5588(1-j\epsilon_p)\ \text{m/s},\\ & && c_s=3387(1-j\epsilon_s)\ \text{m/s},\\ & && \rho=2500\ \text{kg/m}^3,\\ &\text{slow formation:} && c_p=3411(1-j\epsilon_p)\ \text{m/s},\\ & && c_s=1350(1-j\epsilon_s)\ \text{m/s},\\ & && \rho=2200\ \text{kg/m}^3.\end{aligned} \tag{31}$$

The borehole mesh is designed with

$$h=100r_1, \quad L=5r_1. \tag{32}$$

A. Prescribed stresses on the empty borehole surface

A triangular normal stress distribution:

$$t_n(z)=T_0\left(1-\frac{|z|}{l}\right), \tag{33}$$

is applied on the surface of the empty borehole on a height $2l=100r_1$. The spectrum of the applied stress in the wave number domain is expressed analytically and combined with Eqs. (A1)–(A3) to give the reference solution. Figure 3 compares the displacements computed analytically and numerically on the borehole surface and in the fast formation ($\epsilon_p=\epsilon_s=0.0$) at reduced frequency $k_s r_1=0.928$. The computational error is defined as

$$\epsilon=\frac{1}{N}\sqrt{\sum_{i=1}^{N}\left|\frac{u_i^2-U_i^2}{U_i^2}\right|}. \tag{34}$$

The variation of the computational error with mesh density is displayed in Fig. 4. Contrary to classical finite-element modeling where mesh density is related to wavelength, the wave number decomposition used to describe the formation does not require any mesh density criterion. This is a direct consequence of the use of Fourier integrals (9) to describe the spatial variations of the physical fields along the surface. Therefore, the accuracy of the final result is directly related to the accuracy in the computation of Fourier integrals. This result only holds for the discretized wave number decomposition used to describe the formation. When this formulation is coupled to finite elements which describe the internal part of the borehole (as in the next sections), the description of the internal fields still requires the usual mesh density/wavelength criterion.

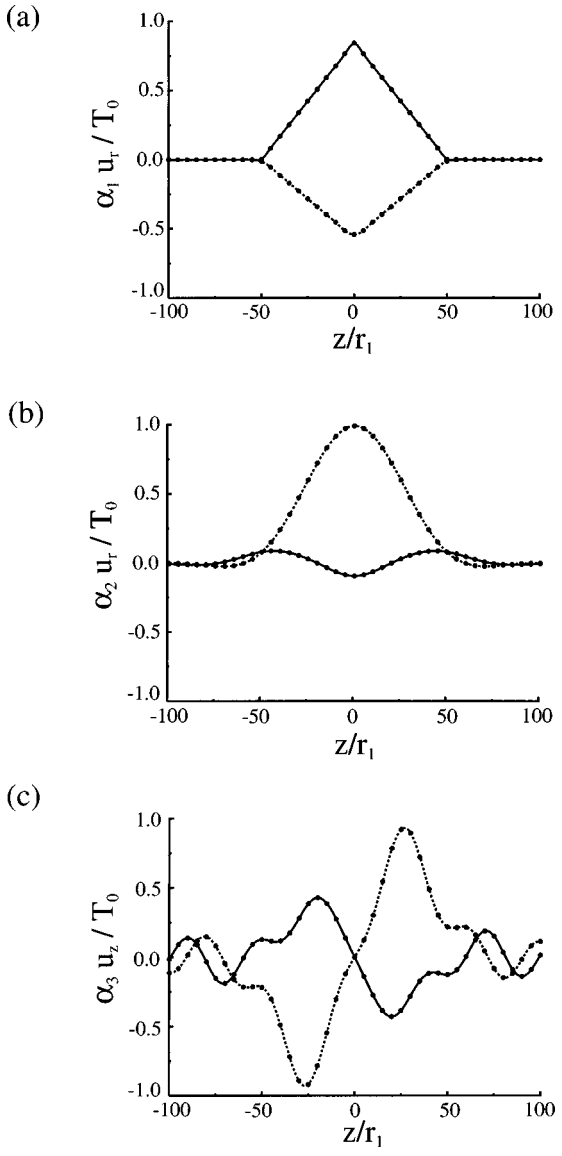

FIG. 3. Displacements generated in the formation by a triangular distribution of normal stress on an empty borehole surface at $k_s r_1=0.928$. Solid line: real part of analytical results; dashed line: imaginary part of analytical results, dots: numerical results. (a) Radial displacements on borehole surface; (b) radial displacements at $r=20r_1$; (c) axial displacements at $r=20r_1$. $\alpha_1=9.8408\times10^{10}$ Pa/m, $\alpha_2=5.9149\times10^{11}$ Pa/m, $\alpha_3=1.6919\times10^{13}$ Pa/m.

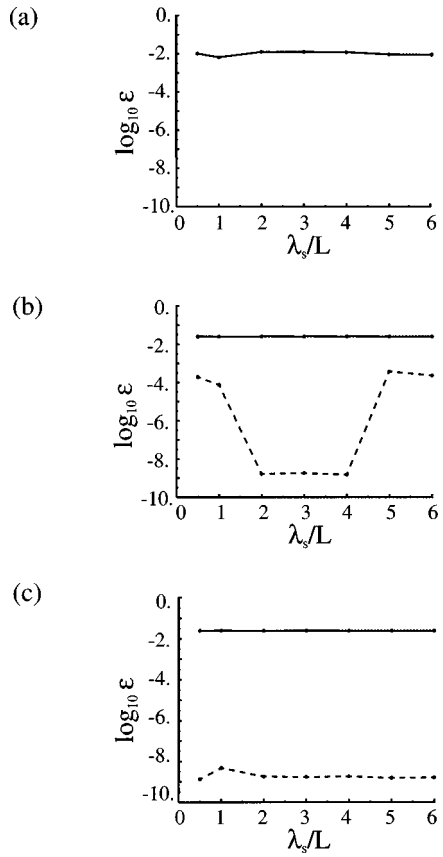

FIG. 4. Variation of the computational error with borehole surface mesh density. Case of an empty borehole with prescribed stress. Solid line: error on radial displacement; dashed line: error on axial displacement. (a) Displacement at $r=r_1$; (b) displacement at $r=20r_1$; (c) displacement at $r=50r_1$.

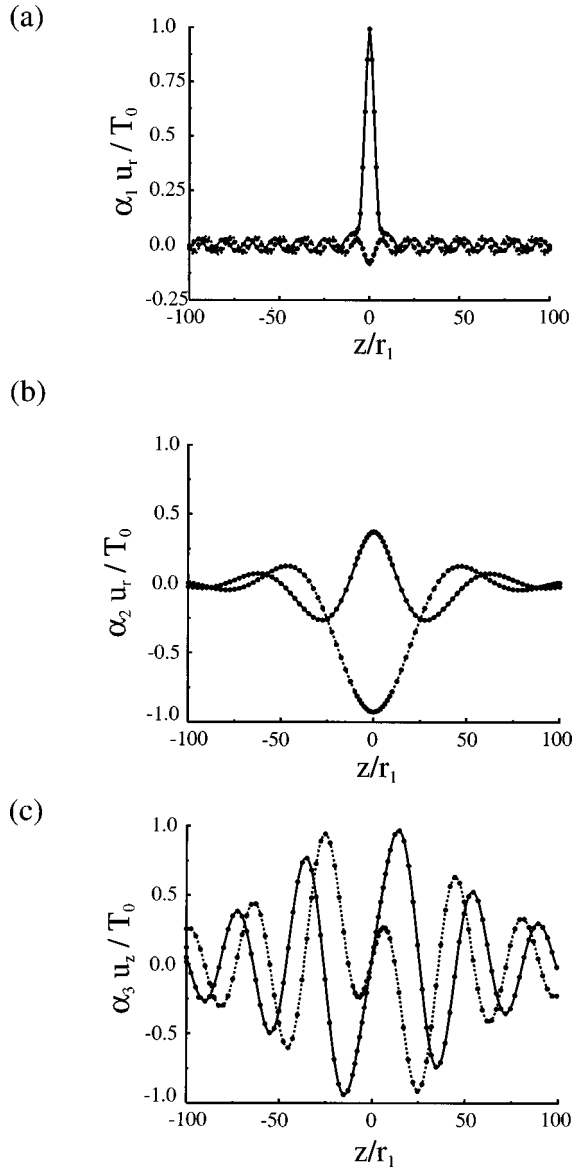

FIG. 5. Displacements generated in the fast formation by a triangular distribution of normal stress on a fluid-filled borehole surface at $k_f r_1 = 0.441$. Solid line: real part of analytical results; dashed line: imaginary part of analytical results; dots: numerical results. (a) Radial displacements on borehole surface; (b) radial displacements at $r = 20 r_1$; (c) axial displacements at $r = 20 r_1$. $\alpha_1 = 1.6072 \times 10^{11}$ Pa/m, $\alpha_2 = 8.3693 \times 10^{12}$ Pa/m, $\alpha_3 = 1.2715 \times 10^{13}$ Pa/m.

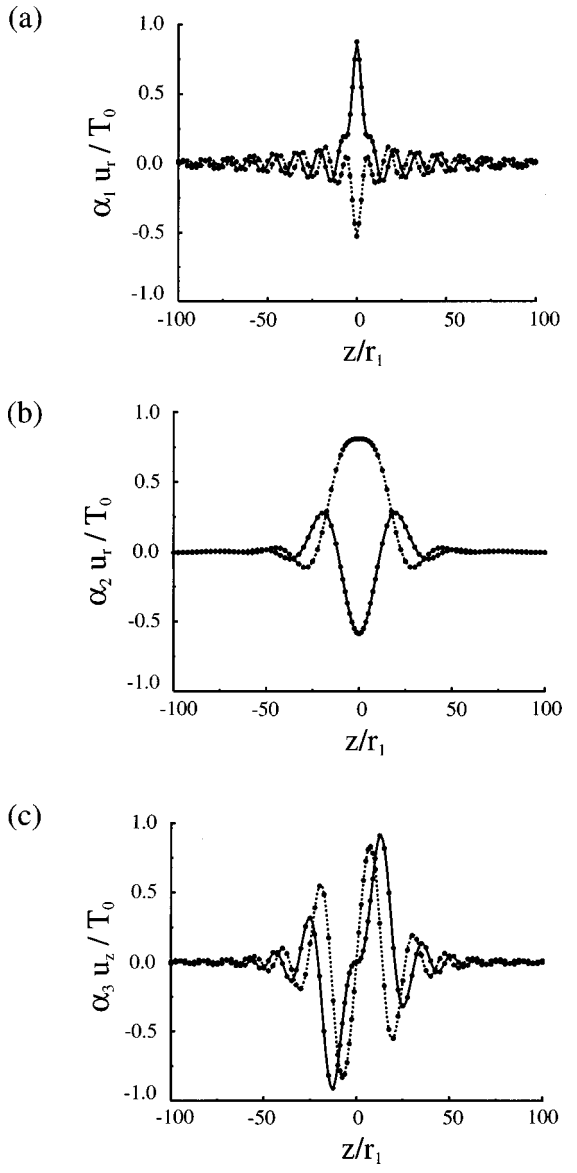

FIG. 6. Displacements generated in the slow formation by a triangular distribution of normal stress on a fluid-filled borehole surface at $k_f r_1 = 0.441$. Solid line: real part of analytical results; dashed line: imaginary part of analytical results; dots: numerical results. (a) Radial displacements on borehole surface; (b) radial displacements at $r = 20 r_1$; (c) axial displacements at $r = 20 r_1$. $\alpha_1 = 3.3869 \times 10^{10}$ Pa/m, $\alpha_2 = 2.3340 \times 10^{12}$ Pa/m, $\alpha_3 = 1.3498 \times 10^{13}$ Pa/m.

B. Prescribed stresses on the fluid-filled borehole surface

A triangular normal stress given by Eq. (33) is applied on the surface of the fluid-filled borehole on a height $2l = 10 r_1$. The spectrum of the applied stress in the wave number domain is expressed analytically and combined with Eqs. (A1)–(A3) and boundary conditions on borehole surface to give the reference solution. Figures 5 and 6 compare the displacements computed analytically and numerically on the borehole surface at reduced frequency $k_f r_1 = 0.441$ in the fast ($\epsilon_p = \epsilon_s = 0.05$) and slow ($\epsilon_p = \epsilon_s = 0.5$) formations, respectively. Tables I and II display the characteristics of the corresponding tube waves. It can be noted that the tube wave travels faster than the shear wave in the slow formation when $k_f r_1 > 0.220$ and therefore radiates in the far field. Variations of the computational error with the distance between the source (the origin) and the mesh boundary (covers) is displayed in Fig. 7.

TABLE I. Characteristics of tube wave for a fast formation ($c_p/c_f = 3.921$, $c_s/c_f = 2.377$).

$k_f r_1$	k_T'/k_s	k_T''/k_s
0.0441	1.0261	0.0000
0.2205	1.0128	0.0000
0.4409	1.0074	0.0000
1.1023	1.0017	0.0000

TABLE II. Characteristics of tube wave for a slow formation ($c_p/c_f=2.394$, $c_s/c_f=0.947$).

$k_f r_1$	k_T'/k_s	k_T''/k_s
0.0441	1.1102	0.0000
0.2205	1.0002	−0.0074
0.4409	0.9762	−0.1321
1.1023	0.9525	−0.7433

C. Point source in the fluid-filled borehole

The analytical solution of a point source acting at ($z=0$, $r=0$) in a fluid-filled borehole surrounded by a fast formation ($\epsilon_p=\epsilon_s=0.05$) is considered. At low frequency, an analytical solution is available.[2] Figure 8 compares the pressures computed analytically and numerically on the borehole axis at two frequencies.

D. Piezoelectric transducer in a fluid-filled borehole

The problem of a piezoelectric transducer radiating in a PVC (poly vinyl chloride) oil-filled tube (external diameter: 50.6 mm, internal diameter: 47.6 mm) surrounded by water is considered (Fig. 9). The transducer is a radially polarized PZT5A (lead zirconate–titanate) ceramic ring the dimensions of which are:

external diameter: 39.0 mm,
internal diameter: 34.2 mm, height: 25.4 mm. (35)

The physical constants of the PZT5A ceramics from the Morgan-Matroc Company are given in Table III. Starting with usual PZT5A ceramic constants, the values of s_{11}^E, d_{31}, and ϵ_{33}^T are fitted to match the *in vacuo* characteristics of the ring transducer. Then, the same relative change is applied to the other elastic, piezoelectric, and dielectric constants. Oil and water sound velocities and densities are:

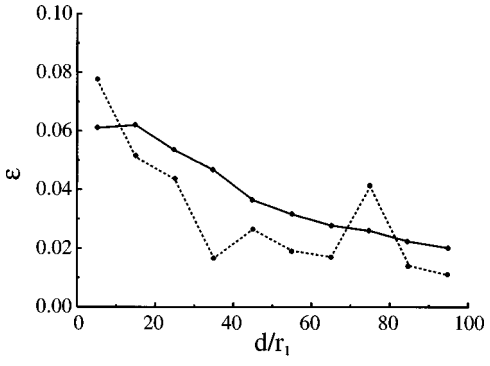

FIG. 7. Variation of the computational error on the borehole surface radial displacement with position of the mesh boundary. Case of a fluid-filled borehole with prescribed stress at $k_f r_1=0.441$. Solid line: fast formation; dashed line: slow formation. $d=2(h-l)$ is the shortest distance between the prescribed stress and the mesh boundary (cover).

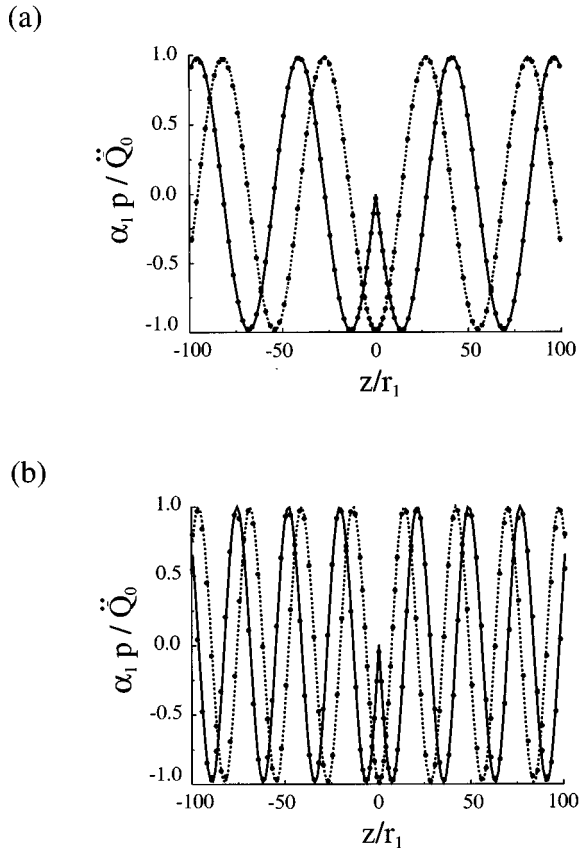

FIG. 8. Pressures generated by a point source on the axis of a borehole surrounded by a fast formation. Solid line: real part of analytical results; dashed line: imaginary part of analytical results; dots: numerical results. (a) $k_f r_1=0.110$; (b) $k_f r_1=0.220$. $\alpha_1=3.7723\ \mathrm{m^3/(Pa\cdot s^2)}$.

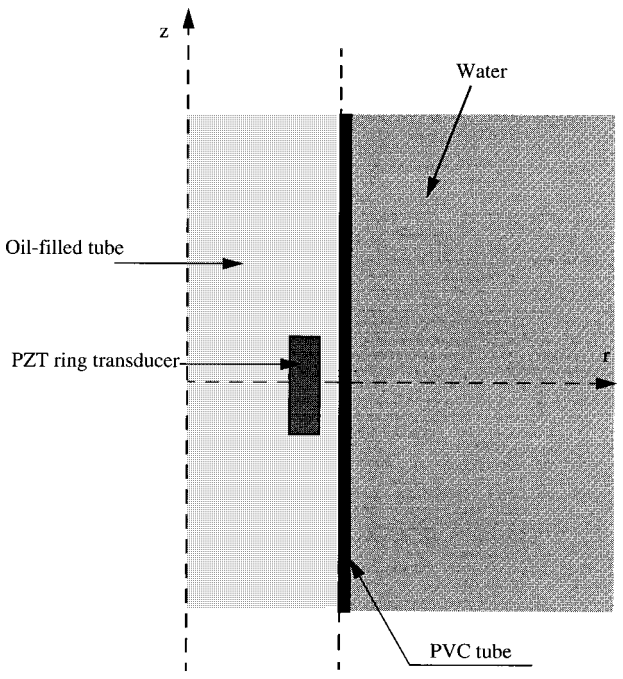

FIG. 9. Geometry of the PZT ring transducer in the oil-filled borehole surrounded by water.

TABLE III. Physical characteristics of PZT5A ceramics.

$s_{11}^E = 19.4\times10^{-12}$ m^2/N	$s_{12}^E = -6.79\times10^{-12}$ m^2/N	$s_{13}^E = -8.54\times10^{-12}$ m^2/N
$s_{33}^E = 22.2\times10^{-12}$ m^2/N	$s_{44}^E = 56.2\times10^{-12}$ m^2/N	$\rho_c = 7072$ kg/m^3
$d_{15} = 536\times10^{-12}$ m/V	$d_{31} = -157\times10^{-12}$ m/V	$d_{33} = 343\times10^{-12}$ m/V
$\epsilon_{11}^T = 16.6\times10^{-9}$ F/m	$\epsilon_{33}^T = 16.3\times10^{-9}$ F/m	

$$c_{\text{oil}} = 1005 \text{ m/s}, \quad \rho_{\text{oil}} = 930 \text{ kg/m}^3, \tag{36}$$

$$c_{\text{water}} = 1458 \text{ m/s}, \quad \rho_{\text{water}} = 1000 \text{ kg/m}^3.$$

Specific modifications were made in the formulation, to replace the elastic formation by a fluid. They are described in Appendix C.

The fluids are separated by the PVC tube which is not modeled. To verify the acoustic transparency of the tube, the pressure radiated by the transducer is measured in the infinite water medium and water-filled tube surrounded by water configurations. Differences are less than 1 dB in the 10–30 kHz frequency range, as long as the distance to the tube axis is larger than 300 mm.

Figures 10 and 11 display computed and measured pressures in the oil-filled tube and in water respectively when the transducer is excited by a voltage $\Phi_0 = 100$ V. Excellent agreement is obtained. The electrical impedance of the transducer and the active electrical input power are shown in Fig. 12. Around 10 kHz, in the frequency range corresponding to the cavity mode of the transducer, a shift in the frequency of the response peak is observed. The difference is probably due to the fact that the PVC tube is not modeled.

III. CONCLUSION

A numerical method, based on a coupled finite-element wave number decomposition, is proposed to describe the radiation of piezoelectric transducers in boreholes in the frequency domain. The spatial discretization of the wave number decomposition leads to a mutual mechanical matrix relating nodal displacements and forces on the borehole surface. Tube waves and radiation in the formation are also considered. A validation is provided by comparison with analytical values for test problems. The accuracy of the method is demonstrated for the case of a piezoelectric ring transducer radiating in an oil-filled tube surrounded by water. The proposed model is an efficient tool to describe the coupling of the transducer with different waves and therefore to optimize acoustic sources for boreholes.

The wave number decomposition technique provides a discretized surface representation of an infinite elastic me-

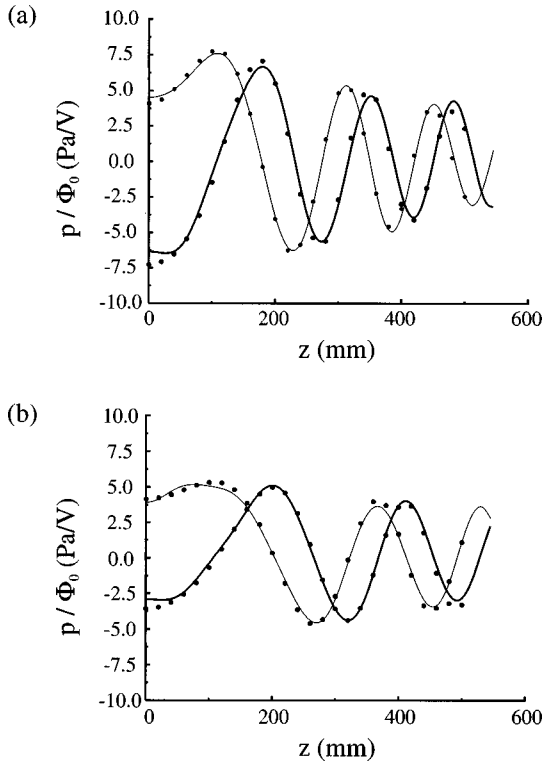

FIG. 10. Pressures generated by the ring transducer in the surrounding water at 15 kHz. Thick line: real part of numerical results; thin line: imaginary part of numerical results; dots: measurements. (a) Pressure at $r = 400$ mm; (b) pressure at $r = 600$ mm.

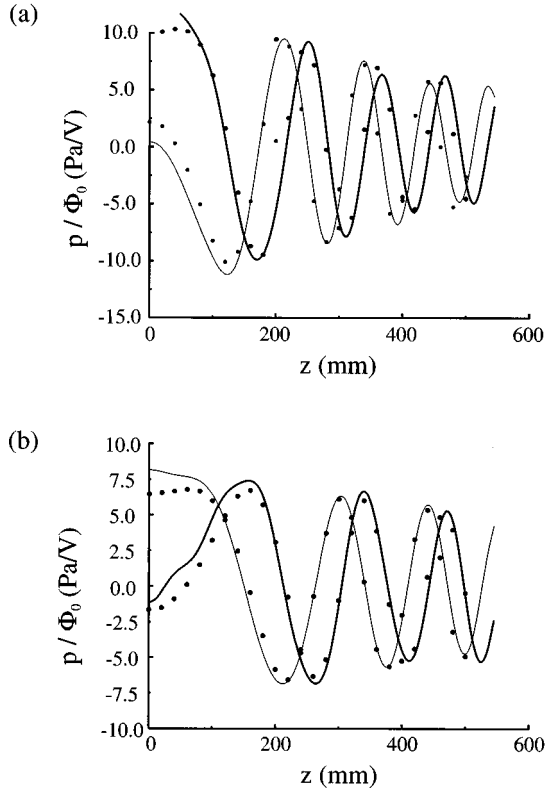

FIG. 11. Pressures generated by the ring transducer in the surrounding water at 20 kHz. Thick line: real part of numerical results; thin line: imaginary part of numerical results; dots: measurements. (a) Pressure at $r = 400$ mm; (b) pressure at $r = 600$ mm.

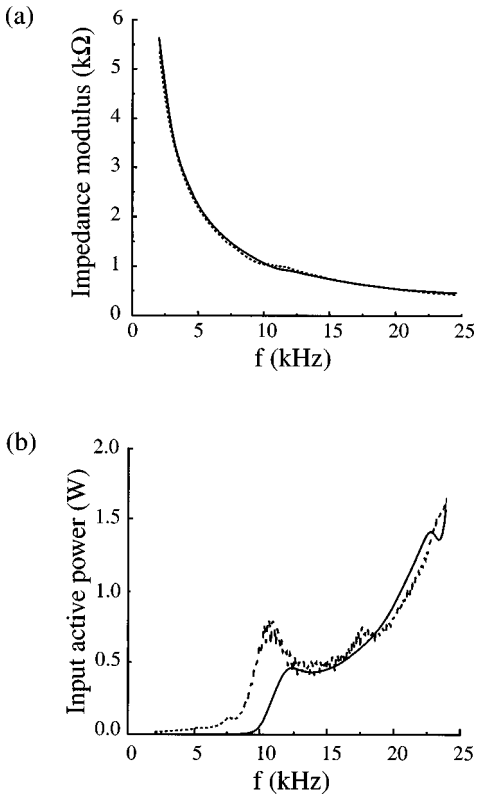

FIG. 12. Variation of electrical input characteristics of the transducer with frequency. Solid line: numerical results; dashed line: measurements. (a) Modulus of input impedance; (b) active input electrical power.

dium which can be directly integrated in any finite-element software. The extension to other problem geometries (e.g., semi-infinite elastic medium) is straightforward.

APPENDIX A

The complex constants of Eqs. (3)–(4) are

$$\overline{u}_{0p}(k_z)=\frac{-\hat{k}_s H_0'^{(2)}(\hat{k}_s r_1)\overline{t}_n(r_1,k_z)}{\Delta}, \tag{A1}$$

$$\overline{u}_{0s}(k_z)=\frac{-jk_z H_1^{(2)}(\hat{k}_p r_1)\overline{t}_n(r_1,k_z)}{\Delta}, \tag{A2}$$

with

$$\Delta=\left[(\lambda+2\mu)\hat{k}_p H_1^{(2)}(\hat{k}_p r_1)+\frac{\lambda}{r_1}H_1^{(2)}(\hat{k}_p r_1)\right] \times\hat{k}_s H_0'^{(2)}(\hat{k}_s r_1)+\lambda k_z^2 H_0^{(2)}(\hat{k}_s r_1)H_1^{(2)}(\hat{k}_p r_1). \tag{A3}$$

APPENDIX B

For a three-noded isoparametric finite element, the interpolation function vector is defined as

$$\mathbf{N}_T^{et}=[N_{T1}^e(z),N_{T2}^e(z),N_{T3}^e(z)], \tag{B1}$$

$$N_{Ti}^e(z)=a_i z^2+b_i z+c_i, \tag{B2}$$

$$a_1=\frac{z_2-z_3}{\Delta'},\quad b_1=\frac{z_3^2-z_2^2}{\Delta'},\quad c_1=\frac{z_3z_2^2-z_2z_3^2}{\Delta'},$$

$$a_2=\frac{z_3-z_1}{\Delta'},\quad b_2=\frac{z_1^2-z_3^2}{\Delta'},\quad c_2=\frac{z_1z_3^2-z_3z_1^2}{\Delta'}, \tag{B3}$$

$$a_3=\frac{z_1-z_2}{\Delta'},\quad b_3=\frac{z_2^2-z_1^2}{\Delta'},\quad c_3=\frac{z_2z_1^2-z_1z_2^2}{\Delta'},$$

$$\Delta'=z_1z_3^2+z_2z_1^2+z_3z_2^2-z_1z_2^2-z_2z_3^2-z_3z_1^2, \tag{B4}$$

where subscript i denotes the node number. The corresponding $\overline{\mathbf{N}}_T^e$ vector is written as

$$\overline{\mathbf{N}}_T^{et}=[\overline{N}_{T1}^e(k_z),\overline{N}_{T2}^e(k_z),\overline{N}_{T3}^e(k_z)], \tag{B5}$$

$$\overline{N}_{Ti}^e(k_z)=\begin{cases}\dfrac{a_i}{3}(z_2^3-z_1^3)+\dfrac{b_i}{2}(z_2^2-z_1^2)+c_i(z_2-z_1) & \text{for } k_z=0\\ \left\{-j\dfrac{a_i}{k_z}z_2^2+\left(2\dfrac{a_i}{k_z^2}-j\dfrac{b_i}{k_z}\right)z_2+\left(2j\dfrac{a_i}{k_z^3}+\dfrac{b_i}{k_z^2}-j\dfrac{c_i}{k_z}\right)\right\}e^{jk_z z_2} & \\ \quad-\left\{-j\dfrac{a_i}{k_z}z_1^2+\left(2\dfrac{a_i}{k_z^2}-j\dfrac{b_i}{k_z}\right)z_1+\left(2j\dfrac{a_i}{k_z^3}+\dfrac{b_i}{k_z^2}-j\dfrac{c_i}{k_z}\right)\right\}e^{jk_z z_1} & \text{for } k_z\neq 0.\end{cases} \tag{B6}$$

APPENDIX C

For an empty borehole surrounded by a fluid (denoted by subscript 2), the pressure spectrum in the fluid $\overline{p}(r,k_z)$ is related to the spectrum of the pressure normal derivative $\overline{\psi}(r_1,k_z)$ on the borehole surface by

$$\overline{p}(r,k_z)=-\frac{\overline{\psi}(r_1,k_z)}{\hat{k}_{f2}H_0'^{2}(\hat{k}_{f2}r_1)}H_0^{(2)}(\hat{k}_{f2}r),\quad \text{for } r\geqslant r_1, \tag{C1}$$

with

$$\hat{k}_{f2}^2=k_{f2}^2-k_z^2. \tag{C2}$$

The spatial discretization of the borehole surface using three-noded line elements is performed according to the description of Sec. I B and leads to

$$\mathbf{P}^e = \left(\frac{1}{2\pi} \int_{-\infty}^{\infty} \frac{-H_0^{(2)}(\hat{k}_{f2} r) \overline{\mathbf{N}}_T^{et}}{\hat{k}_{f2} H_0'^{2}(\hat{k}_{f2} r_1)} \begin{bmatrix} e^{-jk_z z_1} \\ \cdot \\ e^{-jk_z z_N} \end{bmatrix} dk_z \right) \mathbf{\Psi}^e = [Y_2^e] \mathbf{\Psi}^e. \tag{C3}$$

Integration is performed in the complex plane by avoiding the poles at $k_z = k_{f2}$ and $k_z = -k_{f2}$. After setting $r = r_1$ in Eq. (C3) and assembling, a matrix equation relating nodal pressures and nodal flux velocities on the borehole surface is obtained

$$[Z_2]\mathbf{P} = \mathbf{\Psi}. \tag{C4}$$

For the case of the fluid-filled borehole (denoted by subscript 1) surrounded by another fluid (denoted by subscript 2), the boundary conditions on the borehole surface are the continuity of pressure and normal displacement. The wave number k_T of the tube wave is the first root of the determinant of the resulting matrix equation

$$g_2(k_z) = \frac{\hat{k}_{f1}}{\omega^2 \rho_{f1}} J_0'(\hat{k}_{f1} r_1) H_0^{(2)}(\hat{k}_{f2} r_1) - \frac{\hat{k}_{f2}}{\omega^2 \rho_{f2}} J_0(\hat{k}_{f1} r_1) H_0'^{(2)}(\hat{k}_{f2} r_1). \tag{C5}$$

The damping element is then constructed as described in Sec. I C. The final set of equations is obtained by combining Eqs. (1), (26), and (C4):

$$\begin{bmatrix} [K_{uu}] - \omega^2 [M] & [K_{u\varphi}] & -[L] \\ [K_{u\varphi}]^t & [K_{\varphi\varphi}] & [0] \\ -\rho_{f1}^2 c_{f1}^2 \omega^2 [L]^t & [0] & [H] + [Z_2] - \omega^2 [M_1] - j\rho_{f1} c_{f1}^2 k_T [D] \end{bmatrix} \begin{bmatrix} \mathbf{U} \\ \mathbf{\Phi}_0 \\ \mathbf{P} \end{bmatrix} = \begin{bmatrix} \mathbf{F} \\ -\mathbf{Q}_0 \\ \mathbf{0} \end{bmatrix}. \tag{C6}$$

Radiation in fluid 2 is obtained using the procedure previously described for an elastic formation (Sec. I D).

[1] B. Froelich, ''Transducer needs for petroleum acoustics,'' in *Power Transducers for Sonics and Utrasonics*, edited by B. F. Hamonic, O. B. Wilson, and J.-N. Decarpigny (Springer-Verlag, New York, 1990), pp. 22–34.

[2] M. W. Lee and A. H. Balch, ''Theoretical seismic wave radiation from a fluid-filled borehole,'' Geophysics **47**, 1308–1314 (1982).

[3] A. L. Kurkjian and S.-K. Chang, ''Acoustic multipole sources in fluid-filled boreholes,'' Geophysics **51**, 148–163 (1986).

[4] S. Kostek and C. J. Randall, ''Modeling of a piezoelectric transducer and its application to full wave acoustic logging,'' J. Acoust. Soc. Am. **95**, 109–122 (1994).

[5] R. R. Smith, J. T. Hunt, and D. Barach, ''Finite element analysis of acoustically radiating structures with applications to sonar transducers,'' J. Acoust. Soc. Am. **54**, 1277–1288 (1973).

[6] J.-N. Decarpigny, ''Application de la méthode des éléments finis à l'analyse de transducteurs piézoélectriques,'' Doctoral thesis, Université des Sciences et Techniques de Lille (1984) (in French).

[7] R. Bossut and J.-N. Decarpigny, ''Finite element modeling of radiating structure using dipolar damping elements,'' J. Acoust. Soc. Am. **86**, 1234–1244 (1989).

[8] P. Germain and P. Muller, *Mécanique des milieux continus* (Masson, Paris, 1986) (in French), 2nd ed.

[9] O. C. Zienkiewicz and R. L. Taylor, *The Finite Element Method* (McGraw-Hill, New York, 1989), 4th ed.

[10] A. D. Pierce, *Acoustics: An Introduction to Its Physical Principles and Applications* (Acoustical Society of America, New York, 1989).

[11] J. E. White, *Underground Sound* (Elsevier Science, New York, 1983), pp. 193–210.

[12] B. Davies, ''Locating the zeros of an analytic function,'' J. Comput. Phys. **66**, 36–49 (1981).

[13] D. Ekeom, ''Modélisation par la méthode des éléments finis du rayonnement d'un transducteur piézoélectrique dans un puits de forage,'' Ph. D. Thesis, Université des Sciences et Techniques de Lille (1997) (in French).

Design and optimization of unipolar pressure pulse generators with a single transducer

Stéphane Holé[a] and Jacques Lewiner
Laboratoire d'Électricité Générale, École Supérieure de Physique et de Chimie Industrielles de la Ville de Paris, 10, rue Vauquelin, 75005 Paris, France

(Received 4 May 1998; accepted for publication 24 July 1998)

In this paper a broad bandwidth elastic wave generator is described which can produce unipolar (half-oscillation) longitudinal pressure pulses. Such systems are of great interest in many fields: for instance, in nondestructive testing when spatial resolution is needed in lossy materials. The emitter is composed of a thin piezoelectric transducer coupled with a waveguide and a backing medium. Depending on the impedance of each material, both broad proportional and differential bandwidth can be obtained. The theoretical description, which takes into account the connection to an electrical generator, is presented. It allows for optimization of the performance of the system. These developments are in good agreement with the experiments which have been carried out. A bandwidth of 185% of the central frequency and pressure pulses of 1.5-MPa amplitude are obtained.
 [S0001-4966(98)00811-X]

PACS numbers: 43.38.Fx, 43.35.Zc [SLE]

INTRODUCTION

Elastic wave techniques are intensively used to probe materials in nondestructive testing. For instance, in echographic techniques,[1,2] a short ultrasonic pulse propagates through a material to be tested and is partially reflected on impedance mismatches or flaws. The depth of a mismatch is determined by measuring the delay between the beginning of the ultrasonic pulse and the beginning of the echo. In the case of tomographic techniques,[3] a set of measurements is performed at various angles of incidence in order to determine the spatial position of each mismatch. In a third example, the propagation of an ultrasonic pulse is used to obtain information on the electrical and mechanical properties of materials.[4–6] In all cases the quality of measurements is directly connected to the spatial resolution which can be obtained. For this reason it is favorable to use as short as possible ultrasonic pulses. However, the presence of oscillations of pressure in the pulse has a negative impact, particularly in lossy materials in the first two examples and in any materials in the last example. Various reasons are responsible for this negative impact. First, the presence of oscillations within the pulse has the effect to shift the Fourier spectrum of the pulse toward higher frequencies without improving the resolution. Since the attenuation and the dispersion increase drastically with the frequency in lossy materials, oscillations lead to a loss of information. Second, oscillations tend to average any localized phenomena leading again to a loss of information. Third and as it is well known, the presence of oscillations may drastically downgrade the solutions obtained in signal processing, for instance, when using inverse convolution, polarity, or envelope detection. For these reasons, it is highly desirable to produce unipolar, that is to say, having the shape of half an oscillation, pressure pulses. With such a pulse the Fourier spectrum is no longer shifted; measurements are no longer averaged and signal processing is simplified.

Unipolar pressure pulses can be generated using piezoelectric transducers in various configuration.[7,8] It is possible to use a thick transducer electrically supplied through its thickness by a uniform field,[9,10] a thick transducer supplied by a divergent field,[11] or a thin transducer supplied by a uniform field.[12] In the first configuration, reducing the thickness of the transducer increases the amplitude of the pressure wave generated for a given applied voltage. However, since the pressure wave in the transducer is reflected at its boundaries, the thicker the transducer is, the more delayed echoes are induced. A compromise has hence to be found to make the system generate the highest-pressure wave amplitude with the most delayed echoes for a given applied voltage. In the second configuration, an electrical divergent field is produced in a very thin layer of a thick transducer. In this case the pressure wave amplitude does not depend on the thickness of the transducer. Unfortunately, electrodes that induce the divergent field must be carefully insulated in order to withstand large electric fields outside the transducer which could lead to electrical breakdowns. In the third configuration, a thin transducer is subjected to a voltage applied to its opposite faces. The limiting factor in this case is the breakdown strength of the transducer itself. We have focused our study on thin transducers because they lead to simple configurations that give both a high amplitude response and a high voltage insulation between the electrodes.

This paper is separated into five parts. In the first part, after a brief description of the principle and design used, the transfer function, which characterizes the dependence on the applied voltage of the emitted pressure wave, is established. In the second part the optimization of the performance, in terms of high amplitude pressure wave and a large bandwidth, by choosing proper materials is discussed. The morphology of the transfer function is especially studied in order to show that it is possible to produce short unipolar pressure

[a]Laboratoire des Instruments et Systèmes, Université Pierre et Marie Curie 10, rue Vauquelin, 75005 Paris, France. stephane.hole@espci.fr

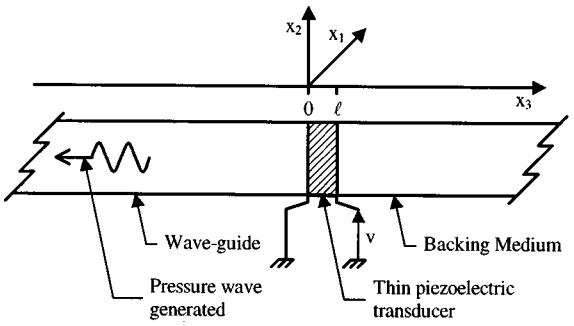

FIG. 1. Structure of the elastic wave generator.

pulses by applying to the transducer a particular voltage. The third part presents a way to optimize the matching between the acoustic part and the electrical part of the system. The last two parts are devoted, respectively, to bonding effects and to a presentation of experimental results.

I. DESCRIPTION AND TRANSFER FUNCTION

A. Description

The general design of the elastic wave generator is shown in Fig. 1. It is composed essentially of three materials—a waveguide, a thin piezoelectric transducer, and a backing medium. The waveguide, coupled to one side of the piezoelectric transducer, transmits the pressure wave generated by the system to where it is being used. It can be the sample to be tested itself or an intermediate medium. In the latter case, its length must be sufficient to delay nondesired echoes. The backing medium loads the other side of the piezoelectric transducer in order to modify the shape of the generator response. Its length must also be sufficient to reject spurious echoes. The thin transducer transforms electrical energy into mechanical energy. Its thickness must be small as compared to its radial dimensions in order to reduce boundary effects. In addition, electrodes, bonding, and coupling layers are necessary to electrically supply the transducer and to transmit the elastic wave to the sample.

In the present study, the waveguide and the backing medium are supposed to be of infinite length, which means that echoes are avoided and boundary effects negligible. All theoretical developments are performed at this stage without taking into account the effect of electrodes, bonding and other couplings.

B. Transfer function

The transfer function is obtained by combining the state equations (1) and the boundary conditions, which are the continuity of the displacement and of the normal stress at the interfaces. In Eqs. (1), T is the stress, S the strain, E the electrical field, and D the electrical displacement field. The various coefficients are c^E_{ijkl} the elastic stiffness at zero electric field, e_{ijk} the piezoelectric tensor, and ϵ^S_{ij} the dielectric tensor at no deformation. The exponents E and S used in the former terms mean, respectively, at constant electric field E, or constant deformation S:

$$\begin{aligned} T_{ij} &= c^E_{ijkl} S_{kl} - e_{kij} E_k, \\ D_i &= \epsilon^S_{ij} E_j + e_{ijk} S_{jk}. \end{aligned} \tag{1}$$

As shown in Eqs. (2), in the case of quasi-static problems, the strain S derives from the displacement u and the electrical field E from the potential Φ. This is clearly the case since the speed of light is much larger than the speed of sound, so that the electric field reaches its equilibrium quasi-instantaneously as compared to the mechanical motions:

$$S_{ij} = \frac{1}{2}\left(\frac{\partial u_j}{\partial x_i} + \frac{\partial u_i}{\partial x_j}\right), \quad E_i = \frac{\partial \Phi}{\partial x_i}. \tag{2}$$

In the configuration of Fig. 1, where the thickness of the transducer (x_3 axis) is small as compared to its radial dimensions (x_1 and x_2 axes), the displacement u and the electric potential Φ can be considered as constant in a section perpendicular to the x_3 axis. Thus only S_{33} and F_3 are different from zero. In fact, only D_3 is also different from zero except for triclinic and some monoclinic crystals. Furthermore, when no space charge is trapped in the piezoelectric material, Poisson's law indicates that D_3 must be constant along the x_3 axis. It can be calculated by integrating over the transducer thickness l the second relation of the state equations. This leads to

$$lD_3 = \epsilon^S_{33} v + e_{333}(u_3(l) - u_3(0)), \tag{3}$$

where v is the potential difference applied between the two sides of the transducer (see Fig. 1). The stress T_{ij} in the transducer can be obtained by combining relation (3) with the first relation of the state equations. One has

$$\begin{aligned} T_{ij} = {} & \frac{\epsilon^S_{33} c^E_{ij33} + e_{3ij} e_{333}}{\epsilon^S_{33}} S_{33} \\ & - \frac{e_{3ij} e_{333}}{l \epsilon^S_{33}} (u_3(l) - u_3(0)) - \frac{e_{3ij}}{l} v. \end{aligned} \tag{4}$$

In the waveguide and in the backing medium, which are nonpiezoelectric materials, the stress is directly given by Hooke's equation:

$$T_{ij} = c_{ij33} S_{33}. \tag{5}$$

It is now possible, using the above expressions for the stress and adding the boundary conditions, to calculate the stress in the waveguide as a function of the voltage applied to the transducer. Since the interfaces are all perpendicular to the x_3 axis, as shown in Fig. 1, the introduction of the boundary conditions leads to the system of Eqs. (6). In these expressions the variables are marked with a ''g'' or a ''b,'' respectively, for the waveguide and for the backing medium:

$$\begin{aligned} & T_{i3g}(0) = T_{i3}(0), \quad u_{3g}(0) = u_3(0), \\ & T_{i3}(l) = T_{i3b}(l), \quad u_3(l) = u_{3b}(l). \end{aligned} \tag{6}$$

In this configuration, we see that the only component of T which is needed is T_{13}, but, except for triclinic and some monoclinic crystals, T_{13} and T_{23} are equal to zero. For this reason, if these symmetries are avoided, all spatial indexes needed for solving the boundary equations are equal to 3 and assuming that x_3 is the z-axis, the boundary conditions can

be rewritten by introducing the quantity $e=e_{333}$, $\epsilon^S=\epsilon^S_{33}$, $c=c_{3333}$, $c^E=c^E_{3333}$, and $u=u_3$. One has

$$
\begin{aligned}
&c_g \frac{\partial u_g}{\partial z}(0)=\frac{\epsilon^S c^E+e^2}{\epsilon^S}\cdot\frac{\partial u}{\partial z}(0)-\frac{e^2}{l\epsilon^S}(u(l)-u(0))-\frac{e}{l}v,\\
&u_g(0)=u(0),\\
&\frac{\epsilon^S c^E+e^2}{\epsilon^S}\cdot\frac{\partial u}{\partial z}(l)-\frac{e^2}{l\epsilon^S}(u(l)-u(0))-\frac{e}{l}v=c_b\frac{\partial u_b}{\partial z}(l),\\
&u(l)=u_b(l).
\end{aligned}
\tag{7}
$$

The pressure waves propagate from the transducer toward decreasing z in the waveguide and toward increasing z in the backing medium. In the transducer, both directions of propagation must be considered. If the displacement is an harmonic plane wave of circular frequency ω, then:

$$
\begin{aligned}
&u_g(z)=b_g e^{i(\omega t+k_g z)},\\
&u(z)=a e^{i(\omega t-kz)}+b e^{i(\omega t+kz)},\\
&u_b(z)=a_b e^{i(\omega t-k_b z)}.
\end{aligned}
\tag{8}
$$

In these expressions a and b are the displacement amplitudes for each plane wave, k the wave vector, and t the time. The displacement amplitudes are, respectively, indexed by ''g'' or ''b'' to refer to the waveguide or to the backing medium. With these values, Eqs. (7) can be expressed as

$$
\begin{aligned}
&i\omega Z_g b_g=-i\omega Z\left(a-b+\frac{K^2}{ikl}(a(e^{-ikl}-1)+b(e^{ikl}-1))\right)-\frac{e}{l}v,\\
&b_g=a+b,\\
&-i\omega Z\left(a e^{-ikl}-b e^{ikl}+\frac{K^2}{ikl}(a(e^{-ikl}-1)+b(e^{ikl}-1))\right)-\frac{e}{l}v=-i\omega Z_b a_b e^{-ik_b l},\\
&a e^{-ikl}+b e^{ikl}=a_b e^{-ik_b l}.
\end{aligned}
\tag{9}
$$

In these expressions the coupling coefficient K, the normalized circular frequency w, the specific acoustic impedances of the waveguide Z_g, of the transducer Z and of the backing medium Z_b are defined by

$$
\begin{aligned}
&K=e/\sqrt{\epsilon^S c^E+e^2},\\
&w=kl,\\
&Z_g=k_g c_g/\omega,\\
&Z=k(\epsilon^S c^E+e^2)/\omega\epsilon^S,\\
&Z_b=k_b c_b/\omega.
\end{aligned}
\tag{10}
$$

The system of the four equations (9) can be used to determine the four unknown values $i\omega Z_g b_g$, a, b, and $a_b e^{-ik_b l}$. The first of these values is of great interest since it describes the pressure wave emitted in the waveguide. One has

$$
i\omega Z_g b_g=\frac{iwZ_g[Z(\cos(w)-1)+iZ_b\sin(w)]}{Z^2[2K^2(1-\cos(w))-w\sin(w)]-Z_g Z_b w\sin(w)+iZ(Z_g+Z_b)[w\cos(w)-K^2\sin(w)]}\cdot\frac{ev}{l}. \tag{11}
$$

The transfer function h_g (12) between the voltage applied to the transducer and the pressure wave emitted in the waveguide is equal to:

$$
h_g=\frac{iwZ_g[Z(\cos(w)-1)+iZ_b\sin(w)]}{Z^2[2K^2(1-\cos(w))-w\sin(w)]-Z_g Z_b w\sin(w)+iZ(Z_g+Z_b)[w\cos(w)-K^2\sin(w)]}\cdot\frac{e}{l}. \tag{12}
$$

II. CONSEQUENCES

The analysis of this transfer function shows that it is possible, by choosing the proper materials, to have either a proportional or a differential behavior below the resonance frequency. It may also be used to apply a particular voltage shape in order to produce short width unipolar pressure pulses. These different points are described in the following chapter.

A. Broad constant bandwidth

When Z_g and Z_b are both larger than Z, h_g exhibits a broad proportional bandwidth response. This behavior can easily be physically explained. Both surfaces of the transducer generate pressure waves which have the same shape as that of the applied voltage but of opposite polarities and delayed one with respect to the other one by the transit time of sound waves in the transducer. The resulting pressure in the waveguide, which is more or less the sum of these two waves, has the same shape as the time derivative of the applied voltage. Moreover, because the waveguide and backing medium impedances are larger than that of the transducer, the reflected waves at the interfaces have the same polarity as the incident pressure waves, which has an integrating effect. The derivation followed by the integration leads to an emitted pressure wave proportional to the electrical excitation. This simple explanation cannot be applied to all frequencies. Indeed, in the high frequency range, that is to say, when the transit time in the transducer is long as compared to the period of the wave, the transducer acts no longer as a derivator because of the fixed time delay. In the low frequency range, that is to say, when the transit time in the transducer is short as compared to the period of the wave, reflections no longer have an integrating effect because of the attenuation

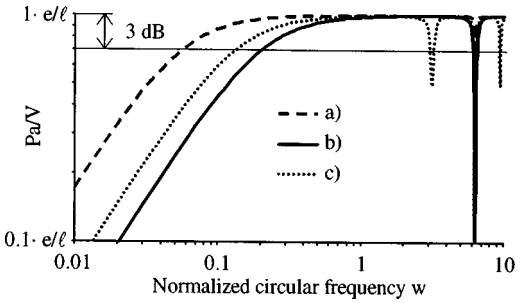

FIG. 2. Normalized circular frequency dependence of h_g in the case of a broad flat bandwidth generator with a PVDF transducer: (a) Steel waveguide and backing medium. (b) Fused silica waveguide and backing medium. (c) Fused silica waveguide and brass backing medium.

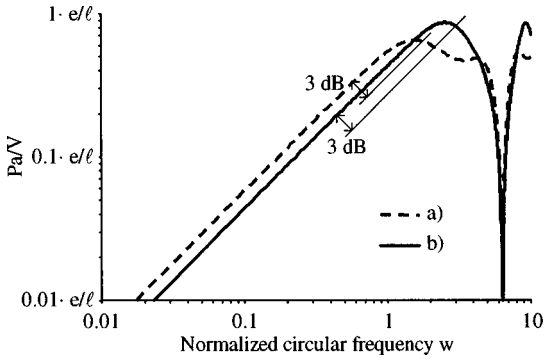

FIG. 3. Normalized circular frequency dependence of h_g in the case of a broad differential bandwidth generator with a piezoelectric ceramic transducer: (a) Fused silica waveguide and brass backing medium. (b) Fused silica waveguide and aluminum backing medium.

produced by the transmission of pressure, at least in the waveguide. This leads to a flat proportional bandwidth between a low and a high cutoff frequencies. The lower cutoff normalized circular frequency w_L can be estimated by carrying a limited development of h_g at low w:

$$w_L = \frac{Z(Z_g+Z_b)(1-K^2)}{Z^2(1-K^2)+Z_gZ_b}. \tag{13}$$

The higher cutoff normalized circular frequency w_H depends on the choice of Z_g and Z_b. If they are different, w_H is almost equal to π and if they are equal w_H is slightly less than 2π. Such a configuration is well suited for thin polymeric transducers such as those made with polyvinylidene fluoride (PVDF). Indeed they have specific acoustic impedance of the order of 1.5 Pa·s/m.

The bandwidth, defined relative to the central frequency, when $Z_g=Z_b=Z'$, is given by

$$2\frac{w_H-w_L}{w_H+w_L} \approx 2\frac{Z(\pi Z-Z')(1-K^2)+\pi Z'^2}{Z(\pi Z+Z')(1-K^2)+\pi Z'^2}. \tag{14}$$

This bandwidth can theoretically reach 200% if Z' is infinite. In practice, if the waveguide and the backing media are made of steel and the transducer of PVDF, the bandwidth is of the order of 196%. It falls to 186% if steel is replace by fused silica. Figure 2 shows h_g for configurations in which the transducer is made of PVDF and the waveguide and the backing media made either with steel, silica, or brass. It can be observed that the absorption at $w=\pi$ in the case of a fused silica waveguide and a brass backing medium is negligible when $Z_g=Z_b$.

The gain H of the elastic wave generator is given by

$$H = \frac{Z_gZ_b}{Z^2(1-K^2)+Z_gZ_b} \cdot \frac{e}{l}. \tag{15}$$

In this configuration Z is lower than Z_g and Z_b, so that the gain is approximately equal to the ratio e/l.

B. Broad differential bandwidth

It has been seen above that the positive reflections at both surfaces of the transducer lead to an integrating behavior. Hence, breaking this configuration lets the generator just act as derivator. The advantage of the differential bandwidth is that it starts from dc. The application of a step voltage to the transducer generates a unipolar pressure pulse in the waveguide.[12] At low frequency h_g behaves as

$$h_g \approx \frac{Z_gZ_b}{Z_g+Z_b} \cdot \frac{iw}{Z^2(1-K^2)} \cdot \frac{e}{l}. \tag{16}$$

Replacing w, Z, and K in (16) by their values leads to

$$h_g \approx \frac{Z_gZ_b}{Z_g+Z_b} \cdot \frac{e}{c^E}\, i\omega. \tag{17}$$

In this expression $i\omega$ is the Fourier transform of the time derivative operator. The gain of this operator has two parts, the first one depending on the waveguide and on the backing medium impedances, and the other one depending on the ratio e over c^E, which is the piezoelectric coefficient d of the transducer. Unlike as in the former broad constant bandwidth case, the gain of the differential operator does not depend on the transducer thickness.

When the waveguide has to transmit the pressure wave to a sample of specific acoustic impedance Z_s, the transmission coefficient of the pressure from the waveguide to the sample has to be taken into account. Here the overall gain is optimized when the waveguide impedance Z_g^{opt} is equal to the geometrical average of the impedances of the backing medium and of the sample:

$$Z_g^{\text{opt}} = \sqrt{Z_sZ_b}. \tag{18}$$

Concerning the bandwidth, a choice of Z_b between 1 and 1.5 times Z is a good compromise between amplitude and bandwidth. In that case the higher cutoff normalized circular frequency is slightly larger than $\pi/2$. If Z_b is slightly smaller than Z, the bandwidth can be increased to almost π. Figure 3 shows h_g when the transducer is made of a piezoelectric ceramic, the waveguide of fused silica, and the backing medium either of brass or aluminum.

C. Short unipolar pressure pulse

So far the linear bandwidth of the elastic wave generator has been studied in the frequency domain. In this paragraph the generation of short unipolar pressure pulses is especially analyzed. Indeed, it is possible to express the numerator of the transfer function h_g as a sum of the Fourier transform of two adjacent pulses:

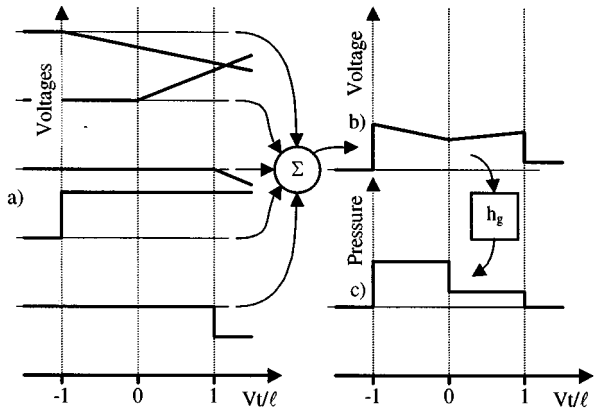

FIG. 4. Voltage shape that must be applied to h_g to make the generator produce two adjacent pressure pulses: (a) Decomposition of the voltage into three ramps and two steps. (b) Voltage shape resulting from the summation of the five voltage terms. (c) Pressure shape generated.

$$
\begin{aligned}
&Z(\cos(w)-1)+iZ_b\,\sin(w)\\
&\Rightarrow iw\,\frac{Z+Z_b}{2}\left(\frac{\sin(w/2)}{w/2}\,e^{iw/2}\right.\\
&\quad\left.+\frac{Z_b-Z}{Z+Z_b}\cdot\frac{\sin(w/2)}{w/2}\,e^{-iw/2}\right).
\end{aligned}
\tag{19}
$$

The generator will generate two adjacent pulses if the voltage applied to the transducer has a Fourier transform proportional to the inverse of the residual terms of h_g. It can be recalled that a similar procedure has been used in the audible range.[13] The Fourier transform of this particular voltage is proportional to the sum of the five following terms:

$$
\begin{aligned}
&-\frac{ZK^2(2Z+Z_g+Z_b)}{Z_g(Z+Z_b)}\cdot\frac{e^{iw}}{(iw)^2},\\
&+\frac{4Z^2K^2}{Z_g(Z+Z_b)}\cdot\frac{1}{(iw)^2},\\
&-\frac{ZK^2(2Z-Z_g-Z_b)}{Z_g(Z+Z_b)}\cdot\frac{e^{-iw}}{(iw)^2},\\
&+\frac{(Z+Z_g)}{Z_g}\cdot\frac{e^{iw}}{iw},\\
&-\frac{(Z-Z_g)(Z-Z_b)}{Z_g(Z+Z_b)}\cdot\frac{e^{-iw}}{iw}.
\end{aligned}
\tag{20}
$$

The three first terms, in $1/(iw)^2$, are Fourier transforms of ramp voltages starting respectively from -1, 0, and 1 in a normalized timescale, whereas the last two terms, in $1/(iw)$, are Fourier transforms of step voltages. They take place in the same normalized timescale at time -1 and 1. The dependence in the normalized timescale of the voltages associated with the five terms is shown Fig. 4(a). Figure 4(b) shows the result of the summation of these five terms. Figure 4(c) shows the resulting pressure wave response in the waveguide. One can notice that the ramps are proportional to K^2. If the coupling coefficient is small, which is the case for PVDF and piezoelectric crystals in general, the five voltage terms can be reduced to only two step voltages. It can be noticed that even if the coupling coefficient is larger, which is the case for piezoelectric ceramics and some crystal cuts, the influence on the pressure response of the ramp voltage term is still not as important as compared to that of the two step voltage terms. For these reasons two adjacent pressure pulses can be almost perfectly generated by the simple application of two step voltages delayed by the resonance period of the transducer.

It must be pointed out that a similar result can be obtained by a digital signal processing. A single step voltage is generated from which is subtracted a delayed and properly amplitude modified copy of this voltage. This technique does not physically produce a short pressure pulse but rather a long one eventually with oscillations. However, the measured signal resulting from this pressure wave can be processed to retrieve the information as if it were a short pressure pulse. With this technique, the beginning and the amplitude of the second step can be optimized by previous measurements. Another advantage is the simplification of the experiment: it is easier to generate a single step voltage than a sequence of two having specific amplitudes and proper timing. On the other hand, the signal-to-noise ratio is decreased by a factor of $\sqrt{2}$ due to the sum of two white noises. Figure 5 shows the result of this process for both low and high transducer coupling coefficients K. It can be noticed that the pulses are better defined with a low K transducer. As it has been explained above, the ramp voltage terms do not introduce significant modification of the shape of the emitted pressure in the waveguide.

III. ELECTRICAL CONNECTION

So far, the purely acoustic response of a generator has been discussed, assuming a perfect match with the electrical generator which supplies it. In this section, the influence of the connection between the electrical and the acoustical parts of the system is discussed. A method is proposed to design and choose the appropriate elements for the whole system.

A. Cable effect

The elastic wave generator emits a pressure wave proportional to the voltage applied to the transducer. But this voltage depends on the electrical input impedance of the elastic wave generator, on the cable properties, and on the output impedance of the electrical generator. If there were no cable and an electrical generator with an almost zero output impedance, the problem would be solved. Because it is hard to reach such a configuration within a large bandwidth, the electrical input impedance of the elastic wave generator must be taken into account. It can easily be calculated by introducing in relation (7) the expression of the current density j versus the electrical displacement field D:

$$
j_i=-\frac{\partial D_i}{\partial t}. \tag{21}
$$

In the case of an harmonic excitation and taking into account the fact that D_1 and D_2 are equal to zero, j can be expressed from the following:

$$-j\left(\frac{1}{i\omega}+\delta(\omega)\right)=\frac{\epsilon^S}{l}v+\frac{e}{l}(u(l)-u(0)). \tag{22}$$

When the mean current is equal to zero, the electrical impedance is

$$\frac{v}{j}=\left(1-K^2\frac{Z(Z_g+Z_b)\sin(w)+2iZ^2(1-\cos(w))}{w[Z(Z_g+Z_b)\cos(w)+i(Z^2+Z_gZ_b)\sin(w)]}\right)\times\frac{l}{i\omega\epsilon^S}. \tag{23}$$

Below resonance, the impedance behaves as a planar capacitor of thickness l made of a dielectric having the dielectric constant at zero stiffness ϵ^T of the transducer. The exponent T used for ϵ^T means at constant stress T. One has

$$\frac{v}{j}=(1-K^2)\frac{l}{i\omega\epsilon^S}=\frac{l}{i\omega\epsilon^T}. \tag{24}$$

Since l is small, the equivalent capacitance of the transducer is large. This makes it difficult to supply the higher frequencies. Two cases can be considered. First, the electrical generator is matched to the cable and the electrical circuit can be considered as a RC circuit, where R is the output impedance of the electrical generator and C the input impedance of the elastic wave generator. In this case, the electrical bandwidth F_e is $1/(2\pi RC)$. Second, the electrical generator is not matched to the cable and the electrical circuit can be considered, if the length of the cable is short enough, as a RLC circuit where L is the inductance of the cable. In that case, the electrical bandwidth F_e is $1/(2\pi\sqrt{LC})$.

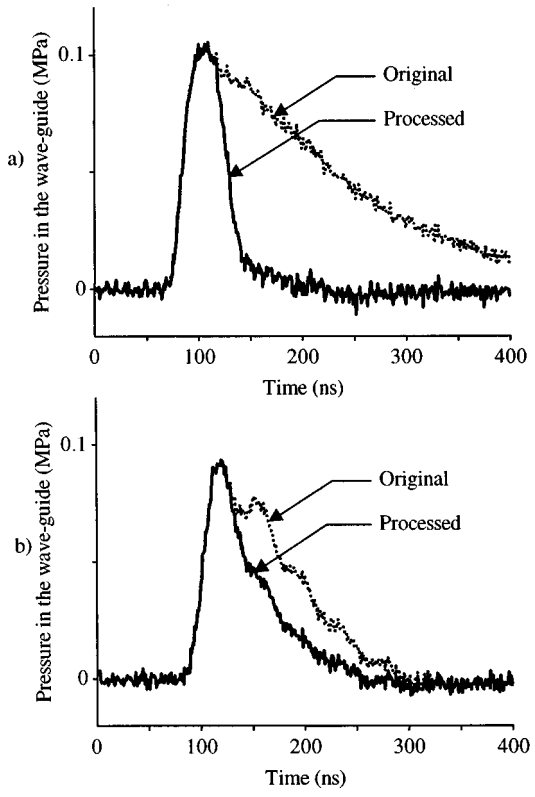

FIG. 5. Pressure in the waveguide as a function of time and time compression signal obtained by digital processing. The elastic wave generators have a fused silica waveguide and a brass backing medium: (a) Case of a low piezoelectric coupling coefficient (40-μm PVDF transducer supplied by a 540-V step voltage). (b) Case of a high piezoelectric coupling coefficient (120-μm piezoelectric ceramic transducer supplied by a 52-V step voltage).

B. Case of a differential bandwidth generator

In this paragraph the optimization of a differential bandwidth generator is considered. The problem is to obtain the largest pressure amplitude for a given voltage generator, acoustical bandwidth, coaxial cable, and transducer area. It has been shown above that the bandwidth of the elastic wave generator is proportional to the thickness of the transducer. Thus its equivalent capacitance C can be calculated from the acoustical bandwidth F_a, the transducer sound velocity V, and the area S taking $\pi/2$ as the normalized cutoff circular frequency. One has

$$l=\frac{V}{4F_a}, \tag{25}$$

which leads to

$$C=\frac{4\epsilon^T SF_a}{V}. \tag{26}$$

The bandwidth of the whole system depends not only on the transducer parameters but also on the electrical parameters. If the acoustical bandwidth F_a is lower than the electrical bandwidth F_e, then the amplitude of the emitted pressure is optimized when the transducer has the highest piezoelectric coefficient d, as shown in Eq. (17). Suppose now that F_e is lower than F_a one must decrease the capacitance seen by the electrical generator by introducing a serial capacitor C_s in the circuit in order to reach at least $F_e=F_a$. Using the expressions for F_e obtained in Sec. III A, it is possible to determine C_s in the case of matched cables or of short length cables. In the case of matched cables one has

$$C_s=\frac{4\epsilon^T SF_a}{8\pi R\epsilon^T SF_a^2-V}, \tag{27}$$

and with short length cables C_s is given by

$$C_s=\frac{4\epsilon^T SF_a}{(4\pi)^2L\epsilon^T SF_a^3-V}. \tag{28}$$

This serial capacitor increases the electrical bandwidth but also decreases the voltage applied to the transducer by a factor M for a given electrical generator voltage. Since the value of C_s depends on the transducer dielectric constant and on the sound velocity, M has to be taken into account for the choice of the transducer material. For matched cables M is equal to

$$M=\frac{V}{8\pi R\epsilon^T SF_a^2}, \tag{29}$$

and for short length cables M is equal to

$$M=\frac{V}{(4\pi)^2L\epsilon^T SF_a^3}. \tag{30}$$

As can be seen in both cases, this factor is directly proportional to the ratio of V/ϵ^T. The pressure wave amplitude is thus optimized when the transducer has the highest $V \cdot g$ product, where g is the classical piezoelectric coefficient as defined by the ratio d/ϵ^T.

We have considered the effect of two types of connections. It is now possible to analyze the best one for a given application. If the electrical bandwidth is larger than the acoustical one, both types of connections are equivalent. On the contrary, if a serial capacitor has to be added, then it is more favorable to choose the type which is associated with the smallest M factor. The ratio of M_m, obtained in the case of a matched connection, over M_s, obtained in the case of a short length connection, is

$$\frac{M_m}{M_s} = \frac{2\pi L F_a}{R} = 2\pi F_a \sqrt{\mu\epsilon}\, l_c . \tag{31}$$

In this expression μ and ϵ are, respectively, the insulator permeability and the dielectric constant of the coaxial connecting cable and l_c its length. For a 1-m length polyethylene insulated coaxial cable, the best matched connection is obtained when F_a is higher than 32 MHz.

In the case of the generation of two adjacent pressure pulses, the electrical bandwidth has to be larger than the acoustical one in order to include the spectrum of these two pulses. For instance, F_e must be eight times larger than F_a to generate pressure pulses having edges four times smaller than their width. Assuming that n is the ratio of F_e over F_a, M_m is divided by a factor n and M_s by a factor n^2. Thus M_m/M_s is also reduced by a factor n so that the matched connection type may always be used.

IV. BONDING

All analysis has been made assuming in the elastic wave generator a perfect coupling between the waveguide and the transducer and between the transducer and the backing medium. Unfortunately, this is not the case because these interfaces include electrodes and a bonding material. The introduction of such layers on both sides of the transducer changes the transfer function of the generator. It is well accepted to consider that layers of thickness smaller than 5% of the wavelength do not produce any serious degradation. For instance, with a 20-MHz bandwidth, 5% of the wavelength in an Epoxy layer leads to a thickness of less than 5 μm. If the layer is thicker then some effects are visible on the bandwidth. The influence of these layers can be taken into account. They change the impedance according to

$$Z'_{\text{seen}} = Z_l \frac{Z' + iZ_l \tan(\omega l_l / V_l)}{Z_l + iZ' \tan(\omega l_l / V_l)}, \tag{32}$$

where Z_l, l_l, and V_l are, respectively, the layer impedance, the thickness, and the sound velocity, and Z' is either the waveguide or the backing medium impedance. It can be observed that Z'_{seen} is progressively changed from Z' to iZ_l as the frequency increases. Above the resonance frequency of the layer, the impedance oscillates between Z' and iZ_l, and produces resonances and antiresonances in the acoustical bandwidth. When the layer is relatively thin, the resulting h_g amplitude is enhanced when the layer impedance is larger than Z' and is reduced in the opposite case.

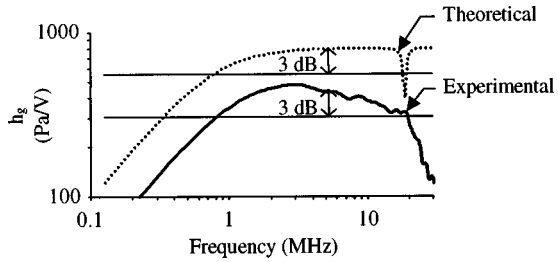

FIG. 6. Broad flat bandwidth elastic wave generator.

V. EXPERIMENTAL RESULTS

Some results in the time domain have already been shown above. In the present part, experimental spectra are compared with the theoretical calculation of h_g established in the first part of this paper.

We have used two types of piezoelectric transducers either made of ceramic or of PVDF. In order to measure the emitted pressure wave an electrical method involving a short circuit capacitor is used.[12] When the pressure wave enters into the insulating part of the capacitor, the short circuit current i_{sc} is proportional to the pressure shape:

$$T_g(t) = -\frac{Z_s}{\tau C_s} \cdot \frac{l_s}{V_s}\, i_{sc}(t). \tag{33}$$

In this expression Z_s, l_s, and C_s are, respectively, the specific acoustic impedance, the thickness, the capacity of the sample, and V_s is the applied voltage. From the short circuit current and the shape of the voltage applied to the transducer, it is possible to derive h_g.

Figure 6 shows a comparison between the experimental and the theoretical spectra of a broad flat bandwidth generator made of a fused silica waveguide, a brass backing medium, and a 40-μm-thick 1.75-cm^2 active surface PVDF transducer. As expected, the two spectra are very similar, except for their amplitude, exhibiting a bandwidth of almost 185% spread from 800 kHz to 20 MHz. The difference of the amplitude over this bandwidth, which corresponds to a shift of -5 dB, can be attributed to pressure losses in the transducer, in the waveguide, and in the coupling media and also to the uncertainty of characteristic coefficients of the materials used in the experiment. The spectrum has been calculated with the ''original'' pressure of Fig. 5(a) generated by a step

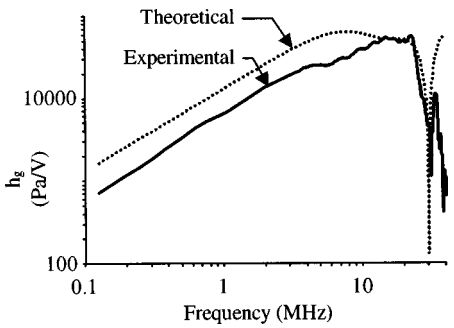

FIG. 7. Broad differential bandwidth elastic wave generator.

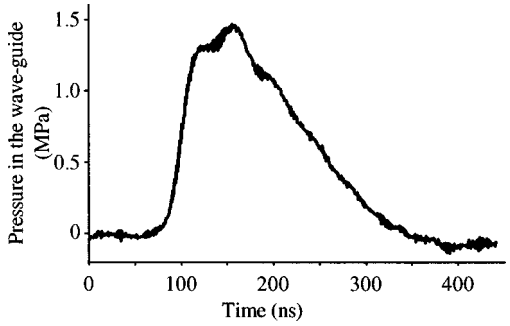

FIG. 8. Pressure shape response to a 175-V step voltage of an elastic wave generator made of an aluminum wave guide, a piezoelectric ceramic, and a brass backing medium.

voltage of only 175 V. This voltage could be 10 times larger and still not reach the breakdown voltage. Such a voltage could generate a pressure of 1 MPa in the waveguide.

Figure 7 shows a comparison between the experimental and the theoretical spectra of a broad differential bandwidth generator made of an aluminum waveguide, a brass backing medium, and a 120-μm-thick 1.75-cm^2 active surface ceramic transducer.[14] Here again the general shapes are very similar and the difference of the amplitude over the spectrum corresponds to a shift of -5 dB for the same reasons as mentioned above. The time response of this elastic wave generator to a 175-V step voltage is illustrated in Fig. 8. The peak pressure amplitude is 1.5 MPa for a 30-ns rise time and a 135 ns width. Some oscillations due to the bonding appear on the peak but vanish rapidly.

VI. CONCLUSION

In this paper we have shown that it is possible to generate high power pressure pulses using a thin transducer coupled on each of its sides with a waveguide and a backing medium. We have analyzed the behavior of such a system taking into account the specific acoustic impedance of the components of the elastic wave generator. Depending on the goal, very broad flat or differential bandwidth generators can be designed. It is also possible to generate very well defined pressure pulses using two consecutive step voltages of properly chosen amplitudes with one delayed with respect to the other one by the resonance period. The influence of the electrical connections has been taken into account in order to make possible the design of a system giving the highest amplitude pressure wave with the lowest electrical applied voltage. Experiments have been carried out which show a very good agreement between theory and experiments.

[1] D. A. Sotiropoulos and J. D. Achenbach, ''Reflection of elastic waves by a distribution of coplanar cracks,'' J. Acoust. Soc. Am. **84**, 752–759 (1988).
[2] M. De Billy, L. Adler, and G. Quentin, ''About the use of ''trailing echoes'' for the detection of disbond at solid-solid interface,'' J. Phys IV Colloque C5 **4**, 917–920 (1994).
[3] M. N. Rychagov and H. Ermert, ''Reconstruction of fluid motion in acoustic diffraction tomography,'' J. Acoust. Soc. Am. **99**, 3029–3035 (1996).
[4] P. Laurenceau, G. Dreyfus, and J. Lewiner, ''New principle for the determination of potential distributions in dielectrics,'' Phys. Rev. Lett. **38**, 46–49 (1977).
[5] C. Alquié, G. Dreyfus, and J. Lewiner, ''Stress-wave probing of electric field distributions in dielectrics,'' Phys. Rev. Lett. **47**, 1483–1487 (1981).
[6] T. Ditchi, C. Alquié, and J. Lewiner, ''Broadband determination of ultrasonic attenuation and phase velocity in insulating material,'' J. Acoust. Soc. Am. **94**, 3061–3066 (1993).
[7] A. F. Brown and J. P. Weight, ''Generation and reception of wideband ultrasound,'' Ultrasonics **12**, 161–167 (1974).
[8] F. S. Foster and J. W. Hunt, ''Generation and characterization of short pulse ultrasound transducers,'' Ultrasonics **16**, 116–122 (1978).
[9] W. Eisenmenger and M. Haardt, ''Observation of charge compensated polarization zones in polyvinylidenfluoride (PVDF) films by piezoelectric acoustic step-wave response,'' Solid State Commun. **41**, 917–920 (1982).
[10] M. Maeda, S. Takahashi, T. Takada, and M. Ide, ''Measurement of charge distributions in organic photoconductor using pulse ulrasonic wave,'' Proceedings of 11th Symposium on Ultrasonic Electronics, Kyoto 1990, Jpn. J. Appl. Phys. **30**, Supplement 30-1, 74–76 (1991).
[11] L. J. van der Pauw, ''The planar transducer—A new type of transducer for exciting longitudinal acoustic waves,'' Appl. Phys. Lett. **9**, 129–131 (1966).
[12] S. Holé and J. Lewiner, ''Single transducer generation of unipolar pressure waves,'' Appl. Phys. Lett. **69**, 3167–3169 (1996).
[13] T. G. Winter, J. Pereira, and J. Bee Bednar, ''On driving a transducer to produce pulses shorter than the natural period of the transducer,'' Ultrasonics **13**, 110–112 (1975).
[14] Piezoelectric ceramic Pz24 purchased from Ferroperm A/S.

The ring-type all-fiber Fabry–Pérot interferometer hydrophone system

Donglin Li and Shuquan Zhang
Department of Underwater Acoustic Engineering, Harbin Engineering University, Harbin, 150001, People's Republic of China

(Received 21 January 1997; revised 12 April 1998; accepted 13 May 1998)

A compact theory and the detailed design of the ring-type all-fiber Fabry–Pérot interferometer hydrophone system has been developed here. The system is composed of four parts: the optical part with the laser source, the ring interferometer of all-fiber suited for the acoustical structure, the acoustical structure, and the stabilization maintaining the feedback servo mechanism and signal demodulation part. For this reason it differs greatly in many ways from the traditional concept of hydrophone which is commonly made up with one or several functional material elements such as the piezoelectric ceramic or the PVDF ones. So, on accuracy ground it is named the Fiber Hydrophone System instead of Hydrophone. The fiber-optic hydrophone itself, not including the laser source and the electric servo part, has the compact size of $\phi 40 \times 80$ mm, specific gravity of less than 1, and the system has a free-field open-circuit voltage sensitivity level of above -140 dB *re*: 1 V/μPa. Experimental results show an exciting future of this kind of fiber-optic hydrophone system for the application of all optical towed arrays. © *1998 Acoustical Society of America.* [S0001-4966(98)01209-0]

PACS numbers: 43.38.Zp, 43.30.Yj [SLE]

INTRODUCTION

Perhaps one of the most important breakthroughs in sonar technology after World War II is the towed array sonar system. This breakthrough had forced the submarine to be developed into a quieter state. As a follow-up to the coming out of the quieter state submarine the need for some new sonar concepts which can keep in step with the up-to-date progress of technology becomes clear. An optic towed array is such a new concept and the fiber-optic hydrophone is its kernel part.

Optic fiber sensing technology began in the late 1970s, optic fiber hydrophones were first demonstrated by Bucaro *et al.* in 1977.[1] During 20 years of development significant progress has been achieved. Now there are tens of different kinds of fiber-optic hydrophones being reported. Among these works, Dandridge's contribution is the most noticeable.[2–5] From the point of view of the acousto-optic transduction mechanism, the fiber-optic hydrophone systems can be classified into three types: the intensity modulation type, the polarization modulation type, and the phase generated interference type. This has been well demonstrated in the published literature.

Now, the main interests of the study in sonar use are focused on the phase generated interference type. Since the working principles are exactly the same with traditional optic interferometers except that the light paths are confined within the optic fibers, the hydrophone systems of this type are also named the interferometer hydrophone systems. Hydrophones of this type have sensitivities of 2 to 3 orders of magnitude higher than that of the piezoelectric ceramic counterparts that are now in active service.

Figure 1 shows several all-fiber interferometers suitable for hydrophone systems.

The Mach–Zehnder and the Michelson interferometers belong to the two-beam interference kind which have two fiber arms; one is the sensory arm, the other is the reference beam arm. An acoustically induced change on the sensory arm will generate a phase difference between the two arms; if we suitably select the linear region of its output intensity versus the change of phase difference as its working scope, the phase difference will be proportional to the acoustic change. However, there are some inconveniences in forming a hydrophone with these kinds of interferometers, such as its reference arm will also be sensitive to the acoustic pressure and this requires solving the acoustical shielding problem, which is a difficult matter. A push–pull idea which makes both arms sensory arms seems to some extent to provide a solution to the problem, but this idea limits the hydrophone's structure to an impractical case.[6] In addition, this kind of interferometer hydrophone needs two fiber couplers, making the system arrangement more complex. But there are also some advantages of this kind, for example, it does not need the laser source to be highly coherent and this will reduce the technical requirement for the laser source greatly.

The Sagnac and the Fabry–Pérot interferometers belong to the multibeam interference kind.

An all-fiber Sagnac interferometer operates in such a principle that the light beam from the laser source is coupled to a directional coupler which splits the beam into two. It makes the two beams transmit in opposite directions with each other in a closed fiber ring, and then they return to the same terminal of a photodetector. If the system gets a small rotation in the direction perpendicular to the plane where light beams are in, there will be an optical path difference between the two beams. So it is sensitive to the rotation

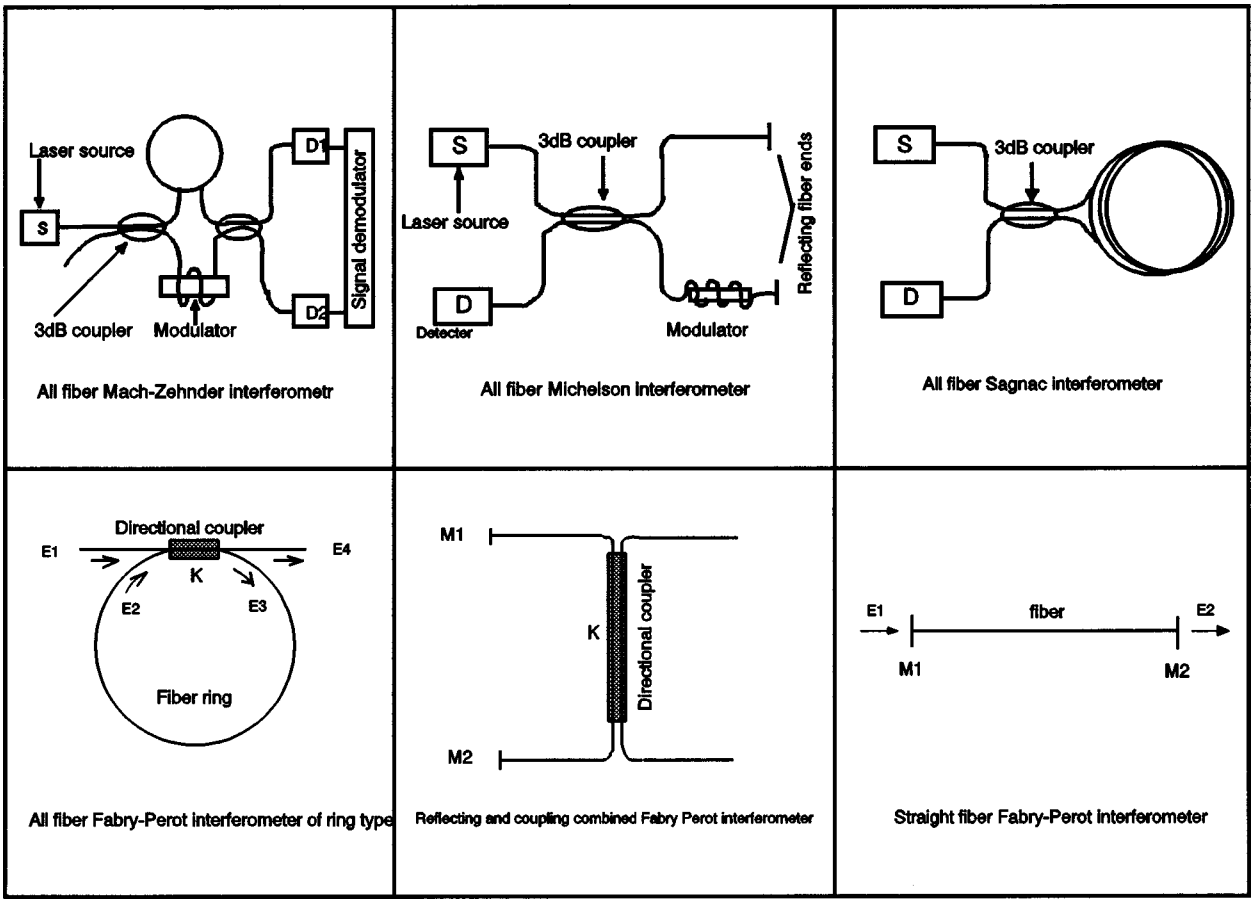

FIG. 1. Some typical all-fiber interferometers.

effects and often used as a gyroscope system. When it is used as a hydrophone system, we have to add another coupler and a polarizer to distinguish the sensory beam and the reference one.

All-fiber Fabry–Pérot interferometers can be arranged in two forms in their construction. One is by plating certain medium films which have a high reflecting ratio onto both ends of a piece of single-mode fiber to form a Fabry–Pérot resonator. This form has advantages of simplicity and high sensitivity. But its high reflection back to the laser source will induce an unstable source problem, so an isolator is needed. Another problem is the technical difficulty of connecting the communicating fiber to the two ends. These limit its real application in constructing a practical hydrophone. The other form of an all-fiber Fabry-Pérot interferometer is by using a so-called fiber ring resonator to form a Fabry–Pérot counterpart. It usually has a fineness of tens or several hundreds. Theoretically speaking, a Fabry–Pérot interferometer has a fineness of 1 to 2 orders of magnitude higher than that of the Mach–Zehnder and Michelson ones. In reality, it is the finest displacement-sensing instrument known today. So, theoretically the hydrophones of Fabry–Pérot interferometer type have the highest sensitivity.

Therefore we choose the ring form of all-fiber Fabry–Pérot interferometer in our hydrophone system.

I. THEORIES

A. The principles of the ring-type all-fiber Fabry–Pérot interferometer

Traditionally a Fabry–Pérot interferometer is made up of two parallel mirrors, it is an open cavity and requires the two mirrors to be strictly parallel with each other. Any slight tilt would induce a rapid geometrical loss, so it is very difficult to have a relatively long cavity interferometer.

While a ring-type all-fiber Fabry–Pérot interferometer employs the single-mode optical fiber and a directional coupler to make up a closed cavity, it is necessary that the multibeam interference be completed by means of a ring optical fiber path. Having overcome this problem, there is another difficulty which we will meet when we make a practical hydrophone; that is the winding loss, which will be discussed later.

The working principles of a ring-type all-fiber Fabry–Pérot interferometer are shown in Fig. 2. It is commonly named a ring resonator in the optical fiber communication field.

An incident light E1 from the laser source is split by the coupler into two, the E3 and E4. By passing through the ring, E3 becomes another incident light E2 which again will be partially coupled into E4, and partially into E3 by the coupler. This endless circulation forms the multibeam interference at the output end of E4.

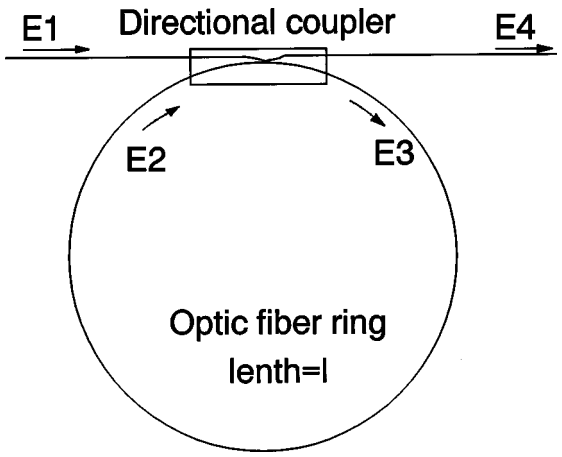

FIG. 2. A ring type all-fiber Fabry–Pérot interferometer.

If we use α_c to indicate the coupling loss, α_f, the transmitting loss of light in the fiber, and K, the coupling coefficient of the coupler, and assume the ring has a length of l, the optical traveling time needed in one circulation in the ring will be

$$\tau = l/v, \tag{1}$$

where v is the velocity of light in the fiber. Thus we can express the light amplitudes as follows:

$$E_1(t) = E_0 \exp[-i(2\pi\nu_0 t + \varphi(t))], \tag{2}$$

$$E_2(t) = \exp(-2\alpha_f l/2) E_3(t+\tau), \tag{3}$$

$$E_3(t) = \exp(-\alpha_c/2)[(1-K^2)^{1/2} E_1(t) + iKE_2(t)], \tag{4}$$

$$E_4(t) = \exp(-\alpha_c/2)[iKE_1(t) + (1-K^2)^{1/2} E_2(t)]. \tag{5}$$

The fiber ring length l cannot be very long, so the optical transmitting loss factor $\alpha_f l$ in the fiber ring is relatively very small compared with the coupling loss α_c, in fact it can be neglected in Eq. (3), so we can approximately express Eq. (3) as

$$E_2(t) = E_3(t+\tau). \tag{6}$$

With the recurrence relations of Eqs. (2)–(5), we can get

$$E_4(t)/E_1(t) = A\left\{ B + A(1-K^2)\sum_{n=1}^{\infty} (AB)^{n-1} \times \exp[-i2\pi n\nu_0\tau + i(\varphi(t) - \varphi(t+n\tau))] \right\}, \tag{7}$$

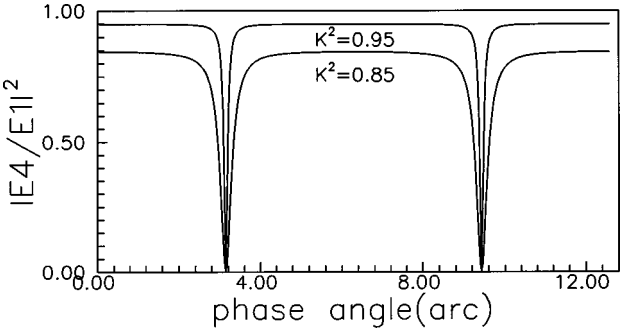

FIG. 3. Ring resonance properties.

where $A = \exp(-\alpha_c/2)$, $B = iK$. By taking the mean square of the above equation with respect to time, we finally obtain the input–output light intensity ratio of the ring-type all-fiber Fabry-Pérot interferometer as

$$|E_4(t)/E_1(t)|^2 = A^2\{1 - G/[1 - H\sin^2(\theta/2)]\}, \tag{8}$$

where

$$G = (1-K^2)(1-A^2K^2C^2)(1-A^2)/(1+AKC)^2(1-A^2K^2), \tag{9}$$

$$H = 4AKC/(1+AKC)^2, \tag{10}$$

$$C = \exp(-2\pi\Delta\nu\tau), \tag{11}$$

$$\theta = 2\pi\nu_0\tau - \pi/2. \tag{12}$$

Equation (8) includes the information of random-phase perturbation of the laser source. Here we can make a brief discussion on its output properties.

(a) Suppose $A^2 = K^2$, this means the coupling coefficient K is matching with the coupler loss coefficient A, in addition, suppose the laser source is monochromatic, or the spectrum line width (of the laser source) $\Delta\nu = 0$, thus from Eq. (8) we know

$$\left|\frac{E_4(t)}{E_1(t)}\right|^2 = K^2 \frac{1-(1-K^2)^2}{(1+K^2)^2 - 4K^2\sin^2(\theta/2)}, \tag{13}$$

this is the ideal case, its resonating output properties are shown in Fig. 3 and, at this case we say the coupling coefficient K is the resonance coupling coefficient.

(b) Again, in the matching case of $A^2 = K^2$, but the effects of the spectrum line width have been taken into consideration, that is, $\Delta\upsilon \neq 0$. Substituting $\tau = l/v$, $\Delta\nu = \nu\Delta\lambda/\lambda$, and (the coherence length) $L_c = \lambda^2/\Delta\lambda$ into (8) and we have

$$\left|\frac{E_4(t)}{E_1(t)}\right|^2 = K^2\left\{1 - \frac{(1-K)^2(1+K^2\exp(-2\pi l/L_c))/(1+K^2)}{1-4K^2\exp(-2\pi l/L_c)\sin^2(\theta/2)/(1+K^2\exp(-2\pi l/L_c))^2}\right\}. \tag{14}$$

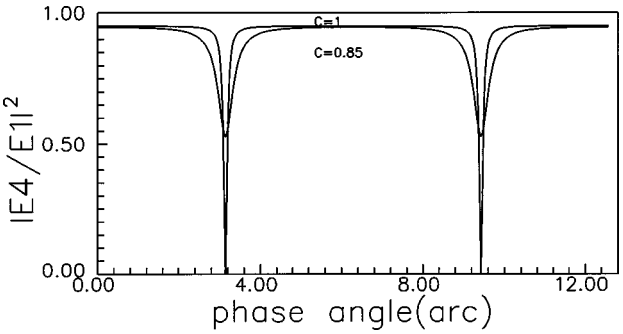

FIG. 4. Relations with coherence length.

Figure 4 shows the changes of the resonance output properties of the ring resonator with respect to the coherence length of the laser source.

B. The elastic theories of the back structure of the hydrophone

One of the advantages of an optical fiber hydrophone is that you can design it in any shape you need. The shape can be formed by the so-called elastic back structure of the hydrophone. In fact it is the back structure which will respond to the acoustic pressure impinged on the hydrophone, and corresponding results ensue when the back structure issues elastic strains in accordance with the pressure. The strains can be sensed by the fiber ring of the interferometer being wound around the back structure. In our case, we choose the back structure to be a hollow cylinder with end caps at both ends to keep an air cavity inside the structure in order to obtain a maximum response to the acoustic pressure (see Fig. 5).

We are concerned here with only the low-frequency range, or in other words, the maximum dimension of the hydrophone is small compared with the acoustic wavelength, so we can use the quasistatic analysis method to solve this problem. However, it may be proper to say a few words about an objection brought forward by Bucaro,[7] which tends to invalidate this usual calculation and suggest a dynamic correction. When the thickness of the cylinder has thinned to any considerable extent, our calculation of quasistatic analysis would have to be greatly modified.

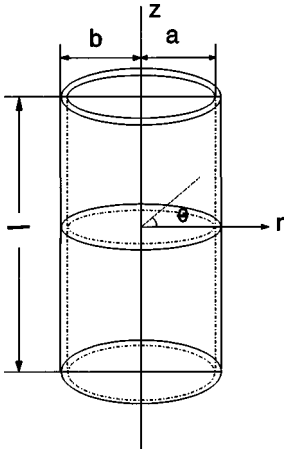

FIG. 5. PVC elastic cylinder as the back structure.

In the quasistatic state the problem can be solved by evaluating only the stresses. Here as usual we use 1, 2, and 3 to represent the cylindrical coordinate components of r, θ, and z, respectively. The stress components of the back structure (Fig. 5) should satisfy the equilibrium and the accordant equations, and also the boundary conditions, which are as follows. The axisymmetric equilibrium equations:

$$\frac{\partial T_1}{\partial r}+\frac{\partial T_6}{\partial z}+\frac{T_1-T_2}{r}=0, \tag{15}$$

$$\frac{\partial T_3}{\partial z}+\frac{\partial T_6}{\partial r}+\frac{T_6}{r}=0. \tag{16}$$

The axisymmetric accordant equations:

$$\Delta^2 T_1-\frac{2}{r}(T_1-T_2)+\frac{1}{1+\sigma}\frac{\partial^2\Theta}{\partial r^2}=0, \tag{17}$$

$$\Delta^2 T_2+\frac{2}{r}(T_1-T_2)+\frac{1}{1+\sigma}\frac{1}{r}\frac{\partial^2\Theta}{\partial r^2}=0, \tag{18}$$

$$\Delta^2 T_3+\frac{1}{1+\sigma}\frac{\partial^2\Theta}{\partial z^2}=0, \tag{19}$$

$$\Delta^2 T_6-\frac{1}{r^2}T_6+\frac{1}{1+\sigma}\frac{\partial^2\Theta}{\partial r\,\partial z}=0, \tag{20}$$

where $\Delta^2=\partial^2/\partial r^2+1/r\ \partial/\partial\theta+\partial^2/\partial z^2$, $\Theta=T_1+T_2+T_3$, and σ is the Poisson's ratio of the material. If we introduce the stress potential Φ here to simplify the problem, we have the relations:

$$T_1=\frac{\partial}{\partial z}\left(\sigma\Delta^2\Phi-\frac{\partial^2\Phi}{\partial r^2}\right), \tag{21}$$

$$T_2=\frac{\partial}{\partial z}\left(\sigma\Delta^2\Phi-\frac{1}{r}\frac{\partial\Phi}{\partial r}\right), \tag{22}$$

$$T_3=\frac{\partial}{\partial z}\left[(2-\sigma)\Delta^2\Phi\ \frac{\partial^2\Phi}{\partial z^2}\right], \tag{23}$$

$$T_6=\frac{\partial}{\partial r}\left[(1-\sigma)\Delta^2\Phi-\frac{\partial^2\Phi}{\partial z^2}\right]. \tag{24}$$

Substituting Eqs. (21)–(24) into (15)–(20), Φ satisfies

$$\Delta^2(\Delta^2\Phi)=0. \tag{25}$$

The general solution of the above equation is

$$\Phi=z(A\ln r+Br^2+C)+Dz^3, \tag{26}$$

where the constants A, B, C, and D can be determined by the following boundary conditions:

$$\begin{aligned} &T_1|_{r=a}=0,\ T_1|_{r=b}=-P_0,\\ &T_3|_{z=-1/2}=T|_{3z=1/2}=-P_0\frac{b^2}{b^2-a^2},\\ &T_6|_{r=a}=0,\ T_6|_{r=b}=0, \end{aligned} \tag{27}$$

where P_0 denotes the incident acoustic pressure, and therefore we get the solutions of the stresses T_i of the back structure induced by the incident acoustic pressure P_0:

$$\begin{bmatrix} T_1 \\ T_2 \\ T_3 \\ T_6 \end{bmatrix} = P_0 \frac{b^2}{b^2-a^2} \begin{bmatrix} \frac{a^2}{r^2}-1 \\ -\frac{a^2}{r^2}+1 \\ 1 \\ 0 \end{bmatrix}. \tag{28}$$

Having had the solution of the stresses T_i, the corresponding strains S_i are obtained at once:

$$\begin{bmatrix} S_1 \\ S_2 \\ S_3 \\ S_6 \end{bmatrix} = \frac{P_0 b^2}{Y(b^2-a^2)} \begin{bmatrix} \frac{a^2(1+\sigma)}{r^2}-(1-2\sigma) \\ \frac{-a^2(1+\sigma)}{r^2}-(1-2\sigma) \\ -1+2\sigma \\ 0 \end{bmatrix}. \tag{29}$$

C. The free-field open-circuit voltage sensitivity level of the hydrophone

Suppose the phase of the traveling light in the ring is

$$\varphi = knl = \beta l + \varphi_0, \tag{30}$$

where k is the wave number of light in vacuum and n is the refractive index of the fiber core.

Any response to the incident acoustic pressure of the back structure will introduce a phase change in the ring interferometer being wound on it, we may write it as

$$\Delta\varphi = \beta\Delta l + l\Delta\beta = \beta\Delta l + l[k\Delta n + (\partial\beta/\partial a_0)\Delta a_0], \tag{31}$$

where a_0 is the radius of the fiber core, the term $(\partial\beta/\partial a_0)\Delta a_0$, which represents the frequency dispersion, is very small compared with $k\Delta n$, so we can approximately rewrite (31) as

$$\Delta\varphi = \beta l \frac{\Delta l}{l} + \beta l \frac{\Delta n}{n}. \tag{32}$$

The second term of above equation can be evaluated by making use of the photoelastic relation:

$$\Delta\left(\frac{1}{n^2}\right)_y = \sum_l^{k,l} p_{ijkl}\epsilon_{kl}, \tag{33}$$

where ϵ_{kl} are the strain components of the fiber core and p_{ijkl} is the photoelastic coefficients. Hitherto we have supposed the fiber to be a homogeneous material, so only two of p_{ijkl} are independent. Note also the relations of $\Delta l/l = \epsilon_{33}$, $\epsilon_{11} = \epsilon_{22}$, we have

$$\Delta\varphi = \epsilon_{33}\beta l - \frac{n^2}{2}\beta l[(p_{11}+p_{12})\epsilon_{11} + p_{12}\epsilon_{33}], \tag{34}$$

hence, if assuming the fiber has been wound tightly on the back structure, i.e., the elastic changes will be transmitted directly into the fiber without any loss, or in other words, we provide that the strains on the connecting boundaries between the fiber and the back structure are continuous, then, by noticing the difference between the two coordinate systems, we can obtain

$$\epsilon_{33} = (S_1+S_2)|_{r=b}, \tag{35}$$

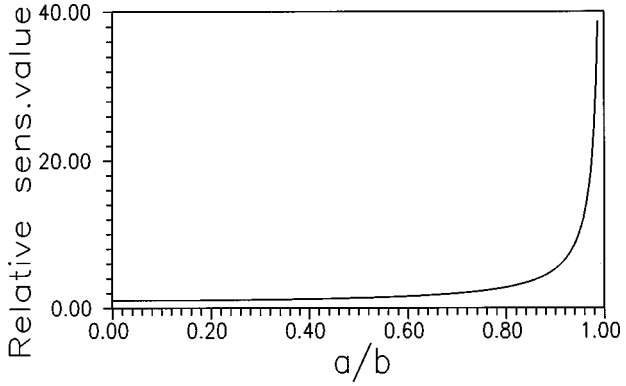

FIG. 6. Relative-relations of phase-pressure sensitivity $\Delta\phi/p_0$, with the radius ratio, a/b.

$$\epsilon_{11} = S_3|_{r=b}, \tag{36}$$

by substituting (29) into (35) and (36), and then by using (34), we get

$$\Delta\varphi = \frac{P_0\beta l b^2(2\sigma-1)}{Y(b^2-a^2)}\left[1-\frac{n^2}{2}(p_{11}+2p_{12})\right]. \tag{37}$$

This means the pressure-phase sensitivity is

$$\frac{\Delta\varphi}{P_0} = \frac{\beta l b^2(2\sigma-1)}{Y(b^2-a^2)}\left[1-\frac{n^2}{2}(p_{11}+2p_{12})\right]. \tag{38}$$

Figure 6 shows the relations of the pressure-phase sensitivity Δ/P_0 with the back structure's radius ratio a/b.

Another important design parameter is the optimum sensing point. If we define

$$S_\theta = \frac{\partial}{\partial\theta}\left|\frac{E_4(t)}{E_1(t)}\right|^2 \tag{39}$$

as the phase sensitivity of the Fabry–Pérot interferometer, then there will exist a most sensitive point $\theta = \theta_0$ which satisfies

$$\left.\frac{\partial S_\theta}{\partial\theta}\right|_{\theta=\theta_0} = \frac{\partial^2}{\partial\theta^2}\left|\frac{E_4(t)}{E_1(t)}\right|^2_{\theta=\theta_0} = 0. \tag{40}$$

From Eqs. (8) and (39) we have

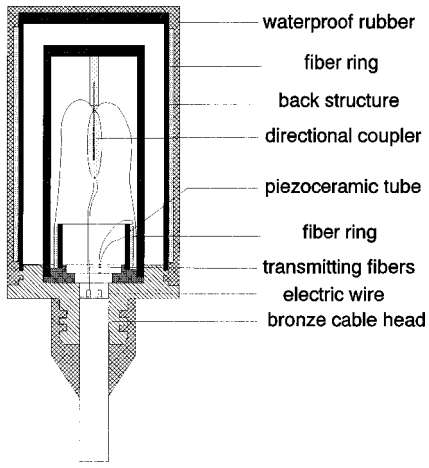

FIG. 7. Diagram of the hydrophone head.

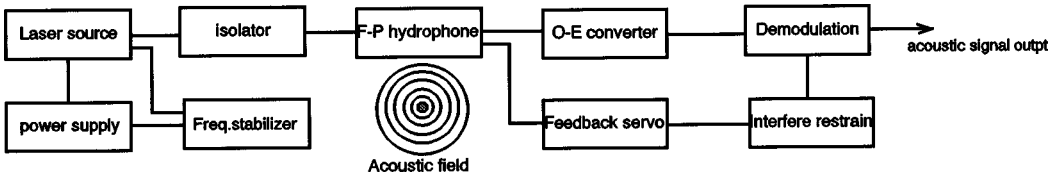

FIG. 8. The schematic diagram of Fabry–Pérot interferometer hydrophone.

$$\theta_0 = \arccos \frac{1}{2}\left\{\left(\frac{2}{H}-1\right) \pm \left[\left(\frac{2}{H}-1\right)^2 + 8\right]^{1/2}\right\}. \tag{41}$$

Substituting (41) into (39), the optimum phase sensitivity of the Fabry–Pérot interferometer is obtained

$$S_{\theta_0} = -\frac{A^2 G \cos^2 \theta_0}{2H \sin^3 \theta_0}. \tag{42}$$

Equation (42) represents the change per unit phase shift of the unified output light power from the interferometer.

An incident acoustic pressure P_0 acts on the hydrophone and induces a phase shift of $\Delta\varphi$, this will induce a power change of the output light:

$$\Delta W_{\text{out}} = \Delta\varphi S_{\theta_0} W_{\text{in}}, \tag{43}$$

where W_{in} denotes the input light power from the laser source. By inserting (38) into the above equation, ΔW_{out} becomes

$$\Delta W_{\text{out}} = -\frac{A^2 G \cos^2 \theta_0}{2H \sin^3 \theta_0} \cdot \frac{P_0 \beta l b^2 (2\sigma - 1)}{Y(b^2 - a^2)} \times \left[1 - \frac{n^2}{2}(p_{11} + 2P_{12})\right] W_{\text{in}}. \tag{44}$$

Then the output current induced by ΔW_{out} has the form

$$i_{\text{out}} = \Delta W_{\text{out}} \frac{qe}{h\nu}, \tag{45}$$

where q is the light quantum coefficient of the photodiode at the output end of the hydrophone, e is the electricity of one electron, h is the Plank constant, and ν is the light frequency. If, in addition, the photodiode has a load resistance R, then the output voltage signal of the hydrophone will be

$$V_{\text{out}} = i_{\text{out}} R = \Delta W_{\text{out}} \frac{qe}{h\nu} R, \tag{46}$$

thus we obtain the free-field open-circuit voltage sensitivity of the hydrophone:

$$M_0 = \frac{V_{\text{out}}}{P_0} = \frac{qe}{h\nu} R \frac{\beta l b^2 (2\sigma - 1)}{Y(b^2 - a^2)} \frac{A^2 G \cos^2 \theta_0}{2H \sin^3 \theta_0} \times \left[\frac{n^2}{2}(p_{11} + p_{12}) - 1\right] W_{\text{in}} \tag{47}$$

and the corresponding sensitivity level:

$$M_L = 20 \log(M_0 / M_{\text{ref}}), \tag{48}$$

where M_{ref} is the reference sensitivity with the value of 1 V/μPa.

II. THE SYSTEM ARRANGEMENT

A. The diagrams of the system and the hydrophone head

The ring-type all-fiber Fabry–Pérot interferometer hydrophone system has four main parts: the optical part with the laser source, the ring interferometer of all-fiber suited for the acoustical structure, the acoustical structure, and the stabilization maintaining the feedback servo mechanism with the signal demodulation part. Figure 7 shows the hydrophone head arrangement. The scheme diagram of the system is shown in Fig. 8. We will give a brief discussion below.

B. The requirements for the laser source

From Sec. I B we know the spectrum line width $\Delta\nu$ of the laser source affects the hydrophone's coherence properties greatly. And from Eq. (46) in Sec. I C we can see that the stability of the output power of the laser source also has a direct influence on the hydrophone's sensitivity. So it requires that the laser source have a narrow-band spectrum together with a highly stable output power. We choose a

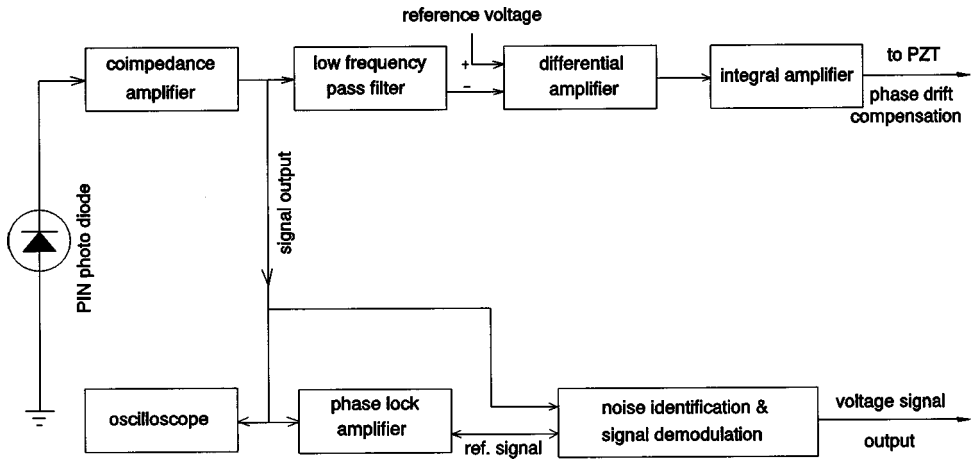

FIG. 9. Block diagram of signal processing and demodulation scheme.

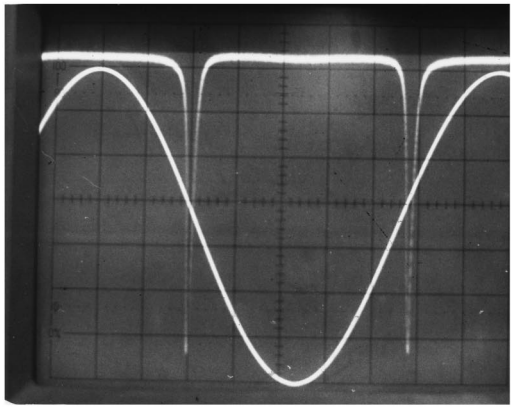

(a)

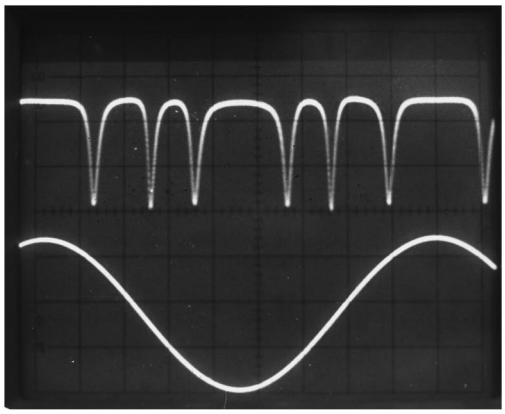

(b)

FIG. 10. (a) Ring resonator's coherence properties (a) at its natural state, and (b) after round winding.

He–Ne laser source with the wave length of $\lambda = 0.6328\ \mu$m, and make use of the thermal Q-controlling technique to adjust the cavity length of the laser source automatically, locking the frequency in a certain point. The technical parameters are as follows: frequency stability: (1–10 s square-error) 10^{-10}; frequency repeatability: prior to $\pm 1 \times 10^{-7}$; output power stability: 1%; spectrum line width: $\Delta\nu < 300$ kHz.

C. Signal demodulation and hydrophone stabilization

We used the noise-free p-i-n-type photodiode at the output terminal of the hydrophone as a photoelectric con-

FIG. 11. Photo of an experimental hydrophone head (number 3).

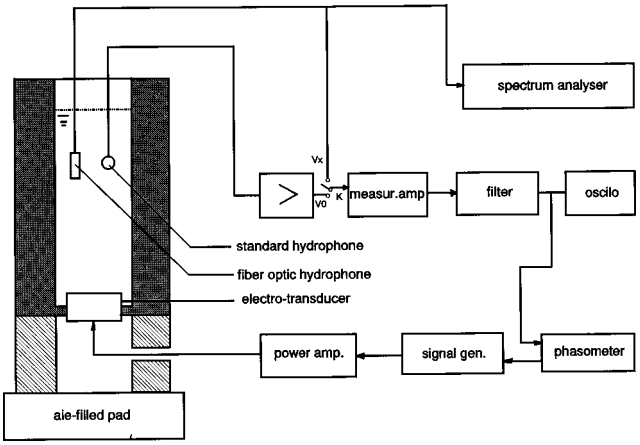

FIG. 12. Fluid column vibrating calibration system.

verter, and a coimpedance amplifier at the front stage of the receiving circuit to detect and amplify the faint output current signal from the photodiode. The frequency range is from 50 to 5000 Hz, and the bandpass filters are used to absorb noise. In general, both the acoustical and the electrical noise shielding methods would have already been well considered at the design stage, so the high-frequency band suppression filter used in the system seems to have little use, but in reality we have a piezoelectric ceramic tube inside the hydrophone to serve as a reacting mechanism for maintaining the ring interferometer in its optimum sensing point, and this mechanism may, under certain circumstances, have some slight vibrating effects due to its resonance frequencies, which will cause a wrong feedback controlling signal and the corresponding mechanism reactions. In such a case the high-frequency band suppression filter takes its effects. Below 50 Hz, the perturbation has relatively higher amplitudes, and the lower the frequency, the more difficult to purify it, so the acoustic shielding is necessary. Figure 9 is the illustration diagram of this part.

D. The interferometer and the back structure

The all-fiber Fabry–Pérot interferometer is made of the single-mode fiber with the cutoff wavelength $\lambda = 0.579\ \mu$m, and the directional coupler used has a loss fac-

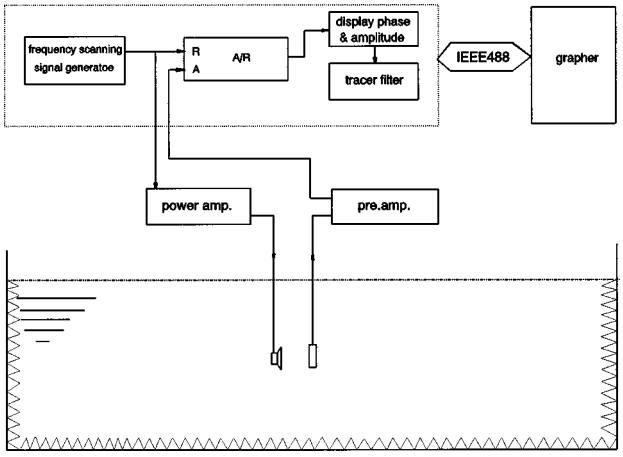

FIG. 13. Sound absorbing water pool with the measuring system.

TABLE I. Measured results of the sensitivity level and relative phase stability of the hydrophone numbered 3 (0 dB re: 1 V/μPa).

Measuring order	First time		Second time		Third time		Fourth time	
f(Hz)	M(dB)	Φ(deg)	M(dB)	Φ(deg)	M(dB)	Φ(deg)	M(dB)	Φ(deg)
63	−137.9	328.1	−136.8	328.4	−137.9	327.9	−137.0	328.3
80	−130.0	170.1	−128.6	170.2	−129.0	170.1	−130.0	170.1
100	−127.1	175.0	−126.6	175.0	−126.9	175.1	−127.0	175.0
125	−126.6	174.3	−126.2	173.9	−127.1	173.6	−126.8	173.6
160	−126.8	202.3	−126.1	202.7	−126.3	202.7	−126.1	202.7
200	−125.6	200.6	−125.6	200.6	−125.4	200.4	−125.6	200.4
250	−125.9	202.4	−125.0	202.2	−125.9	202.1	−125.6	202.2
315	−124.7	217.6	−124.1	217.6	−125.3	217.9	−125.1	217.6
400	−125.2	227.8	−125.5	227.8	−125.2	228.0	−125.8	227.9
500	−126.2	230.9	−125.7	231.0	−125.7	231.0	−125.9	230.9
630	−127.1	245.7	−125.7	245.7	−126.6	245.7	−127.0	245.7
800	−131.6	106.4	−130.5	106.9	−130.2	106.1	−130.4	106.2
1000	−132.5	14.2	−132.2	14.3	−132.7	14.4	−132.5	14.2
*1000	−129.5	−35.2	−129.9	−35.7	−127.5	−36.0	−128.9	−35.7
1250	−127.2	−33.9	−129.3	−34.0	−129.0	−33.5	−129.2	−34.0
1600	−128.1	−30.3	−128.9	−29.3	−128.9	−30.1	−129.0	−30.1
2000	−127.9	−30.0	−128.1	−29.9	−129.1	−29.9	−130.5	−30.0
2500	−128.5	−60.7	−129.3	−60.2	−127.5	−61.0	−129.0	−60.2
3150	−128.0	−102.7	−129.5	−102.5	−129.3	−102.5	−128.9	−102.2
4000	−129.5	−145.9	−131.2	−145.8	−130.3	−145.0	−129.0	−145.0
5000	−129.8	176.1	−130.1	176.4	−130.5	176.4	−131.0	176.5

tor which is less than 0.3 dB. According to the theory and considering the coherence length of the laser source, we choose the fiber ring length to be $l=8$ m. The sensitivity of the hydrophone is proportional to the ring length l, but the length is constrained due to the winding loss. Figure 10 shows the pictures of the resonance output properties of the ring interferometer before and after the round winding. We can see in the pictures the coherence fineness dropped from above 50 to about 5. The coupling coefficient is chosen to be $K=0.95$. There is an isolator between the input terminal of the hydrophone and the output terminal of the laser source which is used to protect the back reflection from the fiber end to the laser source; another method for protecting the back reflection is to grind the input fiber end into an angle, say, about 6°. The geometric parameter of the back structure is chosen to be $a/b=0.95$, and the outside dimension of the hydrophone is $\phi 40\times 80$ mm. Figure 11 shows the photo picture of the experimental hydrophone head numbered 3.

III. THE EXPERIMENTAL RESULTS

The sensitivity level and the phase consistent measurements were carried out in two ways according to the different frequency ranges. From 50 to 1000 Hz the measurements were done by making use of the fluid column vibrating calibration system, as shown in Fig. 12, and from 1000 to 5000 Hz the measurements were made in the sound absorbing water pool, the arrangement is shown in Fig. 13.

The experimental results are listed in Table I and Fig. 14 shows the sensitivity levels, both theoretical and experimental, of the hydrophone numbered 3.

As to the minimum detectable acoustic pressure (level), we have done such a test in the sound absorbing water pool, that is, by reducing the acoustic source's level gradually until the B&K 8103 standard hydrophone's output is nothing but noise, then from this level continue the reduction (about 6 dB) until the acoustic source cannot work properly, we failed to catch the minimum detectable acoustic pressure (level) of the optic fiber hydrophone.

From the above table we can see that there is a disagreement between the two rows at $f=1000$ Hz, this is due to the systematic errors between the two different calibration systems. Figure 14 shows the mean experimental sensitivity levels of the above results compared with the theoretical one that is expressed in a line. The phase values are the relative ones being compared with the standard hydrophone under the same circumstance. From Fig. 14 we can see that the experiment sensitivity level is higher than that of the predicted one, and at both the low- and the high-frequency ends the sensitivity level has the tendency to descend, this having much to do with the ''free waves'' which, by using the dynamic elastic theory instead of the quasistatic one, has been demonstrated by Bucaro.[7] Also the descent of the sensitivity level from 800 to 1000 Hz may be caused partly by the upper frequency limit of $f_{\mathrm{Hoff}}=800$ Hz of the fluid column vibrating calibration system, and the lower frequency limit of $f_{\mathrm{Loff}}=1000$ Hz of the sound absorbing water pool.

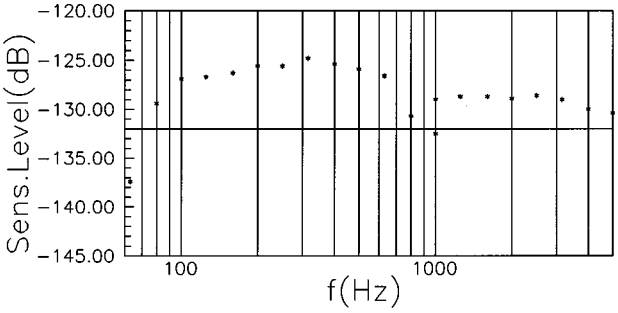

FIG. 14. The theoretical (−) and the measured (*) sensitivity levels.

IV. CONCLUSIONS

We have introduced here the theoretical formulations and the practical arrangements of the all-fiber Fabry–Pérot interferometer hydrophone system. The system has a sensitivity level of above -140 dB, and the hydrophone head has a compact size of $\phi 40 \times 80$ mm. Still, two matters need to be improved in this system. One is the linear dynamic range, which depends on the depth of the slope of the coherence curve represented by the ratio $|E4/E1|^2$ as a function of the phase shift, as shown in Figs. 6 and 7. This system has a relatively small dynamic range compared with normal hydrophones, that means, when the incident acoustic signal is slightly strong, the system would be out of its linear range and give out a distortion electric output. This problem can be improved by increasing the coherence fineness of the interferometer and by reducing the winding loss. Another matter is the permanent stability. Mostly the instability is induced by thermal perturbation, because this kind of interferometer is also a kind of thermal sensor. The strain released in the fiber is also a reason to cause the instability. Now that certain fibers used for special purposes are commercially available, it seems the problem can be solved. The authors are now engaging in a new system with a semiconductor laser as the light source, which can be adjusted in wavelength due to the feedback signal from the ring resonator, in order to keep the system in a certain steady resonant state. So this new system needs no piezoelectric ceramic mechanism to serve as a feedback activator, and there will be no electric wire inside the hydrophone head. This work will be published in another paper.

ACKNOWLEDGMENT

The project was supported by National Natural Science Foundation of China.

[1] J. A. Bucaro, J. H. Cole, N. Lagakos, and T. G. Giallorenzi, ''Fiber optic transduction,'' in *Physical Acoustics* (Academic, New York, 1982), Vol. 16, Chap. 7.
[2] A. Dandridge and A. B. Tveten, ''Phase compensation in interferometric fiber-optic sensors,'' Opt. Lett. **7**, 279–281 (1982).
[3] A. Dandridge and A. D. Kersey, ''Overview of Mach-Zehnder sensor technology and applications,'' Proceedings SPIE—The International Society for Optical Engineering, Vol. 985, Fiber Optic and Laser Sensors **VI**, 34–52 (1988).
[4] A. Dandridge, ''The development of fiber optic sensor system,'' 10th Optical Fiber Sensor Conference Invited Paper (unpublished), pp. 154–161.
[5] A. D. Kersey, ''Recent progress in interferometric fiber sensor technology,'' Proceedings SPIE—The International Society for Optical Engineering, Vol. 1376, Fiber Optic and Laser Sensors **VIII**, 2–12 (1990).
[6] D. L. Gardner, D. A. Brown, and S. L. Garrett, ''Fiber-optic push-pull acoustic sensor systems research at NPS,'' Acustica **76**, 106 (1992).
[7] J. A. Bucaro, ''Fiber-optic air-backed hydrophone transduction mechanisms,'' J. Acoust. Soc. Am. **89**, 451–453 (1991).

Complex acoustic waveforms excited with multiple picosecond transient gratings formed using specially designed phase-only beam-shaping optics

John A. Rogers
Bell Laboratories, Lucent Technologies, Murray Hill, New Jersey 07974

(Received 13 May 1998; accepted for publication 24 July 1998)

This paper describes a method for using a pulsed laser and specialized low cost beam-shaping optics to launch complex acoustic waveforms with user-definable geometries; diffraction of a continuous wave probe laser from these waveforms reveals their temporal evolution in real time. Methods are introduced for designing and fabricating simple binary phase optics for beam-shaping that is useful for high-frequency measurements on thin films. Experiments on films of platinum on silicon demonstrate the approach. © *1998 Acoustical Society of America.* [S0001-4966(98)01011-X]

PACS numbers: 43.38.Zp, 43.35.Sx [SLE]

INTRODUCTION

Basic scientific interest in high-frequency acoustics and applications in nondestructive evaluation motivate the development of techniques for using picosecond and femtosecond pulsed lasers to excite surface acoustic waves, and optical methods to detect these disturbances. Two methods are particularly useful. One, based on transient grating spectroscopy[1,2] and known as impulsive stimulated thermal scattering (ISTS),[3,4] uses temporal and spatial overlap of a pair of excitation pulses to produce a grating interference pattern. Interaction of these crossed pulses with the sample launches a material disturbance whose orientation and wavelength match the interference pattern. In many cases, slight absorption causes mild, spatially periodic heating, and the ensuing thermal expansion launches counterpropagating acoustic waves and thermal disturbances; both of these motions are monitored through diffraction of probe light that is overlapped with the excitation pulses. Mathematical descriptions of excitation and detection in this case are given in Refs. 1, 3, and 5–7. The utility of the ISTS technique has been demonstrated through studies of high-frequency acoustics in bulk solids,[8,9] liquids,[10] and surfaces,[11,12] and on supported[13–15] and free standing[16–18] films and multilayer assemblies.[19,20]

Another valuable method for acoustically examining films and surfaces uses impulsive heating induced by the cylindrically focused output of a pulsed laser.[21,22] In this case, thermal expansion yields a broadband ''line source'' for surface-propagating acoustic pulses; the pulses are probed interferometrically or with beam deflection at one or more locations separated from the excitation. Fourier transformation of data collected in this type of experiment gives acoustic velocities over a range of wavelengths determined by the narrow dimension of the focused excitation laser. Procedures for performing this type of analysis, and mathematical descriptions of the excitation are contained in Refs. 21 and 23. The ability of this technique to rapidly determine the dependence of the acoustic velocity on wavelength is attractive, and has been exploited in the past to characterize a variety of films and surfaces.[24–26] Accurate measurements of the velocities and attenuation rates, however, require probing at two precisely known locations. In addition, interpreting data that include multiple acoustic velocities at a single wavelength (e.g., multiple modes in an acoustic waveguide) is nontrivial. Although conventional ISTS is extremely effective for accurately and conveniently determining attenuation rates and acoustic velocities of single and multiple acoustic modes in bulk and waveguide structures, it has the disadvantage that acoustic waves with only a single wavelength are excited and monitored in a single experiment.

This paper describes an experimental approach that combines many advantages of the line source and ISTS methods. It uses multiple transient gratings to excite acoustic waveforms characterized by many wave vectors, and diffraction to probe these disturbances. The technique has attractive characteristics that include the capability for (i) single-shot measurement of wavelength dependent elastic and loss moduli in bulk samples and dispersion properties of single and multiple modes in acoustic waveguides, such as thin films or multilayer structures (which we demonstrate in this paper), (ii) simultaneous determination of acoustic properties in many directions in anisotropic materials, and (iii) investigations of nonlinear interactions between high-frequency acoustic waves with different, but well defined, wavelengths. The experiment relies on specialized beam-shaping optics and commercially available imaging lenses to divide and then recombine the output of an excitation laser. The beam-shaping optics and the magnification of the lenses determine the geometry of the acoustic waveform that the excitation laser stimulates; diffraction of light from a probe laser determines its temporal evolution in real time.

We begin by outlining the experimental technique and apparatus. We then describe several simple binary phase optics specially designed to produce a variety of excitation beam geometries, and we illustrate a low cost means for fabricating these optics. Experiments on silicon supported thin metal films demonstrate how the optics can be used to excite complex acoustic waveforms, and how diffraction can be used to probe them. We conclude with a description of future improvements that may increase the sensitivity and flexibility of the experiment.

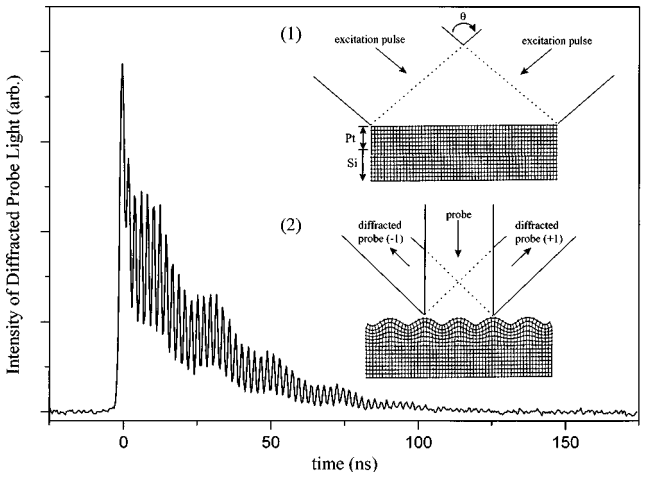

FIG. 1. Time dependence of the intensity of light diffracted from a film of platinum (~70 nm) on silicon excited by a pulsed laser. The inset shows a schematic illustration of the experiment. Crossed picosecond excitation pulses give rise to a grating interference pattern whose periodicity is defined by the crossing angle and the optical wavelength. Slight absorption by the film leads to mild impulsive heating in a periodic geometry. Thermal expansion launches acoustic and thermal disturbances at the wavelength of the optical interference pattern. Surface ripple associated with these responses diffracts light from a continuous wave probe laser. (For ease of illustration, this figure shows the probe beam normal to the surface of the sample. Measurements described in this paper were carried out with the probe beam incident on the sample at ~30° with respect to the surface normal.) The time dependence of the intensity of the diffracted light reveals the temporal characteristics of the material motions. The data displayed here show oscillations with a frequency and damping rate determined by the acoustic wavelength and the viscoelastic properties of the film-substrate system. Thermal diffusion in and out of the plane of the film causes the nonoscillatory component of the signal to decay in a few tens of nanoseconds.

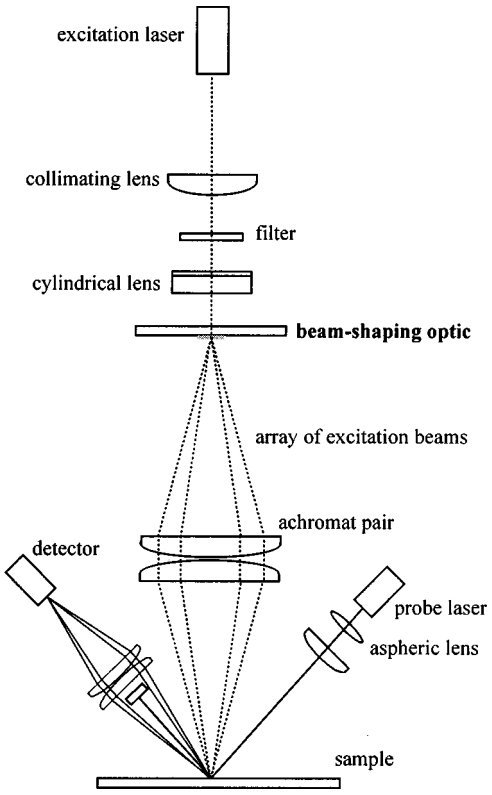

FIG. 2. Schematic illustration of the experimental setup. Pulses of light from an excitation laser (passively Q-switched microchip Nd:YAG) are collimated and then cylindrically focused onto a beam-shaping mask optimized for operation at 1064 nm, the wavelength of the microchip laser. An achromat pair recombines selected diffracted orders from this mask. The crossed pulses induce acoustic and thermal disturbances with wavelengths defined by the pattern on the mask and the magnification of the imaging lenses. A lens pair collects and focuses onto an avalanche photodiode the probe light diffracted by the time-dependent ripple induced on the surface of the sample by the excitation pulses. A transient digitizing oscilloscope records the output of the photodiode. The achromat pair gives 1:1 imaging; its separation from the phase optic and the sample is ~12 cm.

I. EXPERIMENT

A. Experimental arrangement

Figure 1 schematically illustrates the ISTS, or transient grating, experiment and displays typical data collected from a film of Pt (~70 nm) on a silicon wafer. Crossed picosecond excitation pulses coherently launch counterpropagating acoustic waves whose wavelengths (Λ) are defined by the wavelength of the excitation pulses (λ_L) and the crossing angle (θ) according to

$$\Lambda = \frac{\lambda_L}{2\sin(\theta/2)}. \tag{1}$$

The time dependence of light diffracted from the surface ripple and index modulation associated with the material disturbance reveals the temporal evolution of the response. The wavelength of the acoustic wave and the mechanical properties of the sample determine the acoustic frequency and damping rate of the acoustic component of the signal. Thermal diffusion in and out of the plane of the film governs the decay of the nonoscillatory component.

In a conventional experiment, a beamsplitter divides the output of an excitation laser into two parts, and mirrors and lenses recombine the resulting beams at an angle. Our recent work demonstrates how simple gratings and imaging lenses can replace the beamsplitter, mirrors, and lenses used in the standard experiment.[27,28] In the approach introduced here, beam-shaping optics produce many excitation beams and imaging lenses cross these beams at the sample. Figure 2 illustrates the specific experimental arrangement. A Nd:YAG laser produces ~300-ps, 10-μJ pulses at 1064 nm with a repetition rate of up to 10 kHz. A spherical lens collimates the output from this laser, and a cylindrical lens focuses it onto a beam-shaping mask optimized for operation at 1064 nm. Selected beams generated by diffraction from this mask are imaged (1:1) onto the surface of the sample. Diffraction of light from a continuous wave diode laser whose output is overlapped with the excitation pulses is collected by a lens pair and focused onto the surface of an avalanche photodiode. (A beam block prevents undiffracted probe light from reaching the detector.) A transient digitizing oscilloscope records the output of the photodiode in real time, and can be used to average multiple waveforms. For experiments described here, acceptable signal-to-noise ratios could be obtained in a single shot of the excitation laser; data displayed in all of the figures resulted from averaging of 300 shots.

B. Design and fabrication of binary surface relief phase optics

Custom beam-shaping optics were designed to generate many excitation beams for stimulating complex, but well de-

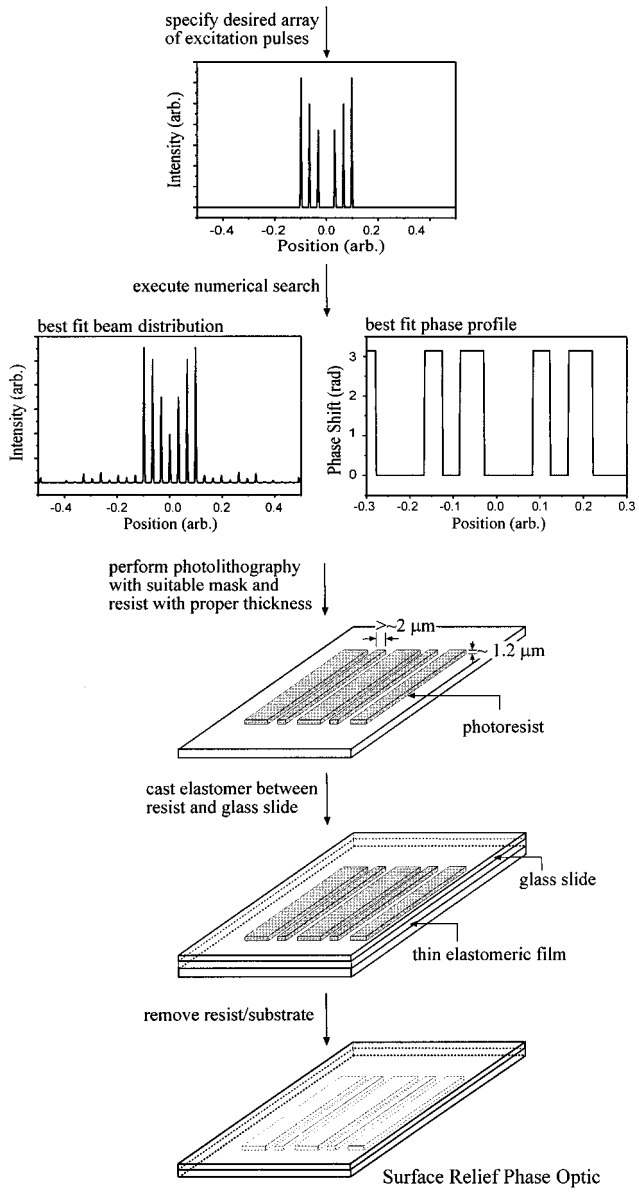

FIG. 3. Steps for computing and fabricating custom binary phase optics. A binary phase profile that produces diffraction that best fits a desired pattern defines a phase optic. (Only a small fraction of the profile is illustrated here.) Photoresist patterned with an amplitude photomask whose geometry is determined by the best fit phase profile serves as a template for molding a film (100–1000 μm thick) of elastomeric prepolymer supported by a rigid glass backing. Curing and removing the polymer from the patterned photoresist yields a phase optic. The index of the elastomer, the wavelength of the excitation light, and the phase shift required by the best fit phase profile define the thickness of photoresist.

fined, acoustic disturbances. We examined only pure phase optics because they often enable more efficient use of excitation light than ones that include amplitude modulation, and because optics that absorb light can, in certain extreme situations, be damaged by the excitation pulses. It should be noted, however, that for arbitrary manipulations, phase and amplitude modulating optics must be used.

Figure 3 illustrates the steps for designing and fabricating the phase optics. The first step involves specifying a desired beam configuration by identifying the intensities and positions of excitation beams in an array. (Although the relative phases of the beams can also be specified, we ignored this information since it only determines the relative spatial phase of interference patterns that form when the beams are recombined.) A numerical search identifies phase optics that produce beam distributions that best match the desired ones. Minimization of the sum of squares error between the desired intensities and positions of the excitation beams and the far field diffraction pattern calculated for a trial phase optic guides the search. The diffraction pattern was computed by Fourier transformation of the transmission function, $\tau(x,y)$, of the optic.[29] The transmission function determines how the optic modulates light that passes through it. If the (approximately two dimensional) optic lies at $z=0$, $E(x,y,z=0^+)$ is the field immediately after the optic, and $E(x,y,z=0^-)$ is the field immediately before it, then

$$E(x,y,z=0^+)=E(x,y,z=0^-)\tau(x,y). \tag{2}$$

For pure phase gratings, the transmission function takes the form

$$\tau(x,y)=\exp\{if(x,y)\}, \tag{3}$$

where $f(x,y)$ is a real function that determines the phase profile. Because we wished to design optics that could be fabricated easily with low cost procedures, we heavily constrained the search by requiring (i) single-level phase profiles [i.e., the value of $f(x,y)$ is binary], and (ii) feature sizes no smaller than one-third of the size of those in a grating that generates first order diffraction at angular positions of the outermost specified beams. We also only examined optics with profiles that varied in one dimension. The search was performed using a simplex optimization algorithm with a simple square-wave basis set cut off at a frequency determined by the minimum feature size. Details of the search procedure will be described elsewhere.

After numerically locating the binary phase profile that produces diffraction that best fits the desired beam configuration, a chrome-on-quartz amplitude photomask was generated with patterns defined by the geometry of this profile. Photolithography with this mask was then used to pattern a film of photoresist spin-coated onto a silicon wafer. Casting and curing a thin elastomeric polymer (polydimethylsiloxane) between the patterned resist and a clean glass slide, followed by removal of the silicon wafer and photoresist, yields a binary surface relief phase optic with the geometry of the amplitude mask. The depth of surface relief, the index of refraction of the elastomer, and the wavelength of the excitation light determine the depth of modulation of the phase. The thickness of the photoresist, which is determined by the spin speed used for spin-coating, was selected to yield the required phase modulation. (Fabrication procedures similar to the ones described here have been used in the past to produce simple rubber optical elements and other elastomeric microstructures.[30–32])

We used the method outlined in Fig. 3 to generate phase optics for efficient beamsplitting (i.e., square-wave profile, with a modulation of the phase of π), and for producing diffraction patterns that match the various beam configurations illustrated in Fig. 4. We chose these configurations because they are useful for evaluating, for example, dispersion in thin films where frequencies at a number of wavelengths

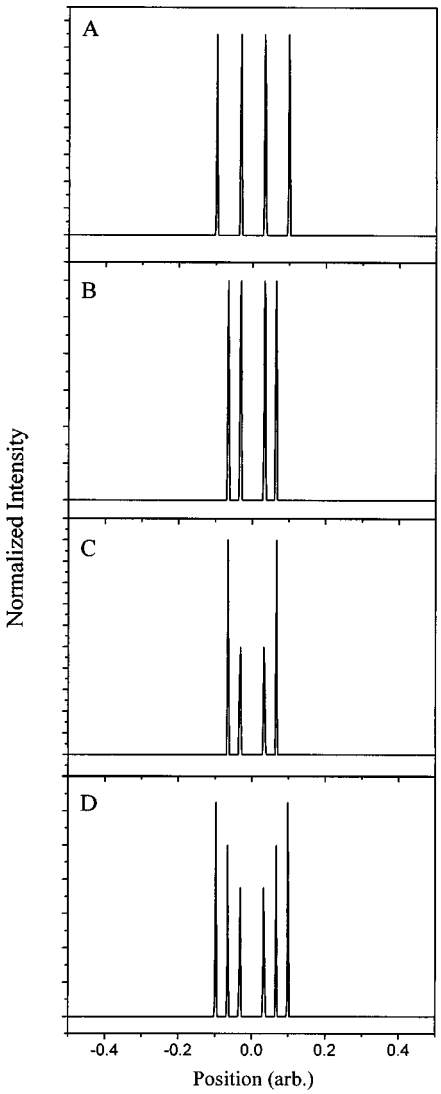

FIG. 4. Several arrays of excitation beams useful for launching complex acoustic waveforms for characterizing thin films. Labels A, B, C, and D defined in this figure are used throughout the main text to refer to optics that best fit the beam configurations illustrated in the top through the bottom frames, respectively.

are required, and where signal often decreases with increasing wave vector. The first consideration leads to beam profiles that consist of multiple excitation beams; interference associated with overlap of each pair of beams yields an intensity pattern with a characteristic wavelength. The second consideration motivates the choice of configurations that have intensities that increase with diffracted order as illustrated in parts C and D of Fig. 4. We evaluated the diffraction properties of the optics, and their performance in high-frequency acoustic measurements of a film of Pt (~70 nm) on silicon.

II. RESULTS

To verify that the fabrication procedures described in the experimental section can yield high quality phase optics for use in ISTS experiments, we first built and tested optics with geometries similar to those of commercial gratings that we used in previous experiments: square-wave phase masks with depths (~1.2 μm) optimized for diffraction at 1064 nm.[27]

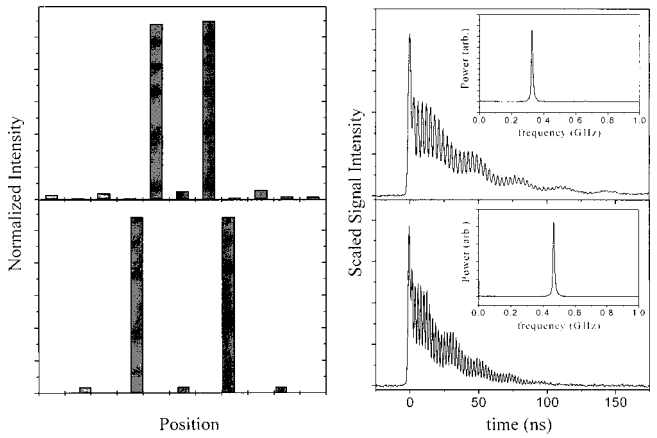

FIG. 5. Left frames: Normalized intensity of light diffracted from a binary square-wave phase grating with a depth optimized for diffraction. Data in the upper and lower frames were collected using gratings with 30- and 20-μm periodicity, respectively. The data show that the gratings, made according to procedures outlined in Fig. 3, diffract with ~75% efficiency into the first orders; this efficiency compares well with the theoretical maximum efficiency (~80%) for a grating with similar geometry. Right frames: Intensity of probe light diffracted from a sample of Pt (~70 nm)/Si excited with light from 1:1 imaging of first order beams diffracted from gratings that produce diffraction patterns illustrated in the left frames. The signals in the upper and lower frames are from acoustic and thermal disturbances with wavelengths of 19.0 and 10.0 μm, respectively.

The upper and lower frames of Fig. 5 show diffraction patterns measured in the far field, and signals measured using gratings with 30.0- and 20.0-μm periods, respectively, and fabricated according to procedures described in the previous section. Both gratings diffract light into the first orders with an efficiency of ~74%, a value close to the theoretical maximum (~80%) and comparable to the efficiency of commercial gratings produced with sophisticated fabrication techniques. The signals illustrated in the upper and lower frames on the right correspond to surface acoustic waves and thermal modes with 15.0- and 10.0-μm wavelengths, respectively, excited in a film of Pt (~70 nm) on Si by recombining the $+1$ and -1 diffracted orders produced by the molded elastomeric gratings. (Note that 1:1 imaging with only the $+/-1$ orders produces an intensity pattern whose periodicity is one-half of that of the grating. This relationship is useful for interpreting results from complex gratings.) The data are essentially identical to those collected using commercial gratings.

Figure 6 illustrates the calculated far field diffraction patterns and phase profiles of binary phase optics that best reproduce the patterns illustrated in Fig. 4. In all cases, the best fit patterns provide reasonable approximations to the desired ones. The correspondence is not exact because only binary phase optics with feature sizes larger than a fixed value were considered. The fraction of light that passes through the optic and appears in the desired positions is one quantity that characterizes the efficiency of the optic. According to this measure, designs for optics A, B, and C, have calculated efficiencies of ~60%, and optic D has an efficiency of ~70%.

The frames on the right in Fig. 7 show far field diffraction patterns generated with phase optics designed according to profiles illustrated in Fig. 6, and fabricated using proce-

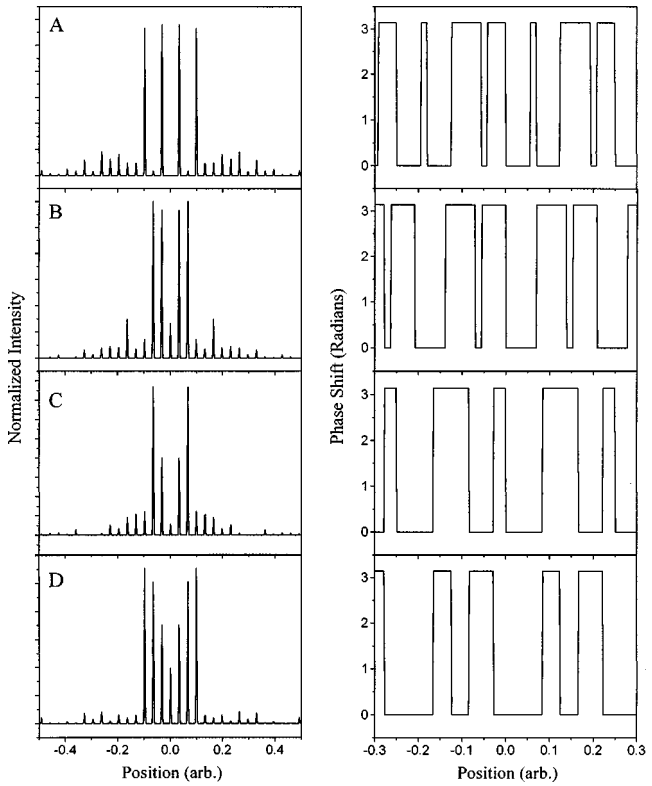

FIG. 6. Left frames: Calculated diffraction from binary phase optics optimized to generate beam configurations that best fit those illustrated in Fig. 4. Right frames: Phase profiles of binary phase optics that produce the diffraction patterns shown on the left. For each of these optics, more than 60% of the diffracted light passes appears in the desired locations.

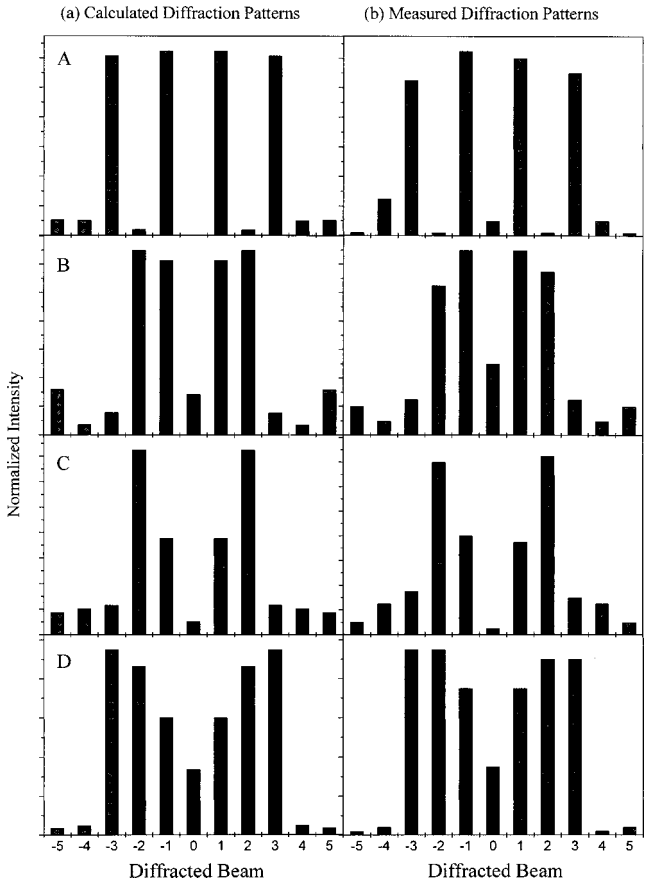

FIG. 7. Calculated and measured diffraction patterns from binary phase optics with geometries illustrated in Fig. 5, and fabricated according to procedures illustrated in Fig. 6. The data show that for each optic, the calculated and measured diffraction patterns are similar; slight deviations are likely due to some combination of (i) small differences between the geometry of the amplitude mask and the patterned photoresist that result from limitations in the resolution ($\sim$0.5 μm) of the photolithography, (ii) cross sectional profiles of the patterned resist that are not perfectly rectangular, and (iii) deviations of the actual from the required depth of surface relief that arise from nonuniformities in the thickness of the spin-coated resist.

dures outlined in Fig. 3. The frames on the left in Fig. 7 show the relative intensities of beams in the calculated diffraction patterns shown in Fig. 6. A comparison of the right and left frames indicates that the measured diffraction corresponds reasonably well to the calculated diffraction. The measured efficiencies of optics A, B, C, and D are 58%, 61%, 57%, and 65% respectively; these values are close to the calculated ones (see previous paragraph). We believe that differences between calculated and measured properties result primarily from imperfections in the fabricated optics caused by (i) nonuniformities in the thickness of the photoresist, (ii) deviations of the cross section of the patterned resist from rectangular, and (iii) limited resolution ($\sim$0.5 μm) of the mask aligner that was used to expose the resist.

We collected data from films of Pt ($\sim$70 nm) on silicon using the apparatus shown in Fig. 2 and optics whose properties are illustrated in Figs. 6 and 7. For these experiments, optics with designs A, B, C, and D had minimum feature sizes of 3.0, 3.0, 6.0, and 9.0 μm, respectively, and 1:1 imaging optics were used. We inserted beam blocks immediately before the imaging lens pair to remove diffracted beams that did not appear at the desired locations (e.g., diffracted beams 0, and $\pm4,\pm5,\pm6,...$ for optic D). Figure 8 illustrates typical data; power spectra in the insets show that more than two acoustic frequencies were present in each case. The positions and widths of peaks in the power spectrum provide accurate measures of the frequencies and damping rates of the various acoustic components of the excited waveform. The wavelengths of these components are simply related to the configuration of the excitation beams and the imaging. For example, the signal waveform generated using optic A (top frame) shows three acoustic frequencies, each associated with a different wavelength. The highest frequency is associated with the interference pattern formed by beams 3 and -3 and the lowest is due to beams 1 and -1; the intermediate frequency is generated by beam pairs -1 and 3, and by 1 and -3. The second frame in Fig. 8 shows four acoustic frequencies generated with optic B. In this case, the frequencies are associated with diffracted beams (i) -2, -1 and 2,1, (ii) -1, $+1$, (iii) -2, $+2$, and (iv) -1, 2 and 1, -2. Similar arguments explain the frequency components observed with the optics C and D. In general, the assignments can be determined by selectively blocking excitation beams at the imaging lens. In practice, it is often not crucial to know the assignments since the sizes of features on the phase optics and the magnification of the lenses determine the precise values of the acoustic wavelengths associated with the waveform and, therefore, can be used to estimate the expected frequencies.

Figure 9 shows data measured from a waveform pro-

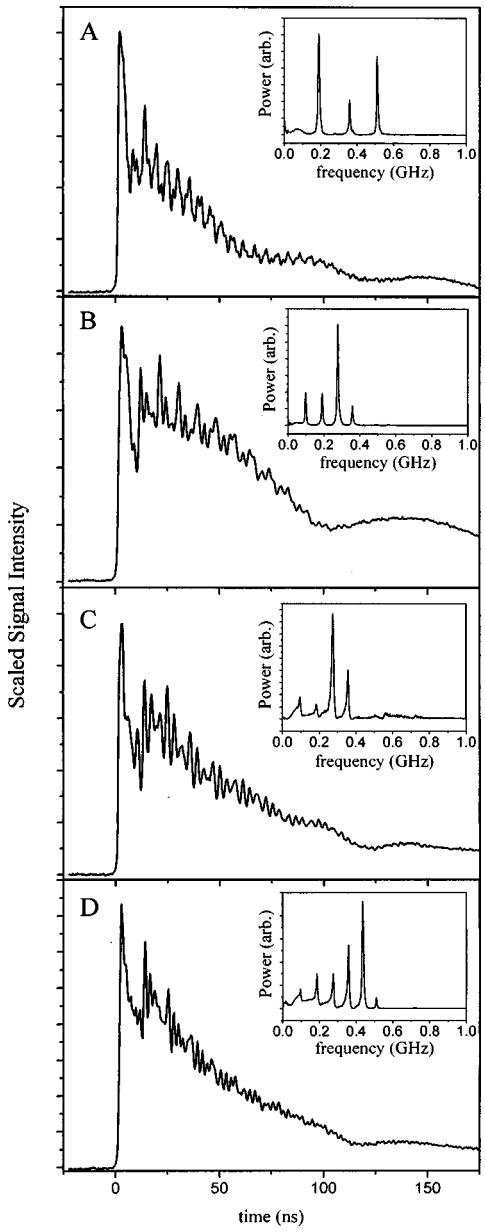

FIG. 8. Intensity of probe light diffracted from a film of Pt (~70 nm) excited using binary phase optics whose diffraction patterns are shown in Fig. 7, with the apparatus illustrated in Fig. 2. In all cases, the data show acoustic frequencies that are consistent with spatial frequencies that characterize the interference patterns produced by recombining selected beams diffracted from the phase optics.

duced by using optic D (smallest feature 9.0 μm) and 1:1 imaging lenses to excite a waveform with wavelength components at 54.0, 27.0, 18.0, 13.5, 10.8, and 9.0 μm. This figure illustrates how data collected by diffraction from complex acoustic waveforms can reveal the dispersion in the velocity in one experiment, and, if necessary, with a single shot of the excitation laser. In addition to mapping the dispersion in a single experiment, it is possible to perform sequential measurements with a series of beam-shaping optics. Figure 10 shows measurements made with three optics that have the basic design of optic A, but differ in the overall lateral length scale of the phase profile. The optic used for the top, middle, and bottom frames had minimum feature sizes of 5.0, 3.0, and 2.0 μm, respectively. (The highest-frequency component

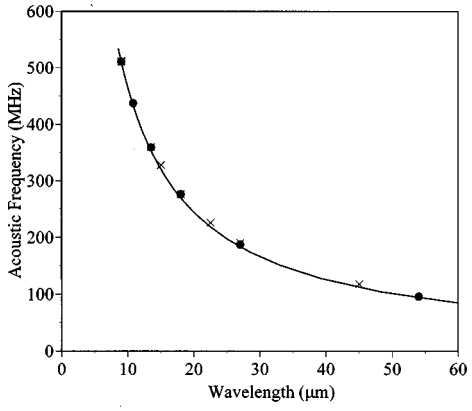

FIG. 9. Acoustic frequency as a function of wavelength in a film of platinum on silicon (i) measured using optic D (solid circles), (ii) measured with three different optics with the phase profile of optic A (crosses), and (iii) calculated using the literature values of the densities and elastic properties of platinum and silicon (solid line).

in the bottom frame was not visible because the diffracted probe light from the shortest acoustic wavelength in this case was not captured by the lenses that focus signal light onto the detector.) The measurements shown in Fig. 10 provide points on the dispersion curve at wavelengths of 45.0, 27.0, 22.5, 18.0, 15.0, 13.5, and 9.0 (twice) μm; these data are shown in

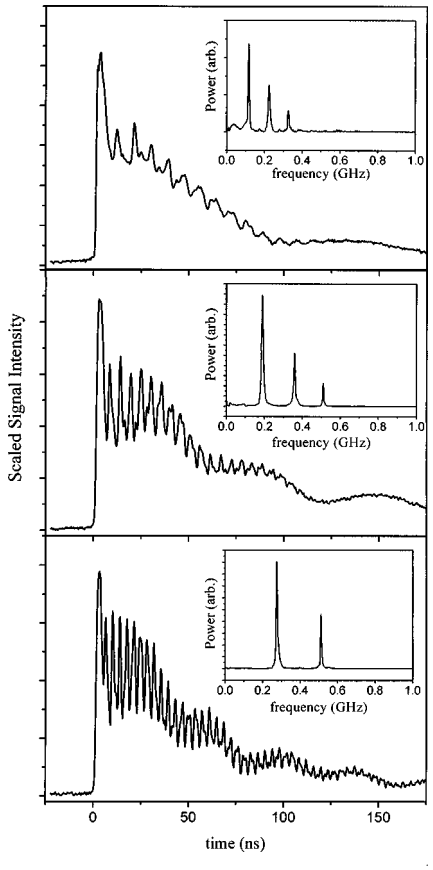

FIG. 10. Intensity of probe light diffracted from a film of Pt (~70 nm) excited using binary phase optics with phase profiles like the one shown in the upper frame of Fig. 6. Data in the upper, middle, and lower frames were collected using optics whose smallest features were 5.0, 3.0, and 2.0 μm. These data illustrate tunability that can be achieved by changing the overall lateral length scale of features on the phase optic.

Fig. 9. All of the measurements are consistent with calculations[33] that use the bulk acoustic properties and density for platinum[34] and the density and Voigt-averaged isotropic moduli for silicon.[34] (See Fig. 9.)

Finally, although the positions and widths of peaks in the power spectrum provide enough data to allow viscoelastic characterization of the sample, the relative amplitudes of these peaks in principle provide additional information. We observed, however, that while the positions and widths of peaks in the power spectra of measured signal remained constant when the distance between the sample and the phase optic was varied slightly, their relative amplitudes in general did not. We believe that movement of the sample causes shifts in the relative phase of interference patterns formed with different pairs of excitation beams, and that these shifts give rise to variations in the amplitudes of certain frequency components. The data displayed in Fig. 8 were collected with the sample positioned to yield the maximum overall signal in the time domain. The variation of the signal with position of the sample, the dependence of excitation, and detection efficiencies on acoustic wavelength in thin films, and the sensitivity of the signal to precise alignment make quantitative interpretation of the relative amplitudes of frequency components difficult. Analysis of relative amplitudes is, nevertheless, the subject of current study.

III. CONCLUSIONS AND DISCUSSION

In this paper we described a method to extend the utility of the transient grating, or ISTS, technique. The method uses specialized beam-shaping optics and a pulsed laser to excite acoustic waveforms with user-specified geometries, and diffraction of a continuous wave laser to probe these waveforms. We demonstrated excitation and detection of acoustic disturbances characterized by as many as six wavelengths. Although the optics allow for waveforms with many more than six wavelengths, peaks in the power spectrum of the signal will begin to overlap when large numbers of wavelengths are present. Significant overlap of adjacent frequency components will diminish the ability to determine accurately the frequencies and attenuation rates. The upper limit on the useful number of wavelengths will, therefore, be a function of the damping rate and the accuracy that is required. For the apparatus and sample used here, we expect accuracy to begin to degrade for more than $\sim$30 wavelengths. We also note that probing of many wavelengths can potentially lead to heterodyning of signal beams against one another, an effect that was not considered here.

In summary, we believe that the use of beam-shaping optics for performing sophisticated types of transient grating experiments is new, and that it should be applicable to experiments that involve different timescales (e.g., femtosecond) and excitation mechanisms (e.g., electrostiction) than those investigated here. We are currently exploring extensions of the approach that exploit two dimensional binary and holographic optical elements, and heterodyne detection schemes.[27,28,35]

[1] H. J. Eichler, P. Gunter, and D. W. Pohl, *Laser-Induced Dynamical Gratings* (Springer-Verlag, Berlin, 1986).
[2] M. D. Fayer, Annu. Rev. Phys. Chem. **33**, 63 (1982).
[3] K. A. Nelson and M. D. Fayer, J. Chem. Phys. **72**, 5202 (1980).
[4] K. A. Nelson, D. R. Lutz, M. D. Fayer, and L. Madison, Phys. Rev. B **24**, 3261 (1981).
[5] Q. Shen, A. Harata, and T. Sawada, Jpn. J. Appl. Phys. **35**, 2339 (1996).
[6] S. M. Gracewski and R. J. D. Miller, J. Chem. Phys. **103**, 1191 (1995).
[7] J. A. Rogers and K. A. Nelson, J. Appl. Phys. **75**, 1534 (1994).
[8] I. C. Halalay and K. A. Nelson, J. Chem. Phys. **97**, 3557 (1992).
[9] S. M. Silence, S. R. Goates, and K. A. Nelson, Chem. Phys. **149**, 233 (1990).
[10] A. R. Duggal and K. A. Nelson, J. Chem. Phys. **94**, 7677 (1991).
[11] J. J. Kasinski, L. Gomez-Jahn, K. J. Leong, S. M. Gracewski, and R. J. D. Miller, Opt. Lett. **13**, 710 (1988).
[12] A. Harata, H. Nishimura, and T. Sawada, Appl. Phys. Lett. **57**, 132 (1990).
[13] A. R. Duggal, J. A. Rogers, and K. A. Nelson, J. Appl. Phys. **72**, 2823 (1992); A. R. Duggal, J. A. Rogers, K. A. Nelson, and M. Rothschild, Appl. Phys. Lett. **60**, 692 (1992).
[14] J. S. Meth, C. D. Marshall, and M. D. Fayer, J. Appl. Phys. **67**, 3362 (1990); J. S. Meth, C. D. Marshall, and M. D. Fayer, Chem. Phys. Lett. **162**, 306 (1989).
[15] M. J. Banet, M. Fuchs, J. A. Rogers, R. Logan, A. A. Maznev, and K. A. Nelson, Appl. Phys. Lett. **73**, 169 (1998).
[16] J. A. Rogers, L. Dhar, and K. A. Nelson, Appl. Phys. Lett. **65**, 312 (1994); J. A. Rogers and K. A. Nelson, IEEE Trans. Ultrason. Ferroelectr. Freq. Control **42**, 555 (1995).
[17] J. A. Rogers and K. A. Nelson, J. Adhes. **50**, 1 (1995).
[18] J. K. Cocson, C. S. Hau, P. M. Lee, C. C. Poon, A. H. Zhong, J. A. Rogers, and K. A. Nelson, Polymer **36**, 4069 (1995).
[19] L. Dhar, J. A. Rogers, K. A. Nelson, and F. Trusell, J. Appl. Phys. **77**, 4431 (1995).
[20] A. Harata and T. Sawada, Jpn. J. Appl. Phys. **32**, 2188 (1993).
[21] A. Neubrand and P. Hess, J. Appl. Phys. **71**, 227 (1992).
[22] P. Hess, Appl. Surf. Sci. **106**, 429 (1996).
[23] V. Gusev, C. Desmet, W. Lauriks, C. Glorieux, and J. Thoen, J. Acoust. Soc. Am. **100**, 1514 (1996).
[24] H. Coufal, K. Meyer, R. K. Grygier, M. de Vries, D. Jenrich, and P. Hess, Appl. Phys. A: Solids Surf. **59**, 83 (1994).
[25] C. Desmet, V. Gusev, W. Lauriks, C. Glorieux, and J. Thoen, Appl. Phys. Lett. **68**, 2939 (1996).
[26] U. Kawald, C. Desmet, W. Lauriks, C. Glorieux, and J. Thoen, J. Acoust. Soc. Am. **99**, 926 (1996).
[27] J. A. Rogers, M. Fuchs, M. J. Banet, J. B. Hanselman, R. Logan, and K. A. Nelson, Appl. Phys. Lett. **71**, 225 (1997).
[28] J. A. Rogers, Ph.D. thesis, MIT, 1995.
[29] J. W. Goodman, *Introduction to Fourier Optics* (McGraw-Hill, New York, 1968).
[30] J. A. Rogers, O. J. A. Schueller, C. Marzolin, and G. M. Whitesides, Appl. Opt. **36**, 5792 (1997).
[31] J. L. Wilbur, R. J. Jackman, G. M. Whitesides, E. Cheng, L. Lee, and M. Prentiss, Chem. Mater. **8**, 1380 (1996).
[32] Y. Xia, E. Kim, X.-M. Zhao, J. A. Rogers, M. Prentiss, and G. M. Whitesides, Science **273**, 347 (1996).
[33] G. W. Farnell and E. L. Adler, in *Physical Acoustics, Principles and Methods*, edited by W. P. Mason and R. N. Thurston (Academic, New York, 1969), Vol. 6, pp. 109–166.
[34] G. Simmons and H. Wang, *Single Crystal Elastic Constants and Calculated Aggregate Properties: A Handbook* (MIT, Cambridge, 1971), 2nd ed.
[35] A. A. Maznev, J. A. Rogers, and K. A. Nelson, Opt. Lett. **23**, 1319 (1998).

Modeling and measurement of nonlinear dynamic behavior in piezoelectric ceramics with application to 1-3 composites

T. J. Royston[a)]
The University of Illinois at Chicago, Chicago, Illinois 60607-7022

B. H. Houston
Naval Research Laboratory, Code 7136, Washington, DC 20375-5350

(Received 31 March 1998; accepted for publication 4 August 1998)

The nonlinear vibratory behavior of a 1-3 piezoceramic composite is characterized theoretically and experimentally. The developed theoretical model for the electroelastic behavior of the 1-3 composite follows conventional assumptions made by prior investigators but includes nonlinear terms to account for hysteresis in the embedded PZT phase. Experimental measurements of the quasistatic and dynamic mechanical response of the 1-3 with embedded PZT-4 or PZT-5H phases to harmonic electrical excitation over a range of excitation frequencies and two different mechanical loading conditions quantify the nature and level of nonlinearity and illustrate its dependence on the type of PZT material and the mechanical coupling conditions of the 1-3 to its surroundings. Good agreement exists between theoretical predictions and experimental measurements. © *1998 Acoustical Society of America.* [S0001-4966(98)03211-1]

PACS numbers: 43.40.At, 43.40.Ga, 43.38.Fx [CBB]

INTRODUCTION

There is a continuing need for improvements in vibro-acoustic transduction and control in numerous applications for reasons of market competitiveness, protection and functionality of sensitive equipment and instrumentation, increased reliability, reduced operating costs, stealth, and protection of individuals. Applications range from structural noise and vibration control in commercial, industrial, military, and scientific equipment to medical diagnostic imaging, nondestructive testing, health monitoring of machinery, MEMS technology, and precision manufacturing. To meet such needs, in recent years there has been much research on the use of so-called smart materials and structures with integrated actuation and sensing to enable a greater ability to manipulate and measure vibro-acoustic energy.

Even though all dynamic systems are inherently nonlinear, the majority of analyses are typically based on the underlying assumption of system linearity. But, while vibration of many conventional (passive) structural systems is often reasonably described by linear system theory, particularly in the audio and ultrasonic frequency ranges with relatively low dynamic displacement amplitudes, the vibration of systems employing so-called smart materials often are not due to the relatively large dynamic amplitudes or strong nonlinearities present in the coupled electrical and/or magnetic variables. Significant nonlinear behavior has been observed in many of the primary smart material technologies, such as piezoelectric,[1–8] electrostrictive,[7–9] magnetostrictive,[7–12] and electro-rheological fluid.[13–15] Ferroelectric material advancements on the horizon, e.g., thin film and single crystal piezoelectrics and electrostrictives, are expected to bring the issue of nonlinearity even further to the forefront in smart material applications. While these devices hold the promise for vastly increased strain rates and actuation authority, they also have been shown to exhibit nonlinear behavior.[16]

Nonlinearities can significantly affect system performance in several ways at different levels, including: (i) a degradation or loss of actuation authority; (i) a degradation or loss of stability; and/or (iii) a degradation or loss of system functionality. Nonlinear effects, such as hysteresis and nonproportional parameter relationships, allow multiple output states for a given input state, thus frustrating open-loop control, and generate unwanted amplitude-dependent phase shifts and harmonic distortion which reduce the effectiveness of feedback control. Nonlinear behavior like harmonic distortion, frequency modulation, and chaotic response represent a loss of order in the spectral content of the vibro-acoustic phenomenon as it is broadened from one or a few discrete frequencies into potentially numerous subharmonics, superharmonics, combination tones, or broadband random behavior. This leads to greater difficulty and confusion in sensing, interpreting and controlling the vibro-acoustic event.

On the other hand, in addition to its inherent presence, it sometimes is desirable to intentionally introduce a well-defined nonlinearity as a means of greater control capability or system functionality. Improved piezo-based vibration control designs utilizing nonlinearity have been considered.[1,17,18] Before smart material nonlinearities can be properly accounted for and/or utilized in control algorithms, system models, and design strategies, their effect on system behavior must be better understood. This is the principle focus of this article which presents preliminary theoretical and experimental studies of a common smart material component, a 1-3 piezoceramic composite.

The 1-3 piezoelectric ceramic composite considered in this study is shown schematically in Fig. 1. It consists of PZT-4 or PZT-5H rods oriented in the thickness or 3 direction, which are uniformly spaced and separated by a compli-

a)Electronic mail: troyston@uic.edu

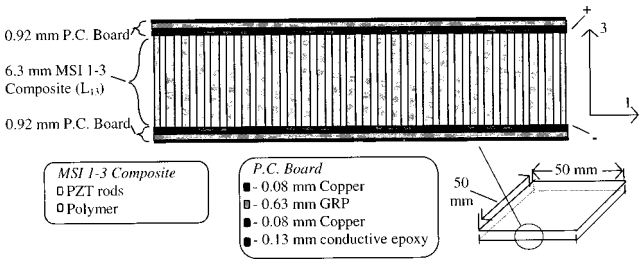

FIG. 1. Cross section of 1-3 piezoelectric ceramic composite. The conductive copper and epoxy on the interior of the PC boards act as the electrodes for the PZT rods. Note the name ''1-3'' is not associated with the mode of PZT electromechanical interaction that is utilized in this device. Here, the electric field is applied in the ''3'' direction of the PZT and mechanical strain in the ''3'' direction is the mechanical actuation output of interest.

ant polymer material. The volume fraction of rods considered in this study is $\nu = 15\%$. Any change in the length of the rods (3 direction), due to the application of a voltage across the electrodes, will appear as a change in the thickness of the entire layer. Conversely, any lateral strain in the rods (1 and 2 direction) is ideally absorbed by the compliant material. In terms of volume displacement, this results in an actuator with greater authority than that of an equivalent volume of PZT. Also, by varying the percentage of PZT rod volume to that of the compliant polymer, different boundary impedance conditions and electromechanical coupling conditions can be achieved. This ability to custom-design the 1-3's electromechanical authority and its boundary dynamics, along with its conformability and wide frequency range, make it an ideal embedded transducer of vibro-acoustic energy in numerous applications[19–24] that include medical diagnostic imaging, vibration isolation and structural acoustic control, nondestructive testing, and underwater acoustic sensing, to name a few. Dimensions for the components studied, which were fabricated by MSI Inc.[25] using an injection molding process, are given in Fig. 1 and Table I.

The specific objectives addressed in this article include:

- A review of prior theoretical and experimental studies of nonlinearity in 1-3 and PZT-based devices.
- A theoretical formulation of the nonlinear constitutive equations for the 1-3 composite.
- Measurements of the nonlinearity of the 1-3 device under a range of static and dynamic excitation conditions with comparison to theoretical predictions.

I. LITERATURE REVIEW

A. Nonlinearity in the piezoelectric effect

While a theoretical nonlinear formulation for thermoelectroelasticity specifically for 1-3 piezoceramic composites has not been previously developed to the best of the authors' knowledge, numerous studies considering nonlinearity in piezoelectric materials have been conducted. Early studies on the nonlinear thermoelectroelastic theory of dielectrics[26–28] were based on continuum mechanics and employed fundamental thermodynamic principles. These studies predict that both large mechanical stresses and electrical fields can result in significant reversible nonlinear behavior. A more recent article[29] formulates the nonlinear thermoelectroelastic constitutive equations specifically for piezoelectric materials by keeping higher order terms in the Taylor series expression for the thermodynamic Gibbs potential. Hence, one is not assuming that strain, electric displacement, and entropy depend linearly on stress, electrical field, and temperature. The resulting constitutive equations include higher order terms in electrical field-potential variables, mechanical stress–strain variables, and coupled electrical and mechanical variables.

TABLE I. Test configuration parameter values.

1–3 Piezoceramic composite Parameter	PZT-4 1-3[a]	PZT-5H 1-3[a]
A (m^2)	0.0025 (measured)	0.0025 (measured)
b_{13} (N s/m)	5×10^5 (compare w/ exp.)	5×10^5 (compare w/ exp.)
c_{11} (N/m^2)	3.4×10^9 (60)	3.4×10^9 (60)
c_{12} (N/m^2)	2.9×10^9 (60)	2.9×10^9 (60)
$\overline{c}^D_{33}$ (N/m^2)	17.0×10^9 [Eq. (2)]	14.1×10^9 [Eq. (2)]
c^E_{33} (N/m^2)	115×10^9 (66)	68.0×10^9 (25)
c^E_{13} (N/m^2)	$0.77c^E_{33}$ (60)	$0.77c^E_{33}$ (60)
c^E_{11} (N/m^2)	$1.22c^E_{33}$ (60)	$1.22c^E_{33}$ (60)
c^E_{12} (N/m^2)	$0.79c^E_{33}$ (60)	$0.79c^E_{33}$ (60)
e_{31} (C/m^2)	-5.2 (66)	-6.5 (66)
$\underline{e}_{33}$ (C/m^2)	15.1 (66)	23.3 (66)
h_{33} (v)	2.67×10^9 [Eq. (2)]	1.76×10^9 [Eq. (2)]
$\underline{L}_{13}$ (m)	0.0063 (measured)	0.0063 (measured)
β^s_{33} (V/C)	1.13×10^9 [Eq. (2)]	0.49×10^9 [Eq. (2)]
ν [ν']	0.15 [0.85] (25)	0.15 [0.85] (25)
ϵ^S_{33} (C/V m)	$635\epsilon^0$ (66)	$1470\epsilon^0$ (66)
MRC hysteresis model parameter values estimated by comparison with PZT-5H 1–3 experimental data		
$\overline{\beta}^{S(1)}=0.80\overline{\beta}^S_{33}$; $\overline{\beta}^{S(2)}=0.125\overline{\beta}^S_{33}$; $\overline{\beta}^{S(3)}=0.06\overline{\beta}^S_{33}$; $\overline{\beta}^{S(4)}=0.015\overline{\beta}^S_{33}$;		
$e^{(1)}_{rc}=100\overline{\beta}^{S(1)}$; $e^{(2)}_{rc}=0.0006\overline{\beta}^{S(2)}$; $e^{(3)}_{rc}=0.0001\overline{\beta}^{S(3)}$; $e^{(4)}_{rc}=0.00001\overline{\beta}^{S(4)}$		
Additional parameters for Basic Test Configuration (BTC)[a]		
$L_{pl}=0.0063$ m (measured)	$c_{pl}=5.93\times10^9$ N/m^2 (67)	$b_{pl}=3\times10^3$ N s/m (compare w/exp.)

[a]Number or remark in parentheses following value indicates reference source.

Such an approach does not make the distinction between intrinsic and extrinsic piezoeffects and does not consider irreversible nonlinearities, such as hysteresis, which are generally associated with extrinsic effects. Intrinsic piezoeffects are dependent on the homogeneous (unit cell) deformation caused by the electric field. Extrinsic piezoeffects represent the elastic deformation caused by the motions of non-180 degree domain walls (partially domain switching) and the interphase interfaces. In commonly used ferroelectric ceramics, such as PZT, the extrinsic effects are believed to be more dominant in many applications over a wide range of field levels.[30–33]

Numerous experimental studies of the nonlinear behavior of piezoelectric ceramics have also been conducted. Many can be classified as static or quasistatic analyses of the strain–stress, charge density field, and electromechanical interaction curves where a test specimen is placed under a range of mechanical compressive (or tensile) loads and/or electrical field loads and mechanical strain/stress and electrical charge/voltage values are measured.[5,34–38] Another group of studies may be classified as resonance techniques, where the piezoelectric element is driven at its resonance at different amplitude levels and the resonant frequency value and mechanical Q factor are measured.[2,33,39–41] Typically, what is found is that as the vibration amplitude level increases, the resonant frequency and mechanical Q-values decrease. In fact, this softening stiffness quality of PZT can lead to jump behavior where the backbone curve of the resonance peak is bent down in frequency and a multi-solution regime exists. These changes in resonant frequency and Q-values are attributed to some degree to temperature increases as vibration levels increase which affect ferroelectric domain wall mobility.

In more recent years there has been an increase in the number of studies, both theoretical and experimental, of nonlinearity in piezoelectrics. These studies, to some degree, may be categorized based on their principle intention or related application, which may be that of basic research in solid state physics and materials[16,29,32,33,35,38,42–45] or applied research with application to vibro-acoustic transducers[2,7,8,40,41,46] or actuators for high precision positioning.[5,47–54] Related objectives may focus on understanding the underlying constitutive relations at a fundamental physical level or quantifying a particular piezoelectric material characteristic, in terms of static or dynamic indices, e.g., displacement accuracy or harmonic distortion. Additionally, some application-driven studies focus not on the nonlinearity in the piezoelectric relations but rather on the dynamics of the system or structure mechanically coupled to the piezoelectric element.[6,55–57]

The principle goals of the study and its related application, if any, will affect how the nonlinearity is mathematically described. The two principle approaches are in terms of reversible nonlinearities, such as higher order polynomial expressions in the constitutive relations,[2,7,8,46] expressed in the time or frequency domain, or irreversible nonlinearities, such as rate-independent hysteretic behavior.[5,47–54] In addition to being driven by their end use, the types of nonlinear functions employed are also dependent on the types of experimental studies which are conducted in their construction. For example, quasistatic mechanical stress–strain versus electrical field-displacement studies may be used to directly observe hysteretic properties under static load conditions. Harmonic excitation may be employed to measure harmonic distortion levels, which then are usually simulated with polynomial nonlinearities but also can be described with hysteresis nonlinearities. Finally, transfer function approaches using broadband excitation, although inherently invalid for nonlinear systems, may be applied to assess the general frequency and amplitude dependence of certain relationships.

Summarizing the literature, nonlinearity in the electroelastic relations of piezoceramics may best be described using a combination of reversible functions, like higher order polynomials in the constitutive relations, and irreversible operators, specifically rate-independent hysteretic behavior. Under high field levels, one may expect both, while under low field levels only nonlinear hysteretic behavior may be evident. How the nonlinear behavior of piezoelectric ceramics may couple into resonant mechanical systems has not been seriously addressed either theoretically or experimentally.

B. The dynamics of 1-3 piezoceramics

As mentioned, there are no theoretical models available which describe the nonlinear dynamics of 1-3 piezoceramic composites. Numerous researchers, however, have formulated linear models.[20,58–60] These essentially involve a weighted averaging of the elastic, dielectric, and piezoelectric properties of the PZT and passive polymer materials based on their volume fraction in the composite. Just as there have been no theoretical studies, there have been no experimental studies of 1-3 piezoceramic composites specifically directed at characterizing nonlinear phenomena. Prior investigators have focused on measuring transfer function indices of the 1-3 as a function of PZT volume fraction.[19,20,24,61] Indices have included specific acoustic impedance, electromechanical coupling, electrical impedance, and transmit voltage response. Usually, an impulsive excitation is applied to the device and the response and excitation are recorded and used to construct a frequency response of the output with respect to the input. This method is inadequate in determining the presence and nature of system nonlinearity. Any transfer function quantity is inherently based on the assumption of linearity in that the response at a given frequency is only due to excitation at that frequency. Such methods also neglect any amplitude dependence in the response and the inherent initial condition dependence of nonlinear systems. Proper measurement of system nonlinearities requires a steady-state excitation condition and, in some cases, sensitivity to the initial conditions.

II. THEORY

A. Integrating irreversible nonlinearity into the electroelastic constitutive equations for 1-3's

Smith and Auld[60] derive a *linear* constitutive model for thickness oscillations of the 1-3 that is valid for frequencies whose wavelengths in the composite are much greater than

the composite's lateral spatial scale; i.e., the composite can be treated as a homogeneous medium. Also, their model does not hold at extreme values of the volume fraction ν of PZT, i.e., $\nu \approx 0$ or $\nu \approx 1$. For the components and conditions of interest here, these limitations are not restrictive. Ferroelectric materials, such as the PZT phase embedded in the 1-3, couple elastic and electrical properties and can be described by phenomenological equations of state which relate mechanical stress (T), mechanical strain (S), electric field (E), and electric displacement (D). As part of Smith and Auld's model, the following equalities hold which relate these properties in both the PZT and nonferroelectric polymer phase:

$$T_3 = \nu T_3^c + \nu' T_3^p, \tag{1a}$$

$$D_3 = \nu D_3^c + \nu' D_3^p, \tag{1b}$$

$$E_3 = E_3^c = E_3^p, \tag{1c}$$

$$S_3 = S_3^c = S_3^p. \tag{1d}$$

Here, subscripts denote the direction (3 thickness direction), $\nu' = 1 - \nu$ is the volume fraction of the polymer, and superscripts c and p denote the ceramic and polymer phases, respectively. It is noted that T_3, S_3, E_3, and D_3 are assumed to be independent of lateral location (1 or 2 directions) within the 1-3. Given Eqs. (1a)–(d) and assumptions detailed in Ref. 60, the linear constitutive equations take the following form analogous to PZT by itself (without the overhead bars):

$$T_3 = \overline{c}_{33}^{D} S_3 - \overline{h}_{33} D_3, \tag{2a}$$

$$E_3 = -\overline{h}_{33} S_3 + \overline{\beta}_{33}^{s} D_3, \tag{2b}$$

where

$$\overline{c}_{33}^{D} = \overline{c}_{33}^{E} + (\overline{e}_{33})^2 / \overline{\epsilon}_{33}^{s}, \tag{2c}$$

$$\overline{h}_{33} = \overline{e}_{33} / \overline{\epsilon}_{33}^{s}, \tag{2d}$$

$$\overline{\beta}_{33}^{s} = 1 / \overline{\epsilon}_{33}^{s}, \tag{2e}$$

and

$$\overline{c}_{33}^{E} = \nu [c_{33}^{E} - 2\nu'(c_{13}^{E} - c_{12})^2 / \kappa] + \nu' c_{11}, \tag{2f}$$

$$\overline{e}_{33} = \nu [e_{33} - 2\nu' e_{31}(c_{13}^{E} - c_{12}) / \kappa], \tag{2g}$$

$$\overline{\epsilon}_{33}^{s} = \nu [\epsilon_{33}^{s} + 2\nu'(e_{31})^2 / \kappa] + \nu' \epsilon_{11}, \tag{2h}$$

with

$$\kappa = \nu(c_{11} + c_{12}) + \nu'(c_{11}^{E} + c_{12}^{E}). \tag{2i}$$

Here, nomenclature generally follows that of ANSI/IEEE standard 176-1987 on piezoelectricity. The conventional compressed subscript notation is employed with the following relationships: 1=11, 2=22, 3=33, 4=23 or 32, 5=13 or 31, and 6=12 or 21. This is possible due to symmetry: e.g., $c_{ij} = c_{ji}$. In addition to this symmetry, $c_{11}^{E} = c_{22}^{E}$, $c_{13}^{E} = c_{23}^{E}$, $\epsilon_{11}^{S} = \epsilon_{22}^{S}$, $e_{13} = e_{23}$, and $e_{14} = e_{24} = e_{15} = e_{25}$. Superscripts E, D, and S refer to ''at constant'' electrical field, displacement, or mechanical strain, respectively. The terms c_{ij}^{E}, e_{ij}, and ϵ_{33}^{S} refer to elastic moduli, piezoelectric strain constants, and the dielectric constant, respectively, of the PZT material. The terms c_{ij} and ϵ_{11} refer to elastic moduli and the dielectric constant of the polymer matrix material.

Material parameter values for the experimental studies presented in Sec. III are provided in Table I. The nonpiezoelectric polymer phase in most 1-3 devices is significantly more compliant than the PZT phase and it may seem logical to ignore its contribution in Eqs. (2f)–(i). Constitutive equation coefficients for the PZT-5H 1-3 under study are calculated for both the case of including and ignoring polymer elasticity. Only the effective elastic moduli of the 1-3 is significantly changed from 10.6×10^9 to 14.1×10^9 C/m^2 with the inclusion of the polymer properties.

A number of studies have shown that, even at relatively low electrical and/or mechanical stress levels, piezoelectric ceramics exhibit substantial rate-independent hysteretic behavior in their electroelastic interaction which is not accounted for in the linear formulation of the electroelastic equations (2(a)–(b)) for the 1-3. For example, Goldfarb and Celanovic[47] and Main *et al.*[51–53] have measured a strong hysteretic relation between electrical displacement D and field E. Take hysteretic behavior in the 1-3 to be in the dielectric $\overline{\beta}_{33}^{s}$ relation. It will be denoted as a bracket $\{\ \}$ in the following equations where, from this point forward a simplified notation will be employed by dropping the overhear bar ($\overline{\ }$) and subscripts ''3'' and ''33'' from the electroelastic variables and coefficients;

$$T = c^{D} S - hD \tag{3a}$$

$$E = -hS + \{\beta^{S} D\} \tag{3b}$$

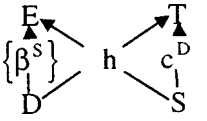

Before specifically defining the hysteresis operator, consider where it would appear in other formulations of the constitutive equations with different independent variable sets. Rearrangement leads to the following:

$$S = \{s^{E} T\} + \{dE\} \tag{4a}$$

$$D = \{dT\} + \{\varepsilon^{T} E\} \tag{4b}$$

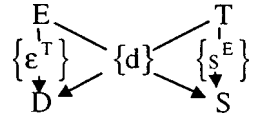

$$S = s^{D} T + gD \tag{5a}$$

$$E = -gT + \{\beta^{T} D\} \tag{5b}$$

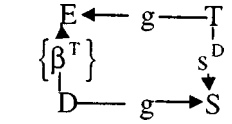

$$T = \{c^{E} S\} - \{eE\} \tag{6a}$$

$$D = \{eS\} + \{\varepsilon^{S} E\} \tag{6b}$$

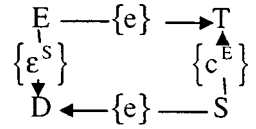

For visualization, diagrams next to Eqs. (3)–(6) show how the hysteresis is manifested depending on which variables are treated as independent. Note that the displayed diagrams do agree in analogy with experimental observations of PZT reported in the literature. For example, Goldfarb and Celanovic[47] observed that the applied electrical displacement (D) vs strain (S) relation under zero stress (T) was reversible, *g*, but that applied electric field (E) vs S under zero T was not, *d*. They also observed that the mechanical stress–strain relation under constant electric displacement, c^D, was reversible whereas the relation under constant electric field was hysteretic, c^E. Damjanovic[42] observed that the applied stress vs electrical displacement relation was hysteretic (*d*).

Several different models for hysteretic behavior of piezoelectric ceramics have been proposed in the literature. Only rate-independent hysteresis models are considered here which do not depend on higher derivatives of the state variables but which will depend on previous values of the state variables, i.e., nonlocal memory. Some models, such as the Rayleigh law for magnetism which was applied to piezoceramics by Damjanovic,[42] or the polynomial model used by Chonan *et al.*,[54] are restricted to steady-state oscillatory behavior and assume an *a priori* knowledge about the extrema values reached. A phenomenological, rate-independent, nonlocal memory hysteresis model which does not rely on noncausal knowledge is the Preisach hysteresis model.[5,48–50] There are, in fact, a number of forms of the Preisach model, as explained in the text by Mayergoyz.[62]

Another rate-independent, causal hysteresis model for piezoelectric ceramics which will be applied here is the ''Maxwell resistive capacitor (MRC)'' element as proposed by Goldfarb and Celanovic.[47] The MRC is based on the Maxwell slip model developed by James C. Maxwell in the mid-1800's. Although it has its roots in describing mechanical hysteresis between stress and strain in terms of spring elements and Coulomb friction elements, hence both reversible and irreversible components, it is not domain specific. The MRC model is schematically presented in Fig. 2. The formulation here is in terms of electrical field and displacement, E and D. Referring to Fig. 2, the model may be implemented into the otherwise linear constitutive equations (3a–b) as follows:

$$T = c^D S - hD \tag{7a}$$

$$E = -hS + \mathrm{MRC}(\beta^S D), \tag{7b}$$

with

$$\mathrm{MRC}(\beta^S D) = \sum_{i=1}^{n} E_{rc}^{(i)} \quad \text{where} \tag{7c}$$

$$\text{if } |\beta^{S(i)}(D - D_b^{(i)})| < e_{rc}^{(i)} \quad \text{then} \quad E_{rc}^{(i)} = \beta^{S(i)}(D - D_b^{(i)}),$$

otherwise $E_{rc}^{(i)} = e_{rc}^{(i)} \mathrm{sign}[\dot{D}]$ and $D_b^{(i)}$ is set such that $|\beta^{S(i)}(D - D_b^{(i)})| = e_{rc}^{(i)}$.

Here, the terms β^S, e_N, μ, e_{rc}, and D_b may be viewed as electrical analogies to a mechanical spring stiffness, normal force, Coulomb friction coefficient, the force due to Coulomb friction, and the displacement from an equilibrium position of the massless box. Note that if the model is reduced to one Coulomb friction, and linear spring pair ($n = 1$) and the threshold electric field value for motion of the Coulomb component is never reached ($|\beta^{S(1)}(D - D_b^{(1)})| < e_{rc}^{(1)}$, $D_b^{(1)} = 0$), then the underlying linear dielectric impermeability relation $\beta^S D$ is recovered. More generally, n linear springs in parallel *without* the Coulomb friction effect would lead to $\beta^S = \Sigma_{i=1}^{n} \beta^{S(i)}$. Hysteretic behavior, an irreversible nonlinearity, is introduced by allowing for Coulomb friction motion to occur, i.e., $D_b^{(1)} \neq 0$.

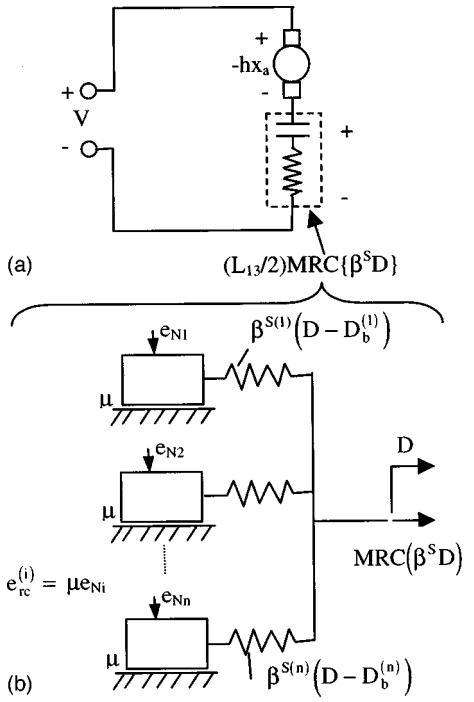

FIG. 2. Maxwell resistive capacitor (MRC) hysteresis model. (a) Equivalent electric circuit of Eq. (8d). (b) Equivalent mechanical analogy of MRC operator of Eq. (7c).

B. Application to a basic test configuration

The dynamic response of the 1-3 component to steady-state electrical sinusoidal excitation is considered. First, the theoretical model of an experimental setup, shown in Fig. 3 and referred to as the basic test configuration (BTC), is developed. The 1-3 element is epoxied between two plexiglass blocks which enable isolation of the high voltage electrodes from the surrounding environment. The plexiglass blocks also provide a mounting location for the accelerometers which are used to measure the motion on either side of the

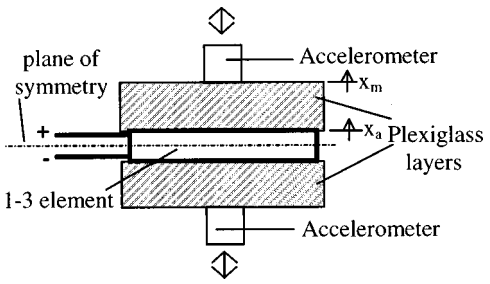

FIG. 3. Basic test configuration (BTC).

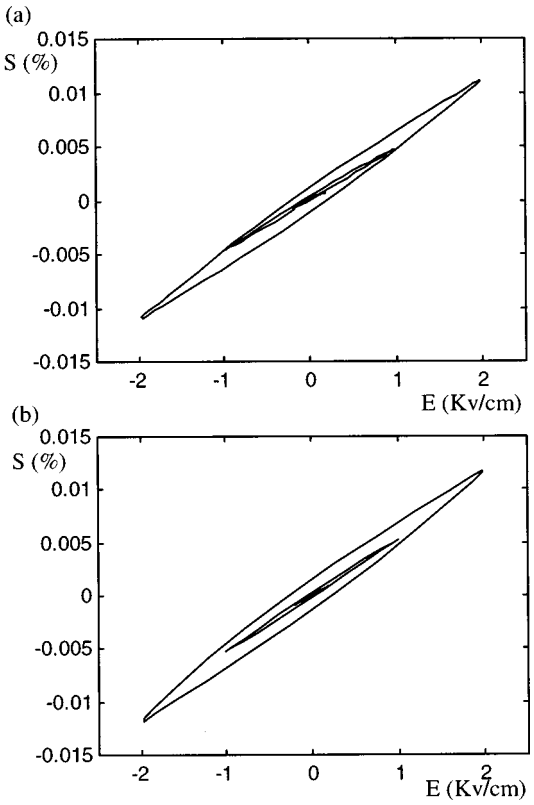

FIG. 4. Strain versus electric field of the PZT-5H 1-3 piezoceramic composite under negligible mechanical stress and subject to a steady-state 50-Hz sinusoidal excitation at three different amplitude levels. (a) Experimental measurement. (b) Theoretical prediction.

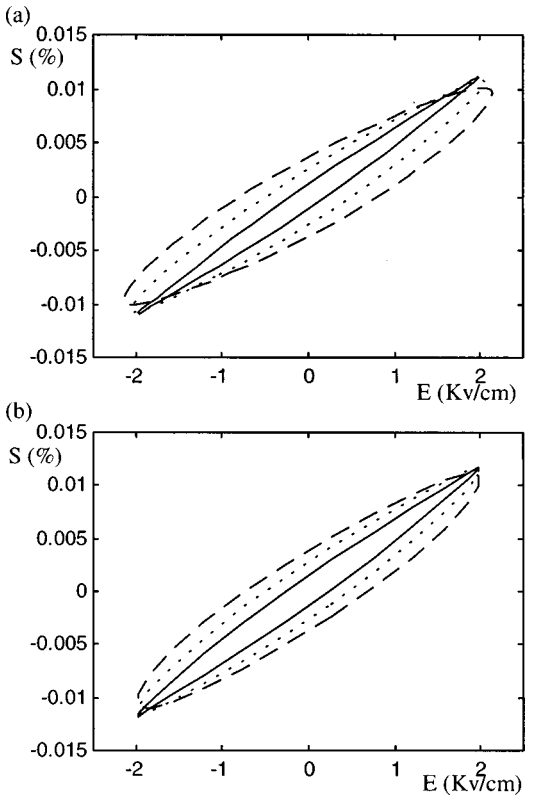

FIG. 5. Strain versus electric field of the PZT-5H 1-3 piezoceramic composite under negligible mechanical stress and subject to a steady-state sinusoidal excitation at three different frequencies. Key: ——— $\omega/2\pi = 50$ Hz; ---- $\omega/2\pi = 500$ Hz; ——— $\omega/2\pi = 1000$ Hz. (a) Experimental measurement. (b) Theoretical prediction.

1-3. The BTC has a plane of symmetry as denoted in Fig. 3. For the low frequency range of interest, less than 1 kHz, the following modeling assumptions are made: (1) motion at the plane of symmetry is zero with equal and opposite motions and forces occurring on either side of this plane; and (2) since this is well below any resonant frequencies in the ''3'' direction of the BTC, an equivalent SDOF mass–spring–damper can be applied with reasonable accuracy. With these assumptions and referring to the diagram in Fig. 3, the following equations can be derived:

$$M\ddot{x}_m(t)+b_{pl}(\dot{x}_m(t)-\dot{x}_a(t))+k_{pl}(x_m(t)-x_a(t))=0, \tag{8a}$$

$$b_{pl}(\dot{x}_m(t)-\dot{x}_a(t))+k_{pl}(x_m(t)-x_a(t)) = AT(t)+2b_{13}\dot{x}_a(t), \tag{8b}$$

$$AT(t)=\frac{2Ac^D}{L_{13}}x_a(t)-AhD(t), \tag{8c}$$

$$V(t)=-hx_a(t)+\frac{L_{13}}{2}\,\mathrm{MRC}\{\beta^S D(t)\}. \tag{8d}$$

Here, note that $E=2V/L_{13}$ where V is the applied voltage and L_{13} is the thickness of the 1-3 and $S=2x_a/L_{13}$, where x_a is the absolute displacement at the 1-3 electrode surface in the ''3'' direction. The term M denotes the lumped equivalent system mass which, for stress-free boundary conditions, is approximated as the half the plexiglass block mass plus the accelerometer mass. The term $k_{pl}=\pi^2 c_{pl}A/8L_{pl}$ denotes the equivalent plexiglass block stiffness Also, x_m, b_{pl}, c_{pl}, and L_{pl} refer to the absolute position of mass M, and the thickness, elastic modulus, and linear viscous damping coefficient, respectively, for the plexiglass block. Finally, b_{13}, A, and F_{ext} refer to the linear viscous damping coefficient for thickness-mode motion of the 1-3, the lateral area of the 1-3 and plexiglass block, and the value of any external force applied to the BTC. (The values of M and k_{pl} here are relatively unimportant with respect to the experimental tests described in Secs. III A–D. They were conducted well below the fundamental resonant frequency ($\sqrt{k_{pl}/M}\approx 16.4$ kHz). Inertial effects were negligible; thus, $x_a \approx x_m$. In the ''loaded'' studies of Sec. III E, M is significantly higher, lowering resonant frequencies and $x_a \neq x_m$). Measured system physical property values are given in Table I.

C. Numerical simulation

Equations (8a)–(d) represent a set of coupled nonlinear differential equations which cannot be solved via simple linear transform techniques. While direct time numerical integration is certainly a viable solution option, for the specific excitation and response conditions of interest here (steady-state periodic excitation and response), a far more efficient solution approach is the multi-term harmonic balance technique. Many numerical implementations of this can be found in the literature; a specific weighted residual approach[63–65] with some modifications was employed in this study.

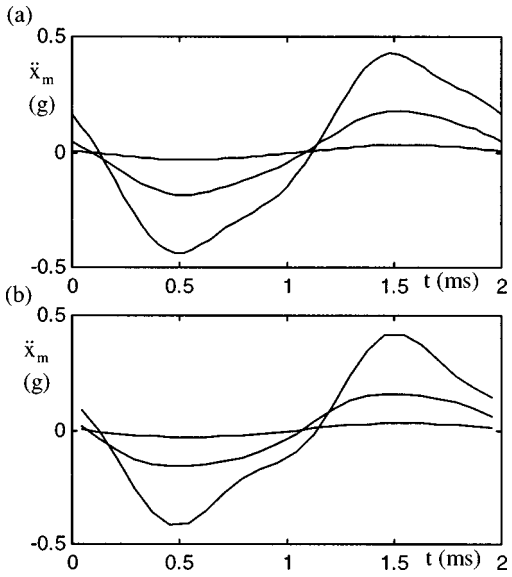

FIG. 6. Acceleration versus time of the PZT-5H 1-3 BTC piezoceramic composite under negligible mechanical stress and subject to a steady-state 500-Hz sinusoidal excitation at three different amplitude levels: $V=1300$, 650, and 130 V (peak). (a) Experimental measurement. (b) Theoretical prediction.

The nonlinearity in the system is confined to Eq. (8d). By nondimensionalizing in time with $\tau=\omega t$, where ω is the sinusoidal excitation frequency of the voltage input and V_a is its amplitude, this equation can be rewritten as follows:

$$0=V_a\,\sin(\tau)+hx_a(\tau)-\frac{L_{13}}{2}\,\mathrm{MRC}\{\beta^S D(\tau)\}. \tag{9}$$

For harmonic motion, Eqs. (8a)–(c) can then be expressed in the frequency domain via a transfer function between x_a and D as follows:

$$x_a(\omega')=tf(\omega')D(\omega')$$

$$\text{where } tf(\omega')=\frac{hAa_{11}(\omega')}{[a_{11}(\omega')a_{22}(\omega')-a_{12}(\omega')a_{21}(\omega')]},$$

$$a_{11}(\omega')=k_{pl}+j\omega' b_{pl}-\omega'^2 M,$$

$$a_{12}(\omega')=a_{12}(\omega')=a_{21}(\omega')=k_{pl}+j\omega' b_{pl}, \tag{10}$$

$$\text{and } a_{22}(\omega')=\left(k_{pl}+\frac{2Ac^D}{L_{13}}\right)+j\omega'(b_{pl}+b_{13}).$$

The variable ω' denotes a response frequency which may be equal to ω or an integer multiple (superharmonic) of it. Now an approximate solution to the set of equations above for D and x_a assumes that up to N_p harmonics of the excitation frequency, ω, are present in the response:

$$D(\tau)=a_0^D+\sum_{n=1}^{N_p} a_{2n-1}^D\,\sin(n\tau)+a_{2n}^D\,\cos(n\tau), \tag{11a}$$

$$x_a(\tau)=a_0^x+\sum_{n=1}^{N_p} a_{2n-1}^x\,\sin(n\tau)+a_{2n}^x\,\cos(n\tau). \tag{11b}$$

The following set of $4N_p+1$ determining equations can be defined based on the above expressions:

$$G_0(\alpha)\equiv \mathrm{Re}[tf(0)]a_0^D-a_0^x=0, \tag{12a}$$

$$G_{2n-1}(\alpha)\equiv \mathrm{Re}[tf(n\omega)]a_{2n-1}^D+\mathrm{Im}[tf(n\omega)]a_{2n}^D - a_{2n-1}^x=0,\quad n=1,...,2N_p, \tag{12b}$$

$$G_{2n}(\alpha)\equiv \mathrm{Re}[tf(n\omega)]a_{2n}^D-\mathrm{Im}[tf(n\omega)]a_{2n-1}^D-a_{2n}^x=0,\quad n=1,...,2N_p. \tag{12c}$$

Here, $\alpha\equiv[a_0^x\ a_1^x\ldots a_{4N_p}^x\ a_0^D\ a_1^D\ldots a_{4N_p}^D]$ and Re and Im denote real and imaginary, respectively. The computational method essentially employs an iterative Newton–Raphson technique with QR decomposition and continuation to find a path of approximate steady-state solutions to Eqs. (9) and (12a)–(c) as a system parameter, such as excitation frequency, is varied. The solutions are approximate in that, in

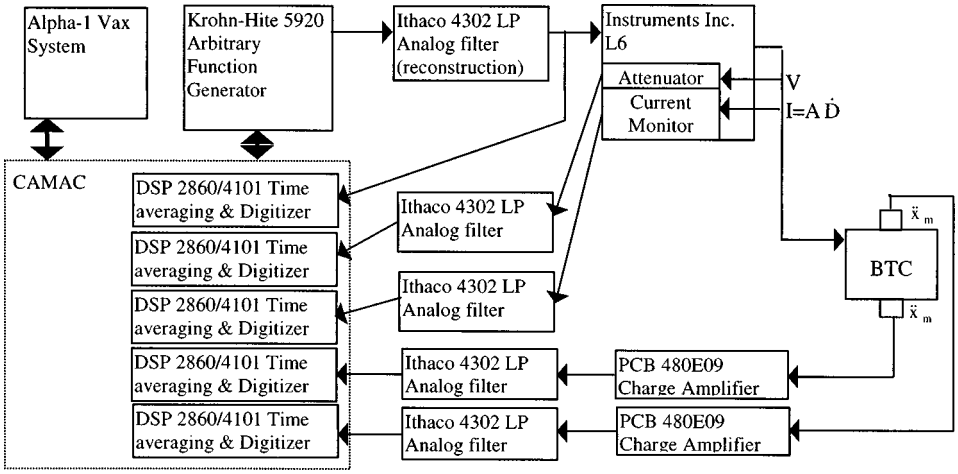

FIG. 7. Instrumentation schematic for dynamic electrical excitation studies. Accelerometers, $\ddot{x}_m$ and $-\ddot{x}_m$, are PCB Model Q353B44 with nominal gain of 300 mv/g.

TABLE II. Arbitrary function parameters for harmonic distortion measurement.

Function	Sweep range increment (Hz)	Low-pass filter (kHz)	Sampling freq f_s (kHz)	Sampling period (μs)	Function length (s)
A	20–120 (10)	1	5	200	6.55
B	120–210 (10)	3.15	16.67	60	1.97
C	210–340 (10)	4	20	50	1.64
D	340–500 (10)	5	25	40	1.31
E	500–670 (10)	8	33.3	30	0.983
F	670–810 (10)	10	50	20	0.655
G	810–990 (10)	10	50	20	0.655
H	210–240 (5)	4	20	50	1.64
I	240–275 (5)	4	20	50	1.64
J	275–315 (5)	4	20	50	1.64
K	315–360 (5)	4	20	50	1.64
L	360–415 (5)	4	20	50	1.64

the time domain, Eq. (9), convergence is forced only at discrete time points. In the frequency domain, Eqs. (12a)–(c), convergence up to only a finite number of harmonics is forced; these harmonics are related to the discrete points in the time domain via the discrete Fourier transform. Further details of the method can be found in Refs. 63–65.

III. EXPERIMENT AND COMPARISON TO THEORY

A. Quasistatic mechanical strain versus electric field

The electromechanical strain-field relationship for the PZT-5H 1-3 sample was determined under nearly stress-free conditions by driving it with a quasistatic (50-Hz sinusoidal) voltage from an Instruments, Inc. L6 linear power amplifier (limit$\approx\pm$1300 V) and Krohn-Hite 5920 arbitrary function generator. The excitation condition is considered quasistatic as no change in the displacement response was observed for sinusoidal voltage excitation with frequencies ranging from 70 Hz down to 40 Hz, the lower limit of the ac amplifier. Velocity was measured using a TSI, Inc. model 1940/30 laser Doppler vibrometer and controller with sensitivity of 5×10^{-4} m/s V. Input and output signals were appropriately filtered, digitized, and processed in Matlab software to obtain the mechanical strain versus electric field, shown in Fig. 4(a). Hysteretic behavior is clearly evident in the relationship with an effective softening nonlinearity as E increases. In Fig. 4(b), predictions based on the theoretical model developed in Sec. II are shown. Parameter values used in the theoretical model are provided in Table I. (Most are based on values reported in the literature.[25,60,66,67] A few are directly measured.) The experimental measurements suggested that the hysteresis was the only dominant form of nonlinearity for the electric field levels considered. A hysteresis model, as depicted by Eqs. (7b)–(c), with $n=4$, was empirically adjusted to achieve good agreement with experiment.

B. Steady-state dynamic electrical excitation and response measurement

The 1-3 was electrically excited with a sinusoidal input and its mechanical velocity was recorded as described in the previous section, but now at several different excitation frequencies above 70 Hz where rate dependence in the response was observed. It is accounted for in the theoretical model as linear viscous damping, b_{13}, for which a value is obtained by comparison with experimental results over a range of excitation frequencies. Experimental mechanical strain versus electric field results are shown in Fig. 5(a) for excitation frequencies of 50, 500, and 1000 Hz. With this rate-dependent linear viscous damping term added, the theoretical model predictions as a function of excitation frequency match experimental measurements fairly well, as shown in Fig. 5(b). Shown in Fig. 6 are experimental measurements and theoretical predictions of the mechanical acceleration under sinusoidal excitation of 500 Hz made using a PCB model No. 353B52 (500 mV/g) accelerometer. Experiment and theory agree fairly well.

C. Harmonic distortion under steady-state dynamic electrical excitation

Measurements of the harmonic distortion of the 1-3 basic test configuration (BTC) to steady-state electrical sinusoidal excitation from 20 to 1000 Hz were conducted. Electrical excitation amplitudes from 130 to 1300 V (peak) were used. Two mounting conditions were considered: (1) a freely suspended, ''in-air'' BTC, and (2) a compressive mechanical load on the BTC (described in Sec. III E). Measured parameters included the electrical voltage and current applied to the 1-3 and the two accelerometer responses (which were virtually identical). Automated measurements were made in 10-Hz increments using the CAMAC system of the Physical Acoustics branch at NRL and data-processing algorithms de-

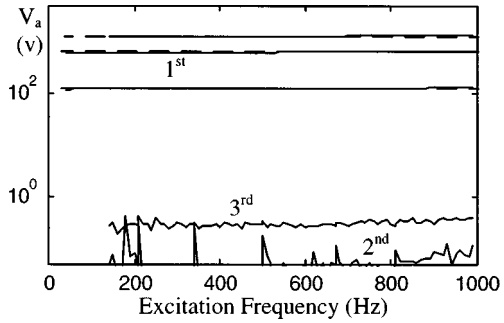

FIG. 8. Electrical excitation voltage, V, of PZT-5H 1-3 BTC in ''in-air unloaded'' condition. Nominally, $V=1300$, 650, and 130 V (peak). Fundamental harmonic shown for all voltage levels. Higher harmonics shown for 1300-V case. Key: ——— experimental measurement; — — — theoretical prediction.

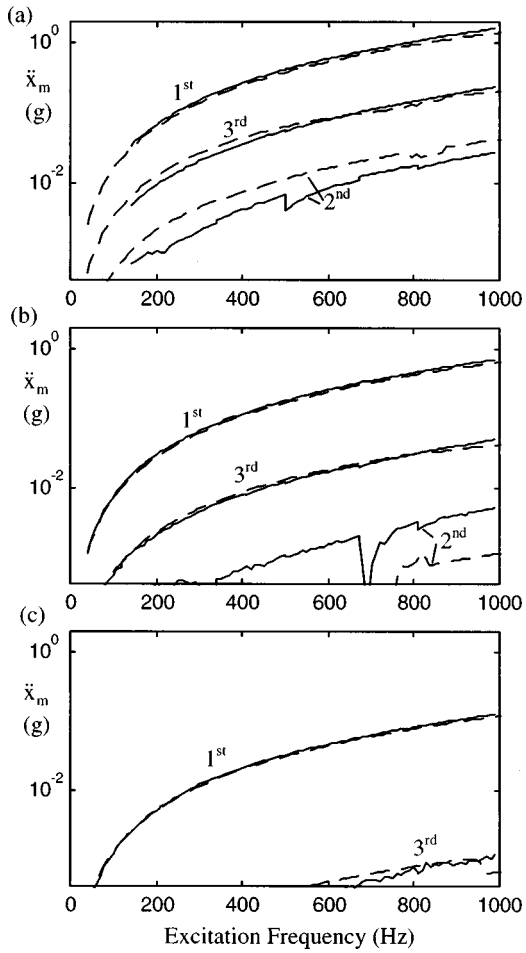

FIG. 9. Mechanical acceleration response, $\ddot{x}_m$, of PZT-5H 1-3 BTC in ''in-air unloaded'' condition. Key: ——— experimental measurement; — — — theoretical prediction. (a) $V=1300$ V (peak). (b) $V=650$ V (peak). (c) $V=130$ V (peak).

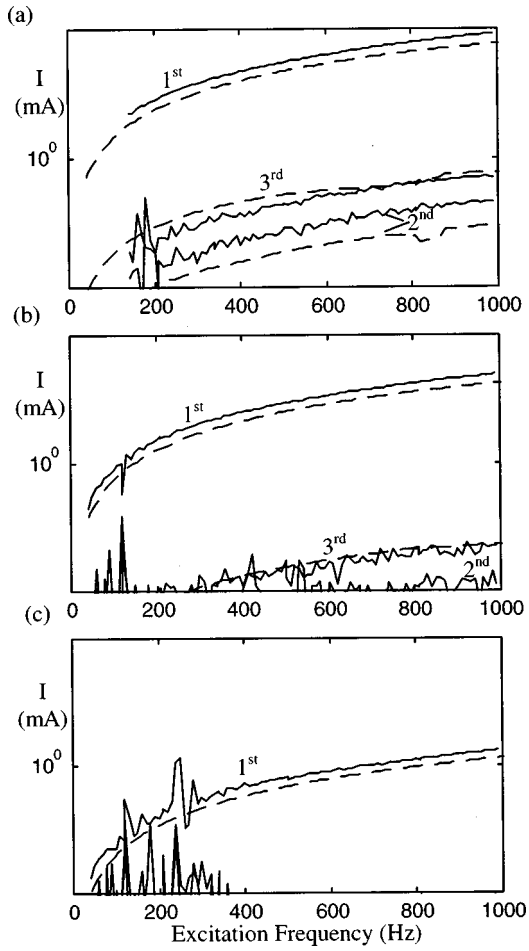

FIG. 10. Electrical current response, I, of PZT-5H 1-3 BTC in ''in-air unloaded'' condition. Key: ——— experimental measurement; — — — theoretical prediction. (a) $V=1300$ V (peak). (b) $V=650$ V (peak). (c) $V=130$ V (peak).

veloped by the first author in Matlab software. The experimental system instrumentation is shown schematically in Fig. 7.

To efficiently and accurately ''track'' the higher harmonic content of the 1-3's over a wide frequency range, a series of arbitrary functions were generated in Matlab and loaded into the Kronhite 5920 arbitrary function generator. Each arbitrary function consisted of a sinusoidal wave that stayed at a fixed frequency for a sufficient number of cycles, 30 to 50, to achieve a steady-state excitation condition. The sinusoid frequency is then increased by a 10-Hz discrete increment and then held at this frequency value for a sufficient number of cycles to again achieve steady state. A continuous sinusoidal excitation was applied at a number of the more resonant excitation frequencies to verify that a sufficient time was given for steady-state convergence. The process is continued throughout the length of the arbitrary function. Due to limitations on the number of allowable data points in the arbitrary function (32 768 points) and the need to satisfy Nyquist's sampling theory, only a finite number of frequency increments can be included in a particular arbitrary function. Given the available equipment, this method of system excitation is optimal since a range of deterministic steady-state dynamic conditions can be rapidly achieved as variations in response from one frequency increment to the next are usually minimal with transients quickly dissipating. Also, a well defined initial condition is recorded which often is necessary in studying nonlinear systems which are initial-condition-dependent. The group of arbitrary functions used in this study and the related instrumentation sampling and filtering parameter values are given in Table II. A four-pole low-pass Bessel filter was used for anti-aliasing and excitation signal

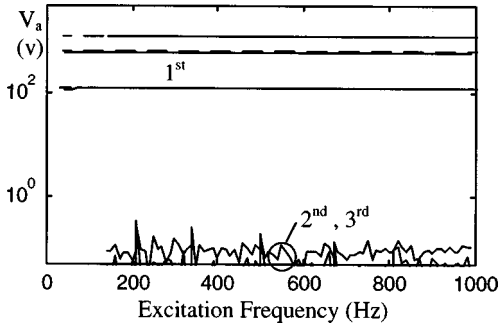

FIG. 11. Electrical excitation voltage, V, of PZT-4 1-3 BTC in ''in-air unloaded'' condition. Nominally, $V=1300$, 650, and 130 V (peak). Fundamental harmonic shown for all voltage levels. Higher harmonics shown for 1300-V case. Key: ——— experimental measurement; — — — theoretical prediction.

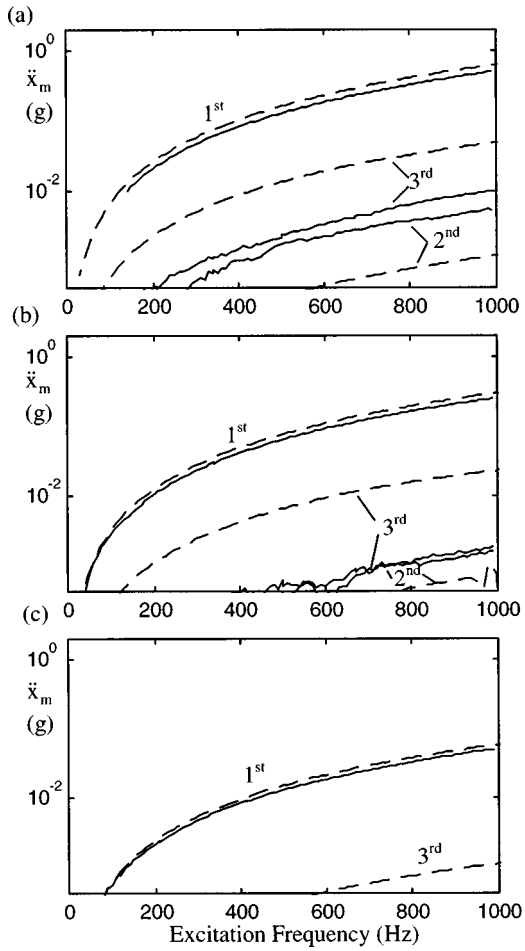

FIG. 12. Mechanical acceleration response, $\ddot{x}_m$, of PZT-4 1-3 BTC in ''in-air unloaded'' condition. Key: ——— experimental measurement; — — — theoretical prediction. (a) $V=1300$ V (peak). (b) $V=650$ V (peak). (c) $V=130$ V (peak).

reconstruction. The sampling frequency and the low-pass filter break point frequency were selected sufficiently high and separated from one another to achieve the necessary reduction in aliased response for a wide frequency band which included a minimum of the first five harmonics of the excitation.

Thirty-two time-averaged system response measurements were captured using the DSP 2860/4101 time averaging and digitizer unit. Four units were used to simultaneously record the attenuated excitation voltage, V, and current, I, and the two acceleration signals, $\ddot{x}_m$ and $-\ddot{x}_m$. The time-averaged records were then stored in a file on the VAX system. From here, they were converted into MATLAB format for post-processing. To avoid errors in harmonic content measurement, the time signals were then nondimensionalized in time and cubic spline fitted to obtain a time-symmetric spacing of data points for the discrete time frequency analysis. Individual harmonic content was extracted via convolution with the appropriate sinusoidal function. It was verified with simulated data that ''numerical noise'' in the digitizing process was sufficiently low.

Results. Results of the higher harmonic measurements for the ''unloaded'' in-air configuration are shown in Figs. 8–10 for the PZT-5H 1-3 alongside theoretical predictions. The first three harmonics of the excitation input (electrical voltage), electric displacement output (current), and mechanical displacement output (acceleration) are shown for three different amplitude levels. (Fourth and higher harmonics for all measured responses were below the measurement noise floor.) The primary harmonic of the response indicates a system being driven in the elastic region with acceleration increasing logarithmically at 40 dB/decade. This agrees with equivalent single-degree-of-freedom calculations given in the previous section. In Fig. 8, the second and third harmonics of the 1300-V (peak) input case are the only ones shown as the other two cases produced similar levels, suggesting that this is, in fact, a noise floor of the measurement and signal processing technique. Nonetheless, it is observed that even for the 1300-V excitation case, harmonic distortion of the input is about four orders of magnitude below the fundamental, or 0.01%. In Figs. 9 and 10, it is seen that this is not the case for the acceleration and current outputs, with harmonic distortion of 15.6% for mechanical acceleration (5.7% for velocity) and 5.6% for electric current. Note the dominance of the odd order (symmetric) third harmonic over that of the second harmonic, indicative of a system with a predominantly symmetric nonlinearity. Also note that the level of harmonic distortion increases as the excitation input amplitude increases. The theoretical model of Eqs. (8a)–(d) with the MRC hysteresis operator ($n=4$) and parameter values provided in Table I, accurately predicts the response of the system variables at the excitation frequency (the fundamental harmonic) and at the third harmonic. Predictions of the second harmonic are better than expected given that there was essentially no asymmetry in the theoretical model aside from minor initial-condition-dependent biases in the slip mechanisms of the MRC hysteresis operator.

D. Parametric study: Different PZT phase in 1-3

Measurements of harmonic distortion levels like those discussed in Sec. III C were conducted on a 1-3 sample

TABLE III. Summary of harmonic distortion levels for in-air study (HDD).

Excitation amplitude (V)	Harmonic distortion in terms of acceleration mean %		Harmonic distortion in terms of velocity mean %		Harmonic distortion in terms of displacement mean %	
	PZT-4	PZT-5H	PZT-4	PZT-5H	PZT-4	PZT-5H
1300	3.0	15.6	1.2	5.7	0.5	2.2
650	1.3	7.7	0.5	2.8	0.2	1.1
130	0.5[a]	2.2[a]	0.2[a]	0.7[a]	0.1[a]	0.2[a]

[a]Numbers may be affected by signal-to-noise ratio.

TABLE IV. Amplitude normalized harmonic distortion levels in terms of displacement. HDD/Displacement amplitude/10^5—see Table III.

Excitation amplitude (v)	PZT-4	PZT-5H
1300	2.4	4.2
650	2.0	4.3
130	4.1[a]	6.4[a]

[a]Numbers may be affected by signal-to-noise ratio.

which incorporated the ''harder'' PZT-4 ceramic in place of the PZT-5H ceramic. In Figs. 11 and 12 the measured electrical excitation and resulting mechanical acceleration are shown alongside theoretical predictions. Note the overall reduced response levels at the fundamental harmonic due to the substantially lower piezoelectric coefficient. The theoretical predictions are based on parameter values provided in Table I for PZT-4. Linear coefficient values again were based on values found in the literature. The identical hysteresis model that was matched to the PZT-5H 1-3 behavior was employed here for theoretical predictions. Note that the theoretical predictions of distortion using this model are significantly greater than those measured, suggesting that the PZT-4 1-3 does in fact have a reduced level of hysteresis relative to PZT-5H 1-3.

Higher harmonic levels for PZT-4 and PZT-5H samples are summarized in Table III in terms of distortion in the acceleration, velocity, and displacement. The percentage values represent the total contribution of all of the dominant higher harmonics, typically only the second and third harmonics. Perhaps a better comparison of nonlinearity in PZT-4 vs PZT-5H 1-3's is given in Table IV, where the harmonic distortion levels are normalized with respect to the achieved displacement levels. Note that while it may require roughly twice the voltage using PZT-4 to produce the same displacement as that obtained using PZT-5H, the level of harmonic distortion using PZT-4 will still be roughly half of that when using PZT-5H.

E. Parametric study: 1-3 under resonant-dynamic and static-bias mechanical loading

In some applications, such as vibration isolation in structural systems, the 1-3 may be subjected to significant static mechanical bias forces and/or be coupled to a highly resonant mechanical boundary condition which may produce large variations as a function of frequency in the effective mechanical impedance that the 1-3 is expected to actuate. Recall from the constitutive equations that the PZT response is dependent on both mechanical stress and strain. The impact of nonnegligible mechanical stress, static, and/or dynamic on the PZT and 1-3 behavior, particularly in terms of the level of nonlinearity, has not yet been addressed in this article, nor has it been thoroughly analyzed by other researchers.

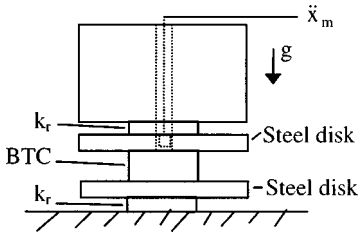

FIG. 13. Schematic of BTC under static bias and resonant-dynamic load.

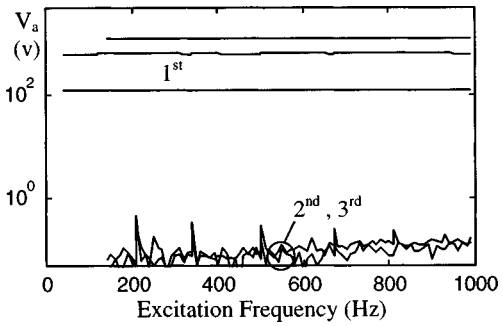

FIG. 14. Electrical excitation voltage, V, of PZT-5H 1-3 BTC under static bias and resonant-dynamic load condition of Fig. 13. Nominally, $V = 1300$, 650, and 130 V (peak). Fundamental harmonic shown for all voltage levels. Higher harmonics shown for 1300 V case. Key: ——— experimental measurement.

The experimental condition, shown in Fig. 13, involved a mounting arrangement in which the 1-3 is subjected to some level of static mechanical compression and a resonant mechanical load in the frequency range of interest. In the test

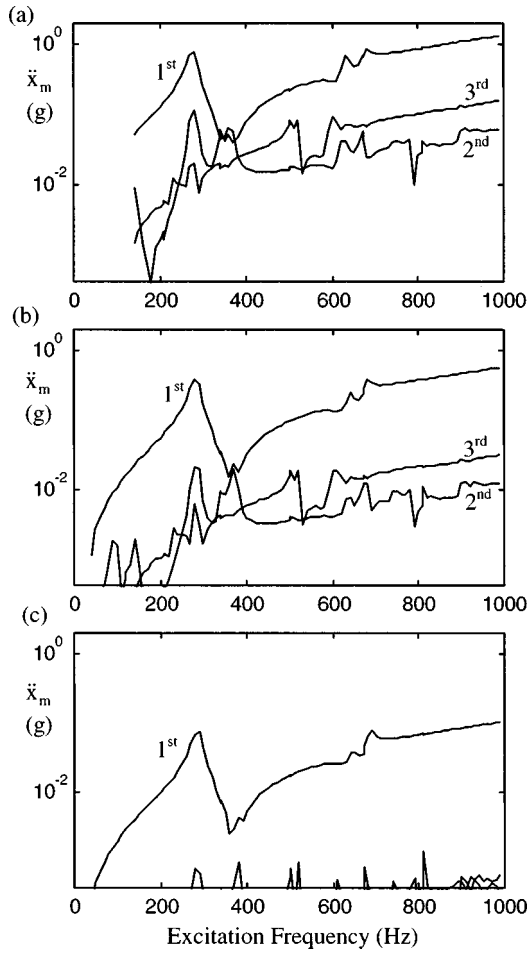

FIG. 15. Mechanical acceleration response of PZT-5H 1-3 BTC under static bias and resonant-dynamic load condition of Fig. 13. Key: ——— experimental measurement. (a) $V = 1300$ V (peak). (b) $V = 650$ V (peak). (c) $V = 130$ V (peak).

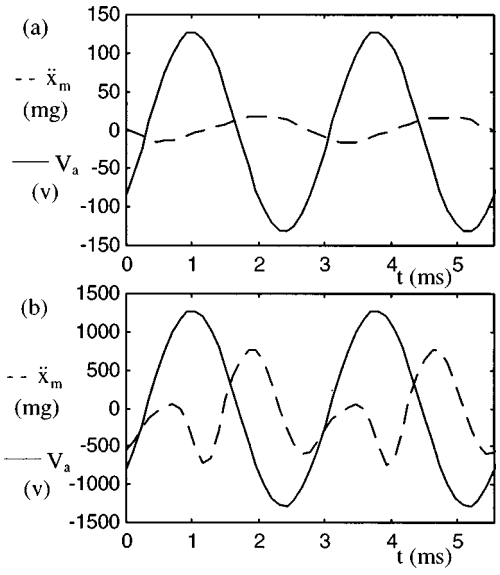

FIG. 16. Electrical excitation/mechanical response of PZT-5H 1-3 BTC under static bias and resonant-dynamic load condition of Fig. 13 and sinusoidal excitation of frequency $\omega/2\pi=360$ Hz. (a) Small amplitude excitation. (b) Large amplitude excitation. Key: ——— applied voltage V; — — — acceleration $\ddot{x}_m$.

studies, the BTC was exposed to a static compressive load of 1113.6 N [pressure of 445 kPa (64.4 psi) on the 1-3 itself]. The stiffness of each rubber layer shown in the figure is estimated to be on the order of 1×10^5 N/m. Ideally, with vertical motion only and this stiffness value being sufficiently low, the BTC and the two steel rings directly in contact with it (each of 22.7-kg mass) may be considered dynamically isolated above 20 Hz. Again, there is a plane of symmetry through the BTC as in Fig. 3. Except now, there is a substantial resonant load in the frequency range of interest. As a rough first approximation, the plexiglass block mass is lumped with the steel disk and its spring stiffness is given by $k_{pl}=c_{pl}A/L_{pl}=(5.93\times10^9\ \mathrm{N/m^2})(0.002\ \mathrm{m^2})/(0.0254\ \mathrm{m})=4.67\times10^8$ N/m. If the disk mass is treated as rigid, then a resonant frequency of $\sqrt{4.67\times10^8/22.7}/2\pi \approx 720$ Hz is predicted. But, the steel disk (radius of 0.19 m and mean thickness of 0.0254 m with Young's modulus of 207 GPa and density of 7850 kb/m^3) flexural modes under free boundary conditions can be estimated using formulas by Liessa.[68] The only axisymmetric mode with a natural frequency below 1000 Hz, is the first with a value of about 250 Hz. A more thorough analysis of the resonant loading condition would require a detailed numerical treatment because of the complex coupling conditions and actual disk geometry (center hole and thickness variation) and would still be approximate given some modeling uncertainties. It is beyond the scope of this article; nonetheless, the above theoretical predictions suggest there may be more than one resonance below 1000 Hz.

Experimental measurements for the PZT-5H 1-3 under the loading condition of Fig. 13 are shown in Figs. 14–16. For this case, the response has become significantly more complex and frequency dependent. Measured harmonic distortion in the excitation voltage is now about 0.1%. This was true for all three of the excitation levels considered. In Fig. 15, note the general increase in the asymmetric second harmonic response of the mechanical acceleration, eclipsing the symmetric third harmonic at some excitation frequencies. This is a common occurrence in nonlinear systems subject to some sort of bias load.[69] A strong resonance in the fundamental and higher harmonic acceleration responses occurs at about 280 Hz. Its peak frequency decreases slightly with increasing excitation amplitude, sign of a softening stiffness nonlinearity (or hardening stiffness nonlinearity under a bias load).[69] Approximate theoretical predictions suggest that this may be associated with the first axisymmetric flexural mode of the steel disk. Note in Fig. 15(b) the excitation of this strong resonance at excitation frequencies of one-half and one-third the resonant frequency evident in the second and third higher harmonic traces, respectively. Resonant behavior at all three excitation amplitude levels is evident near excitation frequencies of 640 and 690 Hz in the fundamental harmonic. Note that resonances in the higher harmonics which roughly correspond to these are evident at about 330 and 360 Hz in the second harmonic and to a less degree at about 230 Hz in the third harmonic. In fact, the second harmonic response at an excitation frequency of 360 Hz apparently due to a system resonance at twice this frequency dominates the spectrum as the fundamental harmonic response at 360 Hz is in an antiresonance. In other words, it appears that the multi-resonant dynamics of the structure the 1-3 is driving has led to a condition of greater that 100% harmonic distortion, a condition not encountered when the 1-3 was subject to much simpler mechanical coupling. This is clearly evident in the time domain plots of Fig. 16. Table V summarizes the harmonic distortion levels and variability for this loading condition.

IV. CONCLUSION

The principle contributions of this study are summarized. Preliminary theoretical formulations of the nonlinear constitutive equations for 1-3's have been developed which account for irreversible (hysteretic) dielectric behavior in the PZT phase. Preliminary experimental studies of a 1-3 piezoceramic element have detected nonlinear behavior, particu-

TABLE V. Summary of harmonic distortion levels for biased-resonant study (PZT-5H).

Excitation amplitude (V)	Harmonic distortion in terms of acceleration mean (range) %	Harmonic distortion in terms of velocity mean (range) %	Harmonic distortion in terms of displacement mean (range) %
1300	28.3 (2.2–204)	11.6 (0.8–92.3)	5.0 (0.3–42.9)
650	14.1 (0.7–111)	5.8 (0.2–50.6)	2.5 (0.1–23.7)
130	2.5 (0–26.7)	1.1 (0–12.5)	0.5 (0–6.0)

larly in terms of hysteresis under quasistatic excitation conditions and higher harmonic response (harmonic distortion) under dynamic excitation conditions. Dependence on excitation amplitude level and frequency has been measured. Response predictions based on the nonlinear theoretical model have shown good agreement with experiment, particularly for low externally applied mechanical stress conditions.

A significant dependence of the level of nonlinearity on the coupling conditions of the 1-3 to its surroundings has been measured. This may have serious repercussions with respect to integrating 1-3's in applications where they will be subjected to significant resonant dynamic mechanical loading such as in structural vibro-acoustic control applications. Further theoretical and experimental research on this particular issue are needed. Finally, comparative studies of nonlinearity in PZT-4 vs PZT-5H 1-3's indicate that, even if the reduced actuation authority of the PZT-4 is taken into account, the level of harmonic distortion using PZT-4 is significantly less than when using PZT-5H.

While this study has focused on the 1-3, some of the utilized techniques are applicable to the wide range of conventional and smart components and structures with significant nonlinearity. Smart materials in which nonlinearity has been reported include piezoelectric, electrostrictive, magnetostrictive, electrorheological, and shape memory alloy. Nonlinearity may be especially prevalent in piezoelectric and electrostrictive single-crystal and thin film devices in the coming years as electric field levels are expected to be very high in their application. A better fundamental understanding of nonlinear vibration transmission, transduction, dissipation, and production in components and structures utilizing these technologies will ultimately have wide benefit.

ACKNOWLEDGMENTS

The first author acknowledges the financial support of the ASEE/NRL Summer Faculty Program. Both authors acknowledge the technical support of the Physical Acoustics Branch of the Naval Research Laboratory.

[1] G. S. Agnes and D. J. Inman, ''Nonlinear piezoelectric vibration absorbers,'' Smart Mater. Struct. **5**, 704–714 (1996).
[2] N. Aurelle, D. Guyomar, C. Richard, P. Gonnard, and L. Eyraud, ''Nonlinear behavior of an ultrasonic transducer,'' Ultrasonics **34**, 187–191 (1996).
[3] M. D. Bryant and R. F. Keltie, ''A characterization of the linear and non-linear dynamic performance of a practical piezoelectric actuator. Part 1: Measurements,'' Sens. Actuators **9**, 95–103 (1986).
[4] M. D. Bryant and R. F. Keltie, ''A characterization of the linear and non-linear dynamic performance of a practical piezoelectric actuator. Part 2: Theory,'' Sens. Actuators **9**, 105–114 (1986).
[5] D. Hughes and J. T. Wen, ''Preisach modeling of piezoceramic and shape memory alloy hysteresis,'' Smart Mater. Struct. **6**, 287–300 (1997).
[6] F. Lalande, Z. Chaudhry, and C. A. Rogers, ''A Simplified Geometrically Nonlinear Approach to the Analysis of the Moonie Actuator,'' IEEE Trans. Ultrason. Ferroelectr. Freq. Control **42**, 21–27 (1995).
[7] C. H. Sherman and J. L. Butler, ''Analysis of harmonic distortion in electroacoustic transducers,'' J. Acoust. Soc. Am. **98**, 1596–1611 (1995).
[8] C. H. Sherman, J. L. Butler, and A. L. Butler, ''Analysis of harmonic distortion in electroacoustic transducers under indirect drive conditions,'' J. Acoust. Soc. Am. **101**, 297–314 (1997).
[9] M. L. R. Fripp and N. W. Hagood, ''Distributed structural actuation with electrostrictors,'' J. Sound Vib. **203**, 11–40 (1997).
[10] M. J. Dapino, F. T. Calkins, A. B. Flatau, and D. L. Hall, ''Measured Terfenol-*D* material properties under varied applied magnetic field levels,'' SPIE Proceedings **2717**, 697–708 (1996).
[11] A. G. Jenner, R. D. Greenough, D. Allwood, and A. J. Wilkinson, ''Control of Terfenol-*D* under load,'' J. Appl. Phys. **76**, 7160–7162 (1994).
[12] M. B. Moffet, A. E. Clark, M. Wun-Fogle, J. Linberg, J. P. Teter, and E. A. McLaughlin, ''Characterization of Terfenol-*D* for magnetostrictive transducers,'' J. Acoust. Soc. Am. **89**, 1448–1455 (1991).
[13] G. M. Kamath and N. M. Wereley, ''A nonlinear viscoelastic-plastic model for electrorheological fluids,'' Smart Mater. Struct. **6**, 351–359 (1997).
[14] D. J. Peel, R. Stanway, and W. A. Bullough, ''Dynamic modeling of an ER vibration damper for vehicle suspension applications,'' Smart Mater. Struct. **5**, 591–606 (1996).
[15] A. H. Shiang and J. P. Coulter, ''A comparative study of ac and dc electrorheological material based adaptive structures in small amplitude vibration,'' J. Intell. Mater. Syst. Struct. **7**, 455–469 (1996).
[16] S.-E. Park and T. R. Shrout, ''Ultrahigh strain and piezoelectric behavior in relaxor based ferroelectric single crystals,'' J. Appl. Phys. **82**, 1804–1811 (1997).
[17] J. R. Pratt, S. S. Oueini, and A. H. Nayfeh, ''A Terfenol-*D* nonlinear vibration absorber,'' SPIE Proceedings **3041**, 56–66 (1997).
[18] D. J. Warkentin and N. W. Hagood, ''Nonlinear piezoelectric shunting for structural damping,'' SPIE Proceedings **3041**, 747–757 (1997).
[19] R. D. Corsaro, B. H. Houston, and J. A. Bucaro, ''Sensor-actuator tile for underwater surface impedance control studies,'' J. Acoust. Soc. Am. **102**, 1573–1581 (1997).
[20] G. Hayward and J. A. Hossack, ''Unidimensional modeling of 1-3 composite transducers,'' J. Acoust. Soc. Am. **88**, 599–608 (1990).
[21] W. A. Smith, ''The role of piezocomposites in ultrasonic transducers,'' in *Proceedings of the 1989 IEEE Ultrasonics Symposium* (IEEE, New York, 1989), pp. 755–766.
[22] W. A. Smith, ''The application of 1-3 piezocomposites in acoustic transducers,'' in *Proceedings of the 1990 IEEE 7th International Symposium on Ferroelectrics* (IEEE, New York, 1991), pp. 145–152.
[23] R. Y. Ting and T. R. Howarth, ''Underwater evaluation of piezocomposite panels as active surfaces,'' SPIE Proceedings **2721**, 214–221 (1996).
[24] Q. M. Zhang, W. Cao, H. Wang, and L. E. Cross, ''Characterization of the performance of 1-3 type piezocomposites for low-frequency applications,'' J. Appl. Phys. **73**, 1403–1410 (1993).
[25] MSI (1997) Material Systems Inc., Private correspondence.
[26] J. C. Baumhauer and H. F. Tiersten, ''Nonlinear electroelastic equations for small fields superposed on a bias,'' J. Acoust. Soc. Am. **54**, 1017–1034 (1973).
[27] H. F. Tiersten, ''On the nonlinear equations of thermoelectroelasticity,'' Int. J. Eng. Sci. **9**, 587–604 (1971).
[28] R. A. Toupin, ''The elastic dielectric,'' Journal of Rational Mechanical Analysis **5**, 849–915 (1956).
[29] S. P. Joshi, ''Nonlinear constitutive relations for piezoceramic materials,'' Smart Mater. Struct. **1**, 80–83 (1992).
[30] D. Berlincourt, ''Piezoelectric ceramics: Characteristics and applications,'' J. Acoust. Soc. Am. **70**, 1586–1595 (1981).
[31] D. Berlincourt and H. H. A. Krueger, ''Domain processes in lead titanate zirconate and barium titanate ceramics,'' J. Appl. Phys. **30**, 1804–1810 (1959).
[32] S. Li, W. Cao, and L. E. Cross, ''The extrinsic nature of nonlinear behavior observed in lead zirconate titanate ferroelectric ceramic,'' J. Appl. Phys. **69**, 7219–7224 (1991).
[33] S. Li, W. Cao, R. E. Newnham, and L. E. Cross, ''Electromechanical nonlinearity of ferroelectric ceramics and related non-180 degree domain wall motions,'' Ferroelectrics **139**, 25–49 (1993).
[34] R. F. Brown and G. W. McMahon, ''Material constants of ferroelectric ceramics at high pressures,'' Can. J. Phys. **40**, 672–674 (1962).
[35] H. Cao and A. G. Evans, ''Nonlinear deformation of ferroelectric ceramics,'' J. Am. Ceram. Soc. **76**, 890–896 (1993).
[36] H. H. Krueger and D. Berlincourt, ''Effects of high static stress on the piezoelectric properties of transducer materials,'' J. Acoust. Soc. Am. **33**, 1339–1344 (1961).
[37] H. H. Krueger, ''Stress sensitivity of piezoelectric ceramics: Part 1. Sensitivity to compressive stress parallel to the polar axis,'' J. Acoust. Soc. Am. **42**, 636–644 (1967).
[38] T. Tanimoto, K. Okazaki, and K. Yamamoto, ''Tensile stress–strain behavior of piezoelectric ceramics,'' Jpn. J. Appl. Phys., Part 1 **9B**, 4233–4236 (1993).
[39] R. Gerson, ''Dependence of mechanical Q and Young's modulus of ferro-

electric ceramics on stress amplitude,'' J. Acoust. Soc. Am. **32**, 1297–1301 (1960).
[40] S. Takahashi and S. Hirose, ''Vibration-level characteristics of lead-zirconate-titanate ceramics,'' Jpn. J. Appl. Phys. **31**, 3055–3057 (1992).
[41] S. Takahashi, S. Hirose, and K. Uchino, ''Stability of PZT piezoelectric ceramics under vibration level change,'' J. Am. Ceram. Soc. **77**, 2429–2432 (1994).
[42] D. Damjanovic, ''Stress and frequency dependence of the direct piezoelectric effect in ferroelectric ceramics,'' J. Appl. Phys. **82**, 1788–1797 (1997).
[43] D. V. Taylor and D. Damjanovic, ''Evidence of domain wall contribution to the dielectric permittivity in PZT thin films at sub-switching fields,'' J. Appl. Phys. **82**, 1973–1975 (1997).
[44] D. Damjanovic and R. E. Newnham, ''Electrostrictive and piezoelectric materials for actuator applications,'' J. Intell. Mater. Syst. Struct. **3**, 190–208 (1992).
[45] Q. M. Zhang, H. Wang, N. Kim, and L. E. Cross, ''Direct evaluation of domain-wall and intrinsic contributions to the dielectric and piezoelectric response and their temperature dependence on lead zirconate-titanate ceramics,'' J. Appl. Phys. **75**, 454–459 (1994).
[46] D. Guyomar, N. Aurelle, and L. Eyraud, ''Piezoelectric ceramics nonlinear behavior. Application to Langevin transducer,'' J. Phys. III **7**, 1197–1208 (1997).
[47] M. Goldfarb and N. Celanovic, ''A lumped parameter electromechanical model for describing the nonlinear behavior of piezoelectric actuators,'' ASME Journal of Dynamic Systems, Measurement and Control **119**, 478–485 (1997).
[48] P. Ge and M. Jouaneh, ''Generalized Preisach model for hysteresis nonlinearity of piezoceramic actuators,'' Precis. Eng. **20**, 99–111 (1997).
[49] P. Ge and M. Jouaneh, ''Tracking control of a piezoceramic actuator,'' IEEE Transactions on Control Systems Technology **4**(3), 209–216 (1996).
[50] P. Ge and M. Jouaneh, ''Modeling hysteresis in piezoceramic actuators,'' Precis. Eng. **17**, 211–221 (1995).
[51] J. A. Main and E. Garcia, ''Design impact of piezoelectric actuator nonlinearities,'' J. Guid. Control. Dyn. **20**, 327–332 (1997).
[52] J. A. Main and E. Garcia, ''Piezoelectric stack actuators and control system design: Strategies and pitfalls,'' J. Guid. Control. Dyn. **20**, 479–485 (1997).
[53] J. A. Main, E. Garcia, and D. V. Newton, ''Precision position control of piezoelectric actuators using charge feedback,'' J. Guid. Control. Dyn. **18**, 1068–1073 (1995).
[54] S. Chonan, Z. Jiang, and T. Yamamoto, ''Nonlinear hysteresis compensation of piezoelectric ceramic actuators,'' J. Intell. Mater. Syst. Struct. **7**, 150–156 (1996).
[55] Y. Y. Yu, ''Some recent advances in linear and nonlinear dynamical modeling of elastic and piezoelectric plates,'' J. Intell. Mater. Syst. Struct. **6**, 237–254 (1995).
[56] H. S. Tzou and Y. Bao, ''Nonlinear piezothermoelasticity and multi-field actuations, Part 1: Nonlinear anisotropic piezothermoelastic shell laminates,'' ASME Journal of Vibration and Acoustics **119**, 374–381 (1997).
[57] H. S. Tzou and Y. H. Zhou, ''Nonlinear piezothermoelasticity and multi-field actuations, Part 2: Control of nonlinear deflection, buckling and dynamics,'' ASME Journal of Vibration and Acoustics **119**, 382–389 (1997).
[58] W. Cao, Q. M. Zhang, and L. E. Cross, ''Theoretical study on the static performance of piezoelectric ceramic-polymer composites with 1-3 connectivity,'' J. Appl. Phys. **72**, 5814–5821 (1992).
[59] J. A. Hossack and G. Hayward, ''Finite-element analysis of 1-3 composite transducers,'' IEEE Trans. Ultrason. Ferroelectr. Freq. Control **38**, 618–629 (1991).
[60] W. A. Smith and B. A. Auld, ''Modeling of 1-3 composite piezoelectrics: Thickness-mode oscillations,'' IEEE Trans. Ultrason. Ferroelectr. Freq. Control **38**, 40–7 (1991).
[61] T. Bui, H. L. W. Chan, and J. Unsworth, ''Specific acoustic impedances of piezoelectric ceramic and polymer composites used in medical applications,'' J. Acoust. Soc. Am. **83**, 2416–2421 (1988).
[62] I. D. Mayergoyz, *Mathematical Models of Hysteresis* (Springer-Verlag, New York, 1991).
[63] M. Urabe and A. Reiter, ''Numerical computation of nonlinear forced oscillations by Galerkin's procedure,'' J. Math. Anal. Appl. **14**, 107–140 (1966).
[64] T. J. Royston and R. Singh, ''Vibratory power flow through a nonlinear path into a resonant receiver,'' J. Acoust. Soc. Am. **101**, 2059–2069 (1997).
[65] T. J. Royston and R. Singh, ''Periodic response of mechanical systems with local nonlinearities using an enhanced Galerkin technique,'' J. Sound Vib. **194**, 243–263 (1996).
[66] G. S. Kino, *Acoustic Waves: Devices, Imaging, and Analog Signal Processing* (Prentice-Hall, Englewood Cliffs, NJ, 1987).
[67] N. Lagakos, J. Jarzynski, J. H. Cole, and J. A. Bucaro, ''Frequency and temperature dependence of elastic moduli of polymers,'' J. Appl. Phys. **59**, 4017–4031 (1986).
[68] A. Leissa, *Vibration of Plates* (Acoustical Society of America, Woodbury, NY, 1993).
[69] T. J. Royston and R. Singh, ''Experimental study of mechanical systems with mean-loaded localized continuous stiffness nonlinearities,'' J. Sound Vib. **198**, 279–298 (1996).

Active control of sound transmission through a double-leaf partition by volume velocity cancellation

X. Pan, T. J. Sutton, and S. J. Elliott
Institute of Sound and Vibration Research, University of Southampton, Southampton SO17 1BJ, United Kingdom

(Received 7 November 1997; accepted for publication 4 August 1998)

The paper considers the active control of harmonic sound transmitted through a double-leaf partition by cancelling the volume velocity of the radiating panel. The double-leaf partition consists of a pair of small plates, 300×380 mm, separated by a 100-mm air-gap. The panel volume velocity can be sensed by a single shaped film of piezoelectric PVDF material attached to the plate. Cancellation of volume velocity using a single point force is compared with the result using a matched, *distributed* actuator which applies a uniform force to the plate and does not give rise to control spillover. Comparison with earlier work in which the volume velocity of a single plate was cancelled [Johnson and Elliott, J. Acoust. Soc. Am. **98**, 2174–2186 (1995)] shows that substantial reductions in the transmitted sound power are only possible up to around 350 Hz, as opposed to 600 Hz in the single panel case. A radiation mode analysis of the panels shows that the double-leaf construction provides good passive attenuation of the first radiation mode at high frequencies, so that inefficiently radiating even modes of the radiating panel make a dominant contribution to the radiated sound power. Thus there is no advantage in controlling volume velocity in this frequency range. © *1998 Acoustical Society of America.* [S0001-4966(98)02811-2]

PACS numbers: 43.40.Dx, 43.40.Vn, 43.55.Rg [PJR]

INTRODUCTION

Double-leaf partitions are often used in noise control engineering when high sound transmission loss has to be achieved with lightweight structures: an example is an aircraft fuselage shell. However, the sound transmission loss decreases rapidly toward low frequencies, where it is generally poorer than that of a single panel.[1,2] Active noise control offers a solution to this problem.

A recent paper on the active control of sound radiation[3] has discussed the strategy of cancelling the net volume velocity of a vibrating panel in order to reduce the sound power radiated from it at low frequencies. The net volume velocity of a thin plate can be obtained directly using a single distributed piezoelectric sensor attached to the plate surface.[4] No knowledge of the mode shapes of the plate vibration is needed. In the earlier work[3] the effect of cancelling the volume velocity of a single thin plate was examined, and it was seen that the radiated power could be reduced significantly, not only at very low frequencies as might have been expected (i.e., for $kl \ll 1$, where k is wave number and l is the longest dimension of the plate), but also up to $kl = 4$, where a 10-dB reduction was calculated. In order to achieve this attenuation, it was assumed that the control was applied by a single *distributed* secondary actuator. The distributed actuator was designed to avoid control spillover by exerting a uniform force over the plate surface; such an actuator formed a matched pair with the volume velocity sensor and only excited those plate modes which are observed by the volume velocity sensor. One advantage of cancelling plate volume velocity is that no remote error microphones are required to sense the radiated sound. A further advantage is that of simplicity because the volume velocity measurement can be made by a single distributed sensor.

In this paper the philosophy of cancelling the net volume velocity of a panel by active means will be applied to a double-leaf partition. As in the work on single panels,[3] it will be assumed that a measurement of the spatially integrated volume velocity of the radiating panel is available and either a single point force or a uniform-force actuator will be used for control. Previous work on the active control of sound transmission through a double-leaf partition has generally involved reducing the sound pressure at discrete microphone locations. Carneal and Fuller[5] carried out an experimental study of the active control of a double-leaf partition using three PZT actuators for control. At single frequencies, the controller acted to minimize the sum of squared sound pressure measurements using three error microphones in a receiving room. In the experiment the PZT actuators were first placed on the incident panel and then on the radiating panel. On the incident panel it was found that the control acted to suppress the modes of the plate and reduce their source strength; while with the actuators on the radiating panel the modes were restructured so that the odd–odd modes (which are efficient radiators) were suppressed while the inefficiently radiating even modes were generally increased in amplitude.

Another investigation of the active control of a double-leaf partition was carried out by Sas *et al.*[6,7] who inserted small loudspeakers into the space between the two panels. In different experiments they minimized the sum of squared sound pressures at two microphones placed either inside the cavity between the panels or external to the partition assembly at various distances from the radiating panel. The use of microphones in the cavity gave good transmission loss at frequencies where vibration of the coupled structural-acoustic system was dominated by one or two modes. How-

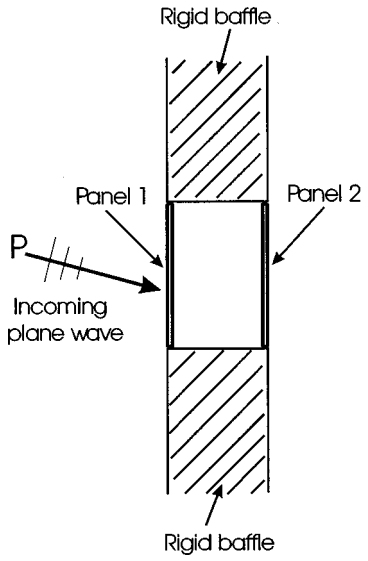

FIG. 1. Double panel partition.

ever, the transmission loss was generally slightly better when the microphones were placed externally in the radiated sound field.

In this paper, radiation modes are used as a tool to analyze the radiated power from a double-panel partition. In the radiation mode approach the surface vibration is decomposed into a set of independently radiating velocity distributions which roughly correspond to monopole, dipole, and higher-order acoustic radiators. For example, the first (monopole-type) radiation mode simply expresses the net volume velocity of the plate. The application of a single uniform-force actuator to one or other panel of a double-panel partition is investigated, and compared with the reduction in radiated power achieved using a point actuator.

I. THEORY

A. Description of double-panel model

Previous work on sound transmission into a rectangular enclosure[6,8,9] indicates that a fully coupled structural-acoustic model is required to describe the double-leaf partition adequately. Kim and Brennan[10] set out a fully coupled structural-acoustic model to investigate the minimization of the acoustic potential energy for reducing sound transmission into a rectangular enclosure using both structural and acoustic actuators. In this model the vibration of the fully coupled system is expressed in terms of the amplitudes of the structural and acoustic modes of the uncoupled subsystems. Our analysis extends the model[10] to active control of sound transmission into a free field, through a double-leaf partition where full coupling exists among the acoustical modes in the sound field between the two panels and the structural modes on each panel. Figure 1 shows a double-leaf partition in an infinite rigid baffle. An incident plane wave P excites panel 1. Through the coupling of panel 1, the acoustical enclosure between the double panels and panel 2, sound power is radiated from the right hand side of the baffle. The coordinates of panel 1, which is excited by plane wave (P), are shown in Fig. 2(a), and the coordinates of panel 2 are shown in Fig. 2(b). The sound radiation from panel 2 is calculated using a number of elemental radiators.[3]

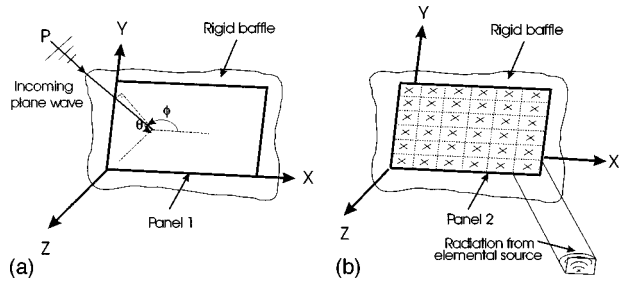

FIG. 2. (a) Coordinates of panel 1 which is excited by an incident plane wave P; (b) coordinates of panel 2 and sound radiation from the panel using a number of elemental radiators.

B. Structural-acoustic coupled response

If the acoustic pressure and the structural vibration are assumed to be described by summation of N and M modes, respectively, the acoustic pressure at a location (x,y,z) inside the enclosure and the structural vibration velocities at a location (x,y) on panel 1 and panel 2 are given, respectively,

$$p(x,y,z,\omega)=\sum_{n=0}^{N-1}\psi_n(x,y,z)a_n(\omega)=\mathbf{\Psi}^T\mathbf{a}, \tag{1}$$

$$v_{p1}(x,y,\omega)=\sum_{m=1}^{M}\phi_m(x,y)b_{p1m}(\omega)=\mathbf{\Phi}^T\mathbf{b_{p1}}, \tag{2}$$

and

$$v_{p2}(x,y,\omega)=\sum_{m=1}^{M}\phi_m(x,y)b_{p2m}(\omega)=\mathbf{\Phi}^T\mathbf{b_{p2}}, \tag{3}$$

where the N-length column vectors[11] $\mathbf{\Psi}$ and $\mathbf{a}$ consist of the array of uncoupled acoustic mode shape functions $\psi_n(x,y,z)$ and the complex amplitude of the acoustic pressure modes $a_n(\omega)$, respectively. Similarly, the M-length column vectors[12] $\mathbf{\Phi}$, $\mathbf{b_{p1}}$, and $\mathbf{b_{p2}}$ consist of the array of uncoupled vibration mode shape functions $\phi_m(x,y)$ and the complex amplitude of the vibration velocity modes $b_{p1m}(\omega)$ and $b_{p2m}(\omega)$, respectively, in which it is assumed that both panels have the same boundary conditions and hence mode shapes.

Following the approach of Kim and Brennan,[10] we can extend the expressions for the amplitude of the uncoupled acoustic modes and structural modes to a double-panelled partition by considering all the modal forces applied to each panel; also the modal velocity of each panel applied to the enclosed volume. The amplitudes of the acoustic modes and the amplitudes of the structural modes on panel 1 and panel 2 can be written, respectively, as follows:

$$\mathbf{a}=\mathbf{Z_a}(\mathbf{C_1}\mathbf{b_{p1}}+\mathbf{C_2}\mathbf{b_{p2}}), \tag{4}$$

$$\mathbf{b_{p1}}=\mathbf{Y_{p1}}(\mathbf{g_p}-\mathbf{p_{c1}}-\mathbf{C_1}^T\mathbf{a}), \tag{5}$$

and

$$\mathbf{b_{p2}}=\mathbf{Y_{p2}}(-\mathbf{p_{c2}}+\mathbf{C_2}^T\mathbf{a}), \tag{6}$$

where $\mathbf{Z_a}=(\rho c^2/V)\mathbf{A}(\omega)$. In the following analysis, the subscript i refers to panel 1 or panel 2. ρ is the density of air, c is the speed of sound in air, V is the volume of the enclosure, the matrix $\mathbf{A}(\omega)$ is a $(N\times N)$ diagonal matrix in which each diagonal term $(n\times n)$ consists of the acoustic resonance of the nth acoustic mode, given by

$$A_n(\omega)=\frac{j\omega}{\omega_n^2-\omega^2+j2\xi_n\omega_n\omega}, \tag{7}$$

in which ω_n and ξ_n are, respectively, the natural frequency and damping ratio of the nth acoustic mode and it has been assumed that the acoustic modes are normalized, such that $(1/V)\int_V \psi_n^2=1$. $\mathbf{C_i}$ is the structural-acoustic mode shape coupling matrix $(N\times M)$ in which each element (C_{inm}) is given by

$$C_{inm}=\int_{S_{pi}} \psi_n \phi_m \, ds, \tag{8}$$

where S_{pi} is the area of panel i. The superscript T refers to transpose. $\mathbf{Y_{pi}}$ is an $(M\times M)$ diagonal matrix in which each diagonal term (m,m) can be written by

$$Y_{pim}=\frac{1}{\rho_s h_i S_{pi}} B_{im}(\omega), \tag{9}$$

where ρ_s is the density of the plate material, h_i is the thickness, and B_{im} is the structural resonance of the mth structural mode of panel i which has a similar form to Eq. (7). The M-length column vector $\mathbf{g_p}$ is the generalized modal vector due to the primary excitation in which each term consists of the coupling between a structural mode and the primary plane wave excitation.[3] It should be noted that the effect of pressure generated in the external fluid by the motion of the panels has been assumed to be negligible compared with the effect of the internal pressure in the cavity. The M-length column vector $\mathbf{p_{ci}}$ is the structural force vector (i.e., due to control forces) which will be determined in the following section. The minus sign in Eqs. (5) and (6) is because of the sign convention used. Substituting Eqs. (5) and (6) into Eq. (4), we get

$$\mathbf{a}=[\mathbf{I}+\mathbf{Z_a}(\mathbf{C_1Y_{p1}C_1^T}-\mathbf{C_2Y_{p2}C_2^T})]^{-1}$$
$$\mathbf{Z_a}[\mathbf{C_1Y_{p1}}(\mathbf{g_p}-\mathbf{p_{c1}})-\mathbf{C_2Y_{p2}p_{c2}}]. \tag{10}$$

Substituting Eq. (10) into Eqs. (5) and (6) and the results into Eqs. (1), (2), and (3), we can get fully coupled structural-acoustic responses.

C. Cancellation of volume velocity with a single control actuator

The cancellation of the volume velocity of the radiating plate will be used as a strategy for the active control of sound power transmission. The net complex volume velocity Q_i of panel i is simply the sum of the complex velocities at each elemental position multiplied by the elemental area, and can be written in terms of a velocity vector,[3] $\mathbf{v_i}$, of length d:

$$Q_i=\mathbf{q_i v_i}, \tag{11}$$

where $\mathbf{q_i}$ is a d-length row vector in which every element is equal to the elemental area. If we define the total volume velocity of the surface as a sum of contributions from the primary and control sources, we have

$$Q_i=\mathbf{q_i v_{pi}}+\mathbf{q_i v_{ci}}, \tag{12}$$

where $\mathbf{v_{pi}}$ is the velocity of each element due to the primary source and $\mathbf{v_{ci}}$ is the velocity due to the control sources. We can define $\mathbf{v_{ci}}$ as being a combination of the velocity due to a unit force, $\mathbf{v_{ci-f}}$, times a force of complex amplitude F_{ci}. Therefore, Eq. (12) can be written as

$$Q_i=\mathbf{q_i v_{pi}}+\mathbf{q_i}F_{ci}\mathbf{v_{ci-f}}. \tag{13}$$

We can calculate the force F_{ci} which is required to cancel the volume velocity by setting Q_i in Eq. (13) equal to zero:

$$F_{ci}=\frac{\mathbf{q_i v_{pi}}}{\mathbf{q_i v_{ci-f}}}. \tag{14}$$

If a point control force is applied on panel i, each element (P_{cim}) in the modal vector $\mathbf{p_{ci}}$ in Eq. (10) for a simply supported panel can be written as[11]

$$P_{cim}=\frac{4F_{ci}}{l_x l_y}\sin\left(\frac{m_1\pi x_{ci}}{l_x}\right)\sin\left(\frac{m_2\pi y_{ci}}{l_y}\right), \tag{15}$$

where l_x and l_y are the dimensions of the panels in the x and y directions (the dimensions of the two panels are assumed the same), m_1 and m_2 are the structural mode number in the x and y directions (the structural mode numbers of the two panels are assumed the same), and (x_{ci},y_{ci}) is the location of the control force.

If instead a uniform-force actuator is applied on panel i, each element (P_{cim}) in the force term $(\mathbf{p_{ci}})$ in Eq. (10) for a simply supported panel can be written as[10]

$$P_{cim}=\int_0^{l_x}\int_0^{l_y}\frac{4F_{ci}}{l_x l_y}\sin\left(\frac{m_1\pi x}{l_x}\right)\sin\left(\frac{m_2\pi y}{l_y}\right)dx\,dy. \tag{16}$$

Substituting Eq. (15) or (16) into Eqs. (10), (5), and (6) and the results into Eqs. (1), (2), and (3), we can get fully coupled structural-acoustic responses due to a point force or a uniform-force actuator, respectively.

D. Transmission of sound power

Many of the results quoted in the following sections will be expressed in terms of power transmission ratio. This is defined as the sound power radiated by panel 2 divided by the sound power incident on panel 1 if the panel were rigid. The power incident on panel 1 if it is rigid is[3]

$$W^{in}=|P|^2 l_x l_y \cos\theta/2\rho c, \tag{17}$$

where P is the incident pressure on panel 1 (Fig. 1). The sound radiation by panel 2 is (see the example for a single panel[3])

$$W^r=\mathbf{v_2}^H\mathbf{R}\mathbf{v_2}, \tag{18}$$

where $\mathbf{v_2}=\mathbf{v_{p2}}+F_{c2}\mathbf{v_{c2-f}}$ is the d-length vector of elemental velocities due to both primary and control source excitations, H is the Hermitian transpose (complex conjugate transpose), and $\mathbf{R}$ is a $d\times d$ matrix giving the real part of the acoustic transfer impedance between each pair of elemental areas of

TABLE I. Structural resonance of panel 1 ($h_1=1$ mm). Note: 1,2...,6 in the first column are the mode numbers in the x-direction and 1,2,...,6 in the first row are the mode numbers in the y direction.

Natural frequency (Hz)	1	2	3	4	5	6
1	44	126	262	453	698	998
2	95	177	313	504	749	1049
3	180	262	398	589	834	1134
4	299	381	517	708	953	1253
5	452	534	670	861	1106	1406
6	639	720	857	1048	1293	1593

panel 2. The sound transmission ratio (T) can then be written as

$$T=W^r/W^{in}. \tag{19}$$

E. Radiation modes

As the matrix $\mathbf{R}$ is real, symmetric, and positive definite, it has an eigenvector-eigenvalue decomposition $\mathbf{R}=\mathbf{Q}\mathbf{\Lambda}\mathbf{Q}^T$, where $\mathbf{Q}$ is a real and unitary matrix of orthogonal eigenvectors and $\mathbf{\Lambda}$ is a diagonal matrix of eigenvalues $\lambda_j (j=1,...,d)$ which are all positive real numbers. Equation (18) can be modified to give

$$W^r=\mathbf{v_2}^H\mathbf{Q}\mathbf{\Lambda}\mathbf{Q}^T\mathbf{v_2}. \tag{20}$$

Therefore, we can express the radiated power as a sum of radiation mode amplitudes $\mathbf{y}$. The d-length vector $\mathbf{y}$ of radiation mode amplitudes will be given by $\mathbf{y}=\mathbf{Q}^T\mathbf{v_2}$. Each radiation mode is a weighted sum of the element velocities $\mathbf{v_2}$. The radiation mode shapes are given by the eigenvectors in $\mathbf{Q}$. We can then rewrite Eq. (20) as

$$W^r=\mathbf{y}^H\mathbf{\Lambda}\mathbf{y}=\sum_{j=1}^{d}\lambda_j|y_j|^2. \tag{21}$$

Equation (21) shows that radiation modes radiate sound independently.

II. NUMERICAL RESULTS

A. Natural resonance and response

The numerical results presented here have been calculated for aluminium panels with Young's modulus $E=71$ GPa, structural density $\rho_s=2720$ kg/m^3, Poisson's ratio $\nu=0.33$, and structural damping ratio $\xi_s=0.002$. Each panel has dimensions $l_x=380$ mm and $l_y=300$ mm, the thickness of panel 1 $h_1=1$ mm, the thickness of panel 2 $h_2=1.1$ mm, and the distance between the double panels $l_z=100$ mm. The panel 1 is excited by a plane wave incident at $\theta=45°$ and $\phi=45°$ (with the exception of Sec. II D). The enclosure is with density of air $\rho=1.21$ kg/m^3 and speed of sound $c=343$ m/s (with the exception of Sec. II C), and modal damping ratio of air $\xi_n=0.01$. The structural modes up to $(m_1=m_2=6)$, the acoustical modes up to $(n_1=n_2=2,\ n_3=1)$, and the number of the elemental radiators $(d\times d=9\times 9)$ are assumed for the calculations in this paper, although the results are not substantially changed if many more modes are also included in the calculation. In Sec. II C, results are given for various gases which have different values ρ and c, altering the coupling between the plates. In Sec. II D, results are given for various incident waves and a diffuse incident sound field.

The results presented in this paper represent the control possible using a feedforward control system with a perfectly correlated reference signal.

The uncoupled structural natural frequencies of panel 1 and panel 2 are shown in Table I and Table II, respectively,

TABLE II. Structural resonance of panel 2 ($h_2=1.1$ mm).

Natural frequency (Hz)	1	2	3	4	5	6
1	48	138	288	498	768	1098
2	104	194	344	554	824	1154
3	198	288	438	648	918	1248
4	329	419	569	779	1049	1379
5	497	587	737	947	1217	1547
6	703	793	943	1153	1422	1752

TABLE III. Acoustical resonance in the enclosure.

Mode number in the enclosure	Natural frequency (Hz)
(0,0,0)	0
(1,0,0)	451
(0,1,0)	571
(1,1,0)	728
(2,0,0)	902
(2,1,0)	1068
(0,2,0)	1143
(1,2,0)	1229
(2,2,0)	1456
(0,0,1)	1715
(1,0,1)	1773
(0,1,1)	1807
(1,1,1)	1863
(2,0,1)	1938
(2,1,1)	2020
(0,2,1)	2061
(1,2,1)	2110
(2,2,1)	2250

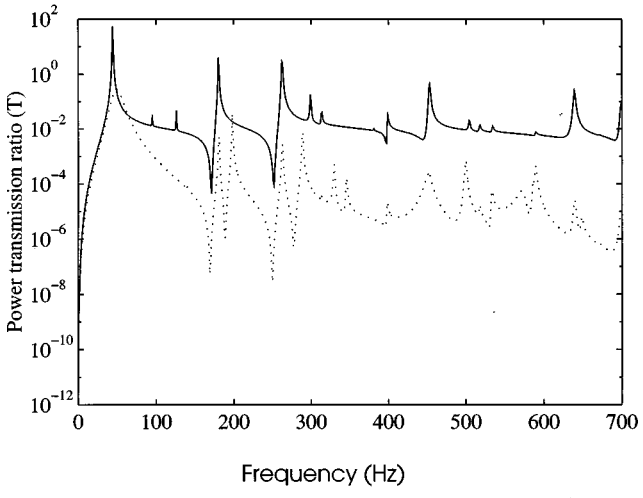

FIG. 3. Uncontrolled power transmission ratios for both a single panel and double panel partition. ——— Single panel; ····· double panel partition.

and the uncoupled acoustical natural frequencies of the enclosure are shown in Table III. Comparing these three tables, it can be seen that at frequency below 700 Hz (the case considered here) there are many more structural modes than acoustical modes.

Figure 3 presents the uncontrolled power transmission ratio for both a single panel (panel 1 only) and double panel partitions for the same incident plane wave excitation. The power transmission ratio (T) is defined to be the ratio of the power radiated by the plate to the power incident on a rigid panel [Eq. (19)]. In certain circumstances the vibration of the panel can cause the power absorbed by the baffled panel from the incident acoustic wave to be greater than that incident on a rigid surface, and if most of this power is transmitted through the structure then T can be numerically greater than unity, even though energy is conserved.

As expected, there is an overall improvement in power transmission loss from the introduction of the second-panel, particularly at high frequencies. However, the double panel partition has a relatively poor sound insulation at some low frequencies, due to effective coupling of the wall structural modes and acoustical modes in the sound field between them. The sound transmission loss is worst at the mass-air-mass resonance of the partition (49 Hz).

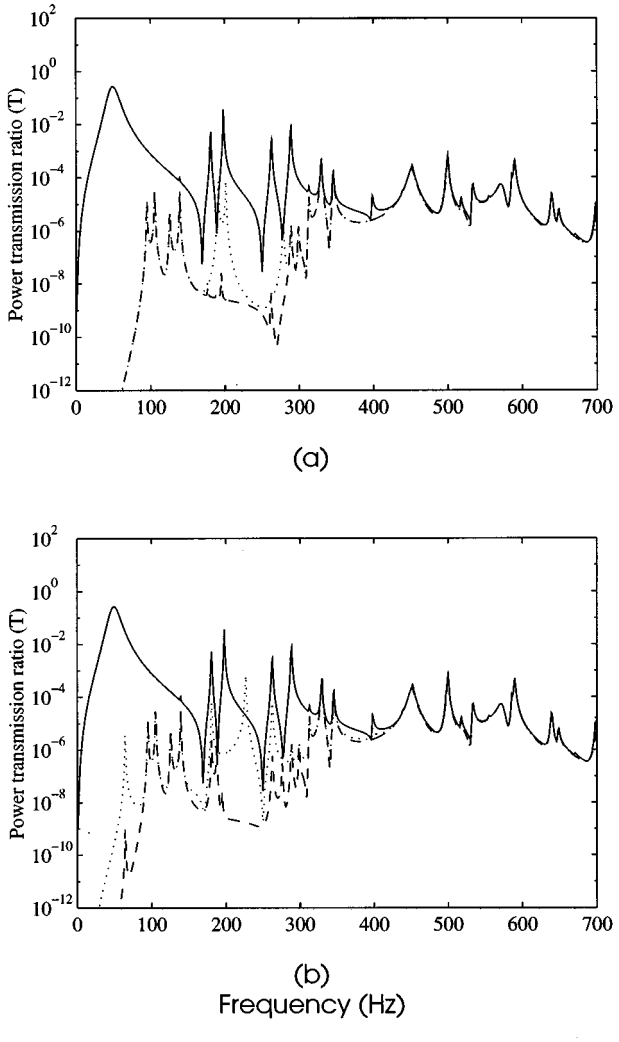

FIG. 4. Power transmission ratios of the double panel partition, for both without and with control by driving a structural actuator on either panel to cancel volume velocity. ——— Without control; ····· using a central point force; ---------- using a uniform-force actuator.

B. Cancellation of volume velocity with a point force or a uniform-force actuator

Figure 4(a) shows the power transmission ratio when the volume velocity of the radiating panel (panel 2) is cancelled using an actuator applied to panel 1. Even when a single point force is used, the control is effective over a range of frequencies up to 350 Hz. At around 200 Hz the control with a point force is poor due to excitation of high-order modes on panel 1 (control spillover). However, if a uniform-force actuator is used, the spillover problem disappears.

In Fig. 4(b) the same secondary actuator is applied to panel 2. Here the result using a uniform-force actuator is little changed from the previous case when the control was applied to panel 1; however, the result of using a point force on panel 2 gives significantly worse results than on panel 1. This arises for two reasons:

(1) High-order modes of panel 2 are excited by the point force and contribute directly to radiation by high-order structural modes which are not cancelled by driving the plate volume velocity to zero. On the other hand, high-order modes on panel 1 are attenuated to some degree by the intervening cavity.
(2) There is some loss of control at 65 Hz which corresponds to the natural frequency of panel 1 (which is uncontrolled) on the compliance of the air in the cavity.

It can be concluded that good reductions of power transmission are achieved by driving a uniform-force actuator on either panel 1 or panel 2 to cancel the volume velocity on panel 2. The best results appear to be obtained by driving constant force on panel 1 to cancel volume velocity on panel 2.

C. Active control at high frequencies

Figure 4 shows that virtually no reduction in power transmission is achievable above 400 Hz for the plate configuration considered. This is in contrast with the corresponding result for a single panel having the same dimensions (given in Fig. 11 in the paper by Johnson and Elliott[3]) where reductions in radiated sound power approaching 10 dB were possible up to 600 Hz.

In order to explain the poor reduction in the high frequency range, radiated power by each radiation mode has been determined for both uncontrolled and controlled cases. Figure 5(a) shows the radiated power by the first eight radiation modes with no control. 0 dB represents the total power radiated equal to the sound power incident on panel 1. It can be seen that in the low frequency range virtually all the radiated power is due to the first radiation mode. However, in the frequency range above about 400 Hz, the power due to the second radiation mode is very high and exceeds that due to the first radiation mode at some points. Figure 5(b) shows the contribution of each radiation mode at 25 Hz both with

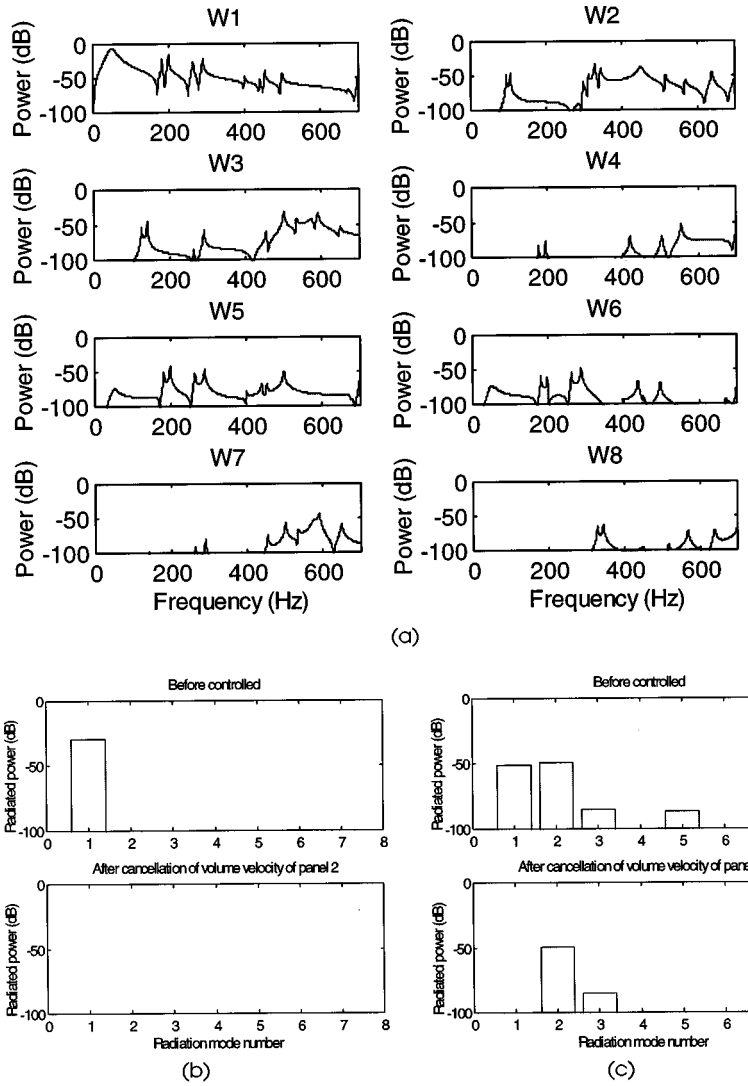

FIG. 5. Radiated power by the first eight radiation modes. (a) without control; (b) contribution of each radiation mode at 25 Hz both with and without control; (c) contribution of each radiation mode at 350 Hz both with and without control.

and without control using a uniform force on panel 2 to cancel volume velocity on panel 2. From Fig. 5(b), it can be seen that before control the first radiation mode dominates, as would be expected because the plate is very small compared with an acoustic wavelength. After control, all the radiated power is reduced as the volume velocity is driven to a low value. This results in the reduction of total power transmission at this frequency. Figure 5(c) shows the corresponding results at 350 Hz. At this frequency, before control there are two significantly excited radiation modes. After control, the power due to the first mode is reduced significantly. However, the power due to the second radiation mode remains unchanged, so the total radiated power stays almost the same as in the uncontrolled case. Thus it is a feature of the uncontrolled double panel system that at high frequencies much of the sound radiation is due to dipole-type motions of the radiating panel (which is not detected by a volume velocity sensor).

It is likely that the (1,0,0) and (0,1,0) acoustic modes of the cavity are responsible for this strong coupling to even modes of the radiating plate. In order to check this possibility, it is of interest to consider different gases in the enclosure between the two panels. To examine the effect of gas filling in the enclosure (outside of the enclosure is still air), Fig. 6 shows power transmission ratios for three types of gases. Comparing Fig. 6(a) and (b) with Fig. 4(b), it can be seen that oxygen [Fig. 6(a)] and CO_2 [Fig. 6(b)] produce similar attenuation as air [Fig. 4(b)] under each control condition. This is because the acoustic density and acoustic speed of these three gases are similar.

Figure 6(b) shows the results for helium which has high acoustic speed. It shows that good reductions of sound transmission are achieved using helium, especially at high frequencies. This is because that the high acoustic speed results in long acoustic wavelength. As a result, the (1,0,0) and (0,1,0) acoustic modes (see Table III) are shifted up out of the frequency range of interest, giving less coupling to the even modes of plate 2. Therefore, the first radiation mode dominates so reducing volume velocity means reducing sound power.

The above simulations show that the double panel construction provides passive attenuation of the first radiation mode above about 200 Hz. Comparing the radiated power from a single panel with no control (Fig. 3) the radiated power from a double panel partition is significantly reduced in the high frequency range by purely passive means. There-

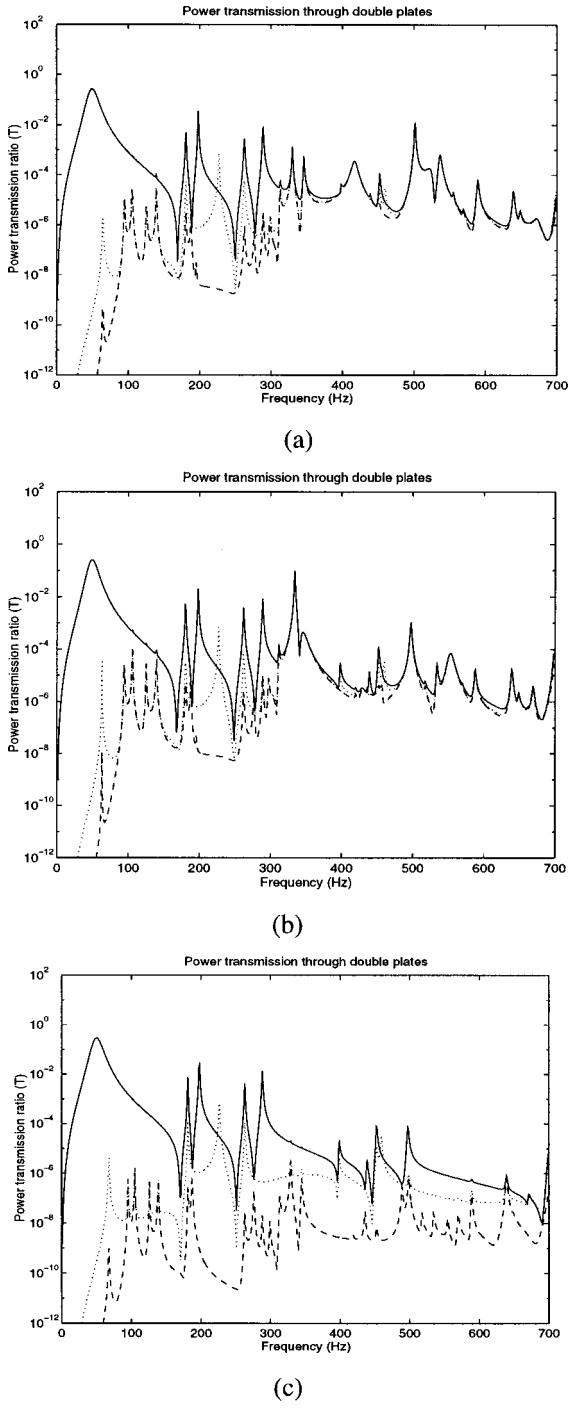

FIG. 6. Power transmission ratios of the double panel partition, for both without and with control by driving a structural actuator on panel 2 to cancel volume velocity on panel 2, and for various gases. (a) Oxygen ($\rho = 1.43$ kg/m^3, $c = 317.2$ m/s); (b) CO_2 ($\rho = 1.98$ kg/m^3, $c = 258$ m/s); (c) helium ($\rho = 0.18$ kg/m^3, $c = 971.9$ m/s). ——— Without control; ····· using a central point force; ---------- using a uniform-force actuator.

fore, in the high frequency range, there is no advantage in controlling only the volume velocity of a double panel partition; if further attenuation is required, the second and third radiation modes must be controlled as well.

D. Effect of direction of incoming plane wave

In the examples discussed so far, only a plane wave incident at $\theta = 45°$ and $\phi = 45°$ has been considered. To test the effect of the direction of the incident wave, Fig. 7(a)–(c) shows power transmission ratios for the incident wave at three individual directions. From these figures, it can be seen that reductions of power transmission ratios decrease as θ and ϕ increase simultaneously ($0 \leqslant \theta = \phi \leqslant \pi/4$), especially at high frequencies. The best reductions of power transmission are achieved when the normal incident wave [Fig. 7(a)] is used. This is because the normal incident wave does not excite any even modes of the plate, while an oblique incident plane wave excites all the plate modes in general. As a result, cancellation of volume velocity reduces the sound transmission to a very low value. Figure 7(d) shows the results for the incident plane waves from all the directions ($\theta = 0$, $\pi/S, \ldots, \pi/2$ and $\phi = 0, 2\pi/4, \ldots, 2\pi$) which provides a crude approximation to the diffuse field which would be presented in a reverberant room. The results are obtained by calculating the total velocity vector [$\mathbf{v_2}$ in Eq. (18)] due to all 25 incident waves above both without and with control. Figure 7(d) shows that at low frequencies (frequencies$\leqslant$400 Hz) the power transmission ratios are reduced significantly except for a few discrete points. At high frequencies (frequencies$>$400 Hz), virtually no reduction in power transmission is achievable. These results are similar to those shown in Fig. 4 for an incident plane wave at $\theta = 45°$ and $\phi = 45°$. Therefore, the analysis and results shown in Sec. II C (active control at high frequencies) can be applied to the case of sound transmission from a diffuse incident field.

Other numerical simulations have shown using a uniform-force actuator on either panel to cancel the volume velocity on panel 2 produces slight better results than using these actuators to cancel the volume velocity on panel 1. To save space, only the results of canceling the volume velocity on panel 2 are shown here.

III. CONCLUSIONS

The transmission of the sound power through a double panel partition can be reduced significantly by the cancellation of volume velocity on either panel at low frequencies (below 350 Hz). At high frequencies and in air, inefficiently radiating even modes of the radiating panel make a dominant contribution to the radiated sound power and so there is no advantage in controlling volume velocity alone in this frequency range. However, the transmission of the sound power from the double panel partition is significantly reduced at high frequencies by purely passive means. If further attenuation is required, two respects could be considered which are active structural control of the second and third radiation modes, or possibly the introduction of acoustic sources into the air-gap between the panels to control the (1,0,0) and (0,1,0) acoustic modes.

The use of a single point force actuator on either panel causes spillover at some frequencies. To achieve the best control, it is suggested that a uniform-force actuator should be driven on either panel to cancel the volume velocity on panel 2. These findings provided an opportunity to design an active control system for sound transmission through a double panel partition.

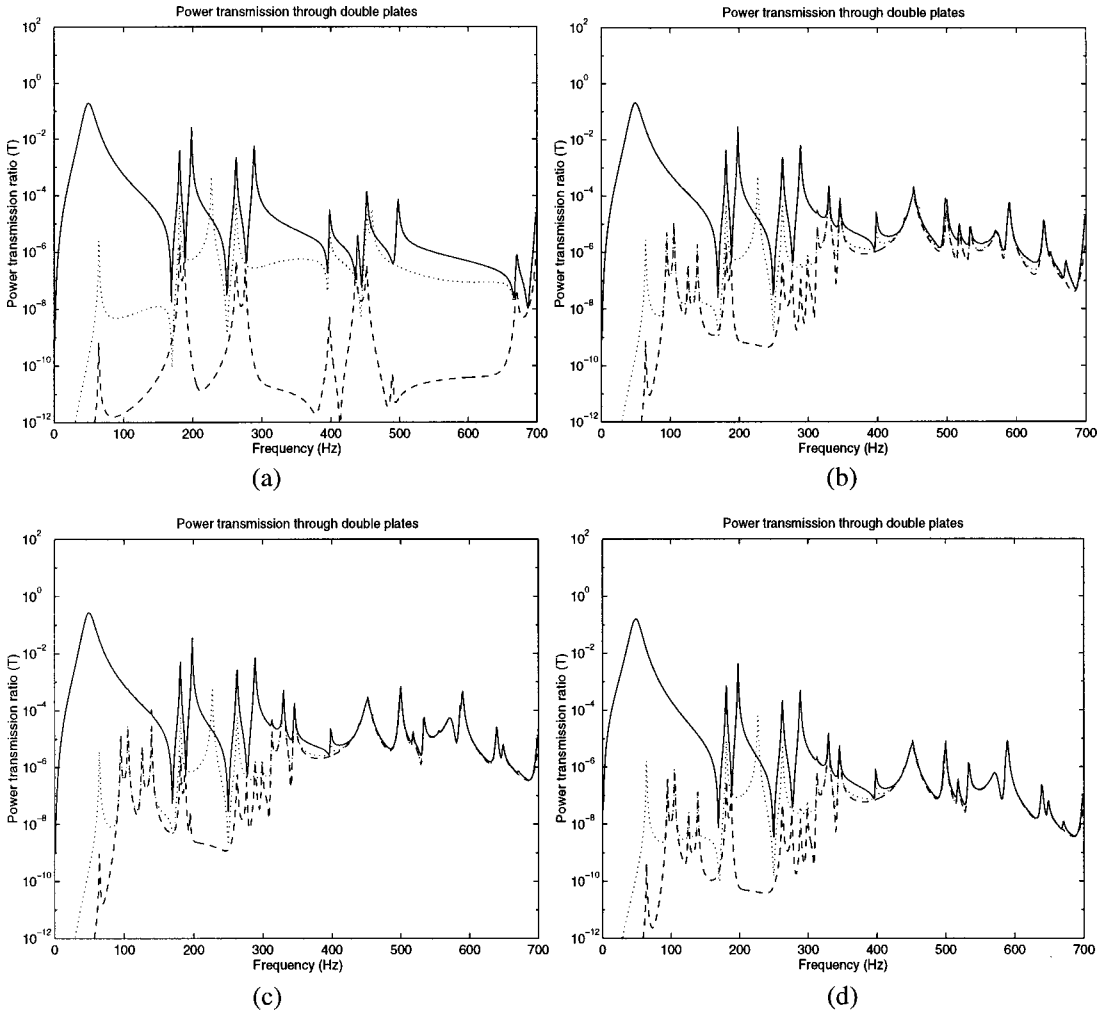

FIG. 7. Power transmission ratios of the double panel partition, for both without and with control by driving a structural actuator on panel 2 to cancel volume velocity on panel 2, and for various incident waves and a diffuse incident sound field. (a) $\theta=0$, $\phi=0$; (b) $\theta=\pi/8$, $\phi=\pi/8$; (c) $\theta=\pi/4$, $\phi=\pi/4$; (d) all the directions ($\theta=0,...,\pi/2$, $\phi=0,...,2\pi$). ——— Without control; ····· using a central point force; ---------- using a uniform-force actuator.

ACKNOWLEDGMENT

The authors are pleased to acknowledge that the work presented here was funded by the European Commission under the Framework IV program (Contract No. BRPR-CT96-0154).

[1] L. L. Beranek and G. A. Work, ''Sound transmission through multiple structures containing flexible blankets,'' J. Acoust. Soc. Am. **21**, 419–428 (1949).

[2] A. London, ''Transmission of reverberant sound through double walls,'' J. Acoust. Soc. Am. **22**, 270–279 (1950).

[3] M. E. Johnson and S. J. Elliott, ''Active control of sound radiation using volume velocity cancellation,'' J. Acoust. Soc. Am. **98**, 2174–2186 (1995).

[4] M. E. Johnson and S. J. Elliott, ''Volume velocity sensors for active control,'' Proc. Inst. Acoust. **15**, 411–420 (1993).

[5] J. P. Carneal and C. R. Fuller, ''Active structural acoustic control of noise transmission through double-panel systems,'' AIAA J. **33**, 618–623 (1995).

[6] P. Sas, C. Bao, F. Augusztinovicz, and W. Desmet, ''Active control of sound transmission through a double panel partition,'' J. Sound Vib. **180**, 609–625 (1995).

[7] P. De Fonseca, W. Desmet, A. Cops, J. Cooper, and P. Sas, ''Active control of the sound transmission through a double-glazing window,'' Inter-noise 96, Liverpool, UK, 1811–1816 (1996).

[8] J. Pan, C. H. Hansen, and D. A. Bies, ''Active control of noise transmission through a panel into a cavity: I. Analytical study,'' J. Acoust. Soc. Am. **87**, 2098–2108 (1990).

[9] J. Pan and C. Bao, ''Active attenuation of noise transmission through elastic partitions with high modal densities,'' Inter-noise 96, Liverpool, UK, 1055–1060 (1996).

[10] S. M. Kim and M. J. Brennan, ''Active Control of sound transmission into a rectangular enclosure using both structural and acoustic actuators,'' Sixth International Conference on Recent Advances in Structural Dynamics (1997).

[11] P. A. Nelson and S. J. Elliott, *Active Control of Sound* (Academic, London, 1992), pp. 312–313.

[12] C. R. Fuller, S. J. Elliott, and P. A. Nelson, *Active Control of Vibration* (Academic, London, 1996), pp. 240–251.

Scattering by an elastic sphere embedded in an elastic isotropic medium

Jean-Pierre Sessarego, Jean Sageloli, and Régine Guillermin
CNRS/Laboratoire de Mécanique et d'Acoustique, 31 ch. Joseph Aiguier, 13402, Marseille Cedex 20, France

H. Überall
Department of Physics, Catholic University of America, Washington, DC 20064

(Received 30 June 1997; accepted for publication 13 July 1998)

The scattering of acoustic waves by an elastic sphere embedded in an elastic isotropic medium is investigated. Expressions for the scattered waves are given in terms of monostatic and bistatic scattering cross sections. The resonances of the solid sphere were determined numerically in the individual normal mode amplitudes; dispersion curves for the phase velocities of the circumferential waves were also obtained. Computations and experimental results for an aluminum sphere embedded in Plexiglas were in good agreement. © *1998 Acoustical Society of America.* [S0001-4966(98)05610-0]

PACS numbers: 43.40.Ey, 43.20.Gp [CBB]

INTRODUCTION

The aim of this work is the understanding of the mechanisms of acoustic scattering by objects embedded in sediments. Nowadays, detection of objects buried in sediments[1] seems to be a challenging problem, even if the object is covered by only a thin layer of sediment. This problem arises frequently in the offshore domain, where there is a need for inspecting pipes or cables laying on the sea bottom. It also arises for military applications.

Buried objects are generally difficult to detect because of the influence of the interface between water and sediment and because of the complex nature of sediments. In this paper we made the simplifying assumption that the object is sufficiently far from the interface so that the interaction between the interface and the object is negligible. On the other hand, it is well known that, in most cases, since sediments can support shear waves, we used a modeling in which the embedding medium is elastic, homogeneous, and isotropic. Moreover, we used an elastic sphere to simulate the buried object.

Acoustic scattering by elastic spheres in water has been widely investigated[2–6] in the last 40 years. Here, our objective was to extend this work to the scattering by spheres embedded in an elastic medium. This problem has been investigated too,[7–10] but to our knowledge there have been no experimental results given in the literature. Our objective was to fill this gap and verify by tank experiments the validity of computational results. A physical interpretation of the observed phenomena is given in terms of circumferential waves.

Special attention has been paid to the resonance behavior of the target. It has been observed that if some of the resonances are connected to $P-P$ scattering (incident P-wave, received P wave), others are directly connected to $P-S$ scattering (incident P wave, received S wave). This could be very useful for an inverse problem strategy.

Our theoretical approach was from the point of view of elasticity theory (i.e., computation of stress tensor and displacements, inside and outside the object).

I. GENERAL SOLUTION TO THE PROBLEM

In an elastic medium the displacement vector $\mathbf{u}$ may be represented in terms of a scalar potential ϕ and a vector potential $\boldsymbol{\psi}$ by the equation

$$\mathbf{u}=\text{grad}\ \phi+\text{rot}\ \boldsymbol{\psi}, \tag{1}$$

where ϕ and $\boldsymbol{\psi}$ satisfy the equations

$$\nabla^2\phi+k_L^2\phi=0, \quad \nabla^2\psi+k_T^2\psi=0. \tag{2}$$

In a problem with spherical symmetry the vector potential ψ has only one component and can be written in the form: $\boldsymbol{\psi}=(0,0,\psi)$, where ψ is a scalar.

In these conditions the scalar potentials ϕ and ψ satisfy the two equations

$$\nabla_{r\theta}^2\phi+k_L^2\phi=0, \quad \nabla_{r\theta}^2\psi+k_T^2\psi=0, \tag{3}$$

where

$$k_L=\frac{\omega}{c_L}, \quad k_T=\frac{\omega}{c_T}, \qquad c_L=\sqrt{\frac{\lambda+2\mu}{\rho}}, \quad c_T=\sqrt{\frac{\mu}{\rho}}. \tag{4}$$

$\nabla_{r\theta}^2$ is the Laplacian operator in spherical coordinates. We denote by (1) the surrounding medium and by (2) the object medium (Fig. 1).

In medium (1) we suppose the incident field to be produced by a plane compressional wave

$$\phi_{\text{inc}}(x_2)=\phi_0 e^{i(k_{1L}x_2-\omega t)}, \tag{5}$$

where ϕ_0 is an arbitrary constant. This field can be expanded using spherical wave functions in the form:

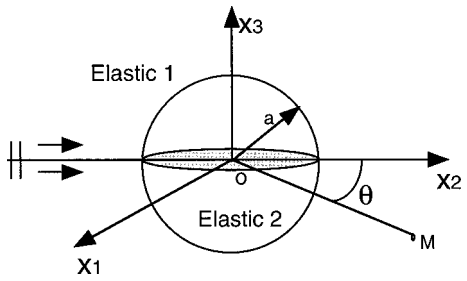

FIG. 1. Geometry of the problem.

$$\phi_{\text{inc}} = \phi_0 e^{-i\omega t} \sum_{n=0}^{\infty} i^n (2n+1) j_n(k_{1L} r) P_n(\cos\,\theta), \tag{6}$$

where $P_n(\cos\theta)$ are the Legendre polynomials and j_n the spherical Bessel functions of order n. θ is the angle between the direction of the incident wave and the direction of observation (Fig. 1).

Once the incident wave has been scattered by the object, two waves (a compressional wave and a shear wave) can be produced in medium (1), whose expressions are given by

$$\phi_1^{(s)} = \phi_0 e^{-i\omega t} \sum_{n=0}^{\infty} i^n (2n+1) b_n h_n^{(1)}(k_{1L} r) P_n(\cos\,\theta) \tag{7}$$

and

$$\psi_1^{(s)} = \phi_0 e^{-i\omega t} \sum_{n=0}^{\infty} i^n (2n+1) c_n h_n^{(1)}(k_{1T} r) P_n(\cos\,\theta). \tag{8}$$

In the medium inside the object, we have

$$\phi_2^{(s)} = \phi_0 e^{-i\omega t} \sum_{n=0}^{\infty} i^n (2n+1) d_n j_n(k_{2L} r) P_n(\cos\,\theta), \tag{9}$$

$$\psi_2^{(s)} = \phi_0 e^{-i\omega t} \sum_{n=0}^{\infty} i^n (2n+1) f_n j_n(k_{2T} r) P_n(\cos\,\theta). \tag{10}$$

The four coefficients b_n, c_n, d_n, f_n are obtained from the boundary conditions at the elastic–elastic interface which state that at $r=a$ contact is complete (continuity of displacements and stresses). In spherical coordinates the displacement components are

$$\begin{aligned} u_r &= \frac{\partial}{\partial r}\left[\phi + \frac{\partial}{\partial r}(r\psi)\right] + r k_T^2 \psi, \\ u_\theta &= \frac{1}{r}\frac{\partial}{\partial \theta}\left[\phi + \frac{\partial}{\partial r}(r\psi)\right], \\ u_\varphi &= 0, \end{aligned} \tag{11}$$

and the stress tensor components can be expressed as

$$\begin{aligned} \sigma_{rr} &= -\lambda k_L^2 \phi + 2\mu\left[\frac{\partial^2}{\partial r^2}\left(\phi + \frac{\partial}{\partial r}(r\psi)\right) + k_T^2 \frac{\partial}{\partial r}(r\psi)\right], \\ \sigma_{r\vartheta} &= \mu\left[2\frac{\partial}{\partial r}\left(\frac{1}{r}\frac{\partial}{\partial \vartheta}\left(\phi + \frac{\partial}{\partial r}(r\psi)\right)\right) + k_T^2 \frac{\partial \psi}{\partial \vartheta}\right], \end{aligned} \tag{12}$$

$$\begin{aligned} \sigma_{\vartheta\vartheta} &= -\lambda k_L^2 \phi + 2\mu\left[\left(\frac{1}{r}\frac{\partial}{\partial r} + \frac{1}{r^2}\frac{\partial^2}{\partial \vartheta^2}\right)\left(\phi + \frac{\partial}{\partial r}(r\psi)\right) + k_T^2 \psi\right], \\ \sigma_{\phi\phi} &= -\lambda k_L^2 \phi + 2\mu\left[\left(\frac{1}{r}\frac{\partial}{\partial r} + \frac{\cot g\,\vartheta}{r^2}\frac{\partial}{\partial \vartheta}\right) \times \left(\phi + \frac{\partial}{\partial r}(r\psi)\right) + k_T^2 \psi\right]. \end{aligned}$$

The four equations given by the boundary conditions when we express the continuity of displacements (u_r and u_θ) and stresses (σ_{rr} and $\sigma_{r\theta}$) determine the four coefficients given in Eqs. (7)–(10). This system of equations can be solved by Cramer's rule. The coefficients b_n and c_n of the scattered longitudinal wave and the scattered shear wave, respectively, are given by the ratios

$$b_n = \frac{\det D_n^{(1)}}{\det D_n^*} = \frac{\begin{bmatrix} A_1 & a_{12} & a_{13} & a_{14} \\ A_2 & a_{22} & a_{23} & a_{24} \\ A_3 & a_{32} & a_{33} & a_{34} \\ A_4 & a_{42} & a_{43} & a_{44} \end{bmatrix}}{\begin{bmatrix} a_{11} & a_{12} & a_{13} & a_{14} \\ a_{21} & a_{22} & a_{23} & a_{24} \\ a_{31} & a_{32} & a_{33} & a_{34} \\ a_{41} & a_{42} & a_{43} & a_{44} \end{bmatrix}}, \tag{13}$$

$$c_n = \frac{\det D_n^{(2)}}{\det D_n^*} = \frac{\begin{bmatrix} a_{11} & A_1 & a_{13} & a_{14} \\ a_{21} & A_2 & a_{23} & a_{24} \\ a_{31} & A_3 & a_{33} & a_{34} \\ a_{41} & A_4 & a_{43} & a_{44} \end{bmatrix}}{\begin{bmatrix} a_{11} & a_{12} & a_{13} & a_{14} \\ a_{21} & a_{22} & a_{23} & a_{24} \\ a_{31} & a_{32} & a_{33} & a_{34} \\ a_{41} & a_{42} & a_{43} & a_{44} \end{bmatrix}}. \tag{14}$$

(The elements a_{ij} and A_i of these determinants are given in the Appendix.)

Once coefficients b_n and c_n are known, the scattered field around the object can be obtained in a straightforward manner.

II. NUMERICAL RESULTS

The backscattered field $\phi_1^{(s)}$ corresponding to the longitudinal scattered waves has been computed for the case where the embedded object is a sphere made of aluminum and the surrounding medium is made of Plexiglas. Physical properties of these materials are listed in Table I. For the calculations we supposed that the media were not dissipative, and that no energy was lost by absorption.

Studies of acoustical scattering by objects in water showed[10] that the quantity of interest was the normalized bistatic scattering cross section, which is defined by

TABLE I. Physical characteristics of the materials used in the numerical tests and in the experiment.

Material	Density (kg/m^3)	Longitudinal wave velocity (m/s)	Shear wave velocity (m/s)
Aluminum	2761	6363	3161
Plexiglas	1180	2878	1394
Water	1000	1480	···

$$|F_\infty(\theta)|^2=\left(\frac{2}{a}\right)^2\frac{d\sigma}{d\theta}=\frac{4}{(ka)^2}\left|\sum_n f_n(\theta)\right|^2, \tag{15}$$

where $F_\infty(\theta)$ is the so-called form function,

$$f_n(\theta)=(2n+1)b_nP_n(\cos\theta), \tag{16}$$

ka is the dimensionless frequency, θ is the angle between the incident direction and the direction of observation, and σ is an energy flux.

For an object embedded in an elastic medium, the problem is more complex because two bistatic scattering cross sections can be defined, one for *P*-wave excitation and *P*-wave reception $[F_\infty^{pp}(\theta)]$ and the other for *P*-wave excitation and *S*-wave reception $[F_\infty^{ps}(\theta)]$.

According to Ying and Truel,[7] we can define a normalized differential scattering cross section as

$$\left(\frac{4}{a^2}\right)\frac{d\sigma}{d\theta}=\frac{4}{(k_{1L}a)^2}\left(\left|\sum_{n=0}^{\infty} f_n^{pp}(\theta)\right|^2+\frac{k_{1L}}{k_{1T}}\left|\sum_{n=1}^{\infty} f_n^{ps}(\theta)\right|^2\right), \tag{17}$$

with

$$f_n^{pp}(\theta)=(2n+1)b_nP_n(\cos\theta),$$

$$f_n^{ps}(\theta)=(2n+1)c_n\frac{\partial}{\partial\theta}P_n(\cos\theta).$$

Relation (17) can also be put into the form

$$|F_\infty(\theta)|^2=|F_\infty^{pp}(\theta)|^2+\frac{k_{1L}}{k_{1T}}|F_\infty^{ps}(\theta)|^2 \tag{18}$$

with

$$|F_\infty^{pp}(\theta)|^2=\frac{4}{(k_{1L}a)^2}\left|\sum_{n=0}^{\infty} f_n^{pp}(\theta)\right|^2, \tag{19}$$

$$|F_\infty^{ps}(\theta)|^2=\frac{4}{(k_{1L}a)^2}\left|\sum_{n=1}^{\infty} f_n^{ps}(\theta)\right|^2. \tag{20}$$

$F_\infty^{ss}(\theta)$ and $F_\infty^{sp}(\theta)$, which correspond to a shear wave excitation, could have been defined as well, but in our problem where only a *P*-wave excitation is used, these functions do not have to be calculated. If an *S*-wave excitation had been used, the expression of $F_\infty^{ss}(\theta)$ and $F_\infty^{sp}(\theta)$ would have been obtained using the same method as the one given in Ref. 8.

Figure 2 gives both the backscattering form function $F_\infty^{pp}(\pi)$ of the aluminum sphere embedded in Plexiglas [Fig. 2(a)] and the backscattering form function of the same sphere in water [Fig. 2(b)].

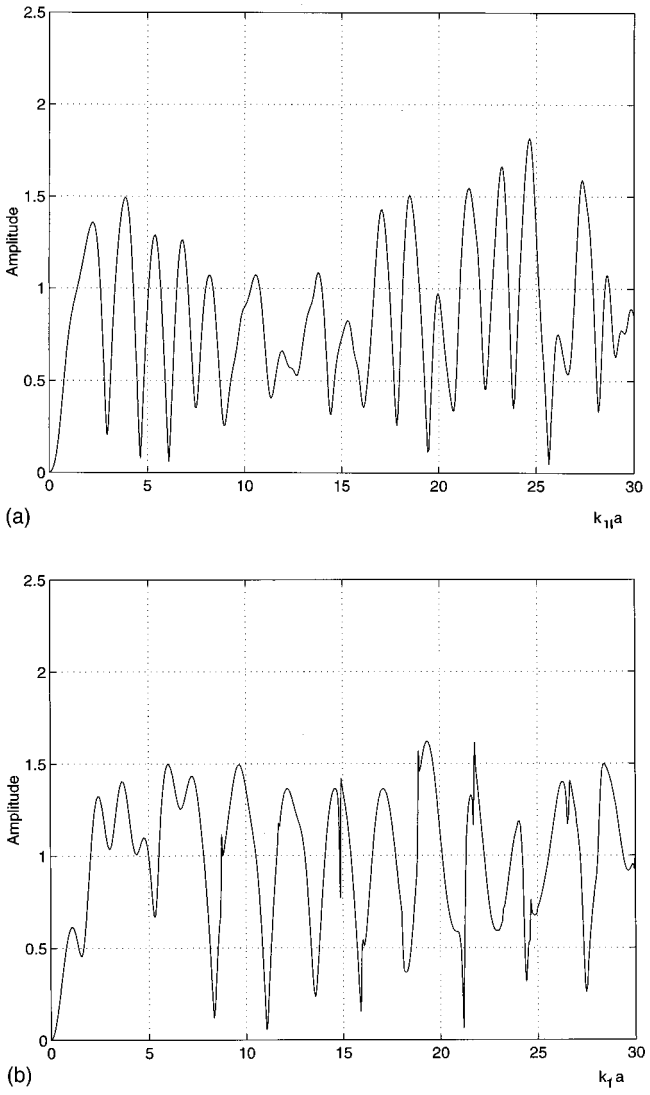

FIG. 2. Backscattering form function $F_\infty^{pp}(\pi)$ of an aluminum sphere, (a) embedded in Plexiglas ($k_{1L}=\omega/c_{1L}$, and c_{1L} is the longitudinal velocity in Plexiglas); (b) immersed in water ($k_1=\omega/c_1$, and c_1 is the longitudinal velocity in water).

The physical interpretation of these curves is not easy because the form function results from the sum of a series and cannot give the different contributions to the scattering separately. To get more information on the object response, we used a technique based on the resonance scattering theory[10–12] (RST), which has been widely developed for scattering by elastic objects in water. This theory establishes how to isolate the elastic behavior of a target from the total scattered field. Each partial wave is decomposed into two contributions—a background and the resonances. In general, the main difficulty comes from the choice of the background. For an elastic sphere in water, the rigid background (corresponding to the case of an impenetrable sphere with Neuman boundary conditions) gives acceptable results. For an aluminum sphere in Plexiglas the impedance ratio $\rho_2c_{2L}/\rho_1c_{1L}$ is greater than 1, but is not infinite (namely $\rho_2c_{2L}/\rho_1c_{1L}\approx 5$).

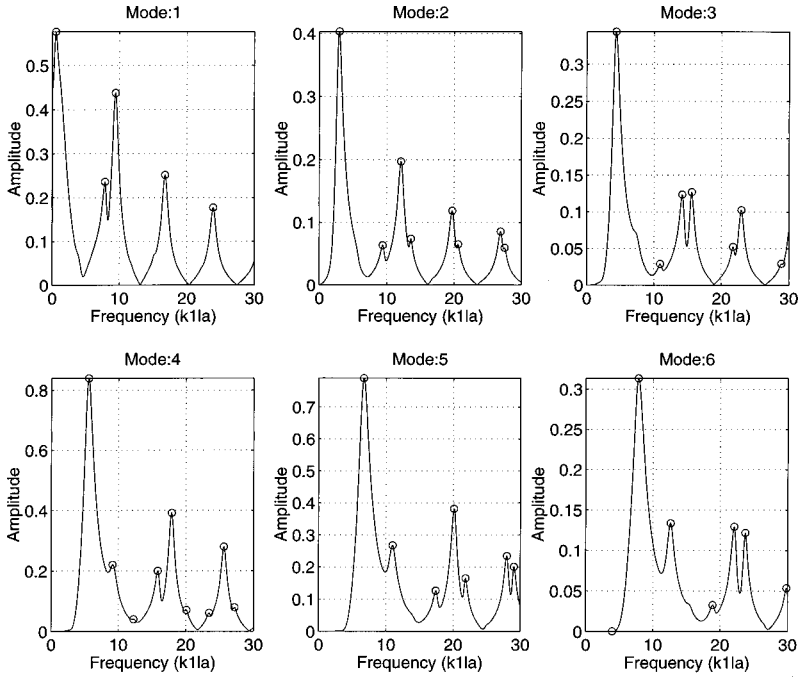

FIG. 3. Plot of function $|f_n^{pp}(\pi)-f_n^{pp(R)}(\pi)|$ for $n=1$ to 6.

We again chose a rigid background to isolate the elastic behavior of the target, but the validity of this choice is to be questioned; some *a posteriori* verifications are therefore given below. In this case the rigid background corresponds to the scattering by an impenetrable sphere embedded in an elastic material, but herein, two rigid backgrounds can be defined, one for *P*-wave excitation and *P*-wave reception and the other for *P*-wave excitation and *S*-wave reception.

We thus have

$$f_n^{pp(r)}(\theta)=(2n+1)u_nP_n(\cos\ \theta),$$
$$f_n^{ps(r)}(\theta)=(2n+1)\nu_n\frac{\partial}{\partial\theta}P_n(\cos\ \theta), \tag{21}$$

where u_n and v_n are determined from the boundary conditions, namely,

$$u_n=\frac{\det D_n^{(1)(r)}}{\det D_n^{*(r)}},\quad \nu_n=\frac{\det D_n^{(2)(r)}}{\det D_n^{*(r)}}. \tag{22}$$

For an impenetrable sphere embedded in Plexiglas we obtain

$$\det D_n^{1(r)}=\begin{vmatrix}A_4 & a_{42}\\ A_2 & a_{22}\end{vmatrix},\quad \det D_n^{2(r)}=\begin{vmatrix}a_{41} & A_4\\ a_{21} & A_2\end{vmatrix},$$
$$\det D_n^{*(r)}=\begin{vmatrix}a_{41} & a_{42}\\ a_{21} & a_{22}\end{vmatrix}. \tag{23}$$

The elements of the determinants are given in the Appendix. In Fig. 3, the function $|f_n^{pp}(\pi)-f_n^{pp(r)}(\pi)|$ has been plotted for $n=1$ to 6. Each peak on these curves gives the position of the resonances of the sphere.

To test the validity of RST we also computed the zeros of $\det D_n^*$, given in Eqs. (13) and (14). Zeros of this determinant have been computed[13] for integer values of the index n and for complex values of $k_{1L}a$. Results are given in Table II for modes 1 to 5 (in this table, only the real part of $k_{1L}a$ is given). The two methods were in good agreement, but some resonances are not recovered by the RST when only *P*-wave excitation and *P*-wave reception are used. However, computation of the function $|f_n^{ps}(\theta)-f_n^{ps(r)}(\theta)|$ giving the resonances of mode n for *P*-wave excitation and *S*-wave reception allows all the resonances missing in the previous case to be recovered. Figure 4 gives the shape of the function $|f_n^{ps}(\pi/4)-f_n^{ps(r)}(\pi/4)|$, plotted for $n=1$ to 6, and Table III compares resonances obtained by RST to resonances obtained by computation of the zeros of the determinant D_n^*. Agreement was very good, which proves that the rigid background was adequate to isolate the resonances of our target. Computation of $f_n^{ps}(\theta)$ and $f_n^{ps(r)}(\theta)$ has been done for the particular case $\theta=\pi/4$. If we come back to the definition of these functions, both $f_n^{ps}(\theta)$ and $f_n^{ps(r)}(\theta)$ have an angular variation given by the derivative of Legendre polynomial. These Legendre polynomial have many zeros according to the value of θ. The choice we made ($\theta=\pi/4$), is a good compromise which, for the integers n we have considered ($n=1,6$), gives no trivial values for both $f_n^{ps}(\theta)$ and $f_n^{ps(r)}(\theta)$.

RST can also be used to obtain Regge trajectories where, for a given mode number, resonance frequencies are plotted. On such representations, resonances appear to be aligned on trajectories called Regge trajectories. Each trajectory is associated with a circumferential wave involved in the scattering process. From these diagrams, and according to the relation given by Überall:[9]

$$\frac{(k_{1L}a)^*}{(n+\frac{1}{2})}=\frac{C_{ph}}{C_{1L}}, \tag{24}$$

the phase velocity of the different waves can be computed. In Eq. (24), n is the mode number, $(k_{1L}a)^*$ the value of $k_{1L}a$ at a resonance, and C_{1L} the *P*-wave velocity in the surrounding medium.

TABLE II. Comparison between resonances obtained by computation of the function $|f_n^{pp}(\pi)-f_n^{pp(R)}(\pi)|$ and exact determination of the zeros of the determinant $\det D_n^*$ for modes 1 to 5 (nr. means: not recovered).

	Mode									
	1		2		3		4		5	
ka	RST	Det	RST	Det	RST	Det	RST	Det	RST	Det
	7.86	7.99	9.38	9.50	4.34	4.28	5.57	5.50	nr.	4.46
	9.44	9.44	12.08	12.13	nr.	7.49	9.21	9.25	6.74	6.64
	nr.	11.80	13.55	13.52	10.91	10.99	12.26	12.49	10.97	10.95
	nr.	15.26	nr.	16.87	14.19	14.28	15.84	15.96	nr.	13.99
	16.77	16.79	19.71	19.73	15.60	15.55	17.89	17.88	17.42	17.49
	nr.	18.80	20.59	20.53	nr.	18.46	20.06	20.07	20.12	20.13
	nr.	22.26	nr.	23.90	21.76	21.83	23.40	23.44	21.82	21.78
	23.87	23.90	26.92	26.96	22.93	22.92	25.63	25.62	nr.	25.01
	nr.	25.75	27.51	27.48	nr.	25.52	27.21	27.17	27.98	28.05
	nr.	29.20	nr.	30.86	28.91	28.93	nr.	30.55	29.09	29.02
	30.91	30.94	34.02	34.07	30.15	30.16	33.02	33.02	nr.	32.14
	nr.	32.68	34.43	34.41	nr.	32.50	34.19	34.17	35.31	35.41
	nr.	36.13	nr.	37.80	nr.	35.93	nr.	37.55	36.25	36.23
	37.95	37.94	41.06	41.13	37.30	37.30	40.23	40.26	nr.	39.17
	nr.	39.60	41.41	41.33	nr.	39.45	41.17	41.14	42.46	42.53
	nr.	43.05	nr.	44.72	nr.	42.89	nr.	44.52	43.46	43.43
	44.93	44.93	48.09	48.14	44.40	44.38	47.39	47.41	nr.	46.15
	nr.	46.51	48.33	48.26	nr.	46.39	48.09	48.08	49.50	49.55

Figure 5 is a plot of Regge trajectories where the different waves circumnavigating the obstacle are labeled by numbers 1,2,3,... and Fig. 6(a) is a plot of the phase velocity. In this figure, the *y* axis represents the relative phase velocity C_{ph}/C_{t2} (phase velocity is normalized by the shear wave velocity of the wave propagating in the object). In order to test if a Stoneley wave can be generated at a plane interface between two materials such as aluminum and Plexiglas, the Stoneley wave dispersion equation was set up. In the case of Plexiglass and aluminum no root was obtained. It is well known[14] that Stoneley wave solutions do not always exist on the boundary of two elastic media. The existence of such a wave depends on the density and on the shear wave velocity ratios. We verified that according to the relations given in Ewing *et al.*,[14] Stoneley waves do not exist at the interface between Plexiglass and aluminum.

In the high frequency limit the curves approach an horizontal asymptotic value [Fig. 6(a)]. This asymptotic value cannot be the Stoneley wave velocity because it has been shown that this wave cannot exist; instead, this asymptotic value is close to the shear wave velocity in the aluminum material, as mentioned by Überall[9,10] for other types of ma

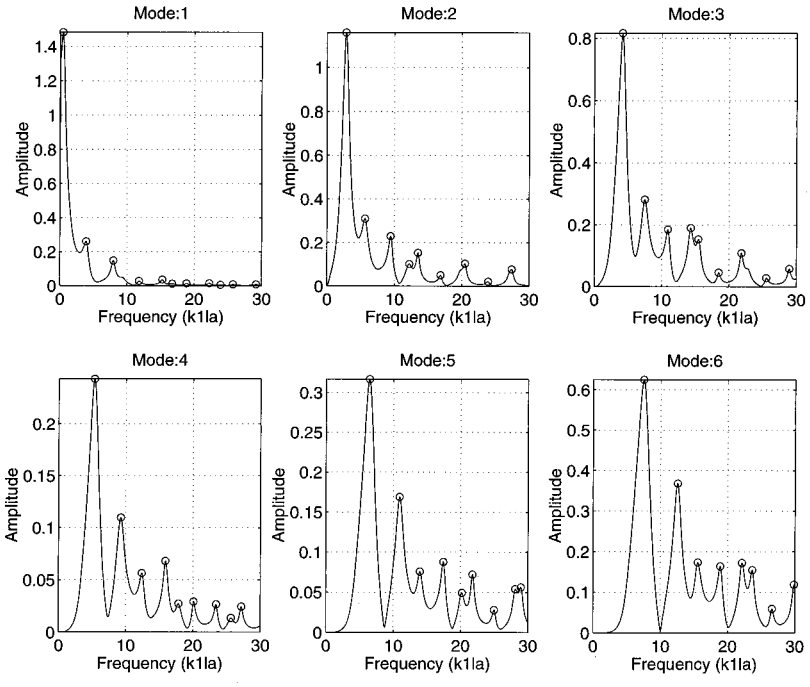

FIG. 4. Plot of function $|f_n^{ps}(\pi/4)-f_n^{ps(R)}(\pi/4)|$ for $n=1$ to 6.

TABLE III. Comparison between RST (*P*-wave excitation and *P*-wave reception combined with *P*-wave excitation and *S*-wave reception) and exact determination of the zeros of the determinant det D_n^* for modes 1 to 5.

	Mode									
	1		2		3		4		5	
ka	RST	Det	RST	Det	RST	Det	RST	Det	RST	Det
	7.86	7.99	9.38	9.50	4.34	4.28	5.57	5.50	----	4.46
	9.44	9.44	12.08	12.13	7.51	7.49	9.21	9.25	6.74	6.64
	11.85	11.80	13.55	13.52	10.91	10.99	12.26	12.49	10.97	10.95
	15.25	15.26	16.83	16.87	14.19	14.28	15.84	15.96	13.96	13.99
	16.77	16.79	19.71	19.73	15.60	15.55	17.89	17.88	17.42	17.49
	18.83	18.80	20.59	20.53	18.48	18.46	20.06	20.07	20.12	20.13
	22.23	22.26	23.87	23.90	21.76	21.83	23.40	23.44	21.82	21.78
	23.87	23.90	26.92	26.96	22.93	22.92	25.63	25.62	24.99	25.01
	25.75	25.75	27.51	27.48	25.57	25.52	27.21	27.17	27.98	28.05
	29.21	29.20	30.85	30.86	28.91	28.93	30.50	30.55	29.09	29.02
	30.91	30.94	34.02	34.07	30.15	30.16	33.02	33.02	32.14	32.14
	32.67	32.68	34.43	34.41	32.55	32.50	34.19	34.17	35.31	35.41
	36.13	36.13	37.77	37.80	35.89	35.93	37.54	37.55	36.25	36.23
	37.95	37.94	41.06	41.13	37.30	37.30	40.23	40.26	39.18	39.17
	39.59	39.60	41.41	41.33	39.47	39.45	41.17	41.14	42.46	42.53
	43.05	43.05	44.69	44.72	42.87	42.89	44.52	44.52	43.46	43.43
	44.93	44.93	48.09	48.14	44.40	44.38	47.39	47.41	46.16	46.15
	46.51	46.51	48.33	48.26	46.39	46.39	48.09	48.08	49.50	49.55

terials. Figure 6(b) gives the group velocity dispersion curves, where as above, in the high frequency limit the different curves tend to a horizontal asymptotic value corresponding to the shear wave velocity in the aluminum material.

III. EXPERIMENTS

To verify our computational results, we did an experiment with an aluminum sphere embedded in a parallelepipedic volume made of Plexiglas. The physical parameters of this sphere are given in Table I. Transducers were directly applied on the faces of this parallelepiped; perfect transmission was obtained by using glycol as a coupling fluid. A description of the experimental arrangement is given in Fig. 7.

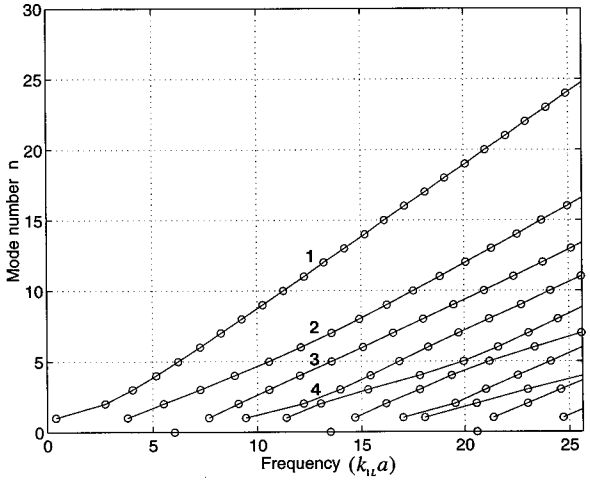

FIG. 5. Regge trajectories for the aluminum sphere in Plexiglas.

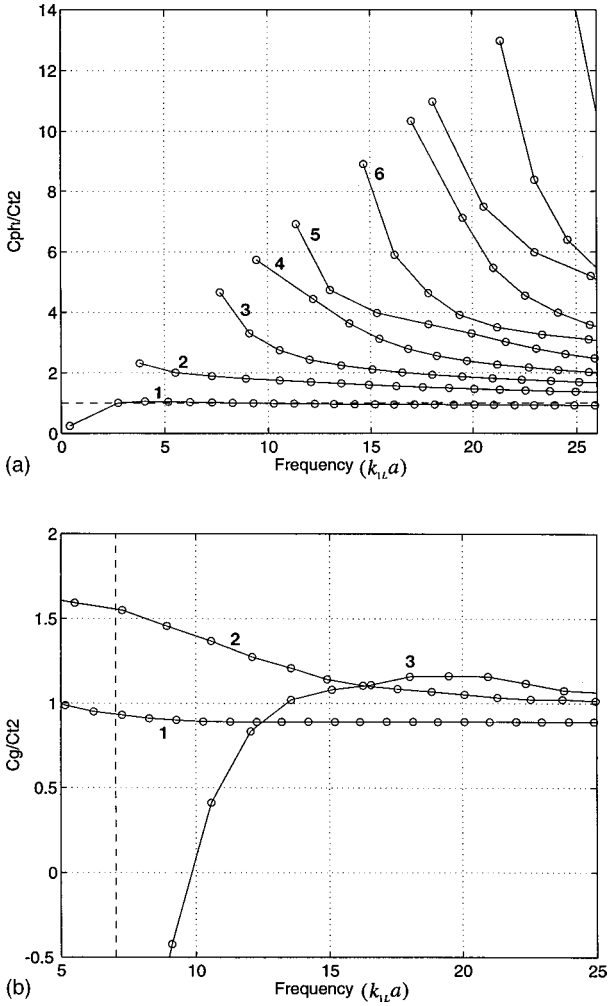

FIG. 6. (a) Phase velocity dispersion curves; (b) group velocity dispersion curves.

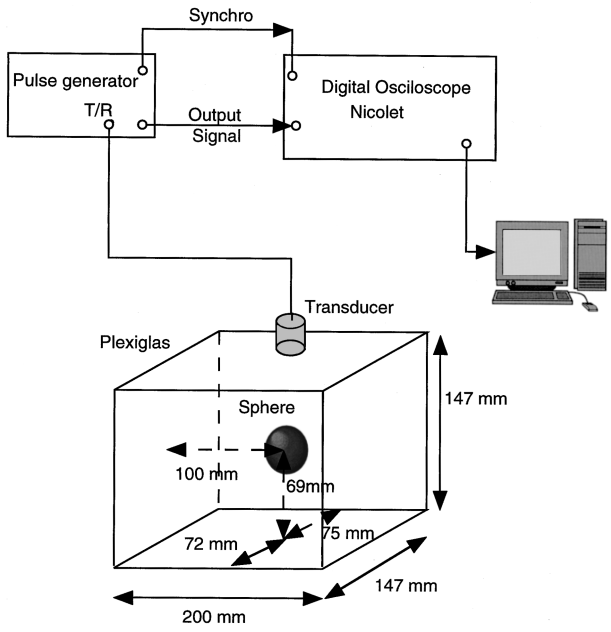

FIG. 7. Diagram of the experimental arrangement.

In the first experiment we applied a *P*-wave transducer (transducer *T*1) on the face of the parallelepiped in order to transmit a wide-band signal whose central frequency was around 250 kHz. Figure 8 gives an example of the spectrum of this signal (amplitude and phase). First, the echo of the target was received on the same transducer acting as a receiver (backscattering conditions); the spectrum and the received echo are given, respectively, in Fig. 9(a) and (b); Second, the echo of the target was received by another transducer at a 90° angle with the direction of insonification. The spectrum and the received echo are given in Fig. 9(c) and (d). On the time signals of Fig. 9(b) and (d) appear two main contributions: a specular echo and a surface wave. This statement will be verified in the following. The same experiment was done with another wide-band transducer (transducer *T*2) whose response is given in Fig. 10. For backscattering conditions, the spectrum and the echo are given, respectively, in Fig. 11(a) and (b) and, for bistatic conditions ($\theta=90°$), in Fig. 11(c) and (d).

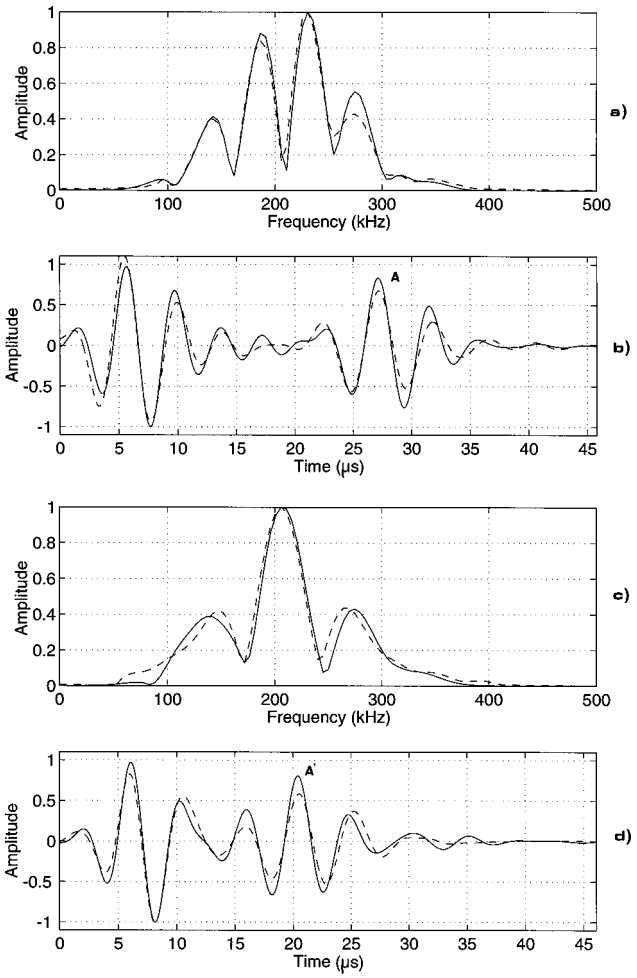

FIG. 9. Comparison between experiment and theory for *P*-wave excitation and *P*-wave reception; transducer T1 for emission and reception; (a) spectrum (backscattering conditions); (b) received echo (backscattering conditions); (c) spectrum ($\theta=90°$); (d) received echo ($\theta=90°$). ——— Experiment; ----- Theory.

Comparison between experiment and theory cannot be done immediately because in the experiment the transmitted

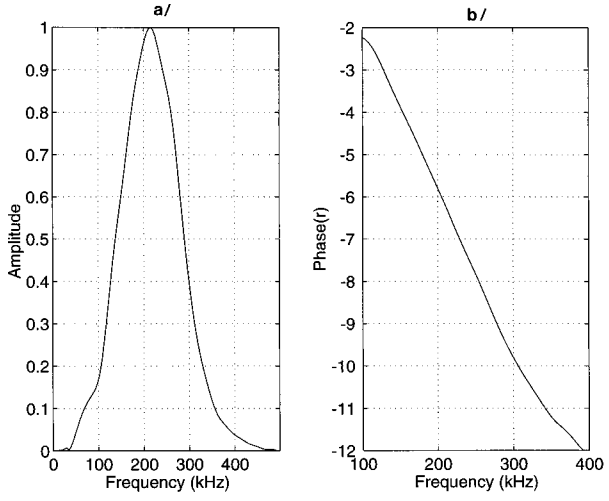

FIG. 8. Spectral characteristics of signals transmitted by transdducer T1 (250 kHz); (a) spectral amplitude; (b) phase.

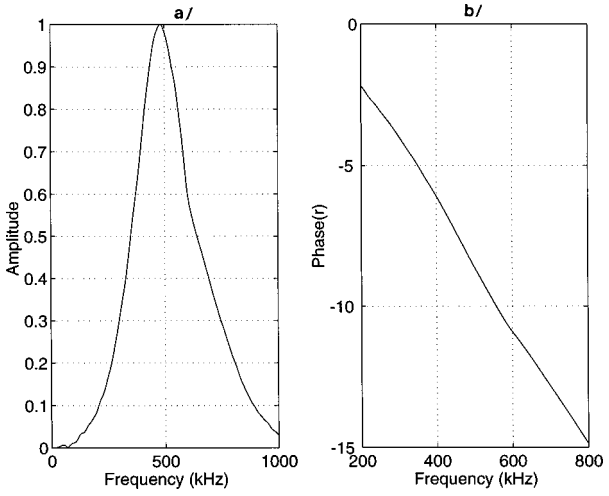

FIG. 10. Spectral characteristics of signals transmitted by transducer T2 (500 kHz); (a) spectral amplitude; (b) phase.

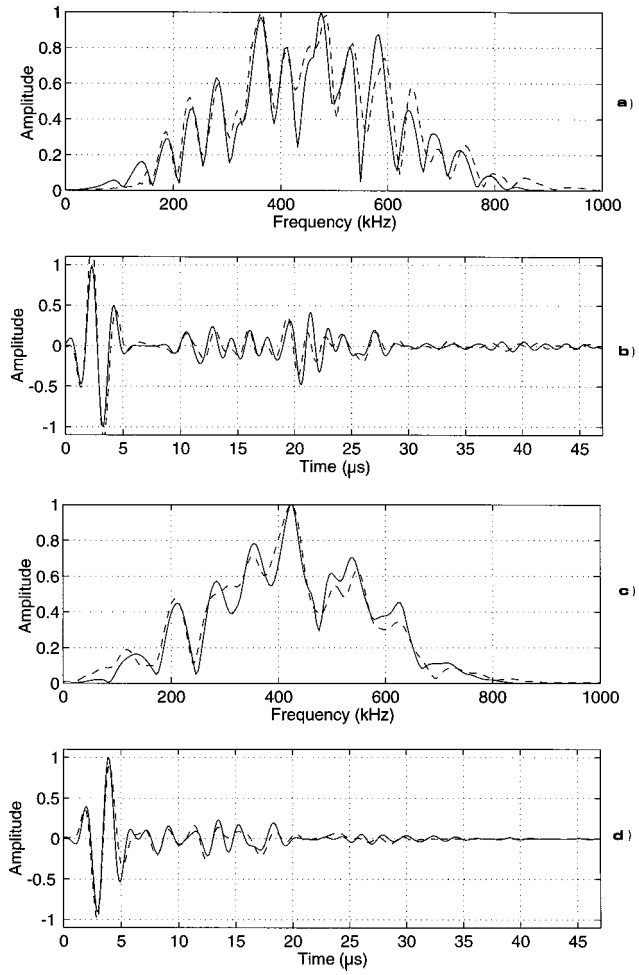

FIG. 11. Comparison between experiment and theory for *P*-wave excitation and *P*-wave reception; transducer T2 for emission and reception; (a) spectrum (backscattering conditions); (b) received echo; (c) spectrum ($\theta = 90°$); (d) received echo ($\theta = 90°$). ——— Experiment; ----- Theory.

and received signals are modified by the frequency response of the transducer—amplitude and phase [Fig. 8(a) gives the spectral amplitude of the signal]. Thus to compare experiment and theory, we used a weighting function simulating the frequency response of the transducer to modify the computed form function, both for monostatic and bistatic conditions (in the following, an easy implemented Kaiser–Bessel function was used). The result is given in Fig. 9(a) and (c) for the case of a weighting function simulating the effect of transducer $T1$ (central frequency: 250 kHz) and in Fig. 11(a) and (c) for the case of a weighting function simulating the effect of transducer $T2$ (central frequency: 500 kHz). Figures 9(b), (d), 11(b), and (d) give (respectively) the time signals obtained via a Fourier transform of Figs. 9(a), (c), 11(a), and (c). A detailed analysis of these figures shows that there is a good agreement between theory and experiment.

In the second experiment, we applied a *P*-wave transducer to the face of the parallelepiped in order to transmit, as before, a wide-band signal centered around 250 kHz. Reception was obtained by using a shear wave transducer (transducer $T3$) fixed to the parallelepiped by a shear wave coupling material; the two transducers formed an angle of 90°. Results are given in Fig. 12. As was mentioned before, experiment and theory cannot be compared immediately. First, the function $F_{\infty}^{ps}(\pi/2)$ was computed, and then a weighting function simulating the effect of transducer T_1 was applied. Results are given in Fig. 12; agreement between experiment and theory was also good. This proves again that our computational method is correct.

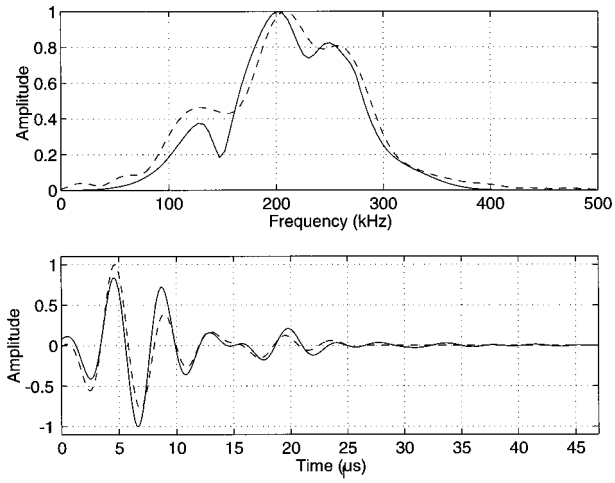

FIG. 12. Comparison between experiment and theory for *P*-wave excitation and *S*-wave reception; transducer T1 for emission and transducer T3 for reception; (a) spectrum for $\theta = 90°$; (b) received echo. ——— Experiment; ----- Theory.

Coming back to the signals in Fig. 9(b) and (d), there are two main arrivals. The first is a specular echo, and the second, labeled A in Fig. 9(b) and A′ in Fig. 9(d), could be expected to be related to a circumferential wave. If this is the case, by measuring the difference of the arrival times between echoes A and A′ (from the same origin), and the difference in propagation path, we can determine the velocity of the wave. The difference in propagation paths corresponds to 1/4 of the total circumference of the sphere ($\Delta l = 2\pi a/4$). From these measurements, the group velocity of the wave under study was obtained: $C_g = 2925$ m/s (or in a dimensionless form: $C_g/C_{t2} = 0.925$). This measured velocity is in an excellent agreement with the computed group velocity of the circumferential wave labeled 1 in Fig. 6(b). Note, from the analysis of Fig. 9(b) and (d), that this wave radiates a large part of its energy during its circumnavigation on the sphere interface, because no signal can be observed after the first surface wave arrival, labeled A in Fig. 9(b) and A′ in Fig. 9(d). Moreover, it seems that surface waves having higher group velocities cannot be detected.

In Fig. 11, corresponding to the high frequency case, the time signal has a more complicated structure; in fact, it seems that in this case, several interface waves are present, but they are so close that it is impossible to separate them to find their phase and group velocities.

IV. CONCLUSION

We have calculated the field scattered by an object of simple shape embedded in an isotropic elastic medium. The obtained results are in good agreement with experimental data, which confirms the validity of our theoretical model. As for an elastic sphere in water, surface waves circumnavi-

gating the object were evidenced, and resonances can still be observed even if some of them, corresponding to Rayleigh waves, have disappeared. Moreover, because of the mass effect of the embedding medium, the damping of the observed resonances is higher than for a sphere in water and they are not clearly observable in the form function. In the case of an elastic sphere embedded in an elastic medium, we have shown that some resonances can be detected by transmitting and receiving *P* waves, but others can be detected only when in addition a shear wave receiver is used. We have just proved that when using *P* waves only, part of the information coming back to the receiver is missing. This conclusion could be important for an identification strategy.

APPENDIX: ELEMENTS OF THE 4×4 DETERMINANT

The nondimensionalized elements of the determinant are as follows:

$$a_{11}=-\frac{\rho_1}{\rho_2}\left[\frac{\lambda_1 h_n^{(1)}(k_{1L}a)-2\mu_1 h_n''(k_{1L}a)}{\lambda_1+2\mu_1}\right],$$

$$a_{12}=2\frac{\rho_1}{\rho_2}\,n(n+1)(k_{1T}a)^{-2}[(k_{1T}a)h_n'(k_{1T}a) - h_n(k_{1T}a)],$$

$$a_{13}=[\lambda_2 j_n(k_{2L}a)-2\mu_2 j_n''(k_{2L}a)]\cdot\frac{1}{\lambda_2+2\mu_2},$$

$$a_{14}=-2n(n+1)(k_{2T}a)^{-2}[(k_{2T}a)j_n'(k_{2T}a) - j_n(k_{2T}a)],$$

$$A_1=\frac{\rho_1}{\rho_2}\left[\frac{\lambda_1 j_n^{(1)}(k_{1L}a)-2\mu_1 j_n''(k_{1L}a)}{\lambda_1+2\mu_1}\right],$$

$$a_{21}=-h_n^{(1)}(k_{1L}a),$$

$$a_{22}=-[h_n^{(1)}(k_{1T}a)+(k_{1T}a)h_n'(k_{1T}a)],$$

$$a_{23}=j_n(k_{2L}a),$$

$$a_{24}=[j_n(k_{2T}a)+(k_{2T}a)j_n'(k_{2T}a)],$$

$$A_2=j_n(k_{1L}a),$$

$$a_{31}=-2[(k_{1L}a)h_n'(k_{1L}a)-h_n(k_{1L}a)],$$

$$a_{32}=-[(k_{1T}a)^2 h_n''(k_{1T}a)+(n+2)(n-1)h_n^{(1)}(k_{1T}a)],$$

$$a_{33}=2[(k_{2L}a)j_n'(k_{2L}a)-j_n(k_{2L}a)]\,\frac{\mu_2}{\mu_1},$$

$$a_{34}=[(k_{2T}a)^2 j_n''(k_{2T}a)+(n+2)(n-1)j_n(k_{2T}a)]\,\frac{\mu_2}{\mu_1},$$

$$A_3=2[(k_{1L}a)j_n'(k_{1L}a)-j_n(k_{1L}a)],$$

$$a_{41}=-(k_{1L}a)h_n'(k_{1L}a),$$

$$a_{42}=-n(n+1)h_n^{(1)}(k_{1T}a),$$

$$a_{43}=(k_{2L}a)j_n'(k_{2L}a),$$

$$a_{44}=n(n+1)j_n(k_{2T}a),$$

$$A_4=(k_{1L}a)j_n'(k_{1L}a).$$

[1] R. Lim, J. L. Lopes, R. H. Hackman, and D. G. Todoroff, ''Scattering by objects buried in underwater sediments: Theory and experiment,'' J. Acoust. Soc. Am. **93**, 1762–1783 (1993).

[2] J. J. Faran, ''Sound scattering by solid cylinders and spheres,'' J. Acoust. Soc. Am. **23**, 405–418 (1951).

[3] R. Hickling, ''An analysis of echoes from a solid elastic sphere in water,'' J. Acoust. Soc. Am. **34**, 1582–1592 (1962).

[4] N. Gespa, *La diffusion acoustique par des cibles élastiques de forme géométrique simple: Théorie et expériences*, Préface de H. Überall (ceDOCar, Paris, 1986).

[5] R. R. Goodman and R. Stern, ''Reflection and transmission of sound by elastic spherical shells,'' J. Acoust. Soc. Am. **34**, 338–344 (1962).

[6] H. Überall, L. R. Dragonette, and L. Flax, ''Relation between creeping waves and normal modes of vibration of a curved body,'' J. Acoust. Soc. Am. **61**, 711–715 (1977).

[7] C. F. Ying and R. Truell, ''Scattering of a plane longitudinal wave by a spherical obstacle in an isotropically elastic solid,'' J. Appl. Phys. **25**, 1086–1097 (1956).

[8] N. G. Einspruch, E. J. Witterholt, and R. Truell, ''Scattering of a plane transverse wave by a spherical obstacle in an elastic medium,'' J. Appl. Phys. **31**, 806–818 (1960).

[9] L. Flax and H. Überall, ''Resonant scattering of elastic waves from spherical solid inclusions,'' J. Acoust. Soc. Am. **65**, 1432–1442 (1980).

[10] L. Flax, G. C. Gaunaurd, and H. Überall, ''Theory of resonance scattering,'' in *Physical Acoustics*, edited by W. P. Mason and R. N. Thurston (Academic, New York, 1981), Vol. 15, pp. 191–294.

[11] G. C. Gaunaurd and H. Überall, ''RST analysis of monostatic and bistatic acoustic echoes from an elastic sphere,'' J. Acoust. Soc. Am. **73**, 1–12 (1983).

[12] L. Flax, L. R. Dragonette, and H. Überall, ''Theory of elastic resonance excitation by sound scattering,'' J. Acoust. Soc. Am. **63**, 123–131 (1978).

[13] P. Cristini, ''Calcul des zéros d'une fonction analytique avec points de branchements,'' J. Phys. IV **4**, 869–872 (1994).

[14] W. M. Ewing, W. S. Jardetzky, and F. Press, *Elastic Waves in Layered Media*, International Series in the Earth Sciences (McGraw-Hill, New York, 1957), pp. 109–113.

Supersonic acoustic intensity on planar sources

Earl G. Williams
Physical Acoustics, Code 7137, Naval Research Laboratory, Washington, DC 20375-5350

(Received 9 February 1998; accepted for publication 16 July 1998)

The concept of supersonic acoustic intensity was developed in 1995 out of a need to locate the sources of radiation on an internally excited, submerged cylindrical shell. Supersonic intensity is obtained through signal processing of near-field holographic data to remove the subsonic part of the helical or plane wave spectrum, leaving only the radiating components. This eliminates the out-of-plane circulation of the acoustic intensity vector which results from evanescent waves. The resulting supersonic intensity on the surface is generally only positive, representing outgoing power flow from the surface. Since negative intensity regions of a vibrator are removed, sources of radiation are readily located on the surface of the vibrator. Since the earlier work concentrated on a cylindrical geometry, the theory is presented here for a planar geometry. In many ways the theory for the planar case is simpler and more straightforward. Numerical examples are given for simply supported, baffled plates. It is shown how the supersonic intensity reconstructions, and resulting location of radiating source regions are consistent with the popular theories of corner and edge mode radiation from plates. [S0001-4966(98)05810-X]

PACS numbers: 43.40.Rj, 43.30.Jx, 43.20.Ye [CBB]

INTRODUCTION

Identification of regions on a vibrating structure which radiate to the far field is critical in many areas of acoustics. Acoustic intensity measurement devices have been popular for this reason, and are often used to help identify regions of a structure which radiate to the far field, and to quantify the strength of these regions.[1] Wave bearing structures containing flat and curved plates may pose difficulties for source localization if the waves are subsonic (traveling slower than the speed of sound). This problem arises from the generation of adjacent positive and negative intensity regions on the structure which cancel almost completely in the process of radiation, making source identification difficult.

Supersonic intensity was introduced in 1995.[2] It resulted from the study of radiation from submerged cylindrical shells and the need to locate the radiating regions on the surface of these shells. Because the flexural waves, which dominate the vibration of thin shells underwater, are highly subsonic, the resulting acoustics power flow is circulatory, flowing out of the shell and back into the shell in adjacent regions. This circulation makes it difficult to locate regions which have a net (uncanceled) power flow to the far field. It was demonstrated from actual experiments on point-driven shells[2] that if the subsonic trace waves were filtered out, leaving only the supersonic trace waves on the surface of the shell, then the resulting supersonic intensity identified regions on the shell which radiate to the far field. This identification also yielded the source strength levels of these regions in watts per square centimeter. It was concluded in that paper that the extension to planar coordinates was straightforward, although the actual details were not discussed, nor any examples given. It would have been more informative to present the theory and results for the planar geometry first, since those results provide valuable insight to applications in other geometries. We hope to right that oversight in this paper.

The choice, perhaps confusing at first sight, of the term supersonic to describe this new quantity arises from the fact that only waves which have a trace velocity greater than the speed of sound are included. To an observer on the plane these included waves appear to travel faster than the speed of sound. Of course, their actual speed is sonic.

The outline of the paper is as follows. First we deal with the development of the theory, based on the plane wave spectrum. We note that the theory leads to a conservation of power which is exact for the planar geometry. That is, the sum total over the vibrating surface of all the supersonic sources adds up to the correct total power radiated to the far field. This was not the case for the cylindrical geometry due to the fact that helical waves, which are barely subsonic in the circumferential direction, do leak power to the far field. However, this leads to only small errors in the conservation of power which can be ignored.

Second we provide the supersonic intensity for a baffled point source. Understanding of the point source leads the way to interpretation of the results from more complicated vibrators. Finally, examples are given for the radiation from baffled, simply supported plates vibrating in a natural mode. It is shown that the sources localized by the supersonic intensity on the surface correspond to the predictions made by the classical theory of edge and corner mode radiation.[3–5]

I. THEORY FOR A PLANAR VIBRATOR

Consider a rectangular coordinate system with the plane of interest located at $z=0$, parallel to the (x,y) coordinate plane. This plane is coincident with the vibrator. The region $z>0$ is source free. The pressure in the half-space $z\geqslant 0$ can be uniquely represented by the angular spectrum:[6]

$$p(x,y,z)=\frac{1}{4\pi^2}\int\int_{-\infty}^{\infty}P(k_x,k_y)e^{ik_x x}e^{ik_y y}e^{ik_z z}\,dk_x\,dk_y, \tag{1}$$

where $P(k_x,k_y)$ is the complex amplitude of the plane waves in the decomposition and $e^{-i\omega t}$ is the suppressed time dependence. Equation (1) must satisfy the homogeneous Helmholtz equation in $z \geqslant 0$: $\nabla^2 p + k^2 p = 0$, where $k = \omega/c$, which leads to the important relationship

$$k_z = \sqrt{k^2 - (k_x^2 + k_y^2)}.$$

When $(k_x^2 + k_y^2) \leqslant k^2$, k_z is real and the plane wave extends to the far field without loss of amplitude. Since the trace speed of this wave in the (x,y) plane is faster than the speed of sound, we call this wave a supersonic plane wave. When $(k_x^2 + k_y^2) > k^2$, k_z is purely imaginary and the plane wave is an evanescent wave which decays exponentially from $z=0$ and does not reach the far field. The evanescent wave components of the plane wave spectrum are called subsonic waves since they travel at phase speeds less than the speed of sound.

At $z=0$ both the pressure and the normal velocity distributions in the plane can be given, respectively, by the inverse Fourier transforms:

$$p(x,y,0) = \frac{1}{4\pi^2} \int \int_{-\infty}^{\infty} P(k_x,k_y) e^{ik_x x} e^{ik_y y} \, dk_x \, dk_y, \tag{2}$$

and

$$\dot{w}(x,y,0) = \frac{1}{4\pi^2} \int \int_{-\infty}^{\infty} \dot{W}(k_x,k_y) e^{ik_x x} e^{ik_y y} \, dk_x \, dk_y, \tag{3}$$

where $P(k_x,k_y)$ and $\dot{W}(k_x,k_y)$ are the complex amplitudes of the plane wave decompositions of the pressure and normal velocity. Since Eqs. (2) and (3) are two-dimensional inverse Fourier transforms, the complex amplitudes are given by the corresponding forward transforms:

$$P(k_x,k_y) = \int \int_{-\infty}^{\infty} p(x,y,0) e^{-i(k_x x + k_y y)} \, dx \, dy, \tag{4}$$

and

$$\dot{W}(k_x,k_y) = \int \int_{-\infty}^{\infty} \dot{w}(x,y,0) e^{-i(k_x x + k_y y)} \, dx \, dy. \tag{5}$$

From Euler's equation for fluids, $i\rho c k \dot{w}(x,y,0) = [\partial p(x,y,0)/\partial z]$, $P(k_x,k_y)$ and $\dot{W}(k_x,k_y)$ are related by

$$P(k_x,k_y) = \frac{\rho c k}{k_z} \dot{W}(k_x,k_y). \tag{6}$$

We now construct the supersonic intensity out of the supersonic trace plane wave components of the pressure and normal velocity in the $z=0$ plane. Define the supersonic pressure $p^{(s)}$ and supersonic normal velocity $\dot{w}^{(s)}$ through

$$p^{(s)}(x,y,0) \equiv \frac{1}{4\pi^2} \int \int_{S_r} P(k_x,k_y) e^{ik_x x} e^{ik_y y} \, dk_x \, dk_y, \tag{7}$$

and

$$\dot{w}^{(s)}(x,y,0) = \frac{1}{4\pi^2} \int \int_{S_r} \dot{W}(k_x,k_y) e^{ik_x x} e^{ik_y y} \, dk_x \, dk_y, \tag{8}$$

where S_r is the area in the radiation circle, that is, the integration is over values of k_x and k_y such that $k_x^2 + k_y^2 \leqslant k^2$. The superscript s indicates a supersonic quantity. Thus $p^{(s)}$ and $\dot{w}^{(s)}$ are constructed by filtering out the evanescent (and nonradiating) plane wave components, keeping only the supersonic parts. The supersonic intensity (normal component) is defined in the same way as the actual normal intensity, except that supersonic pressure and velocity are used:

$$I^{(s)}(x,y,z) \equiv \tfrac{1}{2} \operatorname{Re}[p^{(s)}(x,y,z) \dot{w}^{(s)}(x,y,z)^*]. \tag{9}$$

Eliminating the subsonic plane wave components from the intensity eliminates the circulation of power flow which arises from the presence of subsonic and supersonic trace plane wave components near vibrating structures bearing subsonic flexural waves.

The credibility of the concept of supersonic intensity lies in the fact that power is conserved. That is, the total (real) power passing through a plane is identical to the supersonic power which passes through that plane. That is,

$$\int \int_{-\infty}^{\infty} I^{(s)}(x,y,z_0) dx \, dy = \int \int_{-\infty}^{\infty} \frac{1}{2} \operatorname{Re}[p(x,y,z_0) \dot{w}(x,y,z_0)] dx \, dy, \tag{10}$$

where p and $\dot{w}$ are the nonfiltered fields.

The proof Eq. (10) is quite simple. Expanding $p^{(s)}$ and $\dot{w}^{(s)}$ in their Fourier transforms, the left hand side becomes:

$$\Pi^{(s)}(\omega) = \frac{1}{2} \operatorname{Re}\left[\frac{1}{(4\pi^2)^2} \int \int_{-\infty}^{\infty} \int \int_{S_r} \int \int_{S_r'} P(k_x,k_y,z) \times \dot{W}(k_x',k_y',z)^* e^{i(k_x - k_x')x} e^{i(k_y - k_y')y} \times dx \, dy \, dk_x \, dk_y \, dk_x' \, dk_y' \right]. \tag{11}$$

The right hand side of Eq. (10), which is the actual power $\Pi(\omega)$, is given by the same expression with S_r and S_r' replaced with infinity. In Eq. (11) the integral over x and y yields $4\pi^2 \delta(k_x - k_x') \delta(k_y - k_y')$ so that the right hand side collapses to a double integral. Using Eq. (6) to eliminate $P(k_x,k_y,z)$ yields

$$\Pi^{(s)}(\omega) = \frac{\rho_0 c k}{8\pi^2} \int \int_{S_r} \operatorname{Re}\left[\frac{1}{k_z}\right] |\dot{W}(k_x,k_y,z)|^2 \, dk_x \, dk_y.$$

Since $\Pi(\omega)$ is also given by Eq. (11) with S_r replaced with infinity, and since k_z is purely imaginary outside S_r, giving $\operatorname{Re}[1/k_z] = 0$, then $\Pi^{(s)}(\omega) = \Pi(\omega)$ and power is conserved. To show the utility of the supersonic intensity for source localization, we study the supersonic intensity for a point source.

A. Supersonic intensity for a point source

The concept of supersonic intensity, and its ability to locate the regions on a structure which radiate to the far field, is clarified by considering a point source in an infinite baffle. Let the source plane be located at $z=0$. The source has a strength given by its volume flow, Q_h. The velocity in the source plane is

$$\dot{w}(x,y,0)=Q_h\delta(x)\,\delta(y),$$

since $Q_h \equiv \int\int \dot{w}(x,y)dx\,dy$. Thus from Eq. (5) $\dot{W}(k_x,k_y)=Q_h$.

Following the definition, Eq. (8), the supersonic surface velocity is

$$\dot{w}^{(s)}(x,y)=\frac{Q_h}{4\pi^2}\int\int_{S_r} e^{ik_x x}e^{ik_y y}\,dk_x\,dk_y.$$

Transforming from rectangular to polar coordinates, (ρ,ϕ), and using

$$\oint d\phi' e^{-ik_\rho \rho\cos(\phi-\phi')}=2\pi J_0(k_\rho\rho), \tag{12}$$

yields

$$\dot{w}^{(s)}(x,y)=\frac{Q_h}{2\pi}\int_0^k J_0(k_\rho\rho)k_\rho\,dk_\rho=\frac{kQ_h}{2\pi}\frac{J_1(k\rho)}{\rho}, \tag{13}$$

where we have used the definite integral relation $\int J_0(x)x\,dx=xJ_1(x)$.

Similarly, following the definition of the supersonic pressure, Eq. (7), in the plane $z=0$, along with Eq. (6) we have

$$p^{(s)}(x,y)=\frac{1}{4\pi^2}\int\int_{S_r} P(k_x,k_y)e^{ik_x x}e^{ik_y y}\,dk_x\,dk_y$$

$$=\frac{\rho_0 ck}{4\pi^2}\int\int_{S_r}\frac{\dot{W}(k_x,k_y)}{k_z}e^{ik_x x}e^{ik_y y}\,dk_x\,dk_y.$$

Again transforming to polar coordinates and using Eq. (12) we find

$$p^{(s)}(x,y)=\frac{Q_h\rho_0 ck}{2\pi}\int_0^k\frac{J_0(k_\rho\rho)}{\sqrt{k^2-k_\rho^2}}k_\rho\,dk_\rho.$$

The integral is given in tables,[7] and integrates to a sinc function:

$$\int_0^1\frac{J_0(\gamma x)}{\sqrt{1-x^2}}x\,dx=\frac{\sin\gamma}{\gamma},$$

so that finally

$$p^{(s)}(x,y)=\frac{Q_h\rho_0 ck^2}{2\pi}\frac{\sin k\rho}{k\rho}. \tag{14}$$

The supersonic pressure follows a sinc function. Inserting these results into Eq. (9) the normal component of the supersonic intensity is

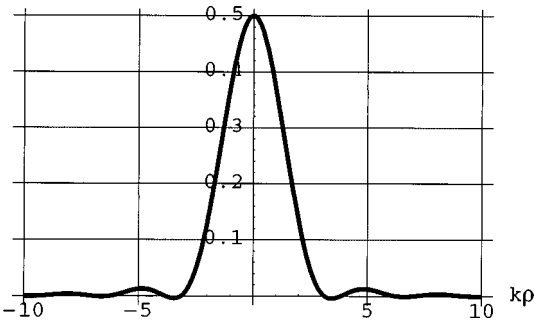

FIG. 1. Plot of $[J_1(k\rho)\sin(k\rho)/(k\rho)^2]$. Note the regions of negative intensity are almost nonexistent, and the side lobes are small.

$$I^{(s)}(x,y)=\frac{Q_h^2\rho_0 ck^2}{8\pi^2}\frac{J_1(k\rho)\sin(k\rho)}{\rho^2}. \tag{15}$$

$I^{(s)}(x,y)$ is a purely real quantity. Although true for the point source, the reactive part of the supersonic intensity is generally not zero for more complicated vibrators such as the baffled plates discussed later in this paper.

Figure 1 is a plot of $f(k\rho)=[J_1(k\rho)\sin(k\rho)/(k\rho)^2]$, the spatial variation of the supersonic intensity over the plane. Note that there are almost no negative values and the side lobes are small in level. To clearly show the side lobe levels, Fig. 2 provides a decibel plot of $f(k\rho)$. The first major side lobe is 16 dB below the main peak. The small sidelobes in between the larger ones are the small regions where the intensity is negative.

Figure 1 clarifies the assertion that the supersonic intensity localizes the sources on a vibrating structure, identifying the location of the ''hot spots'' which radiate to the far field. Even though $I^{(s)}$ spreads over the whole plane, it is mainly confined to an area $\lambda/2$ on either side of the actual location of the point source. The side lobes which appear as rings around the actual source are an inevitable result of the sharp k-space cutoff at $k_\rho=k$.

To demonstrate that the total power is conserved for the point source we calculate the integral of $I^{(s)}$ over the source plane:

$$\Pi^{(s)}=\frac{Q_h^2\rho_0 ck^2}{8\pi^2}\int_0^\infty\int_0^{2\pi}\frac{J_1(k\rho)\sin(k\rho)}{\rho^2}\rho\,d\rho\,d\phi$$

$$=\frac{Q_h^2\rho_0 ck^2}{4\pi},$$

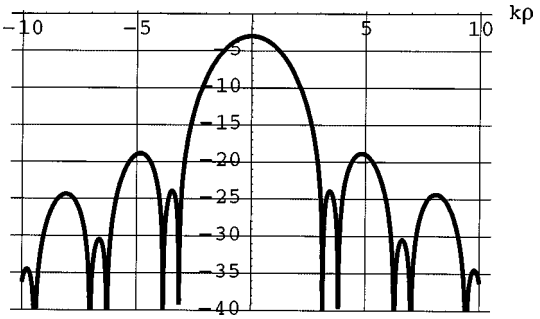

FIG. 2. $10\,\mathrm{Log}_{10}(|f(k\rho)|)$ to show more clearly the sidelobe levels.

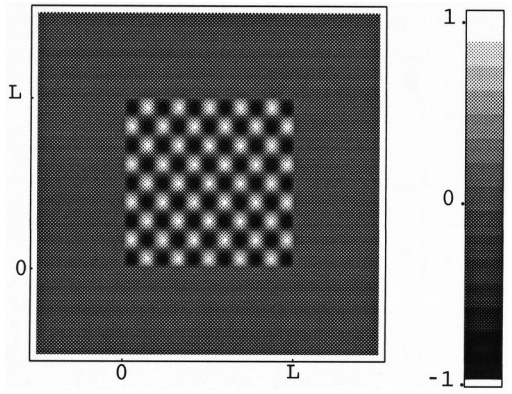

FIG. 3. Mode shape shown in gray scale for a $m=11$, $n=9$ mode of a square plate, $\Psi_{mn}(x,y)=\sin(11\pi x/L_x)\sin(9\pi y/L_y)$ and $L=L_x=L_y=2$. The baffle is shown surrounding the plate.

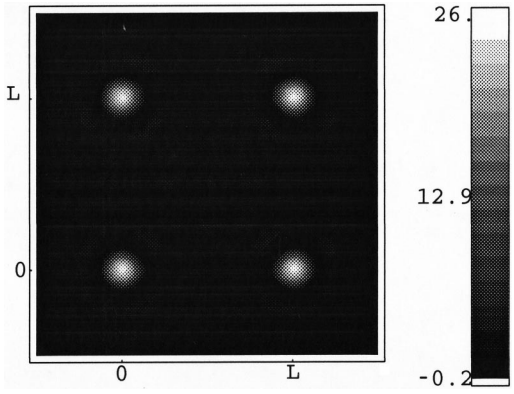

FIG. 4. Supersonic intensity for the normal mode shown in Fig. 3. The intensity is almost always positive, with black near zero level. White indicates maximum level and locates the regions of the plate which radiate to the far field. Very faint sidelobe rings circle the main source regions, consistent with Fig. 2.

where we have used the relation[7] $\int_0^\infty [J_1(k\rho)\sin(k\rho)/\rho]d\rho=1$. This is identical to the power radiated from a point source with volume flow Q_h in an infinite baffle. Thus power is conserved.

B. Supersonic intensity of a mode of a simply supported plate

Consider a normal mode of a baffled square plate. If the plate is simply supported then the mode shape is given by $\sin(m\pi x/L_x)\sin(n\pi y/L_y)$. For this example we choose $m=11$, $n=9$, and $L_x=L_y=2$. Figure 3 shows the mode shape with unit amplitude using a density plot, with white and black indicating maximum positive and negative values, respectively. Part of the infinite baffle is shown surrounding the plate. The legend indicates the corresponding levels of vibration. We assume that this mode is forced into excitation at a frequency such that $kL=6$. The actual eigenfrequency for this mode is irrelevant since we are not considering any of the elastic details and we are interested only in the radiation. The plate is excited below coincidence, since $kL<k_nL_y<k_mL_x$ ($k_mL_x=11\pi$, $k_nL_y=9\pi$), and according to the radiation classification this mode is a corner mode.[5] The wavelength in the fluid is larger than the structural wavelengths in either direction.

The pressure on the plate and baffle was computed using Rayleigh's integral.[8] Fourier transforms of the resulting surface pressure and specified velocity (mode shape) provided the integrands for Eqs. (7) and (8). These equations were then used to compute the supersonic intensity, using Eq. (9) for this mode. The result is shown in Fig. 4. The gray scale indicates that the intensity is dominantly positive throughout. One of the beneficial aspects of the supersonic intensity is the removal of the circulating power flow, evidenced by the disappearance of negative intensity regions. Furthermore, the largest levels of intensity (w/m^2), shown in white, localize the regions on the plate which radiate to the far field. Clearly the sources are the four corner regions of the plate, perfectly consistent with the theory of mode classification.[5] In this theory this mode is classified as a corner mode, as explained in Fig. 5. This figure illustrates the corner mode concept, given a (3,4) mode, in which the volume flow from adjacent regions of opposite sign cancel leaving four corners of uncanceled volume flow. The cross-hatched regions shown in the figure illustrate two of the canceled regions.

The power radiated by each identified source is easily obtained by computing the surface integral over the source region so that, if S_s is the area identified as a source, then the power radiated from the identified source is

$$\Pi^s=\int\int_{S_s} I^{(s)}(x,y)dx\,dy.$$

One can divide the plate into radiating regions and the conservation of power, Eq. (10), guarantees that the sum of all the powers from all the regions must equal the actual power radiated.

As a point of comparison, Fig. 6 is a plot of the actual normal intensity on the surface, which includes all the subsonic waves. We note that it is positive and negative throughout, which arises from the beating as subsonic and supersonic plane waves and indicates circulation of the intensity vector. The actual source regions which radiate to the far field are not as evident now, although the four corners are still the strongest source regions. Four large negative sinks (black) of energy are located close to the corners. Compared with the supersonic intensity the maximum intensity level is about 20 times higher. The supersonic intensity provides a special kind of spatial average, averaging the negative and

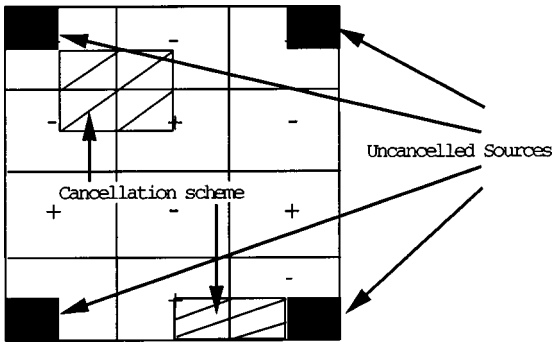

FIG. 5. Example of a corner mode for a simply supported, $m=3$, $n=4$ mode. The cross-hatched regions illustrate the cancelation of adjacent cells which occurs over the whole plate except at the four corners, where there are no adjacent regions to cancel. The four corners form a corner mode.[4]

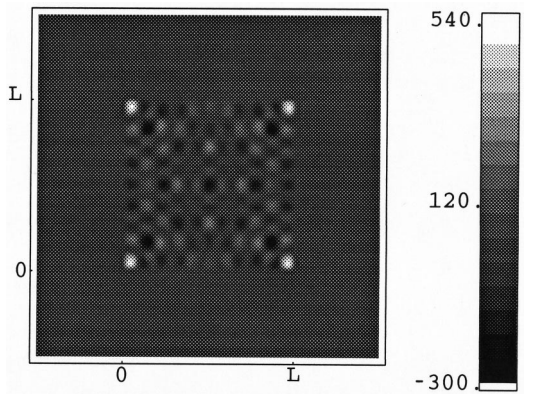

FIG. 6. Normal acoustic intensity including subsonic waves for the normal mode shown in Fig. 3. The intensity is both positive (white) and negative (black), indicating circulating intensity flow. The source regions are not as clearly identifiable as they were for the supersonic intensity.

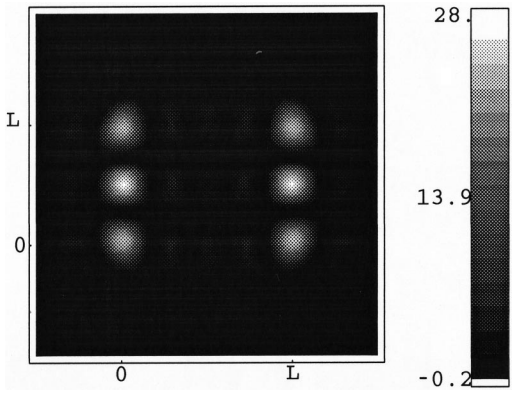

FIG. 8. Supersonic intensity for the normal mode shown in Fig. 7. The intensity is almost always positive, with black near zero level. White indicates maximum level and locates the regions of the plate which radiate to the far field. The edge mode radiation occurs.

positive intensity regions to produce positive intensity images over the real sources. This averaging process, however, reduces the spatial resolution as noted above, limiting the resolution to $\lambda/2$.

C. Supersonic intensity for an edge mode

Consider now the situation in which the structural wavelength in the x direction is smaller, and in the y direction larger than the acoustic wavelength ($k_y < k < k_x$). This leads to a radiation condition called an edge mode. The cancellation of adjacent sections of the normal mode on the plate occurs now only in the x direction, with no cancellation in the perpendicular direction. By the scheme discussed with respect to Fig. 5, the two edges on the left and right sides of the plate are left uncanceled. For this case we consider an $m=11$, $n=3$ mode on a baffled plate, shown in Fig. 7. The supersonic intensity on the surface of this plate for this mode is shown in Fig. 8 and the actual intensity in Fig. 9. The frequency is chosen so that $kL=17.2$ and thus a corner mode is produced since $k_nL < kL < k_mL$ ($k_m=11\pi$, $k_n=3\pi$).[4] In Fig. 8 the edge mode is clearly indicated, whereas the actual intensity in Fig. 9 shows strong positive and negative regions throughout the plate. The supersonic intensity is almost always positive as the scale indicates.

The cancellation of adjacent regions of the plate for this mode is not as complete as in the case of the corner mode illustrated above. As the wave number in k-space of the edge mode approaches the radiation circle the interior regions of the plate become stronger sources, since the cancellation of volume flow becomes less and less complete. Note these regions are not side lobes, however, as discussed in Fig. 2, since they do not form a ring around the dominant source regions.

II. SUMMARY

Supersonic intensity allows us to locate, with a spatial resolution of one half an acoustic wavelength, the ''hot spots'' of radiation on planar sources. It is especially useful for wave-bearing plates with subsonic waves since the circulating power flow from the surface has been removed, uncovering an image of the radiating regions. These regions are quantified by the power per unit area which they give off to the far field. The sum total of all these regions provides a total power which is equal to the actual power radiated to the far field.

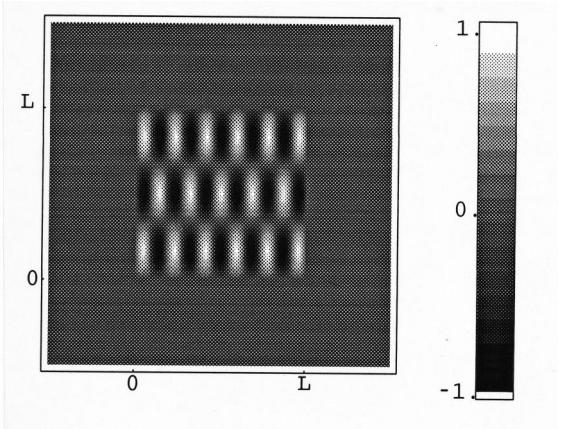

FIG. 7. Mode shape shown in gray scale for a $m=11$, $n=3$ mode of a plate, $\Psi_{mn}(x,y)=\sin(11\pi x/L_x)\sin(3\pi y/L_y)$. The baffle is shown surrounding the plate.

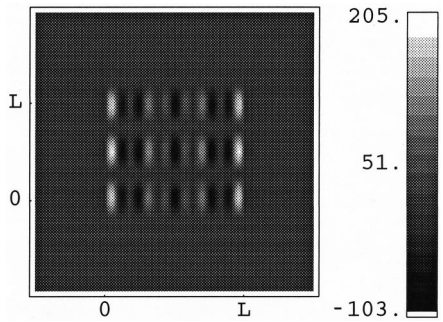

FIG. 9. Actual real intensity for the normal mode shown in Fig. 7. Note that the levels are higher than the supersonic intensity case, and the negative regions are much stronger.

ACKNOWLEDGMENTS

This work was supported by ONR.

[1] Second International Congress on Acoustic Intensity, CETIM, Senlis, France, September 1985.
[2] E. G. Williams, ''Supersonic acoustic intensity,'' J. Acoust. Soc. Am. **97**, 121–127 (1995).
[3] P. Smith and R. Lyon, ''Sound and structural vibration,'' NASA Report CR-160, 1965.
[4] G. Maidanik, ''Response of ribbed panels to reverberant acoustic fields,'' J. Acoust. Soc. Am. **34**, 809–826 (1962).
[5] G. Maidanik, ''Vibrational and radiative classifications of modes of a baffled finite panel,'' J. Sound Vib. **34**, 447–455 (1974).
[6] J. W. Goodman, *Introduction to Fourier Optics* (McGraw-Hill, New York, 1968).
[7] I. S. Gradshteyn and I. M. Ryzhik, *Tables of Integrals, Series and Products* (Academic, New York, 1965).
[8] E. G. Williams and J. D. Maynard, ''Numerical evaluation of the Rayleigh integral for planar radiators using the FFT,'' J. Acoust. Soc. Am. **72**, 2020–2030 (1982).

Acoustic shape sensitivity analysis using the boundary integral equation

Bon-Ung Koo, Jeong-Guon Ih,[a] and Byung-Chai Lee
Department of Mechanical Engineering, Korea Advanced Institute of Science and Technology, Science Town, Taejon 305-701, Korea

(Received 19 March 1996; revised 21 July 1998; accepted 28 July 1998)

Boundary integral equations are formulated for the shape sensitivity analysis of the acoustic problems. The concept of the material derivative is employed in deriving the sensitivity equations. Since the equation is derived by the direct differentiation of the boundary integrals containing the field values, it is expected that the sensitivity would be computed more effectively and accurately than the conventional finite difference method. In addition, the equation has the potential to be applied to many complex acoustic problems, because the derived equation is regularized by using the integral identity that incorporates the one-dimensional propagating wave and its material derivative. The validity of the formulations is demonstrated through examples having regular shapes such as the three-dimensional pulsating sphere and the one-dimensional duct, for which the analytical solutions are available. As an example for an irregular domain, the two-dimensional model of an automotive interior cavity is dealt with in the view point of the noise level at the passenger's ear position. The results show that the present method can be an effective tool for the shape optimization in designing the desired sound field. It is noted that the present method permits accurate sensitivities of the acoustic pressure on the boundary as well as at the field points. The present method is thought to be an alternative to the previous finite difference techniques for computing the shape sensitivity using the boundary element method and the formal derivative method using the finite element method.
[S0001-4966(98)02111-0]

PACS numbers: 43.50.Gf [GAD]

INTRODUCTION

There have been considerable research activities in the area of computational methods for the shape optimization. The goal of shape optimization is to find the best design parameters defining the desired shape of the given structure under certain constraints. For the optimization process, it is often desirable to utilize the shape design sensitivity which represents the rate of change of object function or constraint values with respect to the design parameters. Once the sensitivities of the given configuration to the design variables can be determined, an improved design can be obtained after the iterative calculations. Much work has been done on the evaluation of the design sensitivity; Ding[1] and Kwak[2] have provided excellent reviews on numerous previous works.

In the numerical implementation of the sensitivity analysis, either the finite element method (FEM)[3] or the boundary element method (BEM) can be used. The BEM has advantages compared with the FEM in terms of accuracy on the boundary and the ease of the remeshing process. Furthermore, the vibro-acoustic radiation into the infinite region can be easily dealt with by using the BEM.

There have been several studies reported on the computation of the design sensitivity for the acoustic problems by using the BEM. Kane *et al.*[4] presented a shape design sensitivity analysis formulation method by using the implicit differentiation of the discretized Helmholtz integral equation. Cunefare and Koopmann[5] studied the sensitivity of radiated acoustic power to the change of acoustic velocity for a given geometric configuration. Smith and Bernhard[6] computed the sensitivity by differentiating the discretized boundary integral equation. The derivative of the system matrix was approximated by adopting the finite difference concept. Although the finite difference method (FDM) is straightforward and very available for utilization, the method has some weak points as follows. If the relationship between design variables of the system is not linear, the result will not be exact and, consequently, the precision would be highly dependent on the magnitude of perturbations. In addition, the computational cost might be high owing to the reconstruction of the system matrix adapting for the perturbed shape.

The direct differentiation of the boundary integral equation can be an effective alternative to the FDM. Kane and Saigal[7] computed the sensitivities by the analytical differentiation of the system matrix for elastic problems. Singular behavior of the integral equation was observed to originate from the analytic differentiation. In order to avoid the singular behavior, they placed the source point outside the domain. Barone and Yang[8,9] located the source point on the boundary to clear the ambiguity of Kane's method and the recovery process was introduced into the singularity reduction by using the rigid body condition.

In this paper, an analytic expression for the design sensitivity of the acoustic problems is to be presented by differentiating the conventional boundary integral equation and employing the material derivative concept.[10] In order to re-

[a]Electronic mail: ihih@sorak.kaist.ac.kr

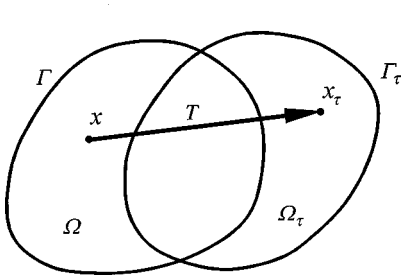

FIG. 1. Deformation of the domain by the mapping.

duce the singularity of the sensitivity equation, the uniform potential field is brought into the solution process, because the singularity of the fundamental solution of the potential field is similar to that of the acoustic field near the source point. Combining the potential equation with the governing equation, the acoustic sensitivity equation can be expressed by the weakly singular integral. However, this potential-combined weakly singular sensitivity equation can increase the computational cost and requires singular integration to obtain the accurate solution. In order to complement these weak features, the sensitivity equation is further regularized and only the acoustic equation is used. The singularities of the integrands in the integral representation can be removed by adopting an integral identity utilizing the one-dimensional propagating wave component.[11] In this way, a regular representation of sensitivity equation can be derived. In order to validate the derived formula, the exterior acoustic field from a pulsating sphere and the interior field in a duct are selected as two typical examples, for which the analytical solutions are available. As an example for the irregular boundary, the simple two-dimensional model of an automotive cabin is optimized for reducing the noise level at the passenger's ear position.

I. MATHEMATICAL FORMULATIONS

A. Material derivative

As a first step toward shape design sensitivity analysis, a relationship is required between the variation in shape and the resulting changes in functionals. Since the shape of the domain will vary in the design process, it is convenient to regard the domain Ω as a continuous medium, to which the material derivative method of the continuum mechanics can be applied.

Consider domain Ω and its deformed shape Ω_τ as shown in Fig. 1 and suppose that only one parameter τ defines the transformation T. In Fig. 1, Γ and Γ_τ represent the boundaries before and after the transformation, respectively. The mapping $T:\mathbf{x}\rightarrow\mathbf{x}_\tau(\mathbf{x})$, $\mathbf{x}\in\Omega$, can be written as[10]

$$\mathbf{x}_\tau = T(\mathbf{x},\tau). \tag{1}$$

The mapping in Eq. (1) may be thought of as a dynamic process of the deforming continuum, where τ plays the role of time. Then, the design velocity, $\mathbf{V}(\mathbf{x}_\tau,\tau)$, can be defined as

$$\mathbf{V}(\mathbf{x}_\tau,\tau)\equiv\frac{d\mathbf{x}_\tau}{d\tau}=\frac{\partial T(\mathbf{x},\tau)}{\partial\tau}, \tag{2}$$

because the initial point $\mathbf{x}$ does not depend on τ. Ignoring the high order terms, $\mathbf{x}_\tau$ can be rewritten in the neighborhood of $\tau=0$ as follows:

$$\mathbf{x}_\tau = T(\mathbf{x},\tau)=\mathbf{x}+\tau\frac{\partial T}{\partial\tau}(\mathbf{x},0)=\mathbf{x}+\tau\mathbf{V}(\mathbf{x}). \tag{3}$$

Here, $\mathbf{V}(\mathbf{x})\equiv\mathbf{V}(\mathbf{x},0)$ represents the design velocity of the initial shape. By using the foregoing relations, the material derivatives of the boundary variables can be expressed in terms of the design velocity. The expressions are well known and can be seen in the Appendix.

B. Design sensitivity equation

Consider the acoustic field Ω subject to the prescribed time-harmonic acoustic pressure $\bar{p}$ or surface velocity $\bar{v}_n$ on the boundary Γ. When the field Ω contains no active sources and the medium is homogeneous and lossless, the boundary integral equation for the acoustic pressure p at point $\boldsymbol{\xi}$, $\boldsymbol{\xi}\in\Omega$, can be expressed as

$$p(\boldsymbol{\xi})=-j\omega\rho_0\int_\Gamma G(\boldsymbol{\xi},\mathbf{x})v_n(\mathbf{x})d\Gamma(\mathbf{x}) - \int_\Gamma F(\boldsymbol{\xi},\mathbf{x})p(\mathbf{x})d\Gamma(\mathbf{x}). \tag{4}$$

Here, ω is the circular frequency, $j=\sqrt{-1}$, ρ_0 is the density of the initially quiescent medium, and v_n is the outward normal component of the boundary velocity. $G(\boldsymbol{\xi},\mathbf{x})$ and $F(\boldsymbol{\xi},\mathbf{x})$ are well known singular free-field functions given by

$$G(\boldsymbol{\xi},\mathbf{x})=\begin{cases} jH_0^{(1)}(kr)/4, & \text{in } 2\text{D},\\ \exp(-jkr)/4\pi r, & \text{in } 3\text{D},\end{cases} \tag{5a}$$

$$F(\boldsymbol{\xi},\mathbf{x})=\frac{\partial F(\boldsymbol{\xi},\mathbf{x})}{\partial n(\mathbf{x})} =\begin{cases} -\dfrac{jk}{4}H_1^{(1)}(kr)\dfrac{\partial r}{\partial n}, & \text{in } 2\text{D},\\ -(1+jkr)\dfrac{\exp(-jkr)}{4\pi r^2}\dfrac{\partial r}{\partial n}, & \text{in } 3\text{D},\end{cases} \tag{5b}$$

where $H_n^{(1)}$ denotes the nth order Hankel function of the first kind, $k=\omega/c$ the wave number, c the speed of sound, and r the distance between $\boldsymbol{\xi}$ and $\mathbf{x}$.

The sensitivity equation can be obtained by taking the material derivative of the Kirchhoff–Helmholtz integral equation (4) with respect to the design variables as follows:

$$\dot{p}(\boldsymbol{\xi}) = -j\omega\rho_0 \int_\Gamma G(\boldsymbol{\xi},\mathbf{x})\dot{v}_n(x)d\Gamma(\mathbf{x}) - \int_\Gamma F(\boldsymbol{\xi},x)\dot{p}(\mathbf{x})d\Gamma(\mathbf{x}) - j\omega\rho_0 \int_\Gamma \dot{G}(\boldsymbol{\xi},\mathbf{x})v_n(\mathbf{x})d\Gamma(\mathbf{x}) - \int_\Gamma \dot{F}(\boldsymbol{\xi},\mathbf{x})p(\mathbf{x})d\Gamma(\mathbf{x})$$
$$- j\omega\rho_0 \int_\Gamma G(\boldsymbol{\xi},\mathbf{x})v_n(\mathbf{x})J^s(\mathbf{x})d\Gamma(\mathbf{x}) - \int_\Gamma F(\boldsymbol{\xi},\mathbf{x})p(\mathbf{x})J^s(\mathbf{x})d\Gamma(\mathbf{x}). \tag{6}$$

Here, the dot over a variable denotes the material derivative with respect to the design variable and $J^s(\mathbf{x})$ means the rate of change of the differential boundary at $\mathbf{x}$ due to the shape change, i.e., $J^s(\mathbf{x}) = d\dot{\Gamma}(\mathbf{x})/d\Gamma(\mathbf{x})$.

In Eq. (6), the sensitivity of the acoustic pressure at any point $\boldsymbol{\xi}$ is represented in terms of the fundamental solutions as well as the velocity and the acoustic pressure on the boundary. The free terms in the left-hand side of Eqs. (4) and (6) to be multiplied by the solid angle $\Lambda(\boldsymbol{\xi})$ due to the strong singularity of $F(\boldsymbol{\xi},\mathbf{x})$. The solid angle depends on the geometry of the boundary near the source point $\boldsymbol{\xi}\in\Gamma$. In order to obtain the sensitivity of the boundary value accurately, $\Lambda(\boldsymbol{\xi})$ and the design load vector should be evaluated accurately where the latter implies the effect of shape change.

The strong singularity in Eq. (6) can be eliminated by combining Eq. (6) with the sensitivity representation of the uniform potential field as follows:

$$\dot{p}(\boldsymbol{\xi}) = \dot{p}(\boldsymbol{\eta}) - j\omega\rho_0 \int_\Gamma [G(\boldsymbol{\xi},\mathbf{x})\{\dot{v}_n(\mathbf{x}) + v_n(\mathbf{x})J^s(\mathbf{x})\}$$
$$+ \dot{G}(\boldsymbol{\xi},\mathbf{x})v_n(\mathbf{x})]d\Gamma(\mathbf{x})$$
$$- \int_\Gamma [F(\boldsymbol{\xi},\mathbf{x})\dot{p}(\mathbf{x}) - q^*(\boldsymbol{\xi},\mathbf{x})\dot{p}(\boldsymbol{\eta})]d\Gamma(\mathbf{x})$$
$$- \int_\Gamma [\dot{F}(\boldsymbol{\xi},\mathbf{x})p(\mathbf{x}) - \dot{q}^*(\boldsymbol{\xi},\mathbf{x})p(\boldsymbol{\eta})]d\Gamma(\mathbf{x})$$
$$- \int_\Gamma [F(\boldsymbol{\xi},\mathbf{x})p(\mathbf{x}) - q^*(\boldsymbol{\xi},\mathbf{x})p(\boldsymbol{\eta})]J^s(\mathbf{x})d\Gamma(\mathbf{x}). \tag{7}$$

Here, $q^*(\boldsymbol{\xi},\mathbf{x})$ denotes the flux of the fundamental solution of the potential problems. Defining reference point $\boldsymbol{\eta}$ as the nearest boundary point from source point $\boldsymbol{\xi}$, one can find that the strong singularity related to $F(\boldsymbol{\xi},\mathbf{x})$ is regularized by combining the potential equation. Since the boundary integrals in Eq. (7) are continuous on the boundary, the jump term, which arises in the conventional boundary integral equation, does not appear in the numerical procedure. Furthermore, Eq. (7) is weakly singular that the sensitivity can be obtained accurately by using singular integral for the continuos design velocity.

The boundary element method is very effective in dealing with the sound radiation from the vibrating body and the sensitivity equation can be derived for the exterior problems. In order to derive the exterior sensitivity equation, the effects of integration over the infinite boundary should be known. When the Sommerfeld radiation condition is considered, the net effect of acoustic pressure over the infinite boundary vanishes, while the effect of integration of the potential equation over the infinite boundary still remains. From the causality condition, source point $\boldsymbol{\xi}$ is confined to exist inside the infinite boundary, that the effect of the potential term is the same as the pressure sensitivity value at the reference point. Consequently, the sensitivity equation for exterior problems can be stated as

$$\dot{p}(\boldsymbol{\xi}) = -j\omega\rho_0 \int_\Gamma [G(\boldsymbol{\xi},\mathbf{x})\{\dot{v}_n(\mathbf{x}) + v_n(\mathbf{x})J^s(\mathbf{x})\}$$
$$+ \dot{G}(\boldsymbol{\xi},\mathbf{x})v_n(\mathbf{x})]d\Gamma(\mathbf{x})$$
$$- \int_\Gamma [F(\boldsymbol{\xi},\mathbf{x})\dot{p}(\mathbf{x}) - q^*(\boldsymbol{\xi},\mathbf{x})\dot{p}(\boldsymbol{\eta})]d\Gamma(\mathbf{x})$$
$$- \int_\Gamma [\dot{F}(\boldsymbol{\xi},\mathbf{x})p(\mathbf{x}) - \dot{q}^*(\boldsymbol{\xi},\mathbf{x})p(\boldsymbol{\eta})]d\Gamma(\mathbf{x})$$
$$- \int_\Gamma [F(\boldsymbol{\xi},\mathbf{x})p(\mathbf{x}) - q^*(\boldsymbol{\xi},\mathbf{x})p(\boldsymbol{\eta})]J^s(\mathbf{x})d\Gamma(\mathbf{x}). \tag{8}$$

C. Regularized sensitivity equation

The potential-combined weakly singular sensitivity equation has been derived in the foregoing section. However, the amount of computation increases by introducing the potential equation into the problem and the remaining weak singularity may cause errors in the numerical calculation.

It is already shown[11] that the singularity condition can be further lowered and one can get an accurate solution, if the propagating wave mode is utilized. The integral identity expressing the wave propagation in the arbitrary domain can be written as:

$$\exp[jk(\boldsymbol{\xi}-\boldsymbol{\eta})\cdot\mathbf{a}] = jk\int_\Gamma G(\boldsymbol{\xi},\mathbf{x})\mathbf{n}(\mathbf{x})\cdot\mathbf{a}\,\exp(jr_a)d\Gamma(\mathbf{x})$$
$$- \int_\Gamma F(\boldsymbol{\xi},\mathbf{x})\exp(jr_a)d\Gamma(\mathbf{x}). \tag{9}$$

Here, $\boldsymbol{\eta}$ refers to an arbitrary reference point, $\mathbf{a}$ denotes an arbitrary unit vector, and $r_a = k(\mathbf{x}-\boldsymbol{\eta})\cdot\mathbf{a}$. As a special case of Eq. (9), the following cosine or sine wave representation can be obtained by adding or subtracting the propagating waves directed to $-\mathbf{a}$:

$$\cos[k(\boldsymbol{\xi}-\boldsymbol{\eta})\cdot\mathbf{a}] = -k\int_\Gamma G(\boldsymbol{\xi},\mathbf{x})\mathbf{n}(x)\cdot a\,\sin(r_a)d\Gamma(\mathbf{x})$$
$$- \int_\Gamma F(\boldsymbol{\xi},\mathbf{x})\cos(r_a)d\Gamma(\mathbf{x}), \tag{10a}$$

$$\sin[k(\boldsymbol{\xi}-\boldsymbol{\eta})\cdot\mathbf{a}] = k\int_\Gamma G(\boldsymbol{\xi},\mathbf{x})\mathbf{n}(x)\cdot\mathbf{a}\,\cos(r_a)d\Gamma(\mathbf{x}) - \int_\Gamma F(\boldsymbol{\xi},\mathbf{x})\sin(r_a)d\Gamma(\mathbf{x}). \tag{10b}$$

Using the relations in Eqs. (10), a regular boundary integral representation for the acoustic pressure can be derived as

$$\begin{aligned} p(\boldsymbol{\xi}) = \alpha[p^0\,\cos\{k(\boldsymbol{\xi}-\boldsymbol{\eta})\cdot\mathbf{n}^0\} - j\rho_0 c v_n^0\,\sin\{k(\boldsymbol{\xi}-\boldsymbol{\eta})\cdot\mathbf{n}^0\}] \\ - j\omega\rho_0\int_\Gamma G(\boldsymbol{\xi},\mathbf{x})[v_n(\mathbf{x}) - v_n^0\mathbf{n}^0\cdot\mathbf{n}(\mathbf{x})\cos(r_n) \\ + jp^0\mathbf{n}^0\cdot\mathbf{n}(\mathbf{x})\sin(r_n)/\rho_0 c]d\Gamma(\mathbf{x}) - \int_\Gamma F(\boldsymbol{\xi},\mathbf{x})[p(\mathbf{x}) \\ - p^0\,\cos(r_n) + j\rho_0 c v_n^0\,\sin(r_n)]d\Gamma(\mathbf{x}), \end{aligned} \tag{11}$$

where $r_n = k(\mathbf{x}-\boldsymbol{\eta})\cdot\mathbf{n}^0$, $(Q)^0$ denotes the physical quantity Q at the reference point $\boldsymbol{\eta}$ on the boundary and α is the variable depending on the problem type: $\alpha=1$ for interior problems and $\alpha=0$ for exterior problems. Even though $\boldsymbol{\xi}$ is located on the boundary or near the boundary, all the integrands in Eq. (11) become regular by defining the reference point $\boldsymbol{\eta}$ as the nearest boundary point from $\boldsymbol{\xi}$. Finally, an accurate and stable numerical solution can be obtained by using the standard Gaussian quadrature for evaluating all the integrals within the domain as well as near the boundary.

Similarly, the singular integrands in Eq. (6) can be regularized. Taking material derivatives of Eqs. (10a) and (10b), one can derive the following equations:

$$\begin{aligned} & k\{\mathbf{V}(\boldsymbol{\xi})-\mathbf{V}^0\}\cdot\mathbf{a}\,\sin\{k(\boldsymbol{\xi}-\boldsymbol{\eta})\cdot\mathbf{a}\} \\ & = k\int_\Gamma\{\dot G(\boldsymbol{\xi},\mathbf{x}) + G(\boldsymbol{\xi},\mathbf{x})J^s(x)\}\mathbf{n}(\mathbf{x})\cdot\mathbf{a}\,\sin(r_a)d\Gamma(\mathbf{x}) + k\int_\Gamma G(\boldsymbol{\xi},\mathbf{x})\mathbf{a}\cdot[\dot{\mathbf{n}}(\mathbf{x})\sin(r_a) + k\mathbf{n}(\mathbf{x})\{\mathbf{V}(\mathbf{x})-\mathbf{V}^0\}\cdot\mathbf{a} \\ & \times\cos(r_a)]d\Gamma(\mathbf{x}) + \int_\Gamma\{\dot F(\boldsymbol{\xi},\mathbf{x}) + F(\boldsymbol{\xi},\mathbf{x})J^s(\mathbf{x})\}\cos(r_a)d\Gamma(\mathbf{x}) - k\int_\Gamma F(\boldsymbol{\xi},\mathbf{x})\{\mathbf{V}(\mathbf{x})-\mathbf{V}^0\}\cdot\mathbf{a}\,\sin(r_a)\cdot d\Gamma(\mathbf{x}), \end{aligned} \tag{12a}$$

$$\begin{aligned} & k\{\mathbf{V}(\boldsymbol{\xi})-\mathbf{V}^0\}\cdot\mathbf{a}\,\cos\{k(\boldsymbol{\xi}-\boldsymbol{\eta})\cdot\mathbf{a}\} \\ & = k\int_\Gamma\{\dot G(\boldsymbol{\xi},\mathbf{x}) + G(\boldsymbol{\xi},\mathbf{x})J^s(\mathbf{x})\}\mathbf{n}(\mathbf{x})\cdot\mathbf{a}\,\cos(r_a)d\Gamma(\mathbf{x}) + k\int_\Gamma G(\boldsymbol{\xi},\mathbf{x})\mathbf{a}\cdot[\dot{\mathbf{n}}(\mathbf{x})\cos(r_a) - k\mathbf{n}(\mathbf{x})\{\mathbf{V}(\mathbf{x})-\mathbf{V}^0\}\cdot\mathbf{a} \\ & \times\sin(r_a)]d\Gamma(\mathbf{x}) - \int_\Gamma\{\dot F(\boldsymbol{\xi},\mathbf{x}) + F(\boldsymbol{\xi},\mathbf{x})J^s(\mathbf{x})\}\sin(r_a)d\Gamma(\mathbf{x}) - k\int_\Gamma F(\boldsymbol{\xi},\mathbf{x})\{\mathbf{V}(\mathbf{x})-\mathbf{V}^0\}\cdot\mathbf{a}\,\cos(r_a)\cdot d\Gamma(\mathbf{x}). \end{aligned} \tag{12b}$$

After multiplying Eq. (12a) by p^0, viz., acoustic pressure at reference point, and replacing $\mathbf{a}$ by the unit normal vector $\mathbf{n}^0$, one can obtain the following equation by combining the resultant equation with Eq. (6):

$$\begin{aligned} \dot p(\boldsymbol{\xi}) = & -j\omega\rho_0\int_\Gamma G(\boldsymbol{\xi},\mathbf{x})[\dot v_n(\mathbf{x}) - p^0 k\mathbf{n}^0\cdot\{\dot{\mathbf{n}}(\mathbf{x})\sin(r_n) + k\mathbf{n}(x)V_{rn}\,\cos(r_n)\}/j\omega\rho_0]d\Gamma(\mathbf{x}) \\ & - \int_\Gamma F(\boldsymbol{\xi},\mathbf{x})[\dot p(\mathbf{x}) + p^0 kV_{rn}\,\sin(r_n)]d\Gamma(\mathbf{x}) - j\omega\rho_0\int_\Gamma\{\dot G(\boldsymbol{\xi},\mathbf{x}) + G(\boldsymbol{\xi},\mathbf{x})J^s(\mathbf{x})\} \\ & \times[v_n(\mathbf{x}) - p^0 k\mathbf{n}^0\cdot\mathbf{n}(\mathbf{x})\sin(r_n)/j\omega\rho_0]d\Gamma(\mathbf{x}) \\ & - \int_\Gamma\{\dot F(\boldsymbol{\xi},\mathbf{x}) + F(\boldsymbol{\xi},\mathbf{x})J^s(\mathbf{x})\}[p(\mathbf{x}) - p^0\,\cos(r_n)]d\Gamma(\mathbf{x}) - p^0 k\{\mathbf{V}(\boldsymbol{\xi})-\mathbf{V}^0\}\cdot\mathbf{n}^0\,\sin\{k(\boldsymbol{\xi}-\boldsymbol{\eta})\cdot\mathbf{n}^0\}, \end{aligned} \tag{13a}$$

$$V_{rn} = \{\mathbf{V}(\mathbf{x})-\mathbf{V}^0\}\cdot\mathbf{n}^0. \tag{13b}$$

Similarly, when Eq. (12a) is multiplied by $\dot p^0$ and $\mathbf{n}^0$ is substituted into $\mathbf{a}$, the following acoustic pressure sensitivity at an interior point $\boldsymbol{\xi}$ can be derived by combining the result with Eq. (13a):

$$\dot{p}(\boldsymbol{\xi}) = -j\omega\rho_0 \int_\Gamma G(\boldsymbol{\xi},\mathbf{x})[\dot{v}_n(\mathbf{x}) - k\mathbf{n}^0 \cdot \{p^0 \dot{\mathbf{n}}(\mathbf{x})\sin(r_n) + p^0 k\mathbf{n}(x) V_{rn}\cos(r_n) + \dot{p}^0 \mathbf{n}(\mathbf{x})\sin(r_n)\}/j\omega\rho_0] d\Gamma(\mathbf{x}) - \int_\Gamma F(\boldsymbol{\xi},\mathbf{x})[\dot{p}(\mathbf{x})$$
$$- \dot{p}^0 \cos(r_n) + p^0 k V_{rn} \sin(r_n)] d\Gamma(\mathbf{x}) - j\omega\rho_0 \int_\Gamma \{\dot{G}(\boldsymbol{\xi},\mathbf{x}) + G(\boldsymbol{\xi},\mathbf{x}) J^s(\mathbf{x})\}[v_n(\mathbf{x}) - p^0 k\mathbf{n}^0 \cdot \mathbf{n}(\mathbf{x})\sin(r_n)/j\omega\rho_0] d\Gamma(\mathbf{x})$$
$$- \int_\Gamma \{\dot{F}(\boldsymbol{\xi},\mathbf{x}) + F(\boldsymbol{\xi},\mathbf{x}) J^s(\mathbf{x})\}[p(\mathbf{x}) - p^0 \cos(r_n)] d\Gamma(\mathbf{x}) - p^0 k\{\mathbf{V}(\boldsymbol{\xi}) - \mathbf{V}^0\} \cdot \mathbf{n}^0 \sin\{k(\boldsymbol{\xi} - \boldsymbol{\eta}) \cdot \mathbf{n}^0\}$$
$$+ \dot{p}^0 \cos\{k(\boldsymbol{\xi} - \boldsymbol{\eta}) \cdot \mathbf{n}^0\}. \tag{14}$$

It is noted in Eq. (14) that the sensitivity of acoustic pressure at an interior point is represented by the values at the reference point and using the weakly singular boundary integral. Therefore, the accuracy of the calculated sensitivity based on Eq. (14) is expected to be nearly the same with that of the potential-combined sensitivity equation (7).

The remaining weak singularity in Eq. (14) can be further regularized. As the first step for regularizing the weak singularity in Eq. (14), one can multiply Eq. (12b) by q^0 and Eq. (10b) by $\dot{q}^0$, where

$$q^0 \equiv j\rho_0 c v_n^0, \tag{15a}$$

$$\dot{q}^0 \equiv j\rho_0 c \dot{v}_n^0. \tag{15b}$$

Next, $\mathbf{n}^0$ is substituted into **a** in both equations. Lastly, the consequent equations are combined with the weakly singular representation of Eq. (14). The final regularized sensitivity equation can be written as

$$\dot{p}(\boldsymbol{\xi}) = -j\omega\rho_0 \int_\Gamma G(\boldsymbol{\xi},\mathbf{x})[\dot{v}_n(\mathbf{x}) - \dot{v}_n^0 \mathbf{n}(\mathbf{x}) \cdot \mathbf{n}^0 \cos(r_n) - k\mathbf{n}^0 \cdot \{p^0 \dot{\mathbf{n}}(\mathbf{x})\sin(r_n) + p^0 k\mathbf{n}(\mathbf{x}) V_{rn}\cos(r_n) + \dot{p}^0 \mathbf{n}(\mathbf{x})\sin(r_n)\}/j\omega\rho_0$$
$$- v_n^0 \mathbf{n}^0 \cdot \{\dot{\mathbf{n}}(\mathbf{x})\cos(r_n) - k\mathbf{n}(\mathbf{x}) V_{rn}\sin(r_n)\}] d\Gamma(\mathbf{x}) - \int_\Gamma F(\boldsymbol{\xi},\mathbf{x})[\dot{p}(\mathbf{x}) - \dot{p}^0 \cos(r_n) + p^0 k V_{rn}\sin(r_n) + q^0 k V_{rn}\cos(r_n)$$
$$+ \dot{q}^0 \sin(r_n)] d\Gamma(\mathbf{x}) - j\omega\rho_0 \int_\Gamma \{\dot{G}(\boldsymbol{\xi},\mathbf{x}) + G(\boldsymbol{\xi},\mathbf{x}) J^s(\mathbf{x})\}[v_n(\mathbf{x}) - v_n^0 \mathbf{n}^0 \cdot \mathbf{n}(\mathbf{x})\cos(r_n) - p^0 k\mathbf{n}^0 \cdot \mathbf{n}(\mathbf{x})\sin(r_n)/j\omega\rho_0] d\Gamma(\mathbf{x})$$
$$- \int_\Gamma \{\dot{F}(\boldsymbol{\xi},\mathbf{x}) + F(\boldsymbol{\xi},\mathbf{x}) J^s(\mathbf{x})\}[p(\mathbf{x}) - p^0 \cos(r_n) + q^0 \sin(r_n)] d\Gamma(\mathbf{x}) - [p^0 k\{\mathbf{V}(\boldsymbol{\xi}) - \mathbf{V}^0\} \cdot \mathbf{n}^0 + \dot{q}^0]\sin\{k(\boldsymbol{\xi} - \boldsymbol{\eta}) \cdot \mathbf{n}^0\}$$
$$+ [\dot{p}^0 - q^0 k\{\mathbf{V}(\boldsymbol{\xi}) - \mathbf{V}^0\} \cdot \mathbf{n}^0]\cos\{k(\boldsymbol{\xi} - \boldsymbol{\eta}) \cdot \mathbf{n}^0\}. \tag{16}$$

Note that all the integrands in Eq. (16) are regular, if the boundary is smooth near source point $\boldsymbol{\xi}$ and the design velocity is continuous. However, consideration for weak singularity is required near a sharp corner or edge. The discontinuous element can be used for this purpose.[11]

For exterior problems, one can easily find that free terms in Eq. (16) are equivalent to the integral effect of the one-dimensional wave component over the infinite boundary. The regularized sensitivity equation for exterior problems can be derived as

$$\dot{p}(\boldsymbol{\xi}) = -j\omega\rho_0 \int_\Gamma G(\boldsymbol{\xi},\mathbf{x})[\dot{v}_n(\mathbf{x}) - \dot{v}_n^0 \mathbf{n}(\mathbf{x}) \cdot \mathbf{n}^0 \cos(r_n) - k\mathbf{n}^0 \cdot \{p^0 \dot{\mathbf{n}}(\mathbf{x})\sin(r_n) + p^0 k\mathbf{n}(\mathbf{x}) V_{rn}\cos(r_n) + \dot{p}^0 \mathbf{n}(\mathbf{x})\sin(r_n)\}/j\omega\rho_0$$
$$- v_n^0 \mathbf{n}^0 \cdot \{\dot{\mathbf{n}}(\mathbf{x})\cos(r_n) - k\mathbf{n}(\mathbf{x}) V_{rn}\sin(r_n)\}] d\Gamma(\mathbf{x}) - \int_\Gamma F(\boldsymbol{\xi},\mathbf{x})[\dot{p}(\mathbf{x}) - \dot{p}^0 \cos(r_n) + p^0 k V_{rn}\sin(r_n) + q^0 k V_{rn}\cos(r_n)$$
$$+ \dot{q}^0 \sin(r_n)] d\Gamma(\mathbf{x}) - j\omega\rho_0 \int_\Gamma \{\dot{G}(\boldsymbol{\xi},\mathbf{x}) + G(\boldsymbol{\xi},\mathbf{x}) J^s(\mathbf{x})\}[v_n(\mathbf{x}) - v_n^0 \mathbf{n}^0 \cdot \mathbf{n}(\mathbf{x})\cos(r_n) - p^0 k\mathbf{n}^0 \cdot \mathbf{n}(\mathbf{x})\sin(r_n)/j\omega\rho_0] d\Gamma(\mathbf{x})$$
$$- \int_\Gamma \{\dot{F}(\boldsymbol{\xi},\mathbf{x}) + F(\boldsymbol{\xi},\mathbf{x}) J^s(\mathbf{x})\}[p(\mathbf{x}) - p^0 \cos(r_n) + q^0 \sin(r_n)] d\Gamma(\mathbf{x}). \tag{17}$$

As aforementioned, the sensitivities of boundary variables are known to obtain the sensitivity at the field. The sensitivities of

boundary variables can be obtained by placing the source on the boundary and collocating the reference point $\boldsymbol{\eta}$ to $\boldsymbol{\xi}$ in the sensitivity equation for internal points. In this fashion, the sensitivity equation for a boundary variable can be expressed as

$$\alpha\dot{p}(\boldsymbol{\xi}) = -j\omega\rho_0 \int_\Gamma G(\boldsymbol{\xi},\mathbf{x})[\dot{v}_n(\mathbf{x}) - \dot{v}_n^0 \mathbf{n}(\mathbf{x})\cdot\mathbf{n}^0 \cos(r_n) - k\mathbf{n}^0\cdot\{p^0\dot{\mathbf{n}}(\mathbf{x})\sin(r_n) + p^0 k\mathbf{n}(\mathbf{x})V_{rn}\cos(r_n) + \dot{p}^0\mathbf{n}(\mathbf{x})\sin(r_n)\}/j\omega\rho_0$$

$$- v_n^0\mathbf{n}^0\cdot\{\dot{\mathbf{n}}(\mathbf{x})\cos(r_n) - k\mathbf{n}(\mathbf{x})V_{rn}\sin(r_n)\}]d\Gamma(\mathbf{x}) - \int_\Gamma F(\boldsymbol{\xi},\mathbf{x})[\dot{p}(\mathbf{x}) - \dot{p}^0\cos(r_n) + p^0 kV_{rn}\sin(r_n) + q^0 kV_{rn}\cos(r_n)$$

$$+ \dot{q}^0\sin(r_n)]d\Gamma(\mathbf{x}) - j\omega\rho_0\int_\Gamma\{\dot{G}(\boldsymbol{\xi},\mathbf{x}) + G(\boldsymbol{\xi},\mathbf{x})J^s(\mathbf{x})\}[v_n(\mathbf{x}) - v_n^0\mathbf{n}^0\cdot\mathbf{n}(\mathbf{x})\cos(r_n) - p^0 k\mathbf{n}^0\cdot\mathbf{n}(\mathbf{x})\sin(r_n)/j\omega\rho_0]d\Gamma(\mathbf{x})$$

$$- \int_\Gamma\{\dot{F}(\boldsymbol{\xi},\mathbf{x}) + F(\boldsymbol{\xi},\mathbf{x})J^s(\mathbf{x})\}[p(\mathbf{x}) - p^0\cos(r_n) + q^0\sin(r_n)]d\Gamma(\mathbf{x}), \tag{18}$$

where α is 0 for field points in the interior domain and 1 in the exterior domain.

II. NUMERICAL METHOD

For the numerical implementation of the derived sensitivity equations, coordinates of the reference point should be found to obtain the sensitivities at the given field points near the boundary. The first step is to find the closest element to source point $\boldsymbol{\xi}$. This element can be determined among elements, on which the closest node to the source point lies. Then, the coordinates of the closest point can be found by employing the various optimization techniques.[12,13] The sequential quadratic programming method and the inaccurate line search algorithm are used in the present study.

Choosing an orthonormal basis on the boundary causes another problem in obtaining the rates of change of the boundary surface and the normal vector. Although the normal vector can be defined uniquely, two orthogonal tangential vectors can be chosen arbitrarily. The tangential vectors can be determined by the following manner. Suppose that the element is mapped on reference coordinate (u,v) as shown in Fig. 2 and a unit tangential vector **s** is chosen to be parallel with the u axis in the reference coordinate system. Then, another unit tangential vector **t** can be uniquely determined by using the orthonormality of **s**, **t**, and **n** as follows:

$$\mathbf{t} = \mathbf{n}\times\mathbf{s}. \tag{19}$$

The tangential derivatives can be obtained by the chain rule and the shape function. Let the auxiliary unit tangential vector **w** in the global coordinate system be defined such that it is parallel with the v axis in the reference coordinate system. Then, the two directional derivatives can be obtained as

$$\frac{\partial}{\partial s} = \frac{\partial}{\partial u}\frac{du}{ds}, \tag{20a}$$

$$\frac{\partial}{\partial w} = (\mathbf{s}\cdot\mathbf{w})\frac{\partial}{\partial s} + (\mathbf{t}\cdot\mathbf{w})\frac{\partial}{\partial t} = \frac{\partial}{\partial v}\frac{dv}{dw}. \tag{20b}$$

Using Eqs. (20), the tangential derivative with respect to **t** can be expressed as

$$\frac{\partial}{\partial t} = \left[\frac{\partial}{\partial v}\frac{dv}{dw} - (\mathbf{s}\cdot\mathbf{w})\frac{\partial}{\partial u}\frac{du}{ds}\right] \Big/ (\mathbf{t}\cdot\mathbf{w}). \tag{21}$$

It can be said that all the integrals in the propagating-wave-combined regularized sensitivity equation can be evaluated by using the standard Gaussian quadrature. However, the singular integral scheme is needed to utilize the potential-combined weakly singular representation for calculating the accurate sensitivity.

III. APPLICATION EXAMPLES

A. Exterior sound field of the pulsating sphere

The sound radiation from a uniformly pulsating sphere is chosen as an example for exterior problems. The spherical radius a was designated as the design variable, while the same surface velocity was maintained for every situation. The sensitivity of the acoustic pressure due to the variation of the radius was calculated at a field point and compared with the analytic solution. For a vibrating sphere with a uniform radial velocity v_n, the analytic pressure sensitivity at a field point is given by

$$\dot{p}(r) = \frac{\rho_0 c v_n ka[(kar - ka^2 - ja)(1+jka) + 2jr]}{r^2(1+k^2a^2)(1+jka)} \times\exp\{-jk(r-a)\}, \tag{22}$$

where r is the radial distance between the center of the sphere and the field point of interest.

For the numerical sensitivity analysis, the three-dimensional computer program was written and the boundary surface of the pulsating sphere with an initial radius of $a = 0.5$ m was discretized into 48 triangular, isoparametric,

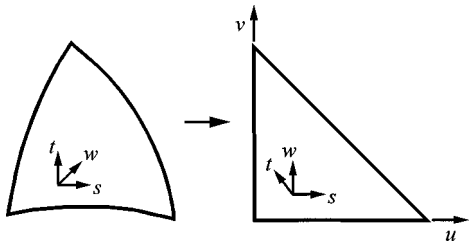

FIG. 2. Mapping of tangential vectors on the boundary.

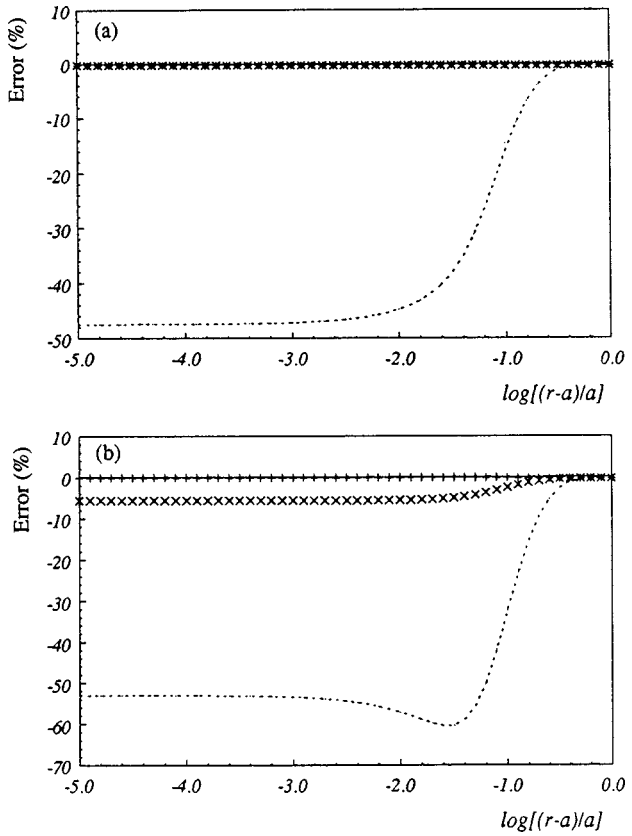

FIG. 3. Sensitivity of the acoustic pressure with respect to the change of the radius of the three-dimensional pulsating sphere: +, propagating-wave-combined regularized representation; ×, potential-combined weakly singular representation; ·····, strongly singular (conventional) representation. (a) Real part, (b) imaginary part.

quadratic elements. Sensitivity was calculated for $ka=0.5$ at some field points by approaching from the far field to the vibrating surface.

The nonuniqueness problem occurs in dealing with exterior problems due to the inherent mathematical nature of the Fredholm integral equation. In this study, the well-known overdetermined method is used for unique solutions in nonregular frequencies. However, the determination of reference point $\boldsymbol{\eta}$ is not easy for the overdetermination point $\boldsymbol{\xi}$ and this job can be done as follows: first, find the nearest node point from $\boldsymbol{\xi}$. Second, find all boundary elements that include this nearest node point. Third, find the nearest point $\boldsymbol{\eta}^e$ for each element by employing the optimization technique of which the object function is the distance from $\boldsymbol{\xi}$ and the constraint is the boundary of the element. Finally, select the smallest one from the calculated $\boldsymbol{\eta}^e$ set and this defines reference point $\boldsymbol{\eta}$. In general, all the points $\boldsymbol{\eta}^e$ except $\boldsymbol{\eta}$ converge to the points lying on the element boundaries due to the imposed constraints.

Figure 3 compares the accuracy of the predicted sensitivities of acoustic pressure by using the propagating-wave-combined regular representation in Eq. (17), by the potential-combined weakly singular representation in Eq. (8), and by the conventional representation in Eq. (6) containing the strong singularity. It is observed that all three equations can predict the sensitivity accurately at the far field and the material derivative concept is useful for the computation of

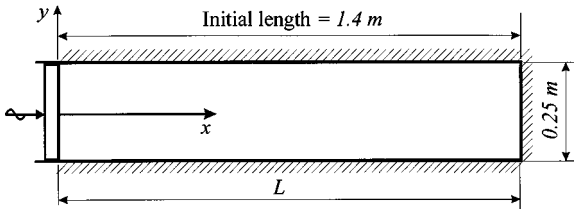

FIG. 4. Piston-driven rigid one-dimensional duct model.

acoustic sensitivity. However, the difference in accuracies of the three methods is very clear in the near field. Examining the behavior in the near field, one can find that the conventional singular method is very inaccurate. The inaccuracy of the conventional method is caused from the abrupt change of the coefficient of free term on the boundary. There is no change of the free term coefficient in the weakly singular and the regular formulas. The predicted sensitivity of the imaginary part using the potential-combined equation shows small error and this is definitely due to the remaining weak singularity. On the other hand, propagating-wave-combined regular representation predicts the sensitivity very accurately at all points. However, if the far field sensitivity is only of concern, the conventional representation provides enough accuracy for the sensitivity.

B. Interior sound field of the one-dimensional duct

As an example for interior problems, a uniform duct with a rigid termination which is harmonically driven at the other end[3] is taken for testing the applicability, as depicted in Fig. 4. Here, the sensitivity of the acoustic pressure due to the variation of duct length is to be calculated at interior field points.

The analytic pressure at an axial position x is given by

$$p(x)=\frac{A\cos(kL)}{k\sin(kL)}\cos(kx)+\frac{A}{k}\sin(kx), \tag{23}$$

where A is the normal gradient of the acoustic pressure on the driving piston, k is the wave number, and L is the duct length. From Eq. (23), one can easily obtain the following analytic sensitivity of the acoustic pressure with respect to the change of the length:

$$\frac{dp(x)}{dL}=-A\frac{\cos(kx)}{\sin^2(kL)}. \tag{24}$$

For the numerical sensitivity analysis, the boundary of the two-dimensional duct model with 1.4 m long and 0.25 m wide was discretized into 16 quadratic isoparametric line elements, and the discontinuous elements were used at corners to describe the abrupt change in boundary conditions.[11]

The calculation was performed for 100 Hz, $A=157$ and the design velocity $\mathbf{V}(\mathbf{x})$ of the boundary point at $\mathbf{x}$ was given by

$$V_x(x)=x/1.4 \tag{25a}$$

and

$$V_y(x)=0, \tag{25b}$$

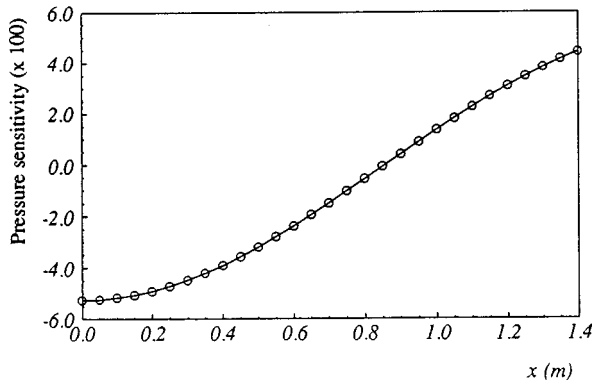

FIG. 5. Pressure sensitivity due to the length change of the duct: ○, BEM solution; ———, analytic solution.

while the design velocity at internal point was zero. Figure 5 shows the sensitivity of pressure obtained by the derived regular equation and compares it with the analytic solution in Eq. (24). One can find that the derived equation predicts the pressure sensitivity very accurately. The maximum relative error was 1.99% and occurs at the point having zero pressure sensitivity.

C. Automotive interior cavity

In the foregoing examples, the accuracy and applicability of the derived sensitivity formulations using the material derivative concept are investigated for regular geometries having analytic solutions. As an example for irregular domains, a simple two-dimensional automotive interior cavity[3] is taken for optimally reducing the noise level at the driver's ear position. The model is illustrated in Fig. 6 where the boundary is discretized into 120 quadratic line elements. Boundary conditions were given such that the harmonically vibrating velocity of the boundary between A and B, viz. the simplified dash panel, was 0.01 m/s uniformly for all frequencies and the other walls were assumed rigid. It was intended to optimize the depths of the cavity under the front seat, a, and the cavity between the rear seat and the tailgate, b, for minimizing the mean-squared acoustic pressure at the driver's ear position at a frequency or frequency band. To

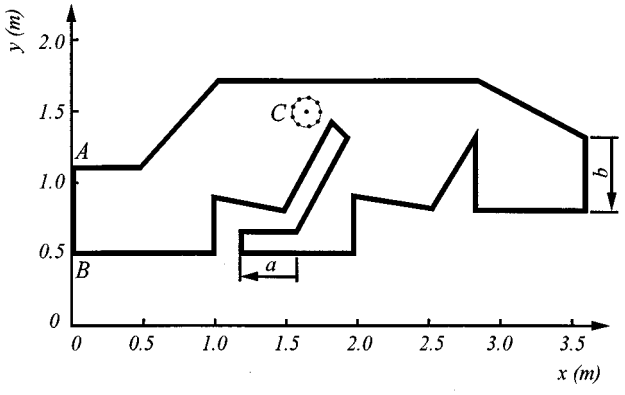

FIG. 6. Two-dimensional rigid wall model of an automotive interior cavity (Ref. 3). The excitation will be given to the section A-B with uniform velocity.

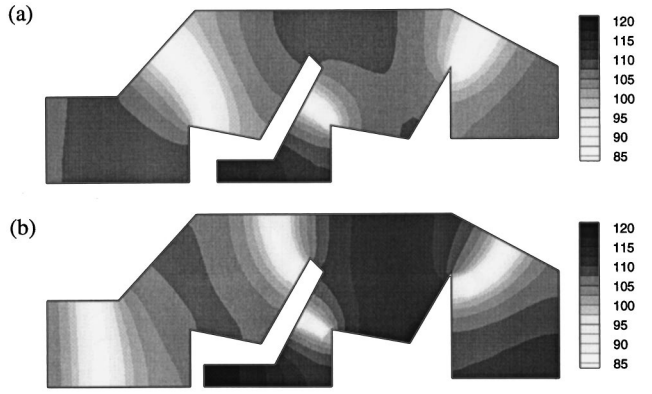

FIG. 7. Noise distribution in the car cavity at 105 Hz. (a) Initial shape, (b) optimal shape.

this end, 10 points denoted as region C near the driver's ear position were selected for calculating the noise level.

The object function and the upper and lower bounds of the design variables were as follows:

$$\text{minimize} \quad \Pi = \frac{1}{10} \sum_{i=1}^{10} p(\mathbf{x}^i) p^*(\mathbf{x}^i), \tag{26}$$

$$\text{subject to} \quad 0.1 \leqslant a \leqslant 0.5 \tag{27a}$$

and

$$0.1 \leqslant b \leqslant 0.8. \tag{27b}$$

Here, $\mathbf{x}^i$ is the location of the ith point in the region C selected for the calculation of the noise level and the asterisk denotes the complex conjugate. Initial starting values of a and b were 0.4 and 0.5, respectively. Before attempting to optimize, acoustic resonance frequencies and modes of the automotive cavity were estimated and the lowest four resonance frequencies were at 38.6, 68.4, 93.2, and 115.6 Hz.

Using the above conditions, the sizes of a and b were optimized for each vibrating frequency between 90 and 110 Hz at a spacing of 1 Hz by using the automated design synthesis (ADS). Figure 7 compares the sound field of optimal shape with initial one at 105 Hz and one can observe that the quiet region is adjusted from the front of the driver to the driver's head position. It was found that the lengths of a and b became longer than the initial ones at 105 Hz, but a and b became shorter for 93 Hz that was below the third longitudinal cavity mode.

When the transient operating condition is of concern, it can be said that the optimal shape for a frequency may no longer be the low noise configuration for other excitation frequencies. In practice, the firing frequency and its harmonics of the internal combustion engine vary with the engine rotational speed. In order to optimize the cavity shape adapting for the changing frequency condition, the frequency band concept should be introduced to the object function expression as follows:

$$\text{minimize} \quad \Pi = \frac{1}{10N_f} \sum_{i=1}^{10} p(\mathbf{x}^i, \omega) \mathbf{p}^*(\mathbf{x}^i, \omega). \tag{28}$$

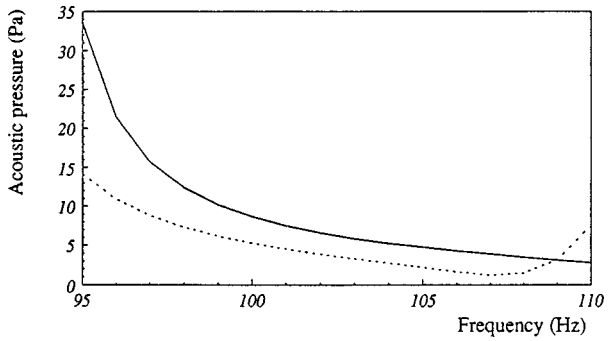

FIG. 8. Predicted acoustic pressure at the driver's head for frequencies between 95 and 110 Hz: ———, initial shape; ·····, optimal shape.

Here, N_f denotes the number of discrete frequencies for actual calculation within the frequency band of interest and the constraints are the same with Eq. (27).

Using the modified object function, the car cavity was optimized for the arbitrary frequency band between 95 and 110 Hz. Within this frequency range, the object function was evaluated at a spacing of 1 Hz. The acoustic pressure of the optimal shape is compared with the initial shape in Fig. 8, where optimum values were converged to $a=0.5$ and $b=0.6246$. In this figure, one can find that the noise is reduced below 108 Hz and increased above 109 Hz. Figure 9 shows the sound field in the interior of the band-optimized car cavity and a substantial reduction in noise level can be found at the driver's ear position.

IV. CONCLUDING REMARKS

The acoustic sensitivity equations for the shape design have been derived for acoustic problems based on the boundary integral equation. The sensitivity equations were derived by adopting the material derivative concept in the continuum mechanics. In order to investigate the precision and applicability of the derived formula, a pulsating sphere and a piston-driven duct were selected for typical exterior and interior problems, respectively.

Although the sensitivity in the far field can be accurately obtained by employing the material derivative concept, the predicted sensitivity in the near field by using the conventional method is very inaccurate. In order to resolve the problem, the singularity of integrands in the sensitivity equation has been reduced by usin the potential field and the one-dimensional wave propagation equations. Although the potential-combined approach is more accurate than the conventional method in the near field by removing the strong singularity, the predicted result still contains small error due to the remaining weak singularity. When the propagating-wave-combined regularized equation is used, all the singularities can be removed and very accurate sensitivity can be obtained near the boundary as well as in the far field. In this case, the potential field is no longer required to obtain the sensitivity, because the regularized equation uses the wave equation only.

Through three example calculations, the present method is found to be accurate and it is expected that the method can be applied to many acoustic problems, although, depending on the method and platforms in the implementation, the complexity of the formula and the computing time may not be advantageous compared to the method utilizing the finite difference technique.

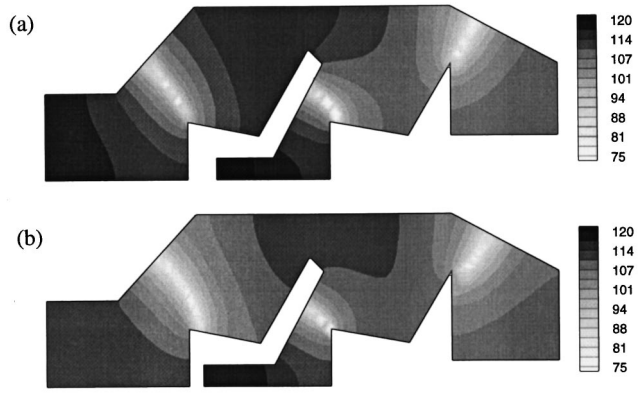

FIG. 9. Noise distribution in the car cavity at 98 Hz. (a) Initial shape; (b) optimal shape for the frequency band between 95 and 110 Hz.

ACKNOWLEDGMENTS

The authors wish to thank Dr. B.-K. Kim and I.-Y. Jeon for helping to prepare some of the figures in this work and appreciate Professor R. J. Bernhard at Purdue University for helpful discussions.

APPENDIX: MATERIAL DERIVATIVES OF VARIABLES

The material derivatives of point vectors can be written as

$$\dot{\mathbf{x}}=\mathbf{V}(\mathbf{x}), \quad \dot{\boldsymbol{\eta}}=\mathbf{V}(\boldsymbol{\eta}), \quad \dot{\boldsymbol{\xi}}=\mathbf{V}(\boldsymbol{\xi}). \tag{A1}$$

The material derivatives of the displacement vector and the distance are given by

$$\dot{\mathbf{r}}(\mathbf{x},\boldsymbol{\xi})=\mathbf{V}(\mathbf{x})-\mathbf{V}(\boldsymbol{\xi}), \tag{A2a}$$

$$\dot{r}(\mathbf{x},\boldsymbol{\xi})=[\mathbf{V}(\mathbf{x})-\mathbf{V}(\boldsymbol{\xi})]\cdot\mathbf{r}(\mathbf{x},\boldsymbol{\xi})/r, \tag{A2b}$$

where $\mathbf{r}(\mathbf{x},\boldsymbol{\xi})$ denotes the vector from $\boldsymbol{\xi}$ to $\mathbf{x}$ and $r(\mathbf{x},\boldsymbol{\xi})$ means the distance between $\boldsymbol{\xi}$ and $\mathbf{x}$.

The changes of boundary and normal vectors can be expressed as

$$d\dot{\Gamma}=(V_{i,s}s_i+V_{i,t}t_i)d\Gamma, \tag{A3}$$

$$\dot{n}_i=-V_{j,s}n_js_i-V_{j,t}n_jt_i, \tag{A4}$$

where **s** and **t** are two unit tangential vectors, and **s**, **t** and **n** are mutually orthonormal.

[1] Y. Ding, ''Shape optimization of structures: A literature survey,'' Comput. Struct. **24**, 985–1004 (1986).
[2] B. M. Kwak, ''A review on shape optimal design and sensitivity analysis,'' J. Structural Mechanics and Earthquake Engineering—JSCE **483**, 1–16 (1994).
[3] J. E. Huff and R. J. Bernhard, ''Acoustic shape optimization using parametric finite elements,'' Proc. 1995 ASME Design Engineering Technical Conferences, Vol. 3, part B, 577–584 (1995).
[4] J. H. Kane, S. Mao, and G. C. Everstine, ''A boundary element formulation for acoustic sensitivity analysis,'' J. Acoust. Soc. Am. **90**, 561–573 (1991).
[5] K. A. Cunefare and G. H. Koopmann, ''Acoustic design sensitivity for structural radiators,'' Trans. ASME, J. Vib. Acoust. **114**, 178–186 (1992).

[6] D. C. Smith and R. J. Bernhard, ''Computation of acoustic shape design sensitivity using a boundary element method,'' Trans. ASME, J. Vib. Acoust. **114**, 127–132 (1992).
[7] J. H. Kane and S. Saigal, ''Design-sensitivity analysis of solids using BEM,'' J. Eng. Mech.—ASCE **114**, 1703–1721 (1988).
[8] M. R. Barone and R. J. Yang, ''Boundary integral equations for recovery of design sensitivities in shape optimization,'' AIAA J. **26**, 589–594 (1988).
[9] M. R. Barone and R. J. Yang, ''A boundary element approach for recovery of shape sensitivities in three-dimensional elastic solids,'' Comput. Methods Appl. Mech. Eng. **74**, 69–82 (1989).
[10] E. J. Haug, K. K. Choi, and V. Komkov, *Design Sensitivity Analysis of Structural Systems* (Academic, New York, 1986).
[11] B.-U. Koo, B.-C. Lee and J.-G. Ih, ''A non-singular boundary integral equation for acoustic problems,'' J. Sound Vib. **192**, 263–279 (1996).
[12] D. G. Luenberger, *Linear and Nonlinear Programming*, 2nd ed. (Addison-Wesley, Menlo Park, 1984).
[13] M. S. Bazaraa and C. M. Shetty, *Nonlinear Programming* (Wiley, New York, 1979).

Potential of microperforated panel absorber

Dah-You Maa
Institute of Acoustics, Academia Sinica, P.O. Box 2712, Beijing 100080, People's Republic of China

(Received 7 November 1997; accepted for publication 16 July 1998)

Many applications have been found for the microperforated panel (MPP) absorber, on which the perforations are reduced to submillimeter size so that they themselves will provide enough acoustic resistance and also sufficiently low acoustic mass reactance necessary for a wide-band sound absorber. The most important parameter of the MPP is found to be the perforate constant k which is proportional to the ratio of the perforation radius to the viscous boundary layer thickness inside the holes. This, together with the relative (to the characteristic acoustic impedance in air) acoustic resistance r and the frequency f_0 of maximum absorption of the MPP absorber, decides the entire structure of the MPP absorber and its frequency characteristics. In other words, the MPP absorber may be designed according to the required absorbing characteristics in terms of the parameters k, r, and f_0. Formulas and curves are presented toward this end. It is shown that the MPP absorber has tremendous potential for wide-band absorption up to 3 or 4 octaves and for low-frequency absorption with a cavity of depth small compared to the wavelength. Techniques of making minute holes (of 0.1–0.3 mm, say) have to be developed, though. [S0001-4966(98)05710-5]

PACS numbers: 43.50.Gf, 43.55.Ev, 43.50.Jh [MRS]

INTRODUCTION

Perforated panels have been developed and used for some years,[1] but the necessary use of porous materials with it has reduced it to protective covering material.[2] Microperforated panels (MPP) were developed in the late sixties of the twentieth century, when a robust sound absorber was needed for severe environments, without fibrous, porous materials. An approximate theory was presented later.[3] Unlike ordinary perforated panels where the perforations are in millimeters or even centimeters, with scarcely little inherent acoustic resistance, the perforations in MPP were reduced to submillimeter size (diameter 0.5–1 mm), so as to provide, by themselves, enough acoustic resistance and low acoustic mass reactance necessary for wide-band sound absorber, without additional fibrous, porous materials. Up to the present, the MPP absorber has usually provided sound absorption in a frequency band of one to two octaves, a wide band which no other resonator-absorber can do. But still, it is not quite enough for a general purpose sound absorber. Double resonators with two MPPs in tandem have been developed,[4,5] and special design problems considered,[6] to broaden the absorption band.

The MPP absorbers have a simple structure and absorption characteristics that are exactly predictable. The panel may be made of any material from cardboard, plastic, plywood to sheet metal, with any finishing or decoration to suit the purpose.[7] The fact that the designs within the framework of the existing theory have limited absorption band is due to reasons not in the MPP absorber itself, but in the approximation made in the existing theory. It is the purpose of the present work to find the exact solution of the MPP equations in order to get a full view of the possibilities of the MPP absorber to facilitate better exploitation of the MPP absorbers.

It is found that the structure and frequency characteristics of the MPP absorber depend on its relative acoustic resistance r, the resonance frequency f_0, and the perforate constant $k=r_0\sqrt{\rho_0\omega/\eta}$ of the perforations, where r_0 is the radius of the perforations, ω the angular frequency, and η the coefficient of viscosity. The maximum absorption coefficient occurs at the resonance frequency f_0 and the possible band width is found to be given by the frequency interval (the ratio of the upper to lower half-absorption frequencies) $B=\pi/\cot^{-1}(1+r)-1$, which may be very large when r is large. But the realization of the tremendous potential of the MPP absorber depends on the key parameter k. For a considerable range of k values, the maximum possible bandwidth becomes reality or near to reality. The absorption band narrows down quickly when k is increased beyond a certain value. But a small value of k calls for minute holes. Thus the perforate constant is essential for the MPP absorber design structure as well as characteristics.

I. THE MICROPERFORATED PANEL[1]

The MPP may be considered a lattice of short narrow tubes, separated by distances much larger then their diameters, but small compared to the wavelength of impinging sound wave. The propagation of a sound wave in a tube was treated by Lord Rayleigh,[8] and the treatment was simplified by Crandall[9] for short tubes. The equation of aerial motion in a tube short compared to the wavelength is

$$j\omega\rho_0 u-\frac{\eta}{r_1}\frac{\partial}{\partial r_1}\left(r_1\frac{\partial}{\partial r_1}u\right)=\frac{\Delta p}{t}, \tag{1}$$

where Δp is the sound pressure difference between the ends of the tube, t the length of the tube (equal to the thickness of the panel), ρ_0 the density of air, η its coefficient of viscosity, and r_1 the radius vector of cylindrical coordinates inside the tube. The equation may be solved for the particle velocity u, and the ratio of Δp to the average value of u over the cross-

sectional area of the tube gives the specific acoustic impedance of the short tube

$$Z_1=\frac{\Delta p}{\overline{u}}=j\omega\rho_0 t\left[1-\frac{2}{k\sqrt{-j}}\frac{J_1(k\sqrt{-j})}{J_0(k\sqrt{-j})}\right]^{-1}, \tag{2}$$

where $k=r_0\sqrt{\rho_0\omega/\eta}$ (x had been used for this quantity in earlier papers,[1] it is changed here to avoid confusion), r_0 is the radius of the tube, J_1 the Bessel function of the first kind and first order, and J_0 same of zeroeth order. It is seen that the quantity k is proportional to the ratio of the radius to the viscous boundary layer thickness inside the tube, and may be termed as the perforate constant. The limiting values of Z_1 for small and large values of k were given by Crandall as

$$Z_1\rightarrow\frac{4}{3}j\omega\rho_0 t+\frac{32\eta t}{d^2}, \quad \text{as } k<1, \tag{3a}$$

$$\rightarrow j\omega\rho_0 t+\frac{4\eta t}{d}\sqrt{\frac{\omega\rho_0}{2\eta}}(1+j), \quad \text{as } k>10. \tag{3b}$$

These formulas have been used since Zwikker and Kosten[1] in the theory of absorbing materials. But the intermediate values of k between 1 and 10 are very important, especially for the MPP. An approximate formula,

$$Z_1=\frac{32\eta t}{d^2}\left(1+\frac{k^2}{32}\right)^{1/2}+j\omega\rho_0 t\left(1+\left(3^2+\frac{k^2}{2}\right)^{-1/2}\right), \tag{4}$$

has been developed to be valid for all k values by combining Eqs. (3a) and (3b) so that it becomes Eq. (3a) when k^2 terms in the brackets are omitted (k small) and Eq. (3b) when the k^2 terms are only retained (k large). The maximum error is only about 6% at some value of k between 1 and 10 from the exact value given by Eq. (2).

In Eq. (4) it is necessary to add the end corrections which have been discussed by Morse and Ingard.[10] In his resonator paper,[11] Ingard suggested the use of values due to Rayleigh,[12] viz., the resistance due to air flow friction on the surface of the panel, $(1/2)\sqrt{2\omega\rho_0\eta}$ (the value used in earlier papers[3] was too high, error is introduced when k is large), as the air flow is squeezed into the small area of the inlet end of the hole; and the mass reactance due to the piston sound radiation at both ends, 0.85 d. For normal incidence of sound wave on the panel, the wave motion in all the short tubes is in-phase and additive. The relative (to the characteristic impedance $\rho_0 c$ in air) acoustic impedance of the MPP is then

$$z=Z_1/(\sigma\rho_0 c)=r+jx_m=r+j\omega m, \tag{5}$$

where

$$r=\frac{32\eta t}{\sigma\rho_0 c d^2}k_r, \quad k_r=\left[1+\frac{k^2}{32}\right]^{1/2}+\frac{\sqrt{2}}{32}k\frac{d}{t}, \tag{5a}$$

$$\omega m=\frac{\omega t}{\sigma c}k_m, \quad k_m=1+\left[1+\frac{k^2}{2}\right]^{-1/2}+0.85\frac{d}{t}, \tag{5b}$$

and

$$k=d\sqrt{\omega\rho_0/4\eta}, \tag{6}$$

where d is the orifice diameter, and t the panel thickness. [A useful design formula obtained from Eq. (6) is $k=d\sqrt{f/10}$, where d is specified in mm and f, in Hz.] The ratio d/t is usually nearly one and is taken so, small variations of the actual value are not important. The resistance coefficient k_r, mass reactance coefficient k_m, and their ratio k_m/k_r, important in the computation of r, m, and x_m, are plotted in Fig. 1 as functions of k. It is seen that k_m is practically constant, varying only by 2% in the range from 0.1 to 5 of k, but the resistance coefficient k_r increases with k significantly, especially when k is larger than 1. The maximum error of the approximate formula of acoustic impedance (5) is also 6% compared to the exact value from Eq. (2). Measurement techniques have been proposed for the orifice.[10,13,14] Experiments[15] agree well with the theoretical results (5) within 10% when the sound intensity is low, and further end corrections are necessary due to jet formation at the ends of the tubes,[15,16] when the sound pressure level is well over 100 dB, depending on the perforation area ratio and resonance condition (about 100 dB at resonance when $\sigma=0.01$). The end correction of the mass reactance, however, decreases with increasing intensity, perhaps due to the fact that the piston radiation at the ends of the narrow tube is partly blown away by the jet formed at the high intensity and it is proposed[16] that the end correction of the acoustic mass should change the last term of k_m to $0.85(d/t)(1+u_0/\sigma c_0)^{-1}$, where u_0 is the peak particle velocity inside the tube and σ the perforation ratio. The linear and nonlinear end corrections do not seem to be directly additive. Only the linear end corrections exist when the sound intensity is low, and the end corrections gradually change from linear values to nonlinear values after the particle velocity inside the tubes exceeds a certain value.

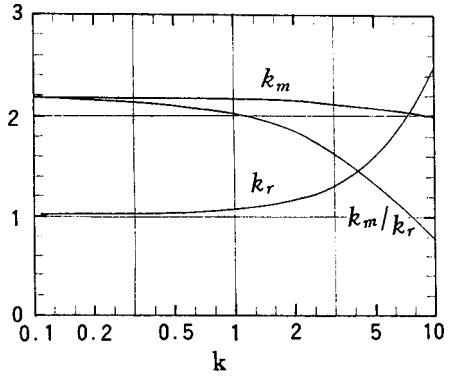

FIG. 1. Constants of MPP as functions of the perforate constant. k_r—resistance coefficient; k_m—mass reactance coefficient.

The perforation area ratio may be found from the resistance equation (5a) to be given by

$$\sigma/t=\frac{32\eta}{\rho_0 c}k_r/(rd^2). \tag{7}$$

The value of this ratio is important, while a small change of σ or t is usually allowed (t is ordinarily taken to be equal to d, because it is nearly so) the exact value is necessary here. Substituting this ratio into Eq. (5b), it yields the mass reactance

$$x_m=(k_m/8k_r)rk^2. \tag{8}$$

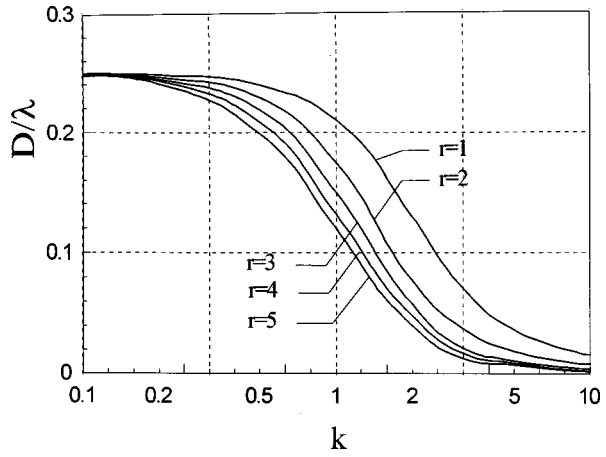

FIG. 2. Relative cavity depth D/λ as function of perforate constant k for different values of relative acoustic resistance.

This does not change the value of x_m; it only relates x_m to the choice of r. The value of the ratio k_m/k_r is approximately 2 in the range of k from 0.5 to 2, which is the most important region in MPP design. Equation (8) may be taken as $x_m = 0.25rk^2$ in this region.

II. THE MPP ABSORBER

A microperforated panel fixed before a solid surface with a cavity of thickness D makes an MPP absorber. The relative acoustic resistance r and mass reactance $x_m = \omega m$ are given by Eq. (5) and the relative acoustic reactance of the cavity is $-\cot \omega D/c$. For normal incidence, the sound absorption coefficient is

$$\alpha = \frac{4r}{(1+r)^2 + (\omega m - \cot(\omega D/c))^2}. \tag{9}$$

Its maximum value

$$\alpha_0 = 4r/(1+r)^2 \tag{10}$$

occurs at the resonance frequency f_0 given by

$$\omega_0 m - \cot \frac{\omega_0 D}{c} = 0. \tag{11}$$

This gives

$$\frac{\omega_0 D}{c} = \cot^{-1}\ \omega_0 m \tag{12}$$

and the cavity depth ratio is obtained by a division with 2π

$$\frac{D}{\lambda} = \frac{1}{2\pi} \cot^{-1}\ \omega_0 m, \tag{13}$$

λ being the wavelength corresponding to the resonance frequency f_0, Thus given the values of k, r and f_0, the structure of the MPP absorber is completely determined. The cavity depth ratio as given by Eq. (13) is plotted in Fig. 2. It is 1/4 for all r values, when k is zero, it decreases linearly but slowly as k increases, with a rate proportional to r at first, and then the rates increase to a maximum and finally it levels off to a rather small value when k is large. This gives the possibility of a very thin absorber for low frequency. An

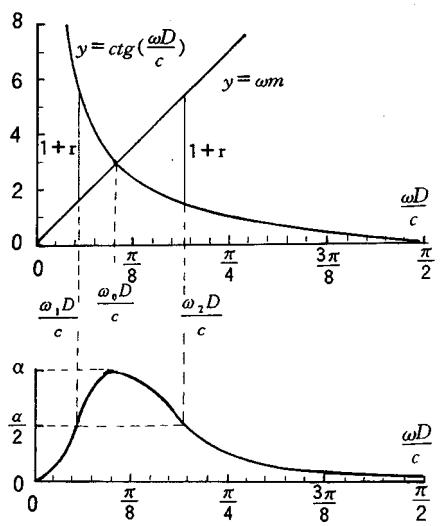

FIG. 3. Absorption band of MPP absorber.

important quantity is the ratio of ωm to $\omega_0 D/c$, or the ratio of the mass and cavity reactances at low frequency,

$$g = mc_0/D = \omega_0 m/\cot^{-1}\ \omega_0 m, \tag{14}$$

which is essentially a constant of the MPP, practically independent of frequency, and will prove to be important in the frequency characteristics of the MPP absorber.

The absorption coefficient α is one-half of the maximum value (10) at the frequencies given by

$$\omega m - \cot(\omega D/c) = \pm(1+r). \tag{15}$$

The resonance and half-absorption points are shown graphically in Fig. 3 of the ωm and $\omega D/c$ curves. In the figure, $\omega D/c$ is taken as the abscissa, which is proportional to the frequency. Thus the cotangent curve is valid for all designs, and the ωm line is nearly a straight line with a slope g given by Eq. (14). The lines intersect at the point of resonance, and their values differ by $1+r$ at half-absorption points. It is evident that the absorption band is wider as the value of $\omega_0 m$ is smaller, and also as r is larger. This is important when a wide-band MPP absorber is designed.

III. ABSORPTION BANDWIDTH

Equation (15) may be converted into an equation of the half-absorption frequencies,

$$\frac{\omega D}{c} = \cot^{-1}\left[\mp(1+r) + g\ \frac{\omega D}{c} \right], \tag{16}$$

with the help of Eq. (14), where the plus and minus sign is for the lower and higher half-absorption frequencies, respectively. The equation is quite simple, but an exact solution is not readily available. An approximate solution is, however, easy when g is small. From the derivative of the arccotangent function

$$\frac{d}{dx} \cot^{-1}\ \frac{x}{a} = -\frac{a}{a^2 + x^2}. \tag{17}$$

Equation (16) becomes, for the lower half-absorption frequency,

TABLE I. Absorption bandwidth possible of MPP absorber for different values of r ($k=0$, $D/\lambda=0.25$).

r	1	2	3	4	5
α_0	1	0.89	0.75	0.64	0.56
$(f_2-f_1)/f_0$	1.41	1.59	1.69	1.75	1.79
f_2/f_1	5.78	8.76	11.82	14.91	18.02

$$\frac{\omega_1 D}{c}=\cot^{-1}\left[(1+r)+g\,\frac{\omega_1 D}{c}\right],$$

$$=\cot^{-1}(1+r)-\frac{1}{1+(1+r)^2}\cdot g\,\frac{\omega_1 D}{c}, \tag{18}$$

for low values of g. Solving

$$\frac{\omega_1 D}{c}=\cot^{-1}(1+r)\Big/\left[1+\frac{g}{1+(1+r)^2}\right] \tag{19}$$

to the first order of approximation. Similarly, for the upper half-absorption frequency,

$$\frac{\omega_2 D}{c}=[\pi-\cot^{-1}(1+r)]\Big/\left[1+\frac{g}{1+(1+r)^2}\right]. \tag{20}$$

The frequency interval is the ratio of Eq. (20) to (19)

$$B=f_2/f_1=[\pi/\cot^{-1}(1+r)]-1, \tag{21}$$

which is constant to the first order of approximation, as g is small compared to unity. Thus the frequency interval of the absorption band of the MPP absorber is practically constant so far as rk^2 is smaller than 1. The possible values of B as well as the relative band width $F=(f_2-f_1)/f_0$ are tabulated in Table I, for different values of r. As the absorption coefficient α_0 is not sensitive to the variation of acoustic resistance r, Eq. (21) as well as Table I demonstrate the possibility of exchanging bandwidth with absorption. The resonance frequency, however, varies with k all the way, as

$$\frac{\omega_0 D}{c}=\cot^{-1}(\omega_0 m)=\cot^{-1}[(k_r/8k_m)rk^2],$$

from Eqs. (8) and (11). It is $\pi/2$ when k is zero, and decreases slowly as k increases, exactly in the fashion of the cavity depth ratio (13), because the difference is only by a constant factor. It can be found that the resonance frequency is nearly the average of f_1 and f_2 when k is very small and gradually changes to their geometric mean when k is large.[3,5] The resonance-absorption curve changes gradually from symmetrical to unsymmetrical, accordingly. The ratio of the resonance frequency to the lower half-absorption frequency is of interest, and may be found as

$$FR=\frac{f_0}{f_1}=\left(1+r+\frac{g+1/3}{1+r}\right)\cot^{-1}(\omega_0 m), \tag{22}$$

if $g+1/3$ is small compared to $(1+r)^2$, $\omega_0 m$ is given by Eq. (8).

IV. ROLE OF THE PERFORATE CONSTANT *k*

Exact solution of Eq. (15) is desirable in order to have a view of the whole picture of the frequency characteristics of the MPP absorber. Numerical techniques were used to find the frequency interval in terms of r and k. The result is plotted in Fig. 4, showing the dependence of the frequency interval of absorption on the perforate constant k for different values of the acoustic resistance r. The magnitude of r decides the maximum possible bandwidth, but its realization is controlled by the value of k. The maximum possible values tabulated in Table I occur only when $k=0$. The values of B change little when k is small, reducing, for instance, only by 1% when k is increased to 0.9 (for $r=1$) or to 0.7 (for $r=5$). Shortly after these, the values of B drop rather steeply, more so for higher r, and the values for different r come closer and closer, at increasing values of k. The curves for r equal 2 and up cross each other between the values 1.25 and 1.6 of k, and the curve for $r=1$ comes slightly later. The order of the curves reverses after each crossing, and the curve for higher r lies lower, or the bandwidth is narrower for larger r. Thus, it is meaningless to take higher values of r if k is large. In other words, small values of k are essential for the wide-band MPP absorber. Larger values of k, however, are found important when r is small.

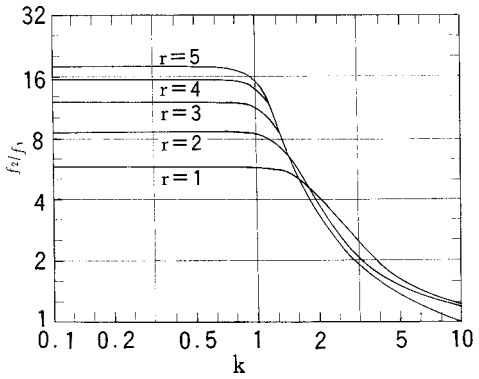

FIG. 4. Frequency interval of MPP absorption band as a function of the perforate constant k for different values of relative acoustic resistance.

V. ABSORPTION IN DIFFUSE SOUND FIELD

The above sections are all for normal incidence of sound on the MPP absorber. In the case of oblique incidence, the MPP itself, as a locally reacting material, has its acoustic impedance $r+j\omega m$ unchanged. But in the cavity behind the panel, sound travels in direction θ to the normal, the same as the angle of incidence in the field, and the incident and reflected waves in the cavity have path difference $2D\cos\theta$ instead of $2D$ for normal incidence. Thus the relative acoustic impedance of the cavity becomes $(1/j\cos\theta)\times\cot((\omega D/c)\cos\theta)$. The relative acoustic impedance on a unit area of the panel surface for oblique-incident wave is thus

$$z=(r+j\omega m)\cos\theta-j\cot\left(\frac{\omega D}{c}\cos\theta\right),$$

and the absorption coefficient may be calculated as[5]

$$\alpha_0=\frac{4r\cos\theta}{(1+r\cos\theta)^2+\left(\omega m\cos\theta-\cot\dfrac{\omega D}{c}\cos\theta\right)^2} \tag{23}$$

as the case discussed in Morse and Ingard.[17,18] As a result, r, m, and D are all multiplied by the cosine. A multiplication of r by $\cos\theta$ means an increase of the absorption coefficient, if r is larger than one. The multiplication of m and D by the cosine is equivalent to a multiplication of ω by $\cos\theta$, as m and D of the MPP are fixed constants. Thus the resonance and the half-absorption frequencies are increased by the ratio $1/\cos\theta$, and the absorption band is shifted to higher frequencies. In a diffuse field, sound is incident at all angles on the MPP, and the absorption band extends continually to higher frequencies, and is broadened. Moreover, the cotangent curve is many branched, and the absorption band shown in Fig. 3 repeats itself when the argument is increased by π and its multiples, and there are many absorption bands along the frequency scale. The gap between the bands depends on the bandwidth of each band. The gaps between absorption bands will be, more or less, filled up if the bandwidth of each band is broad enough. Thus the absorption range of the MPP absorber is extended considerably in a diffuse sound field.

VI. DISCUSSION

It has been shown that the important parameters of the MPP absorber are its relative acoustic resistance r, determining its maximum absorption coefficient α_0, the resonance frequency f_0 of the maximum absorption, and the perforate constant $k=r_0\sqrt{\rho_0\omega/\eta}$. These three parameters determine the structure and frequency characteristics of the MPP absorber.

The maximum absorption coefficient and maximum possible absorption bandwidth are decided by the value of r. An extremely wide band with good absorption is found to be possible with the MPP absorber, but its realization is limited by the value of the perforate constant. With the aid of Fig. 4, the values of k, r, and f_0 necessary to fulfill the frequency characteristics required of the absorber may be chosen. The resonance frequency is found from the frequency ratio (22). The desired frequency characteristics of the absorber are converted to a set of parameters. The design of the absorber may then be started from the absorption requirements of the absorber, expressed by the values of the parameters k, r, and f_0. The perforation diameter required is found from Eq. (6) as

$$d=2k\sqrt{\eta/\omega\rho_0}. \tag{24}$$

From Eq. (5a) of the relative acoustic resistance of the MPP, it may be solved by Eq. (7) for the perforation area ratio σ for panel thickness t, while k_r is given by Eq. (5a) and plotted in Fig. 1, taking $t/d=1$. The exact value of t/d is not important for the value of k_r unless it is far from 1, because it is in the correction term, and does not affect much. σ is the perforation area ratio and related to the ratio d/b as

$$\sigma=(\pi/4)(d/b)^2, \tag{25}$$

b being the separation of the perforations, if they are arranged in square lattices, and equivalently,

$$b=d\sqrt{\pi/4\sigma}. \tag{26}$$

Thus the constants of the microperforated panel are all determined, and the cavity depth ratio D/λ, which is given in Eq. (13) and plotted in Fig. 2, determines the cavity depth. The mass reactance is given in Eq. (8), and the factor k_m/k_r which is plotted in Fig. 1. Thus the design of the MPP absorber from the required k, r, and f_0 is simple and straightforward.

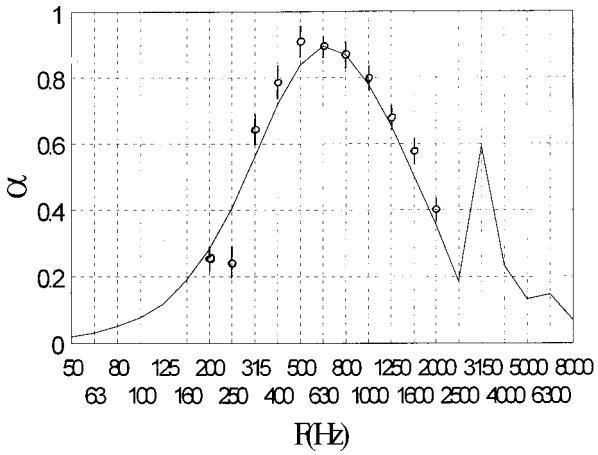

FIG. 5. Absorption curve of MPP absorber designed for 250–2000 Hz. $d=t=0.2$ mm, $b=2.5$ mm, $D=0.06$ m, ——— theory, ○○○ experimental points.

Take, for example, a general purpose sound absorber, an absorption band from 250–2000 Hz being desirable. This requires a frequency interval of 8. The family of f_2/f_1 curves in Fig. 4 indicate that this can be satisfied with a value of 1.25 for k and a value of r slightly over 2. The ratio of the resonance frequency to the lower half-absorption frequency for these k and r values is found from Eq. (22) as 3.05, and hence f_0 is to be 760 Hz. From these parameters, the constants of the MPP may be found as $d=t=0.144$ mm, $\sigma=0.52\%$, or $b=1.77$ mm; the cavity depth formula (13) gives a value of 0.14 for D/λ, and D is 0.064 m. Thus the design is completed. An absorber with maximum absorption coefficient 0.88 and half-absorption between 250 and 2000 Hz is obtained. This calls for the making of minute holes, new techniques needed to be developed to realize the wideband and high absorption possibility of the MPP absorber. Otherwise, some compromise must be made; if a lower resonance frequency is taken, for instance, $f_0=380$ Hz. The design will become $d=t=0.2$ mm, $b=2.5$ mm, and $D=0.12$ m. The realization is easier, but the frequency range of absorption drops to 125–1000 Hz. The result is shown in Fig. 5, in which the solid line is the theoretical curve and the circles are obtained in measurements in a standing wave tube.

ACKNOWLEDGMENTS

This work has been supported by a grant from the National Natural Science Foundation of China. The figures were prepared by Professor Ke Liu.

[1] C. Zwikker and C. W. Kosten, *Sound Absorbing Materials* (Elsevier, New York, 1949), Chap. II.
[2] L. L. Beranek, Ed., *Noise and Vibration Control* (McGraw-Hill, New York, 1971), p. 267.
[3] D.-Y Maa, ''Theory and design of microperforated-panel sound-absorbing construction,'' Sci. Sin. **XVIII**, 55–71 (1975).

[4] D.-Y. Maa, ''Wide band sound absorber based on microperforated panels,'' *Proc. Inter-noise 84* (Honolulu, 1984), pp. 415–420; Chin. J. Acoust. **4**, 197–208 (1985).
[5] D.-Y. Maa, ''Microperforated Panel wide-band absorber,'' Noise Control Eng. J. **29**, 77–84 (1987).
[6] D.-Y. Maa, ''Design of microperforated panel construction,'' Acta Acust. **13**, 174–180 (1988); Chin. J. Acoust. **7**, 193–200 (1988).
[7] H. V. Fuchs and X. Zha, ''Transparente Vorsatzschalen als alternative Schallabsorber im Plenarsaal des Bundestages,'' Bauphysik **16**, 69–80 (1994); ''Einsatz microperforierter Platten als Schallabsorber mit inharenter Dampfung,'' Acustica **81**, 107–116 (1995).
[8] Lord Rayleigh, *Theory of Sound II* (MacMillan, New York, 1929 ed.), p. 327.
[9] I. B. Crandall, *Theory of Vibration System and Sound* (Van Nostrand, New York, 1926), pp. 229 et seq.
[10] P. M. Morse and U. Ingard, *Theoretical Acoustics* (McGraw-Hill, New York, 1968), pp. 460–463.
[11] U. Ingard, ''On the theory and design of acoustic resonators,'' J. Acoust. Soc. Am. **25**, 1044 (1953).
[12] Lord Rayleigh, Ref. 8, pp. 317–318, 487–491.
[13] M. R. Stinson and A. E. G. Shaw, ''Acoustic impedance of small circular orifices in the plates,'' J. Acoust. Soc. Am. **77**, 2039–2042 (1985).
[14] D.-Y. Maa, ''Measurements of acoustic impedences,'' in *Proc. ICA 12* (Toronto, 1986), M3-1.
[15] D.-Y. Maa, ''Direct and accurate measurements of acoustic impedance of the microperforated panel,'' Acta Acust. (in Chinese) **8**, 257–261 (1983).
[16] D.-Y. Maa, ''Microperforated panel at high sound intensity,'' *Proc. Inter-noise 94* (Yokohama, 1994), pp. 1511–1514; Acta Acust. **21**, 257–262 (1996).
[17] Reference 10, Eq. (6.3.8), p. 264.
[18] K. U. Ingard and H. Ising, ''Acoustical nonlinearity of an orifice,'' J. Acoust. Soc. Am. **42**, 6–17 (1967).

Acoustic attenuation performance of circular flow-reversing chambers

A. Selamet and Z. L. Ji
Department of Mechanical Engineering and The Center for Automotive Research, The Ohio State University, Columbus, Ohio 43210-1107

(Received 16 September 1997; accepted for publication 25 July 1998)

A three-dimensional analytical approach is developed to determine the transmission loss of circular flow-reversing chambers in the absence of bulk flow. The study couples the continuity conditions of the acoustic pressure and particle velocity at the inlet and outlet with the orthogonality relations of Fourier–Bessel functions. The present analytical results are compared with the boundary element predictions to assess the approach, as well as with previous works to examine the effect of nonplanar wave decay in end ducts. The acoustic attenuation due to flow-reversing chamber is then investigated in detail as a function of the length-to-diameter ratio of the chamber and the relative locations of the inlet/outlet. © *1998 Acoustical Society of America.* [S0001-4966(98)01711-1]

PACS numbers: 43.50.Gf, 43.20.Ks [MRS]

INTRODUCTION

Several studies[1–3] have developed analytical approaches for concentric and asymmetric (with offset inlet/outlet) expansion chambers. The inlet and outlet in these works are located on separate endplates. The present study concentrates on a configuration where both inlet and outlet are located on the same endplate. This configuration is known as the flow-reversing chamber, which is an important component of the exhaust mufflers in production vehicles. The higher order modes are excited at the area discontinuities of these silencers, and do not decay fully before reaching the other opening because of the close proximity of inlet and outlet. Therefore multi-dimensional wave propagation needs to be considered both in the chamber and the end ducts for an accurate prediction of the acoustic attenuation performance of these chambers even at low frequencies. Young and Crocker[4] studied the acoustic characteristics of short flow-reversing chambers with elliptical cross section, using the finite element method (FEM), and concluded that the flow-reversing chambers have two completely different transmission loss characteristics: one is similar to that of the simple expansion chamber and the other to that of a side-branch resonator. Ih and Lee[5] developed a three-dimensional analytical approach for circular flow-reversing chambers, and their results matched the experimental transmission loss fairly well over a wide frequency range. The chamber is modeled as a piston-driven circular rigid tube and the sound pressures on the inlet and outlet are averaged over the cross-sectional area. Thus they have chosen to exclude the inlet and outlet ducts. The resulting predictions in the absence of these ducts are expected to show some difference relative to the experiments performed with the end ducts, particularly for shorter chambers due to the importance of nonplanar wave decay.

The objective of the present study is to develop a three-dimensional analytical approach to determine the transmission loss of circular flow-reversing chambers including the end ducts. This approach is used to investigate the effect of the length-to-diameter ratio of the chamber and the relative locations of the inlet/outlet on the acoustic attenuation performance of flow-reversing chamber. The boundary element method (BEM), which has been applied successfully to predict the transmission loss of expansion chamber mufflers,[6,7] is also employed to examine the analytical approach.

Following the Introduction, Sec. I describes the three-dimensional analytical approach, while deferring some details to Appendixes A and B. Section II presents and discusses the results, and Sec. III concludes the study with final remarks.

I. THREE-DIMENSIONAL ANALYTICAL APPROACH

For a circular flow-reversing chamber with inlet/outlet ducts shown in Fig. 1, the sound field in each cylindrical section may be expressed analytically as described in Appendix A. Equations (A2) and (A8) can be used for waves *A*, *C*, and *E* traveling in the positive *z* direction, and Eqs. (A3) and (A9) for waves *B*, *D*, and *F* traveling in the negative *z* direction. At the right side of chamber, the rigid endplate boundary condition gives

$$(U_C+U_D)|_{z=l}=0. \tag{1}$$

Substitution of Eqs. (A8) and (A9) into Eq. (1) yields

$$D_{00}=C_{00}e^{-j2kl}, \quad D_{0n}=C_{0n}e^{j2k_{0n}l},$$
$$D^{+}_{mn}=C^{+}_{mn}e^{j2k_{mn}l}, \quad D^{-}_{mn}=C^{-}_{mn}e^{j2k_{mn}l}. \tag{2}$$

At the left side of chamber, the continuity conditions reveal, for the pressure,

$$(P_A+P_B)|_{z=0}=(P_C+P_D)|_{z=0} \quad (\text{on } S_1) \tag{3}$$

$$(P_C+P_D)|_{z=0}=(P_E+P_F)|_{z=0} \quad (\text{on } S_2) \tag{4}$$

and the continuity and boundary conditions, for the velocity,

$$(U_A+U_B)|_{z=0}=(U_C+U_D)|_{z=0} \quad (\text{on } S_1), \tag{5}$$

$$(U_C+U_D)|_{z=0}=(U_E+U_F)|_{z=0} \quad (\text{on } S_2), \tag{6}$$

$$(U_c+U_D)|_{z=0}=0 \quad (\text{on } S-S_1-S_2); \tag{7}$$

where S, S_1, and S_2 are the cross-sectional areas of chamber, inlet, and outlet ducts, respectively. In order to establish a set of independent equations to determine the amplitude coefficients, the foregoing equations are coupled with the orthogonality of Fourier–Bessel functions for the pressure and velocity conditions.

For the pressure condition at inlet, multiply both sides of Eq. (3) by $J_t(\alpha_{ts} r_1/a_1)e^{jt\varphi}\,dS$ and integrate over S_1 to get, for $t=0$ and $s=0$,

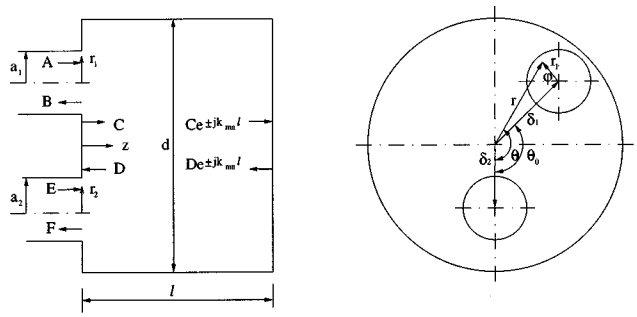

FIG. 1. Geometry of the circular flow-reversing chamber.

$$[A_{00}+B_{00}]\,\frac{a_1^2}{2}=C_{00}(1+e^{-j2kl})\,\frac{a_1^2}{2}+\sum_{n=1}^{\infty}C_{0n}(1+e^{j2k_{0n}l})\,\frac{aa_1}{\alpha_{0n}}\,J_0(\alpha_{0n}\delta_1/a)J_1(\alpha_{0n}a_1/a)$$
$$+\sum_{m=1}^{\infty}\sum_{n=0}^{\infty}[C_{mn}^{+}e^{-jm\theta_0}+C_{mn}^{-}e^{jm\theta_0}](1+e^{j2k_{mn}l})\,\frac{aa_1}{\alpha_{mn}}\,J_m(\alpha_{mn}\delta_1/a)J_1(\alpha_{mn}a_1/a), \tag{8}$$

for $t=0$ and $s=1,2,\ldots,\infty$,

$$[A_{0s}+B_{0s}]\,\frac{a_1^2}{2}\,J_0(\alpha_{0s})=\sum_{n=1}^{\infty}C_{0n}(1+e^{j2k_{0n}l})J_0(\alpha_{0n}\delta_1/a)\quad\frac{\alpha_{0n}a_1/aJ_0'(\alpha_{0n}a_1/a)}{(\alpha_{0s}/a_1)^2-(\alpha_{0n}/a)^2}$$
$$+\sum_{m=1}^{\infty}\sum_{n=0}^{\infty}[C_{mn}^{+}e^{-jm\theta_0}+C_{mn}^{-}e^{jm\theta_0}](1+e^{j2k_{mnl}})J_m(\alpha_{mn}\delta_1/a)\,\frac{\alpha_{mn}a_1/aJ_0'(\alpha_{mn}a_1/a)}{(\alpha_{0s}/a_1)^2-(\alpha_{mn}/a)^2}, \tag{9}$$

for $t=1,2,\ldots,\infty$ and $s=0,1,\ldots,\infty$,

$$[A_{ts}^{+}+B_{ts}^{+}]\,\frac{a_1^2}{2}\left(1-\frac{t^2}{\alpha_{ts}^2}\right)J_t(\alpha_{ts})=\sum_{n=1}^{\infty}C_{0n}(1+e^{j2k_{0n}l})J_t(\alpha_{0n}\delta_1/a)\,\frac{\alpha_{0n}a_1/aJ_t'(\alpha_{0n}a_1/a)}{(\alpha_{ts}/a_1)^2-(\alpha_{0n}/a)^2}$$
$$+\sum_{m=1}^{\infty}\sum_{n=0}^{\infty}[C_{mn}^{+}J_{m+t}(\alpha_{mn}\delta_1/a)e^{-jm\theta_0}+C_{mn}^{-}(-1)^tJ_{m-t}(\alpha_{mn}\delta_1/a)e^{jm\theta_0}]$$
$$\times(1+e^{j2k_{mnl}})\,\frac{\alpha_{mn}a_1/aJ_t'(\alpha_{mn}a_1/a)}{(\alpha_{ts}/a_1)^2-(\alpha_{mn}/a)^2}. \tag{10}$$

Multiply both sides of Eq. (3) by $J_t(\alpha_{ts}r_1/a_1)e^{-jt\varphi}\,dS$ and integrate over S_1 to obtain, for $t=1,2,\ldots,\infty$ and $s=0,1,\ldots,\infty$,

$$[A_{ts}^{-}+B_{ts}^{-}]\,\frac{a_1^2}{2}\left(1-\frac{t^2}{\alpha_{ts}^2}\right)J_t(\alpha_{ts})=\sum_{n=1}^{\infty}C_{0n}(1+e^{j2k_{0n}l})J_t(\alpha_{0n}\delta_1/a)\,\frac{\alpha_{0n}a_1/aJ_t'(\alpha_{0n}a_1/a)}{(\alpha_{ts}/a_1)^2-(\alpha_{0n}/a)^2}$$
$$+\sum_{m=1}^{\infty}\sum_{n=0}^{\infty}[C_{mn}^{+}(-1)^tJ_{m-t}(\alpha_{mn}\delta_1/a)e^{-jm\theta_0}+C_{mn}^{-}J_{m+t}(\alpha_{mn}\delta_1/a)e^{jm\theta_0}]$$
$$\times(1+e^{j2k_{mnl}})\,\frac{\alpha_{mn}a_1/aJ_t'(\alpha_{mn}a_1/a)}{(\alpha_{ts}/a_1)^2-(\alpha_{mn}/a)^2}. \tag{11}$$

For the outlet, using the same procedure as the inlet, Eq. (4) gives, for $t=0$ and $s=0$,

$$[E_{00}+F_{00}]\,\frac{a_2^2}{2}=C_{00}(1+e^{-j2kl})\,\frac{a_2^2}{2}+\sum_{n=1}^{\infty}C_{0n}(1+e^{j2k_{0n}l})\,\frac{aa_2}{\alpha_{0n}}\,J_0(\alpha_{0n}\delta_2/a)J_1(\alpha_{0n}a_2/a)$$

$$+\sum_{m=1}^{\infty}\sum_{n=0}^{\infty}[C_{mn}^{+}+C_{mn}^{-}](1+e^{j2k_{mn}l})\,\frac{aa_2}{\alpha_{mn}}\,J_m(\alpha_{mn}\delta_2/a)J_1(\alpha_{mn}a_2/a), \tag{12}$$

for $t=0$ and $s=1,2,...,\infty$,

$$[E_{0s}+F_{0s}]\,\frac{a_2^2}{2}\,J_0(\alpha_{0s})=\sum_{n=1}^{\infty}C_{0n}(1+e^{j2k_{0n}l})J_0(\alpha_{0n}\delta_2/a)\,\frac{\alpha_{0n}a_2/aJ_0'(\alpha_{0n}a_2/a)}{(\alpha_{0s}/a_2)^2-(\alpha_{0n}/a)^2}$$

$$+\sum_{m=1}^{\infty}\sum_{n=0}^{\infty}[C_{mn}^{+}+C_{mn}^{-}](1+e^{j2k_{mn}l})J_m(\alpha_{mn}\delta_2/a)\,\frac{\alpha_{mn}a_2/aJ_0'(\alpha_{mn}a_2/a)}{(\alpha_{0s}/a_2)^2-(\alpha_{mn}/a)^2}, \tag{13}$$

for $t=1,2,...,\infty$ and $s=0,1,...,\infty$,

$$[E_{ts}^{+}+F_{ts}^{+}]\,\frac{a_2^2}{2}\left(1-\frac{t^2}{\alpha_{ts}^2}\right)J_t(\alpha_{ts})=\sum_{n=1}^{\infty}C_{0n}(1+e^{j2k_{0n}l})J_t(\alpha_{0n}\delta_2/a)\,\frac{\alpha_{0n}a_2/aJ_t'(\alpha_{0n}a_2/a)}{(\alpha_{ts}/a_2)^2-(\alpha_{0n}/a)^2}$$

$$+\sum_{m=1}^{\infty}\sum_{n=0}^{\infty}[C_{mn}^{+}J_{m+t}(\alpha_{mn}\delta_2/a)+C_{mn}^{-}(-1)^tJ_{m-t}(\alpha_{mn}\delta_2/a)]$$

$$\times(1+e^{j2k_{mn}l})\,\frac{\alpha_{mn}a_2/aJ_t'(\alpha_{mn}a_2/a)}{(\alpha_{ts}/a_2)^2-(\alpha_{mn}/a)^2}, \tag{14}$$

and

$$[E_{ts}^{-}+F_{ts}^{-}]\,\frac{a_2^2}{2}\left(1-\frac{t^2}{\alpha_{ts}^2}\right)J_t(\alpha_{ts})=\sum_{n=1}^{\infty}C_{0n}(1+e^{j2k_{0n}l})J_t(\alpha_{0n}\delta_2/a)\,\frac{\alpha_{0n}a_2/aJ_t'(\alpha_{0n}a_2/a)}{(\alpha_{ts}/a_2)^2-(\alpha_{0n}/a)^2}$$

$$+\sum_{m=1}^{\infty}\sum_{n=0}^{\infty}[C_{mn}^{+}(-1)^tJ_{m-t}(\alpha_{mn}\delta_2/a)+C_{mn}^{-}J_{m+t}(\alpha_{mn}\delta_2/a)]$$

$$\times(1+e^{j2k_{mn}l})\,\frac{\alpha_{mn}a_2/aJ_t'(\alpha_{mn}a_2/a)}{(\alpha_{ts}/a_2)^2-(\alpha_{mn}/a)^2}. \tag{15}$$

For the three velocity conditions, multiply Eqs. (5), (6), and (7) by $J_t(\alpha_{ts}r/a)e^{jt\theta}\,dS$, and integrate them over S_1, S_2, and $S-S_1-S_2$, respectively, and then add these three integral equations to give, for $t=0$ and $s=0$,

$$[A_{00}-B_{00}]a_1^2+[E_{00}-F_{00}]a_2^2=C_{00}(1-e^{-j2kl})a^2, \tag{16}$$

for $t=0$ and $s=1,2,...,\infty$,

$$k[A_{00}-B_{00}]\,\frac{aa_1}{\alpha_{0s}}\,J_0(\alpha_{0s}\delta_1/a)J_1(\alpha_{0s}a_1/a)-\sum_{n=1}^{\infty}k_{1,0n}[A_{0n}-B_{0n}]J_0(\alpha_{0s}\delta_1/a)\,\frac{\alpha_{0s}a_1/aJ_0(\alpha_{0n})J_0'(\alpha_{0s}a_1/a)}{(\alpha_{0n}/a_1)^2-(\alpha_{0s}/a)^2}$$

$$-\sum_{m=1}^{\infty}\sum_{n=0}^{\infty}k_{1,mn}[(A_{mn}^{+}-B_{mn}^{+})+(A_{mn}^{-}-B_{mn}^{-})]J_m(\alpha_{0s}\delta_1/a)\,\frac{\alpha_{0s}a_1/aJ_m(\alpha_{mn})J_m'(\alpha_{0s}a_1/a)}{(\alpha_{mn}/a_1)^2-(\alpha_{0s}/a)^2}$$

$$+k[E_{00}-F_{00}]\,\frac{aa_2}{\alpha_{0s}}\,J_0(\alpha_{0s}\delta_2/a)J_1(\alpha_{0s}a_2/a)-\sum_{n=1}^{\infty}k_{2,0n}[E_{0n}-F_{0n}]J_0(\alpha_{0s}\delta_2/a)\,\frac{\alpha_{0s}a_2/aJ_0(\alpha_{0n})J_0'(\alpha_{0s}a_2/a)}{(\alpha_{0n}/a_2)^2-(\alpha_{0s}/a)^2}$$

$$-\sum_{m=1}^{\infty}\sum_{n=0}^{\infty}k_{2,mn}[(E_{mn}^{+}-F_{mn}^{+})+(E_{mn}^{-}-F_{mn}^{-})]J_m(\alpha_{0s}\delta_2/a)\,\frac{\alpha_{0s}a_2/aJ_m(\alpha_{mn})J_m'(\alpha_{0s}a_2/a)}{(\alpha_{mn}/a_2)^2-(\alpha_{0s}/a)^2}$$

$$=-k_{0s}C_{0s}(1-e^{j2k_{0s}l})\,\frac{a^2}{2}\,J_0^2(\alpha_{0s}), \tag{17}$$

for $t=1,2,...,\infty$ and $s=0,1,...,\infty$,

$$\Bigg\{k[A_{00}-B_{00}]\,\frac{aa_1}{\alpha_{ts}}\,J_t(\alpha_{ts}\delta_1/a)J_1(\alpha_{ts}a_1/a)-\sum_{n=1}^{\infty}k_{1,0n}[A_{0n}-B_{0n}]J_t(\alpha_{ts}\delta_1/a)\,\frac{\alpha_{ts}a_1/aJ_0(\alpha_{0n})J_0'(\alpha_{ts}a_1/a)}{(\alpha_{0n}/a_1)^2-(\alpha_{ts}/a)^2}$$

$$-\sum_{m=1}^{\infty}\sum_{n=0}^{\infty}k_{1,mn}[(A_{mn}^{+}-B_{mn}^{+})J_{t+m}(\alpha_{ts}\delta_1/a)+(A_{mn}^{-}-B_{mn}^{-})(-1)^mJ_{t-m}(\alpha_{ts}\delta_1/a)]\,\frac{\alpha_{ts}a_1/aJ_m(\alpha_{mn})J_m'(\alpha_{ts}a_1/a)}{(\alpha_{mn}/a_1)^2-(\alpha_{ts}/a)^2}\Bigg\}e^{jt\theta_0}$$

$$+k[E_{00}-F_{00}]\,\frac{aa_2}{\alpha_{ts}}\,J_t(\alpha_{ts}\delta_2/a)J_1(\alpha_{ts}a_2/a)-\sum_{n=1}^{\infty}k_{2,0n}[E_{0n}-F_{0n}]J_t(\alpha_{ts}\delta_2/a)\,\frac{\alpha_{ts}a_2/aJ_0(\alpha_{0n})J_0'(\alpha_{ts}a_2/a)}{(\alpha_{0n}/a_1)^2-(\alpha_{ts}/a)^2}$$

$$-\sum_{m=1}^{\infty}\sum_{n=0}^{\infty}k_{2,mn}[(E_{mn}^{+}-F_{mn}^{+})J_{t+m}(\alpha_{ts}\delta_2/a)+(E_{mn}^{-}-F_{mn}^{-})(-1)^mJ_{t-m}(\alpha_{ts}\delta_2/a)]\,\frac{\alpha_{ts}a_2/aJ_m(\alpha_{mn})J_m'(\alpha_{ts}a_2/a)}{(\alpha_{mn}/a_2)^2-(\alpha_{ts}/a)^2}$$

$$=-C_{ts}^{+}k_{ts}(1-e^{j2k_{ts}l})\,\frac{a^2}{2}\left(1-\frac{t^2}{\alpha_{ts}^2}\right)J_t^2(\alpha_{ts}),\tag{18}$$

where

$$k_{mn}=k[1-(\alpha_{mn}/ka)^2]^{1/2},\quad k_{1,mn}=k[1-(\alpha_{mn}/ka_1)^2]^{1/2},\quad k_{2,mn}=k[1-(\alpha_{mn}/ka_2)^2]^{1/2}$$

are the axial wave numbers in chamber, inlet and outlet ducts. The detailed derivation of Eq. (18) is deferred to Appendix B. Multiply Eqs. (5), (6), and (7) by $J_t(\alpha_{ts}r/a)e^{-jt\theta}\,dS$, integrate them over S_1, S_2, and $S-S_1-S_2$, and then add these three integral equations to give, for $t=1,2,...,\infty$ and $s=0,1,...,\infty$,

$$\Bigg\{k[A_{00}-B_{00}]\,\frac{aa_1}{\alpha_{ts}}\,J_t(\alpha_{ts}\delta_1/a)J_1(\alpha_{ts}a_1/a)-\sum_{n=1}^{\infty}k_{1,0n}[A_{0n}-B_{0n}]J_t(\alpha_{ts}\delta_1/a)\,\frac{\alpha_{ts}a_1/aJ_0(\alpha_{0n})J_0'(\alpha_{ts}a_1/a)}{(\alpha_{0n}/a_1)^2-(\alpha_{ts}/a)^2}$$

$$-\sum_{m=1}^{\infty}\sum_{n=0}^{\infty}k_{1,mn}[(A_{mn}^{+}-B_{mn}^{+})(-1)^mJ_{t-m}(\alpha_{ts}\delta_1/a)+(A_{mn}^{-}-B_{mn}^{-})J_{t+m}(\alpha_{ts}\delta_1/a)]\,\frac{\alpha_{ts}a_1/aJ_m(\alpha_{mn})J_m'(\alpha_{ts}a_1/a)}{(\alpha_{mn}/a_1)^2-(\alpha_{ts}/a)^2}\Bigg\}e^{-jt\theta_0}$$

$$+k[E_{00}-F_{00}]\,\frac{aa_2}{\alpha_{ts}}\,J_t(\alpha_{ts}\delta_2/a)J_1(\alpha_{ts}a_2/a)-\sum_{n=1}^{\infty}k_{2,0n}[E_{0n}-F_{0n}]J_t(\alpha_{ts}\delta_2/a)\,\frac{\alpha_{ts}a_2/aJ_0(\alpha_{0n})J_0'(\alpha_{ts}a_2/a)}{(\alpha_{0n}/a_2)^2-(\alpha_{ts}/a)^2}$$

$$-\sum_{m=1}^{\infty}\sum_{n=0}^{\infty}k_{2,mn}[(E_{mn}^{+}-F_{mn}^{+})(-1)^mJ_{t-m}(\alpha_{ts}\delta_2/a)+(E_{mn}^{-}-F_{mn}^{-})J_{t+m}(\alpha_{ts}\delta_2/a)]\,\frac{\alpha_{ts}a_2/aJ_m(\alpha_{mn})J_m'(\alpha_{ts}a_2/a)}{(\alpha_{mn}/a_2)^2-(\alpha_{ts}/a)^2}$$

$$=-k_{ts}C_{ts}^{-}(1-e^{j2k_{ts}l})\,\frac{a^2}{2}\left(1-\frac{t^2}{\alpha_{ts}^2}\right)J_t^2(\alpha_{ts}).\tag{19}$$

Equation (19) can be derived similar to Eq. (18).

To determine the transmission loss of flow-reversing chamber, (1) the dimensions of the inlet duct are assumed such that the incoming wave A is planar, and its magnitude A_{00} is chosen to be unity for convenience, and (2) an anechoic termination is imposed at the exit of the chamber by setting the reflected wave E to zero. Thus Eqs. (8)–(19) give a large (theoretically infinite) number of relations $3(2t+1)(s+1)$ for a large number of unknowns $3(2m+1)(n+1)$. The unknowns are the pressure magnitudes for incident and reflected waves in the inlet duct, the chamber, and outlet duct (B_{mn}, C_{mn}, and F_{mn}). Since the higher modes have a diminishing effect on the solution, and t and m can be truncated to p terms and s and n to q terms resulting in $3(2p+1)(q+1)$ equations with $3(2p+1)(q+1)$ unknowns. The numbers of terms, p and q, needed for a converged solution depend both on the magnitude of the area transition and the length of the chamber. In order to analyze the convergence problem and determine the number of modes used in each region for the electromagnetic waveguide with area discontinuity, Mittra and Lee[8] presented the concept of ''relative convergence'' and imposed the so-called ''edge condition.'' Hudde and Letens[9] introduced the edge condition to acoustic duct with area discontinuity to determine the modal ratio in a transition. For circular concentric ducts, they suggested a modal ratio at a transition of two concentric ducts equal to the radius ratio, which ensures a rapid convergence. The present study, however, considers an asymmetric configuration rather than a concentric one and employs the addition of velocity equation. In view of these differences, the number of modes used in three regions (chamber, inlet, and outlet ducts) is retained the same. For the geometries and frequencies investigated here, $p=5$ for the asymmetric modes and $q=5$ for the radial modes were

found to be sufficient. The convergence was assessed by comparing the analytical solutions for consecutive (p,q) pairs. These results are also compared with boundary element predictions. Once Eqs. (8)–(19) are solved, the transmission loss is determined in the center of duct by

$$\mathrm{TL} = -20 \log_{10}\left\{ (a_2/a_1)\left| F_{00} e^{-jkl_2} + \sum_{n=1}^{p} F_{0n} e^{jk_{2,0n} l_2} \right| \right\}. \tag{20}$$

Below the planar wave cutoff frequency for inlet and outlet ducts, the higher order modes leaving the chamber in outlet duct will decay rapidly with distance l_2. Thus even for a short distance l_2, the effect of decaying Σ terms in Eq. (20) becomes negligible, simplifying the transmission loss to

$$\mathrm{TL} = -20 \log_{10}[(a_2/a_1)|F_{00}|], \tag{21}$$

which is now uniquely defined independent of location[10] (beyond l_2).

Setting $p=0$ and $q=0$ in Eqs. (8), (12), and (16) readily gives the classical transmission loss of a one-dimensional flow-reversing chamber as, for $a_1=a_2$,

$$\mathrm{TL} = 10 \log_{10}[1 + \tfrac{1}{4} m^2 \tan^2 kl], \tag{22}$$

which is identical to the behavior of a side-branch resonator with length l and cross-sectional area ratio of m ($m = S_b/S_m$; S_b and S_m are the cross-sectional areas of the branch and main duct, respectively). Note the area ratio m here for the flow-reversing chamber is significantly larger than unity, whereas it is usually less than unity for a typical side branch resonator. Thus the flow-reversing chambers have broader acoustic attenuation than the side branch resonators. Equation (22) reveals that the attenuation maxima are repeated when $kl=(2n+1)\pi/2$, leading to resonance frequencies of

$$f_r = (2n+1)\frac{c}{4l} \quad (n=0,1,2,\ldots). \tag{23}$$

The broad attenuation behavior of the flow-reversing chambers coupled with the resonance over the bandwidth $kl=\pi$ is referred to ''wide peak'' hereafter in the present paper.

II. RESULTS AND DISCUSSION

Three configurations are considered here with $l/d=0.205$ (short chamber), $l/d=1.843$ (mid-length chamber), and $l/d=3.525$ (long chamber), and all with $d=15.318$ cm, $d_1=d_2=4.859$ cm, $\delta_1=\delta_2=5.10$ cm, and the relative offset angles $\theta_0=180°$ and $\theta_0=90°$, respectively. These dimensions (length, diameter, and expansion ratio) were chosen to match three of the nine configurations fabricated for the experiments of Selamet *et al.*[1–3] The short chamber is clearly the most relevant to the present study, while the other two configurations are also included to illustrate the trend with changing chamber length. To validate the analytical model, a numerical study based on the boundary element method is also conducted for these chambers. In the present BEM calculations, a length of 0.10 m is used both for the inlet and outlet ducts. The boundary surfaces are discretized into eight-node quadrilateral and six-node triangular elements with the longest size being smaller than $\frac{1}{6}$ wavelength at the highest frequency. Further details of the numerical procedure using quadratic isoparametric elements for three-dimensional analysis can be found elsewhere.[6,7]

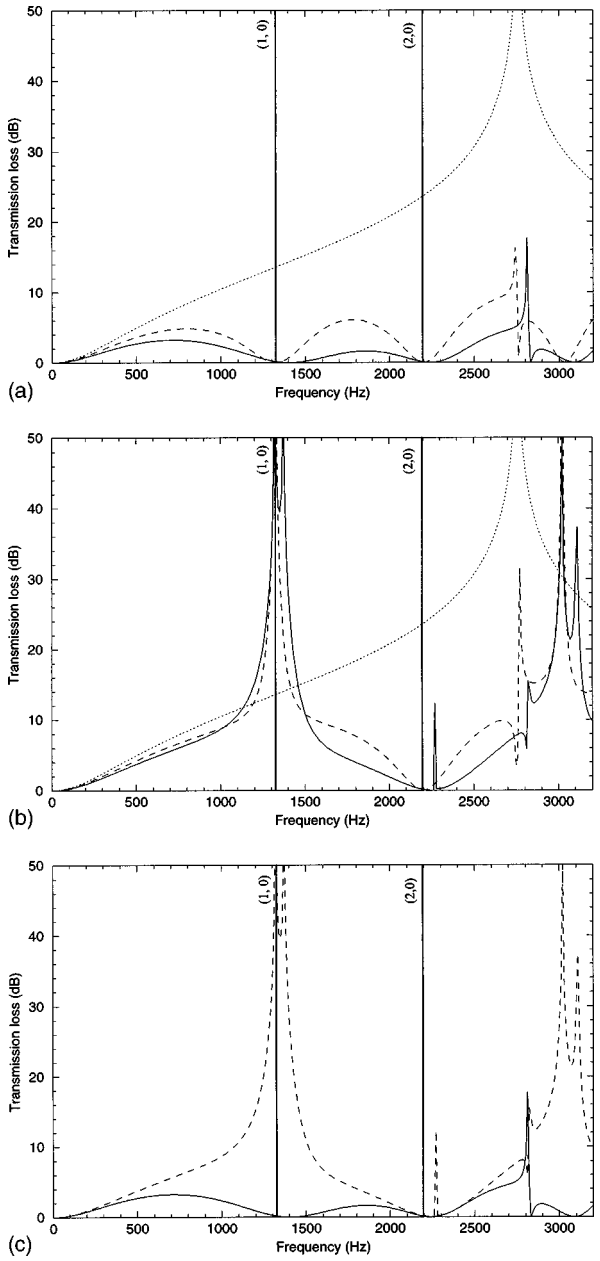

FIG. 2. Transmission loss of circular flow-reversing chamber with $l/d=0.205$. (a) $\theta_0=180°$: solid line, analytical, present; dashed line, analytical, piston-driven model; dotted line, plane wave; (b) $\theta_0=90°$: solid line, analytical, present; dashed line, analytical, piston-driven model; dotted line, plane wave; (c) comparison: solid line, $\theta_0=180°$; and dashed line, $\theta_0=90°$.

A number of comparisons are presented in Fig. 2 for $l/d=0.205$, Fig. 3 for $l/d=1.843$, and Fig. 4 for $l/d=3.525$. Each figure consists of three graphs: the first one (a) represents 180° offset configuration; the second (b) 90° offset configuration; and the third (c) the comparison of 180° and 90° orientations of (a) and (b). Figures 2(a), (b), 3(a), (b), and 4(a), (b) compare the transmission loss results from the present analytical approach, the analytical approach of Ih and Lee for piston-driven chambers, and the simple one-

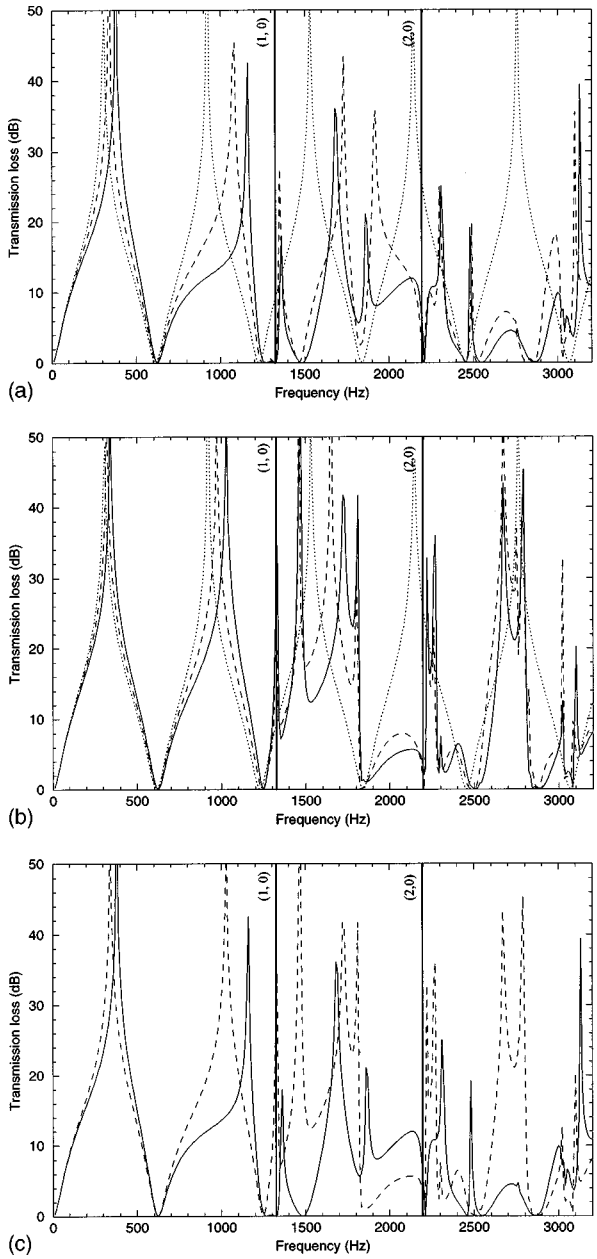

FIG. 3. Transmission loss of circular flow-reversing chamber with $l/d = 1.843$. (a) $\theta_0 = 180°$: solid line, analytical, present; dashed line, analytical, piston-driven model; dotted line, plane wave; (b) $\theta_0 = 90°$: solid line, analytical, present; dashed line, analytical, piston-driven model; dotted line, plane wave; (c) comparison: solid line, $\theta_0 = 180°$; and dashed line, $\theta_0 = 90°$.

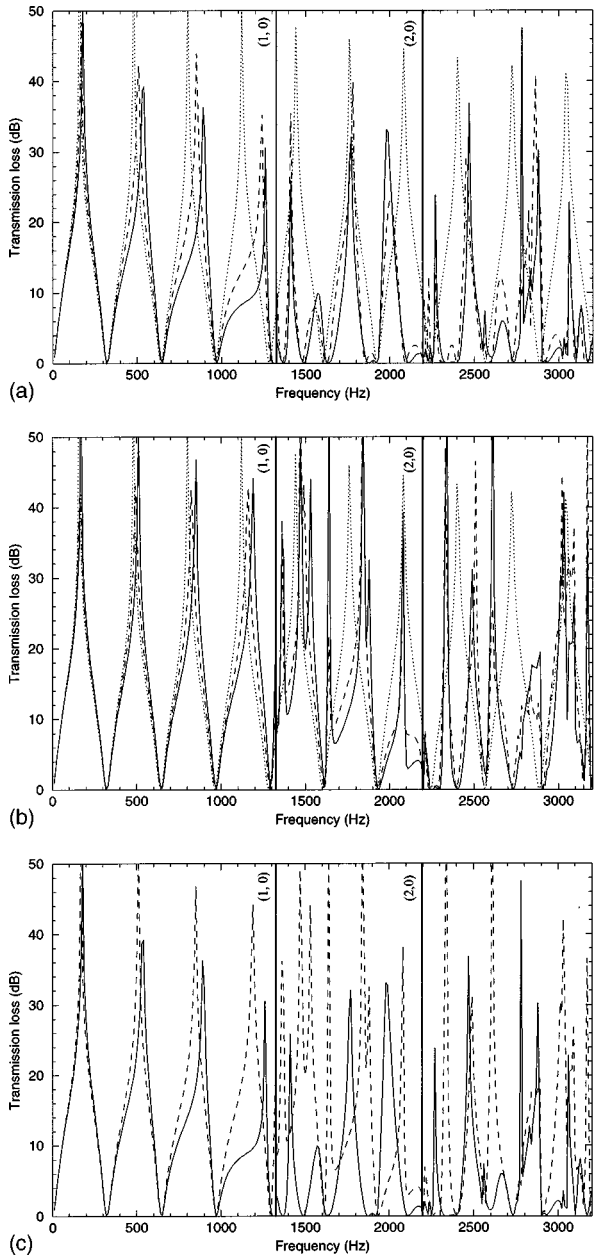

FIG. 4. Transmission loss of circular flow-reversing chamber with $l/d = 3.525$. (a) $\theta_0 = 180°$: solid line, analytical, present; dashed line, analytical, piston-driven model; dotted line, plane wave; (b) $\theta_0 = 90°$: solid line, analytical, present; dashed line, analytical, piston-driven model; dotted line, plane wave; (c) comparison: solid line, $\theta_0 = 180°$; and dashed line, $\theta_0 = 90°$.

dimensional approximation [Eq. (22)]. Comparison of the present study with that of the piston-driven chamber model illustrates the effect of the decay of nonplanar waves in the inlet and outlet ducts. The differences become less pronounced with increasing length of the chamber, as expected. The effect of length on the acoustic attenuation of flow-reversing chambers can be observed from Figs. 2–4. The short flow-reversing chamber of Fig. 2 shows clearly no similarity between the one-dimensional (axial) and three-dimensional predictions. This behavior is similar to the acoustic attenuation characteristics of short expansion chambers due to dominant transverse propagation.[2,3] The short flow-reversing chamber in Fig. 2(a) with 180° separation exhibits a domelike behavior of the one-dimensional expansion chamber with the smaller effective expansion ratio in the transverse direction, while Fig. 2(b) with 90° separation shows a dominant resonant peak, resembling a side-branch resonator. The relative behavior of the 180° and 90° offset inlet/outlet configurations may best be illustrated by combining the present 3-D analytical results from Fig. 2(a) and (b) in Fig. 2(c). For longer flow-reversing chambers, a shift in the resonant frequencies and noticeable magnitude differences between the one-dimensional (axial) and three-dimensional predictions are observed in Figs. 3 and 4. This observation demonstrates the importance of multi-dimensional wave propagation in the flow-reversing cham-

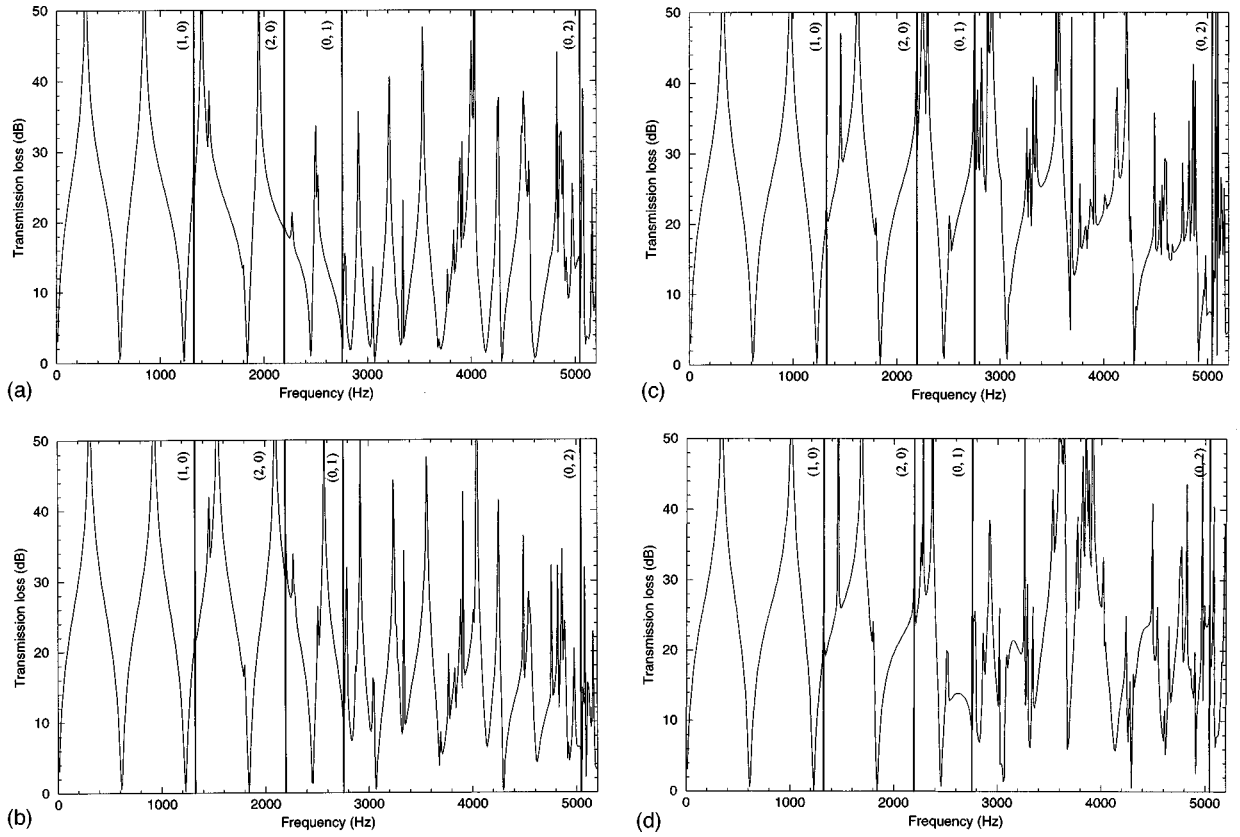

FIG. 5. Transmission loss of circular flow-reversing chamber with $l/d=1.843$ and $\delta_1=0$. (a) $\delta_2=3.0$ cm; (b) $\delta_2=4.0$ cm; (c) $\delta_2=4.807$ cm$=0.6276a$; and (d) $\delta_2=6.0$ cm.

bers. Figures 3(a) and 4(a) show the repeating wide-peak behavior characteristic of one-dimensional propagation in flow-reversing chambers below the cutoff frequency of the first asymmetric (1,0) mode. For the one-dimensional wide peaks, Eq. (A6) can be rearranged to provide a relationship between the l/d ratio of the chamber and the number of repeating wide peaks, kl/π, before higher order modes begin to dominate, as

$$\frac{kl}{\pi}<\frac{2\alpha_{mn}}{\pi}\left(\frac{l}{d}\right). \tag{24}$$

The number of wide peaks can then be approximated for the 180° offset flow-reversing chamber by introducing $\alpha_{10}=1.841$ (corresponding to $f_{10}=1324$ Hz) into Eq. (24). This suggests that geometries with an l/d ratio of less than 0.853 will have no complete wide peaks, one wide peak for $l/d=0.854$ to 1.706, two wide peaks for $l/d=1.707$ to 2.560, three wide peaks for $l/d=2.561$ to 3.413, and four wide peaks for $l/d=3.414$ to 4.266. These values show good agreement with the actual number of wide peaks in Figs. 3(a) and 4(a).

Since the inlet and outlet locations can significantly affect the excitation and suppression of higher order modes, the effect of inlet and outlet locations on the acoustic attenuation performance of the flow-reversing chambers is examined next. Similar to expansion chambers,[3] the detrimental effect of asymmetric mode (1,0) observed in Figs. 3(a) and 4(a) for the flow-reversing chambers could partially be eliminated by rotating the outlet 90°, thus setting $\theta_0=90°$. The results are depicted in Figs. 3(b) and 4(b), respectively, which exhibit increased transmission loss over the 180° case, particularly in the frequency range between the (1,0) and (2,0) modes. Also, the shift in the resonant frequencies between the one-dimensional and three-dimensional results is reduced in comparison with that of $\theta_0=180°$. In addition to the familiar one-dimensional behavior until the (1,0) mode, Figs. 3(b) and 4(b) reveal that, by ignoring some narrow peaks (spikes), the repeating wide-peak behavior continues up until the (2,0) mode begins to propagate. Thus for the 90° offset chamber, substituting $\alpha_{20}=3.054$ (corresponding to $f_{20}=2196$ Hz) into Eq. (24) predicts $l/d=0.514$ for transition, suggesting no (axial) one-dimensional wide peak for Fig. 2(b), three wide peaks for Fig. 3(b), and six wide peaks for Fig. 4(b). Examination of Figs. 2(b), 3(b), and 4(b) suggests that this is a reasonable estimate. The relative behavior of the 180° and 90° offset inlet/outlet for these two longer chambers is illustrated in Figs. 3(c) and 4(c).

The BEM predictions obtained for all six configurations of Figs. 2–4 are excluded from these figures, simply because the results match the present 3-D analytical solution throughout the frequency range of interest to the degree that they cannot be distinguished.

Also similar to expansion chambers, by centering the inlet and offsetting the outlet suitably, the acoustic attenuation performance can be improved, resulting in effective plane wave propagation inside the flow-reversing chamber until much higher frequencies. To investigate this effect, the inlet and outlet diameters of the mid-length chamber l/d

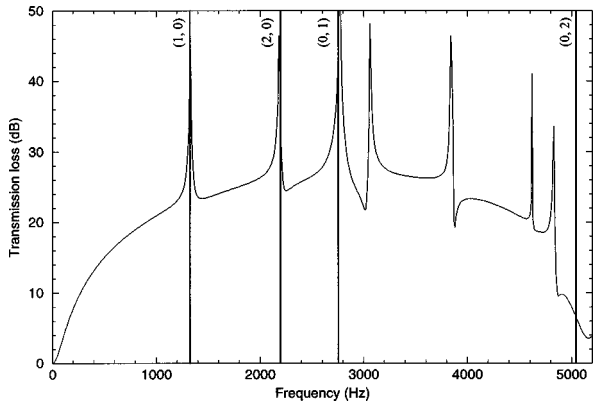

FIG. 6. Transmission loss of circular flow-reversing chamber with $l/d=0.205$, $\delta_1=0$ and $\delta_2=4.807$ cm$=0.6276a$.

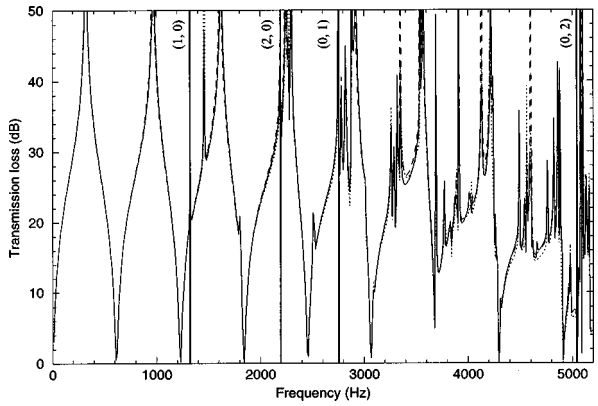

FIG. 8. The effect of terms on transmission loss of circular flow-reversing chamber with $l/d=1.843$ ($\delta_1=0$, $\delta_2=4.807$ cm$=0.6276a$): dotted line, $p=q=3$; dashed line, $p=q=4$; solid line, $p=q=5$.

$=1.843$ are halved ($d_1=d_2=2.430$ cm) in Fig. 5, thereby supporting only planar wave propagation in end ducts below 8346 Hz (for a speed of sound of 346 m/s). With the outlet approaching the pressure nodal circle of the (0,1) mode while maintaining the inlet centered, the acoustic attenuation performance is improved, particularly in the frequency range between the (0,1) and (0,2) modes. Beyond the pressure nodal circle, the attenuation starts deteriorating again. Thus offsetting the outlet by a radial distance of 0.6276 times the radius of the chamber [the pressure nodal circle of the (0,1) mode] maximizes the acoustic attenuation performance and extends the effective attenuation band to the (0,2) mode cutoff frequency (corresponding to $f_{02}=5045$ Hz). This benefit is also illustrated for the short chamber ($d_1=d_2=2.430$ cm) in Fig. 6.

Finally, the effect of mode number on the convergence of solution is shown in Figs. 7 and 8, which correspond to the configurations of Figs. 2(a) and 5(c). Within the frequency range of interest of the present work, $p=5$ for the asymmetric modes and $q=5$ for the radial modes appear to be sufficient for the convergence. While these two configurations are arbitrarily chosen for demonstration purposes here, the convergence as a function of p and q has been examined for all figures presented in the study.

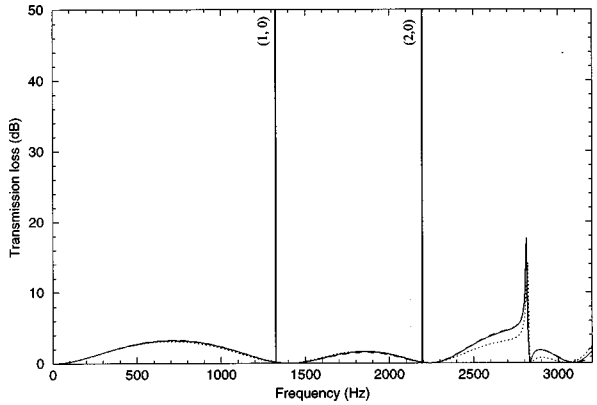

FIG. 7. The effect of terms on transmission loss of circular flow-reversing chamber with $l/d=0.205$ ($\delta_1=\delta_2=5.10$ cm, $\theta_0=180°$): dotted line, $p=q=3$; dashed line, $p=q=4$; solid line, $p=q=5$.

III. CONCLUDING REMARKS

A three-dimensional analytical approach is presented for the prediction of the acoustic attenuation performance of circular flow-reversing chambers, and compared by the boundary element predictions. The effect of inlet and outlet ducts on transmission loss is illustrated by comparing the present predictions with the ducts attached to those with the ducts removed (simple openings). Particularly, for short chambers, the higher order mode propagation and decay in the end ducts are found to be pronounced. This effect has led to the present three-dimensional analytical approach, which couples the wave propagation in the chamber and two end ducts.

The short flow-reversing chambers have acoustic attenuation characteristics similar to the short expansion chambers because of the dominant transverse propagation. The long flow-reversing chambers show a shift in the resonant frequencies and noticeable magnitude differences between the one-dimensional and three-dimensional predictions. For the 180° offset chambers with $l/d>0.853$, the repeating one-dimensional wide-peak behavior appears below the cutoff frequency of the first asymmetrical (1,0) mode, while the acoustic attenuation is reduced above this frequency. The short flow-reversing chamber exhibits a domelike behavior similar to an expansion chamber with the smaller effective expansion ratio in the transverse direction. Rotating the outlet such that $\theta_0=90°$ may improve the acoustic attenuation and extends the effective frequency band to the (2,0) second diametral mode. The flow-reversing chambers of $l/d>0.514$ show the repeating one-dimensional wide-peak behavior, while the short chambers reveal a dominant narrow resonant peak, resembling a side-branch resonator. For the flow-reversing chambers with concentric inlet, the effective acoustic attenuation frequency band is also stretched from (0,1) to the (0,2) radial mode by offsetting the outlet by a radial distance of 0.6276 times the chamber radius, which demonstrates the benefit of the concentric inlet and offset outlet arrangement in the silencer design.

APPENDIX A: SOUND PROPAGATION IN CIRCULAR DUCT

For the three-dimensional sound propagation in circular duct, the governing equation is the well-known Helmholtz equation[10]

$$\nabla^2 P + k^2 P = 0, \tag{A1}$$

where P is the acoustic pressure, $k=\omega/c$ is the wave number, ω is the angular frequency, and c is the speed of sound. By employing the separation of variables, the following general solutions of the sound pressure can be written for a wave C traveling in the positive z direction:

$$P_C = C_{00}e^{-jkz} + \sum_{n=1}^{\infty} C_{0n}J_0(\alpha_{0n}r/a)e^{jk_{0n}z} + \sum_{m=1}^{\infty}\sum_{n=0}^{\infty}(C_{mn}^{+}e^{-jm\theta} + C_{mn}^{-}e^{jm\theta}) \times J_m(\alpha_{mn}r/a)e^{jk_{mn}z}, \tag{A2}$$

and for a wave D traveling in the negative z direction:

$$P_D = D_{00}e^{jkz} + \sum_{n=1}^{\infty} D_{0n}J_0(\alpha_{0n}r/a)e^{-jk_{0n}z} + \sum_{m=1}^{\infty}\sum_{n=0}^{\infty}(D_{mn}^{+}e^{-jm\theta} + D_{mn}^{-}e^{jm\theta}) \times J_m(\alpha_{mn}r/a)e^{-jk_{mn}z}, \tag{A3}$$

where C_{mn} and D_{mn} are the constants corresponding to the waves traveling in the positive and negative z directions, in which superscripts $+$ and $-$ designate the positive and negative θ directions; $J_m(x)$ is the Bessel function of the first kind of order m; α_{mn} is the root satisfying the radial boundary condition of

$$J_m'(\alpha_{mn}) = 0, \tag{A4}$$

and m and n denote the asymmetrical and radial mode numbers (see, for example, Table 1 of Ref. 2 for α_{mn}); a is the duct radius; and

$$k_{mn} = k[1-(\alpha_{mn}/ka)^2]^{1/2} \tag{A5}$$

is the axial wave number of the mode (m,n). Examining Eq. (A5) for any high order mode (m,n), k_{mn} will be imaginary when

$$f < \frac{c}{2\pi}\left(\frac{\alpha_{mn}}{a}\right). \tag{A6}$$

The sign difference between the planar and higher order modes in the exponential terms of Eqs. (A2) and (A3) ensures that for a wave traveling, for example, in the positive direction, the magnitude of all modes will decrease exponentially to zero with increasing distance when Eq. (A6) is satisfied. The axial particle velocities for waves C and D are obtained, in view of the harmonic time dependence $\exp(j\omega t)$, from the momentum equation,

$$j\rho\omega\mathbf{U} = -\nabla P, \tag{A7}$$

as

$$U_C = \frac{1}{\rho\omega}\left\{kC_{00}e^{-jkz} - \sum_{n=1}^{\infty} k_{0n}C_{0n}J_0(\alpha_{0n}r/a)e^{jk_{0n}z} - \sum_{m=1}^{\infty}\sum_{n=0}^{\infty} k_{mn}(C_{mn}^{+}e^{-jm\theta} + C_{mn}^{-}e^{jm\theta}) \times J_m(\alpha_{mn}r/a)e^{jk_{mn}z}\right\} \tag{A8}$$

and

$$U_D = -\frac{1}{\rho\omega}\left\{kD_{00}e^{jkz} - \sum_{n=1}^{\infty} k_{0n}D_{0n}J_0(\alpha_{0n}r/a)e^{-jk_{0n}z} - \sum_{m=1}^{\infty}\sum_{n=0}^{\infty} k_{mn}(D_{mn}^{+}e^{-jm\theta} + D_{mn}^{-}e^{jm\theta}) \times J_m(\alpha_{mn}r/a)e^{-jk_{mn}z}\right\}. \tag{A9}$$

APPENDIX B: DERIVATION OF EQUATION (18)

For the velocity boundary conditions, multiply both sides of Eqs. (5), (6), and (7) by $J_t(\alpha_{ts}r/a)e^{jt\theta}\,dS$, integrate Eq. (5) over S_1, Eq. (6) over S_2, and Eq. (7) over $S-S_1-S_2$, and then adding these three integral equations to get

$$\int_0^{2\pi}\int_0^{a_1}\left\{k[A_{00}-B_{00}] - \sum_{n=1}^{\infty} k_{1,0n}[A_{0n}-B_{0n}]J_0(\alpha_{0n}r_1/a_1) - \sum_{m=1}^{\infty}\sum_{n=0}^{\infty} k_{1,mn}[(A_{mn}^{+}-B_{mn}^{+})e^{-jm\varphi} + (A_{mn}^{-}-B_{mn}^{-})e^{jm\varphi}] \times J_m(\alpha_{mn}r_1/a_1)\right\}J_1(\alpha_{ts}r/a)e^{jt\theta}r_1\,dr_1\,d\varphi + \int_0^{2\pi}\int_0^{a_2}\left\{k[E_{00}-F_{00}] - \sum_{n=1}^{\infty} k_{2,0n}[E_{0n}-F_{0n}]J_0(\alpha_{0n}r_2/a_2) - \sum_{m=1}^{\infty}\sum_{n=0}^{\infty} k_{2,mn}[(E_{mn}^{+}-F_{mn}^{+})e^{-jm\varphi} + (E_{mn}^{-}-F_{mn}^{-})e^{jm\varphi}]J_m(\alpha_{mn}r_2/a_2)\right\}J_t(\alpha_{ts}r/a)e^{jt\theta}r_2\,dr_2\,d\varphi$$
$$= \int_0^{2\pi}\int_0^{a}\left\{kC_{00}(1-e^{-j2kl}) - \sum_{n=1}^{\infty} k_{0n}C_{0n}(1-e^{j2k_{0n}l})J_0(\alpha_{0n}r/a) - \sum_{m=1}^{\infty}\sum_{n=0}^{\infty} k_{mn}[C_{mn}^{+}e^{-jm\theta} + C_{mn}^{-}e^{jm\theta}] \times (1-e^{j2k_{mn}l})J_m(\alpha_{mn}r/a)\right\}J_t(\alpha_{ts}r/a)e^{jt\theta}r\,dr\,d\theta. \tag{B1}$$

Using the Graf's addition theorem for Bessel functions[11]

$$J_m(\mu r)e^{jm\theta}=\sum_{P=-\infty}^{\infty} J_{m+P}(\mu\delta_1)J_P(\mu r_1)e^{j(P\varphi+m\theta_0)} \tag{B2}$$

for the left side of Eq. (B1) to transform the coordinates of chamber to those of the inlet duct, and then integrating over φ for the left side and θ for the right side yields

$$\begin{aligned}
&\int_0^{a_1}\Bigg\{k[A_{00}-B_{00}]J_t(\alpha_{ts}\delta_1/a)J_0(\alpha_{ts}r_1/a)-\sum_{n=1}^{\infty}k_{1,0n}[A_{0n}-B_{0n}]J_0(\alpha_{0n}r_1/a_1)J_t(\alpha_{ts}\delta_1/a)J_0(\alpha_{ts}r_1/a)\\
&\quad-\sum_{m=1}^{\infty}\sum_{n=0}^{\infty}k_{1,mn}[(A_{mn}^{+}-B_{mn}^{+})J_{t+m}(\alpha_{ts}\delta_1/a)+(A_{mn}^{-}-B_{mn}^{-})(-1)^mJ_{t-m}(\alpha_{ts}\delta_1/a)]J_m(\alpha_{mn}r_1/a_1)J_m(\alpha_{ts}r_1/a)\Bigg\}\\
&\quad\times e^{jt\theta_0}r_1\,dr_1+\int_0^{a_2}\Bigg\{k[E_{00}-F_{00}]J_t(\alpha_{ts}\delta_2/a)J_0(\alpha_{ts}r_2/a)-\sum_{n=1}^{\infty}k_{2,0n}[E_{0n}-F_{0n}]J_0(\alpha_{0n}r_2/a_2)J_t(\alpha_{ts}\delta_2/a)J_0(\alpha_{ts}r_2/a)\\
&\quad-\sum_{m=1}^{\infty}\sum_{n=0}^{\infty}k_{2,mn}[(E_{mn}^{+}-F_{mn}^{+})J_{t+m}(\alpha_{ts}\delta_2/a)+(E_{mn}^{-}-F_{mn}^{-})(-1)^mJ_{t-m}(\alpha_{ts}\delta_2/a)]J_m(\alpha_{mn}r_2/a_2)J_m(\alpha_{ts}r_2/a)\Bigg\}r_2\,dr_2\\
&\quad=-\int_0^{a}\sum_{n=0}^{\infty}k_{tn}C_{tn}^{+}(1-e^{j2k_{tn}l})J_t(\alpha_{tn}r/a)J_t(\alpha_{ts}r/a)r\,dr.
\end{aligned} \tag{B3}$$

Integrating over r_1, r_2, and r for the left and right sides of Eq. (B3), and using the integral relation for Bessel functions,[11]

$$\int rJ_m(\lambda r)J_m(\mu r)dr=\begin{cases}\dfrac{r}{\lambda^2-\mu^2}\{\mu J_m(\lambda r)J_m'(\mu r)-\lambda J_m(\mu r)J_m'(\lambda r)\} & (\lambda\neq\mu)\\[2ex] \dfrac{r^2}{2}\left\{[J_m'(\lambda r)]^2+\left[1-\dfrac{m^2}{\lambda^2r^2}\right]J_m^2(\lambda r)\right\} & (\lambda=\mu)\end{cases}, \tag{B4}$$

and applying Eq. (A4) for radial boundary condition gives

$$\begin{aligned}
&\Bigg\{k[A_{00}-B_{00}]\frac{aa_1}{\alpha_{ts}}J_t(\alpha_{ts}\delta_1/a)J_1(\alpha_{ts}a_1/a)-\sum_{n=1}^{\infty}k_{1,0n}[A_{0n}-B_{0n}]J_t(\alpha_{ts}\delta_1/a)\frac{\alpha_{ts}a_1/aJ_0(\alpha_{0n})J_0'(\alpha_{ts}a_1/a)}{(\alpha_{0n}/a_1)^2-(\alpha_{ts}/a)^2}\\
&\quad-\sum_{m=1}^{\infty}\sum_{n=0}^{\infty}k_{1,mn}[(A_{mn}^{+}-B_{mn}^{+})J_{t+m}(\alpha_{ts}\delta_1/a)+(A_{mn}^{-}-B_{mn}^{-})(-1)^mJ_{t-m}(\alpha_{ts}\delta_1/a)]\\
&\quad\times\frac{\alpha_{ts}a_1/aJ_m(\alpha_{mn})J_m'(\alpha_{ts}a_1/a)}{(\alpha_{mn}/a_1)^2-(\alpha_{ts}/a)^2}\Bigg\}e^{jt\theta_0}+k[E_{00}-F_{00}]\frac{aa_2}{\alpha_{ts}}J_t(\alpha_{ts}\delta_2/a)J_1(\alpha_{ts}a_2/a)\\
&\quad-\sum_{n=1}^{\infty}k_{2,0n}[E_{0n}-F_{0n}]J_t(\alpha_{ts}\delta_2/a)\frac{\alpha_{ts}a_2/aJ_0(\alpha_{0n})J_0'(\alpha_{ts}a_2/a)}{(\alpha_{0n}/a_2)^2-(\alpha_{ts}/a)^2}-\sum_{m=1}^{\infty}\sum_{n=0}^{\infty}k_{2,mn}[(E_{mn}^{+}-F_{mn}^{+})J_{t+m}(\alpha_{ts}\delta_2/a)\\
&\quad+(E_{mn}^{-}-F_{mn}^{-})(-1)^mJ_{t-m}(\alpha_{ts}\delta_2/a)]\frac{\alpha_{ts}a_2/aJ_m(\alpha_{mn})J_m'(\alpha_{ts}a_2/a)}{(\alpha_{mn}/a_2)^2-(\alpha_{ts}/a)^2}=-k_{ts}C_{ts}^{+}(1-e^{j2k_{ts}l})\frac{a^2}{2}\left(1-\frac{t^2}{\alpha_{ts}^2}\right)J_t^2(\alpha_{ts}),
\end{aligned} \tag{B5}$$

which is identical to Eq. (18).

[1] A. Selamet and P. M. Radavich, ''The effect of length on the acoustic attenuation performance of concentric expansion chambers: An analytical, computational, and experimental investigation,'' J. Sound Vib. **201**, 407–426 (1997).

[2] A. Selamet and Z. L. Ji, ''Acoustic attenuation performance of circular expansion chambers with offset inlet/outlet: I. Analytical approach,'' J. Sound Vib. **213**, 601–617 (1998).

[3] A. Selamet, Z. L. Ji, and P. M. Radavich, ''Acoustic attenuation performance of circular expansion chambers with offset inlet/outlet: II. Comparison with experimental and computational studies,'' J. Sound Vib. **213**, 619–641 (1998).

[4] C.-I. J. Young and M. J. Crocker, ''Acoustical analysis, testing and design of flow-reversing muffler chambers,'' J. Acoust. Soc. Am. **60**, 1111–1118 (1976).

[5] J. G. Ih and B. H. Lee, ''Theoretical investigation of flow-reversing chamber,'' J. Sound Vib. **112**, 261–273 (1987).

[6] A. F. Seybert and C. Y. R. Cheng, ''Application of the boundary element method to acoustic cavity response and muffler analysis,'' Journal of Vibration, Acoustics, Stress, and Reliability in Design **109**, 15–21 (1987).

[7] Z. L. Ji, Q. Ma, and Z. H. Zhang, ''Application of the boundary element

method to predicting acoustic performance of expansion chamber mufflers with mean flow,'' J. Sound Vib. **173**, 57–71 (1994).
[8] R. Mittra and S. W. Lee, *Analytical Techniques in the Theory of Guided Waves* (MacMillan, New York, 1971).
[9] H. Hudde and U. Letens, ''Scattering matrix of a discontinuity with a nonrigid wall in a lossless circular duct,'' J. Acoust. Soc. Am. **78**, 1826–1837 (1985).
[10] M. L. Munjal, *Acoustics of Ducts and Mufflers* (Wiley, New York, 1987).
[11] C. J. Tranter, *Bessel Functions with Some Physical Applications* (Hart, New York, 1969).

Active control of sound transmission using structural error sensing

Ben S. Cazzolato and Colin H. Hansen
Department of Mechanical Engineering, The University of Adelaide, South Australia 5005, Australia

(Received 13 May 1997; revised 15 June 1998; accepted 28 July 1998)

The active minimization of harmonic sound transmission into an arbitrarily shaped enclosure using error signals derived from structural vibration sensors is investigated numerically. It is shown that by considering the dynamics of the coupled system, it is possible to derive a set of ''structural radiation'' modes which are orthogonal with respect to the global potential energy of the coupled acoustic space and which can be sensed by structural vibration sensors. Minimization of the amplitudes of the ''radiation modes'' is thus guaranteed to minimize the interior acoustic potential energy. The coupled vibro-acoustic system under investigation is modelled using finite element analysis which allows systems with complex geometries to be investigated rather than limiting the analysis to simple analytically tractable systems. Issues regarding the practical implementation of sensing the orthonormal sets of structural radiation modes are discussed. Specific examples relating to the minimization of the total acoustic potential energy within a longitudinally stiffened cylinder are given, comparing the performance offered using error sensing of the radiation modes on the structure against the more traditional error criteria; namely, the discrete sensing of the structural kinetic energy on the boundary and the acoustic potential energy in the enclosed space. [S0001-4966(98)02211-5]

PACS numbers: 43.50.Ki [GAD]

INTRODUCTION

The use of vibration control sources to minimize sound transmission through lightweight structures into coupled enclosures offers two advantages over the use of more conventional acoustic sources: fewer secondary sources are generally required for global control of the interior noise field;[1] and surface mounted actuators are far less intrusive than bulky speaker/cabinet arrangements. However, the gains in system compactness are not necessarily realized in practice when microphones placed throughout the cavity are used to provide the controller error signals to achieve global control.

As an alternative, surface mounted structural vibration sensors have also been used as error sensors and, although a reduction in the vibration of the structure has been achieved, a reduction in the interior sound field did not necessarily follow, particularly at low frequencies where the modal density is low.[2] Clearly a control system using structural error sensors to directly measure the surface vibration is unsuitable for the control of sound transmission. However, it has been shown recently that is possible to calculate a quantity from the vibration of the structure which is directly proportional to the sound radiated into the enclosed space.[3]

This paper develops a procedure in which the sound transmission from a structure into an enclosed space can be sensed using structural vibration error sensors. It draws from the work of previous researchers who have investigated the sound power radiated into free field from vibrating beams,[4,5] plates,[6–12] and shells[13–17] using orthogonal surface velocity patterns, commonly referred to as acoustic ''radiation modes.'' The approach involves decomposing the surface vibration, usually via a singular value decomposition, into a number of surface velocity distributions which contribute independently to the radiated sound field. Snyder and Tanaka[3] have extended the work to include a brief study of the active control of sound transmitted into a coupled rectangular enclosure. However, their work failed to address many of the practical implementation issues discussed in this paper.

It has been shown that for both free-field radiation and transmission problems only a very limited number of radiation modes contribute to the sound radiated from the vibrating structure and it is the number of efficiently radiating modes, rather than the modal response of the structure, which defines the system dimensionality[13] and subsequently, the control system order. Distributed parameter modal sensors called ''smart sensors'' may then be employed to measure the modal amplitudes of the radiation modes and to provide inputs into an active control system.[18,19]

The use of independent (orthogonal) error signals for active noise control problems has been shown to offer a number of practical advantages, as it can: reduce convergence time for controllers; provide robustness to system parameter uncertainty; and minimize the number of sensors and actuators, and corresponding system dimensionality.[20,21]

The primary objective of the work described here was to extend the technique of active control of sound transmission into enclosures using radiation modal control, to the point where it may be used in a real active control system.

A second objective was to investigate the mechanisms of sound transmission into a stiffened cylindrical enclosure and the subsequent implications on the design and performance of active systems for controlling sound transmission through the boundaries. It is shown that the interior radiation mode shapes are frequency dependent. This makes the application of modal control very difficult for real systems. A new technique for overcoming this application problem is derived which allows the use of fixed shape modal sensors.

A third objective was to determine the most suitable means of sensing radiation modes using structural vibration measurements. Both discrete and continuous shaped sensors have been investigated for use as modal sensors, with the latter being more practical for large, modally dense (structural) systems.

The active control of sound transmission into a longitudinally stiffened cylinder with an integral floor, excited by an external vibration source is investigated numerically to illustrate the implementation of the extended technique and to gain some understanding of the associated physical processes. The structure and the acoustic space enclosed by the cylinder have been modeled numerically using the commercially available finite element package ANSYS, which has enabled the investigation to be extended to geometrically complex, modally dense systems that are typically found in most real situations.

I. GENERAL THEORY

In this section the theory of sound transmission through a structure into a contiguous cavity is developed. The transmitted sound field is derived in terms of radiation modes and the implications for structural vibration sensing of the radiation modes is also discussed. Using the modal-interaction approach to the solution of coupled problems, the response of the structure is modeled in terms of its *in vacuo* mode shape functions and the response of the enclosed acoustic space is described in terms of the rigid-wall mode shape functions.[22] The response of the coupled system is then determined by solving the modal formulation of the Kirchhoff–Helmholtz integral equation.

A. Global error criteria

An appropriate global error criterion for controlling the sound transmission into a coupled enclosure is the total time-averaged frequency-dependent acoustic potential energy, $E_p(\omega)$, in the enclosure[23]

$$E_p(\omega)=\frac{1}{4\rho_0 c_0^2}\int_V |p(\mathbf{r},\omega)|^2 d\mathbf{r}, \tag{1}$$

where $p(\mathbf{r},\omega)$ is the acoustic pressure amplitude at some location $\mathbf{r}$ in the enclosure, ρ_0 is the density of the acoustic fluid (air), c_0 is the speed of sound in the fluid, and V is the volume over which the integral is evaluated. The frequency dependence, ω, is assumed in the following analysis but this factor will be omitted in the equations for the sake of brevity. Using the modal interaction approach to the problem,[22] the acoustic pressure at any location within the cavity is expressed as an infinite summation of the product of rigid-wall acoustic mode shape functions, ϕ_i, and the modal pressure amplitudes, p_i, of the cavity

$$p(\mathbf{r})=\sum_{i=1}^{\infty} p_i \phi_i(\mathbf{r}). \tag{2}$$

The modal expansion for the acoustic potential energy evaluated over n_a acoustic modes is then given by

$$E_p=\mathbf{p}^H \mathbf{\Lambda} \mathbf{p}, \tag{3}$$

where $\mathbf{p}$ is the $(n_a\times 1)$ vector of acoustic modal amplitudes and $\mathbf{\Lambda}$ is a $(n_a\times n_a)$ diagonal weighting matrix, the diagonal terms of which are

$$\Lambda_{ii}=\frac{\Lambda_i}{4\rho_0 c_0}, \tag{4}$$

where Λ_i is the modal volume of the ith cavity mode, defined as the volume integration of the square of the mode shape function,

$$\Lambda_i=\int_V \phi_i^2(\mathbf{r})\, dV(\mathbf{r}). \tag{5}$$

The pressure modal amplitudes, $\mathbf{p}$, within the cavity, arising from the vibration of the structure are given by the product of the $(n_s\times 1)$ structural modal velocity vector, $\mathbf{v}$, and the $(n_a\times n_s)$ modal structural-acoustic radiation transfer function matrix,[24] $\mathbf{Z}_a$,

$$\mathbf{p}=\mathbf{Z}_a \mathbf{v}. \tag{6}$$

The l, ith element of the radiation transfer function matrix $\mathbf{Z}_a$ is the pressure amplitude of the acoustic mode l generated as a result of structural mode i vibrating with unit velocity amplitude. Substituting Eq. (6) into Eq. (3) gives an expression for the acoustic potential energy with respect to the normal structural vibration,

$$E_p=\mathbf{v}^H \mathbf{\Pi} \mathbf{v}, \tag{7}$$

where the error weighting matrix $\mathbf{\Pi}$ is given by

$$\mathbf{\Pi}=\mathbf{Z}_a^H \mathbf{\Lambda} \mathbf{Z}_a. \tag{8}$$

It should be noted that the error weighting matrix $\mathbf{\Pi}$ is not necessarily diagonal, which implies that the normal structural modes are not orthogonal contributors to the interior acoustic pressure field. It is for this reason that minimization of the modal amplitudes of the individual structural modes (or kinetic energy) will not necessarily reduce the total sound power transmission.

B. Diagonalization of the error criteria

As $\mathbf{\Pi}$ is real symmetric, it may be diagonalized by the orthonormal transformation;

$$\mathbf{\Pi}=\mathbf{U}\mathbf{S}\mathbf{U}^T, \tag{9}$$

where the unitary matrix $\mathbf{U}$ is the (real) orthonormal transformation matrix representing the eigenvector matrix of $\mathbf{\Pi}$ and the (real) diagonal matrix $\mathbf{S}$ contains the eigenvalues (singular values) of $\mathbf{\Pi}$. The physical significance of the eigenvectors and eigenvalues is interesting. The eigenvalue can be considered a radiation efficiency (or coupling strength[25]) and the associated eigenvector gives the level of participation of each normal structural mode to the radiation mode; thus it indicates the modal transmission path.[25]

Substituting the orthonormal expansion of Eq. (9) into Eq. (7) results in an expression for the potential energy of the cavity as a function of an orthogonal radiation mode set,

$$E_p=\mathbf{v}^H \mathbf{U}\mathbf{S}\mathbf{U}^T \mathbf{v}=\mathbf{w}^H \mathbf{S} \mathbf{w}, \tag{10}$$

where the elements of **w** are the velocity amplitudes of the radiation modes defined by

$$\mathbf{w}=\mathbf{U}^T\mathbf{v}. \tag{11}$$

Equation (11) demonstrates that each radiation mode is made up of a linear combination of the normal structural modes, the ratio of which is defined by the eigenvector matrix **U**. As the eigenvalue matrix, **S**, is diagonal, Eq. (10) may be written as follows:

$$E_p=\sum_{i=1}^{n} s_i|w_i|^2, \tag{12}$$

where s_i are the diagonal elements of the eigenvalue matrix **S** and w_i are the modal amplitudes of the individual radiation modes given by Eq. (11).

The potential energy from any radiation mode is equal to the square of its amplitude multiplied by the corresponding eigenvalue. The radiation modes are therefore independent (orthogonal) contributors to the potential energy and the potential energy is directly reduced by reducing the amplitude of any of the radiation modes. As mentioned previously, the normal structural modes are not orthogonal radiators since the potential energy arising from one structural mode depends on the amplitudes of the other structural modes. The orthogonality of the radiation modes is important for active control purposes as it guarantees that the potential energy will be reduced if the amplitude of any radiation mode is reduced.[10]

C. Advantages of diagonalization

For shells radiating into free space,[6,7,13,17] the eigenvalues of the radiation modes rapidly decrease in magnitude with respect to the largest eigenvalue. Therefore, in practice it is necessary to only include the first few (efficient) radiation modes with the largest radiation efficiencies to account for majority of the sound power radiated from the structure into the free field. The same principle applies for interior radiation modes. When calculating the transmission of sound from the structure into the cavity only the few most efficient radiation modes need to be used in the transmission loss calculations. It is therefore possible to neglect the nonefficient radiation modes with no appreciable loss in accuracy of the transmission loss estimates.

With the acoustic potential energy in the form of Eq. (12) the above property can be exploited. Therefore, if only the first n_r terms in the eigenvalue matrix are of significance (say greater than 1% of the maximum), then the error weighting matrix may be approximated by[5]

$$\mathbf{\Pi}\approx\sum_{i=1}^{n_r} s_i\mathbf{u}_i\mathbf{u}_i^H, \tag{13}$$

which in matrix form yields

$$\mathbf{\Pi}\approx\mathbf{U}\mathbf{S}\mathbf{U}^T, \tag{14}$$

where $\mathbf{S}\approx\mathrm{diag}(s_1,s_2,...,s_{n_r})$ is a $(n_r\times n_r)$ matrix and $\mathbf{U}\approx[\mathbf{u}_1,\mathbf{u}_2,\ldots,\mathbf{u}_{n_r}]$ is a $(n_s\times n_r)$ matrix.

It is in this truncation of the system equations where the benefits of using radiation modes to provide error signals in active control systems become apparent. For example, ''real'' systems tend to be modally dense structures with several hundred normal structural modes contributing to the overall response of the structure. It will be shown that it is possible to truncate the radiation matrix used in the simulations from a (200×200) matrix to a (5×5) matrix with almost no loss in accuracy. This greatly reduces both the computation times for the simulation and the complexity of the physical control system.

D. Structural sensing of radiation modes

To evaluate the potential energy using Eq. (12) it is necessary to know the amplitudes of the radiation modes. The process of extracting the amplitudes of radiation modes from measurements of the structural vibration, known as modal filtering, is discussed in detail by Tanaka *et al.*[19] and relies on the principle of orthogonality, i.e.,

$$\int_S \theta_m(\mathbf{r})\,\theta_n(\mathbf{r})\,dS=\begin{cases}0, & m\neq n,\\ 1, & m=n,\end{cases} \tag{15}$$

where θ_m is the mth mode of some orthogonal set of natural modes. Post multiplying Eq. (15) by the mth modal velocity, w_m, and summing over all modes gives

$$\int_S v(\mathbf{r})\,\theta_m(\mathbf{r})\,dS=w_m, \tag{16}$$

where $v(\mathbf{r})=\Sigma_{i=1}^{\infty}w_i\theta_i(\mathbf{r})$ is the velocity of the structure at some location **r**. The modal filters can be constructed by implementing Eq. (16) in its discrete form using weighted measurements of the structural vibration at discrete locations, or in a continuous form using shaped sensors such as piezo-electric film.

An alternative approach to modal filtering described above uses a least-squares formulation rather than numerical integration and is derived below in matrix form for discrete sensors which are a subset of continuous sensors. The structural velocity levels at the (n_e) discrete error sensor locations are given by the following finite matrix modal expansion,

$$\mathbf{v}_e=\mathbf{\Psi}_e\mathbf{v}, \tag{17}$$

where $\mathbf{v}_e$ is the $(n_e\times1)$ vector of velocity levels for the sensors and $\mathbf{\Psi}_e$ is the $(n_e\times n_s)$ mode shape matrix at the sensor locations. The normal structural modal amplitudes are then given by

$$\mathbf{v}=\mathbf{\Psi}_e^{-1}\mathbf{v}_e. \tag{18}$$

Inserting Eq. (18) into (11), an expression is obtained for the velocity amplitudes of the radiation modes as a function of the velocity levels at the error sensor locations

$$\mathbf{w}=\mathbf{Z}_t\mathbf{v}_e, \tag{19}$$

where $\mathbf{Z}_t$ is the $(n_r\times n_e)$ radiation mode structural transfer function matrix (or modal filter matrix) which relates the vibration velocity levels at the discrete error sensor locations to the modal velocity amplitudes of the radiation modes and is given by

$$\mathbf{Z}_t=\mathbf{U}^T\mathbf{\Psi}_e^{-1}. \tag{20}$$

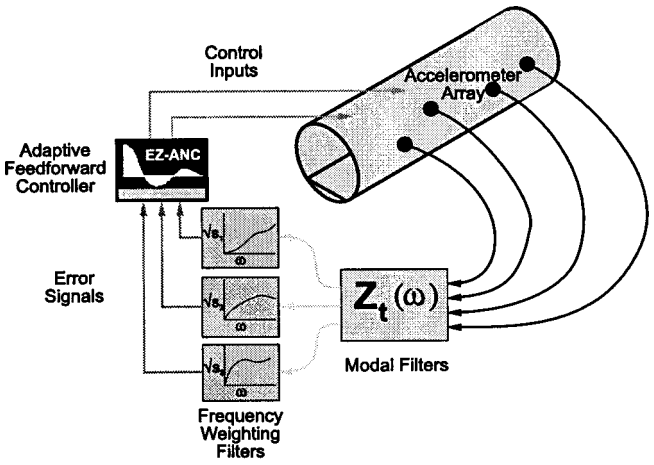

FIG. 1. Schematic of modal and eigenfilter for an ANVC system.

The elements of each row of this modal filter matrix represent a weighting value, which when applied to the signal from the vibration sensors and summed for all sensors, will provide a measure of the amplitudes of the radiation modes.

The expression for the velocity at any point on the surface of the structure given by Eq. (17) can be expanded, using the properties of a unitary matrix and Eq. (11), to give the following:

$$\mathbf{v}_e = \mathbf{\Psi}_e \mathbf{U}\mathbf{U}^{-1}\mathbf{v} = \mathbf{\Psi}_e \mathbf{U}\mathbf{U}^{T}\mathbf{v} = [\mathbf{\Psi}_e \mathbf{U}]\mathbf{w}. \tag{21}$$

It follows that the term $\mathbf{\Psi}_e\mathbf{U}$ in Eq. (21) is the mode shape matrix of the radiation modes evaluated at the n_e error sensor locations, $\mathbf{\Theta}_e$. Therefore, the radiation mode shape is obtained by post-multiplying the mode shape matrix of the normal structural modes by the eigenvector matrix, i.e.,

$$\mathbf{\Theta} = \mathbf{\Psi}\mathbf{U}. \tag{22}$$

In most practical systems the number of discrete error sensors (n_e) will be much less than the number of significant normal structural modes (n_s); therefore, the error sensor mode shape matrix, $\mathbf{\Psi}_e$, will be underdetermined. It is therefore necessary to evaluate the inverse via a pseudo (least squares) inverse. Note that this technique is an approximation and will reduce the fidelity of the sensing system much like evaluating Eq. (16) over some subspace of the surface rather than the complete surface. It is shown in the following section that the reduction in sensor fidelity will lead to a reduction in controller performance.

The practical implementation of the control system may look something like that shown in Fig. 1, where an accelerometer array would be used to measure the velocity levels on the surface of the shell. The modal filters, $\mathbf{Z}_t$, given by Eq. (20) would be used to decompose the velocity signal to modal amplitudes of the radiation modes. The frequency weighting (eigenvalue) filters, **S**, would then be used to weight the modal amplitudes to provide inputs to the controller.

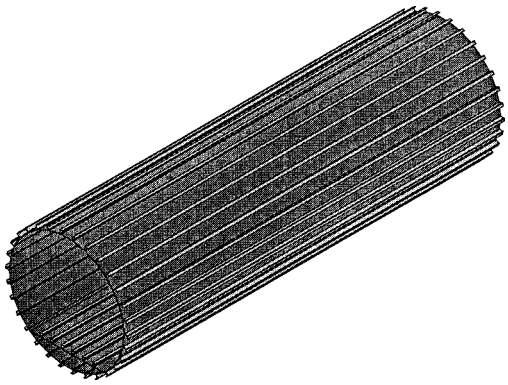

FIG. 2. Solid model of the longitudinally stiffened cylinder with an integral floor.

II. SOUND TRANSMISSION THROUGH A STIFFENED CYLINDER

The active control of sound transmission through the 3.0-m-long, 0.9-m-diam longitudinally stiffened cylinder with an integral floor shown in Fig. 2 has been investigated. The floor was rigidly fixed to the shell and subtended an angle of 80 degrees. The shell was constructed from 1-mm-thick stainless steel with 30 longerons around the circumference of the cylinder and 6 along the floor. The boundary conditions of the ends of the structure were shear diaphragm and the acoustic boundary conditions of the end caps were rigid. Damping of the system was light with the modal loss factor for both the structure and the cavity set to 2%.

Studies of the importance of representative structural models for aircraft interior acoustics have shown that it is necessary to account for the stiffness and mass provided by stiffeners attached to the skin as well as interior structures such as the floor. Omitting to account for such elements leads to poor correlation between the numerical model and experimental results.[26] Therefore the geometry of the cylinder was designed to reflect the complex, modally dense nature of a typical fuselage.

A. Finite element analysis

The cylinder and the contiguous acoustic space were modeled separately using the FEA package ANSYS, then coupled using modal coupling theory[22] within MATLAB. The FE models of the structure and the cavity are shown in Fig. 3

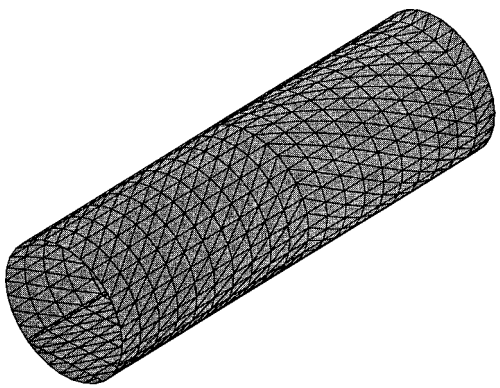

FIG. 3. Finite element model of the structure.

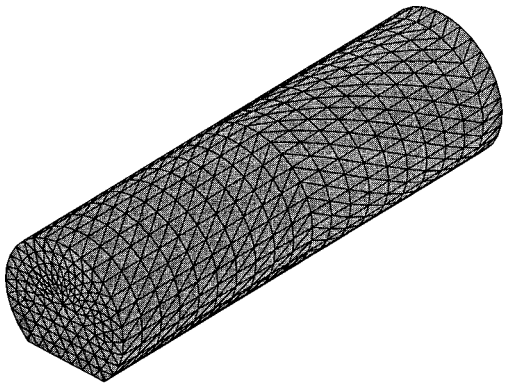

FIG. 4. Finite element model of the acoustic space.

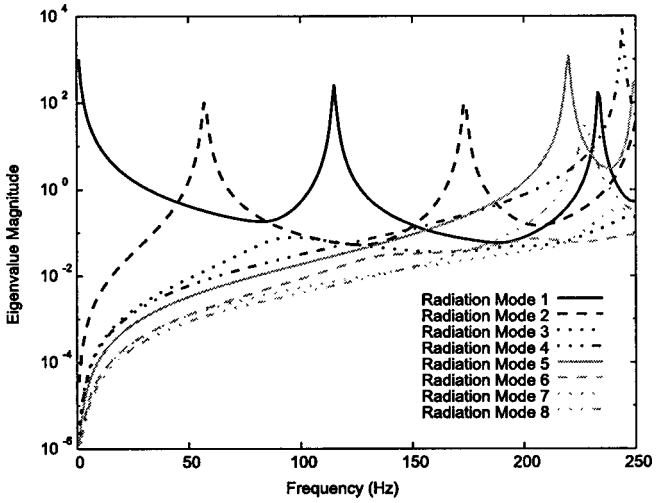

FIG. 5. Eigenvalue magnitudes (radiation efficiencies) for the first eight radiation modes.

and Fig. 4, respectively. The structural FE model consisted of 2280 triangular shell elements and 4032 degrees of freedom. The C-section longerons attached to the shell were modeled using 3-D beam elements. The acoustic model consisted of 11 242 acoustic tetrahedral elements and 2341 degrees of freedom.

ANSYS has the facilities to analyze a fully coupled vibroacoustic system. However, a fully coupled approach results in an unsymmetric system of equations, the solution of which is computationally intensive. In the interests of keeping the model size manageable and keeping track of the modal coupling mechanisms, it was decided to analyze the two subsystems individually, then post-couple the two modal models using the modal interaction approach.[22] The structural and acoustic models have been meshed with coincident nodes to facilitate coupling of the FE models in MATLAB. This resulted in an excessively fine acoustic model but did not significantly extend the time taken for the forced response analysis.

The first 50 acoustic modes and the first 400 normal structural modes were extracted using the finite element model described previously. The natural frequencies of the lowest 10 acoustic modes are shown in Table I.

Cunefare and Currey[4] found that the low order (free-space) radiation modes of rectangular panels converge quickly to their true shape after considering only a limited number of structural modes. It was found in the work discussed in the paper that this is not the case for interior radiation modes of a complex three-dimensional structure and many hundreds of modes (400) were required to achieve partial convergence to the ''true'' shape of the radiation mode.

TABLE I. Natural frequencies of the first ten acoustic modes.

Mode	Natural frequency (Hz)
0	0
1	57
2	117
3	173
4	220
5	228
6	233
7	244
8	250
9	251

When calculating the sound transmission from the structure into the enclosed space it was only necessary to consider the structural modes that were resonant or close to resonance within the frequency bandwidth of interest, namely 0 to 250 Hz. Therefore, for the sake of computational efficiency, only 100 structural modes were used during the simulation to calculate the system response.

B. Radiation modes—mode shapes and radiation efficiencies

The eigenvalues and eigenvectors of the radiation matrix were calculated within MATLAB using the method and model outlined above. A singular value decomposition (SVD) was used to calculate the orthonormal transformation of the radiation matrix rather than other eigenextraction routines because of the singular nature of the problem. As the radiation efficiencies of the radiation modes rapidly approach zero, the condition number of the matrices becomes infinite and thus ill-conditioned. This being the case, many of the other techniques which use simple eigenroutines to construct the orthonormal radiation mode set, such as Gram–Schmidt orthogonalization, suffer severely from round-off problems.

The eigenvalues for the first eight (most efficient) radiation modes are shown as a function of frequency in Fig. 5. As can be seen, the eigenvalues are very frequency dependent with the peaks in the radiation efficiency corresponding to the natural frequencies of the cavity. Figure 5 shows qualitatively that in general (at least at low frequencies) a single radiation mode will dominate the sound transmission from the structure into the acoustic space. It is this property that enables significant control within a limited frequency range to be achieved by controlling a single radiation mode. It should be noted that at the ''crossover'' frequencies where two radiation modes have the same eigenvalue, there will be at least two radiation modes contributing to the sound transmission into the cavity. It is not critical that the active control system perform optimally in the crossover regions as

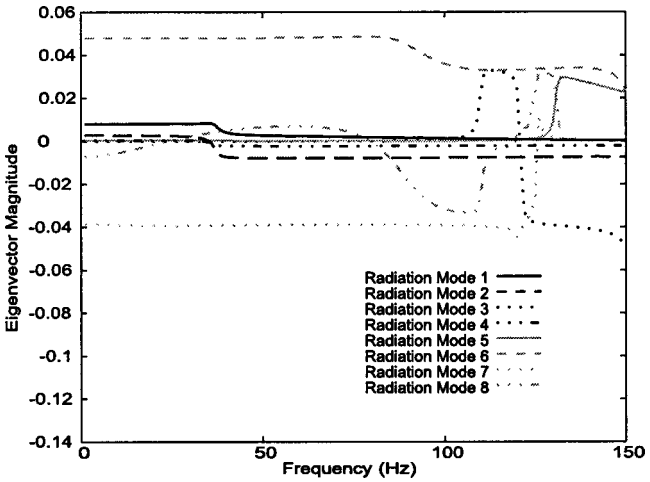

FIG. 6. First eight eigenvectors for the eleventh structural mode.

these regions are likely to occur at frequencies where the radiation efficiencies are low and therefore the sound transmission is also low.

The frequency dependence is also reflected in the eigenvectors, with particularly high variation at the ''crossover'' frequencies where there is a change in the ranking of eigenvalues. Physically, this means that the shape of the modal sensors used to measure the radiation modal amplitude is frequency dependent. As an example, the eigenvector weighting of the first eight radiation modes for the eleventh normal structural mode is shown in Fig. 6. This weighting is typical for all the normal structural modes and demonstrates how the importance of each normal structural mode alters with respect to frequency as the response of the acoustic space is dominated by different acoustic modes.

As very few radiation modes contribute to the sound transmission, only a few low order IIR filters are needed to implement the frequency dependent eigenvalues. However, due to the large number of structural modes needed to derive the radiation modes, the frequency dependence of the eigenvectors (mode shapes) presents a significant burden for practical implementation of the control system shown in Fig. 1. Obviously, because of the frequency dependence of the radiation mode shapes, the modal amplitudes of these modes can only be calculated through discrete sensors weighted with digital filters rather than using fixed shape sensors. This

FIG. 8. Mode shape of the most efficient radiation mode at 117 Hz.

effectively prohibits the calculation of the modal amplitudes using Eq. (20) for all but the simplest physical systems. Consider for example the particular case, where 5 radiation modes are to be controlled using 16 tap IIR filters, upward of 8000 (5 radiation modes$\times$16 taps$\times$100 sensors) multiplications may be required, presenting a significant burden even for high speed DSPs. A technique for overcoming this limitation is detailed in Sec. III.

The mode shape functions of the most efficient radiation modes calculated for the stiffened cylinder model, at 57 Hz and 117 Hz (corresponding to the natural frequencies of the first two acoustic modes) were derived using Eq. (22). These are shown in Figs. 7 and 8 in an exploded format to show more clearly the vibration profile of the floor. It becomes apparent that the radiation modes reflect the dominant acoustic modes at the driving frequency, as shown in Figs. 9 and 10.

As the floor of the cylinder is significantly more compliant than the shell, the modal masses of the majority of the structural modes are dominated by the floor motion. Subsequently, the calculated radiation mode shapes are more accurate for the floor than for the rest of the shell. If a greater number of structural modes were used to estimate the radiation mode shapes, then the shell motion would more closely resemble that of the dominant acoustic mode shape.

When compared to the normal structural modes of similar frequency (see Figs. 11 and 12) the radiation modes have a much lower circumferential wave number. This property is beneficial when implementing modal sensing for the control

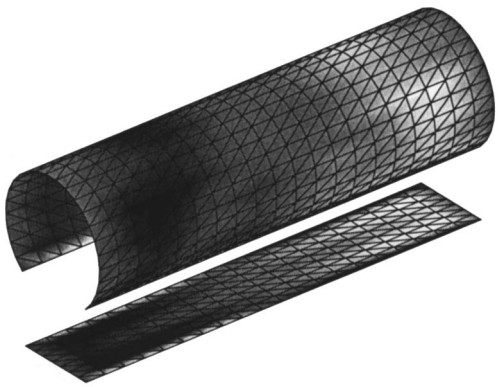

FIG. 7. Mode shape of the most efficient radiation mode at 57 Hz.

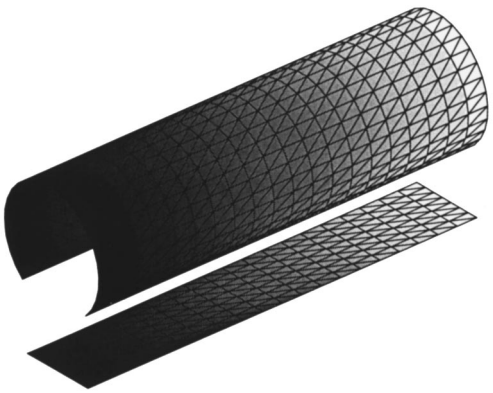

FIG. 9. Mode shape of the first acoustic mode (57 Hz).

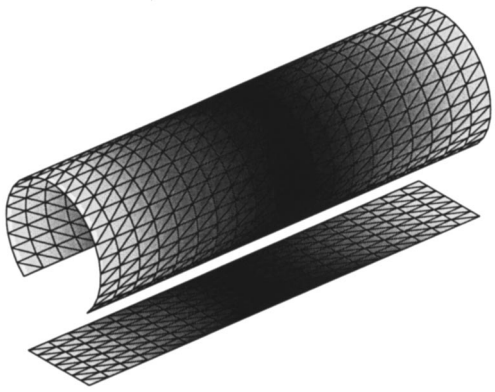

FIG. 10. Mode shape of the second acoustic mode (117 Hz).

FIG. 12. Mode shape of the fourth normal structural mode (34 Hz).

system, as modes with lower wave numbers are easier to measure with distributed modal sensors.

It is not surprising that the structural radiation mode shape functions are similar to the mode shapes of the dominant acoustic modes at the structure boundary, for it is well known that the coupling efficiency between acoustic and structural modes is high when the acoustic and structural mode shape functions are similar. This has important implications when it comes to designing the control system. Instead of calculating the radiation modes as was done in Sec. I, for structural/acoustic systems with ''regular'' geometries, it may be adequate to assume the radiation mode shape function is the same as the acoustic mode shape function as a first approximation.

It is also interesting to note that the calculation of the radiation mode shapes allows identification of regions of high power transmission (which are not necessarily colocated with the areas of maximum structural vibration). It may be possible to use this information prudently to optimize the location of structural control sources.

When the eigenvalues corresponding to a particular excitation frequency are returned by the eigensolver, they are always sorted in either ascending or descending order with respect to the magnitudes. This ''ranking'' of the eigenvalues and eigenvectors has the benefit of arranging the modes from the biggest contributors to the sound transmission to the smallest. Therefore, only the important modes are sensed and controlled which leads to a reduction in the number of error and control signals required by the control system.

FIG. 11. Mode shape of the third normal structural mode (33 Hz).

For example, the ranked eigenvalues for the first eight (most efficient) radiation modes are shown in Fig. 13. It can be seen that the ranking of the eigenvalues creates a discontinuity in the slope of the eigenvalues at the crossover frequencies. This manifests itself as step changes in the modes shapes of the radiation modes, so the mode shape of the most efficient mode at 40 Hz does not resemble the mode shape of the most efficient mode at 60 Hz.

In comparing Fig. 5 and Fig. 13, it can be seen that with the radiation modes ranked with respect to their radiation efficiencies, only two radiation modes need to be considered at each frequency up to 250 Hz to account for most of the sound transmission, otherwise six or seven ''unranked'' radiation modes would need to be considered to account for a similar level of sound transmission.

It should be noted that because of the discontinuities in the slope of the ranked eigenvalues at the crossover frequencies, a greater number of taps in the digital filters used to shape the error signal input to the controller (see Fig. 1) are required. However, the system requirements are not significantly greater than for the unranked case because fewer (ranked) radiation modes contribute to the sound transmission.

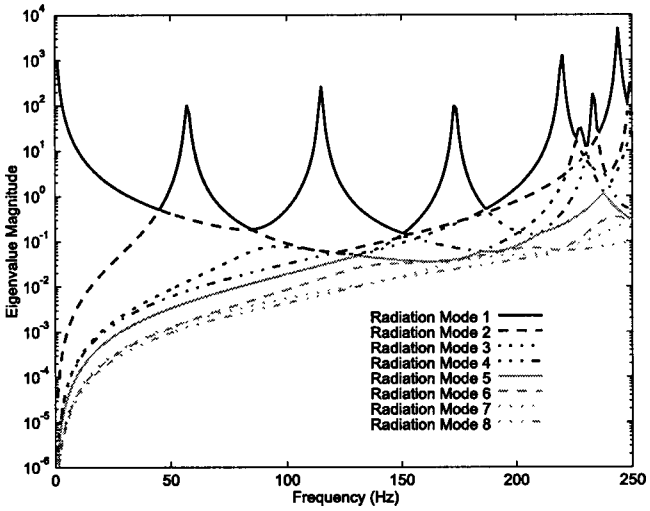

FIG. 13. Calculated (ranked) eigenvalue magnitudes of the first eight most efficient radiation modes.

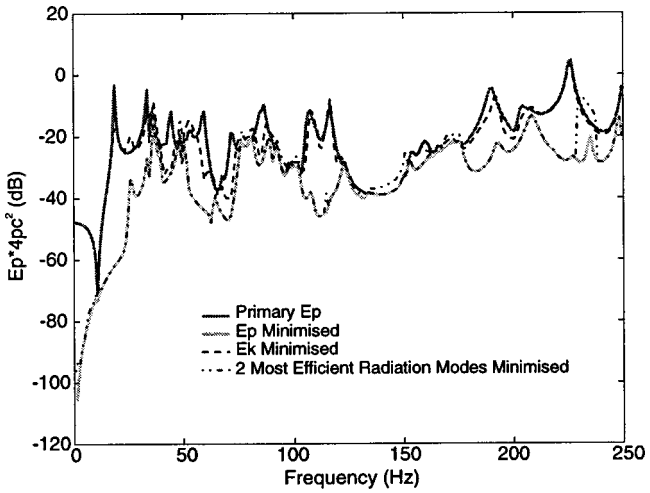

FIG. 14. Reduction in acoustic potential energy—Conventional error criteria versus radiation modal sensing.

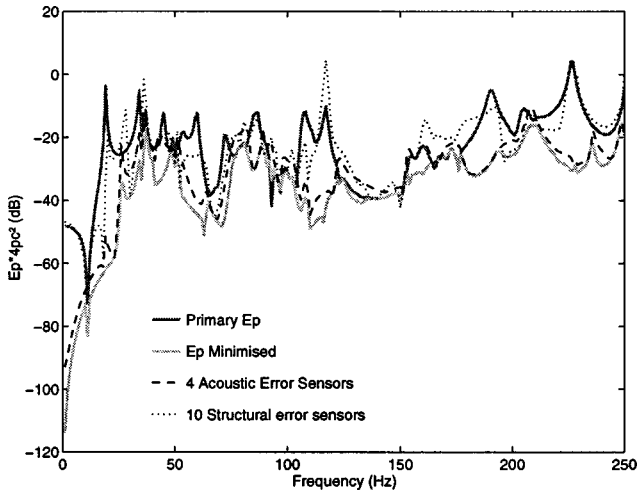

FIG. 15. Effect of insufficient structural sensors on performance and Control using four acoustic error sensors.

C. Active control of sound transmission—traditional error criteria versus radiation modes

A simulation was conducted where a single point force was placed randomly in a nonsymmetric location on the outside of the cylinder to provide the primary excitation source (78° at 1.35 m). A single secondary source was symmetrically located with respect to the floor on the shell to provide the control force (258° at 1.35 m). It should be noted that the location of the control force was not optimized in any way as this was not the aim of the study. The research objective was to show that it is possible to use a structural error sensor to provide an error signal which would result in a similar reduction in enclosure potential energy as obtained by using the enclosure potential energy as the error signal.

Figure 14 compares the reduction in the acoustic potential energy obtained when minimizing the two most efficient radiation modes against that obtained using conventional error criteria; namely, the acoustic potential energy (which provides an upper limit of control performance) and the structural kinetic energy. The cost function of Eq. (12) was optimized using conventional quadratic optimization to determine the optimum control force magnitude and phase. The velocity amplitudes of the radiation modes were estimated using the modal filter matrix given by Eq. (19). There were as many error sensors (100) as normal structural modes used to calculate the modal filter matrix (of the radiation modes) so as to provide an upper bound on the performance offered by the technique. A lesser number would have required the use of a pseudo-inverse to evaluate Eq. (20) which would have resulted in a decrease in the control performance. At the frequencies where the eigenvalues cross (in Fig. 13) there is an increase in the potential energy as a result of minimizing the amplitudes of the two radiation modes. This occurs for two reasons: (1) As several radiation modes contribute to the power transmission at these crossover frequencies, a single control force (used in the simulation) is unable to provide enough independent control channels to achieve control. Subsequently, the amount of control is low for all cost functions. The corollary is that the reduction in sound transmission is greatest where the radiation efficiencies peak. (2) Insufficient radiation modes were used to measure the power transmission, and this is particularly apparent in the frequency bands 140–160 Hz and 230–240 Hz. If more modes were used then the controlled levels would approach that of the potential energy controlled case.

It will be shown in the following section, for the frequency range of interest, that it is sufficient to consider only the first five dominant radiation modes (see Fig. 13) to achieve attenuation levels equal to those achieved by using the potential energy as a cost function.

Figure 15 shows the effect of having significantly fewer error sensors than the number of dominant structural modes. A practical number of ten error sensors were randomly located around the circumference of the cylinder and on the floor. As can be seen in this example, ten error sensors were insufficient to accurately resolve the modal amplitudes of the normal structural modes, resulting in observation spillover. In fact, it was found that it was necessary to have at least half the number of error sensors (50) as normal structural modes before an acceptable estimate of the structural modal amplitudes using Eq. (18) was obtained. This limitation associated with discrete error sensing has also been reported by others.[19,21]

Also shown in Fig. 15 is the acoustic potential energy when the squared sum of four acoustic error sensors is used as the error criterion. When comparing Fig. 15 against modal control in Fig. 14, it becomes clear that two radiation modal sensors outperform four traditional pressure field sensors (provided a sufficient number of structural sensors are used to properly measure the radiation modes). One may argue that it is not valid to draw comparisons between a structural system with 50–100 point sensors and an acoustic system with only 4 sensors. However, it should be noted that for active control applications it is the number of error signals, be they composite or point sensors, which define the system dimensionality.

The conclusion is that error signals derived from the radiation modes outperform conventional structural and acoustic error sensing and that excellent control is achieved with very few error signals. Although the radiation mode

formulation as it is described above using many discrete error sensors is unworkable for a practical control system because of the frequency dependence of the eigensystem and the large number of point sensors required, it can be used as a benchmark against which the performance of simplifications can be compared. The limitation arising from the frequency dependence will be addressed and techniques for overcoming it will be presented in the following section.

III. PRACTICAL IMPLEMENTATION AND APPROXIMATIONS

A. Background theory

As already shown in the preceding section, the eigenvalue and eigenvector matrices are highly frequency dependent and it is possible in a practical control system to generate an eigenvalue filter set using a low order digital filter for each radiation mode. However, the same cannot be said about the eigenvector matrix. In the case of the cylinder, for each radiation mode of interest, the eigenvector filter would consist of several hundred individual frequency dependent digital filters, one filter for every structural sensor used to measure each radiation mode. It is difficult to store the necessary filter coefficients to model the eigenvector matrix over a large bandwidth and definitely beyond the ability of current DSP systems to implement such filters in real time. It is also impractical in most cases to implement the required number of physical error sensors.

Studies of the power flow from cylinders[16] and rectangular panels using either vibration error sensors[18] or acoustic error sensors[6] have found that by exploiting the property that the radiation mode shapes (eigenvectors) varied slowly with respect to frequency, it was possible to select a frequency such that the radiation mode shapes at that frequency were representative of the mode shapes over a frequency range with little loss in accuracy. This was achieved by fixing the radiation transfer function matrix to that at some desired frequency (known as the *normalization* frequency), *f*, resulting in a set of eigenvectors independent of frequency which can be implemented by a fixed gain. This greatly reduces the number of digital filters required for the control system.

Applying this approach to the current set of equations yields[6]

$$\mathbf{U}=\mathbf{K}\mathbf{U}_f, \tag{23}$$

where $\mathbf{U}_f$ is the eigenvector matrix corresponding to the chosen frequency, *f*, and $\mathbf{K}$ is a $(n_r \times n_r)$ correction matrix and is given by

$$\mathbf{K}=\mathbf{U}\mathbf{U}_f^{-1}. \tag{24}$$

The correction matrix is highly diagonal and by neglecting the off-diagonal terms there is little loss in accuracy; that is,

$$\mathbf{K}=\mathrm{DIAG}[\mathbf{U}\mathbf{U}_f^{-1}]. \tag{25}$$

Substituting Eq. (23) into Eq. (10), an expression for the potential energy is obtained;

$$E_p \approx \mathbf{v}^H\mathbf{U}_f^H\mathbf{S}\mathbf{U}_f\mathbf{v}, \tag{26}$$

where $\mathbf{S}_f$ is the frequency normalized eigenvalue matrix,

$$\mathbf{S}_f=\mathbf{K}^H\mathbf{S}\mathbf{K}. \tag{27}$$

Although the radiation modes for internal acoustic spaces exhibit a significantly greater frequency dependence than free-field radiation modes (at frequencies below the critical frequency) it is possible to apply the same technique here with surprisingly little degradation in performance.

A more elegant and accurate way of obtaining an ''orthonormal'' set of equations than just described is to diagonalize the eigenvalue matrix after it has been pre- and post-multiplied by the correction matrix. Thus the following expansion may be made:

$$\mathbf{U}\mathbf{S}\mathbf{U}^T=\mathbf{U}_f[\mathbf{U}_f^{-1}\mathbf{U}\mathbf{S}\mathbf{U}^T\mathbf{U}_f]\mathbf{U}_f^{-1}. \tag{28}$$

By using the property of the unitary matrix ($\mathbf{U}^{-1}=\mathbf{U}^T$) it is possible to rearrange Eq. (28) to derive a orthonormal basis independent of frequency

$$\mathbf{U}\mathbf{S}\mathbf{U}^T=\mathbf{U}_f[\mathbf{S}_f]\mathbf{U}_f^T, \tag{29}$$

where $\mathbf{S}_f$ is the fixed frequency eigenvalue matrix given by

$$\mathbf{S}_f=\mathbf{U}_f^T\mathbf{U}\mathbf{S}\mathbf{U}^T\mathbf{U}_f. \tag{30}$$

In this format the eigenvalue matrix is not diagonal (except at the normalization frequency) but fully populated. It is therefore necessary to diagonalize the fixed frequency eigenvalue matrix to retain the benefits associated with the orthonormal transformation:

$$\hat{\mathbf{S}}_f=\mathrm{DIAG}[\mathbf{U}_f^T\mathbf{U}\mathbf{S}\mathbf{U}^T\mathbf{U}_f]. \tag{31}$$

As with the diagonalization of Eq. (24), very little loss in mass (accuracy) occurs when diagonalizing the highly diagonal frequency normalized eigenvalue matrix $\mathbf{S}_f$, particularly adjacent to the normalization frequency. The acoustic potential energy given by Eq. (10) can now be approximated as

$$E_p \approx \mathbf{v}^T\mathbf{U}_f\hat{\mathbf{S}}_f\mathbf{U}_f^T\mathbf{v}. \tag{32}$$

Likewise the fixed shape modal filter, Eq. (20), can be written as

$$\mathbf{Z}_{t|_f}=\mathbf{U}_f^T\Psi_e^{-1}. \tag{33}$$

The modal amplitudes of the fixed shape radiation modes are given by

$$\mathbf{w}=\mathbf{Z}_{t|_f}\mathbf{v}_e. \tag{34}$$

With the modal filter in a form independent of frequency, shaped sensors may be used to decompose the surface velocity into modal amplitudes (Fig. 16), thereby doing away with the many point sensors and associated eigenvector digital filters required in Fig. 1. Therefore, unlike the system in Fig. 1, only the eigenvalues need be implemented with digital filters (see Fig. 16). It should be noted that because of the discrete nature of the finite element simulations, ''continuous meta sensors'' were approximated from the summed output of a line of discrete point sensors.

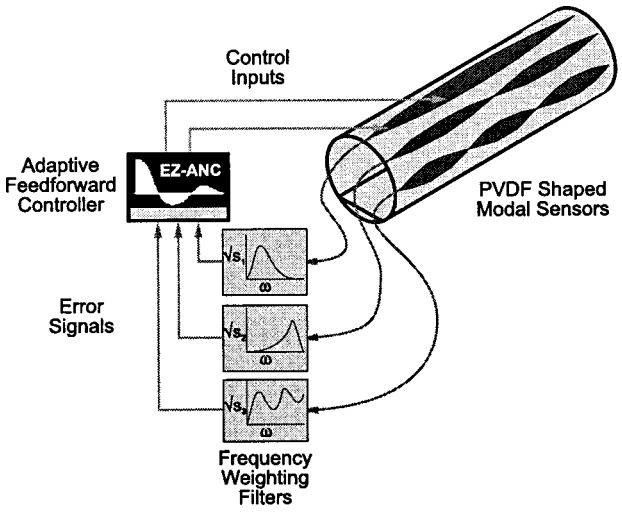

FIG. 16. Modal filter arrangement with frequency normalization of modal filter.

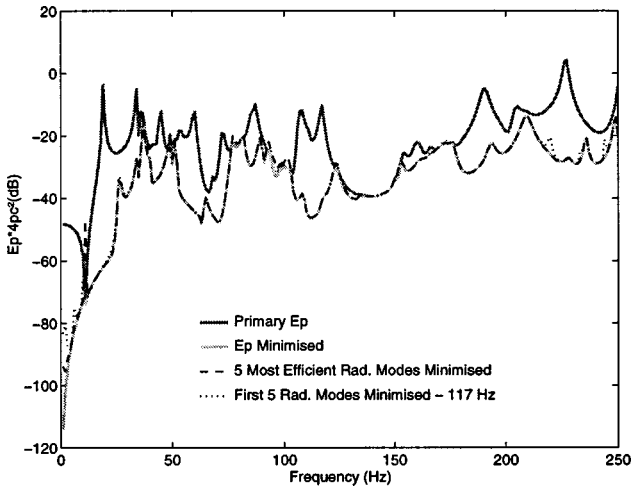

FIG. 18. Cost function comparison between frequency normalized radiation modes (117 Hz) and unmodified (frequency dependent) radiation modes.

The use of shaped error sensors made from piezo film and means for relating the charge output to the flexural motion of the surface to which they are fixed is discussed in detail by Hansen and Snyder.[27]

B. Results

As discussed previously, a decrease in accuracy is expected from neglecting the off-diagonal terms in the fixed frequency eigenvalue matrix [see Eq. (31)]. The error manifests itself as an increase in the number of efficient radiation modes away from the normalization frequency. This physically means that more ''orthogonal'' modes are necessary to account for the power transmission. Figure 17 illustrates the effect of fixing the eigenvectors to the values at a particular frequency has on the eigenvalues (as compared to Fig. 5).

As can be seen from Fig. 17, the eigenvalues around the frequency at which the system of equations is fixed (117 Hz) resembles the original frequency dependent data (Fig. 5). However, away from 117 Hz more radiation modes contribute significantly to the power transmission and as a result more modes will need to be measured to keep the control system performance equal to that of the frequency dependent case. A higher order digital filter is required to model the eigenvalues than was previously necessary in Fig. 5. However, this is still very easy to implement in a practical system.

As a benchmark, the performance achieved using the five most efficient radiation modes has been compared against that achieved using the first five fixed-shape radiation modes normalised at 117 Hz (see Fig. 18). This figure clearly shows that the two techniques yield almost identical levels of control (with the exception of 200–250 Hz where the acoustic modal density is high) demonstrating that frequency normalization of the mode shape is an excellent and highly efficient means of simplifying the control system when using radiation modal sensors.

Obviously, if fewer fixed-shape radiation modes are used, then the level of control will be subsequently reduced, particularly away from the normalization frequency. Figure 19 shows the reduction in the acoustic potential energy using

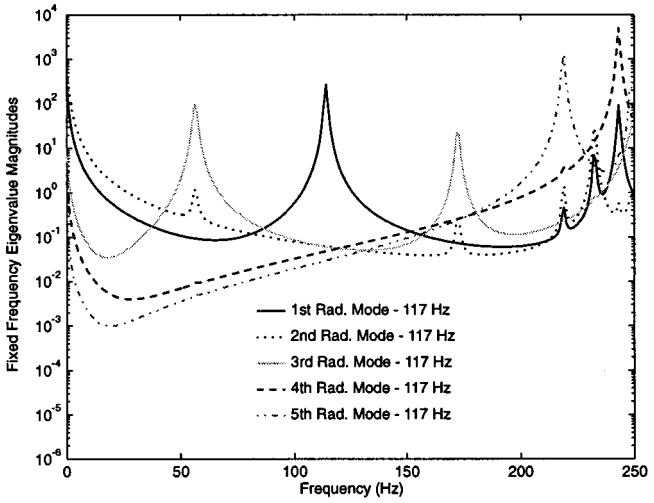

FIG. 17. Fixed frequency eigenvalues normalized to 117 Hz.

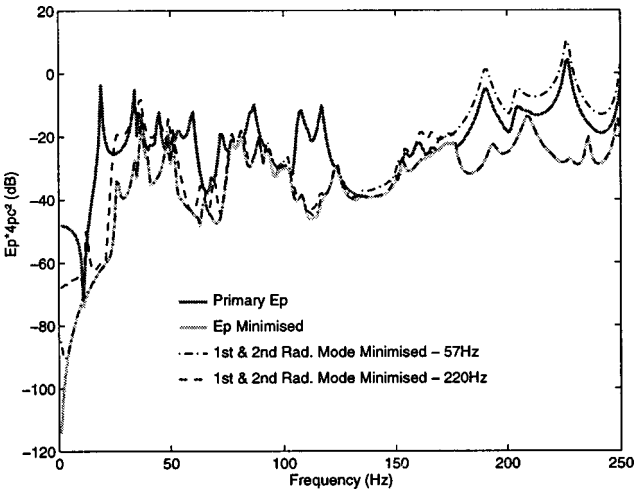

FIG. 19. Reduction in acoustic potential energy when minimizing frequency normalized mode shape functions.

the first two radiation modes when normalized to the first and fourth (nonzero) natural frequency of the cavity (57 and 220 Hz, respectively). For both cases, it can be seen that the performance drops away from the normalization frequency as the number of efficient radiation modes increases.

A close look at the results shows that control with the first two radiation modes fixed at 57 Hz is good between 10 and 140 Hz. Inspection of the mode shapes of the two most efficient fixed-shape radiation modes (fixed at 57 Hz) found that these reflected the first two acoustic modes (57 and 117 Hz). It is for this reason that control was only achieved up to 140 Hz. Likewise, when the radiation mode shapes were fixed to their shapes at 220 Hz, the first two radiation mode shapes matched the 173- and 220-Hz acoustic mode and good control was only achieved around the bandwidth bounded by these two frequencies.

C. Control without eigenvalue filters

In a real system, the eigenvalue (radiation efficiency) filter may be inconvenient to implement as most commercial active control systems do not have the facility to apply a frequency dependent filter to each individual channel. By not weighting the modal amplitudes by the square root of the radiation efficiencies (eigenvalue filter), neither the modal volume nor the acoustic impedance is accounted for in the cost function. As a result, the level of control afforded by the system will be reduced.

The five most efficient radiation modes were identified and their shape calculated at the natural frequencies of the first five acoustic modes, respectively. The modal amplitudes of these five fixed-shape radiation modes were then used as error signals for the control system over the entire frequency range of control. Figure 20 shows the acoustic potential energy levels obtained when minimizing the five most efficient fixed-shape radiation modes normalized to the natural frequencies of the first five acoustic modes without using an eigenvalue filter in the control system.

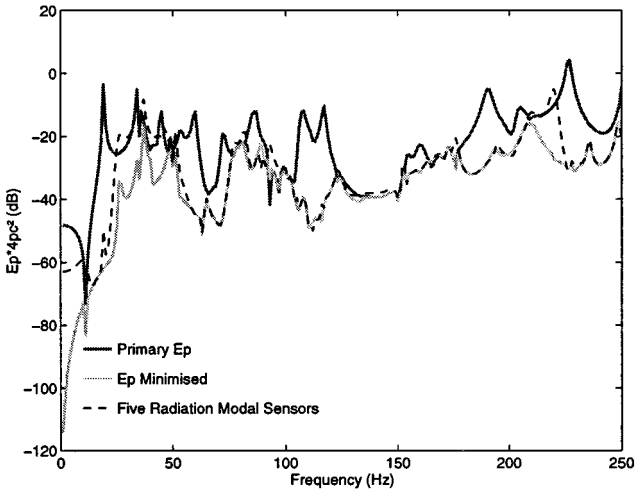

FIG. 20. Multi-channel frequency normalized radiation modal sensors without radiation efficiency weighting filter.

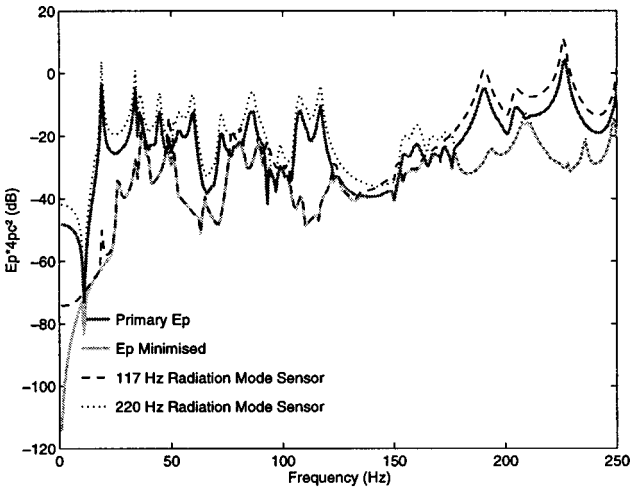

FIG. 21. Single channel frequency normalized radiation modal sensors without radiation efficiency weighting filter.

As can be seen, the reduction in the potential energy is less than that shown in Fig. 18. The poor performance is a result of not accounting for the frequency dependent radiation efficiency of the individual radiation modes. As a result, much of the control effort is spent in reducing the amplitudes of the less efficient modes, which do not significantly contribute to the sound transmission.

If only a single fixed-shape radiation mode is sensed, then 100% of the control effort is used in controlling that mode. Such an approach gives good results over a limited bandwidth around the frequency at which the mode shape is fixed. Figure 21 shows the level of control achieved by using the ''raw'' (unweighted) signal derived from a single radiation mode sensor whose shape was normalized at either 117 or 220 Hz. If a single channel control system were to use these two modal sensors with a crossover at approximately 170 Hz, this would provide almost optimal control over the 0–250 Hz frequency band. It should be noted that although such an approach is suitable for a system with a single control source, it is unlikely that it will work as well for systems using multiple control sources.

IV. CONCLUSIONS

It has been shown that it is possible to decompose a large number of discrete surface vibration measurements into a small number of high quality error signals for an active noise control system and obtain similar or improved results to conventional acoustic and structural error sensing. The decomposed structural vibration signals are formed so that they represent amplitudes of ''radiation modes'' which are orthogonal in terms of their contribution to the acoustic potential energy in the enclosure. The result of using such error signals is an increase in stability of the active noise control system and reduced dimensionality achieved through the reduction of the condition number of the control system transfer function matrix. Modal sensing of radiation modes provides the highest level of control with noninvasive sensors. Frequency normalization permits the use of shaped modal sensors rather than numerous discrete sensors to provide the

required error signals to minimize the enclosure acoustic potential energy. The work derived is not limited to stiffened cavities and may be applied to any coupled vibro-acoustic system. Preliminary experimental investigations involving the use of the technique to control the sound transmission from a small curved panel into an enclosed box have been very promising, although more work is needed in understanding the sensitivity of the control system to shape and fidelity errors before acceptable potential energy reductions will be achieved with large vibro-acoustic systems.[28]

ACKNOWLEDGMENTS

The authors gratefully acknowledge the financial support for this work provided by Australian Research Council and the Sir Ross & Keith Smith Fund. The authors would also like to thank colleagues Dr. K. A. Burgemeister and Dr. S. D. Snyder for their most enlightening discussions and contributions.

[1] F. Charette, C. Guigou, and A. Berry, ''Development of volume velocity sensors for plates using pvdf film,'' in Active 95, pp. 241–252 (1995).
[2] J. Pan, C. Hansen, and D. Bies, ''Active control of noise transmission through a panel into a cavity: I. Analytical study,'' J. Acoust. Soc. Am. **87**, 2098–2108 (1990).
[3] S. Snyder and N. Tanaka, ''On feedforward active control of sound and vibration using error signals,'' J. Acoust. Soc. Am. **94**, 2181–2193 (1993).
[4] K. Cunefare and M. Currey, ''On the exterior acoustic radiation modes of structures,'' J. Acoust. Soc. Am. **96**, 2302–2312 (1994).
[5] K. Naghshineh and G. Koopmann, ''Active control of sound power using acoustic basis functions as surface velocity filters,'' J. Acoust. Soc. Am. **93**, 2740–2752 (1993).
[6] K. Burgemeister, ''Novel methods of transduction for active control of harmonic sound radiated by vibrating surfaces,'' Ph.D. dissertation, The University of Adelaide, 1996.
[7] S. Elliott and M. Johnson, ''Radiation modes and the active control of sound power,'' J. Acoust. Soc. Am. **94**, 2194–2204 (1993).
[8] S. Snyder and K. Burgemeister, ''Performance enhancement of structural/acoustic active control systems via acoustic error signal decomposition,'' in *Inter-Noise 96* (Liverpool), pp. 1141–1146 (1996).
[9] M. Currey and K. Cunefare, ''The radiation modes of baffled finite plates,'' J. Acoust. Soc. Am. **98**, 1570–1580 (1995).
[10] M. Johnson and S. Elliott, ''Active control of sound radiation using volume velocity cancellation,'' J. Acoust. Soc. Am. **98**, 2174–2186 (1995).
[11] K. Burgemeister and S. Snyder, ''Active minimisation of radiated acoustic power using acoustic sensors,'' J. Acoust. Soc. Am. (submitted).
[12] S. Snyder, N. Tanaka, K. Burgemeister, and C. Hansen, ''Direct-sensing of global error criteria for active noise control,''in Active 95, pp. 849–860 (1995).
[13] G. Borgiotti, ''The power radiated by a vibrating body in an acoustic fluid and its determination from boundary measurements,'' J. Acoust. Soc. Am. **88**, 1884–1893 (1990).
[14] D. Photiadis, ''The relationship of singular value decomposition to wave-vector filtering in sound radiation problems,'' J. Acoust. Soc. Am. **88**, 1152–1159 (1990).
[15] P.-T. Chen and J. Ginsberg, ''Complex power, reciprocity, and radiation modes for submerged bodies,'' J. Acoust. Soc. Am. **98**, 3343–3351 (1995).
[16] G. Borgiotti and K. Jones, ''Frequency independence property of radiation spatial filters,'' J. Acoust. Soc. Am. **96**, 3516–3524 (1994).
[17] G. Borgiotti and K. Jones, ''The determination of the acoustic far field of a radiating body in an acoustic field from boundary measurements,'' J. Acoust. Soc. Am. **93**, 2788–2797 (1993).
[18] S. Snyder, C. Hansen, and N. Tanaka, ''Shaped vibration sensors for feedforward control of structural radiation,'' in *The Second Conference on Recent Advances in Active Control of Sound and Vibration* (Virginia Tech, Blacksburg, VA, 1993).
[19] N. Tanaka, S. Snyder, and C. Hansen, ''Distributed parameter modal filtering using smart sensors,'' Trans. ASME, J. Vib. Acoust. **118**, 630–640 (1996).
[20] R. Clark, ''Adaptive feedforward modal space control,'' J. Acoust. Soc. Am. **98**, 2639–2650 (1995).
[21] D. Morgan, ''An adaptive modal-based active control system,'' J. Acoust. Soc. Am. **89**, 248–256 (1991).
[22] F. Fahy, *Sound and Structural Vibration: Radiation, Transmission, and Response* (Academic, London, 1985).
[23] P. Nelson, A. Curtis, S. Elliott, and A. Bullmore, ''The active minimization of harmonic enclosed sound fields, part I: Theory,'' J. Sound Vib. **117**, 1–13 (1987).
[24] S. Snyder and C. Hansen, ''The design of systems to actively control periodic sound transmission into enclosed spaces, part 1: Analytical models,'' J. Sound Vib. **170**, 433–449 (1994).
[25] F. Bessac, L. Gagliardini, and J.-L. Guyader, ''Coupling eigenvalues and eigenvectors: A tool for investigating the vibroacoustic behaviour of coupled vibrating systems,'' J. Sound Vib. **191**, 881–899 (1996).
[26] M. Mercadal and A. Flowtow, ''On the importance of representative structural models in turboprop acoustics,'' J. Sound Vib. **188**, 753–759 (1995).
[27] C. Hansen and S. Snyder, *Active Control of Noise and Vibration* (E&FN Spon, London, 1997).
[28] B. Cazzolato and C. Hansen, ''Structural sensing of sound transmission into a cavity for active structural-acoustic control,'' in *Proceedings of the Fifth International Congress and Vibration* (The International Institute of Acoustics and Vibration, Adelaide), pp. 2391–2401 (1997).

A field survey on the annoyance caused by sounds from large firearms and road traffic[a)]

Edmund Buchta
Institut für Lärmschutz, Düsseldorf, Germany

Joos Vos
TNO Human Factors Research Institute, Soesterberg, The Netherlands

(Received 24 February 1998; revised 10 July 1998; accepted 19 July 1998)

Subjective reactions to artillery sounds were determined for over 400 respondents divided among 17 different residential areas. Also, for the same respondents, the subjective effects of road-traffic sounds were determined enabling a comprehensive comparison of the dose-response relations. For the sake of comparison with other field surveys, the noise dose for the shooting sounds was, among other things, expressed as the yearly average C-weighted day–night level (CDNL) and that for the road-traffic sounds was expressed as the A-weighted day–night level (ADNL). Similarly, for both sound types the community response was expressed as the percentage of respondents being ''highly annoyed.'' From the comparison of the two dose-response relationships it could be concluded that for numerically equal day–night levels, the artillery sounds were more annoying than the road-traffic sounds. Overall, the difference was equivalent to the change in annoyance produced by a 5-dB shift in the yearly average day–night levels of the sounds. With equal day–night levels for ''downwind'' conditions, the artillery and road-traffic sounds were equally annoying. Results from the present highly controlled field survey provided a new opportunity to optimize the parameter values in Schomer's rating procedure $y=(1/\beta)(L_{\mathrm{CE}}-\mathrm{PNSE})+\mathrm{PNSE}$, in which the noise exposure for impulsive sounds (y) is expressed as the A-weighted SEL of equally annoying vehicle sounds. PNSE represents the point at which the impulsive and vehicle sounds with numerically equal levels are also equally annoying. With PNSE fixed at 103 dB, an optimal solution was found with slope β set to 1.3. With the previously recommended slope $\beta=0.67$, the rating sound level for artillery sounds would be underestimated by almost 12 dB. © *1998 Acoustical Society of America.* [S0001-4966(98)06110-4]

PACS numbers: 43.50.Qp, 43.50.Ba, 43.50.Pn [MRS]

INTRODUCTION

The spectrum of artillery sounds such as the muzzle bangs from 120, 155, and 203 mm calibre weapons and the bangs from detonating high-explosive shells and other explosions is dominated by the energy in low-frequency bands. In contrast with the impulses from small firearms, these artillery sounds can excite noticeable vibration of dwellings. The induced vibration in dwellings might generate additional annoyance beyond that due to the audibility of the impulses because of house rattling, startle, and fear for structure damage.

For many years, procedures for the assessment of community response to this kind of high-energy impulsive sounds (CHABA, 1981) have been based on the results from only two field surveys: the sonic-boom study in the Oklahoma City area (Borsky, 1965) and a field survey on artillery noise reported by Schomer (1982). On the basis of the results from these two studies, together with additional results from studies on, among other things, the annoyance of sonic booms relative to that of airplane flyover noise (see Kryter, 1985, Chap. 5), CHABA Working Group 84 (1981) in fact proposed to express the dose of the impulses in the average C-weighted day–night level (CDNL, L_{Cdn}), and concluded that for $L_{\mathrm{Cdn}}>60$ dB, the annoyance rises more rapidly than is indicated by a comparable relation between the A-weighted day–night level (ADNL, L_{Adn}), and the annoyance caused by transportation noise.

In the last 10–15 years, additional results from field surveys on the annoyance caused by artillery sounds have been reported (Bullen *et al.*, 1991; Rylander and Lundquist, 1996; Schomer, 1985), and a portion of the available data has recently been revised (Schomer, 1994). After a comparison of the various dose-response relations for the artillery sounds with the dose-response relation for transportation sounds (air-, road-, and rail-traffic), as synthesized by Schultz (1987), it might be concluded that for numerically equal day–night levels, the artillery sounds are more annoying than the transportation sounds. Overall, the difference in annoyance between the artillery and transportation sounds is equivalent to the change in annoyance produced by a shift of 8–12 dB in the day–night level. Moreover, the data suggest that the difference in annoyance slightly decreases with increasing level of the artillery and transportation sounds. In line with the conclusions drawn in NRC (1996), however, additional information about the annoyance caused by high-energy impulsive sounds is highly needed.

In the present study, the relationship between the annoy-

[a)]A portion of this article is an abridged and revised version of *Belästigung durch Kanonenlärm in dB(C) und Straßenverkehrslärm in dB(A)*, published by Institut für Lärmschutz, February 1993.

ance caused by artillery and (road-)traffic sounds is investigated further. Since the subjective effects of artillery and (local) road-traffic sounds were determined for the *same* respondents, and with a *uniform* questionnaire, the comparison between the community response to these two different sound sources is highly controlled.

With the present design, unwanted influences of climatic (season of survey), cultural (e.g., items related to the language: wording of the questions, number and wording of response alternatives), personal (noise sensitivity, ability to cope with the noise), physical (dwelling type, single or double glazing), and methodological factors (location of questions in the questionnaire, mode of administration of the questionnaire), as well as various possible interactions of these factors (window opening patterns, amount of outdoor activity around the dwelling) on the comparison are reduced as much as possible (Fields and Walker, 1982; Fields and Hall, 1987; Guski *et al.*, 1978).

In addition to the more conventional rating procedure for artillery sounds, which is based on CDNL, preferably in combination with, as indicated above, either a constant or a level-dependent adjustment, two alternative rating procedures have recently been proposed.

In one of these procedures, the A-weighted and C-weighted sound levels of the impulses, either measured with the time constant of 125 ms, or expressed as the A-weighted and C-weighted sound exposure levels (ASEL and CSEL) of the impulses (Buchta, 1996; Krahé and Buchta, 1994; Vos, 1996) are the two relevant parameters.

In the other alternative procedure, a level-dependent conversion of the CSELs of the impulses into the ASELs of equally annoying vehicle passby sounds is applied (Schomer, 1994). In a recent re-analysis (Vos, 1997) it was shown that at least for artillery sounds, the optimal parameter values to be used in this level-dependent conversion procedure were different from those suggested by Schomer.

The experimental results of the present field survey provide a new opportunity to optimize Schomer's conversion procedure. This effort is especially interesting because here, in contrast to previous analyses, large sets of different CSEL-values per residential area are available, and, as a result of the features of the present survey design, it might be expected that the estimation of the adequate parameter values is highly reliable.

I. METHODS

A. General

To allow the determination of dose-response relationships, 17 residential areas (zones) at different distances from the military training fields (MTFs) of Bergen and Munster were selected for interviews. For 15 of the 17 zones, the number of personal interviews completed ranged between 23 and 28 (Table I). For two zones the number of completed interviews was 13 or 56. For the 17 zones around the MTFs, 433 interviews were completed in total. For the 82 respondents in the 3 noise zones of Unterlüß, the questionnaires also included items on the subjective effects of the shooting sounds produced at the Rhein Metall test area located north of the village of Unterlüß.

The questionnaire consisted of about 100 questions; many of these questions had been used in previous studies (e.g., see Buchta, 1990). For 5% of the respondents the age was lower than 20 years, and for 20% of the respondents the age was higher than 60 years. For the remaining 75%, the age was evenly distributed between 20 and 60 years. There were slightly more female than male respondents (53% vs 47%). The interviews were carried out in the summer of 1991.

B. Description of the training and residential areas

In 16 zones, the exposure to shooting noise was to a large extent determined by the bangs from detonating grenades and explosions (zones 1–3, 4a–6a, 7–14, 16, 17; see Table I). In most zones, the muzzle bangs from the 120 mm cannon (zones 1–3, 4a–5a, 7–11, 16) and those from the 120 mm cannon and the 155 mm howitzer (zones 6a, 12, 13) contributed significantly as well. In addition to the detonations/explosions, in zone 14 the muzzle bangs from the howitzer, and in zone 17, the muzzle bangs from the 20 and 120 mm weapons were important. In zones 5b and 6b, the exposure was determined by the muzzle bangs from the 20 and 35 mm guns, whereas in zone 4b, the exposure was determined by the muzzle bangs from the 35, 120 and 155 mm caliber weapons. In zone 15, the exposure was determined by the muzzle bangs from the 120 mm cannon.

In addition to the shooting sounds, the respondents in each zone were exposed to local road-traffic sounds.

C. Computation of the noise dose on a yearly basis

1. Shooting sounds

In many cases the shooting sounds produced by firearms are composed of various components: the muzzle report, the projectile report, and especially for the large firearms, the detonation of the grenade in the target area.

As long as the speed of the projectile exceeds the velocity of sound in air, a shock front is produced. The projectile shock forms a cone whose vertex is centered on the moving projectile at any time and whose sides are tangent to the muzzle blast front. As a result, the area in which the projectile bang occurs is limited to a relatively narrow sector in front of the weapon. Since shooting occurs from the edges to the center of the MTF, the projectile bang has to travel over a much longer distance before arriving at the residential area than the part of the muzzle bang propagating backward. Moreover, due to spectral differences, the level reduction with distance is greater for the projectile bang than for the muzzle bang. Because of these two factors, the sound-pressure levels of the projectile reports in the residential areas are always considerably lower than those of the muzzle reports. For the community response, the projectile reports are therefore of minor importance and excluded from computation of the yearly noise dose.

For zones 1–17, detailed information about the ammunition spent in 1989 and 1990 was provided by the opera-

TABLE I. C-weighted yearly average sound level (CLEQ) of shooting noise and percentage of ''highly annoyed'' respondents, for 17 noise zones around military training fields Bergen/Munster. The number of respondents in each zone is indicated by n. CLEQs are given for the daytime and the nighttime separately; the overall noise dose is expressed as the C-weighted day–night level (CDNL). The community response to the artillery sounds is given for two different questions (A1 and A2) explained in the text. In three of these 17 noise zones, the respondents were also exposed to the shooting sounds produced at the Test Area of Unterlüß Rhein Metall. The community response to these sounds, as well as the relevant CLEQ- and CDNL-values are given in the lower part of the table.

			CLEQ in dB			% highly annoyed		
No. (1)	Noise zone (2)	n (3)	Day (4)	Night (5)	CDNL (6)	A1 (7)	A2 (8)	M (9)
			Military Training Areas Bergen/Munster:					
1	Eschede	24	42.3	36.8	44.3	4.2	4.2	4.2
2	Schneverdingen	23	41.9	36.4	43.9	18.2	8.7	13.5
3	Neuenkirchen	23	45.7	37.3	46.3	17.4	21.7	19.6
4a	Unterlüß-Nord	27	48.0	43.4	50.6	15.4	13.8	14.6
5a	Unterlüß-Mitte	28	47.7	43.0	50.2	10.7	10.2	10.5
6a	Unterlüß-Süd	27	47.2	42.5	49.7	0.0	1.8	0.9
7	Sülze	23	53.6	46.6	54.9	26.1	17.4	21.8
8	Soltau	23	54.8	48.0	56.1	18.2	8.7	13.5
9	Bomlitz	23	55.9	45.7	55.8	34.8	26.1	30.5
10	Bergen	24	59.6	52.7	60.9	29.2	33.3	31.3
11	Fallingbostel	25	63.5	52.7	63.3	52.0	32.0	42.0
12	Wietzendorf	23	67.3	62.4	69.7	30.4	43.5	37.0
13	Munster-Nord	56	68.4	63.8	71.0	32.7	30.4	31.6
14	Munster-Süd	13	70.9	66.3	73.5	46.2	7.7	27.0
15	Meißendorf	23	64.7	55.6	65.0	47.8	34.8	41.3
16	Westenholz	23	70.7	60.9	70.8	60.9	65.2	63.1
17	Dorfmark	25	65.0	53.6	64.6	72.0	64.0	68.0
		433						
			Test Area Rhein Metall:					
4b	Unterlüß-Nord	27	63.3	···	61.5	48.2	44.4	46.3
5b	Unterlüß-Mitte	28	50.6	···	48.8	21.4	17.9	19.7
6b	Unterlüß-Süd	27	47.9	···	46.1	3.7	11.1	7.4

tional planning section of the relevant MTFs. For zones 4b–6b, such information was available for 1991. From these reports the number of shots fired in a representative calendar year was computed for the daytime and the nighttime separately. These calculations were performed for each firearm and for each firing range, yielding emission data for over 100 separate cases relevant to zones 1–17, and for about 25 cases relevant to zones 4b–6b.

The CSELs of the various bangs, as received in the specific residential areas, was calculated with ''LARMLAST.'' This computer program was developed by the ''Institut für Lärmschutz'' and includes an advanced propagation model based on a large number of sound measurements performed in the field (Hirsch and Buchta, 1993). From the CSEL-values and the corresponding total numbers, the yearly C-weighted equivalent level (CLEQ, L_{Ceq}) for the daytime (06–22 h) was computed for the time period of 4160 h [$=52$ (weeks)$\times 5$ (days)$\times 16$ h], and the yearly CLEQ for the nighttime (22–06 h) was computed for 2080 h.

Since the CSEL-values, as predicted by ''LARMLAST,'' are only relevant for ''downwind'' conditions, the yearly CLEQ had to be corrected. In a related field survey, appropriate corrections to downwind CLEQ ranged between -2.3 and -3.8 dB (Buchta, 1988). For lack of such specific information for the separate zones in the present study, an average correction of -3.3 dB was applied to CLEQ in all noise zones.

2. Road-traffic sounds

In each noise zone the levels of local road-traffic sounds were measured between 6 and 22 h for various time periods ranging from 15 to 30 min. On the basis of these data the A-weighted equivalent level (ALEQ, L_{Aeq}) for the daytime was computed. ALEQ in the nighttime was typically 10 dB lower than ALEQ in the daytime. ADNL of the road-traffic sounds, with a 10 dB nighttime penalty applied between 22 and 6 h, was therefore equal to ALEQ as determined between 6 and 22 h.

D. The questionnaire

The questionnaire included various items assessing, among other things, general disturbance, specific annoyance, emotional experiences, habituation, and so on. Since the CSELs of the single bangs around the dwellings of the respondents were all lower than 105 dB, aspects such as hearing damage and vegetative functional disorders were not considered.

The wording of most questions occurred by means of one of three possible formats. More than 20 questions were preceded by the introductory question ''To what extent is

this sentence correct?'' In these cases the respondents had to select their answers from (1) ''quite correct'' (in German: ''stimmt sehr''), (2) ''considerably correct'' (''stimmt ziemlich''), (3) ''correct on the average'' (''stimmt mittelmäßig''), (4) ''a little correct'' (''stimmt wenig''), and (5) ''not correct'' (''stimmt nicht''). Twenty additional questions were preceded by the introductory question ''How often are you affected by...,'' after which the respondents had to select their answers from (1) ''never'' (''nie''), (2) ''seldom'' (''selten''), (3) ''sometimes'' (''manchmal''), (4) ''often'' (''oft''), and (5) ''very often'' (''sehr oft''). In a portion of the remaining questions, the degree of annoyance, loudness or habituation was determined directly with the help of the appropriate verbally labeled response scales.

For example, a question that is very relevant to the analyses in Secs. II A–B read ''Could you please indicate to which extent you are disturbed in your residential area by the noise from cannons, grenades, and explosions?'' A similar question was asked to determine the disturbance caused by road-traffic sounds. The respondents had to select their answers from (1) ''not disturbing'' (''stört nicht''), (2) ''weakly disturbing'' (''stört schwach''), (3) ''clearly disturbing'' (''stört deutlich''), (4) ''strongly disturbing'' (''stört stark''), and (5) ''very strongly disturbing'' (''stört sehr stark'').

II. DOSE-RESPONSE RELATIONSHIPS

A. Dose-response relationships for shooting sounds

For the various noise zones, Table I shows the CLEQs for the day- and the nighttime in columns 4 and 5, respectively. As a conventional measure of the overall noise dose, CDNL is given in column 6.

There were basically two questions that informed about the degree of annoyance caused by shooting sounds. In one of these questions (question A1) the respondents had to select their answers from verbally labeled 5-point rating scales (see last paragraph in Sec. I D). In the other question (question A2) a 9-point rating scale with, at the extremes, the labels ''not annoying'' and ''extremely strongly annoying'' was used.

In many field surveys on the effects of noise, the community response is expressed as a percentage of the respondents being ''highly annoyed'' (e.g., see Fidell *et al.*, 1991; Hall *et al.*, 1981; Rylander *et al.*, 1972, 1974; Schomer, 1982, 1985; Schultz, 1978; Vos, 1985, 1995) or ''seriously affected'' (Bullen *et al.*, 1991; Hede and Bullen, 1982). For comparability with related studies, the subjective effect of artillery noise, as found in the present study, will be expressed as the percentage of respondents being ''highly annoyed'' as well. For question A1 all respondents who indicated being ''strongly,'' or ''very strongly disturbed'' were considered to be ''highly annoyed.'' For question A2, all respondents who selected one of the three upper response categories were considered to be ''highly annoyed.''

For each noise zone the percentages of ''highly annoyed'' respondents, as determined with questions A1 and A2, are given in columns 7 and 8 of Table I. Overall, question A1 yielded a percentage ''highly annoyed'' respondents which was five percentage points higher than that of question A2. The correlation coefficient, r, between the percentages obtained by the two questions was equal to 0.80. In these annoyance questions, no reference was made to the experiences in a specific part of the day. The questions were intended to elicit overall responses. In line with this, the community response (percentages ''highly annoyed'' obtained with questions A1 and A2) will first be related to CDNL.

The function

$$y = \Phi[(L_{\mathrm{Cdn}} - \mu)/\sigma] \tag{1}$$

was fitted to the data, in which μ is the expected value for $y = 50\%$, and σ is a measure for the steepness of the function. $\Phi(z)$ denotes the cumulative normal (Gaussian) distribution. The values of μ and σ are obtained by means of maximum-likelihood estimation.

The statistical association between the percentages ''highly annoyed'' and CDNL [as determined with Eq. (1)] was stronger for question A1 than it was for question A2. The variance explained in the percentages by the day–night level and the cumulative distribution function was 58% and 39% for questions A1 and A2, respectively. On the basis of the mean percentages of ''highly annoyed'' respondents (column 8 in Table I), the explained variance was 53%.

Since there were various zones in which the noise dose was almost equal, it was decided to stratify the data from Table I. With the class intervals given in Table II, a comprehensive re-grouping of the respondents was obtained. In contrast with the previous analyses, the predictability of the community response from the day–night level was about the same for question A1 and question A2: The variance explained in the percentages was as high as 73% for question A1 and 77% for question A2.

On the basis of the mean percentages of ''highly annoyed'' respondents (seventh column in Table II), the explained variance was 77%. Figure 1 shows these mean percentages (y) obtained in the various class intervals as a function of CDNL. The equation of the cumulative distribution function (dashed line) fitted to the data in Fig. 1 is given by $y = \Phi[(L_{\mathrm{Cdn}} - 70.6)/20.8]$.

B. Dose-response relationship for road-traffic sounds

On the basis of their corresponding ADNLs of the road-traffic sounds, the annoyance ratings of the respondents were assigned to one of the eight classes given in Table III. The lower and higher boundaries of the class intervals were chosen in such a way that at least for six intervals the mean A-weighted levels were very close to mean C-weighted levels for the shooting sounds (Table II). The differences ranged between 0.2 and 0.6 dB. The number of respondents in each class interval is given in the fourth column of Table III. Percentages of ''highly annoyed'' respondents were determined for two questions, B1 and B2, which were identical to questions A1 and A2 (Sec. II A) with respect to both the wording of the questions and with respect to the response alternatives.

The variance explained in the percentages by ADNL (column 3 in Table III) and the cumulative distribution function was 85% and 86% for questions B1 and B2, respec-

TABLE II. Stratification of the data given in Table I. Lower and higher boundaries of the class intervals, as well as the mean value for each class interval, are expressed as the C-weighted yearly day–night level (CDNL in dB) of the shooting sounds. The number of respondents in each class interval is indicated by n. The community response to the artillery sounds was determined with questions A1 and A2, as explained in the text, and is expressed as (1) percentages of ''highly annoyed'' respondents, (2) as percentages of ''clearly and highly annoyed'' respondents, and (3) as the mean of the annoyance ratings from all respondents. M represents the mean of the percentages or the ratings; σ_M is the estimated standard error of the mean.

CDNL boundary				% of respondents annoyed							
				Highly			Clearly and highly			Annoyance ratings	
Lower (1)	Higher (2)	Mean CDNL (3)	n (4)	A1 (5)	A2 (6)	M (7)	A1 (8)	A2 (9)	M (10)	M (11)	σ_M (12)
43	45	44.1	47	10.6	6.4	8.5	15.2	25.2	20.4	2.0	0.17
46	47	46.2	50	10.0	16.0	13.0	30.0	28.0	29.0	2.3	0.15
48	51	49.8	110	11.9	11.0	11.5	22.9	30.3	26.6	2.0	0.10
54	57	55.6	69	26.5	17.4	21.9	38.2	39.1	38.7	2.5	0.16
60	62	61.2	51	39.2	39.2	39.2	52.9	62.7	57.8	3.1	0.18
63	66	64.3	73	57.5	43.8	50.7	76.7	72.6	74.7	3.6	0.15
68	74	71.0	115	39.5	37.4	38.5	58.8	61.7	60.3	3.1	0.12

tively. On the basis of the mean percentages of ''highly annoyed respondents'' (seventh column in Table III) the explained variance was 89%. These mean percentages are included in Fig. 1. The equation of the cumulative distribution function (solid line) fitted to the data in Fig. 1 is given by $y=\Phi[(L_{\mathrm{Adn}}-73.1)/17.8]$.

C. Adjustment for shooting noise

From the two dose-response relationships shown in Fig. 1, it can be concluded that even if the average yearly day–night level for artillery sounds is C-weighted, a correction is needed. For a criterion of, for example, 20% ''highly annoyed'' respondents, an adjustment of 5.0 dB has to be added to obtain ADNL of equally annoying road-traffic sounds; for a criterion of 40% ''highly annoyed'' respondents, the adjustment is 3.2 dB. These results imply that the adjustment is not significantly dependent on the overall level of the shooting sounds, and that application of a 4-dB adjustment would be adequate.

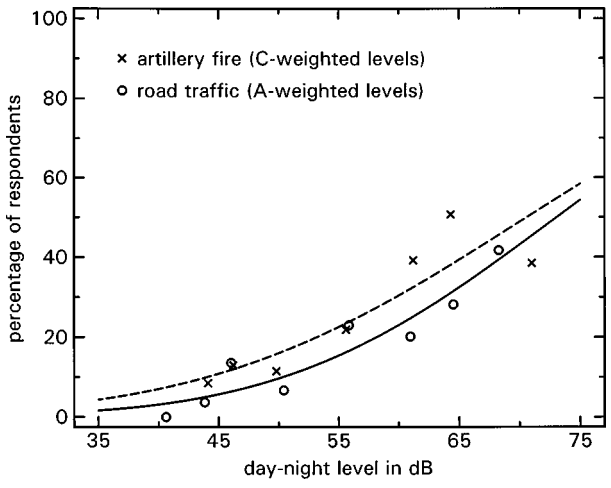

FIG. 1. Percentage of respondents describing themselves as ''highly annoyed'' as a function of the yearly average C-weighted day–night level for the shooting sounds, and as a function of the A-weighted day–night level for the road-traffic sounds. For each sound source, the percentages are based on the responses to two questions. The inserted dashed and solid lines are regression functions for the shooting and road-traffic data, respectively.

III. OPTIMIZATION OF A LEVEL-DEPENDENT CONVERSION PROCEDURE

A few years ago Schomer (1994) developed a new rating procedure for high-energy impulsive sounds, in which a level-dependent conversion of the CSELs of the impulses into the ASELs of equally annoying vehicle sounds was applied. In a recent re-analysis Vos (1997) showed that at least for *artillery sounds* the optimal parameter values to be used in this level-dependent conversion procedure were different from those suggested by Schomer. The experimental results from the present field survey provide a new opportunity to optimize the conversion procedure.

A. Recent laboratory results

In various field-laboratory studies—carried out at the MTF of Munster, Germany, and at Aberdeen Proving Ground, Maryland—listeners were presented with high-energy impulse sounds produced by blasting-charges (0.2–4 kg TNT), with sounds produced by various types of wheeled vehicles passing by, and with loudspeaker-generated white noise control sounds (Schomer *et al.*, 1994; Schomer and Wagner, 1995). The studies were designed as paired comparison tests where the listeners were presented with the impulse test sounds and the vehicle or white-noise control sounds and were asked, for each pair, to indicate which sound was more annoying, the first or the second one. On the basis of the responses of the subjects, the average ASELs of the vehicle or white-noise sounds were determined at which these reference sounds were as annoying as the impulse sound.

A typical result is shown in Fig. 2, where the boldly printed solid line relates the levels of equally annoying vehicle and impulse sounds. In the present example, slope β in the function $L_{\mathrm{CE}}(\mathrm{impulse})=\alpha+\beta L_{\mathrm{AE}}(\mathrm{vehicle})$ equals 0.5, which implies that for a similar shift in the annoyance, a 1-dB increase in CSEL of the impulse sound requires a 2-dB

TABLE III. Stratified data for 432 respondents from all 17 noise zones together. Lower and higher boundaries of the class intervals, as well as the mean value for each class interval, are expressed as the A-weighted yearly day–night level (ADNL in dB) of the road-traffic sounds. The number of respondents in each class interval is indicated by n. The community response to the road-traffic sounds was determined with questions B1 and B2, as explained in the text, and is expressed as (1) percentages of ''highly annoyed'' respondents, (2) as percentages of ''clearly and highly annoyed'' respondents, and (3) as the mean of the annoyance ratings from all respondents. M represents the mean of the percentages or the ratings; σ_M is the estimated standard error of the mean.

ADNL boundary				% of respondents annoyed							
				Highly			Clearly and highly			Annoyance ratings	
Lower (1)	Higher (2)	Mean ADNL (3)	n (4)	B1 (5)	B2 (6)	M (7)	B1 (8)	B2 (9)	M (10)	M (11)	σ_M (12)
35.5	42.4	40.6	21	0.0	0.0	0.0	4.8	0.0	2.4	1.5	0.12
42.5	45.0	43.8	68	4.4	2.9	3.7	10.3	10.3	10.3	1.7	0.10
45.1	47.5	46.0	33	18.2	9.1	13.6	24.2	27.3	25.8	2.0	0.22
47.6	52.7	50.4	89	6.7	6.7	6.7	20.2	20.2	20.2	2.0	0.11
52.8	58.4	55.8	69	18.8	27.1	23.0	36.2	38.6	37.4	2.6	0.16
58.5	62.9	61.0	89	19.1	21.4	20.2	36.0	47.2	41.6	2.6	0.12
63.0	67.9	64.5	39	30.8	25.6	28.2	48.7	48.7	48.7	2.8	0.20
68.0	69.4	68.3	24	41.7	41.7	41.7	62.5	58.3	60.4	3.2	0.25
			432								

(=$1/\beta$ dB) increase in ASEL of the vehicle passby sound. According to the relation in Fig. 2, the impulse sound at $L_{CE}=85$ dB is as annoying as the vehicle sound at $L_{AE}=70$ dB. Consequently, an adjustment of $70-85=-15$ dB should be added to CSEL of the impulse sound to obtain ASEL of the equally annoying vehicle sound.

At the point where the function $L_{CE}=\alpha+\beta L_{AE}$ crosses the line $L_{CE}=L_{AE}$, the correction is reduced to 0 dB. At this *point*, the sounds presented at *numerically* equal CSEL- and ASEL-values are also *subjectively equal* (PNSE). For levels higher than PNSE (in Fig. 2 at $L_{CE}=L_{AE}=100$ dB) a positive correction is required. For example, the impulse sound at $L_{CE}=110$ dB is as annoying as the vehicle sound at $L_{AE}=120$ dB. As a result, an adjustment of $120-110=10$ dB should be added to CSEL of the impulse sound to obtain ASEL of the equally annoying vehicle sound.

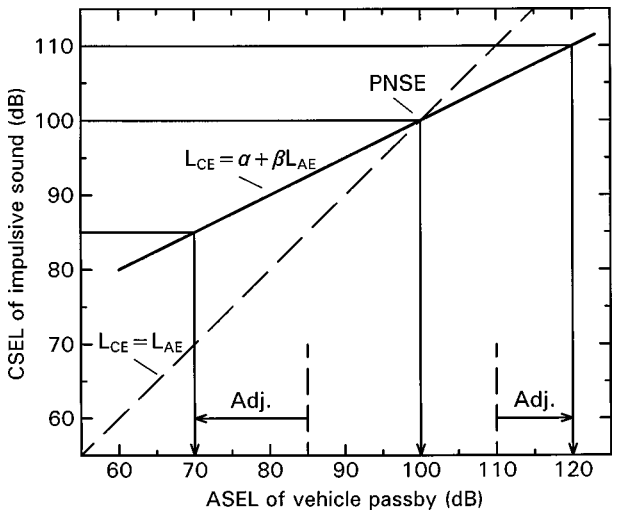

FIG. 2. Illustration of a typical result obtained in field-laboratory tests from Schomer and colleagues. The boldly printed solid line relates the levels of equally annoying impulsive and vehicle sounds. The significance of the adjustments (Adj.) is explained in the text.

B. Schomer's newly developed model

After a new analysis of the results obtained in field surveys, Schomer (1994) concluded that the discrepancy between dose-response relations for (a) artillery shooting sounds and sonic booms, and (b) transportation sounds, could be minimized by using a slope of $\beta=0.67$ in the transformation of the various CSEL-values. In Schomer's analysis, PNSE was set to values between 100 and 104 dB, all of which yielded, in combination with $\beta=0.67$, similar results.

In a recent re-analysis of the field data used in Schomer (1994), Vos (1997) showed that application of Schomer's newly developed model (with PNSE=103 dB and β equal to 0.67) would result in a systematic underestimation of the rating sound level for high-energy impulsive sounds. For rating procedures which are based on sound levels determined in free-field conditions, Vos (1997) showed that an adequate prediction of ADNL of equally annoying traffic sound could be obtained with, for example, PNSE equal to 80 dB, instead of 103 dB, in combination with slope β close to the previously found value of 0.67.

C. An additional test on the basis of the present results

The experimental results from the present field survey provide a new opportunity to test the validity of the transformation as suggested by Schomer (1994). The present effort is especially interesting because here, in contrast to previous analyses, large sets of different CSEL-values per residential area are available, and the annoyance ratings for the impulsive and road-traffic sounds had been determined with similar questions and for the same group of respondents, facilitating a comprehensive estimate of the adequate parameter values. Moreover, in addition to including various values for slope β, the effect of PNSE will be tested for a broad range as well.

The conversion of the equivalent-energy-average CSEL of the impulsive sounds into the ASEL of equally annoying

TABLE IV. Grouped cumulative frequency distributions (in %) of single event CSEL for all residential areas. Based on the yearly number of impulses with $L_{CE} \geqslant 45$ dB. For all columns, the midpoints of the class intervals (with a size equal to 5 dB) are indicated. The total number of impulses per year considered, N_T, is given in multiples of 1000.

		C-weighted sound exposure level in dB												
No.	Residential area	47.5	52.5	57.5	62.5	67.5	72.5	77.5	82.5	87.5	92.5	97.5	102.5	N_T
	Military Training Areas Bergen/Munster:													
1	Eschede	30.3	39.2	65.3	82.2	100.0	100.0	100.0	100.0	100.0	100.0	100.0	100.0	509
2	Schneverdingen	41.3	61.2	73.4	95.3	100.0	100.0	100.0	100.0	100.0	100.0	100.0	100.0	567
3	Neuenkirchen	22.4	38.1	65.3	92.0	97.5	99.3	100.0	100.0	100.0	100.0	100.0	100.0	784
4a	Unterlüß-Nord	0.0	15.6	40.9	53.3	69.6	100.0	100.0	100.0	100.0	100.0	100.0	100.0	305
5a	Unterlüß-Mitte	0.0	7.7	35.1	49.2	67.8	100.0	100.0	100.0	100.0	100.0	100.0	100.0	282
6a	Unterlüß-Süd	0.0	17.5	43.9	58.2	71.6	100.0	100.0	100.0	100.0	100.0	100.0	100.0	320
7	Sülze	0.0	18.6	26.1	55.2	67.7	90.7	100.0	100.0	100.0	100.0	100.0	100.0	706
8	Soltau	0.0	0.0	0.0	53.0	59.0	75.0	95.5	100.0	100.0	100.0	100.0	100.0	533
9	Bomlitz	0.0	0.0	24.0	63.1	81.5	86.7	97.4	99.1	100.0	100.0	100.0	100.0	872
10	Bergen	0.0	0.0	0.0	32.3	50.8	65.5	89.9	97.0	99.9	100.0	100.0	100.0	764
11	Fallingbostel	0.0	0.0	0.0	35.0	50.7	74.8	86.4	94.2	97.8	99.0	100.0	100.0	804
12	Wietzendorf	0.0	0.0	0.0	0.0	21.3	21.3	27.9	31.7	54.9	99.2	100.0	100.0	260
13	Munster-Nord	0.0	0.0	0.0	0.0	0.0	17.3	21.8	29.6	43.6	97.4	100.0	100.0	226
14	Munster-Süd	0.0	0.0	0.0	0.0	0.0	0.0	0.0	18.3	25.5	45.4	99.4	100.0	185
15	Meißendorf	0.0	0.0	6.5	55.5	65.2	76.3	80.3	88.9	93.7	99.9	100.0	100.0	679
16	Westenholz	0.0	0.0	1.1	46.8	55.9	71.0	76.5	87.8	91.1	92.2	99.9	100.0	749
17	Dorfmark	0.0	0.0	0.0	11.1	30.0	71.0	91.4	95.0	96.8	99.3	100.0	100.0	814
	Test Area Rhein Metall:													
4b	Unterlüß-Nord	0.0	0.0	0.0	2.9	2.9	4.1	6.1	6.2	87.4	87.4	98.4	100.0	49
5b	Unterlüß-Mitte	0.0	0.0	2.9	2.9	4.1	6.1	56.2	100.0	100.0	100.0	100.0	100.0	49
6b	Unterlüß-Süd	0.0	0.0	2.9	4.1	6.1	46.3	100.0	100.0	100.0	100.0	100.0	100.0	49

vehicle sounds was performed in exactly the same way as in Schomer (1994).

First, for each type of muzzle blast and for each type of detonation, the mean CSEL of the impulses of the higher-level distribution, as described in Schomer and Luz (1994), L_{CM}, was set equal to CSEL as predicted by ''LARMLAST'' for downwind conditions.

Second, for each impulsive noise type, standard deviation σ of the higher-level distribution was calculated from

$$\sigma = 3.5 + 1.1 \ \lg(d), \tag{2}$$

in which d represents the distance between the relevant shooting range and the residential area in km.

For specific combinations of PNSE and $1/\beta$, ASEL of equally annoying vehicle sound, L_{AV}, was found from

$$L_{AV} = \mathrm{PNSE} + (1/\beta)(L_{CM} - \mathrm{PNSE}) + 0.115(1/\beta)^2(\sigma)^2. \tag{3}$$

Before computing yearly average levels of equally annoying traffic sound, an adjustment factor had to be determined that accounted for the fact that only a percentage of the impulsive sounds belong to the higher-level distribution described in Schomer and Luz (1994). This adjustment, Δh, which varies with the distance d is given in decibels by

$$\Delta h = -3.8 - 0.23d. \tag{4}$$

The A-weighted average level of road-traffic sound with the same annoyance as the impulsive sounds produced in the daytime, $L_{\mathrm{Aeq06-22h}}$, was now found from

$$L_{\mathrm{Aeq06-22h}} = 10 \lg\left(\sum_{i=1}^{j} N_{\mathrm{day}(i)} 10^{[L_{\mathrm{AV}(i)} + \Delta h(i)]/10} \right) - 71.8 \ \mathrm{dB}, \tag{5}$$

in which $N_{\mathrm{day}(i)}$ represents the yearly number of rounds produced in the daytime for source i. Since it was decided to compute the average level for a time period of 4160 h [$=52$ (weeks)$\times 5$ (days)$\times 16$ h], the constant to be subtracted equaled 71.8 dB.

For the nighttime, the A-weighted average level of equally annoying road-traffic sound, $L_{\mathrm{Aeq22-06h}}$, was found from

$$L_{\mathrm{Aeq22-06h}} = 10 \lg\left(\sum_{i=1}^{j} N_{\mathrm{night}(i)} 10^{[L_{\mathrm{AV}(i)} + \Delta h(i)]/10} \right) - 68.8 \ \mathrm{dB}, \tag{6}$$

in which $N_{\mathrm{night}(i)}$ represents the yearly number of rounds produced in the nighttime for source. i. ADNL of equally annoying road-traffic sound was computed from the two average levels defined in Eqs. (5) and (6).

In the present analysis, for each residential area about 40 shooting range/weapon type combinations with relatively high contributions to the overall CLEQ in the daytime were included. For the nighttime the number of such combinations was equal to about 40 as well.

In Table IV, detailed information is given about the frequency distribution of CSEL. Since the distributions for the shooting sounds produced in the daytime were not basically different from the distributions in the nighttime, the cumula-

TABLE V. Mean differences (in dB) between the transformed A-weighted day–night levels for the impulse sounds and the A-weighted day–night levels for the equally annoying road-traffic sounds, determined for the various combinations of PNSE and $1/\beta$. Each mean is based on 20 values, one for each residential area. Root mean squares of the differences (rms, in dB) are given between parentheses. Corresponding values for β are given as references.

	$1/\beta$:	0.50	0.625	0.75	0.875	1.0	1.125	1.25	1.375	1.50	1.625	1.75
PNSE	β:	2	1.6	1.3	1.14	1	0.89	0.8	0.73	0.67	0.62	0.57
53		−18.8	−15.3	−11.7	−7.8	−3.8	**0.3**	4.6	9.0	13.5	18.1	22.8
		(20.3)	(17.0)	(13.6)	(10.6)	(8.2)	**(7.6)**	(9.3)	(12.5)	(16.4)	(20.7)	(25.3)
63		−13.8	−11.6	−9.2	−6.6	−3.8	**−0.9**	2.1	5.2	8.5	11.8	15.3
		(15.7)	(13.7)	(11.6)	(9.7)	(8.2)	**(7.6)**	(8.3)	(10.1)	(12.6)	(15.6)	(18.8)
73		−8.8	−7.8	−6.7	−5.3	−3.8	−2.2	**−0.4**	1.5	3.5	5.6	7.8
		(11.6)	(10.7)	(9.7)	(8.9)	(8.2)	(7.9)	**(8.0)**	(8.8)	(10.0)	(11.6)	(13.5)
83		−3.8	−4.1	−4.2	−4.1	−3.8	−3.4	−2.9	−2.3	−1.5	−0.7	0.3
		(8.4)	(8.3)	(8.2)	(8.2)	(8.2)	(8.3)	(8.5)	(8.9)	(9.5)	(10.2)	(11.0)
93		1.2	**−0.3**	−1.7	−2.8	−3.8	−4.7	−5.4	−6.0	−6.5	−6.9	−7.2
		(7.6)	**(7.3)**	(7.3)	(7.6)	(8.2)	(8.9)	(9.7)	(10.5)	(11.4)	(12.3)	(13.2)
103		6.2	3.4	**0.8**	−1.6	−3.8	−5.9	−7.9	−9.8	−11.5	−13.2	−14.7
		(9.7)	(8.0)	**(7.1)**	(7.3)	(8.2)	(9.6)	(11.3)	(13.0)	(14.8)	(16.6)	(18.4)
113		11.2	7.2	3.3	**−0.3**	−3.8	−7.2	−10.4	−13.5	−16.5	−19.4	−22.2
		(13.5)	(10.2)	(7.8)	**(7.1)**	(8.2)	(10.4)	(13.2)	(16.1)	(19.0)	(21.9)	(24.8)
123		16.2	10.9	5.8	**0.9**	−3.8	−8.4	−12.9	−17.3	−21.5	−25.7	−29.7
		(17.9)	(13.1)	(9.2)	**(7.1)**	(8.2)	(11.3)	(15.2)	(19.3)	(23.5)	(27.6)	(31.7)
133		21.2	14.7	8.3	2.2	−3.8	−9.7	−15.4	−21.0	−26.5	−31.9	−37.1
		(22.5)	(16.4)	(10.9)	(7.4)	(8.2)	(12.3)	(17.4)	(22.7)	(28.1)	(33.5)	(38.7)
143		26.2	18.4	10.8	3.4	−3.8	−10.9	−17.9	−24.8	−31.5	−38.1	−44.3
		(27.2)	(19.8)	(13.0)	(7.9)	(8.2)	(13.3)	(19.6)	(26.2)	(32.9)	(39.4)	(45.6)

tive frequency distributions (in percentages) for successive 5-dB class-intervals in Table IV are collapsed for the day- and the nighttime shooting activities.

Table IV shows that there were great differences in the range of downwind CSEL of the impulses received among the residential areas: for example, there were two residential areas (numbers 1 and 2 in Table IV) in which downwind CSEL of the impulses ranged between 45 and 70 dB, three residential areas (numbers 4a, 5a, and 6a) in which CSEL ranged between 50 and 75 dB, and five residential areas (numbers 11, 12, 13, 15, and 17) in which CSEL ranged between 55–70 and 100 dB.

For the first 17 residential areas the total number of impulses, combined at a yearly basis for the day- and the nighttime, ranged between about 200 000 and 800 000. For residential areas 4b–6b the total number of these impulses was equal to 49 000.

In the present analysis, PNSE ranged in 10-dB steps from 53 to 143 dB. For each PNSE-value, the exchange ($1/\beta$) between CSEL and ASEL was varied in 0.125-steps between 0.25 and 2.25, corresponding to β values between 4 and 0.44. From the ASEL-values, the yearly ADNLs were determined for each combination of PNSE and $1/\beta$. Next, the differences between these transformed day–night levels and the original day–night levels of equally annoying road-traffic sounds were calculated for each of the 20 conditions (Table I) separately. The utilized dose-response relationship for road-traffic sound was described in Sec. II B and was shown in Fig. 1.

D. A test on the basis of the results from the present study

For a portion of the combinations of PNSE and $1/\beta$, both the mean difference between the transformed day–night levels for the impulse sounds and the day–night levels for the equally annoying road-traffic sounds, and the root mean square, rms, of these differences are given in Table V.

For the neutral situation ($1/\beta = 1$), i.e., the condition in which the same increase in the levels of the impulse and vehicle sounds yields a similar shift in the annoyance, the mean difference was equal to −4 dB, the rms was equal to 8 dB. In Table V it can be seen that there are two clusters of $1/\beta$ and PNSE combinations for which both the (absolute) mean and the rms of the differences were lower than the values obtained for combinations in which $1/\beta$ equals 1.

In the first cluster relatively low absolute mean differences (e.g., those $\leqslant 1$ dB) and slightly lower rms-values (e.g., those $\leqslant 8$ dB) were obtained in conditions in which PNSE ranged between 53 and 73 dB and $1/\beta$ ranged between 1.125 and 1.25. In Table V, the figures in the relevant combinations are printed boldly. In the second cluster low mean differences and slightly lower rms values were obtained in conditions in which PNSE ranged between 93 and 123 dB and $1/\beta$ ranged between 0.625 and 0.875.

In the first cluster the specific combinations of PNSE and slope β imply that a (positive) adjustment has to be added to the shooting sounds with CSEL-values greater than 53–73 dB. From the information given in Table IV it can be verified that for all 20 residential areas there were impulse sounds with $L_{CE} > 53$ dB, and that there were 18 areas in which there were impulse sounds with $L_{CE} > 73$ dB. In the second cluster the specific combinations of PNSE and slope β imply that a (positive) adjustment has to be added to the shooting sounds with CSEL smaller than 93–123 dB. In Table IV it can be seen that for PNSE-values of 113 and 123 dB, all impulse sounds in all residential areas receive positive adjustments. For PNSE = 103 dB, there are only three areas (numbers 14, 16, and 4b in Table IV) in which 1% of the impulses do not receive positive adjustments, and for

TABLE VI. Values for $1/\beta$ which in combination with the specific PNSE-values yielded unbiased fits between the predicted and the originally obtained A-weighted day–night levels of equally annoying road-traffic sounds (mean differences equal to 0 dB). Corresponding values for β are given as references. Root mean squares (rms, in dB) are given in the last column.

PNSE	$1/\beta$	β	rms
53	1.12	0.89	7.5
63	1.17	0.85	7.7
73	1.28	0.78	8.2
83	1.72	0.58	10.8
93	0.60	1.68	7.3
103	0.79	1.27	7.1
113	0.86	1.16	7.1
123	0.90	1.11	7.1
133	0.92	1.10	7.1
143	0.93	1.08	7.1

PNSE=93 dB, there are three areas (numbers 12, 13, and 14) in which about 10%–30% of the impulses do not receive positive adjustments.

E. Parameter values for an optimal fit

Table V shows that for the combination of PNSE=103 dB and $\beta=0.67$, which was previously indicated to be an optimal combination for the prediction of ADNL of equally annoying transportation sounds (Schomer, 1994), the rating sound level for the impulse sounds in the present study would be underestimated by almost 12 dB. For Schomer's data set Vos (1997) considered the combination of PNSE=80 dB and β close to 0.67 more appropriate. For the data from the present study, this combination yielded an unbiased solution as well (mean difference equal to 0 dB); the rms of the differences, however, was 9.4 dB and therefore 2 dB higher than several other unbiased solutions.

In order to find, for the set of relevant PNSE-values, those $1/\beta$-values for which the mean differences between the predicted and the obtained day–night levels were equal to 0 dB, additional computations were performed. From the results shown in Table VI, it can be concluded that such unbiased solutions with reasonably low rms values of about 7 dB were obtained with PNSE ranging between 93 and 143 dB, and $\beta>1$.

An adequate prediction of ADNL of equally annoying road-traffic sound was obtained with, for example, PNSE equal to 103 dB and slope β equal to 1.27. Using a more rounded value for PNSE of 100 dB, β was equal to 1.33.

IV. DISCUSSION

A. Relative importance of day- and nighttime shooting

The average day–night level is a rather global measure that embodies assumptions such as (a) the exchangeability of single event level and number of events, and (b) a 10 dB penalty for sounds produced in the nighttime, which are not necessarily the key factors that explain the annoyance caused by artillery sounds. Additional analyses might yield more insight into the mechanism that caused the significant correlation between this dose and the community response.

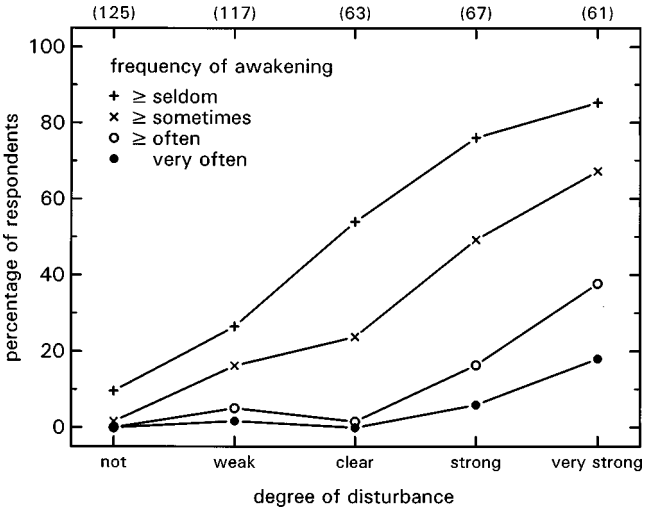

FIG. 3. Cumulative percentages of respondents who reported about their frequency of awakening, as a function of their corresponding disturbance rating. For the various response alternatives of the disturbance question, the number of respondents who selected these alternatives is given along the top axis of the figure.

One could hypothesize that the community response has been determined by shooting during the night. Since for the first 17 noise zones in the present study the average level for the daytime is highly correlated with the average level for the nighttime ($r=0.97$), the association strengths between these time-period specific levels and the community response are about equal as well. It is therefore impossible to conclude from differences in association strength that it is more likely that the community response has been elicited by shooting during the night than by shooting during the day.

However, up to a point, a test for such a hypothesis is provided by the results of an analysis of the responses to (1) a question asking the frequency at which one has been awakened by the shooting sounds; and (2) a question asking the frequency at which one had to close the windows for getting to sleep.

A regression analysis performed on the 433 individual responses to one of the questions (question A1) asking the degree of disturbance and the responses to the question asking the frequency of awakening showed that r was equal to 0.60, which is highly significant ($t=15.5$, $p<0.001$).

Figure 3 shows the cumulative percentages of respondents who reported about their frequency of awakening, as a function of their corresponding disturbance rating. In Fig. 3 it can be seen that of the (63) respondents who said that they were ''clearly disturbed,'' almost none of them reported being awakened ''often'' or ''very often,'' whereas this percentage increased to about 40% for those (61) respondents who indicated being ''very strongly disturbed.''

Even for a group of respondents, however, who can all be considered being ''highly annoyed,'' such as those in Fig. 3 with responses in the ''strongly'' or ''very strongly disturbed'' categories, only 25% of them reported that they had at least often been awakened by shooting noise. Consequently, these results show that although awakening was significantly related to general disturbance, for the respondents

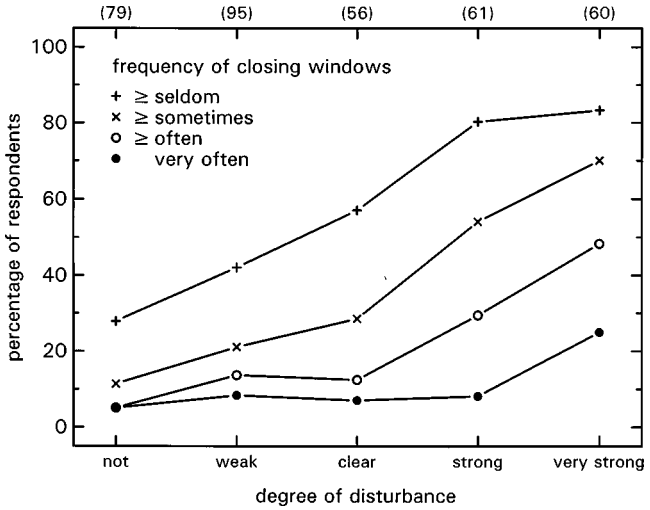

FIG. 4. Cumulative percentages of respondents who reported about their frequency of closing the windows in order to get to sleep, as a function of their corresponding disturbance rating.

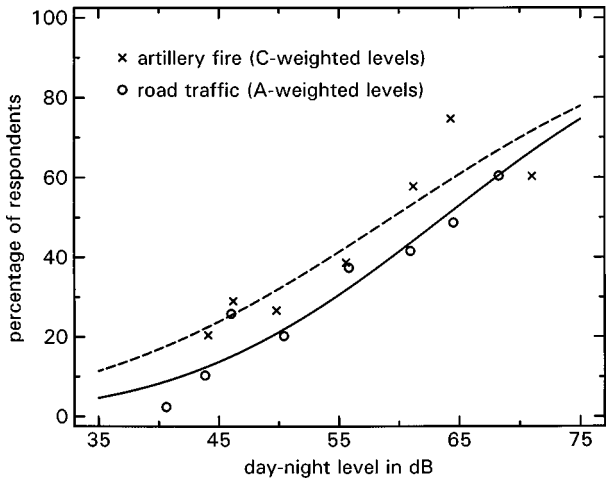

FIG. 5. As in Fig. 1, but now the community response is expressed as the percentage of respondents describing themselves as ''clearly or highly annoyed.''

in the present study, it was not nearly a necessary condition for being ''highly annoyed.''

For the second question the responses of 351 subjects could be included, because for residential areas 4a–6a (see Table I) the question about how often one had to close the windows had not been asked. Again, the correlation between disturbance and the frequency at which the windows had to be closed was highly significant ($r=0.45$; $t=9.4$, $p<0.001$).

As in Fig. 3, Fig. 4 shows the cumulative percentages. In Fig. 4, it can be seen that of the (56) respondents who had reported being ''clearly disturbed,'' slightly more than 10% of them indicated closing the windows ''often'' or ''very often,'' whereas this percentage increased to about 50% for those (60) respondents who had reported being ''very strongly disturbed.'' For the ''highly annoyed'' respondents about 20% of them reported that, for getting to sleep, they had to close the windows ''often,'' and about 15% of them reported that they had to close the windows ''very often.''

As in the previous analysis on awakening, the results show that although closing the windows was significantly related to general disturbance, it was in the present study not a necessary condition for being ''highly annoyed.'' The hypothesis that the community response had been determined by shooting during the night has therefore to be rejected. It appears more likely that the community response had been determined both by shooting in the daytime and by shooting in the nighttime.

B. The ''highly annoyed'' criterion as a definition for community response

In spite of the fact that in most field surveys the community response is expressed as percentages of respondents describing themselves as ''highly annoyed,'' this criterion is more or less arbitrary. At least in some countries, decision makers would like to include in the analyses also those respondents who indicated being ''moderately'' or ''clearly annoyed.'' Moreover, from a methodological point of view, it might be preferred to take the statistical distribution of the annoyance rating, as characterized by a mean and a variance, into account instead of treating the scores in a categorical way (e.g., see Griffiths, 1983). Because of this, it is verified in the next two sections whether inclusion of (1) the ''clearly annoyed'' respondents, and (2) the ratings from all respondents would result in a change in the adjustment for shooting sound.

1. Inclusion of ''clearly annoyed'' respondents

For the same sets of respondents described in Table I, alternative dose-response relationships for shooting sound were determined. For the 5-point rating scale (question A1), the percentages were not only based on the respondents who reported to be ''strongly'' or ''very strongly disturbed,'' but also on those who reported being ''clearly disturbed.'' For the 9-point rating scale the respondents were considered to be ''clearly or highly annoyed'' if they selected scores 5, 6, 7, 8, or 9. With this criterion the coefficient of determination, r^2, as determined between the 20 percentages obtained for the 5-point and 9-point rating scales, was equal to 0.73. If for the 9-point rating scale only the scores 6 up to 9 had been taken into account, a considerably lower r^2-value of 0.56 would have been obtained.

As in Sec. II A, the data were stratified. For the relevant class intervals the percentages respondents being ''clearly or highly annoyed,'' as determined with question A1 and question A2, as well as the percentages averaged across these two questions, are given in columns 8–10 of Table II.

Figure 5 shows these mean percentages as a function of CDNL. The equation of the function (dashed line) fitted to the data in Fig. 5 is given by $y=\Phi[(L_{\mathrm{Cdn}}-59.4)/20.3]$. The regression line explains 83% of the variance in the mean percentages.

For the road-traffic sounds, the various percentages of respondents being ''clearly or highly annoyed'' are given in columns 8–10 of Table III. Figure 5 shows the mean percentages as a function of ADNL. The equation of the func-

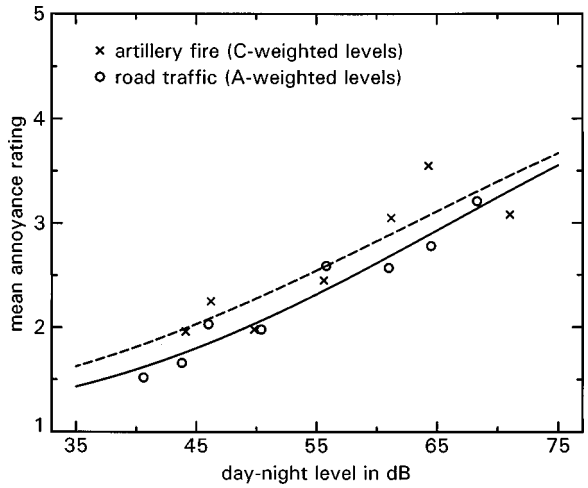

FIG. 6. As in Fig. 1, but now the community response is expressed as the mean of the annoyance ratings from all respondents in the various class intervals.

tion (solid line) fitted to the data in Fig. 5 is given by $y = \Phi[(L_{\mathrm{Adn}} - 63.7)/17.1]$. The regression line explains 93% of the variance in the mean percentages.

From the two dose-response relations shown in Fig. 5, the adjustment for shooting sound can be derived. For a criterion of 20% ''clearly or highly annoyed'' respondents, an adjustment of 7 dB has to be added to CDNL of the shooting sounds to obtain ADNL of equally annoying road-traffic sounds; for a criterion of 40% ''clearly or highly annoyed'' respondents, the adjustment is equal to 5 dB. These results imply that the adjustment is not significantly dependent on the overall level of the shooting sounds, and that application of a 6-dB adjustment would be adequate.

2. Inclusion of the ratings from all respondents

For the sets of respondents described in Table I, mean annoyance ratings for the shooting sounds were determined. To enable a direct comparison between the responses given on the 9-point rating scale with those given on the 5-point rating scale, the original raw scores (x_{original}) for the 9-point rating scale were converted to the 5-point rating scale range by using the rule $x_{\mathrm{converted}} = 1 + (x_{\mathrm{original}} - 1)/2$.

As in Sec. II A the data were stratified. For the various class-intervals mean ratings and estimated standard errors of the mean were determined for the various questions separately. Within each sound type, the results obtained with the two questions were almost equal. The overall results for the shooting and road-traffic sounds are given in the last two columns of Tables II and III, respectively.

The mean ratings are also shown in Fig. 6. Overall, the mean annoyance ratings for the shooting sounds were higher than those for the road-traffic sounds, provided that the day–night levels were the same. For each sound type the function

$$S(L_{\mathrm{dn}}) = 1 + 4 \cdot \Phi[(L_{\mathrm{dn}} - \mu)/\sigma] \tag{7}$$

was fitted to the data. $S(L_{\mathrm{dn}})$ denotes the mean score on the annoyance rating scale, and is a function of L_{dn}. As in Eq. (1), $\Phi(z)$ denotes the cumulative normal distribution; this function has now been rescaled such that it covers the entire rating scale from 1 to 5.

For the shooting sounds the optimal values of μ and σ, as estimated by a least-squares fit of Eq. (7) to the mean ratings, were equal to 63.0 and 27.8 dB, respectively ($r^2 = 0.77$). For the road-traffic sounds the optimal values of μ and σ were equal to 66.1 and 25.1 dB ($r^2 = 0.94$). From the two regression functions shown in Fig. 6, an adjustment for shooting sound can be derived. For a mean annoyance rating between 2 and 3, corresponding with $43 < L_{\mathrm{Cdn}} < 63$ dB, the adjustment ranges between 5 and 3 dB.

For a powerful test of the statistical significance of any adjustment, the annoyance scores of the respondents (averaged across the two questions) were subjected to a two-way analysis of variance [with sound type (shooting or road traffic) and day–night level (6 mean levels between $L_{\mathrm{dn}} \sim 44$ dB and $L_{\mathrm{dn}} \sim 65$ dB) as between-subjects variables]. The ratings for road traffic with $L_{\mathrm{Adn}} < 42$ dB could not be included because there were no data available for the shooting sounds at corresponding levels. The ratings given in the conditions with $L_{\mathrm{dn}} \geqslant 68$ dB had to be excluded because, for an appropriate comparison, the difference between the mean levels for the shooting sounds (last class interval in Table II) and the road-traffic sounds (last class interval in Table III) was too large.

The effect of the day–night level was highly significant [$F(5,775) = 27.9$, $p < 0.000\,01$]. More importantly, however, is the finding that the ratings for the shooting sounds were significantly higher than those for the road-traffic sounds [$F(1,775) = 11.5$, $p = 0.0007$]. There was also a moderately significant interaction effect between sound type and day–night level [$F(5,775) = 2.9$, $p = 0.013$]. The relatively large difference in annoyance between the shooting and road-traffic sounds at $L_{\mathrm{dn}} \sim 64$ dB is responsible for this interaction effect. From the data set subjected to the analysis of variance, it might be predicted that for the shooting sounds the adjustment increases with increasing CDNL. From the mean rating obtained for the 115 respondents who were exposed to $68 < L_{\mathrm{Cdn}} < 74$ dB, however, it must be concluded that any notion about such a level-dependent adjustment to CDNL must be rejected.

3. Conclusion

With the community response expressed as the percentage of ''highly annoyed'' respondents, the adjustment to CDNL of the shooting sounds was about 4 dB. With the effect expressed as the percentage of ''clearly and highly annoyed'' respondents, the adjustment was about 6 dB, and with the effect expressed as the mean annoyance ratings, the adjustment was about 4 dB. From these findings it must be concluded that the adjustment for shooting sounds is a rather robust measure: its size is not greatly affected by either a shift in the criterion for including respondents in the dose-response relationship or by an alternative analysis in which the ratings from all respondents were included. Contrary to Griffiths's (1983) suggestion, the choice of the ''highly annoyed'' measure did not lead to an error in the prediction of the adjustment.

From the present study it might be concluded that application of a 5-dB adjustment would be adequate. This value is not greatly different from the adjustment that can be derived from Schomer's field survey results for the Ft. Lewis and Ft. Bragg artillery ranges (Schomer, 1985, 1994). For obtaining ADNL of equally annoying transportation sounds (the widely known ''Schultz curve''), an average adjustment of 8 dB had to be added to CDNL (as determined in free-field conditions) of the shooting sounds (also see Table I in Vos, 1997).

If, in the present study, the day–night levels of the shooting and road-traffic sounds had been computed for 365 instead of for 260 days per year, the discrepancy of 3 dB would have been reduced to about 1.5 dB.

C. Adjustments in rating procedures based on sound levels in ''downwind'' conditions

In the present paper the adjustment was derived from the difference between the yearly average CDNL of the artillery sounds and the yearly average ADNL of equally annoying road-traffic sounds. In several European countries, however, the rating sound level is determined only for more unfavorable sound propagation conditions in which the wavefronts are diffracted downwards to the ground (Gerretsen, 1996; Gottlob, 1995). Although it is understood that downward diffraction is the combined result of wind and temperature effects, this type of sound propagation is often labeled as ''downwind'' propagation.

For the artillery sounds, which propagate over distances of about 1 km up to more than 15 km, the day–night levels in the ''downwind'' conditions were estimated to be about 3 dB higher than the levels determined at a yearly basis, including all possible propagation conditions ranging from ''downwind'' to ''upwind'' (see Sec. I C 1).

Since for the (local) road-traffic sounds the distances between the source and the receiver were much smaller (about 10–50 m), the day–night levels in the ''downwind'' conditions were hardly different from those in the ''upwind'' conditions. As a result, the adjustment for the shooting sounds is smaller with the noise dose expressed as the day–night levels in ''downwind'' conditions than with the noise dose expressed as the yearly average day–night levels.

This is illustrated in Fig. 7, where the community response is expressed as the percentage of ''highly annoyed'' respondents (cf. Fig. 1). The dose-response relationships for the artillery and road-traffic sounds (broken and solid line in Fig. 7) almost coincide. With the community response expressed as (a) the percentage of ''clearly or highly annoyed'' respondents (cf. Fig. 5), or (b) the mean of the annoyance ratings from all respondents (cf. Fig. 6), similar results were obtained.

By using a procedure similar to that described in Sec. IV B 2, the annoyance scores of the respondents were subjected to an analysis of variance (with sound type and ''downwind'' day–night level as between-subjects variables). Overall, the ratings for the shooting sounds were not significantly different from those for the road-traffic sounds [$F(1,654)=0.3$, $p=0.60$]. Moreover, there was no significant interaction effect between sound type and ''downwind'' day–night level [$F(5,654)=1.6$, $p=0.15$]. These results confirm that with the noise dose expressed as day–night levels in ''downwind'' conditions, application of an adjustment to the C-weighted level of artillery sounds is not justified.

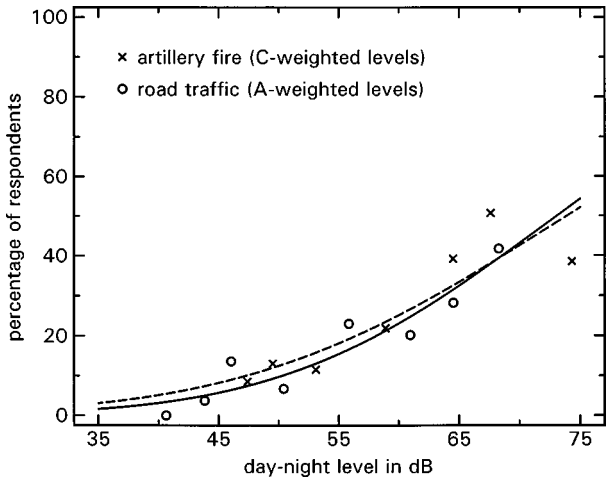

FIG. 7. Percentage of respondents describing themselves as ''highly annoyed'' as a function of the yearly average day–night level of the shooting and road-traffic sounds, for ''downwind'' conditions. The inserted dashed and solid lines are regression functions for the shooting and road-traffic data, respectively.

V. GENERAL CONCLUSIONS

(1) For numerically equal yearly average day–night levels, the (C-weighted) artillery sounds were more annoying than the (A-weighted) road-traffic sounds. Overall, the difference was equivalent to the change in the community response produced by a 5-dB shift in the day–night level.

(2) The 5-dB adjustment to the C-weighted day–night level of the artillery sounds is a robust measure: within 1 dB, similar adjustments were found with the community response expressed as (a) the percentage of ''highly annoyed'' respondents, (b) the percentage of ''clearly and highly annoyed'' respondents, and (c) the mean annoyance ratings from all respondents.

(3) The 5-dB adjustment is not greatly different from the 8-dB adjustment derived from previous survey results for the Ft. Lewis and Ft. Bragg artillery ranges (Schomer, 1985, 1994). If, in the present study, the yearly average day–night levels had been computed for 365 instead of for 260 days per year, the 3-dB discrepancy would have been reduced to about 1.5 dB.

(4) With equal day–night levels for ''downwind'' conditions, the artillery and road-traffic sounds were equally annoying.

(5) The results from the present highly controlled field survey provided a new opportunity to optimize the parameter values in Schomer's level-dependent conversion procedure $y=(1/\beta)(L_{CE}-\mathrm{PNSE})+\mathrm{PNSE}$, in which the noise exposure for impulsive sounds (y) is expressed as the A-weighted sound exposure level of equally annoying vehicle passby sounds. With PNSE fixed at 103 dB, an optimal solution was found with slope β set to 1.3. With the previously recommended slope $\beta=0.67$, the rating sound level for artillery sounds would be underestimated by almost 12 dB.

ACKNOWLEDGMENT

This research was supported by the German Ministry of Defence/Staatshochbauamt Munster.

Borsky, P. N. (**1965**). ''Community reactions to sonic boom in the Oklahoma City area,'' AMRL-TR-65-37. (Wright-Patterson Air Force Base, Ohio).

Buchta, E. (**1988**). *Pilotprojekt für passive Schallschutzmassnahmen am Truppenübungsplatz Grafenwöhr* (Institut für Lärmschutz, Düsseldorf, Germany).

Buchta, E. (**1990**). ''A field survey on annoyance caused by sounds from small firearms,'' J. Acoust. Soc. Am. **88**, 1459–1467.

Buchta, E. (**1996**). ''Annoyance caused by shooting noise—Determination of the penalty for various weapon calibers,'' in *Proceedings Internoise 1996* (Institute of Acoustics, St. Albans, U.K.), Book 5, pp. 2495–2500.

Bullen, R. B., Hede, A. J., and Job, R. F. S. (**1991**). ''Community reaction to noise from an artillery range,'' Noise Control Eng. J. **37**, 115–128.

CHABA (**1981**). Assessment of community response to high-energy impulsive sounds. Report Working Group 84, Committee on Hearing, Bioacoustics, and Biomechanics. Assembly of Behavioral and Social Sciences. (National Research Council, Washington, D.C., National Academy Press).

Fidell, S., Barber, D. S., and Schultz, T. J. (**1991**). ''Updating a dosage-effect relationship for the prevalence of annoyance due to general transportation noise,'' J. Acoust. Soc. Am. **89**, 221–233.

Fields, J. M., and Hall, F. L. (**1987**). ''Community effect of noise,'' in *Transportation Noise Reference Book*, edited by P. M. Nelson (Butterworths, London, U.K.), Chap. 3.

Fields, J. M., and Walker, J. G. (**1982**). ''Comparing the relationships between noise level and annoyance in different surveys: A railway noise vs aircraft and road traffic comparison,'' J. Sound Vib. **81**, 51–80.

Gerretsen, E. (**1996**). ''Environmental noise descriptors in Europe—Comparison of definitions and prediction methods'' (TNO Institute of Applied Physics, Delft, The Netherlands), Report TPD-HAG-RPT-960059.

Gottlob, D. (**1995**). ''Regulations for community noise,'' Noise/News International, 223–236.

Griffiths, I. D. (**1983**). ''Review of community response to noise,'' in *Proceedings of the 4th International Congress on Noise as a Public Health Problem*, edited by G. Rossi (Centro Ricerche e Studi Amplifon, Milano, Italy), Turin, Italy, Vol. 2, pp. 1031–1048.

Guski, R., Wichmann, U., Rohrmann, B., and Finke, H-O. (**1978**). ''Konstruktion und Anwendung eines Fragebogens zur sozialwissenschaftlichen Untersuchung der Auswirkungen von Umweltlärm,'' Zeitschrift für Sozialpsychologie **9**, 50–65.

Hall, F. L., Birnie, S. E., Taylor, S. M., and Palmer, J. E. (**1981**). ''Direct comparison of community response to road traffic noise and to aircraft noise,'' J. Acoust. Soc. Am. **70**, 1690–1698.

Hede, A. J., and Bullen, R. B. (**1982**). ''Community reaction to noise from a suburban rifle range,'' J. Sound Vib. **82**, 39–49.

Hirsch, K. W., and Buchta, E. (**1993**). ''Zum Standardverfahren für die Berechnung der Schallimmissionen in der Umgebung von Truppenübungslätzen,'' *Fortschritte der Akustik—DAGA 1993* (Bad Honnef, Germany), DPG-GmbH, pp. 656–659.

Knall, V., and Schümer, R. (**1983**). ''The differing annoyance levels of rail and road traffic noise,'' J. Sound Vib. **87**, 321–326.

Krahé, D., and Buchta, E. (**1994**). ''Bestimmung der Lästigkeit von impulsartigen Geräuschen auf Basis der Lautheit,'' *Fortschritte der Akustik—DAGA 1994* (Bad Honnef, Germany), DPG-GmbH, pp. 1117–1120.

Kryter, K. D. (**1985**). *The Effects of Noise on Man* (Academic, Orlando, FL).

NRC (**1996**). ''Community response to high-energy impulsive sounds: an assessment of the field since 1981,'' Working group on assessment of community response to high-energy impulsive sounds, Committee on Hearing, Bioacoustics, and Biomechanics, National Research Council (National Academy Press, Washington, D.C., 1996).

Rylander, R., and Lundquist, B. (**1996**). ''Annoyance caused by noise from heavy weapon shooting ranges,'' J. Sound Vib. **192**, 199–206.

Rylander, R., Sörensen, S., Berglund, K., and Brodin, C. (**1972**). ''Experiments on the effect of sonic boom exposure on humans,'' J. Acoust. Soc. Am. **51**, 790–798.

Rylander, R., Sörensen, S., Andrae, B. O., Chatelier, G., Espmark, Y., Larsson, T., and Thackray, R. I. (**1974**). ''Sonic boom exposure effects—A field study on humans and animals,'' J. Sound Vib. **33**, 471–486.

Schomer, P. D. (**1982**). ''A model to describe community response to impulse noise,'' Noise Control Eng. J. **18**, 5–15.

Schomer, P. D. (**1985**). ''Assessment of community response to impulsive noise,'' J. Acoust. Soc. Am. **77**, 520–535.

Schomer, P. D. (**1994**). ''New descriptor for high-energy impulsive sounds,'' Noise Control Eng. J. **42**, 179–191.

Schomer, P. D., and Luz, G. A. (**1994**). ''A revised statistical analysis of blast sound propagation,'' Noise Control Eng. J. **42**, 95–100.

Schomer, P. D., and Wagner, L. R. (**1995**). ''Human and community response to military sounds—Part 2: Results from field-laboratory tests of sounds of small arms, 25-mm cannons, helicopters, and blasts,'' Noise Control Eng. J. **43**, 1–13.

Schomer, P. D., Wagner, L. R., Benson, L. J., Buchta, E., Hirsch, K.-W., and Krahé, D. (**1994**). ''Human and community response to military sounds: Results from field-laboratory tests of small arms, tracked-vehicle, and blast sounds,'' Noise Control Eng. J. **42**, 71–84.

Schultz, T. J. (**1978**). ''Synthesis of social surveys on noise annoyance,'' J. Acoust. Soc. Am. **64**, 377–405.

Vos, J. (**1985**). ''A review of field studies on annoyance due to impulse and road-traffic sounds,'' in *Proceedings Internoise 1985* (Bundesanstalt für Arbeitsschutz, Dortmund, Germany), Vol. 2, pp. 1029–1032.

Vos, J. (**1995**). ''A review of research on the annoyance caused by impulse sounds produced by small firearms,'' in *Proceedings Internoise 1995* (Newport Beach, California), Vol. 2, pp. 875–878.

Vos, J. (**1996**). ''Annoyance caused by impulse sounds produced by small, medium-large, and large firearms,'' in *Proceedings Internoise 1996* (Institute of Acoustics, St. Albans, U.K.), Book 5, pp. 2231–2236.

Vos, J. (**1997**). ''A re-analysis of the relationship between the results obtained in laboratory and field studies on the annoyance caused by high-energy impulsive sounds,'' Noise Control Eng. J. **45**, 123–131.

An innovative design of a probe-tube attachment for a $\frac{1}{2}$-in. microphone

Linda P. Franzoni
Department of Mechanical Engineering and Materials Science, Duke University, Durham, North Carolina 27708-0300

Christopher M. Elliott
Center for Sound and Vibration, Department of Mechanical and Aerospace Engineering, North Carolina State University, Raleigh, North Carolina 27695-7910

(Received 25 October 1997; accepted for publication 24 July 1998)

Nonintrusive devices are needed to measure sound pressure levels in the mid- to high-frequency range. This need arises due to the small acoustic wavelengths which are present at these frequencies, and the interference caused by conventional microphones which are typically of relatively large diameter. Smaller microphones are less sensitive, and may not be small enough to be useful at very high frequencies or when physical size constraints are limiting. Simple probe attachments have been developed by others to address these problems; however, generally the transfer functions of these devices have possessed undesirable peaks due to the presence of standing waves within the transducers. In this paper, several possible options for making a microphone attachment that will convert a standard $\frac{1}{2}$-in.-diam microphone into a probe-tube are discussed. Recommendations are made with regard to the particular use and ease of construction of the attachment. The new concepts eliminate standing waves, within certain frequency bands that are controlled by the geometry of the attachment, *without* the addition of damping material in the sound path. [S0001-4966(98)00711-5]

PACS numbers: 43.58.Vb, 43.38.Kb [SLE]

INTRODUCTION

Probe microphones can be used to measure sound pressure levels in a variety of acoustical spaces in which the size of a typical microphone would interfere with the sound field, or where space limitations require a small diameter device. In order for the acoustical measurements to be accurate for a particular frequency, the device cross section should be small compared to a wavelength at that frequency. In the mid- to high-frequency range, the wavelengths are small and can be on the order of the microphone diameter. For example, the diameter of a $\frac{1}{2}$-in. microphone is roughly the size of a quarter-wavelength at 6600 Hz. If the microphone is relatively large compared to the wavelength, sound waves reflected by the microphone can change the sound field. Furthermore, the microphone itself becomes directional and wave pressures may vary considerably over the diaphragm causing large measurement errors.

To avoid these problems, smaller microphones and/or small diameter probe-tubes are often used for measurements at high frequency. However, small diameter microphones are less sensitive than larger diameter microphones. A seemingly appropriate solution is to build a simple adapter which couples a large diameter microphone to a small diameter probe tube. This ''traditional design'' has been employed for use with a $\frac{1}{2}$-in. microphone by Bruel and Kjaer (B&K)[1] and has been further investigated by researchers Copeland and Hill[2] who designed such an adapter for a 1-in. microphone. The basic concept of these designs is shown in Fig. 1.

There are problems with this design that often render it undesirable for measuring high-frequency sound fields. Primarily, the resonant behavior of this probe-tube results in large peaks in its transfer function, as can be seen in Fig. 2. Although it is possible to correct for this rapidly varying transfer function in subsequent digital processing, this situation is potentially susceptible to large errors. Since large, rapidly varying corrections must be applied, any subsequent shift in the probe behavior relative to the correction procedure may lead to large errors. Changes in probe response could occur due to a variety of effects, including; varying end conditions if the probe tip is near a boundary; temperature changes; and alterations in microphone/probe attachment geometry. Therefore, it is expected that a device that provides a smooth transfer function, one without sharp resonance peaks, will be more robust than one possessing these resonances.

To produce a smooth transfer function with the traditional attachment design, damping material must be inserted along the entrance path of the probe tube, as is suggested by B&K.[1] This application of damping lowers the signal-to-noise ratio of the measurements, since the amplitude of the incident sound wave will decrease before reaching the microphone. Because probe tubes are often used for high-frequency measurements, this effect is often more pronounced.

In this paper, innovative concepts for microphone attachments will be presented. The main goal of these designs is to obtain a useable, easily built probe-tube with a smooth transfer function, without introducing damping material. Some of the designs presented are intellectually interesting, while others are more practical.

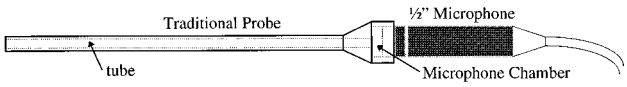

FIG. 1. Schematic of the traditional probe tube attachment.

I. TRADITIONAL DESIGN

In Fig. 1, the traditional probe-tube design is sketched. In this design, the protective cap of a $\frac{1}{2}$-in. microphone is removed, and the probe attachment is screwed onto the microphone housing. One problem with this design is that the tube behaves roughly like an ''open–closed'' one-dimensional waveguide with numerous resonances across the frequency range of interest. The transfer function between the probe-tube and an unmodified microphone contains sharp peaks at these resonant frequencies as can be seen in Fig. 2. To remove the sharp resonance peaks from the transfer function, B&K recommends filling the tube with steel wool, noting that ''the degree of damping will depend on the compactness of the filling;... by a trial and error method an almost linear characteristic can be obtained over a wide frequency range.'' Damping of each probe-tube would therefore be done on an individual basis, and since it could not be quantified precisely, response inconsistencies from one probe to the next would be expected. In addition, and more importantly, introduction of damping material into the path of the propagating sound wave from the source to the microphone would be expected to substantially reduce the probe's signal-to-noise ratio.

Two advantages of the traditional design are that the probe-tube is completely removable and that it is fairly simple to construct. The fact that the probe is removable means that the microphone can be used in other ways and is not dedicated to probe-tube applications.

II. DESCRIPTION OF NEW DESIGN

A new probe tube design was developed which possesses the advantages of the traditional design: it is detachable and simple to construct. However, it does not have an undesirable sharply peaked transfer function. A prototype probe-tube attachment for a $\frac{1}{2}$-in. microphone was built in order to experimentally analyze different configurations. The prototype probe-tube, as shown in Fig. 3, is modular to allow

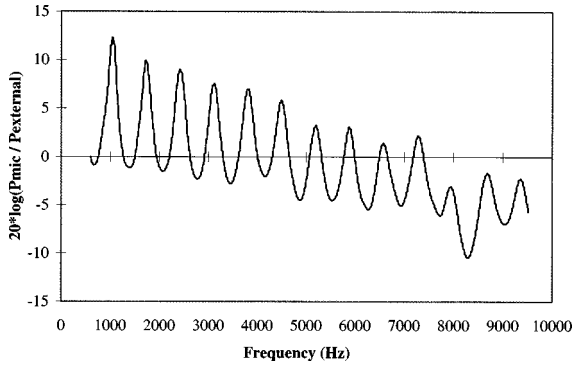

FIG. 2. Traditional probe tube attachment transfer function (FFT). Experimental data only.

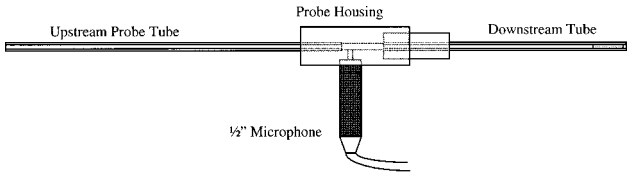

FIG. 3. Novel modular probe tube design.

for flexibility in the geometric parameters that could be used to achieve the desired acoustical characteristics. For example, any length tube (standard stock steel tubing) can be attached to the front of the device. The tube to the rear, if long enough, can provide an almost anechoic termination. By adjusting different lengths and diameters of tubing within the probe housing, interior dimensions can be altered to create expansions or contractions. A single expansion or contraction or a combination of both may result in a desirable transfer function which is smooth and fairly flat over the frequency range of interest.

In order to attach the microphone to the probe's housing, a cylindrical cavity was milled to approximately $\frac{1}{2}$-in. in diameter to accommodate the microphone. A pressure-tap was made between the main tube and the cavity containing the microphone. This physical system behaves like a Helmholtz resonator directly above the microphone. Adjustable parameters (i.e., expansions, contractions, etc.) were used to counteract the dynamics of this resonator. The probe-tube was modeled theoretically using a one-dimensional acoustic analysis, and a mathematical/computer model was then used to study different configurations for optimization of the final design (Mathcad® by MathSoft, Inc. was used to for computer modeling).

III. THEORETICAL MODEL

The microphone probe-tube was modeled as a one-dimensional transmission line with a series of length and area changes including a Helmholtz resonator cavity in front of the microphone, and a branch analysis of the intersection between the upstream tube, the resonator cavity opening, and the downstream tube. This model is shown in Fig. 4. Variables in the model were the lengths and cross-sectional areas. The dimensions of the Helmholtz resonator were principally governed by the $\frac{1}{2}$-in. microphone. It was required to fit as closely as possible without damaging the microphone diaphragm and without leaking energy from the system. Experimentally, a small insert (as in the traditional B&K design) was placed against the microphone diaphragm and the top of the cavity. This insert reduced the size of the cavity and

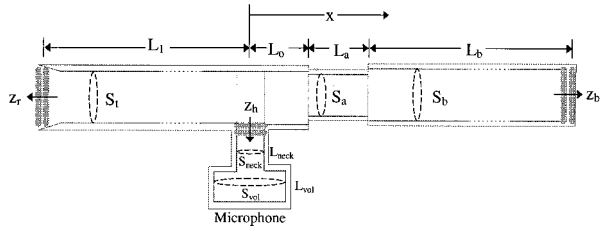

FIG. 4. Schematic view of modular probe. Acoustical parameters are labeled.

increased the natural frequency of the resonator. The termination specific acoustic impedance, z_b, at the end of the downstream tube was a variable in the model, both ''hard wall'' (large real impedance) terminations and ''infinite tube'' (ρc impedance) terminations were investigated.

The relationship between the external acoustic pressure and the acoustic pressure at the microphone was determined theoretically using a one-dimensional analysis, described in the next section. The one-dimensional acoustics assumptions that are used in this analysis can be found in most acoustics textbooks, for example, Ref. 3.

A. Formulation of the theoretical model

Geometric variables, lengths, and areas are described by the letters L and S, with subscripts to differentiate them, as shown in Fig. 4. Specific acoustic impedances (pressure/velocity) at different points in the probe-tube are labeled using the letter z with an appropriate subscript. The locations of the impedances designated are shown in Fig. 4. All impedances are specific acoustic impedances (pressure/velocity), unless otherwise noted, and are normalized by the characteristic impedance, ρc of air. The probe-tube coordinate system has its origin at the center of the microphone port and is positive in the downstream direction.

1. Downstream subsystems

Define the impedance, normalized by the specific acoustic impedance of air (ρc), at the termination point to be z_b. Referring to Fig. 4, at a distance L_b away from the termination point (in the direction of decreasing x), in a one-dimensional tube of area S_b, the normalized impedance, z_1, is

$$z_1(\omega)=\frac{z_b+i\cdot\tan(kL_b)}{1+i\cdot z_b\,\tan(kL_b)}, \tag{1}$$

where k is the wave number ($k=\omega/c$). Next, an area change, either an expansion or a contraction, was built into the model. The normalized impedance just to the left of this area change is

$$z_2(\omega)=z_1(S_a/S_b), \tag{2}$$

where S_a is the new area of the tube, and S_b is the area of the terminating tube.

This procedure is repeated through the next length L_a, the next area change from S_a to S_t, and the subsequent length L_0. The formula for transferring impedances over a length is given by Eq. (1) and the impedance formula for an area change is given by Eq. (2). The normalized impedance at $x=0^+$ just to the right of the microphone centerline is $z_{\rm rhs}$, given by the equation

$$z_{\rm rhs}=\left(\frac{z_2+i\cdot\tan(kL_a)}{1+i\cdot z_2\,\tan(kL_a)}\cdot\frac{S_t}{S_a}-i\cdot\tan(kL_0)\right)\times\left(1+i\cdot\frac{z_2+i\cdot\tan(kL_a)}{1+i\cdot z_2\,\tan(kL_a)}\cdot\frac{S_t}{S_a}\cdot\tan(kL_0)\right)^{-1}. \tag{3}$$

2. Helmholtz resonator

The dynamic system ''looking into'' the microphone port from the main tube can be modeled as a Helmholtz resonator. The cavity in which the microphone is placed can be thought of as an airspring; the fluid in the neck (port) between the probe-tube and this volume can be modeled as a mass attached to the airspring. If the neck of the resonator has length L_h, area S_h, and volume V_h, then the normalized specific acoustic impedance at the centerline of the microphone ($x=0$ in Fig. 4), looking into the resonator cavity that houses the microphone is

$$z_h(\omega)=r_h+i(kL_h-S_h/kV_h), \tag{4}$$

where r_h represents the acoustic resistance of the resonator. The only dissipation in the microphone probe system is viscous damping. This dissipative effect will be incorporated into the mathematical probe-tube model by using a complex sound speed (a complex wave number, k, in the above formula), as explained later, in Sec. III C. Therefore, r_h in the resonator model is assumed to be zero.

3. Branch analysis

The impedance ''looking to the right'' at a point just *left* of the centerline of the microphone ($x=0$) is defined as $z_{\rm lhs}$ (see Fig. 4). This impedance $z_{\rm lhs}$ is modeled as the net effect of branches consisting of z_h and $z_{\rm rhs}$, thus

$$z_{\rm lhs}(\omega)=S_t[z_{\rm rhs}z_h/(S_tz_h+S_hz_{\rm rhs})]. \tag{5}$$

4. The upstream tube

The probe-tube itself is modeled as a one-dimensional waveguide of length L_1 and diameter S_t with the following boundary conditions at each end. At the $x=0$ end, the impedance is $z_{\rm lhs}$. At the open end, $x=-L_1$, the pressure is equal to the external pressure p_e minus the radiated pressure due to the open end. The radiated pressure is equal to the radiation specific acoustic impedance z_r times the velocity just inside the tube. The specific acoustic radiation impedance z_r is modeled as being equivalent to the mechanical impedance of an unflanged piston given in Kinsler[3] divided by the area of the tube S_t:

$$z_r=(\tfrac{1}{4}(kr)^2+i(0.06)kr)/S_t. \tag{6}$$

Solving the one-dimensional wave equation for waves in the tube, with the above boundary conditions, gives an expression for the pressure anywhere in the tube, from $x=-L_1$ to $x=0$. The complex pressure at $x=0$ can be expressed in terms of the radiation impedance z_r, the external pressure p_e, and the impedance $z_{\rm lhs}$:

$$p(0,t)=\frac{z_{\rm lhs}p_e e^{i\omega t}}{(z_rz_{\rm lhs}+1)i\,\sin kL_1+(z_r+z_{\rm lhs})\cos kL_1}. \tag{7}$$

This expression gives the pressure at the top of the Helmholtz resonator ''looking into'' the microphone, but it is *not* equal to the pressure *at* the microphone. The desired transfer function for the probe-tube analysis is a ratio of the pressure at the microphone p_m to the external pressure p_e.

5. Solving for microphone pressure

In order to relate the above pressure $p(0,t)$ to the microphone pressure, an analysis of the resonator is necessary. The pressure $p(0,t)$ at the top of the neck of the resonator causes a deflection, δy, of the fluid (mass) in the neck. This slightly reduces the volume of the airspring by an amount equal to $(\delta y)S_h$. The pressure on the diaphragm of the microphone is

$$p_m = -B(\delta V/V_h), \tag{8}$$

where B is the adiabatic bulk modulus of air. For a perfect gas, $B=\rho_0 c^2$. Assuming the acoustic fluctuation to be harmonic, the pressure $p(0,t)$, the normalized specific acoustic impedance z_h, and the velocity (time derivative of δy) at the top of the resonator are related by

$$i\omega\rho c\,\delta y = p(0)/z_h. \tag{9}$$

Invoking all of the above relations, and Eq. (7), yields the transfer function expression:

$$\frac{P_m}{P_e} = \frac{S_h}{ikV_h}\frac{z_{\text{lhs}}}{z_h}\frac{1}{(z_{\text{lhs}}+z_r)\cos(kL_1)+i(1+z_r z_{\text{lhs}})\sin(kL_1)}, \tag{10}$$

where P_m is the *amplitude* of the harmonic microphone pressure p_m, and P_e is the *amplitude* of the external harmonic pressure p_e. This transfer function can also be measured experimentally by determining the ratio of the external pressure measured with an ordinary condenser microphone to that obtained by a microphone with a probe-tube attachment. The experimental results were used to verify the theoretical model and to determine the amount of viscous damping.

B. Verification of the model

The theoretical model was verified experimentally for several configurations, which differed by the type of termination beyond the microphone. Some of the terminations included downstream tubes of different lengths which were closed at the end, others consisted of combinations of different diameters and lengths before terminating with a closed end.

The experiments were performed in an anechoic chamber with a white noise sound source. All experimental plots shown are transfer functions, presented as a ratio of external pressure measured by a standard $\frac{1}{2}$-in. condenser microphone and the pressure measured by the probe-tube microphone. The tip of the probe-tube and the standard microphone diaphragm were carefully located so that they could be as close as possible to each other. The experimental transfer functions include calibrations of each bare microphone using a standard pistonphone. Both microphones were attached to preamps and the data were processed simultaneously by a dual channel spectrum analyzer.

In Fig. 5, an example verification is shown for the case of a ''hard wall'' termination immediately following the microphone. At approximately 8700 Hz, a quarter wavelength is equal to the distance between the microphone port and the ''hard wall'' termination (pressure maximum), therefore both the experimental and theoretical transfer functions have a minimum at that frequency. This configuration most closely resembled the original traditional design (Fig. 1) whose experimental transfer function was shown in Fig. 2, and can be used as a baseline to judge the relative merits of the alternative designs. The physical dimensions of the probe tube attachment for this case are given in Table I.

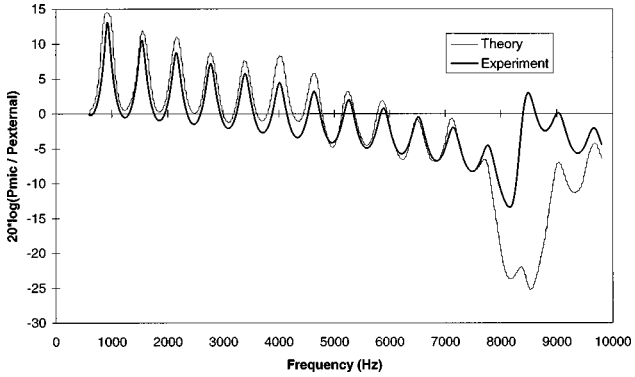

FIG. 5. Transfer function for modular probe tube with a hard ending instead of the ''downstream tube,'' as a verification of the mathematical model.

C. Damping

Viscous damping was included in the theoretical model by using a complex sound speed. The exact numerical values of the real and imaginary parts of the sound speed were determined using experimental data. The functional dependence of viscous damping on frequency was determined from a theoretical analysis. In the analysis, the damping was modeled as viscous/thermal losses in the acoustic boundary layers on the probe-tube internal surfaces. In Ref. 4, the energy dissipated per unit area and time at the surface is

$$\left(\frac{d^2E}{dA\,dt}\right)_{\text{diss}} = \xi\cdot\sqrt{\omega}\cdot I, \tag{11}$$

where I is the intensity and is equal to $I=\overline{p^2}/\rho\cdot c$ for a plane wave, and ξ is a factor which depends upon the density of the fluid, the viscosity, the thermal conductivity, and the specific heat at constant pressure and is taken to be independent of frequency. For the purposes of modeling the viscous losses in the probe-tube, the important result is that the rate of energy dissipation is proportional to the square root of angular frequency. To correctly implement this dependence in the mathematical model, the imaginary part of the sound speed was multiplied by the inverse square-root of angular frequency. The approximate numerical values of c_{Re} and c_{Im}, the real and imaginary parts of the sound speed, were determined from curve fitting the theoretical model with the experimental data. In the previously shown verification plot (Fig. 5) the complex sound speed given below was used:

$$c(\omega) = \left(1+\frac{3.5}{\sqrt{\omega}}\,i\right)c_{\text{constant}}, \tag{12}$$

where c_{constant} is the sound speed of air in meters per second (343 m/s) and ω is the angular frequency in radians per second.

TABLE I. Dimensions used for parameters defined in Fig. 4 for the cases shown in Figs. 5, 7, 8, and 9.

Dimension (refer to Fig. 4)	''Hard End'' (Fig. 5)	''Infinite Termination'' (Fig. 7)	''Tuned Resonators'' (Fig. 8)[a]	''Horn Termination'' (Fig. 8)[b]	''Constriction'' (Fig. 9)
L_1	10.3 in.	10.3 in.	10.3 in.	10.3 in.	10.3 in.
S_t	0.0125 in.^{2}	0.0125 in.^{2}	0.0125 in.^{2}	0.0125 in.^{2}	0.0125 in.^{2}
L_0	0.0125 in.	1.0 in.	0.0 in.	0.0 in.	0.042 in.
S_0	0.0125 in.^{2}	0.0125 in.^{2}	N.A.	N.A.	0.0033 in.^{2}
L_a	0 in.	24.4 in.	0.0 in.	0.0 in.	26 in.
S_a	N.A.	0.0125 in.^{2}	N.A.	N.A.	0.0125 in.^{2}
L_b	0 in.	5 ft	∞	∞	5 ft
S_b	N.A.	0.011 in.^{2}	0.0125 in.^{2}	N.A.	0.0110 in.^{2}
L_{neck}	0.06 in.	0.06 in.	0.04 in.	0.04 in.	0.06 in.
S_{neck}	0.0035 in.^{2}	0.0035 in.^{2}	0.004 in.^{2}	0.004 in.^{2}	0.0035 in.^{2}
L_{vol}	0.013 in.	0.013 in.	0.013 in.	0.013 in.	0.013 in.
S_{vol}	0.125 in.^{2}	0.125 in.^{2}	0.125 in.^{2}	0.125 in.^{2}	0.125 in.^{2}

[a]This probe configuration differs from Fig. 4. At the junction where $x=0$, there are three branches. One of them is the Helmholtz resonator due to the microphone tap, another is an infinite tube with cross section S_t, and the third is another Helmholtz resonator. The dimensions of this second resonator corresponding to the plot in Fig. 8 are $L_{\text{neck2}}=0.097$ in., $S_{\text{neck2}}=0.0013$ in.^{2}, $L_{\text{vol2}}S_{\text{vol2}}=0.025$ in^3. See Fig. 6(b).

[b]This probe configuration differs from Fig. 4 in that an exponentially flared horn starts at $x=0$. The flare constant for the plot shown in Fig. 8 was 60.0 (refer to Sec. IV C of the text for more information on the model). See Fig. 6(c).

IV. DESIGN POSSIBILITIES

The traditional probe-tube design, shown in Fig. 1 with a microphone placed at the end of the tube, resulted in undesirable standing waves in the tube. This resonant behavior caused peaks in the transfer function. As shown in Fig. 3, it was thought that placing the microphone at the *side* of the tube, rather than ''head on,'' and placing an absorptive termination at the end of the tube would eliminate the standing waves. However, standing waves still exist, due to the reflections from the microphone side branch. The goal of the various designs discussed below is to eliminate reflections, and therefore standing waves in the probe-tube. The elimination of reflections will result in a smooth transfer function without the use of damping material in the sound path between source and receiver, and the associated loss in signal-to-noise ratio. At the branch, the sound waves propagating from the open end encounter two impedances, the impedance of the resonator leading to the microphone and the impedance of the downstream termination. Assuming that the resonator dimensions are fixed (due to physical constraints regarding the microphone itself), different downstream terminations can be chosen that make the branch (including the effects of both downstream impedances) look ''transparent,'' at least for some bandwidth about a fixed center frequency.

The different downstream terminations that were explored consisted of: a long (infinite) tube; a flared tube (horn) termination; a canceling (tuned) resonator with an infinite tube; and a narrow constriction (masslike behavior) followed by an infinite tube. These designs are sketched in Fig. 6. In order to choose the best design, several factors were considered along with the shape of the transfer function. The recommended design is a probe-tube adapter with a downstream constriction followed by an anechoic termination. This design can be implemented easily and produces a smooth transfer function. For completeness, the other designs described will be discussed in the sections that follow. Physical dimensions for the experimental prototypes corresponding to each configuration are given in Table I.

A. Anechoic termination

If the downstream termination were a very long (infinite) tube (Fig. 6), the normalized specific acoustic impedance z_{rhs} would equal unity. The ''infinite tube'' was constructed experimentally by attaching a few feet of flexible tubing to a few inches of hollow steel tubing. Both had approximately the same inner diameters, and the flexible plastic tube was pressed onto the steel tube. This created a slight discontinuity, which could have been eliminated by matching the diameters more accurately. Comparisons between the experimental transfer function and the theoretically calculated transfer function are shown in Fig. 7.

Experimentally, it is difficult to achieve a perfectly anechoic termination with a long flexible tube. Surprisingly, enough viscous damping was provided by the long tube that reflected sound waves were much smaller in magnitude than incident waves. This allowed the termination to be approxi-

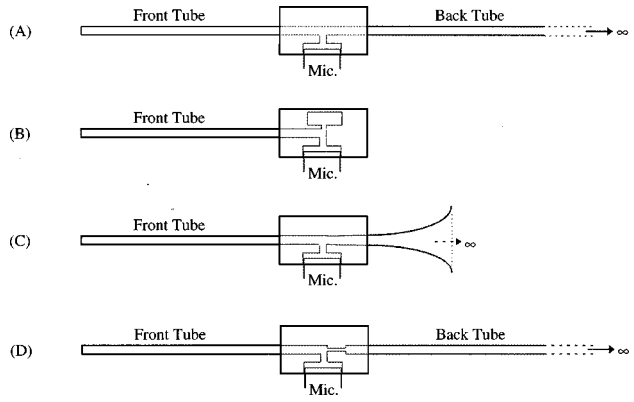

FIG. 6. Design concepts for termination of probe tube: (a) infinite tube ending, (b) tuned resonator at branch, (c) infinite exponential horn, and (d) constriction followed by infinite tube.

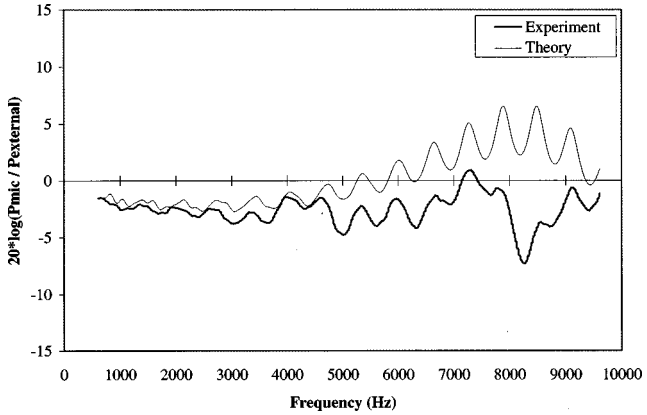

FIG. 7. Experimental and theoretical data: ''infinite'' termination.

mately modeled as anechoic. The discrepancies between the two curves (theoretical and experimental) in Fig. 7 are due to this approximation. The rough agreement between the two curves suggests that the model is a fairly good estimate of the physical system described. The presence of standing waves in these plots, especially in the theoretical plot, suggests that the sound is reflected from the *branch* containing the microphone rather than the final termination itself, since it is nearly anechoic. It is the *combination* of impedances at the branch which must be transparent to the waves in order to eliminate the resonances.

B. Tuned resonator

Since it is the combination of impedances at the branch that act together to eliminate the reflections back into the probe-tube, an additional resonator was introduced at the branch along with the infinite tube, in an attempt to create a net anechoic impedance at the branch (see Fig. 6). If the frequency of the sound waves to be measured is below the resonance frequency of the resonator (microphone cavity), then that resonator acts dynamically like an acoustic spring. The additional resonator which is added at the branch can be sized so that its resonance frequency is well below that of the first resonator (microphone cavity) and also below that of the sound waves to be measured. At these frequencies, the additional resonator will behave dynamically like an acoustic mass. In other words, its specific acoustic impedance will be positive, purely imaginary, and will be proportional to frequency. Since the original resonator (microphone cavity) behaves like an airspring, its impedance is negative, purely imaginary, and inversely proportional to frequency. At a fixed frequency, the two resonators (of opposite sign and purely imaginary) can be used to cancel each other, leaving only the ''infinite tube'' effects at the branch.

The idea of tuning resonators to cancel sound waves at a center frequency was successfully used by Bliss *et al.* for interior noise cancellation, and was called alternate resonance tuning (ART).[5] This work did not involve resonators, *per se*, but consisted of structural panels. Based on mass and stiffness properties, the panels had resonance frequencies above or below a given center frequency. The panels were arranged in an alternating pattern (checkerboard style) with panels whose resonance frequency was above a certain frequency next to panels whose resonance frequency was below this targeted frequency. In that work, sound cancellation was achieved over a wide frequency band.

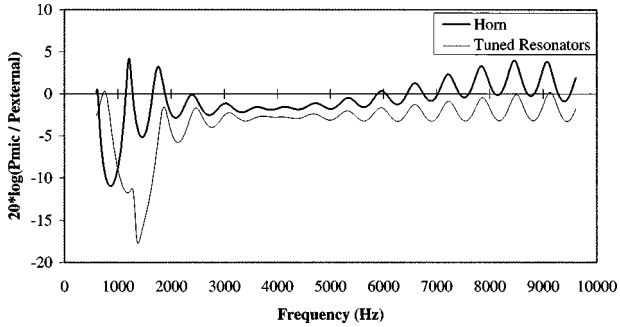

FIG. 8. Optimization at 4000 Hz using tuned resonators and horn termination. Theoretical data only.

In Fig. 8, two theoretical transfer functions are shown. One of these is for a case where a canceling resonator is introduced at the branch. The dimensions of the added resonator were chosen so that its resonance frequency was well below that of the original resonator, and so that the magnitude of the impedances would cancel at 4000 Hz. The effect appears to spread out over a band from approximately 3500 to 5500 Hz, as exhibited by the smoother transfer function at those frequencies. However, a major drawback of this design is the poor performance (i.e., large peaks in the transfer function) outside this frequency range, especially at the lower resonance frequency of the added resonator.

C. Horn termination

A similar effect was produced by terminating the probe-tube with an ''infinite'' exponential horn (Fig. 6). Once again, the object of the analysis is to make the impedance $z_{\mathrm{lhs}}=1$. This is the impedance ''looking into'' the branch. A modification of Eq. (5) for a horn termination (i.e., $z_{\mathrm{rhs}}=z_{\mathrm{horn}}$ and the opening into the horn has area S_t) is

$$\frac{1}{z_{\mathrm{lhs}}}=\frac{S_h/S_t}{z_h}+\frac{1}{z_{\mathrm{horn}}}, \tag{13}$$

where the normalized horn impedance for an exponential horn with flare constant μ is[3]

$$z_{\mathrm{horn}}=\frac{c}{\omega}\left(i\,\frac{\mu}{2}+\sqrt{\frac{\omega^2}{c^2}-\frac{\mu^2}{4}}\right). \tag{14}$$

Assuming that the microphone cavity behaves like an airspring at frequencies below its resonance and that $\omega/c \gg \mu/2$, Eq. (13) for the ideal case of $z_{\mathrm{lhs}}=1$ becomes

$$1=i\,\frac{S_h}{S_t}\,\frac{\omega}{S_h c/V_h}+1-i\,\frac{c\mu}{2}. \tag{15}$$

Solving (15) for the choice of flare constant that makes this statement true,

$$\mu=\frac{2}{c}\,\frac{S_h}{S_t}\,\frac{\omega^2}{(S_h c/V_h)}. \tag{16}$$

Unfortunately, this result implies that an infinite exponentially flared horn termination can only cancel the standing

waves in the probe-tube at a single frequency. However, as shown in Fig. 8, the impedance effect is gradual and the transfer function remains flat over a wide frequency range. Choices of μ dictate at which center frequency the transfer function will remain flat, or vice versa. In Fig. 8, μ was calculated from Eq. (16) using the dimensions of the prototype S_h, V_h, S_t, and an angular frequency, ω, equal to 8000π radians/second (or equivalently $f=4000$ Hz). The theoretical transfer function shows the horn termination effectively removes the standing waves between 3500–5500 Hz. In practice, this design would be difficult to implement since machining the exponential flare of the horn would require special effort. In theory, the horn was modeled as infinite, which poses an additional challenge for implementing the design.

D. Constriction

Another choice for a downstream termination at ''the branch'' is a constriction followed by an ''infinite'' tube (Fig. 6). The combination of a length of tube of one cross-sectional area joined on both ends to a tube of larger cross-sectional area creates a constriction. Define the length of the constriction as L_c, and its area as S_c. Looking into the branch, the impedance is z_{lhs} [Eq. (5)]. For the ideal probe-tube design, this normalized impedance should equal 1. Therefore, standing waves would not exist in the tube because there would be no reflections from the branch.

From one-dimensional acoustics, the impedance ''looking into'' the constriction, assuming an infinite tube beyond the constriction, is

$$z_c=\frac{1+i(S_t/S_c)\tan(kL_c)}{1+i(S_c/S_t)\tan(kL_c)}. \tag{17}$$

Assuming $kL_c \ll 1$, this expression approximates to

$$z_c=1+i\left(\frac{S_t}{S_c}-\frac{S_c}{S_t}\right)\frac{L_c}{c}\,\omega=1+im_c\omega. \tag{18}$$

In other words, the effect of the constriction is similar to adding a small mass m_c, which depends upon the area of the constriction and the length of the constriction. Looking into the branch at the microphone centerline,

$$\frac{1}{z_{\text{lhs}}}=\frac{S_h/S_t}{z_h}+\frac{1}{1+im_c\omega}, \tag{19}$$

which is equivalent to Eq. (5), with $z_{\text{rhs}}=1+im_c\omega$, and division by S_t, the cross-sectional area of the tube. Below the resonance frequency of the microphone cavity (a Helmholtz resonator), its impedance is approximately equal to (an air-spring)

$$z_h=-iS_hc/\omega V_h, \tag{20}$$

where S_h and V_h are the area of the neck of the resonator and the volume of the resonator, respectively, and c is the speed of sound. Requiring that $m_c\omega$ of the constriction be small compared to 1, Eq. (19) can be rewritten for the ideal case of $z_{\text{lhs}}=1$:

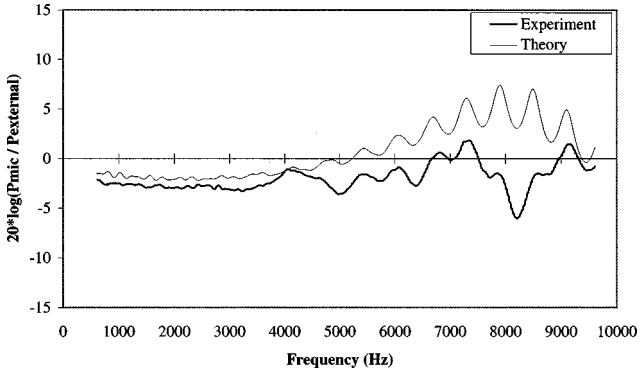

FIG. 9. Transfer function resulting from optimization using a constriction. Experimental and theoretical data.

$$1=i\left[\frac{S_h/S_t}{(S_hc/V_h)}\right]\omega+1-im_c\omega. \tag{21}$$

To satisfy this equation, $m_c=V_h/(S_tc)$. Recalling that $m_c\omega=(S_t/S_c-S_c/S_t)(L_c/c)\omega$ leads to an equation which relates the dimensions of the constriction to the dimensions of the microphone cavity,

$$\frac{V_h}{S_t}=\left(\frac{S_t}{S_c}-\frac{S_c}{S_t}\right)L_c. \tag{22}$$

For a given cavity volume V_h, Eq. (22) can be used to size the constriction. It appears that this formula is independent of frequency, but there are two assumptions which limit the range of applicability of this result. The first is $kL_c \ll 1$, which was used to simplify Eq. (17). This assumption limits the frequency range, depending on the length of the constriction, which is coupled to the area of the constriction by Eq. (22). The second, and perhaps more limiting, assumption is that the microphone cavity behaves as an airspring. This assumption is only valid for frequencies that are well below the natural frequency of the microphone cavity (Helmholtz resonator, in the model). Using the dimensions of the prototype with the plastic spacer inserted, theoretically, the resonance frequency of the cavity was around 9300 Hz. This seemed to limit the frequency range over which the constriction would work to around 5500 Hz. Increasing the resonance frequency of the microphone cavity would extend the frequency range over which the constriction would cancel the standing waves.

The constriction termination design worked well over a large frequency range. As shown in Fig. 9, the transfer function is almost completely flat until 5000 Hz. Between 5000 and 7000 Hz, the experimentally measured transfer function varies by only a few decibels. Above this there are significant variations in the transfer function. Notice the signal does not roll off to any significant degree over the entire frequency range shown since no damping material has been added in the sound path and since the resonance frequency of the microphone cavity is so high.

The constriction is easy to implement, since standard stock steel tubing is readily available in contiguous diameters. To create a constriction, a smaller diameter tube can be nested inside a larger diameter tube. The desired cross-sectional area of the constriction, S_c, and length of the constriction, L_c, can be obtained by using tubes of different size

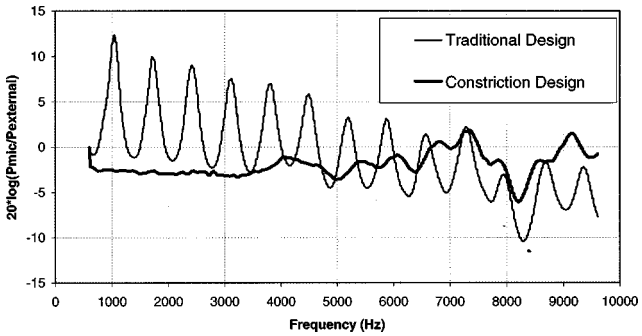

FIG. 10. Experimental transfer functions: the original traditional probe-tube design versus the recommended design.

inner diameters cut to different lengths. Knowing the inner diameter of tubing available, the appropriate length of the constriction can be calculated from Eq. (22). However, the chosen values must be such that kL_c is small [a limitation of Eq. (18)] for the desired frequency application.

V. RECOMMENDATIONS

Both the horn termination and the tuned resonator termination worked well in a particular frequency band. However, above and below the band the transfer functions ceased to be flat. Therefore, if the chosen application is for a particular band of interest, either of these designs could be used. The tuned resonator would be much more easily constructed than the horn termination.

The constriction design provided a smoother transfer function over a wider frequency range and is simple to construct. A downstream constriction followed by an ''infinite tube'' is easily achievable using standard materials. A minimum amount of simple machining is required. For these reasons, this is the recommended design. As a final comparison, Fig. 10 shows transfer functions for the original traditional probe tube design versus this constriction design, i.e., Figs. 2 and 9 (experimental only) are overlaid on the same scale.

For high-frequency applications of the probe-tube, it is also recommended that the resonance frequency of the cavity which contains the microphone be as high as possible. This can be accomplished through appropriate choices of the dimensions for the pressure tap (''neck'' of the resonator) and the space above the microphone (''volume'' of the resonator). The volume should be as small as possible. The neck of the resonator affects the resonance frequency in two ways: increasing its cross-sectional area increases the resonance frequency; increasing the length of the neck decreases the resonance frequency of the resonator. However, in practice, if the neck port is too large, the ''lumped parameter'' assumptions fail, and the resonance frequency cannot be predicted from this model. The results of having experimented with several different size microphone ports (i.e., the neck of the resonator) would lead us to recommend a relatively small port.

As a final recommendation, damping material should *not* be placed in the sound path, as in previous designs. Using the designs described in this paper, damping is not needed to smooth the transfer function and will only reduce the signal-to-noise ratio.

VI. SUMMARY

It is possible to achieve a smooth transfer function between a microphone with a probe-tube attachment and a bare microphone if certain design specifications are followed. The design concepts presented in this paper were for terminations downstream from a $\frac{1}{2}$-in. microphone which is mounted in the side of a tube. In the best design, the combination of the housing cavity for the microphone and a downstream termination of a constriction followed by an ''infinitely'' long tube creates a branch impedance that appears to be transparent to sound waves impinging upon it. Therefore, with this combination, sound waves do not reflect and standing waves are eliminated in the probe-tube. Damping material was not placed between the source and the receiver in any of the designs presented.

ACKNOWLEDGMENTS

The authors would like to thank Dr. Donald Bliss of Duke University for technical discussions and insight regarding the probe-tube designs and Dr. Kevin Shepherd of NASA Langley Research Center for originally inspiring the idea to design a probe-tube with the microphone attached to a side branch. Also, the authors would like to thank Cameron Loper and Sean Connolly, former North Carolina State University students who have contributed to this project. The authors appreciate the financial support which has been made available from the following sources: Oak Ridge Associated Universities and the National Science Foundation.

[1] Brüel and Kjaer Instruments, Inc., *Instructions and Applications: Half-Inch Condenser Microphone Types 4133, 4134, 4147, 4149, 4163* (Corboe Print, Copenhagen, 1973), pp. 63–64.
[2] A. B. Copeland and D. Hill, ''Design of a probe-tube adapter for use with a 1-inch condenser microphone,'' J. Acoust. Soc. Am. **48**, 1036 (1970).
[3] C. E. Kinsler, A. R. Frey, A. B. Coppens, and J. V. Sanders, *Fundamentals of Acoustics* (Wiley, New York, 1982), 3rd ed.
[4] A. D. Pierce, *Acoustics: An Introduction to Its Physical Principles and Applications* (Acoustical Society of America, New York, 1989), p. 529.
[5] J. A. Gottwald, *Alternate Resonance Tuning*, Ph.D. dissertation, Duke University, under the direction of Donald B. Bliss, 1991.

Study on verifying technology of rms detector characteristics of sound level meters

Mingduo Zhang
Applied Acoustics Institute, Shaanxi Normal University, Xi'an 710062, People's Republic of China

(Received 6 September 1997; accepted for publication 16 July 1998)

Current standards have defined the methods to verify the rms (root-mean-square) detector characteristic of sound level meters. When using these methods, there will be a systematic error in the measuring results. The results then cannot accurately express the error in the rms detector characteristic of a sound level meter. The reason for this is that the effect of the difference between the frequency-weighting characteristics of the sound level meter to be inspected and that of the standard system is ignored. So, an erroneous judgment may be made. Aiming at this problem, this paper contains some theoretical analysis and quantitative calculation in detail. An improved verifying method is put forward. © *1998 Acoustical Society of America.*
[S0001-4966(98)00311-7]

PACS numbers: 43.58.Vb [SLE]

INTRODUCTION

The rms (root-mean-square) detector characteristic is one of the important properties of a sound level meter. The instrument is used to measure audio signal and its frequency range is 20–20 000 Hz generally. The range is much smaller than that of general electric meters. For a signal under measuring, the rms value given by the instrument is different from that by a general electric meter. To verify the rms detector characteristic of the instrument, a special method is needed. Current standards[1–4] have defined some correlative verifying methods. However, these methods ignored the effect of the difference between the frequency-weighting characteristics of the standard system and that of the sound level meter to be tested on the measuring results. This paper is to analyze the effect by means of both theoretical analysis and quantitative calculation. An improved method of verification is then given.

I. THEORETICAL ANALYSIS

The rms detector characteristics of all classes of sound level meters are defined by current standards[1–4] and shown in Table I. These standards also define the method used for verifying the rms detector characteristics. The measuring principle is shown in Fig. 1. Here, the standard system must have the same frequency-weighting network as that of the sound level meter to be tested. First, the signal generator produces a continuous sine signal of given frequency and conveys it to the sound level meter being tested and the standard system simultaneously to cause each of the two systems to produce a reading. Second, the signal generator produces one of the testing signals shown in Table II and conveys it as above. Adjust the amplitude of the signal so that the standard system's reading is equal to that for the previous sine signal. Then the error of the rms detector characteristic of the sound level meter can be expressed as

$$\delta = D_1 - D_2, \tag{1}$$

where D_1 and D_2 are the readings of the sound level meter responding to the sine signal and the testing signal, respectively, and δ is the error. For other testing signals, repeat the measuring procedures as above.

This method is based on the following. First, the two readings of the standard system are identical, which implies that both signals produced by the signal generator successively should have the same rms values. Second, measuring error resulting from the deviations of frequency-weighting characteristics of the sound level meter will be offset when calculating δ by using Eq. (1). However, it is not the truth. Listed below are the major reasons for this.

First, the standard system and the sound level meter are independent of each other. It is impossible to ensure that the standard system has the same frequency-weighting network as every sound level meter under test. Shown in Table III are the specified tolerances of frequency-weighting characteristics of all classes of sound level meters defined by the relevant standards.[1–3] This means that the frequency-weighting characteristics of both systems are up to standard provided they conform to the definition of Table III. This does not mean, however, that their frequency-weighting networks are the same.

Second, it can be seen from Table III that the specified tolerances of frequency-weighting characteristics are different from range to range. That is to say that the network makes the input signals change nonlinearly in different frequency bands. So, the measuring error, which results from the deviation of the frequency-weighting characteristics, correlates with the spectrum of the input signal.

The rms detector is set after the network in a sound level

TABLE I. Allowable error of rms value detector characteristics of sound level meters (unit: dB).

Class of sound level meter	0 and 0I	1I	1	2I	2	3
Crest factor=3	±0.5	±0.5	±0.5	±1	±1	±1.5
5	±0.5	±1	⋯	±1	⋯	⋯
10	±1	±1.5	⋯	⋯	⋯	⋯

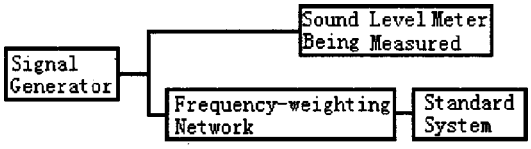

FIG. 1. Measuring principle of current verifying method.

meter. Thus, the detector receives different signals during verification according to the method shown in Fig. 1. It is unreasonable to express the error of rms value detector characteristics of the sound level meters by Eq. (1). Instead, it should be expressed as

$$\delta_{Ss}-\delta_{Sf}=\delta-(\Delta_{Ss}-\Delta_{Bs})+(\Delta_{Sf}-\Delta_{Bf})+(\delta_{Bs}-\delta_{Bf}),$$

where δ_{Sf} and δ_{Bf} are the respective errors of rms detector characteristics of the sound level meter and the standard system when a continuous sine signal of frequency f is conveyed, δ_{Ss} and δ_{Bs} are the respective errors of the rms detector characteristics when a testing signal is conveyed, Δ_{Sf} and Δ_{Bf} are the respective measuring errors of rms detector characteristics resulting from the deviation of frequency-weighting characteristics of the sound level meter and the standard system when the continuous sine signal of frequency f is conveyed, and Δ_{Ss} and Δ_{Bs} are the respective measuring errors resulting from the deviation when the testing signal is conveyed. Usually, the effect of δ_{Sf}, δ_{Bs}, and δ_{Bf} can be ignored. Then,

$$\delta_{Ss}=\delta-(\Delta_{Ss}-\Delta_{Bs})+(\Delta_{Sf}-\Delta_{Bf}). \tag{2}$$

It can be seen from Eq. (2) that unless the frequency-weighting characteristics of the two systems are exactly identical ($\Delta_{Ss}=\Delta_{Bs}$ and $\Delta_{Sf}=\Delta_{Bf}$), δ_{Ss} will not equal δ.

II. QUANTITATIVE CALCULATING ANALYSIS

Considering the qualitative analysis above, the following are quantitative calculations aimed at specific testing signals.

It is known that a function $f(t)$ with period of $T=2l$ can be expressed as a Fourier series:

$$f(t)=a_0+\sum_{n=1}^{\infty} a_n\cos\left(\frac{n\pi}{l}t\right)+b_n\sin\left(\frac{n\pi}{l}t\right),$$

where

$$a_0=\frac{1}{2l}\int_{-l}^{l}f(t)dt,\quad a_n=\frac{1}{l}\int_{-l}^{l}f(t)\cos\left(\frac{n\pi}{l}t\right)dt,$$

and

$$b_n=\frac{1}{l}\int_{-l}^{l}f(t)\sin\left(\frac{n\pi}{l}t\right)dt.$$

So, a rectangular pulse signal and a continuous tone burst signal used for testing can be expressed as

$$f_J(t)=\frac{2A\tau}{T}\left(1-\frac{\tau}{T}\right)+\sum_{n=1}^{\infty}\frac{2A}{n\pi}\left(1-\frac{2\tau}{T}\right)\times\sin\left(\frac{n\pi\tau}{T}\right)\cos\left[\frac{2n\pi}{T}\left(t-\frac{\tau}{2}\right)\right], \tag{3}$$

$$f_C(t)=\frac{B}{\omega T}\sin(\omega\tau)+\sum_{n=1}^{\infty}P_n\cos\left[\frac{2n\pi}{T}\left(t-\frac{T}{2n\pi}\alpha_n\right)\right], \tag{4}$$

where T and τ are the period and duration of the testing signal, respectively, A is the peak-to-peak value of the rectangular pulse signal, B is the peak value of the continuous tone burst signal, ω is the angular frequency of the sine signal used for forming the tone burst signal,

$$P_n=\frac{B\sqrt{A_n^2+B_n^2}}{(\omega T)^2-(2n\pi)^2},$$

$$A_n=2\omega T\sin(\omega\tau)\cos\left(\frac{2n\pi\tau}{T}\right)-4n\pi\cos(\omega\tau)\sin\left(\frac{2n\pi\tau}{T}\right),$$

TABLE II. Testing signals. (Note: Frequency of the sine signal used for forming continuous tone burst signal is equal to 2 kHz.)

Type of testing signal	Rectangular pulse			Continuous tone burst		
T (ms)	2	5.2	20	25	25	25
τ (ms)	0.2	0.2	0.2	5.56	2	0.5

TABLE III. Allowable deviation of frequency-weighting characteristics of sound level meters (unit: dB).

f (Hz)	10–16	20	25	31.5	40	50	63	80	100	125–1k	1.25k
Class 0	+2,−∞	±2	±1.5	±1	±1	±1	±1	±1	±0.7	±0.7	±0.7
Class 1	+3,−∞	±3	±2	±1.5	±1.5	±1.5	±1.5	±1.5	±1	±1	±1
Class 2	+5,−∞	±3	±3	±3	±2	±2	±2	±2	±1.5	±1.5	±1.5
Class 3	+5,−∞	+5,−∞	+5,−∞	±4	±4	±3	±3	±3	±3	±2	±2.5
f (Hz)	1.25k	1.6k–2k	2.5k	3.15k	4k	5k	6.3k	8k	10k	12.5k	16k–20k
Class 0	±0.7	±0.7	±0.7	±0.7	±0.7	±1	+1,−1.5	+1,−2	+2,−3	+2,−3	+2,−3
Class 1	±1	±1	±1	±1	±1	±1.5	+1.5,−2	+1.5,−3	+2,−4	+3,−6	+3,−∞
Class 2	±1.5	±2	±2.5	±2.5	±3	±3.5	±4.5	±5	+5,−∞	+5,−∞	+5,−∞
Class 3	±2.5	±3	±4	±4.5	±5	±6	±6	±6	+6,−∞	+6,−∞	+6,−∞

TABLE IV. Calculated results for rectangular pulse signal (Δ_J, unit: dB). (Note: CF is the crest factor of sound level meters.)

Class of sound level meter		0	1	2	3
Without deviation	CF=3	−0.0839	−0.0839	−0.0839	−0.0839
	CF=5	−0.0983	−0.0983	−0.0983	−0.0983
	CF=10	−0.1078	−0.1078	−0.1078	−0.1078
Maximum deviation (positive)	CF=3	+0.3332	+0.5267	+1.3276	+2.0835
	CF=5	+0.5653	+0.8558	+1.8888	⋯
	CF=10	+0.6271	+0.9476	⋯	⋯
Maximum deviation (negative)	CF=3	−0.4921	−0.6727	−1.1103	−2.6216
	CF=5	−0.7779	−1.0868	−1.8417	⋯
	CF=10	−0.8722	−1.2263	⋯	⋯

$$B_n = 2\omega T \sin(\omega\tau)\sin\left(\frac{2n\pi\tau}{T}\right) + 4n\pi\left[\cos(\omega\tau)\cos\left(\frac{2n\pi\tau}{T}\right) - 1\right],$$

and

$$\alpha_n = \tan^{-1}(B_n/A_n).$$

As stated above, a sound level meter is used to measure audio signals (20–20 000 Hz). Only audio signals are to be conveyed to the rms detector for detecting and indicating. Considering this aspect and the testing signal defined by Table II, as well as the deviation of frequency-weighting characteristics of the instrument, Eqs. (3) and (4) should be rewritten as

$$F_J(t) = \frac{2A\tau}{T}\left(1 - \frac{\tau}{T}\right) + \sum_{n=1}^{N} \frac{2A\delta_n}{n\pi} \times \left(1 - \frac{2\tau}{T}\right)\sin\left(\frac{n\pi\tau}{T}\right)\cos\left[\frac{2n\pi}{T}\left(t - \frac{\tau}{2}\right)\right], \quad (5)$$

$$F_C(t) = \frac{B}{\omega T}\sin(\omega\tau) + \sum_{n=1}^{N} \delta_n P_n \times \cos\left[\frac{2n\pi}{T}\left(t - \frac{T}{2n\pi}\alpha_n\right)\right], \quad (6)$$

where $N = 20\,000T$ and δ_n is the deviating factor corresponding to different frequencies. In Eq. (6), if $n = 50$, then $\alpha_n = 0$ and $P_n = -B\tau/T$. The respective rms value of the signal corresponding to Eqs. (5) and (6) is

$$R_J = \sqrt{\frac{1}{T}\int_0^T F_J^2(t)dt}, \quad (7)$$

$$R_C = \sqrt{\frac{1}{T}\int_0^T F_C^2(t)dt}. \quad (8)$$

The respective true rms values of the two testing signals are

$$\mathrm{rms}_J = \frac{A\tau}{T}\sqrt{\frac{T}{\tau - 1}}, \quad (9)$$

$$\mathrm{rms}_C = B\sqrt{\frac{\tau}{2T}}. \quad (10)$$

Thus, for a given sound level meter and the two testing signals, the respective measuring error of the rms detector characteristics resulting from the deviation of the frequency-weighting of the instrument can be expressed as

$$\Delta_J = 20\lg(R_J/\mathrm{rms}_J), \quad (11)$$

$$\Delta_C = 20\lg(R_C/\mathrm{rms}_C). \quad (12)$$

Within the specified tolerances defined by the standards, the frequency-weighting characteristic of a sound level meter changes in many ways. It is very difficult, and unnecessary, too, to provide the affecting degree of the deviation on verifying the rms detector characteristics for all conditions. As special samples, we made some calculation on three cases. In

TABLE V. Calculated results for continuous tone burst signal (Δ_C, unit: dB). (Note: CF is the crest factor of sound level meters.)

Class of sound level meter		0	1	2	3
Without deviation	CF=3	−0.0763	−0.0763	−0.0763	−0.0763
	CF=5	−0.0222	−0.0222	−0.0222	−0.0222
	CF=10	−0.0895	−0.0895	−0.0895	−0.0895
Maximum deviation (positive)	CF=3	+0.1562	+0.2330	+0.5185	+0.8533
	CF=5	+0.0384	+0.0673	+0.1774	⋯
	CF=10	+0.0740	+0.0666	⋯	⋯
Maximum deviation (negative)	CF=3	−0.1530	−0.2095	−0.3765	−0.5139
	CF=5	−0.0745	−0.0947	−0.1531	⋯
	CF=10	−0.1027	−0.1078	⋯	⋯

the first case, deviation of frequency-weighting characteristics, is equal to naught in the audio range ($\delta_n \equiv 1$). In the second case, all the deviations reach positive maximum value. In the third case, all the deviations reach negative maximum value. For the maximum deviation, δ_n can be obtained from converting the numerical value shown in Table III. Calculated results are shown in Tables IV and V. The first case reflects the effect of filter characteristics of the sound level meter with ideal frequency-weighting characteristics on verifying rms detector characteristics. The later two reflect the effect on the verification of which frequency-weighting characteristics reached maximum deviation. The major reasons of analyzing the cases with maximum deviation are the following. First, sound level meters with maximum deviation of frequency-weighting characteristics are also considered as up to standard. Second, although deviation of the overwhelming majority of sound level meters is smaller than the specified tolerances, the possibility for individual sound level meters to have the maximum deviation could not be removed.

III. A NEW METHOD FOR VERIFICATION

From Eq. (2) and Tables IV and V, the effect of the deviation of frequency-weighting characteristics on verification is clear. That is the case especially when maximum deviation is reached. The affecting degree is closely connected with the spectrum of testing signal. So, the verifying results cannot accurately express the error of the rms detector characteristics of the sound level meter according to current standards. Erroneous judgment may be made. The key to solve this problem is that either the measured results should not depend on the frequency-weighting network or the effect of the network on the measured results can be ignored.

For this reason, the verifying method should be modified as shown in Fig. 2. Compared with Fig. 1, the difference is that the standard system is connected to ''ac output'' of the sound level meter to be tested. It is unnecessary to set a special frequency-weighting network. The measuring methods are equal to that of current standards. As the ''ac output'' is set between network and detector of the instruments, the standard system has the same frequency-weighting network as that of the sound level meters to be tested. Detectors of the two systems will receive exactly the same signal. Thus, it can remove the systematic measurement error resulting from the difference between the frequency-weighting characteristics of the two systems. Furthermore, the deviation of the frequency response of the standard system is chosen so small that we can ignore its effect on the measured results. So, we can say that the unique difference between the two systems is that their rms detectors are different from each other.

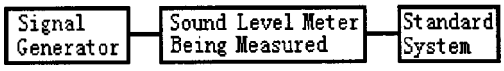

FIG. 2. Measuring principle of new verifying method.

Suppose rms_{Sf} and rms_{Bf} are the respective true rms values of the signal received by the sound level meter to be tested and the standard system when a continuous sine signal of frequency f is conveyed, rms_{Ss} and rms_{Bs} are the respective true rms values when the testing signal is conveyed, and D is the reading of the standard system for both signals. According to Fig. 2 and the testing procedure we have

$$D = \mathrm{rms}_{Bf} + \delta_{Bf} + \Delta_{Sf} = \mathrm{rms}_{Bs} + \delta_{sf} + \Delta_{Ss},$$

$$D_1 = \mathrm{rms}_{Sf} + \delta_{Sf} + \Delta_{Sf}, \quad D_2 = \mathrm{rms}_{Ss} + \delta_{Ss} + \Delta_{Ss},$$

$$\mathrm{rms}_{Ss} - \mathrm{rms}_{Sf} = \mathrm{rms}_{Bs} - \mathrm{rms}_{Bf}.$$

According to these equations we have

$$\delta_{Ss} - \delta_{Sf} = \delta + \delta_{Bs} - \delta_{Bf}.$$

Similarly as above, the effect of δ_{Sf}, δ_{Bs}, and δ_{Bf} can be ignored, so

$$\delta_{Ss} = \delta.$$

Clearly the measured results are unconnected with the frequency-weighting network of the two systems. That is to say that the error of the rms detector characteristics of the sound level meter can be expressed as Eq. (1) when the verifying method shown in Fig. 2 is adopted.

IV. SUMMARY

According to current standards, there is a systematic error in the verifying results. The error results from the difference between the frequency-weighting characteristics of the standard system and that of the sound level meter under test. It should not be ignored. So, the verifying results cannot express the rms characteristic of a sound level meter accurately. This paper puts forward a new method. In the new method, it is unnecessary to set a special frequency-weighting network for the standard system and the error of the rms detector characteristics of a sound level meter can be expressed simply by Eq. (1) as in the current standard. However, the new verifying method can overcome the shortcomings and remove the systematic error existing in the current method. It can therefore improve the measurement accuracy of verification.

ACKNOWLEDGMENTS

I am very grateful to Professor W. X. Jiang for his helpful advice on this paper, and to help given by my colleagues S. J. Wu and M. X. Ding.

[1] IEC651-1979, *Sound Level Meters*.
[2] GB3785-83, *Electric, Sonic Properties and Measuring Method for Sound Level Meters* (in Chinese).
[3] SJ/T10423, *General Specifications for Sound Level Meters* (in Chinese).
[4] JJG188-90, *Verification Regulation of Sound Level Meters* (in Chinese).

The Wagstaff's integration silencing processor filter: A method for exploiting fluctuations to achieve improved sonar signal processor performance

Ronald A. Wagstaff
Naval Research Laboratory, Stennis Space Center, Mississippi 39529-5004

(Received 1 October 1995; revised 20 April 1998; accepted 23 July 1998)

There is a class of signal processing algorithms that achieves gain by exploiting the amplitude fluctuations in the spectrum analyzed acoustic power. One of those processors is presented. The causes of fluctuations that influence the performance of such processors are discussed, and processed results from a fluctuation-based processor are presented. Gains relative to the average power processor in signal-to-noise ratio (SNR) of as much as 10 dB, and gains in spatial and spectral resolution, minimum detectable levels, and other measures of processor performance have been achieved. For the most part, the additional gains from exploiting fluctuations are independent of the frequency resolution and the array aperture (or number of elements if the noise is ''white'') and depend on the number of averages and percent of overlap of consecutive time-to frequency fast Fourier transforms (FFT). [S0001-4966(98)00511-6]

PACS numbers: 43.60.Cg, 43.30.Re, 43.30.Wi [JCB]

INTRODUCTION

The study of fluctuations in underwater acoustics is not new. Research has been going on for more than 30 years. Many measurements have been made; various fluctuation generation mechanisms have been investigated, and models have been proposed. Summaries of fluctuation research are provided by Gaunaurd,[1] Fortuin,[2] and Horton.[3] Fisher[4] gives an annotated bibliography of more than 130 papers on various aspects of the subject. Urick[5,6] gives brief discussions of fluctuations in the ocean and their influence on the detection of a signal from a submarine. He indicates that the presence of fluctuations can extend the detection range. Simanin[7] suggests that the amplitude distribution of the signal from a submerged source can provide a clue to determining the propagation paths between the source and the receiver and, hence, the depth of the source. Outside of those two noteworthy exceptions, the general rule of thumb seems to be that fluctuations are considered a nuisance that degrades the signal processor's performance and should be ignored or avoided whenever possible.

Some of the causes of fluctuations in signals and noise propagating in the undersea acoustic environment that are considered to be important, for periods of the order of a few minutes and less, are the following:

(i) temporally and spatially variable thermal and salinity finestructure (patches or blobs),[8,9]
(ii) internal waves,[5,8–11]
(iii) turbulent particle velocities,[12]
(iv) ray path or wave front reflection from the moving, irregular sea surface,[13,14]
(v) changes in source–receiver range separation,[15]
(vi) rocking dipole effect of the radiation directivity pattern of a ship at the sea surface (not a propagation effect),
(vii) source and/or receiver vertical motion causing temporal changes in propagation modes or ray paths,[13]
(viii) source radiation amplitude instability (not a propagation effect),
(ix) interference of multipath arrivals, and[5,14–16]
(x) variable sea surface height above the source or receiver due to sea surface motion (sea and swell) causing changes in the decoupling depth or Loyd's mirror effect.[5,13,17]

For specific detail see Refs. 5–17, and see Refs. 1–4 for more general detail.

Figure 1 presents three time histories of spectrum analyzer output from data measured by a deep sensor in the ocean. Each is for a frequency bin width (BW) of 0.1 Hz and 75% overlap of consecutive temporal fast Fourier transforms (FFT). The middle trace, designated N, is from a ''noise only'' bin. It has a random nature and large amplitude fluctuations that are characteristic of broadband background noise that is generated by sources at the surface, such as ships and winds and waves. It has a standard deviation of the decibel time history of 5.8 dB. The top trace, designated $C+N'$, is from a frequency bin that, in addition to noise (N'), contains a clutter signal (C), or tonal clutter, from a surface ship. It also has large amplitude fluctuations with a standard deviation of 5.4, nearly the same as the noise trace. The bottom trace, designated $S+N'$, is from a frequency bin that contains background noise (N') and a signal from a deep projector (S) which has not had significant interaction with the sea surface. It has a distinctly nonrandom character with small fluctuations in amplitude compared to the previous two traces (i.e., clutter and noise). It is this type of trace, with its relatively low amplitude fluctuations, that a fluctuation-based processor will preferentially preserve, while severely attenuating the other two types of traces. However, as the signal-to-noise ratio (SNR) in the bin of this last trace decreases, its fluctuation character will approach that of the ''noise only'' (N) trace with corresponding reductions in the gains achieved by fluctuation-based signal processors. The additional gains that could be achieved will disappear when there

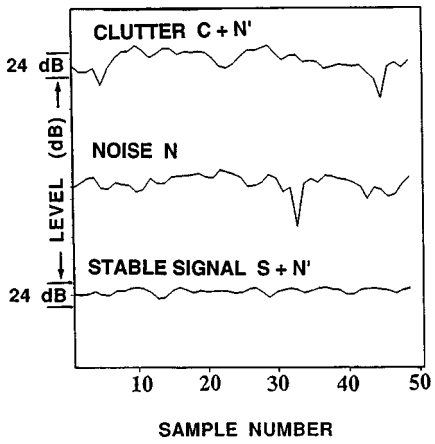

FIG. 1. Narrow-band acoustic power time histories of ambient noise (N, middle), clutter signal plus noise ($C+N'$, top), and submerged source signal plus noise ($S+N'$, bottom).

are no discernible differences between the fluctuations in the resulting highly corrupted signal plus noise ($S+N'$) bin and the ''noise only'' bins. Similarly, the additional gains will also vanish if the projector is raised to a depth near the sea surface where the projected signal (S) paths interact with the fluctuation generators near the ocean surface. The signal, S, will then have the fluctuation character that is nearly identical to the second trace, the clutter signal (C), and will also appear to the fluctuation-based processor the same as noise, even though it originated as a low fluctuation amplitude tonal. Furthermore, during conditions of extreme multipath interference (e.g., reinforcement and cancellation), the signal fluctuations can even exceed those of the noise.

The causes of amplitude fluctuations listed above are not all of the causes that are known. They are simply those that are believed to be the most important for the two fluctuation-based processors of particular interest in this paper. The first one, designated Wagstaff's Integration Silencing Processor (WISPR), derived its name from the Office of Naval Research (ONR) exploratory development (6.2) research project called WISPR Filter Development and Evaluation which was started in 1988. The WISPR filter has been known by that acronym ever since. The second algorithm, designated as DELTA (a name, not an acronym), is related to both WISPR and the average power processor. It will be defined later.

I. GOVERNING EQUATIONS

The potential for achieving additional gain by exploiting fluctuations will be demonstrated by using the average power processor AVGPR, as the designated reference to which the performance of the WISPR processor will be compared, where

$$\mathrm{AVGPR}=\frac{1}{n}\sum_{i=1}^{n} X_{i,} \tag{1}$$

$X_{i,}=i$th output power from a given spectral bin containing either signal and noise ($S+N'$) or only noise (N), N' = noise that also occupies the bin containing the signal, and n = total number of time samples.

The average power processor (AVGPR) is dominated by the highest power values in the data sequence.[18] Stories are numerous that relate the inability of AVGPR processor-driven undersea passive sonar systems to function properly in the presence of high-level impulsive noise from such sources as seismic prospectors, snapping shrimp, and ''carpenter fish.'' In such impulsive noise environments and AVGPR processing, ''normal'' signals and background noise are masked beyond recognition. Experience has shown the output of the average power processor on ambient noise measured in the ocean is approximately equivalent to the 75 percentile of the decibel time history of the narrow-band spectrum analyzer output. Of course, the AVGPR processor operates on powers and not power levels. However, the statistics of the decibel values are useful quantities.

The rational for the development of an improved processor was based on the realization that the AVGPR processor was biased upward by the high values. Such a processor, it seemed, should not be optimum when the SNR is very low. For such a case, it appeared to make more sense to bias the processor toward the lower levels and away from the high levels. The challenge was how to do that. Perhaps one could ''turn the processor upside down,'' which would make high-level clutter and noise unimportant and low-level signals important. For example, if one turns Fig. 1 upside down, the low level minimum in both the noise (N) and the clutter plus noise ($C+N'$) time histories become high level transients that would ''capture'' the AVGPR processor, but the signal plus noise ($S+N'$) time history would not be greatly affected by the inversion process.

One approach to inverting the processor is to establish a high-level decibel reference (e.g., 200 dB) and measure from that high-level reference line down to each decibel value in the power level time history. Each modified value would then be the reference level minus the individual power level. In other words, they become negative decibels. When these new negative decibels, with their high-level reference, are converted to powers and summed, a power value approximately equal to the 75 percentile decibel level could be expected. However, since the measurement is in the downward (negative) direction, the actual power value, when the reference level is removed, should be approximately the 25 percentile decibel level, i.e., the 75 percentile decibel level in the downward direction. The equation in power that results from such a procedure is the WISPR filter, which is simply the reciprocal of the average of the reciprocals of the individual power values and is also recognized within the statistical community as the harmonic mean. Verification of that is left as an exercise for those who are interested. The author was unaware of the harmonic mean until several years after using it as the WISPR filter and documenting previous results. It was given the acronym of WISPR because of its noise suppression ability. It never was, nor or is it now, the intention of the author to claim invention of the harmonic mean. However, since the WISPR processor involves more than the harmonic mean (i.e., includes DELTA) and much work has already appeared under the WISPR banner, that designation will continue to be used herein.

The above two paragraphs give the intuitive approach to

deriving the WISPR filter. The mathematical definition of the WISPR filter (or harmonic mean) is

$$\text{WISPR}=\left[\frac{1}{n}\sum_{i=1}^{n}X_i^{-1}\right]^{-1}, \tag{2}$$

and the previous definitions for X_i and n apply. In addition, the constraint that $X_i \neq 0$ is required to avoid division by zero.

The WISPR SNR gain is defined for each frequency bin containing signal plus noise ($S+N'$) and for adjacent bins containing only noise (N) as

$$\text{WISPR SNR gain}=\left[\frac{(\text{WISPR/AVGPR})_{S+N'}}{(\text{WISPR/AVGPR})_N}\right]. \tag{3}$$

Alternatively, Eq. (3) can be written as

$$\text{WISPR SNR gain}=\left[\frac{S+N' \text{ suppression}}{N \text{ suppression}}\right], \tag{4}$$

where

$$S+N' \text{ suppression}=(\text{WISPR/AVGPR})_{S+N'}, \tag{5}$$

and

$$N \text{ suppression}=(\text{WISPR/AVGPR})_N. \tag{6}$$

The ratio AVGPR/WISPR for a sequence is a valuable measure of fluctuation content that is designated in results below as:

$$\text{DELTA}=\frac{\text{AVGPR}}{\text{WISPR}}. \tag{7}$$

In order to quantify DELTA, tests have been conducted on more than 10^8 measured time histories of FFT outputs ranging in size (n) from as few as 2 points to more than 4000 points. They include consecutive FFTs with overlaps ranging from 0% to 99%. The frequency bin widths range from 0.012 Hz to about 10 Hz. Data are also included from single sensors, and from linear and multidimensional arrays with as many as 200 elements and apertures from a few meters to 3 nmi in shallow and deep water, and in areas of light to heavy shipping traffic with sea states from 0 to 5, and frequencies from 1 to 1500 Hz. Signals from submerged projectors [$S+N'$ in Eqs. (1)–(7)] that varied in range from tens of meters to more than 400 nmi, geophysical prospecting sources, innumerable nearby and distant ships, and most varieties of noise [N in Eqs. (1)–(7)] one might expect to measure in the oceans, including the Arctic near the ice, were also included in the data. The data came from more than 18 separate measurement exercises. Based on the processing and analysis of those data, an empirical threshold was determined, such that when

$$\text{DELTA} \leqslant 1.41 (\text{or } 1.5 \text{ dB}), \tag{8}$$

it indicates that the sequence of powers from which DELTA was obtained has an extremely high probability of having originated from a submerged projector. In fact, the empirically determined false alarm rate for identifying low fluctuation amplitude signals from submerged projectors by that means was found to be less than 10^{-5}.

A plot of the DELTA curve [Eq. (7)] provides a simple and rapid means for visually identifying the submerged source signals (illustrated in some of the figures below). The submerged source signal identifications can also be easily and rapidly accomplished in an unalerted and automatic manner by the computer.

II. APPROACH

Theoretical, analytical, and empirical studies of the SNR gain and other enhancements due to WISPR processing (i.e., WISPR and DELTA) have been conducted. Only empirical results will be presented in this paper. Results from processing spatial domain (beam-formed) and spectral domain data are included. In presenting the results, it is assumed that the power averaging processor, AVGPR [Eq. (1)], is sufficiently well understood that it can be used for and designated as a standard, or bench mark, against which corresponding WISPR processing [Eqs. (2) and (7)] results can and will be compared. Furthermore, the comparisons will be facilitated by plotting (as appropriate) the two different but corresponding results, AVGPR and WISPR, on the same plot. In some cases, the ratio of the two, or DELTA [Eq. (7)], will also be displayed at the bottom of the same plot to designate which components of the spectral or spatial spectrum pass the submerged source test [Eq. (8)].

III. RESULTS AND DISCUSSION

Quantitative and qualitative measures of performance for the WISPR processor and the fluctuation exploitation (FE) gain it achieves are given below.

A. Independence of FE gain from frequency binwidth gain

The plots in Fig. 2 illustrate the independence of FE gain from frequency bin width (BW) gain with two sequences (time histories) of ''typical'' measured ambient noise data (bottom curves) and two sequences of measured signal data (top curves). Each sequence contains 400 FFT output data points. The data sequences in Fig. 2(a) are from a 1024-point time domain FFT (BW of 0.2 Hz) with consecutive FFTs overlapped (O.L.) by 55%. The three statistics AVGPR, WISPR, and DELTA associated with each data sequence are listed in the top row of Table I. For the plots in Fig. 2(a) and the top row of statistics in Table I, the DELTA for the noise (N suppression) is 9.2 dB, while the DELTA for the signal ($S+N'$ suppression) is 1.0 dB. Hence, the average WISPR SNR gain (FE) is approximately 9.2 dB -1.0 dB$=8.2$ dB.

Each successive row of Table I is for a doubling of the FFT size and corresponding reduction in the BW by a factor of 2. Hence the results range from a BW of 0.2 Hz for a 1024-point FFT with 55% overlap (top row) to a BW of 0.012 Hz for the 16384-point FFT with 97% overlap (bottom row). The plots in Fig. 2(b) and last row of statistics in Table I contain the results for the 16 384-point FFT with corresponding FE gain of 11.2 dB-0.2 dB$=$11.0 dB. The FE gains in Table I show some scatter, but no definite trend that is

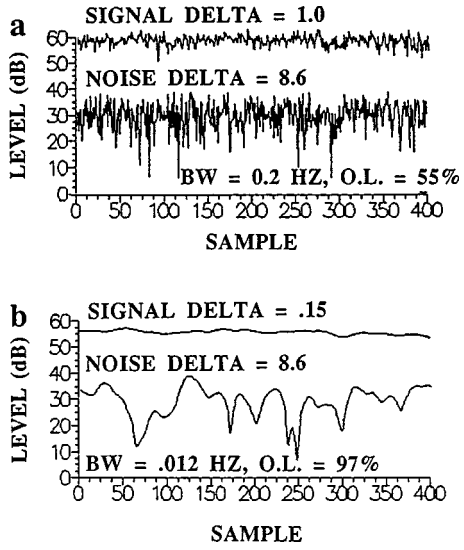

FIG. 2. Time histories of spectrum analyzed acoustic data for typical ambient noise (bottom curves) and signal plus noise bin (top curves) for two BW sizes. The FFT sizes and corresponding statistics of AVGPR, WISPR, and status DELTA are included in rows 1 and 5 of Table I.

related to the FFT size, or BW. Similar processing of other data sets support the notion that the FE gain is independent of the BW.

B. Independence of FE gain from directivity index (DI) gain

Figure 3 illustrates the independence of FE gain from DI gain. Each of the four plots contains three curves. The top curves are the beam output levels versus beam number (related to steering angle) that were obtained from power averaging [AVGPR, Eq. (1)] of the beam-former outputs. The middle curves are the corresponding outputs from WISPR processing [Eq. (2)]. The bottom curves are the decibel differences (or ratio in power) between the previous two curves [DELTA, Eq. (7)] in the same plot. They have been clipped on the plots to avoid having them interfere with the WISPR curves and confusing the display. The DELTA curve is where the gain of the WISPR processing, relative to the AVGPR processing, shows up. The average noise suppression part of the FE gain (for noise only) is the average level of the DELTA curve (before clipping). Each plot corresponds to a given aperture of a towed horizontal-line array, as denoted by the directivity index (DI) in the upper right-hand corners of the plots. Figure 3(a) is for an array with a DI of 1.8 dB. The FE gain indicated by the average of the bottom curve is about 7 dB. A signal is barely distinguishable at the location designated by ''S'' (i.e., $S+N'$). Figure 3(b) is for an array of about twice the directivity index (4.6 dB). In this case, the average FE gain is approximately 7 dB. Figure 3(c) is for another doubling of the DI (7.6 dB). The average FE gain is still about 7 dB. The final plot, Fig. 3(d), is for another doubling of the DI (10.6 dB), and the average FE gain is again about 7 dB. The increase in the DI with the progression in the plots (three factors of 2, or 9 dB) is obvious from the corresponding enhanced resolution in the top curves (AVGPR) of each plot. In all, this figure presents results to support the notion that the FE gain is independent of the DI gain. The DI varied over a range of 12 dB, and yet the average FE gain remained approximately 7 dB. Other tests of a similar nature have been conducted, and the results have been nearly identical; the FE gain was independent of the DI gain.

C. Independence of FE gain from both BW and DI gains

Figures 2 and 3 illustrate the independence of the FE gain from the BW and DI gains, respectively, by keeping the FE gains approximately constant while the other two gains are varied over factors of 16 (12 dB) and 8 (9 dB), respectively. In those cases, the FE gains, within a reasonable degree of scatter, were about 7–8 dB. Figure 4 presents results obtained from data measured by a sonobuoy during sea state

TABLE I. Comparisons of various statistics for typical time histories of narrow-band noise in an FFT bin (N) and signal plus noise ($S+N'$). The number of averages is 400. The time histories for the FFT sizes of 1024 and 16384 are included in Fig. 2.

FFT size	Bin width (Hz)	Overlap %	Bin type	AVGPR (dB)	WISPR (dB)	DELTA (dB)	SNR gain (dB)
1024	0.2	55	N	32.6	23.4	9.2	8.2
			$S+N'$	44.1	43.1	1.0	
2048	0.1	78	N	32.3	24.5	7.9	7.3
			$S+N'$	46.9	46.4	0.6	
4096	0.05	89	N	31.1	21.1	9.9	9.6
			$S+N'$	49.9	49.5	0.3	
8192	0.025	95	N	31.4	25.7	5.7	5.5
			$S+N'$	52.8	52.6	0.2	
16 384	0.012	97	N	31.7	20.5	11.2	11.0
			$S+N'$	55.8	55.6	0.2	

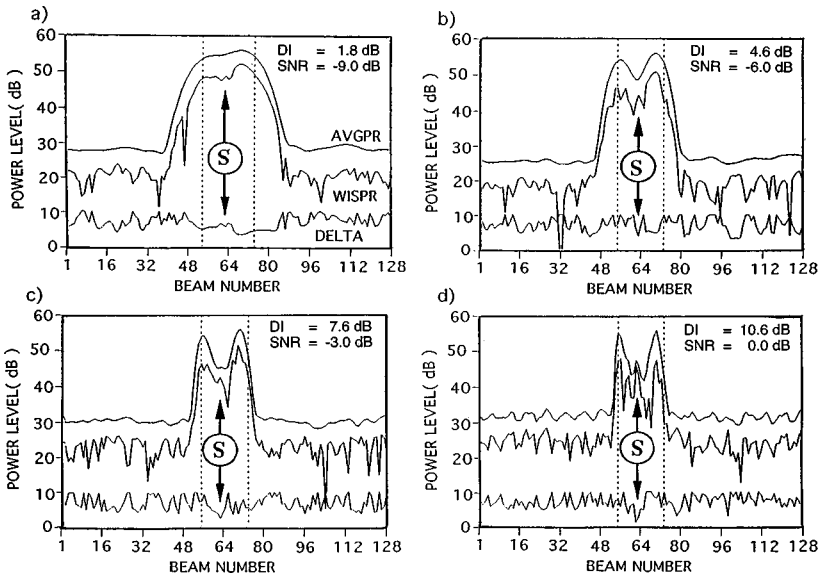

FIG. 3. Spatial resolution of the AVGPR processor (top curves), the WISPR filter (middle curves), and the difference between the two (DELTA, bottom curves) for four aperture sizes that decrease by a factor of 2 from top left to bottom right. The directivity index (DI) and SNR are included in each plot. The location of a submerged source signal is identified by ''S.''

3 to illustrate the case when the BW and DI gains are held constant, while the FE gains are varied. The relevant processing parameters for the FE gain are the number of spectrum-analyzed data points being processed by the WISPR filter or, correspondingly, the number of averages, n, in Eqs. (1) and (2) and the percentage of overlap of the time domain data prior to spectral analysis, e.g., percent of overlap of consecutive FFTs. Whereas, for DI and BW gains, the relevant parameters are the aperture length in wavelengths (or correspondingly the number of sensors) and the frequency bin width (or size of the time domain FFT). The values for noise suppression (DELTA for noise) have been averaged over 361 adjacent bins in frequency to increase the statistical significance of the results. The results in Fig. 4 are for a BW of 1 Hz and an aperture size of 0 (one sensor only). However, nearly identical results have been obtained for similar overlaps and averages when the aperture sizes ranged up to 99 wavelengths (198 sensors at half-wavelength spacing), and the BW changed from 0.012 to 4.6 Hz.

The family of curves in Fig. 4 shows that the noise suppression [Eq. (6)] ranges from 0 to 11 dB as n ranges from 1 to 2000 at 0% overlap, while it varies from 1.25 to 6 dB as the overlap ranges from 99% to 0% at $n=10$. These noise suppression levels are comparable to the SNR gains that have been achieved for reasonably stable signals (bins of $S+N'$). These results indicate that by overlapping 99% and an average of 101 overlapped FFTs, 5-dB noise suppression can be achieved with only the amount of original time domain data that it takes to form two contiguous FFTs. On the other hand, by averaging two contiguous FFTs, an incoherent gain of only 1.5 dB (5 log 2 for incoherent averaging to suppress noise only) can be achieved. Hence, there is about a 3-dB advantage for WISPR processing in this case. The advantage increases as the number of averages increases and the percentage of overlap decreases. This can be an important source of gain for small data samples.

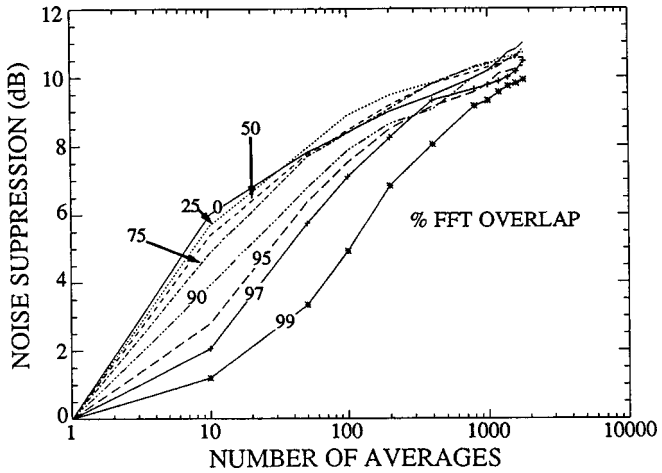

FIG. 4. The WISPR filter noise suppression versus number of averages for percentages of overlap in the consecutive FFTs ranging from 0% to 99%.

D. Functional form of FE gain

An equation for the noise suppression part of FE gain [the upper bound for the FE gain, Eq. (6)], can be determined from a least squares fit to the family of curves in Fig. 4. The resulting equation (in decibels) is

$$\mathrm{FE}_{\mathrm{noise}}=6[\log(n)]^{1/2}\left\{1-\frac{\%\,\mathrm{overlap}}{100}\right\}+1.03[\log(n)]^{2}\left\{\frac{\%\,\mathrm{overlap}}{100}\right\}^{8}, \tag{9}$$

where $n=$the numerical size of the WISPR sum and % overlap=the percentage of overlap in successive FFTs.

The signal plus noise ($S+N'$) suppression [Eq. (5)] is required to completely quantify the WISPR SNR gain (or FE gain). However, it can be ignored if one is only interested in the upper bound to the SNR gain, which is dominated by the noise suppression part for low fluctuation amplitude signals (and noise).

E. Enhanced SNR

Figure 5 illustrates the SNR enhancement of the WISPR filter compared to the AVGPR processor. The x axis is beam number, and the y axis is relative level. There are three

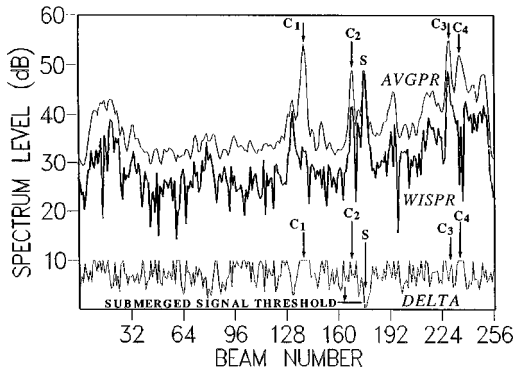

FIG. 5. Beamformer output levels versus beam number for the conventional power average, AVGPR (top), the WISPR (middle), and the DELTA (bottom) curves. An amplitude stable signal (S) is located at beam number 176. Ship clutter signals are denoted $C_1, C_2 \cdots$.

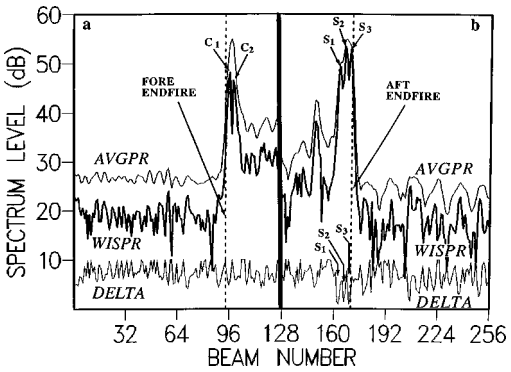

FIG. 6. Horizontal towed array beamformer output levels versus beam number for the conventional power average, AVGPR (top), the WISPR (middle), and the DELTA curves (bottom). Left and right halves of plot are for different data. Results show increased resolution for the WISPR filter especially (a) near the forward endfire beams (numbers 96–100) where there are two clutter source signals (C_1 and C_2) and (b) near aft endfire (numbers 161–167) where there are three submerged source signals (S_1, S_2, and S_3).

curves in this plot. The top curve is due to the AVGPR processor (AVGPR) and the middle one is the corresponding WISPR filter (WISPR) result. The bottom curve is the submerged source curve (DELTA) and will not be discussed until the next subsection. The results in Fig. 5 are for a BW of 0.1 Hz, for an n of 60 contiguous FFTs, and a towed horizontal line array with an aperture of 60 wavelengths. There are many clutter signals present in the results of both processors, some with large SNR relative to the base background noise and some with small SNR. However, there is only one signal that is relatively stable from a distant projector that was located deep within the Sofar channel about 200 miles from the array. The array was also within the Sofar channel over the Blake Plateau in the North Atlantic Ocean. That submerged projector signal, designated ''S,'' was received on beam number 176. It has a SNR of approximately 8 dB in the AVGPR results. However, the SNR of the same signal is 15 dB in the WISPR filter results. Hence, the increase in SNR of that relatively stable signal, due to the WISPR filter, compared to the results of the AVGPR processor is 7 dB. Furthermore, some of the other clutter signals were suppressed by the WISPR filter even more than the amount by which the stable signal's SNR was enhanced, e.g., 21 dB for the signal at beam 138 (C_1), and 14 dB for the signal at beam 236 (C_4). Finally, it is interesting to note that, in the AVGPR result, the submerged source signal is not the largest signal, but it is in the WISPR result. However, this is not the most important result of the WISPR processing. The most important result is that the signal was not significantly suppressed in the WISPR processing.

F. Submerged source identification

The bottom curve in Fig. 5 is a result of plotting (in decibels) the ratio of the outputs of the AVGPR processor and the WISPR filter [Eq. (7)]. When that ratio is less than or equal to 1.41 (1.5 dB in the plot), the existence of a signal (plus noise) with a low fluctuation amplitude is indicated. The implication is that for the power of the signal plus the noise in the frequency bin to be relatively stable in amplitude, the source must have been at a depth sufficiently deep to minimize the opportunities for the fluctuation generation mechanisms near the sea surface to cause the signal plus noise to fluctuate. In the case of the results in Fig. 5, there are many clutter signals from surface ships (e.g., designated $C_1, C_2, \ldots$); some have large SNR, and some have small SNR. However, there is only one signal from a submerged projector, designated by ''S'' (beam 176) for which the DELTA curve is less than the 1.5-dB detection threshold [Eq. (8)]. Without a DELTA value such as that, the signal from the submerged source would be indistinguishable from the other highly fluctuating clutter signals from sources near the sea surface (i.e., shipping tonal clutter). Hence, Eq. (8) and the resulting DELTA curve [Eq. (7)] can be important for characterizing the fluctuation content of signals and noise and for identifying signals (plus noise) from submerged sources with small fluctuation amplitudes.

G. Enhanced resolution

Figure 6 contains two halves of beam noise plots with AVGPR, WISPR, and DELTA results in a format that is similar to Fig. 5. The relevant half of each plot has been kept to illustrate the same point of enhanced resolution for fluctuating signals from a surface ship, Fig. 6(a), and low fluctuation amplitude signals from a submerged projector, Fig. 6(b). Both of these figures are good examples of the enhanced resolution that is provided by the WISPR filter, when compared to the AVGPR processor as the standard.

Figure 6(b) contains a signal (plus noise) that is relatively stable in amplitude on the aft endfire beam of these output results from a towed horizontal line array spatial FFT beam former. There is evidence in the AVGPR results that a signal appears as two separate arrivals near beam number 168, one much higher in level than the other and covering more beams. However, those two arrivals are separated into three distinct arrivals with relatively little suppression in the WISPR results, at least at the signal peaks in the arrival structure. The small amount of suppression in those three arrivals in the DELTA curve indicates that they are low fluctuation amplitude signals from a submerged source. Furthermore, all of the other signals and noise have been attenuated by the WISPR filter from about 5 to 20 dB.

The results in Fig. 6(a) are for a nearly identical case as in Fig. 6(b) except the single signal response in beams 95–100 of the AVGPR processor has been divided into two distinct arrival peaks by the WISPR filter, and the signal has been significantly suppressed in the DELTA curve rather than preserved as the stable signal (plus noise) was in Fig. 6(b).

The reason that the signal in Fig. 6(a) was not preserved by the WISPR filter is because it was not a low fluctuation amplitude signal from a submerged projector. It was a clutter signal with high amplitude fluctuations from a ship at an unknown distance from the array along the forward endfire direction. The reason that the signals were separated into two or three separate arrivals in Fig. 6(a) and (b), respectively, is because those were the number of vertical arrival angles that correspond to the vertical multipaths of the signals at the array. There were three separate vertical arrival angles of the signal from the distant projector [Fig. 6(b)] and two from the ship [Fig. 6(a)]. Sometimes it is easy to forget that the beam former forms steering angles relative to the axis of the line array. Near broadside to the array, those angles correspond nicely to angles in the horizontal plane, and near endfire they correspond nicely to angles in the vertical plane and not to angles in the horizontal plane. Nevertheless, it is clear that the spatial resolutions of the two signals have been increased sufficiently by the WISPR filter to identify the separate arrivals, while they were not separated by the AVGPR processor. Furthermore, when the two WISPR filter results in Fig. 6(a) and (b) are compared, it is evident that both have improved resolution, but only the signal in Fig. 6(b) has the additional SNR gain enhancement associated with a low fluctuation amplitude signal from a submerged projector.

The enhanced resolution that was achieved in these two signal cases, one with high fluctuation amplitudes and the other with low fluctuation amplitudes, is due to the mutual interference of the phases of the different multipaths on the beams between the ''stable'' main arrivals (or on the edges of their response patterns). The resolution is improved by increasing the beam pattern overlap, thus maximizing the opportunities for mutual signal or clutter interference and accompanying high amplitude fluctuations. The net result is a discrimination capability that is enhanced well beyond the actual reduction in the width of the beam response pattern caused by the fluctuation processor. The ''effective width'' is determined by the fluctuation-based processor's ability to discriminate between the fluctuations due to two or more closely separated sources. It is clear that the effective beam width achieved is well below half the beam width of that for the AVGPR processor in both cases of vertical multipath arrivals from the endfire direction of the horizontal line array, two in one case [Fig. 6(a), beams 95–100] and three in the other [Fig. 6(b), beams 163–170]. Similar results could be expected for signals near broadside with close azimuthal (or horizontal) spacing.

Figure 7(a) and (b) illustrate a case of enhanced resolution that is similar to that in Fig. 6, except it is for the spectral domain. Figure 7(a) presents a segment of a frequency spectrum from measured data for frequency bins 300–330. The top curve is the AVGPR processor result, and

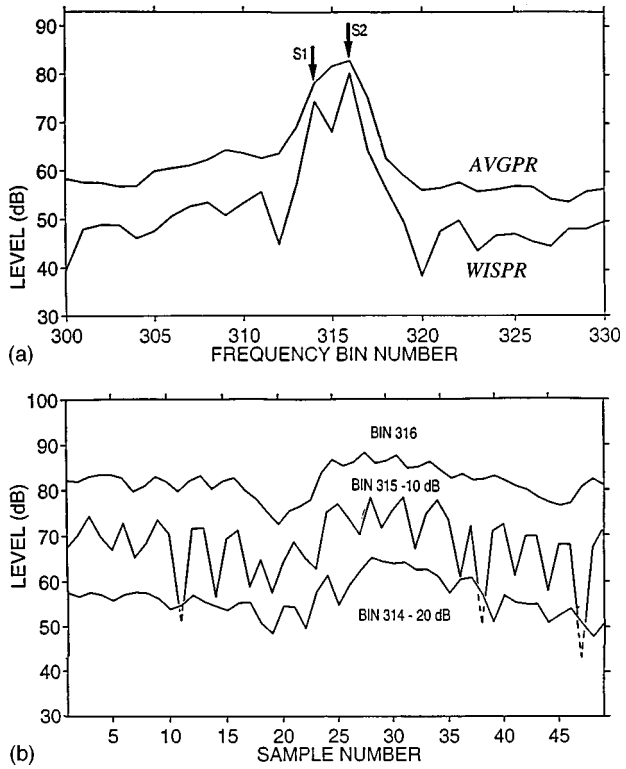

FIG. 7. Illustration of (a) two signals S1 and S2 being separated by the WISPR filter (bottom curve) but not by the AVGPR processor (top curve) and (b) the acoustic power time histories for frequency bins 314 (S1), 315, and 316 (S2). Curves for bins 315 and 314 have been displaced downward for clarity by 10 and 20 dB, respectively.

the bottom curve is the corresponding WISPR filter result. There are two signals from a single source in these results, designated S1 and S2, at frequency bin numbers 314 and 316, respectively. The AVGPR curve shows only a single maximum at bin number 316. There is no evidence in this curve to suggest that there is more than one signal present. In other words, only signal S2 could be considered detected by the AVGPR processor. However, there are two local maxima in the WISPR curve at bin numbers 314 and 316. Hence, both S1 and S2 can be considered detected by the WISPR filter.

The reason that the WISPR filter successfully separates and detects the two closely spaced signals in Fig. 7(a) is illustrated by Fig. 7(b). The same principles apply to the spatial resolution results in Fig. 6. Figure 7(b) presents the power level time histories for frequency bin numbers 314 (bottom), 315 (middle), and 316 (top). The time histories for bins 314 and 316 are similar in nature, but not exactly the same, as would be expected from the same source and for only a small difference in the frequency. The three curves have been vertically separated on the plot for visual clarity. Their AVGPR and WISPR levels are the values plotted at the corresponding bin numbers in Fig. 7(a). The time history for bin number 315 is radically different from the other two, although the general trends are similar. The curve for bin 315 has an oscillatory nature (i.e., large fluctuations) that is a result of reinforcement and cancellation of the acoustic pressures due to the two signals contributing to bin 315, but not always being in phase. Hence, cancellation and reinforce-

ment takes place to spread the levels. The low values do not appreciably affect the AVGPR calculation, but they substantially suppress the WISPR filter value, which accounts for the local minimum at bin 315 that separates S1 and S2. That interference behavior permits the two signals to be separated by the WISPR filter, but not by the AVGPR processor. Two signals will continue to be separated by the WISPR filter as they get closer until they are both in the same frequency bin. At that point, they will appear as one signal to both processors.

H. Enhanced minimum detectable level

An enhancement in minimum detectable level (MDL) has been observed for the WISPR filter. However, a systematic and comprehensive study of the MDL of the WISPR filter has not yet been done. Plans to acquire the necessary MDL data are currently being carried out. However, many examples of low-level signal detections made possible by the WISPR filter that were not detected by the AVGPR processor suggest that the MDL for the WISPR filter is several decibels below that of the AVGPR processor. For example, the results in Fig. 3 for four different array aperture lengths provide evidence that the WISPR filter has a lower MDL than the AVGPR processor. The data in Fig. 3(d) for the array with the 10.6 dB DI indicate that the SNR is approximately 0 dB (equal signal and noise will give a local maximum of 10 log 2, or 3 dB). That being the case, it is a simple matter to estimate the SNR of the other three results by reducing the SNR by 3 dB each time that the DI is reduced by a factor of 2, which gives SNRs of -3, -6, and -9 dB for Fig. 3(c), (b), and (a), respectively. Then, using the results in Fig. 3 as a visual metric, one can estimate at what SNR is it possible to begin to detect the presence of the signal, S. Its presence is obvious in the results of the AVGPR and WISPR curves in Fig. 3(d), and it is also distinguishable in the DELTA curve as a signal from a submerged source (DELTA$\leqslant$1.5 dB). However, as the DI and the SNR decrease, the signal is questionably detectable in the AVGPR curve at a SNR of -3 dB [Fig. 3(c)]. At the same time it is easily detected in the WISPR curve, although it does not pass the test for being a signal from a submerged source. However, that designation is determined by whether the signal crosses the 1.5-dB threshold. For low SNR signals, a different threshold could be established. Such a modification of the threshold has not been done. The signal is not detectable in the AVGPR curves at SNR's of -6 dB [Fig. 3(b)] and -9 dB [Fig. 3(a)], while it is detectable in the WISPR curves. In the case of -9-dB SNR, the local maximum due to the source is only about 1.5 dB, but it is still more detectable than the ''questionable'' local maximum in the AVGPR curve for the -3-dB SNR case [Fig. 3(c)]. These results indicate that the MDL of the WISPR filter is lower than that for the AVGPR processor, but not how much lower it is. That issue needs to be addressed systematically. However, these results suggest that the MDL of the WISPR filter is at least 6 dB lower than for the AVGPR processor.

The reason that the WISPR filter has a lower MDL than the AVGPR processor is that in the summations for the AVGPR and WISPR processors, Eqs. (1) and (2), respectively, the average [Eq. (1)] is biased upward toward the higher values in the sequence, while the average of the reciprocals [Eq. (2)] is biased downward toward the lower values. Hence, high values are more detectable by the AVGPR processor and low values are more detectable by the WISPR filter. The amount by which the WISPR filter is able to depress the MDL is not sufficiently well understood to provide firm quantitative results. However, the broad range of data that has been processed suggests that the WISPR filter depresses the MDL in excess of 6 dB.

I. Essence of WISPR filter

Previous discussions identified and illustrated various characteristics of the WISPR filter as applied to passive undersea sonar data. The enhancements achieved suggest that the WISPR filter could be an attractive alternative or augmentation to the AVGPR processor for some applications. The results in Fig. 8 illustrate one practical application of the WISPR processor.

Figure 8 presents the results of a detection experiment that was conducted in a deep water region of moderate shipping traffic. The objective of the experiment was to detect a signal from a deep projector among the background noise and interfering clutter from the shipping traffic. The task was an unusually challenging one because the signal had a relatively low level and there was no *a priori* knowledge of the signals' frequency or spatial orientation relative to the measurement array, a towed horizontal line array.

The first thing done in the detection chain to detect the signal among the clutter and noise was time histories of spectrum-analyzed (FFT output) power values for each frequency bin-beam number cell were calculated (e.g., for an n of 125, a BW of 0.1 Hz, and the FFTs overlapped 90%). Next, corresponding values for AVGPR [Eq. (1)], WISPR [Eq. (2)], and DELTA [Eq. (7)] were calculated for each frequency bin-beam number cell. The results formed three surfaces in frequency bin-beam number space corresponding to the AVGPR, WISPR, and DELTA results. The AVGPR surface is plotted in Fig. 8(a). The DELTA surface (not shown) was then thresholded at 1.41 (or 1.5 dB), and the result is plotted as the surface in Fig. 7(b). Visual observation of that surface, or automatic interrogation by the computer, identifies the location of the signal from the submerged source at the coordinates of 15 Hz and beam 101. That was the actual detection stage of the process, and it was, for all practical purposes, an unalerted detection.

Given the coordinates of the detected signal, a cut across beam number at 15 Hz and across frequency at beam number 101 can be made to investigate in greater detail the signal and noise performance of the two WISPR processors (WISPR and DELTA). Those results are presented in Fig. 8(c) and (d). A visual evaluation of those two plots in conjunction with the previous two [Fig. 8(a) and (b)] in Fig. 8 indicates that the gains that have been achieved by the WISPR processors (WISPR and DELTA) include the following:

(i) SNR increase (about 12 dB near the signal),
(ii) clutter/noise reduction [DELTA in Fig. 8(c) and (d), about 8 dB],

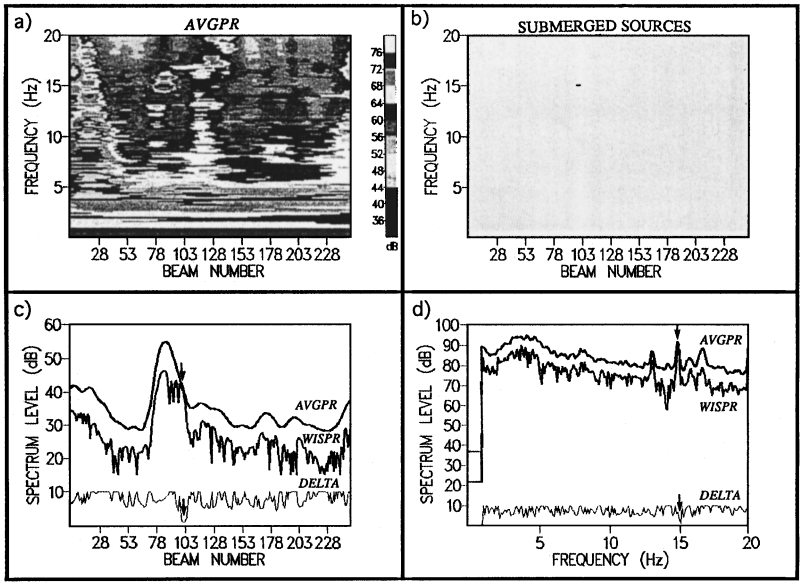

FIG. 8. The WISPR filter processing products: frequency versus beam number surfaces for (a) AVGPR and (b) signals from submerged sources (DELTA, black dot at 15 Hz and beam 101), and plots of level versus (c) beam number (at 15 Hz) and (d) frequency (for beam 101) with curves for AVGPR, WISPR, and DELTA. The presence of the submerged source signal in plots (c) and (d) is indicated by arrows.

(iii) clutter elimination [submerged source signal only in Fig. 8(b)],
(iv) unalerted detection and submerged source identification [DELTA in Fig. 8(c) and (d), and dot in Fig. 8(b)],
(v) enhanced spatial and spectral resolution [WISPR in Fig. 8(c) and (d)],
(vi) enhanced bearing determination [WISPR combined with DELTA in Fig. 8(c)],
(vii) enhanced MDL [WISPR in Fig. 8(c)].

The achievement of each of these various enhancements contributed to the accomplishment of a task that was an extremely difficult one for the unalerted conventional processor (AVGPR), especially considering that neither the frequency nor the beam number (i.e., bearing) of the source was known in advance. However, detection and identification (i.e., submerged/not submerged) was a simple matter for the WISPR processors, which simultaneously provided other gains and processor enhancements.

IV. SUMMARY AND OBSERVATIONS

Some of the major sources of fluctuations were identified. The WISPR filter and a derivative of it called DELTA were introduced, and their abilities to suppress fluctuating quantities were demonstrated. A particularly important aspect of that suppression is that a SNR enhancement is achieved when the fluctuation amplitudes of the clutter noise are greater than those of the signal plus noise, which is often the case for signals from submerged sources. Examples were shown and results were presented in which the SNR gain enhancements were well in excess of 8 dB. Other processor enhancements were demonstrated such as improved spatial resolution, lower MDL, clutter reduction, and unalerted (and automatic) detection of signals from submerged sources (i.e., clutter elimination). Furthermore, the fluctuation exploitation (FE) gains were shown to be independent of the BW and the aperture size of an array (DI). Finally, the relevant signal processing parameters for optimizing the WISPR filter gain were shown to be the number of averages (gain increases with increasing averages) and the percentage of FFT overlap in the time domain (gain increases with decreasing overlap), and a functional form for the noise suppression part of the FE gain (normally the major part for low fluctuation amplitude signals from submerged sources) was presented.

When one considers the broad range of gains that the WISPR filter achieves, compared to the conventional average power processor, it is evident that to quantify only the improvement in a single quantity such as SNR enhancement is an over simplification. Some of the enhancements achieved are in characteristics in which it does not make much sense to compare them with the average power processor such as clutter reduction and unalerted detection.

ACKNOWLEDGMENTS

This work was conducted as part of the WISPR Filter Development and Evaluation Project funded under program element number 602314N by Tommy Goldsberry of the Office Naval Research, Code 321. For that support, the author is grateful. Appreciation is also expressed to fellow workers who helped in various ways, with special thanks to Dr. Joel Newcomb, Dr. Jacob George, Jackson Mobbs, Stephanie Kooney, and Edward J. Yoerger. A special thanks is expressed to Laura Hart and her technical staff at Alliant Techsystems in San Diego, CA, for programing and data processing support. Finally, appreciation is expressed for the valuable comments and suggestions of the journal's reviewers which improved the presentation and the clarity of the material presented in this paper.

[1] G. C. Gaunaurd, ''Categorized Bibliography of the Topics of Underwater Sound Transmission Fluctuations,'' Naval Ordinance Laboratory Report NOLTR 73-176 (1973).
[2] L. Fortuin, ''Survey of literature on reflection and scattering of sound waves at the sea surface,'' J. Acoust. Soc. Am. **47**, 1209–1228 (1070).
[3] C. W. Horton, Sr., ''A review of reverberation, scattering, and echo structure,'' J. Acoust. Soc. Am. **51**, 1049–1061 (1972).
[4] C. A. Fisher, ''A Bibliography, with Abstracts and Annotations, of Publications on the Related to Underwater Acoustic Fluctuations,'' Naval Research Laboratory Report NRL/MR/7176-94-7563, 1995.

[5] R. J. Urick, ''Models of the amplitude fluctuations of narrow-band signals in the sea,'' J. Acoust. Soc. Am. **62**, 878–887 (1977).
[6] R. J. Urick, *Principles of Underwater Sound for Engineers* (McGraw–Hill, New York, 1983), 3rd ed.
[7] A. A. Simanin, ''Possibility of classifying water and surface rays by amplitude fluctuations of the received signal,'' Sov. Phys. Acoust. **36**, 622–624 (1990).
[8] T. E. Ewart, ''A numerical simulation of the effects of oceanic finestructure on acoustic transmission,'' J. Acoust. Soc. Am. **67**, 496–503 (1980).
[9] S. M. Flatte, R. Leung, and S. Y. Lee, ''Frequency spectra of acoustic fluctuations caused by oceanic internal waves and other finestructure,'' J. Acoust. Soc. Am. **68**, 1773–1779 (1980).
[10] D. E. Weston and H. W. Andrews, ''Acoustic fluctuations due to shallow-water internal waves,'' J. Sound Vib. **31**, 357–367 (1973).
[11] F. Dyson, W. Munk, and B. Zetler, ''Interpretation of multipath scintillation's Eleuthera to Bermuda in terms of internal waves and tides,'' J. Acoust. Soc. Am. **59**, 235–247 (1976).
[12] D. Di Iorio and D. M. Farmer, ''Path-averaged turbulent dissipation measurements using high-frequency acoustic scintillation analysis,'' J. Acoust. Soc. Am. **96**, 1056–1069 (1994).
[13] C. S. Clay, Y.-Y. Wang, and E.-C. Shang, ''Sound field fluctuations in a shallow water wave guide,'' J. Acoust. Soc. Am. **77**, 424–428 (1985).
[14] H. A. De Ferrari, ''Time-varying multipath interference of broad-band signals over a 7-nmi range in the Florida Straits,'' J. Acoust. Soc. Am. **53**, 162–180 (1973).
[15] I. Dyer, ''Statistics of sound propagation in the ocean,'' J. Acoust. Soc. Am. **48**, 337–345 (1970).
[16] R. H. Nichols and H. J. Young, ''Fluctuations in low-frequency acoustic propagation in the ocean,'' J. Acoust. Soc. Am. **43**, 716–722 (1968).
[17] J. A. Scrimger, ''Signal amplitude and phase fluctuations induced by surface waves in ducted sound propagation,'' J. Acoust. Soc. Am. **33**, 239–247 (1961).
[18] R. A. Wagstaff and J. L. Berrou, ''Is power averaging the best estimator for acoustic data?,'' SACLANT Undersea Research Centre, Report CP-32 Part 2, pp. 17-1 to 17-16, June 1982.

Comparison between intensity and pressure as measures of sound level in the ear canal

Stephen T. Neely[a] and Michael P. Gorga
Boys Town National Research Hospital, 555 North 30 Street, Omaha, Nebraska 68131

(Received 12 March 1998; accepted for publication 28 July 1998)

In-the-ear calibration of sound pressure level may be problematic at frequencies above 2 kHz, because the pressure can vary significantly along the length of the ear canal, due to reflection of sound waves at the eardrum. This issue has been investigated by measuring behavioral thresholds to tones in a group of human subjects ($N=61$) for two different insertion depths of an insert earphone. The change in insertion depth was intended to alter the distribution of pressure in the ear canal, shifting the frequency at which spectral notches occur. The inset earphone or ''probe'' (Etymotic ER-10C) also contained a calibrated microphone, allowing the recording of sound pressure levels in the ear canal. Prior to the threshold measurements in each subject, the Thevenin acoustic source characteristics of the probe were determined by a special calibration procedure. This calibration allowed the expression of the sound level at threshold in terms of acoustic intensity (W/m^2). The impact of changes in insertion depth was determined by measuring behavioral threshold at each depth. Because cochlear sensitivity remained constant, the level of sound entering the ear at threshold should have been the same (within measurement error) for both insertions. The difference in sound pressure level (SPL) at threshold between the two probe insertions was greatest at the notch frequency of the first insertion. At this notch frequency, the SPL at threshold increased by an average of 11.4 dB. The change in sound intensity level (SIL) at threshold was almost always less than the change in SPL. At the notch frequency, the SIL decreased, on average, by only 0.5 dB. These results suggest that SIL may be a better indicator than SPL of the sound level entering the ear, especially for frequencies in the 4–8 kHz range. [S0001-4966(98)03011-2]

PACS numbers: 43.64.Ha, 43.64.Jb, 43.64.Yp [BLM]

INTRODUCTION

In-the-ear sound pressure calibration has become increasingly popular in recent years due to the availability of high quality, calibrated probe microphones (e.g., Etymotic ER-7C and ER-10C). It is generally agreed that the pressure at the eardrum is a better measure of the stimulus than the pressure at the earphone (e.g., Siegel, 1994). However, due to the difficulty of measuring sound pressure at the eardrum, the pressure at the earphone is often used to calibrate stimuli. For example, most commercial distortion-product otoacoustic emission (DPOAE) systems rely on pressure at the earphone for stimulus calibration.

The accuracy with which pressure measurements at the earphone estimate the pressure at the eardrum is frequency dependent (Siegel, 1994; Siegel and Hirohata, 1994). For frequencies below about 2 kHz, pressure throughout the ear canal is more nearly uniform, because the quarter wavelength of the signal is large compared with the dimensions of the ear canal. This situation does not exist at higher frequencies, where standing waves can result in a partial cancellation of the sound pressure seen at the microphone. As a result, the pressure seen at the measurement microphone could potentially underestimate the pressure at the eardrum for these higher frequencies. Obviously, the dimensions of the ear canal also influence the accuracy of these measurements. All other things being equal, the upper frequency limit for which pressure measurements at the plane of the probe indicate pressure at the eardrum will decrease as the length of the ear canal increases.

An alternative measure of stimulus level is acoustic *intensity*, defined as the acoustic power per unit area (e.g., W/m^2). Intensity at the earphone will be a good indicator of the intensity at the eardrum whenever ear canal losses are small (Keefe *et al.*, 1993). It is expected that specifying the stimulus level in terms of acoustic power avoids the problem of standing wave notches (e.g., Marlan *et al.*, 1994). However, power measurements require more information about the acoustic load than pressure measurements. Microphones directly measure acoustic *pressure*. To convert a pressure measurement into a power or intensity value, the *conductance* of the acoustic load must also be determined. One way to estimate the conductance of the load is to first calibrate the acoustic source characteristics of the probe (Møller, 1960; Rabinowitz, 1981; Allen, 1986; Keefe *et al.* 1992).

The probe can be characterized by its Thevenin-equivalent source pressure and source impedance (Allen, 1986). These source parameters can be estimated by a special calibration procedure which uses a set of acoustic cavities to provide known acoustic loads (Allen, 1986). Once the source parameters are known, the probe can be used to measure the conductance of any given acoustic load.

The study described in this paper investigates two related questions: (1) How well do sound pressure measure-

[a]Electronic mail: neely@boystown.org.

ments in the ear canal describe the level of sound that enters the ear? and (2) Do sound intensity measurements provide a better (i.e., more reliable) description of stimulus level than sound pressure measurements? To investigate these questions, we used behavioral threshold to maintain a nearly constant level of sound entering the ear and manipulated the distribution of pressure in the ear canal by varying the insertion depth of an insert earphone and microphone (probe). Since it is assumed that behavioral thresholds do not vary (at least within a test session), any variances in behavioral threshold must reflect inaccuracy in the calibration procedure. By calibrating in both SPL and SIL, we can compare the relative accuracy of pressure and intensity measurements over a wide range of frequencies.

I. METHODS

A. Probe

An ER-10C probe microphone (Etymotic Research) was used to deliver stimuli and to measure sound pressure level in the ear canal. This microphone is well suited for making pressure measurements because it has a nearly constant sensitivity of about 0.05 V/Pa, over a wide range of frequencies. This means that at the output of the preamp, a measurement expressed in terms of dB *re*: μV can be interpreted as a measurement of dB SPL (*re*: 20 μPa).

The Thevenin acoustic source characteristics were estimated (using locally developed software) for the ER-10C probe by a method similar to the one described by Allen (1986). [See also Keefe *et al.* (1992) and Voss and Allen (1994).] Five brass tubes (11/32 in. o.d., 8 mm i.d.) of varying lengths (21, 24, 28, 34, and 42 mm) were closed at one end and mounted vertically for use as acoustic cavities by gluing one end of each tube to a single brass plate.

In order to attach the ER-10C probe to the open ends of the calibration tubes, a simple coupler was made by gluing a short (20 mm) section of the same diameter tube inside a slightly longer (30 mm) section of the next larger diameter tube (3/8 in. o.d.). The foam eartip of the ER-10C probe was compressed and inserted into the smaller end of the coupler. The larger end of the coupler was seated on top of the open end of the acoustic cavity providing a good acoustic seal between the probe and the cavity. The coupler effectively extended the tube length by about 3 mm.

The pressure response of each of the five cavities to a wide-band chirp stimulus was measured by the ER-10C microphone. The stimulus was generated and the response recorded digitally by a Turtle Beach ''Tahiti'' soundcard at a sample rate of 44.1 kHz. Although the ER-10C probe contains two receivers (loudspeakers), only one receiver was used in this study. The chirp stimulus delivered to the receiver was 112-mV peak-to-peak (40-mV rms) with a flat spectrum from 0 to 20 kHz. Synchronous averaging of repeated stimuli was used to reduce noise in the calibration measurement. The total averaging time was about 37 s per chirp-response measurement (corresponding to 80 repetitions of a 46.4-ms chirp).

Because the probe calibration is sensitive to temperature, the acoustic cavities were maintained at a temperature between 34 and 40 °C (monitored by an oral thermometer inserted into the tallest tube). This was intended to warm the *probe* to approximately the same temperature during calibration as when it was inserted into a human ear canal. As a result, the speed of sound in the interior air spaces of the probe should have been about the same during probe calibration as when the probe was inserted into an ear canal.

The acoustic impedance of each cavity was computed by a formula derived by Keefe (1984). This formula requires that the length, diameter, and temperature of the tubes be known. The length of the acoustic cavities (including the coupler) could not be determined with sufficient accuracy by direct measurement, so an initial estimate of this length, based on the frequency of the first prominent spectral peak, was subsequently improved by numerical iteration. The procedure used an overspecified set of five linear equations, based on both the measured cavity pressures and the calculated cavity impedances, to generate an error term, and sought to minimize the error by adjusting the estimated tube lengths iteratively (Allen, 1986). The Thevenin source impedance and pressure for the ER-10C probe was determined by this procedure.

Acoustic intensity is, in general, a vector quantity equal to the product of fluid velocity and pressure. In this paper, we consider only the direction normal to the plane of the probe and treat intensity as a scalar quantity. For a particular frequency component, intensity can be computed as

$$I(f)=\tfrac{1}{2}\mathrm{Re}[v(f)^{*}\cdot p(f)],$$

where $v(f)$ and $p(f)$are, respectively, the complex Fourier components of velocity and pressure at that frequency. (Re[] extracts the real part of a complex number, and the * denotes a complex conjugate.) *Specific* acoustic impedance (or unit area acoustic impedance) is defined as the ratio of the pressure and velocity

$$Z_s(f)=\frac{p(f)}{v(f)}$$

(Pierce, 1981). If the specific impedance is known, then intensity can be computed as

$$I(f)=G_s(f)\cdot p_{\mathrm{rms}}^2(f),$$

where $p_{\mathrm{rms}}(f)$is the rms pressure and $G_s(f)=\mathrm{Re}[Z_s^{-1}(f)]$ is the specific conductance. The specific impedance of air (at 37 °C) is $\rho c=401$ Pa s/m (Keefe, 1984).

The characteristic impedance of the brass tubes used for probe calibration is $Z_0=\rho c/A_0=8.0\times10^6$ Pa s/m^3 (=80 cgs acoustic ohms) where $A_0=5.0\times10^{-5}$ m^2 is the cross-sectional area of each tube. The source impedance of the probe Z_{prb} and the load impedance of the ear canal Z_{ec}, which are derived from the calibration procedure, have the same units as Z_0. For simplicity, the source and load impedances are normalized by Z_0 when they are presented in Sec. II.

Because the foam eartip was changed for each subject, the probe calibration was repeated for each subject either immediately before or immediately after behavioral threshold measurements were made. The entire probe calibration procedure was completed in about 5–10 min.

B. Subjects

Subjects were seated in a comfortable chair in a sound-attenuating booth. The ER-10C probe (with the same foam eartip that was used for probe calibration) was inserted into the subject's ear canal. Special effort was made to obtain an initial insertion as deep as possible. A pressure response was measured in the ear canal using the same wide-band chrip stimulus. The ear canal (load) pressure, together with the previously determined source pressure and impedance, provided enough information to calculate the specific conductance of the ear canal. The *notch frequency* was identified by a peak in the conductance curve in the 1–8 kHz range. Conductance was used to determine the notch frequency instead of pressure because the conductance maximum was easier to locate. The notch occurs in the pressure magnitude (versus frequency) curve because reflected sound from the eardrum arrives back at the probe with a 180 degrees phase shift at this frequency and tends to cancel the forward-going sound being emitted by the probe. This sound-wave cancellation is also responsible for the observed peak in the conductance curve.

Following the measurements of the ear canal pressure response, behavioral threshold measurements were made. The subjects were asked to press a response button each time they heard a tone. The tones were presented 100 times at each of 12 frequencies. The tone was initially presented at 40 dB SPL, decreased in level on the next trial by 5 dB if the subject indicated that the tone was heard, and increased by 5 dB if the subject did not respond. The 1-s interval between tones was extended if the subject had not yet released the button. Thresholds were measured at the five octave frequencies from 0.5 to 8 kHz and at seven additional frequencies in the vicinity of the notch frequency. The first set of ear canal calibration and threshold measurements required about 35 min to complete.

The seven additional frequencies extended from one octave below to one-half octave above the notch frequency in quarter-octave steps. This asymmetric pattern was selected to maximize our observations around the notch frequencies of both probe insertions, where we expected the calibration errors to be greatest. The second probe insertion was always less deep than the first insertion and was expected to have a notch frequency about one-half octave lower than the notch frequency of the first insertion. By designing our threshold estimates to extend one octave below the initial notch frequency, we expected the estimates to also extend one-half octave below the notch frequency of the second insertion.

Thresholds were determined by a maximum-likelihood procedure (Green, 1993). Likelihood values, based on all 100 trials, were computed using a logistic function to approximate the psychometric function describing percent of ''yes'' votes (Green, 1995). The parameters of the logistic function were (1) upper asymptote, (2) lower asymptote, (3) slope, and (4) threshold. Values for these four parameters were chosen by numerical iteration to obtain a maximum likelihood value, given the history of responses to the 100 trials. The threshold of the psychometric function with the maximum likelihood was selected as the behavioral threshold for that tone.

After a short break, the probe was again inserted into the subjects' ear canal, but this time not as deep as the first time. During this probe insertion procedure, a new notch frequency (determined from the conductance peak) was computed online and updated on the computer screen every few seconds. The insertion depth was adjusted until the notch frequency shifted (usually downward) by about $\frac{1}{2}$ octave (at least $\frac{1}{4}$ and not more than $\frac{3}{4}$ octave), compared to the initial probe insertion. The ear canal conductance and threshold at the same 12 frequencies were again measured in the same way as they were for the initial deeper insertion.

The threshold measurements provided a way to control the level of the sound entering the ear that was independent of any measurements from the probe microphone. We assumed that behavioral threshold over the duration of a test session was relatively constant. Therefore, any difference in threshold between the two probe insertions could not be a consequence of a change in middle-ear or cochlear function. The threshold differences can be attributed to two sources (1) threshold estimation errors and (2) calibration errors. The threshold estimation errors should be unbiased (i.e., equally likely to be larger or smaller for the second insertion). Therefore, any tendency for the pressure or intensity at threshold to be consistently larger or smaller for the second insertion must reflect an error in the corresponding pressure or intensity calibration. The extent to which the behavioral thresholds vary provides an estimate of the error in the pressure (SPL) or intensity (SIL) calibration.

The experimental protocol was completed on 75 subjects ranging in age from 14 to 78 years. All subjects were presumed to have ''normal'' hearing, based on informal questioning; however, this was not confirmed by clinical audiometric assessment because normal hearing was not a requirement for this experiment. It was only necessary for the subjects to be able to hear the tones and for their threshold to remain constant over the course of participation in the experiment, which typically lasted less than 2 h.

In seven subjects, it was not possible to shift the notch frequency by at least $\frac{1}{4}$ octave, because the frequency remained nearly the same even when the probe was withdrawn to the shallowest possible insertion. Since the primary objective of the experiment was to investigate the effect of changing the pressure distribution in the ear canal, the data from these seven subjects were excluded from further analysis. In seven other subjects, the SPL at threshold at one or more frequencies changed by more than 40 dB, probably because the subject fell asleep during the test. Because this threshold shift was larger than could be accounted for by the change in probe insertion depth, the data from these seven subjects were also excluded from further analysis. The data reported are from the remaining 61 subjects.

II. RESULTS

A. Probe

When chirp-response measurements were made in each of the five calibration tubes, the first resonant peaks occurred at 3.8, 4.6, 5.5, 6.3, and 7.1 kHz. The corresponding tube lengths, determined by the iterative procedure described

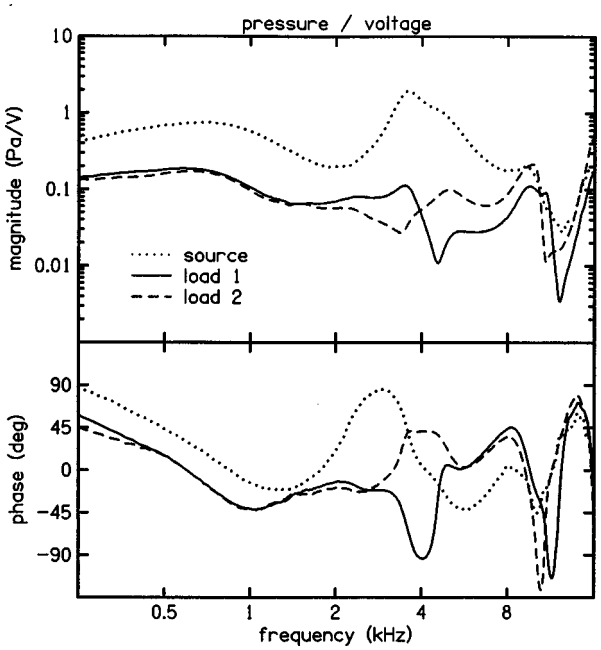

FIG. 1. Thevenin source and load pressures. The dotted lines represent the source pressure of the ER-10C. The solid and dashed lines represent the load pressure of the ear canal for the first and second insertions, respectively. The pressure magnitudes (upper panel) are normalized by the voltage to the probe. A linear phase, corresponding to a constant delay of 1.45 ms, was subtracted from all phase curves (lower panel) for clarity.

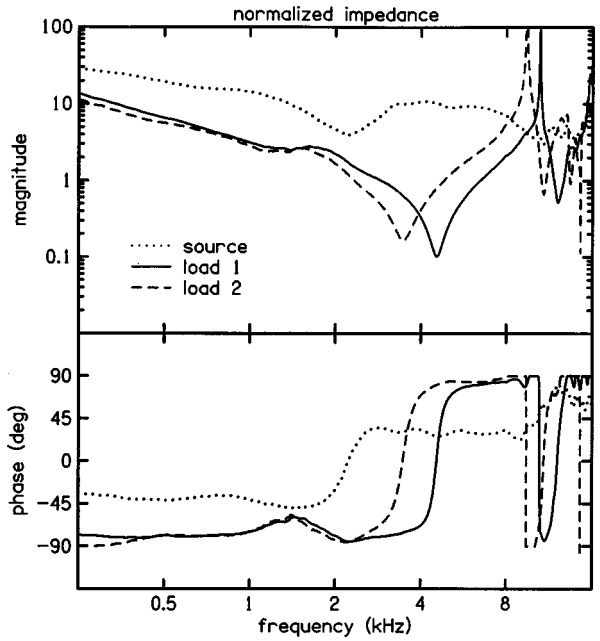

FIG. 2. Thevenin source and load impedance. The dotted lines represent the source impedance of the ER-10C probe. The solid and dashed lines represent the load impedance of the ear canal for the first and second insertions, respectively. The impedance magnitude (upper panel) is normalized by the characteristic impedance of the calibration cavities $Z_0 = 8 \times 10^6$ Pa/m^2 (=80 cgs acoustic ohms). The phase of the load impedance (lower panel) was restricted to the range between −90 and +90 by forcing the real part of the impedance to remain positive (see text).

above, were (on average) 45.2, 37.6, 31.1, 27.4, and 24.2 mm. The standard deviations associated with these tube lengths were 0.74, 0.78, 078, 0.78, and 0.77 mm, respectively. The similarity of these standard deviations across all of the different tube lengths suggests a common source of variability, such as the insertion depth of the probe tip into the coupler that was used for these calibrations.

The Thevenin acoustic source characteristics of ER-10C probe were obtained as a result of the calibration procedure. These computations were done in the frequency domain, with independent estimates for the source pressure and source impedance at each frequency. Typical results derived from one set of tube measurements are shown by the dotted lines in Figs. 1 and 2.

The source pressure/voltage ratio in Fig. 1 was computed by dividing the derived source pressure by the Fourier transform of the voltage waveform delivered to the probe. The magnitude of the source pressure (upper panel) decreases gradually between 0.5 and 8 kHz, except for a shallow dip around 2 kHz and a peak near 3.5 kHz. The phase (lower panel) has a corresponding peak near 3 kHz. A linear phase corresponding to a constant delay of 1.45 ms was subtracted from the measured phase to show details more clearly. Digital processing as the signal passes through the soundcard accounts for 1.21 ms of this delay. Electrical and acoustic propagation through the ER-10C accounts for the remaining (~0.24 ms) delay.

The source impedance in Fig. 2 was derived from the same tube measurements used to derive the source pressure shown in Fig. 1. The impedance magnitude is normalized by the characteristic impedance of the calibration tubes Z_0. The magnitude of the source impedance, like the pressure, is relatively constant across the frequency range of interest, except for a dip near 2 kHz. The phase has a 90-degree phase increase near 2 kHz, going from −45 degrees at low frequencies to +45 degrees at high frequencies. The magnitude and phase behavior near 2 kHz suggests that the ER-10C probe has an internal cavity that resonates at this frequency. The magnitude and phase functions should have a minimum-phase relationship because they represent the impedance of a physical system. Our tests to confirm this minimum-phase relation were inconclusive due to uncertainties about the impedance below 100 Hz and above 10 kHz.

Repeated measurements of the source pressure and impedance produced slightly different results. For example, across the 61 separate measurements on the same ER-10C probe, the normalized magnitude of the source impedance ranged from about 12 to 30 at 0.5 kHz and from about 2 to 9 at 8 kHz. These variations might be due to slight differences in compression of the foam eartip of the probe or due to instabilities in the analysis methods used to derive these quantities.

To access the accuracy of the probe calibration, the impedance of a test load of known impedance was also measured. The test load was a 60.0-mm brass tube of the same diameter (8.0 mm), but longer than any of the five tubes used for the probe calibration. Figure 3 compares the measured impedance of the test load (solid line) with the theoretical value calculated for this tube (Keefe, 1984). The agreement between the measured and the calculated impedances appears to be excellent from 0.5 to 8 kHz, which is the frequency range of interest.

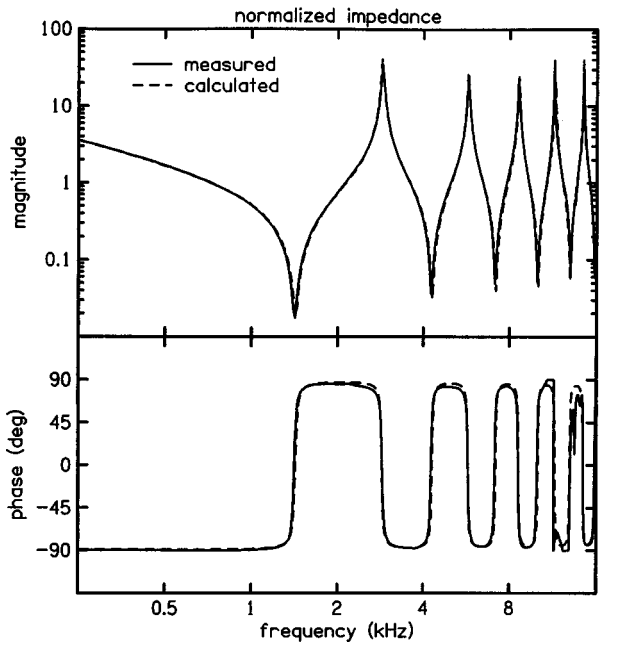

FIG. 3. Measured and calculated impedance for test load. The test load was a closed, brass tube at room temperature (25 °C) with 8-mm diameter and 60-mm length. The calculated impedance is based on equations from Keefe (1984). The impedance magnitude (upper panel) is normalized by $Z_0 = 8 \times 10^6$ Pa/m^2 (=80 cgs acoustic ohms).

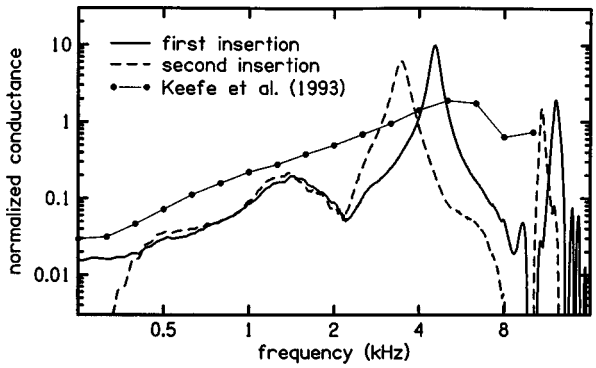

FIG. 4. Thevenin load conductance. The solid and dashed lines represent the conductance of the ear canal for the first and second insertions, respectively. These conductances correspond with the load impedance measurements shown in Fig. 2. The solid circles represent average, third-octave conductance values from ten adult subjects measured by Keefe *et al.* (1993). The conductance magnitude is normalized by Z_0, the characteristic impedance of the calibration cavities.

B. Ear canal

When the probe is inserted into an ear canal, the ear canal becomes the acoustic load being driven by the acoustic source within the probe. A typical measurement of an ear canal pressure is shown in Fig. 1. The solid line represents the first (deeper) insertion and the dashed line represents the second (shallower) insertion. The pressure/voltage ratio was computed by dividing the Fourier transform of the pressure waveform recorded from the probe by the Fourier transform of the voltage waveform delivered to the probe. Compared with the source pressure, the magnitude of the load pressure is generally smaller (by about 10 dB) and the phase shows no obvious difference in slope (that would be evidence of an additional delay).

The initial notch frequency can be seen in the pressure magnitude (solid line) at about 4.6 kHz. The notch moves down to about 3.3 kHz for the second insertion (dashed line). This shift of -0.4 octaves is a result of increasing the length of the air space between the plane of the probe and the eardrum. A downward shift of the notch frequency was observed in most subjects; however, in five subjects, the notch frequency shifted upward by more than 0.25 octaves. This was an unexpected result for which a definitive explanation is not known. We assume that the upward shift, occurring in 8% of our subjects, must be due to unusual curvature or cross-sectional area in these subjects' ear canals. While the upward shift is difficult to explain, its occurrence has no influence on the primary purpose of this shift namely, to determine the reliability of ear canal estimates of pressure and intensity. In the subset of 56 subjects where the notch frequency shifted downward (as expected), the initial notch frequency ranged from 3.4 to 8.1 kHz and the second notch frequency ranged from 2.6 to 5.3 kHz. In the other five subjects, where the notch frequency shifted upward, the initial notch frequency ranged from 2.4 to 6.2 kHz and the second notch frequency ranged from 3.2 to 8.4 kHz.

The solid and dashed lines in Fig. 2 show the ear canal normalized impedance corresponding to the ear canal pressure shown in Fig. 1. The ear canal impedance Z_{ec} at each frequency was computed from the probe pressure P_{prb}, probe impedance Z_{prb}, and ear canal pressure P_{ec}, according the formula $Z_{ec} = Z_{prb} \cdot P_{ec}/(P_{prb} - P_{ec})$. Note that the notch frequencies appear more distinct when they are observed in the impedance magnitude (Fig. 2) than when they are observed in the pressure magnitude (Fig. 1). This was always the case and made it easier (and more reliable) to determine the notch frequency from the impedance instead of the pressure. The impedance phase crosses zero at the notch frequency, going from -90 degrees at lower frequencies to $+90$ degrees at higher frequencies.

Occasionally, the phase of the impedance would become greater than $+90$ degrees or less than -90 degrees. For example, where the dashed line in the lower panel of Fig. 2 is equal to $+90$ degrees between 8 and 9 kHz, the computed impedance value was actually greater than $+90$ degrees. This meant that the real part of the complex impedance was negative, which was a nonphysical result for a passive system. The negative real impedance may have been due to measurement errors (noise), instability in the analysis methods used to compute the probe impedance, or changes in the probe impedance between probe calibration and ear canal insertion. The small amount by which the phase exceeded $+90$ degrees would have seemed insignificant when plotted, but the corresponding effect on the real part of the impedance greatly influences our estimate of acoustic intensity. Our method for dealing with these nonphysical impedances is described below.

The conductance values in Fig. 4 are for the same two probe insertions for which the pressure and impedance were presented in Figs. 1 and 2. Conductance is defined as the real part of $1/Z_{ec}$. Note that the conductance peaks in Fig. 4 occur at the notch frequencies of the pressure in Fig. 1 and the

impedance in Fig. 2. This means that if we know the frequency of the conductance peak, we also know the notch frequency. This method was used to determine the notch frequency for this experiment because it proved more reliable than using the pressure magnitude. For comparison, conductance values measured by Keefe *et al.* (1993) are also shown in Fig. 4.

When the real part of the impedance is negative, the conductance also becomes negative. In the example shown in Fig. 4, the conductance values were negative above 9.6 kHz for the first insertion (solid line) and above 8.1 kHz (and below 0.3 kHz) for the second insertion (dashed line). In this subject, the conductance values were positive over the frequency range of interest (0.5–8 kHz). However, in other subjects, negative conductance values sometimes occurred in the 0.5–8 kHz range. Dealing with negative conductance values presented the greatest challenge for this method of determining acoustic intensity in the ear canal. Because negative conductance values were considered unrealistic, a minimum (normalized) conductance value of 0.01 was established for the purpose of computing intensities. Whenever the conductance value was less than the minimum value, it was set equal to the minimum value. This adjustment made it possible to compute intensity values for all subjects at all frequencies of interest. Without this adjustment, 19 of the 61 subjects would have had negative values at one or more of the frequency at which behavioral thresholds were measured. This is not an ideal solution to the problem of negative conductance values. We hope that a better solution can be found to deal with this problem in the future.

The two ear canal pressure-to-voltage ratios shown in the upper panel of Fig. 1 as solid and dashed lines represent in-the-ear SPL calibrations. Using these curves, it is possible to determine the voltage needed to produce any desired SPL at any frequency. The differences in pressure-to-voltage ratio between the two insertion depths, by as much as an order of magnitude (20 dB) at some frequencies (near 4.2 kHz), illustrate the primary issue addressed in this paper. Specifically, in-the-ear SPL calibration cannot provide a reliable indication of the signal level entering the ear at some frequencies because it is so sensitive to the insertion depth of the probe.

Ear canal conductance provides the additional information needed to transform an SPL calibration into an SIL calibration. Figure 5 shows two in-the-ear SIL calibrations constructed from the pressure-magnitudes in Fig. 1 and the conductance in Fig. 4. The solid and dashed lines represent the first and second probe insertions, respectively. The difference between the two SIL calibrations in Fig. 5 is much smaller than the difference between the two SPL calibrations in Fig. 1. Multiplication by the conductance has effectively removed the ''standing-wave'' notches seen in SPL curves. The relative insensitivity of the SIL calibration to changes in probe insertion depth is an important advantage of this approach to calibration.

C. Thresholds

In Fig. 6, thresholds are shown for the five octave frequencies (0.5, 1, 2, 4, and 8 kHz). The circles indicate the mean values for the 61 subjects. The error bars indicate the

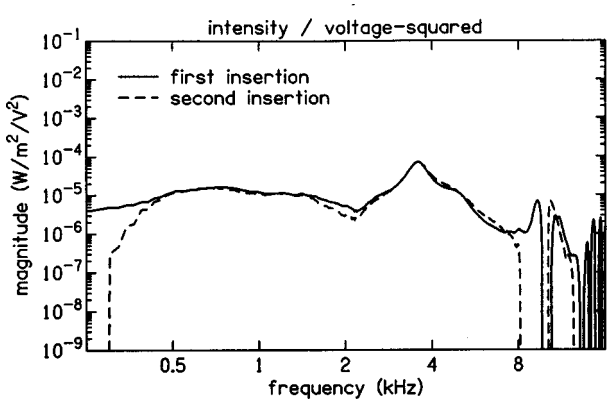

FIG. 5. Acoustic intensity in the ear canal. The solid and dashed lines represent the ratio of intensity in the ear canal to voltage squared at the probe for the first and second insertions, respectively. Note that intensity in the ear canal is less sensitive (between 0.5 and 8 kHz) to the change in probe insertion depth than the pressure magnitude shown in Fig. 1. To facilitate comparison, the vertical scales in Fig. 1 and in this figure both span an 80-dB signal range.

standard error of the mean. For each subject, the threshold values for the two probe insertions were averaged. The open circles indicate the sound pressure level (dB SPL) at threshold. For comparison, the triangles indicate the ANSI (1996) standard reference equivalent threshold (RETSPL) for an occluded ear simulator and the asterisks indicate the minimum audible pressure (MAP) at hearing threshold at the eardrum estimated by Killion (1978).

There is general agreement between the present mean thresholds and the average thresholds described in the na-

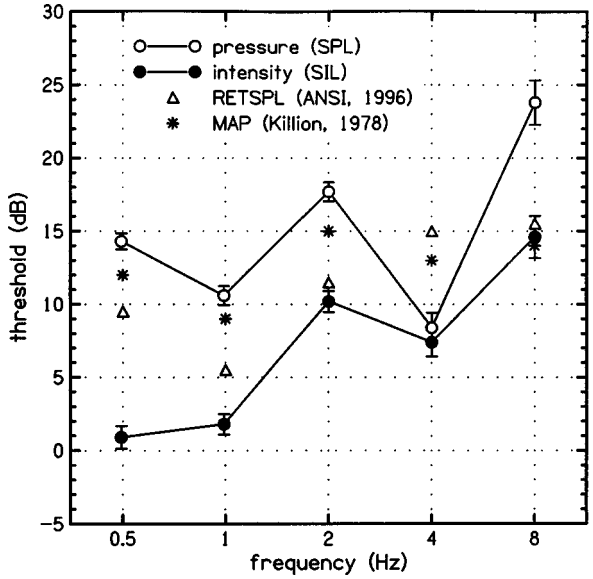

FIG. 6. Behavioral thresholds to tones. The open circles represent the mean SPL thresholds for our subjects in dB *re*: 20 μPa rms. The filled circles represent the mean SIL threshold in dB *re*: 10^{-12} W/m^2. (The filled circles also represent the mean power threshold in dB *re*: 5×10^{-17} W.) The SPL and SIL values were determined from the same threshold measurements using the ear canal conductance to convert SPL values to SIL values. The error bars indicate the standard error of the mean. For comparison, the triangles represent the ANSI (1996) reference equivalent thresholds (RETSPL) for an occluded ear simulator and the asterisks represent the minimum audible pressure (MAP) at the eardrum estimated by Killion (1978).

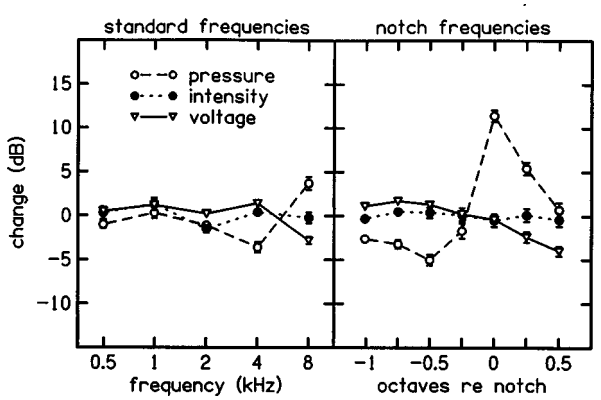

FIG. 7. SPL, SIL, and voltage threshold changes due to change of insertion depth. The open circles represent the mean change in SPL threshold, the closed circles represent the mean change in SIL threshold, and the triangles represent the change in voltage (dBV) to the probe at threshold. The error bars represent standard error of the mean. The five standard frequencies are shown in the left panel. The seven additional frequencies near the notch frequency are shown in the right panel.

tional standards and by Killion. The present threshold values were higher than the previously published values, except at 4 kHz. This is probably descriptive of the subjects population, since normal hearing was not a requirement for inclusion in this study. The lower threshold in our subjects at 4 kHz is probably an artifact of the spectral notch in pressure magnitude that was usually observed at frequencies near 4 kHz.

The filled circles show the sound intensity level (SIL) at threshold expressed in dB *re:* 1 pW/m^2. No standard for the SIL at behavioral threshold has yet been established for use with insert earphones. The threshold SIL is not constant across frequency; it is 13.7 dB higher at 8 kHz than at 0.5 kHz, suggesting a trend for the threshold SIL to increase with frequency by about 3 dB/octave. This is greater than the change in MAP, which is only 2 dB larger at 8 kHz than at 0.5 kHz.

The change in threshold between the two probe insertions is shown in Fig. 7. The open circles indicate the mean SPL change and the filled circles indicate the mean SIL change. The error bars represent the standard error of the mean. Results of the five octave frequencies (0.5, 1, 2, 4, and 8 kHz) are shown in the left panel, while the threshold changes at the seven additional frequencies (-1, $-\frac{3}{4}$, $-\frac{1}{2}$, $-\frac{1}{4}$, 0, $\frac{1}{4}$, and $\frac{1}{2}$ octaves relative to the initial notch frequency) are shown in the right panel. At 2 kHz and below (left panel), the mean threshold change at the standard frequencies is about 1 dB or less for both SPL and SIL measures of threshold. The difference between SPL and SIL is less than 1 dB at 2 kHz and below. The mean SPL change decreases by about 3 dB at 4 kHz and increases by about 3 dB at 8 kHz. These deviations are probably due to the reflection of sound waves at the eardrum. The mean SIL change is less than 1 dB at 4 and 8 kHz.

A greater contrast between the mean SPL change and the mean SIL change is seen in the right panel of Fig. 7. The fact that the SPL change is negative for frequencies below the initial notch frequency is evidence of the downward shift of the notch frequency by about $\frac{1}{2}$ octave for the second probe insertion. The mean SPL change is most positive (11.4 dB) at the initial notch frequency and most negative (-5.0 dB) at one-half octave below this frequency. By contrast, the SIL change is never more than ± 0.5 dB at any frequency in the vicinity of the notch frequency. Since we assumed that behavioral thresholds have not changed between the two probe insertions, the large SPL changes must indicate that the SPL at the plane of the probe differs from the SPL at the eardrum.

An alternative to in-the-ear calibration (SPL or SIL) is to calibrate the insert earphone in an occluded ear simulator or other coupler attached to a calibrated microphone (ANSI, 1996). With this calibration method, the voltage required to produce a given SPL in the coupler is assumed to produce the same SPL at the eardrum. To assess the effect of using a voltage reference in place of in-the-ear calibration, the triangles in Fig. 7 show the mean change in voltage (dBV) delivered to the earphone at threshold. In general, the voltage change appears to be less than the SPL change, but greater than the SIL change. This suggests that a voltage reference may be more reliable than in-the-ear pressure calibration, especially for frequencies at which a notch in the SPL occurs; however, calibrating the voltage reference presents its own set of problems, as discussed below.

III. DISCUSSION

The method used to obtain ear canal impedance by first determining the Thevenin acoustic source characteristics generally follows the description provided by Allen (1986) and Keefe *et al.* (1992). The choice of five calibration tubes was a compromise between the four tubes recommended by Allen and the six tubes recommended by Keefe. The tube lengths also represent a compromise between the slightly shorter tubes used by Voss and Allen (1994), which ranged from 11.2 to 30.2 mm, and the much longer tubes used by Keefe *et al.* (1992), which ranged from 238 to 500 mm. The tube lengths used in this study were selected so that the frequencies of the first resonant peaks (at the half-wave resonance) would span the frequency range of greatest interest (4–8 kHz) with approximately uniform spacing.

Our decision to heat the calibration tubes to body temperature was based on a suggestion by Allen (personal communication) and some preliminary comparisons that we made between calibrations performed at room temperature and at body temperature. We observed phase shifts in the source impedance and source pressure as the temperature was raised from room temperature to body temperature. These phase shifts were larger at higher frequencies and were consistent with the increased speed of sound due to the temperature increase. More importantly, negative conductance values occurred less frequently in our initial tests when the probe calibration was performed at the same temperature as the test load. While this result was not definitive, it did suggest that heating our calibration tubes to body temperature for this study might be worth the effort.

Others have demonstrated that probe calibration is possible using only two acoustic loads (e.g., Rosowski *et al.*, 1990; Puria *et al.*, 1997; Lynch *et al.*, 1994). The two-load method was not used in this study because it was not known whether the unevenness and inconsistency of the foam tip on

the ER-10C would interfere with the accurate determination of effective tube lengths. There was also some concern about the effect of temperature on the calibration. When the tube lengths are determined by an iterative procedure, a small error in the temperature specification can be partially corrected by adjusting the effective tube length appropriately. The only successful probe calibrations for the ER-10C that were known at the time that this study was initiated were those of Allen (personal communication) using four tubes and Keefe (personal communication) using six tubes, which formed the basis for the selection of five tubes for this study.

An independent calibration of the ER-10C probe was recently reported by Huang *et al.* (1998). Huang *et al.* recommend that the ER-10C probe be modified to extend the microphone tube 3–4 mm beyond the earphone tube to reduce evanescent effects, which were found to be significant (see also Rabinowitz, 1981). This may represent a source of calibration error in the present study, since we did not modify the microphone tube in this manner. For example, the small phase errors we observed between measured and calculated impedance values (see Fig. 5) might be due to evanescent effects.

The probe calibration procedure used in this study appears to be efficient and reliable in most cases. However, the large number of subjects for which negative conductance values occurred at frequencies of interest (19 out of 61) suggests that some improvement in this method is warranted before it is adopted for routine use. Incorporation of additional physical constraints (perhaps by physical modeling) may be useful. The results of the experiment would have been nearly the same if we had excluded the 19 subjects with negative conductance, suggesting that the main effects we observed were robust. Including all 61 subjects in the data analysis (by setting a minimum value for the conductance) gives a more realistic assessment of the results that can be obtained by currently available methods.

The Thevenin acoustic source pressure and impedance shown in Figs. 1 and 2 have not previously been published for the ER-10C; although source reflectance, derived from the source impedance, has been published by Keefe (1997). Informal comparisons were made of the Thevenin source impedance shown in Fig. 2 with that obtained (using similar methods) by Allen (personal communication) and Keefe (personal communication) for the ER-10C. Results of these comparisons indicate as much as a factor of 3 difference between the lowest and highest impedance values at any given frequency. This discrepancy is about the same as the range of values across the 61 probe calibrations obtained in this experiment alone. The variability in results among these probe calibrations can be attributed to variations in the eartip, instabilities in the analysis methods, and, in the comparisons with Allen's and Keefe's results, physical differences among the different ER-10C probes. Significantly better agreement among source impedance estimates should be possible with improvements in the methods used to derive the Thevenin source characteristics.

In Fig. 6, the difference between the ANSI standard RETSPL and the mean value of our measured SPL at threshold is about 4 dB at 500 Hz and increases to about 8 dB at 8 kHz. There may be several reasons for this discrepancy: (1) The occluded ear simulator used in the ANSI standard might not be representative of the average ear canal of our subjects. Note that below 8 kHz, our group means are closer to Killion's MAP than the RETSPL. Killion's MAP values have been confirmed in a comparison with other studies (Wilbur *et al.*, 1988) and may be more reliable than the ANSI RETSPL values. (2) Our technique measures SPL at the probe whereas ANSI standard and Killion's MAP both refer to SPL at the eardrum. (3) The average threshold of our subjects was probably not exactly 0 dB HL (*re*: ANSI, 1996) at all frequencies. We did not obtain (standard clinical) audiometric thresholds on these subjects because the focus of this experiment was on threshold changes rather than absolute thresholds. Finally, (4) there may be errors or biases in our threshold measurement methods. One possible source of measurement error is subject inattention. Failure to respond to audible tones inappropriately elevates the threshold estimate obtained by our automated threshold procedure. Another possible source of measurement error is the deviation of the ER-10C microphone calibration from a constant value. In our calculations, we assumed that the microphone sensitivity was 0.05 V/Pa at all frequencies. The calibration chart for this microphone supplied by the manufacturer indicates that the error in this assumption is at most 1 or 2 dB over the frequency range of interest (0.5–8 kHz).

In Fig. 4, we compare our measured conductance values for one subject with the third octave conductance values obtained by Keefe *et al.* (1993) for the mean of ten subjects. Below 2 kHz, the conductance values obtained by Keefe *et al.* are similar to those obtained by Møller (1960), who also presented the mean of ten subjects, but did not measure above 2 kHz. The mean conductance values of Keefe *et al.* do not show the distinct peaks and dips that are apparent in the conductance of a single ear canal; however, an average of the conductance values we obtained in all 61 subjects would be similar to their mean value.

In-the-ear pressure calibration is the method currently used by most commercial DPOAE measurement systems. Siegel (1994) has shown that such calibration can lead to significant errors in the measured DPOAE amplitudes. The reason for the DPOAE amplitude errors is that the stimulus levels measured at the plane of the probe were not always a good indication of the stimulus level at the eardrum. The results shown in Figs. 5 and 7 indicate that in-the-ear intensity calibration would not have the same problems as pressure calibrations and could, therefore, lead to more reliable measures of DPOAE amplitude because the stimulus level would be more reliably determined. This improvement in accuracy of the stimulus level is obtained despite the problems with current methods (such as negative conductance) described above.

One disadvantage of using in-the-ear intensity calibration is the additional time (5–10 min) required to recalibrate the probe before each ear canal measurements. It is, therefore, of interest of know whether similar results could be obtained with fewer probe calibrations. We repeated the analysis using the same probe calibration (the one illustrated

in Figs. 1, 2, and 4) for all ears. The mean SPL and SIL values for the change in threshold were within 1 dB of the values shown in Fig. 7, despite a much more frequent occurrence of negative conductance values. Thus, it appears that in-the-ear SIL calibration retains its advantage over SPL calibration even with a single probe calibration.

An alternative to in-the-ear calibration is to calibrate the probe in an occluded ear simulator or other coupler attached to a calibrated microphone. With this method, the voltage that produces the desired SPL in the coupler would be assumed to produce the same SPL in the ear canal. To assess this calibration method, it is of interest to know whether a given voltage to the earphone always produces the same level of sound entering the ear. The triangles in Fig. 7 show that the change in threshold is greater at most frequencies for a voltage reference than it is for an intensity reference. The voltage change is greatest at 8 kHz or above the notch frequency. In general, based on these results, it would appear that coupler calibration may be preferable to in-the-ear SPL calibration, but not as good as in-the-ear SIL calibration. However, there are other problems associated with coupler calibrations. For example, if the coupler impedance is much different than the ear-canal impedance, then the pressure measured in the coupler (by the calibration microphone) can be much different than the pressure presented to the eardrum. Thus one could obtain errors from coupler calibrations that are as large as those observed with in-the-ear pressure calibrations.

If intensity is a better indicator of stimulus level than pressure, then the question arises whether the ear is detecting pressure or power. In Fig. 6, we see that neither the pressure nor the intensity at threshold is constant across frequency. Puria *et al.* (1997) provided evidence from measurements in human cadaver ears that behavioral threshold corresponds to constant pressure (28 dB SPL) in the vestibule of the cochlea. With this observation in mind, we can interpret our results in the following way. Pressure at the probe is not constant at threshold across frequency because it is not a good indicator of pressure in the cochlea, due to reflected waves from the eardrum and middle ear. Intensity at the probe is not constant across frequency because the ear is not a power detector.

If behavioral threshold is determined by pressure at the entrance to the cochlea (Puria *et al.*, 1997), then calibrating sound levels to a pressure reference may be preferable to using an intensity reference. Direct measurement of pressure at the eardrum avoids the problem of notches due to standing waves (Siegel, 1994), but the procedure may be too difficult for routine use. Another way to obtain estimates of pressure at the eardrum is to use a calibrated probe, estimate the ear canal diameter and distance between the probe and the eardrum, and calculate the propagated pressure at the eardrum assuming cylindrical geometry (Rabinowitz, 1981; Huang *et al.*, 1988; Stevens *et al.*, 1987).

IV. CONCLUSIONS

Currently available methods for estimating acoustic source pressure and impedance of a probe allow the determination of sound intensity level (SIL) in addition to sound pressure level (SPL) in the ear canal. Above 2 kHz the in-the-ear SIL measurement appears to provide a better indication of the level of sound entering the ear than in-the-ear SPL calibration, judged by the sensitivity of behavioral thresholds to changes in probe insertion depth. Coupler calibration may be better than in-the-ear SPL calibration, but does not appear to be as good as in-the-ear SIL calibration. Below 2 kHz, SIL and SPL calibrations appear to perform equally well.

ACKNOWLEDGMENTS

Jan Kaminski performed the measurements on all subjects included in this study. Douglas Keefe, Huanping Dai, Meade Killion, and an anonymous reviewer made many helpful suggestions for improvements in this paper. This work was supported by a grant (P60-DC00982) from the National Institutes of Health.

Allen, J. B. (**1986**). ''Measurement of eardrum acoustic impedance,'' in *Peripheral Auditory Mechanisms*, edited by J. B. Allen, J. L. Hall, A. Hubbard, S. T. Neely, and A. Tubis (Springer-Verlag, New York).

ANSI (**1996**). ANSI S3.6-1996, ''Specifications for audiometers'' (American National Standards Institute, New York).

Green, D. M. (**1993**). ''A maximum-likelihood method for estimating thresholds in a yesno task,'' J. Acoust. Soc. Am. **93**, 2096–2105.

Green, D. M. (**1995**). ''Maximum-likelihood procedures and the inattentive observed,'' J. Acoust. Soc. Am. **97**, 3749–3760.

Huang, G. T., Rosowski, J. J., Puria, S., and Peake, W. T. (**1998**). ''Noninvasive technique for estimating acoustic impedance at the tympanic membrane (TM) in ear canals of different size,'' Assoc. Res. Otolaryngol. Abs. **21**, 487.

Keefe, D. H. (**1984**). ''Acoustical wave propagation in cylindrical ducts: Transmission line parameter approximations for isothermal and nonisothermal boundary conditions,'' J. Acoust. Soc. Am. **75**, 1386–1391.

Keefe, D. H., Ling, R., and Bulen, R. C. (**1992**). ''Method to measure acoustic impedance and reflection coefficient,'' J. Acoust. Soc. Am. **75**, 1386–1391.

Keefe, D. H. (**1997**). ''Otoreflectance of the cochlea and middle ear,'' J. Acoust. Soc. Am. **102**, 2849–2859.

Keefe, D. H., Bulen, J. C., Hoberg, K., and Burns, E. M. (**1993**). ''Ear-canal impedance and reflection coefficient of human infants and adults,'' J. Acoust. Soc. Am. **94**, 2617–2638.

Killion, M. C. (**1978**). ''Revised estimate of minimum audible pressure: Where is the missing 6 dB?'' J. Acoust. Soc. Am. **63**, 1501–1508.

Lynch, T. J. III, Peake, W. T., and Rosowski, J. J. (**1994**). ''Measurement of the acoustic input impedance of cat ears: 10 Hz to 20 kHz,'' J. Acoust. Soc. Am. **96**, 2184–2209.

Marlan, R. S., Kim, D. O., LaBrie, L., and Leonard, G. (**1994**). ''Specification of high frequency stimulus level in terms of acoustic power using Thevenin equivalent source in the measurement of DPOAEs,'' Assoc. Res. Otolaryngol. Abs. **17**, 55.

Møller, A. R. (**1960**). ''Improved technique for detailed measurements of middle-ear impedance,'' J. Acoust. Soc. Am. **32**, 250–257.

Pierce, A. D. (**1981**). *Acoustics: An Introduction to its Physical Principles and Applications* (McGraw-Hill, New York), p. 107.

Puria, S., Peake, W. T., and Rosowski, J. J. (**1997**). ''Sound-pressure measurements in the cochlear vestibule of human-cadaver ears,'' J. Acoust. Soc. Am. **101**, 2754–2770.

Rabinowitz, W. M. (**1981**). ''Measurement of the acoustic immittance of the middle ear,'' J. Acoust. Soc. Am. **70**, 1025–1035.

Rosowski, J. J., Davis, P. J., Merchant, S. N., Donahue, K. M., and Coltrera, M. D. (**1990**). ''Cadaver middle ears as models for living ears: comparisons of middle ear input, immittance,'' Ann. Otol. Rhinol. Laryngol. **99**, 403–412.

Siegel, J. H. (**1994**). ''Ear-canal standing-waves and high-frequency sound calibration using otoacoustic emission probes,'' J. Acoust. Soc. Am. **93**, 3308–3319.

Siegel, J. H., and Hirohata, X. (**1994**). ''Sound calibration and distortion product otoacoustic emissions at high frequencies,'' Hearing Res. **80**, 146–152.

Stevens, K. N., Berkovitz, R., Kidd, Jr., G., and Green, D. M. (**1987**). ''Calibration of ear canals for audiometry at high frequencies,'' J. Acoust. Soc. Am. **81**, 470–484.
Voss, S. E., and Allen, J. B. (**1994**). ''Measurement of acoustic impedance and reflectance in the human ear canal,'' J. Acoust. Soc. Am. **95**, 372–384.
Wilber, L. A., Kruger, B., and Killion, M. C. (**1988**). ''Reference thresholds for the ER-3A insert earphone,'' J. Acoust. Soc. Am. **82**, 669–676.

Click train encoding in primary auditory cortex of the awake monkey: Evidence for two mechanisms subserving pitch perception

Mitchell Steinschneider[a)]
Departments of Neurology and Neuroscience, Albert Einstein College of Medicine, Rose F. Kennedy Center, Bronx, New York 10461

David H. Reser and Yonatan I. Fishman
Department of Neuroscience, Albert Einstein College of Medicine, Bronx, New York 10461

Charles E. Schroeder
Program in Cognitive Neuroscience and Schizophrenia, Nathan Kline Institute for Psychiatric Research, Orangeburg, New York 10962

Joseph C. Arezzo
Departments of Neurology and Neuroscience, Albert Einstein College of Medicine, Bronx, New York 10461

(Received 23 January 1998; revised 29 June 1998; accepted 24 July 1998)

Multiunit activity (MUA) and current source density (CSD) patterns evoked by click trains are examined in primary auditory cortex (A1) of three awake monkeys. Temporal and spectral features of click trains are differentially encoded in A1. Encoding of temporal features occurs at rates of 100–200 Hz through phase-locked activity in the MUA and CSD, is independent of pulse polarity pattern, and occurs in high best frequency (BF) regions of A1. The upper limit of ensemble-wide phase-locking is about 400 Hz in the input to A1, as manifested in the cortical middle laminae CSD and MUA of thalamocortical fibers. In contrast, encoding of spectral features occurs in low BF regions, and resolves both the f_0 and harmonics of the stimuli through local maxima of activity determined by the tonotopic organization of the recording sites. High-pass filtered click trains decrease spectral encoding in low BF regions without modifying phase-locked responses in high BF regions. These physiological responses parallel features of human pitch perception for click trains, and support the existence of two distinct physiological mechanisms involved in pitch perception: the first using resolved harmonic components and the second utilizing unresolved harmonics that is based on encoding stimulus waveform periodicity. © *1998 Acoustical Society of America.* [S0001-4966(98)01611-7]

PACS numbers: 43.64.Qh, 43.64.Ri, 43.66.Hg [RDF]

INTRODUCTION

Pitch perception is a fundamental feature of human audition, subserving functions as diverse as speech recognition, music appreciation, and auditory source identification. Despite this crucial role in hearing, little is known about the central nervous system mechanisms that underlie the encoding of pitch. Elucidating these neural mechanisms requires detailed investigations of the auditory cortex, as profound deficits in pitch perception occur following lesions of the posterior temporal lobe (e.g., Zatorre, 1988; Divenyi and Robinson, 1989; Robin *et al.*, 1990). While these lesion studies suggest a specialized role of auditory cortex in the nondominant hemisphere for pitch perception, neuroanatomical and functional imaging studies indicate that primary auditory cortex (A1) of both hemispheres is involved in the initial stages of cortical processing (Galaburda and Pandya, 1983; Zatorre *et al.*, 1992, 1994; Morel *et al.*, 1993; Pandya and Rosene, 1993). These considerations suggest that A1 is a critical component of the neural network involved in pitch processing, and support the need to examine relevant activity that would serve as input for later auditory processing stages.

Electrophysiological analysis is critical for defining physiological mechanisms important for pitch perception in A1. Functional imaging studies can identify brain regions involved with pitch perceptual tasks, but cannot delineate the associated physiological events within the activated cortical areas. Noninvasive recordings of human event-related potentials and magnetic-evoked responses provide temporally dynamic pictures of complex sound encoding, but are also limited in their ability to characterize the specific neural processes that generate the waveform components. Resolution of these physiological mechanisms requires intracranial recordings. Ethical considerations, however, preclude extensive investigations in humans.

Fortunately, key features of complex sound perception that mirror human responses occur in some animals. This indicates that animals can serve as models for detailing some of the neural events underlying pitch encoding. Monkeys and cats respond to the pitch of harmonic tone complexes determined by a missing fundamental frequency (f_0) in a manner similar to humans (Heffner and Whitfield, 1976; Tomlinson and Schwarz, 1988). This ability is lost in cats after bilateral ablation of the auditory cortex (Whitfield, 1980). The capacity to discriminate amplitude-modulated noise is nearly iden-

a)Electronic mail: steinsch@aecom.yu.edu

tical in monkeys and humans, and both species demonstrate qualitatively similar critical bands and psychoacoustical sensitivities for multiple phonetic contrasts of speech sounds (Gourevitch, 1970; Kuhl and Padden, 1982, 1983; Sinnott and Adams, 1987; Sinnott and Kreiter, 1991; Sommers *et al.*, 1992; Pfingst, 1993). Monkeys also exhibit categorical perception of species-specific vocalizations, aphasia-like deficits following auditory cortical lesions, and human-like hemispheric specialization (Petersen *et al.*, 1978; Heffner and Heffner, 1986, 1989; May *et al.*, 1989). Thus, many higher-order capacities in complex sound perception are determined by general principles of auditory system physiology, and can be adequately examined in a primate model.

In this study, neural activity associated with pitch encoding of click trains is investigated by examining neuronal ensemble responses in A1 of awake monkeys. Click trains composed of individual pulses with same and alternating polarity are used as stimuli because they elicit pitch perceptions that are apparently based on two distinct psychoacoustical mechanisms that lend themselves to physiological analysis (Flanagan and Guttman, 1960a, 1960b; Guttman and Flanagan, 1964; Rosenberg, 1965). The pitch of click trains with pulse rates less than 100 Hz equals the pulse rate regardless of the click polarity pattern. In contrast, the pitch of click trains with f_0's greater than 200 Hz is determined by the f_0 and is dependent on the click polarity pattern. The intervening frequency region is a transition zone where pitch based on rate and f_0 are in conflict, leading to determinations of a single pitch that are often unsatisfactory. These two pitch mechanisms are mediated by distinct auditory channels, with pitch perception equal to pulse rate encoded by high-frequency channels, and pitch perception based on f_0 mediated by low frequency channels. Furthermore, pitch determined by pulse rate is thought to be determined by temporal mechanisms, whereas spectral encoding processes are thought to mediate pitch encoded by the f_0.

There is controversy, however, about the need to postulate the existence of two distinct pitch mechanisms. A unitary model of pitch encoding using autocorrelation within individual auditory processing channels and subsequent aggregation of periodicity estimates across channels has been proposed (Meddis and Hewitt, 1991; Meddis and O'Mard, 1997). Physiological data based on autocorrelation of auditory nerve fiber activity support this hypothesis (Cariani and Delgutte, 1996a, 1996b). Other studies describe differential processing of resolved and unresolved harmonics that support dual pitch mechanisms (Carlyon and Shackleton, 1994; Shackleton and Carlyon, 1994). As discussed above, auditory cortex is required for complex pitch perceptions. Therefore, if a dual mechanism of pitch processing is valid, physiological support using click train stimuli may be evident in A1. Specifically, we hypothesize that click train stimulation should engage two neural mechanisms relevant for pitch encoding. The first should be based in low-frequency tonotopic regions of A1 and encode spectral features of click trains, the second should be present in high-frequency areas and contain temporal patterns of activity that encode click trains presented at rates up to 100–200 Hz.

I. METHODS

Three male monkeys (*Macaca fascicularis*) weighing between 2 and 3 kg were studied following approval by our institutional Animal Care and Use Committee. Animals were housed in our AAALAC-accredited Animal Institute and their health was monitored daily. Surgery was performed using sterile techniques under barbiturate anesthesia and involved the implantation of electrode guides for repeated intracortical recordings. Electrode guides were 18-gauge stainless steel tubes glued together to form matrices that rested upon the intact dura. Implants were positioned above and anterior to A1 at a 30-degree angle, permitting electrode penetrations nearly orthogonal to the surface of A1. The implants and bars permitting painless head fixation during the later recordings were embedded in dental acrylic and secured to the skull with screws and inverted bolts keyed into the bone. Perioperative medications were used to minimize animal discomfort and the risk of infection. Recordings began 2 weeks after surgery.

Intracortical recordings were performed with multicontact electrodes constructed in our laboratory (Barna *et al.*, 1981). They contained 14 electrodes evenly spaced at 150-μm intervals ($<$10% error) that permitted simultaneous recordings from the entire laminar width of A1. Individual electrodes were 25-μm insulated stainless steel wires that were fixed in place within the sharpened distal portion of a 30-gauge needle. Each channel had an impedance of 0.1 to 0.4 MΩ at 1 kHz. Headstage preamplification was followed by amplification with a frequency bandpass down 6 dB at 3 Hz and 3 kHz. The reference was an occipital bone electrode. Auditory evoked potentials (AEPs) were averaged on-line by computer with a sampling rate of 1673 Hz. Input signals were simultaneously high-pass filtered above 500 Hz (rolloff 24 dB/oct), further amplified by a factor of 8, full-wave rectified, digitized at a sampling rate of 3346 Hz, and averaged by computer for acquisition of multiunit activity (MUA).

MUA is a measure of the weighted sum of action potentials recorded from neuronal ensembles surrounding the recording contacts (for details see Vaughan and Arezzo, 1988). Electrode impedance determines the radius of recording. Electrodes used in the present study are capable of recording sharply differentiated MUA at 75-μm spacing (Schroeder *et al.*, 1990). Increases of MUA above prestimulus baseline levels indicate net cellular excitation, while decreases denote a net decrement in the firing rate of the sampled population of neurons. While multichannel MUA recordings offer the advantage of rapidly sampling synchronized unit activity simultaneously from multiple cortical laminae, the technique does have important limitations that include: a greater weight in the response from larger cells and those closer to the recording tips, an inability to define the cell types that contribute to the response, and the masking of response patterns contributed by individual neurons.

One-dimensional current source density (CSD) analyses were calculated from the laminar profiles of the AEPs using an algorithm that approximated the second spatial derivative of the field potential voltages (V) from 3 adjacent points:

$$D = -(V(r-h) - 2V(r) + V(r+h))/h^2,$$

where D is the second spatial derivative approximation, r is the point at which D is calculated, and h is the spacing of the recording sites (Freeman and Nicholson, 1975). CSD analysis determines net transmembrane current flow by calculating scalar quantities that indicate whether a recording site acts as an extracellular current source or sink at each time point of the AEP. Sources and sinks represent locations where current is either injected or removed from the extracellular space, and primarily index sites of synaptic activity or associated, circuit completing current flow. CSD analysis is enhanced when active sinks and sources are differentiated from passive currents effecting circuit closure. Thus, a sink can index a site of net depolarization or it can represent passive current drawn to balance hyperpolarization at an adjacent site. A source can occur at a site of net hyperpolarization or represent circuit completing current flow for an adjacent depolarization. These possibilities are distinguished by using MUA as an independent measure of cellular excitation and inhibition. A sink coincident with increased MUA indicates that the sink represents EPSPs, while a source associated with a reduction in MUA suggests that the source indexes hyperpolarization.

Multiple requirements must be met for accurate one-dimensional CSD analysis (for reviews see Mitzdorf, 1985; Vaughan and Arezzo, 1988; Vaughan *et al.*, 1992; Schroeder *et al.*, 1995). One requirement is the need for relatively uniform activation of neurons in the planes perpendicular to the trajectory of the recording electrode, thereby canceling current flow in all directions except that orthogonal to the cortical surface. The stimuli in this study evoke nonuniform patterns of activation that might violate basic requirements for valid CSD analysis. However, CSD along the vertical dimension is not distorted by lateral current flow when the diameter of a neuronal ensemble generating a specific current is one to two times the vertical length of the associated sources and sinks (Nicholson and Freeman, 1975). The extended widths of dendritic trees of auditory cortical pyramidal cells indicate that synchronous activation of only a small group of adjacent neurons will satisfy our requirements for CSD analysis (Winer, 1984; Mitani *et al.*, 1985). These theoretical considerations are exemplified by demonstrations that, despite nonuniform activation, reliable one-dimensional CSD profiles are obtained that reflect the A1 tonotopic organization (Steinschneider *et al.*, 1995; Fishman *et al.*, 1998). Another concern of CSD analysis is the frequency response characteristics of the technique, which might lead to spectral aliasing of the responses. However, at frequencies of interest ($<$1 kHz), capacitive, inductive, magnetic, and propagative effects of the extracellular medium can be ignored (Mitzdorf, 1985). Furthermore, except for lamina 1, variation in resistance across cortical laminae is less than 10% (Hoeltzell and Dykes, 1979; Mitzdorf and Singer, 1980). This indicates that CSD components predominantly reflect changes in current flow induced by stimulation, and not changes in tissue resistance. To minimize the possibility of spatial aliasing, wherein interelectrode spacing is too wide to resolve differential activity occurring between adjacent recording contacts, we use electrode spacing (150 μm) capable of recording from even the narrowest of cortical laminae. Finally, we did not analyze the CSD when there was significant deviation ($>$20 degrees) from a perpendicular electrode penetration into A1, as this might also introduce error into the computations.

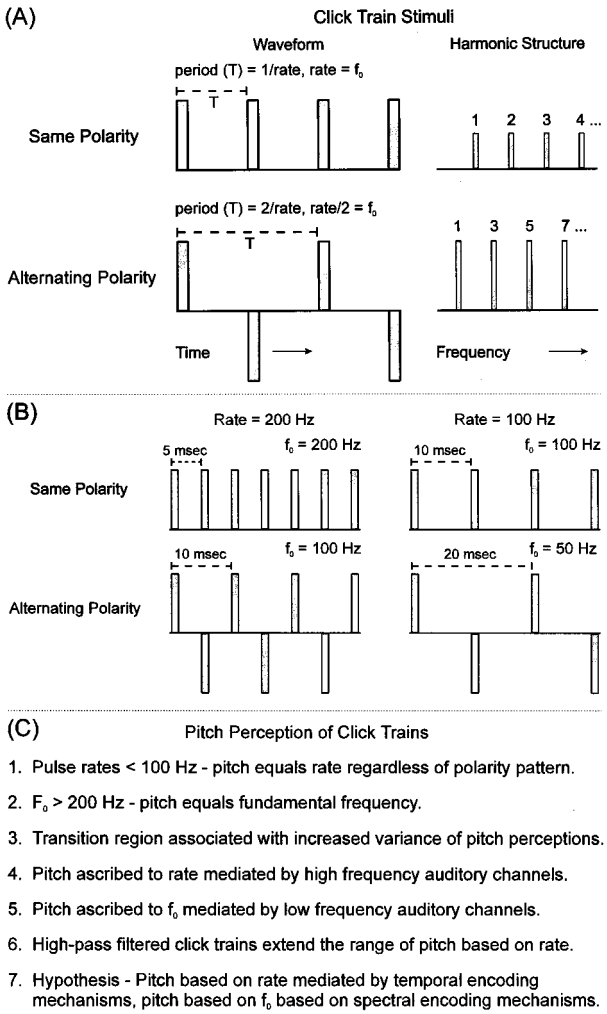

FIG. 1. (a) Schematic diagram of the click train stimuli used in the present study. Trains were composed of pulses that were either of uniform or alternating polarity. The fundamental frequency of alternating polarity click trains was one-half the same polarity trains presented at an equal rate. Same polarity click trains contained sequential harmonics, while alternating polarity stimuli were composed of odd-numbered harmonics that were each twice the amplitude of the former stimuli. (b) Schematic diagram of same and alternating polarity click trains presented at pulse rates of 200 and 100 Hz. (c) Summary of pitch perception findings for click trains (based on Flanagan and Guttman, 1960a, b; Guttman and Flanagan, 1964; Rosenberg, 1965).

Stimuli were click trains with pulse rates of 10 Hz to 2 kHz. They were digitally constructed from clicks 100 μs in duration that were either of the same or alternating polarity (Fig. 1). Alternating polarity click trains had a f_0 that was one-half that of the same polarity click trains presented at the same rate. The alternating polarity click trains also contained odd-numbered harmonic components that were twice the amplitude of the same polarity trains, which were composed of both odd and even harmonics. Trains were 175 ms in maximum duration, with the absolute duration dependent on the click rate. Tone bursts ranging in frequency from 0.2–12.0 kHz were presented to define the tonotopic specificity of the recording sites. They were 175 ms in duration, with 10-ms

linear rise–decay times. All stimuli were digitally constructed, edited, and delivered at a sampling frequency of 44.1 kHz (*Macintosh* computer using *digidesign Turbosynth* and *Sound Designer II* software and hardware). In one animal, high-pass filtered click trains (cutoff 2 kHz) were also delivered. Fourier analysis confirmed the adequacy of the filtering process. Inter-stimulus-interval was 658 ms. Stimuli were presented via a dynamic headphone (*Sony, MDR-7502*) coupled to a 60-cc plastic tube that was placed against the ear contralateral to the recording sites. A *Rane GE60* graphic equalizer was used to enhance the headphone's frequency-response characteristics for one animal. All stimuli were presented at 60 dB SPL (rms), and occasionally at 80 dB. Acoustic calibrations were performed with the microphone of a sound level meter (*Brüel & Kjaer, type 2236*) placed in the same relative position as the animal's ears.

Recordings were performed in an electrically-shielded and sound-attenuated chamber. The animals were painlessly restrained in custom-fitted primate chairs with their heads immobilized using pressure fits against the bars implanted at the time of surgery. Monkeys maintained an alert state throughout the recordings. Positive food reinforcements were given periodically. Intracortical positioning of the electrodes was guided by the on-line analysis of the AEP and MUA evoked by isolated clicks (80 dB). Click trains and tone bursts were presented when the multicontact electrode straddled the inversion of the AEP components and middle electrode channels recorded MUA of cortical origin. Response averages were generated from 75 or 100 stimulus repetitions.

Animals were deeply anesthetized with sodium pentobarbital and perfused through the heart with physiologic saline and 10% buffered formalin when recordings were completed. A1 was anatomically delineated using published criteria (Morel *et al.*, 1993), and the electrode tracks were identified and reconstructed in coronal sections stained with cresyl violet. Laminar locations of the recording sites were defined using a combined histological and physiological procedure. Depths of the earliest click-evoked current sinks and concurrent sources were used to locate lamina 4 and lower lamina 3 (Steinschneider *et al.*, 1992). The physiologic laminar profiles of the CSD and MUA were then correlated with the measured widths of A1 and its laminae for each electrode penetration, and checked by relating the remainder of the laminar CSD and MUA profiles to expected locations for prominent current sources and sinks (Steinschneider *et al.*, 1994). MUA recorded in subjacent white matter and with onset and peak latencies earlier than intracortical activity was ascribed to activity in thalamocortical afferents.

II. RESULTS

Results are based on 40 electrode penetrations into A1. Consistent with earlier studies, a tonotopic organization in the tone-evoked CSD and MUA is observed, with low best frequencies (BF) located anterolaterally and higher BFs posteromedially (e.g., Merzenich and Brugge, 1973; Morel *et al.*, 1993). BFs ranged from 200–12 000 Hz in 37 penetrations. Three penetrations in histologically identified posteromedial A1 are included in the sample and are assumed to have BFs greater than 12 000 Hz. Twenty-two penetrations have a BF less than 2000 Hz. No differences are noted among the responses from the three animals or from the left and right hemispheres.

A. Encoding of click trains in low BF regions of A1

Spectral features of click trains are predominantly encoded within low BF regions of A1. Responses reflect the entire harmonic structure of the click trains and not just the pitch, or f_0, of the sounds. Demonstrating this result first requires an illustration of how spectral sensitivity of recording sites is determined. Figure 2 depicts tone-evoked responses recorded at an electrode penetration site (site A) with a BF of 700–800 Hz. The laminar profile of CSD evoked by the 700 Hz tone is shown in the left-hand column, with approximate laminar locations shown at the far left of the figure. A characteristic sequence of cortical activation is engaged. Initial current sinks are located in the thalamorecipient zone of lamina 4 and lower lamina 3 (depths 5 and 6). The location and timing of these sinks and surrounding current sources are consistent with the initial depolarization of lamina 4 stellate cells, basilar regions of lower lamina 3 pyramidal cells and terminal portions of thalamocortical afferents (Steinschneider *et al.*, 1992; Tenke *et al.*, 1993). These initial sinks are rapidly followed by supragranular activation, shown by the current sinks at depths 3 and 4, with associated passive current sources in more superficial laminae (depths 1 and 2). This dipolar configuration indicates depolarization of more apical portions of pyramidal cells. These initial components are followed by more variable sources and sinks that will not be further discussed.

The middle column of Fig. 2 depicts the lower lamina 3 CSD profiles (depth 5) evoked by the indicated tone bursts. There is an increase in the size of the initial current sink as tone frequency increases from 200 to 700 Hz, a plateau between 700 and 1000 Hz, and a rapid change from a current sink to initial current sources at higher tone frequencies. The MUA patterns parallel the CSD findings, as shown in the right-hand column of the figure. There is an increase in both the initial burst of MUA and the sustained activity as tone frequency increases to 700 Hz, a decline in activity at slightly higher frequencies, and a sustained decrease of MUA to levels below baseline for tone frequencies greater than 1000 Hz. Association of the decreases in MUA with concurrent sources in the CSD indicate that these lamina 3 current sources represent active hyperpolarization of local neurons. Absence of a large excitatory current sink and associated MUA increases preceding the hyperpolarization indicate that the current sources index synaptically mediated inhibition and not passive afterhyperpolarization.

Data are quantified in the graphs at the bottom of Fig. 2, which depict both the area (solid lines) and peak responses (dotted lines) elicited by the tones. Area and peak measures are taken from 5 to 35 ms following stimulus onset for the initial CSD sinks at depths 5 and 6, and 15 to 45 ms for the later supragranular activity. There is a consistent maximum between 700 and 800 Hz in the CSD peak and area measures across the granular and supragranular laminae. MUA responses are measured from 5 ms following stimulus onset

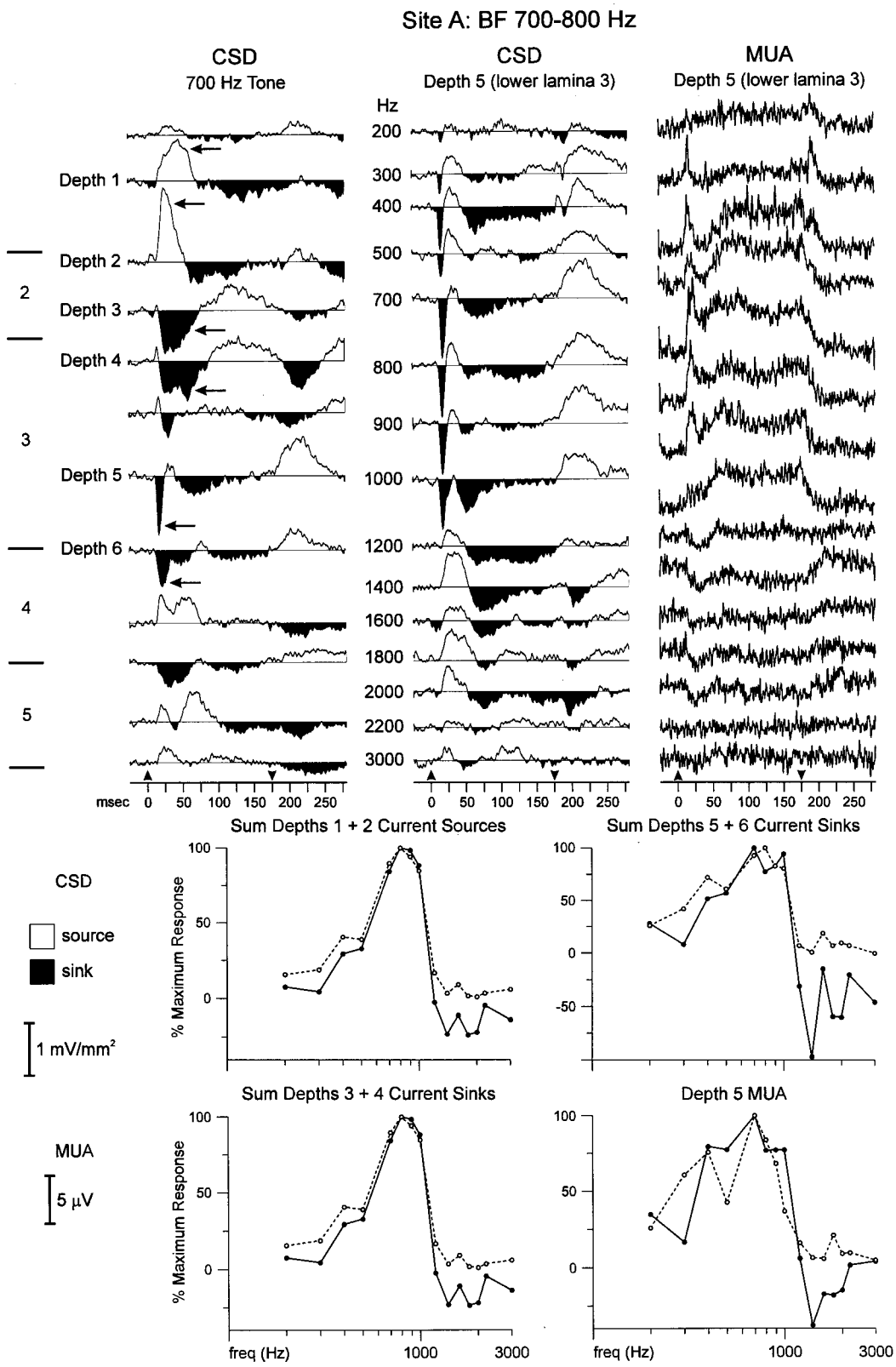

FIG. 2. Tone-evoked CSD and MUA recorded from an A1 site whose BF is 700–800 Hz. The CSD laminar profile elicited by the 700-Hz tone is shown in the left-hand column. Arrows denote locations of principal current sources and sinks, beginning with the earliest activation in lower lamina 3 and lamina 4 (initial sinks at depths 5 and 6), followed by later supragranular sinks (depths 3 and 4). The sources at depths 1 and 2 reflect passive current return for the deeper sinks. Approximate laminar boundaries are shown at the far left of the figure. CSD and MUA recorded to the presented tones in lower lamina 3 (depth 5) are shown in the middle and right-hand columns, respectively. Tone frequencies are shown to the left of the middle column. Arrowheads immediately above the timelines indicate stimulus onset and offset. The graphs at the bottom of the figure illustrate the spectral sensitivity of the CSD components and the lower lamina 3 MUA. Solid curves denote area measurements of the responses, while dotted curves denote peak responses. Maximum responses occur to the 700- and 800-Hz tones in all cases. See text for details.

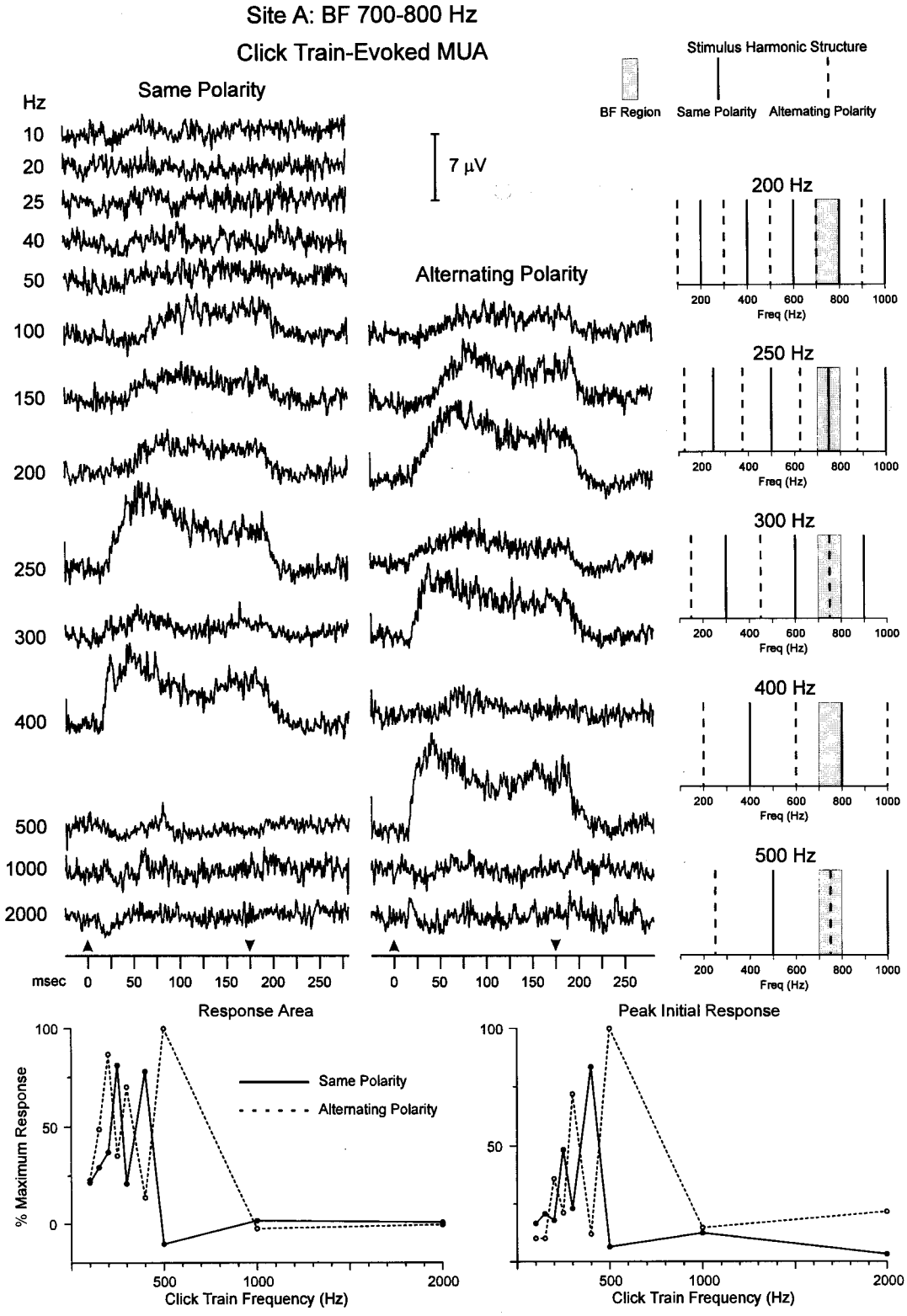

FIG. 3. MUA recorded from the same lower lamina 3 site (depth 5) as that shown in Fig. 2. Responses evoked by the same and alternating polarity click trains are shown in the left-hand and middle columns, respectively. Click train rate is shown at the far left of the figure. Note the absence of phase-locked activity elicited by the lower rate click trains. Complex changes in response amplitudes are related to the relationship between the harmonic structure of the stimuli and the spectral sensitivity of the recording site. The right-hand column depicts this relationship by illustrating the harmonic structure of the click trains in relation to the 700–800 Hz region of maximum spectral sensitivity. Large amplitude responses contain harmonics within this spectral region. The bottom graphs summarize measurements of sustained and peak responses to the same (solid lines) and alternating (dotted lines) polarity click trains. See text for details.

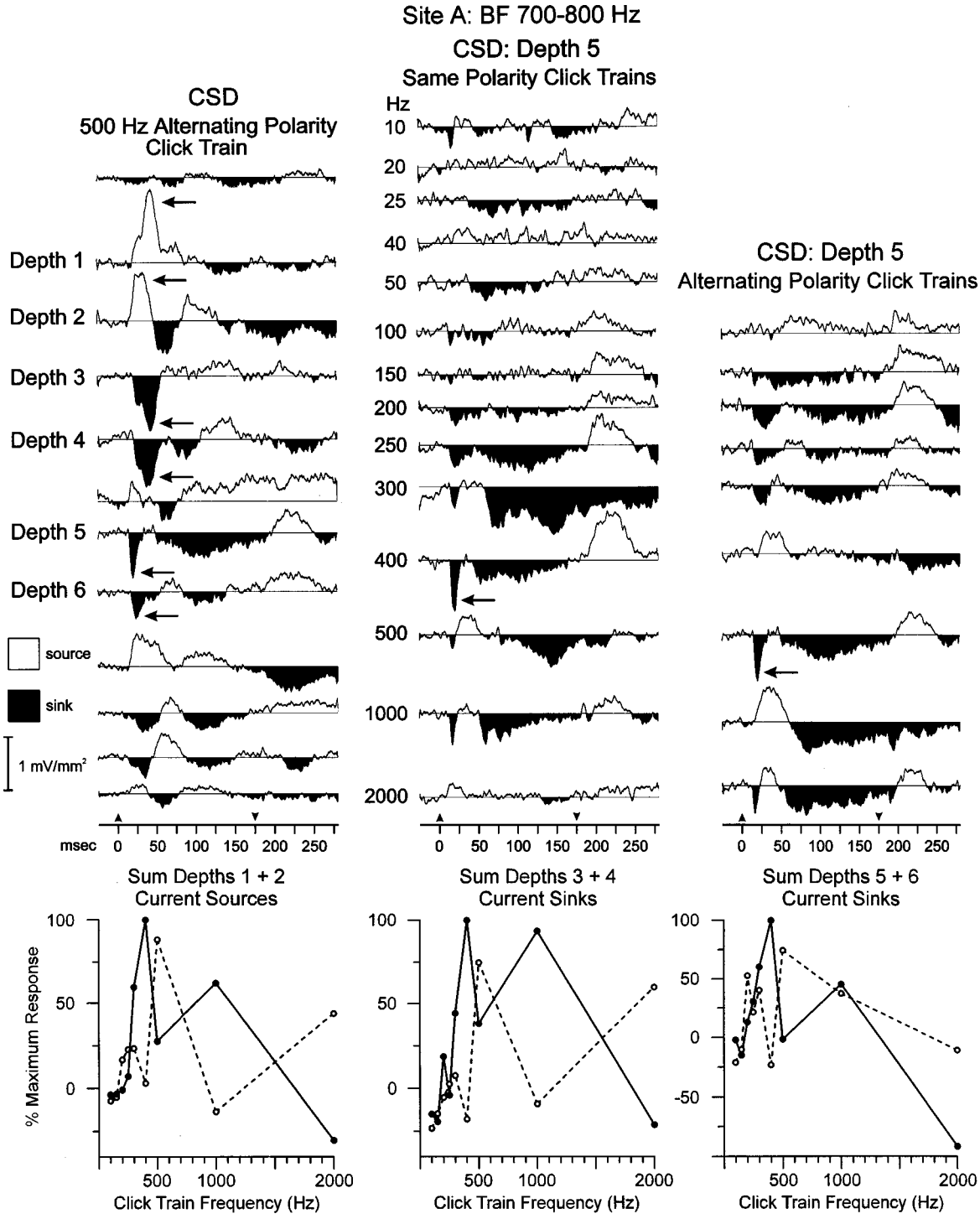

FIG. 4. CSD evoked by the click trains during the same electrode penetration as that shown in Figs. 2 and 3. The left-hand column depicts the laminar CSD profile evoked by the 500-Hz alternating polarity click train. This stimulus, which evokes large amplitude MUA in lower lamina 3, also initiates a sequence of current sources and sinks nearly identical to the 700-Hz BF tone. Arrows denote the principal current sources and sinks. The middle and right-hand columns illustrate the lower lamina 3 (depth 5) CSD evoked by the same and alternating polarity click trains, respectively. Largest amplitude responses are evoked by the 400-Hz same polarity and 500-Hz alternating polarity click trains (arrows), which can be ascribed to low-order harmonics of these stimuli lying within the BF region of this site. Graphs at the bottom of the figure depict area response measures at the principal sites of sources and sinks. In all cases, the 400-Hz same polarity and 500-Hz alternating polarity click trains evoke maximal or near maximal responses.

until tone offset. This excludes an ''off'' response from the analysis that might reflect postinhibition rebound of neural activity. The area and initial peak of the lower lamina 3 MUA are maximal at 700 Hz. There is a marked decrease in activity evoked by tone frequencies higher than 1000 Hz in both the CSD and MUA, with area measurements generally falling below baseline levels. This finding indicates the presence of a flanking, inhibitory region at frequencies somewhat higher than the BF.

Responses to click trains reflect the tonotopic sensitivity of recording site A. Figure 3 illustrates MUA recorded from the same lower lamina 3 site (depth 5) as shown in the pre-

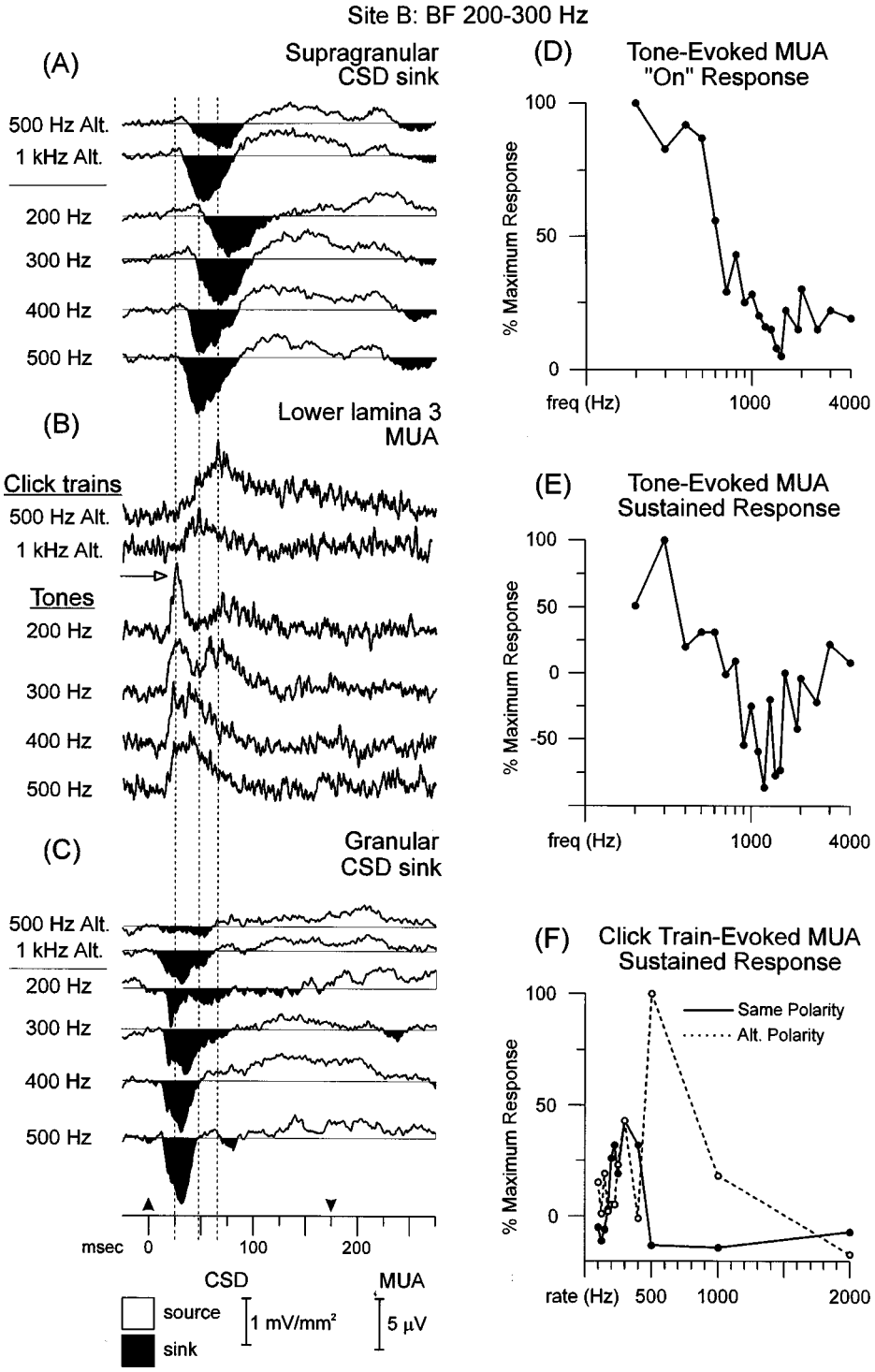

FIG. 5. Salient CSD and MUA waveforms evoked by the 500- and 1000-Hz alternating click trains and low-frequency tones from an electrode site whose BF is 200–300 Hz: (A) depicts the supragranular sink, (B) the lower lamina 3 MUA, and (C) the granular CSD sink. Lower lamina 3 MUA is recorded 600 μm below the supragranular sink and 150 μm above the granular sink. Tone-evoked lower lamina 3 MUA ''on'' (D) and sustained (E) response graphs indicate maximum activity at 200 and 300 Hz, respectively; (F) illustrates the click train-evoked MUA, and shows that the 500-Hz alternating polarity click train ($f_0 = 250$ Hz) elicits the largest response. Drop lines facilitate comparisons between tone- and click train-evoked MUA and CSD components. In (B), note that the ''on'' response in the MUA evoked by low-frequency tones (unfilled arrow) is absent in the click train responses. See text for details.

vious figure. Comparisons between responses to the same polarity (left-hand column) and alternating polarity (middle column) click trains reveal a complex pattern of activity that is best explained by relating the harmonic structure of the stimuli to the tonotopic specificity. For instance, MUA to the 500-Hz alternating polarity click train is much larger than the response to the 500-Hz same polarity click train. The third harmonic of the alternating polarity train falls within the BF response area of the site, in contrast to the harmonics of the same polarity stimulus (right-hand column). Furthermore, the third harmonic of the same polarity click train (1500 Hz) lies within the maximum inhibitory surround of this record-

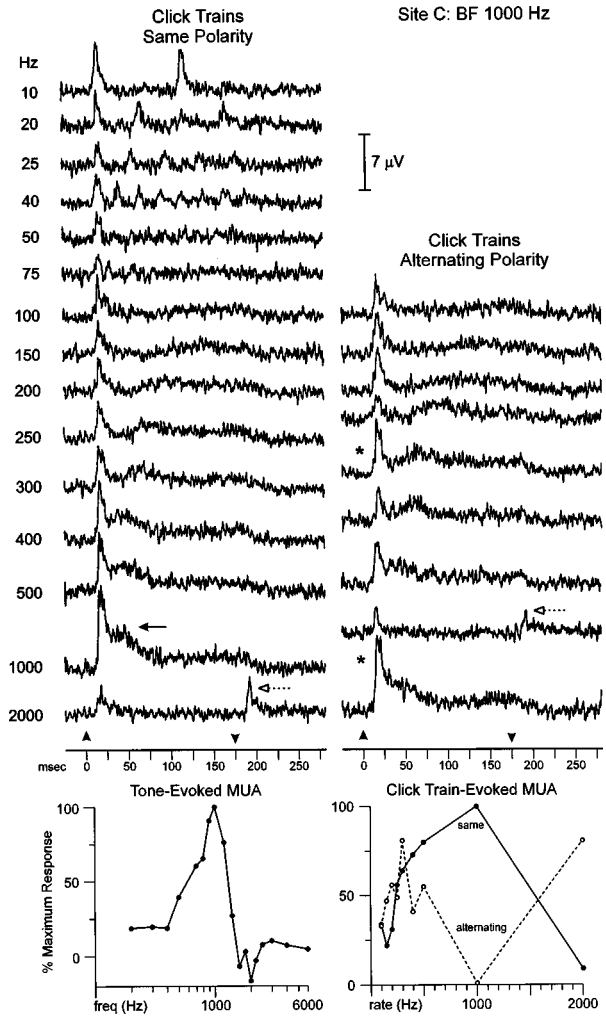

FIG. 6. Click train-evoked MUA recorded from a lower lamina 3 site. The lower left-hand graph depicts the sustained activity evoked by the tones. Maximum activity is evoked by the 1000-Hz tone. Frequencies between 1600 and 2500 Hz elicit sustained inhibition. Same polarity and alternating polarity click train responses are shown in the left- and right-hand columns, respectively. Click train rate is shown at the far left of the figure. Phase-locked activity is only evoked by click trains with rates less than 50 Hz. The lower right-hand graph depicts the sustained MUA amplitudes evoked by the click trains. The largest amplitude sustained response is evoked by the 1000 Hz same polarity click train (solid arrow in the above waveforms), consistent with the BF of this site. The largest alternating polarity click train responses are evoked at rates of 300 and 2000 Hz (asterisks). The seventh harmonic of the former, and the f_0 of the latter click train, are near the BF. ''Off'' responses are evoked by the 2000-Hz same polarity and 1000-Hz alternating polarity click trains (unfilled arrows).

ing site. Similarly, the second harmonic of the 400-Hz same polarity click train is near the BF, while harmonics of the alternating polarity click train fall outside this spectral region. These differential spectral patterns explain the markedly enhanced response evoked by the 400-Hz same polarity click train when compared to its alternating polarity counterpart. Identical rationales can explain the differences in response sensitivity for the other click train comparisons. For instance, the 300-Hz alternating polarity click train elicits a much larger response than its same polarity counterpart. The fifth harmonic of the alternating polarity stimulus is near the BF, in contrast to the harmonics of the same polarity click train. A 50-Hz reduction in click train rate evokes a larger response for the same polarity stimulus. Now, the third harmonic of the 250-Hz same polarity click train lies near the BF, while the harmonics of the alternating polarity fall outside this region. There is also a lack of response to the 1000- and 2000-Hz click trains in both the same and alternating polarity conditions. For these four stimuli, low harmonic components are present in the inhibitory surround flank of the spectral sensitivity curve and appear to dominate the response to the total sound. Of importance is the absence of synchronized phase-locked activity in the neuronal ensembles to the individual click pulses for even the lowest frequency click trains.

Response differences are quantified at the bottom of Fig. 3. The 500-Hz alternating polarity click train elicits the maximum area response (left-hand graph). The next largest response is to the 200-Hz alternating polarity click train. Its seventh harmonic is at the BF of 700 Hz. The 250- and 400-Hz same polarity click trains elicit the next largest responses, and their harmonics are also near the BF. Similar patterns, with minor variation, are seen for the peak initial responses (right-hand graph).

CSD profiles at site A demonstrate comparable features of spectral sensitivity to click trains (Fig. 4). The left-hand column illustrates the laminar CSD profile elicited by the 500-Hz alternating polarity click train. This stimulus, which elicits large amplitude MUA as shown in the previous figure, produces a laminar profile of activity very similar to that evoked by the 700-Hz tone (see Fig. 2, left-hand column). This finding indicates that excitatory stimuli engage a similar sequence of synaptic events across laminae and illustrates the stability of the multicontact electrode recordings over time. The middle and right-hand columns depict the lower lamina 3 CSD at depth 5 to same and alternating polarity click trains. Once again, there is a near absence of ensemble-wide phase locking to the individual click pulses. The largest initial current sinks are evoked by the 400-Hz same polarity and 500-Hz alternating polarity click trains (arrows), mirroring the MUA responses shown in Fig. 3. Furthermore, this relative specificity is maintained in the amplitudes of the other granular and supragranular current sources and sinks, as depicted in the graphs at the bottom of the figure. For all three measures, the 400-Hz same polarity and 500-Hz alternating polarity click trains evoke maximal or near maximal responses. Thus, the combined data for the MUA and CSD indicate that this site is sensitive to the spectral content of click trains, and responds most vigorously when low number harmonics are in the vicinity of the 700-Hz BF.

Remarkably, the previous example demonstrates that differential spectral encoding of click trains in A1 can begin with the earliest depolarization in the thalamorecipient zone of lamina 4 and lower lamina 3. Spectral encoding occurs despite the fact that all trains contain the same initial click at stimulus onset. Thus, there is a very rapid integration of information pertaining to spectral content in the earliest cortical responses, suggesting that subcortical processing performs some form of spectral encoding. However, onset responses evoked by thalamocortical fiber input may not be a consistent indicator of click train spectral content. Instead, later and more sustained activity reflecting intracortical pro-

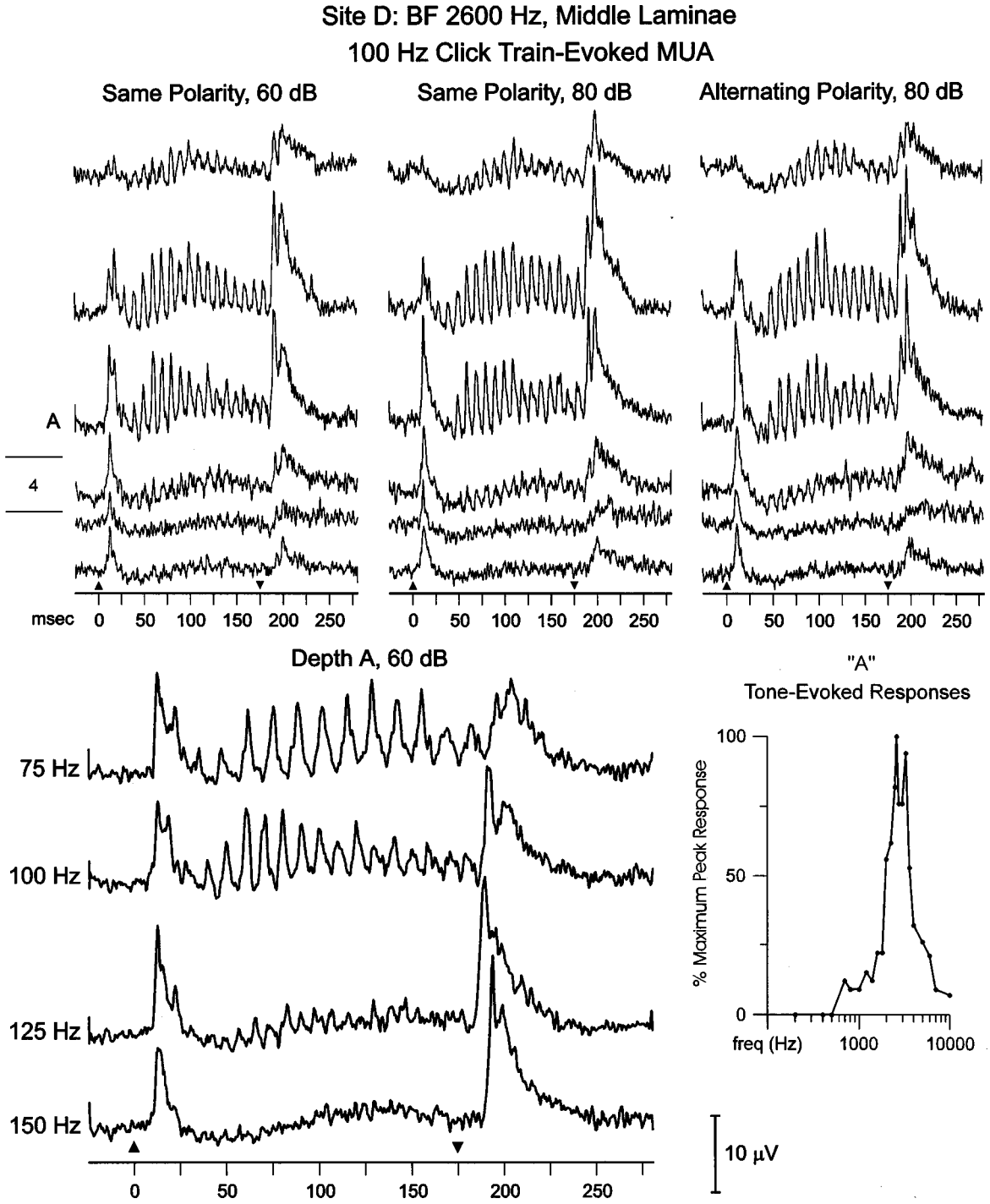

FIG. 7. The upper half of the figure depicts middle laminae MUA simultaneously recorded at 150-μm intervals in response to 100-Hz click trains presented as same polarity stimuli and at 60 dB (left-hand column), 80 dB (middle column), and as an alternating polarity train at 80 dB (right-hand column). Approximate depth of lamina 4 is indicated at the far left of the figure. Peak tone-evoked responses at depth ''A,'' located in lower lamina 3, are shown in the lower right-hand graph and indicate a maximum response at 2600 Hz. Responses at the same middle laminae locations are nearly identical, demonstrate ensemble-wide phase-locking at 100 Hz, and are independent of suprathreshold intensity and pulse polarity pattern. MUA evoked by same polarity click trains presented at 60 dB and recorded from depth ''A'' are shown in the bottom of the figure, and demonstrate phase-locked activity that dissipates at rates above 125 Hz.

cessing may represent a better measure of the spectral composition of these complex stimuli (Fig. 5, site B). At this site with a BF of 200–300 Hz, tone-evoked MUA consist of an initial ''on'' response (unfilled arrow) followed by later and more sustained activity [Fig. 5(B)]. Alternating click trains of 500 and 1000 Hz fail to evoke an ''on'' response. In the granular layer, CSD sinks are temporally coincident with the initial ''on'' response components in the MUA to the low-frequency tones [Fig. 5(C), left-most vertical drop line]. Despite the presence of these current sinks evoked by the click trains, they are not associated with coincident MUA responses.

In contrast, the later, supragranular sinks shown in Fig. 5(A), located 600 μm above (B), are associated with the

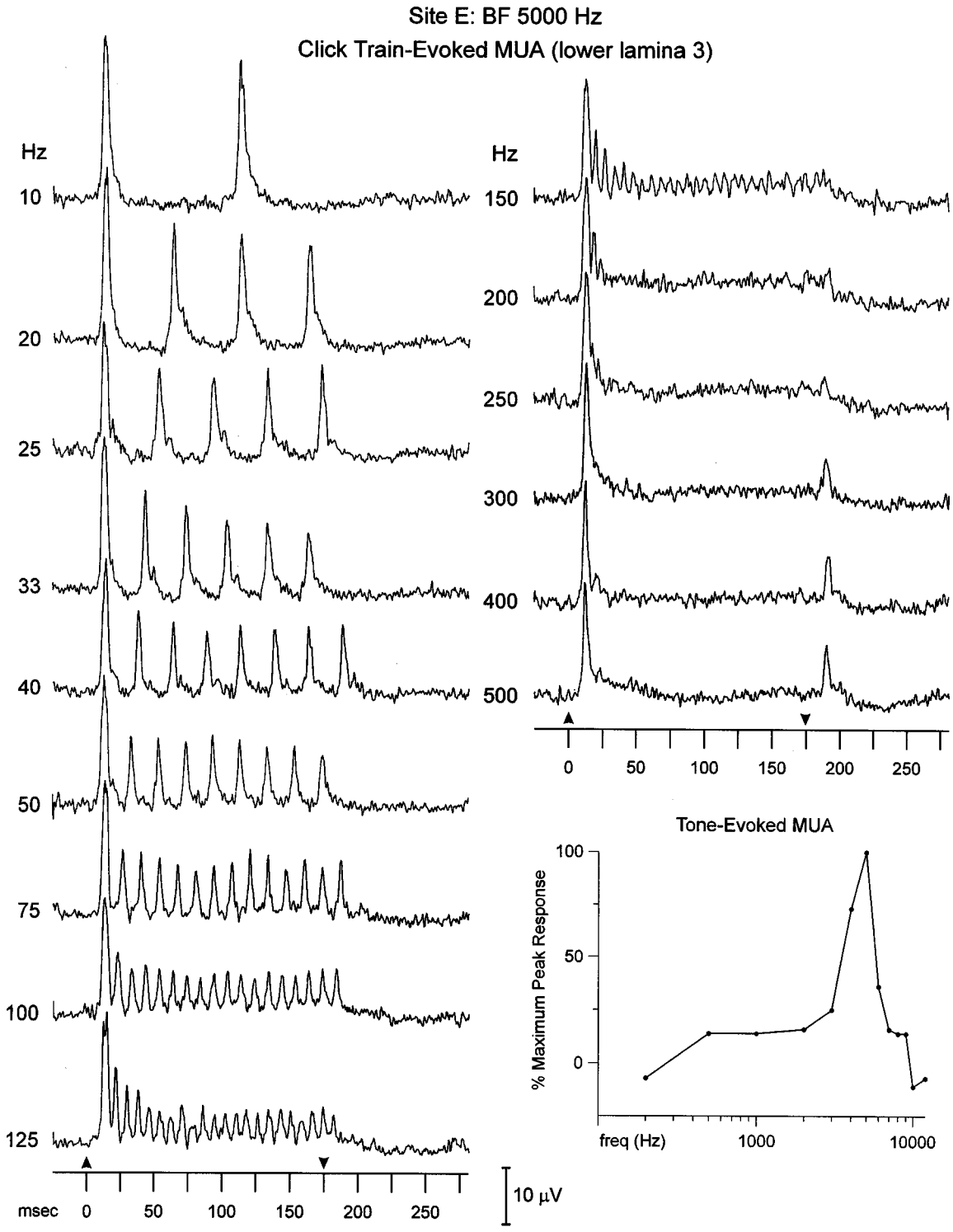

FIG. 8. MUA recorded from a lower lamina 3 site with a maximum tone-evoked response elicited at 5000 Hz (lower right-hand graph). Phase-locked responses are evoked by same polarity click trains at rates as high as 150 Hz.

click train-evoked MUA and demonstrate the spectral encoding of these stimuli. The current sinks in Fig. 5(A) evoked by the tones are characterized by an increase in latency as the frequency of stimulation decreases from 500 to 200 Hz. Timing of these supragranular sinks is nearly identical to the peaks of the more sustained tone-evoked MUA in Fig. 5(B). The current sink in Fig. 5(A) evoked by the 500-Hz alternating polarity click train is longer in latency than that associated with the 1000-Hz alternating polarity click train, and the peaks of these sinks are temporally coincident with the peaks in the sustained MUA to the same stimuli. Latencies of the supragranular sink and MUA to the 500-Hz alternating polarity click train are nearly coincident with those elicited by the 200- and 300-Hz tones. The latter are near the f_0 of this click train. A different pattern is seen for the 1000-Hz alternating polarity click train, where timing of the supragranular

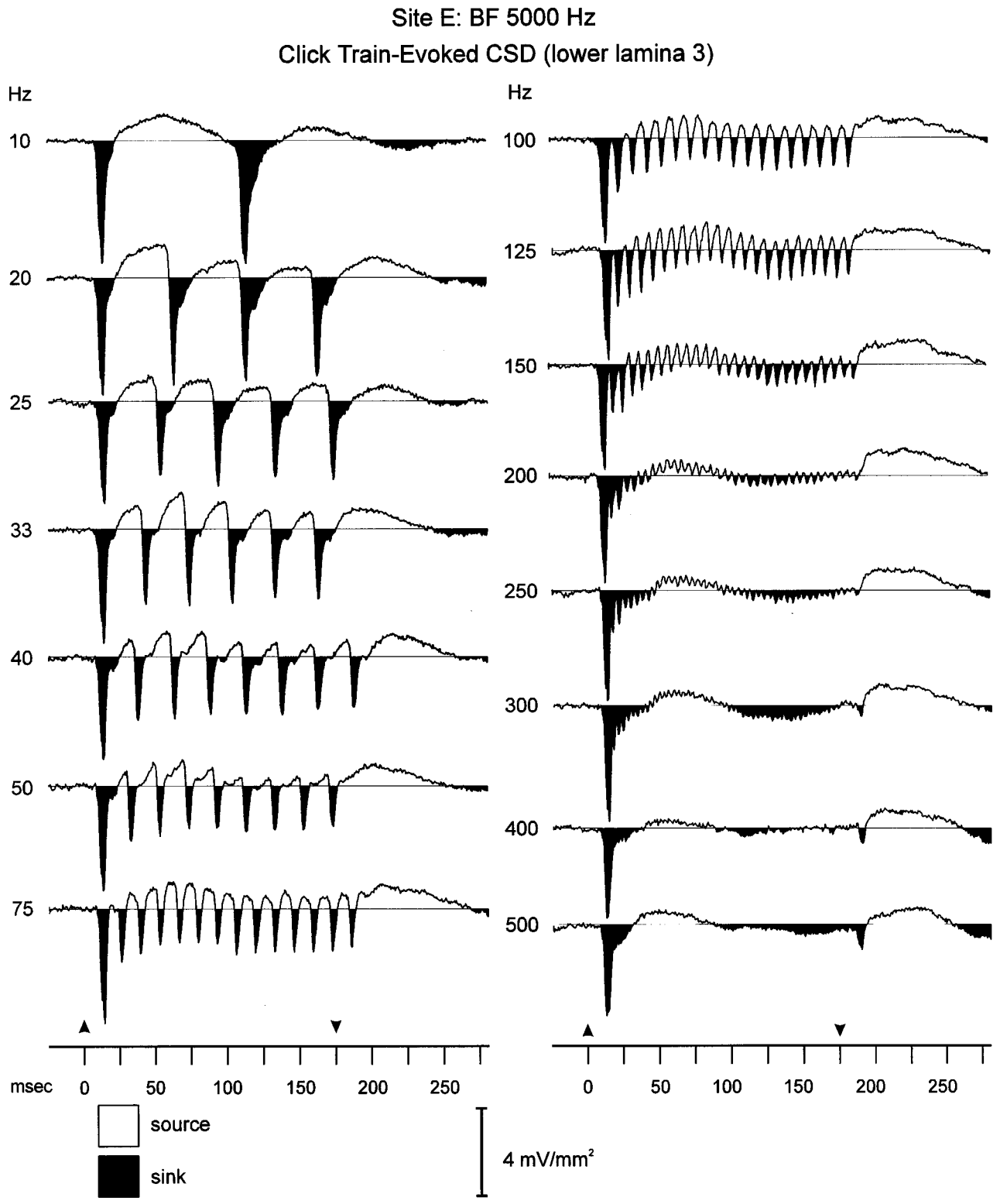

FIG. 9. CSD recorded from the same lower lamina 3 site shown in the previous figure. Phase-locked CSD components are evoked by click trains at rates up to 300 Hz.

sink and MUA is coincident with the 500-Hz tone, consistent with its f_0. These findings illustrate that the click train-evoked MUA is dependent on the tonotopic sensitivity of this site, and that this sensitivity is based on activity derived from intracortical processing and not the initial cortical activation.

Responses are quantified in the graphs shown in (D), (E), and (F) of Fig. 5. The 200-Hz tone evokes the largest MUA initial ''on'' response [Fig. 5(D)] and the 300-Hz tone elicits the largest sustained response [Fig. 5(E)]. A trough that dips below baseline levels between about 1000 and 2000 Hz is also observed, suggesting an inhibitory flank at these

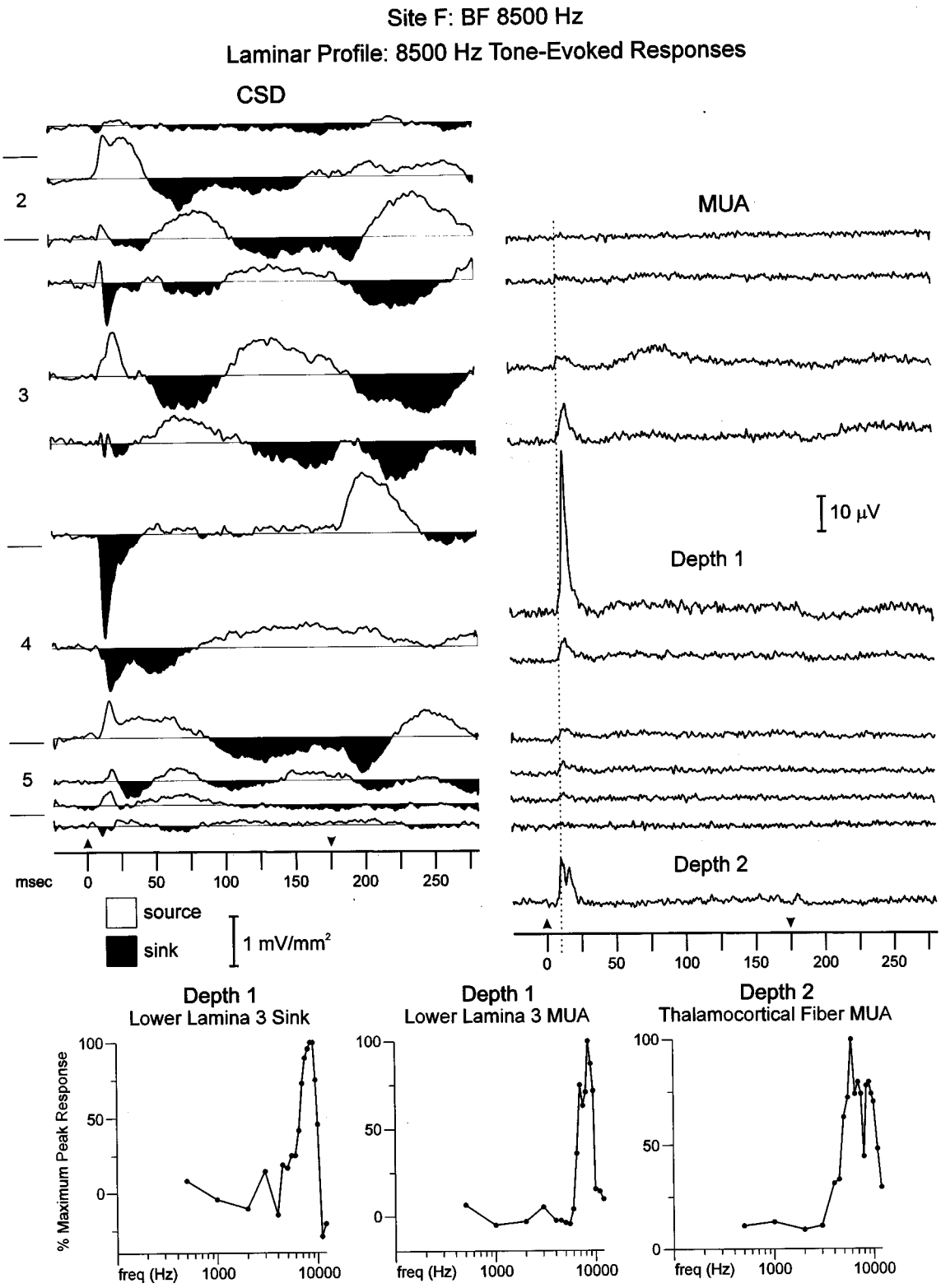

FIG. 10. CSD and MUA laminar profiles simultaneously recorded at 150-μm intervals in response to an 8500-Hz tone. CSD and MUA located at depth 1 are maximally responsive to the 8500-Hz tone (left and center graphs). MUA recorded 900 μm deeper at depth 2, located at the boundary of lamina 6 and the white matter, has an onset and peak that is 3 ms earlier than that at depth 1. This indicates the MUA is of thalamocortical fiber origin. The dotted drop line in the MUA profile facilitates this comparison. These afferents are maximally responsive to a 6000-Hz tone, suggesting that they are primarily fibers of passage.

higher frequencies. As predicted by the tone response specificity, the 500-Hz alternating polarity click train with its 250-Hz f_0 yields the largest response for this class of stimuli [Fig. 5(F)]. The largest same polarity click train response occurs when the rate is 300 Hz, again consistent with the tonotopic organization of this site. The pronounced difference between the maximum response observed for the same and alternating polarity click trains may reflect inhibitory

harmonic interactions that are more intense for the former stimuli. This in turn may be due to a greater number of harmonics lying within the inhibitory surround region of this site. While not shown, the lowest rate click trains (i.e., 10–100 Hz) fail to elicit phase-locked activity in the ensemble responses.

MUA phase-locked to individual click train pulses is not a prominent feature of the responses at most low BF sites. When it does occur, the upper limit is almost always less than 100 Hz (Fig. 6, site C). MUA at this lower lamina 3 site is phase-locked to individual pulses at rates less than 50 Hz. It is important to stress that the absence of phase-locking in the synchronized activity of neuronal ensembles at higher rates, as measured in the MUA or CSD, does not preclude the possibility that isolated neurons are capable of generating a phase-locked response in these low BF regions of A1. The BF of site C is 1000 Hz, as measured by sustained activity from 35 ms after tone onset until offset (lower left-hand graph). Suppression of MUA to levels below baseline occurs from 1600 to 2500 Hz. Similar to other low BF sites, this location encodes click train spectral content. Because ''on'' responses evoked by click trains at this site contain spectrally insensitive activity elicited by isolated clicks, sustained MUA beginning immediately after the transient responses dissipate at 35 ms and extending until stimulus offset at 175 ms is quantified (lower right-hand graph). Maximum MUA is evoked by the 1000-Hz same polarity click train, which has a f_0 equal to the BF of this site (solid arrow). The next best same polarity click train response occurs at a stimulation rate of 500 Hz. Now, the second harmonic equals the BF. The largest responses evoked by alternating polarity click trains occur at rates of 300 and 2000 Hz (asterisks). The seventh harmonic of the 300-Hz alternating polarity click train and the f_0 of the 2000-Hz train are near the BF. The 2000-Hz same polarity click train and the 1000-Hz alternating polarity train elicit minimal sustained activity. The f_0 of the former, and third harmonic of the latter, fall within the inhibitory flank of the spectral sensitivity curve. Both responses contain an ''off'' component, presumably due to a rebound from inhibition (open arrows). The CSD profiles and MUA from other depths evoked by the tones and click trains demonstrate a similar organization (not illustrated).

B. Encoding of click trains in high BF regions of A1

The previous section demonstrates that low BF regions of A1 are sensitive to the spectral composition and polarity pattern of the click trains, and have response maxima determined by the tonotopic organization. Phase-locking within neuronal ensembles consistently remains below 100 Hz, the psychoacoustic boundary for temporal encoding of click train pitch. In contrast, higher BF regions of A1 display a different pattern of activity in response to click trains. These locations are relatively insensitive to spectral characteristics of click trains, but are instead sensitive to temporal stimulus features.

Figure 7(D) depicts, in its upper half, MUA simultaneously recorded at 150-μm intervals through middle cortical laminae in response to 100-Hz click trains of same polarity presented at 60 and 80 dB, and alternating polarity presented at 80 dB. The BFs of these locations are about 2600 Hz. Peak tone-evoked response measures for depth ''A,'' located in lower lamina 3, are shown in the graph in the lower right-hand portion of the figure. This site responds to 100-Hz click trains with prominent ensemble-wide phase-locking to the click rate that is insensitive to suprathreshold intensity changes, as well as changes in pulse polarity that alter the stimulus spectrum. Phase-locked responses are maximal in lamina 3, and are presumably dominated by synchronized action potentials of local pyramidal cells. Additionally, the phase-locked activity in lower lamina 3 MUA dissipates above 125 Hz, within the transition zone demarcating temporal from spectral pitch perception mechanisms (bottom left portion of figure).

As discussed earlier, temporal encoding mechanisms determining click train pitch are dominant at rates less than 100 Hz and are mediated by high-frequency auditory channels (Rosenberg, 1965). An ever decreasing degree of pitch based on temporal periodicity, however, occurs for click trains at f_0's up to 200 Hz. If phase-locked activity in A1 is related to this temporal pitch representation, then evidence of periodic responses at these higher repetition rates should be present at the cortical level. Supporting evidence is observed in the temporal encoding capabilities of a lower lamina 3 site with a 5000-Hz BF (Fig. 8, site E). Tone frequency plotted against peak response amplitude is shown in the lower right-hand portion of the figure. Synchronized phase-locked activity is present at click train rates up to 150 Hz. However, the CSD simultaneously recorded from the same site contains phase-locking of the current sources and sinks at click rates up to 300 Hz (Fig. 9). This finding indicates that synchronized synaptic activity in A1, derived from subcortical input, can phase-lock to click rates that support even the higher rates of click train pitch perception based on temporal periodicity.

Confirmation that A1 has access to synchronized thalamocortical fiber input with the capacity to temporally encode click trains at rates of at least 300 Hz is provided by a penetration into a site with a BF of 8500 Hz (Fig. 10, site F). Laminar recordings at 150-μm intervals in response to presentation of an 8500-Hz tone reveal a cortical MUA maximum at the base of lamina 3 that principally represents ensemble activity of cortical cells (depth 1). The MUA at this depth occurs at the focus of the earliest, large amplitude current sink. The MUA at depth 2 is recorded near the boundary between the gray and white matter (900 μm below depth 1). This activity has a peak latency 3 ms earlier than that recorded from depth 1, and primarily reflects activity within thalamocortical afferent fibers. The graphs at the bottom of the figure illustrate that maximum amplitudes of the lower lamina 3 sink and MUA are elicited by the 8500-Hz tone. The thalamocortical fibers have a different BF from the cortical MUA and CSD (6000 Hz), suggesting that these afferents are primarily fibers of passage.

Comparison of click train-evoked MUA simultaneously recorded from lower lamina 3 (depth 1) and thalamocortical fiber afferents (depth 2) illustrates the differential capacity for phase-locking between the two populations (Fig. 11). Synchronized activity in the cortical responses at this loca-

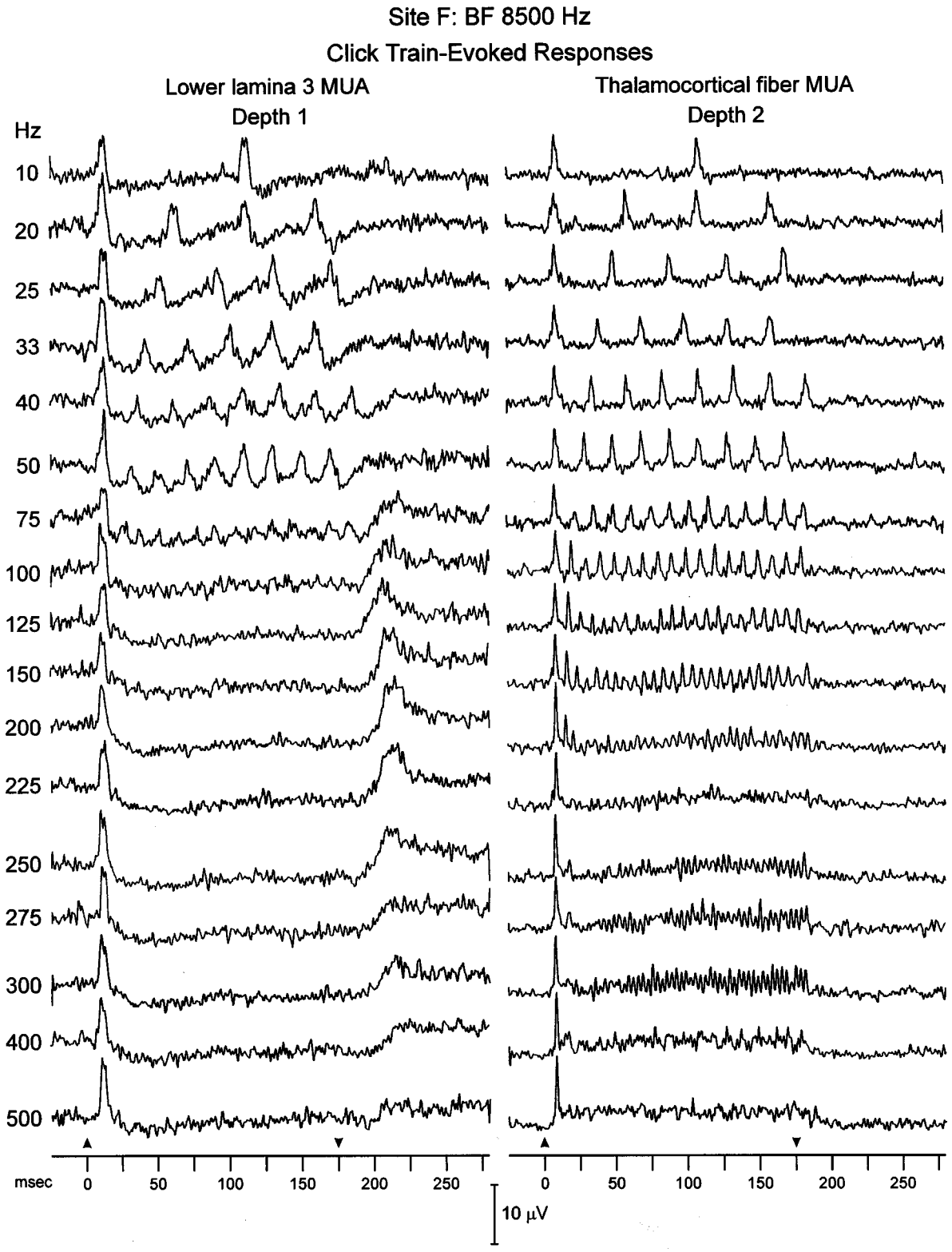

FIG. 11. MUA evoked by click trains at depths 1 and 2 shown in the previous figure. MUA of cortical origin in lower lamina 3 contains phase-locked activity that dissipates above 75 Hz. In contrast, the simultaneously recorded MUA of thalamocortical fiber origin contains prominent phase-locked activity at rates of 300 Hz.

tion is markedly diminished at a rate of 100 Hz (left-hand column), whereas thalamocortical fiber MUA contains a phase-locked response through rates of 300 Hz (right-hand column). In our sample, five penetrations (12.5%) contain thalamocortical fiber afferent MUA in infragranular laminae or subjacent white matter that phase-lock to click trains at high rates. The upper limit of synchronized phase-locking is 300 Hz in three cases, 400 Hz in another, and 200 Hz in the last.

Synchronized phase-locking to the 100-Hz click train are segregated in the higher BF regions of A1 (Fig. 12). This summary depiction of all recorded lower lamina 3 MUA

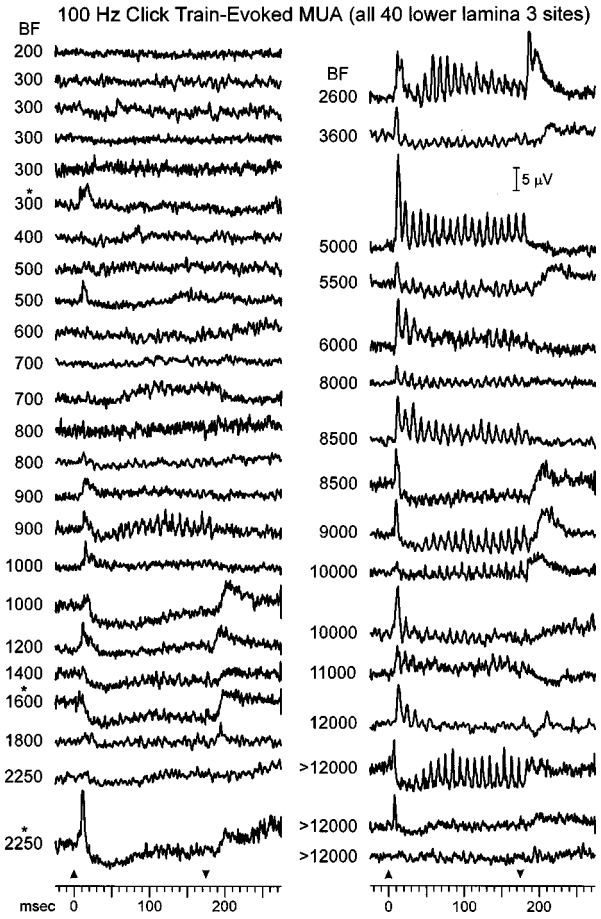

FIG. 12. Summary of all MUA recorded in lower lamina 3 and evoked by 100-Hz click trains from the 40 electrode penetrations of the study. BF of the sites are indicated to the left of the waveforms. Asterisks above the BF indicate click train presentation at 80 dB. Phase-locked activity is differentially distributed within higher BF sites.

sites reveals that of the 24 penetrations whose BFs are 2250 Hz or less, only 1 location (900-Hz BF) has prominent phase-locking of the MUA at 100 Hz. MUA at six of eight penetrations with a BF of 1000–2250 Hz consists of an ''on'' and ''off'' response with an intervening period of suppression that is most pronounced immediately after the ''on'' response and persists throughout the duration of the stimulus. At locations with a BF less than 1000 Hz, the 100-Hz click train either fails to evoke a clear MUA response, or the stimulus elicits an ''on'' or low-amplitude sustained response. In contrast, phase-locked activity is evoked by the 100-Hz click train at 12 of 16 locations with a BF of 2600 Hz or greater. This activity can be superimposed on either sustained increases or decreases in the MUA. At sites where there is both phase-locked activity and MUA suppression below baseline levels, there is a tendency for the periodic responses to be delayed and begin following an initial ''on'' response and period of MUA inhibition.

A greater extent of synchronized phase locking to the 100-Hz click train occurs in the CSD profiles at the same lower lamina 3 sites (not illustrated). Phase-locking is observed at 13 of 17 locations with a BF between 500 and 2250 Hz, and at the higher BF sites that do not display this response pattern in the MUA. This finding indicates that there

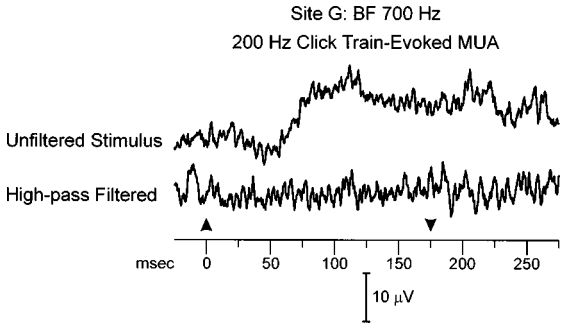

FIG. 13. MUA summed across middle laminae evoked by a 200-Hz click train that is unfiltered and high-pass filtered above 2 kHz. BF of this site is 700 Hz. The sustained response evoked by the unfiltered stimulus is eliminated after filtering. See text for details.

is a greater capacity for phase-locking at 100 Hz in the synchronized activity of thalamocortical afferents, which in turn evokes synchronized synaptic responses as manifested in the CSD. There is also a greater extent of phase-locking in the cortical MUA at lower repetition rates. For instance, the 50-Hz click train was presented during 38 of 40 electrode penetrations into A1. Synchronized responses occur at most sites with a BF greater than 700 Hz. The 50-Hz click train evokes minimal activity at the lowest BF sites in our sample.

The effects of increasing click intensity from 60 to 80 dB on the encoding of click train rate was examined during four penetrations with BFs ranging from 2600–10 000 Hz. No increase in the upper limit of synchronized responses was observed in the CSD and MUA, though a modest increase in response amplitude was seen at one site. At two sites with lower BFs where 100-Hz click trains presented at 60 dB did not evoke synchronized responses, increasing the intensity to 80 dB failed to elicit a qualitative change in the response

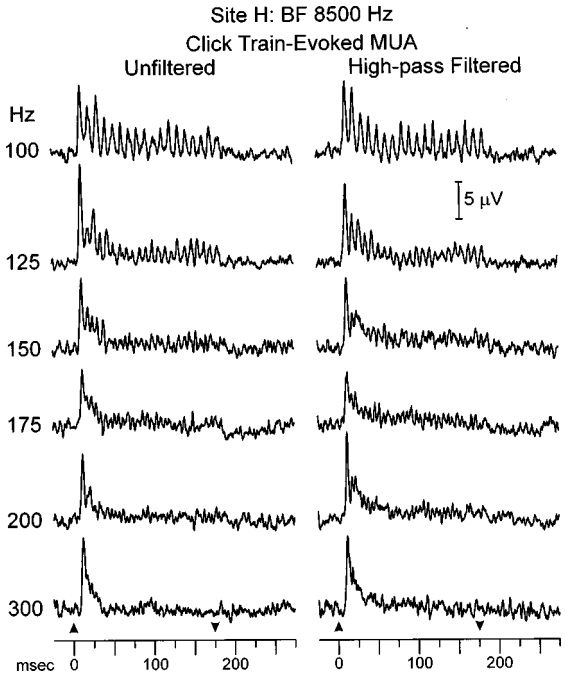

FIG. 14. Click train-evoked MUA at a lower lamina 3 site whose BF is 8500 Hz. Phase-locked activity is present at rates up to 200 Hz. High-pass filtering has no significant effect on the response patterns.

patterns. These findings suggest that stimulus intensity is not a major determinant of the synchronized responses at these suprathreshold levels.

C. Effects of high-pass filtered click trains on A1 responses

High-pass filtering of click trains raises the perceptual boundary at which the transition from periodicity to spectral pitch occurs to levels above the usual 100–200 Hz range (Guttman and Flanagan, 1964). This effect could be due to an increase in the upper limit of synchronized phase-locked responses in higher BF regions of A1. On the other hand, high-pass filtering could decrease competing spectral encoding information emanating from lower BF regions of A1, thereby making more salient weaker temporally based response patterns, especially at high rates of stimulation. Additionally, phase-locked activity could appear in lower BF regions. In order to investigate these possibilities, we examined the physiological effects produced by click trains high-pass filtered above 2 kHz during 15 electrode penetrations in one monkey.

High-pass filtering elicits characteristic changes in the evoked activity within low and middle BF regions of A1 that are related to effects on spectral encoding of the stimuli. Typically, there is a decrease in the degree of excitation produced by click trains, exemplified by the summed, middle laminae MUA from a site with a BF of 700 Hz (Fig. 13, site G). An unfiltered 200-Hz click train evokes MUA with a sustained increase above baseline levels that persists for more than 100 ms after stimulus offset. The response is most likely based on harmonic components of the stimulus falling within the spectral response area of the recording site. This supposition is supported by the absence of evoked activity when the same stimulus is high-pass filtered above 2 kHz. In this condition, remaining spectral components lie outside the spectral response area of the site and fail to elicit evoked activity. This pattern is observed in six of eight penetrations with a low to moderate BF. In the seventh penetration, sustained suppression produced by a 100-Hz click train at a site with a BF of 600 Hz is decreased following high-pass filtering. In the eighth site with a BF of 2250 Hz, a high-pass filtered 100-Hz click train elicits a stronger sustained response than its unfiltered counterpart, presumably because low-frequency harmonic components that evoke inhibition are removed from the stimulus. In no case did phase-locked responses appear in these BF regions following high-pass filtering of the click trains. High-pass filtering has no major effect on synchronized phase-locked activity in high BF regions, exemplified by the lower lamina 3 MUA from a site with a BF of 8500 Hz (Fig. 14, site H). Both filtered and unfiltered click trains evoke phase-locked activity of similar amplitude at rates up to 200 Hz.

III. DISCUSSION

A. Summary of findings and relationship to click train pitch perception

Correlating neural responses with psychoacoustical phenomena is a necessary first step for identifying physiological mechanisms that underlie pitch perception. Ideally, neural responses would be identified that differentiate between encoding of click train pitch based on pulse rate and f_0 (Flanagan and Guttman, 1960a, b; Guttman and Flanagan, 1964; Rosenberg, 1965). f_0 encoding of click trains should occur at f_0's greater than 200 Hz and be dependent on the polarity pattern of the clicks. Pitch based on pulse repetition rate should be independent of click polarity pattern, and occur at rates of at least 100 Hz. Furthermore, f_0 encoding of click train pitch should occur in low-frequency channels of the auditory system, while rate encoding should be located in high-frequency channels. A1 responses conform to these perceptual requirements. Both temporal and spectral forms of click train encoding are demonstrated. Rate of stimulation is temporally encoded at pulse rates below 100–200 Hz through synchronized phase-locked responses of neuronal ensembles, is independent of click polarity pattern, and occurs in higher BF regions. Limiting frequencies for ensemble-wide phase-locking occurs in the transition zone between which the spectral and temporal forms of click train pitch predominate. In contrast, the spectral form of encoding is dependent on the polarity pattern of the stimuli, occurs in lower BF regions, and resolves both the f_0 of higher click train rates and the major harmonics of the stimuli through local maxima of activity. These maxima are determined by the tonotopic organization of the A1 sites.

Boundary shifts between spectral pitch and pitch based on repetition rate elicited when high-pass filtered click trains are used, or when low- or high-frequency masking noise is simultaneously presented with the click trains, can be explained by A1 activity (Guttman and Flanagan, 1964; Rosenberg, 1965). The temporal form of pitch perception gradually weakens at rates above 100 Hz as the upper limit of synchronized phase-locked activity is approached. High-frequency noise would mask the less secure and lower amplitude phase-locked activity to faster click train rates, allowing the competition in pitch perception between temporal encoding within high BF regions of A1 and spectral encoding in low BF regions to shift in favor of the latter. In contrast, low-frequency noise or high-pass filtered click trains would degrade the spectral representation of very low f_0's and shift the perception towards a temporally based pitch encoded in higher BF regions.

Compelling evidence supporting the existence of two separate mechanisms for pitch perception is presented in a series of experiments by Carlyon and colleagues (Carlyon and Shackleton, 1994; Shackleton and Carlyon, 1994; Plack and Carlyon, 1995). In these studies, harmonic complexes were summed in either same or alternating phase, and then bandpass filtered to accentuate low, middle, or high frequencies. The pitch of alternating phase complexes was an octave higher (i.e., twice the pitch) than that generated by summing same phase harmonics when the sounds were high-pass filtered. This finding is consistent with the pitch of the sounds being determined from the periodicity of the stimulus waveforms, because the high-pass filtered alternating phase stimuli had twice the number of waveform peaks than the same phase complexes. Low-pass filtered complexes were equated according to f_0, and not stimulus periodicity. Band-

pass filtering at moderate frequencies produced two different results based on the resolvability of the harmonics. With higher f_0's and resolved harmonic components, pitch was determined by the f_0. At lower f_0's and filtered stimuli containing only unresolved harmonics, pitch was based on stimulus periodicity. Transition between the two forms of pitch perception occurred at a f_0 of about 125 Hz. Sensitivity to f_0 differences was best when the combination of f_0 and low-, middle-, or high-pass filtering was such that both stimuli were composed of only resolved or unresolved harmonics, and worse when comparisons were between stimuli with resolved versus unresolved harmonics. Furthermore, f_0 encoding using only unresolved components was degraded with stimuli less than 100 ms in duration, whereas the same task using resolved harmonics was accurate even when sounds had a duration of only 25 ms. These experiments provide strong evidence that resolved and unresolved harmonics are processed using different perceptual mechanisms, and that the mechanism associated with unresolved harmonic components uses waveform periodicity as a key feature in the process.

Our data are in agreement with these results, providing additional weight to the hypothesis that temporal encoding within A1 based on synchronized phase-locked activity is a physiological finding relevant for pitch perception and not just an epiphenomenon of cortical activity. For instance, we find that neural activity in A1 reflects twice the f_0 at lower rates of stimulation for alternating polarity components, and that 125 Hz is within a transition region between spectral and periodicity encoding. When the extent of ensemble-wide phase-locking in A1 between 50- and 100-Hz click trains was compared, we found that periodic MUA responses extend into middle BF regions at the lower stimulus repetition rate. This finding parallels those of Carlyon and colleagues, and indicates that an important parameter determining whether phase-locking in A1 occurs is the critical band of specific BF regions. Thus, when multiple harmonic components fall within a critical band of a BF region, phase-locked responses will be generated and repetition pitch will be augmented. There are also parallels in our data and the requirement that pitch encoding of unresolved harmonics needs a prolonged stimulus duration, while spectral encoding can be performed within 25 ms. Examination of Fig. 12 reveals that at many A1 locations, phase-locking is delayed relative to stimulus onset. Additionally, measures of pitch based on pulse rate would require a number of stimulus cycles to occur in order for rate to be determined in the neural responses. In contrast, spectral components of click trains can be resolved in the initial cortical responses, though sustained activity does yield more accurate measures.

The ability of amplitude-modulated (AM) noise and other sounds with absent spectral cues to evoke sensations of pitch and melody provides additional evidence for the existence of pitch-related mechanisms based on the encoding of waveform periodicity (Burns and Viemeister, 1981; Warren and Wrightson, 1981; Pierce, 1991). Upper limits of periodicity pitch ranged from 200 to 500 Hz, higher than the phase-locked activity observed in our sample of cortical MUA. However, thalamocortical fiber MUA input into A1 and subsequent thalamorecipient zone CSD components do phase-lock at these higher rates, suggesting that information relevant for temporal pitch at high rates has a cortical correlate. Higher stimulus repetition rates generally evoke very weak pitch perceptions based on timing cues, perhaps secondary to the inability of A1 ensembles to synchronously fire at rapid rates of stimulation. It must be conceded, however, that weak periodicity pitch at high rates of stimulation may be based solely on other mechanisms, including its mediation by subcortical auditory centers.

Phase-locked activity in A1 populations may also be a relevant mechanism for the perception of sensory consonance and dissonance. Sensations of roughness, the perceptual correlate for audible beats in a sound, correlate with judgments of sensory dissonance (Terhardt, 1974a, 1977). These beats are thought to be encoded by the temporal envelope of evoked neural responses (Terhardt, 1974b). The pronounced amplitude fluctuations in the cortical responses evoked by lower frequency click trains could be a powerful signal for sensory roughness. Psychoacoustical studies indicate that consonance of two-tone complexes is maintained when the frequency difference exceeds the critical bandwidth, while maximal dissonance occurs when the frequency difference is about one quarter the bandwidth (Plomp and Levelt, 1965). Published values of maximum dissonance for specific mean frequencies of two-tone complexes and for click trains are in accord with present findings (Plomp and Steeneken, 1968; Terhardt, 1974b), wherein high BF regions display synchronized phase-locking at 100 Hz, while synchronized phase-locking in regions with BFs between 700 and 2000 Hz are generally limited to rates of 50 Hz.

Present data support models of pitch perception that utilize template matching of resolved, harmonic components to determine the f_0 (e.g., Goldstein, 1973; Terhardt, 1974a). Responses within low BF regions of A1 encode stimulus harmonics, without special regard to the f_0. Foci of maximum activity are determined by the harmonic structure of the stimulus interacting with the excitatory and inhibitory frequency bands of the A1 sites. Our findings thus support evidence indicating that A1 utilizes a rate code for encoding the spectral structure of complex stimuli, producing distributed patterns of activation across tonotopically organized auditory cortex unique for each sound (e.g., Ehret, 1997; Schreiner, 1998). However, this scheme does not identify mechanisms that might be used for template matching in order to form a unitary perception of virtual pitch. It is also unclear whether these distributed patterns of A1 activation are capable of supporting the fine pitch discrimination capacities for the f_0 of harmonic sounds. Most importantly, these findings do not exclude other mechanisms, such as those that use autocorrelation, which might be operative in A1 but underappreciated by our techniques, or occurring at other levels of the auditory system (e.g., Meddis and O'Mard, 1997).

B. Relationship to other auditory physiological studies

Cariani and Delgutte (1996a, b) provide powerful experimental data supporting an autocorrelation method of pitch perception by demonstrating that most pitch phenom-

ena can be adequately explained by defining the peaks in all-order interspike interval distributions within the summed activity of auditory nerve fibers. The major difficulty with their analysis was the failure to account for pitch based on rate for lower frequency alternating polarity click trains. To account for this discrepancy, the authors suggest that a more likely mechanism uses phase-locking to click rate in the auditory nerve fiber population, especially those with higher BFs. This conclusion is similar to that presented here, and suggests that mechanisms important for low-frequency periodicity pitch is initiated in the auditory nerve and maintained through A1.

For stimuli that might engage autocorrelation methods within the auditory nerve to encode pitch, a transformation from a temporal code to a code utilizing rate of excitation and topographic organization has been suggested to occur in the inferior colliculus (Langner and Schreiner, 1988; Schreiner and Langner, 1988). This finding suggests the development of a topographic organization based not on spectral content, but rather one based on pitch. A pitch representation in human auditory cortex has been proposed from analysis of neuromagnetic responses to multiharmonic tone complexes (Pantev *et al.*, 1989, 1996). While provocative, this and other studies found no evidence for an A1 organization based on the f_0 of harmonic sounds (Schwartz and Tomlinson, 1990; Fishman *et al.*, 1998). In contrast, responses reflect the harmonic structure of the stimuli and their relationship to spectral tuning curves. Other means of pitch encoding are clearly not excluded by these data, and include the possibility of differential activity along isofrequency lines in A1 to distinguish stimuli with similar spectral content but different pitches, or pitch representation due to spectral integration within nonprimary auditory cortex (Rauschecker *et al.*, 1995; Langner *et al.*, 1997). The latter possibility is especially intriguing, since studies in the human have indicated that nonprimary auditory cortex in the nondominant hemisphere plays a key role in pitch processing (Zatorre, 1988; Divenyi and Robinson, 1989; Robin *et al.*, 1990; Zatorre *et al.*, 1992, 1994). In this scheme, A1 activity encoding temporal and spectral features of harmonic complexes would serve as input for later processing stages within secondary auditory cortex in order to extract the pitch of the sounds.

There is close correspondence between the present results and previous examinations of click train-evoked phase-locking activity in A1. The upper limit of phase-locked evoked potentials in the unanesthetized cat is 200 Hz (Goldstein *et al.*, 1959). Isolated pyramidal cells recorded from the unanesthetized cat typically phase-lock to the repetition rate of click trains with a median limiting rate of 50–100 Hz, a limiting rate greater than 100 Hz in 32%, and an upper limit greater than 300 Hz (Ribaupierre *et al.*, 1972). An additional population of cortical neurons, characterized by short duration action potentials (''thin spikes'') and thought to represent lamina 4 stellate cells, is able to phase-lock to click trains at rates up to 400 Hz. The present study has shown phase-locking in the cortical CSD and thalamocortical afferent MUA at rates comparable to both the ''thin spiking'' cells in A1 and other studies examining click train encoding in the medial geniculate nucleus (Rouiller *et al.*, 1981; Rouiller and Ribaupierre, 1982). Thus, it appears that phase-locked input into auditory cortex may reflect the upper limit of pitch encoding based on temporal mechanisms.

Limiting rates for A1 phase-locked activity in both our ensemble data and in the studies cited above are greater than similar investigations examining single unit responses in A1 of anesthetized cats (e.g., Eggermont, 1991, 1994; Eggermont and Smith, 1995; Schreiner and Raggio, 1996). In these studies, phase-locked responses always dissipate at rates greater than 32 Hz. However, a profound decrease in phase-locked activity occurs in cat A1 following administration of barbiturates (Goldstein *et al.*, 1959; Mäkelä *et al.*, 1990; Eggermont and Smith, 1995). This consideration minimizes the discrepancy between the upper limit of synchronized phase-locking to clicks trains in our study using awake monkeys and those performed in anesthetized cats.

Finally, it is necessary to address the relevance of ensemble activity as physiological indices important for encoding of click trains. Using a technique of MUA recording very similar to that utilized in the present study, Nelken and colleagues (1994) determined that ensemble recordings are statistically more stable than single unit activity in cat A1, and have comparable temporal and spectral response specificities. These findings indicate that ensemble recordings gain fidelity without significant loss of response specificity present in single unit responses. Additionally, analysis of responses in A1 evoked by complex stimuli has led to the conclusion that synchronized activity of neuronal ensembles is more likely relevant for sound processing than the activity of single neurons, may more accurately encode important sound parameters, and may lead to improved activation of cortical areas involved in further sensory processing (Creutzfeldt *et al.*, 1980; Eggermont, 1994; Wang *et al.*, 1995; deCharms and Merzenich, 1996).

IV. SUMMARY AND CONCLUSIONS

Encoding of click trains in primary auditory cortex of awake monkeys is examined in order to clarify neural mechanisms associated with pitch perception. A1 differentially encodes temporal and spectral features of click trains. Temporal features are encoded within high best frequency regions, and occur at rates less than 100–200 Hz via synchronized phase-locked activity in the responses of cortical ensembles. Activity reflecting thalamocortical input into A1 has an upper limit of ensemble-wide phase-locking about twice that of the cortical ensembles. Spectral features of click trains are encoded in low best frequency regions of A1, and occur at higher rates of stimulation. Responses in low best frequency regions are sensitive to the pitch polarity pattern, and encode both the f_0 and other harmonics of the trains via a rate code that is determined by the tonotopic sensitivity of the recording sites. High-pass filtered click trains decrease spectral encoding in low best frequency regions but do not alter phase-locked activity in other locations. Physiological responses parallel multiple features of human pitch perception for click trains, and support the existence of two, distinct mechanisms in A1 involved in pitch perception. The first mechanism utilizes resolved harmonic components, produc-

ing patterns of distributed neural activity across A1 with response maxima based on the tonotopic organization and harmonic composition of the sounds. This form of neural encoding supports models of pitch perception that hypothesize template matching of spectral patterns as a key component for determining the f_0 of complex sounds. The second mechanism uses unresolved harmonics, is based on the encoding of stimulus waveform periodicity, and is dominant at lower rates of stimulation.

ACKNOWLEDGMENTS

This research was supported in part by Grant No. DC00657 from NIH, the Beth Abraham Hospital Institute for Music and Neurologic Function, and the Rose F. Kennedy Center at Albert Einstein College of Medicine Core Grant. The authors thank the two journal reviewers for their insightful comments, and C. Freeman, M. Huang, M. Litwak, L. O'Donnell, and S. Seto for excellent technical, secretarial, and histological assistance.

Barna, J., Arezzo, J. C., and Vaughan, Jr., H. G. (**1981**). ''A new multicontact array for the simultaneous recording of field potentials and unit activity,'' Electroencephalogr. Clin. Neurophysiol. **52**, 494–496.

Burns, E. M., and Viemeister, N. F. (**1981**). ''Played-again SAM: Further observations on the pitch of amplitude-modulated noise,'' J. Acoust. Soc. Am. **70**, 1655–1660.

Cariani, P. A., and Delgutte, B. (**1996a**). ''Neural correlates of the pitch of complex tones. I. Pitch and pitch salience,'' J. Neurophysiol. **76**, 1698–1716.

Cariani, P. A., and Delgutte, B. (**1996b**). ''Neural correlates of the pitch of complex tones. II. Pitch shift, pitch ambiguity, phase invariance, pitch circularity, rate pitch, and the dominance region for pitch,'' J. Neurophysiol. **76**, 1717–1734.

Carlyon, R. P., and Shackleton, T. M. (**1994**). ''Comparing the fundamental frequencies of resolved and unresolved harmonics: Evidence for two pitch mechanisms?'' J. Acoust. Soc. Am. **95**, 3541–3554.

Creutzfeldt, O., Hellweg, F-C., and Schreiner, C. (**1980**). ''Thalamocortical transformation of responses to complex auditory stimuli,'' Exp. Brain Res. **39**, 87–104.

deCharms, R. C., and Merzenich, M. M. (**1996**). ''Primary cortical representation of sounds by the coordination of action-potential timing,'' Nature (London) **381**, 610–613.

Divenyi, P. L., and Robinson, A. J. (**1989**). ''Nonlinguistic auditory capabilities in aphasia,'' Brain and Language **37**, 290–326.

Eggermont, J. J. (**1991**). ''Rate and synchronization measures of periodicity coding in cat primary auditory cortex,'' Hearing Res. **56**, 153–167.

Eggermont, J. J. (**1994**). ''Neural interaction in cat primary auditory cortex. II. Effects of sound stimulation,'' J. Neurophysiol. **71**, 246–270.

Eggermont, J. J., and Smith, G. M. (**1995**). ''Synchrony between single-unit activity and local field potentials in relation to periodicity coding in primary auditory cortex,'' J. Neurophysiol. **73**, 227–245.

Ehret, G. (**1997**). ''The auditory cortex,'' J. Comp. Physiol. A **181**, 547–557.

Fishman, Y. I., Reser, D. H., Arezzo, J. C., and Steinschneider, M. (**1998**). ''Pitch versus spectral encoding of harmonic complex tones in primary auditory cortex of the awake monkey,'' Brain Res. **786**, 18–30.

Flanagan, J. L., and Guttman, N. (**1960a**). ''On the pitch of periodic pulses,'' J. Acoust. Soc. Am. **32**, 1308–1319.

Flanagan, J. L., and Guttman, N. (**1960b**). ''Pitch of periodic pulses without fundamental component,'' J. Acoust. Soc. Am. **32**, 1319–1328.

Freeman, J. A., and Nicholson, C. (**1975**). ''Experimental optimization of current source density technique for anuran cerebellum,'' J. Neurophysiol. **38**, 369–382.

Galaburda, A. M., and Pandya, D. N. (**1983**). ''The intrinsic architectonic and connectional organization of the superior temporal region of the rhesus monkey,'' J. Comp. Neurol. **221**, 169–184.

Goldstein, J. L. (**1973**). ''An optimum processor theory for the central formation of the pitch of complex tones,'' J. Acoust. Soc. Am. **54**, 1496–1516.

Goldstein, Jr., M. H., Kiang, N. Y-S., and Brown, R. M. (**1959**). ''Responses of the auditory cortex to repetitive acoustic stimuli,'' J. Acoust. Soc. Am. **31**, 356–364.

Gourevitch, G. (**1970**). ''Detectability of tones in quiet and in noise by rats and monkeys,'' in *Animal Psychophysics*, edited by W. C. Stebbins (Appleton-Century-Crofts, New York), pp. 67–97.

Guttman, N., and Flanagan, J. L. (**1964**). ''Pitch of high-pass-filtered pulse trains,'' J. Acoust. Soc. Am. **36**, 757–765.

Heffner, H. E., and Heffner, R. S. (**1986**). ''Effect of unilateral and bilateral auditory cortex lesions on the discrimination of vocalizations by Japanese macaques,'' J. Neurophysiol. **56**, 683–701.

Heffner, H. E., and Heffner, R. S. (**1989**). ''Effect of restricted cortical lesions on absolute thresholds and aphasia-like deficits in Japanese macaques,'' Behavioral Neuroscience **103**, 158–169.

Heffner, H. E., and Whitfield, I. C. (**1976**). ''Perception of the missing fundamental by cats,'' J. Acoust. Soc. Am. **59**, 915–919.

Hoeltzell, P. B., and Dykes, R. W. (**1979**). ''Conductivity in the somatosensory cortex of the cat—evidence for cortical anisotopy,'' Brain Res. **177**, 61–82.

Kuhl, P. K., and Padden, D. M. (**1982**). ''Enhanced discriminability at the phonetic boundaries for the voicing feature in macaques,'' Percept. Psychophys. **32**, 542–550.

Kuhl, P. K., and Padden, D. M. (**1983**). ''Enhanced discriminability at the phonetic boundaries for the place feature in macaques,'' J. Acoust. Soc. Am. **73**, 1003–1010.

Langner, G., and Schreiner, C. E. (**1988**). ''Periodicity coding in the inferior colliculus of the cat. I. Neuronal mechanisms,'' J. Neurophysiol. **60**, 1799–1822.

Langner, G., Sams, M., Heil, P., and Schulze, H. (**1997**). ''Frequency and periodicity are represented in orthogonal maps in the human auditory cortex: Evidence from magnetoencephalography,'' J. Comp. Physiol. A **181**, 665–676.

Mäkelä, J. P., Karmos, G., Molnár, M., Csépe, V., and Winkler, I. (**1990**). ''Steady-state responses from the cat auditory cortex,'' Hearing Res. **45**, 41–50.

May, B., Moody, D. B., and Stebbins, W. C. (**1989**). ''Categorical perception of conspecific communication sounds by Japanese macaques, *Macaca fuscata*,'' J. Acoust. Soc. Am. **85**, 837–847.

Meddis, R., and Hewitt, M. J. (**1991**). ''Virtual pitch and phase sensitivity of a computer model of the auditory periphery. I: Pitch identification,'' J. Acoust. Soc. Am. **89**, 2866–2882.

Meddis, R., and O'Mard, L. (**1997**). ''A unitary model of pitch perception,'' J. Acoust. Soc. Am. **102**, 1811–1820.

Merzenich, M. M., and Brugge, J. F. (**1973**). ''Representation of the cochlear partition on the superior temporal plane of the macaque monkey,'' Brain Res. **50**, 275–296.

Mitani, A., Shimokouchi, M., Itoh, K., Nomura, S., Kudo, M., and Mizuno, N. (**1985**). ''Morphology and laminar organization of electrophysiologically identified neurons in the primary auditory cortex in the cat,'' J. Comp. Neurol. **235**, 430–447.

Mitzdorf, U. (**1985**). ''Current source-density method and application in cat cerebral cortex: Investigation of evoked potentials and EEG phenomena,'' Physiol. Rev. **65**, 37–100.

Mitzdorf, U., and Singer, W. (**1980**). ''Monocular activation of visual cortex in normal and monocularly deprived cats: Analysis of evoked potentials,'' J. Physiol. (London) **304**, 203–220.

Morel, A., Garraghty, P. E., and Kaas, J. H. (**1993**). ''Tonotopic organization, architectonic fields, and connections of auditory cortex in macaque monkeys,'' J. Comp. Neurol. **335**, 437–459.

Nelken, I., Prut, Y., Vaadia, E., and Abeles, M. (**1994**). ''Population responses to multifrequency sounds in the cat auditory cortex: One- and two-parameter families of sounds,'' Hearing Res. **72**, 206–222.

Nicholson, C., and Freeman, J. A. (**1975**). ''Theory of current source-density analysis and determination of conductivity tensor for anuran cerebellum,'' J. Neurophysiol. **38**, 356–368.

Pandya, D. N., and Rosene, D. L. (**1993**). ''Laminar termination patterns of thalamic, callosal, and association afferents in the primary auditory area of the rhesus monkey,'' Exp. Neurol. **119**, 220–234.

Pantev, C., Hoke, M., Lütkenhöner, B., and Lehnertz, K. (**1989**). ''Tonotopic organization of the auditory cortex: Pitch versus frequency representation,'' Science **246**, 486–488.

Pantev, C., Elbert, T., Ross, B., Eulitz, C., and Terhardt, E. (**1996**). ''Binaural fusion and the representation of virtual pitch in the human auditory cortex,'' Hearing Res. **100**, 164–170.

Petersen, M. R., Beecher, M. D., Zoloth, S. R., Moody, D. B., and Stebbins, W. C. (**1978**). ''Neural lateralization of species-specific vocalizations by Japanese macaques (*Macaca fuscata*),'' Science **202**, 324–327.

Pfingst, B. E. (**1993**). ''Comparison of spectral and nonspectral frequency difference limens for human and nonhuman primates,'' J. Acoust. Soc. Am. **93**, 2124–2129.

Pierce, J. R. (**1991**). ''Periodicity and pitch perception,'' J. Acoust. Soc. Am. **90**, 1889–1893.

Plack, C. J., and Carlyon, R. P. (**1995**). ''Differences in frequency modulation detection and fundamental frequency discrimination between complex tones consisting of resolved and unresolved harmonics,'' J. Acoust. Soc. Am. **98**, 1355–1364.

Plomp, R., and Levelt, J. M. (**1965**). ''Tonal consonance and critical bandwidth,'' J. Acoust. Soc. Am. **38**, 548–560.

Plomp, R., and Steeneken, H. J. M. (**1968**). ''Interference between two simple tones,'' J. Acoust. Soc. Am. **43**, 883–884.

Rauschecker, J. P., Tian, B., and Hauser, M. (**1995**). ''Processing of complex sounds in the macaque nonprimary auditory cortex,'' Science **268**, 111–114.

de Ribaupierre, F., Goldstein, Jr., M. H., and Yeni-Komshian, G. (**1972**). ''Cortical coding of repetitive acoustic pulses,'' Brain Res. **48**, 205–225.

Robin, D. A., Tranel, D., and Damasio, H. (**1990**). ''Auditory perception of temporal and spectral events in patients with focal left and right cerebral lesions,'' Brain and Language **39**, 539–555.

Rosenberg, A. E. (**1965**). ''Effect of masking on the pitch of periodic pulses,'' J. Acoust. Soc. Am. **38**, 747–758.

Rouiller, E., and de Ribaupierre, F. (**1982**). ''Neurons sensitive to narrow ranges of repetitive acoustic transients in the medial geniculate body of the cat,'' Exp. Brain Res. **48**, 323–326.

Rouiller, E., de Ribaupierre, Y., Toros-Morel, A., and de Ribaupierre, F. (**1981**). ''Neural coding of repetitive clicks in the medial geniculate body of the cat,'' Hearing Res. **5**, 81–100.

Schreiner, C. E. (**1998**). ''Spatial distribution of responses to simple and complex sounds in the primary auditory cortex,'' Audiology and Neuro-Otology **3**, 104–122.

Schreiner, C. E., and Langner, G. (**1988**). ''Periodicity coding in the inferior colliculus of the cat. II. Topographic organization,'' J. Neurophysiol. **60**, 1823–1840.

Schreiner, C. E., and Raggio, M. W. (**1996**). ''Neuronal responses in cat primary auditory cortex to electrical cochlear stimulation. II. Repetition rate coding,'' J. Neurophysiol. **75**, 1283–1300.

Schroeder, C. E., Tenke, C. E., Givre, S. J., Arezzo, J. C., and Vaughan, Jr., H. G. (**1990**). ''Laminar analysis of bicuculline-induced epileptiform activity in area 17 of the awake macaque,'' Brain Res. **515**, 326–330.

Schroeder, C. E., Steinschneider, M., Javitt, D. C., Tenke, C. E., Givre, S. J., Mehta, A. D., Simpson, G. V., Arezzo, J. C., and Vaughan, Jr., H. G. (**1995**). ''Localization of ERP generators and identification of underlying neural processes,'' in *Perspectives of Event-Related Potentials Research (EEG Suppl. 44)*, edited by G. Karmos, M. Molnár, V. Csépe, I. Czigler, and J. E. Desmedt (Elsevier, Amsterdam), pp. 55–75.

Schwarz, D. W. F., and Tomlinson, R. W. W. (**1990**). ''Spectral response patterns of auditory cortex neurons to harmonic complex tones in alert monkey (*Macaca mulatta*),'' J. Neurophysiol. **64**, 282–298.

Shackleton, T. M., and Carlyon, R. P. (**1994**). ''The role of resolved and unresolved harmonics in pitch perception and frequency modulation discrimination,'' J. Acoust. Soc. Am. **95**, 3529–3540.

Sinnott, J. M., and Adams, F. S. (**1987**). ''Differences in human and monkey sensitivity to acoustic cues underlying voicing contrasts,'' J. Acoust. Soc. Am. **82**, 1539–1547.

Sinnott, J. M., and Kreiter, N. A. (**1991**). ''Differential sensitivity to vowel continua in Old World monkeys (*Macaca*) and humans,'' J. Acoust. Soc. Am. **89**, 2421–2429.

Sommers, M. S., Moody, D. B., Prosen, C. A., and Stebbins, W. C. (**1992**). ''Formant frequency discrimination by Japanese macaques (*Macaca fuscata*),'' J. Acoust. Soc. Am. **91**, 3499–3510.

Steinschneider, M., Reser, D., Schroeder, C. E., and Arezzo, J. C. (**1995**). ''Tonotopic organization of responses reflecting stop consonant place of articulation in primary auditory cortex (A1) of the monkey,'' Brain Res. **674**, 147–152.

Steinschneider, M., Schroeder, C. E., Arezzo, J. C., and Vaughan, Jr., H. G. (**1994**). ''Speech-evoked activity in primary auditory cortex: Effects of voice onset time,'' Electroencephalogr. Clin. Neurophysiol. **92**, 30–43.

Steinschneider, M., Tenke, C. E., Schroeder, C. E., Javitt, D. C., Simpson, G. V., Arezzo, J. C., and Vaughan, Jr., H. G. (**1992**). ''Cellular generators of the cortical auditory evoked potential initial component,'' Electroencephalogr. Clin. Neurophysiol. **84**, 196–200.

Tenke, C. E., Schroeder, C. E., Arezzo, J. C., and Vaughan, Jr., H. G. (**1993**). ''Interpretation of high-resolution current source density profiles: A simulation of sublaminar contributions to the visual evoked potential,'' Exp. Brain Res. **94**, 183–192.

Terhardt, E. (**1974a**). ''Pitch, consonance, and harmony,'' J. Acoust. Soc. Am. **55**, 1061–1069.

Terhardt, E. (**1974b**). ''On the perception of periodic sound fluctuations (Roughness),'' Acustica **30**, 201–213.

Terhardt, E. (**1977**). ''The two-component theory of musical consonance,'' in *Psychophysics and Physiology of Hearing*, edited by E. F. Evans and J. P. Wilson (Academic, London), pp. 381–389.

Tomlinson, R. W. W., and Schwarz, D. W. F. (**1988**). ''Perception of the missing fundamental in nonhuman primates,'' J. Acoust. Soc. Am. **84**, 560–565.

Vaughan, Jr., H. G., and Arezzo, J. C. (**1988**). ''The neutral basis of event-related potentials,'' in *Human Event-Related Potentials. EEG Handbook, Vol. 3 (Revised Series)*, edited by T. W. Picton (Elsevier, Amsterdam), pp. 45–96.

Vaughan, Jr., H. G., Schroeder, C. E., and Arezzo, J. C. (**1992**). ''The genesis of cortical event-related potentials: Excitatory and inhibitory contributions,'' in *Slow Activity Changes In The Brain*, edited by W. Haschke and E.-J. Speckmann (Birkhauser, Boston), pp. 111–127.

Wang, X., Merzenich, M. M., Beitel, R., and Schreiner, C. E. (**1995**). ''Representation of a species-specific vocalization in the primary auditory cortex of the common marmoset: Temporal and spectral characteristics,'' J. Neurophysiol. **74**, 2685–2706.

Warren, R. M., and Wrightson, J. M. (**1981**). ''Stimuli producing conflicting temporal and spectral cues to frequency,'' J. Acoust. Soc. Am. **70**, 1020–1024.

Whitfield, I. C. (**1980**). ''Auditory cortex and the pitch of complex tones,'' J. Acoust. Soc. Am. **67**, 644–647.

Winer, J. A. (**1984**). ''The pyramidal neurons in layer III of cat primary auditory cortex (A1),'' J. Comp. Neurol. **229**, 476–496.

Zatorre, R. J. (**1988**). ''Pitch perception of complex tones and human temporal-lobe function,'' J. Acoust. Soc. Am. **84**, 566–572.

Zatorre, R. J., Evans, A. C., and Meyer, E. (**1994**). ''Neural mechanisms underlying melodic perception and memory for pitch,'' J. Neurosci. **14**, 1908–1919.

Zatorre, R. J., Evans, A. C., Meyer, E., and Gjedde, A. (**1992**). ''Lateralization of phonetic and pitch discrimination in speech processing,'' Science **256**, 846–849.

Frequency discrimination of stylized synthetic vowels with two formants

Johannes Lyzenga[a] and J. Wiebe Horst
Department of Otorhinolaryngology/Audiology, University Hospital Groningen, P.O. Box 30.001, 9700RB Groningen, The Netherlands

(Received 20 July 1997; accepted for publication 23 July 1998)

Just-noticeable differences (jnd's) in the formant frequencies of synthetic two-formant ''vowels'' were measured for normal hearing subjects. The jnd's were examined for a change in only the first or the second formant, and for a combined change of both formants. For the combined change two quantitative relations between the formant frequencies were used; one with equal relative changes in both formants, and one with a double relative change for the first formant. Formant frequencies were 500, 550, and 600 Hz in the first, and 2000, 2050, and 2100 Hz in the second formant region. Both formants had either shallow or steep slopes. For the fundamental frequency of the complexes we used 100 and 200 Hz. For the single-formant changes, a ''natural,'' and a random-phase relation were used between the individual components of the complexes. These results were compared to jnd's for a Gaussian noise that was filtered with the same spectral envelopes as the harmonic complexes. For the combined formant changes only the natural phase relation was used. A three-interval, three-alternative forced-choice task was used. All measurements were performed with roving stimulus level. For the single formant changes, the phase relations had no effect on the results. For the harmonic stimuli, jnd's were mostly smaller for the formants between two harmonics than for those at a harmonic. The results for the harmonic stimuli as well as the noise bands could be described by a model using a spectral profile comparison. For the combined formant changes smaller jnd's were found than for the single changes. These jnd's could be explained by combining measures of the perceived differences from the two separately changed formants. In this combination these measures were summed as independent variables. [S0001-4966(98)03411-0]

PACS numbers: 43.66.Ba, 43.66.Fe, 43.71.Es [WJ]

INTRODUCTION

This is the last paper in a series of three on formant-frequency discrimination for synthetic vowels. The investigations were started using highly stylized vowels with just a single formant (Lyzenga and Horst, 1995). By stepwise increasing the complexity of the stimuli via more natural one-formant vowels (Lyzenga and Horst, 1997), we now have arrived at synthetic vowels containing two formants. The vowels in natural speech contain a number of formants, the first two or three of which characterize the vowel. In the present study, the two formants of our stimuli are either changed separately or simultaneously in the same direction.

In the first paper (Lyzenga and Horst, 1995) we investigated jnd's for the center frequency of synthetic vowels with a single formant near 2000 Hz. The stimuli had either a triangular or a trapezoidal spectral envelope. We found that the position of the formant relative to the nearest harmonics was an important influence on the jnd. The nature of this influence, however, was roughly the inverse for the two envelope shapes. This divided the results into more than one group, which required us to use more than one model to describe these data. The need to use a hybrid model was corroborated in a subsequent paper (Lyzenga and Horst, 1997). In this paper we reported jnd's for synthetic vowels with a single formant in the range of either the first or the second formant. Again the stimuli were characterized by two spectral envelope shapes, but now we used the triangular envelope and a more natural envelope according to the Klatt synthesizer (Klatt, 1980). We found phase effects in the jnd's for the second-formant region when a low fundamental frequency was used, indicating temporal discrimination processes. Under the remaining conditions no phase effects were found. To describe our data, we proposed models that use changes in the envelopes of the stimulus waveforms for the conditions where we found evidence for temporal discrimination processes. For the triangular envelopes, under conditions where the formants were not halfway between two harmonics, we proposed a model based on the modulation depth of the stimuli. For stimuli with unresolved harmonics and a formant positioned halfway between two harmonics, we proposed a model based on the sharpness of the minima of the temporal envelope of the stimuli. On the other hand, for the stimuli in the first formant region and for the remaining stimuli in the second formant region, we proposed a modified place model (for a short description, see experiment 1) in which information was combined over a limited frequency range by comparing the spectral profiles of the two presented stimuli. One of the questions we wish to address in the present investigation is whether it is necessary to use such combined spectral-temporal modeling to describe formant-

[a]Current address: MRC Cognition and Brain Sciences Unit, 15 Chaucer Road, Cambridge CB2 2EF, United Kingdom.

frequency discrimination for stimuli containing two formants.

In the present investigation we combined two of the stimuli of Lyzenga and Horst (1997) with the Klatt-shaped envelope, to form a synthetic vowel with two formants. To study the influence of the presence of a second peak in the spectrum, we investigated the jnd while changing one formant and keeping the other stationary. So, either the first formant was changed and the second was stationary, or vice versa. Earlier investigations using vowels that contain more than one formant, while changing them separately, have been performed by e.g., Flanagan (1955), Mermelstein (1978), Kewley-Port and Watson (1994), Hawks (1994), and Kewley-Port *et al.* (1996). A large range of relative jnd's was found in these studies. Flanagan, like Kewley-Port and Watson, investigated jnd's for a change of either the first or the second formant for a range of widely spread formant frequencies. Kewley-Port and Watson and Kewley-Port *et al.* found jnd's decreasing rather abruptly from 7% (female speaker) or 4% (male speaker) to 2% for formant frequencies from 200 to 800 Hz and then gradually sloping to about 1% for a formant frequency of 2800 Hz. Over this range Flanagan found relative jnd's decreasing from 5% to 3%. Mermelstein (1978) and Hawks (1994) investigated jnd's for single and combined changes of the first two formants. The relative jnd's Mermelstein found for a single change in the first formants of two vowels (14% and 5.5%) were slightly larger than those for a single change in the second formants (4.2% and 7%). Hawks found jnd's near 2% for a single change in both the first and the second formant. All in all, in most of these studies jnd's were larger for the first than for the second formant region. Together, these studies provide a good overview of the discrimination of single-formant changes as a function of formant frequency range. In the first experiment of the present study we make a detailed study of the effects of adding a stationary formant to a single-formant ''vowel'' (from our previous work) to arrive at stimuli closer resembling those used in the aforementioned studies.

For the first experiment of the present study, we used an orderly set of stimulus parameters to enable thorough testing of possible models to describe formant-frequency discrimination. Under a number of stimulus conditions, Lyzenga and Horst (1997) found a phase effect, which indicated that temporal discrimination processes were involved. To check the occurrence of such temporal processes for the two-formant vowels, we used two different phase relations between the harmonics of the stimuli. The first is the phase relation as generated by the Klatt synthesizer. This condition resembles hearing a speaker from close by. The second is a random-phase relation, more akin to hearing a speaker in a room where the original phase relation of the sound has been disturbed by the added reflections of the walls. Another important aspect of the stimuli is the position of the formant relative to the harmonics. In our previous studies (Lyzenga and Horst, 1995, 1997), we found that this position is an important influence on the jnd's. Likewise, Kewley-Port and Watson (1994) and Kewley-Port *et al.* (1996) reported ''unusually high thresholds'' for formants located very close to a harmonic. To take the influence of formant position into account, we employed the two positions also used by Lyzenga and Horst (1997): at a harmonic, and halfway between two harmonics. We used two fundamentals and for both formant peaks we used either shallow or steep slopes.

In the second experiment we allowed both formants to change simultaneously. Hawks (1994) reported smaller jnd's (i.e., a bigger effect) for two-formant changes in which the directions of the changes were parallel rather than opposite. Mermelstein (1978) used parallel formant changes. Since we wanted to compare our results with those from the studies of Mermelstein and Hawks, we changed the two formants in the same direction. We used two different quantitative relations between the two formant frequencies. With the choice of these rules we tried to cover a range in which the changes in both formants were roughly of equal influence on the discrimination. According to the first rule, the relative change in the first formant was twice that of the second formant ($\Delta F_1/F_1 = 2\Delta F_2/F_2$). This rule was chosen to compensate for the fact that in most studies larger jnd's were found for the first than for the second formant region. According to the second rule, the changes in the first and the second formant were chosen equal ($\Delta F_1/F_1 = \Delta F_2/F_2$). This rule was chosen because we expected that the jnd's for the second formant would be disturbed more by the presence of a first formant than vice versa (in many vowels the level of the first formant is much larger than that of the second formant). We used the same fundamentals and slopes as in the first experiment. For both formants we used the position at a harmonic and halfway between two harmonics.

Mermelstein (1978) measured jnd's for single and combined changes of the first two formants. Hawks (1994) investigated discrimination for single changes of the second formant, and for a number of combinations of changes in the first three formants. In a ''pilot fashion'' he measured jnd's for single and combined changes in the first two formants. Both Mermelstein and Hawks found smaller jnd's for a parallel combined change of two formants than for single changes of these formants. Mermelstein proposed a model for the prediction of jnd's for combined formant changes from the separate formant changes. In this model the frequency changes in the separate formants are added as ''independent parameters'' to form a measure of the combined frequency change. For parallel formant changes, Hawks proposed a ''weighted Euclidean distance model'' that predicts a jnd for combined formant changes directly from the jnd's for single formant changes. In the present study we will check for our stimuli which rule is the more appropriate one.

I. GENERAL METHODS

A. Stimuli

The experiments were carried out using bandlimited harmonic complexes as stimuli. We used a rounded spectral envelope, equal to the steady-state spectrum of two-formant vowels as generated by the digital Klatt synthesizer (Klatt, 1980). Two formant resonators of the synthesizer were used in series, and their center frequencies (F_C) were set in the regions of the first and second formants. We first calculated the amplitude and the phase spectrum, after which the har-

monic components were added with the appropriate amplitudes and phase angles. This procedure allowed us to use any phase spectrum. The fundamental frequency (F_0) of the harmonic complexes was either 100 or 200 Hz. The center frequencies of the formants were chosen either to coincide with a harmonic, or in the middle between two harmonics. In the first formant region the center frequencies were 500 and either 550 or 600 Hz, and in the second formant region they were 2000 and either 2050 or 2100 Hz. Two combinations of values for the slope (G) were employed for the formants: 50 dB/oct for the first and 100 dB/oct for the second formant, or 100 dB/oct for the first and 200 dB/oct for the second formant. These slope values corresponded with the steepest parts of the spectral slopes (the associated bandwidths for the Klatt synthesizer can be derived from the relation $bw = 4.8F_C/G$). In the first experiment we used two phase relations between the harmonics of the complexes: the phase relation as it is generated by the digital Klatt synthesizer (from here on called the Klatt-phase relation), and a random phase. For the stimuli with the Klatt phase, the stationary formant could be either at a harmonic or between two harmonics. In the presentations, the results will be arranged according to the position of the changing formant relative to the harmonics. For the stationary formant the positions at a harmonic and between two harmonics will be referred to as Klatt/peak 1 and Klatt/peak 2, respectively (note that the numbers 1 and 2 reflect the number of major components in this formant). For the stimuli with the random phase, the stationary formant always coincided with a harmonic; this condition will be referred to as random/peak 1. In the first experiment, we also investigated the jnd for a Gaussian noise that was filtered with the same spectral envelopes (from here referred to as the noise bands). In the second experiment we only used the Klatt-phase relation in the stimulus generation. The formant positions at a harmonic, and between two harmonics were used for both the first and the second formant. The relative changes in the two formants were either equal, or twice as large in the first as in the second formant. In this experiment, the jnd's will be considered in terms of either the first or the second formant, depending on which formant was found to have the greater effect on the frequency discrimination. This strategy, which, of course, does not alter the actual data, helps in providing a clear presentation of the data. For the remaining, less influential formant, the positions at a harmonic and between two harmonics will be referred to as the peak relations 1 and 2, respectively.

Using the series version of the Klatt synthesizer, the relative formant peak levels in the spectral envelope depend on the distance between these two formants. Furthermore, the actual formant peak levels depend on the positions of the formants relative to the harmonics. Because of this we found attenuation values of the second formant peak relative to the first between 0 and 27 dB (dependent of the stimulus parameters). This is illustrated in Fig. 1, in which examples are shown of the harmonic stimulus spectra used in both experiments. For the stimuli shown in panels (c) and (g), the attenuations of the second formants are about 18 and 0 dB, respectively. For the noise bands, the attenuations of the second formant peaks relative to the first were between 15 and 18 dB, depending on the distance between the two formants.

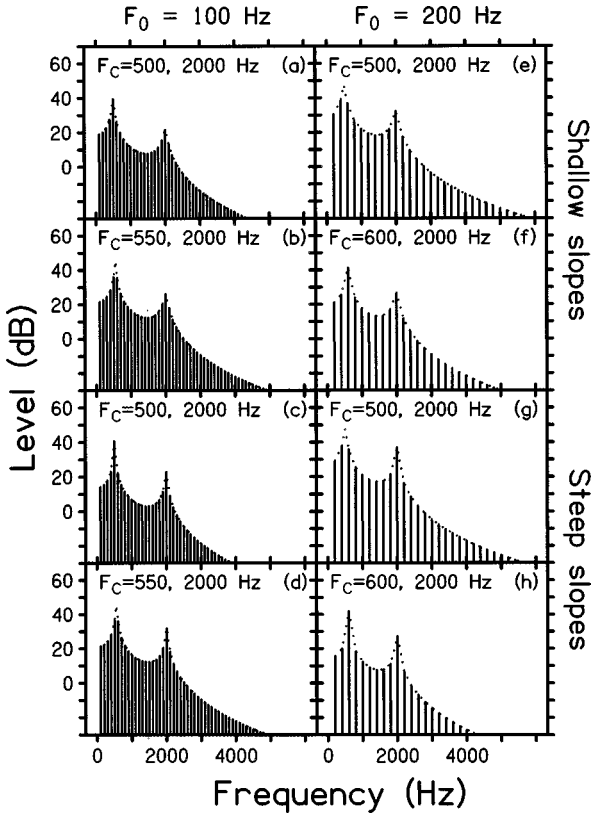

FIG. 1. Examples of stimulus spectra. The left column shows stimuli for the 100-Hz fundamental, and the right column for the 200-Hz fundamental. The two rows at the top display the stimuli with the shallow slopes, and the two rows at the bottom those with the steep slopes. The dotted lines indicate the spectral envelopes according to the Klatt synthesizer.

The stimulus generation and presentation procedures were equal to those described by Lyzenga and Horst (1995) for the roving level condition. For the noise stimuli and the stimuli with random-phase relations, three sets of stimuli were made with different random relations. During the measurements each stimulus was picked at random from one of these three sets. In this way the correlation between the stimuli was reduced.

B. Procedure

The jnd's were measured using an adaptive three-interval, three-alternative forced-choice method (3IFC). Before the actual jnd measurements, the absolute threshold of the reference tone was estimated, after which stimuli were presented at a level about 40 dB above this threshold. We added a pink background noise to the stimuli at a level of −40 dB relative to the stimuli; therefore, this procedure produced background noise levels close to the absolute thresholds. We used a ''roving level'' condition for the tones in all presentation intervals: in this condition the levels of all stimuli were randomized, around one fixed level value, within trials over a 16-dB range in 0.5-dB steps (Henning, 1966). The background noise was roved in level along with the stimulus, keeping the signal-to-noise ratio in the stimulus constant.

The procedure by which the jnd's were estimated was equal to the one used, and described in detail by Lyzenga and Horst (1995). In short, subjects were asked to identify the odd tone in a series containing two reference tones and one target tone. They were given immediate feedback. The frequency difference between the target and the reference tones was adapted according to decision rules that were chosen so that the procedure converges at 63% correct responses, which corresponds to a d' of 1 for the 3IFC paradigm. Data were collected until the direction of the formant frequency adaption was reversed five times. On average, 1 jnd measurement contained 71 trials. The whole set of jnd's was measured 3 times (involving at least 200 trials per jnd), in 1 group containing the stimuli of both experiments in a pseudorandom order. The jnd's were estimated from the averaged scores with the same algorithm as used by Lyzenga and Horst (1995). Since the subjects' bias toward one of the three signal intervals was found to be very small, it has been neglected in the calculations.

C. Subjects

Six normal-hearing subjects participated in the experiments. All were adults, four female and two male, with ages ranging from 25 to 48 years. For the harmonic stimuli, all subjects participated for different sets of phase conditions, in such a way that three subjects participated for each condition. In the first experiment an exception was the Klatt/peak 1 condition, where four subjects participated. All subjects participated for the noise bands. All subjects had participated in frequency discrimination experiments before and were well trained. For all six subjects no improvements in the scores were observed during the course of the measurements.

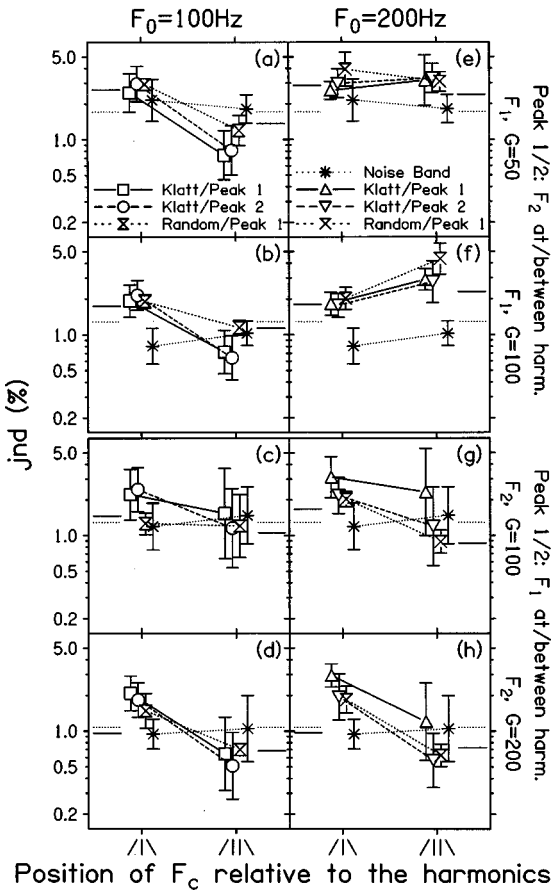

FIG. 2. Average jnd's for single-formant changes. Each row contains the jnd's measured for one formant region and slope combination. The left column contains the averages for the 100-Hz, and the right column for the 200-Hz fundamental. The error bars indicate the standard deviations of the averages. The little solid and dotted line segments at the side of each panel indicate the expectations of the modified place model for the harmonic stimuli, and the noise bands, respectively.

II. EXPERIMENT 1. SINGLE-FORMANT CHANGES

The average jnd's across subjects for the single formant changes are shown in Fig. 2. The columns on the left and on the right contain averages for the fundamentals of 100 Hz and 200 Hz, respectively. Each panel contains jnd's for two values of the formant frequency; one coinciding with and one halfway between the stimulus harmonics, denoted as /I\ and /II\, respectively. The smaller value of these pairs of formant frequencies is plotted on the left and the larger on the right, except for the first formant region with the 200-Hz fundamental. Here they are plotted in reversed order (i.e., 600 Hz, 500 Hz), because here the condition where the formant frequency coincides with a harmonic occurs for the higher frequency of the two. For the 100-Hz fundamental, the jnd's for the Klatt/peak 1, Klatt/peak 2, and random/peak 1 conditions are shown as square, circular, and hourglass symbols, respectively. For the 200-Hz fundamental, the jnd's for these three conditions are shown as triangular-up, triangular-down, and picnic table symbols. For clarity the jnd's for these conditions are connected with a solid, a long dashed, and a short dashed line, respectively. For the noise bands (the asterisks, connected by a dotted line) the value of the formant frequency relative to the position of the harmonics is not relevant; we chose 500 and 600 Hz for the first formant and 2000 and 2100 Hz for the second formant, plotted at the positions /I\ and /II\, respectively.

For comparison, the predictions of a modified place model are shown for each condition by means of the little line segments at the sides of each panel. The solid and the dotted line segments represent the expected jnd's for the harmonic stimuli and the noise bands, respectively. For a detailed description of this modified place model see Lyzenga and Horst (1997). In short, the model consists of a linear filter bank followed by a detector of level differences. The filter bank consists of 3400 Roex filters (rounded exponential) with a Q of 5. To form an excitation pattern over all channels, the outputs of the filters are converted to a level in dB. As a representation of the absolute threshold, a noise floor with a power of 1 (i.e., a level of 0 dB) is added to the output power of each filter before it is converted to dB. A level difference detector compares the excitation patterns for two tones. This detector has been modified to apply the model to experiments with roving stimulus levels: the excitation levels of the presented tones are roughly equalized (by matching their overall levels), after which the largest positive excitation difference and the absolute value of the largest

negative difference are summed. Last, this sum is compared with a 2-dB detection threshold.

In the region of the first formant ($F_C \approx 500$ Hz), the average jnd's for the filtered noise bands are 2.0% for a slope of 50 dB/oct, and 0.9% for a 100-dB/oct slope. These values correspond to just audible level differences in the flanks of the spectral envelopes of the stimuli of 1.4 dB and 1.3 dB, respectively. In the second formant region ($F_C \approx 2000$ Hz) the average jnd's are 1.3% and 1.0% for the slopes of 100 and 200 dB/oct, respectively. These jnd's correspond to level differences of 1.9 and 2.9 dB. So, for the second formant we find a larger level difference in the flanks of the stimulus envelopes, necessary for discrimination, than for the first formant. For both formant regions, Lyzenga and Horst (1997) found a level difference of just over 1 dB for noise bands with one formant. So, for the two-formant noise bands discrimination of a change in the first formant is not affected by the presence of the second formant, whereas for the second formant the jnd's are increased by the presence of the first formant. Furthermore, for the second formant region, Lyzenga and Horst (1997) found a poor correspondence between the jnd's and the predictions of the modified place model. For these stimuli a temporal discrimination process was suggested. For all of the present noise band jnd's in Fig. 2 we find good correspondence between the data and the modified place model: The sum of the squared relative errors between predictions and data, summed over eight data points, is 0.51. This correspondence implies that for the second formant the frequency discrimination mechanism is affected by the presence of the stationary first formant in such a way that it can no longer use temporal information and has to resort to a spectral process.

As expected, the harmonic jnd's of the first formant region are on average somewhat larger than those of the second formant region (with a factor of 1.6, which a *t*-test performed on the ratios between the jnd's for both formants revealed to be significantly larger than unity: df=23, $t=-3.29$, $p<0.01$). Similar tests revealed that all jnd's show modest, but significant, dependencies on slope (df=23, $t=4.62$, $p<0.01$), fundamental (df=23, $t=4.86$, $p<0.01$), and position of the formant frequency relative to the harmonics (df=23, $t=-5.00$, $p<0.01$). This is in agreement with our earlier findings (Lyzenga and Horst, 1995, 1997).

A *t*-test on the ratios between the jnd's for harmonic stimuli for the two phase conditions (Klatt/peak 1 and random/peak 1) revealed that the average ratio does not differ significantly from unity (df=15, $t=-1.50$, $p>0.05$).[1] Therefore, we can assume that the jnd's for harmonic stimuli are independent of the phase conditions. The same test, performed on the data for the two positions of the stationary formants (Klatt/peaks 1 and 2), revealed that jnd's for stationary formants at a harmonic are just significantly smaller than for stationary formants between two harmonics with a factor of 1.2 (df=15, $t=-2.17$, $p<0.05$).[2] So, we find that the position of the stationary formants had an effect on the jnd's, but this effect is very small. The predictions of the modified place model are practically equal to those for the single-formant stimuli of Lyzenga and Horst (1997). For the second formant region for the 200-dB/oct slope and a formant frequency coinciding with a harmonic [left sides of panels (d) and (h)], the predictions of the model are somewhat lower than the jnd's. Under most conditions, the predictions of the modified place model are close to the jnd's for the harmonic stimuli (the sum of the squared relative errors, summed over 48 data points, is 5.9).

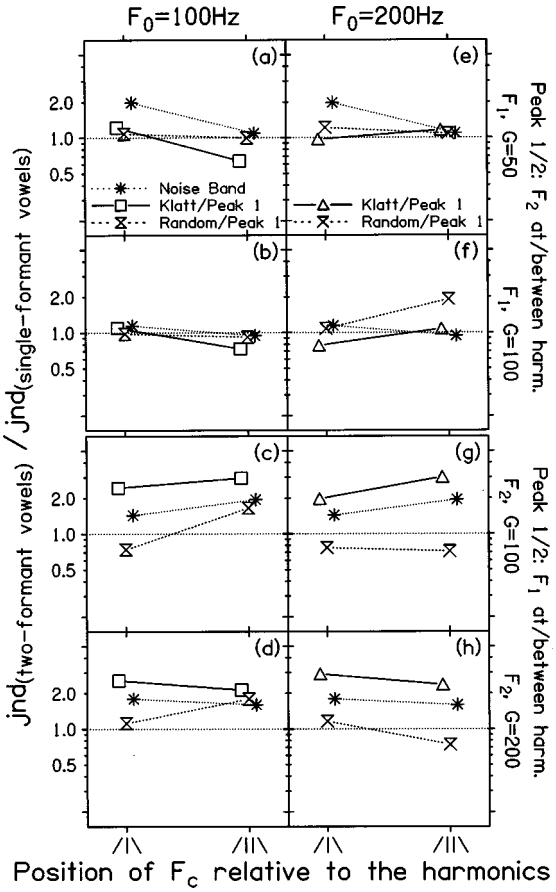

FIG. 3. The average jnd's for single-formant changes in two-formant vowels related to single-formant jnd's. The format of this figure is identical to that of Fig. 2. Each entry is the quotient of the jnd for a single-formant change of Fig. 2 and that of the corresponding single-formant stimulus of Lyzenga and Horst (1997). No entries are given for the Klatt/peak 2 condition.

Figure 3 shows a direct comparison of the present data with the data found by Lyzenga and Horst (1997) for single-formant vowels. Each entry in this figure shows the quotient of the present two-formant jnd for a stationary formant at a harmonic (peak relation 1) and the single-formant jnd. So, this figure shows the direct influence of adding a stationary formant to a single-formant vowel. A value larger than unity indicates a larger two-formant than single-formant jnd, a smaller value indicates the opposite. In the first formant region we find no consistent deviations from unity (as confirmed by *t*-tests on the ratios between the present and the single-formant jnd's; Klatt phase: df=7, $t=-0.53$, $p>0.05$; random phase: df=7, $t=1.41$, $p>0.05$; Noise bands: df=3, $t=1.24$, $p>0.05$). For the second formant region we find a consistent increase in the noise band jnd's (df=3, $t=6.25$, $p<0.01$), and in the harmonic jnd's for the Klatt-phase relation (df=7, $t=4.52$, $p<0.01$). For the 100-Hz fundamental and a formant position halfway between

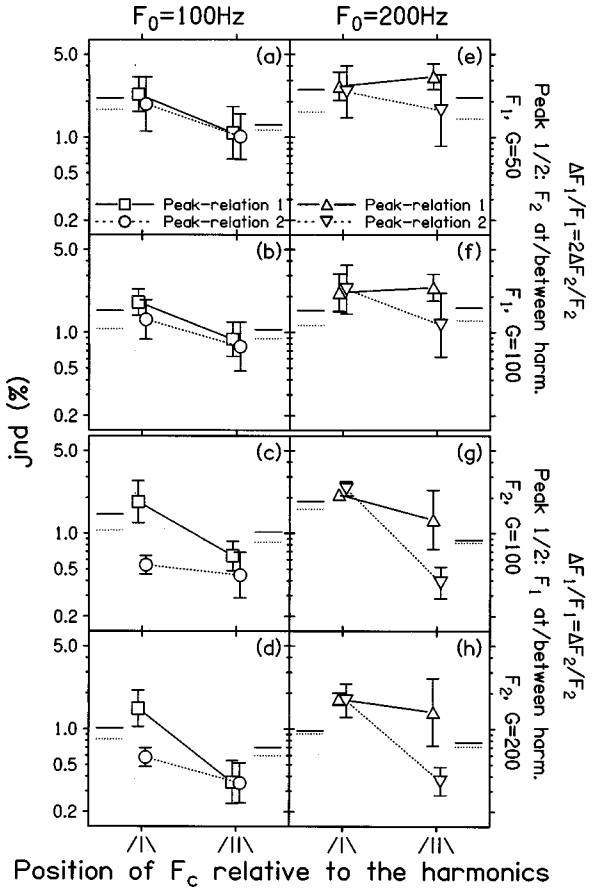

FIG. 4. Average jnd's for combined formant changes. The format of this figure is the same as that of Fig. 2. The error bars indicate the standard deviations of the averages. The little solid and dotted line segments at the side of each panel indicate the expectations of the extended modified place model for the peak relations 1 and 2, respectively.

harmonics, we find an increase for both the Klatt and the random phase (df=3, $t=3.88$, $p<0.05$). So, Fig. 3 shows that the jnd's of the first formant region are hardly affected by adding a stationary second formant to the stimuli, and that for the second formant region many jnd's are increased when a stationary first formant is added.

III. EXPERIMENT 2. COMBINED FORMANT CHANGES

The average jnd's for combined formant changes are shown in Fig. 4. All stimuli have a Klatt-phase relation. The jnd's for the 100-Hz and the 200-Hz fundamental are shown in the left and right columns, respectively. The upper half of the figure contains the jnd's for the formant relation: $\Delta F_1/F_1=2\Delta F_2/F_2$. These jnd's are expressed as a percentage of the change in the first formant, because the first formant was found to have the greater effect on the discrimination process (see below). For these jnd's, the position of the first formant relative to the harmonics is indicated by the annotations /I\ and /II\. The position of the second formant, either at a harmonic or between two harmonics, is indicated by the peak relations 1 and 2, respectively. The lower half of Fig. 4 contains the jnd's for the relation: $\Delta F_1/F_1=\Delta F_2/F_2$. These jnd's are expressed as a percentage of the change in the second formant, because it was found that the changes in this formant were the more important in the discrimination process here (see below). For these jnd's the position of the first formant relative to the harmonics is indicated by the peak relations 1 and 2. In all panels of Fig. 4, jnd's for the peak relations 1 and 2 are shown as square and circular symbols for the $F_0=100$ Hz, and as triangular-up and triangular-down symbols for $F_0=200$ Hz. For clarity, the jnd's for peak relations 1 and 2 are connected with solid and dashed lines, respectively.

The predictions of the modified place model are shown for all conditions by means of the little line segments at the sides of each panel of Fig. 4. The solid and the dotted line segments represent the expected jnd's for the peak relations 1 and 2, respectively. The model has been extended with a summation rule to predict the jnd for combined formant changes from the changes in the excitation due to both formants. The excitation difference of the first formant ΔE_1 (calculated below 1250 Hz) and that of the second formant ΔE_2 (calculated above 1250 Hz) are summed as independently perceived variables.[3] The total perceived excitation difference ΔE is defined as:

$$\Delta E=\sqrt{\Delta E_1^2+\Delta E_2^2}. \tag{1}$$

The value of ΔE that ensues is compared with the detection threshold of 2 dB.

The upper half of Fig. 4 shows the jnd's for a relative change in the first formant that is twice that of the second formant. These jnd's for peak relations 1 and 2 are very close to those of a singly changed first formant for the corresponding conditions (Klatt/peaks 1 and 2, respectively) shown in the upper half of Fig. 2 (the ratios between the individual jnd's do not differ significantly from unity; peak relation 1: df=23, $t=0.09$, $p>0.05$; peak relation 2: df=23, $t=0.97$, $p>0.05$). However, the averaged jnd's for peak relation 1 (F_2 at a harmonic) are slightly larger than those for peak relation 2 (F_2 between harmonics) (on average they differ with a factor of 1.4, which a *t*-test on the individual data revealed to be significantly larger than unity: df=23, $t=-3.32$, $p<0.01$). This indicates that the changes in the second formants have only a small influence on the jnd's (especially when the second formant coincides with a harmonic). So, we find that the first formant dominates the discrimination process here. The predictions of the modified place model extended with the summation rule are not far from those of the modified place model for the first formant as they are shown in Fig. 2, and, in agreement with the jnd's, we consistently find slightly smaller predictions for peak relation 2 than for peak relation 1. Most jnd's in the upper half of Fig. 4 are close to the predictions of this extended model (the sum of the squared relative errors, summed over 16 data points, is 0.9).[4] All in all, when the relative change in the first formant is twice that of the second, the change in the first formant dominates both the data and the model results.

When the changes in both formants are equal (the lower half of Fig. 4), the jnd's for the two positions of F_1 (peak relations 1 and 2) show a large difference under four conditions, indicating that the changes in the first formants have influenced the discrimination. The differences between the two F_1 positions are found for the 100-Hz fundamental when the F_2 coincides with a harmonic [left sides of panels (c) and

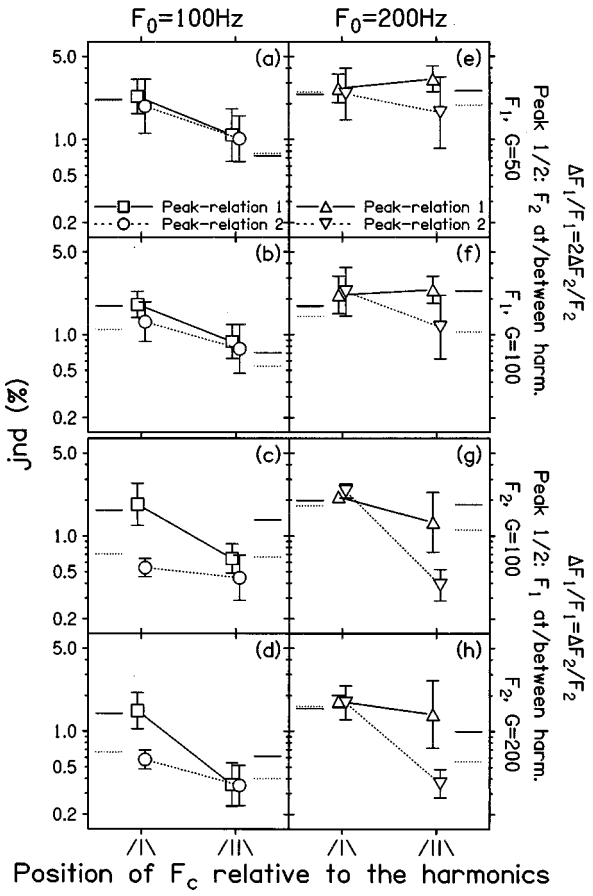

FIG. 5. Average jnd's for combined formant changes, replotted from Fig. 4. The format of this figure is the same as that of Fig. 4. The little solid and dotted line segments at the side of each panel indicate the expectations calculated by combining the jnd's for single-formant changes using Eq. (2).

(d)], and for $F_0 = 200$ Hz when F_2 lies halfway between two harmonics [right sides of panels (g) and (h)]. A *t*-test proved these differences to be just significant in the individual results (shown in Fig. A2; first condition: df=5, $t = -3.18$, $p < 0.05$, second condition: df=5, $t = -2.24$, $p < 0.05$).[5] Under these conditions, the predictions of the extended modified place model show much smaller differences between the two F_1 positions. The sum of the squared relative errors between data and predictions, over all 16 data points in the lower half of Fig. 4, is 7.6. So, we find reasonably good correspondence between the jnd's for equal formant changes and the predictions of the extended modified place model.

IV. GENERAL DISCUSSION

A. Single-formant changes

An important goal of these experiments was the comparison of jnd's for single-formant changes of two-formant vowels with those of single-formant stimuli (of Lyzenga and Horst, 1997). Figure 3 shows the quotients of the average jnd's for the former and the latter stimuli. For the noise bands, this comparison shows that jnds for stimuli in the region of the first formant are hardly influenced by the addition of a stationary second formant. For noise bands in the second formant region, jnd's are affected by the addition of a stationary first formant. For single noise bands in the second formant region, Lyzenga and Horst (1997) could not describe their jnd's accurately with the modified place model, and assumed that a temporal discrimination mechanism was involved. For the present two-formant stimuli, all the noise band jnd's show good correspondence with the predictions of the modified place model. This indicates that for these stimuli only spectral discrimination mechanisms are involved.

For the harmonic stimuli, adding a stationary second formant to a stimulus with a changing formant in the region of the first formant hardly influences the jnd. Adding a stationary first formant to a stimulus with a changing second formant increases the jnd under a number of conditions: for the Klatt phase, and for the 100-Hz fundamental combined with a formant frequency halfway between two harmonics. For many of these conditions Lyzenga and Horst (1997) proposed a temporal mechanism to describe their jnd's. For the first formant region they found no temporal mechanisms, and in the present study, such jnd's are hardly influenced by the addition of a stationary second formant. Furthermore, all present jnd's for the two-formant stimuli show good correspondence with the modified place model. So, in analogy with our findings for the noise bands, we can conclude that the addition of a stationary first formant disturbs the temporal discrimination mechanisms in the region of the second formant, and thereby reduces the discrimination to spectral mechanisms only.

The level differences between the first and the second formants (as discussed Sec. I A) do not depend on the phase relation of the components of the stimuli. Therefore, these level differences are the same for corresponding stimuli of the Klatt/peak 1 and random/peak 1 conditions. However, in the bottom half of Fig. 3 we can see that the jnd's for these two phase relations are influenced quite differently by the addition of a stationary first formant. This implies that the influence of the first formant on the second depends on phase effects (and discrimination mechanisms, as was argued in the previous paragraph) rather than on level differences between the two formants (under the restriction that the level of the second formant is either equal to, or lower than, that of the first one). If the two formants were interacting with each other at the level of the cochlea, an effect of the relative levels would be expected. This implies that, for formants that are sufficiently distant to avoid interactions at the level of the cochlea, the influence of the first formant takes place at a later stage along the auditory pathway than the cochlea. This is an indication that the observed transition from temporal to spectral formant-frequency discrimination occurs beyond the cochlea, in central auditory processes.

B. Combined formant changes

A second important goal of this study was the comparison of jnd's for combined formant changes with those for single-formant changes. When considering the jnd's for combined formant changes with a relative change in the first formant that is twice that of the second formant, we find that all jnd's for an F_2 at a harmonic are very close to, and those for an F_2 between two harmonics are only slightly smaller than those for a singly changed first formant (this can be seen

TABLE I. Table of the results of Mermelstein (1978) and predictions of the various models. $Hawks_1$, and $Hawks_2$ refer to the first and second weighting option used by Hawks (1994). The sums of the squared relative errors were calculated over the individual jnd's. V: vowel alone. B: vowel in /b/ context. G: vowel in /g/ context.

Comparison of predictions		$Subj_1$	$Subj_2$	$Subj_3$	$Subj_4$	$Subj_5$	Mean
Jnds for parallel	V	66	63	54	76	63	64
formant changes of	B	142	66	80	88	63	88
Mermelstein (1978)	G	101	53	80	78	63	75
Predictions Mermelstein	V	111	53	83	93	66	81
Σ(Rel. Error)=1.19	B	105	69	77	96	53	80
	G	114	59	80	101	86	88
Present predictions	V	110	53	83	92	66	81
Σ(Rel. Error)=1.27	B	105	69	77	96	53	80
	G	113	59	84	101	94	90
Predictions $Hawks_1$	V	142	68	145	138	105	120
Σ(Rel. Error)=16.32	B	173	113	183	151	104	145
	G	203	91	172	191	171	166
Predictions $Hawks_2$	V	105	50	96	95	71	83
Σ(Rel. Error)=2.66	B	116	76	117	103	68	96
	G	134	62	111	125	113	109

by comparing the top halves of Figs. 4 and 2). So, here the changes in the first formant have the greater effect on the discrimination mechanism (especially when the second formant coincides with a harmonic). These jnd's are in good agreement with the extended modified place model.

For equal relative formant changes, the changes in the second formants exert the largest influence upon the jnd's, but there are several jnd's with a clear influence of the changes in the first formants (as can be seen by comparing the bottom halves of Figs. 4 and 2). The occurrences of these influences show no correspondence with the relative levels of the two formants. [Under four conditions the jnds for the two positions of F_1 (at a harmonic and between two harmonics) show a large difference; in contradiction to our expectations, the influence of the first formant is larger when this formant is actually lower in level.] For the 200-Hz fundamental and an F_2 positioned halfway between two harmonics [right side of panels (g) and (h), Fig. 4], the jnd's show a difference between the two positions of F_1 that is not found in the predictions of the model. Nevertheless, most predictions of the extended modified place model are in good agreement with the data.

Using the summation rule for independently perceived variables, predictions for the jnd's for combined formant changes can also be computed directly from those for single-formant changes. Under the assumption that the perceived difference is proportional to the frequency difference, an expectation for the jnd for combined formant changes can be derived from Eq. (1) as:

$$\text{jnd}=\sqrt{\frac{1}{(\omega_1/\text{jnd}_1)^2+(\omega_2/\text{jnd}_2)^2}}, \tag{2}$$

where ω_1 and ω_2 are weights that reflect the amounts of change in the first and the second formants, respectively. With the proper weights, this relation can be used to calculate predictions in terms of both formants, and it can be used when the jnd's are expressed in units of Hz as well as in percent. When calculating predictions in terms of the first formant, ω_1 must be equal to unity, and for predictions in terms of the second formant ω_2 must equal unity. The weight of the remaining formant must be chosen equal to the change in this formant divided by that in the formant in terms of which the predictions are expressed. For this the amounts of change must be expressed in the same units as the jnd's (in either Hz or percent). So, for the formant-frequency relation $\Delta F_1/F_1=2\Delta F_2/F_2$ the weights are $\omega_1=1$ and $\omega_2=1/2$, because the predictions are calculated in terms of the first formant and the relative change in the second formant is half that of the first formant. For the relation $\Delta F_1/F_1=\Delta F_2/F_2$ both weights are equal to unity.

The described weighting rules correspond with the behavior of Eq. (1). When the changes in both formants are equal, the excitation differences for each formant will have a certain value. When the amount of change in the second formant is halved, the corresponding excitation difference will be reduced to approximately half of its original value too. So, ΔE_2 in Eq. (1) will be reduced with a factor of 2. When the change in the second formant is halved, the value of ω_2/jnd_2 in Eq. (2) needs to be halved for these reductions to have corresponding effects in both equations. This is equal

TABLE II. Table of the results of Hawks (1994) and predictions of the various models.

Comparison of predictions	AH-UH	EH-AE
jnd's for parallel formant changes of Hawks (1994)	1.87	1.10
Present predictions Σ(Rel. Error)=0.025	1.75	0.94
Predictions $Hawks_1$ Σ(Rel. Error)=0.044	2.24	1.02
Predictions $Hawks_2$ Σ(Rel. Error)=0.038	1.94	0.89

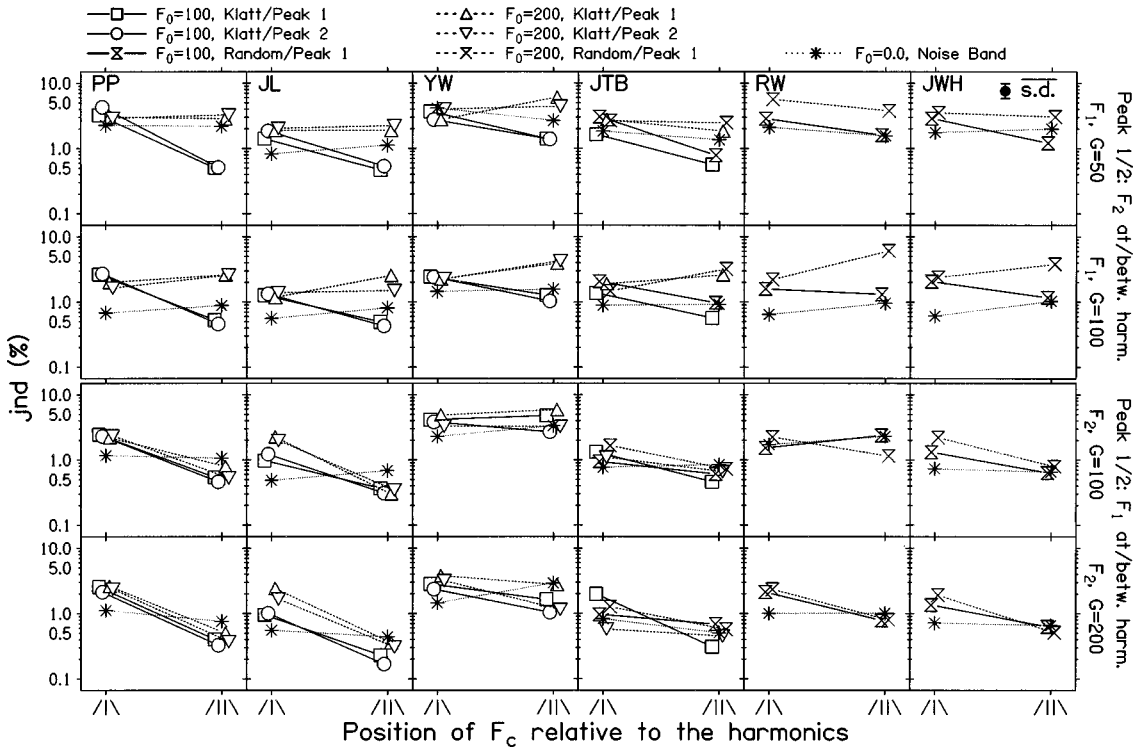

FIG. A1. Individual jnd's for single-formant changes. The rows show jnd's for the same conditions as in Fig. 2. The error bar in the right top corner indicates the mean standard deviation of the individual results. The meaning of the symbols is the same as in Fig. 2.

to the introduction of a weight $\omega_2 = 1/2$ in Eq. (2).

The predictions calculated with Eq. (2) are shown in Fig. 5, along with the replotted jnd's of Fig. 4. In general these predictions are close to those of the extended modified place model in Fig. 4. However, they approximate the data somewhat better, especially where we found different jnd's for the two peak relations. Under the conditions where the change in the first formant is two times that of the second (the upper half of Fig. 5) the sum of the squared relative errors over 16 data points is 0.6, where it was 0.9 for the extended place model, and for the equal formant changes (lower half of Fig. 5) this sum is 6.5, where it was 7.6. This indicates that the accuracy of the modeling slightly decreases when the modified place model is extended for the description of combined formant changes, but in both the Figs. 4 and 5 we find good correspondence between data and predictions.

When the relative change in the first formant (at approximately 500 Hz) is twice that of a second formant (at approximately 2000 Hz), the absolute change of the second formant is twice that of the first formant. This relation is identical to the one used by Mermelstein (1978) for his measurements with combined formant changes. Because the center frequency of his second formant was six times that of the first formant ($F_2 = 2100$ Hz and $F_1 = 350$ Hz), the relative change in the first formant was three times as large as for the second formant. So, when comparing this condition with the relative amounts of change in the present study, we expect that the changes in the first formant are dominant in his data. This effect can be observed in the averages of his jnds; for a single change in the first formant the average jnd is 49 Hz, and for a combined change it is 38 Hz (in terms of the first formant). For the second formant this decrease is much more dramatic; for a change in the second formant the average jnd is 172 Hz, compared with 76 Hz for a combined formant change (in terms of the second formant). So, the changes in the first formant dominated these jnd's.

Mermelstein predicted his jnd's for combined formant changes from those for single-formant changes (see Table I) by considering ''F_1 and F_2 to be independent parameters that contribute information to discriminability given by $\sqrt{\omega_1(\Delta F_1)^2 + \omega_2(\Delta F_2)^2}$, where ω_1 and ω_2 are appropriate weighting factors.'' Using this relation, Hawks (1994) could not replicate Mermelstein's predictions exactly. We were able to reproduce Mermelstein's predictions (which are in Hz and in terms of F_2) by using our Eq. (2) with the weights $\omega_1 = 1/2$ and $\omega_2 = 1$. In Mermelstein's experiments, the absolute change in the first formant was half that of the second formant. So, in disagreement with his formula, it appears that Mermelstein actually used a relation, equivalent to Eq. (2), in which the weights were squared as well as the independent parameters. Table I shows that the present, and Mermelstein's, predictions are closer to the data than both versions of Hawks' model.

Hawks (1994) used identical relative changes for the first and the second formant, but he performed only a few measurements with a single change in the first formant. For his predictions, he used the formula of Mermelstein (1978) to predict jnd's directly. In a first option he used the weights $\omega_1 = \Delta F_1/(\Delta F_1 + \Delta F_2)$, and $\omega_2 = \Delta F_2/(\Delta F_1 + \Delta F_2)$. In a second option he used the relative changes of the formants instead of the absolute changes in these relations. Since these relative changes were equal, both ω_1 and ω_2 were equal to 1/2. In these calculations the jnd's were expressed in Hz, and

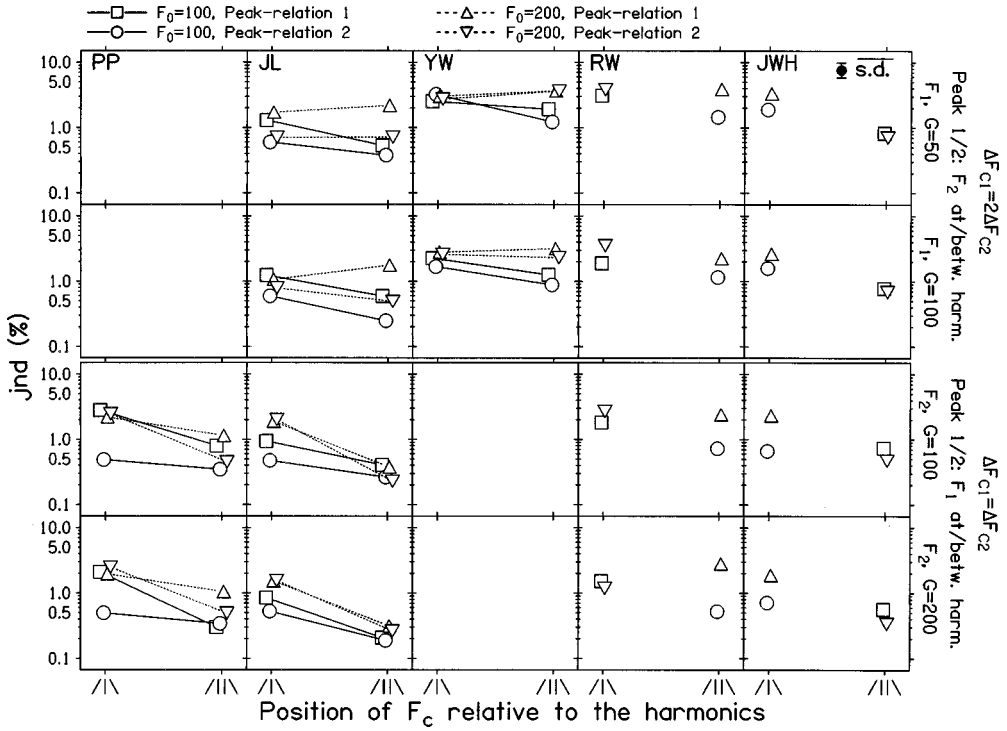

FIG. A2. The individual jnd's for combined formant changes. The format of this figure is the same as in Fig. 2. The meaning of the symbols is the same as in Fig. 4. The error bar in the right top corner indicates the mean standard deviation of the individual results. The uppermost two rows display data for a relative change in the first formant that was twice that of the second formant. The lowermost two rows display data for equal relative changes in both formants.

the predictions were given in terms of the second formant. For his vowels AH-UH and EH-AE he measured jnd's for parallel formant changes of 1.87% and 1.10%, respectively (in terms of F_2). Table II shows these jnd's and the corresponding predictions for Eq. (2) and for the first (Hawks_1) and second weighting option (Hawks_2) of Hawks. The sums of the squared relative errors show that the present model functions slightly better.

When applying the model of Hawks (1994) to the present data, we find better correspondence between predictions and data when using the weights of the second option. The sum of the squared relative errors between the predictions and the data is 129 for the first option and 68 for the second option (summed over 32 data points). However, the predictions calculated using our Eq. (2) approximate the data better than those of the model of Hawks for both weighting options. For this model the sum (over 32 data points) of the squared relative errors between predictions and data is 7.1. A comparison of the squared absolute errors between predictions and data provides the same conclusion. The most important aberrations of Hawks' model are encountered when the jnd's for the single-formant changes are about equal. Under such conditions the predictions are equal to, instead of smaller than these jnd's. This problem can be avoided when using Eq. (2).

The extensive data of Hawks' actual experiments show clearly that jnd's for parallel combined changes are smaller than those for single formant changes. His jnd's for opposite changes in the first two formants are practically equal to those for a single change of the second formant. So, for opposite combined formant changes the Eqs. (1) and (2) do not apply, they are only valid for parallel formant changes.

For the artificial vowels with two formants, one of which was changing, we found that the temporal discrimination mechanisms that were observed for single formants made way for a spectral process. For the two-formant vowels with parallel formant changes we could describe the data using a spectral model that was extended with a summation rule for these combined formant changes. So, for both cases of two-formant vowels we found that spectral rather than temporal processes were involved in the formant frequency discrimination. This implies that temporal discrimination processes only occur for single formants, and it seems very unlikely that listeners will be using them for discriminating between natural vowels.

V. CONCLUSIONS

For frequency discrimination of single-formant changes we find no influence of adding a stationary second formant to a stimulus containing a changing first formant. For changing second formants, the addition of a stationary first formant increases the jnd under many conditions. The resulting jnd's are in good agreement with the predictions of the modified place model. It can, therefore, be concluded that adding a stationary formant disturbs temporal discrimination processes, and limits the discrimination mainly to spectral processes. This transition from temporal to spectral formant-frequency discrimination appears to occur in central auditory processes.

Under many conditions, we found smaller jnd's for combined formant changes than for the corresponding single-formant changes. A good description of most of these data could be achieved with the modified place model, by extend-

ing this model with a summation rule for the individual excitation differences of the two changed formants.

Using the summation rule directly in Eq. (2), we could accurately predict the jnd's for combined formant changes from those for single-formant changes. With this equation we could also describe the data for parallel combined formant changes of Mermelstein (1978) and Hawks (1994). For his predictions, Mermelstein apparently used a relation equivalent to Eq. (2). To predict his data for combined formant changes, Hawks used a ''weighted Euclidean distance model.'' The predictions calculated with Eq. (2) agree better with the present and with Mermelsteins data than those from the model of Hawks.

Increasing the complexity of the stimuli appears to decreases the number of feasible mechanisms used for discrimination. For the more complex stimuli of our investigations, temporal discrimination mechanisms have disappeared and only spectral mechanisms, analogous to the modified place model, remain.

ACKNOWLEDGMENTS

This research was supported by the Netherlands Organization for Scientific Research (NWO) through the Foundation for Behavioral Sciences (SGW), and the Heinsius Houbolt Fund. The authors would like to thank J. W. Hawks and an anonymous reviewer for their constructive comments on an earlier version of this manuscript.

APPENDIX

A. Individual jnd's of experiment 1

The individual jnd's of the first experiment are presented in Fig. A1. Each row contains the just-noticeable differences, measured for one region of the center frequency of the changed formant and one value of the slope, in six panels with individual results. The columns contain the jnd's for the four combinations of formant frequency and slope. The meaning of the symbols, and the annotations /|\ and /||\, is the same as in Fig. 2. For clarity, the jnd's for the 100-Hz fundamental are connected with a solid, and those for the 200-Hz fundamental with a dashed line. The jnd's for the filtered noise bands are shown as asterisks, connected by a dotted line.

B. Individual jnd's of experiment 2

The individual jnd's for the combined formant changes of the second experiment are presented in Fig. A2. The format of each panel is identical to those of Fig. A1. All stimuli have a Klatt-phase relation. Each row contains the just-noticeable differences, measured for one combination of the slopes of the two formants, in five panels with individual results. The uppermost two rows contain jnds for the formant relation: $\Delta F_1/F_1 = 2\Delta F_2/F_2$, and the lowermost two rows for the relation: $\Delta F_1/F_1 = \Delta F_2/F_2$. The meaning of the symbols is the same as in Fig. 3. For clarity, the jnd's for the 100-Hz and 200-Hz fundamentals are connected with a solid and a dashed line, respectively. Due to an unfortunate choice in the distribution of the stimulus conditions over the subjects, RW and JWH contributed half the jnd series for both peak relations; under each condition their jnd's for the center frequencies at and between harmonics belong to a different peak relation. Therefore, their jnd's for each fundamental are not connected with lines.

[1]Since different groups of subjects participated for the different phase conditions, between-subject variations may have caused some spread in the averages, but the individual results in Fig. A1 of the Appendix show that jnd's are mostly very consistent over subjects.

[2]In these statistics, the data of subjects PP, JL, YW, and JTB were included in the averaging, although subject JTB only contributed jnd's for the Klatt/peak 1 condition. Excluding JTB from the analysis produced a ratio of 1.3, significant at the 1% level.

[3]The value of 1250 Hz was chosen at a location where the excitation showed a minimum between both formants, thus separating the excitation differences caused by these formants.

[4]For $F_0 = 200$ Hz and a formant halfway between harmonics [right sides of panels (e) and (f), Fig. 4], the average jnd's for peak relation 2 are smaller than those for peak relation 1. These relatively small jnds for peak relation 2 can also be seen in Fig. A2 in the individual results of subject JL, but not in those of subject YW. This inconsistency between subjects is reflected in the relatively large standard deviation of the averages in Fig. 4. So, here the changes in F_2 may have been used in the discrimination by subject JL, and possibly by JWH, but not by YW.

[5]In both cases, the differences between the individual jnd's for peak relations 1 and 2 bear inconsistencies between the subjects. In the lower half of Fig. A2, differences between the individual jnd's for both peak relations are found for subject PP, but not for subject JL. These inconsistencies are reflected in the relatively large standard deviations of the averages for peak relation 1. So, here the changes in F_1 may have been used in the discrimination by subject PP, and possibly by JWH, but not by JL.

Flanagan, J. L., (**1955**). ''A difference limen for vowel formant frequency,'' J. Acoust. Soc. Am. **27**, 613–617.

Hawks, J. W., (**1994**). ''Difference limens for formant patterns of vowel sounds,'' J. Acoust. Soc. Am. **95**, 1074–1084.

Henning, G. B., (**1966**). ''Frequency discrimination of random-amplitude tones,'' J. Acoust. Soc. Am. **39**, 336–339.

Kewley-Port, D., and Watson, C. S., (**1994**). ''Formant-frequency discrimination for isolated English vowels,'' J. Acoust. Soc. Am. **95**, 485–496.

Kewley-Port, D., Xiaofeng, L., Zheng, Y., and Neel, A. T., (**1996**). ''Fundamental frequency effects on thresholds for vowel formant discrimination,'' J. Acoust. Soc. Am. **100**, 2462–2470.

Klatt, D. H., (**1980**). ''Software for a cascade/parallel formant synthesizer,'' J. Acoust. Soc. Am. **67**, 971–995.

Lyzenga, J., and Horst, J. W., (**1995**). ''Frequency discrimination of band-limited harmonic complexes related to vowel formants,'' J. Acoust. Soc. Am. **98**, 1943–1955.

Lyzenga, J., and Horst, J. W., (**1997**). ''Frequency discrimination of stylized synthetic vowels with a single formant,'' J. Acoust. Soc. Am. **102**, 1755–1767.

Mermelstein, P., (**1978**). ''Difference limens for formant frequencies of steady-state and consonant-bound vowels,'' J. Acoust. Soc. Am. **63**, 572–580.

Modeling temporal asymmetry in the auditory system

Roy D. Patterson
Centre for the Neural Basis of Hearing, Physiology Department, University of Cambridge, Downing Street, Cambridge, CB2 3EG, United Kingdom

Toshio Irino
ATR Human Information Processing Research Laboratories, 2-2 Hikaridai Seika-cho, Soraku-gun Kyoto, 619-0288, Japan

(Received 24 July 1997; accepted for publication 14 August 1998)

Sound sources in the environment produce waves that are almost invariably asymmetric in time, and human listeners are highly sensitive to temporal asymmetry. The spectral analysis and neural transduction processes in the cochlea enhance temporal asymmetry, as do time-domain models of cochlear processes, but it appears that the resulting asymmetry is not sufficient to explain the observed perceptual asymmetry. In the auditory image model (AIM) of hearing, the temporal asymmetry in the neural activity produced by the cochlea is further enhanced by the ''strobed'' temporal integration that converts the neural activity pattern into an auditory image, and the temporal asymmetry in the auditory image is sufficient to explain the perceptual asymmetry. Modern versions of the ''duplex model'' of pitch have time-domain cochlea simulations that produce neural activity with temporal asymmetry similar to that produced by AIM. In the final stage, however, they apply autocorrelation to the neural pattern and autocorrelation is a symmetric process in time. In this paper the effect of autocorrelation on temporal asymmetry is examined in a range of auditory models with varying forms of auditory filterbank, compression, and neural transduction. It is concluded that autocorrelation does not enhance temporal asymmetry and often reduces it, and that autocorrelogram models cannot explain the magnitude of the perceptual asymmetry in their current form. Then, the original version of strobed-temporal-integration is reviewed with regard to temporal asymmetry, and the delta-gamma theory of temporal asymmetry [Irino and Patterson, J. Acoust. Soc. Am. **99**, 2316–2331 (1996)] is used to develop a new version of strobed-temporal-integration that is more robust and physiologically more plausible. [S0001-4966(98)05711-7]

PACS numbers: 43.66.Ba, 43.66.Jh, 43.66.Mk [RVS]

INTRODUCTION

A. The perception of temporal asymmetry

The ASA set of ''auditory demonstrations'' (Houtsma *et al.*, 1987) includes a very compelling illustration of the effects of short-term temporal asymmetry on auditory perception (No. 29). A piece of music is played on the piano, and then it is repeated with the waves for the individual notes reversed in time. The melody and harmony are largely unaffected by the manipulation, but the instrument is perceived to change from a piano to a reed organ whose notes end in disruptive complex transients. The existence of the demonstration shows that the effect of time reversal has been known for some time. Nevertheless, there was little research on the topic until Patterson (1994a, 1994b) initiated a systematic study of auditory temporal asymmetry with ''damped'' and ''ramped'' sinusoids. The damped sinusoid has a repeating, exponentially decaying envelope, and is illustrated with a 4-ms half-life in Fig. 1(a); the ramped sinusoid has a repeating, exponentially rising envelope, shown with the same half-life in Fig. 1(b). The perceptions produced by these sounds have two components: a drumming component produced by the stream of abrupt transients at the start of each cycle of the envelope, and a continuous tonal component with the pitch and timbre of the carrier. As the half-life increases from 1 to 100 ms, the relative loudness of the drumming component decreases while that of the tonal component increases.

What makes the sounds interesting for auditory modellers is that pairs with the same half-life have identical power spectra when calculated over an integer number of periods, but they are, nevertheless, discriminable over a wide range of half-lives, envelope periods, and carrier frequencies. Thus, they pose a serious problem for traditional spectral models of auditory perception (Patterson, 1994a). Akeroyd and Patterson (1995) extended the phenomenon to noise carriers using the same discrimination technique. The carrier is heard as hiss rather than a tone, and listeners were asked to discriminate damped and ramped pairs with the same half-life on the basis of the relative loudness of the drumming and hiss components. The long-term power spectra of pairs with the same half-life are the same, and, in this case, the short-term power spectra are the same, except the level changes in the short-term spectra of the ramped sound come in the reverse order to those of the damped sound. In a spectral model, then, the fact that the ramped noise produces a relatively louder hiss component would have to be explained, *post hoc*, on the basis of the order of the short-term spectra. Fay *et al.* (1996) showed that goldfish, which have no basilar membrane, can nevertheless discriminate damped and ramped sinusoids, and that generalization from a ramped

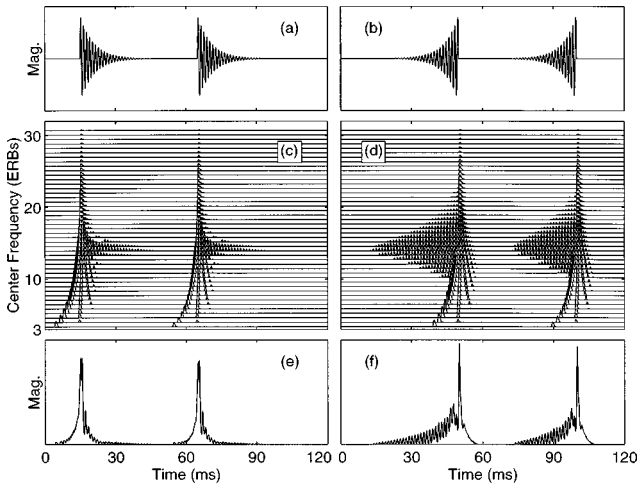

FIG. 1. Phase-compensated NAPs for damped (left) and ramped (right) sinusoids. The top row shows two cycles of the damped (a) and ramped (b) waves. The middle row shows the damped (c) and ramped (d) NAPs produced by the ***gtf/2dat*** model. The ordinate is channel center frequency on an ERB scale. The bottom row shows damped (d) and ramped (f) summary NAPs. The peak concentration is the activity in a 4-ms region about the peak divided by the activity in the complete cycle, and it is greater for the damped sound.

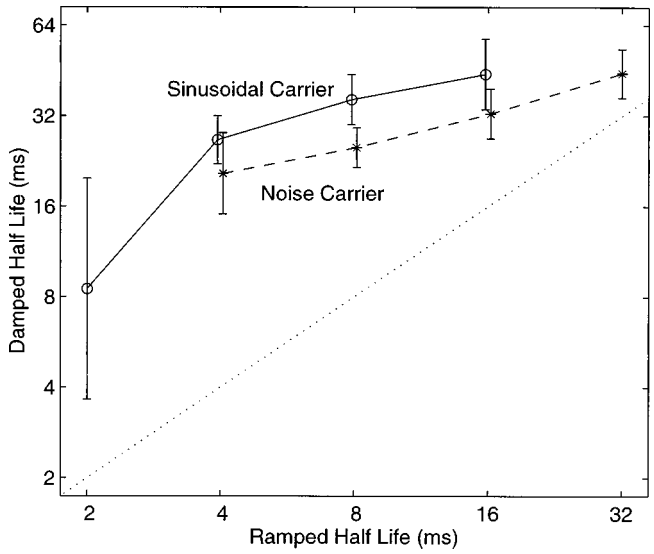

FIG. 2. Matching half-life values for damped and ramped sounds with sinusoidal carriers (open circles) and noise carriers (stars). Average data for four listeners. The matching half-life is the damped half-life required to produce the same perceptual click/carrier ratio as that produced by a given ramped sound. The equal half-life line is shown by the dotted diagonal; the average distance from the data to the diagonal is the measure of temporal asymmetry.

sinusoid to a flat-envelope sinusoid is stronger than generalization from a damped sinusoid to a flat-envelope sinusoid. Lorenzi *et al.* (1997) showed that cochlear implantees can discriminate damped and ramped sinusoids when the stimuli are presented on a single electrode, and that their performance was far superior to that of normals at longer half-lives. Since the implant bypasses the cochlea and stimulates the auditory nerve directly, it is difficult to see how a spectral model could explain this discrimination.

B. The measurement of temporal asymmetry

Irino and Patterson (1996) refined the damped/ramped discrimination experiment to provide a direct measure of auditory temporal asymmetry. The experiment is described in some detail because the measurement and quantification of the perceptual asymmetry are central to the modeling studies presented in the paper that follows. In a two-alternative, forced-choice experiment, listeners were presented a ramped sinusoid in one interval and a damped sinusoid having the same *or greater* half-life in the other interval. In one version of the experiment, the listeners were asked to choose the interval containing the sound with the louder tonal component; in another version with the same stimuli, they were asked to choose the interval with the louder drumming component. Between trials, the half-life of the damped sinusoid was varied to determine the ''matching point,'' that is, the half-life of the damped sinusoid required to equate the probability of choosing either the ramped or damped stimulus as the one with the louder tonal or drumming component. Then the experiments were repeated using noise carriers, and listeners were asked to choose either the interval with the louder hiss component or the interval with the louder drumming component, relative to the other component. The results showed that listener variability was exceptionally low; the type of response did not affect either the form *or the horizontal position* of the psychometric functions with either carrier, and so the data were averaged over listener and response type.

The average matching-point data for the sinusoidal and noise carriers are presented by open circles and asterisks, respectively, in Fig. 2 (Fig. 4 of Irino and Patterson, 1996). The abscissa is the half-life of the ramped sound, and the figure shows the half-life that the damped sound must have to produce a perception in which the two components have the same relative loudness. If there were no perceptual asymmetry, the data would lie along the dotted diagonal. All of the data lie well above this line, indicating that, relative to the drumming component, the carrier is substantially louder in the ramped sounds when the half-life is in the range 2–32 ms. The open circle above 4 ms shows the extreme case; the damped sinusoid has to have a half-life of about 25 ms to produce a tonal component with the same relative loudness as that produced by the 4-ms ramped sinusoid. In other words, to match the tonal component of the ramped sound in Fig. 1(b), the half-life of the damped sinusoid in Fig. 1(a) has to be extended to the point where the amplitude of the carrier at the end of the envelope cycle is still fully half the starting height! Comparison of the open circles and asterisks shows that the asymmetry with the sinusoidal carrier is greater than the asymmetry with the noise carrier. Irino and Patterson (1996) suggested that the main effects could be simply summarized for modeling purposes in terms of two ''asymmetry factors,'' one for the sinusoidal carrier and one for the noise carrier. The asymmetry factor was defined as the average distance in logarithmic units between the matching half-life and the equal half-life (dotted diagonal) for all of the ramped half-lives associated with one carrier. For the data in Fig. 2, the asymmetry factors for the sinusoidal and noise carriers

are 2.1 and 1.4, respectively.[1] That is, the matching half-lives of the damped sounds are, on average, about 4 and 2.5 times larger than those of the ramped sounds, respectively. The data in Fig. 2 and the asymmetry factors are the focus of the asymmetry modeling in this paper.

C. Modeling temporal asymmetry

In the damped/ramped papers mentioned above, the authors explain the perceptual asymmetries in terms of temporal asymmetries in the auditory image model (AIM) (Patterson *et al.*, 1992, 1995). The model consists of an auditory filterbank that produces a representation of basilar membrane motion (BMM), a multi-channel, neural transduction mechanism that produces a representation of the neural activity pattern (NAP) in the auditory nerve, and a bank of ''strobed'' temporal integration units that produce the model's representation of the auditory image that we hear in response to the sound. Irino and Patterson (1996) showed that all three stages of the model enhanced temporal asymmetry as the information passed through, and they argued that all three transformations were required to explain the magnitude of the perceptual asymmetry shown in Fig. 2. They summarize their studies in terms of a general ''delta-gamma'' theory of temporal asymmetry in the auditory system.

AIM has essentially the same architecture as the original autocorrelogram model of pitch perception proposed by Licklider (1951), computational versions of which have been developed by Lyon and colleagues (Lyon, 1982, 1984; Slaney and Lyon, 1990), Assmann and Summerfield (1989, 1990), Meddis and Hewitt (1991a, b, 1992), and Brown and Cooke (1994) among others. Brown and Cooke (1994) present a review of autocorrelation models and their uses. In each of these autocorrelogram (ACG) models there is an auditory filterbank that simulates BMM, a multi-channel transduction mechanism that simulates the NAP, and a bank of autocorrelators to produce the ACG, and so the primary difference between AIM and the traditional ACG model is in the final stage, where the former has strobed temporal integration and the latter has autocorrelation. AIM and the ACG model often produce very similar results. For example, both have been used to explain the pitch and pitch strength of high-pass filtered iterated rippled noise (IRN) (Yost *et al.*, 1996; Patterson *et al.*, 1996; Yost *et al.*, 1998), which appears to be beyond the capabilities of spectral model of hearing, even those based on short-term spectra. The delay-and-add process used to generate IRN, introduces a ripple into the power spectrum of the stimulus that can be used to explain the pitch in a spectral model when the ripple is resolved in the auditory system. However, the pitch persists when the stimulus is high-pass filtered to remove the frequency region where the ripple would be resolved.

AIM and the ACG model produce similar predictions for the pitch and the pitch strength of IRN (Yost *et al.*, 1996; Patterson *et al.*, 1996), which led to the question as to whether AIM and the ACG model could be distinguished by their ability to explain the perception of temporal asymmetry. The reason for doubting the ACG model was that autocorrelation is a symmetric process in time; given a periodic wave like a static vowel with an intraperiod waveform that is asymmetric in time, the autocorrelation of the sound is, nevertheless, symmetric within the autocorrelation cycle. For example, see the auditory image and the ACG of the vowel /ae/ presented in Figs. 2(c) and 3(c) of Patterson *et al.* (1995). Irino and Patterson (1996) argued that the strobed temporal integration mechanism in AIM accentuates the shape of ramped features in the NAP but not those of damped features (see Sec. III). As a result, it enhances the asymmetry of ramped and damped sounds in the auditory image to the level where it can explain the magnitude of the perceptual asymmetry shown in Fig. 2. If autocorrelation reduces temporal asymmetry rather than enhancing it, then it seems likely that ACG models will not produce sufficient temporal asymmetry to explain the magnitude of the observed differences in relative loudness.

D. Overview of the paper

In Sec. I, the temporal asymmetry produced by the default version of AIM (Release 7) is compared with that observed when AIM's strobed temporal integration is replaced by autocorrelation. Then, the temporal asymmetry observed with the autocorrelation model of Meddis and Hewitt (1991a, b) is compared with that observed when the autocorrelation module in that model is replaced by strobed temporal integration. In both cases, strobed temporal integration produces sufficient temporal asymmetry to explain the magnitude of the perceptual asymmetry, and, in both cases, autocorrelation does not produce sufficient temporal asymmetry to explain the perceptual asymmetry.

The first stage of both AIM and the Meddis and Hewitt model is a linear gammatone filterbank. Cochlear filtering, however, is nonlinear and arguably more asymmetric in time than gammatone filtering. Accordingly, in Sec. II, the gammatone filterbank of the Meddis and Hewitt model is replaced with the active cochlea simulation of Giguère and Woodland (1994) to determine whether this will lead to more asymmetry in the resulting ACGs. Once again the analysis reveals insufficient asymmetry to explain the magnitude of the perceptual asymmetry.

The form of compression varies from model to model and it was suggested that this might affect temporal asymmetry, and so a separate study was performed in which three forms of compression were crossed with three forms of neural transduction to determine the effects on asymmetry. It is concluded that compression has little effect on asymmetry and so the studies are presented as an Appendix.

The analysis of asymmetry in the auditory images produced by the default version of AIM (R7) (Sec. I E) reveals that the original strobe mechanism explains the form and magnitude of the perceptual asymmetry better than the more physiological ''delta-gamma'' strobe mechanism developed in Irino and Patterson (1996). In Sec. III, we first determine why this is so, and then use this information to develop a more robust version of the delta-gamma strobe that can explain the form and magnitude of the perceptual asymmetry.

Terminology: Over the course of this paper, upwards of a dozen different auditory models are reviewed with regard to their temporal asymmetry. To assist in distinguishing the models, they are referred to by abbreviations involving the

processes that they employ, and these labels are presented in bold, italic, lower-case symbols. The auditory representations produced by the models are distinguished by abbreviations presented in unbold, upper-case symbols. The Meddis and Hewitt (1991a) model consists of a gammatone auditory filterbank, ***gtf***, to simulate basilar membrane motion (BMM), a bank of Meddis (1986, 1988) haircells, ***med***, to simulate the neural activity pattern (NAP) in the auditory nerve, and a bank of autocorrelators, ***ac***, to produce the autocorrelogram (ACG). It is referred to as a ***gtf/med/ac*** model. AIM has the identical auditory filterbank for spectral analysis, it uses two-dimensional adaptive thresholding, ***2dat***, to simulate the NAP, and it uses strobed temporal integration, ***sti***, to produce the auditory image (AI) (Patterson *et al.*, 1995). So it is a ***gtf/2dat/sti*** model. The modules required to assemble the default version of AIM (R7) and the Meddis and Hewitt (1991a) model are available in the software package described by Patterson *et al.* (1995).[2]

I. ASYMMETRY IN AIM R7 AND MEDDIS AND HEWITT (1991a)

The filtering and transduction processes in the AIM and Meddis and Hewitt (1991a, b) are *all asymmetric in time*. It is a natural property of causal, physical systems. Thus, the question, as noted by Irino and Patterson (1996), is not so much 'Where does asymmetry arise in the auditory system?' but rather, 'Which asymmetry dominates and is primarily responsible for the perceptual asymmetry we hear?' To answer the question and evaluate the effect of ***ac*** on asymmetry, we follow the approach set out by Irino and Patterson. That is, we identify structures associated with the transient and carrier components of the perceptions in the model output, and develop a measure of the relative loudness of the components (the peak concentration, PC), a measure that is applicable to all of the representations of sounds produced by these models. The matching point for a given ramped sound is determined by calculating its PC and then finding the damped half-life required to produce the same PC value. In this way, the matching points for all conditions in the experiment can be calculated for a particular form of model output and converted to asymmetry factors to compare with those of the experimental data.

A. Asymmetry measures derived from auditory models

The auditory models described in this paper begin with 75-channel auditory filterbanks covering the frequency range 100 to 6000 Hz, and all of the NAPs, ACGs, and AIs have the same number of channels. The asymmetry information is distributed both in time and frequency in all these different representations. The decision statistic developed by Irino and Patterson to summarize the asymmetries and predict listeners' performance is illustrated in Fig. 1, which is adapted from Fig. 8 of Irino and Patterson (1996). The upper panels show two cycles of damped and ramped sinusoids with carrier frequencies of 800 Hz, half-lives of 4 ms, and envelope periods of 50 ms. The middle panels show phase-aligned NAPs produced by the AIM in response to the stimuli. Patterson (1994a) argued that the drumming component of the perception arises from the vertical structure in the NAP which is produced by the transient in each cycle of the stimulus, whereas the tonal component of the perception arises from the horizontal triangular structure associated with the carrier in each cycle; the triangular structure follows the vertical structure in the damped NAP and precedes it in the ramped NAP.

To provide a measure of the relative loudness of the transient and carrier components, Irino and Patterson (1996) averaged the NAPs across frequency to produce summary NAPs, as shown in Fig. 1(e) and (f). Information about the transient component is concentrated about the peak in the NAP while information about the carrier is contained in the region away from the peak. Information about the timbre of the components is contained in the fine structure of the summary NAP. For example, the time intervals in the ramped summary NAP are highly regular, like those in the NAP itself, indicating that the timbre of the carrier is a tone and the pitch of the tone is 1/1.25 ms, or 800 Hz. The summary NAP of the ramped noise has a similar envelope but the time intervals in the region away from the peak are highly irregular, revealing that the timbre of the carrier is a hiss, and there is no pitch (see Akeroyd and Patterson, 1995, Fig. 4). In the experiment of Irino and Patterson (1996), however, the listeners were not required to identify the carrier; rather they were instructed to focus on the relative loudness of the carrier component (tone or hiss) compared to the transient component (drumming sound). The information about relative loudness is contained in the areas occupied by the transient and carrier portions of the summary NAP. There is relatively more activity in the region of the peak in the summary NAP of the damped sinusoid, which produces the perception with the louder drumming component, and there is relatively more carrier activity away from the peak in the summary NAP of the ramped sinusoid, which produces the perception with the louder tonal component. This led them to suggest that the relative loudness of the drumming component of the perception might be characterized by the ''peak concentration'' in the NAP; that is, the ratio of ''the average activity level in the 4-ms segment around the peak'' to ''the average activity level in the remainder of the cycle.''

The decision statistic was defined to be the peak concentration of the damped sound over the peak concentration of the ramped sound, and it was designated the peak concentration ratio (PCR). To predict the matching point for a given ramped sound, the half life of the damped sinusoid was varied to find the value that produced a PCR of unity. That is, the summary NAP of a given ramped sound was generated and used to calculate its peak concentration, and then summary NAPs and peak concentration values were generated for damped sounds with varying half-lives to find the one that produced the same peak concentration value as that of the ramped sound. The process was repeated for all ramped half lives, separately with the tone and noise carriers, to generate a complete set of matching points to compare with those in Fig. 2; then the logarithms of the matching-point values were averaged to produce asymmetry-factor values for the tone and noise carriers. The details of the PCR cal-

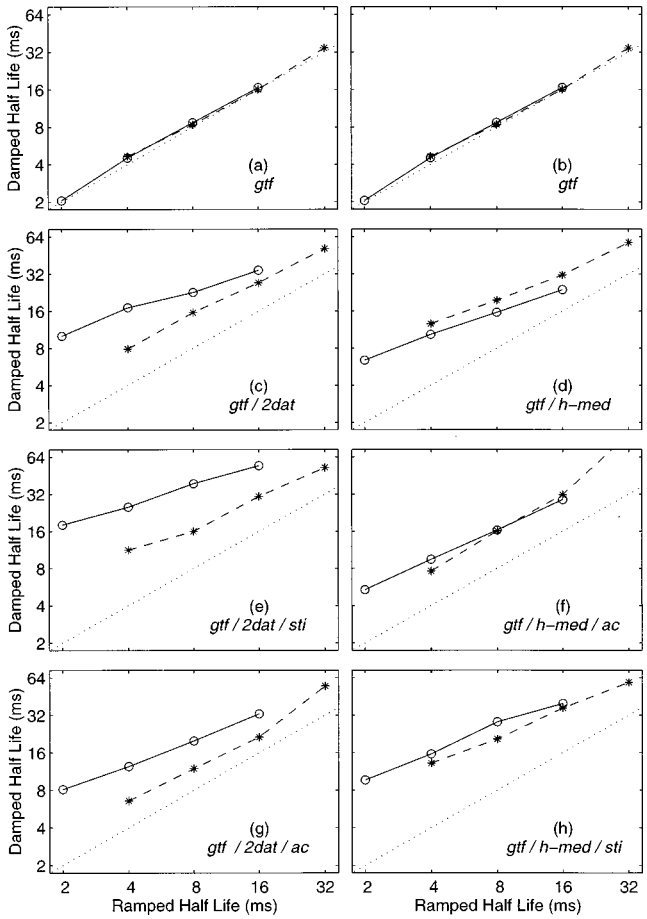

FIG. 3. Matching half-lives for sinusoidal (open circles) and noise (stars) carriers produced by the three stages of AIM (left column, ***gtf/2dat/sti***) and Meddis and Hewitt (1991) (right column, ***gtf/med/ac***). The gammatone filterbank [(a) and (b)] produces asymmetry only at 4 ms and the asymmetry is minimal. The cochlea simulation in AIM (c) produces more asymmetry than that of the Meddis and Hewitt model (d). The ***sti*** mechanism enhances asymmetry measured in the NAP (e) and (g); the ***ac*** module does not enhance asymmetry on average (f) and (h).

culation are presented in Appendix B of Irino and Patterson (1996).

B. Asymmetry in the auditory image model

The matching half-lives were determined for all of the conditions in the damped/ramped experiments at the output of each stage of the default version of AIM. The results are plotted in the upper three panels of the left-hand column of Fig. 3; each panel has the same format as the experimental data in Fig. 2. Then the ***sti*** module was replaced with an ***ac*** module and matching points were calculated from the resulting ACGs. The values are plotted in the bottom panel of the left-hand column of Fig. 3. Note that whenever there is asymmetry, it is invariably the case that the damped half-life is greater than the ramped half life. In this subsection, we compare the magnitude of the asymmetry at each level with that in the experimental data.

(i) ***gtf***: The measurement of asymmetry at the ***gtf*** stage was based on half-wave rectified versions of the individual filtered waves, which were phase aligned and averaged to produce a summary BMM in the same way as described for the summary NAP. The simulated matching-point data are presented in Fig. 3(a), which shows that there is virtually no measurable asymmetry for either carrier except at the 4-ms half-life where there is a small amount for both carriers. The impulse response of the gammatone filter has an exponential tail and its half-life is on the order of 4 ms in the region of 800 Hz. In this region, the response to the transient in the damped sound is slightly more concentrated than the response to the transient in the ramped sound. At shorter half-lives both ramped and damped sounds are like impulses to the gammatone filter; at longer half-lives the output just follows the stimulus with a short lag and the peak concentration is essentially the same for damped and ramped sounds. Thus, although it is true that gammatone filtering is asymmetric in time, and responses to ramped and damped sounds are different, the size of the difference is far too small for the PCR to explain the magnitude of the perceptual asymmetry observed in the experiments.

(ii) ***gtf/2dat***: The neural encoding stage in the AIM is a form of two-dimensional, adaptive thresholding ***2dat***, (Patterson and Holdsworth, 1996; Patterson *et al.*, 1995). It converts AIM's simulation of BMM into its simulation of the NAP. The adaptation in this module is highly asymmetric in time; the output of the module rises almost instantaneously with membrane amplitude, but the rate of decrease in the output after a peak is restricted to values on the order of 1 dB/ms. As a result, the asymmetry in adaptive thresholding interacts with that of the damped and ramped sounds over a larger range of half-lives than for gammatone filtering, increasing the negative slope of damped features and decreasing the positive slope of ramped features. The operation of adaptive thresholding and its role in asymmetry are discussed at length in Irino and Patterson (1996). The matching half-lives produced by sinusoidal and noise stimuli with ***gtf/2dat*** are presented in Fig. 3(c). The pattern of asymmetries is correct inasmuch as both carriers produce substantial asymmetry, and that for the sinusoidal carrier is greater than that for the noise carrier. The degree of asymmetry, however, is not as large as that observed in the experiments in the range 4–16 ms. The asymmetry factors for the experimental data (2.1 and 1.4 for the tone and noise carriers, respectively) are shown by the leftmost pair of bars in Fig. 4; they summarize the two sets of data presented in Fig. 2. The asymmetry factors for ***gtf/2dat*** [Fig. 3(c)] are presented by the second pair of columns in Fig. 4 over ''***2dat***,'' and they show in a more compact form that the asymmetry produced by ***gtf/2dat*** has the correct form but it is not large enough to explain the magnitude of the perceptual asymmetry.

(iii) ***gtf/2dat/sti***: The ***sti*** mechanism that converts NAPs into AIs in the original version of the AIM, employs an adaptive threshold somewhat like that in ***2dat***; it rises rapidly with level prior to a NAP peak and falls

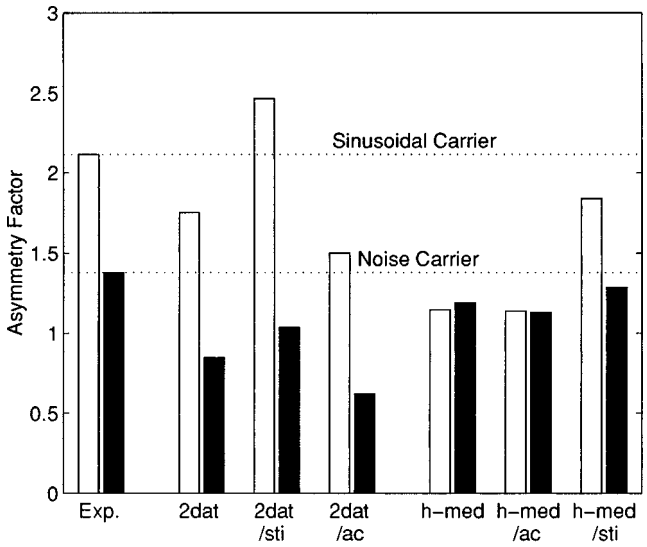

FIG. 4. Asymmetry factors calculated from the matching half-lives measured in the perceptual experiment (Exp), and from the representations underlying the predicted matching points in panels (c)–(h) of Fig. 3: on the left, the NAPs (***2dat***), AIs (***2dat/sti***), and ACGs from AIM (***2dat/ac***); on the right, the NAPs (***h-med***), ACGs (***h-med/ac***), and AIs (***h-med/sti***) from Meddis and Hewitt (1991a). Whereas ***sti*** enhances temporal asymmetry in the NAP, ***ac*** does not.

slowly after the NAP peak. In this version of ***sti***, however, the rate of decrease is 2%/ms, which is much slower than in ***2dat***. The strobe asymmetry enhances the damped/ramped asymmetry in the auditory image over that in the NAP, but in a different way; it has virtually no effect of damped features because they decay faster than the strobe threshold, but it does reduce the positive slope of ramped features because the ramped features induce multiple strobes per envelope period. The effect is described in detail in Sec. III B.

(iv) Auditory images are automatically phase aligned by the ***sti*** mechanism because it works asynchronously on individual channels, and the NAP peak that initiates temporal integration is mapped to the 0-ms interval in the auditory image (Patterson *et al.*, 1992). Thus, the PCR measure developed for NAPs is directly applicable to AIs. The matching-point data produced by damped and ramped sounds with sinusoidal and noise carriers in the auditory image, using the default version of the AIM, are presented in Fig. 3(e); the asymmetry factors are presented in the third pair of columns in Fig. 4. The pattern of asymmetries is correct, and, in this case, the average degree of asymmetry is close to that in the data. The matching points produced by sinusoidal carriers are a little greater than those observed in the experiments, and the matching points for noise carriers are a little less than those observed. Nevertheless, it is an excellent fit when compared with the problems of explaining temporal asymmetry with spectral models and leaky-integrator models (Patterson, 1994a; Akeroyd and Patterson, 1995; Patterson and Irino, 1996).

(v) ***gtf/2dat/ac***: To provide a direct comparison of the effect of ***ac***, a ***gtf/2dat/ac*** version of an autocorrelogram model was assembled using the first two stages of the AIM, that is, ACGs were generated from the AIM NAPs that produced the matching points in Fig. 3(c). The NAP asymmetry is relatively large and the asymmetry for the sinusoidal carrier is substantially greater than that for the noise carrier, so these NAPs might be expected to provide a sensitive test of the effects of ***ac***. The matching points from the ACGs are presented in Fig. 3(g) and the asymmetry factors are presented in the fourth pair of columns in Fig. 4. Comparison of Fig. 3(g) with Fig. 3(e) shows that, when applied to the same NAPs, ***ac*** produces less temporal asymmetry than ***sti***. Comparison of the second and fourth pairs of columns in Fig. 4 shows that ***ac*** actually reduces the temporal asymmetry of the NAPs presented as input to the ACG module.

C. Asymmetry in the model of Meddis and Hewitt (1991a, b)

AIM was not originally designed as an autocorrelogram model and so the analysis was repeated with the autocorrelogram model of Meddis and Hewitt (1991a, b) which is perhaps the most commonly referenced computational version of Licklider's (1951) autocorrelation model. Matching half-lives were determined for all of the conditions in the damped/ramped experiments at the output of each stage of the Meddis and Hewitt model (***gtf/med/ac***), and the results were plotted in the upper three panels of the right-hand column of Fig. 3. Then the ***ac*** module used to construct the ACGs was replaced with the ***sti*** module used to construct auditory images in the AIM, and matching points were calculated from the AIs to compare with those from the ACGs. The matching points are plotted in the bottom panel of the right-hand column of Fig. 3.

(i) ***gtf***: The Meddis and Hewitt model (***gtf/med/ac***.) employs the same gammatone auditory filterbank as the default version of the AIM, and so the matching points produced by this stage, and plotted in Fig. 3(b), are the same as those for the AIM, plotted in Fig. 3(a). The subfigure is included simply to maintain the parallel presentation of the two models.

(ii) ***gtf/med***: In the Meddis and Hewitt model the transduction is performed by a bank of haircell simulators (Meddis, 1986, 1988). Table I of Meddis (1988) presents two sets of parameter values for haircells that lead to medium- and high-spontaneous rate firing in primary fibers, and Table II of Meddis *et al.* (1990) presents two different sets of parameter values. The default parameter values for the Meddis module in the AIM software package are those associated with the medium spontaneous-rate fiber in Meddis *et al.* (1990) which will be referred to as ***m-med***. It has the greatest dynamic range and so is least restricted by the maximum firing rate of the haircell. Matching points were calculated with this version of the haircell and they are positive, indicating that the asymmetry associated with adaptation in the Meddis haircell does interact with the asymmetry of the stimuli. The size of

the asymmetry, however, was not nearly large enough to explain the perceptual asymmetry. The asymmetry factors for the sinusoidal and noise carriers were about 0.4 and 0.6, respectively.

(iii) The AIM package also includes parameter values for the high-rate fiber of Meddis *et al.* (1990) which will be referred to as ***h-med***. The high-rate fiber is more reactive than the medium-rate fiber, with a stronger onset response and stronger adaptation that together make ***h-med*** more asymmetric in time; the dynamic range of ***h-med***, however, is about 40 dB rather than the 60 dB of ***m-med***. Matching points produced by ***gtf/h-med*** are presented in Fig 3(d), the asymmetry factors are presented by the fifth pair of columns in Fig. 4, over ''***h-med***.'' They show that ***h-med*** produces much more asymmetry than ***m-med***, but it is still less than that required to explain the perceptual asymmetry. Comparison of Fig. 3(d) with Fig. 3(c) shows that, on average, the asymmetry produced by ***gtf/h-med*** is about the same as that produced by ***gtf/2dat***; however, with ***h-med***, the sinusoidal carrier produces *less* asymmetry than the noise carrier, which is incorrect.

(iv) ***gtf/h-med/ac***: The multi-channel NAPs from the Meddis haircell are converted into ACGs by applying ***ac*** separately to each channel of the NAP. The resulting ACGs are automatically phase aligned because ***ac*** is phase insensitive. So the PCR measure developed for NAPs is directly applicable to ACGs. The matching-point data produced by ***gtf/h-med/ac*** in response to sinusoidal and noise stimuli are presented in Fig. 3(f), and the asymmetry factors are presented in the sixth pair of columns in Fig. 4, over ''***h-med/ac***.'' Both figures show that the asymmetry in the ACG is essentially the same as that in the NAP from which it was derived [compare Fig. 3(f) with Fig. 3(d), and compare the fifth and sixth pairs of columns in Fig. 4]. Thus, the ***ac*** process in the Meddis and Hewitt model neither enhances nor attenuates the temporal asymmetry observed in the NAPs.

(v) ***gtf/h-med/sti***: The ***ac*** module was replaced by the ***sti*** module in the default version of the AIM and the matching points produced by the resultant ***gtf/h-med/sti*** model are presented in Fig. 3(h); the asymmetry factors appear in the rightmost pair of columns in Fig. 4. The pattern of asymmetries has the correct form and the average level of asymmetry is almost large enough to explain the magnitude of the perceptual asymmetry. The difference in asymmetry between sinusoidal and noise carriers is rather smaller than in the perceptual data.

(vi) ***Summary***: The fact that autocorrelation does not enhance temporal asymmetry was to be expected, inasmuch as autocorrelation is a symmetric process in time. Nevertheless, it seemed important to begin by demonstrating that the ACGs produced by the Meddis and Hewitt (1991a, b) model, or the AIM with ***ac*** in place of ***sti***, do not have sufficient temporal asymmetry to explain the magnitude of the perceptual contrast between damped and ramped sounds. A similar conclusion has recently been reported by de Cheveigné (1998). It seems likely that the ACG models of Assmann and Summerfield (1989, 1990) and Brown and Cooke (1994) cannot explain the magnitude of the perceptual asymmetry either, insofar as they employ very similar filterbanks for their spectral analyses and the same Meddis haircell models for neural transduction. It is possible that an extra stage could be added to the ACG model to enhance the temporal asymmetry of the ACG, but the prospects for this solution do not seem good inasmuch as the asymmetry with sinusoidal carriers is barely greater than that with noise carriers.

II. ASYMMETRY AND AUTOCORRELATION WITH A LEVEL-DEPENDENT AUDITORY FILTERBANK

Whereas the gammatone filterbank is linear, cochlear filtering is level dependent; the bandwidth of the filter increases and the duration of the impulse response decreases as the intensity of the stimulus increases (Evans, 1977). The dynamic range of damped and ramped sounds is large, so there are significant changes in the duration of the impulse response over the cycle of the sound. The nonlinear cochlear filter has a relatively broadband response to the peak amplitude in the transient and a relatively narrow-band response to the low-level portion of the carrier, and it is difficult to predict how the nonlinearities might interact with the temporal asymmetry of damped and ramped sounds. It is also the case that the phase response of the cochlea differs from that of the gammatone filterbank and the difference has measurable perceptual effects. Kohlrausch and Sander (1995) and Carlyon and Datta (1997) have measured masking period patterns for time-reversed, temporally asymmetric sounds (positive and negative Schroeder-phase waves) and shown that the peak factor in the internal representation of the two sounds is different. But again, it is not clear how this might interact with the temporal asymmetry of damped and ramped sounds.

A. Meddis and Hewitt (1991) with a level-dependent filterbank

There are several level-dependent filterbanks which are used to simulate cochlear filtering, and they can assist in understanding the interaction of level and temporal asymmetry (e.g., Lyon, 1982; Strube, 1985; Giguère and Woodland, 1994). The latter two of these filterbanks have separate, nonlinear, feedback circuits in the individual sections of the filterbank to simulate the effects of outer haircells. The compression in the feedback circuit is similar in form to that thought to exist in the cochlea (Giguère and Woodland, 1994), and so these filterbanks are arguably more appropriate as preprocessors for the Meddis haircell than the gammatone filterbank. The original Meddis (1986) haircell algorithm has an input compressor that is not properly part of the haircell simulation. It was included to control the dynamic range of the haircell input when the haircell is driven by a linear filterbank as in Meddis and Hewitt (1991). The physiological version of the AIM (Patterson *et al.*, 1995, Fig. 1, right column) is like a Meddis and Hewitt (1991) model with a some-

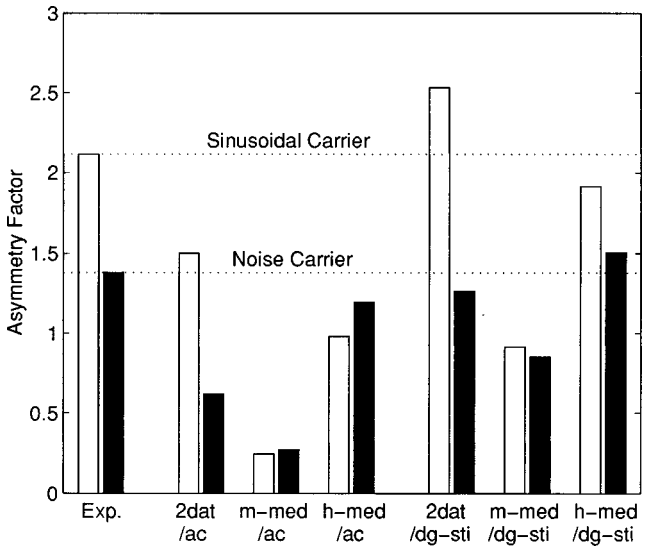

FIG. 5. Asymmetry factors calculated from the matching half-lives measured in the perceptual experiment (Exp), and from the matching half-lives predicted from six auditory models: On the left, three level-dependent ***(tlf)*** ACG models with different neural transduction stages (***2dat, m-med,*** and ***h-med***); they show that ***ac*** does not produce more asymmetry with a level-dependent filterbank ***(tlf)***. On the right, three level-independent (***gtf***) AI models (***dg-sti***) with the same neural transduction stages (***2dat, m-med,*** and ***h-med***); they show that ***dg-sti*** enhances temporal asymmetry in each case.

what more realistic cochlea simulation, that is, a level-dependent filterbank with compression. It is a combination of the Giguère and Woodland (1994) transmission-line filterbank (***tlf***), the Meddis *et al.* (1990) haircell model without the input compressor (***med***), and autocorrelation (***ac***). In this section, asymmetry factors for damped/ramped discrimination are calculated from the ACGs produced by this physiological version of the AIM (***tlf/med/ac***) using both the medium- and high-rate fibers from Meddis *et al.* (1990) to determine whether this would lead to greater asymmetry in the ACGs as suggested by Slaney (1994) (personal communication).

B. Phase-alignment in physiological NAPs

When calculating the PCR, phase alignment across channels is important for preserving the peak associated with the transient, as described in Sec. II A (Fig. 1). In the case of gammatone filtering, the appropriate phase compensation is a fixed temporal shift for a given channel, independent of level. This is not the case with transmission-line filtering, however, and we were not able to establish a reliable method of phase alignment and peak preservation for damped and ramped sounds. As a result, there are no asymmetry measures for the NAPs of the physiological model on their own. Nevertheless, ***ac*** produces phase alignment automatically, and so the temporal asymmetry of the model can be measured in the ACG.

C. Asymmetry in the level-dependent ACG

The asymmetry factors measured with the ***tlf/med/ac*** model are shown in the third and fourth pairs of columns in Fig. 5 for the medium- and high-rate fibers, respectively. They are essentially the same as the results produced with ***gtf*** in the original version of the Meddis and Hewitt model. There is not enough asymmetry to explain the magnitude of the perceptual asymmetry, and the asymmetry with sinusoidal carriers is not greater than that for noise carriers. The first pair of columns shows asymmetry factors measured in the experiment, as before. The second pair of columns shows the asymmetry factors produced by ***gtf/2dat/ac*** for comparison; these are the same values as in the fourth column of Fig. 4. Note that it is the combination of ***h-med*** with ***ac***, or ***m-med*** with ***ac***, that is the problem. In Sec. I C it was revealed that AIs produced with ***gtf/h-med/sti*** produce sufficient asymmetry, on average, to explain the magnitude of the perceptual asymmetry. And looking ahead briefly, in Sec. III B we show that AIs produced with ***tlf/h-med/dg-sti*** produce sufficient asymmetry to explain the perceptual asymmetry. So the problem is more with autocorrelation than with the Meddis haircell.

D. The effect of compression on asymmetry

The form of compression in the Meddis and Hewitt (1991) model is different from that in AIM, and the asymmetry measured at the output of the compressor stage in the AIM is a little greater than that with the filterbank on its own (Irino and Patterson, 1996, Fig. 5). It is also the case that the adaptation is different in the two models (***2dat*** vs. ***med***). As a result, we investigated the effect of compression on asymmetry using three forms of compression (none, square-root, and log), crossed with three forms of neural transduction (***2dat***, ***m-med***, and ***h-med***), to determine the contribution of compression to asymmetry. The analysis of these nine auditory models, and the argument as to why they represent a sufficient investigation of the compression issue, is fairly lengthy. Moreover, the analysis reveals that the form of compression has surprisingly little effect on asymmetry. As a result, the discussion is deferred to the Appendix.

III. ASYMMETRY IN STROBED TEMPORAL INTEGRATION

In Secs. I and II it was revealed that it is actually rather difficult to explain the pattern of asymmetries in the matching point data from the damped/ramped experiments, and that the successful fits produced by the AIM with the original version of ***sti*** are, in retrospect, somewhat surprising [Figs. 3(e) and (h)]. These asymmetry studies, with the original ***sti*** were performed explicitly for the comparisons described in Sec. I and had not been reported before; the asymmetry studies reported in Irino and Patterson (1996) were performed with the ''delta-gamma'' version of ***sti***. In this section of the paper, we examine the original strobe mechanism to determine how it enhances temporal asymmetry. Then, the results of the analysis are used to develop a new version of ***dg-sti*** which is more robust and physiologically more plausible, and which produces a slightly better fit to the asymmetry data. Finally, this new version of ***dg-sti*** is applied to the NAPs produced by the Meddis and Hewitt (1991) model to determine whether there is inherently sufficient temporal asymmetry in these NAPs to explain the perceptual asymmetry.

A. Ramped sounds and the original *sti*

The purpose of the strobe mechanism in the original version of AIM (Patterson *et al.*, 1992) was to identify local maxima in the NAP which were then used to initiate temporal integration. The NAPs of periodic sounds typically have only one maximum per cycle, and if integration is initiated on this maximum, the resulting auditory image is a stabilized copy of the pattern of pulses in the NAP. The local maxima are identified with the aid of an adaptive threshold and there is an independent adaptive threshold for each channel of the NAP. The operation is as follows: Threshold rises rapidly with NAP level on the leading edge of each NAP pulse up to the pulse peak, and the time of the peak is marked as a candidate strobe point. After the peak passes, the adaptive threshold decays at a rate of about 2%/ms. Before initiating temporal integration, however, the mechanism waits for up to 5 ms (the strobe lag) to see if another larger peak appears. If one does, the peak of the larger pulse becomes the strobe candidate and the strobe lag is reset to 5 ms. Eventually, the strobe lag times out, temporal integration is initiated, and the mechanism is reset.[3]

The NAPs of most natural periodic sounds have damped asymmetry, and they are readily stabilized by the simple strobe algorithm. The same is not true, however, for ramped sounds. Consider the response to a ramped sound with a long envelope period, say 500 ms, and a long half-life, say 64 ms. The strobe unit in the carrier channel would continually find larger NAP peaks on the way up the ramp and would keep on resetting the strobe lag to 5 ms until the end of the ramp. Thus, the sound level would be above absolute threshold for as much as 500 ms without any activity reaching the auditory image, which in the AIM means without the listener hearing anything. This is clearly incorrect; we would hear the onset of a slowly rising tone long before the local maximum at the offset of the tone. To solve this problem an extra condition was added to the strobe criterion; namely, ''Once a NAP pulse has been encountered, limit the duration of the search for a local maximum to a total of 10 ms.'' This version of ***sti*** is surprisingly successful in producing clean auditory images of ramped sinusoids; that is, images which preserve the carrier intervals of the horizontal triangular structure in the NAP *and* the filter-ringing intervals of the vertical structure in the NAP, even when the two occur adjacent to each other in the same channel. Patterson and Irino (1998) have shown that when carrier and filter-ringing intervals occur together in one channel, ***ac*** averages them and the ACG contains a range of time intervals that do not appear in the NAP.

This revised ***sti*** does not, however, produce an exact copy of repeating ramped NAP structures in the auditory image. In channels near the carrier frequency, the triangular structure is elongated horizontally and elevated in level because the mechanism strobes once or twice on the way up the ramp as well as at the end of the ramp. The time intervals in these channels are all carrier periods, both before and after the end of the ramp, and so the asynchronous strobing does not distort the fine structure in these channels. In channels farther away from the carrier region, the mechanism does not alter either the size or the form of the vertical transient structure. As a result, the peak concentration, which is the ratio of transient activity to carrier activity, is reduced for ramped sounds. This, in turn, means that the half-life of the matching damped sound has to be extended to reduce its peak concentration and restore the PCR to unity. Thus, the strobe mechanism enhances the asymmetry of damped/ramped sounds over that observed in the NAP.

The perception of the carrier component of a ramped sinusoid is pure, which in AIM means that there is the minimum of distortion of carrier intervals in the auditory image. Accordingly, the three strobe parameters, threshold decay rate, strobe lag, and strobe-lag limit, were varied to determine the values that would minimize time-interval distortion. The values of both strobe lag and strobe-lag limit were found to have little effect on image distortion over a fairly wide range and so they were left fixed at the default values of 5 and 10 ms, respectively. Threshold decay rate was found to have a substantial effect on strobe rate, and the value in the default version of the AIM (R7), 5%/ms, was found to produce too much strobing. Distortion in the image was reduced by decreasing the decay rate to 2%/ms, and this is the rate that was used to produce the matching points and asymmetry factors in Figs. 3 and 4. No parameter sets were found that produced one strobe per envelope period for the full range of ramped sounds. It seems that enhancement of temporal asymmetry is an unavoidable property of ***sti***—a property that emerges from the principles of image stabilization in the AIM.

B. Modification of the delta-gamma strobe

The original version of ***sti*** is based on logic; it is a simple algorithm for finding local maxima in NAP functions without regard to its physical or physiological plausibility. The ''delta-gamma'' version of ***sti*** developed by Irino and Patterson (1996) represents an attempt to move forward to a physical model in hopes of discovering general physical principles of auditory processing—principles that might eventually lead to a full physiological model of ***sti***. The delta gamma version of ***sti*** also has a better dynamic response than the original ***sti***; it overshoots less at onset and adapts to level changes faster. In this subsection we describe a revised version of ***dg-sti*** that produces the best asymmetry results to date. The process is illustrated with an extended example of the response of ***dg-sti*** to the NAPs of damped and ramped sounds with 16-ms half-lives and 50-ms periods, shown by the upper traces in Fig. 6(a) and (b), respectively. These are individual NAP functions from a channel about 200 Hz above the carrier frequency, 800 Hz. The perception of the damped sinusoid has the stronger click-to-tone ratio. In the AIM, this means that the mechanism issues strobe pulses less frequently for the damped sinusoid than for the ramped sinusoid. The bottom traces in Fig. 6(a) and (b) mark the strobe points issued by the modified version of ***dg-sti*** for

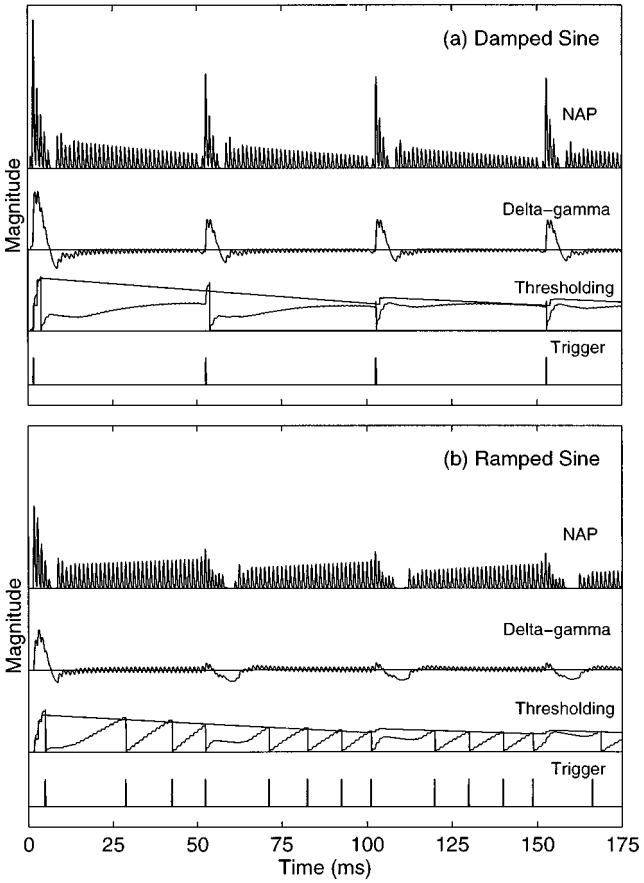

FIG. 6. Response of the delta-gamma strobe mechanism to damped (a) and ramped (b) sinusoids in the channel centred on 1.0 kHz. Delta-gamma (row 2) is the smoothed derivative of the NAP (row 1). It controls the rate at which activity accumulates for comparison with an adaptive threshold (row 3). When threshold is exceeded, a strobe pulse is issued (row 4). After the initial strobe pulse, delta-gamma causes activity to accumulate faster in the auditory image of the ramped sinusoid, thus enhancing temporal asymmetry.

these NAPs, and they show that strobing asymmetry occurs in ***dg-sti*** as in the original ***sti***. In this subsection we explain the operation of ***dg-sti*** and the matching-point data produced by this version of the AIM.

1. The architecture of the delta-gamma strobe

In AIM, there is a strobe unit for each channel of the NAP and they operate independently. The architecture of the ***dg-sti*** mechanism is presented in Fig. 7. The multi-channel NAP is represented schematically by the left-hand column of the figure. All of the modules to the right of the NAP column pertain to ***dg-sti*** for one NAP channel; namely, the one marked by the central, bold arrow of the set entering the summation. Delta-gamma is defined as the derivative of the smoothed envelope of the NAP. The envelope extractor is represented in Fig. 7 by the column of leaky integrators (LI) and the summation sign just to the right of the NAP column. The envelope is the weighted average of the smoothed NAPs from channels in a 3-ERB band about the given channel. Tc-short is 3 ms and the weighting is a Hamming function with unit area. The inclusion of the frequency dimension in the envelope calculation reduces the variability of the envelope estimate for a given time constant. The envelope is fed to the delta-gamma operator shown in the bottom panel of the central column. The envelope is also fed to an adaptive threshold (top panel) and an accumulator (middle panel) which between them determine precisely when a strobe should be issued. The delta-gamma operator controls the rate at which activity from the NAP accumulates in the decision process. When the level of activity in the accumulator exceeds the level of the adaptive threshold, a strobe pulse is issued and temporal integration is initiated.

Delta-gamma is basically the derivative of the envelope of the NAP. In this implementation, the derivative operator is preceded and followed by leaky integrators with a short Tc, 3 ms, to smooth the input and output. To limit the influence of extreme values, the delta-gamma value is passed through a sigmoid function with floor and ceiling values of 0 and 1, respectively. The slope of the sigmoid near its midpoint is a parameter of the model and in the current fits it is 2.

The output of the delta-gamma sigmoid controls the proportion of the NAP envelope that enters the accumulator which is a simple LI with a long Tc, 30 ms. The output of the accumulator is compared with the level of an adaptive

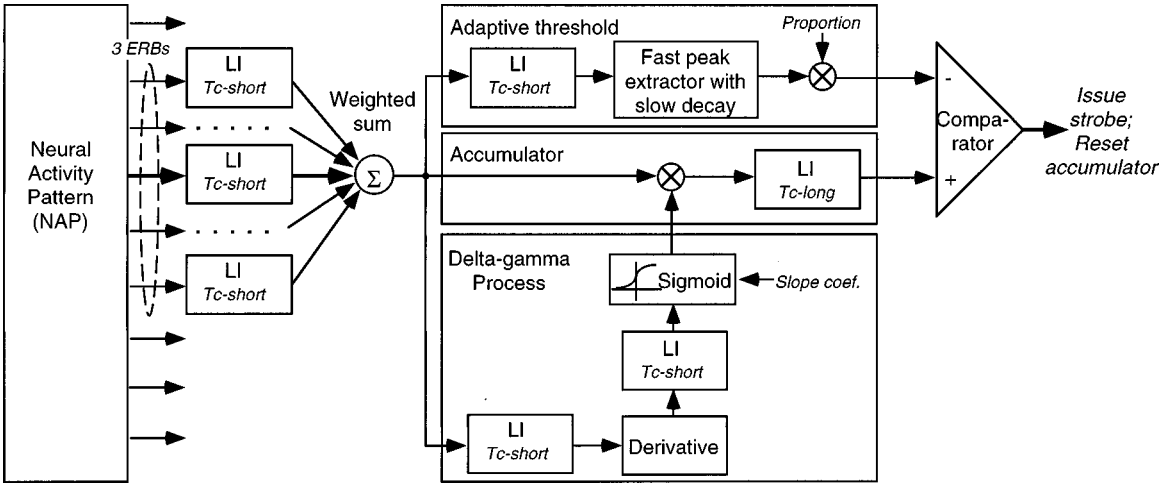

FIG. 7. Architecture of the delta-gamma strobe mechanism: The envelope of the NAP (col. 1) is extracted (col. 2) and fed to the delta-gamma process (col. 3) which determines the rate at which activity accumulates in the comparator (col. 4). When the activity level exceeds the adaptive threshold level, a strobe pulse is issued and it is reset.

threshold. The purpose of the adaptive threshold is to maintain the comparison value in roughly the same range as the level in the NAP channel. In order to strobe promptly in response to abrupt onsets, the mechanism must estimate the NAP level rapidly, and so the onset time-constant for the adaptive threshold is short (3 ms). In order to hold the estimated level for comparison over a reasonable length of time, the mechanism has a relatively slow decay (0.2%/ms). With these onset and offset characteristics, the adaptive threshold value tends to be set by onset responses where the neural transduction mechanisms are inclined to overshoot. As a result, the peak value is scaled down by a fixed proportion before being used for comparison; in the current simulations the proportion is about 0.15.

2. The operation of the delta-gamma strobe

The delta-gamma functions produced in response to the damped and ramped NAPs at the top of Fig. 6(a) and 6(b) are shown by the traces directly under those NAPs. The adaptive thresholds and accumulation functions produced in response to the damped and ramped NAPs are shown by the pair of traces directly under the delta-gamma traces. The slowly decaying trace is the adaptive threshold; the sawtooth function is the accumulator output. Every time the accumulator value exceeds the adaptive threshold, a strobe pulse is issued, as shown in the bottom trace of each figure, and then the accumulator is rest to zero.

Delta-gamma rises rapidly at the onset of both NAPs but the positive peak of the delta-gamma is greater for the damped sound and so the adaptive threshold for the damped NAP in Fig. 6(a) rises faster and to a higher level than that for the ramped NAP in Fig. 6(b). However, the accumulation rate is very high for both NAPs and so the accumulation value exceeds adaptive threshold shortly after onset in both cases and strobe pulses are issued. Shortly thereafter, delta gamma turns negative. The value is more negative for the damped sound because the recovery from overshoot is stronger in the damped sound. Moreover, the average value remains negative for the damped sound longer than for the ramped sound because the slope of the envelope of the NAP is negative for the damped sound, whereas it is positive for the ramped sound. As a result, the accumulation of NAP activity is relatively slow for the damped sound, and, since the adaptive threshold is relatively high, the accumulator does not exceed threshold until the start of the next cycle. The rising slope of the ramped sound leads to greater output from the delta-gamma operator, and, so, activity from the ramped NAP accumulates relatively quickly. The adaptive threshold is lower for the ramped NAP and so the level in the accumulator soon exceeds the adaptive threshold. The result is that ***dg-sti*** strobes two or three times during the rising portion of the cycle of the ramped sinusoid.

3. Asymmetry factors with the modified dg-sti

The asymmetry factors produced by the modified ***dg-sti*** operating on NAPs from the default version of AIM (R7) are presented by the fifth pair of columns in Fig. 5. The corresponding values with the same NAPs and the original version of ***sti*** were presented in the third pair of columns in Fig. 4. The comparison reveals that the modified ***dg-sti*** increases the noise asymmetry factor, bringing it closer to the observed values. The matching-point values produced by the modified ***dg-sti*** are a little smaller than the observed values for the shorter half-lives, and a little larger than the observed values for the longer half-lives; in general, however, they are closer to the observed values than those from the original version of ***sti***.

The final two pairs of columns show the asymmetry factors produced by ***dg-sti*** for NAPs from the level-dependent Meddis model, ***tlf/med/dg-sti***. With medium-rate fibers, ***dg-sti*** produces more asymmetry than ***ac*** (compare the sixth and third pairs of columns), but it is not sufficient to explain the magnitude of the observed asymmetry, and there is no carrier difference. With the high-rate fibers, ***dg-sti*** produces sufficient asymmetry to explain the observed asymmetry (seventh pair of columns), and there is a carrier difference that is in the correct direction. It is not as great as the observed carrier difference, but it is large enough to suggest that with a little tuning, ***tlf/h-med/dg-sti*** could explain the data as well.

IV. SUMMARY AND CONCLUSIONS

The autocorrelogram (ACG) model of hearing was developed to explain the pitch of complex sounds and it does this exceptionally well, including the pitch of high-passed iterated rippled noise which is beyond the scope of spectral models of pitch. This paper attempted to determine whether the ACG model could be extended to explain the timbre differences between spectrally matched pairs of damped and ramped sounds. Patterson and colleagues had demonstrated that the auditory image model (AIM) could explain the perception of damped and ramped sounds, and the initial stages of AIM are quite similar to those of ACG models. Accordingly, damped and ramped sounds were presented to two general forms of ACG model–the well-known Meddis and Hewitt (1991a, b) model and a version of AIM in which the strobed-temporal-integration (***sti***) module was replaced with an autocorrelation (***ac***) module. The results showed that neither form of ACG model could explain the magnitude of the perceived temporal asymmetry; that is, the fact that listeners require half-lives in damped sounds to be three to four times greater than those in ramped sounds to equate the relative loudness of the transient and carrier components of the perception. When the ***ac*** module of the Meddis and Hewitt model is replaced with an ***sti*** module, it produces sufficient asymmetry to explain the perceptual asymmetry provided the parameters of the Meddis haircell are set to simulate a high-spontaneous-rate fiber.

A series of studies was then performed with the autocorrelation model to determine whether damped/ramped asymmetry in the autocorrelogram, ACG, could be enhanced using a level-dependent auditory filterbank (Giguère and Woodland, 1994) and/or different forms of compression prior to the transduction stage in these models. The manipulations led to minor changes in the size and form of the temporal asymmetry, but there was never sufficient asymmetry in the ACG to explain the magnitude of the perceptual asymmetry. This suggests that, while autocorrelation models

are very successful in explaining pitch perception, they will need modification, and probably the addition of an extra stage, to explain the magnitude of the timbre discriminations associated with temporal asymmetry.

An analysis of the temporal integration of damped and ramped sounds with the original version of ***sti*** revealed that it is particularly difficult to stabilize the patterns of phase-locking information produced by periodic sounds where a rising tonal component ends in a transient (e.g., a ramped sinusoid). The analysis led to the development of a new version of delta-gamma strobe (***dg-sti***) that can stabilize ramped sounds accurately and explain the magnitude of the perceptual asymmetry quantitatively. The new form of ***dg-sti*** is also more plausible physiologically.

ACKNOWLEDGMENTS

Much of the modeling work and the first version of the paper were produced while the first author was a visiting researcher at NTT Basic Research Laboratories, Atsugi, Japan in the autumn of 1996. The authors would like to thank Malcolm Slaney for his suggestions with regard to reorganizing and simplifying the paper.

APPENDIX: COMPRESSION AND ASYMMETRY

1. The form of compression in AIM and Meddis and Hewitt (1991)

In the default version of AIM (R7) (Patterson *et al.*, 1995), there is logarithmic compression at the input to the neural transduction module, ***2dat***. The logarithmic function was chosen because the tail of the impulse response of the gammatone filter is a decaying exponential; log compression linearizes the decay function which greatly simplifies the adaptive thresholding algorithm. Log compression was also justified on the grounds that the pitch and timbre of complex sounds is largely invariant with level and log compression best captures this property; that is, the patterns that appear in the NAP vary least with level when the compression is logarithmic. In the Meddis and Hewitt (1991a, b) model, there is quasi-log compression at the input to the haircell module, ***med***, and there is a limit on the output firing rate that operates as a compressor at higher levels. It is this which limits the dynamic range of ***m-med*** to about 60 dB, and that of ***h-med*** to about 40 dB. In this Appendix, we investigate the effect of compression on asymmetry using three forms of compression (none, square-root, and log), crossed with three forms of neural transduction (***2dat***, ***m-med***, and ***h-med***).

We installed a variable compressor unit in the AIM software package after the filterbank and before the neural transduction modules (***2dat*** and ***med***). The unit was capable of applying no compression, log compression, or power-function compression. Several authors have recently reported that a power-law compressor with an exponent in the region of 0.5 (applied to amplitude) is a reasonable approximation to the compression applied by outer haircells over a wide range of levels in the normal cochlea (e.g., Allen, 1996; Plack, 1996; Oxenham, 1996). Consequently, we used power-function compression with an exponent of 0.5, that is, square-root compression as applied to amplitude.

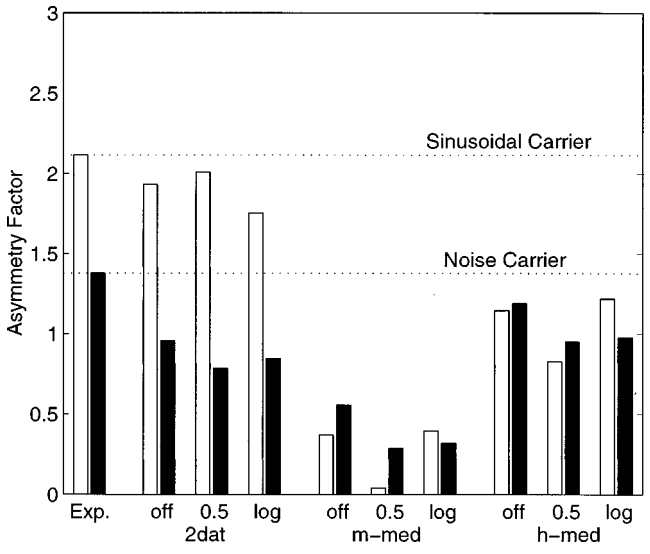

FIG. A1. Asymmetry factors calculated from the matching half-lives measured in the perceptual experiment (Exp), and from the NAPs produced by three auditory models, each with three different forms of compression, none (off), square root (0.5), and logarithmic (log). The NAPs were produced by AIM (***gtf/2dat***), and the Meddis and Hewitt model with medium-rate fibers (***gtf/m-med***) and high-rate fibers (***gtf/h-med***) fibers. The figure shows that the asymmetry factor is largely independent of compression.

2. Compression Effects in AIM and Meddis and Hewitt (1991)

The results are presented in terms of asymmetry factors in Fig. A1. The analysis was restricted to auditory models with the linear filterbank ***gtf***, since the analysis of models with the level-dependent filterbank, ***tlf***, revealed that the resultant ACGs had essentially the same temporal asymmetry. The linear filterbank has one further advantage with regard to the space of auditory models that need to be investigated; the PCR measure can be applied directly to the NAPs produced with ***gtf***, which is not the case for ***tlf***, as noted above in Sec. III B. This means that the effect of compression on asymmetry can be assessed independent of the effects of ***ac*** or ***sti***, which, in turn, reduces the number of auditory models that need to be assessed considerably.

The asymmetry factors produced with AIM (***gtf/2dat***) are presented over the ''***2dat***'' section of the abscissa. They show that the asymmetry factor is largely independent of compression. The ''log'' values are the asymmetry factors for the default version of AIM as shown in Fig. 3(c). Thus, for all three types of compression, there is sufficient asymmetry to explain the perceptual asymmetry when ***gtf/2dat*** is accompanied by ***sti*** in either the original form or the delta-gamma form. Moreover, the asymmetry has the correct form; the asymmetry for the sinusoidal carrier is greater than that for the noise carrier. This indicates that it is the asymmetric adaptation in ***2dat***, rather than compression, that dominates in the production of asymmetry at the NAP level in AIM.

The asymmetry factors for the Meddis and Hewitt model with medium-rate fibers and with high-rate fibers are presented over the ''***m-med***'' and ''***h-med***'' sections of the abscissa, respectively. In both cases, the asymmetry factor is largely independent of compression. The medium-rate model, ***m-med***, does not produce sufficient asymmetry to

explain the experimental data. Moreover, the asymmetry factors for the sinusoidal carriers are less than those for the noise carriers when there is no compression or power-function compression. The high-rate model, ***h-med***, produces more asymmetry and, if accompanied by ***sti***, it would probably be sufficient to explain the average magnitude of the perceptual asymmetry. However, there is insufficient difference between the asymmetry factors for sinusoidal and noise carriers to explain the perceptual data.

3. Summary

The results indicate that compression does not have a large effect on temporal asymmetry as measured by the asymmetry factor. With hindsight, perhaps this is not surprising. The PCR measure and the asymmetry factor are both relative measures. Compression is instantaneous and monotonic, and so when ratios are computed the effect of the compression is minimized. Nevertheless, it is useful to know that compression is not a complicating factor when modeling temporal asymmetry in the auditory system.

[1]The asymmetry factor reported by Irino and Patterson (1996) for sinusoidal carriers, 2.3, is incorrect. It should be *2.1* as stated in this paper rather than 2.3. This means that, in round numbers, the matching half-life for a damped sinusoid is about *four* times the ramped half-life rather than five times the ramped half life as reported in Irino and Patterson (1996).

[2]The package is available by ftp from ftp.mrc-cbu.cam.ac.uk. Alternately, see the web page for AIM on the internet at http://www.mrc-cbu.cam.ac.uk/aim.

[3]The strobe-criterion details are presented with demonstrations in the AIM documentation file '/docs/aimStrobeCriterion'.

Akeroyd, M. A., and Patterson, R. D. (**1995**). ''Discrimination of wideband noises modulated by a temporally asymmetric function,'' J. Acoust. Soc. Am. **98**, 2466–2474.

Allen, J. B. (**1996**). ''A review of active and passive basilar membrane cochlear mechanics,'' J. Acoust. Soc. Am. **99**, 2582.

Assman, P. F., and Summerfield, A. Q. (**1989**). ''Modelling the perception of concurrent vowels: Vowels with the same fundamental frequency,'' J. Acoust. Soc. Am. **85**, 327–338.

Assman, P. F., and Summerfield, Q. (**1990**). ''Modelling the perception of concurrent vowels: Vowels with different fundamental frequencies,'' J. Acoust. Soc. Am. **88**, 680–697.

Brown, G. J., and Cooke, M. (**1994**). ''Computational auditory scene analysis,'' Comput. Speech Lang. **8**, 297–336.

Carlyon, R. P., and Datta, A. J. (**1997**). ''Masking period patterns of Schroeder-phase complexes: Effects of level, number of components, and phase of flanking components,'' J. Acoust. Soc. Am. **101**, 3648–3657.

de Cheveigné, A. (**1998**). ''Cancellation model of pitch perception,'' J. Acoust. Soc. Am. **103**, 1261–1271.

Evans, E. F. (**1977**). ''Frequency selectivity at high signal levels of single units in cochlear nerve and nucleus,'' in *Psychophysics and Physiology of Hearing*, edited by E. F. Evans and J. P. Wilson (Academic, London), pp. 185–192.

Fay, R. R., Patterson, R. D., and Chronopoulos, M. (**1996**). ''The sound of a sinusoid: Perception and neural representations in the goldfish,'' Aud. Neurosci. **2**, 377–392.

Giguère, C., and Woodland, P. C. (**1994**). ''A computational model of the auditory periphery for speech and hearing research. I. Ascending path,'' J. Acoust. Soc. Am. **95**, 331–342.

Houtsma, A. J. M., Rossing, T. D., and Wagenaars, W. M. (**1987**). ''Auditory Demonstrations,'' CD (IPO, Acoust. Soc. Am., Eindhoven, The Netherlands).

Irino, T., and Patterson, R. D. (**1996**). ''Temporal asymmetry in the auditory system,'' J. Acoust. Soc. Am. **99**, 2316–2331.

Kohlrausch, A., and Sander, A. (**1995**). ''Phase effects in masking related to dispersion in the inner ear. II. Masking period patterns of short targets,'' J. Acoust. Soc. Am. **97**, 1817–1829.

Licklider, J. C. R. (**1951**). ''A duplex theory of pitch perception,'' Experientia **7**, 128–133. Reprinted in E. D. Schubert (ed.), *Psychological Acoustics* (Dowden, Hutchinson and Ross, Stroudsburg, PA, 1979).

Lorenzi, C., Gallego, S., and Patterson, R. D. (**1997**). ''Discrimination of temporal asymmetry in cochlear implantees,'' J. Acoust. Soc. Am. **102**, 482–485.

Lyon, R. F. (**1982**). ''A computational model of filtering, detection, and compression in the cochlea,'' in *Proc. IEEE Int. Conf. Acoust. Speech Signal Processing*, Paris, France.

Lyon, R. F. (**1984**). ''Computational models of neural auditory processing,'' in *Proc. IEEE Int. Conf. Acoust. Speech Signal Processing*, San Diego, CA.

Meddis, R. (**1986**). ''Simulation of mechanical to neural transduction in the auditory receptor,'' J. Acoust. Soc. Am. **79**, 702–711.

Meddis, R. (**1988**). ''Simulation of auditory-neural transduction: Further studies,'' J. Acoust. Soc. Am. **83**, 1056–1063.

Meddis, R., and Hewitt, M. J. (**1991a**). ''Virtual pitch and phase sensitivity of a computer model of the auditory periphery: I. Pitch identification,'' J. Acoust. Soc. Am. **89**, 2866–2882.

Meddis, R., and Hewitt, M. J. (**1991b**). ''Virtual pitch and phase sensitivity of a computer model of the auditory periphery: II. Phase sensitivity,'' J. Acoust. Soc. Am. **89**, 2883–2894.

Meddis, R., and Hewitt, M. J. (**1992**). ''Modelling the identification of concurrent vowels with different fundamental frequencies,'' J. Acoust. Soc. Am. **91**, 233–245.

Meddis, R., Hewitt, M., and Shackleton, T. (**1990**). ''Implementation details of a computational model of the inner-haircell/auditory-nerve synapse,'' J. Acoust. Soc. Am. **87**, 1813–1816.

Oxenham, A. J. (**1996**). ''Peripheral origins of the upward spread of masking,'' J. Acoust. Soc. Am. **99**, 2542.

Patterson, R. D. (**1994a**). ''The sound of a sinusoid: Spectral models,'' J. Acoust. Soc. Am. **96**, 1409–1418.

Patterson, R. D. (**1994b**). ''The sound of a sinusoid: Time-interval models,'' J. Acoust. Soc. Am. **96**, 1419–1428.

Patterson, R. D., and Holdsworth, J. (**1996**). ''A functional model of neural activity patterns and auditory images,'' in *Advances in Speech, Hearing and Language Processing*, edited by W. A. Ainsworth, Vol. 3, Part B (JAI, London), pp. 547–563.

Patterson, R. D., and Irino, T. (**1998**). ''Auditory Temporal Asymmetry and Autocorrelation,'' in *Psychophysical and Physiological Advances in Hearing*, edited by A. Palmer, A. Rees, Q. Summerfield, and R. Meddis (Whurr, London), pp. 554–562.

Patterson, R. D., Allerhand, M., and Giguère, C. (**1995**). ''Time-domain modelling of peripheral auditory processing: A modular architecture and a software platform,'' J. Acoust. Soc. Am. **98**, 1890–1894.

Patterson, R. D., Handel, S., Yost, W. A., and Datta, A. J. (**1996**). ''The relative strength of the tone and noise components in iterated rippled noise,'' J. Acoust. Soc. Am. **100**, 3286–3294.

Patterson, R. D., Robinson, K., Holdsworth, J., McKeown, D., Zhang, C., and Allerhand M. (**1992**). ''Complex sounds and auditory images,'' in *Auditory Physiology and Perception*, edited by Y Cazals, L. Demany, and K. Horner (Pergamon, Oxford), pp. 429–446.

Plack, C. J. (**1996**). ''Basilar membrane non-linearity and the growth of masking,'' J. Acoust. Soc. Am. **99**, 2543.

Slaney, M. (**1994**). Personal communication.

Slaney, M., and Lyon, R. F. (**1990**). ''A perceptual pitch detector,'' in *Proc. IEEE Int. Conf. Acoust. Speech Signal Processing*, Albuquerque, NM.

Strube, H. W. (**1985**). ''A computationally efficient basilar-membrane model,'' Acustica **58**, 207–214.

Yost, W. A., Patterson, R. D., and Sheft, S. (**1996**). ''A time-domain description for the pitch strength of iterated rippled noise,'' J. Acoust. Soc. Am. **99**, 1066–1078.

Yost, W. A., Patterson, R. D., and Sheft, S. (**1998**). ''The role of the envelope in processing of iterated rippled noise,'' J. Acoust. Soc. Am. **104**, 2349–2361.

Response distributions in intensity resolution and speech discrimination

M. E. H. Schouten and A. J. van Hessen
Research Institute for Language and Speech, University of Utrecht, Trans 10, 3512 JK Utrecht, The Netherlands

(Received 25 November 1996; revised 18 June 1998; accepted 2 July 1998)

In this paper the assumption of an equal, Gaussian distribution of the response to each stimulus in an experiment, an assumption which has to be met if d' is to be estimated by calculating the difference between $z(\mathrm{H})$ and $z(\mathrm{FA})$, is tested for two different sets of stimuli: 1000-Hz tones differing in level only, and a continuum of stop consonants, obtained by full spectral interpolation between /p/, /t/, and /k/. Response distributions were measured directly by means of a form of non-numerical magnitude estimation, in which subjects had to indicate the position of each stimulus on a quasi-continuous rating scale. It could be shown that, in general, all distributions were sufficiently unimodal, but that their variances differed. The consequences for the calculation of d' are unlikely to be serious. © *1998 Acoustical Society of America.* [S0001-4966(98)00211-2]

PACS numbers: 43.66.Ba, 43.66.Fe, 43.66.Lj, 43.71.An [RHD]

INTRODUCTION

In an ideal world, every estimate of stimulus resolution expressed in terms of d' would be obtained by fitting a ROC (receiver operating characteristic) curve through a large number of paired hit (H) and false-alarm (FA) proportions. Each pair of proportions would be the result of a separate experiment involving the same stimuli and the same conditions, but with a different decision criterion for the observer in each experiment. Criteria may be influenced by manipulating the *a priori* probability of the stimuli or by changing the reward for a hit or the penalty for a false alarm.

Signal detection theory states that successive presentations of a stimulus give rise to a range of sensations distributed around a mean. These sensation distributions are usually assumed to be Gaussian and all distributions in an experiment are usually assumed to have equal variance. If these conditions are met, and if we plot the H and FA pairs along normal coordinates [i.e., $z(\mathrm{FA})$ vs $z(\mathrm{H})$], then the ROC fitted through them is a straight line with unit slope, and d' equals the intercept along the $z(\mathrm{H})$ axis. If the distributions are not Gaussian, a straight line will not provide a good fit; if the variances are unequal, slope will not be unity (see Swets *et al.*, 1961). This only makes sense, incidentally, if the variances of the distributions are expressed in terms of physical units or of perceptual units psychoacoustically derived from physical units.

It is fairly easy to check the Gaussian and equal variance assumptions, but it is also rather costly, since it requires a number of stimulus presentations that should be large enough for reliable estimates of hit and false-alarm probabilities over a wide range of criterion positions along the rating scale. As a consequence, experimenters usually restrict themselves to one criterion, yielding single estimates of $z(\mathrm{H})$ and $z(\mathrm{FA})$ which are then subtracted to yield a d' estimate, under the assumption that they define a straight line with a slope of unity. However, in an experiment with visual stimuli presented by Swets *et al.* (1961), a doubling of the mean stimulus value resulted in a 25% increase in variance, although the distributions appeared to be Gaussian. On the other hand, most of the available evidence indicates that, for simple auditory stimuli, the assumption is a tenable one. For example, Braida and Durlach (1972) provide magnitude-estimation and absolute-identification data obtained with 1000-Hz tones differing only in intensity; the various sets of $z(\mathrm{H})$ vs $z(\mathrm{FA})$ data points for the stimulus pairs are quite well described by straight lines of unit slope. The authors are careful to point out, however, that theirs is not really a rigorous test of the degree to which the data do or do not violate the assumption of Gaussian, equal-variance distributions.

This assumption may constitute a good approximation to the probability-density functions which underlie the rating distributions that are usually associated with simple auditory stimuli. However, the situation is likely to be quite different for more complicated stimuli, especially if these are associated with well-learned categories, such as speech sounds. The hypothetical decision axis is, in such cases, not just a combination of sensation axes related to the various stimulus parameters, but it may be greatly affected by higher-order concepts, such as category boundaries or prototypes. An increasing number of speech perception researchers have come to apply a signal-detection analysis to their data, e.g., Pisoni (1973), Macmillan *et al.* (1977), Rosner (1984), Cowan and Morse (1986), Samuel (1987), Macmillan *et al.* (1987, 1988), Uchanski *et al.* (1992), Schouten and van Hessen (1992), and van Hessen and Schouten (1992). In each of these studies, d' estimates are based on single $z(\mathrm{H})-z(\mathrm{FA})$ pairs and therefore on the assumption that all members of a series of stimuli cause equal, Gaussian variances.

The present authors are engaged in a series of experiments concerning the categorical perception of speech sounds. In our previous papers, cited in the last paragraph, we have found that stop consonants are perceived categorically, and we have attempted to model the discrimination of stop consonants as a function of time. All of this has, however, been done on the rather shaky foundation of an assumption which may be incorrect. Before proceeding with

our experiments, we therefore wanted to put this assumption to the test in a rating-scale experiment, not to obtain a large number of $z(\mathrm{H})-z(\mathrm{FA})$ pairs, but to get a more direct picture of perceptual variance, in a way that will be described briefly in the next paragraph. Since our method involves a type of magnitude estimation, it was decided to first try and replicate the relevant experiment of Braida and Durlach (1972) in experiment I and only then to apply it to speech sounds in experiment II.

We reasoned that it should be possible to obtain a good picture of a subject's perceptual variance by presenting each stimulus often enough and requiring the subject to give a non-numerical estimation of its magnitude, the advantage of a non-numerical estimate being that it does not anchor subjects to, e.g., whole numbers or multiples of 10, but encourages them to use the resolution they are capable of using. In all other respects, this task is equivalent to the one employed by Braida and Durlach (1972), in which subjects were instructed to assign the number 100 to the loudness of a stimulus just below the middle of the range (which was presented ten times before each group of 100 trials). They had to use a ratio scale to rate the loudness of all subsequent stimuli (50 meant half as loud, 200 twice as loud). In our experiments, subjects performed their task by placing a mouse pointer at the appropriate spot of a horizontal bar which spanned the width of their monitor screen, and which represented the full stimulus range used in the experiment. Three reference points were regularly reinforced: the end points of the scale, which represented two stimuli just outside the experimental range (by exactly one stimulus step), and the exact middle of the range. The method made it undesirable to give any form of feedback, since this would have provided subjects with the information that the number of different stimuli was very limited. It was therefore decided to give subjects extensive training with the same stimuli, but using a different task—absolute identification—in such a way that they would not realize that they were being trained and that the same limited number of stimuli was used in both experiments.

Our expectations were that the intensity differences in experiment I would lead to distributions which would be unimodal and have approximately the same variance, especially after training. The timbre differences in experiment II, however, were expected to have a relatively low associated variance near the best representatives of a speech category (phoneme), but a much higher variance for stimuli near a phoneme boundary. The reason for this expectation is to be found in the notion of categorical perception, which says that stimuli that belong to the same category are perceived as identical and will therefore be given the same rating on our rating scale; moreover, the variance associated with this rating will be small, since subjects do not have access to variations in sensation that are due to sensory noise. On the other hand, this same sensory variance will cause a stimulus near a category boundary to be classified both ways, resulting either in a bimodal rating distribution, or in a much wider distribution if the stimulus is actually perceived as being not readily classifiable. We therefore preferred a direct picture of the rating distributions, particularly those evoked by the speech stimuli, over ROC curves, which could easily be constructed from the same rating data by shifting the criterion along the rating scale.

I. EXPERIMENT I: 1000-Hz TONES

Experiment I consisted of two parts: experiment Ia, in which extensive identification training was given, but which will be only selectively reported, since the data showed that the response range had been too narrow, and experiment Ib, which was carried out a year later using a much wider response range, but without training and with a smaller number of subjects. In effect, experiment Ia served as a pilot study for experiment Ib, the main experiment.

A. Method

1. Stimuli

Since experiment I was in many ways intended as a replication of the magnitude-estimation experiment by Braida and Durlach (1972), the stimuli were as similar to theirs as circumstances allowed. There were ten basic stimuli, consisting of 1000-Hz tones of 500-ms duration and with 25-ms cosine-shaped onset and offset windows. Stimuli 1–10 had levels of 50, 54, 58, 62, 66, 70, 74, 78, 82, and 86 dB SPL. In addition, there were three reference stimuli: stimulus 0 had a level of 46 dB, and stimulus 11 one of 90 dB; a third reference stimulus, one of 68 dB in the middle of the range, will not be used in the presentation of the results and was therefore not given a number.

Sampling frequency was 20 kHz, and resolution was 16 bits.

2. Subjects

Six subjects took part in experiment Ia—five female students and one male student of Utrecht University, all in their early twenties. Four of them returned a year later for experiment Ib. They received a basic hourly rate, apart from bonuses and penalties for correct and incorrect responses in absolute identification.

3. General procedure

Experiment Ia consisted of seven tests, taken on consecutive weekdays:

(i) ME-1: magnitude estimation without feedback,
(ii) AI-1 to AI-5: absolute identification with feedback,
(iii) ME-2: magnitude estimation without feedback.

AI-1 to AI-5 were primarily intended as a form of training for ME-2.

Experiment Ib consisted of a single magnitude-estimation test, but with a wider response range.

Magnitude estimation trials involved only stimuli 1–10 (50–86 dB SPL); for absolute identification stimuli 0 and 11 (46 and 90 dB) were added, so the number of identification categories was twelve.

All tests were carried out with subjects seated in one of two sound-treated, but not completely insulated booths—SPL of the least intense stimulus (the one of 46 dB) could

not be measured directly, due to low-frequency ambient noise interference, so to check the level of this particular stimulus an A-weighting had to be used.

Stimuli were presented binaurally over Beyerdynamic DT 770 PRO headphones, which were chosen in preference over the standard Beyer DT 49 headphones, since the latter would have been unsuitable for the speech stimuli in experiment II, in view of their poor frequency response above 4000 Hz. Moreover, the DT 770 are much more comfortable to wear over long periods. Calibration was carried out by means of an artificial ear.

4. Procedure for magnitude estimation

Subjects were seated in front of a monitor screen on which an undivided horizontal bar was displayed; the left end of this bar was marked with the word ''soft,'' the right end with the word ''loud.''

Prior to each block of 100 trials, the two (Ib) or three (Ia) reference stimuli were presented five times in a fixed order: 46 dB (stimulus 0), 68 dB, and 90 dB (stimulus 11), with an interstimulus interval of 2.5 s. In experiment Ia a marker was visible during this interval at the extreme left, in the exact middle, or at the extreme right of the bar. In experiment Ib, the 68-dB reference in the middle of the range was left out, and the positions of reference stimuli 0 and 11 were pulled toward the center of the response bar by two stimulus steps. As a result, the extreme ends of the response bar were much further away from the actual stimulus range than they were in experiment Ia, producing enough latitude to accommodate both tails of each response distribution.

The test itself consisted of 400 presentations of each of the stimuli 1–10, in a completely random order (interrupted by the reference stimuli after every 100 presentations). Subjects responded by moving the mouse pointer to the appropriate position along the horizontal bar and then pressing a mouse button. As soon as they had done this, the next stimulus was presented; if they did not press within 2.5 s, a nonresponse was recorded and the next stimulus was presented.

Maximum net duration of the test was 3 h and 50 min for a subject who needed 2.5 s for every decision. Breaks could be taken at any time at the end of a series of 100 trials; nearly all subjects took breaks after every 1000 trials (the number of remaining trials was displayed at the bottom of the screen).

Since there could not be any ''correct'' responses, no feedback was given. In experiment Ia, subjects were not rewarded or punished in any way but in experiment Ib they were told that they could raise their earnings if their ratings were to show the lowest average variance of all four subjects.

5. Procedure for absolute identification (experiment Ia only)

Subjects were seated in front of a monitor screen which displayed a horizontal bar, divided into 12 segments, marked with the numbers 1 to 12, corresponding to stimuli 0–11 (46–90 dB).

Each of the twelve stimuli was presented 150 times in each of the five tests. Order was completely random. Presentation was self-paced, since there was no maximum response time. After the stimulus had been presented, the subject moved the mouse pointer to the chosen segment and recorded her or his response by pressing a mouse button. Feedback was given immediately: in case of a correct response, the word ''OK'' was displayed for one second in the ''correct'' segment; otherwise, a cross was shown for one second in the ''correct'' segment.

Breaks could be taken between any two stimulus presentations; most subjects took one break exactly halfway through the experiment (the number of remaining stimuli was displayed at the bottom of the screen).

An increasingly severe system of rewards and penalties was enforced over the five tests. A correct response was always rewarded with 5 cents, but incorrect responses were punished increasingly severely. Subjects knew at all times how much they had gained or lost on the response they had just given.

B. Results and discussion

1. Experiment Ia

Since all data from experiment Ia are flawed in the same way, only the final identification and magnitude-estimation tests will be presented and discussed, mainly to indicate what lessons can be learned from them and how particular aspects of the results from experiment Ib may be interpreted.

Figure 1 presents the results from the fifth (and last) absolute identification session. Please note that stimuli 0–11 are represented along the vertical axis, whereas the response categories 0–11 are presented horizontally. The data points show each subject's mean identification rating of each stimulus; the thin horizontal bars around them indicate standard deviations. The barely visible thick line connects the average ratings calculated over the six subjects.

The picture presented by Fig. 1 is simple. Feedback was, by itself, enough to produce accurate identification ratings, since the results for the four preceding sessions were almost exactly the same. The only effect of training was that variance decreased between the first and the last session. This can be seen in Fig. 2, where the diamonds represent standard deviations in the first session (AI-1) and the squares standard deviations in the last session (AI-5). A three-way analysis of variance, with subjects (6) as a random independent variable and tests (5) and stimuli (12) as fixed independent variables, showed a significant effect of the tests factor, and no interaction between tests and stimuli.

The mean magnitude-estimation results for ME-2 (after training) are presented in the top panel of Fig. 3. In this figure stimuli are represented along the ordinate and responses along the abscissa, just as in Fig. 1. What is plotted in the top panel is the number of responses of the type indicated along the abscissa; since there were ten different stimuli, there are ten such plots. The bottom panel shows the mean ratings for each subject.

In Fig. 3 we see that most subjects, after five days of identification training, have learned to correctly identify the stimuli. Truncations occur in the extreme stimuli, especially in stimulus 1. In addition, there is what seems to be a bimo-

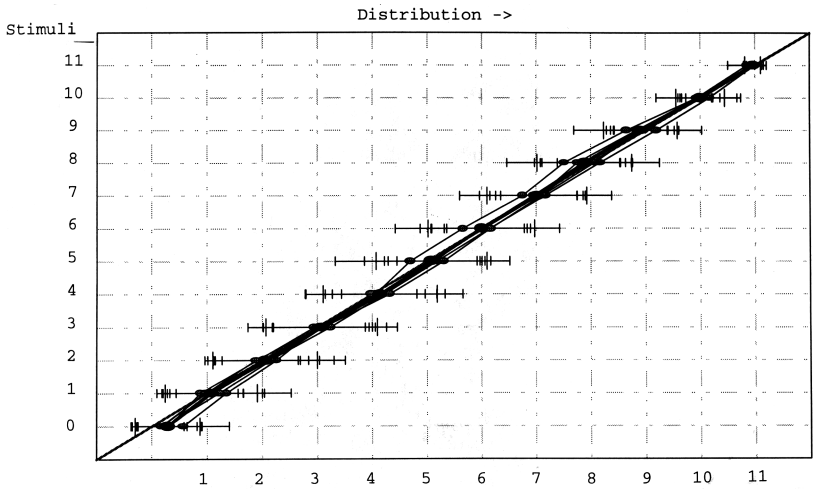

FIG. 1. Experiment Ia, 1000-Hz tones. Distribution means from AI-5 (the last absolute identification session). The stimuli are represented along the ordinate; stimuli 1–10 are the ten test stimuli, while stimuli 0 and 11 are the reference stimuli used in the magnitude-estimation tasks. The response bar, which is represented along the abscissa, contained 12 possible responses. Stimuli range in 4-dB steps from 46 (stimulus 0) to 90 (stimulus 11) dB SPL.

dal distribution in the response to stimuli 4–7, which is shared by half the subjects. These stimuli occupy the middle of the perceptual range; sometimes they are classed with the ''softer'' stimuli (5), sometimes with the ''louder'' ones (7). Some subjects reported that they had three anchors: not only the extreme stimuli, but also the position halfway between these; this was, of course, encouraged by the use of a reference stimulus in the middle of the range.

Figure 4 shows the standard-deviation estimates from ME-1 (before training, diamonds) and those from ME-2 (after training, squares). A certain amount of accuracy has clearly been lost with respect to the lower-level stimuli: standard deviations, expressed in number of stimulus steps, are up after identification training, whereas there is a considerable fall for the other stimuli. A three-way analysis of variance, with subjects (6), tests (2), and stimuli (10) as independent variables, showed that the tests factor did not have a significant effect; it did interact significantly, however, with the stimulus factor.

What is surprising, however, is the difference in shape between the functions marked by square data points in Figs. 2 and 4. Why doesn't the overall improvement in identification (AI-5, Fig. 2) carry over into magnitude estimation (ME-2, Fig. 4)? Average identification σ's fall by 0.28 stimulus steps as a result of training, whereas average estimation σ's decrease by only 0.15 steps. Moreover, there is no across-the-board improvement in magnitude estimation: σ's actually rise for stimuli 1–3. The main effect of training on magnitude estimation of the low-level stimuli seems to be to pull them apart (see the discussion of Fig. 5 below), with no concurrent increase in accuracy, even though Fig. 2

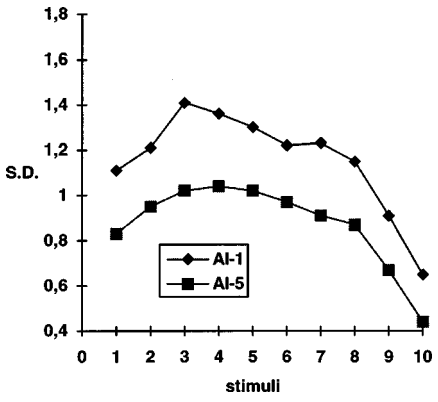

FIG. 2. Experiment Ia, 1000-Hz tones. Standard deviations in absolute identification from the first (AI-1, diamonds) and the last (AI-5, squares) of five identification sessions. Stimuli 1–10 range in 4-dB steps from 50 to 86 dB SPL.

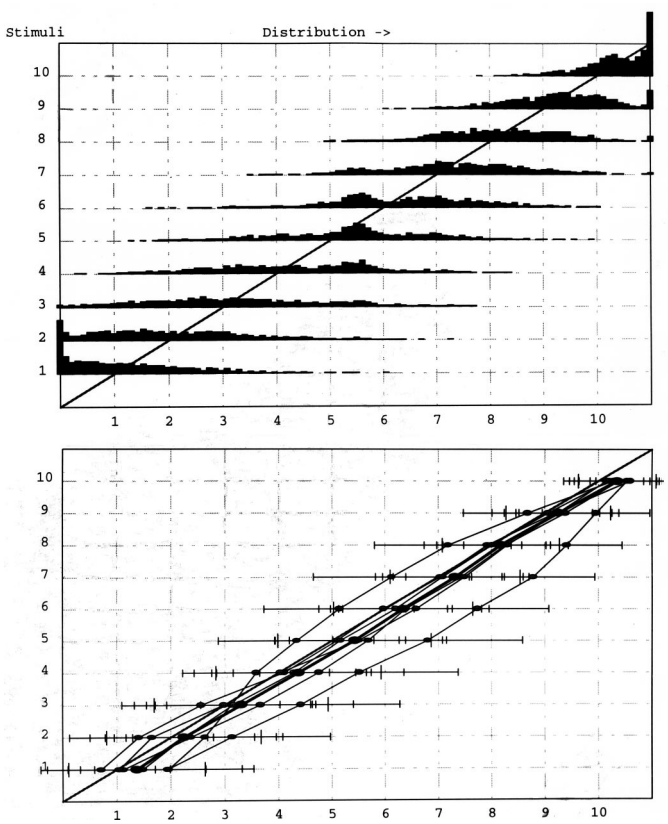

FIG. 3. Experiment Ia, 1000-Hz tones. Mean response distributions (top) and distribution means (bottom) for ME-2 (magnitude estimation after training). The abscissae represent responses along a continuous response bar, and the ordinates represent the ten stimuli. What is plotted is the number of responses of the type indicated along the abscissa; with ten different stimuli, there are ten such plots. In the top panel, the abscissa is divided into 100 segments, corresponding to the accuracy provided by the response bar. In the bottom panel, thin lines connect the distribution means of the separate subjects, and the thick line connects the average distribution means over the six subjects.

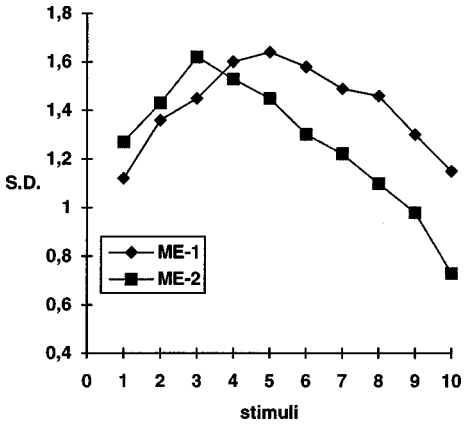

FIG. 4. Experiment Ia, 1000-Hz tones. Standard deviations in magnitude estimation before (ME-1, diamonds) and after (ME-2, squares) identification training. Stimuli range in 4-dB steps from 50 to 86 dB SPL.

shows a clear increase in accuracy for absolute identification. Apparently, accuracy cannot be maintained in the absence of feedback on stimuli that are hard to discriminate.

Braida and Durlach (1972) present d' estimates for their magnitude-estimation experiments, which are based on the discrete numerical responses they obtained from their subjects. We could have ''binned'' our responses to get the same effect, but we decided to use all the available information and therefore to divide the differences between two response means by their averaged standard deviations (separately for each subject), to obtain the d' estimates (averaged over the individual subjects' d' values) shown in Fig. 5. The data points in this figure (stimulus pairs along the abscissa) have been placed halfway between the stimuli that are compared (ticks along the abscissa). Figure 3 has shown that the calculated standard deviations for stimuli 1, 2, and 10 in Fig. 4 are probably too low; this means that the d' values for these stimuli in Fig. 5 are probably too high. If so, the d' values for ME-1 (lower graph) lie on a line that is practically straight. This does not apply to ME-2 (upper graph): as a result of training, all d' values have been lifted, but not all to the same extent. In fact, subjects seem to have learned that

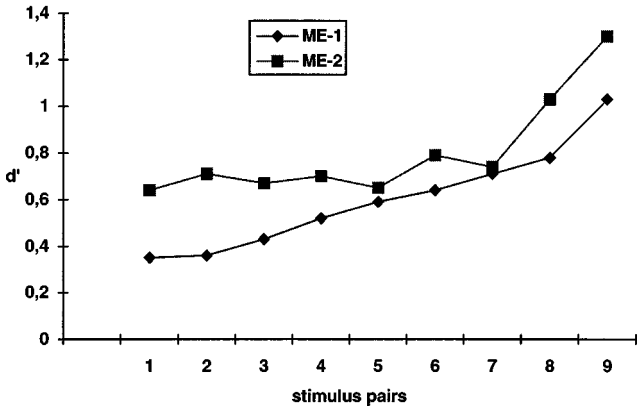

FIG. 5. Experiment Ia, 1000-Hz tones. Magnitude-estimation d' values before (ME-1, diamonds) and after (ME-2, squares) identification training, calculated by dividing the difference in two distribution means by their averaged standard deviations. Stimuli range from 50 to 86 dB SPL in 4-dB steps.

stimuli 1–8 are all at equal distances from each other, namely at the same distance as stimuli 7 and 8.

Cumulative Δ', obtained by simply adding the d' values from left to right, was 5.41 in ME-1 and 7.23 in ME-2, which compares quite well with the value of 6.5 found by Braida and Durlach (1972). The fact that these values are rather low can probably be attributed entirely to the stimulus range, which was the same in both studies (36 dB). As Braida and Durlach (1972) show in their Fig. 3c, which depicts absolute identification results, a stimulus range of 54 dB leads to a (cumulative) Δ' of around 13, whereas for a range of 2 dB (half the stimulus distance in the present experiment), Δ' equals almost 2, even at the low end of the dB range.

Non-numerical magnitude estimation appears to give a good estimate of perceptual variance for 1000-Hz stimuli differing only in level. Variance is a function of stimulus magnitude (see Fig. 4): it seems to be high in the middle of the range and seems to fall towards its edges; this should be taken into account when d' is calculated. However, part of this difference is probably due to the fact that variance is underestimated at the edges of the range, as a result of truncation, whereas it is overestimated in the middle of the range, as a result of the bimodality of the distributions there.

Experiment Ib was set up to remedy these deficiencies. The reference stimulus in the middle of the range was omitted, and the response range was widened by two stimulus steps on each side. Only four of the original six subjects were still available a year after having taken part in experiment Ia.

2. Experiment Ib

The results of the magnitude-estimation session involving 1000-Hz tones are shown separately for the four subjects in Fig. 6. The effect of earlier experience seems to have largely worn off: the ratings are quite similar to what they were before training (ME-1 in experiment Ia, not shown). The main difference is that the end-point stimuli are now accommodated fairly comfortably within the enlarged response range.

Some stimuli still invoke bimodal distributions: 5, 6, 7, and 8 for subject 2, and 6, 7, and 8 for subject 3. As in experiment Ia (Fig. 3), one of the modes coincides with the exact middle of the response range, where there had been an anchor 12 months before. However, it is unlikely that these bimodal distributions are a carryover from experiment Ia: subject 3 was the only subject with bimodal distributions on both occasions, whereas in experiment Ia subject 2 did not exhibit any peaks at or near 5.5 along the abscissa, despite the regularly reinforced anchor in the middle of the range. Subject 2 had apparently changed her strategy between experiments.

Figure 7 presents the standard deviations, averaged over the individual subjects' standard deviations per stimulus. The d' values in Fig. 8 are based directly on these standard deviations. If we compare them to the values from experiment Ia in Fig. 5, we see that they are slightly higher than they were before training for stimulus pairs 1–7, and considerably higher for pairs 8 and 9. The trend in the data is predicted by

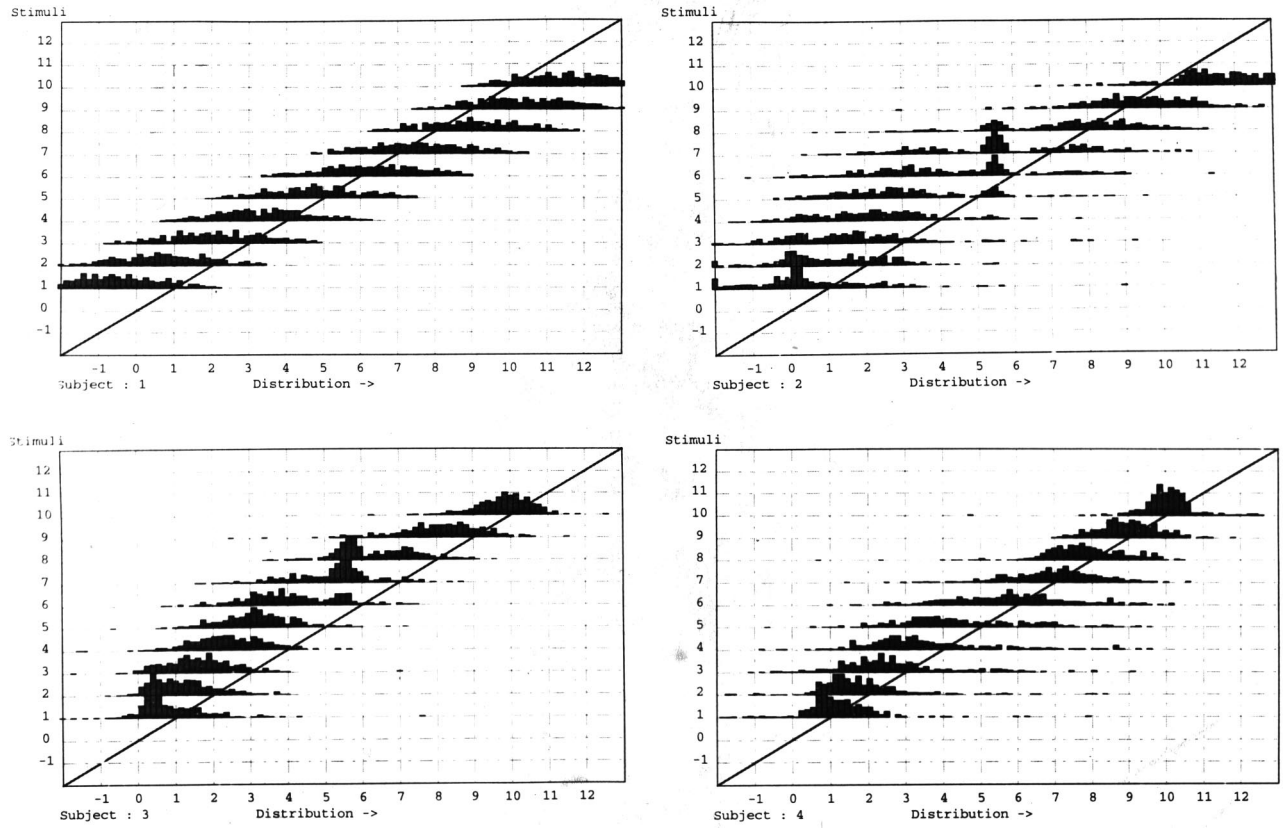

FIG. 6. Experiment Ib, 1000-Hz tones, extended rating scale. Individual magnitude-estimation response distributions. The abscissae represent responses along a continuous response bar divided into 14 positions (from −1 to 12) in the figure, while the ordinates represent the ten stimuli. Stimuli range from 50 to 86 dB SPL in 4-dB steps.

the near miss to Weber's law: resolution is positively correlated with stimulus level.

II. EXPERIMENT II: STOP CONSONANTS

A. Method

1. Stimuli

Just as in experiment I, which was run parallel to experiment II, there were ten stimuli, along with three reference stimuli. The reference stimuli were produced first, as direct resyntheses of the Dutch syllables /pak/, /tak/, and /kak/, pronounced by a male native speaker, using the same source signal for all three syllables (cepstral deconvolution, followed by convolution with one of the source signals). The test stimuli were then calculated by spectral interpolation of the stimuli 1–5 between references /tak/ and /pak/ on the one hand, and of the stimuli 7–11 between references /tak/ and /kak/ on the other [see Schouten and van Hessen (1992) for more details of the method]. As a result of this procedure, there was a gap between stimuli 5 and 7 of the test continuum in experiment IIa, since stimulus 6, the ''original''

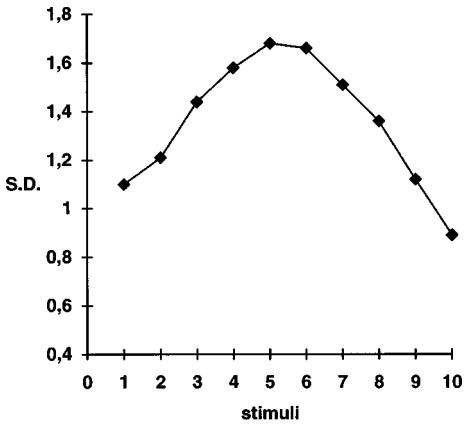

FIG. 7. Experiment Ib, 1000-Hz tones, extended rating scale. Standard deviations for magnitude estimation. Stimuli range in 4-dB steps from 50 to 86 dB SPL.

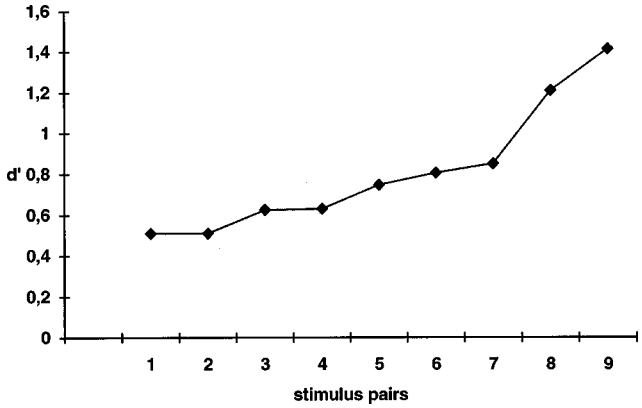

FIG. 8. Experiment Ib, 1000-Hz tones, extended rating scale. Magnitude-estimation d' values, calculated by dividing the difference in two distribution means by their averaged standard deviations. Stimuli range from 50 to 86 dB SPL in 4-dB steps.

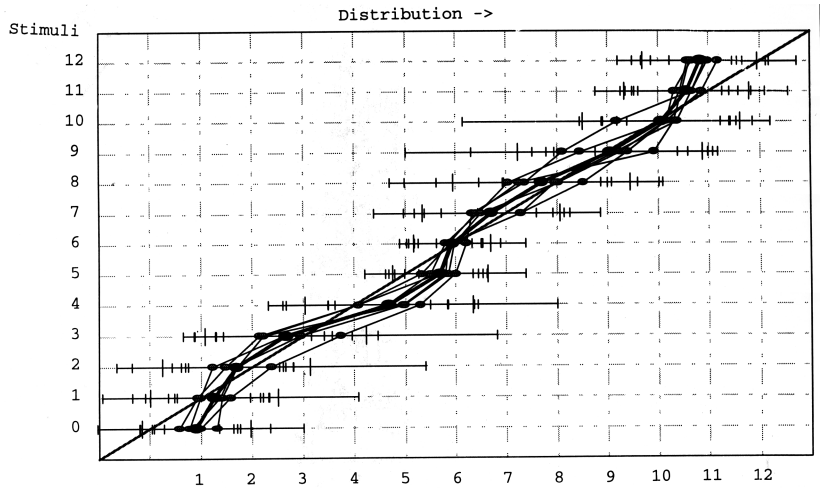

FIG. 9. Experiment IIa, stop consonants. Distribution means for AI-2 (the last absolute identification session). The composition of this figure is the same as that of Fig. 1, except that the ordinate here represents a spectral continuum from /p/ (stimulus 0) via /t/ (stimulus 6) to /k/ (stimulus 12). Stimuli are spectral interpolations between /p/, /t/, and /k/.

/t/, was only used as a reference. In experiment IIb, stimulus 6 was not used as a reference and was included as part of the continuum, which now contained 11 stimuli.

Sampling frequency was 20 kHz, with 16-bit resolution. All stimuli sounded entirely natural—as if they had been pronounced by the original speaker.

2. Subjects

Five of the six subjects in experiment IIa were the same as in experiment I; one female student was replaced by a male student. In experiment IIb, the four subjects were the same as those in experiment Ib.

3. General procedure

It soon turned out that prolonged exposure to the same speech sounds caused nearly all our subjects to hallucinate. They increasingly heard all sorts of sounds that were just not there, but, fortunately, all of them had different experiences (there was nothing wrong with our equipment). We therefore decided to restrict training rather severely: instead of five, there were only two training sessions in experiment IIa: AI-1 and AI-2. These two absolute-identification sessions were preceded and followed by non-numerical magnitude-estimation sessions: ME-1 and ME-2. Experiment IIb consisted of just a single magnitude-estimation session.

4. Procedure for magnitude estimation (ME-1 and ME-2)

Procedure was exactly the same as for the intensity stimuli in experiment I, except that the appropriate points of the response bar were now marked ''p'' and ''k'' instead of ''soft'' and ''loud.'' A second difference was that in both experiments IIa and IIb accuracy was now rewarded financially in view of the limited amount of training that could be given, although subjects did not receive feedback about this after each trial, since it was based on their average rating of the stimuli and on the standard deviations around these ratings.

5. Procedure for absolute identification (AI-1 and AI-2)

Procedure was exactly the same as for the intensity stimuli in experiment Ia, except that the response bar was now divided into 13 segments, marked with the numbers 1–13 (the middle reference stimulus now occupied a segment of its own).

B. Results and discussion

1. Experiment IIa

Figure 9 presents the results of the second absolute identification session (AI-2); stimuli 0, 6, and 12 are the reference stimuli. Accuracy is obviously rather low here: subjects seem to distribute their responses almost randomly over a group of likely candidates, getting increasingly frustrated at the amount of ''negative'' feedback (and the resulting loss of earnings). It is hard to tell whether more training would have been beneficial. Every single subject declared that he or she much preferred the straightforward clarity of experiment I, where hallucinations did not occur and practice really helped performance.

The magnitude-estimation results are presented in Fig. 10 for ME-2 (after training). The most striking aspect of the results is that subjects exhibit a large degree of categorical perception even after training: they appear to give only three different responses (apart from random variation). Before training (not shown), stimuli 1, 2, and 3 belonged to the first category, stimuli 4, 5 (6), 7, and 8 belonged to the second category, and stimuli 9, 10, and 11 to the third. The category in the middle was quite narrow and coincided with the reference /t/; the /p/ and /k/ categories at either end showed much more variance and are severely truncated. After training (Fig. 10), some subjects seem to have acquired a bimodal distribution in the middle of the range, as can be seen in the second peak for stimuli 7 and 8 in Fig. 10. The cause of this is probably that training has taught them to identify stimuli 7 and 8 more accurately, while repeated presentation of the anchor in the middle of the range continues to exert its pull.

Figure 9 shows that perception is not absolutely categorical: each data point is at least slightly to the right of its

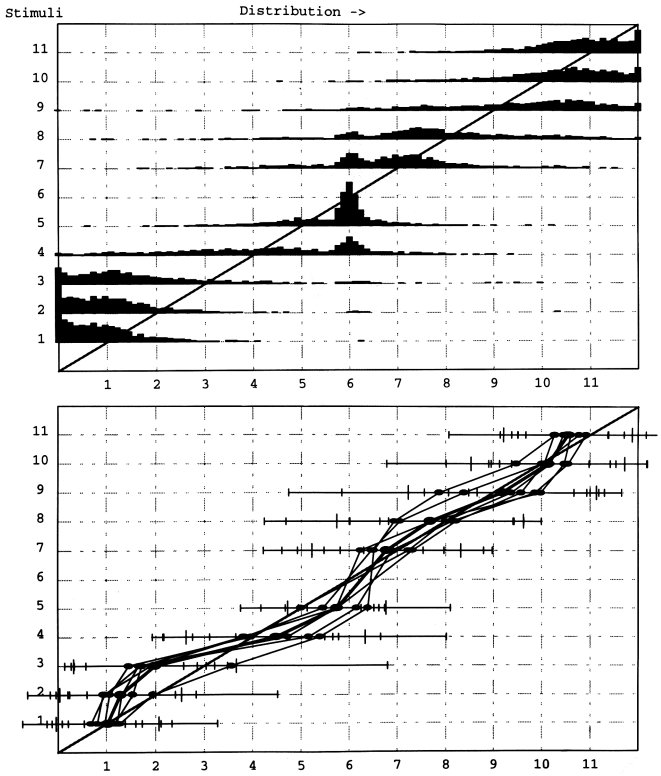

FIG. 10. Experiment IIa, stop consonants. Response distributions for ME-2 (magnitude estimation after training). The composition of this figure is the same as that of Fig. 3, except that the ordinates here represent a spectral continuum from /p/ (stimulus 0) via /t/ (stimulus 6) to /k/ (stimulus 12), and that these three stimuli (0, 6, 12) served only as references and were not used to elicit responses.

lower-number neighbor, so there are audible differences within each of the categories.

Figure 11 displays the overall standard deviations of the distributions from ME-1 (before training) and ME-2 (after training). There is no data point for stimulus 6, since this stimulus served only as a reference. Again, as in Fig. 4, the differences between the stimuli are due in large measure to the truncated nature of many of the distributions, but, also, in the case of stimuli 5 and 7, to proximity to a phoneme category and/or a reference stimulus. The most important aspect of Fig. 11 is, therefore, the significant reduction in variance as a result of identification training ($p<0.05$).

The individual subjects' standard deviations have been

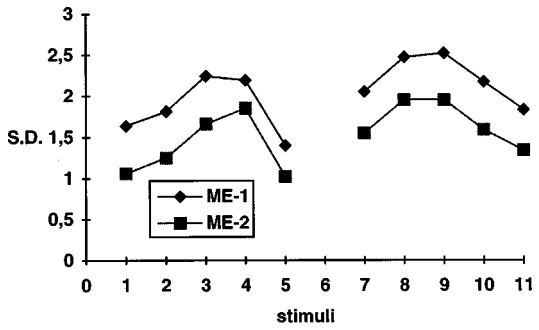

FIG. 11. Experiment IIa, stop consonants. Standard deviations in magnitude estimation before (ME-1, diamonds) and after (ME-2, squares) identification training. Stimuli are spectral interpolations between /p/, /t/, and /k/.

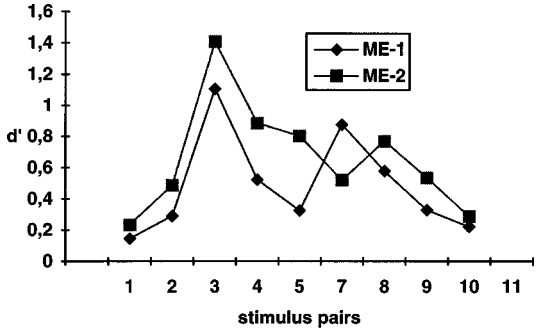

FIG. 12. Experiment IIa, stop consonants. Magnitude-estimation d' values before (ME-1, diamonds) and after (ME-2, squares) identification training, calculated by dividing the difference between two distribution means by their averaged standard deviations. Stimuli are spectral interpolations between /p/, /t/, and /k/.

used to determine the d' values displayed in Fig. 12 (d' equals the difference between the means of the distributions over their averaged standard deviations). Note that the data points denote the perceptual distance between stimuli n and $n+1$ (n being a number along the abscissa), except in the case of 5, where it is the distance between stimuli 5 and 7 that is displayed. In spite of this, before training (ME-1, diamonds), d' is very low for this within-category comparison, almost as low as it is for the other within-category comparisons 1–2 and 10–11. Training has a significant effect here: although it does not affect discriminability of the stimuli at the ends of the range, it does teach subjects to tell stimuli 5 and 7 apart. On the other hand, stimuli 7 and 8 become more similar through training.

Experiment IIb was set up for exactly the same reasons as experiment Ib: to avoid truncations by widening the response range, and to avoid the effect of an anchor in the middle of the range. The subjects were the same as in experiment Ib, as was the procedure.

2. Experiment IIb

The results of the magnitude-estimation session involving stop consonants are shown in Fig. 13, separately for each of the four subjects. Subjects 1, 2, and 3 had three response categories; the one on the left and the one in the middle were well separated, but there was some uncertainty about the demarcation between the middle category and the one on the right, leading to some bimodality in the response distributions. Subject 4 did not have a middle category: he divided the /t/-like stimuli into two classes. The patterns for all four subjects had remained the same with respect to the middle stimuli since experiment IIa had been run nearly a year before, but this need not mean that the effect of training had persisted over the intervening period: it is inevitable that, if only three categories are heard, they come to be positioned the way they are here by subjects 1, 2, and 3.

Apart from some bimodality in the distributions of subjects 2 and 3, mainly evoked by stimuli 7 and 8, distributions in Fig. 13 are fairly normal. As long as we calculate d' for individual subjects, therefore, there is not much that can go wrong. This was done in Fig. 15 on the basis of the average calculated standard deviations shown in Fig. 14.

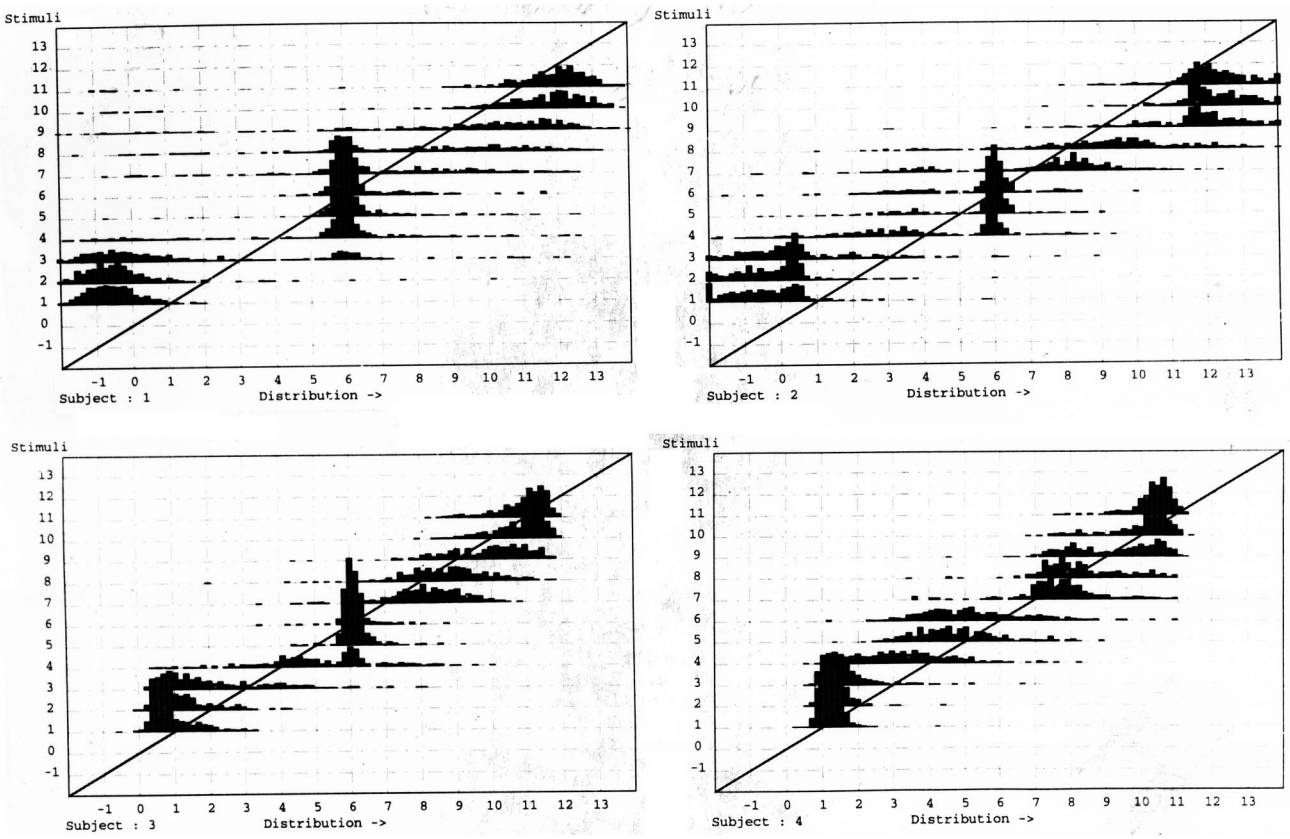

FIG. 13. Experiment IIb, stop consonants. Individual magnitude-estimation response distributions. Stimuli are spectral interpolations between /p/, /t/, and /k/.

III. GENERAL DISCUSSION

The assumption behind all the experiments reported in this paper is that it is possible, in principle, to obtain a good impression of the way the stimuli of a series are represented along a subject's hypothetical internal decision axis, by performing magnitude estimation or absolute identification. Both procedures should, we assume, yield the same response means for the stimuli but different variances, since part of the variance of any response, but not its mean, is determined by the task. Given the same conditions, i.e., the same knowledge about the stimuli, the means should always be at the same points on the decision axis, regardless of the task, but the average distribution variance should vary systematically from one task to another. If this is true, we can determine response mean and variance for each stimulus in one magnitude-estimation or absolute-identification experiment, and, using an appropriate equation for task-dependent variance, we can calculate the variance, and thus predict d', for each stimulus in each task. However, in practice it is usually impossible to separate task factors and knowledge of the stimuli. An example of what is meant here can be obtained by comparing Figs. 1 and 3. In principle, the prior conditions are the same in these two figures: subjects have been trained extensively in the identification of these 1000-Hz tones, and now they are asked to identify them (Fig. 1) and to estimate their magnitude (Fig. 3) again. We would therefore expect the same response means for each subject over the two tasks. Figures 1 and 3 show us, however, that, if any subjects behave like this, certainly not all of them do. The reason is, presumably, that no feedback was given during magnitude estimation, so that after a little while, stimulus knowledge fell behind that in absolute identification, where feedback was given after each response. This is a difference between the tasks, but it is mainly a difference in stimulus knowledge (the difference can be turned into a purely task-related one by omitting feedback in identification).

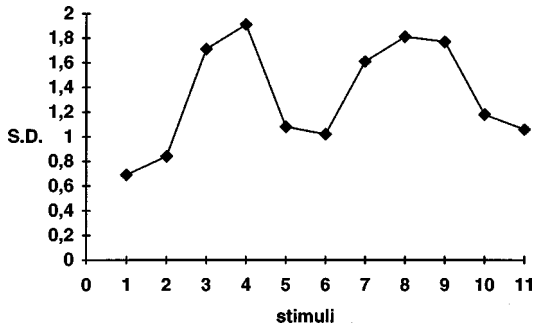

FIG. 14. Experiment IIb, stop consonants. Averaged standard deviations in magnitude estimation. Stimuli are spectral interpolations between /p/, /t/, and /k/.

Despite the differences in response means between identification and magnitude estimation, we feel that it is useful to stick to a model in which each stimulus has its own task-independent mean position on the decision axis, plus an amount of variance that is partly stimulus related, and may vary from stimulus to stimulus, and partly task related. The main advantage of this model is that it makes it possible to talk about the position of a stimulus along a decision axis, even where this position is not measured directly, such as in

any discrimination experiment. In addition, if we treat stimulus- and task-related variance as two independent noise sources, it becomes possible to determine the relative variances in the distributions caused by two stimuli. We need to know this if we want to decide whether these variances are near enough to yield a ROC with a slope of unity; if they are not, we will have to determine d' directly, i.e., by expressing stimulus distance along the decision axis in terms of some form of averaged standard deviation.

On the basis of these assumptions, which were not strongly contradicted by any of the findings, we tested the hypothesis that the distributions caused by pure-tone stimuli differing only in level are equal in variance and Gaussian or at least unimodal, but that a series of speech stimuli, differing in much more complicated ways from each other, and influenced by long-term memory categorization, might not cause equal, Gaussian distributions. We did not know what to predict with respect to the shape of the response distributions for speech sounds, but we did expect relatively large differences in variance, with stimuli from the center of a phoneme category leading to much narrower distributions than stimuli at or near a phoneme boundary, which could be heard as belonging to different categories from one presentation to another, and thus lead to much wider, perhaps even bimodal, response distributions. In short, we expected to confirm that d' for simple psychoacoustic stimuli can safely be calculated in the traditional way, using just one pair of z-transformed hit and false-alarm probabilities, but that the d' values that have up to now been calculated for speech sounds are much less valid.

The experiments have not confirmed the expectations. In both experiments, we have found evidence that, as long as distributions are not affected by lack of response space, they tended to be Gaussian, both for the tones and for the speech stimuli. However, in neither set of stimuli were they equal. This can be seen in Figs. 4, 7, 11, and 14. Tone stimuli (Figs. 4 and 7) from the middle of the range are more difficult to identify than stimuli at either end, which agrees with the anchor effect described by Braida *et al.* (1984): subjects construct their own references, which usually coincide with the end points of the stimulus range, and use a ''noisy ruler'' to measure the distance between each stimulus and these anchors. For speech stimuli, such anchors do not have to be constructed: provided the stimuli are close enough to natural speech sounds, the anchors exist already—they form part of the ''permanent context'' (Schouten and van Hessen, 1992). Figures 11 and 14 show that, as expected, stimuli that are close to such a permanent anchor are easier to position on the decision axis than stimuli that are further away from one; the transition between these two states is, moreover, relatively sudden or ''categorical.'' The d' values calculated on the basis of the standard deviations in Figs. 7 and 14 are shown in Figs. 8 and 15, respectively. One might expect a negative correlation between standard deviation and d', but there seems to be no correlation between Figs. 7 and 8 at all, whereas there appears to be a positive correlation between the speech data in Figs. 14 and 15: a high standard deviation seems to be associated with a high d'. This is due to the rather special, categorical nature of the perception of well-known speech sounds: stimuli belonging to a single category are positioned very closely together, and this is done very consistently.

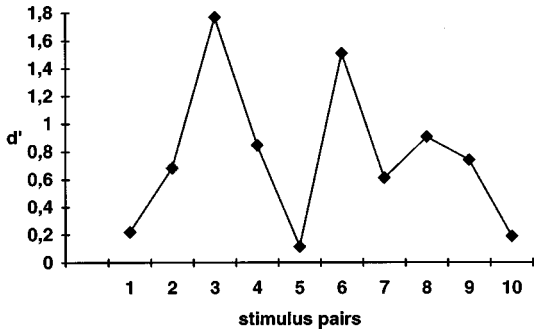

FIG. 15. Experiment IIb, stop consonants. Magnitude-estimation d' values, calculated by dividing the difference between two distribution means by their averaged standard deviations. Stimuli are spectral interpolations between /p/, /t/, and /k/.

What lesson should be learned from all this in relation to the calculation of d'? How serious is the deviation from equal variance, i.e., how much does the slope of the various ROC curves deviate from unity? The answers for intensity perception and speech perception are different. As Figs. 4 and 7 show, standard deviations do not change much from one intensity stimulus to the next, so if stimulus comparisons are restricted to nearest neighbors, one pair of $z(\mathrm{H})$ and $z(\mathrm{FA})$ estimates will produce a d' that is very close to the ''real,'' underlying d'. The deviation will become more serious as more distant stimuli are compared in an experiment.

For speech stimuli (see Figs. 11 and 14) the situation is much more serious: only for stimuli that unambiguously belong to the same category can d' be based on just one $z(\mathrm{H})-z(\mathrm{FA})$ pair; in all other cases we must expect a severe departure from equality of variance. Does this conclusion invalidate all speech d' values that have been collected so far? Fortunately, at least in the present speech data, the negative effects are compensated for: in regions of high variance, perceptual distances are great, due to relatively great distances between mean positions. Although such a compensation should not be taken for granted under all circumstances, it does seem to indicate that the standard procedure for calculating d' is, in most cases, robust enough.

ACKNOWLEDGMENTS

This research was supported by the Foundation for Language, Speech, and Logic (TSL), which is subsidized by the Netherlands Organisation for Scientific Research (NWO). The authors would like to thank Dick Pastore and Neil Macmillan for helping us to get a better grip on our own concerns.

Braida, L. D., and Durlach, N. I. (**1972**). ''Intensity perception. II. Resolution in one-interval paradigms,'' J. Acoust. Soc. Am. **51**, 483–502.

Braida, L. D., Durlach, N. I., Lim, J. S., Berliner, J. E., Rabinowitz, W. M., and Purks, S. R. (**1984**). ''Intensity perception. XIII. Perceptual anchor model of context coding,'' J. Acoust. Soc. Am. **76**, 722–731.

Cowan, N., and Morse, P. A. (**1986**). ''The use of auditory and phonetic memory in vowel discrimination,'' J. Acoust. Soc. Am. **79**, 500–507.

Macmillan, N. A., Braida, L. D., and Goldberg, R. F. (**1987**). ''Central and peripheral processes in the perception of speech and nonspeech sounds,'' in *The Psychophysics of Speech Perception*, edited by M. E. H. Schouten (Martinus Nijhoff, The Hague), pp. 28–45.

Macmillan, N. A., Goldberg, R. F., and Braida, L. D. (**1988**). ''Resolution for speech sounds: Basic sensitivity and context memory on vowel and consonant continua,'' J. Acoust. Soc. Am. **84**, 1262–1280.

Macmillan, N. A., Kaplan, H. L., and Creelman, C. D. (**1977**). ''The psychophysics of categorical perception,'' Psychol. Rev. **84**, 452–471.

Pisoni, D. B. (**1973**). ''Auditory and phonetic memory codes in the discrimination of consonants and vowels,'' Percept. Psychophys. **13**, 253–260.

Rosner, B. S. (**1984**). ''Perception of voice-onset-time continua: A signal detection analysis,'' J. Acoust. Soc. Am. **75**, 1231–1242.

Samuel, A. G. (**1987**). ''Lexical uniqueness effects on phonemic restoration,'' Journal of Memory and Language **26**, 36–56.

Schouten, M. E. H., and van Hessen, A. J. (**1992**). ''Modeling phoneme perception. I: Categorical perception,'' J. Acoust. Soc. Am. **92**, 1841–1855.

Swets, J. A., Tanner, W. P., and Birdsall, T. G. (**1961**). ''Decision processes in perception,'' Psychol. Bull. **68**, 301–340.

Uchanski, R. M., Millier, K. M., Reed, C. M., and Braida, L. D. (**1992**). ''Effects of token variability on resolution for vowel sounds,'' in *The Auditory Processing of Speech: From Sounds to Words*, edited by M. E. H. Schouten (Mouton De Gruyter, Berlin), pp. 291–302.

van Hessen, A. J., and Schouten, M. E. H. (**1992**). ''Modeling phoneme perception. II. A model of stop consonant discrimination,'' J. Acoust. Soc. Am. **92**, 1856–1868.

Detection of sinusoidal amplitude modulation at unexpected rates

Beverly A. Wright[a)]
Audiology and Hearing Sciences Program, Northwestern University, 2299 North Campus Drive, Evanston, Illinois 60208-3550

Huanping Dai
Boys Town National Research Hospital, 555 N. 30th Street, Omaha, Nebraska 68131

(Received 11 March 1998; accepted for publication 12 August 1998)

The detectability of sinusoidal amplitude modulation at unexpected modulation rates was assessed using a probe-signal method. With this method, three listeners were led to expect a target modulation rate (4, 32, or 256 Hz) by presenting the signal most often at that rate, and sensitivity to modulation at six other unexpected rates between 4 and 256 Hz was measured via occasionally presented probe modulation rates. The modulation phase was random on each two-interval forced-choice trial and the overall level of the 500-ms broadband carrier was randomly varied between 55 and 75 dB SPL across intervals. The modulation depth at each rate was set so that the modulation was detected on about 90% of the trials when only that rate was presented. Performance at the unexpected rates depended upon the target rate. For the 4-Hz target, modulation at all rates was detected on about 80% of the trials. For the 32- and 256-Hz targets, unexpected modulation rates of 16 Hz and above were detected on 80%–90% of the trials, but modulation rates below 16 Hz were detected nearly at chance. The influence of expectation of modulation rate on the detection of sinusoidal amplitude modulation is not readily predicted by current models of modulation detection. [S0001-4966(98)04611-6]

PACS numbers: 43.66.Ba, 43.66.Mk [JWH]

INTRODUCTION

Previous probe-signal experiments have shown that listeners are poor at detecting a tone masked by continuous noise when the frequency (Greenberg and Larkin, 1968; Scharf *et al.*, 1987; Dai *et al.*, 1991; Schlauch and Hafter, 1991) or duration (Wright and Dai, 1994; Dai and Wright, 1995) of that tone differs from the expected one. Those results indicate that listeners detect masked tones through a time-frequency window whose shape is determined by the duration and spectrum of the expected signal. The aim of the present project was to determine whether listeners also detect amplitude modulation through a template matched to the modulation rate. The listener's task in two experiments was to indicate in which of two presentations a gated noise was sinusoidally amplitude modulated.

The main experiment employed a variation of the probe-signal method (Greenberg and Larkin, 1968) to manipulate the listener's expectation of the rate of modulation to be detected. A target modulation rate was presented on most trials, leading the listener to expect that rate, and unexpected probe rates were presented only occasionally. The decision statistics employed in existing models of modulation detection do not include any dependence on the expectation of modulation rate. Nevertheless, those models make implicit predictions about the influence of expectation. If modulation is detected by a decision maker monitoring the output of a bandpass filter, followed by a half-wave rectifier, and then a low-pass filter (Viemeister, 1979), then unexpected modulation rates should be detected as well as expected ones regardless of the decision statistic used (see Strickland and Viemeister, 1996 for an overview of these statistics): rms envelope power (Viemeister, 1979), fourth moment of the envelope (Hartmann and Pumplin, 1988), crest factor (Hartmann and Pumplin, 1988), ratio of the maximum to the minimum envelope amplitude (Forrest and Green, 1987), or the average magnitude of the slope of the envelope (Richards, 1992). This is because the value of the statistic will be larger in the modulated than the unmodulated interval at every modulation rate up to the highest rate that the model can detect. Alternatively, if modulation is detected through modulation filters analogous to spectral-frequency filters (e.g., Bacon and Grantham, 1989; Houtgast, 1989; Yost and Sheft, 1989; Dau *et al.*, 1997), then it seems likely that unexpected modulation rates falling outside of the passband of the modulation filter centered on the expected rate would be poorly detected, just as unexpected spectral frequencies are.

Psychometric functions for the detection of sinusoidal amplitude modulation in gated noise carriers were measured in a second experiment. Their slopes were used to transform the percent-correct values obtained in the probe-signal experiment to decibels of attenuation of modulation depth.

I. METHOD

A. Listeners

Three listeners, ranging in age from 21 to 23 years, were paid for their participation. All had hearing within 15 dB of

[a)]Electronic mail: b-wright@nwu.edu

0 dB HL between 100 and 10 000 Hz, as measured with a Bekesy audiometer, and had previous experience in other psychoacoustic tasks.

B. Stimuli

The listeners were asked to detect sinusoidal amplitude modulation of a gated, low-pass noise carrier that had an upper cutoff frequency of 10 000 Hz. The modulated noise was created by multiplying the noise carrier by the function

$$m(t) = 1 + m \sin(2\pi f_m t + \phi), \quad (1)$$

where m is the modulation depth, $0 < m < 1$, f_m is the modulation frequency, and ϕ is the starting phase of modulation. Throughout this paper, the modulation depth is expressed in decibels as $20 \log m$. The starting phase of the modulation was randomly chosen from a uniform distribution on each presentation. The total duration of both the carrier and the modulation was 500 ms, as measured between the half-amplitude points on 16.8-ms rise and decay cosine-squared envelopes. The overall stimulus level was randomly chosen on each observation interval from the range of 55–75 dB SPL, corresponding to 15 and 35 dB SPL spectrum level. This level variation was adopted to help deter the listeners from using as a cue to detection the increase in power by $1 + m^2/2$ of the modulated compared with the unmodulated noise. The waveforms were generated digitally (TDT AP2) and played through a 16-bit digital-to-analog converter (TDT DA1) at a sampling period of 30.5 μs (32 787 Hz), followed by a 10-kHz low-pass filter (TDT). A different noise waveform was created on every observation interval.

C. Procedure: Unexpected modulation rates

The detectability of modulation with unexpected rates was evaluated using a multi-probe procedure (Dai *et al.*, 1991). In the multi-probe condition, seven rates of modulation were employed in each block of 64 trials. A *target* modulation rate was presented on 46 of the 64 trials to direct the listener to expect that rate. On the remaining 18 trials, the other 6 unexpected or *probe* rates were presented on 3 trials each. The probe trials were randomly distributed with the provisions that one of every four consecutive trials (e.g., trials 1–4, 5–8, etc.) was a probe trial, and that two probe trials could not occur in succession. The listeners were not informed about the presence of the probe rates. The seven modulation rates were: 4, 8, 16, 32, 64, 128, and 256 Hz. This spacing is in accord with one modulation-filter model which proposes that the filter bandwidths for modulation rates from 10 to 10 000 Hz are logarithmically scaled with a Q value constant at 2 (Dau *et al.*, 1997). The target modulation rate was 4, 32, or 256 Hz in different tests, and the probe rates were the remaining six rates. The reported functions relating percent correct to modulation rate were each based on 1380 trials for the target rate and on 90 trials for each of the probe rates.

The modulation depth at each modulation rate in the multi-probe condition was fixed at a value at which the modulation could be detected on about 90% of the trials when only that rate was presented. The 90% values were confirmed in the probe-alone condition. The mean depths used, as estimated from a minimum of 150 trials at each modulation rate, were −13 dB ($20 \log m$) for 4 Hz, −17 dB for 8 Hz, −18 dB for 16 Hz, −17 dB for 32 Hz, −16 dB for 64 Hz, −15 dB for 128 Hz, and −12 dB for 256 Hz. This pattern of modulation depths across the various rates is similar to that reported by Viemeister (1979) for gated carriers. To determine the stability of performance in the probe-alone condition, percent correct in that condition was remeasured each of the three times data collection was completed in a multi-probe condition. Each reevaluation was based on 100–150 trials at each modulation rate.

The task was two-interval forced-choice with feedback. The listener indicated in which interval the noise was modulated, and the dependent variable was the percentage of correct responses for each of the seven modulation rates. No cue interval was used.[1] The listener received the stimuli monaurally through Sennheiser HD450 earphones while seated in a sound-treated room.

D. Procedure: Psychometric functions

In order to estimate the attenuation of the modulation depth of each unexpected rate of modulation, psychometric functions were measured for the detection of each of the three target rates using an adaptive method (Dai, 1995). With this method, the depth of modulation was varied adaptively using the three-down, one-up rule of Levitt (1971). However, unlike with the standard implementation of this adaptive technique, the step size was not reduced after a given number of reversals, but was instead fixed at 3 dB. Fifteen blocks of 60 two-interval forced-choice trials were collected from each listener for the 3 target rates, and the modulation depth and response stored after each trial. A subsequent sorting of the modulation depths and corresponding responses yielded a percent correct at each level. Percent-correct values based on fewer than 50 responses or that were less than one standard deviation away from 50% and 100% correct were omitted from the analyses. Each reported psychometric function is based on an average of 820 trials. The slopes of the psychometric functions were used to convert the percent-correct values obtained in the multi-probe conditions to decibels of attenuation of modulation depth.

II. RESULTS

A. Percent correct for the expected and unexpected modulation rates

Figure 1 shows the individual and mean data (rows) for each of the three target modulation rates (columns). All three listeners showed generally similar results. Mean performance in the probe-alone condition, in which only the expected modulation rate was presented, ranged from 88% to 91% correct before (long-dashed line) and from 86% to 94% correct after (short-dashed line) data were collected in the multi-probe condition. The ''after'' values represent the mean of

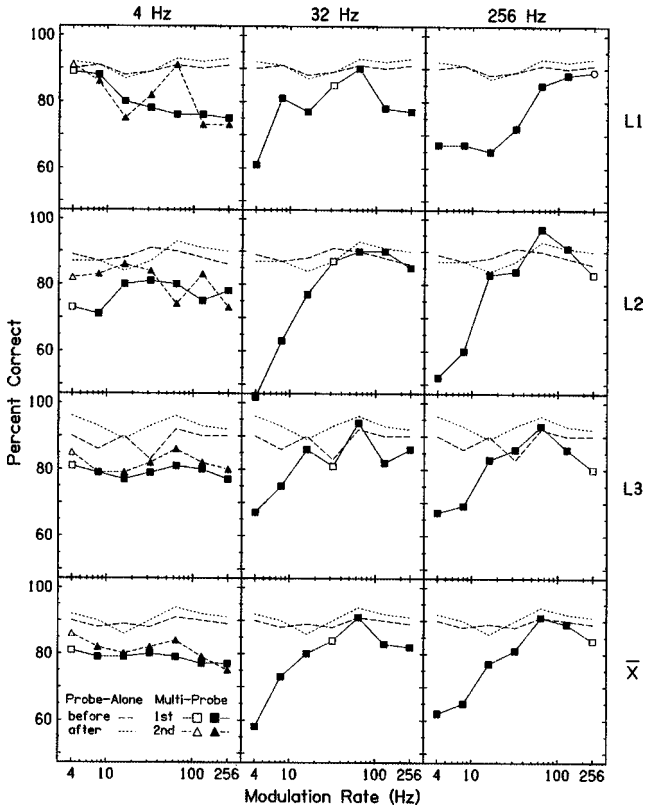

FIG. 1. The percentage of correct responses in the probe-alone and multi-probe conditions. Performance in the probe-alone condition was measured both before (long-dashed line) and after (short-dashed line) data had been collected in the multi-probe condition. Performance for both the expected (open symbols) and unexpected (filled symbols) modulation rates in the multi-probe condition was evaluated at three different target rates: 4 Hz (left column; squares for first measurement, triangles for second), 32 Hz (middle column), and 256 Hz (right column). The top three rows show the individual data of the three listeners. The bottom row shows the mean values.

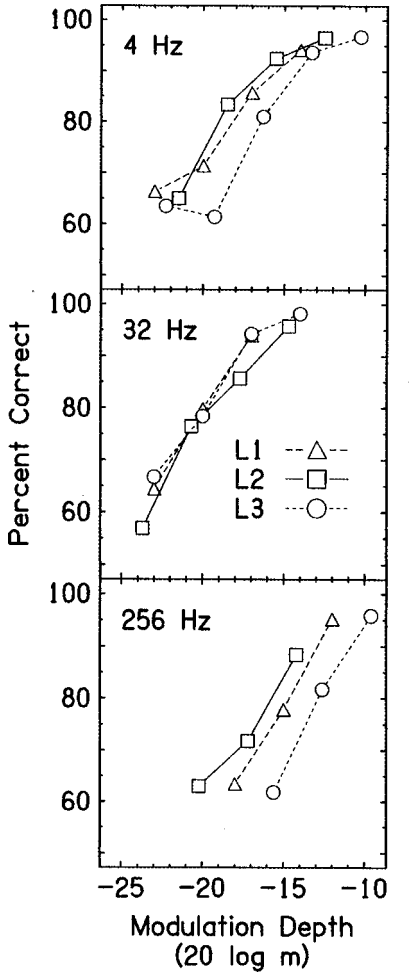

FIG. 2. Psychometric functions for the three target rates (panels) for the three individual listeners: L1 (triangles), L2 (squares), and L3 (circles).

the three remeasurements of performance in the probe-alone condition. The similarity in the before and after results indicate that the percent correct in the probe-alone condition was fairly stable throughout the experiment.

The results in the multi-probe condition (lines with symbols), in which unexpected modulation rates (filled symbols) were mixed in with the expected one (open symbols), depended on the modulation rate of the target. When the expected rate was 4 Hz (left column of Fig. 1), the mean number of correct detections decreased by about 10% relative to the probe-alone condition at every modulation rate. Similar results were obtained in two separate measurements of this condition (squares for first, triangles for second). When the expected rate was 32 Hz (middle column) or 256 Hz (right column), mean performance decreased by about 0%–10% correct for modulation rates at and above 16 Hz, but decreased considerably more for the slowest modulation rate. Mean performance for the 4-Hz rate was 58% correct when the 32-Hz rate was expected and 62% correct when the 256-Hz rate was expected, compared to around 91% correct when only the 4-Hz rate was presented. These data are discussed in Sec. III.

B. Psychometric functions for the expected modulation rates

Plotted in Fig. 2 are the individual psychometric functions for the three target modulation rates. To estimate the slope of each function, the percent correct values were converted to d' values and a straight line was fitted to $20 \log d'$ vs $20 \log m$ by minimizing the chi-square error between the obtained and fitted percent-correct values. The slope increased with modulation rate for all three listeners. The mean slopes were 1.3 for the 4-Hz rate (top panel), 1.7 for the 32-Hz rate (middle panel), and 2.1 for the 256-Hz rate (bottom panel). Increases in the psychometric slope with increasing modulation rate have also been reported by Eddins (1993) and Gifford *et al.* (1997). The values of modulation depth necessary for 90% correct on the psychometric function are in good agreement with the levels used in the probe-signal experiment.

C. Attenuation of the modulation depth of unexpected modulation rates

The attenuation in decibels of the modulation depth of unexpected modulation rates is shown in Fig. 3. These values were obtained for each listener by transforming the percent

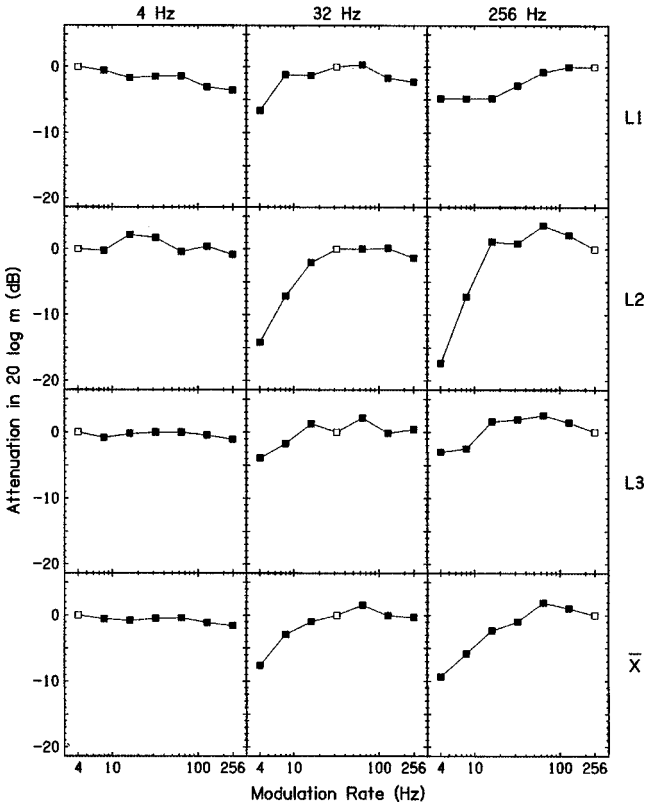

FIG. 3. Effective attenuation converted from the percent-correct values in Fig. 1 via the slopes of the psychometric functions in Fig. 2. The results for the 4-Hz modulation rate are based on the mean of the two measurements of that multi-probe condition. Otherwise as in Fig. 1.

correct measured for each probe rate in the multi-probe condition (from Fig. 1) into decibels of attenuation using a psychometric function with the mean slope of the three target rates (from Fig. 2).[2] The same general results emerge from this analysis as from the original one. On average, the modulation depth of the most poorly detected probes was attenuated by 8 dB (20 log *m*) relative to the expected rate, and by 10 dB relative to the best detected rate.

III. DISCUSSION

The present results show that modulation at unexpected rates $\geqslant$16 Hz is detected only slightly more poorly than modulation at expected rates, regardless of the expected rate of modulation. However, modulation at unexpected rates $<$16 Hz is poorly detected when the expected rate is $>$16 Hz.

A. Heard but not heeded

These results cannot be attributed easily to the idea that in probe-signal experiments listeners can actually hear expected and unexpected signals equally well, but reject the unexpected signals if they do not sound sufficiently like the expected one (Scharf *et al.*, 1987). Here perhaps the primary argument against that heard-but-not-heeded hypothesis is the fact that the pattern of results depended upon the modulation rate of the target. For example, when the target rate was 4 Hz, the 256-Hz probe rate was well detected, but when the target rate was 256 Hz, the 4-Hz probe rate was poorly detected. It is difficult to see how the listener could reject the probe rate because it was different from the target rate in one condition but not in the other. This is especially the case because in the two-interval forced-choice task, the standard was an unmodulated noise, so any sound different from that standard could have been used as the detection cue. A different account is necessary.

B. Two cues to modulation detection

A simple and reasonable qualitative explanation for the present data is that they reflect the different percepts produced by slow and fast rates of sinusoidal amplitude modulation. Listeners hear the individual fluctuations in amplitude at rates lower than about 20 Hz, and hear roughness or pitch at higher modulation rates (Terhardt, 1974; Burns and Viemeister, 1976, 1981; Patterson *et al.*, 1978). One interpretation of the current data is that both of these percepts are used as cues to the detection of modulation, and that the roughness cue is more prominent. According to this view, all modulation rates $>$16 Hz were detected well because those rates sounded rough and the roughness cue is particularly salient. The modulation rates $<$16 Hz were only detected when those rates were at or near the expected rate, because only then was the listener expecting the less pronounced individual-fluctuation cue.

Consistent with the roughness explanation, when the target modulation rate was 32 or 256 Hz, mean performance was actually best for the unexpected rate of 64 Hz, a value close to the 70-Hz rate which produces the greatest roughness for broadband noise carriers (Fastl, 1977). Detection of the 64-Hz rate was also better on average than for neighboring rates in the second measurement of performance with the 4-Hz target rate. Note that because of the shallow modulation depths used in the probe-signal experiment, the relative roughness of the modulation rates $>$16 Hz was probably minimal, but was nevertheless greater than that of the rates $<$16 Hz (Fastl, 1977).

It is interesting to speculate that listeners may be accessing the individual-fluctuation and roughness cues at different levels along the auditory pathway. The ability of neurons to follow rapid fluctuations in amplitude is greatest at the periphery and decreases substantially at higher stations (for a review, see Schreiner and Langner, 1988). For example, neurons in the inferior colliculus respond best to amplitude modulation at rates from about 50 to 120 Hz, and thus may encode the roughness cue (Fastl, 1990), whereas neurons in the primary auditory field (AI) respond best to amplitude modulation rates of 10–20 Hz (Schreiner and Urbas, 1988), and thus may encode the individual-fluctuation cue. If true, the current results indicate that the cue encoded in the inferior colliculus is readily processed, while the cue encoded in AI is processed only selectively and so is influenced by expectation. Some indirect evidence for this comes from a recent investigation of the influence of random variations along two dimensions of a consonant–vowel stimulus: pitch, which corresponds to the present roughness cue, and place of articulation, which loosely corresponds to the present individual-fluctuation cue because phonemes in speech occur at a rate of about 15 Hz (Plomp, 1983). Both behavioral and

neurophysiological measures showed that random variations in the pitch of a consonant–vowel stimulus are more disruptive to the discrimination of place of articulation than are random variations in the place of articulation to the discrimination of pitch (Scharma, 1994).

C. Models

These data do not provide clear support for either of the two model types described in the Introduction. The expectation of a particular modulation rate influenced performance more than is predicted by a low-pass filter model using a variety of proposed decision statistics, but less than might be anticipated for a modulation-filter model.

1. Low-pass filter model

Contrary to the predictions of the low-pass filter model (e.g., Viemeister, 1979), modulation at slow rates was poorly detected when a fast rate was expected. If the heard-but-not-heeded hypothesis is rejected, then this performance pattern indicates that listeners had difficulty hearing the modulation at the unexpected slow rates. None of the decision statistics examined for the low-pass filter model predict any influence of expectation (Viemeister, 1979; Forrest and Green, 1987; Hartmann and Pumplin, 1988; Richards, 1992).

2. Modulation-filter model

The present data also provide little support for the proposed sharply tuned filters of the modulation-filter model (e.g., Bacon and Grantham, 1989; Houtgast, 1989; Yost and Sheft, 1989; Dau *et al.*, 1997), because the fast rates of modulation were always detected well. Previous probe-signal experiments have shown that long duration tones in continuous noise are poorly detected when they are presented at unexpected frequencies outside of the spectral filter centered on the expected frequency (e.g., Greenberg and Larkin, 1968). One motivation for conducting the present experiment was to see if, in parallel, modulation would be poorly detected at unexpected rates outside of the proposed passband of the modulation filter centered on the expected rate. Those passbands are proposed to be about 5, 16, and 128 Hz wide for modulation rates of 4, 32, and 256 Hz, respectively (Dau *et al.*, 1997). The results showed much less influence of expectation than was anticipated if there were indeed modulation filters.

This, however, should not be taken as strong evidence against the presence of modulation filters. If tuned modulation filters exist, listeners may monitor multiple filters simultaneously and thereby show good performance for a wide range of unexpected modulation rates. Listeners clearly do this in the spectral-frequency domain. For example, brief duration tones in continuous noise are well detected even when they are presented at unexpected frequencies outside of the spectral filter centered on the expected frequency (Wright and Dai, 1994). Furthermore, the performance cost for expecting masked spectral-frequency signals with a variety of frequencies (e.g., Green, 1961) or durations (Dai and Wright, 1995) is minimal. Thus the good performance for a wide range of unexpected modulation rates does not preclude the existence of modulation filters. It does indicate that the template-matching detector in the most elaborate of the modulation-filter models should be able to simultaneously monitor multiple templates (Dau *et al.*, 1997). It also raises the question of why listeners would always monitor the high-rate filters, but only monitor the low-rate filters when a low rate was expected.

IV. CONCLUSIONS

(1) Listeners detect modulation at expected and unexpected rates $\geqslant$16 Hz similarly well, but only perform well at rates $<$16 Hz when a slow rate is expected.
(2) These results appear to indicate that listeners use two different cues for the detection of modulation: an individual-fluctuation cue at low rates, and a roughness or pitch cue at higher rates.
(3) No current psychoacoustic model of modulation detection readily predicts the observed influence of the expectation of modulation rate.

ACKNOWLEDGMENTS

These data were presented at the 129th Meeting of the Acoustical Society of America [B. A. Wright and H. Dai, J. Acoust. Soc. Am. **97**, 3329 (A) (1995)]. We thank Quang Nguyen for technical assistance and Therese McGee for helpful discussions. Research Grants Nos. R29 DC02997 (Wright) and R29 DC01827 (Dai) from the National Institute on Deafness and Other Communication Disorders, National Institutes of Health, helped support this work.

[1]In many probe-signal experiments an example of the expected signal is presented in a cue interval prior to every trial to help the listener focus on the expected stimulus. The effect of a cue interval was not evaluated in the present experiment, but has been shown to have little effect on the detection of tones presented at unexpected frequencies (Greenberg and Larkin, 1968; Scharf *et al.*, 1987).

[2]There are two reasons to be cautious about this transformation. First, the slope of the psychometric function depends on the modulation rate. Second, the slope at a given modulation rate may be different between expected and unexpected conditions. These possible differences are ignored in the current analysis.

Bacon, S. P., and Grantham, D. W. (**1989**). ''Modulation masking: Effects of modulation frequency, depth, and phase,'' J. Acoust. Soc. Am. **85**, 2575–2580.

Burns, E. M., and Viemeister, N. F. (**1976**). ''Nonspectral pitch,'' J. Acoust. Soc. Am. **60**, 863–869.

Burns, E. M., and Viemeister, N. F. (**1981**). ''Played-again SAM: Further observations on the pitch of amplitude-modulated noise,'' J. Acoust. Soc. Am. **70**, 1655–1660.

Dai, H. (**1995**). ''On measuring psychometric functions: A comparison between the adaptive up–down and constant-stimulus methods,'' J. Acoust. Soc. Am. **98**, 3135–3139.

Dai, H., and Wright, B. A. (**1995**). ''Detecting signals of unexpected or uncertain durations,'' J. Acoust. Soc. Am. **98**, 798–806.

Dai, H., Scharf, B., and Buus, S. (**1991**). ''Effective attenuation of signals in noise under focused attention,'' J. Acoust. Soc. Am. **89**, 2837–2842.

Dau, T., Kollmeier, B., and Kohlrausch, A. (**1997**). ''Modeling auditory processing of amplitude modulation. I. Detection and masking with narrow-band carriers,'' J. Acoust. Soc. Am. **102**, 2892–2905.

Eddins, D. A. (**1993**). ''Amplitude modulation detection of narrow-band noise: Effects of absolute bandwidth and frequency region,'' J. Acoust. Soc. Am. **93**, 470–479.

Fastl, H. (**1977**). ''Roughness and temporal masking patterns of sinusoidally amplitude modulated broadband noise,'' in *Psychophysics and Physiology of Hearing*, edited by E. F. Evans and J. P. Wilson (Academic, London), pp. 403–414.
Fastl, H. (**1990**). ''The hearing sensation roughness and neuronal responses to AM-tones,'' Hearing Res. **46**, 293–296.
Forrest, T. G., and Green, D. M. (**1987**). ''Detection of partially filled gaps in noise and the temporal modulation transfer function,'' J. Acoust. Soc. Am. **82**, 1933–1943.
Gifford, R. H., Trine, T. D., and Grantham, D. W. (**1997**). ''Amplitude modulation detection thresholds and associated psychometric functions,'' J. Acoust. Soc. Am. **101**, 3083(A).
Green, D. M. (**1961**). ''Detection of auditory sinusoids of uncertain frequency,'' J. Acoust. Soc. Am. **33**, 897–903.
Greenberg, G. S., and Larkin, W. D. (**1968**). ''Frequency-response characteristics of auditory observers detecting signals of a single frequency in noise: The probe-signal method,'' J. Acoust. Soc. Am. **44**, 1513–1523.
Hartmann, W. M., and Pumplin, J. (**1988**). ''Noise power fluctuations and the masking of sine signals,'' J. Acoust. Soc. Am. **83**, 2277–2289.
Houtgast, T. (**1989**). ''Frequency selectivity in amplitude-modulation detection,'' J. Acoust. Soc. Am. **85**, 1676–1680.
Levitt, H. (**1971**). ''Transformed up-down methods in psychoacoustics,'' J. Acoust. Soc. Am. **49**, 467–477.
Patterson, R. D., Johnson-Davies, D., and Milroy, R. (**1978**). ''Amplitude-modulated noise: The detection of modulation versus the detection of modulation rate,'' J. Acoust. Soc. Am. **63**, 1904–1911.
Plomp, R. (**1983**). ''The role of modulation in hearing,'' in *Hearing—Physiological Bases and Psychophysics*, edited by R. Klinke and R. Hartman (Springer-Verlag, Berlin), pp. 270–275.
Richards, V. M. (**1992**). ''The detectability of a tone added to narrow bands of equal-energy noise,'' J. Acoust. Soc. Am. **91**, 3424–3435.
Scharf, B., Quigley, S., Aoki, C., Peachy, N., and Reeves, A. (**1987**). ''Focused auditory attention and frequency selectivity,'' Percept. Psychophys. **42**, 215–223.
Scharma, A. (**1994**). ''Multidimensional processing of pitch and place of articulation: Behavioral and neurophysiologic correlates,'' Doctoral dissertation, Northwestern University, p. 89.
Schlauch, R. S., and Hafter, E. R. (**1991**). ''Listening bandwidths and frequency uncertainty in pure-tone signal detection,'' J. Acoust. Soc. Am. **90**, 1332–1339.
Schreiner, C. E., and Langner, G. (**1988**). ''Coding of temporal patterns in the central auditory nervous system,'' in *Auditory Function*, edited by G. M. Edelman, W. E. Gall, and W. M. Cowan (Wiley, New York), pp. 337–361.
Schreiner, C. E., and Urbas, J. V. (**1988**). ''Representation of amplitude modulation in the auditory cortex of the cat. II. Comparison between cortical fields,'' Hearing Res. **32**, 49–64.
Strickland, E. A., and Viemeister, N. F. (**1996**). ''Cues for discrimination of envelopes,'' J. Acoust. Soc. Am. **99**, 3638–3646.
Terhardt, E. (**1974**). ''On the perception of periodic sound fluctuations (roughness),'' Acustica **30**, 201–213.
Yost, W. A., and Sheft, S. (**1989**). ''Across-critical-band processing of amplitude-modulated tones,'' J. Acoust. Soc. Am. **85**, 848–857.
Viemeister, N. F. (**1979**). ''Temporal modulation transfer functions based upon modulation thresholds,'' J. Acoust. Soc. Am. **66**, 1364–1380.
Wright, B. A., and Dai, H. (**1994**). ''Detection of unexpected tones with short and long durations,'' J. Acoust. Soc. Am. **95**, 931–938.

The role of level, spectral, and temporal cues in children's detection of masked signals

Prudence Allen, Rhiannon Jones, and Pamela Slaney
School of Communication Sciences and Disorders, University of Western Ontario, 1500 Elborn College, London, Ontario N6G 1H1, Canada

(Received 2 April 1998; accepted for publication 12 August 1998)

Preschool-aged children and adults were asked to detect masked signals in four conditions that evaluated the role of level, spectral, and temporal cues on performance. Psychometric functions fitted to percent correct data at several signal-to-noise ratios showed higher thresholds and shallower slopes for the children in all conditions. Performance was similar in fixed and roving level conditions for both age groups suggesting use of level-invariant cues. When the signal was moved to the spectral edge of the masker the performance of the adults improved but that of the children did not. This suggested that children did not benefit from the additional cues provided by the off-center signal. Children's performance worsened when the signal was a narrow-band noise rather than a pure tone but the adults' did not, suggesting children's reliance on temporal changes in the masker with the introduction of the signal. Analyses of the stimuli suggested that the children's thresholds corresponded to signal-to-noise ratios at which multiple cues were present at magnitudes that were great enough to be discriminable.
[S0001-4966(98)04711-0]

PACS numbers: 43.66.Dc [JWH]

INTRODUCTION

Preschool-aged children's detection of masked signals is generally poorer than that of adults. Their thresholds are higher, sometimes by as much as 15–20 dB, and their psychometric function slopes are often shallower (Allen and Wightman, 1994). One proposed explanation for these results is that children may not listen for the signal by focusing their attention consistently, and as narrowly as possible, at the expected signal frequency (Allen and Wightman, 1994, 1995). Yet when signals and maskers are simultaneously gated on and off, even adult listeners are unlikely to use highly frequency specific listening strategies (Dai and Buus, 1991; Wright and Dai, 1994). This makes it less likely that adult–child differences in frequency selective attention would be adequate to explain the age-related differences in detection accuracy.

An alternative explanation may be that children are less able to focus their attention on the acoustic cues that facilitate detection at low signal-to-noise ratios or that they attend to cues that are present or large enough to be discriminable, only at high signal-to-noise ratios. For example, when a tonal signal is added to a noise masker the overall level of the signal plus masker combination will be greater than that of the masker alone, the spectral shape of the masker will change reflecting the increased energy in the frequency region of the signal and the temporal structure of the masker may change, depending on the fine structure of each component and their relative gating. The strength of each of these cues will vary with signal-to-noise ratio.

Adults are likely able to use multiple cues to detect signals, integrating information from several cues (Ahumada and Lovell, 1970) and/or switching attention from one cue to another when some cues are removed (Hartmann and Pumplin, 1988; Kidd *et al.* 1993; Richards and Nekrich, 1993; Richards, 1992). But children may not have the same flexibility. In two recent studies of children's processing of complex sounds, age-related trends in the optimal use of acoustic information were found (Allen and Bond, 1997; Allen and Nelles, 1996). In general, the salience and/or resolution of acoustic features was reduced for children relative to that observed for adult listeners, and children showed less integration of acoustic information. These findings predict that children's ability to detect signals in noise may be reduced relative to that of adults if the magnitude of the acoustic features are small, if the integration of multiple features is required, and/or if it is important to be able to switch attention between cues. This paper reports a series of conditions that enabled comparison of children and adults' performance in detection tasks for which several acoustic cues were systematically manipulated. The cues selected were those that could be present in a more holistic evaluation of the signals, assuming that the listeners may not use a highly selective listening strategy because the signals and maskers were of relatively brief duration and simultaneously gated on and off. These cues included overall level, spectral shape, and temporal fine structure.

The first comparison addressed whether children, like adults, use level-invariant cues for detection. When a signal is added to a masker the level of the combination will be greater than that of the masker alone thus providing the listener with a cue to the presence of the signal. But this cue is not essential for adult detection performance to remain high (Kidd *et al.*, 1989). When the overall levels of the stimuli are randomized, absolute level information is removed but adults' detection accuracy remains the same. Although the magnitude of age-related trends in detection thresholds has been similar in studies using both fixed (Allen *et al.*, 1989; Allen and Wightman, 1994, 1995) and roving (Allen and

Wightman, 1992) level procedures, there has been no direct study of children's use of level information. This study, therefore, included comparison of detection performance in fixed and roving level conditions.

The addition of a signal to a flat-spectrum noise masker may also produce a change in the spectral shape of the masker. This change is likely a very important cue for adults' detection of and discrimination between stimuli (Green, 1988). But Allen and Wightman (1992) showed that children's ability to use spectral information was very poor when compared to that of older listeners. Children consistently required greater spectral contrast than did adults to discriminate between similar signals and their discrimination accuracy was quite poor when the signals were presented in noise. Thus their ability to use spectral information in detection tasks is likely reduced.

One of the perceptual correlates of spectral shape is pitch (e.g., Berg *et al.*, 1992; Feth, 1974; Feth and O'Malley, 1977; Versfeld and Houtsma, 1995). When the components of a complex stimulus are not fully resolved, its overall pitch will be based on a weighted average of the frequencies of the individual components. But when a tonal signal is presented in the spectral center of a flat noise masker, the pitch shift from that of the masker alone may not be large, particularly at low signal-to-noise ratios. If children were therefore listening for a change in the pitch of the signal plus masker combination, it may only be noticeable at fairly high signal-to-noise ratios where the frequency content of the signal will dominate the stimulus and thus provide a more focused pitch cue. But, if the signal is placed asymmetrically within the masker, the pitch shift from the masker alone would likely be more salient and may facilitate detection at lower signal-to-noise ratios. Similarly, moving the signal nearer to the spectral edge of the masker could also provide an additional spectrally related cue in the form of an increase in signal-to-noise ratio, if the listener were to shift their attention to the spectral edge of the masker. This study therefore evaluated detection performance in conditions for which the signal was a tone spectrally centered in the noise masker and another for which the signal was placed at the spectral edge of the masker, where it was expected that a pitch cue would be most salient and local signal-to-noise ratios may be enhanced.

In a recent study of children's and adults' perception of unfamiliar, complex sounds, Allen and Bond (1997) suggested that temporal fine structure may be a salient feature for young children. Results of a multi-dimensional scaling analysis of paired comparisons similarity data provided by school-aged children and adults suggested that the adults evaluated the stimuli based on an equally weighted integration of spectral and temporal information that could be seen in a single dimension of the fitted solution. The spectral coding included the number of spectral peaks in the signals, separating stimuli with compact or flat spectra from those with energy distributed unevenly throughout the frequency range; and absolute frequency. The temporal coding included the average number of components within each critical band, thus separating pure tones, multi-tonal complexes, and noises. In contrast, the ratings of the children suggested less integration of spectral and temporal features with spectral shape, temporal structure, and average frequency coded in separate dimensions. Although coding of spectral information was similar for the children and the adults, coding of temporal information may have been coarser for the children. Analysis of the adult data suggested coding of both temporal fine structure and envelope but the data from the younger children suggested coding of only the presence or absence of a periodic fine structure. Tones and multi-tonal complexes with their periodic fine structure were rated similarly to one another but differently from the noises, which were more aperiodic. This binary distinction between the stimuli and its high contribution to the overall ratings suggests that temporal fine structure information may provide a salient cue for children and may therefore affect their performance on detection tasks. That is, children may judge that a signal is present only when the periodicity in the signal plus masker combination exceeds that of the masker alone. Hartmann and Pumplin (1988) have shown that adults in masked detection tasks may use temporal fine structure cues, especially when maskers are fairly broad and little frequency selective listening is applied. This study therefore included evaluation of children's use of temporal fine structure information by comparing performance in conditions for which the signal was a narrow-band noise, with a less periodic structure, with that obtained when the signal was a pure tone, for which the periodicity cue would be expected to be strong.

In summary, three experimental questions were addressed through planned comparisons of performance in four conditions. The first comparison was made between two conditions for which the signal was a 1000-Hz pure tone, spectrally centered in a noise masker but in which the overall level of the masker was fixed (condition 1) or randomized (condition 2) enabling assessment of the relative contribution of level cues to detection. The second comparison was between data obtained when the signal was a 1000-Hz pure tone and the level was roved (condition 2), and another roving level condition in which the signal was an 1175-Hz pure tone (condition 3), thus allowing evaluation of the contribution of spectral cues to detection, particularly pitch shifts and off-frequency listening. The final comparison was made between performance in conditions 2 and 4 for which the signal was a narrow-band noise, also spectrally centered in the masker, like the pure tone of condition 2. Because the noise signal was assumed to have lower periodicity than the pure tone, the role of temporal fine structure cues to detection could be estimated from this comparison.

I. METHOD

A. Listeners

Listeners were 6 adults (mean age: 25.2 years, range 24.7–25.8 years) and 11 pre-school aged children (mean age: 4.6 years, range 3.7–5.3 years). Adult listeners were recruited from the University of Western Ontario. Each read a letter of information and signed a consent form before participating. Children were recruited from Western Day Care Centre. Their parents read a letter of information and signed a consent form to allow their child to participate. Verbal

consent was also obtained from the children. All listeners were screened for normal hearing sensitivity (<20 dB HL at octave frequencies from 250 through 4000 Hz; ANSI 1989) and normal middle ear function before being admitted to the study (ASHA, 1990). Middle ear status was checked periodically throughout each child's participation if the child, the teacher, or the experimenter suspected difficulties. Information regarding the listeners' prior hearing health history was not solicited but children for whom the teachers suspected behavioral and/or learning difficulties were not included in the study.

B. Stimuli

Stimuli were 328 ms in duration, including 10-ms cosine-squared on/off ramps. Signal and masker combinations were generated digitally, converted to analog form by a 16-bit D/A converter (Ariel) at 25 000 points/s and attenuated by custom built programmable attenuators. The output was low-pass filtered at 8000 Hz and amplified before transduction by an ER-3A insert earphone to the right ear of the listener. The maskers were flat with a bandwidth of 800–1200 Hz, presented at an average spectrum level of 30 dB/Hz SPL. When level was randomized (conditions 2–4), masker spectrum level varied from 25 to 35 dB/Hz. For each condition a series of stimuli were created for which the signal-to-noise ratio (E/N_0) was varied over a 50-dB range, in 5-dB steps. At each of these 11 signal-to-noise ratios, 5 samples of the signal plus masker combination were created, each using a different sample of masker and signal. Ten samples of noise alone were created.[1] Adult listeners were most often tested at the lower range of signal-to-noise ratios, 0–35 dB, while children, because of their poorer performance, were generally tested at higher levels, 15–50 dB. The range of signal-to-noise ratios tested in each block was 25 dB with the levels adjusted up or down in subsequent blocks if required to observe performance at chance and 100% correct. The signal for conditions 1 and 2, investigating the role of level cues, was a 1000-Hz pure tone. The condition 3 signal was an 1175-Hz pure tone and, in conjunction with data from condition 2, estimated the use of spectral cues. The role of temporal cues was determined by examining performance in condition 4, for which the signal was a noise band of 975–1025 Hz, with that obtained in condition 2.

C. Procedure

Adult listeners were tested individually in a double-wall sound-attenuating chamber. The children were tested in a quiet room at the day care center. In a forced choice paradigm, the listener was presented with trials consisting of two listening intervals of 328 ms separated by a 500-ms interstimulus interval. The numbers ''1'' and ''2'' were presented on the computer screen in conjunction with the presentation of each listening interval. Each interval contained either a sample of noise alone or one of the signal plus noise combinations. The interval containing the signal plus noise was chosen randomly with equal *a priori* probability. The listeners' task was to indicate, by pressing either ''1'' or ''2'' on the computer keyboard or pointing to the numbers on the screen, which interval contained the signal. Adults entered their responses into the computer, while an experimenter with the children entered their responses. With each correct response a portion of a picture was revealed to the listener on the computer monitor. Incorrect responses were not reinforced. At the end of a block of trials, the complete picture was revealed to the listeners, indicating that the block was complete.

The four conditions were presented to each listener in blocks of 30 trials. Each block contained five samples of each of six signal-to-noise ratios, chosen randomly throughout the block of trials. Condition was varied randomly between blocks. Each condition required the completion of 120 trials with some listeners completing additional trials with the signal-to-noise ratio adjusted up or down, if needed to observe performance at chance and at 100% correct. Conditions included: 1: tone centered; fixed level; 2: tone centered, roving level; 3: tone off-center, roving level; and 4: noise stimulus, roving level. Children completed up to four blocks of trials each day depending on their willingness to continue. Each block required approximately 4–7 min to complete. Children were tested several times each week until all conditions were completed. The adults completed all of the blocks in one to two sessions.

For each condition, a logistic function was fitted to the percent correct detections as a function of signal-to-noise ratio using the maximum likelihood procedure and the constrained nonlinear function of SPSS-X. Percent correct scores at each signal-to-noise ratio were weighted by the number of observations that contributed to that score. The fitted function was $PC = 0.5 + 0.5/(1 + e^{-2(\text{level}-a)/b})$ where ''level'' is the signal-to-noise ratio, ''*a*'' is the intercept, and ''*b*'' is the slope of the logistic function used to represent the psychometric function. The intercept corresponds to the signal-to-noise ratio at which performance is expected to be 75%. The slope corresponds to the decibel (dB) difference between two points on the linear portion of the function at which performance differs by approximately 20%. Large values of parameter ''*b*'' imply shallow functions and smaller values imply steeper functions. Goodness of Fit was evaluated using the statistic G^2 as recommended by Christensen (1990):

$$G^2 = 2\sum_{i=1}^{n} y_i \log(y_i/p_i) + (1-y_i)\log((1-y_i)/(1-p_i)),$$

where n is the number of trials contributing to the fitted function, y_i indicates whether the response is correct or incorrect (1 for correct, and 0 for incorrect), and p_i is the probability of a correct response predicted from the fitted function. G^2 is evaluated using Chi-square functions with the degrees of freedom equal to the number of trials minus the number of fitted parameters, which is equal to 2 in this case, representing the slope and threshold.

II. RESULTS

All of the six adults completed all four conditions. Figure 1 shows individual obtained percent correct scores in

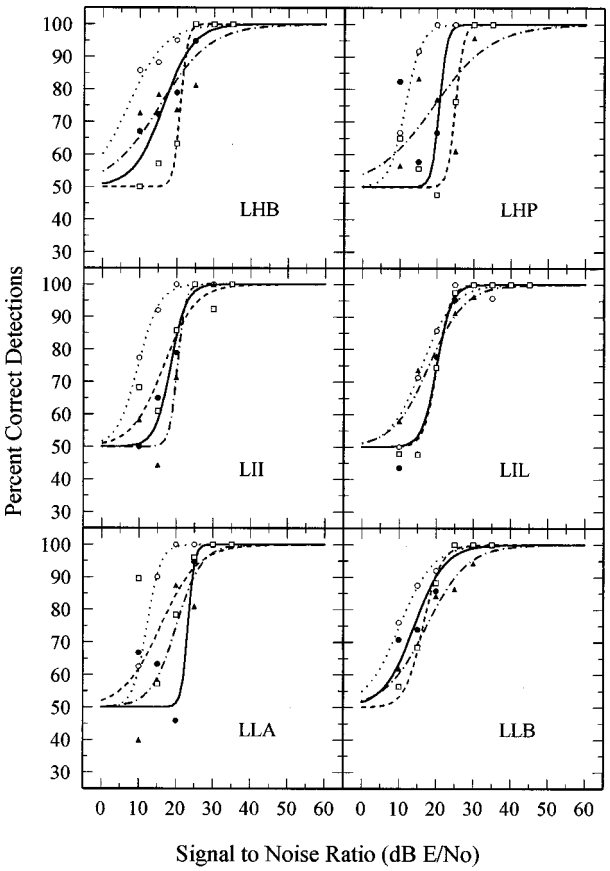

FIG. 1. Individual psychometric functions for adult listeners and the percent correct data from which these functions were fitted. (Each fitted function is based upon at least six percent correct scores at 5-dB intervals from one another. In some cases, scores falling at 100% correct are obscured by other points at the same level of performance for other conditions.) Conditions and symbols are as follows: Tone centered, fixed masker level: dashed lines and open squares; Tone centered, roving level: solid lines and filled circles; Tone spectrally off-center, roving level: dotted lines and open circles; and Narrow-band noise signal, roving level: dash/dot lines and open squares.

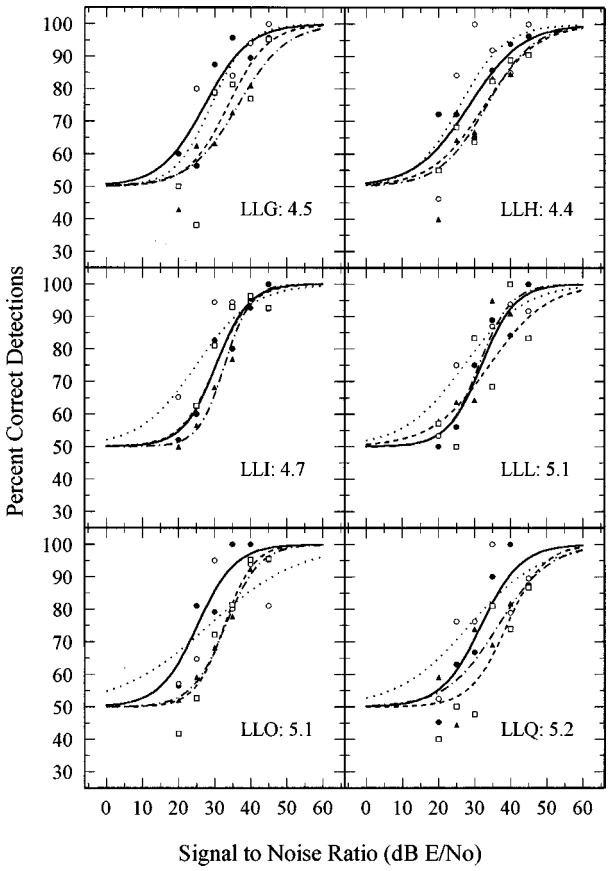

FIG. 2. Individual psychometric functions for child listeners who completed all conditions and the percent correct data from which these functions were fitted. (Each fitted function is based upon at least six percent correct scores at 5-dB intervals from one another. In some cases, scores falling at 100% correct are obscured by other points at the same level of performance for other conditions.) Conditions and symbols are as follows: Tone centered, fixed masker level: dashed lines and open squares; Tone centered, roving level: solid lines and filled circles; Tone spectrally off-center, roving level: dotted lines and open circles; and Narrow-band noise signal, roving level: dash/dot lines and open squares.

each condition plotted as a function of signal-to-noise ratio and the psychometric functions fitted to those data. Each data point reflects performance averaged over approximately 15–25 trials. Data from each listener are shown in separate panels. Listener ID is indicated by the three-letter code in each panel. Performance in condition 1 (tone centered, fixed level) is indicated by the dashed lines and open squares. Solid lines and filled circles show performance in condition 2 (tone centered, roving level). Performance in condition 3 (pure tone, spectrally off-center in the roving level masker) is indicated by the dotted lines and open circles. Data obtained in condition 4 (narrow-band noise, roving level) are shown by the dash/dot lines and filled triangles. All fitted functions showed acceptable G^2 values at the 0.01 level of confidence.

Only 6 of the 11 children produced percent correct data that resulted in fitted psychometric functions with predicted 75% correct thresholds at or below a signal-to-noise ratio of 50 dB, the highest signal-to-noise ratio actually tested, and slopes that were less than 35 dB in all four conditions. Their individual data and fitted functions are shown in Fig. 2. Symbols and lines are as described for the adults in Fig. 1. Listener identification codes and age (in years) are shown in each panel. In general, the fits to the children's data resulted in shallower psychometric function slopes and consequently, higher thresholds, than were observed for the adults. Yet, the fitted functions largely reached asymptote at 100% correct for both groups. Individual thresholds and slopes extracted from the fitted functions for each condition are shown in Fig. 3. Data from the adults and children are shown by the filled and open circles, respectively. The upper panel shows predicted threshold signal-to-noise ratios and the lower panel shows slopes. Filled and open triangles show mean performance for the adults and children, respectively, in each condition.

A repeated measures analysis of variance on the data shown in Fig. 3 showed that thresholds differed significantly as a function of age, $F(1,10)=193.88$, $p<0.0001$, and condition, $F(3,30)=24.5$, $p<0.0001$. Also, the interaction between age and condition was significant, $F(3,30)=3.75$, $p=0.021$, suggesting that the two groups of listeners showed different changes in performance across the various conditions. Slopes differed significantly only as a function of age, $F(1,10)=58.8$, $p<0.0001$.

The effects of age and condition were examined using

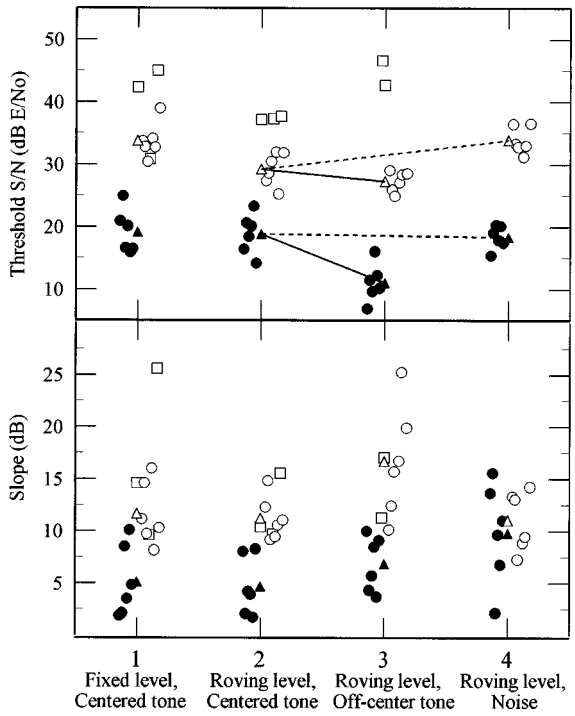

FIG. 3. Upper panel shows individual 75% correct thresholds (signal-to-noise ratios) extrapolated from the fitted psychometric functions for each condition. Filled circles indicate adult data; open circles show data obtained from the six children who completed all conditions; open squares show thresholds obtained from the children who only provided measurable thresholds in some conditions. Filled and open triangles show adults' and children's means. Lower panel shows the slopes of individual fitted pscyhometric functions for each condition. Symbols are as for upper panel.

planned, single degree of freedom contrasts between conditions 1 and 2 (examining level effects); 2 and 3 (examining spectral effects); and 2 and 4 (examining temporal cues). Because the age by condition interaction was significant for thresholds only, contrasts on slopes were not performed.

A. Level cues: Detection in fixed and roving level conditions

When the signal was a tone centered in a noise masker children's thresholds were on average 8.3 dB higher than those of adults, averaged across fixed and roving level conditions (1 and 2). This difference was statistically significant, $F(1,10)=4.834$, $p<0.0001$, but the age by condition interaction was not, $F(1,10)=3.684$, $p=0.084$, suggesting that the children's performance, like that of the adults, was not adversely affected by the removal of absolute level cues. This argues that both groups of listeners were able to use level-invariant detection cues.

B. Spectral cues: Detection of tonal signal as a function of spectral position in the masker

Thresholds obtained when the signal was a tone, spectrally centered in the noise masker (condition 2) and spectrally off-center (condition 3) were significantly different, $F(1,10)=26.086$, $p<0.0001$, as was the age by condition interaction, $F(1,10)=9.510$, $p=0.012$. The solid lines connecting mean thresholds in the upper panel of Fig. 3 illustrate that adult thresholds decreased in the tone off-center condition by an average of 7.8 dB, but the children's thresholds did not. Thus only the adults appeared to take advantage of the additional cue provided by the frequency shift of the signal.

C. Temporal cues: Detection of a narrow-band noise or tonal signal

Thresholds obtained in conditions 2 (tone signal, spectrally centered in the masker) and 4 (narrow-band noise signal, spectrally centered in the masker) differed significantly, $F(1,10)=85.512$, $p=0.041$, as did the age by condition interaction, $F(1,10)=8.373$, $p=0.016$. Examination of the data in Fig. 3 show that children's thresholds increased when the signal was changed from a pure tone to a narrow-band noise by, on average, 6.6 dB. The thresholds of the adults did not. Mean data for the two conditions, connected by the dashed lines in Fig. 3, show that when the signal had a less periodic temporal structure the children's performance worsened but that of the adults did not. This suggests that the younger listeners may have relied more heavily on temporal information than did those in the older age group.

III. DISCUSSION

A. Individual differences

Individual differences in the performance of young children are commonly reported in psychoacoustic studies (e.g., Allen and Wightman, 1992, 1994, 1995). The performance of the six children who were included in the group analyses reported here was quite similar, with both between and within subjects variance quite low and consistent with that observed for the adult listeners. However, the data from the five additional children who participated are consistent with previous reports of high variability. The data from these additional children are plotted in Fig. 4 using the symbols and lines as described for Figs. 1 and 2. The between subject variability is large. At one extreme, for example, is listener LLE who showed very poor performance with fitted psychometric functions falling at chance in all four conditions. At the other extreme is listener LLD who showed comparable performance to the six better performing children in all but the noise condition where performance was very poor. Another difference between these groups of children is that the functions fitted to the data obtained from the five poorer performing children often were flat at chance levels or reached asymptote at levels below 100% correct.

The open squares in Fig. 3 show the thresholds and slopes estimated from the functions fitted to the data obtained from these five children in all conditions for which fitted functions showed thresholds at or below 50-dB signal-to-noise ratio and slopes less than or equal to 35 dB. Note that the fitted thresholds from these five children are generally higher than those of the other listeners, often among the highest of all individuals tested. Exclusion of their data in the overall analysis because of poor performance in some conditions lowered the overall magnitude of adult–child threshold differences. For example, when only the performance of the six better performing children was compared with that of the adults in the fixed–roving comparison, thresholds dif-

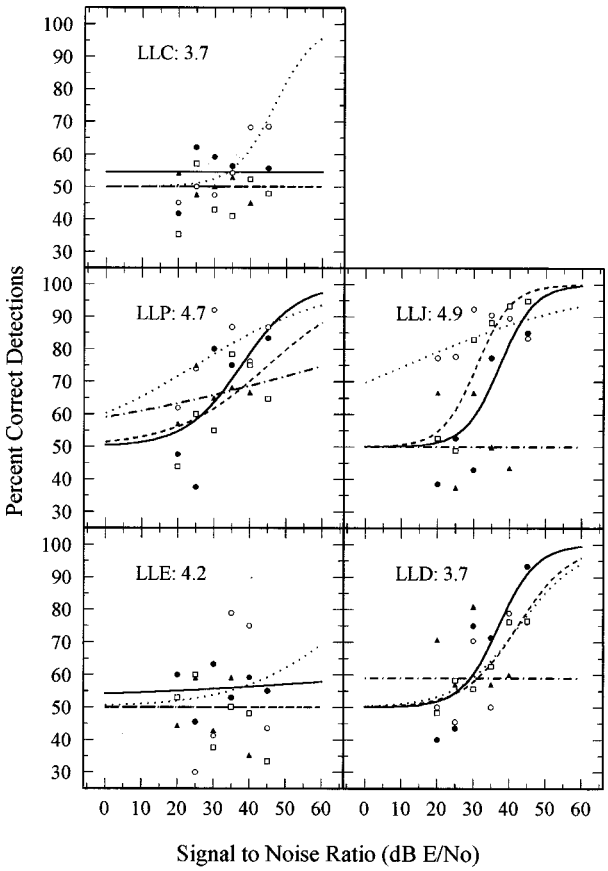

FIG. 4. Individual data and fitted psychometric functions for the five children who provided valid thresholds and slopes in some conditions only. Lines and symbols are as indicated for Figs. 1 and 2.

fered by an average of only 8.3 dB, somewhat lower than that reported in other studies (e.g., Allen and Wightman, 1994). However, when the additional children who completed both fixed and roving level conditions successfully are included in the mean, the children's mean threshold is nearly 15 dB higher than that of the adults.

In spite of the generally poorer performance observed from these five children, the trends in the data with regard to which conditions produced poorest performance are consistent with that observed in the better performers. The children in the poorer performing group showed worst performance for the noise condition in which none of the five produced detection data to which reasonable functions could be fitted. This suggests that, among these poorer performers as well as the better, the reliance on temporal cues may have been substantial.

The mean age of the better and poorer performing children was similar, 4.83 and 4.24 years, respectively, but it was interesting to note that the group of six better performing children included the three oldest children (5.2, 5.1, and 5.1 years) and the five poorer performers included the three youngest children (3.7, 3.7, and 4.2). The remaining children were split between the two groups (4.4, 4.5, and 4.7 for the better group, and 4.7 and 4.9 for the poorer group). Thus it may be that performance is changing fairly rapidly during the 3–5 year period.

B. Acoustic cues to the presence of a signal in a noise masker

It is frequently reported that children's masked detection abilities are poorer than those of adults. Because many aspects of their performance (i.e., higher thresholds, shallower psychometric function slopes, and increased variability) can be modeled by an inattentive listener it has sometimes been suggested that children may be unable to attend consistently and narrowly to a single signal frequency (e.g., Allen and Wightman, 1994). But even adult listeners are unlikely to use a highly frequency selective listening strategy when the signals and maskers are brief in duration and simultaneously gated on and off (Dai and Buus, 1991). A complementary explanation may be that the children attend to acoustic features in noise alone and signal plus noise stimuli that may only be present, or large enough to be discriminable, at relatively high signal-to-noise ratios. Three potential cues were examined in the current study: level, spectral shape (and/or pitch), and periodicity.

1. Absolute level

Absolute level cues were available to the listeners only in condition 1. Comparison of the overall level of the signal plus masker and masker alone stimuli in condition 1 showed that the addition of a signal at the adult threshold signal-to-noise ratios, 15–25 dB, would have raised the overall level of the masker by less than 3 dB. This is a small, but potentially discriminable difference. At the threshold levels measured for the children, on average 30–35 dB signal-to-noise ratio, the signal would have produced an increase of 5–10 dB relative to that of the masker alone. According to children's difference limens for intensity measured by Jensen and Neff (1993), this increase could have been discriminable for the children. Thus discriminable level cues were available to listeners at the signal-to-noise ratios for which threshold were estimated. However, it is unlikely that either group of listeners relied solely on this information, as performance did not deteriorate when it was removed by randomization in condition 2. This suggests that level-invariant cues must have played a role in detection for children, as well as adults.

2. Spectral cues

An important level invariant cue used by adult listeners in masked detection tasks is spectral shape, or evaluation of cross-channel level differences within the stimulus (Green, 1988). Although children may attend to spectral shape information in their encoding of complex sounds (e.g., Allen and Bond, 1997) their resolution for spectral differences is unlikely to be as good as that of older listeners. For example, in a roving level procedure, Allen and Wightman (1992) measured adults' and children's ability to discriminate between tonal complexes with amplitude spectra that were sinusoidally modulated at two different frequencies. Adult listeners required less than 5 dB of spectral contrast (expressed as peak-to-trough ratios) to discriminate between the complexes. But preschool-aged children required at least 20 dB of contrast to discriminate between the stimuli with the same degree of accuracy. In a related roving level procedure, listeners were asked to discriminate between a noise alone and

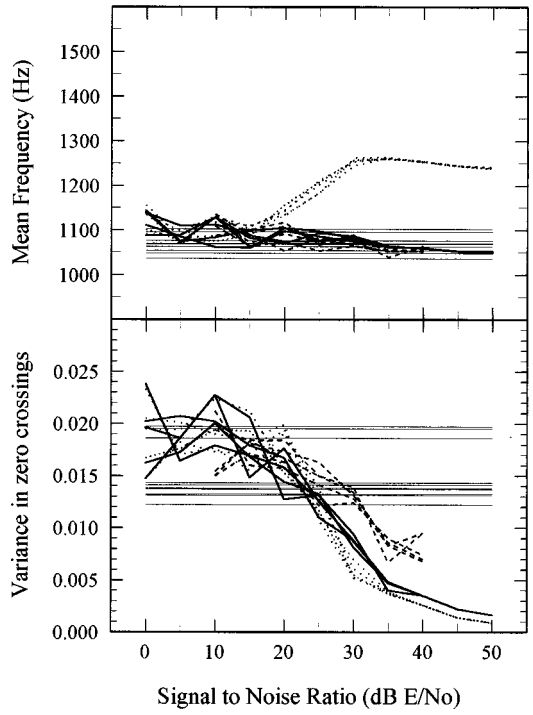

FIG. 5. Upper panel show average frequency of the stimuli, computed from the average interval between successive zero crossings in the time domain waveforms. Mean frequency is represented by 1/(2* mean inter-zero-crossing-interval). Five samples were evaluated at each signal-to-noise ratio. Lines show connections between sampled signals, randomly selected from the five available. Heavy solid lines show the tone centered in the noise masker. Dotted lines show the tone spectrally off-center in the masker. Dashed lines show narrow-band noise signal plus masker combinations. Thin solid lines represent each of the ten masker samples for which there was no signal. Measures for these maskers are therefore plotted at each signal-to-noise ratio for illustrative purposes only. Data in the lower panel show estimates of periodicity which are assumed to be reflected by the variance in the inter-zero-crossing intervals. Lines indicate the same conditions as in the upper panel.

a noise containing one of three signals (a tonal complex, a simulated fricative, and a simulated vowel). The children required signal-to-noise ratios that were 8–18 dB greater than those required by the adults. These data suggest that large spectral contrast is required for children to detect and/or discriminate between signals with adultlike accuracy. Children's higher threshold signal-to-noise ratios measured in the current study are consistent with their need for high contrast and suggest that spectral shape may have contributed to children's ability to detect the signals.

One of the primary perceptual correlates of spectral shape is pitch. A pitch shift with the addition of the signal was unlikely to have occurred for most sounds tested in the current study because the signals were most often centered in the noise masker. Only in condition 3, when the signal was placed asymmetrically within the masker, was a shift in the pitch of the signal plus masker combination relative to that of the noise alone likely and only at high signal-to-noise ratios. The upper panel of Fig. 5 shows estimates of average frequency for the maskers plus the three signals used in this study, each added over a range of signal-to-noise ratios. These estimates were made by analyzing the digital representations of the signals and calculating the average time interval between successive zero crossings. The thin horizontal lines plotted as a constant function of signal-to-noise ratio show data for the ten maskers alone. There were five signal plus noise combinations at each signal-to-noise ratio tested ranging from 0 to 50 dB for the 1000- and 1175-Hz tonal signals and 10–40 dB for the 800–1200 Hz narrow-band noise signals. Samples 1–5 at each signal-to-noise ratio are connected to those at the next higher level. The heavy solid lines show the 1000-Hz signal plus masker combinations used in both the fixed and roving level conditions. The data for the 1175-Hz signal plus masker are shown by the dotted lines; the dashed lines show the narrow-band noise signal plus masker stimuli.

When the signal was an 1175-Hz tone, the mean frequency of the stimulus differs from that of the masker alone only when signal-to-noise ratios of 15 dB are exceeded. Adult detection thresholds were generally obtained at lower signal-to-noise ratios where no frequency differences were observed, arguing against their use frequency differences for detection. But the children's thresholds were obtained at levels for which the average frequency of the signal plus masker stimulus and the masker alone were different by approximately 175 Hz, suggesting that pitch cues may have been available to them.[2] While this frequency difference was not present at a sufficiently low signal-to-noise ratios to result in improved thresholds for the majority of the children, its presence was consistent with the threshold signal-to-noise ratios for the children and was thus a potential cue. It also may have facilitated the performance of some children, particularly those who performed most poorly in the other conditions. As can be seen in Fig. 4, for many of the poorer performing children, best performance was obtained in the tone off-center condition suggesting that the pitch cue may have helped to improve detection accuracy. However, the magnitude of the difference reached asymptote at 30 dB E/N_0 but the thresholds of the poorer performing children were obtained at much higher levels (40–45 dB), suggesting that this cue may not have been the determining factor in their performance.

It is also unlikely that the adult threshold improvement in condition 3 was a result of mean frequency differences as these differences were not available at the signal-to-noise ratios for which adult thresholds were measured. It is more likely that their improvement resulted from off-frequency listening. Because the upper limit of the noise masker was only 1200 Hz and the signal was 1175 Hz, the listeners could have shifted their attention to the spectral edge of the masker, thus improving the signal-to-noise ratio in that region and facilitating detection accuracy. If children's ability to focus their attention at specific frequency regions is poor, as has been suggested earlier (e.g., Allen and Wightman, 1994), it is unlikely that they would have been able to take advantage of off-frequency cues.

3. Periodicity

When the signal was a narrow-band noise (condition 4), the children's performance, but not that of the adults, was poorer than when the signal was a tone (condition 2). One explanation for this result is that the children, in listening for the signals, relied more heavily on changes in the temporal

fine structure of the masker produced with the addition of the signal. This change would have been smaller when the added signal was a noise band. To determine if there were differences in the noise alone and signal plus noise stimuli used in this study and at what signal-to-noise ratios these differences first appeared, an estimate of relative periodicity was obtained from an analysis of the variance in time intervals between successive zero crossings in the time domain representations of each stimulus. Low variance suggested a stimulus with more periodic fine structure than did higher variance. The results of these analyses are shown in the lower panel of Fig. 5. Lines and symbols are as reported for the upper panel.

Adding a tonal signal to the noise masker produced a difference in temporal fine structure when compared to that of the noise alone, for signal-to-noise ratios above 25 dB. Adult thresholds are below this level for all conditions, arguing that they did not use differences in temporal fine structure to detect the signals. However, for all 11 of the children, all detection thresholds for the tonal signals (including the fixed level, roving level, and tone off-center conditions) were at or well above 25 dB where the periodicity differences were available. When a narrow-band noise signal was added to the maskers (condition 4), the masker alone and signal plus masker stimuli began to differ at a signal-to-noise ratio approximately 5 dB above that for the tonal signals, 30 dB. This 5-dB shift is consistent with the average 6.6-dB elevation of children's thresholds in the narrow-band noise condition relative to those obtained with the tonal signals. Without exception all children's thresholds for detection of the narrow-band noise signal were at or above 30-dB signal-to-noise ratio while those of the adults were consistently below this level.

These results suggest that at the signal-to-noise ratios corresponding to the children's detection thresholds, temporal fine structure differences in the signal plus masker, and masker alone stimuli were present and may have been used by the children, either alone or in combination with other cues, to facilitate detection. Especially significant is that when the periodicity difference was decreased, as in condition 4, the children's performance deteriorated accordingly.

Attention to periodicity cues may be useful for explaining children's performance on tasks involving signal and masker uncertainty. Allen and Wightman (1995) found that signal uncertainty produced only a very small effect on children's performance. When young children were asked to detect a tonal signal whose frequency was selected randomly from one of two frequencies (501 and 2818 Hz), their detection accuracy did not change relative to that achieved when the signal frequency was fixed. This was in contrast to the performance of the adults who showed a moderate reduction in accuracy when signal uncertainty was introduced. If the children were listening for increased periodicity associated with the signal plus masker combination, absolute frequency would have been expected to have little effect on performance as long as the frequency of the signals permitted phase locking in the auditory periphery (e.g., $<$4000 Hz, Ruggero, 1992) and a subsequent perception of tonality.

Similarly, listening for changes in periodicity may explain at least some of the very large effect of tonal distracters on detection also reported by Allen and Wightman (1995). When a random frequency, tonal distracter (selected from the ranges 350–700 and 1400–2400 Hz) was presented in each listening interval of a detection task, the majority of the children were unable to detect the 1000-Hz tonal signal at better than chance levels. The level of the distracter was randomized over a 10-dB range (but was always high enough to be clearly audible), thus removing absolute level cues and potentially forcing the children to rely on level-invariant cues. If the children listened for increases in the periodicity of the masker produced when the signal was added, performance would be very poor because the stimuli would always have a relatively high degree of periodicity because of the presence of the tonal distracter. This would reduce the significance of a change produced by the addition of the signal and could disrupt one of the potential cues for detection.

IV. SUMMARY AND CONCLUSIONS

Psychometric functions were fitted to the detection data provided by 6 adults and 11 children in 4 conditions designed to test the relative contribution of level, spectral, and temporal cues to detection. The first question addressed the use of level versus level-invariant cues. Results showed that, consistent with previous findings, children's detection thresholds are generally higher than those obtained from adult listeners and the slopes of their psychometric functions relating performance to signal-to-noise ratio are shallower. However, neither age group showed significant differences in performance in fixed versus roving level conditions. These results are consistent with those previously reported for adult listeners, and add to our understanding of children's performance by suggesting that they too are capable of using level-invariant cues for detection.

In two additional comparisons, the effects of spectral information as provided by the frequency of the signal and its spectral position in the noise masker, and temporal information as provided by the regularities in the temporal fine structure of the signal plus masker combinations, were evaluated. Results suggested that shifting the frequency of the signal off the spectral center of the masker improved the performance of the adults but not the children. Conversely, reducing the periodicity of the signal to be detected resulted in a reduction in the performance of the children, but not the adults.

Collectively, results suggest that both adults and children may have used absolute level differences to facilitate signal detection when levels were fixed and that spectral shape cues likely provided sufficient information to keep performance constant when the level information was removed through randomization. The magnitude of both cues at threshold levels increased with decreasing age in a way that was consistent with previously published reports of children's reduced discrimination ability for changes in intensity and spectral contrast. In spite of these similarities, there were also differences in the children's and adults' performance. For the adults, at the low signal-to-noise ratios associated with threshold, performance was enhanced by the presentation of a signal that was presented asymmetrically within the masker spectrum. It is likely that the adults were able to

enhance detection performance through off-frequency listening but the children were not, probably because of reduced ability to focus attention at specific frequency regions. Also, the children may have attended to another available cue, that provided by changes in the temporal fine structure of the masker when a signal was added. At the higher signal-to-noise ratios associated with children's thresholds, there were changes in periodicity that could have provided an important cue for children's detection in the conditions tested here. Whether this cue is necessary and/or sufficient for performance to remain stable remains questionable until subsequent studies are performed to more thoroughly evaluate its role.

ACKNOWLEDGMENTS

The authors wish to thank the adult listeners and the children, staff, and parents of the Western Day Centre for their participation and the National Sciences and Engineering Research Council of Canada for financial support. We would also like to thank Dr. John Grose and an anonymous reviewer for their comments on an earlier version of this manuscript.

[1]Across all four experimental conditions, each signal-to-noise ratio and signal combination were constructed by adding signals to independent noise samples. Because only ten samples of noise alone were generated it is possible that the adult performance may have been better than that of the children, at least in part, because they were able to learn the spectral and temporal characteristics of these ten noise samples. Our results showed no trend for improved performance as successive blocks of each condition were completed, making it unlikely that the limited number of noise samples contributed significantly to the adult–child performance differences.

[2]The stimuli were created with a mean of zero. Periodicity and relative frequency were therefore estimated from evaluation of the time interval between successive zero crossings in waveforms. The time of the zero crossings, if not occurring at a sampled interval, was estimated as the time corresponding to a sign change in the amplitude values. This introduced some error into the estimates of average frequency. The magnitude of this error was 40–100 Hz for the 400-Hz wide maskers centered at 1000 Hz. When the 1000-Hz signals (pure tones and narrow-band noises) used in conditions 1, 2, and 4 were added to the noise masker there was no change in the estimated mean frequency. When the 1175-Hz pure tones (condition 3) were added to the maskers, the predicted frequency of the combined stimulus exceeded that of the masker alone and that of the masker plus 1000-Hz signals by 150–200 Hz, consistent with the increase in signal frequency. This shift occurred only at the higher signal-to-noise ratios.

Ahumada, A. Jr., and Lovell, J. (**1971**). ''Stimulus features in signal detection,'' J. Acoust. Soc. Am. **49**, 1750–1756.

Allen, P., and Bond, C. A. (**1997**). ''Multidimensional scaling of complex sounds by children and adults,'' J. Acoust. Soc. Am. **102**, 2255–2263.

Allen, P., and Nelles, J. (**1996**). ''Information integration in preschool-aged children,'' J. Acoust. Soc. Am. **100**, 1043–1051.

Allen, P., and Wightman, F. (**1992**). ''Spectral pattern discrimination by children,'' J. Speech Hear. Res. **35**, 222–233.

Allen, P., and Wightman, F. (**1994**). ''Psychometric functions for children's detection of tones in noise,'' J. Speech Hear. Res. **37**, 205–215.

Allen, P., and Wightman, F. (**1995**). ''Effects of signal and masker uncertainty on children's detection,'' J. Speech Hear. Res. **38**, 503–511.

Allen, P., Wightman, F., Kistler, D., and Dolan, T. (**1989**). ''Frequency resolution in children,'' J. Speech Hear. Res. **32**, 317–324.

ANSI (**1989**). ANSI S3.6, 1989 ''Specification for audiometers'' (ANSI, New York).

American Speech-Language-Hearing Association (**1990**). ''Guidelines for Screening for Hearing Impairment and Middle-Ear Disorders,'' Asha **32**, (Supp. 2), 17–24.

Berg, B. G., Nguyen, Q. T., and Green, D. M. (**1992**). ''Discrimination of narrow-band spectra. I: Spectral weights and pitch cues,'' J. Acoust. Soc. Am. **92**, 1911–1918.

Christensen, R. (**1990**). *Log-Linear Models* (Springer-Verlag, New York).

Dai, H., and Buus, S. (**1991**). ''Effect of gating the masker on frequency-selective listening,'' J. Acoust. Soc. Am. **89**, 1816–1818.

Feth, L. (**1974**). ''Frequency discrimination of complex periodic tones,'' Percept. Psychophys. **15**, 375–379.

Feth, L., and O'Malley, H. (**1977**). ''Two-tone auditory spectral resolution,'' J. Acoust. Soc. Am. **62**, 940–947.

Green, D. M. (**1988**). *Profile Analysis: Auditory Intensity Discrimination* (Oxford U.P., New York).

Hartmann, W. M., and Pumplin, J. (**1988**). ''Noise power fluctuations and the masking of sine signals,'' J. Acoust. Soc. Am. **83**, 2277–2289.

Jensen, J., and Neff, D. (**1993**). ''Development of basic auditory discrimination in preschool children,'' Psychol. Sci. **4**, 104–107.

Kidd, G. Jr., Mason, C. R., Brantley, M. A., and Owen, G. A. (**1989**). ''Roving-level tone-in-noise detection,'' J. Acoust. Soc. Am. **86**, 1310–1317.

Kidd, G. Jr., Uchanski, R. M., Mason, C. R., and Deliwala, P. S. (**1993**). ''Discriminability of narrow-band sounds in the absence of level cues,'' J. Acoust. Soc. Am. **93**, 1028–1037.

Richards, V. (**1992**). ''The detectability of a tone added to narrow bands of equal-energy noise,'' J. Acoust. Soc. Am. **91**, 3424–3435.

Richards, V., and Nekrich, R. (**1993**). ''The incorporation of level and level-invariant cues for the detection of a tone added to noise,'' J. Acoust. Soc. Am. **94**, 2560–2574.

Ruggero, M. A. (**1992**). ''Physiology and coding of sound in the auditory nerve,'' in *The Mammalian Auditory Pathway: Neurophysiology*, edited by A. N. Popper and R. R. Fay (Springer-Verlag, New York.), Chap. 2, pp. 34–93.

Versfeld, N. J., and Houtsma, A. J. M. (**1995**). ''Discrimination of changes in the spectral shape of two-tone complexes,'' J. Acoust. Soc. Am. **98**, 807–816.

Wright, B. A., and Dai, H. (**1994**). ''Detection of unexpected tones in gated and continuous maskers,'' J. Acoust. Soc. Am. **95**, 939–948.

Effects of temporal fringes on fundamental-frequency discrimination[a)]

Christophe Micheyl
MRC Cognition and Brain Sciences Unit, 15 Chaucer Road, Cambridge CB2 2EF, England and Department of Experimental Psychology, University of Cambridge, Downing Street, Cambridge CB2 3EB, England

Robert P. Carlyon
MRC Cognition and Brain Sciences Unit, 15 Chaucer Road, Cambridge CB2 2EF, England

(Received 24 November 1997; revised 5 May 1998; accepted 6 August 1998)

It has recently been shown that the ability of listeners to encode the $F0$ of a ''target'' harmonic complex can be disrupted by another complex (the ''fringe'') presented immediately before and after it [R. P. Carlyon, J. Acoust. Soc. Am. **99**, 525–533 (1996)]. This finding has been attributed to listeners overintegrating information about the fringe's $F0$ when estimating that of the target. Here difference limens for $F0$ (DL$F0$s) for a 100-ms harmonic complex target were measured using a two-interval two-alternative forced choice (2I-2AFC) adaptive procedure, in the presence and absence of 200-ms harmonic fringes. The target $F0$s in the signal and standard intervals were geometrically placed around a nominal $F0$ of 88 or 250 Hz; the fringe $F0$, constant throughout a block, was set at either of these two frequencies. The harmonics were bandpass filtered into one of three different frequency regions: low (125–625 Hz), mid (1375–1875 Hz), or high (3900–5400 Hz). In the low and mid regions, the fringes produced a large increase in DL$F0$s when they had a similar $F0$ to the target. This effect was absent or greatly reduced when the fringes and targets either had widely different $F0$s or occupied different frequency regions, and it was not reduced by providing additional spectral cues to the transition between fringes and targets. In the high region, the fringes produced large increases in DL$F0$s whether or not their $F0$ was similar to that of the targets. It is concluded that these results reflect a process of overintegration which, in the low and mid regions, is sensitive both to the $F0$ and to the spectral region of the stimuli. It is suggested that the different results in the high region may reflect the fact that, unlike in the low or mid regions, all the components of the targets and fringes were unresolved by the peripheral auditory system. Finally, the results of all the experiments are discussed in terms of auditory streaming. [S0001-4966(98)03511-5]

PACS numbers: 43.66.Fe, 43.66.Hg, 43.66.Mk [RVS]

INTRODUCTION

Many sounds that we hear in everyday life, such as vowels or musical notes, contain components whose frequencies correspond to integer multiples of a fundamental frequency ($F0$). Such harmonic tones generally elicit a pitch sensation corresponding to the $F0$, even when there is no physical energy at that frequency; this pitch is often referred to as the ''virtual'' or ''periodicity'' pitch. The ability to fuse together frequency components based on the $F0$ and to assign them a single perceptual quality has emerged in recent years as one of the most important processes by which the auditory system sorts out acoustic sources in sound mixtures (Brokx and Nooteboom, 1982; Scheffers, 1983; Moore and Glasberg, 1986; Assmann and Summerfield, 1990; Bregman, 1990; Hartmann *et al.*, 1990; Hartmann, 1996).

The present study is one in a series investigating the mechanisms of $F0$ encoding and how this encoding may be affected by the presence of other sounds, with particular emphasis on the resolvability of the harmonics by the peripheral auditory system (Carlyon *et al.*, 1992; Carlyon, 1994a, b; Carlyon and Shackleton, 1994; Shackleton and Carlyon, 1994; Carlyon, 1995; Plack and Carlyon, 1995; Carlyon, 1996a, b). Recent results obtained in the context of these studies have indicated that the $F0$ discrimination of a ''target'' complex can be disrupted by the presentation of leading and trailing complex tones (''fringes''). Specifically, Carlyon (1996b) reported that difference limens for $F0$ (DL$F0$s) for 200-ms targets could be drastically increased in the presence of fringes consisting of 200-ms complex tones immediately preceding and following the targets, and whose $F0$ was equal to the geometric mean of the $F0$s of the two targets to be compared. After ruling out interpretations of the observed temporal interference effects based on mechanisms such as backward recognition masking or ''blanking'' (Divenyi and Hirsh, 1975; Massaro, 1975; Kelly and Watson, 1986), Carlyon (1996b) suggested that listeners included some of the information about the $F0$ of the surrounding tones in their estimate of the $F0$ of the target. This phenomenon, dubbed ''overintegration,'' can be viewed as an integration of $F0$ information over time, occurring *across*

[a)]Some of this research was presented at the 133rd meeting of the Acoustical Society of America [C. Micheyl and R. P. Carlyon, J. Acoust. Soc. Am. **101**, 3169(A) (1997)].

sounds. This ''overintegration'' of $F0$ information across successive sounds might simply represent a deleterious by-product of the normally advantageous ''integration'' of $F0$ information which occurs *within* a single sound (Hall and Peters, 1981; Plack and Carlyon, 1995; White and Plack, 1998).

Such temporal fringe effects in $F0$ discrimination appear to be of particular interest in that they demonstrate that the ability to encode the $F0$ of complex tones, which is exquisite when the tones are presented in isolation, can be severely degraded by the presence of other, temporally adjacent, complex tones. So far, only a few studies in the literature have addressed temporal interference effects in pitch perception (Ronken, 1972; Leshowitz and Cudahy, 1973; Massaro, 1975; Yost *et al.*, 1976), and in all these studies, pure tones rather than complex tones were used. Consequently, relatively little information is currently available on temporal interference effects in $F0$ discrimination.

In the present study, we set out to investigate further the conditions leading to $F0$ overintegration between successive complex tones. $F0$-discrimination thresholds for target complex tones were successively measured in the absence and in the presence of temporal fringes which, depending on the condition tested, could either have the same or a different $F0$, occupy the same or a different region, have the same or a different status with respect to peripheral harmonic resolvability, and share or not share harmonics with the target.

I. EXPERIMENT 1: INFLUENCE OF TEMPORAL FRINGES ON *F0* DISCRIMINATION AS A FUNCTION OF *F0* AND FREQUENCY REGION

A. Rationale

An important question which remains unanswered is the exact role of harmonic resolvability in the effects of temporal fringes on $F0$ discrimination. This question is tightly linked to that of the nature of the mechanism underlying the fringe effects. Available evidence on $F0$ ''integration'' suggests that this phenomenon is greatest for complex tones composed of unresolved harmonics, and is much less marked for resolved harmonics (Plack and Carlyon, 1995). Thus if overintegration were mediated by the same mechanism as integration, then it too might be greater for unresolved than for resolved harmonics. Because only unresolved harmonics were used in the study by Carlyon (1996b), experiment 1 examined the dependence of $F0$ overintegration on the resolvability of the fringes and targets.

B. Method and stimuli

In all conditions, listeners were presented with two successive harmonic complexes (''targets'') whose $F0$s differed by an amount $\Delta F0$ and were geometrically centered on a nominal $F0$ of either 88 or 250 Hz. These targets could be presented either in isolation or preceded and followed by another complex (the ''fringes'') whose $F0$ was equal to the nominal $F0$. Listeners were required to identify the interval containing the target with the higher $F0$, and received feedback after each 2I, 2AFC trial.

Both the targets and the fringes consisted of a large number of harmonics bandpass filtered into the same frequency region, which, in different conditions, could be the low, mid, or high region; these regions had passbands (corresponding to 3-dB down points) of: 125–625 Hz, 1375–1875 Hz, and 3900–5400 Hz, respectively. According to the definition of resolvability outlined by Shackleton and Carlyon (1994),[1] harmonics of an 88-Hz $F0$ are resolved in the low region but unresolved in the mid and high regions, whereas harmonics of a 250-Hz $F0$ are resolved in both the low and mid regions but unresolved in the high region. The number of harmonics generated varied with $F0$ and region but was always sufficient to ''fill'' the passband and skirts of the bandpass region down to a level of 0 dB SPL. The duration of the target was 100 ms; that of the fringes was 200 ms. All stimuli were gated with 20-ms cosine ramps, and the fringes and the target followed each other without any delay. The overall duration of the fringe-target sequence presented in each interval was thus 500 ms. The inter-interval delay was 500 ms. The level of every component falling in the passband of the filter was 45 dB SPL.

Signals were generated digitally and played out of a CED1401 plus laboratory interface (16-bit DAC) at a sampling rate of 40 kHz before being sent to an anti-aliasing filter (Kemo VBF25.01) with a cutoff frequency of 17.2 kHz (slope of 100 dB/oct). They were then bandpass filtered using a pair of cascaded filters (one high pass, one low pass Kemo VBF25.03, each with slopes of 48 dB/oct). Finally, the signals were attenuated (Wilsonics PATT or Tucker-Davis Technologies PA3) and fed into one input of a headphone amplifier. Pink noise with a cutoff frequency of 20 kHz and a spectrum level of 1 dB/Hz at 1 kHz was presented continuously, and was fed into a second input of the same amplifier. The stimuli were delivered to the listener through one earpiece of a Sennheiser HD414SL headset, and were monitored using an HP3561A spectrum analyzer. Measurements were performed in an IAC double-walled sound-attenuating booth.

C. Procedure and listeners

The difference in $F0$ ($\Delta F0$) between the two targets was adjusted using a 2I, 2AFC procedure with feedback and a two-down one-up geometric adaptive tracking rule (Levitt, 1971) to obtain a threshold. The $\Delta F0$ was divided or multiplied by a factor of 2 until the fourth turnpoint and by a factor of 1.41 after that. In each run, 16 turnpoints were measured overall. Thresholds for each run were estimated as the geometric mean of the last 12 turnpoints; six threshold estimates were measured for each condition and the final estimate corresponded to the geometric mean overall. The different $F0$ conditions were pseudorandomly mixed within blocks of runs corresponding to 2-h testing sessions.

Five listeners took part; all participated in the condition where stimuli were filtered into the mid region, but only four did so in the low and high regions. Their quiet thresholds at octave frequencies between 250 and 8000 Hz were within 15 dB of the 1969 ANSI standard. Four had prior training in psychoacoustic tasks. One was the first author; the others

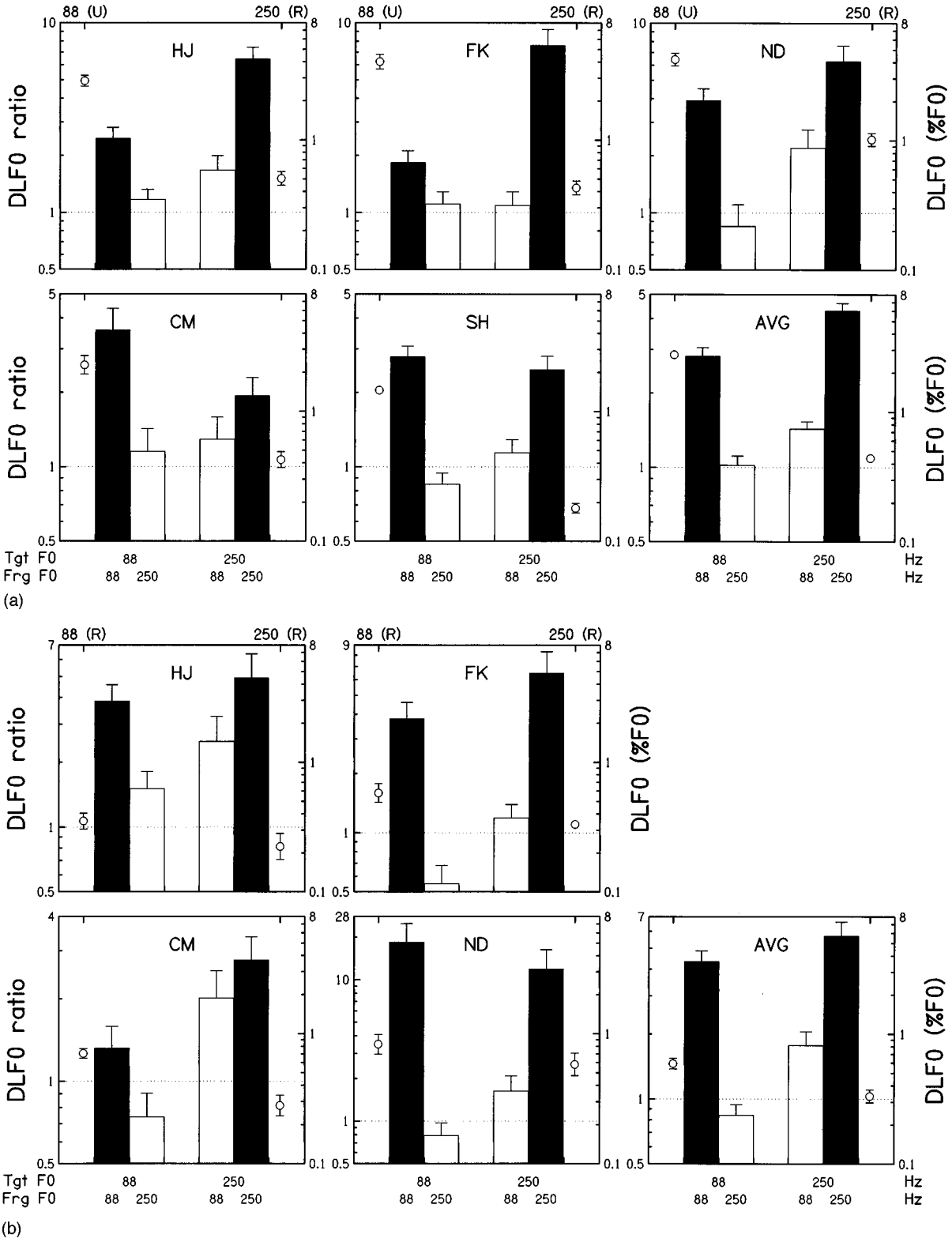

FIG. 1. (a) Hollow circles show DL$F0$s for stimuli presented in the mid region in the absence of a fringe, and are plotted with respect to the top abscissa and right-hand ordinate. Bars show DL$F0$s in the presence of a fringe divided by that with no fringe, are plotted with respect to the bottom abscissa and left-hand ordinate. The two nominal $F0$s at which the DL$F0$s for targets in isolation were measured are shown above the top abscissa, followed by a letter between parenthesis indicating the status of the harmonics: (U) for ''unresolved,'' (R) for ''resolved.'' The target and fringe $F0$s corresponding to the DL$F0$ ratios are shown below the bottom abscissa. The solid bars correspond to the conditions where the target nominal $F0$ was equal to the fringe $F0$; the empty bars correspond to the conditions where the target nominal $F0$ was different from the fringe $F0$. The left-ordinate ranges in the different panels are adjusted in order to adapt to intersubject differences. The dotted horizontal line indicates a DL$F0$ ratio of 1, corresponding to no fringe effect. DL$F0$s and DL$F0$ ratios were computed using the geometrical mean of the six thresholds estimates obtained in each condition in each listener. Error bars show the associated geometrical standard errors. For the DL$F0$ ratios (filled circles) these were calculated from the following formula: $1+\sqrt{(10^{\sigma_a/\sqrt{6}}-1)^2+(10^{\sigma_b/\sqrt{6}}-1)^2}$ where: σ_a and σ_b are the standard deviations of the six log-transformed threshold estimates obtained with and without fringes in a given listener and a given target/fringe $F0$ combination. Figures (b) and (c) are as for (a) but for stimuli in the low and high regions, respectively.

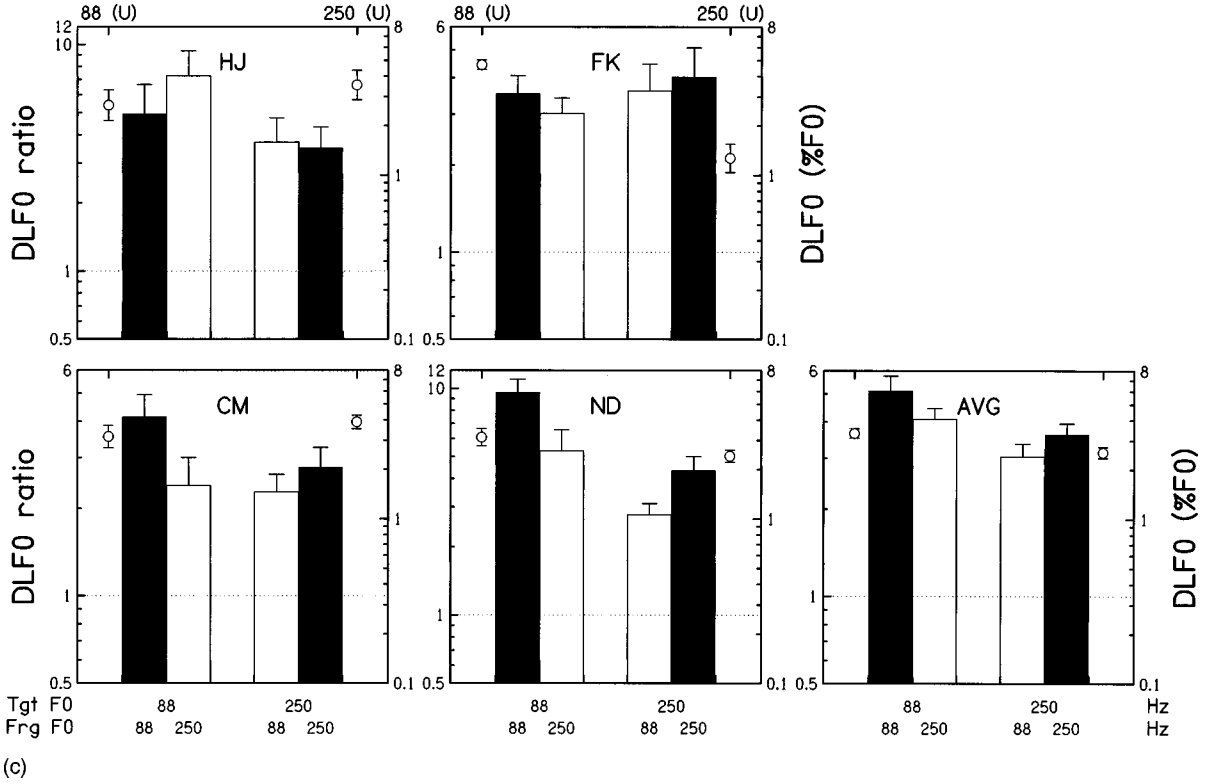

FIG. 1. (*Continued.*)

were paid an hourly wage for their services. All received training in the different conditions of the present study.

D. Statistics

Because the results of preliminary analysis of variance (ANOVAs) involving all listeners indicated significant intersubject differences, all subsequent statistical analyses were performed within, rather than across, listeners. Basically, two types of comparisons were used when analyzing the results: First, in order to test for the significance of the effects of the fringes, Student's paired *t* tests were used to compare the means of the DL*F*0s obtained with fringes to those obtained without fringes. Second, to test for the significance of differences in fringe effects across conditions involving the same target *F*0, Student's *t* tests comparing the DL*F*0s with fringes were used. Six DL*F*0 estimates were obtained in each condition, but given that there was no one-to-one correspondence between any two of the DL*F*0s to be compared and given that the analyses were carried out within listeners, independent-samples *t* tests were used. According to Bonferroni's correction, whenever several *t* tests were performed on the same set of data, the statistical significance level was divided by the number of tests performed. The *p* statistics indicated throughout the text are 2-tailed *p*'s. Prior to each test, the DL*F*0s to be compared were log-transformed.[2]

E. Results and discussion

The open circles in Fig. 1(a) show the DL*F*0s for the stimuli presented in the mid region without fringes, and are plotted with respect to the right-hand ordinate. For all listeners, DL*F*0s were higher for the 88-Hz *F*0 (circle towards left of plot) than for the 250-Hz *F*0 (circle on right). The values of around 3.0% and 0.5% for the two *F*0s compare well to those measured in previous studies, which show higher DL*F*0s for unresolved than for resolved harmonics (Hoekstra, 1979; Shackleton and Carlyon, 1994).

The bars, plotted with respect to the left-hand ordinate, show the mid-region DL*F*0s for the 88- and 250-Hz targets in the presence of a fringe, divided by the DL*F*0 for each target when presented alone. Because of intersubject differences in the size of the ratios, in this figure and in others, the scale on the left-hand ordinate differs across listeners. However, despite the intersubject variability in the size of the ratios, the pattern of results is similar across listeners in that the DL*F*0 ratios are larger when the nominal *F*0s of the target and fringe are similar (solid bars) than when they are different (open bars).

The statistical significance of the effects of the fringes on DL*F*0s was investigated by comparing the DL*F*0s measured in the presence of fringes to those measured in the absence of fringes. The detailed statistical results are provided in Table I(a). They revealed that when the fringe *F*0 was equal to the target nominal *F*0, at either 88 or 250 Hz, the DL*F*0s obtained in the presence of the fringes were larger than those measured without the fringes in all five listeners; the differences proved to be systematically highly significant. On the contrary, with the exception of one case, no significant effect of the fringes on DL*F*0s, when the fringe *F*0, was different from the nominal *F*0 of the target.

The fact that significant fringe effects were observed when the target and fringes had the same *F*0, regardless of whether this *F*0 was 88 or 250 Hz, indicates that overintegration effects can occur not only for targets consisting of

TABLE I. Comparisons between log-transformed DL$F0$s measured in the presence and in the absence of temporal fringes in the various conditions of experiment 1. The rows correspond to subjects, the columns to target-fringe $F0$ combinations. In each cell, the t value, the p value (represented by stars: *: $p<0.05$, **: $p<0.01$, ***: $p<0.005$) and the number of degrees of freedom, noninteger numbers in the cases of unequal variance, are successively indicated. Positive t values correspond to larger DL$F0$s in the presence rather than in the absence of fringes. Cells labeled ''NS'' correspond to nonsignificant differences (i.e., $p>=0.0125$). (a) Results in the mid region. (b) Results in the low region. (c) Results in the high region.

(a)	88/88			88/250			250/88			250/250		
Subject	t	p	df	t	p	df	t	p	df	t	p	df
HJ	7.04	***	10		NS			NS		13.22	***	10
CM	6.21	***	10		NS			NS		3.91	***	10
ND	9.44	***	10		NS			NS		9.63	***	10
FK	4.20	***	10		NS			NS		10.30	***	10
SH	10.64	***	10		NS			NS		7.28	***	10

(b)	88/88			88/250			250/88			250/250		
Subject	t	p	df	t	p	df	t	p	df	t	p	df
HJ	7.71	***	10		NS		3.26	**	10	6.04	***	10
CM		NS			NS		2.97	*	10	5.28	***	10
ND	9.56	***	10		NS			NS		7.58	***	10
FK	6.89	***	10		NS			NS		7.67	***	10

(c)	88/88			88/250			250/88			250/250		
Subject	t	p	df	t	p	df	t	p	df	t	p	df
HJ	5.08	***	10	7.52	***	10	5.21	***	10	5.71	***	6.54
CM	7.99	***	10	3.73	***	10	5.98	***	10	6.52	***	10
ND	16.91	***	10	7.49	***	10	8.67	***	10	10.38	***	10
FK	8.90	***	10	9.21	***	10	6.03	***	6.37	5.97	***	10

unresolved harmonics, but also when those harmonics are resolved. The absence of an effect when the $F0$s of the targets and fringes differed could, on the basis of Fig. 1(a), be due either to differences in resolvability or to differences in $F0$ *per se*. These two factors were unconfounded by the results obtained in the low and high regions, in which the fringes and the targets were always both resolved or both unresolved, respectively, whatever their $F0$.

The results in the low region for four listeners are shown in Fig. 1(b). The DL$F0$s for the targets in isolation were very small at both nominal $F0$s, and did not differ significantly. This finding is consistent with the fact that the harmonics were always resolved in this region, whatever the $F0$ (Shackleton and Carlyon, 1994). Regarding fringe effects, a pattern of results similar to that obtained in the mid region was obtained in this low region: no substantial fringe effect was obtained when the fringe $F0$ was different from the target nominal $F0$ but large fringe effects were obtained when these $F0$s were equal. In the latter condition, statistically significant differences were found between the DL$F0$s measured in the absence and in the presence of fringe at both $F0$s in three out of the four listeners; in one listener (CM), a significant effect was observed only at the 250-Hz $F0$. The detailed statistical results are shown in Table I(b).

The results obtained in the high region for each of the listeners who were tested in this region, the same four as in the low region, are illustrated in Fig. 1(c). Contrary to the pattern observed in the mid region, in the high region, the DL$F0$s obtained in absence of fringes were relatively large at both $F0$s, consistent with the fact that harmonics were always unresolved in this region. More importantly, and in contrast to the low and mid regions, substantial and significant deteriorations were produced by fringes whose $F0$s were markedly different from those of the targets, as well as for fringes and targets with similar $F0$s [as revealed by t tests whose resulting 2-tailed p's were less than the critical probability in all conditions and all listeners, as indicated in Table I(c)].

The results obtained in the various conditions of this first and main experiment can be summarized as follows: In conditions in which at least the fringe or the target contained resolved harmonics, temporal fringes increased DL$F0$s when their $F0$ was equal to the nominal $F0$ of the targets, but had no substantial effect when the fringe and target nominal $F0$s were different. In the high region, where both the fringes and the target consisted entirely of unresolved harmonics, temporal fringes had a large effect on $F0$-discrimination performances even when their $F0$ differed by about 1.5 oct from those of the targets (i.e., 88 vs 250 Hz). Possible mechanisms responsible for this pattern of results will be discussed in Sec. V, after we have described a series of experiments examining the effects of spectral similarity between the fringes and targets on the observed overintegration.

II. EXPERIMENT 2: INFLUENCE OF OFF-FREQUENCY EXTRA FRINGES

A. Rationale and method

Experiment 2 tested whether the fringe effects observed in the first experiment could be explained simply by ''con-

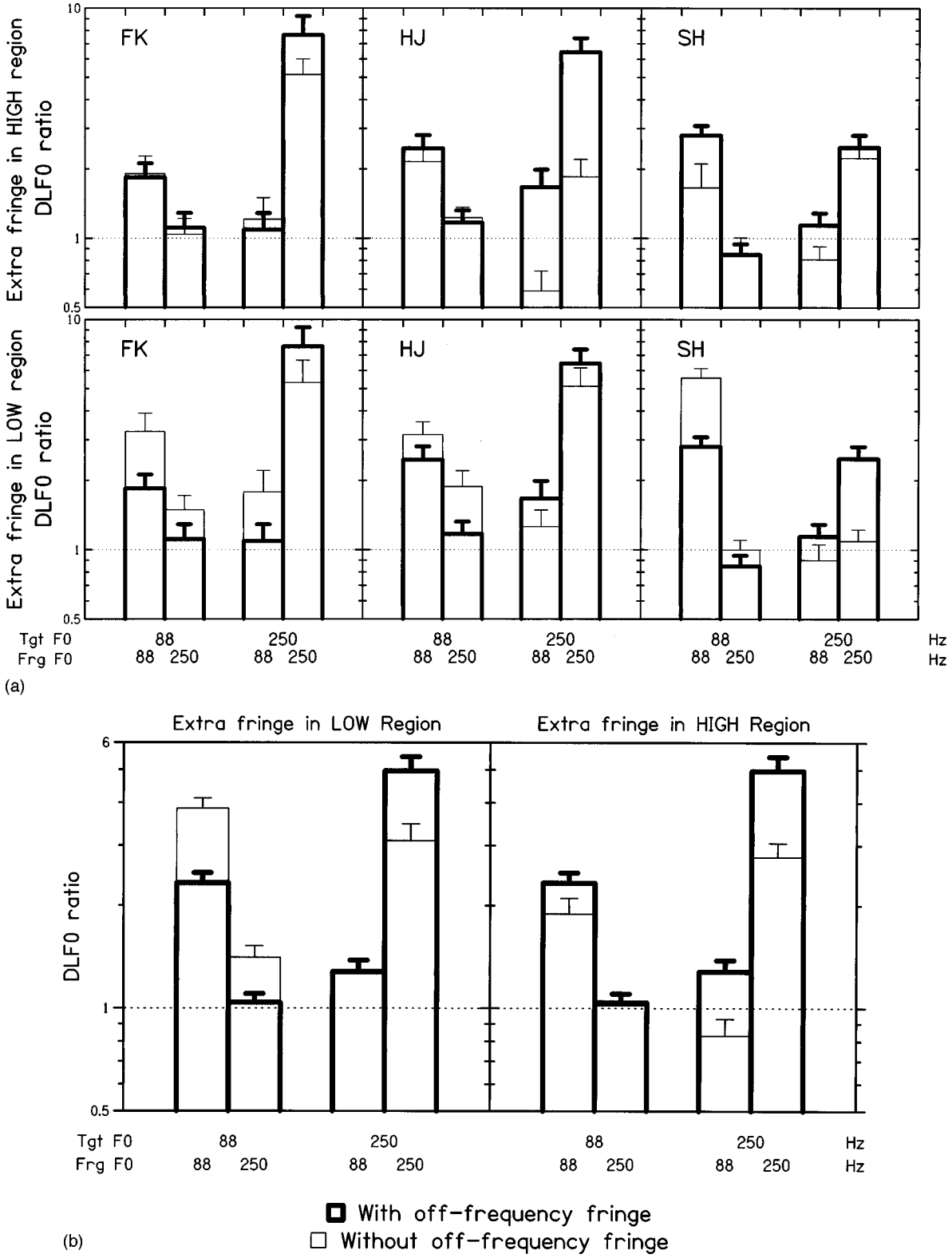

FIG. 2. (a) Thick-contour bars show DL*F*0 ratios for individual listeners for conditions with an additional off-frequency fringe in the low (bottom row) or high (top row) region. The general form of the plot is the same as in Fig. 1. The DL*F*0 ratios from experiment 1 are replotted as thin-contour bars. (b) Data from experiment 2 averaged across listeners. The error bars were calculated as for Fig. 1.

fusion'' between the fringes and the target by the listeners. Indeed, because the fringes and the target immediately succeeded each other and were filtered in the same frequency region, listeners may have experienced difficulties in determining when the fringe stopped and the target started, and vice versa (cf. Neff, 1985). This may have been the case particularly when there were few spectral cues to the transitions between the fringes and the target, as would have occurred in the mid and low conditions when the fringes and targets had similar *F*0s, and in the high region even when

TABLE II. Comparisons between log-transformed DL$F0$s measured in the presence and in the absence of temporal fringes in the various conditions of experiment 2. The rows correspond to subjects, the columns to target-fringe $F0$ combinations. In each cell, the t value, the p value (represented by stars: *: $p<0.05$, **: $p<0.01$, ***: $p<0.005$) and the number of degrees of freedom, noninteger numbers in the cases of unequal variance, are successively indicated. Positive t values correspond to larger DL$F0$s in the presence rather than in the absence of fringes. Cells labeled ''NS'' correspond to nonsignificant differences (i.e., $p>=0.0125$). (a) Extra off-frequency fringe in the low region. (b) Extra off-frequency fringe in the high region.

(a)	88/88			88/250			250/88			250/250		
Subject	t	p	df	t	p	df	t	p	df	t	p	df
HJ	8.64	***	10	3.98	***	10		NS		8.87	***	10
FK	6.20	***	10		NS			NS		7.16	***	10
SH	18.10	***	5.64		NS			NS			NS	
(b)	88/88			88/250			250/88			250/250		
Subject	t	p	df	t	p	df	t	p	df	t	p	df
HJ	6.25	***	10		NS			NS		3.59	***	10
FK	3.64	***	10		NS			NS		10.21	***	10
SH		NS			NS			NS		6.97	***	10

the $F0$s were different. We reasoned that if the effects of the fringe were simply due to confusion, then they should be greatly reduced by the presence of a supplementary timing cue in a neighboring spectral region. Therefore in this second experiment, off-frequency portions were added to the on-frequency fringes. The target and on-frequency fringes were always presented in the mid region. The off-frequency extra fringes were presented simultaneously with the on-frequency fringes but in a different region which corresponded either to the low or to the high previously defined region. Apart from that, the methods and procedure used in this experiment were the same as those used in experiment 1. Three of the five listeners who took part in experiment 1 participated in this second experiment.

B. Results and discussion

The results of experiment 2 are shown for three listeners by the thick-contour bars in Fig. 2(a). Data with the extra fringe in the high and low regions are shown in the top and bottom rows of the figure, respectively. To facilitate comparison, the results obtained in experiment 1 (in the absence of any off-frequency fringe) are also shown as thin-contour bars. As in experiment 1, the fringes had no substantial effect when their $F0$s differed from those of the targets, and so the bulk of this section will focus on those conditions where the target and fringe $F0$s were similar.

The detailed statistical results of this experiment are shown in Table II. Generally speaking, fringes with an $F0$ equal to the nominal $F0$ of the targets still produced a significant increase in DL$F0$s relative to the case with no fringe, despite the presence of off-frequency fringes. As can be seen in the mean data, shown in Fig. 2(b), the average proportional increase in DL$F0$ produced by the fringes ranged across listeners from a factor of about 2 for an $F0$ of 88 Hz with the added high-frequency fringe, to a factor of about 4 with the added low-frequency fringe at $F0$s of either 88 or 250 Hz. Figure 2(a) and (b) also shows that additional off-frequency fringes did not systematically reduce DL$F0$s relative to the case with the on-frequency fringe alone.[3]

The fact that DL$F0$s were not systematically reduced by off-frequency extra fringes indicated that the effects observed in experiment 1 were not entirely due to confusion by the listeners between the fringes and the target because of insufficient spectral cues to differentiate the two. This outcome resembles Carlyon's (1996) finding that the combined effects of a simultaneous masker and on-frequency fringe in the high region could not be reduced by an off-frequency fringe presented in a ''low'' (20–1420 Hz) region. It extends those findings to the case where there is no simultaneous masker present, to two different baseline $F0$s, and to additional fringes both above and below the frequency region occupied by the target. The present result also shows that the added off-frequency fringes have no effect when the fringe and target nominal $F0$s differ.

III. EXPERIMENT 3: INFLUENCE OF OFF-FREQUENCY FRINGES

A. Rationale and method

Experiment 3 tested whether the off-frequency fringes, when presented alone, can produce an increase in DL$F0$s. One reason for this was simply to determine whether ''$F0$ overintegration'' requires the targets and fringes to occupy the same frequency region, as well as having similar $F0$s. Another reason was to shed further light on the absence of a consistent effect of adding such fringes to the on-frequency fringes in experiment 2. Specifically, we wished to test the explanation that the off-frequency fringes could by themselves elevate DL$F0$s, and that this effect could have outweighed any advantageous effects of them producing additional spectral cues to the transitions between fringes and targets. Experiment 3 therefore investigated whether fringes had to be present in the same region as the target in order to alter $F0$-discrimination performance. The targets were always presented in the mid region, and, in different conditions, the fringes were presented in either the low or high region. The same four combinations of target and fringe $F0$s as in the previous experiments were used. Apart from that,

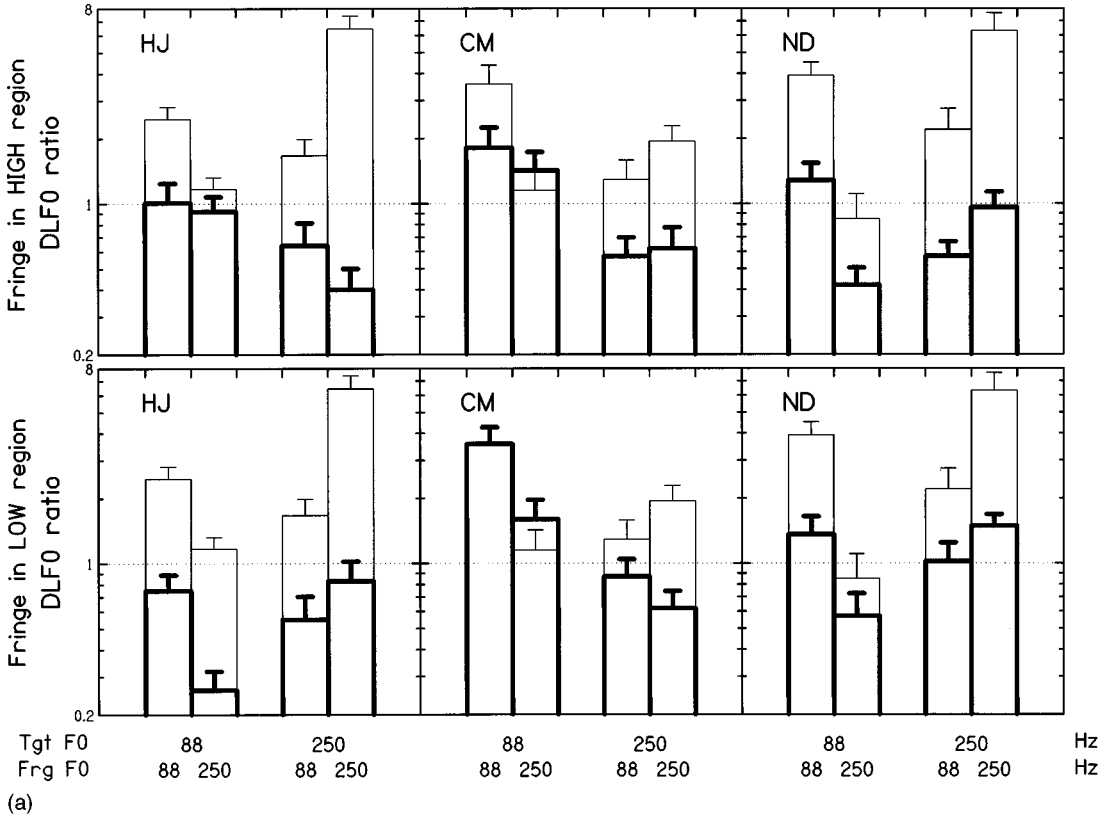

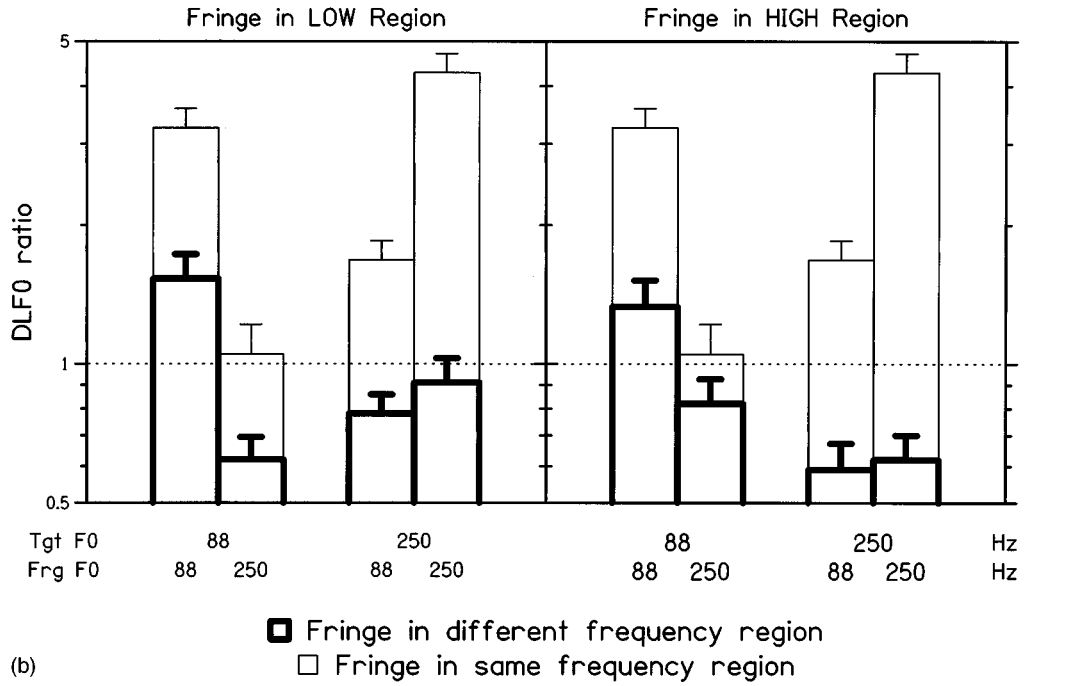

FIG. 3. Same as Fig. 2, but for the conditions with an off-frequency fringe presented without an on-frequency fringe.

the methods and procedures were the same as used in experiment 1. Three of the five listeners who took part in experiment 1 participated in this third experiment.

B. Results and discussion

The results of experiment 3, expressed in terms of DL*F*0 ratios, are shown by the thick-contour bars for each of the three listeners in Fig. 3(a), and for the mean data in Fig. 3(b). Once more, the data from experiment 1 are replotted as thin-contour bars. As can be seen, the off-frequency fringes did not in general increase DL*F*0s relative to the case with no fringe. Statistical analyses, the results of which are shown in Table III, in fact revealed four particular cases where DL*F*0s were significantly smaller with the off-frequency fringes than without them, compared to only two cases where the DL*F*0s were significantly increased by the off-frequency fringes; this effect, however, was absolutely not consistent across listeners and conditions.

TABLE III. Comparisons between log-transformed DL$F0$s measured in the presence and in the absence of temporal fringes in the various conditions of experiment 3. The rows correspond to subjects, the columns to target-fringe $F0$ combinations. In each cell, the t value, the p value (represented by stars: *: $p<0.05$, **: $p<0.01$, ***: $p<0.005$) and the number of degrees of freedom, noninteger numbers in the cases of unequal variance, are successively indicated. Positive t values correspond to larger DL$F0$s in the presence rather than in the absence of fringes; negative t values correspond to smaller DL$F0$s in the presence rather than in the absence of fringes. Cells labeled ''NS'' correspond to nonsignificant differences (i.e., $p>=0.0125$). (a) Off-frequency in the low region. (b) Off-frequency fringe in the high region.

(a)	88/88			88/250			250/88			250/250		
Subject	t	p	df	t	p	df	t	p	df	t	p	df
HJ		NS		6.63	***	10		NS			NS	
CM	7.16	***	10		NS			NS			NS	
ND		NS			NS			NS		3.17	*	10
(b)	88/88			88/250			250/88			250/250		
Subject	t	p	df	t	p	df	t	p	df	t	p	df
HJ		NS						NS		3.94	***	10
CM		NS			NS			NS			NS	
ND		NS		4.20	***	10	3.47	**	10		NS	

The overall lack of an influence of off-frequency fringes is consistent with the results of Carlyon (1996b), who found that fringes in a ''low'' region (20–1420 Hz) had no effect on the DL$F0$s for 210-Hz targets in the high region, and extends those findings to further combinations of target and fringe $F0$s, and to fringes both above and below the frequency region occupied by the targets. Altogether these results demonstrate that fringes lying in a completely different spectral region from the targets have no substantial effect on $F0$ discrimination. One possible interpretation of this result is that, at least under conditions of minimal uncertainty (Neff and Green, 1987), auditory processing can be allocated specifically and almost exclusively to a given frequency region (Mondor and Bregman, 1994).

IV. EXPERIMENT 4: INFLUENCE OF LOCAL HARMONIC COMPARISONS

A. Rationale and method

One possible interpretation of the results presented so far is that fringes impair $F0$ discrimination only when all auditory filters excited by the target components are also driven by a component of the fringe, even when the fringe contains additional, off-frequency, components remote from the target. This would be consistent with the finding in experiment 1, that fringes had their greatest effect when the fringes and targets had similar $F0$s, and/or consisted entirely of unresolved harmonics. It would also account for the finding that off-frequency fringes had little effect when presented either alone (experiment 3) or in combination with an on-frequency fringe (experiment 2). According to this view, then, the importance of the fringes and targets having similar $F0$s is simply due to the resulting local spectral differences, rather than one of $F0$ overintegration.

One means of testing for the role of local spectral similarities is to measure the effect of fringes having the same $F0$ as the target, but which consist of different harmonics of that $F0$. To do this, we took advantage in this fourth experiment of a method devised originally by Moore and Glasberg (1990b) which involves using harmonic numbers 1, 4, 5, 8, 9, 12, 13, etc. (series A) for one complex and 2, 3, 6, 7, 10, 11, etc. (series B) for the other. In one condition (NOVR-A), series A was used for the fringe and series B for the target; in the other condition (NOVR-B), the converse was true. Measurements were performed in the mid region at an $F0$ of 250 Hz. The rationale is that if fringe effects are reduced by spectral differences, then they should be smaller in this experiment than in the condition in experiment 1 in which the fringe and targets consisted of intact harmonic series with $F0$s close to 250 Hz. They should also be smaller than in the experiment 1 conditions with 88-Hz fringes and 250-Hz targets; as can be seen in Fig. 4, the excitation patterns[4] of series-A and series-B stimuli differ by more than do the 250- and 88-Hz stimuli of experiment 1.

B. Results and discussion

The data obtained in the two nonoverlapping harmonic conditions of experiment 4 are shown by the checked bars in Fig. 5, with the data obtained for the 250-Hz targets and fringes in experiment 1 shown by the solid bars. This previous condition will now be referred to as the ''overlapping'' condition to distinguish it from the two new ''nonoverlapping'' conditions. The results at statistical comparisons between the DL$F0$s obtained with and without fringes in the NOVR conditions revealed that the fringes still produced a highly significant increase in these conditions. Examination of the average data panel in Fig. 5 even indicates that, overall, the effects of temporal fringes were at least as large in the two nonoverlapping conditions as in the overlapping condition.

These results reveal that the temporal fringe effects in $F0$ discrimination are not reduced when the target and the fringes contain no common harmonics. As mentioned above and shown in Fig. 4, the differences in excitation pattern between series A and B are considerably larger than those between the 88 and 250-Hz mid-region stimuli of experiment 1. The fact that the former stimuli showed much more over-

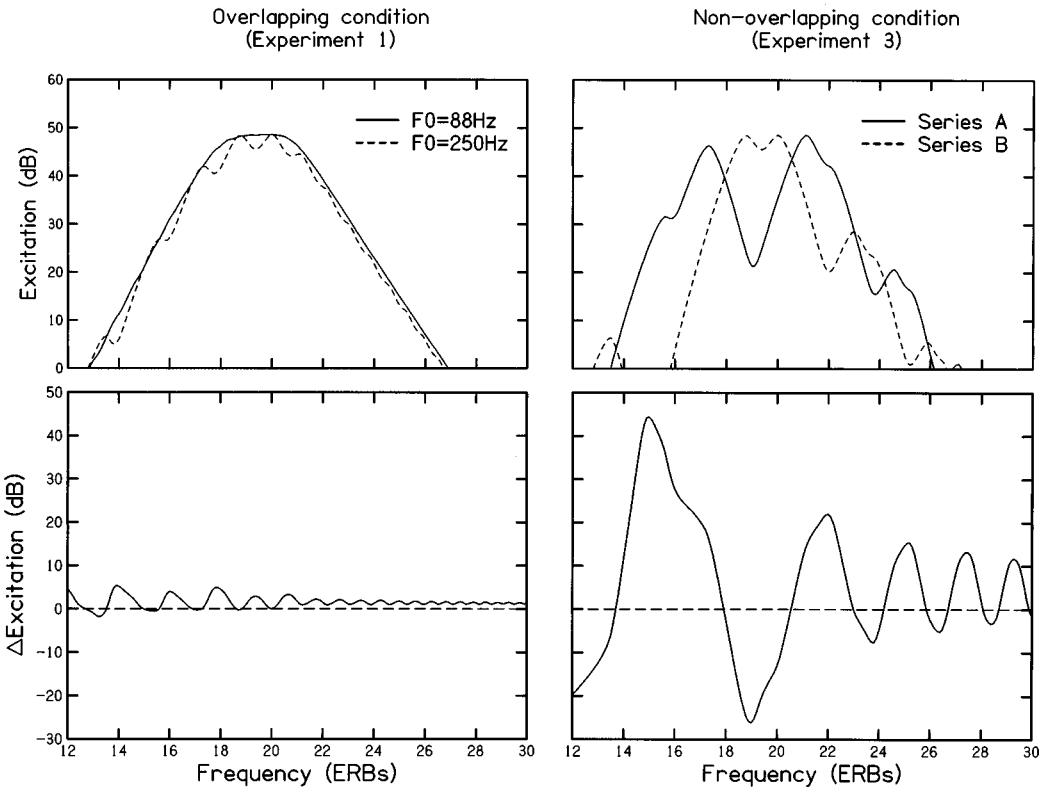

FIG. 4. Simulated excitation patterns (top) and excitation pattern differences (bottom) for the stimuli used in experiments 1 (left) and 3 (right). The abscissa indicates the frequency in ERBs. The ordinate indicates the excitation level or the difference in excitation level, in dB. The solid line in the top-left panel represents the excitation pattern of the 88-Hz-$F0$ (unresolved) harmonic complex in the mid region; the dashed line represents the excitation pattern for the 250-Hz-$F0$ (resolved) harmonic complex in the same region. The solid and dashed line in the top-right panel represent the excitation patterns of the 250-Hz-$F0$ (resolved) nonoverlapping complexes made of harmonic series A and B, respectively. The excitation-pattern differences shown at the bottom were obtained by subtracting the two excitation patterns shown at the top. See footnotes for further details on the excitation pattern calculations.

integration than the latter suggests that the effects of the temporal fringes on $F0$ discrimination proceed from a mechanism sensitive to $F0$ differences, rather than to spectral differences *per se*, between the fringes and the target.

V. GENERAL DISCUSSION

A. Summary of the results

The main results obtained in the present study are summarized in the schema in Fig. 6. A requirement for temporal fringes to exert a substantial effect on $F0$ discrimination is that they lie in the same frequency region. This factor applied independently of all other factors and was therefore placed first. Once this first requirement was met, a second requirement was that the fringe and the target had a similar $F0$. However, this proved to be the case only to the extent that at least the target or the fringes contained resolved harmonics. When both were made of unresolved harmonics, the fringes had large effects, whatever the $F0$ difference between the fringes and the target.

The results of experiment 2, indicating still significant effects of fringes containing off-frequency extra components, strongly argue for the notion that the fringe effects do not simply reflect a global spectro-temporal confusion between the target and the fringes by the listeners.

The results of experiment 4, indicating still significant effects of fringes having no common harmonics with the target, suggest that the presence of local spectral differences between the target and the fringes do not prevent fringe effects.

B. Role of resolvability in temporal fringe effects

The results of experiment 1 are consistent with those of Carlyon (1996b) in revealing detrimental effects of temporal fringes on $F0$ discrimination. The finding of substantial fringe effects for both resolved and unresolved harmonics may be related to the previous finding that, independently of resolvability, listeners are worse at detecting $F0$ differences between two successive complex tones when these tones are very close in time rather than when they are separated by a long silent interval (Plack and Carlyon, 1995). It does not confirm the prediction, inspired from the earlier observation of marked $F0$ integration effects solely for unresolved harmonics (Plack and Carlyon, 1995), that $F0$ *over* integration should also be restricted to unresolved harmonics. This suggests that $F0$ overintegration may not simply be a by-product of the (usually beneficial) integration of $F0$ information within a single sound.

There are several ways to reconcile this apparent discrepancy between the roles of resolvability in $F0$ integration and in $F0$ overintegration. The first is to assume that the observed fringe effects do not reflect an overintegration of $F0$ information at all, but are due instead to another mechanism, such as ''backward recognition masking'' (Massaro,

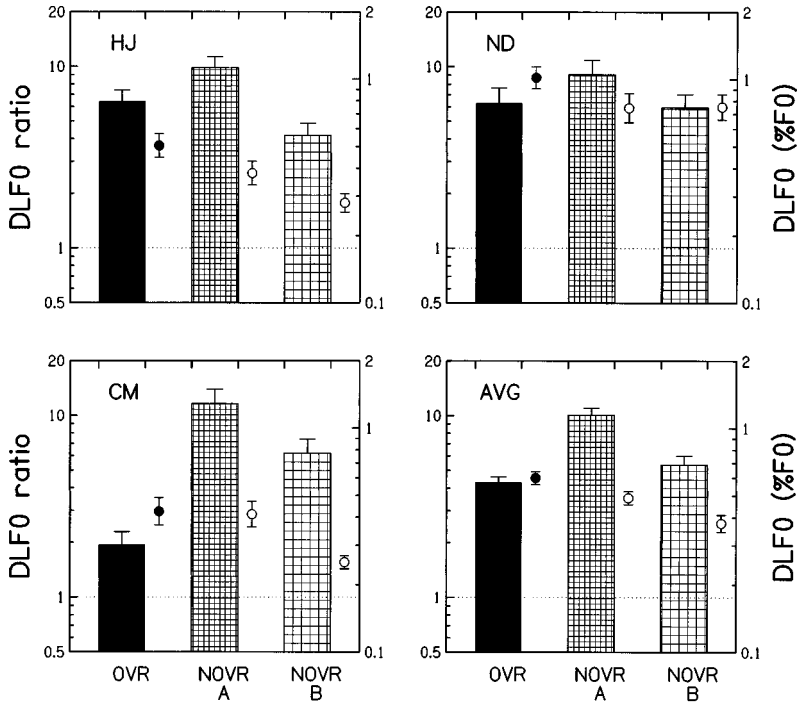

FIG. 5. Results of experiment 4. DL$F0$s (circles, top abscissa, right-hand ordinate) and DL$F0$ ratios (bars, bottom abscissa, and left-hand ordinate) are presented as in Fig. 1. Data are shown for complete harmonic series (''OVR,'' replotted from experiment 1) and for incomplete series (''NOVR'') with the target corresponding to either series A or series B. The different conditions are indicated by labels on the abscissa as well as by different symbols (OVR condition: filled circled; NOVR conditions: hollow circles) and different bar shading (OVR condition: black filling, NOVR-A condition: tight squaring, NOVR-B condition: loose squaring).

1975). However, evidence against this explanation has been reported by Carlyon (1996b), who found that the ''backward'' portion of the fringe (that occurring after the target) had a much smaller effect than the forward portion. Another interpretation of the present results is that the fringe effects do reflect $F0$ overintegration, but that this overintegration comes after the stage in $F0$ extraction at which differences (if any) exist in the processing of resolved and unresolved harmonics. This view would also be consistent with the model for pitch perception proposed by Moore (1977), in which context effects and sequential influences occur after the initial calculation of pitch. However, it does not explain the finding in experiment 1 that $F0$ differences eliminated overintegration when either the target, the fringes, or both were resolved, but not when both were unresolved. Given that experiments 2 and 4 controlled for the effects of spectral differences, this seems to point to a qualitatively different role for resolved and unresolved harmonics in $F0$ overintegration. One, admittedly *post hoc*, explanation is that the $F0$s of resolved harmonics are processed by a parallel array of $F0$-specific ''channels'' while the $F0$s of unresolved harmonics are encoded by the temporal pattern of firing within a single, separate, channel.

The present findings may also appear at first sight difficult to reconcile with an earlier observation that a complex tone masker starting before and ending after a complex tone target did not affect $F0$ discrimination when both the target and masker consisted of resolved harmonics (Carlyon, 1996a). In the present study, fringe effects were observed even when both the target and the fringes consisted of resolved harmonics. However, the comparison between the two studies is limited by the fact that in the previous study, the masker was also present simultaneously with the target. The mechanisms underlying $F0$ discrimination in such a hybrid simultaneous and nonsimultaneous masking condition may have been quite different from those involved in the present study. For instance, one cannot exclude the possibility that in the previous study, the fringe portions actually elicited overintegration effects with both resolved and unresolved harmonics, but that these effects were counteracted by listeners using the fringe to gain information about the masker, in order to more effectively segregate it from the target.

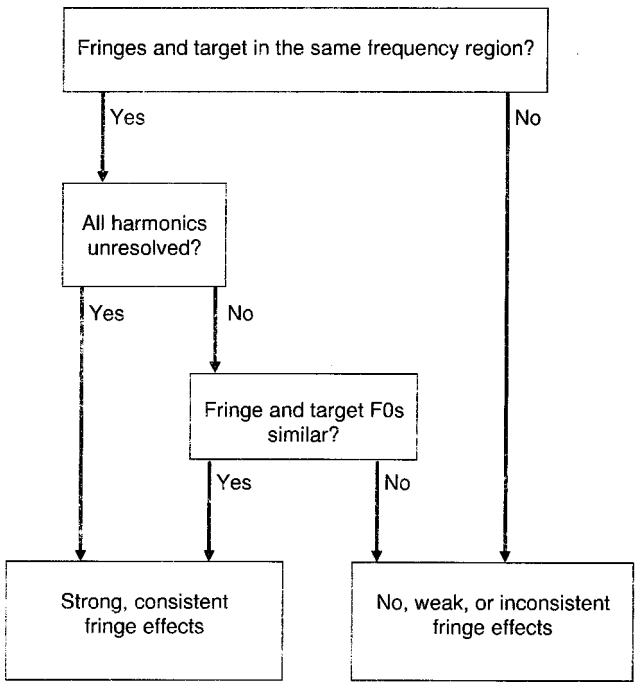

FIG. 6. Schema summarizing the stimulus conditions leading to presence or absence of fringe effects.

C. Overintegration and auditory streaming

Although auditory streaming effects were not directly addressed in the present study, it is worth mentioning the possible existence of a relationship between the observed effects of fringes on target $F0$ discrimination and streaming phenomena. There is evidence in the literature that pure or complex tones presented in a sequence iterated over time can lead to streaming effects (Bregman and Campbell, 1971; van Noorden, 1975; Bregman, 1990). In the present experiment, each run of trials consisted of a large number of presentations of the ''fringe-target-fringe'' stimulus, so that, overall, listeners were presented with a long sequence of tones. Informal reports by the listeners during the course of the experiments suggested that in some conditions they perceived each stimulus as a single sequence consisting of a target embedded between two fringes, whereas in other conditions they were able to focus on the target or on the fringes and could ''hear out'' the targets as a separate stream from the fringes. Interestingly, the conditions in which the target and fringes lay in a single auditory stream happened to be those in which the fringes had a large effect. Although listeners' ability to stream apart the fringes and the target was not measured, it is noteworthy that these conditions also corresponded to those in which, based on existing data in the literature, one might expect the targets and fringes to fall into separate streams.

For sinusoids, there is considerable evidence that the tendency to stream tones apart increases with the frequency separation between them (Miller and Heise, 1950; van Noorden, 1975). Although for such stimuli it is impossible to distinguish the effects of spectral separation from differences in pitch, there is evidence that large spectral differences can cause complex tones having the same $F0$, and therefore similar ''residue'' pitches, to stream apart (e.g., van Noorden, 1975; Bregman, 1990). This could account for the fact that off-frequency fringes had little effect in experiments 2 and 3, as they would have fallen into separate streams from the targets. What is less clear from the literature is whether $F0$ differences can influence streaming independently from the associated spectral cues: the studies which have investigated this have generally used complex tones consisting of consecutive resolved harmonics, with the result that $F0$ differences between stimuli have resulted in spectral differences (Bregman, 1990; Bregman *et al.*, 1990; van Noorden, 1975). What our results show is that, if $F0$ overintegration does depend on auditory streaming, then the streaming must in turn be affected by $F0$ differences, rather than solely by spectral differences (Singh, 1987; Singh and Bregman, 1997; Cusack, 1998). This conclusion follows from the fact that little overintegration occurs between targets and fringes having different $F0$s [e.g., 88 and 250 Hz in experiment 1, Fig. 1(a)], whereas stimuli which show a larger spectral difference but have the same $F0$ show substantial amounts of overintegration (experiment 4, Fig. 5).

ACKNOWLEDGMENTS

This work was supported by a Wellcome Trust grant. The authors would like to thank D. McFadden and F. Wightman for helpful comments on an earlier version of the manuscript. J. Lyzenga is acknowledged for helpful suggestions regarding the modification of the excitation pattern program and several other aspects of the present work. Hedwig Gockel and Rhodri Cusack are gratefully thanked for their detailed reading of the manuscript and their very helpful comments. Ian Nimmo-Smith is acknowledged for helpful suggestions on the statistics. William Hartmann is acknowledged for providing references on temporal interference effects in frequency discrimination. Brian Moore, Roy Patterson, and Lutz Wiegriebe are acknowledged for constructive comments during the course of this study.

[1]The definition of resolvability outlined by Shackleton and Carlyon (1994) includes three criteria: (1) The number of harmonics falling within the 10-dB-down bandwidth of an auditory filter (Patterson *et al.*, 1988) is always greater than three for unresolved complexes and always less than two for resolved complexes. (2) $F0$ discrimination thresholds for fairly long duration, 400 ms, complexes are invariably higher for unresolved than for resolved harmonics. (3) The pitch of unresolved harmonics is approximately doubled when they are summed in alternating phase, whereas that of resolved harmonics stays unchanged.

[2]The initial motivation for this transformation was that we were interested in the ratios rather than in the differences between the thresholds obtained in the presence and in the absence of fringes. Further justification of this procedure came from the fact that after log-transformation, the data were normally distributed, as assessed using a one-sample Kolmogorov–Smirnov's test. Finally, because the variability of DL$F0$s was found to be roughly proportional to their mean, log-transforming the data allowed us to meet the assumption of equal variance in most cases. In the rare cases in which the variance of the two samples to be compared using Student's t test was found to be significantly different, according to Levene's test, the unequal variance correction for the t, p, and df values was considered; these cases can easily be tracked in the tables detailing the statistical results due to the noninteger df values associated with them.

[3]For the conditions where the fringe and target $F0$s were similar, a significant decrease was observed in only two cases (namely: at an $F0$ of 250 Hz, for the added high fringe in listener HJ and for the added low fringe in listener SH, $p<=0.001$ and $df=10$ in both cases). On the other hand, in two other cases, significant increases were observed (at a target $F0$ of 88 Hz and with both the 88- and 250-Hz low extra off-frequency fringe: $p<0.01$, $df=6.22$ and $p<0.005$; $df=10$, respectively, in FK; at a target $F0$ of 88 Hz with the 250-Hz low extra off-frequency fringe in HJ, $p<0.01$, $df=10$; and finally, at a target $F0$ of 88 Hz with the 88-Hz low extra off-frequency fringe in SH, $p<0.001$, $df=10$).

[4]The excitation pattern simulations were performed under MATLAB following the algorithm described in Moore and Glabserg (1990a). In order to avoid discontinuities in the excitation pattern shapes, we modified the algorithm so that the preliminary estimate of the output level, a parameter that controls the slope of the filter, was computed as the output level of a simulated auditory filter having a standard slope, corresponding to a level of 51 dB in the equivalent rectangular bandwidth (ERB), rather than simply integrating over the ERB. The stimuli were generated and processed in the spectral domain. The amplitude of the frequency components was flat within the passband, corresponding to a level of 45 dB SPL, and, as in the experiment, decreased with a slope of 48/dB oct outside the passband. The stimulus spectrum contained 1000 points and had a Nyquist frequency of 10 kHz, allowing for 10-Hz-wide frequency bins. No correction for sound-system or external- and middle-ear transfer functions was applied. Filters with center frequencies between about 700 and 5600 Hz (12 and 30 ERBs) were included. The excitation patterns were normalized with respect to the maximum level of the excitation pattern obtained using the 88-Hz $F0$ complex.

Assmann, P., and Summerfield, Q. (**1990**). ''Modeling the perception of concurrent vowels: vowels with different fundamental frequencies,'' J. Acoust. Soc. Am. **88**, 680–697.

Bregman, A. S. (**1990**). *Auditory Scene Analysis* (MIT, Cambridge, MA).

Bregman, A. S., and Campbell, J. (**1971**). ''Primary auditory stream segregation and the perception of order in rapid sequences of tones,'' J. Exp. Psychol. **89**, 244–249.
Bregman, A. S., Liao, C., and Levitan, R. (**1990**). ''Auditory grouping based on fundamental frequency and formant peak frequency,'' Can. J. Psychol. **44**, 400–413.
Brokx, J. P. L., and Nooteboom, S. G. (**1982**). ''Intonation and the perceptual segregation of simultaneous voices,'' J. Phonetics **10**, 23–36.
Carlyon, R. P. (**1994a**). ''Detecting mistuning in the presence of synchronous and asynchronous interfering sounds,'' J. Acoust. Soc. Am. **95**, 2622–2630.
Carlyon, R. P. (**1994b**). ''Detecting pitch-pulse asynchronies and differences in fundamental frequency,'' J. Acoust. Soc. Am. **95**, 968–979.
Carlyon, R. P. (**1995**).
Carlyon, R. P. (**1996a**). ''Encoding the fundamental frequency of a complex tone in the presence of a spectrally overlapping masker,'' J. Acoust. Soc. Am. **99**, 517–524.
Carlyon, R. P. (**1996b**). ''Masket asynchrony impairs the fundamental-frequency discrimination of unresolved harmonics,'' J. Acoust. Soc. Am. **99**, 525–533.
Carlyon, R. P., and Shackleton, T. M. (**1994**). ''Comparing the fundamental frequencies of resolved and unresolved harmonics: Evidence for two pitch mechanisms?,'' J. Acoust. Soc. Am. **95**, 3541–3554.
Carlyon, R. P., Demany, L., and Semal, C. (**1992**). ''Detection of across-frequency differences in fundamental frequency,'' J. Acoust. Soc. Am. **91**, 279–292.
Cusack, R. (**1998**). ''The role of differences in the temporal characteristics of sounds on their sequential grouping,'' doctoral dissertation, University of Brimingham, England (unpublished).
Divenyi, P. L., and Hirsh, I. J. (**1975**). ''The effect of blanking on the identification of temporal order in three-tone sequences,'' Percept. Psychophys. **17**, 246–252.
Hall, III, J. W., and Peters, R. W. (**1981**). ''Pitch for nonsimultaneous successive harmonics in quiet and noise,'' J. Acoust. Soc. Am. **69**, 509–513.
Hartmann, W. M. (**1996**). ''Pitch, periodicity and auditory organization,'' J. Acoust. Soc. Am. **100**, 3491–3502.
Hartmann, W. M., McAdams, S., and Smith, B. K. (**1990**). ''Hearing a mistuned harmonics in an otherwise periodic complex tone,'' J. Acoust. Soc. Am. **88**, 1712–1724.
Hoekstra, A. (**1979**). ''Frequency discrimination and frequency analysis in hearing,'' Ph.D. thesis, Institute of Audiology, University Hospital, Groningen, The Netherlands.
Kelly, W. J., and Watson, C. S. (**1986**). ''Stimulus-based limitations on the discrimination between different temporal orders of tones,'' J. Acoust. Soc. Am. **79**, 1934–1938.
Leshowitz, B., and Cudahy, E. (**1973**). ''Frequency discrimination in the presence of another tone,'' J. Acoust. Soc. Am. **54**, 882–887.
Levitt, H. (**1971**). ''Transformed up-down methods in psychoacoustics,'' J. Acoust. Soc. Am. **49**, 467–477.
Massaro, D. W. (**1975**). ''Backward recognition masking,'' J. Acoust. Soc. Am. **58**, 1059–1065.
Miller, G. A., and Heise, G. A. (**1950**). ''The trill threshold,'' J. Acoust. Soc. Am. **22**, 637–638.
Mondor, T. A., and Bregman, A. S. (**1994**). ''Allocating attention to frequency regions,'' Percept. Psychophys. **56**, 268–276.
Moore, B. C. J. (**1977**). *An Introduction to the Psychology of Hearing* (Academic, New York).
Moore, B. C. J., and Glasberg, B. R. (**1986**). ''Thresholds for hearing mistuned partials as separate tones in harmonic complexes,'' J. Acoust. Soc. Am. **80**, 479–483.
Moore, B. C. J., and Glasberg, B. R. (**1990a**). ''Derivation of Auditory filter shapes from notched-noise data,'' Hearing Res. **47**, 103–138.
Moore, B. C. J., and Glasberg, B. R. (**1990b**). ''Frequency discrimination of complex tones with overlapping and nonoverlapping harmonics,'' J. Acoust. Soc. Am. **87**, 2163–2177.
Moore, B. C. J., Peters, R. W., and Glasberg, B. R. (**1986**). ''Thresholds for the detection of inharmonicity in complex tones,'' J. Acoust. Soc. Am. **77**, 1861–1867.
Neff, D. L. (**1985**). ''Stimulus parameters governing confusion effects in forward masking,'' J. Acoust. Soc. Am. **78**, 1966–1976.
Neff, D. L., and Green, D. M. (**1987**). ''Masking produced by spectral uncertainty with multicomponent maskers,'' Percept. Psychophys. **41**, 409–415.
Patterson, R. D., Nimmo-Smith, I., Holdsworth, J., and Rice, P. (**1988**). Spiral Vos Final Report, part A: The Auditory Filterbank, Applied psychology unit, Cambridge, England.
Plack, C. J., and Carlyon, R. P. (**1995**). ''Differences in frequency modulation detection and fundamental frequency discrimination between complex tones consisting of resolved and unresolved harmonics,'' J. Acoust. Soc. Am. **98**, 1355–1364.
Ronken, D. A. (**1972**). ''Changes in frequency discrimination caused by leading and trailing tones,'' J. Acoust. Soc. Am. **51**, 1947–1950.
Shackleton, T. M., and Carlyon, R. P. (**1994**). ''The role of resolved and unresolved harmonics in pitch perception and frequency modulation discrimination,'' J. Acoust. Soc. Am. **95**, 3529–3540.
Scheffers, M. T. M. (**1983**). Sifting vowels: auditory pitch analysis and sound segregation. Doctoral dissertation, University of Groningen, The Netherlands.
Singh, P. G. (**1987**). ''Perceptual organization of complex-tones sequences: a tradeoff between pitch and timbre?,'' J. Acoust. Soc. Am. **82**, 886–899.
Singh, P. G., and Bregman, A. (**1997**). ''The influence of different timbre attributes on the perceptual segregation of complex-tone sequences,'' J. Acoust. Soc. Am. **102**, 1943–1952.
van Noorden, L. P. A. S. (**1975**). ''Temporal coherence in the perception of tone sequences,'' doctoral dissertation, Technische Hogeschool Eindhovern, Eindhoven, The Netherlands (unpublished).
White, L. J., and Plack, C. J. (**1998**). ''Temporal processing of the pitch of complex sounds,'' J. Acoust. Soc. Am. **103**, 2051–2063.
Yost, W. A., Berg, K., and Thomas, G. B. (**1976**). ''Frequency recognition in temporal interference tasks: A comparison among four psychophysical procedures,'' Percept. Psychophys. **20**, 353–359.

Sensitivity to changes in level and envelope patterns across frequency

Virginia M. Richards
Department of Psychology, University of Pennsylvania, 3815 Walnut Street, Philadelphia, Pennsylvania 19104

Jennifer J. Lentz
Department of Bioengineering, 120 Hayden Hall and Institute for Research in Cognitive Science, University of Pennsylvania, Philadelphia, Pennsylvania 19104

(Received 4 November 1997; accepted for publication 21 July 1998)

In the first experiment, two measurements were compared—sensitivity to across-frequency changes in level and sensitivity to across-frequency changes in the modulation phase of SAM tones. For the level task, multi-tone stimuli composed of 2–80 tones ranging in frequency from 200 to 5000 Hz were used. For the phase task, the same frequency range was used, and 2–80 SAM tones were tested. For the level task, observers discriminated between a multi-tone, equal-amplitude standard and one of two signals—a one-step or an up–down signal. The one-step signal had higher levels at low frequencies and lower levels at high frequencies. The up–down signal had components with levels that varied high-low–high-low. For the phase task, the standard was the sum of SAM tones with identical modulator phases across frequency. The one-step signal had a common modulator phase at low frequencies and a different common modulator phase at high frequencies. The up–down signal had modulator phases that varied lag-lead–lag-lead. The results suggest that sensitivity to across-frequency changes in level and modulation phase reflect similar initial processing stages. In a second experiment, SAM tones were used, and psychometric functions were measured for the level task, the phase task, and a condition in which changes in level and modulator phase were both present. The standard was ''flat,'' and an up–down signal was to be detected. For one observer, the data suggest that level and phase information are independently represented. For the other two observers, interactions between the two features of the stimuli are apparent. A multiple-looks model was moderately successful in accounting for the data. [S0001-4966(98)01111-4]

PACS numbers: 43.66.Fe, 43.66.Nm [JWH]

INTRODUCTION

In the current experiments, sensitivity to changes in level and modulator phase across frequency is examined as a means of probing the representation of level and envelope pattern information at the output of auditory filters, or what will be referred to as frequency channels. Two experiments are described. The first experiment provides a comparison of the frequency selectivity associated with sensitivity to changes in ''level'' and ''envelope patterns'' across frequency. Because a similar experimental design was used for the phase and level tasks, frequency selectivity for the two tasks could be directly compared. If the frequency selectivity appears similar, it is of interest to determine whether the two types of information are independently represented. The second experiment examines the degree to which information concerning level and envelope patterns across frequency interact when the change to be detected includes changes in (a) level, (b) envelope pattern, or (c) *both* level and envelope patterns.

Consider first frequency selectivity for ''level'' and ''envelope'' processing. In experiment I, a method similar to that used by Bernstein and Green (1987; see also Summers and Leek, 1994) was adopted to provide a gross estimate of frequency selectivity associated with sensitivity to differences in level across frequency (experiment Ia) and sensitivity to differences in modulator phase across frequency (experiment Ib). Bernstein and Green (1987) used a profile analysis task in which observers discriminated between a flat standard and a signal which was sinusoidally rippled, where the sinusoidal ripple was applied to the power spectrum using a logarithmic frequency axis. Their stimuli were spectrally dense, being composed of 161 tones equidistant on a logarithmic frequency axis ranging from 200 to 5000 Hz. The experimental parameter was the number of sinusoidal ripples, which ranged from 1 to 80, and the dependent variable was the threshold depth of the ripple. For small numbers of ripples, thresholds did not depend on the number of ripples. Once the number of ripples exceeded 10, however, thresholds began to rise. Presumably, the increase in threshold indicates limitations in frequency selectivity. For a rectangular filter, once a complete cycle of the sinusoidal variation passes through the filter the power at the output of the filter cannot indicate a difference between a flat standard and rippled signal.

In experiment Ia, the profile analysis or level task, the stimuli were somewhat different from those used by Bernstein and Green (1987). Figure 1 depicts the stimulus set. Two signal configurations were tested. For one configuration, observers discriminated between a flat standard stimu-

lus (left panel) and a one-step signal stimulus (center panel). The flat standard was the sum of N equal-amplitude tones spaced equidistantly on a logarithmic frequency axis and ranging in frequency from 200 to 5000 Hz. N's ranged from 2 to 80; Fig. 1 plots the spectra for an N of 8. The one-step signal was generated by increasing the level of the low-frequency components and reducing the level of the high-frequency components. For the second signal configuration, the discrimination was between a flat standard (left) and an up–down signal (right). For the up–down signal, every other component was incremented/decremented in level relative to the mean stimulus level. Although not indicated in Fig. 1, on each stimulus presentation the overall levels were randomly chosen. Level variation prevents standard/signal discriminations on the basis of a change in level of a single component.

In experiment Ib parallel measurements were obtained for a task in which differences in envelope modulation pattern across frequency were to be detected. Examples of the stimuli used for this phase task are depicted in Fig. 2. Observers discriminated between an in-phase standard (left panel) and either a one-step (center) or an up–down (right) signal. Following the terminology used for the level task, the in-phase standard will be referred to as a ''flat'' standard. For experiment Ib, the stimuli were composed of fully modulated sinusoidally amplitude modulated (SAM) tones. For the flat standard, the N SAM tones had the same modulator phase. For the one-step signal stimulus, the SAM tones with low-frequency carriers had a common modulator phase that was lagging with respect to the common modulator phase of the high-frequency carriers. The up–down signal had modulator phases that varied lag/lead for every other SAM tone.

Both Strickland *et al.* (1989) and Yost and Sheft (1989) have demonstrated that observers are sensitive to changes in SAM modulator phase for two-SAM-tone stimuli. Those studies examined sensitivity to differences in modulator phase as a function of the frequency separation between the two SAM tones. When the two SAM tones were separated by less than $\frac{1}{2}$ octave or so, increases in frequency separation led to higher thresholds. For frequency separations beyond one-half to one octave, however, increasing the frequency separation did not influence thresholds. Presumably, for large frequency separations observers depended on across-frequency comparisons of envelope phases, whereas for small frequency separations, single-channel cues were used (cf. Strickland *et al.*, 1989; Yost and Sheft, 1989). Thus as for the profile analysis task, sensitivity to differences in modulator phase can provide an estimate of frequency selectivity.

Briefly consider expected effects of frequency selectivity for the level and phase tasks used in the current experiments (Figs. 1 and 2). Recall that the frequency range of the stimuli is fixed, meaning that as more components are added the proportional spacing between components decreases. As the number of components increases beyond 2, thresholds are expected to fall as long as the components are passed by independent auditory filters. For the level task, thresholds expressed as a change in level, ΔL in dB, are expected to fall at a rate of $1/\sqrt{N}$, where N is the number of components. This result is predicted by optimal processing models (Durlach *et al.*, 1986) and has been observed empirically for N's as large as 24 or so (Green, 1992).[1] For the phase task, a similar rate of reduction is expected, provided thresholds are measured using an equal-jnd metric. In the absence of such a metric, a reasonable expectation is that thresholds would fall monotonically.

For both the level and phase tasks, the function relating threshold and N is expected to change as two or more components (tones or SAM tones for the level and phase tasks, respectively) are passed through a single auditory filter. For the level task, predictions are fairly straightforward. For the up–down signal, crowding into auditory filters effectively flattens the excitation pattern, making the discrimination between the flat standard and the up–down signal increasingly difficult, leading to higher thresholds (cf. Bernstein and Green, 1987; Summers and Leek, 1994). In contrast, for the one-step stimulus the change in level remains intact—at the output of nearly all auditory filters, levels are high at low frequencies and low at high frequencies. As a result, for the one-step signal, large N's are not expected to generate higher thresholds, although thresholds may approach a flat asymptote.[2]

For the phase task, the effects of crowding into auditory filters are more difficult to predict. For large N's, the flat standard approaches amplitude modulated noise, meaning that the coherent modulation will be somewhat preserved when passed through a bank of auditory filters. For the one-step signal, the logic is similar to that described for the level task, and it seems most likely that the thresholds would mirror those measured in the level task, provided the underlying filter bank is the same. For the up–down stimulus, however, crowding into auditory filters may have two consequences. First, a within-channel cue might be introduced. At the output of a single auditory filter the flat standard remains modulated, but the up–down signal will have a flatter envelope

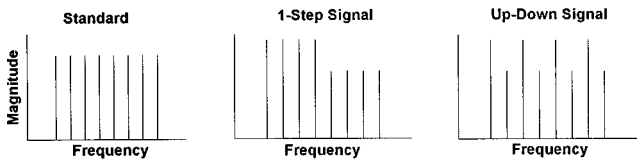

FIG. 1. Spectra for the standard (left), one-step (center), and up–down (right) stimuli are shown. The axis is logarithmic, and $N=8$.

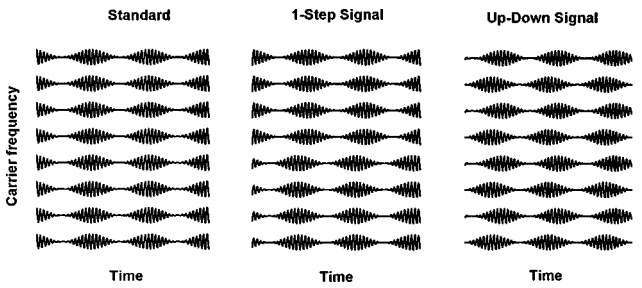

FIG. 2. The stimuli for the phase task are depicted for $N=8$. The abscissa is time, and SAM tones plotted higher in each panel have a higher carrier frequency (not shown in the figure). Three types of stimuli, the flat standard, the one-step signal, and the up–down signal, are plotted in the left, center, and right, panels, respectively.

because the opposing SAM phases tend to cancel. This would lead to lower thresholds, or perhaps thresholds will approach a flat asymptote as the frequency spacing between SAM tones is reduced. Second, due to interactions of carriers within auditory filters, more than one frequency will be present in the envelope, making it more difficult to detect the applied SAM modulation. This factor might lead to higher thresholds for some of the *N*'s tested.

Because parallel stimulus configurations were used in the level and temporal task for experiment I, it was anticipated that the results of experiments Ia and Ib would provide an evaluation of the hypothesis that the same limits in frequency selectivity drive performance in both tasks. The results of experiment I indicate that for both the level and phase task, analogous changes occurred in the function relating thresholds and *N*, suggesting that similar limitations in frequency selectivity underlies both tasks. Given that result, a second experiment was designed to examine the interactions of level and phase information in either the same, or functionally similar, frequency channels. Psychometric functions were obtained for the case that just level cues, just phase cues, or both, were present.

Based on existing data, interactions between level and phase cues were anticipated. Green and Nguyen (1988) found that when across-frequency changes in level applied to SAM tones are to be detected, differences in modulation phase across frequency reduce sensitivity relative to the case that the SAM tones are modulated with the same phase. In one of their experiments, three conditions were tested. In one condition, the standard was the sum of seven sinusoids and the signal was an increment to the level of one of the components of the standard. For the second and third conditions, seven SAM tones were used, and an increment in the level of the central SAM tone was to be detected. In the second condition, the SAM tones were modulated using a single modulator phase. For the third condition, the signal-bearing SAM tone was modulated 180 degrees out of phase relative to the other six SAM tones. They found no difference in thresholds when the SAM tones were coherently modulated and when there was no modulation (i.e., sinusoidal components). For high modulation rates, thresholds were also independent of modulation phase. At modulation rates less than 40 Hz, however, sensitivity to across-frequency differences in level was diminished when incoherent modulation was used. The magnitude of the threshold shift was largest, approximately 10 dB, for the lowest modulation rate tested, 5 Hz. At 20 Hz, the introduction of incoherent modulation led to a 2–3 dB increase in threshold. Such an interaction implies that envelope and level information are not independently represented; if independence holds, no effect of modulation phase would be expected.

Fantini and Moore (1994) also examined sensitivity to across-frequency changes in level and envelope pattern and additionally joint changes in level and envelope pattern. In their experiment, the standard was the sum of five SAM tones coherently modulated, and the signal to be detected was either a change in level, a change in modulation depth, or both, applied to the central ''target'' SAM tone. Their data indicate that the catenation of level and envelope cues led to an improvement in performance—a 5–6 dB threshold reduction when level cues were added to existing envelope cues, and a 1–3 dB improvement when envelope cues were added to existing level cues. Overall, Fantini and Moore (1994) found thresholds were 6–9 dB lower when across-frequency differences in both level and envelope pattern were introduced, as compared to thresholds obtained when the signal was added to just the target SAM tone (e.g., the four ''flanking'' SAM tones were not present, and so across-frequency comparisons were not available).

In contrast to the past work (e.g., Green and Nguyen, 1988; Fantini and Moore, 1994), in experiment II psychometric functions were measured. As a result, interactions between level and phase cues could be examined using combination models based on signal detection theory (Green and Swets, 1974; Macmillan and Creelman, 1991). Additionally, the possibility that a single decision variable underlies sensitivity to across-frequency changes in level and modulator phase is briefly considered.

I. EXPERIMENT I: SENSITIVITY TO CHANGES IN LEVEL AND ENVELOPE PHASE ACROSS FREQUENCY

A. Methods for experiment I

The stimuli were digitally generated and presented through two channels of a 16-bit DAC using a sampling rate of 20 000 samples/s, low-pass filtered at 6 kHz using matched filters (KEMO VBF 8; attenuation skirts approx. 85 dB/oct), and presented diotically by way of two channels of Sennheiser HD410SL headphones. The standard was the sum of *N* equal-amplitude tones (experiment Ia) or *N* equal-amplitude SAM tones (experiment Ib) ranging in frequency from 200 to 5000 Hz and equidistant on a logarithmic frequency scale. *N*'s of 2, 4, 8, 16, 20, 30, 40, and 80 were tested.

1. Experiment Ia

For the level task, one-step and up–down signal stimuli were generated by analog addition of two complexes, the standard and a ''signal,'' where the signal components were either in-phase or anti-phase relative to the components of the standard. The signal level is described as the signal-to-standard amplitude, in dB. The starting phases of the individual components were randomly drawn from a uniform distribution with a range of 2π rad. The mean stimulus level was 50 dB SPL/component, and on each presentation the overall level was chosen using draws from a uniform distribution with a 30-dB range and a 0.1-dB gradation. The stimulus durations were 200 ms, including 17-ms raised cosine onset/offset ramps.

A 2IFC procedure was used, with the signal interval being as likely to be in the first as the second interval. Visual feedback indicated the correctness of each response. Thresholds were estimated using a 3-down 1-up staircase procedure which estimated the 79% correct performance level (Levitt, 1971). Initial signal levels were approximately 10 dB above the ultimate threshold estimates. The initial step size was 4 dB and reduced to 2 dB following three reversals. The last

even number of reversals, excluding at least the first three, were used to estimate threshold. Each threshold estimate was generated using blocks of 50 trials.

The order of completion was not blocked: in any one session, either the one-step or up–down signal was tested, but across sessions the conditions were intermixed. Observers practiced for 10–15 h before data collection began in any one condition. At least 15 threshold estimates were obtained for each number of components tested, and the last 10 averaged to form a final estimate of threshold.

Seven observers participated in this experiment, four of whom also participated in experiment Ib. Of the four that participated in both experiments Ia and Ib, two ran experiment Ia second. For those two observers, threshold estimates were obtained only for N's of 4, 8, 16, 20, and 40. Observers had thresholds in quiet of 20 dB HL or better (for frequencies ranging from 250 to 8000 Hz; a value of 20 dB HL was measured for only one observer at 8000 Hz) and ranged in age from 19 to 21 years. Observers were paid to participate and had no prior experience in psychoacoustic tasks. Tests were conducted with the observer seated in a double-walled soundproof booth.

2. Experiment Ib

As for the level task, one-step and up–down signals were tested, with the change to be detected being a change in the relative phase of the component SAM tones. For the one-step signal, the lower-frequency SAM-tone modulator phase lagged relative to the higher-frequency modulator phase. Likewise, for the up–down signal, the pattern was lag-lead–lag-lead. Unfortunately, due to an undetected programming error, on occasion the pattern of modulation phases varied—the lead replacing lag, and *vice versa*.[3]

The SAM tones were fully modulated at a 20-Hz modulation rate. The stimuli were generated by adding two SAM complexes together. For the signal stimuli, one complex was the sum of the $N/2$ tones with phase leads, and the other the sum of the $N/2$ tones with phase lags. For the standard, all N tones shared a common modulator. The mean starting modulation phase and the phases of the carriers of each SAM tone were randomly chosen prior to each presentation from a uniform distribution with a range of 2π rad. Each SAM tone had a level of 50 dB SPL. The stimulus durations were 500 ms, including 25-ms raised cosine onset/offset ramps.

As in experiment Ia, thresholds were estimated using a 3-down, 1-up staircase procedure which estimated the 79% correct performance level (Levitt, 1971). Each threshold estimate was generated using blocks of 50 trials. The independent variable, $\Delta\phi$, is the change in modulator phase, advanced minus delayed, as a proportion of the period. The magnitude of the $\Delta\phi$ step sizes varied depending on thresholds. In most instances, the initial step size was 0.04, which was reduced to 0.02 following three reversals. When thresholds were small, values of 0.03 and 0.01 were used. The staircase algorithm was constrained so that $\Delta\phi<0$ and $\Delta\phi>0.5$ were not allowed. If values of $\Delta\phi<0$ and $\Delta\phi>0.5$ were reached, $\Delta\phi$ was forced to either 0 or 0.5, but the threshold estimate was not included. If this occurred more than three times, the step sizes/initial signal level were adjusted, and the data recollected. In almost all cases, practice trials sufficed to provide appropriate choice of step sizes. Initial signal levels were approximately four large step sizes above the ultimate threshold. Thresholds will be presented as $\log(\Delta\phi)$ to provide a scale on which small values of $\Delta\phi$ are discernible. Each threshold estimate was translated to $\log(\Delta\phi)$, and the final averaged threshold estimate and the standard errors of the mean are based on translated threshold estimates. At least 15 threshold estimates were measured for each number of components tested, and the last 10 averaged to form a final estimate of threshold.

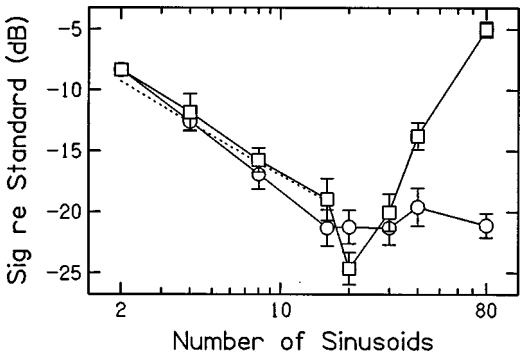

FIG. 3. Results for experiment Ia, the level task, are shown. Average thresholds are plotted as signal-re-standard amplitudes, in dB, as a function of the number of components. Circles are for the one-step signal, and squares are for the up–down signal. The results are averaged across seven observers for N's of 4, 8, 16, 20, and 40, and 5 observers for N's of 2, 30, and 80. Error bars indicate the standard errors of the mean across observers.

II. RESULTS AND DISCUSSION OF EXPERIMENT I

Figure 3 shows the results for experiment Ia, and Fig. 4 shows the results for experiment Ib. In both figures, thresholds averaged across observers are plotted as a function of the number of components, N. Circles show the results for the one-step signal and squares the results for the up–down signal. Error bars indicate the standard error of the mean across observers. There were some individual differences, largely associated with gross differences in sensitivity. One exception was for the level task: for 1 of the 7 observers, the point at which the one-step thresholds flattened out was

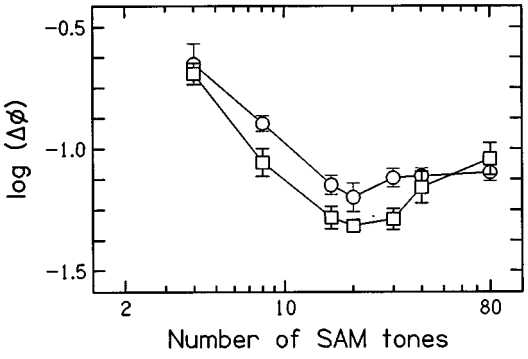

FIG. 4. Results for experiment Ib, the phase task, are shown. Average thresholds are plotted as $\log(\Delta\phi)$, where $\Delta\phi$ is the change in modulator phase across frequency for the signal stimuli, as a proportion of the period. Circles are for the one-step signal and squares are for the up–down signal. The results are averaged across four observers, and error bars indicate the standard errors of the mean across observers.

shifted somewhat toward larger N's. Nonetheless, the averaged data present the trends present for the individual observers. Keep in mind that for the level task, the stimuli were generated by adding sine tones either in-phase or anti-phase to the standard, meaning that a threshold of 0 dB indicates the presence of only $N/2$ components. For the 80-component condition (Fig. 3), threshold estimates sometimes approached this limit, which was protected by the tracking algorithm. When the track was truncated by the tracking algorithm, thresholds were re-estimated. As a result, for the level task, thresholds in the 80-component condition are somewhat underestimated.

Consider first the results of the level task, experiment Ia (Fig. 3). For small N, thresholds fall for both the one-step and the up–down signals. A dashed line drawn on Fig. 3 shows the $1/\sqrt{N}$ prediction of the Durlach *et al.* [1986, based on their Eq. (14)] channel model applied to N's ranging from 2 to 16. The predictions were generated as follows. First the data were transformed to a ΔL dB scale. Then, the parameter to be estimated, the standard deviation of the channel noise, was determined (3.2 dB for the fit shown in Fig. 3) using a least-squares procedure, and the predictions transformed back to a signal-to-standard scale. The data are reasonably well captured by the $1/\sqrt{N}$ prediction.

For N's of 16–20 or larger, thresholds for the one-step signal appear to flatten, indicating a maximum sensitivity. In contrast, for the up–down stimuli, thresholds grow with N. Presumably, the increase in threshold for the up–down signal reflects a flattening of the excitation pattern expected to occur as two or more components crowd into individual auditory filters (cf. Bernstein and Green, 1987; Summers and Leek, 1994).

For the phase task (experiment Ib, Fig. 4), thresholds could not be estimated for just two SAM tones because even 180 degree modulator phase differences did not lead to criterion levels of performance. For the one-step signal, thresholds initially fall as N increases, and then appear to approach an asymptote. This pattern of thresholds is similar to the pattern found for the level task (Fig. 3). Unlike the results for the level task, however, for moderate N's thresholds are somewhat higher for the one-step than the up–down signal. This may reflect any of a number of features of sensitivity to differences in modulator phase across frequency. For example, if sensitivity to modulator phase varies with carrier frequency, thresholds in the up–down condition might be enhanced relative to thresholds in the one-step condition simply because the one-step stimulus requires sensitivity across a wider range of frequencies (e.g., the change is not reflected in adjacent SAM tones). For N's greater than approximately 16–20, thresholds tend to increase for the up–down signal, but the rate of growth is slower than found in the level task. The reasons for this particular pattern of results are far from clear, but presumably reflect interactions of counterbalancing modulator phases and multiple carriers within single auditory filters.

In comparing the results for the level and phase tasks, two consistent results are apparent in the data. First, for the one-step signal, thresholds appear to flatten at approximately the same point. In an effort to quantify the degree of agreement, lines were fitted to the one-step data. The descending portion of the one-step thresholds was fitted using a two-parameter linear estimator, and the flat portion of the one-step thresholds was fitted using a one-parameter estimate (i.e., a slope of zero was assumed). The fitting algorithm took into account the differences in the variability for each data point (Press *et al.*, 1992). Best fits were obtained for all possible allotments of the data into ''descending'' and ''flat'' categories (e.g., thresholds for N's of 2, 4, and 8 might be categorized as descending, and thresholds for N's >8 categorized as flat, etc.). A least-squared error criterion was used to determine the best fitting lines. For the level task, the descending and flat functions intersect at an N of 15.4, and for the phase task, the functions intersect at an N of 14.5. Thus independent of the task, the one-step thresholds level off at an N of 15 or so. Second, the minima in the up–down functions occur at $N=20$, although the minimum is more pronounced for the level task than the phase task. For an N of 15, the proportional frequency spacing factor is 1.26 ($\frac{1}{3}$ of an octave) and for an N of 20, the proportional frequency spacing factor is 1.185 ($\frac{1}{4}$ of an octave).

Before turning to experiment II, a brief digression regarding frequency selectivity is warranted. There are several aspects of auditory processing that might influence the results shown in Figs. 3 and 4. First, due to the presence of a minimal amount of encoding and central noise (cf. Durlach *et al.*, 1986), the one-step thresholds might approach a flat asymptote. It seems unlikely that such a minimum would serendipitously occur at approximately the same N for the level and phase tasks, and so we tentatively suggest that the threshold floor observed in the one-step conditions does not reflect only the actions of central noise. Second, the number of filter outputs integrated into the decision process may change with N. This would lead to $1/\sqrt{N}$ performance for small N's (more filters are incorporated as more components are added), and an upper limit on the number of filters integrated would lead to the threshold floor in the one-step condition. By this account, the ''maximum'' number of filters incorporated is the same in the level and phase tasks. Third, and not independent of the second possibility, crowding of components into single auditory filters might limit the usefulness of a rich excitation pattern. Such crowding is assumed to drive the increase in threshold with increases in N for the up–down signal (Figs. 3 and 4), meaning that the common minimum obtained for the level and temporal tasks implies a common frequency selectivity.

In all, it seems there is sufficient evidence that the thresholds obtained in the level and phase tasks reflect similar limitations in frequency selectivity. As a result, it is reasonable to assume that for sufficiently small N's, the stimulus components may be treated as being independently represented. Moreover, the results of experiment I suggest that it is reasonable to examine interactions between level and phase information that occur within frequency channels, where it is assumed that ''frequency channels'' may be treated as the output of a single set of auditory filters. It should be noted, however, that even in light of the results of experiment I, the conclusion that envelope and level infor-

mation is extracted from a single frequency channel remains tenuous.

III. EXPERIMENT II: PSYCHOMETRIC FUNCTIONS FOR JOINT SENSITIVITY TO CHANGES IN LEVEL AND MODULATION PHASE ACROSS FREQUENCY

In this experiment, psychometric functions were measured for across-frequency changes in level, across-frequency changes in modulation phase, and joint changes in level and modulator phase across frequency. The stimuli are the sum of eight SAM tones with carriers ranging in frequency from 200 to 5000 Hz. An N of 8 was chosen based on the results of experiment I: For both the level and phase tasks, thresholds continue to descend for N's greater than 8, suggesting that for an N of 8, the individual components are passed by independent auditory filters.

Summation experiments, such as this experiment, have at least two benchmarks against which the data may be compared. Denoting the sensitivity for the joint level and phase task as d'_{LP}, and the sensitivity for the level and phase tasks as d'_L, and d'_P, respectively, these benchmarks are:

(A) $d'_{LP}=d'_L+d'_P$,

and

(B) $d'^2_{LP}=d'^2_L+d'^2_P$.

Additivity occurs, for example, when the components are unidimensional (cf. Macmillan and Creelman, 1991). By this interpretation, the signal strengths add, and the variance is the same regardless of the task. The Euclidean metric suggested by option B reflects an optimal combination of independent cues (cf. Green and Swets, 1974; Macmillan and Creelman, 1991). As an example, a random variable associated with cue 1 and an independent random variable associated with cue 2 would be combined so as to maximize the combined d'. If these two random variables have shared variances (e.g., are correlated), the combined d' will fall short of the Euclidean prediction. At the extreme, when the two random variables have completely correlated variances, the d' for the combined cue will be equal to the maximum of the individual d' values. The other region, combined d' values greater than those predicted by the Euclidean metric, but smaller than additivity, is considered below.

Based on the results of Green and Nguyen (1988) there is every reason to expect that the Euclidean prediction $d'^2_{LP}=d'^2_L+d'^2_P$ will not accurately describe the combined d' value. Recall that their results indicate that differences in the modulator phase of the signal component relative to the nonsignal components interfere with the detection of changes in level. If level and phase aspects of the stimuli are independently represented, one might expect that observers could draw on differences in level without any interfering effect of differences in phase. Faced with the obtained interaction, Green and Nguyen (1988) favored the following explanations. At high modulator frequencies, they assumed that filtering of sidebands and interactions of unrelated sidebands led to an effective removal of the modulation pattern (see also Dai and Green, 1991). As a result, no effect of modulation and no effect of modulation phase would be expected. For low modulation rates, they suggested that ''the nonsignal components provide little basis for a simultaneous comparison of signal and nonsignal levels; the nonsignal components are nearly absent when the signal component is in the vicinity of a maximum, and the reverse.'' An alternative explanation is that differences in modulation phase cause the signal SAM tone to be grouped separately from the nonsignal SAM tones, leading to a less efficient comparison of levels[4] (Dai, 1996).

TABLE I. Signal levels for the level and phase task, expressed as ΔL and $\log(\Delta\phi)$, respectively. ΔL is in dB, and $\Delta\phi$ is the change in modulator phase, advanced minus delayed, as a proportion of the period.

	Level task					Phase task				
Obs 1	1.4	1.6	1.8	2.0	2.2	−1.4	−1.3	−1.2	−1.1	−1.0
Obs 2	0.4	0.6	0.8	1.0	1.2	−1.5	−1.4	−1.3	−1.2	−1.1
Obs 3	1.2	1.4	1.6	1.8	2.0	−1.5	−1.4	−1.3	−1.2	−1.1

IV. METHODS FOR EXPERIMENT II

In the primary experiment, three conditions were tested: a level task, a phase task, and a task in which the signal led to differences in both level and phase across frequency. The standard was the sum of eight equal-amplitude SAM tones, fully and coherently modulated. Note that the standard was the same regardless of which of the three conditions was tested. For the level and phase tasks, an up–down signal was used. Compared to experiment I, the primary difference was that for the level task, the change in level was applied to SAM tones. For the joint task, the components which had modulator phase lags also had lower levels, and the components with modulator phase leads had higher levels.

A 2IFC procedure was used, with the signal being as likely to be in the first as the second interval. Psychometric functions are based on five signal levels. For the level task the signal strength is specified in terms of ΔL in dB, where ΔL is either positive or negative, depending on whether the level of a component is incremented or decremented relative to the mean level. For the phase task, the signal strength is specified as $\log(\Delta\phi)$, where $\Delta\phi$ is the difference in phase as a proportion of the period, between adjacent signal SAM tones. The signal levels ultimately used were chosen based on practice data, with the intent that percent correct values would range from 60% to 80% for the level and phase tasks. For the joint task, the same signal strengths were tested as when the level and phase cues were presented in isolation. Of the possible combinations only five were tested: the highest signal level for the phase task was combined with the highest signal level for the level task, etc. Thus for each psychometric function, five signal levels were tested. The signal levels tested are indicated in Table I.

Psychometric functions were measured using two distinct methods. For the first method, all 15 types of trials (5 signal levels, 3 types of tasks) were tested in parallel. In 75-trial blocks, each of the 15 trial types was presented 5 times. A total of 200 trials was collected for each data point. This was the first portion of the experiment finished, and observers practiced 9–14 h prior to data collection. Observer

TABLE II. Signal levels for the level and phase task in the auxiliary experiment, expressed as ΔL and $\log(\Delta\phi)$, respectively. ΔL is in dB, and $\Delta\phi$ is the change in modulator phase, advanced minus delayed, as a proportion of the period. The nonzero static phase and level differences are also shown.

	Static $\log(\Delta\phi)$	Level task					Static ΔL	Phase task				
Obs 1	−1	1.6	2.0	2.4	2.8	3.2	3.6	−1.4	−1.3	−1.2	−1.1	−1.0
Obs 2	−1	0.8	1.0	1.2	1.4	1.6	1.4	−1.5	−1.4	−1.3	−1.2	−1.1
Obs 3	−1	0.6	1.0	1.4	1.8	2.2	2.2	−1.5	−1.4	−1.3	−1.2	−1.1

3, who had considerable difficulty in learning the task and sizable long-term practice effects, repeated this portion of the experiment after finishing the other conditions. Spot checks did not reveal sizable practice effects in the other conditions, but modest practice effects may be present in her data. Observer 3's most recent data are reported.

For the second method, the psychometric functions were obtained one at a time. A total of 100 trials were collected for each data point. For observers 1 and 2, an analysis of variance demonstrated no difference in d' values measured using the mixed and blocked methods. For observer 3, a significant difference was obtained $[F(1,3)=15,\ p<0.05]$. Observer 3's d' values were somewhat higher in the mixed than blocked condition, possibly due to the long-term practice effects mentioned above. Across the three observers, we did not note consistent differences in the pattern of results for the mixed and blocked methods, and so the data from the two conditions were averaged. As a result, the d' values reported below are based on a total of 6 sets of 50 trials: 4 sets of 50 trials in the mixed condition and 2 sets of 50 trials in the blocked condition.

In order to determine whether differences in phase or level influenced sensitivity even when the differences are static, or uninformative, an auxiliary experiment was completed. First consider the level task. For one of the psychometric functions the SAM tones were coherently modulated (similar to the function measured in the primary experiment). For the second psychometric function, the SAM tones varied lag-lead–lag-lead. For all three observers, the static $\log(\Delta\phi)$ value was set at −1.0. Next, consider the phase task. For one psychometric function, the SAM tones were of equal level, as was the case in the primary experiment. For the second psychometric function, the SAM tones had levels that varied low-high–low-high. The magnitude of the static ΔL's was different for the different observers. Table II shows the static values, along with the signal levels tested.

The stimulus generation and presentation method followed that described for experiment Ib, with the following exceptions. The change in level of the ''low'' and ''high'' SAM tones was achieved using programmable attenuators; the stimuli were presented via two channels of a 16-bit DAC using a sampling rate of 50 000 samples/s and low-pass filtered at 10 kHz using matched filters (TDT FT 6-2, attenuation skirts of approximately 300 dB/oct, with a 60-dB stopband attenuation). The mean signal level was 50 dB SPL/component, and on each presentation the overall level was chosen using draws from a uniform distribution with a 30-dB range and a 0.1-dB gradation. The stimulus durations were 500 ms, including 20-ms raised cosine onset/offset ramps.

Three observers participated, and although these observers did not participate in experiment I, they will be referred to as observers 1–3. Observers' hearing was tested and found to be within 15 dB HL for frequencies ranging from 250 to 8000 Hz. The participants, whose ages ranged from 18 to 21 years, had not previously participated in psychoacoustic experiments. One observer, whose results are not shown, was excused from the experiment as she was unable to perform at a level above 75% correct or so after 10 h of practice. Tests were conducted with the observer seated in a double-walled soundproof booth.

V. RESULTS OF EXPERIMENT II

Figure 5 shows the results for the primary experiment. For each observer, squares show the d'_L values for the level task, circles show d'_P for the phase task, and filled triangles

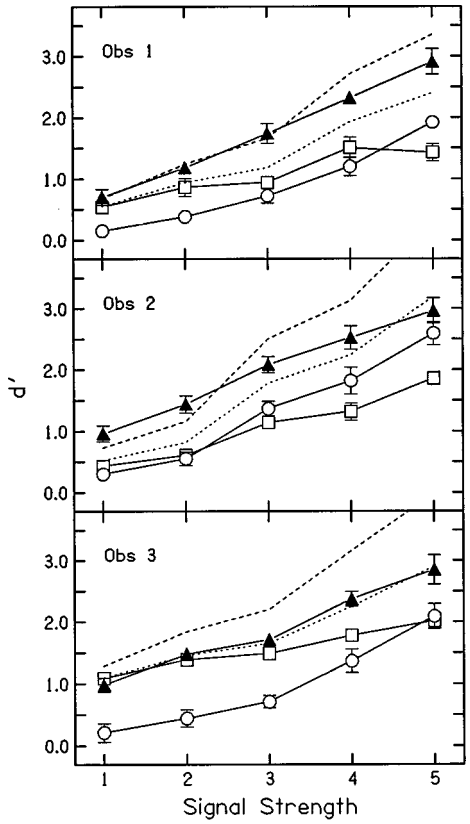

FIG. 5. *D*-prime values are plotted for the level task (squares), the phase task (circles), and the joint task (solid triangles). Error bars show the standard errors of the mean across replicate estimates. Predictions $d'_{LP}=d'_L+d'_P$ and $d'^2_{LP}=d'^2_L+d'^2_P$ are shown using darker and lighter dashed lines, respectively.

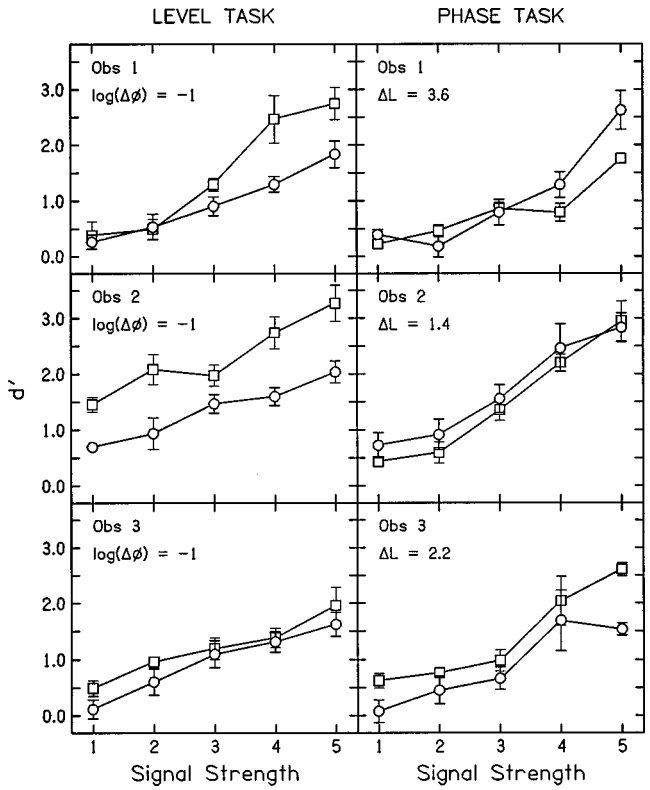

FIG. 6. *D*-prime values are shown for the level (left) and phase (right) tasks. For the level task, the modulation phases of the SAM tones were either in-phase across frequency (squares) or had different, but fixed, modulator phases across frequency (circles). For the phase task, the SAM tones were either equal level across frequency (squares), or had levels that were different, but fixed, across frequency (circles). Error bars show the standard errors of the mean across five replicate estimates.

show the d'_{LP} for the joint condition. Error bars show the standard error of the mean across 6 estimates of d', each estimate being based on 50 trials. The lighter dashed line shows the predictions for the joint condition using $d'^2_{LP} = d'^2_L + d'^2_P$, and the darker dashed line shows the prediction using $d'_{LP} = d'_L + d'_P$. It should be kept in mind that the axis, ''signal strength,'' is somewhat arbitrary, indicating signal levels chosen by the experimenters. Thus differences in the slopes of the level and phase functions, and the relative magnitudes of the d' values reflect the experimenter's talent at choosing appropriate signal levels.

Of particular interest are the d' values for the joint condition compared to the Euclidean and sum-of-d' predictions. In this regard, the individual differences are striking, and those differences were consistent whether d' values were measured using a mixed or a blocked data collection method. For observer 3, the Euclidean prediction fits the data well. For observers 1 and 2, however, d' values in the joint condition are better described as sum-of-d' values for low signal strengths, and intermediate between the sum-of-d' and Euclidean predictions at higher signal strengths (except for the data of observer 2 which at the highest signal strength fall just below the Euclidean prediction).

Figure 6 shows the results of the auxiliary experiment. *D*-prime values are plotted as a function of signal strength for the level (left) and phase (right) tasks. The squares show the results obtained for the level task when the SAM tones were modulated in-phase (left panel) and results for the phase task when the SAM tones were of equal level (right panel). Circles show the effects of a static difference in across-frequency modulation phase in the level task (left panel) and static level differences in the phase tasks (right panel). The magnitude of the static phase [$\log(\Delta\phi)$] and level (ΔL; the change in level, up minus down, is $2\Delta L$) differences are indicated in the upper left corner. Error bars show the standard errors of the mean across 5 sets of d' estimates, each estimate being based on 20 trials.

For observers 1 and 2, clear effects of phase on the sensitivity to changes in level are apparent (left panels). For observer 3, the data are equivocal. This result is consistent with the data plotted in Fig. 5: only observer 3's data are consistent with the hypothesis that level and modulator phase information are independently represented. Such independence might suggest that a fixed modulator phase pattern would not influence sensitivity to differences in level across frequency.

The opposite pattern is not apparent in the results; there does not seem to be a consistent effect of static differences in level when the change to be detected is a change in modulation phase across frequency. The absence of an effect is unlikely to reflect weak perceptual consequences of the static change in level. Examining the psychometric functions for changes in just level and just phase of modulation (Fig. 5), for observer 1 the static level difference applied to the phase task led to a larger d' value than the static modulator phase difference applied to the level task. For the other two observers, the pattern is the opposite. Overall, the individual differences apparent in Fig. 6 do not appear to be tightly linked to differential sensitivities to the static phase/level changes shown in Fig. 5.

VI. DISCUSSION OF EXPERIMENT II

The results of the primary portion of experiment II (Fig. 5) indicate d'_{LP} values midway between the sum of d' and Euclidean predictions for observers 1 and 2, and conform to the Euclidean prediction for observer 3. When thresholds exceed the Euclidean prediction, it might indicate that the single-cue psychometric functions do not reflect optimal processing. Consider, for example, an explanation in which level and envelope ''cues'' are processed linearly, but not optimally[5] (cf. Buell and Hafter, 1991; Heller, 1992). This explanation depends on the observation that whether level, phase, or both cues are present, there is always a pattern of level across frequency and always envelopes at different frequencies. When just level or just phase cues are varied, the other feature is not absent, simply uninformative. It is possible that observers fail to adjust their weights appropriately and cannot help but incorporate these aspects of the stimuli. Consider the case in which the level and phase representations have independent variances. For joint changes in level and phase,

$$d'_{LP} = \frac{(\alpha\Delta_L + \beta\Delta_P)}{\sqrt{(\alpha^2\sigma_L^2 + \beta^2\sigma_P^2)}}, \tag{1}$$

where Δ_L and Δ_P are the mean level and phase changes, σ_L^2 and σ_P^2 are the variances associated with the representations of the level and phase cues, and α and β are the associated weights.

Next, consider the case that the mean difference in either phase or level across frequency is zero:

$$d'_L = \frac{(\alpha\Delta_L + \beta 0)}{\sqrt{(\alpha^2\sigma_L^2 + \beta^2\sigma_P^2)}}, \tag{2}$$

$$d'_P = \frac{(\alpha 0 + \beta\Delta_P)}{\sqrt{(\alpha^2\sigma_L^2 + \beta^2\sigma_P^2)}}. \tag{3}$$

For an optimal decision process, β will be zero when only level cues are present (d'_L) and α will be zero when only phase cues are present (d'_P). Because independence of variances is assumed in Eqs. (1)–(3), such optimal weighting leads to the Euclidean prediction. However, if the observer continues to incorporate the level and phase information, using the same α's and β's in Eqs. (1)–(3), the d' values add; Eqs. (2) and (3) sum to form Eq. (1). Thus additivity of d' values might imply the nonoptimal integration of independent cues.

Next, imagine that observers use optimal weights when both cues are present, but fall short of optimal when only one cue is informative (e.g., the α and β do not fall to zero). Depending on the values of α and β, this scheme will lead to d'_{LP} somewhere between additivity of d' prediction and the Euclidean prediction. In short, the data presented in Fig. 5 may reflect the nonoptimal integration of level and phase information. This possibility rests on the suggestion that there is always a representation of level and envelope patterns across frequency, regardless of whether those features carry information regarding the presence of the signal. Unfortunately, the data of the current experiment do not allow clearcut estimates of the weights for the various conditions and signal levels tested.

A. Consideration of Green and Nguyen's (1988) multiple-looks model

Approaching the results of experiment II at a different level of analysis, it is of interest to evaluate the possibility that sensitivity in both the level and phase tasks depends on a single decision rule. Here, one possible formalization of Green and Nguyen's (1988) multiple-looks model is considered. The model used d' scores based on just two envelopes (channels)—it was assumed that due to the redundant nature of the stimuli across frequency, a d' value based on all eight ''independent'' channels would be proportional to the d' value based on just two channels (e.g., increases from two to eight channels would lead to a doubling of d').

Green and Nguyen suggest that in profile analysis tasks, observers depend on multiple short-term comparisons of level across frequency. In our initial formalization of that idea, the SAM envelopes were averaged using a sequential boxcar averager which led to a limited number of time samples, and the level in dB for the resulting time samples was computed. For the level task, the starting phase of the SAM modulator relative to the starting point of the boxcar averager did not influence the results. For the phase task, however, when window durations of 3 ms or longer were used effects of starting phase were apparent. Thus, when necessary, the starting modulator phase that led to the largest proportion of variance accounted for was chosen, and the results for that particular phase are described.

It was assumed that the sole variance in the task is a zero-mean Gaussian encoding noise added to each time sample, where the deviates were independent and identically distributed across frequency and time. Then a difference vector was generated, and using optimal weights [which are proportional to the difference vector, where the constant of proportionality is the inverse of the (constant) variance of the encoding noise] a decision variable was formed by summing the weighted difference vector. One advantage of this model is that it predicts no difference in d' values for a profile analysis task in which the elements are tones versus SAM tones modulated in phase, and the model produces interference effects when the signal and nonsignal components have different modulation phases and changes in level are to be detected (a result reported by Green and Nguyen, 1988; Fig. 6 for observers 1 and 2).

By construction, this model produces the Euclidean prediction for the joint task. Thus the predictions for this single-variable model are the same as the predictions for the case that independent ''cues'' are optimally combined to form a decision. When nonoptimal weights (e.g., averaging of the absolute value of the difference vector) were used, joint d' values remained near the Euclidean prediction.

The major result is that when the magnitude of the Gaussian deviate is adjusted to provide a good fit to the level data, d' values in the phase condition are vastly overestimated. That is, the model failed to simultaneously fit the level and phase data shown in Fig. 5. The degree of the model's failure can be described in terms of the magnitude of the standard deviation of the Gaussian deviate required to fit only the level data or only the phase data. In general, the shorter the boxcar averager, the larger the mismatch. For example, for a boxcar averager that extended across 1/64th of the SAM tone period (a 0.78-ms window duration), the standard deviation of the encoding noise required to fit the level data was approximately 5–7.5 (depending on observer) times smaller than the standard deviation required to fit the phase data. When the boxcar averager included $\frac{1}{4}$ of the SAM tone period (a 12.5-ms window duration), the largest boxcar averager considered, the ratio of standard deviations ranged from 2.5 to 3.5. This difference in ratios reflects the fact that for the level task, halving the boxcar duration (doubling the number of samples) led to a doubling of the estimated variance whereas for the phase task the rate of growth was more rapid.

When considering just the level data, the model accounted for approximately 97% and 92% of the variance in observers 2 and 3 data, respectively, but for observer 1 only 66% of the variance was accounted for. Considering just the phase data, the success of the predictions depended on window duration, with longer durations generally leading to better fits. For a window duration of 12.5 ms (the longest studied in detail), the model accounted for 73%, 79%, and 74% of the variance for observers 1–3, respectively. For all ob-

servers, the model consistently underpredicted the slope of the psychometric function. That is, the data could not be fitted using a single encoding noise applied to both the phase and level data, but the data were fitted reasonably well when the level and phase data were separately fitted.

The initial model explorations described above suggested that low-pass filtering of the envelope (i.e., using longer-duration boxcar windows) led to better fits to the phase data. Additionally, longer windows led to estimates of encoding noise variance that were more similar for the phase and level tasks. Presumably, when boxcar averages are used, the low-pass filtering associated with longer window durations generates better fits to the phase data because the filtering acts to reduce the modulation depth, thereby reducing the magnitude, as a difference in level, of the change in phase. However, simple boxcar averaging runs into difficulties when long-duration windows are used because the starting point of the integration window compared to the starting phase of the modulator envelope becomes a factor in the quality of the fit. For that reason, we examined the effects of lowpass filtering the SAM envelope using an RC low-pass filter.[6] The filter output was averaged using relatively short-duration boxcar windows (0.78–3.125 ms) so that the sampling strategy did not introduce additional lowpass filtering.

Low-pass filtering did not influence the predictions for the level task: the percent of variance accounted for and the magnitude of the encoding noise did not depend on the filter's cutoff frequency. For the phase data, however, low-pass filtering provided more stable results than when relatively long-duration boxcar averagers were used. For example, the starting modulator phase no longer had an influenced on the results. Also, doubling the number of samples led to estimates of encoding variance that also doubled, which is consistent with linear multiple-looks models.

For the phase data, reducing the cutoff frequency of the RC filter led to higher percent of the variance accounted for and smaller encoding-noise variances. As a result, a cutoff frequency could be found such that the variance of the encoding noise was the same for the phase and level tasks. For observers 1–3, the resulting cutoff frequencies were approximately 15 Hz, 11 Hz, and 9 Hz, respectively. The associated percent of variance accounted for in the phase task was 62%, 75%, and 69%. Again, the predicted psychometric functions were shallower than the empirical data. Lower cutoff frequencies led to slightly higher percent of variance accounted for, but the improvement was modest. It should be noted that the percent of variance accounted for using the lowpass filter (62%, 75%, and 69%) are somewhat smaller than those measured using just a boxcar averager with a large window (73%, 79%, and 74%, listed above). However, it should be remembered that when a long-duration boxcar was used, the percent of variance accounted for depended on the starting modulator phase. The values of (73, 79, 74) percent of the variance accounted for are for the ''best'' starting phase; the values measured using the low-pass filter are within the range measured when the boxcar averager was tested using different starting phases.

To summarize the modeling results, by low-pass filtering the modulation envelopes one may achieve a multiple-looks sampling strategy for which sensitivity to changes in level and changes in phase may be accounted for using a single encoding noise and a single decision rule. By construction, this model predicts Euclidean additivity of d' values, and so is an appropriate descriptor only for observer 3. A low-pass filter is required because sensitivity exhibited by the observers is poorer than would be expected for this model if the 20-Hz SAM tone modulator were represented accurately. By filtering the envelope, the modulation depth is reduced, which in turn reduces the change in level across frequency that is associated with changes in modulator phase across frequency.

In summary, for observer 3, the results of experiment II are consistent with a model in which across-frequency differences in level and modulator phase are processed independently. First, for her, fixed differences in phase did not influence sensitivity in the level task, and fixed differences in level did not influence sensitivity in the phase task. Second, when both level and phase information were present, the Euclidean prediction held. For observers 1 and 2, however, a different conclusion is warranted. First, fixed differences in phase *did* influence sensitivity in the level task. Second, when both level and phase information were present, the d' values were between the sum of d' prediction and the Euclidean prediction. One possible approach in describing these data is to consider a linear model with non-optimal weights. Using an alternative approach (i.e., one that does not depend on independent level and phase representations), by low-pass filtering the envelope an instantiation of the Green and Nguyen (1988) multiple-looks model could be made to simultaneously fit the level and phase data using a single encoding noise and a single decision rule. To fit the data, the low-pass filter required a very low cutoff frequency, approximately 10 Hz. Because our instantiation of the Green and Nguyen model necessarily generates the Euclidean prediction, it is not completely successful in accounting for the data.

VII. SUMMARY

The results of experiment I indicate that estimates of frequency (place) selectivity are largely the same whether the change to be detected is a change in level across frequency or a change in envelope pattern across frequency. The second experiment sought to determine the relationship between representations of level and envelope information as inferred from estimates of sensitivity to differences in level and modulation phase across frequency. The conclusions of this experiment are, to some degree, undermined by individual differences. Using a traditional signal detection theory approach, for one observer, the data are consistent with a model that treats level and envelope information as being independently represented. For the other two observers, however, the d' values in the joint condition are superior to the independent prediction. An explanation based on nonoptimal processing of level and envelope/phase cues can roughly account for these data, but the current data set is not sufficient to provide well-constrained estimates of the weights. Examining the data in terms of just changes in level across frequency, a multiple-looks model suggested by Green and

Nguyen (1988) was applied to the data, and provided it is assumed that the modulator envelope is lowpass filtered at approximately 10 Hz, the phase and level data could be fitted reasonably well using a single decision rule and a single encoding noise. However, the model predicts Euclidean additivity when both level and phase cues are present, and so is not fully in accord with the data. The low-pass filter is required because sensitivity to the phase task is poorer than would be expected if the 20-Hz SAM envelopes are represented with high fidelity.

ACKNOWLEDGMENTS

This work was supported by Grant No. DC 02012 from the National Institutes of Health and an Institute of Research in Cognitive Sciences at the University of Pennsylvania graduate fellowship awarded to Jennifer J. Lentz (NSF STC Grant No. SDR 8920230). Peter Marvit assisted in computer programming, and Matthew R. Matiasek, Peter Marvit, and Robert L. Jones assisted in data collection and analysis. We acknowledge the assistance of two anonymous reviewers whose comments/suggestions improved the manuscript.

[1]Durlach *et al.*'s (1986) channel model predicts that d' grows as $\sqrt{N}$ (and thresholds fall as $1/\sqrt{N}$) for ''balanced'' changes. For a balanced change the sum of the level differences applied to the individual components is zero. Green (1992) found this prediction to hold for profile analysis stimuli.

[2]Such behavior reflects some maximum sensitivity. Because there in no increase in frequency range, three factors are likely to limit performance levels: the amount of internal noise; the degree of correlation across frequency channels (effects of level variation and ''internal'' interchannel correlation impact on thresholds if the stimuli are not ''balanced'' at the output of a bank of auditory filters; see Durlach *et al.*, 1986); and potentially a maximum to the number of auditory filter outputs that can be incorporated into the decision variable.

[3]The programming error affected between approximately 10% to 1% of the trials, depending on the signal level. A subset of the conditions run in experiment II were repeated with and without the error, and the results indicated no significant difference in performance levels. Even though the error carried through all conditions tested (both experiments I and II), it is mentioned only here.

[4]We thank Dr. Gerald D. Kidd, Jr. for alerting us to this alternative explanation.

[5]We are grateful to Dr. David C. Knill for suggesting this alternative to us.

[6]A recursive filter was used: $y_i = c_1 y_{i-1} + c_2(x_i + x_{i-1})$ where x_i is the filter input, and y_i is the filter output for time sample *i*. c_1 is given by $c_1 = (c - \omega_c)/(c + \omega_c)$ and c_2 is given by $c_2 = \omega_c/(c + \omega_c)$, where c is defined by $c = 2/\text{SAMPLE RATE}$ and ω_c is the angular frequency at the 3-dB down point. To ensure that the stimulus onset effects did not influence the modeling results, only the final 1/3 of the digitally filtered envelope was used.

Bernstein, L. R., and Green, D. M. (**1987**). ''The profile-analysis bandwidth,'' J. Acoust. Soc. Am. **81**, 1888–1895.

Buell, T. N., and Hafter, E. R. (**1991**). ''Combination of binaural information across frequency bands,'' J. Acoust. Soc. Am. **90**, 1894–1900.

Dai, H. (**1996**). ''Effect of perceptually separating spectral components on profile discrimination,'' J. Acoust. Soc. Am. **100**, A2681.

Dai, H., and Green, D. M. (**1991**). ''Effect of amplitude modulation on profile detection,'' J. Acoust. Soc. Am. **90**, 836–845.

Durlach, N. I., Braida, L. D., and Ito, Y. (**1986**). ''Toward a model for discrimination of broadband signals,'' J. Acoust. Soc. Am. **80**, 63–72.

Fantini, D. A., and Moore, B. C. J. (**1994**). ''A comparison of the effectiveness of across-channel cues available in comodulation masking release and profile analysis tasks,'' J. Acoust. Soc. Am. **96**, 3451–3462.

Green, D. M. (**1992**). ''The number of components in profile analysis tasks,'' J. Acoust. Soc. Am. **91**, 1616–1623.

Green, D. M., and Nguyen, Q. T. (**1988**). ''Profile analysis: Detecting dynamic spectral changes,'' Hearing Res. **32**, 147–164.

Green, D. M., and Swets, J. A. (**1974**). *Signal Detection Theory and Psychophysics* (Krieger, New York).

Heller, L. H. (**1992**). ''Across-frequency influences in lateralization for interaural time and level differences,'' Doctoral Dissertation, University of Pennsylvania.

Levitt, H. (**1971**). ''Transformed up–down methods in psychoacoustics,'' J. Acoust. Soc. Am. **49**, 167–177.

Macmillan, N. A., and Creelman, C. D. (**1991**). *Detection Theory: A User's Guide* (Cambridge U.P., Cambridge).

Press, W. H., Teukolsky, S. A., Vetterling, W. T., and Flannery, B. P. (**1992**). *Numerical Recipes in C, The Art of Scientific Computing* (Cambridge U.P., Cambridge).

Strickland, E. A., Viemeister, N. F., Fantini, D. A., and Garrison, M. A. (**1989**). ''Within-versus cross-channel mechanism in detection of envelope phase disparity,'' J. Acoust. Soc. Am. **86**, 2160–2166.

Summers, V., and Leek, M. R. (**1994**). ''The internal representation of spectral contrast in hearing-impaired listeners,'' J. Acoust. Soc. Am. **95**, 3518–3528.

Yost, W. A., and Sheft, S. (**1989**). ''Across-critical-band processing of amplitude-modulated tones,'' J. Acoust. Soc. Am. **85**, 848–857.

Some aspects of the lateralization of echoed sound in man. I. The classical interaural-delay based precedence effect

Daniel J. Tollin[a)]
The Sensory Research Unit, Department of Experimental Psychology, The University of Oxford, OX1 3UD United Kingdom

G. Bruce Henning[b)]
Center for Vision and Image Sciences, Department of Psychology, The University of Texas, Austin, Texas 78712

(Received 26 December 1997; revised 26 May 1998; accepted 13 August 1998)

The precedence effect in two-click stimuli was investigated by measuring observers' sensitivity to interaural time delays (ITDs) as a function of interclick interval (ICI). A two-interval two-alternative forced-choice discrimination paradigm was used in two stimulus configurations: type I, a dichotic click with a given ITD preceded a diotic click; and type II, a dichotic click followed a diotic click. Threshold ITDs were measured in each configuration for a finely sampled distribution of ICIs that ranged from 0.1 to 25.6 ms. Performance was characterized by the ''threshold elevation factor'' (TEF) which normalized each of the observers' type I and type II ITD thresholds relative to their ITD threshold for a single dichotic click. The finer sampling of ICIs revealed two novel results: First, for two observers, sensitivity to ITD in the later arriving ITD (type II) oscillated in a consistent and systematic way with changes in ICI. Second, when the ICI reached 12.8 ms, ITD thresholds in the type I and type II configurations were equal but nearly a factor of 2 greater than for a single dichotic click. Some aspects of the data are consistent with the phenomenon of binaural adaptation.
 [S0001-4966(98)04911-X]

PACS numbers: 43.66.Pn, 43.66.Mk, 43.66.Ba [DWG]

INTRODUCTION

In most environments sounds are followed after short delays by reflections coming from many different locations. Fortunately, human observers are not generally aware of echoes and particularly not of the locations from which they arise. The auditory system appears able to sort out direct sounds from echoes, and the ability to correctly localize a sound remains remarkably good despite the large number of reflections that often accompany it. Under echoic conditions, the perceived location of a sound source often appears to be determined, for the most part, by the *localization cues* [not necessarily binaural (Litovsky *et al.*, 1997)] resulting from the first wavefront that reaches the ears (Zurek, 1987).

The precedence effect refers to the phenomenon that arises when similar sounds arrive in close succession, are perceived as a single auditory event, and are localized largely by directional cues carried in the first-arriving sound (Wallach *et al.*, 1949). The mechanisms that produce the precedence effect are thought to underlie the ability to localize sounds in echoic environments. Since echoes abound in natural environments, an important issue in understanding sound localization concerns the effects of echoes on the perceived location of a sound's source. Indeed, a complete understanding of the processes of sound localization, both psychophysical and physiological, cannot be achieved without also understanding how echoes are processed (Tollin, 1998).

The spatial attributes of echoed sounds depend on a variety of acoustical parameters and can be exceedingly complex. One way to simplify their study has been to present stimuli over headphones in configurations that mimic the pattern of stimulation that might occur from a single brief sound and a small number of its early reflections. A particularly important parameter in determining the effects of echoes on the precision of lateralization is the delay between a direct sound and a subsequent echo—the interclick interval (ICI). The effect of ICI on the precision of lateralization has been measured in terms of the lateralizability of the direct sound in comparison to the lateralizability of the echo. An increase in the just-noticeable-differences (jnd's) for interaural delay or interaural level in an echo relative to the jnd's measured for the direct sound can be taken as an indication of the precedence effect (Zurek, 1976, 1980; Gaskell, 1978, 1983). Previous studies of the precedence effect using headphone presentation of transient and broadband sounds have been performed by Békésy (1960) and Wallach *et al.* (1949), and more recently by Zurek (1980), Gaskell (1983), Yost and Soderquist (1984), Saberi and Perrott (1990), Shinn-Cunningham *et al.* (1993), and Stellmack *et al.* (1997). In general, these studies have been interpreted to suggest that the perceived lateral position of pairs of sounds that arrived within about 1–10 ms of each other is largely determined by directional information in the leading sound. The effect is particularly pronounced for delays of 2–3 ms.

The main purpose of the present study was to characterize more accurately the temporal dependence of the precedence effect on ICI. Detailed knowledge of how the prece-

a)Current address: Department of Physiology, University of Wisconsin—Madison, 290 Medical Sciences Building, 1300 University Ave., Madison, WI 53706.
b)On leave from the Department of Experimental Psychology, The University of Oxford, U.K.

dence effect operates with clicks is important for several reasons. First, transient signals are common in natural environments and also seem to be necessary to induce the precedence effect (Wallach *et al.*, 1949; Zurek, 1987). Second, clicks have the unique property of being both temporally punctate and broadband. The punctate nature of clicks make them ideal to study the mechanisms of the precedence effect because, provided the ICI is greater than a few hundred microseconds (see Sec. I), there will be no physical overlap between the leading and the lagging stimuli presented to each ear. Consequently, all observed effects are likely to be due to neural mechanisms and not spectral interference due to overlapping signals. Third, there are several recent neurophysiological studies of the precedence effect (and the related phenomenon, summing localization) that employ clicks: in the inferior colliculus (IC) of anesthetized cat (Yin, 1994; Litovsky and Yin, 1998a, b); in the IC of both the awake rabbit (Fitzpatrick *et al.*, 1995) and the barn owl (Keller and Takahashi, 1996a, b); in the ventral cochlear nucleus of anesthetized chinchillas (Wickesberg, 1996); and in the auditory nerve of unanesthetized cat (Parham *et al.*, 1996). The physiological studies have demonstrated a possible neural correlate of the precedence effect in various auditory structures; relative to the response to the same click presented in isolation, the neural responses to ''echo'' clicks were suppressed for a range of ICIs overlapping the range for which the precedence effect is typically observed. Finally, the construction and evaluation of models of complex binaural phenomenon like the precedence effect require detailed knowledge of the ways in which observers' behavior depends on the ICI.

In this study, the size of the precedence effect was measured in terms of the lateralizability of the sound produced when dichotic clicks were either followed or preceded by a diotic click. A precedence effect at a given ICI was indicated by the conjunction of two criteria: (1) the preceding, or ''direct'' click, made the lateralization of the following, or ''echo'' click, more difficult; and (2) the direct dichotic click is easily lateralized even when followed by a diotic echo. Several other studies of the precedence effect in addition to Zurek (1976, 1980) and Gaskell (1978, 1983) have used similar methods to assess the size of the precedence effect (Saberi and Perrott, 1990; Divenyi, 1992; Shinn-Cunningham *et al.*, 1993; Litovsky and Macmillan, 1994; Tollin and Henning, 1998a).

I. METHODS

A. Stimulus generation

The experimental system was based on the Tucker-Davis-Technologies (TDT) System II. Software was developed to control the generation and delivery of the signals to the earphones, to collect the observers' responses, and to present feedback. Separate signals were generated digitally for the left and the right earphones. From the TDT AP2, the left and right digital signals were each downloaded to the dynamic memory of a TDT DA3-4, 16-bit digital-to-analog converter (DAC) via a fiber-optic data link. A software trigger began the simultaneous conversion of the full scale (16-bit) left and right digital signals to analog voltages by separate DACs at a rate of 200 kHz. From the outputs of the DACs, the analog signals were independently attenuated using two TDT PA4 programmable attenuators. After attenuation, the signals were low-pass filtered at 10 kHz through matched Kemo dual variable VBF/3 filters which had attenuation rates of 24 dB/octave. The signals were then delivered in parallel to three matched pairs of TDH-39 earphones mounted in Grason-Stadler 001 muffs via three TDT HB6 high-impedance dual-channel headphone buffers.

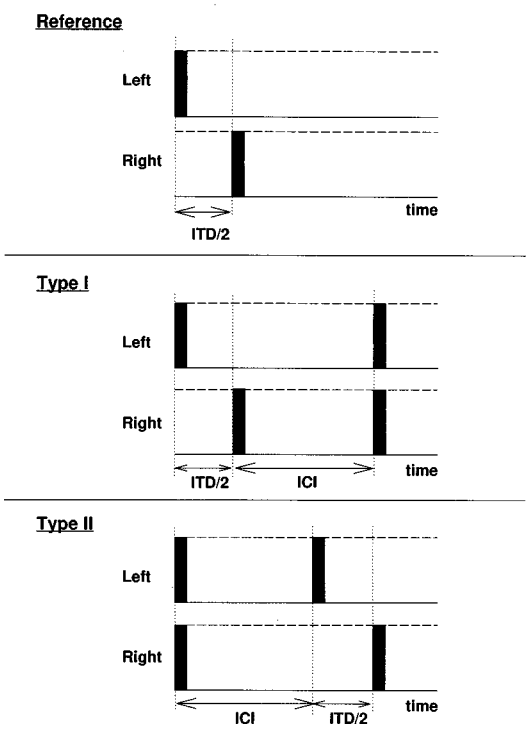

FIG. 1. The three stimulus configurations used in the experiments. Each stimulus was composed of delayed and added 20-μs clicks delivered to the left and right earphone. The top panel shows the reference configuration, the middle panel shows the type I configuration with interaural delay information in the early click, and the bottom panel shows the type II configuration with interaural delay information in the later-arriving click.

B. Stimulus configurations

The three main stimulus configurations used in the experiment are shown schematically in Fig. 1. For each stimulus configuration, the stimuli presented to the left and right earphones in only one observation interval of a two-interval two-alternative forced-choice (2I-2AFC) lateralization discrimination task are shown. In the other observation interval, the signals to the two ears were simply interchanged. Each condition shown in Fig. 1 is the one that was expected to produce the leftmost appearing sound based on the interaural delay in the dichotic pair of clicks.

The basic stimulus was a 20-μs rectangular click. The amplitude of the click delivered to the earphones, when presented diotically, corresponded to approximately 30-dB sensation level; that is, the click was presented 30 dB above the level at which an observer could detect a diotic click 75% of the time in a standard 2I-2AFC detection task.

The reference stimulus configuration (top panel, Fig. 1) comprised a single dichotic click with an interaural time delay (ITD) defined as the delay between the onset of the click presented to one ear and the onset of the click presented to the other. The type I configuration (middle panel, Fig. 1) comprised a ''direct'' dichotic click followed, after an interclick interval (ICI), by a diotic click—the ''echo.'' The ICI for the type I stimulus configuration was defined as the time between the onset of the lagging click of the direct pair and the onset of the diotic echo pair. Finally, the type II configuration (bottom panel, Fig. 1) consisted of a direct diotic click followed, after an ICI, by a dichotic click with an ITD. The ICI for the type II stimulus configuration was defined as the time between the onset of the direct pair and the onset of the leading click of the echo.

Note that the click stimuli shown in Fig. 1 are highly idealized. A single 20-μs click delivered to the TDH-39 earphones generates a pressure waveform that is effectively the impulse response of the earphones. For the TDH-39's we used, the response to the click had a total duration of approximately 500 μs [indicated by observing the signal generated on an oscilloscope by the acoustical output of the earphone seen through a 6-cc coupler by a condenser microphone (Gaskell, 1978)].

C. Psychophysical procedure

The observers were seated in separate sound-attenuating booths and a standard 2I-2AFC procedure was used to measure ITD thresholds for the three stimulus configurations. Each trial was preceded by a 200-ms warning interval signaled by an LED on each observer's response box followed by a 350-ms pause and then the first observation interval. A given stimulus condition was presented in the first observation interval with a probability of 0.5 that the first interval contained the dichotic signal expected to be the leftmost appearing stimulus. In the second observation interval, which followed after a 600-ms pause, the signals to the earphones were interchanged. Before the next trial began, the observers had 1 s to indicate, by pressing one of two buttons on a handheld response box, the interval that had contained the stimulus that had appeared farthest to the left. After each trial, the observers were informed via the LEDs which interval had been ''correct,'' where we arbitrarily defined the ''correct'' signals to be those shown in Fig. 1.

A 3-down 1-up adaptive procedure (Levitt, 1971) was used to measure ITD ''thresholds'' (corresponding to 79.4% correct) for the stimulus configurations shown in Fig. 1. For each adaptive run, one of the three stimulus configurations and a value of ICI were pseudo-randomly chosen by the experimenter. The values of ICI ranged from 0.1 to 25.6 ms; the values for the type I stimuli were 0.1, 0.2, 0.4, 0.8, 1.6, 3.2, 6.4, 9.6, 12.8, and 25.6 ms and 0.1, 0.2, 0.8, 1.6, 2.4, 3.2, 4.8, 6.4, 9.6, 12.8, and 25.6 ms for the type II stimuli. Within an adaptive run, all attributes of the stimulus except the ITD were fixed. The ITD was varied in 40-μs steps for the first 2 reversals of the adaptive run, 10-μs steps for the next 2, and reduced to 5 μs for the final 8 reversals for a total of 12 reversals. The step sizes were chosen so that the ITD would rapidly reach the small range of ITDs for which the observer achieved percentages of correct responses near 79.4%. The initial ITD value was randomly selected from a uniform distribution of large ITDs all of which were expected to produce performance above 79.4%. Neither the experimenter nor the observers knew the initial ITD value on any run.

An ITD threshold estimate was computed as the average of the last 8 of the 12 reversals of each run. A minimum of four such threshold estimates was collected for each stimulus configuration, for each ICI value, and for each observer. On occasion, the ITD threshold estimate was substantially different from estimates obtained in previous runs with the same stimulus conditions. For these conditions, at least two more threshold estimates were collected. No apparent relation was found between stimulus condition and the conditions each observer had to repeat more than four times. Regardless of how many threshold ITD estimates were collected, all data were included in the subsequent analysis. The threshold ITD was then computed for each observer as the arithmetic average of all the ITD threshold estimates obtained for each stimulus condition. Standard errors of the threshold ITD were computed across the threshold estimates obtained in different adaptive runs, of which there were usually between 4 and 8 runs for each condition. Because the observers were highly practiced at lateralizing click stimuli, collecting the data in this way may provide a more accurate measure of the variability of the threshold estimates than is obtained when only the ''best'' estimates of the threshold are taken (Divenyi, 1992).

D. Observers and schedules

Four male observers with normal hearing (FAW, JS, and the authors DJT and GBH) participated in the experiments. Their ages ranged from 20 to 57 years. The authors had extensive experience in lateralization experiments while the other observers had no previous experience. The observers were tested over 1–1.5 h a day. They were given adequate rest between blocks of trials, with longer breaks after 4 or 5 blocks. All observers but JS received at least two weeks training in this task prior to data collection; JS received only one week.

E. Measuring the size of the precedence effect: The threshold elevation factor

There are no detailed accounts in the literature on the dependence of the shape and form of the psychometric functions relating the percentage of correct responses to ITD as a function of ICI in the type II configuration—the configuration most often studied. Gaskell (1983, p. 280) indicates that the psychometric functions for clicks in the type I configuration were ''by and large'' parallel, but did not specify the coordinate system or discuss the implications. Litovsky and Macmillan (1994) reported that a single fixed slope parameter provided good fits to their four observers' psychometric functions for their reference-, type I-, and type II-like configurations at the ICI and azimuths they used when azimuth was plotted on log coordinates. Finally, Tollin (1998) reports that the psychometric functions for clicks in type I and type II configurations for a single observer were parallel to the

same observer's psychometric functions for the reference configuration when ITD was plotted on a logarithmic axis. Based on Tollin's report, we shall assume that, for the ICIs we used, a single slope parameter describes the psychometric functions on semi-logarithmic coordinates. Under this assumption, the measured ITD ''threshold'' corresponding to any reasonable performance level simply indicates the position of the psychometric function along the log-ITD axis for each stimulus configuration and for each ICI.

Another important simplification results when the data are presented in terms of the threshold elevation factor (TEF), defined here as the ratio of the ITD threshold for the type I or type II stimulus to the ITD threshold for the reference stimulus. The TEF can then be used to quantify the size of the precedence effect as a function of the ICI. TEFs were calculated separately for each observer; an observer's performance with the type I and type II stimuli is normalized with respect to his own ability to lateralize the reference stimulus. Thus in the TEF, individual differences in the ability to lateralize clicks are factored out. One reason for using TEFs to describe the data is that performance can readily be compared across observers as well as across different conditions and stimuli. One should bear in mind, however, that the extent to which the observer's underlying psychometric functions across conditions deviate from parallel, the TEF—the estimate of the size of the precedence effect—may vary somewhat if different levels of performance are taken as threshold. Clearly, more attention needs to be paid to the shape and form of the psychometric functions in discrimination studies of the precedence effect, particularly as they relate to measures of the size of the precedence effect as a function of the stimulus parameters being investigated.

When calculated from threshold ITDs measured at a fixed level of performance across all conditions, the TEF can provide some natural benchmarks. For example, a TEF of 1.0 indicates that an observer lateralizes a particular stimulus condition just as well as the reference stimulus. Further, in our experiments, a TEF of 2.0 might be expected to occur if the observer's lateralization were based on the average of the ITDs contained in the direct and echo sounds given that one of them has an ITD of zero. Thus a TEF of around 2.0 for a type II stimulus is not necessarily due to the precedence effect; but a type II TEF significantly larger than 2.0 is one of the signs of a precedence effect. Monte Carlo simulations using each observer's empirical psychometric functions for the reference stimuli, artificially shifted along the log-ITD axis to simulate psychometric functions for type II stimuli based on the assumption that the type II psychometric functions are parallel to those for the reference stimulus (Tollin, 1998), suggest that the type II TEF must be 2.5 or greater to be significantly larger than 2.0. Thus a type II TEF of 2.5 or greater provides some evidence that lateralization of type II stimuli was not based merely on the average of the ITDs contained in the direct and echo sounds, but is due to the precedence effect. Consequently, for a given ICI, a type I TEF near 1.0 together with a type II TEF greater than 2.5 will be taken to indicate a precedence effect for the following reasons: (1) the lateralization of the direct pair (type I) is not much different from the lateralization with the reference stimulus; and (2) the echo (type II) is significantly more difficult to lateralize than both the reference and the average of the ITDs contained in the direct and echo clicks.

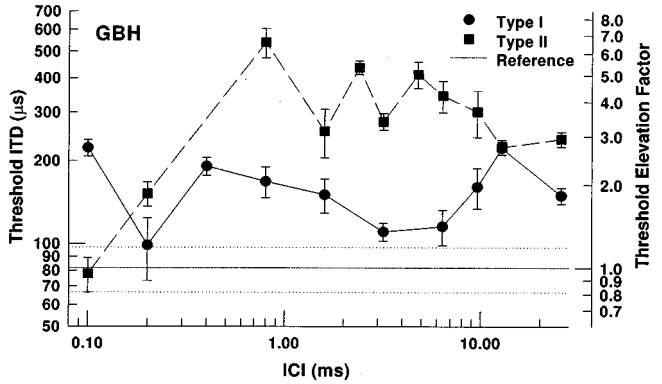

FIG. 2. The mean threshold ITD averaged across different adaptive runs and the standard error of the mean for observer GBH for the type I stimulus (circles) and for the type II stimulus (squares) as a function of the ICI. The mean threshold ITD and standard error of the mean for the reference stimulus, computed in the same way as above, are shown by the solid and dotted horizontal lines, respectively. The right-hand ordinate of each graph gives the threshold elevation factor (TEF).

II. RESULTS

To facilitate comparison of our results with those of others, the interaural time delay of the dichotic clicks (the ITD) was split into two so that the magnitude of the interaural time delay in each of the two observation intervals was ITD/2. The total change in interaural delay across the two observation intervals, then, was ITD, and all data are plotted in terms of ITD. Figures 2–5 show the mean threshold ITDs and standard error of the means of the threshold ITD estimates computed across different adaptive runs as a function of ICI for the type I and type II stimuli for each observer.[1] Threshold ITD (and standard error) for the reference configuration are shown as the solid (and dotted) horizontal lines. The interaural delay thresholds for the reference stimulus were 81.7, 48.0, 48.1, and 119.7 μs for observers GBH, FAW, DJT, and JS, respectively. The threshold elevation factor (TEF) measured with respect to these values is plotted on the right-hand ordinate of each figure.

Provided that the ICI was between 0.8 and 9.6 ms, the type II stimuli were significantly ($p<0.05$) more difficult to

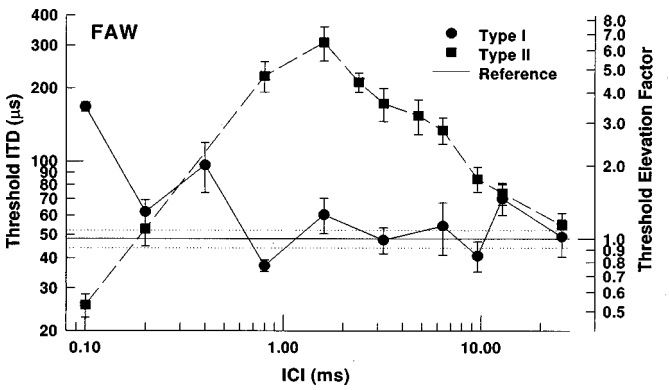

FIG. 3. Same as Fig. 2 but for observer FAW.

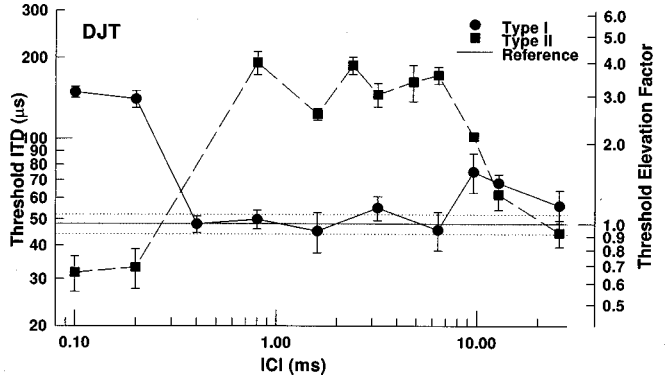

FIG. 4. Same as Fig. 2 but for observer DJT.

lateralize than the type I (except at an ICI of 9.6 ms for GBH and JS, where differences between type I and type II TEFs were not significant). For all observers, the ITDs required to reach the threshold level of performance with type II stimuli for ICIs from 0.8 up to 9.6 ms were both significantly ($p<0.05$) larger than, and ranged from 2 to 7 times, the threshold ITD for the reference stimulus. For all observers but JS, type II TEFs for all ICIs between 0.8 and 6.4 ms were greater than 2.5, indicating a precedence effect. For ICIs between 9.6 and 12.8 ms, the type II thresholds dropped to within a factor of 1.5–3 times the reference threshold. At 12.8-ms ICI, the type II thresholds of three of the observers were still significantly different from and larger than their reference thresholds [$t(12)=6.21$, $p<0.05$ for GBH, $t(10)=3.25$, $p<0.05$ for FAW, and $t(7)=3.47$, $p<0.05$ for JS]. Also at 12.8 ms, none of the four observers' type II thresholds were significantly ($p<0.05$) different from their type I thresholds.

At 25.6-ms ICI, the type II threshold was not significantly different from the reference threshold for FAW and DJT, but the threshold for GBH was significantly larger [$t(12)=6.76$, $p<0.05$]. At the smallest ICI (0.1 ms), two observers achieved thresholds with the type II stimuli that were *smaller* than the reference thresholds as reflected by TEFs significantly below 1.0 [$t(10)=4.22$, $p<0.05$ for FAW and $t(10)=2.62$, $p<0.05$ for DJT]. A similar phenomenon with type II stimuli at small ICIs was reported by Gaskell (1983), but she did not report whether the decrease in threshold was significant. The data in this paper confirm Gaskell's observations.

When the cue for lateralization was in the first click—

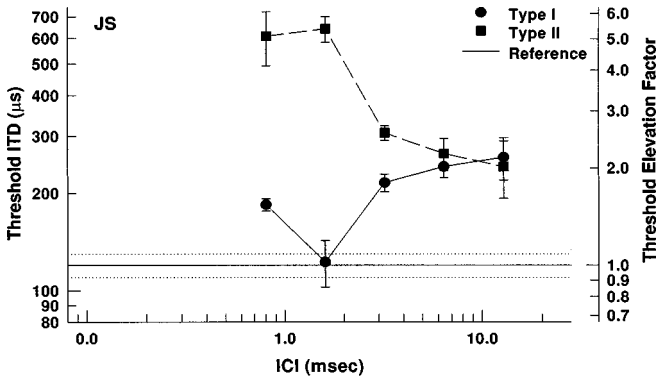

FIG. 5. Same as Fig. 2 but for observer JS.

the type I configuration—the stimuli for many ICIs were generally lateralized nearly as well as with the reference stimulus. This is reflected by threshold elevation factors around 1.0. For observers GBH, FAW, and DJT, there were no significant ($p<0.05$) differences between type I and reference thresholds at ICIs of 3.2 and 6.4 ms. Additionally, neither FAW's nor DJT's type I thresholds at ICIs of 0.8, 1.6, 6.4, and 9.6 ms nor JS's type I threshold at an ICI of 1.6 ms was significantly ($p<0.05$) different from their respective reference thresholds. There were two deviations from this general observation, however. First, for several ICIs less than about 0.4 ms, the type I stimuli were significantly more difficult to lateralize than either the type II or the reference stimuli as reflected by larger ITD thresholds: type I thresholds were significantly larger than type II thresholds for three of the observers at an ICI of 0.1 [$t(12)=6.00$, $p<0.05$ for GBH, $t(10)=15.53$, $p<0.05$ for FAW, and $t(8)=13.35$, $p<0.05$ for DJT], for two observers at 0.4 ms [$t(11)=4.35$, $p<0.05$ for GBH and $t(9)=2.84$, $p<0.05$ for FAW], and for one observer at 0.2 ms [$t(8)=9.63$, $p<0.05$ for DJT]. Second, when the ICI was at 12.8 ms, the type I thresholds did not differ significantly ($p<0.05$) from the type II thresholds for any observer, but thresholds for both configurations were about 1.5–3.0 times greater than the threshold for the reference stimulus. Neither of these two findings has been previously reported.

There was an additional notable characteristic of the data of two observers (GBH and DJT). As the ICI varied from 0.8 to 3.2 ms, the type II TEFs (always above 2.5) appeared to oscillate between high and moderate TEFs. For example, there was a significant decrease in threshold when the ICI was increased from 0.8 to 1.6 ms [$t(9)=3.22$, $p<0.05$ for GBH and $t(6)=2.7$, $p<0.05$ for DJT]. The threshold then increased significantly when the ICI was increased from 1.6 to 2.4 ms [$t(11)=3.38$, $p<0.05$ for GBH and $t(7)=3.08$, $p<0.05$ for DJT]. Observer GBH's threshold significantly decreased again when the ICI was increased further to 3.2 ms [$t(11)=4.53$, $p<0.05$] (observer DJT also showed a decrease in threshold at this ICI that just missed significance [$t(9)=2.04$, $p<0.07$]) and then showed a significant increase at an ICI of 4.8 ms [$t(9)=2.51$, $p<0.05$]. The observation that the TEFs, and thus ITD thresholds for the type II stimuli, oscillated in a consistent way for two observers as a function of ICI was a surprising finding not previously reported.

Finally, Fig. 6 shows the mean TEF as a function of ICI together with the standard error of the mean computed across the four observers' TEFs. The small standard errors reflect the fact that the TEFs for a given combination of stimulus configurations and ICI were often very similar across observers even though the observers' underlying threshold ITDs differed, sometimes by a factor greater than 3. One interesting aspect of the pooled data not generally present in the individual data was the apparent increase in TEF for type I stimuli when the ICI was increased from about 0.8 to 12.8 ms. Statistical analysis shows that the type I TEF at 12.8-ms ICI is significantly larger than the type I TEFs at ICIs of 0.8 ms [$t(3)=7.45$, $p<0.05$], 1.6 ms [$t(3)=3.46$, $p<0.05$], and 3.2 ms [$t(3)=3.2$, $p<0.05$]. A one-way ANOVA indicated

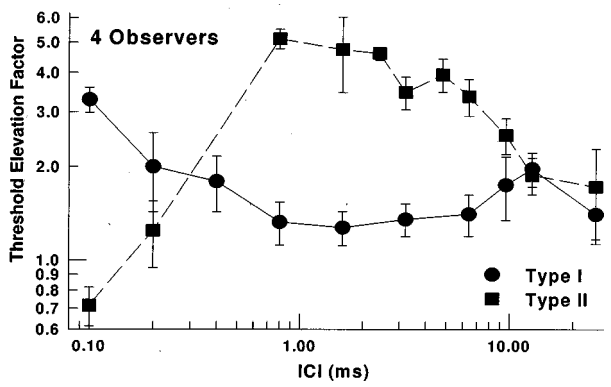

FIG. 6. The mean TEFs computed across the four observers' TEFs are plotted as a function of the ICI in ms for the type I stimulus (circles) and type II stimulus (squares). The error bars show the standard error of the mean computed across the individual observers' TEFs.

that the effect of ICI between 0.8 and 12.8 ms on TEF was significant $[F(5,17)=3.00,\ p<0.05]$—the TEF increased over this range.

III. DISCUSSION

Some of our data are in reasonable agreement with previous headphone-based discrimination studies employing clicks in similar configurations (Gaskell, 1978, 1983; Saberi and Perrott, 1990). For example, for the range of ICIs between 0.8 and 9.6 ms, there was a substantial decrease in the lateralizability of the binaural click pair when it followed an initial diotic pair, as indicated by an increase in ITD threshold, but only a marginal decrease in lateralizability when the cue to lateralization was carried in the initial pair. This finding is consistent with additional discrimination data from both headphone and free-field studies which used brief broadband noise bursts and ICIs over a similar range (Zurek, 1980; Perrott *et al.*, 1989; Shinn-Cunningham *et al.*, 1993; Litovsky and Macmillan, 1994; Tollin and Henning, 1998a). These data are also consistent with the lateralization of the click pairs being determined largely by the interaural information carried in the direct sound (Wallach *et al.*, 1949; Zurek 1976, 1980; Gaskell, 1978, 1983; Yost and Soderquist, 1984; Saberi and Perrott, 1990; Stellmack *et al.*, 1997).

However, our data differ in a number of important ways. First, for ICIs less than 0.4 ms, it was clear that *both* the direct and the echo pair played important roles in the observers' performance. At these small ICIs, it has been shown that the spectral characteristics, and particularly the interaural spectral characteristics, of the sum of the direct and echo stimuli are important (Gaskell, 1978, 1983; Tollin, 1998). One surprising finding was that two observers (FAW and DJT) achieved ITD thresholds with a type II stimuli and an ICI of 0.1 ms significantly *less* than in either their type I or reference configurations. This has not been previously observed.

The data for small ICIs are consistent with what has been called summing localization (Warnke, 1941). The decrease in ITD threshold for type II stimuli and an increase for type I stimuli with small ICIs can be accounted for in part by observing the interaural level and interaural phase-difference spectra of the sum of the direct and echo clicks. It can be easily demonstrated that the interaural phase-difference spectrum for a type I stimulus with a given ICI and ITD (favoring the left ear, for example) is identical to that for a type II stimulus with the same ICI and ITD (favoring the left ear) (Gaskell, 1983). But because of the peaks and notches that occur in the energy-density spectra as a result of adding a delayed copy of the click to itself, the energy-density spectra of both type I and type II stimuli do vary with ICI and ITD. These differences create, in effect, interaural level differences in different bands of frequencies, the sign and size of which depends critically on the ICI, ITD, and frequency region. For example, for a type II stimuli with an ICI of 0.1 ms, these interaural-level differences favor the same ear as the interaural-phase difference spectrum in the frequency region below around 2 kHz in that the ear receiving the delay also receives less energy. One reason why the observers achieved lower thresholds with this stimulus than with the reference stimulus might be due to the observers' use of the additional differences in interaural level that are not present in the reference condition. In type I stimuli, however, the interaural-level differences below 2 kHz are in opposition to the interaural-phase differences. Thus a plausible explanation for the higher ITD thresholds for this condition might be that a kind of time-intensity trade occurs wherein the opposing time and intensity cues partially cancel each other. So to achieve a given discrimination performance level, the ITD of the dichotic click (and hence the interaural-phase difference of the click pair) must be increased to offset the effects of the opposing level difference (which also change when the ITD is changed). Gaskell (1983) first developed this theory to explain results that she observed with type II stimuli for very small ICIs. The present data confirm Gaskell's findings at these very small ICIs and also extend them to include type I stimuli.

A second surprising finding occurred at an ICI of 12.8 ms. At this ICI, although the type I and the type II configurations were equally lateralizable, the observers required about twice the ITD that they required to lateralize the reference stimulus.[2] At this ICI, the observers could easily hear that there were two clicks; an ICI of 12.8 ms is well above the echo threshold for clicks which is the ICI at which an observer reports hearing two events instead of one fused event (Blauert, 1997). The data suggest, however, that even though two clicks could be *detected*, neither the leading nor the lagging click pair could be independently *lateralized*. If the dichotic click in either the type I or type II configuration could have been independently lateralized, TEFs near 1.0 would have been expected for *both* configurations. The fact that the TEFs for both configurations were roughly 2 suggests that at 12.8-ms ICI the perceived lateral position was based on the average of the ITDs in the direct and echo clicks, one of them having zero ITD. This observation closely parallels the phenomenon of summing localization where the interaural characteristics of both the direct sound and its echo together determine the perceived location of the composite stimulus (Warnke, 1941). But our result is paradoxical because the ICI of 12.8 ms is an order of magnitude

larger than the ICI commonly held to the upper bound of summing localization (Blauert, 1997). We suggest that the ICI at which the TEF for both the type I and type II stimuli reach a value of 1.0 can serve as an indication of the temporal upper bound of the precedence effect with click stimuli.

A. The precedence effect and binaural adaptation

Some of the results reported here closely parallel the phenomenon of binaural adaptation (Hafter *et al.*, 1988). In a series of elegant experiments, Hafter and his colleagues have shown that the lateralization of trains of a fixed number of high-frequency, narrow-band clicks depends more and more on interaural information from the onset of the stimulus as the click rate is increased (or the interclick interval decreased). It is supposed that the relative effectiveness of the interaural information extracted from each successive click after onset is reduced by an amount which is highly dependent on the ICI. Based on the findings of several experiments concerning binaural adaptation, Hafter and his colleagues argue that binaural adaptation is likely the result of a peripheral process whose neural substrate is located in the monaural afferents leading to the initial sites of binaural interaction (Hafter *et al.*, 1988; Hafter, 1996).

Our findings are consistent with this interpretation; for ICIs less than 12.8 ms and above the commonly assumed upper limit of roughly 0.8 ms for summing localization with transient stimuli (Blauert, 1997), the dominance of the initial pair of clicks over the echo pair measured in terms of the effectiveness of the interaural cues, increases with decreasing ICI. In this ICI region, two predictions can be made by applying the binaural adaptation hypothesis to the type I and the type II stimuli. First, for the type II stimuli, as the ICI is increased from 0.8 ms, the dichotic echo click should go from being relatively ineffective to being more effective. This would result in a shift of the perceived lateral position of the stimuli *away* from the midline. Thus lower type II TEFs with increasing ICI would be predicted. The same reasoning applied to the type I stimuli predicts that TEFs should actually *increase* from TEFs near 1.0 as the ICI increases. An increasing TEF would be expected because the diotic echo click would begin to be more effective for lateralization and would consequently pull the lateral position of the stimuli back toward the midline. Figure 6 shows that the results for the type II stimuli with ICIs between 0.8 and 12.8 ms are consistent with the first prediction. As for the second prediction, there is some evidence that the across-observer average type I TEF increases over the same range of ICIs, but there is little evidence of an increasing trend in the individual data.

Another prediction from the binaural adaptation hypothesis is that at some ICI, the directional information carried in the echo click will be nearly equal to the information carried by the initial click. Buell and Hafter (1988) used trains of brief high-frequency, narrow-band clicks and found that an ICI of about 10 ms yielded ITD discrimination results that strongly suggested that each click in the train carried equivalent amounts of directional information. From their finding, we should expect that, at some ICI, the directional information carried by the echo click will be nearly equal to the information carried by the initial click *and* the observers should be able to use the information from both the leading and the echo click equally well. Figure 6 shows that when the ICI was 12.8 ms, the TEF was near 2.0 for *both* the type II and the type I stimuli. A TEF of 2 arises when the perceived lateral position of the stimulus lies midway between that of the direct click and that of the echo with one click being dichotic and the other diotic. In other words, at this ICI the direct and echo clicks were not only equally effective in determining lateralization but also the directional information they carried was somehow averaged. This finding suggests that, in terms of ITD threshold at an ICI of 12.8 ms, the type I and type II configurations are equivalent stimuli. It would be interesting to know, with ICIs around 12.8 ms, whether observers can discriminate type I from type II stimuli.

B. Additional observations related to oscillating type II thresholds

The data with the type II configuration revealed TEFs for two experienced observers and ICIs between 0.8 and 3.2 ms that oscillated significantly between high and moderate values. The oscillations were surprising and have not been previously reported with broadband transient stimuli over headphones. [Blauert and Cobben (1978) observed consistent oscillations in the perceived location of narrow-band transients presented from two loudspeakers as a function of the inter-speaker delay for delays up to 3.0 ms, the largest delay they used.] It is possible that previous studies failed to observe the oscillations simply because of sparse sampling of ICIs. Experience may have also played a role because there were no oscillations in the data of the two least experienced observers. One observer in Gaskell's (1983) study of the interaural delay-based precedence effect did exhibit oscillatorylike thresholds for type II stimuli. The ITD thresholds for that observer peaked at an ICI of 1.0 ms but then declined substantially (greater than a factor of 2) when the ICI increased to 2.0 ms. Unfortunately, 2.0 ms was the largest ICI Gaskell used.

Additional examples of oscillating intracranial lateral position occur in the classic study of Wallach *et al.* (1949). Wallach *et al.* used a pair of 1-ms clicks and an ICI of 2 ms, and found an oscillation in the ITD of the direct click required to offset a fixed ITD in the echo; that is, the function relating the ITD of their direct click to the ITD of their echo click required for a centered image was nonmonotonic. Wallach *et al.* confirmed the changes in intracranial position with changes in ITD of the echo using a type II-like configuration where they fixed the ITD of the direct click at zero ITD and varied the ITD of the echo click between -1000 and 1000 μs.

A monotonic function relating the ITD of the direct click required to offset a fixed ITD in the echo might be expected if the precedence effect were based on a mechanism that simply reduced the sensitivity to directional information for a short period of time after the onset of the direct sound (Zurek, 1980, 1987). But this is not what Wallach *et al.* observed. Further, when Wallach *et al.* increased the ITD of the echo click from $+200$ to $+800$ μs, their observers actually

consistently reported the stimulus on the side of the head *opposite* the side that would be expected based on the ITD. In other words, the perceived location of those stimuli crossed the midline, an impossible situation if the precedence effect were based only on an onset-mediated suppression of the ITD in the echo click. In a replication of Wallach's study (but using 100-μs clicks and an ICI of 1 ms), Yost and Soderquist (1984) also found nonmonotonic functions relating the ITD of the direct click to the ITD of the echo click required for a centered image.

Oscillations as a function of ICI were also present in the data of Saberi and Perrott (1995). In that study, trains of 200 40-μs clicks were presented such that the first and last click contained a fixed ITD favoring one ear, while the remaining 198 clicks contained an ITD of equal size favoring the opposite ear. Both the ICI and the ITD were manipulated and the observers were instructed to judge whether the lateral position of the stimulus was to the left or right of the midline. Their data reveal that, for a fixed ITD, the percentage of times the observers judged the lateral position of the stimuli to be consistent with the ITD in the initial click oscillated between higher and lower percentages as a function of ICI. The oscillations were particularly obvious for ICIs less than about 3 ms, consistent with those observed in the present study. For ICIs greater than 3 ms, the data suggest that the observers perceived the lateral position of the stimuli in a fashion consistent with the ITD in the ongoing (middle clicks) click train.

The subjective reports provided by the observers in several studies of the precedence effect provide some insight into a possible cause of the oscillations. In Saberi and Perrott (1995), for stimuli with ICIs between 2 and 4 ms, the observers reported hearing two concurrent images throughout the duration of the stimulus and that the two images were lateralized to opposite sides of the head. Yost and Soderquist (1984) also reported that under certain stimulus conditions, their observers experienced more than one image and reported ''diffuse'' and ''ambiguous'' images for stimuli with large second-click ITDs. Such reports are similar to reports from experiments examining time-intensity trading (Hafter and Jeffress, 1968) and may indicate that a similar phenomenon is occurring in experiments examining the precedence effect.

A neural correlate of these oscillations might be found at the level of the auditory nerve. Parham *et al.* (1996) found that a majority of the responses of a population of auditory nerve fibers of unanesthetized cats to click pairs exhibited some form of ICI-dependent fluctuation over a range of ICIs between 1 and about 10–20 ms. These fluctuations might be dependent on the delay between the two clicks and the frequency tuning of the nerve fibers due to the comb-filtered spectrum of the delayed and added clicks. While it is known that the responses of auditory nerve fibers to click pairs do not behave in any simple linear fashion (Goblick and Pfeiffer, 1969), Hall and Lummis (1973) have demonstrated psychophysically that the monaural detection of click pairs in the presence of a notched-noise masker was highly and, more importantly, *predictably* dependent on both ICI (for ICIs just above 2 ms or less) and the spectral location of the notch in the masking noise. The importance of spectral cues in the lateralization of echoed sound is investigated more completely in the companion paper (Tollin and Henning, 1998b).

IV. SUMMARY

Previous investigations of the ITD-based precedence effect with brief and broadband sounds have suggested that the precedence effect is most effective for ICIs between 1 and 2 ms (Wallach *et al.*, 1949; Zurek, 1980; Gaskell, 1983; Yost and Soderquist, 1984; Saberi and Perrott, 1990; Litovsky *et al.*, 1997). While our data are in general agreement with this analysis, there were two important differences: First, the results for experienced observers with the type II configuration suggest that the size of the precedence effect, as measured by the TEF, may be more dependent on ICI than once believed; significant oscillations of performance with changing ICIs were observed. The subjective reports of observers from other studies of the precedence effect exhibiting oscillatory responses suggest that the oscillations may be due to a kind of time-intensity trade between interaural phase differences and the interaural level differences in the low-frequency region. Second, at an ICI of 12.8 ms, the type I and type II stimuli were equally lateralizable, but threshold ITDs were about a factor of 2 larger than the reference thresholds.

Analysis of our data from the point of view of binaural adaptation revealed close parallels between these two phenomena even though it is commonly held that the mechanism responsible for binaural adaptation is different from that primarily responsible for the precedence effect (Hafter *et al.*, 1988; Hafter, 1996). The conclusions drawn from our data suggest that the mechanism for binaural adaptation, whose neural substrate is currently hypothesized to be located in monaural channels leading to the first sites of binaural interaction, may also be important in the precedence effect. One important mechanism responsible for the ICI-dependent reduction in the sensitivity to the directional attributes of echoes following a direct sound, then, may be located at a site peripheral to the first sites of binaural interaction.

An additional implication of our observations is that even under conditions commonly held to be in the domain of the precedence effect—for brief broadband stimuli and ICIs between about 1 and 10 ms—a process not unlike summing localization occurs. In other words, the echo *always* has some influence on the perceived lateral position of the stimulus although its influence generally decreases with decreasing ICI.

ACKNOWLEDGMENTS

This work was carried out in The Sensory Research Unit, Department of Experimental Psychology, The University of Oxford, U.K., as part of the first author's doctoral dissertation. Financial support was provided to the first author through an O.R.S. Award, a St. Catherine's College (Oxford) Graduate Fellowship, and an University of Oxford Overseas Bursary. The first author was supported by NIH NIDCD Grants Nos. DC00045 and DC00116 during the

preparation of the manuscript. Both authors would like to thank Dr. Erv Hafter, Dr. Dennis McFadden, and Tom Yin for their insightful comments on various drafts of this paper. We'd also like to thank Dr. Wesley Grantham (the Associate Editor), Dr. Ruth Litovsky, and one anonymous reviewer for their suggestions.

[1]Observer JS was not available for the entire experiment. For that reason, type I and type II threshold ITDs were obtained only for the subset of ICIs which included 0.8, 1.6, 3.2, 6.4, and 12.8 ms.

[2]This finding demonstrates why the TEF provides a more illustrative way to quantify the size of the precedence effect than other quantitative measures. For example, one such measure developed by Shinn-Cunningham *et al.* (1993) quantifies the precedence effect in discrimination experiments in terms of ratio of the ITD threshold for type II-like stimuli and the sum of the type I and the type II ITD thresholds at a given ICI. This quantity, called *C*, can range from 0.5 to 1.0. In effect, *C* indicates the relative weight an observer gives to the ITD in the initial sound and (1-*C*) is the weight given to the ITD in the echo sound. Clearly, a *C* value of 1.0 indicates a strong precedence effect; more weight given to the ITD in the initial sound resulting in a very much larger Type II ITD threshold than the type I threshold. A *C* value of 0.5 indicates that the thresholds for the type II and type I configurations are identical. In headphone discrimination experiments with clicks (including the data in this paper) or brief broadband noisebursts, *C* values typically range between 0.6 and 1.0 for ICIs between 1 and 10 ms (Shinn-Cunningham *et al.*, 1993). One shortcoming of the *C* value as a measure of the precedence effect, however, is that there is no common frame of reference by which to judge the absolute size of the effect. For example, in the present data, at an ICI of 12.8 ms the type I and type II thresholds were nearly equal, which would result in a *C* value near 0.5. But the type I and type II ITD thresholds were also nearly equal at an ICI of 25.6 ms for two observers (and would certainly be equal for the other observers at larger ICIs) resulting in a *C* value of 0.5 as well. On its own, the value of *C* would imply that the *size* of the precedence effect at these two ICIs is equivalent, but clearly it was not; the ITD thresholds at 12.8-ms ICI were larger than at 25.6 ms. Threshold elevation factors, however, clearly reveal the differences.

von Békésy, G. (**1960**). *Experiments in Hearing* (McGraw-Hill, New York), pp. 272–301.

Blauert, J. (**1997**). *Spatial Hearing* (MIT, Cambridge).

Blauert, J., and Cobben, W. (**1978**). ''Some considerations of binaural cross correlation analysis,'' Acustica **39**, 96–104.

Blauert, J., and Divenyi, P. L. (**1988**). ''Spectral selectivity in binaural contralateral inhibition,'' Acustica **66**, 267–274.

Buell, T. N., and Hafter, E. R. (**1988**). ''Discrimination of interaural differences in time in the envelopes of high-frequency signals: Integration times,'' J. Acoust. Soc. Am. **84**, 2063–2066.

Divenyi, P. L. (**1992**). ''Binaural suppression of nonechoes,'' J. Acoust. Soc. Am. **91**, 1078–1084.

Fitzpatrick, D. C., Kuwada, S., Stanford, T. R., and Trahiotis, C. (**1995**). ''Neural responses to simple, simulated echoes in the auditory brainstem of the unanesthetized rabbit,'' J. Neurophysiol. **74**, 2469–2486.

Gaskell, H. (**1978**). ''Some aspects of the localization of transient sounds in man,'' Doctoral dissertation, University of Oxford, U.K.

Gaskell, H. (**1983**). ''The precedence effect,'' Hearing Res. **11**, 277–303.

Goblick, T. J., Jr., and Pheiffer, R. R. (**1969**). ''Time-domain measurements of cochlear nonlinearities using combination click stimuli,'' J. Acoust. Soc. Am. **46**, 924–938.

Hafter, E. R. (**1996**). ''Binaural adaptation and the effectiveness of a stimulus beyond its onset,'' in *Binaural and Spatial Hearing in Real and Virtual Environments*, edited by R. H. Gilkey and T. R. Anderson (Earlbaum, Mahwah, NJ), pp. 211–232.

Hafter, E. R., and Jeffress, L. A. (**1968**). ''Two image lateralization of tones and clicks,'' J. Acoust. Soc. Am. **44**, 563–569.

Hafter, E. R., Buell, T. N., and Richards, V. M. (**1988**). ''Onset coding in lateralization: Its form, site and function,'' in *Auditory Function*, edited by G. W. Edelman, E. Gall, and W. M. Cowen (Wiley, New York), pp. 647–676.

Hall, J. L., and Lummis, R. C. (**1973**). ''Thresholds for click pairs masked by band-stop noise,'' J. Acoust. Soc. Am. **54**, 593–599.

Keller, C. H., and Takahashi, T. T. (**1996a**). ''Responses to simulated echoes by neurons in the barn owl's auditory space map,'' J. Comp. Physiol. A **178**, 499–512.

Keller, C. H., and Takahashi, T. T. (**1996b**). ''Binaural cross-correlation predicts the responses of neurons in the owl's auditory space map,'' J. Neurosci. **16**, 4300–4309.

Levitt, H. (**1971**). ''Transformed up-down methods in psychoacoustics,'' J. Acoust. Soc. Am. **49**, 467–477.

Litovsky, R. Y., and Macmillan, N. A. (**1994**). ''Sound localization precision under conditions of the precedence effect: Effects of azimuth and standard stimuli,'' J. Acoust. Soc. Am. **96**, 752–758.

Litovsky, R. Y., and Yin, T. C. T. (**1998a**). ''Physiological studies of the precedence effect in the inferior colliculus of the cat: I. Correlates of psychophysics,'' J. Neurophysiol. **80**, 1285–1301.

Litovsky, R. Y., and Yin, T. C. T. (**1998b**). ''Physiological studies of the precedence effect in the inferior colliculus of the cat: II. Neural mechanisms,'' J. Neurophysiol. **80**, 1302–1317.

Litovsky, R. Y., Rakerd, B, Yin, T. C. T., and Hartmann, W. M. (**1997**). ''Psychophysical and physiological evidence for a precedence effect in the median sagittal plane,'' J. Neurophysiol. **77**, 2223–2226.

Parham, K., Zhao, H. B., and Kim, D. O. (**1996**). ''Responses of auditory nerve fibers of the unanesthetized decerebrate cat to click pairs as simulated echoes,'' J. Neurophysiol. **76**, 17–29.

Perrott, D. R., Marlborough, K., Merrill, P., and Strybel, T. A. (**1989**). ''Minimum audible angle thresholds obtained in conditions in which the precedence effect is assumed to operate,'' J. Acoust. Soc. Am. **85**, 282–288.

Saberi, K., and Perrott, D. R. (**1990**). ''Lateralization thresholds obtained under conditions in which the precedence effect is assumed to operate,'' J. Acoust. Soc. Am. **87**, 1732–1737.

Saberi, K., and Perrott, D. R. (**1995**). ''Lateralization of click-trains with opposing onset and ongoing interaural delays,'' Acustica **81**, 272–275.

Shinn-Cunningham, B. G., Durlach, N. I., and Zurek, P. M. (**1993**). ''Adjustment and discrimination measures of the precedence effect,'' J. Acoust. Soc. Am. **93**, 2923–2932.

Stellmack, M. A., Dye, R. H., and Guzman, S. J. (**1997**). ''Observer weighting of binaural information in source and echo clicks,'' J. Acoust. Soc. Am. **101**, 3083(A).

Tollin, D. J. (**1998**). ''Some aspects of the lateralization of echoed sounds in man,'' Doctoral dissertation, University of Oxford, U.K.

Tollin, D. J., and Henning, G. B. (**1998a**). ''Across-frequency integration in the precedence effect.'' in *Psychophysical and Physiological Advances in Hearing*, edited by A. R. Palmer, A. Rees, A. Q. Summerfield, and R. Meddis (Whurr, London), pp. 329–335.

Tollin, D. J., and Henning, G. B. (**1998b**). ''Some aspects of the lateralization of echoed sound in man. II. The role of stimulus spectrum,'' J. Acoust. Soc. Am. (submitted).

Wallach, H., Newman, E. B., and Rosenzweig, M. R. (**1949**). ''The precedence effect in sound localization,'' Am. J. Psychol. **62**, 315–337.

Warnke, H. (**1941**). ''The fundamentals of room-related stereophonic reproduction in sound films,'' Akust. Z. **6**, 174–188.

Wickesberg, R. E. (**1996**). ''Rapid inhibition in the cochlear nuclear complex of the chinchilla,'' J. Acoust. Soc. Am. **100**, 1691–1702.

Yin, T. C. T. (**1994**). ''Physiological correlates of the precedence effect and summing localization in the inferior colliculus of the cat,'' J. Neurosci. **14**, 5170–5186.

Yost, W. A., and Sonderquist, D. R. (**1984**). ''The precedence effect revisited,'' J. Acoust. Soc. Am. **76**, 1377–1383.

Zurek, P. M. (**1976**). ''An investigation of the binaural perception of echoed sound,'' Doctoral dissertation, Arizona State University.

Zurek, P. M. (**1980**). ''The precedence effect and its possible role in the avoidance of interaural ambiguities,'' J. Acoust. Soc. Am. **67**, 952–964.

Zurek, P. M. (**1987**). ''The precedence effect,'' in *Directional Hearing*, edited by W. A. Yost and G. Gourevitch (Springer-Verlag, New York), pp. 85–106.

The influence of broadband noise on the precedence effect

Yuan-Chuan Chiang and Richard L. Freyman[a)]
Department of Communication Disorders, University of Massachusetts, Amherst, Massachusetts 01003

(Received 2 July 1996; revised 10 September 1997; accepted 22 June 1998)

This study examined the influence of background noise on the localization of lead-lag noise-burst pairs and on echo threshold for the same stimuli. Experiments were conducted in an anechoic chamber with a leading stimulus delivered from a loudspeaker at 45° to the right of center and a lagging stimulus from 45° left. Lead and lag stimuli were 4-ms bursts of Gaussian noise. In experiment 1, with lead and lag at equal levels and the lag delay fixed at 2 ms, the perceived location of the image produced by the lead-lag stimulus was estimated from subjects' left/right judgments relative to bursts from a ''comparitor'' loudspeaker whose position could be adjusted. In experiment 2, the dominance of the leading burst on perceived location was measured by determining the increase in level of the lagging burst necessary to produce an image estimated to be centered at 0° azimuth. Experiment 3 was concerned with echo threshold. Subjects reported whether or not they heard a sound in the vicinity of the lagging loudspeaker as the lag-burst delay was varied. In all three experiments, data were obtained for four to five stimulus levels in quiet and for three levels of background white noise from a loudspeaker at 180°. The results revealed a substantial weakening effect of background noise on the precedence effect in experiments 2 and 3, and a nonsignificant effect in experiment 1. [S0001-4966(98)03310-4]

PACS numbers: 43.66.Qp, 43.66.Pn [RHD]

INTRODUCTION

While participating in an experiment by Thurlow and Parks (1961) in which trains of lead-lag click pairs were presented in a sound field, listeners made the surprising informal observation that echo suppression was broken if they talked during the stimulus presentation. At certain lag-click delays, subjects were aware of only one auditory image when the room was otherwise quiet, but when they talked or someone near them talked the listeners reported hearing both lead and lag clicks separately. Recently we set up a similar configuration in our lab, and this effect of talking during stimulus presentation was also observed and was quite startling. Thurlow and Parks (1961) conducted a followup experiment with thermal noise added instead of subjects talking. The noise was reported to affect two different perceptual phenomena related to the precedence effect. At lag delays sufficiently short that only one image localized toward the lead loudspeaker was heard for stimuli presented in quiet, the image moved by an unspecified amount toward the lag loudspeaker when noise was added. At delays that were longer, the effect of adding a sufficiently intense noise was to allow the lag clicks to be heard as separate events under conditions in which the lead-lag click pair was heard as a single event in quiet. Thurlow and Parks concluded that the addition of a sufficiently intense noise ''removes the suppression effect'' (p. 12).

Leakey and Cherry (1957) studied the influence of noise on the precedence effect using a time-intensity trading paradigm. Subjects sat in an anechoic room, equidistant between two loudspeakers at 32° right and left of midline. Running speech at a quiet conversational level was presented from both loudspeakers. Time delays of up to 2.5 ms were introduced in one of the loudspeakers by moving it away from the listener while maintaining the same azimuth angle. Subjects judged whether the image produced by the lead-lag pair was to the right or left of midline. As expected with the precedence effect, judgments favored the leading loudspeaker. However, the image could be brought to center by increasing the intensity of the lag loudspeaker. The strength of the precedence effect was quantified by the number of dB the lag needed to be increased to produce 50% left-of-center and 50% right-of-center judgments. A wide-band noise presented from a third loudspeaker at 0° was in some conditions switched on and off simultaneously with the speech. The effect of noise was orderly and dramatic. The higher the noise level, the smaller the intensity increase of the lag required for 50% left judgments. For example, as the noise level increased from 50 dB to 10 dB below the level that just masked the speech stimulus, the required intensity increase for the lagging stimulus decreased from 9 dB to 2 dB when the lag delay was 2 ms. These results suggest that the influence of the leading stimulus in localization can be greatly weakened by the addition of a broadband background noise.

To our knowledge, no other reports on the effects of noise on the precedence effect in the free field have been published, although there are at least two related earphone studies. Hall (1959) investigated, among other things, the effect of noise on binaural fusion using the ''three click paradigm'' (Guttman *et al.*, 1960). Pairs of clicks separated by a time delay are presented to one ear while a probe click is presented to the other ear. The probe click is adjusted in time until it fuses with one of the members of the click pair and produces a centered intracranial image. Fusion with the second member of the pair is possible only if its time delay relative to the first click is sufficiently large. Hall (1959) found that a background of noise reduced the required time

a)Electronic mail: rlf@comdis.umass.edu

delay for fusion with the second click. In another earphone study, Babkoff and Sutton (1966) presented a leading click to one ear and a lagging click to the other and measured the lag delay at which subjects reported hearing two rather than one click (the ''lag-click threshold''). The stimulus conditions were not perfectly analogous to the loudspeaker studies of the precedence effect because no attempt was made to simulate the binaural inputs to the two ears with the relevant interaural delays. Nevertheless, Babkoff and Sutton (1966) reported similar findings in noise to the break down in fusion reported by Thurlow and Parks (1961). The lag-click threshold decreased as the level of a broadband white noise increased until the level was 13–38 dB (depending on subject) below the level that would mask the click. At higher noise levels at which the signal approached inaudibility, there was a reversal of the effect. The weakening effect of broadband noise does not appear to be related to the reduced stimulus sensation level produced by the masking effect of the noise. Babkoff and Sutton (1966) showed that the lag-click threshold actually increased with decreased sensation level in the quiet. Shinn-Cunningham *et al.* (1993) reported a similar finding in their study of the lateralization of precedence effect stimuli.

Despite this previous work, information about the influence of noise on the precedence effect is as yet too limited to allow an appreciation of the practical and theoretical significance of the phenomenon. For example, we do not yet have enough information to predict whether background noise is likely to increase the audibility of reflections in acoustic environments outside the laboratory, and whether this would have an impact on speech perception in noisy reverberant spaces. From a theoretical standpoint, it is interesting that noise seems to reduce both echo threshold and the dominance of the leading sound in localization, as these two aspects of the precedence effect are not known to be strongly linked. However, stronger evidence will be necessary to establish the fact that both types of measures are affected by noise. The effect of noise on localization dominance by the leading sound has been studied only by increasing the level of the lag to offset the temporal advantage of the lead (Leakey and Cherry, 1957). The effect on the perceived location of an auditory image in the more realistic case where the lag is not more intense than the lead was mentioned but not quantified by Thurlow and Parks (1961). The report by Thurlow and Parks (1961) that talking or the presentation of noise affected echo suppression was also informal, and we do not yet know whether the effect of noise on fusion of stimuli delivered under headphones (Hall, 1959; Babkoff and Sutton, 1966) is related. At this point there are no published data quantifying the effect of noise on perception of echoes in a sound field environment.

With these limitations in mind, the purpose of the current sound field studies was to quantify the influence of broadband noise on the precedence effect using three different paradigms. Experiment 1 was concerned with the effect of noise on the localization of precedence effect stimuli using direct localization judgments and the model of Shinn-Cunningham *et al.* (1993). These results were compared with those obtained in a second paradigm in which the level of the lag was increased to offset the temporal advantage of the lead (a partial replication of Leakey and Cherry, 1957). The third experiment examined the effect of noise on the delay at which fusion breaks down and echoes are heard as separate events (echo threshold). In all three experiments the level of the noise was varied as well as the signal level in quiet.

I. EXPERIMENT 1: LOCALIZATION

This experiment estimated the perceived location of the auditory event produced by single-source and lead-lag pairs of noise bursts. These estimates were made by comparing (with a ''left'' or ''right'' judgment) the image produced by a target stimulus with that produced by a ''comparitor'' noise burst that could be delivered from varying azimuths in the horizontal plane. Localization of the target was specified as the comparitor location producing 50% ''left'' and 50% ''right'' judgments. The strength of the precedence effect was determined, in both quiet and noisy backgrounds, by comparing localization for lead-lag target stimuli with that for lead-only stimuli.

A. Method

1. Subjects

Listeners in this and the two subsequent experiments were five adults aged 21 to 30 years with pure-tone detection thresholds less than or equal to 20 dB HL *re:* ANSI (1989) in the audiometric frequencies through 6 kHz. Two of the subjects, JF and SS, had participated previously in binaural hearing studies, while the other three subjects had no experience in auditory experiments.

2. Apparatus and procedure

All experiments were conducted in an IAC constructed anechoic chamber measuring $4.9\times4.1\times3.12$ m. The floor, ceiling, and walls of the chamber were lined with 0.72-m foam wedges. Regardless of angle, all loudspeakers were at a distance of 1.65 m from the position of a listener's head when seated in a chair in the center of the room. The center of the loudspeakers was 1.04 m above the wire mesh floor of the chamber, the approximate height of the typical subject's ears while sitting. Loudspeakers delivering the test stimuli were placed on a foam-covered wood-frame semicircular arc covering the front half of the horizontal plane. One additional loudspeaker that was used to deliver noise from directly behind the listener was supported by a stand. The loudspeaker arrangement is diagramed in Fig. 1.

Stimuli were digitally synthesized wide-band Gaussian noise bursts having a total duration of 4 ms, which included 1-ms linear rise/fall periods. The stimuli were presented in two basic types of conditions: (a) a ''precedence effect'' or ''lead-lag'' condition in which a leading burst was presented from a loudspeaker located at $+45°$ (right of center) and a lagging burst (the same sample of noise) was presented from a loudspeaker at $-45°$ (left), and (b) a ''lead only'' or ''single-source'' condition in which only the burst from the right loudspeaker was presented. The stimuli were presented at a 20-kHz rate per channel from a 16 bit D/A converter (TDT QDA2) with a 2-ms delay in the left channel for the

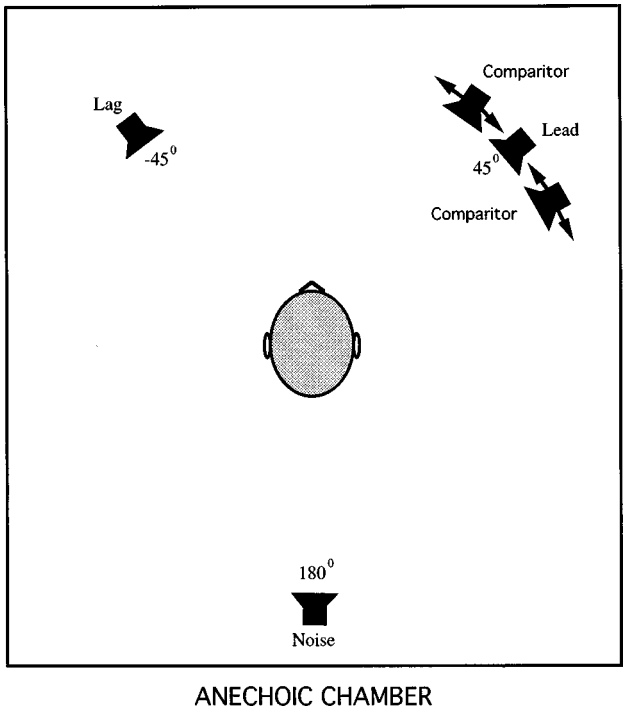

FIG. 1. Diagram of the anechoic chamber for experiment 1. The lead and lag loudspeakers were at ±45°, respectively. The two comparitor loudspeakers were placed symmetrically at variable angles around the lead loudspeaker. The noise was presented from the loudspeaker at 180°.

precedence effect conditions. The short 2-ms delay between the leading and lagging bursts was used to increase the probability that the stimuli were below echo threshold (i.e., only one image is heard). The D/A outputs were low-pass filtered at 8.5 kHz (TTE J1390), attenuated (TDT PAT1), amplified (NAD 2100), multiplexed (TDT MUX1), and delivered to the loudspeakers (Realistic Minimus 7). The background noise, when presented, was generated by a broadband random noise generator (TDT GNS40), amplified (Optimus SA 155), and delivered from a loudspeaker (Minimus 7) at 180°.

Each trial consisted of two temporal intervals as diagrammed in Fig. 2. During the first interval the stimulus burst (or burst pairs in the case of the precedence effect conditions) was presented three times with a 250-ms interval between bursts. The purpose of the repetition was to give subjects multiple opportunities to hear the stimulus before making a judgment. This type of repetition has been used in earphone studies in which lateralization judgments relative to a comparison stimulus were required (e.g., Buell *et al.*, 1993; Freyman *et al.*, 1997). The three repetitions may have also increased the probability of one image being heard because echo threshold is known to increase with repeated stimulation (Clifton and Freyman, 1989). During the second interval a ''comparitor'' stimulus, also a 4-ms Gaussian noise repeated three times, was presented from one loudspeaker only. The subjects' task was to report via a button box held on the lap whether the image heard in second interval was to the right or left of the image heard in the first (signal) interval. To facilitate comparisons across conditions, it was desirable to have an invariant comparitor. The comparitor was always presented in quiet at 56 dB SPL. For conditions in which background noise was presented, this required that the noise be turned off in between target and comparitor presentations. As shown in Fig. 2, the noise was turned on 300 ms before the first stimulus burst and was turned off 500 ms following the third stimulus burst, 300 ms before the comparitor was presented.

Stimuli were delivered in blocks of 20 trials, in which 10 independent samples of the noise bursts were each presented twice. The location of the loudspeaker delivering the comparitor stimulus was fixed within a block, and the percentage of left judgments for that comparitor position was recorded. Across blocks, a total of three different loudspeakers were used to deliver the comparitor, although only one loudspeaker was used in an individual block. Two of these loudspeakers were placed symmetrically around the lead loudspeaker, which was at +45°. The third comparitor loudspeaker was the lead loudspeaker itself. This was used in the blocks in which the comparitor stimulus needed to be delivered at the same azimuth angle as the leading stimulus.

All stimulus variables were fixed in a series of blocks used to estimate the angle producing 50% left judgments for a particular condition. These fixed variables included the level of the stimulus bursts, whether the target presentation was in quiet or in a background of noise, the level of the background noise, when present, and whether the stimulus was a lead-lag pair or lead-only. Within a series of blocks, only the location of the comparitor was changed between blocks. The initial angle of the comparitor stimulus was typically either 4°, 0°, or −4° relative to +45°, the 4° difference being the smallest possible given the loudspeaker size. For

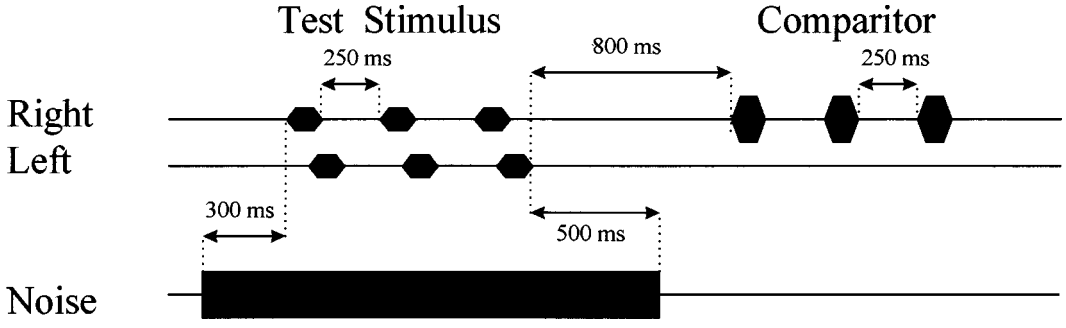

FIG. 2. Schematic diagram of presentation sequence of test stimulus, comparitor, and noise in experiment 1. The test stimulus bursts, which are not to scale with the rest of the figure, were 4 ms in duration, including 1-ms rise and fall times. The comparitor bursts were identical to the leading stimulus, but their level was always 56 dB SPL, while the level of the test stimulus was a variable in the quiet conditions. In the noise conditions, the target was fixed at 46 dB SPL and the level of the noise was varied.

wider relative angles the step change in loudspeaker azimuth was 3°. After the first block, comparitor angles were chosen with the goal of establishing a function relating percentage of left judgments to comparitor angle that clearly bracketed 50%. From two to eight comparitor locations were necessary to establish these functions, although the vast majority required three, four, or five locations, with a median of four locations. Thus 60–100 judgments were typically used to estimate the perceived location of the image for a particular condition.

In between blocks it was usually necessary for the experimenter to enter the chamber and manually move the comparitor loudspeakers to their subsequent locations, although up to three blocks (comparitor locations) could be presented without moving loudspeakers. For example, stimuli from loudspeakers at 41°, 45°, and 49° could be presented from the three different comparitor loudspeakers before the two outer comparitor loudspeakers might need to be moved. Changes in position of these two loudspeakers were always made symmetrically about 45° even if a stimulus block was needed from only one of them. This type of situation occurred when, for example, 35° was necessary to complete a function, but 55° was not. Subjects could see the loudspeakers during the experiments and could see them being moved, but they were unaware of which of the loudspeakers was used for the stimulus and which for the comparitor, or even that the loudspeakers delivering the stimuli were fixed during a block.

Preliminary calibration and threshold testing were conducted to determine the SPLs and approximate SLs of the signals and noise. With no subject in the room, a microphone (B&K 4145) fitted with a random incidence corrector was placed in the position of the center of the subjects' head. The microphone output was routed to a sound level meter (B&K 2204) set to C-weighted ''fast'' response and located outside the chamber. All ten tokens of the bursts were calibrated for both lead and lag loudspeakers by playing them repetitively with no pause in between presentations. Thresholds in quiet were estimated for the first author and three of the subjects using a Bekesy tracking procedure. One token of the three-burst lead-lag stimulus was played repetitively with a 1-s pause between presentations while subjects controlled the level by pressing and releasing a button. Burst thresholds estimated from the mean of six reversals averaged 6 dB SPL (s.d.=3.27 dB) in quiet. A Bekesy tracking procedure was also used to find continuous background noise levels required to mask three different levels of the lead-lag stimulus with the noise at 180°. Noise levels of 43, 52, and 62 dB SPL were required, respectively, to mask signal levels of 23, 33, and 43 dB SPL. This information was used to estimate the stimulus SLs in the noise conditions.[1]

Estimates of the location of the target image were obtained for 16 total conditions for each subject. The target was either lead-only or lead-lag and was presented at three sensation levels in noise and five in quiet. In the noise conditions, the target was presented at 46 dB SPL (which was 40 dB SL in quiet), and noise levels were 55, 45, and 35 dB SPL, which were estimated from the preliminary testing described above to be 10, 20, or 30 dB below that necessary to mask the lead-lag target. For convenience these noise conditions will be referred to as stimulus SLs of 10, 20, and 30 dB, with the lower SLs associated with higher noise SPLs. To compare the effects of noise from the reductions in SL produced by the noise, conditions of 10, 20, and 30 dB SL (16, 26, and 36 dB SPL) were also run in quiet. Two additional conditions in quiet were also included—40 dB SL (46 dB SPL), because it was the stimulus level for the noise conditions, and 50 dB SL (56 dB SPL), because it was the level of the comparitor.

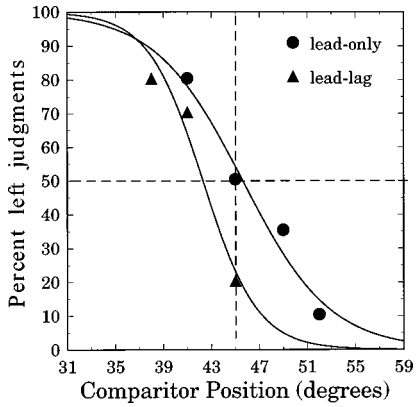

FIG. 3. Example of individual raw data for experiment 1: subject LF at 40 dB SL in quiet. Solid lines are best-fitting logistic equations using a least-squares criterion.

B. Results

1. Perceived location estimates

Two example functions relating percentage of left judgments to comparitor angle are shown in Fig. 3. The functions shown are for subject LF at 40 dB SL in quiet. Circles indicate lead-only and triangles, lead-lag. Because many of the functions were sigmoidal in shape, a logistic equation $[1/(1+e^{-(x-m)/s})]$ was fit to each function, where x was the comparitor loudspeaker angle, m is the midpoint of the function, and s is the slope parameter. Best fitting parameters m and s were estimated with a least-squares criterion using a Levenberg–Marquardt iterative solution. In the few cases where there was a series of consecutive data points at 100% or 0% left judgments, the data point in the series adjacent to the dynamic portion of the function was included in the fit, while the remainder were excluded. The fitting procedure provided good results in the majority of cases, with a median coefficient of determination (r^2) of 0.96. We considered the possibility that the slopes of the functions would less steep in noise or with precedence effect stimuli, but an analysis of variance on the parameter s revealed no significant differences. The assumed centroid of the image produced by the target was determined from the azimuth angle at which the fitted lines crossed 50% (the parameter m). In the examples shown in Fig. 3, this angle was 45.6° for the lead-only condition and 42.3° for the lead-lag condition.

Table I displays all of the estimated perceived locations of the lead-only and lead-lag stimulus conditions in quiet and in noise. The angle values are relative to 45°. The subjects can be divided into two groups based on their data for single-source conditions in quiet. Subjects DL and SF heard the

TABLE I. Estimated perceived locations in degrees (*re*: +45°) for lead-only (SS) and lead-lag (PE) stimuli in experiment 1. Data are for all subjects for all SLs in (Q) quiet and in (N) noise.

	Subject									
	DL		SF		LF		SS		JF	
SL(dB)	SS	PE	SS	PE	SS	PE	SS	PE	SS	PE
Q10	−1.47	−7.91	−4.14	−3.42	11.0	11.1	9.35	7.93	17.9	17.1
Q20	−2.61	−2.65	−2.46	−3.20	7.71	6.29	9.20	8.97	11.9	22.6
Q30	−0.72	−10.7	−0.41	−2.05	2.76	0.28	6.42	0.23	4.97	12.5
Q40	−1.32	−5.16	0.75	−2.5	0.63	−2.70	3.84	3.72	1.08	5.72
Q50	−1.04	−10.0	1.01	−2.00	2.00	−7.32	6.81	2.03	−0.15	4.14
N10	10.5	1.27	0.53	−6.46	23.5	10.8	16.8	8.68	7.74	11.5
N20	4.36	2.27	3.82	−5.73	18.9	12.6	12.9	9.87	8.39	8.19
N30	2.90	2.23	−0.12	−2.18	11.2	11.2	10.1	7.61	2.98	9.56

stimuli close to the actual 45° location across sensation levels. The other three subjects apparently heard the stimuli to the right of 45° at low SLs. The localization judgments for subject SS were also to the right at high SLs, suggesting a bias possibly related to the fixed temporal order of stimulus and comparitor. The 50 dB SL target stimulus, which was identical to the comparitor, should have produced 50% left estimates that were near 0° as it did for the other four subjects.

In noise, the lead-only data were variable, but subjects nearly always heard the stimuli to the right of 45°, with three of the subjects' data shifted more than 10 degrees to the right at the highest noise level. Shifts in perceived horizontal azimuth due to a background noise have been observed previously by Good and Gilkey (1996). For example, with a noise presented from 0 degrees azimuth and a stimulus between 0° and 45° to the right, their subjects nearly always perceived the stimulus to the right of its physical location for a +2 or +8 dB signal-to-noise ratio.

For the lead-lag stimuli in the current study, four of the subjects usually perceived the image to the left (toward the lag) relative to the single-source comparisons in quiet and noise, although one subject (JF) heard them mostly to the right. Thus the bulk of the data are consistent with the idea that the image produced by leading sound plus a simulated or real reflection is pulled slightly toward the delayed sound relative to a lead-only condition (see, for example, Rakerd and Hartmann, 1985; Shinn-Cunningham *et al.*, 1993; and Litovsky and Macmillan, 1994).

2. Computation of c

As in Litovsky and Macmillan (1994), this study used a soundfield analogy of the model of the precedence effect presented by Shinn-Cunningham *et al.* (1993). The target lead-lag stimulus was assumed to produce an image whose perceived location was a weighted combination of lead and lag. The strength of the precedence effect, or the relative weighting of the lead, was measured for each condition by comparing the perceived location of the lead-lag event with that of the lead-only event. This comparison produced the statistic, *c*, the relative weighting of the lead on a scale from 0 to 1.0 (Shinn-Cunningham *et al.*, 1993). Computation of *c* was as follows:

$$c = \frac{\mathrm{per}_{\mathrm{lead,lag}} - \mathrm{phys}_{\mathrm{lag}}}{\mathrm{per}_{\mathrm{lead\text{-}only}} - \mathrm{phys}_{\mathrm{lag}}},$$

where per is the perceived azimuthal location for the subscripted condition, and the physical location of the lag is always −45° left.

If lead-only and lead-lag stimuli are heard at the same location, then the lead completely determines the perceived location and *c* is 1.0. If the lead-lag image is heard halfway between lead-only and lag, then lead and lag contribute equally, and *c* is 0.5. Aside from the fact that loudspeaker locations were used in the computation rather than interaural time delays, the primary difference between our computation and Eq. (2) in Shinn-Cunningham *et al.* (1993) is that the *perceived* location of the lead-only image was used instead of the *physical* location of the lead (45°). This modification was necessary because, as noted in Sec. I above, the perceived and physical locations of the single-source bursts were often different when the signal was in noise or at a low SL in quiet. For example, if $\mathrm{per}_{\mathrm{lead\text{-}lag}}$ was +45° (also the lead's physical position) for a particular condition, it might be assumed that the lag had no effect. However, this would be erroneous if $\mathrm{per}_{\mathrm{lead\text{-}only}}$ for the same condition was actually +50°.[2]

3. Effect of sensation level and noise level on c

Figure 4 displays values of *c* plotted as a function of SL in quiet and in noise for the five subjects. The figure shows that *c* was generally very high in both quiet and noise conditions. These high *c* values, which were almost always above 0.9, reveal an overwhelming dominance of the leading stimulus. The effect of noise on *c* appears to be generally small and is not easily summarized across subjects. As shown in Fig. 4, the data from three subjects (SS, SF, LF) appear to show a slight trend toward decreasing *c* relative to the corresponding condition in quiet as the noise level was increased (SL was decreased). A fourth subject (DL) did not show this trend. For JF, most values of *c* were truncated to 1.0, as her localizations of the lead-lag stimuli were equal to or to the right of the lead-only stimuli (see Table I).

A two-way analysis of variance [background (quiet versus noise)×SL] was conducted for the *c* data using the three values of SL that were in common for the quiet and noise

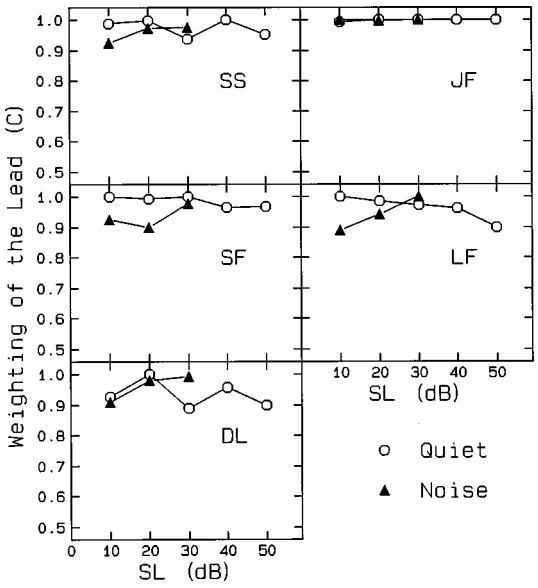

FIG. 4. Values of c plotted as a function of SL in quiet and noise for five individual subjects.

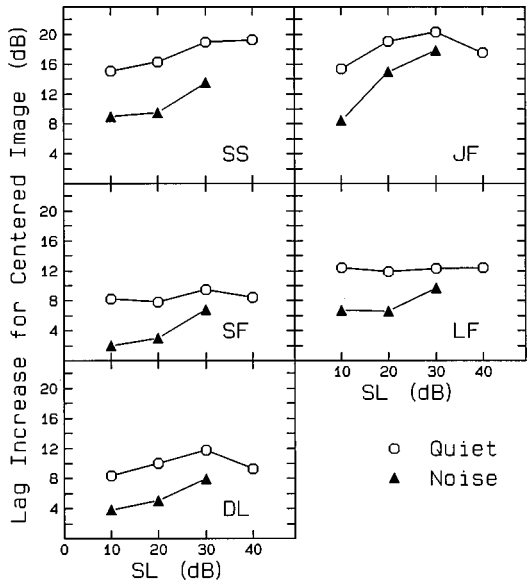

FIG. 5. The increased level of the lagging stimulus estimated to produce a centered image as function of SL in quiet and noise for five individual subjects.

conditions (10, 20, and 30 dB SL). Using an α of 0.05, neither main effect reached statistical significance. The interaction between the variables was significant [$F(2,8)=8.46$, $p=0.011$]. Follow-up t-tests revealed that the differences between quiet and noise conditions were not significant at any of the three SLs. Paired t-tests were also conducted comparing the data from each of the three noise SLs with the results from 40 dB SL in quiet, which was the level of the stimulus used in the noise conditions, with the level of significance adjusted to be $\alpha/3$ using the Bonferroni correction. None of the three tests revealed significant differences between c values obtained in quiet and noise conditions. Thus the majority of the data provide little support for the idea that the relative weighting of leading and lagging sounds in localization is significantly affected by addition of a broadband background noise. This conclusion is in apparent contrast with Leakey and Cherry's (1957) results, where in some conditions the dominance of the lead became exceedingly small when noise was introduced. This contrast is probably due either to the different stimuli (they used speech) or to the different methods of measuring the strength of the precedence effect. The purpose of experiment 2 was to sort out these possibilities by replicating their basic procedure using the present stimuli.

II. EXPERIMENT 2: TIME-INTENSITY TRADING

This experiment investigated the dominance of the leading stimulus in localization using a procedure similar to that employed by Leakey and Cherry (1957). This method determined the degree to which the level of the lagging stimulus needed to be raised in order to offset the temporal advantage of the leading stimulus, producing an image centered at 0° azimuth.

A. Method

Stimuli were the same noise-burst triads used in experiment 1, but only the lead-lag conditions were presented. The noise, when present, was continuous. A Bekesy tracking procedure was used to find the amount of lead-lag level difference necessary for the combined image (or dominant image if there was more than one) to cross 0° azimuth. During a tracking run the noise-bursts triads were presented repetitively with a 500-ms pause between triads. The subjects' task was to press and hold down a button as long as the image was heard to the left of a visual reference used to mark 0° azimuth, and immediately release the button when the image was heard to the right of midline. The initial level of the lag burst was always equal to the level of the lead burst, which was fixed within a tracking run. The level of the lag burst was programmably controlled, decreasing when the button was held and increasing when it was released. The run was terminated after 12 reversals of the tracking and the last 6 reversals were averaged. The procedure was repeated for four quiet conditions (the lead at 10, 20, 30, and 40 dB SL) and three noise conditions (10, 20, and 30 dB SL) with the lead signal at 46 dB SPL. The same detection and masking thresholds from experiment 1 were used to compute the SLs, so the SPLs of the lead stimulus and the noise were the same as in experiment 1.

B. Results

The average results from three tracking runs for each subject and condition are shown in Fig. 5. For all five subjects the increase in the level of the lag necessary to produce a centered image was less in noise than it was in quiet. The lag-level increases obtained in noise were somewhat larger than the minimum of 2 dB reported by Leakey and Cherry (1957), but they still represent a substantial reduction from the values obtained in quiet. A two-way analysis of variance similar to that conducted for experiment 1 revealed a significant difference between quiet and noise backgrounds over the range of 10–30 SL [$F=(1,4)=225.19$, $p<0.001$]. The main effect of SL also showed significant differences [$F(2,8)=12.64$, $p=0.003$], as did the background×SL inter-

action [$F(2,8)=9.22$, $p=0.008$]. Follow-up t-tests revealed that differences between quiet and noise conditions at all three SLs were statistically significant at the 0.017 level ($\alpha/3$). Paired t tests comparing the results from each of the three noise SLs with the results at 40 dB SL in quiet (the stimulus level used for the noise conditions) revealed statistically significant differences for the 10 dB SL [$t(4)=-7.78$, $p=0.001$] and 20 dB SL [$t(4)=-4.66$, $p=0.01$] noise conditions, but not the 30 dB SL condition [$t(4)=2.17$, $p=0.096$].

In summary, the data from this experiment are in agreement with those reported by Leakey and Cherry (1957). When measured as the level of the lagging stimulus necessary to offset the temporal advantage of the leading stimulus, the precedence effect appears to be substantially weakened by broadband noise.

III. EXPERIMENT 3: ECHO THRESHOLD

The purpose of experiment 3 was to measure the effect of background noise on echo threshold, which was defined as the delay at which subjects reported hearing a second sound in the vicinity of the lag loudspeaker. Previous reports by Thurlow and Parks (1961) and Babkoff and Sutton (1966) led to the expectation that echo threshold would be reduced by noise, but data quantifying the effect have not been presented previously for a sound field environment.

A. Method

The stimuli were ten tokens of digitally synthesized 4-ms noise bursts, as in experiments 1 and 2, but lead-lag pairs of bursts were presented with eight different delays ranging from 2 to 16 ms in steps of 2 ms. Unlike the previous two experiments only one, rather than three, pairs of bursts was presented on each trial. This is because previous research has shown that the echo threshold often builds up with repeated stimulation (e.g., Clifton and Freyman, 1989), and it might be difficult for subjects to make a judgment if perception was changing across three repetitions. The lead was always presented from 45° to the right and the lag from 45° to the left. The noise, when present, was continuous. A subjective task was used to find echo threshold. Recent research on echo threshold has been conducted using an objective method where the subject's task is to discriminate the direction of 10 degree shifts in the position of the lag loudspeaker (Freyman *et al.*, 1991; Clifton *et al.*, 1994; Grantham, 1996). Freyman *et al.* (1991) found that there was good agreement between performance on this type of task and subjective audibility of the echo as a separate event. However, pilot testing with the current stimuli revealed that the discrimination task was difficult to perform in noise, even when the lag was clearly audible. Therefore a subjective echo threshold task was employed (as in Clifton and Freyman, 1989), where after each trial subjects were asked to report whether or not they heard a sound in the vicinity of the lag loudspeaker.

Echo threshold measurements were made at 10, 20, 30, 40, and 50 dB SL in quiet and 10, 20, and 30 dB SL in noise. The same detection thresholds obtained for experiment 1 were used to compute the sensation levels, so the SPLs of the stimuli were the same as those in experiment 1. Four blocks of 40 trials were presented for each of the 8 conditions. Within each block, all eight delays were presented five times in a random order. Across the blocks, each subject made a total of 20 judgments per delay per condition.

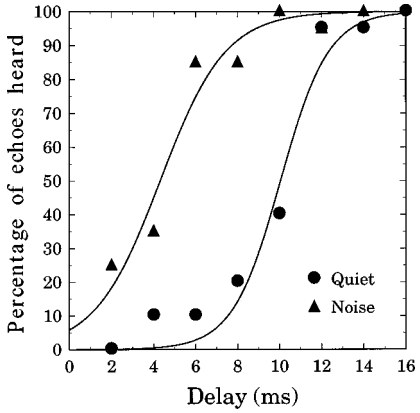

FIG. 6. Example of raw data from experiment 3 for one subject: Subject SS at 20 dB SL. Solid lines are best-fitting logistic equations using a least-squares criterion.

B. Results

An example pair of functions is shown in Fig. 6 for subject SS. The percentage of trials on which an echo was reported is plotted as a function of lag-burst delay for equivalent SLs in quiet and in noise. Like what is shown in figure, for every subject and condition the functions in noise were shifted to the left relative to those in quiet, indicating that noise increased the audibility of echoes. The functions were fitted with logistic equations using the methods described in experiment 1. Echo thresholds were estimated from the parameter m in the equation, which is the delay at which the functions reached 50% echoes reported.

The echo threshold data shown in Fig. 7 indicate that at

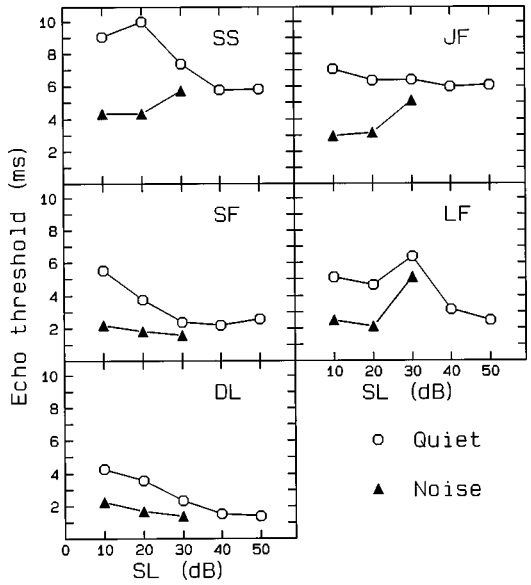

FIG. 7. Echo threshold as function of SL in quiet and noise for five individual subjects.

equivalent SLs echo thresholds for all five subjects were lower in noise than they were in quiet. The difference appears to be greater at 10 and 20 dB SL than it does at 30 dB SL. Analysis of variance conducted on the 10–30 SL data revealed a significant main effect of noise [$F(1,4)=35.98$, $p=0.004$], but not SL [$F(2,8)=0.25$, $p=0.785$]. The background×SL interaction was significant [$F(2,8)=13.22$, $p=0.003$]. Follow-up t tests revealed significant differences between quiet and noise conditions at all three SLs. However, echo threshold for none of the three noise conditions was significantly different from the results for 40 dB SL in quiet, where echo thresholds were consistently lower than those obtained in quiet at the lower SLs. Thus the tendency for noise to reduce echo threshold was only observed in the equal SL comparison.

IV. DISCUSSION

The current data generally support previous anecdotal and published reports indicating that the influence of the lagging sound in a lead-lag stimulus is strengthened by the introduction of background noise. However, the influence of noise was not shown to be as robust as might have been expected from earlier research. In experiment 1, the weighting of the lead c was slightly reduced by noise in several of the subjects, but the differences in the group data did not reach statistical significance. In general, the location of the image produced by lead-lag stimuli was still dominated by the lead even in noise. The relatively small effect of noise on c cannot be compared directly with any published data, although the statement by Thurlow and Parks (1961) that noise moved the image ''toward the median plane'' (p. 11) seems to imply that the shift in the image produced by noise was somewhat larger than observed here. The effect of noise was much more consistent in experiment 2, in which the strength of the precedence effect was measured by increasing the level of the lagging stimulus by an amount necessary to offset the temporal advantage of the lead. Smaller increases in the level of the lag were necessary when noise was added, especially at the higher noise levels. These findings are consistent with those of Leakey and Cherry (1957).

The differences in results between experiments 1 and 2 suggest that under some conditions the methods are not comparable measures of the precedence effect. Experiment 1 is a more direct evaluation of the influence of noise on the weighting of lead and lag stimuli in localization in that it is most unambiguously a localization experiment. While experiment 2 might also be considered a localization experiment, it suffers from the fact that echoes are more intense than the first arriving sound, an unecological condition. An additional problem in interpretation is that the introduction of noise also appears to increase the effect of changing stimulus intensity for simple monaural stimuli. Noise that partially masks a signal produces a loudness recruitmentlike phenomenon in normal-hearing listeners in which the loudness of a stimulus increases sharply as intensity is increased at low SLs in a noise background (Stevens and Guirao, 1967). It is possible that the finding in experiment 2 that the presence of noise increases the effect of changing the intensity of the lag stimulus is related to the mechanisms responsible for the recruitment phenomenon, and may have little to do with the precedence effect. Finally, we should note that in experiment 2 (and experiment 3 also) the noise was continuous, while in experiment 1 it was gated off for a period during each trial so that the comparitor could be heard in quiet. Although informal listening in continuous noise to the stimuli presented in experiment 1 suggested that this was not a source of the differences in results between the experiments, no formal evaluation was conducted.

The results of the third experiment displayed in Fig. 7 indicate that broadband background noise does appear to lower echo threshold substantially and consistently. For each subject and sensation level, the echo threshold in noise was lower than that obtained in quiet. These data are generally in agreement with Thurlow and Parks (1961) and Babkoff and Sutton (1966). One difference from the previous studies is that in the current study large differences were observed only for comparisons at equivalent SLs. The original observation of the effect of talking by Thurlow and Parks (1961), their brief report of the follow-up experiment with a noise background, and data from Fig. 11 in Babkoff and Sutton (1966) together lead to a prediction that the introduction of a broadband noise would increase the audibility of echoes for a fixed SPL stimulus. This effect can be examined in the current data by comparing echo thresholds in noise with those obtained at 40 dB SL in quiet, which was the stimulus level used for the noise conditions. Although the individual data shown in Fig. 7 include several examples of noise lowering echo threshold relative to 40 dB SL in quiet, comparisons of the means revealed nonsignificant differences. In strong agreement with Babkoff and Sutton (1966), however, the current data displayed in Fig. 7 show that any reductions in echo threshold produced by noise are not due to the lowering of sensation level, which in quiet clearly tends to increase echo threshold relative to 40 dB SL.

The data in Fig. 7 indicating that some subjects had very low echo thresholds in noise and at high SLs in quiet suggests that even with the short 2-ms delay, the stimuli used in experiments 1 and 2 were near echo threshold for some subjects and conditions. The three repetitions of the bursts in those experiments may have raised echo threshold (see Clifton and Freyman, 1989). However, the buildup of echo suppression in the presence of noise has not been evaluated. The conservative assumption is that some subjects would have reported hearing an echo during a lead-lag trial in the precedence localization experiments had they been listening for it. From the current data it is not possible to know what effect this might have had on the localization comparison or time-intensity trading results.

The combined results of these studies provide a starting point for considering future work on the influence of noise on the precedence effect. Further research might focus most beneficially on the influence of noise on fusion of a leading sound with simulated or real reflections, as opposed to its effect on localization. Experiment 1 provided little evidence that the noise influences localization of a lead-lag pair substantially more than it does a single-source stimulus. On the other hand, the echo threshold results in experiment 3 largely support earlier related studies showing that noise tends to

break down fusion of lead and lag. To find out why this occurs it will be important of vary parameters such as the frequency content of the noise and signal [which Babkoff and Sutton (1966) varied in some conditions], the location of the noise relative to the signals, and whether the noise is itself delivered from one source or multiple sources. With regard to the last consideration it is important to note that both Thurlow and Parks (1961) and the current study delivered the background noise from a single loudspeaker in a room designed to limit reverberation, while the stimulus itself was presented from two loudspeakers with a delay between them, which simulated a reflection. Thus noise and signal provided inconsistent information about the acoustics of the room. Similar inconsistencies have been shown to break down echo suppression in past studies (Clifton *et al.*, 1994; Yost and Guzman, 1996; Clifton and Freyman, 1997; McCall *et al.*, 1998). Yet to be determined is whether noise also disrupts echo suppression in the more realistic case when it provides acoustic information consistent with the target stimulus.

ACKNOWLEDGMENTS

This research was part of the doctoral dissertation written by the first author. The work was supported by NIH Grant No. DC-01625.

[1]As quiet and masking thresholds were obtained with the lead-lag stimuli, they would be expected to be slightly different with lead-only stimuli. However, no adjustments in the reported SLs were made.

[2]Similarly, data could have been collected for the lag-only condition or, alternatively, an assumption of shifts in lag-only that were symmetric with the lead-only data could have been made. However, these would have produced only very small differences in the values of c. For the example where the estimated perceived location of the lead-only stimulus is $+50°$ and the lead-lag stimulus is $+45°$, the assumption of the perceived location of the lag stimulus being $-50°$ (as opposed to its physical location of $-45°$) would change c only from .947 (90°/95°) to .95 (95°/100°).

ANSI (**1989**). ANSI S3.6-1989, ''Specifications for audiometers'' (American National Standards Institute, New York).

Babkoff, H., and Sutton, S. (**1966**). ''End point of lateralization for dichotic clicks,'' J. Acoust. Soc. Am. **41**, 87–102.

Buell, T. N., Trahiotis, C., and Bernstein, L. R. (**1991**). ''Lateralization of low-frequency tones: Relative potency of gating and ongoing interaural delays,'' J. Acoust. Soc. Am. **90**, 3077–3085.

Clifton, R. K., and Freyman, R. L. (**1989**). ''Effect of click rate and delay on breakdown of the precedence effect,'' Percept. Psychophys. **46**, 139–145.

Clifton, R. K., and Freyman, R. L. (**1997**). ''The precedence effect: Beyond echo suppression,'' in *Binaural and Spatial Hearing in Real and Virtual Environments*, edited by R. H. Gilkey and T. B. Anderson (Lawrence Erlbaum, Hillsdale, NJ).

Clifton, R. K., Freyman, R. L., Litovsky, R. Y., and McCall, D. (**1994**). ''Listener expectations about echoes can raise or lower echo threshold,'' J. Acoust. Soc. Am. **95**, 1525–1533.

Freyman, R. L., Clifton, R. K., and Litovsky, R. Y. (**1991**). ''Dynamic processes in the precedence effect,'' J. Acoust. Soc. Am. **90**, 874–884.

Freyman, R. L., Zurek, P. M., Balakrishan, U., and Chiang, Y. C. (**1997**). ''Onset dominance in lateralization,'' J. Acoust. Soc. Am. **101**, 1649–1659.

Good, M. D., and Gilkey, R. H. (**1996**). ''Sound localization in noise: The effect of signal-to-noise ratio,'' J. Acoust. Soc. Am. **99**, 1108–1117.

Grantham, D. W. (**1996**). ''Left–right asymmetry in the buildup of echo suppression in normal-hearing adults,'' J. Acoust. Soc. Am. **99**, 1118–1123.

Guttman, N., Van Bergeijk, W. A., and David, E. E. (**1960**). ''Monaural temporal masking investigated by binaural interaction,'' J. Acoust. Soc. Am. **32**, 1329–1336.

Hall, J. L. II (**1959**). ''A psychoacoustic study of the mechanism of binaural fusion,'' MS thesis, MIT.

Leakey, D. M., and Cherry, E. C. (**1957**). ''Influence of noise upon the equivalence of intensity differences and small time delays in two-loudspeaker systems,'' J. Acoust. Soc. Am. **29**, 284–286.

Litovsky, R. Y., and Macmillan, N. A. (**1994**). ''Sound localization precision under conditions of the precedence effect: Effects of azimuth and standard stimuli,'' J. Acoust. Soc. Am. **96**, 752–758.

McCall, D. D., Freyman, R. L., and Clifton, R. K. (**1998**). ''Sudden changes in room acoustics influence the precedence effect,'' Percept. Psychophys. **60**, 593–601.

Rakerd, B., and Hartmann, W. M. (**1985**). ''Localization of sound in rooms, II: The effects of a single reflecting surface,'' J. Acoust. Soc. Am. **78**, 524–533.

Shinn-Cunningham, B. G., Zurek, P. M., and Durlach, N. I. (**1993**). ''Adjustment and discrimination measurements of the precedence effect,'' J. Acoust. Soc. Am. **93**, 2923–2932.

Stevens, S. S., and Guirao, M. (**1967**). ''Loudness functions under inhibition,'' Percept. Psychophys. **2**, 459–465.

Thurlow, W. R., and Parks, T. E. (**1961**). ''Precedence-suppression effects for two click sources,'' Perceptual and Motor Skills **13**, 7–12.

Yost, W. A., and Guzman, S. (**1996**). ''Auditory processing of sound sources: Is there an echo in here?'' Current Directions in Psychological Science **5**, 125–131.

Range dependence of the response of a spherical head model

Richard O. Duda
Department of Electrical Engineering, San Jose State University, San Jose, California 95192

William L. Martens
Human Interface Lab, University of Aizu, Aizu-Wakamatsu 965-80, Japan

(Received 28 July 1997; revised 1 July 1998; accepted 2 July 1998)

The head-related transfer function (HRTF) varies with range as well as with azimuth and elevation. To better understand its close-range behavior, a theoretical and experimental investigation of the HRTF for an ideal rigid sphere was performed. An algorithm was developed for computing the variation in sound pressure at the surface of the sphere as a function of direction and range to the sound source. The impulse response was also measured experimentally. The results may be summarized as follows. First, the experimental measurements were in close agreement with the theoretical solution. Second, the variation of low-frequency interaural level difference with range is significant for ranges smaller than about five times the sphere radius. Third, the impulse response reveals the source of the ripples observed in the magnitude response, and provides direct evidence that the interaural time difference is not a strong function of range. Fourth, the time delay is well approximated by well-known ray-tracing formula due to Woodworth and Schlosberg. Finally, except for this time delay, the HRTF for the ideal sphere appears to be minimum-phase, permitting exact recovery of the impulse response from the magnitude response in the frequency domain. [S0001-4966(98)00111-8]

PACS numbers: 43.66.Qp, 43.66.Pn 43.20.Fn [RHD]

LIST OF SYMBOLS

a	radius of the sphere (m)
c	ambient speed of sound (m/s)
f	frequency (Hz)
h	head-related impulse response
h_m	mth-order spherical Hankel function
h'_m	the derivative of h_m with respect to its argument
H	head-related transfer function relative to free field
H_ε	head-related transfer function relative to source
i	$\sqrt{-1}$
j_m	mth-order spherical Bessel function
k	acoustic wave number (/m)
n_m	mth-order spherical Neumann function
p_{ff}	free-field pressure at the center of the sphere (kg/m^2)
p_s	pressure on the surface of the sphere (kg/m^2)
p_ε	pressure at a small sphere surrounding the source (kg/m^2)
P_m	Legendre polynomial of degree m
Q_m	mth-order modified spherical Hankel function
r	distance from the center of the sphere to the source (m)
r_ε	radius of a small sphere surrounding the source
S_ω	magnitude of flow from an ideal point source (m^3/s)
t	time (s)
Δt	time between arrival at observation point and sphere center (s)
$\Delta\tau$	normalized Δt
θ	angle of incidence (rad)
θ_0	angle for tangent incidence (rad)
λ	wavelength (m)
μ	normalized frequency
ρ	normalized distance to the source
ρ_0	density of air (kg/m^3)
τ	normalized time
ω	radian frequency (rad/s)

INTRODUCTION

This paper is concerned with the range dependence of the response of an ideal rigid sphere to a point sound source. The purpose of this study was to gain a better understanding of the behavior of the head-related transfer function (HRTF) at close range. It is hoped that these results will serve as a guide to those engaged in the study of human HRTFs, including their measurement and analysis, and to those engaged in creating spatial sound stimuli by convolving audio signals with these HRTFs. Given the paucity of experimental measurements of HRTF variation at close range, it seemed particularly important to have a foundation upon which to base further acoustical studies of this spatial region. Therefore, the investigation reported in this paper included the numerical evaluation of a theoretical model, the collection of related acoustical measurement data, and the comparison of the theoretical solution to the experimental results.

A classical spherical model of the human head was chosen for this investigation for the traditional reasons—its response can be analyzed mathematically, and the theoretical solution can be evaluated numerically. Even though this model is quite idealized, it exhibits features similar to those observed in the close-range behavior of the human HRTF. For example, sounds from a source that is very close to one's ear are not only louder but also contain relatively more low-frequency energy than do sounds from a distant source. The

simplest model that explains these effects approximates the human head by a rigid sphere of the same average radius and approximates the sound impinging on the sphere as if it were generated by a point source. While this idealization is restricted to relatively low frequencies and obviously becomes problematic very close to the surface of the head, a quantitative understanding of its behavior provides insight into the more complex behavior of the HRTF for an actual human head.

To compute the response at the surface of the sphere for a sound source located at an arbitrary distance from the surface of the sphere, a modification was made to an algorithm for computing the classical solution for a source infinitely far from the sphere. The behavior of the solution was examined in both the frequency domain (the HRTF) and the time domain (the head-related impulse response, or HRIR). The time-domain solution provides insight into some otherwise puzzling behavior of the HRTF. The adequacy and accuracy of the model were confirmed by comparing the numerical results with the results of a corresponding series of impulse response measurements made using an actual physical sphere.

I. THE THEORETICAL SOLUTION

A. Expansion in spherical harmonics

The frequency-domain solution for the diffraction of an acoustic wave by a rigid sphere, which is presented in many textbooks, was obtained by Lord Rayleigh at the end of the 19th century (Strutt, 1904, 1945). If the flow for a complex sinusoidal point source is of the form $S_\omega e^{-i\omega t}$, then the free-field pressure at a distance r from the source is given by

$$p_{ff}(r,\omega,t) = -i\omega \frac{\rho_0 S_\omega}{4\pi r} e^{i(kr-\omega t)}, \tag{1}$$

where $k=\omega/c$.[1] Because multiplication by $-i\omega$ in the frequency domain is equivalent to differentiation in the time domain, this implies that if the flow is a unit step function, the free-field pressure is a Dirac impulse wave whose strength varies inversely with the distance to the source.

The presence of the sphere diffracts the sound wave and modifies the pressure field. Most authors give only Rayleigh's solution for the case where the source is infinitely distant from the center of the sphere. Rabinowitz *et al.* (1993) present the solution for the pressure on the surface of the sphere due to a sinusoidal point source at any range r greater than the sphere radius a. With minor notational changes, their solution can be written as

$$p_s(r,a,\omega,\theta,t) = \frac{i\rho_0 c S_\omega}{4\pi a^2} \Psi e^{-i\omega t}, \tag{2}$$

where Ψ is the infinite series expansion

$$\Psi = \sum_{m=0}^{\infty} (2m+1) P_m(\cos\theta) \frac{h_m(kr)}{h_m'(ka)}, \quad r>a. \tag{3}$$

Here θ is the angle of incidence, the angle between the ray from the center of the sphere to the source and the ray to the measurement point on the surface of the sphere, and normal incidence corresponds to $\theta=0°$. It is conventional to use the time $2\pi a/c$ that it takes for a wave to travel once around the sphere to define the normalized frequency μ,

$$\mu = ka = f\frac{2\pi a}{c}. \tag{4}$$

Define the normalized distance to the source ρ by

$$\rho = \frac{r}{a}, \tag{5}$$

and define the transfer function H by

$$H = \frac{p_s}{p_{ff}}. \tag{6}$$

Then

$$H(\rho,\mu,\theta) = -\frac{\rho}{\mu} e^{-i\mu\rho}\Psi, \tag{7}$$

where

$$\Psi(\rho,\mu,\theta) = \sum_{m=0}^{\infty} (2m+1) P_m(\cos\theta) \frac{h_m(\mu\rho)}{h_m'(\mu)}, \quad \rho>1. \tag{8}$$

This ''head-related transfer function'' H relates the pressure that would be present at the center of the sphere in free field to the pressure that is actually developed at the surface of the sphere.[2] The inverse Fourier transform of H is the normalized ''head-related impulse response'' h [which should not be confused with the m th-order spherical Hankel function h_m in Eq. (8)].

B. Limiting cases

The behavior of the transfer function as the normalized range ρ becomes arbitrarily large can be obtained by using the asymptotic formula (see Morse and Ingard, 1968, Chap. 7.2)

$$h_m(x) = j_m(x) + i n_m(x) \rightarrow \frac{e^{i(x-[(m+1)/2]\pi)}}{x}. \tag{9}$$

This leads to

$$H(\infty,\mu,\theta) = \frac{1}{\mu^2} \sum_{m=0}^{\infty} \frac{(-i)^{m-1}(2m+1)P_m(\cos\theta)}{h_m'(\mu)}, \tag{10}$$

which is Rayleigh's solution for an infinitely distant source. The low-frequency behavior can be obtained from the first two terms in this series, which leads to the well-known result

$$H(\infty,\mu,\theta) \approx 1 - i\tfrac{3}{2}\mu\cos\theta. \tag{11}$$

Thus, at low frequencies, the magnitude of H is essentially unity, and the phase angle is approximately $-\frac{3}{2}\mu\cos\theta$, which corresponds to a group delay of $-\frac{3}{2}a\cos\theta/c$ (Kuhn, 1977).

Since both Eqs. (8) and (10) converge more and more slowly as μ increases, the high-frequency behavior is less obvious. Kuhn (1977) obtained the high-frequency solution by employing an alternative ''creeping wave'' expansion.

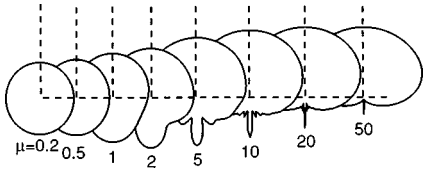

FIG. 1. Polar plots of the magnitude of the transfer function for an infinitely distant source. A bulge in the response starts to become distinct when the normalized frequency is around 1, i.e., when the wavelength equals the circumference of the sphere. As the frequency increases, the response at the front of the sphere approaches twice the free-field response. In addition, the response on the shadowed side of the sphere becomes progressively smaller, except for the celebrated ''bright spot'' at the back of the sphere.

For the special case of normal incidence ($\theta=0$ degrees), one can argue on physical grounds that when the wavelength is small compared to the radius of the sphere, the solution must reduce to that of a plane wave normally incident on a rigid plane surface, where the pressure at the surface becomes twice the free-field pressure. Thus,

$$|H(\infty,\infty,0)|=2. \tag{12}$$

These special case results serve to define interesting limits of the general solution.

II. BEHAVIOR OF THE THEORETICAL SOLUTION

A. Frequency response—distant range

In general, one must use numerical methods to evaluate the transfer function $H(\rho,\mu,\theta)$ for arbitrary values of ρ, μ and θ. Bauck and Cooper (1980) developed a simple but effective algorithm for evaluating the solution for an infinitely distant source. Formulas extending their algorithm to the general case of arbitrary range are given in Appendix A, and a pseudocode implementation of the resulting algorithm is given in Appendix B. This implementation was used to investigate the behavior of the transfer function computationally.

Consider first the well-known results for an infinitely distant source (Strutt, 1904). Figure 1 shows a polar plot of $|H(\infty,\mu,\theta)|$ as a function of the angle of incidence for several different frequencies. As Eq. (11) requires, the response at low frequencies is not directionally dependent, with $|H(\infty,\mu,\theta)|\approx 1$ until the normalized frequency nears unity. Above that frequency, the response around the front of the sphere begins to increase noticeably, and the response around most of the back decreases. However, the minimum response does not occur at the very back. Instead, the very back of the sphere exhibits the so-called ''bright spot,'' which can be explained by arguing that all the waves propagating around the sphere arrive at that point in phase. At very high frequencies, the bright-spot lobe becomes extremely narrow, and the back of the sphere is effectively in a sound shadow. By contrast, the pressure at the front of the sphere is doubled, in agreement with Eq. (12).

Figure 2 shows this same information plotted on a dB scale against normalized frequency for 37 different values of angle of incidence. All of the curves approach 0 dB at low frequencies. The top curve in Fig. 2 shows the 6-dB increase or doubling in magnitude for frontal incidence at high frequencies. The response is approximately 3 dB above the free-field value when the normalized frequency is unity, which supports the statement that the point $\mu=1$ separates low from high frequencies. For the standard 8.75-cm head radius (Hartley and Fry, 1921), this corresponds to about 625 Hz. As the angle of incidence increases, this high-frequency rise changes to a high-frequency rolloff, with the maximum attenuation occurring around $\theta=150$ degrees. The strong interference ripples in the response are visually striking. By contrast, the response at the back of the sphere stays quite flat out to $\mu\approx 20$, which is another manifestation of the bright spot.

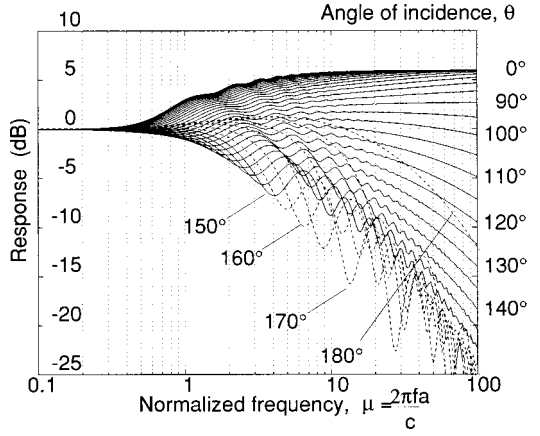

FIG. 2. Magnitude response for an infinitely distant source. Roughly speaking, the response is flat when the angle of incidence is around 100 degrees, exhibits a 6-dB boost at high frequencies near the front of the sphere, and–except for the bright spot at the very back–falls off with frequency around the back of the sphere. Interference effects caused by waves propagating in various directions around the sphere introduce ripples in the response that are quite prominent on the shadowed side.

B. Frequency response—range dependence

The responses at 0 and 150 degrees can be thought of as providing rough bounds on the frequency response. Figure 3 shows that these bounds separate as the source approaches

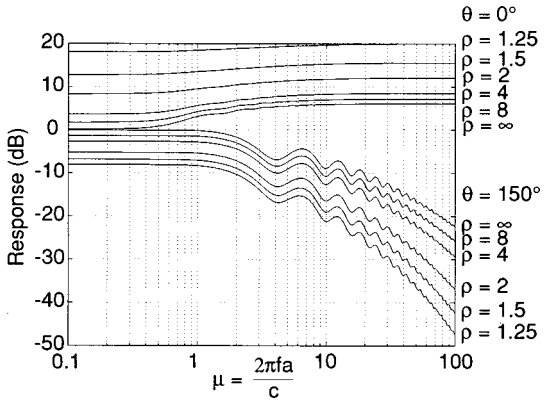

FIG. 3. Effect of range on the magnitude response. (The responses shown are relative to the free-field pressure at the center of the sphere, so that the general inverse range effect is not included.) These curves provide rough bounds on the response at different angles of incidence, with the maximum occurring at $\theta=0$ degrees and the minimum around $\theta=150$ degrees. Note that as the source approaches the sphere, the response increases on the near side and decreases on the far side. This results in the possibility of having large interaural level differences at low frequencies.

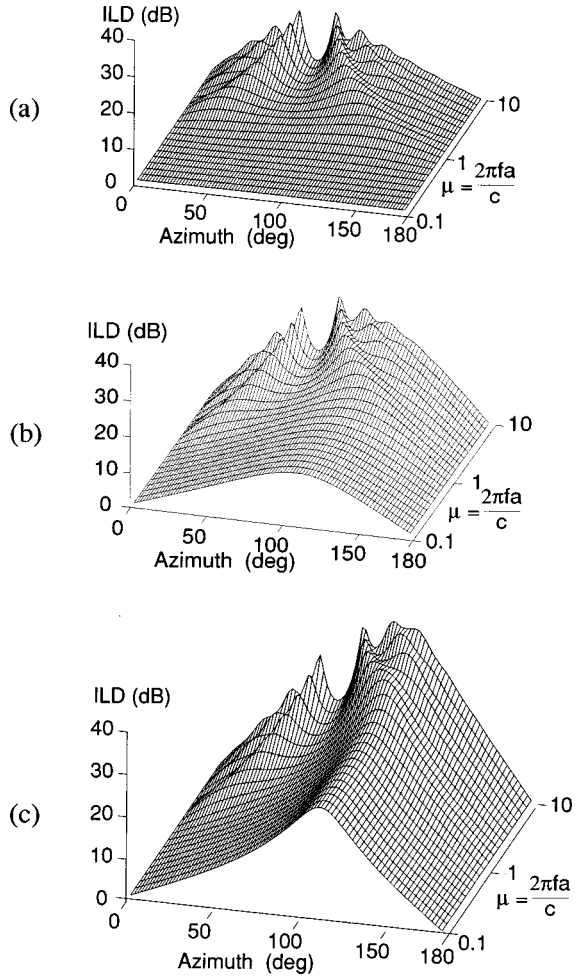

FIG. 4. The interaural level difference (ILD) versus azimuth, assuming that the ears are located at $\theta=\pm 100$ degrees; (a) $\rho=100$, (b) $\rho=2$, (c) $\rho=1.25$. The maximum low-frequency ILD is negligible for a distance source, but becomes quite large as the source approaches the sphere.

the sphere. The response on the near side increases and the response on the far side decreases for all frequencies. It is not surprising that the near-side response gets quite large as the source approaches the sphere, but somewhat less intuitive to see that the response on the far side drops below the free-field response, even at low frequencies.

Another general characteristic is that the difference between the responses at low and high frequencies diminishes on the near side, but increases on the far side. For example, when $\rho=1.25$, the extra high-frequency rise at the front of the sphere, instead of being 6 dB, is only about 2 dB. This is consistent with the informal experience of a relative increase in the low-frequency content of close sound sources.

These two effects combined imply that the low-frequency interaural level difference (ILD) becomes even further exaggerated as the source approaches one ear. As Blauert (1997) points out, human ears are not located across a diameter, but are set back about 10 degrees. Figure 4(a) shows the ILD for an infinitely distant source, assuming that the ''ears'' are located at $\theta=\pm 100$ degrees. Note that the ILD is quite small for normalized frequencies below unity. By contrast, when $\rho=2$, the low-frequency ILD exceeds 10 dB [see Fig. 4(b)], and when $\rho=1.25$ it exceeds 20 dB [see Fig. 4(c)]. Figure 5 shows that the ILD at an azimuth of 100

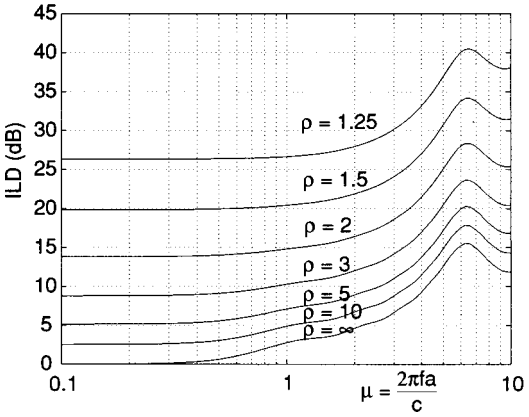

FIG. 5. The ILD when the azimuth to the sound source is 100 degrees. Note that very substantial low-frequency ILD's occur as the source approaches the sphere.

degrees becomes very large as ρ approaches unity, even at low frequencies. This development of a large ILD at low frequencies would seem to be a major cue indicating that a sound source is very close.

C. Impulse response

While the phase response contains useful information about the temporal response, it is more illuminating to invert the transfer function $H(\rho,\mu,\theta)$ and obtain the normalized HRIR $h(\rho,\tau,\theta)$:

$$h(\rho,\tau,\theta)=\int_{-\infty}^{\infty} H(\rho,\mu,\theta)e^{-i2\pi\mu\tau}\,d\mu, \tag{13}$$

where τ is the normalized time given by[3]

$$\tau=\frac{ct}{2\pi a}. \tag{14}$$

Figure 6 shows the results of evaluating this integral numerically for the case of an infinitely distant source. Many features of the frequency response are reflected in the impulse response. For example, notice how the amplitude of the pulse drops off and its width increases as the angle of incidence

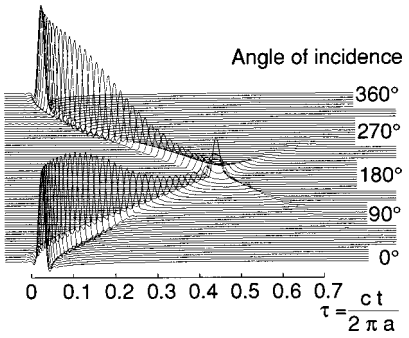

FIG. 6. The theoretical impulse response for an infinitely distant source. The overshoot for small angles of incidence corresponds to the 6-dB boost of high frequencies. As the angle of incidence increases, the pulse is delayed and low-pass filtered by head shadow. Near the back, the effect of waves traveling around the other ''side'' of the sphere becomes more visible. This is the source of the interference ripples in the magnitude response. The ''bright spot'' emerges where the various waves arrive at the back of the sphere in phase.

increases, corresponding to the rolloff in response at high frequencies. The overshoot (negative dip in response) that appears for incidence angles below 90 degrees corresponds to the fact that high frequencies are boosted at those angles.

As the angle of incidence approaches 180 degrees, the bright spot becomes prominent in the HRIR. Moreover, the visual appearance of the graph strongly suggests that the impulse ''ridge'' continues on through the bright spot. One can interpret the overall response as being composed of two ridges, a lower ridge that is due to a wave propagating around one ''side'' of the sphere, and an upper ridge that is due to a wave propagating around the other ''side,'' with the bright spot occurring where these two waves join and reinforce one another. Of course, this is a very crude approximation. In particular, adding just these two ridges does not accurately account for either the height of the bright spot or the nearby behavior. However, it explains why the response for incidence angles between 150 and 170 degrees contains two prominent pulses in the time domain, and it qualitatively explains the corresponding pattern of ripples in the frequency domain at all incidence angles.

Figure 7 shows the HRIR for $\rho=1.25$. As one would expect from Fig. 3, as the source is brought closer to the sphere, the response becomes stronger on the near side and weaker and broader on the far side. There is also a difference in the arrival times. In particular, the difference between arrival at the near side and arrival at the far side is smaller at long ranges (Fig. 6) than at close range (Fig. 7).

D. Time delay and minimum-phase reconstruction

There are several ways to define the arrival time of a pulse. While group delay is frequently employed, it is frequency dependent, being significantly greater at low frequencies than at high frequencies (Kuhn, 1977, 1987). With experimentally measured data, it is convenient simply to use $\Delta t_{0.15}$, the time at which the pulse first exceeds 15% of its maximum amplitude; this same definition is used to compute the normalized arrival time for $h(\rho,\tau,\theta)$, $\Delta\tau=c\Delta t_{0.15}/2\pi a$.

The open circles in Fig. 8 show how this normalized arrival time varies with the angle of incidence for two different normalized ranges, $\rho=1.25$ and $\rho=100$. These two

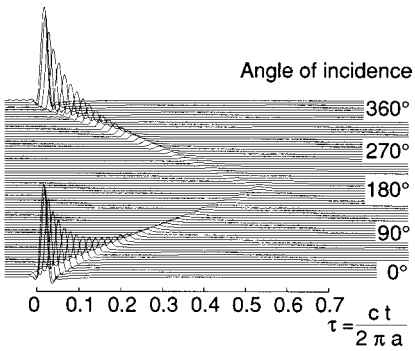

FIG. 7. The theoretical impulse response for a source that is close to the surface of the sphere ($\rho=1.25$). The response drops quite rapidly with azimuth, and the maximum time delay is longer than in Fig. 6.

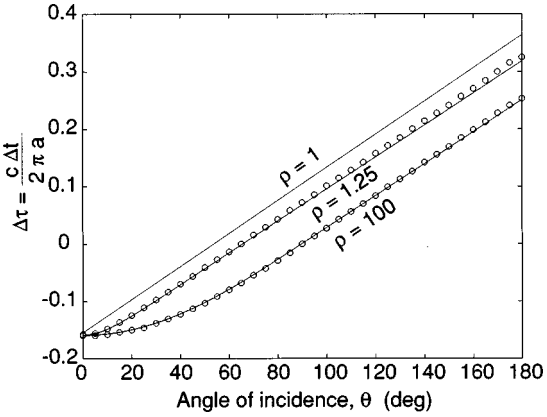

FIG. 8. The delay in arrival time relative to free-field arrival at the center of the sphere. The solid lines are from the Woodworth/Schlosberg ray-tracing formula. The open circles are computed from the theoretical solution as the first time that the impulse response exceeds 15% of its maximum value.

curves are close to the curves for $\rho=1$ and $\rho=\infty$, and thus more or less bound the results at intermediate ranges. Since $\Delta\tau$ is the (normalized) difference between the time of arrival at the surface of the sphere and the free-field time of arrival at the center of the sphere, when the angle of incidence θ is zero, $\Delta\tau$ is negative and is independent of range. At larger incidence angles, $\Delta\tau$ becomes larger as the source approaches the sphere. In addition, the interaural time difference (ITD), which can be computed from $\Delta\tau(\theta+100$ degrees$)-\Delta\tau(\theta-100$ degrees$)$, also becomes larger as the source approaches the sphere.

A different method for measuring the time delay was also investigated. Let $h_{mp}(\rho,\tau,\theta)$ be the minimum-phase reconstruction of $h(\rho,\tau,\theta)$. It is well known that minimum-phase reconstruction removes any linear-phase terms associated with pure time delay (Oppenheim and Schafer, 1989). Indeed, minimum-phase reconstructions are commonly used to time-align impulse responses. When $h_{mp}(\rho,\tau,\theta)$ was computed for many different values of ρ and θ, it was found that, except for time shift, the results were essentially identical to $h(\rho,\tau,\theta)$. The time delay was then computed by maximizing the cross-correlation between $h_{mp}(\rho,\tau,\theta)$ and $h(\rho,\tau,\theta)$. The results were very close to the 15% rise-time results. An interesting byproduct of this investigation was the observation that the HRIR for an ideal sphere appears to be minimum phase for all ranges and incidence angles.

A well-known ray-tracing formula due to Woodworth and Schlosberg (1962) can be extended to get useful approximate equations for the time delay and the ITD (Blauert, 1997, p. 76). As Fig. 9 illustrates, there are two cases, one in which a ray from the source goes directly to the observation point, and one in which the wave must travel from a point of tangency around the sphere to the observation point. If the speed of propagation is assumed to be c both in air and around the surface, a simple geometrical argument shows that the normalized time difference $\Delta\tau$ between the time that the wave reaches the observation point and the time that it would reach the center of the sphere in free field is given by

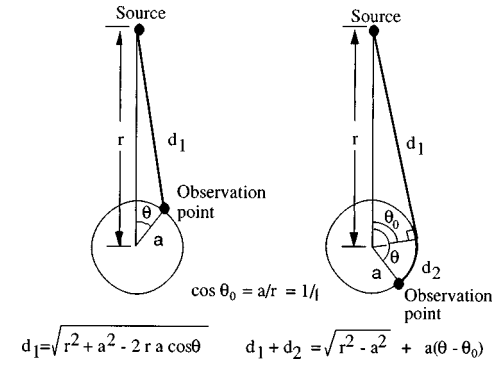

FIG. 9. Geometry for the Woodworth/Schlosberg formula. The wave is assumed to travel with a constant velocity c, whether the distance is the straight line distance d_1 from the source to the observation point, or the sum of distance d_1 from the source to a point of tangency and the distance d_2 around the sphere to the observation point.

$$\Delta\tau = \frac{c\Delta t}{2\pi a} = \begin{cases} \frac{1}{2\pi}(\sqrt{\rho^2 - 2\rho\cos\theta + 1} - \rho), & \text{if } 0 \leqslant \theta \leqslant \theta_0, \\ \frac{1}{2\pi}(\theta - \theta_0 + \sqrt{\rho^2 - 1} - \rho), & \text{if } \theta_0 \leqslant \theta \leqslant \pi, \end{cases} \tag{15}$$

where

$$\theta_0 = \sin^{-1}(1/\rho), \quad \rho \geqslant 1. \tag{16}$$

The solid-line curves in Fig. 8 show the predictions of this simple model for $\rho = 1$, 1.25, and ∞. The agreement with the 15% rise time results is very good, with the maximum error being 2.4% at $\theta = 170$ degrees.

Finally, Fig. 10 shows bounds on the ITD computed from Eqs. (15) and (16) under the assumption that the ears are located at $\theta = \pm 100$ degrees. The upper bound corresponds to a source at the surface of the sphere ($\rho = 1$), and the lower bound corresponds to a source at infinity. Bringing the source closer to the sphere increases the ITD, the maximum increase being 25.7% (0.0908 normalized units, corresponding to 146 μs for the 8.75-cm standard head radius). Brungart and Rabinowitz (1996) obtained essentially the same results using the phase delay. They pointed out that humans are insensitive to time delays above 700 μs, and the results shown here support their conjecture that changes in the ITD probably do not provide significant information about range.

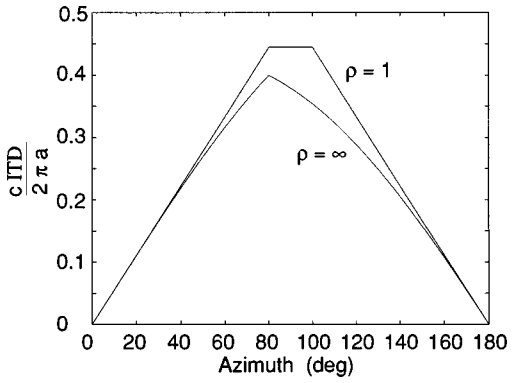

FIG. 10. Bounds on the normalized interaural time difference computed from the Woodworth/Schlosberg formula, assuming that the ears are located at $\theta = \pm 100°$. In general, the ITD is not very sensitive to range.

III. EXPERIMENTAL MEASUREMENTS

The theoretical results presented above are based on assumptions that cannot be met by any physically realizable system (such as the assumption of an ideal point source). Nonetheless, the validity of the basic theory is well established. Although the results of a number of experimental studies of the diffraction of sound by a sphere are reported in the literature, acoustical measurements showing the range dependence of the ILD and ITD were not available. Furthermore, modern techniques for measuring acoustic transfer functions provide a significant improvement over prior techniques, especially in terms of their sensitivity to noise. These considerations led to the following experimental study.

A. Procedure

The response at the surface of a sphere was measured using the same DSP-based techniques currently being employed for measuring human HRTFs. The measurements were made with the Snapshot™ system manufactured by Crystal River Engineering. For each response measurement, this system generated two computer-generated sequences of pseudo-random noise signals called Golay codes. These signals were used to drive a 6.4-cm-diam Bose Acoustimass™ loudspeaker. Signals picked up by the pair of blocked-meatus microphones (typically inserted in the subject's ear canals) were digitized at 44.1 kHz. Snapshot's oneshot function was used to recover the impulse responses without additional compensation or normalization. A record length of 256 samples corresponded to about 5.8 ms and provides a frequency resolution of 172 Hz.

For this study, a single microphone was inserted in a hole drilled through an 3.6-kg, 10.9-cm radius (27-in. circumference) bowling ball. The ball was mounted on a 1.3-cm-diam vertical threaded rod rotated by a motor in 5 degree increments. The ball was positioned in the center of a $5 \times 5 \times 3$-m^3 anechoic chamber at the University of California at Davis. The center of the ball was 1 m from the chamber floor. Preliminary experiments revealed that the blocked-meatus microphone did not exhibit the expected 6-dB rise at high frequencies, presumably because its 9.5-mm diameter (which is a quarter of a wavelength at 9 kHz) was too large relative to the wavelength. A comparison of the directional variation in the response of the blocked-meatus microphone to that of an Etymotic Research ER-7C probe microphone led to the conclusion that the former exhibited substantial reduction in its response at normal incidence. Thus, the blocked-meatus microphone was replaced by an ER-7C probe microphone. The ER-7C's probe tube was 76 mm long, with a 0.95 mm o.d. and 0.5 mm i.d. The body of the microphone was fully contained within the bowling ball, with the probe tip being flush with the bowling ball's surface.

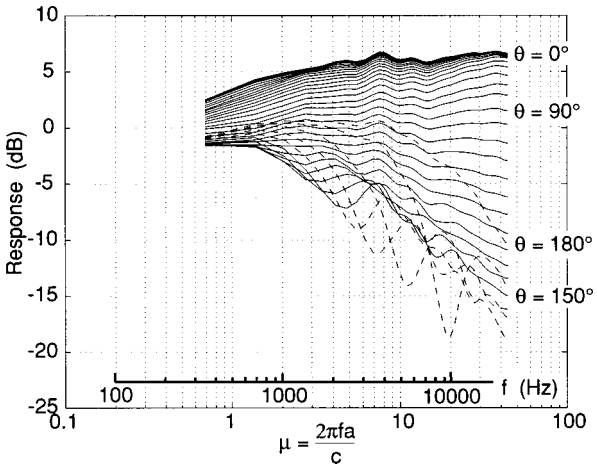

FIG. 11. Experimental measurement of the magnitude response for a 10.9-cm radius bowling ball, $\rho=20$ (cf. Fig. 2). The squared magnitude of the transfer function was smoothed with an auditory filter having a Q of 10.

The loudspeaker, which was mounted on a microphone stand, was located at a distance r from the center of the ball, with the principal axis of the loudspeaker directed at the center of the ball. Measurements were made for $r=13.5$, 16, 22, 33, 55, 109, and 218 cm, which corresponded to $\rho=1.25$, 1.5, 2, 3, 5, 10, and 20, respectively. In addition, free-field measurements were made at each range to allow compensation for the loudspeaker and microphone transfer functions.

B. Measured response

The experimental HRTF was free-field compensated by dividing the FFT of the measured impulse response by the FFT of the free-field response. To reduce the noise and irrelevant fine structure in the measurements, rms values were obtained by smoothing the squared magnitude of the transfer function. A simple constant-Q filter with a Gaussian kernel whose standard deviation was 10% of its center frequency was employed. The resulting frequency response curves for a distant source ($\rho=20$) are shown in Fig. 11. Although there are discrepancies, these results are in general agreement with the theoretical curves shown in Fig. 2. The low-frequency response approaches 0 dB at all incidence angles. At normal incidence ($\theta=0$ degrees), the magnitude response increases with frequency. The response is up about 3 dB at $\mu=1$ and 6 dB at large values of μ. As the angle of incidence increases, the high-frequency response begins to drop off. For $\theta=150$ degrees, the response is down about 13 dB at $\mu=30$, which agrees very well with the theory.

To facilitate comparisons between the theoretical and measured responses, Fig. 12 shows both results for four revealing incidence angles—0, 90, 150, and 180 degrees. Here the theoretical curves are smoothed with the same auditory filter used to smooth the experimental data. Fig. 12(a) is for $\rho=20$, Fig. 12(b) for $\rho=5$, and Fig. 12(c) for $\rho=2$. The results at other ranges are basically similar, and show a good correspondence between theory and measurements. However, for $\rho=1.25$ and $\rho=1.5$ we observed a strong reflection between the ball and the speaker in the vicinity of normal incidence, which produced prominent notches in the 0-degree curve. Physical sound sources are always spatially extended, and one expects the experimental results to depart from theory at close range.

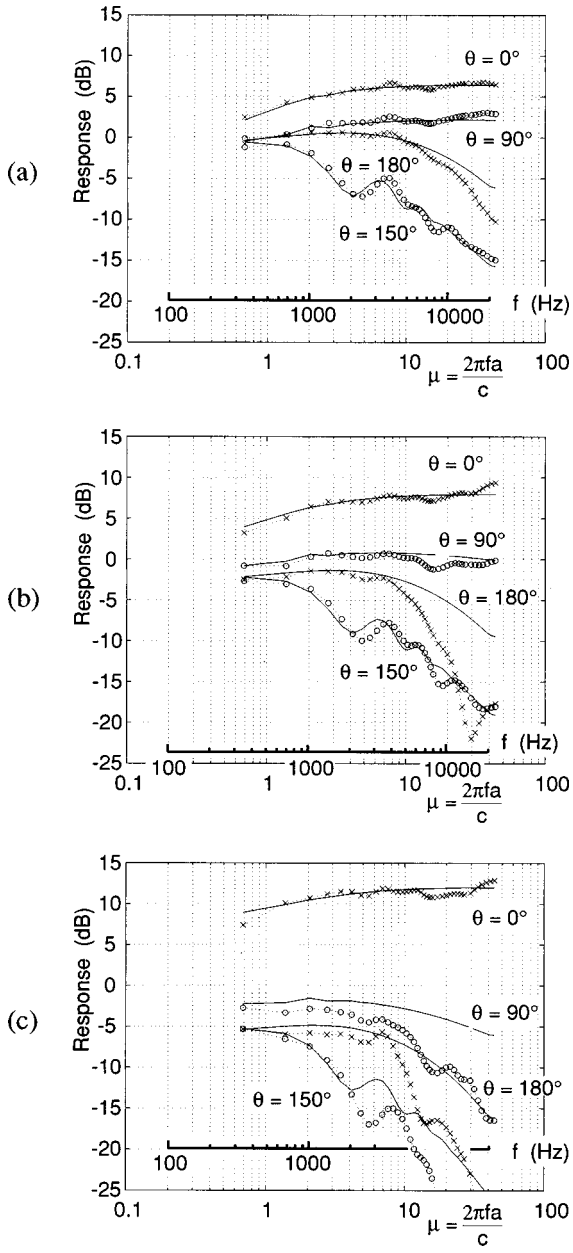

FIG. 12. Comparison between the theoretical and measured responses at four different angles of incidence. (a) $\rho=20$, (b) $\rho=5$, (c) $\rho=2$. For $\rho<2$, the source is no longer well approximated by a point source.

There are two clear differences between the measured and the theoretical results that appear in all of the ranges measured. The first is that there are discrepancies between the ripple patterns above 2 kHz. This is probably due to small angular errors, since the frequencies at which the interference effects occur are quite sensitive to the angle of incidence. The second is a reduction in the measured high-frequency response at $\theta=180$ degrees, which reduces the strength of the bright spot. This is also probably due to small alignment errors, plus the presence of the supporting rod, the exiting microphone cable, and other imperfections that disturb the wave propagation from what would occur with a perfect sphere. These discrepancies could undoubtedly be re-

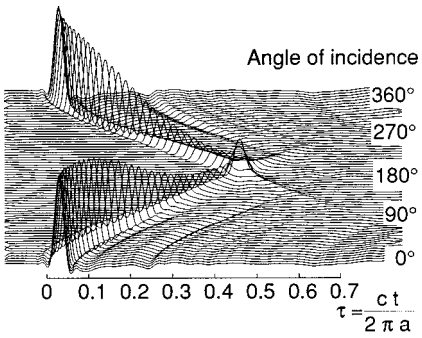

FIG. 13. Experimental measurement of the impulse response for a 10.9-cm radius bowling ball, $\rho=20$ (cf. Fig. 6). The smaller waves following the main pulse are probably due to reflections within the ball.

duced by more careful experimental techniques. However, extremely controlled conditions are not feasible for human HRTF measurements. Since human heads, necks and torsos introduce much greater perturbations, it is not surprising that phenomena such as bright spots that depend critically on geometry can be overlooked in human HRTF measurements.

Figure 13 shows the HRIR obtained by inverse transforming the free-field-compensated HRTF for $\rho=20$ and interpolating by a factor of 4 to smooth the curves. Again, the results are basically similar to the theoretical predictions (cf. Fig. 6). The amplitude of the pulse drops off and broadens in the same way, and a bright spot in fact appears where the two ''ridges'' cross. The visually most prominent difference between experiment and theory appears in the fairly large number of low-amplitude waves that follow the primary response. These are probably due to reflections caused by waves propagating through the interior of the bowling ball.

Figure 14 shows the time delay computed from the experimentally measured HRIR's using the 15% rise-time definition for the cases $\rho=2$ (open circles) and $\rho=20$ ($\times$'s). As in Fig. 8, the solid lines are computed using Woodworth and Schlosberg's approximate formula. Once again, this simple formula provides a very good approximation.

IV. DISCUSSION

There is a long history of research on the diffraction of sound by a rigid sphere that dates back at least to the classical work by Lord Rayleigh (Strutt, 1904, 1945). Hartley and Fry (1921) presented theoretical graphs showing the azimuth and range dependence of the ILD and the interaural phase difference (IPD). They conjectured that the auditory system could determine both the azimuth and the range for the source of a pure tone from the ILD and the IPD taken jointly. Wightman and Firestone (1930) tested this conjecture experimentally, and reported that people were unable to judge the distance to pure tones from this information. Similar failures were later reported by Coleman (1962). Without referring to this earlier work, Hirsch (1968) used a simple inverse-square approximation to show that, in theory, the range to a source could be determined from the ratio of the interaural time difference to a percentage interaural intensity difference. Molino (1973) refined Hirsch's analysis, but again found that human subjects were unable to distinguish five different amplitude normalized sources at ranges of 3 to 38 ft when pure tones (1000 and 8000 Hz) were used.

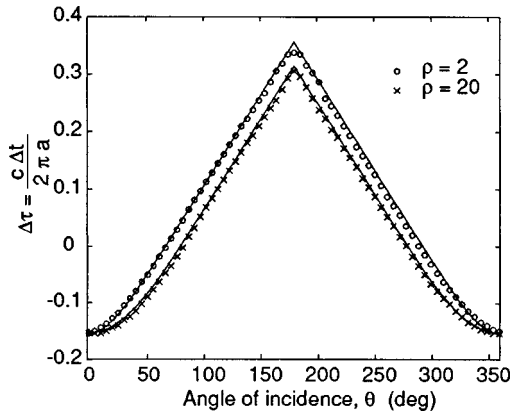

FIG. 14. Comparison of arrival times as measured from the impulse response and calculated by Woodworth and Schlosberg's formula.

It is now understood that such dry, narrow-band stimuli usually do not produce images of auditory events that are heard as external to the listener's head, and so distance judgments will be particularly difficult for subjects to make. The issue of externalization is critically important to psychophysical studies of the apparent distance of stimuli presented via headphones. Not only are wideband signals needed for good directional judgments, but the inclusion of indirect sound (reflections and/or reverberation) is also required for the best externalization (Durlach *et al.*, 1992). Without psychophysical studies of apparent distance employing adequate stimuli, it is difficult to discuss further the importance of the range dependence of the ILD and the IPD in human distance perception.

Earlier work has also been done on comparing acoustical measurements and diffraction theory. Wiener (1947) provided experimental verification of Rayleigh's solution for an infinitely distant source by measuring the pressure at the surface of a smoothly finished 9.7-cm-radius wooden sphere in an anechoic chamber. He used a probe microphone and a sinusoidal source located about 2 m from the center of the sphere. While Wiener's results exhibit considerable variability and do not include range dependence, they do confirm the basic features of the theoretical solution. For the case of an infinitely distant source, Feddersen *et al.* (1957) experimentally confirmed the accuracy of Woodworth and Schlosberg's formula for the ITD, and Kuhn (1977, 1987) used the phase response to derive the ITD from Rayleigh's solution. Rabinowitz *et al.* (1993) presented the range-dependent theoretical solution. Brungart and Rabinowitz (1996) subsequently used this result to determine both the ILD and the ITD as functions of range, and observed that while the ILD varies strongly with range, the ITD is not very sensitive to range.

The results reported in this paper extend this earlier work by presenting an algorithm for computing both the HRTF and the HRIR for any range and angle of incidence, and by confirming these results experimentally. The time-domain results illuminate the somewhat puzzling character of the bright spot, and the ripples that appear in the frequency response in the vicinity of the bright spot. Although

it is an oversimplification to say that these phenomena are due to two waves propagating around the two ''sides'' of the sphere, this interpretation provides a simple and useful first approximation.

V. CONCLUSIONS

To summarize, both the theoretical and experimental data confirm that the variation of low-frequency ILD with range is significant for ranges smaller than about five times the sphere radius. The impulse response provides direct evidence that the ITD is not a strong function of range. The time delay is well approximated by the well-known ray-tracing formula due to Woodworth and Schlosberg. Finally, except for this time delay, the HRTF for the ideal sphere appears to be minimum phase, permitting exact recovery of the impulse response from the magnitude response in the frequency domain.

ACKNOWLEDGMENTS

We are grateful to Professor V. R. Algazi at the University of California at Davis for his help in measuring the experimental data. Intel Corporation donated the probe microphones used to make our experimental measurements. The material in this paper is based upon work supported by the National Science Foundation under Grant Nos. IRI-9402246 and IRI-9619339. Any opinions, findings, and conclusions or recommendations expressed in this material are those of the authors and do not necessarily reflect the views of the National Science Foundation.

APPENDIX A: RECURSION RELATIONS

The basis for the algorithm by Bauch and Cooper (1980) is the following recursion relation for spherical Hankel functions (Morse and Ingard, 1968, Chap 7.2):

$$h_m(x)=\frac{2m-1}{x}h_{m-1}(x)-h_{m-2}(x), \quad m=2,3,\ldots, \tag{A1}$$

where

$$h_0(x)=\frac{e^{ix}}{ix} \quad \text{and} \quad h_1(x)=-i\left[\frac{1}{ix}-\frac{1}{(ix)^2}\right]e^{ix}. \tag{A2}$$

The computation of $h_m(x)$ can be significantly simplified by defining an auxiliary function $Q_m(z)$ through the equation

$$h_m(x)=Q_m\left(\frac{1}{ix}\right)(-i)^m e^{ix}. \tag{A3}$$

It is not hard to show that $Q_m(z)$ satisfies the recursion equation

$$Q_m(z)=-(2m-1)zQ_{m-1}(z)+Q_{m-2}(z), \quad m=2,3,..., \tag{A4}$$

where

$$Q_0(z)=z \quad \text{and} \quad Q_1(z)=z-z^2. \tag{A5}$$

Thus, $Q_m(z)$ is a simple polynomial in z that can easily be computed recursively. Furthermore, by using the recursion relation (see Morse and Ingard, 1968, Chap 7.2)

$$h'_m(x)=\frac{1}{2m+1}[mh_{m-1}(x)-(m+1)h_{m+1}(x)], \tag{A6}$$

one can employ Eqs. (A1) and (A3) to obtain

$$h'_m(x)=\left[Q_{m-1}\left(\frac{1}{ix}\right)-\frac{m+1}{ix}Q_m\left(\frac{1}{ix}\right)\right](-i)^{(m-1)}e^{ix}, \tag{A7}$$

where the case $m=1$ can be included by defining $Q_{-1}(z)=z$. Thus, the derivative of the spherical Hankel function can also be computed directly from the Q polynomials. In addition, the Legendre polynomials can also be computed recursively through

$$P_m(x)=\frac{2m-1}{m}xP_{m-1}(x)-\frac{m-1}{m}P_{m-2}(x), \tag{A8}$$

where

$$P_0(x)=1 \quad \text{and} \quad P_1(x)=x. \tag{A9}$$

Finally, by combining Eqs. (7), (8), (A3), and (A7), we obtain

$$H(\rho,\mu,\theta)=\frac{\rho}{i\mu}e^{-i\mu}\sum_{m=0}^{\infty}(2m+1)P_m(\cos\theta) \times\frac{Q_m(1/i\mu\rho)}{\frac{m+1}{i\mu}Q_m\left(\frac{1}{i\mu}\right)-Q_{m-1}\left(\frac{1}{i\mu}\right)}, \quad \rho>1, \tag{A10}$$

where the complex polynomials P_m and Q_m are computed recursively through Eqs. (A4), (A5), (A8), and (A9). An algorithm based on these relations that can be converted directly into a MATLAB® or a Mathematica™ program is given in Appendix B.

APPENDIX B: THE HRTF ALGORITHM

The following pseudo-code defines an algorithm for evaluating Eq. (A10). It assumes that variables and expressions can have complex values. The first two terms in the series are explicitly computed, and the use of recursion starts with $m=3$. Iteration stops when the fractional change falls below a user-supplied threshold for two successive terms.

```
function H = sphere(a, r, theta, f, c, threshold)
    x = cos(theta);
    mu = (2 * pi * f * a) / c;
    rho = r / a;
    i = sqrt(-1);
    zr = 1 / (i * mu * rho);
    za = 1 / (i * mu);
    Qr2 = zr;
    Qr1= zr * (1 - zr);
    Qa2 = za;
    Qa1 = za * (1 - za);
    P2 = 1;
    P1 = x;
    sum = 0;
    term = zr / (za * (za - 1));
    sum = sum + term;
    term = (3 * x * zr * (zr - 1) ) / (za * (2 * za^2 - 2 * za + 1) );
    sum = sum + term;
    oldratio = 1; newratio = abs(term)/abs(Sum);
    m = 2;
    while (oldratio > threshold) or (newratio > threshold),
       Qr = - (2 * m - 1) * zr * Qr1 + Qr2;
       Qa = - (2 * m - 1) * za * Qa1 + Qa2;
       P = ( (2 * m - 1) * x * P1 - (m - 1) * P2) / m;
       term = ( (2 * m + 1) * P * Qr) / ( (m + 1) * za * Qa - Qa1);
       sum = sum + term;
       m = m + 1;
       Qr2 = Qr1; Qr1= Qr; Qa2 = Qa1; Qa1 = Qa; P2 = P1; P1 = P;
       oldratio = newratio; newratio = abs(term)/abs(Sum);
    end while;
    H = (rho * exp(- i * mu) * Sum) / (i * mu);
end function;
```

[1]See Morse and Ingard (1968, Chap 7). Because we use $e^{i(kr-\omega t)}$ instead of $e^{i(\omega t-kr)}$ to represent a traveling wave, our formulas agree with those in Morse and Ingard (1968) and in Bauck and Cooper (1980), but are the complex conjugates of the formulas in Kuhn (1977) and in Rabinowitz *et al.* (1993).

[2]The classical HRTF relates the pressure at the source to the pressure at the head. While the pressure at an ideal point source is infinite, the pressure p_ε at a small sphere of radius r_ε surrounding the source is approximately $[(-i\omega\rho_0 S_\omega)/(4\pi r_\varepsilon)]e^{i\omega t}$. The transfer function H_ε from this small sphere to the diffracting sphere is given by

$$H_\varepsilon=\frac{p_s}{p_\varepsilon}=\frac{p_s}{p_{ff}}\frac{p_{ff}}{p_\varepsilon}=H\frac{r_\varepsilon}{r}e^{ikr}=H\frac{r_\varepsilon}{r}e^{i\omega(r/c)}.$$

In the time domain, the phase factor $e^{i\omega(r/c)}$ corresponds to the propagation delay of r/c. Thus, except for the uninteresting constant scale factor r_ε, one can use H to find the classical HRTF H_ε merely by adding the effects of propagation delay and dividing by the range.

[3]It should be noted that the time scaling of the impulse response function also leads to amplitude scaling. Thus, the unnormalized impulse response is given by $\hat{h}(r,t,\theta)=(c/2\pi a)h(r/a,ct/2\pi a,\theta)$. This amplitude scaling guarantees that the area under the impulse response is the dc value of the transfer function.

Bauck, J. L., and Cooper, D. H. (**1980**). ''On acoustical specification of natural stereo imaging,'' Preprint 1649 (H-7), 66th Convention Audio Engineering Society, Los Angeles, CA.

Blauert, J. (**1997**). *Spatial Hearing* (revised edition) (MIT, Cambridge, MA). Original edition published as *Räumliches Hören* (Hirzel, Stutgart, Germany, 1974).

Brungart, D. S., and Rabinowitz, W. R. (**1996**). ''Auditory localization in the near field,'' Proc. ICAD 96 (Third International Conference on Auditory Display), Palo Alto, CA (http://www.santafe.edu/~icad/ICAD96/proc96/INDEX.HTM).

Coleman, P. D. (**1962**). ''Failure to localize the source distance of an unfamiliar sound,'' J. Acoust. Soc. Am. **34**, 345–346.

Durlach, N. I., Rigopulos, A., Pang, X. D., Woods, W. S., Kulkarni, A., Colburn, H. S., and Wenzel, E. M. (**1992**). ''On the externalization of auditory images,'' Presence **1**, 251–257.

Feddersen, W. E., Sandel, T. T., Teas, D. C., and Jeffress, L. A. (**1957**). ''Localization of high-frequency tones,'' J. Acoust. Soc. Am. **29**, 988–991.

Hartley, R. V. L., and Fry, T. C. (**1921**). ''The binaural localization of pure tones,'' Phys. Rev. **18**, 431–442.

Hirsch, H. R. (**1968**). ''Perception of the range of a sound source of unknown strength,'' J. Acoust. Soc. Am. **43**, 373–374.

Kuhn, G. F. (**1977**). ''Model for the interaural time differences in the azimuthal plane,'' J. Acoust. Soc. Am. **62**, 157–167.

Kuhn, G. F. (**1987**). ''Physical acoustics and measurements pertaining to directional hearing,'' in *Directional Hearing*, edited by W. A. Yost and G. Gourevitch (Springer-Verlag, New York), pp. 3–25.

Molino, J. (**1973**). ''Perceiving the range of a sound source when the direction is known,'' J. Acoust. Soc. Am. **53**, 1301–1304.

Morse, P. M., and Ingard, K. U. (**1968**). *Theoretical Acoustics* (Princeton U.P., Princeton, NJ).

Oppenheim, A. V., and Schafer, R. W. (**1989**). *Discrete-Time Signal Processing* (Prentice–Hall, Englewood Cliffs, NJ).

Rabinowitz, W. M., Maxwell, J., Shao, Y., and Wei, M. (**1993**). ''Sound localization cues for a magnified head: Implications from sound diffraction about a rigid sphere,'' Presence **2**, 125–129.
Strutt, J. W. (Lord Rayleigh) (**1904**). ''On the acoustic shadow of a sphere,'' Philos. Trans. R. Soc. London, Ser. A **203**, 87–89.
Strutt, J. W. (Lord Rayleigh) (**1945**). *The Theory of Sound* (Dover, New York), 2nd ed., Vols. 1 and 2.
Wiener, F. M. (**1947**). ''Sound diffraction by rigid spheres and circular cylinders,'' J. Acoust. Soc. Am. **19**, 444–451.
Wightman, E. R., and Firestone, F. A. (**1930**). ''Binaural localization of pure tones,'' J. Acoust. Soc. Am. **2**, 271–280.
Woodworth, R. S., and Schlosberg, G. (**1962**). *Experimental Psychology* (Holt, Rinehard and Winston, New York), pp. 349–361.

The effect of changes in hearing status on speech sound level and speech breathing: A study conducted with cochlear implant users and NF-2 patients

Harlan Lane,[a] Joseph Perkell,[b] Jane Wozniak, Joyce Manzella, Peter Guiod, Melanie Matthies,[c] Mia MacCollin,[d] and Jennell Vick
Massachusetts Institute of Technology, Research Laboratory of Electronics, Room 36-511, 50 Vassar Street, Cambridge, Massachusetts 02139

(Received 18 November 1997; accepted for publication 4 August 1998)

According to a dual-process theory of the role of hearing in speech production, hearing helps maintain an internal model used by the speech control mechanism to achieve phonemic goals. It also monitors the acoustic environment and guides relatively rapid adjustments in postural parameters, such as those underlying average speech sound level and rate, in order to achieve suprasegmental goals that are a compromise between intelligibility and economy of effort. In order to obtain evidence bearing on this theory, acoustic and aerodynamic measures were collected from seven adventitiously deaf speakers who received cochlear implants, three speakers who had severe reduction in hearing following surgery for Neurofibromatosis-2, and one hard of hearing speaker. These speakers made recordings of the Rainbow Passage and an English vowel inventory before and after intervention. All but one of the postlingually deaf speakers who received prosthetic hearing reduced speech sound level, SPL. Three of these significantly increased a measure of inferred glottal aperture, $H1-H2$, and their session means for these two parameters were inversely correlated longitudinally. All but one of the speakers terminated respiratory limbs closer to functional residual capacity (FRC) once prosthetic hearing was supplied. Finally, the implant users' average values of air expenditure moved toward normative values with prosthetic hearing. These results are attributed to the mediation of changes in respiratory and glottal posture aimed at reducing speech sound level and economizing effort. [S0001-4966(98)04211-8]

PACS numbers: 43.70.Dn, 43.70Aj, 43.70.Fq, 43.66.Ts [AL]

BACKGROUND

Research on the consequences of long-term changes in hearing for speech has led us to put forth a dual-process theory of the role of auditory feedback in the production of speech (Perkell *et al.*, 1997). Essentially, that theory proposes that the speaker's hearing serves to ensure his or her intelligibility with minimal expenditure of effort. To achieve this, hearing is used to regulate two speech production processes: maintenance of an internal model and posture setting. In the first process, hearing maintains a robust internal model of the relation between articulation and sound output, which is used by the speech control mechanism to achieve acoustic or perceptual phonemic goals that represent a compromise between intelligibility and economy of effort. [On that compromise, see Lindblom and Engstrand (1989).] In the second process, the speaker's hearing monitors the acoustic environment and guides relatively rapid adjustments in his or her postural parameters, such as those underlying average speech sound level and rate, in order to achieve suprasegmental goals that are also a compromise between intelligibility and economy of effort. Those suprasegmental goals include communicatively appropriate values of speech sound level and rate, and inflection of $F0$ and SPL contours (Lane *et al.*, 1997).

In order to test and refine this theoretical framework, we have been eliciting speech samples, over periods as long as 5 years, from two groups of subjects who have undergone long-term changes in hearing status; namely, deafened adults who have received cochlear prostheses, and patients with bilateral vestibular schwannomas (neurofibromatosis-2 patients, NF-2) who experience severe reduction in hearing capacity after surgery for removal of these ''acoustic neuromas.'' It is well known that a particularly robust effect of short-term changes in hearing status is alteration of speech sound level. The speaker's average sound level increases when the perceptible transmission conditions deteriorate through either an increase in noise level (the Lombard effect) or a decrease in signal level [i.e., the level of the speaker's auditory feedback, Black (1951)]. In complementary fashion, the speaker's average sound level decreases with enhanced signal-to-noise (S/N) ratios: speakers whose auditory feedback is amplified speak more softly (Lane *et al.*, 1970; Fletcher *et al.*, 1918), possibly to economize on effort; Russell *et al.* (1998) have shown that as SPL rises above a comfortable speaking level, speech breathing requires more energy. These short-term changes in speech sound level are consistent with the hypothesis that the speaker infers transmission conditions from perceptible signal and noise parameters and makes postural adjustments in speech breathing

[a]Also at Northeastern University, Boston, MA 02115. Electronic mail: lane@speech.mit.edu
[b]Also at Dept. of Brain and Cognitive Sciences, MIT, Cambridge, MA 02139.
[c]Also at Boston University, Boston, MA 02215.
[d]Also at Massachusetts General Hospital, Charlestown, MA 02129.

TABLE I. Subject characteristics and percent correct scores on tests of vowel and consonant identification pre- and/or post-intervention. Speakers with cochlear implants are designated by ''C,'' NF-2 patients who underwent surgery by ''N,'' females by ''F,'' males by ''M'' HMA is a hard-of-hearing male NF-2 patient who received no intervention.

	Cochlear implant users							NF-2 patients			
Speakers	CFA	CFB	CFC	CMA	CMB	CMC	CMD	HMA	NFA	NFB	NMA
Age at onset of change in hearing	18	21	2	0	4	10	0	33	17	17	27
Age at onset of profound loss	33	40	47	31	4	56	36	N/A	27	22	32
Age at intervention	51	50	47	35	46	56	36	N/A	27	22	32
Age at last recording	56	52	49	35	49	59	37	53	31	23	35
Height (cm.)	158	158	170	185	180	185	178	183	168	165	
Weight (kg.)	50	80	59	91	84	84	84	77	67	53	
Smoker	N	Y	N	N	Y	N	N	N	Y	N	N
Vowel ID Pre (% correct)	⋯	⋯	⋯	⋯	⋯	⋯	⋯	40	86	94	23
Vowel ID Post (% correct)	37	80	81	76	50	⋯	65	58	19	75	13
Consonant ID Pre (% correct)	⋯	⋯	⋯	⋯	⋯	⋯	⋯	38	89	94	21
Consonant ID Post (% correct)	48	60	44	49	32	⋯	49	41	22	44	7

and laryngeal parameters that help to maintain adequate levels of intelligibility at minimal expenditure of effort.

In a study of long-term changes in vowel parameters with deafened adults (who later received cochlear prostheses), we found (Perkell *et al.*, 1992) that our speakers read a vowel inventory with anomalously high SPL, averaging 88 dB across the four speakers [about the mean value for ''loud voice'' in normally hearing speakers reported by Holmberg *et al.* (1994); also see Leder *et al.* (1987)]. Those speakers reduced SPL an average of 9 dB (placing them at the Holmberg *et al.* mean for ''normal voice'') once they had received their implants and their speech processors were activated. Thus our speakers seem to have used their hearing to monitor the acoustic environment and to regulate sound level. What adjustments in postural parameters did they make to accomplish this?

In a preliminary report on changes in speech breathing parameters following cochlear prosthesis, with three of the four speakers who served in our vowel study just cited, we found that all subjects, following processor activation, changed their volume of air expended per syllable (LVE/syl) (and their average flow rate) toward normative values during readings of the Rainbow Passage. [Those readings were interleaved in the same recording sessions with the readings of the vowel inventory (Lane *et al.*, 1991)]. We inferred from these findings that our speakers, while deaf, may have adopted unsuitable glottal postures that interacted with respiratory postures, such as those underlying average inspiratory and expiratory levels, in determining air expenditure. We speculated that glottal posture may be difficult to monitor without hearing. Our subsequent study of vowel parameters cited above also reported an indirect index of glottal aperture (the difference in amplitude between the first and second harmonics in the acoustic spectrum, $H1-H2$, during vowel production) along with measures of SPL on the same tokens. The three implant users in the vowel study who reduced speech sound level substantially with processor activation, an average across the speakers of 11.2 dB, increased $H1-H2$ an average of 4.7 dB. Moreover, session means of $H1-H2$ and SPL were correlated longitudinally; the mean product-moment correlation for the three speakers was $r=-0.64$. Thus with some hearing restored, some of the speakers may have achieved SPL reductions, at least in part, with increases in glottal aperture.

To explore further the pattern of changes in speech sound level, speech breathing, and glottal aperture under changes in hearing status, the present study examined changes in six respiratory parameters and two acoustic parameters following interventions that provided or, on the contrary, seriously degraded hearing during speech. Seven of the 11 subjects were deafened adults who received cochlear implants. (Three of these had served for a much shorter period in the preliminary study of speech breathing with cochlear prostheses.) There were also three NF-2 patients whose hearing was severely reduced following surgery for removal of vestibular schwannomas and one NF-2 patient who was hard of hearing and did not undergo any acute change in hearing status.

I. METHOD

A. Subjects

Subject characteristics are given in Table I. Eleven subjects served in this experiment: seven were deaf adults who received cochlear implants (''C'' in the table). Three of these had served in the preliminary study (Lane *et al.*, 1991) for a mean of 11 months after processor activation, but were now followed for an average of 1.8 years longer and now their speech sound levels and inferred glottal apertures were analyzed in conjunction with the respiratory measures. Three subjects were patients with neurofibromatosis-2 (NF-2; designated ''N''), whose auditory nerves were severed during

tumor removal surgery; two of these (NFA and NFB) received an auditory brainstem implant (ABI, Brackman *et al.*, 1993). Finally, there was one NF-2 patient who was hard of hearing (''H'') and did not undergo any acute change in hearing status. (Females are labeled ''F,'' males ''M.'') Also shown are subjects' scores (percent correct) on an identification test containing ten vowels and 12 consonants. For cochlear implant users, those means are averages over 2–4 test sessions after processor activation. For NF-2 speakers, mean identification scores pre-intervention are based on one or two sessions, post-intervention on 2–4 sessions (except for NFA, 7 sessions). For HMA, the ''pre'' scores shown in the table were obtained during his first visit to the laboratory.

Inspection of the left-hand side of Table I (''Cochlear implant users'') shows that hearing loss began in childhood for four of the seven speakers in this study who received cochlear implants. Six of the seven had adult onset of profound hearing loss (CMB is the exception). The period during which the speaker was profoundly deaf without a cochlear prosthesis varied from a few months to as much as 42 years. After two baseline recording sessions, cochlear implant surgery, and activation of the prosthesis speech processor, recordings were made over periods from 1 to 5 years. The table gives the subjects' age at last recording, as well as their height, weight and smoker status. At the time of their last two post-activation recordings, implant users scored an average of 65% correct on vowel identification and 47% correct on consonant identification.

The right-hand column of Table I (''NF-2 patients'') shows that hearing loss began in adulthood for the hard-of-hearing speaker and NF-2 speakers. At least two baseline recordings were made with the NF-2 patients prior to profound loss, which occurred at the time of surgical intervention. These speakers made additional recordings over a period of 1–4 years. Examining their vowel and consonant identification scores in Table I reveals that NFA and NFB were quite accurate in vowel and consonant identification pre-intervention. Following tumor removal surgery and implantation of an ABI, NFA and NFB were much less accurate. However, NFB using her ABI, attained scores comparable to those obtained by the cochlear implant users. NMA, who did not receive an ABI, had low consonant and vowel identification scores both pre- and post-intervention.

B. Speech elicitation

As the methods for elicitation and measurement of respiratory parameters are detailed in Lane *et al.* (1991), and those for elicitation and measurement of vowel acoustics in Perkell *et al.* (1992), they will be only summarized here. In each recording session, the subject read the first paragraph of the Rainbow Passage (Fairbanks, 1960), consisting of six sentences, three times; about 20 min elapsed between each of the three readings. However, CMA, who had a congenital hearing loss and limited English literacy, read instead ''A Trip to the Zoo'' (Wilson, 1979), with seven sentences. There were at least two pre-intervention baseline recording sessions and between three and nine post-intervention recordings depending on when the subjects entered the research program and their availability. The median number of post-intervention recordings was six. Post-intervention recordings with implant users generally were made at intervals of approximately 0, 4, 12, 24, and 48 weeks, and annually thereafter. Recordings with NF-2 patients and the hard of hearing subject were scheduled at intervals of approximately 20, 40, 80, 120, and 160 weeks. The post-intervention recordings began: (1) when the cochlear implant users began to receive electrical stimulation from their Richards (formerly Symbion) multichannel cochlear implants (Youngblood and Robinson, 1988; Eddington, 1983); (2) six (NFB) or 11 (NFA) weeks after the NF-2 patients with ABIs began to receive electrical stimulation from their implants; (3) 20 weeks following surgery for the NF-2 (NMA) patient who did not receive an ABI, (4) in his initial visit to the laboratory for the hard-of-hearing subject (HMA). The post-intervention recordings were scheduled according to a geometric series of time intervals on the evidence from our earlier studies that speech parameters change more rapidly shortly after intervention and then often stabilize after a period of some months or even years, depending on the subject and parameter.

C. Data extraction and signal processing

In order to obtain volumetric measures of speech breathing, from which inspiratory and expiratory levels, respiratory limb volume, and volume of air expended per syllable were derived, we measured changes in lung volume with an inductive plethysmograph (Respitrace, Ambulatory Monitoring Inc.). To compute the change in lung volume resulting from a respiratory maneuver, the abdominal and rib-cage signals from the two plethysmograph amplifiers are summed (in software, after digitizing) after first weighting by a calibration factor to correct for differences in gain between the two channels. In order to determine the correct proportion of the two signals for a given recording session, we had the subject perform isovolume maneuvers at the beginning and again at the end of each session. In order to arrive at a scale factor for converting the summed volume signal to liters, we had each subject exhale and inhale into a plastic bag that had a calibrated volume of 0.8 liters (a ''Spirobag'').

Amplified signals from the Respitrace and the microphone were recorded and subsequently low-pass filtered and digitized simultaneously at two different rates: 10 kHz for speech and 625 Hz for each of the two respiration signals. The digitized signals were demultiplexed into two separate time-aligned files, and the weighted sum of the respiratory signals was computed and displayed. An operator interactively labeled the beginning and end points of each expiratory limb and counted the number of syllables it included, aided by listening to the synchronized acoustic signal. The labeled events were accessed for calculating respiratory limb duration and limb initiation and termination levels in liters above functional residual capacity (FRC). The ratio of the limb excursion to its syllable count is the average volume per syllable in mL. Articulation rate was estimated as the number of syllables in the limb divided by the limb duration (any nonphonated expiratory segments were included in limb duration). To calculate the average SPL of each respiratory limb, the average rms value of the recorded, digitized sound-

pressure signal in each respiratory limb was divided by the rms value of a calibration tone and the ratio expressed in dB. This dB value was then added to the metered SPL of the calibration tone to obtain dB (SPL).

Three readings of a vowel inventory, comprising eight English monophthongs spoken in /hVd/ context, were interleaved with those of the Rainbow Passage in each session. During data extraction from these vowels, the amplitudes of the first and second harmonics of each vowel token were determined at vowel midpoint (with a 51.2-ms window), in order to obtain a measure of inferred glottal aperture. The spectral correlates of increased subglottal coupling include an increase of the relative amplitude of the fundamental and reduced amplitudes of the higher frequency harmonics (Klatt and Klatt, 1990). Thus the amplitude difference between the first two harmonics in the acoustic spectrum, $H1-H2$, is an indirect index of inferred glottal aperture. There is evidence that $H1-H2$ is correlated with the open quotient of the glottal waveform and perceived ''breathiness'' of the voice (cf. Ladefoged, 1981; Bickley, 1981; Klatt and Klatt, 1990). $H1-H2$ is corrected for the influence of $F1$, but the measure is invalid when the frequency of the first or second harmonic in the spectrum is within 150 Hz of the first formant (see Perkell *et al.*, 1992).[1] Therefore $H1-H2$ results are limited to the nonhigh vowels.

II. RESULTS: COCHLEAR IMPLANT PATIENTS

Figure 1 presents longitudinal plots of average sound-pressure level (SPL, left panel), and average lung volume expended per syllable (LVE/syl, middle panel) during readings of the Rainbow Passage by each of seven adventitiously deaf adults before and after receiving cochlear implants. Also shown for each speaker are average values of the index of glottal aperture ($H1-H2$, third panel) for the nonhigh vowels measured during readings of a vowel inventory for English. The vertical line in each graph indicates the reference week when each speaker's implant speech processor was activated. An approximate indication of the range of normative values is given by the dotted lines, whose separation equals one standard error around a normative mean. For SPL, dB means and standard errors for males (77.8, 1.2) and females (74, 0.9) were taken from Holmberg *et al.* (1994). For LVE/syl, the respective ml means and standard errors (49, 5; 38, 3) were taken from Hoit *et al.* (1990). Comparable values of LVE/syl were reported for men (48) by Hoit and Hixon (1987) and for women (35) by Hoit *et al.* (1989). For $H1-H2$, the dB values for women (6.6, 0.9) were taken from Holmberg *et al.* (1995); the mean value for men was set 5.7 dB lower (Klatt and Klatt, 1990).

The effects of changes in hearing status on speech sound level, air expenditure, respiratory limb termination levels, and glottal aperture are considered in turn in the following four sections.

A. Reductions in speech sound level

Inspection of Fig. 1, left-hand panel, reveals that two of the deaf speakers (CFC, CMA) read the Rainbow Passage at mean sound levels within the normative range pre-intervention and yielded similar values, close to or within the normative range, in their final two recording sessions with prosthetic hearing. The remaining five speakers, however, had a mean baseline speech sound level above the normative range initially. In each case, an effect of providing prosthetic hearing was to lower speech sound levels, although CFA and CMD showed an intermediate rise and CFB and CMC resumed speaking at higher levels after some sessions. In spite of this considerable fluctuation, the average speech sound levels in these speakers' last two recording sessions, with prosthetic hearing, were reliably lower than in their first two (baseline) sessions, without prosthetic hearing. Table II contrasts average values of speech parameters measured during the two baseline sessions (pre) with those obtained during each subject's last two recording sessions (post). Also shown are the differences in the mean parameter values (pre-post $=\Delta$), and a t test of those differences using matched pairs of sentences in the Rainbow Passage. The change in mean parameter values is shown in boldface when statistically significant ($p<0.05$).

Inspection of the first block of data in Table II (labeled ''1'') shows that six of the seven cochlear implant users significantly reduced SPL, and one significantly increased it. For all seven cochlear implant users taken together, the mean change in SPL, during readings of the Rainbow Passage, pre- to post-processor activation, was a reduction of 2.7 dB [z of combined t values $=19.7$, $p<0.01$; cf. Rosenthal (1991)]. The change in average SPL determined instead from readings of the vowel inventory (Table III, block 1) was somewhat larger: for all implant users pooled, it was a reduction of 4.3 dB ($z=6.5$, $p<0.01$). When reading the Rainbow Passage pre-intervention, all of the deaf speakers but one (CMA) exceeded the speech sound level normative values in Holmberg *et al.* (1994). The highest female SPL for the passage in this study was 80 dB (Table II, block 1). This is the top of the range for a normal female voice (Holmberg *et al.*, 1994). CMB had the highest SPL pre-intervention of all the speakers, 83 dB; the loudest speaker in Holmberg *et al.* (1994) averaged 85 dB. In summary, these postlingually deaf speakers tended to speak in an abnormally loud voice and, when they received prosthetic hearing, characteristically spoke more softly.

B. Changes in volume of air expended per syllable

In general, implant users' changes in air expenditure pre- to post-activation were in the direction of normative values, although the longitudinal functions show considerable fluctuation. Inspection of the middle panel of Fig. 1 reveals that three of the deafened speakers (CMA, CMB, CMC) initially expended air volumes well above the normative range while reading the Rainbow Passage. Baseline measures of LVE/syl pooled over the three speakers averaged 64 ml/syl in the two sessions preceding activation of their implant speech processors (Table II, block 2). After activation, with prosthetic hearing available, these three speakers rapidly reduced air expenditure and then apparently stabilized within the normative range. Their pooled average in the final two sessions was 47 ml/syl.

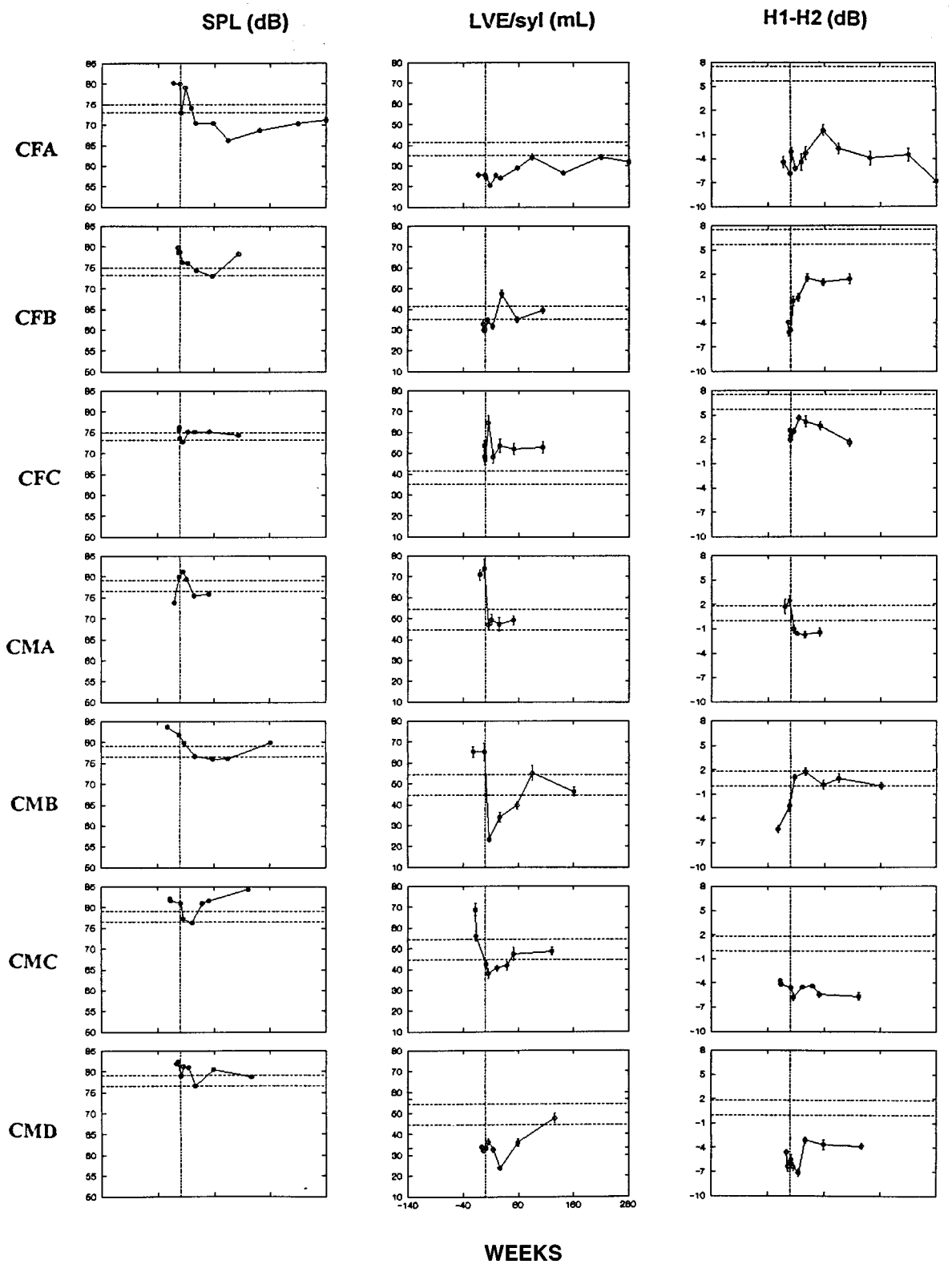

FIG. 1. Longitudinal plots of average sound-pressure level (SPL, left panel), and average lung volume expended per syllable (LVE/syl, middle panel) during readings of the Rainbow Passage by each of seven adventitiously deaf adults before and after receiving cochlear implants. Also shown for each speaker are average values of the index of glottal aperture $H1-H2$, right panel) for the nonhigh vowels measured during readings of a vowel inventory for English. The vertical line in each graph indicates the reference week when each speaker's implant speech processor was activated. An approximate indication of the range of normative values is given by the dotted lines, whose separation equals one standard error around a normative mean.

Three other deafened speakers, in contrast, initially expended air volumes well below the normative range. CFA, CFB, and CMD taken together averaged 29 mL/syl in the baseline sessions. With some self-hearing restored, they gradually (but not monotonically) increased LVE/syl to a pooled mean of 36 ml/syl. Finally, CFC initially expended air volumes a little above the normative range and showed no significant change when comparing baseline and final ses-

TABLE II. Acoustic and speech breathing parameters during readings of the Rainbow Passage by seven cochlear implant users, three NF-2 patients, and a hard-of-hearing subject pre- and post-intervention. The change in mean parameter value pre-post (Δ) is shown in boldface when statistically significant (*t* test for matched pairs; $p<0.05$). ([1]=Volume *re*: FRC.)

			Cochlear implant users							NF-2 patients			
			CFA	CFB	CFC	CMA	CMB	CMC	CMD	HMA	NFA	NFB	NMA
	Number of sentences	*N*	36	36	36	42	36	36	60	60	54	60	30
	Speech sound level	pre	80	79	76	77	83	82	82	63	73	69	65
		post	71	76	75	76	78	83	80	63	72	65	63
1	SPL (dB)	Δ	**9**	**3**	**1**	**1**	**5**	**−1**	**2**	0	1	**4**	**2**
		t	26	5.5	5.1	2.6	9.5	−4.2	9	−1.7	1.8	19.8	11
	Lung volume per syllable	pre	25	30	50	71	63	59	32	35	19	25	26
		post	33	36	51	47	48	47	39	33	19	16	37
2	LVE/syl (ml)[1]	Δ	**−8**	**−6**	−0.6	**21**	**15**	**12**	**−7**	**2**	0.4	**9**	**−9.7**
		t	−7.4	−5.5	−0.4	9.2	8.1	5.8	−6	3	0.3	12.4	−8.5
	Lung volume at limb termination	pre	2.2	77	−72	−53	−122	−265	−62	−184	−83	−139	−14
		post	8.1	−2.8	−71	−43	−25	−231	−11	−103	33	−9	−132
3	LVT (ml)[1]	Δ	−5.9	**80**	−.5	−11	**−97**	−33	**−51**	**−81**	**−95**	**−130**	**118**
		t	−0.4	3.3	−0.02	−0.2	−2.5	−.8	−2.5	−2.5	−3.9	−6.8	7.2
	Lung volume at limb initiation	pre	280	478	321	510	402	450	327	337	326	301	216
		post	410	450	284	349	442	387	476	412	417	322	229
4	LVI (ml)[1]	Δ	**−130**	28	37	**161**	−40	63	**−149**	−75	−67	−21	−15
		t	−3.6	1.1	1.4	2.7	−0.9	1.3	−5.2	−1.9	−1.7	−0.8	−1
	Lung volume per second	pre	94	127	195	183	176	231	136	147	112	142	108
		post	131	162	168	153	149	184	188	141	112	93	135
5	LVE/s (ml/s)[1]	Δ	**−37**	**−35**	**27**	**30**	**26**	**48**	**−52**	**6**	−0.6	**49**	**−17**
		t	−11	−7.5	8.7	5.4	5.6	8.3	−11	2.2	−.1	14	−6.1
	Lung volume of limb	pre	278	400	393	563	523	714	389	521	409	440	230
		post	402	453	355	392	467	618	487	515	384	331	361
6	LVE (ml)[1]	Δ	**−124**	−52	37	**171**	**167**	**96**	**−98**	6	27	**110**	**−133**
		t	−3.8	−1.6	1.5	2.8	2	2.6	−4.1	0.3	1	5.6	−8
	Number syllables per limb	pre	11.9	13.9	8.2	8.5	9	12.8	12.7	14.8	21.2	17.7	9.4
		post	12.1	12.9	7.5	9.1	10.4	13.5	13.5	15.5	21.1	21.3	10.5
7	SYL (N)	Δ	−0.2	1	0.7	−0.6	**−1.4**	−0.7	−0.7	−0.7	0.2	**−3.6**	**−1.6**
		t	−.2	1.1	1.4	−.5	−2.6	−.8	−1.1	−1.8	1.3	−4.4	−2.8
	Number syllables per second	Pre	3.9	4.3	4.1	2.7	2.9	4.1	4.4	4.3	6.2	5.7	4.3
		post	4.1	4.6	3.6	3.4	3.2	4.1	5	4.3	6.1	6.1	3.8
8		Δ	−0.2	**−0.3**	**0.5**	**−0.7**	**−0.3**	−0.1	**−0.7**	−0.1	0.1	**−0.4**	**0.7**
	(N/s)	*t*	−1.6	−3.5	7	−7.9	−7.3	−0.5	−8.2	−0.9	0.4	−3.5	6.6

TABLE III. Mean sound-pressure level and mean index of $H1-H2$ during readings of the vowel inventory by seven cochlear implant users, three NF-2 patients, and a hard of hearing speaker pre- and post-intervention. The change in mean parameter value pre-post (Δ) is shown in boldface when statistically significant (*t* test for matched pairs; $p<0.05$).

			Cochlear implant users							NF-2 patients			
			CFA	CFB	CFC	CMA	CMB	CMC	CMD	HMA	NFA	NFB	NMA
	Speech	pre	86	85	80	85	94	86	88	82	79	84	73
1	sound	post	76	79	78	83	83	89	87	81	81	80	77
	level	Δ	**10**	**6**	**3**	**2**	**11**	**−3**	**1**	**1**	**−2**	**4**	**−4**
		t	20	8	6.7	4.9	10	−6.1	4	3.5	−8.3	12.1	−11.9
	SPL (dB)	*N*	53	54	50	54	51	53	79	80	80	79	40
	Inferred	pre	−5.2	−4.6	2.5	2.1	−3.9	−3.9	−5.4	−2.9	−4.9	−4.0	−3.7
2	glottal	post	−5.2	1.2	2.6	−1.6	0.8	−5.5	−3.7	−2.0	−7.5	−6.6	−2.1
	aperture	Δ	−0.4	**−5.9**	−0.4	**4.3**	**−4.9**	**1.4**	**−2**	**−0.9**	**2.5**	**2.6**	**−1.4**
		t	−0.5	−11.6	−1.1	9.3	−6.5	5.1	−4.9	−2.1	6.9	6.5	−2.5
	$H1-H2$ (dB)	*N*	25	32	23	24	14	26	49	49	49	50	25

sions. Her first session after processor activation, however, showed a rise in air expenditure that was not sustained in later sessions.

We find evidence, then, that prosthetic hearing provided to postlingually deafened adults leads to normalization of their expenditure of air during speech when it was previously abnormal. We did not undertake to collect normative data from hearing speakers; however, several such published studies gave reasonably consistent results. Studying older males, Solomon and Hixon (1993) found an average air expenditure of 47 ml/syl for the Rainbow Passage and Hoit and Hixon (1987) report 48 ml/syl for a different passage. Working with teenagers, Hoit *et al.* (1990) found 49 ml/syl for males and 38 ml/syl for females; these latter means and their standard errors demarcate the ranges in the middle panel of Fig. 1.

C. Changes in limb termination

Five of the seven deaf speakers terminated their respiratory limbs below FRC prior to receiving prosthetic hearing; thus they were encroaching on expiratory reserve. Table II (block 3) shows the average distance from FRC at limb termination pre- versus post-processor activation. Congenitally deaf speakers have also been found to encroach on expiratory reserve (Forner and Hixon, 1977; Itoh and Horii, 1985; Whitehead, 1983). CFA's limb termination levels were very close to FRC while deaf and remained so with prosthetic hearing. All the remaining speakers after receiving prosthetic hearing terminated respiratory limbs closer to FRC. Although those changes, considered individually, are reliable for only three of the six speakers, the combined value of the seven t tests gives a statistically significant result ($z=3.3$, $p<0.01$).

D. Changes in $H1-H2$

Inspection of Fig. 1, right-hand panel, reveals that speakers CFB, CMB, and CMD increased values of $H1-H2$ with prosthetic hearing, moving up toward the normative range (with some fluctuation in CMD's case), indicating that they had adopted a relatively pressed glottal configuration while deaf and assumed a more open posture with stimulation from their implants. Their significant increases in $H1-H2$ (Table III, block 2) were 6, 5, and 2 dB, respectively. Were it not for a drop in $H1-H2$ in their last session, this measure would also have increased significantly for CFA and CFC. Finally, two speakers *reduced* $H1-H2$ after processor activation, indicating that they assumed a more pressed glottal posture: CMA moved from slightly above the normative range to slightly below it, while CMC reduced a low value of $H1-H2$ even further.

For the implant users who increased $H1-H2$ significantly (CFB, CMB, CMD), session means for $H1-H2$ were inversely correlated with those for SPL in readings of the vowel inventory ($r=-0.83$, -0.93, -0.72; $N=8$, 7, 8, respectively; $p<0.05$).

III. RESULTS: HARD-OF-HEARING SPEAKER AND NF-2 PATIENTS

Figure 2 presents longitudinal plots of speech sound level, lung volume expended per syllable, and $H1-H2$ for the hard-of-hearing male speaker (HMA) and the three NF-2 patients who had surgery; the format is comparable to Fig. 1, except for the plots of SPL, where the starting level of the y axis has been lowered to 50 dB to accommodate the lower speaking levels of the NF-2 subjects. The vertical line in each graph indicates the reference week when each NF-2 patient had severe reduction in hearing status and, for NFA and NFB, when each received an auditory brain-stem implant. (For HMA, the vertical line indicates the initial visit to the laboratory.) In the following, we consider first findings for the three parameters for the hard of hearing speaker, then turn to the NF-2 patients and their measures of SPL, LVE/syl, and $H1-H2$.

The hard of hearing subject, HMA, who did not undergo any acute intervention, maintained SPL, LVE/syl, and $H1-H2$ relatively constant over the three years of recording sessions (Fig. 2). Table II (blocks 1 and 2) shows that he did not change speaking level from his first two to his last two sessions, while his LVE/syl dropped 2 ml. This speaker's $H1-H2$ (Table III) increased less than 1 dB. However, since there was little within-session variation of LVE/syl and of $H1-H2$, the small average increases in these parameters were statistically reliable.

If speakers who regain some hearing reduce SPL, as our implant users generally did, then speakers like our NF-2 patients who undergo severe reduction in hearing may be expected to raise SPL. Considering all 11 speakers, the deaf speakers had the highest SPL pre-intervention (80 dB averaged across speakers), whereas the hard of hearing subject and the NF-2 speakers, who had hearing pre-intervention, had the lowest SPL means (68 dB). A comparison of these NF-2 speakers' baseline and final two sessions, showed, contrary to expectation, that mean speech sound levels were *reduced* by 1, 2, and 4 dB; however, these averages obscure considerable variability in speech sound level from session to session. All three speakers showed an initial rise in speech sound level in the session immediately after intervention, as expected (Fig. 2). NFA's average SPL then fell for several sessions, and finally rose again, leaving a comparison of the first and last two sessions with no significant change. NMA's speech sound level also rose initially but then returned to near baseline values. NFB's rise in level post-intervention was attributable to a peculiarly low value just before intervention; final values average 4 dB below baseline. It is difficult to interpret the findings for NFA and NFB in relation to the control of speech sound level by hearing because there is no independent comparison of their perception of the relative loudness of speech before and after receiving their ABIs. NFA achieved stress perception scores as high as 90% correct with her ABI, NFB 80% correct (MTS test; Erber and Alencewicz, 1976). Thus it is possible that these speakers, because of their ABIs, actually perceived their speech to be louder than pre-intervention. NMA, who had a severe reduction in hearing capacity and did not receive an ABI, decreased SPL in the Rainbow Passage by 2 dB (Table II),

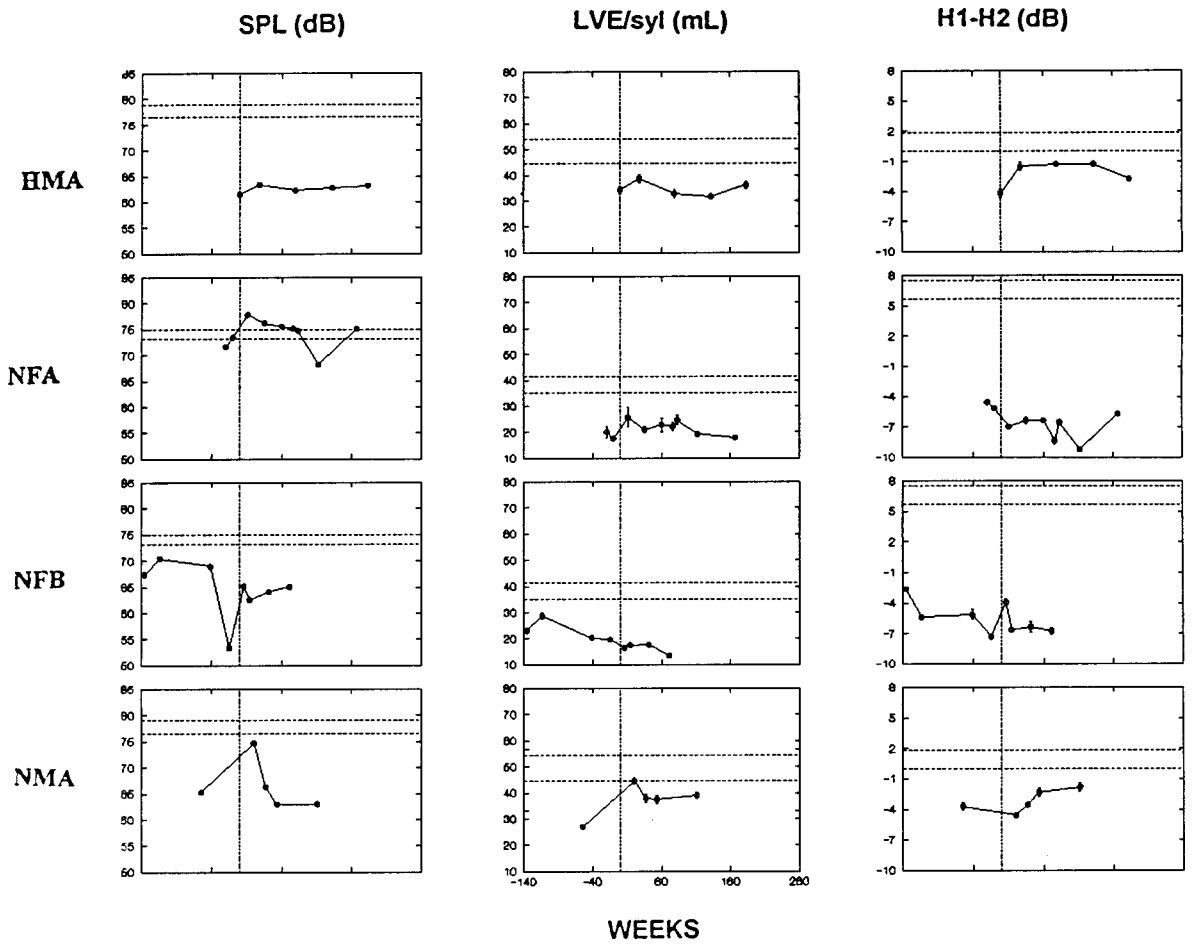

FIG. 2. Longitudinal plots of SPL, LVE/syl, and $H1-H2$ for the hard of hearing male and NF-2 patients; the format is comparable to Fig. 1, except for the plots of SPL, where the starting level of the *y* axis has been lowered to 50 dB to accommodate the lower speaking levels of the NF-2 subjects. The vertical line in each graph indicates the reference week when each NF-2 patient had severe reduction in hearing status and, for NFA and NFB, received an auditory brain-stem implant.

contrary to expectation, but he increased it by 4 dB when reading the vowel inventory (Table III).

Our finding that six of the seven implant users approached normative values of air expenditure during reading once they received some prosthetic hearing leads us to expect that speakers who lose their hearing will deviate from normative values and expend either too little or too much air. Figure 2 shows that all three NF-2 patients had anomalously low LVE/syl while reading prior to their surgery. Following surgery, one speaker maintained low LVE/syl (NFA), one lowered it further (NFB), and one moved toward normative values (NMA). NFA's continued low air expenditure was not the result of particularly shallow speech breathing (Table II, block 4) and may have been due to a pressed glottal posture; the index of her inferred glottal aperture averaged −7.5 dB (Table III, block 2); the female norm reported by Holmberg *et al.* (1995) was +6.6 dB. NFB's further reduction of LVE/syl post-intervention may have been the result of her adopting a more pressed voice (the index of inferred glottal aperture fell to −6.6 dB) and making less incursions below FRC (Table II, block 3). NMA, following severe hearing loss, terminated respiratory limbs well below FRC; this substantially increased the size of his respiratory limbs and hence LVE/syl (block 2). Thus NMA's air expenditure moved towards normative values following hearing loss but it did so because of an anomalous mechanism, he now encroached on expiratory reserve air. Three cochlear implant users also increased LVE/syl but the mechanism they employed was quite different from NMA's use of reserve air: with hearing provided, the CI users who expended more air did so by taking deeper breaths (CFA, CMD) or by extending limbs toward FRC (CFB).

Our finding that five of the seven deaf speakers encroached on expiratory reserve when reading (before receiving prosthetic hearing) leads us to expect that, in general, speakers who become deaf will make greater incursions into expiratory reserve, as did NMA. However, NFA and NFB reduced incursions into reserve air post-intervention (Table II, block 3). This may be related to their receiving ABIs since NMA, who did not receive one, did significantly increase incursions into expiratory reserve after severe hearing loss, as expected. It is unclear, however, what information the ABIs provided that made the difference.

Table III (block 2) shows that the two ABI recipients, NFA and NFB, decreased $H1-H2$. We infer that they assumed more pressed glottal posture. (Although comparison of baseline and final sessions yielded a significant reduction, the time courses for both speakers showed substantial fluc-

TABLE IV. Patterns of change in acoustic and aerodynamic measures following change in hearing status. (A check mark indicates the pattern described at the left was found, while ''No'' indicates a result contrary to the pattern. ns=no significant change or correlation. An asterisk indicates a result that, taken individually, followed the pattern but was not reliable; however, combining the probabilities of a type I error across speakers showed that pattern to be statistically significant.)

		Cochlear implant users							NF-2 patients			
	Speakers:	CFA	CFB	CFC	CMA	CMB	CMC	CMD	HMA	NFA	NFB	NMA
A	Decreased speech sound level	√	√	√	√	√	No	√	ns	ns	√	√
B	Approached normative air expenditure	√	√	ns	√	√	√	√	ns	ns	No	√
C	Limb termination approached FRC	ns	√	√*	√*	√	√*	√	ns	√	√	No
D	Increased inferred glottal aperture	√*	√	ns	No	√	No	√	√	No	No	√

tuation; cf. Fig. 2.) It may be that their very low rates of air expenditure post-intervention reflected in part a substantially reduced subglottal pressure, and their pressed glottal postures were required to sustain phonation. NMA had much higher rates of air expenditure post-intervention than NFA and NFB and did not decrease his index of inferred glottal aperture, indeed, he increased $H1-H2$ by 1.4 dB (Table III, block 2).

All three subjects who were able to hear speech to some extent before *and* after intervention, NFA and NFB because of their ABIs, HMA because he was hard of hearing, read at the highest rates in this study (Table II, block 8: averaging across speakers, their pre-intervention speaking rate was 5.4 syl/s, post-intervention, 5.5 syl/s). They also took the fewest breath pauses, and thus had the largest number of syllables per limb (Table II, block 7): an average of 17.9 and 19.3 pre- and post-intervention, respectively. Perhaps influenced by their ability to hear speech, these speakers frequently uttered an entire sentence, or more than one sentence, in each breath group, which led them to draw on reserve air and may have contributed to their low lung volumes expended per syllable. Finally, the patients who received ABIs reduced these incursions into expiratory reserve significantly from baseline to the final two sessions. High rate, infrequent breath pauses, low levels of air expenditure, and low SPL; this pattern of results is consistent with a strategy of speaking fluently and intelligibly while minimizing energy expenditure.

IV. GENERAL DISCUSSION

In spite of considerable fluctuation in session means for speech sound level, air expenditure, and inferred glottal aperture, a generally coherent picture emerges from these results. Of the 11 speakers in this study, the seven who were deaf pre-intervention had the highest SPL pre-intervention and six of the seven lowered their SPL when the processors of their implants were activated.

Consistent with these results, the dual-process theory leads to the prediction that speakers will increase their sound level if they undergo severe hearing reduction since, following hearing loss, transmission conditions appear to the speaker to be degraded, the perceived signal level goes to zero while other indices of a communication breakdown arise from listener behaviors. In complementary fashion, when an adventitiously deaf speaker receives prosthetic hearing, apparent signal level increases and that speaker will speak more softly when compatible with the current communicative demands.

With some hearing restored, each of the speakers came closer, on the average, to terminating respiratory limbs near FRC (except for CFA who terminated limbs close to FRC while deaf and continued to do so with prosthesis). This result is also consistent with the dual-process theory: under changing conditions for speech transmission, the speaker seeks to ensure adequate speech sound level for intelligibility while minimizing effort. Although we do not measure effort directly, we hypothesize that more effort is expended when the speaker sustains phonation below FRC than above. In order to sustain subglottal pressure below FRC, the speaker must work against the recoil pressures of the respiratory system which are inspiratory. Russell *et al.* (1998) conclude from their study of ventilatory responses during passage reading that ''the respiratory system is controlled during speech to minimize energy expenditure'' (p. 246) and Forner and Hixon (1977) have suggested that when their congenitally deaf speakers were encroaching on reserve air, they were using excessive muscle pressure.

Table IV shows patterns of change in acoustic and aerodynamic measures of the speech of implant users and NF-2

patients following intervention. (A check mark indicates the pattern described at the left was found, while ''No'' indicates a result contrary to the pattern. ns=*no* significant change or correlation; an asterisk indicates a result that, taken individually, followed the pattern but was not reliable; however, combining the probabilities of a type I error across speakers showed that pattern to be statistically significant.) Six of the seven implant users decreased speech sound level (row A). The same number modified their air expenditure in the direction of normative values (B). Six of the speakers also terminated respiratory limbs closer to FRC (C). Four of the speakers increased $H1-H2$ (D).

The pattern of individual results for the implant users (Table IV) indicates that, in several cases, SPL reductions were most likely achieved by increasing glottal aperture, thereby increasing coupling to the trachea, which acts like an antiresonance in the vocal-tract transfer function and attenuates the first formant of low vowels (Perkell *et al.*, 1992). This idea is supported by the observation reported above that three of the four implant users with the largest SPL reductions post-intervention also showed increased $H1-H2$ and reliable longitudinal correlations of SPL and $H1-H2$; the fourth speaker fits this pattern except for her most recent recording. All the speakers who received prosthetic hearing, both cochlear prostheses and ABIs, terminated respiratory limbs closer to FRC post-intervention, by hypothesis to economize on effort. Conversely, the NF-2 patient who had severe hearing loss and did not receive an ABI subsequently read with substantial incursions into expiratory reserve capacity.

Finally, inference from our findings suggests that the implant users' increases and decreases in air expenditure toward normative values with prosthetic hearing were not directly regulated by hearing but were rather a by-product of changes in respiratory and glottal posture made to achieve reductions in SPL (which were directly regulated by hearing) and reductions in the effort expended to initiate expiratory limbs and sustain them with reserve air.

The findings concerning changes in rate of speaking with changes in hearing status are also reasonably consistent with the dual process theory. All of the seven adults with adventitious deafness read the Rainbow Passage initially at articulation rates below the normative range found with 14 hearing males reading the Rainbow Passage (Solomon and Hixon, 1993): 4.9 syl/s +/− 0.3, see Table II, block 8. [Lane and Grosjean (1973) reported a similar average articulation rate of 4.8 syl/s for 12 hearing speakers reading a different passage.] Slower reading rates are associated with ''clear speech'' [e.g., Picheny *et al.* (1986)] and with greater intelligibility [e.g., Picheny *et al.* (1985)]. When prosthetic hearing was provided to those speakers, five of the seven implant users increased articulation rate (four of them reliably), one did not change, and one decreased. (The prosthesis effect may be confounded with a practice effect, although the hard of hearing subject who received no intervention did not alter speaking rate significantly over five sessions spanning more than three years.) The slower articulation rates associated with deafness and with clear speech may come with a greater cost in effort. Following this line of reasoning, speakers chose to reduce that effort once transmission conditions appear to have improved. Thus like the findings for speaking level, those for articulation rate support the view that speakers use self-hearing to monitor transmission conditions and regulate speech parameters in order to achieve a compromise between intelligibility and effort.

ACKNOWLEDGMENTS

Syltinsy Jenkins and Erik Strand assisted with data analysis. We are grateful for assistance to Lorraine Delhorne and Dr. William Rabinowitz, Research Laboratory of Electronics, Massachusetts Institute of Technology; Dr. Donald Eddington, Massachusetts Eye and Ear Infirmary; Dr. Priscilla Short, Massachusetts General Hospital; and Dr. Steven Otto, House Ear Institute. This work was supported by the following N.I.D.C.D. grants: DC00361 to the Massachusetts Eye and Ear Infirmary, Dr. Joseph B. Nadol, Jr., Principal Investigator; DC 01291 and 03007 to the Massachusetts Institute of Technology, Dr. Joseph Perkell, Principal Investigator.

[1]The correction for the influence of $F1$ in dB subtracted from the first and second harmonic amplitudes was $20*\log_{10}(1/(1-(f_{H1}/f_{F1})^2))$ (where f_{H1} is the frequency of the harmonic and f_{F1} is the frequency of the first formant).

Bickley, C. (**1981**). ''Acoustic analysis and perception of breathy vowels,'' MIT Speech Communication Laboratory Working Papers **1**, 71–80.

Black, J. (**1951**). ''The effect of noise-induced temporary deafness upon vocal intensity,'' Sp. Monogr. **18**, 74–77.

Brackmann, D. E., Hitselberger, W. E., Nelson, R. A., Moore, J., Waring, M. D., Portillo, F., Shannon, R. V., and Telischi, F. F. (**1993**). ''Auditory brainstem implant I. Issues in surgical implantation,'' Otolaryngol.-Head Neck Surg. **108**, 624–633.

Eddington, D. (**1983**). ''Speech recognition in deaf subjects with multichannel intracochlear electrodes,'' Ann. (N.Y.) Acad. Sci. **405**, 241–258.

Erber, N., and Alencewicz, C. (**1976**). ''Audiologic evaluation of deaf children,'' J. Speech Hear. Dis. **41**, 256–267.

Fairbanks, G. (**1960**). *Voice and Articulation Drill Book* (Holt, Rinehart and Winston, New York).

Fletcher, H., Raff, G. M., and Parmley, F. (**1918**). ''Study of the effects of different amounts of sidetone in the telephone set,'' Western Electric Company Report No. 19412, Case Number 120622.

Forner, L., and Hixon, T. J. (**1977**). ''Respiratory kinematics in profoundly hearing impaired speakers,'' J. Speech Hear. Res. **20**, 373–408.

Hoit, J. D., and Hixon, T. J. (**1987**). ''Age and speech breathing,'' J. Speech Hear. Res. **30**, 351–366.

Hoit, J. D., Hixon, T. J., Altman, M. E., and Morgan, W. J. (**1989**). ''Speech breathing in women,'' J. Speech Hear. Res. **32**, 353–365.

Hoit, J. D., Hixon, T. J., Watson, P. J., and Morgan, W. J. (**1990**). ''Speech breathing in children and adolescents,'' J. Speech Hear. Res. **33**, 51–69.

Holmberg, E., Hillman, R., Perkell, J. S., and Gress, C. (**1994**). ''Relationships between intra-speaker variation in aerodynamic measures of voice production and variation in SPL across repeated recordings,'' J. Speech Hear. Res. **37**, 484–495.

Holmberg, E. B., Hillman, R. E., Perkell, J. S., Guiod, P. C., and Goldman, S. L. (**1995**). ''Comparisons among aerodynamic, electroglottographic, and acoustic spectral measures of female voice,'' J. Speech Hear. Res. **38**, 1212–1223.

Itoh, M., and Horii, Y. (**1985**). ''Airflow, volume, and durational characteristics of oral reading by the hearing-impaired,'' J. Commun. Disorders **18**, 393–407.

Klatt, D. H., and Klatt, L. C. (**1990**). ''Analysis, synthesis, and perception of voice quality variations among female and male talkers,'' J. Acoust. Soc. Am. **87**, 820–57.

Ladefoged, P. (**1981**). ''The relative nature of voice quality,'' J. Acoust. Soc. Am. **69**, S67(A).

Lane, H., and Grosjean, F. (**1973**). ''Perception of reading rate by speakers and listeners,'' J. Exp. Psychol. **97**, 141–147.
Lane, H. L., Perkell, J., Svirsky, M., and Webster, J. (**1991**). ''Changes in speech breathing following cochlear implant in postlingually deafened adults,'' J. Speech Hear. Res. **34**, 526–533.
Lane, H., Tranel, B., and Sisson, C. (**1970**). ''Regulation of voice communication by sensory dynamics,'' J. Acoust. Soc. Am. **47**, 618–624.
Lane, H., Wozniak, J., Matthies, M., Svirsky, M., Perkell, J., O'Connell, M., and Manzella, J. (**1997**). ''Changes in sound pressure and fundamental frequency contours following changes in hearing status,'' J. Acoust. Soc. Am. **101**, 2244–2252.
Leder, S. B., Spitzer, J. B., Milner, P., Flevaris-Phillips, C., Kirchner, J. C., and Richardson, F. (**1987**). ''Voice intensity of prospective cochlear-implant candidates and normal-hearing adult males,'' Laryngoscope **97**, 224–227.
Lindblom, B., and Engstrand, O. (**1989**). ''In what sense is speech quantal?'' J. Phonetics **17**, 107–121.
Perkell, J., Lane, H., Svirsky, M., and Webster, J. (**1992**). ''Speech of cochlear implant patients: A longitudinal study of vowel production,'' J. Acoust. Soc. Am. **91**, 2961–2978.
Perkell, J. S., Matthies, M. L., Lane, H., Guenther, F. H., Wilhelms-Tricarico, R., Wozniak, J., and Guiod, P. (**1997**). ''Speech motor control: Acoustic goals, saturation effects, auditory feedback and internal models,'' Speech Commun. **22**, 227–250.
Picheny, M. A., Durlach, N. I., and Braida, L. D. (**1985**). ''Speaking clearly for the hard of hearing I: Intelligibility differences between clear and conversational speech,'' J. Speech Hear. Res. **28**, 96–103.
Picheny, M. A., Durlach, N. I., and Braida, L. D. (**1986**). ''Speaking clearly for the hard-of-hearing II: Acoustic characteristics of clear and conversational speech,'' J. Speech Hear. Res. **29**, 434–446.
Rosenthal, R. (**1991**). *Meta-analytic Procedures for Social Research* (Sage, Newbury Park).
Russell, B. A., Cerny, F. J., and Stathopoulos, E. T. (**1998**). ''Effects of varied vocal intensity on ventilation and energy expenditure in women and men,'' J. Speech Lang. Hear. Res. **41**, 239–248.
Solomon, N., and Hixon, T. (**1993**). ''Speech breathing in Parkinson's disease,'' J. Speech Hear. Res. **36**, 294–310.
Whitehead, R. L. (**1983**). ''Some respiratory and aerodynamic patterns in the speech of the hearing impaired,'' in *Speech of the Hearing Impaired*, edited by I. Hochberg, H. Levitt, and M. J. Osberger (University Park Press, Baltimore, MD), pp. 97–116.
Wilson, K. (**1979**). *Voice Problems of Children* (Williams and Wilkins, Baltimore).
Youngblood, J., and Robinson, S. (**1988**). ''Ineraid (Utah) multichannel cochlear implants,'' Laryngoscope **98**, 5–10.

A geometrical fuzzy clustering-based solution to glottal wave estimation

Yair Shapira and Isak Gath
Department of Biomedical Engineering, Technion, Israel Institute of Technology, 32000 Haifa, Israel

(Received 25 June 1997; accepted for publication 10 August 1998)

Accurate estimation of the glottal waveform (GW) is required for purposes such as natural speech synthesis, speaker recognition, physiological speech processing, etc. Most methods available for GW estimation are based on inverse filtering of the speech signal through the vocal tract, and they all suffer from inaccuracies due to incorrect assumptions. The method for GW estimation developed in the present study is based on fuzzy clustering of quasi-linear geometrical substructures, represented within the signal shifts hyperspace. Algorithms for estimation of the driving function to the vocal tract are presented and evaluated on simulated and real data. Comparison of the fuzzy clustering-based method with the PSIAIF and Wong's closed-phase algorithms shows that the present method is superior with respect to both the GW estimation and determination of GW event time instants. © *1998 Acoustical Society of America.* [S0001-4966(98)04411-7]

PACS numbers: 43.72.Ar, 43.70.Aj [JLH]

INTRODUCTION

The glottal waveform (GW) is the volume velocity flow of air through the vocal folds and into the vocal tract. The GW serves as the driving function of the speech production apparatus, the vocal tract filter. There is great significance in accurately estimating the GW, in particular for purposes such as data reduction, natural speech synthesis, speaker recognition, physiological speech processing, pathological speech production, etc.

Accurate estimation of the GW encounters certain difficulties. Sondhi (1975) suggested a method for GW estimation based on reduction of the effects of the vocal tract on the GW by speaking into a reflectionless uniform tube. However, most of the common methods are based on inverse filtering of the speech signal through the vocal tract filter, requiring knowledge of the vocal tract filter parameters. The vocal tract filter in vowels is usually modeled by an all-pole filter, and is therefore estimated using AR estimators. However, AR algorithms assume a white innovation, which the GW does not satisfy.

One way to overcome this difficulty is simply to ignore it. Analog nets were proposed by Miller (1959) for inverse filtering of the first formants and the lip radiation, and later developed to digital filters. These methods often result in an estimation which bears no resemblance to a glottal waveform.

Algorithms such as the closed-phase inverse filtering (Wong, 1979) make use of the typical shape of the GW. In low pitch speakers, the vocal folds are closed for a relatively long time interval, manifested as the flat segment in the GW. During this segment (the closed phase) the GW can be regarded as a white signal. In order to use these algorithms a knowledge of closed-phase timing is required. However, the assumption that during the closed phase the glottis is really closed is not accurate. Glottal models (Hedelin, 1986; Fant *et al.*, 1985) suggest a mild slope in the signal during the so-called closed phase. In addition, the closed phase in high pitch voices is usually very short or even missing, and thus the estimators' statistical properties are not constant, due to the variability in the closed-phase length.

Other methods, such as IAIF (Alku *et al.*, 1990) or the later PSIAIF (Alku, 1992), iterate between glottal envelope estimation and vocal tract estimation. These methods estimate the glottal envelope using a low order AR estimator, and inverse filter the speech signal through the glottal envelope, to get a pure vocal tract AR signal. These methods suffer from a ripple caused by inaccurate estimation of the vocal tract coefficients. In vowels such as /u/ or /i/ the results are often very poor.

Parametric methods, such as Hedelin's (1986), assume a modeled GW, which does not always fit the real GW. These algorithms involve numerical optimization and are computationally expensive.

Fuzzy clustering has been shown to be useful in signal and image processing, and may be used to solve the GW estimation problem as well. The method described here is based on fuzzy clustering of the quasi-linear geometrical structures, generated by the speech signal in signal shifts' hyperspace. Linear structures in this hyperspace are regarded as AR filtered signals, generated by a constant driving function. Hence, the clustering algorithm estimates the vocal tract filter on noncontinuous analysis windows.

The advantages of the suggested algorithm are: (a) There is no need to rigidly define the analysis window as with the closed-phase and PSIAIF methods. (b) The whole data set may be employed in the estimation, including both the opening and the closing phases. (c) The algorithm is nonparametric. (d) As a byproduct, events in the GW can be easily detected. (e) The average slope of the segment can be derived from the linear cluster.

Section I introduces the methods developed and used in the present study. The geometrical framework and the fuzzy hyperplane clustering algorithm are presented, and the methods employed to estimate the GW and its events are explained. In Sec. II the performance of the new methods is evaluated on simulated and real data and compared to the

performance of other algorithms, by means of precision as well as computational complexity. Section III contains conclusions.

I. METHODS

A. The geometrical framework

This paper proposes a new approach to the GW estimation problem, based on fuzzy clustering of hyperplanes in signal shifts' hyperspace. The rationale behind the suggested method is that the glottal waveform can be approximated to first order by three segments with constant slopes: opening, closing, and closed phases. The derivative of these segments constitutes a piecewise constant driving function to the vocal tract. Assuming this rough approximation and a constant AR vocal tract filter, the shift vectors should form three hyperplanes reflecting the three phases of the GW. The normal vectors to these hyperplanes are the AR coefficients of the vocal tract filter.

The vocal tract is assumed to be an all-pole filter of order N, with a coefficient vector $\mathbf{a}=(a_1,a_2,\ldots,a_N)$. The filter's driving function is referred to as the combination of the GW and lip radiation, i.e., the glottal derivative $\mathbf{q}=\mathbf{g}'$. The relation between subsequent samples of the speech signal is therefore:

$$\begin{aligned} x_n &= q_n + \sum_{i=1}^{N} a_i x_{n-i}, \\ x_n - \sum_{i=1}^{N} a_i x_{n-i} &= q_n, \\ \sum_{i=0}^{N} r_i x_{n-i} &= q_n, \\ \mathbf{r}\cdot\mathbf{x}_n^T &= q_n, \end{aligned} \tag{1}$$

where $\mathbf{x}_n$, the signal shifts vector, is defined by $\mathbf{x}_n=(x_n,x_{n-1},\ldots,x_{n-N})$, and the vector $\mathbf{r}$ is defined by $r_i=-a_i$ $r_0=1$. In segments where $\mathbf{q}$ is constant (denoted by c_k), the points $\mathbf{x}_n$ in the N-dimensional signal shifts hyperspace satisfy a hyperplane equation:

$$\mathbf{r}\cdot\mathbf{x}_n^T=c_k. \tag{2}$$

B. Fuzzy *K* hyperplanes

The method suggested involves an algorithm for clustering a pool of vectors in the N-dimensional signal shifts' hyperspace into K hyperplanes. Given a pool of M points as a matrix $\mathbf{X}_{N\times M}$, the aim is to find K hyperplanes which best fit the data. One solution is given by the fuzzy-C-varieties (FCV) algorithm (Bezdek *et al.*, 1981a, 1981b). The FCV clusters points into hyperellipsoids, and linear varieties of dimension r are fitted to these hyperellipsoids. The linear varieties pass through the centroids of the hyperellipsoids, and the dominant (with the highest eigenvalues) eigenvectors, being equivalent to the longest hyperellipsoid axes, are their spanning vectors. This algorithm suffers from instability and initial condition problems. A more geometrical intuitive approach, based on multivariate linear regression, is suggested. The classical statistical approach is here modified by using weighted regression, where the weights are the fuzzy membership functions.

The objective function to be optimized, J, is a weighted sum of the squared distances between a hyperplane and its related points:

$$J(\mathbf{U},\mathbf{R};\mathbf{c})=\sum_{k=1}^{K}\sum_{m=1}^{M} u_{k,m}d_{k,m}^2, \tag{3}$$

where $\mathbf{U}_{K\times M}$ is the membership matrix and $u_{k,m}$ is the degree of membership of the mth point in the kth cluster. The rows of $\mathbf{R}_{K\times N}$ consist of the normal vectors $\mathbf{r}_k$ to the K hyperplane clusters. $\mathbf{c}$ is a column vector of length K, whose elements are c_k [Eq. (2)]. $d_{k,m}$ is the distance between the mth point and the kth hyperplane.

The intuitive geometrical error is the metric of the Euclidean distance between a point $\mathbf{x}$ and a hyperplane [see Eq. (2)]:

$$\begin{aligned} d(\mathbf{x},\mathbf{r},c) &= \frac{|\mathbf{r}\cdot\mathbf{x}^T-c|}{\|\mathbf{r}\|}, \\ d_{k,m} &= \frac{|\mathbf{r}_k\cdot\mathbf{x}_m^T-c_k|}{\|\mathbf{r}_k\|}, \end{aligned} \tag{4}$$

where $\|\cdot\|$ is the Euclidean norm.

The algorithm iterates between updating the membership matrix, and updating the normal vectors to the hyperplanes.

The normal equations for the membership functions are similar to those of the fuzzy K-means algorithm (Bezdek, 1981), and therefore yield a similar updating formula:

$$u_{k,m}=\left[\sum_{l=1}^{K}\frac{d_{k,m}}{d_{l,m}}\right]^{-1}. \tag{5}$$

In order to optimize the objective function by updating the normal vectors $\mathbf{R}$, Eq. (3) is differentiated obtaining the normal equation:

$$\begin{aligned} \frac{\partial J}{\partial \mathbf{r}_k} &= 2\sum_{m=1}^{M} u_{k,m}d_{k,m}\mathbf{x}_m \\ &= \frac{2}{\|\mathbf{r}_k\|}\sum_{m=1}^{M} u_{k,m}(\mathbf{r}_k\mathbf{x}_m^T-c_k)\mathbf{x}_m=0, \end{aligned}$$

$$\sum_{m=1}^{M} u_{k,m}\mathbf{r}_k\mathbf{x}_m^T\mathbf{x}_m=\sum_{m=1}^{M} u_{k,m}c_k\mathbf{x}_m,$$

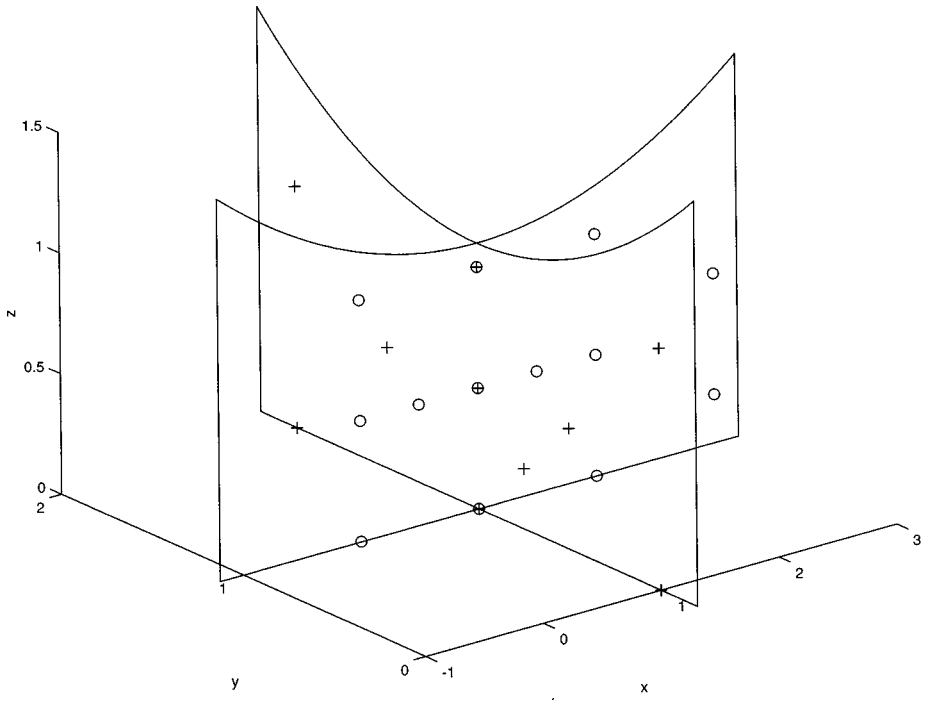

FIG. 1. ''Two fences'' data (Bezdek *et al.*, 1981b). Twenty data points arranged in two orthogonal two-dimensional planes. Results of clustering with the fuzzy *K*-hyperplanes algorithm. ''0'' and ''+'' denote data points belonging to different planes. Three of the data points are distributed along the intersection line between the two planes, and acquire, therefore, a degree of membership of 0.5 in each of the planes.

where $\mathbf{c}_k$ is the column vector of length N, whose elements are all c_k. And in a matrix notation, the weighted linear regression formula is derived:

$$\mathbf{X}\mathbf{U}_k\mathbf{X}^{\mathbf{T}}\mathbf{r}_k=\mathbf{X}\mathbf{U}_k\mathbf{c}_k,$$
$$\mathbf{r}_k^T=[\mathbf{X}\mathbf{U}_k\mathbf{X}^T]^{-1}\mathbf{X}\mathbf{U}_k\mathbf{c}_k, \tag{6}$$

where $\mathbf{U}_k$ is defined by the diagonal $M\times M$ matrix

$$u_{k_{i,j}}=\begin{cases} u_{k,j}, & i=j \\ 0, & i\neq j \end{cases}.$$

In the general case the vectors $\mathbf{x}_n$ are linearly independent, and therefore the matrix $\mathbf{X}$ is regular (and so is $\mathbf{X}^T$). Since $\mathbf{U}_k$ is a diagonal matrix: $|\mathbf{U}_k|=\Pi_{m=1}^{M}u_{k,m}$. In order for the matrix $\mathbf{X}\mathbf{U}_k\mathbf{X}^T$ to be invertible, $u_{k,m}\neq 0 \quad \forall k,m$ is required.

The hyperplane equation [Eq. (2)] holds a redundancy. A specific hyperplane can be given by an infinite number of equations, differing only by a multiplication factor. There is no need for $N+1$ ($\mathbf{r}$ is of length N, and c) variables in order to specify a hyperplane. *Almost all* hyperplanes can be described by an equation of N-variables, while holding the $N+1$ variable equal to 1. For instance, the equation $(1,r_2,r_3,\ldots,r_N)\cdot\mathbf{x}^T=c, \quad c\neq 0$ describes all hyperplanes which are *not parallel* to the x_1 axis. The equation:

$$\mathbf{r}\cdot\mathbf{x}^T=1 \tag{7}$$

describes all hyperplanes which *do not cross* the origin. Nevertheless, hyperplanes which *do cross* the origin can arbitrarily be approximated using such an equation. This latter choice will be used here and subsequently, so that $\forall 1<k<K$: $c_k=1$.

Figure 1 demonstrates two linear planes in a three-dimensional space, using the ''2 fences data'' (Bezdek *et al.*, 1981b). These planes were estimated using the fuzzy-*K*-hyperplanes algorithm, from the 20 marked data points. The initial conditions were chosen randomly. The points distributed on the intersection line between the two planes acquire a degree of membership of 0.5 in each plane cluster, and belong therefore equally to both clusters.

C. The triangular glottal approximation

The GW is approximated to first order by a triangular pulse, where the three slopes reflect the opening, closing, and closed phase of the GW. As mentioned above, the corresponding driving function to the AR vocal tract filter is piecewise constant. Using this rough approximation, the points in the N-dimensional signal shifts hyperspace will be distributed across three hyperplanes.

As long as the closed phase in the triangular approximation has the slightest positive slope, the driving function is not 0. Hence, the fuzzy-*K*-hyperplanes algorithm can estimate the corresponding hyperplanes.

The matrix $\mathbf{X}$, of the points to be clustered, is a Toeplitz matrix, containing the signal shifts vectors:

$$\mathbf{X}=\begin{pmatrix} x_{N-1} & x_N & x_{N+1} & \cdots & x_{M-2} & x_{M-1} & x_M \\ x_{N-2} & x_{N-1} & x_N & \ddots & & x_{M-2} & x_{M-1} \\ \vdots & & \ddots & \ddots & \ddots & & \vdots \\ x_0 & x_1 & x_2 & \cdots & & & x_{M-N+1} \end{pmatrix}$$
$$=(x_{N-1}^T,\ x_N^T,\ x_{N+1}^T,\ldots,x_M^T). \tag{8}$$

The GW estimate is derived from Eq. (1) by projecting the K normal vectors on the $\mathbf{X}$ matrix. The final GW is chosen from the K estimates, as explained in Sec. I D.

The single interval algorithm is summarized as follows:

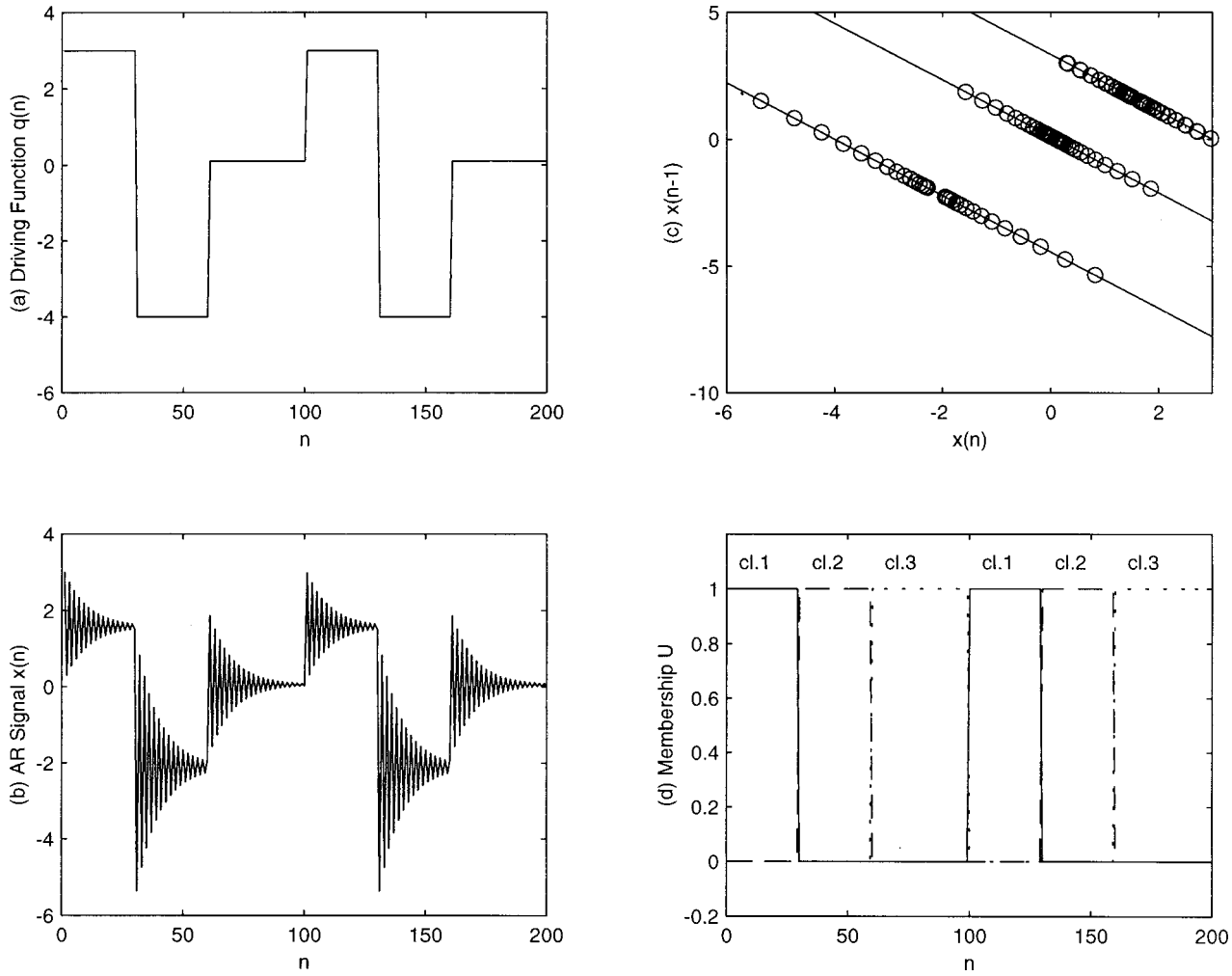

FIG. 2. Estimation of a synthetic GW using a 1st order AR filter. (a) The piecewise constant driving function resembling two periods of the glottal derivative triangular approximation. (b) The temporal filtered signal after passing the driving function in (a) through a first order AR filter. (c) The signal in its two-dimensional shifts space, the points cluster along three linear structures (lines). (d) The three different membership functions (continuous, dashed and dotted lines), calculated by the fuzzy-*K*-hyperplanes algorithm, accurately segment the signal into the three corresponding phases of the driving function.

Algorithm 1:

1. Fix parameters:
   1a. Fix termination criterion, ϵ.
   1b. Choose arbitrary initial conditions $\mathbf{R}$.
2. Generate the Toeplitz matrix $\mathbf{X}$ from the speech signal using Eq. (8).
3. For every k,m calculate the distance $d_{k,m}=|\mathbf{r_k}\cdot\mathbf{x}_m^T-1|/\|\mathbf{r}_k\|$ [Eqs. (4), (7)].
4. Calculate the membership $u_{k,m}$ for every k, m, from Eq. (5).
5. If the change in $\mathbf{U}$ is smaller than ϵ goto 8.
6. For every k estimate $\mathbf{r}_k^T=[\mathbf{X}\mathbf{U}_k\mathbf{X}^T]^{-1}\mathbf{X}\mathbf{U}_k\mathbf{c}_k$ [Eq. (6)], where c is a vector of 1's.
7. Goto 3.
8. The GW estimated by the kth cluster is: $\mathbf{q}_k=\mathbf{r}_k\cdot\mathbf{X}$ [from Eq. (1)].

Figure 2 demonstrates estimation of a synthetic GW using a first order AR filter. A signal was synthesized by passing a piecewise constant driving function [Fig. 2(a)] resembling two periods of the glottal derivative triangular approximation, through a first order AR filter: $x_n=-0.9x_{n-1}+u_n$. The temporal filtered signal is depicted in Fig. 2(b). Figure 2(c) shows the signal in its two-dimensional shifts space. As stated, the points cluster along three linear structures (lines). The fuzzy-*K*-hyperplanes algorithm easily identifies these three lines. The three different membership functions, calculated by the algorithm and depicted in Fig. 2(d), accurately segment the signal into the various corresponding phases of the driving function.

D. Estimation of the real driving function

The constant slope assumption is only an approximation of the true nature of the GW, and hence the shift vectors are not distributed across the hyperplanes but close to them. The further a point is from a hyperplane, the smaller its degree of membership in this hyperplane, and in turn its contribution to the estimation of the hyperplane [see Eqs. (5), (6)]. Hence, the estimation of the vocal tract filter coefficients uses a flexible weighted analysis window, which may even be noncontinuous.

After estimating the three normal vectors to the three

hyperplane clusters, these vectors are employed to estimate the true driving function. A moving average (MA) filter, the coefficients of which are the elements of the normal vectors, is assumed to be the inverse filter to the vocal tract AR filter. Therefore $q_n = \mathbf{r}_k \cdot \mathbf{X}_n^T$, as stated in Eq. (1), and the K whole-length excitation waves can be estimated by the projection of the normal vectors on $\mathbf{X}$:

$$\mathbf{q}_k = \mathbf{r}_k \cdot \mathbf{X}. \tag{9}$$

However, due to the true nature of the GW, the driving function in the opening and closing phases is not necessarily constant as modeled. In addition, the GW may even include AR elements of itself and these AR elements are strong enough for algorithms like the IAIF (Alku *et al.*, 1990) to make use of them. The autoregressive elements cause the normal vectors to be the convolution of both the vocal tract filter and the GW AR elements, and to deviate from the original $\mathbf{r}$. Of all three GW components, the closed-phase shift vectors are nearest to the closed-phase hyperplane, and its normal vector resembles mostly the true vocal tract inverse filter. The closed phase is usually modeled by a slight positive constant slope, equivalent to a low positive constant driving function.

A closed-phase cluster is *very seldom* obtained when clustering a high order AR filtered signal into three hyperplanes. Instead of obtaining the three components of the triangular glottal approximation, the signal is usually segmented into: (a) opening; (b) GW peak; (c) closing, while the closed phase is generated from a mixture of these three clusters. It was thus found that clustering with $K=2$ (two clusters) results in a more accurate description of the opening and closing phases of the GW.

In order to achieve a better estimate of *all three* components of the GW, a second step is suggested, following the $K=2$ clustering. In this step the signal is clustered with $K=3$. The initial guess is derived from the previous two-clusters step. The closed-phase slope was empirically found to be $\sim 1/20$ of the opening phase slope: $\mathbf{g}'_{\text{closed}} \cong \mathbf{g}'_{\text{opening}}/20 \Rightarrow \mathbf{q}_{\text{closed}} \cong \mathbf{q}_{\text{opening}}/20$. In order to satisfy Eq. (9), the normal vector of the closed phase must therefore be ~ 20 times larger than the normal vector of the opening phase: $\mathbf{r}_{\text{closed}} \cong 20 \cdot \mathbf{r}_{\text{opening}}$. The initial $\mathbf{R}$ matrix for the second step is therefore:

$$\mathbf{R} = \begin{bmatrix} \mathbf{r}_{\text{opening}} \\ \mathbf{r}_{\text{closing}} \\ 20 \cdot \mathbf{r}_{\text{opening}} \end{bmatrix}. \tag{10}$$

Running this second step yields a new cluster. The points having a high value of the membership function in this third cluster belong usually to the closed phase, and sometimes to the GW peak as well. The GW estimated using the third cluster normal vector is usually smoother than the GW estimated using the opening cluster or the closing cluster. Figure 3 demonstrates estimation of the GW employing the suggested two steps algorithm. An /a/ vowel was synthesized by passing a synthetic GW [Fig. 3(a)] through a six order AR filter (three formants). The synthesized vowel [Fig. 3(b)] was processed by the suggested two steps algorithm. The first step yielded a rippled estimation [Fig. 3(c)]. The $K=2$ membership functions can be crisped (converted to hard rather than the fuzzy partition) to segment the signal into the opening (op) and closing (cl) phases [Fig. 3(d)]. In the second step a smooth GW was obtained [Fig. 3(e)]. The results of the crisped clustering [Fig. 3(f)] are very precise, and accurately segment the signal into opening (op), closing (cl), and closed (cd) phases.

E. Estimation of the driving function of a long signal segment

When dealing with a long speech signal (more than a few pitch periods), the assumption of a constant vocal tract filter is very rough, and the hyperplanes are corrupted. The computational resources needed to implement the algorithm on a long stretch of signal as a single interval are excessive. The solution to these problems is cutting the signal into analysis intervals of reasonable length (2–3 pitch periods). The GW is estimated in each interval, and all the GWs are concatenated to a fully estimated glottal waveform.

Other methods of GW estimation (Wong *et al.*, 1979; Alku, 1992) demand synchronization of the analysis intervals to specific events in the excitation wave, and this requirement is critical to the consistency and accuracy of the estimation. Due to the flexible analysis window, used in the present method, the algorithm is not sensitive to these timings, assuming that subsequent intervals have similar vocal tract filters.

This last assumption can also be used to reduce the computational load. There is no need to rerun the first step ($K=2$) in order to obtain a rough estimation. The normal vectors from the last analysis interval can be used as an initial guess for the next interval. The first step should, therefore, be computed only once, on the first analysis interval. The algorithm is summarized as follows:

Algorithm 2:

1. Choose ΔT, the interval length (2–3 pitch periods). Fix the timing of the beginning of the first interval, $T_0 = N-1$. Fix $i=0$.
2. $\mathbf{X} = \{\mathbf{x}_{T_i}, \mathbf{x}_{T_i+1}, \ldots, \mathbf{x}_{T_i+\Delta T}\}$, i, the index of current interval.
3. If $i=1$ then estimate $\mathbf{R}$ on $\mathbf{X}$ with $K=2$ and random initial conditions, using algorithm 1. Generate initial guess for the three-clusters estimation, using Eq. (10).
4. Estimate $\mathbf{R}$ and $\mathbf{g}$ on $\mathbf{X}$ with $K=3$, using algorithm 1. Initial conditions are the last estimated $\mathbf{R}$.
5. Concatenate $\mathbf{g}$ to obtain the estimated GW.
6. If end of signal has not been reached, then $T_{i+1} = T_i + \Delta T + 1$, $i = i+1$, go to 2. Else end.

F. Tracking events in the GW

As mentioned, the membership function, utilized as a weighting function for the regression, can also be used for tracking events—glottal opening, maximal opening, and closing. The membership of a sample is a measure of its

affinity to the different clusters, and a phase should therefore consist of a sequence of samples which all have their highest membership in the same cluster.

In order to find these sequences, the membership function should be first crisped. This is carried out by utilizing the criterion of maximal membership. In addition, a crisping threshold can be used, so that fuzzy samples are crisped to a noise cluster:

$$\tilde{u}_{k,m}=\begin{cases}1, & k=\arg\max\limits_{1\leqslant k\leqslant K}(u_{k,m}) \quad \text{and} \quad \max\limits_{1\leqslant k\leqslant K}(u_{k,m})\geqslant th \\ 0, & \text{otherwise}\end{cases}, \tag{11}$$

where th is a given threshold.

Sequences of samples, which belong to the same cluster, are marked using a heuristic approach. Only sequences longer than a predefined length threshold (smaller than the *a priori* phase length) are considered. A tolerance factor, which serves as a noise rejecting filter, can be added, by ignoring in each sequence up to two samples that have their maximal degree of membership in the wrong cluster. A condition of minimal time interval between sequences of the same cluster may also be used.

The acoustic events are at the boundaries of these sequences. Some additional heuristic considerations must be made to ignore event timings. It has been found that segmentation of real data with $K=2$ is often simpler than with $K=3$. The two clusters, opening and closing, exactly match the acoustic phases, while the closed phase does not contain sequences of either clusters. The opening event is, therefore, the beginning of the opening cluster sequence, maximal opening is obtained at the junction between opening and closing cluster sequences, and the closing event is the end of the closing cluster sequence.

II. PERFORMANCE EVALUATION

A. Simulations

Signals of various voiced phonemes (vowels and consonants) were synthesized with a sampling rate of 11 kHz. All signals were 100 pitch periods long ($\sim$1 s). The pitch was normally distributed with $N(100,2.5)$. Hedelin's parametric GW (Hedelin, 1986) was synthesized. The vocal tract was modeled by three formants and the formant frequencies were adapted from Witten (1987). The filtered signal was differentiated using a first order differentiator.

The signals were processed using the fuzzy hyperplane approach, with $K=3$. The best GW estimate was the one obtained by the closed-phase cluster. The membership function was crisped using a crisping threshold of 0.5. Sequences of 12 samples or more in the same cluster were detected, and employed for event estimation.

For comparison, the GW was also estimated using Alku's PSIAIF method (Alku, 1992), which was found to give the best waveform estimation. Events were estimated by Wong's closed-phase method (Wong *et al.*, 1979), which exhibited the best results.

Estimation errors were calculated for both event timing and waveform estimation. Computed timing of the opening and closing events was compared to that given by the simulation parameters and a vector of errors was saved for the opening and closing events in Wong's method and in the fuzzy clustering-based method.

The computed glottal waveform itself was compared to the simulated GW by means of MSE. The dc component of the estimated GW was subtracted for each frame of comparison (200 samples), so that a residue with a zero baseline would be calculated. The residue vector was squared and averaged to obtain the MSE.

Performance of the three methods was compared using the following criteria:

1. The errors' *bias* was estimated using the error median in order to reduce the effect of outliers. A small bias is satisfactory, as long as the dispersion is small.
2. The *success rate* is the proportion of the GW events successfully detected using the algorithm. Outliers are discarded in this criterion. The success rates achieved by the present method and by Wong's closed-phase method were compared using the Welch test.
3. As a measure of *dispersion* the standard deviation of the events error was calculated in order to determine the consistency of the estimation. The vector of errors is often non-Gaussian, and therefore, a nonparametric test is indicated. The Siegel–Tuckey sum of ranks test (Siegel and Castellan, 1988) for dispersion differences was utilized.
4. The *approximation accuracy* was measured by the MSE between the estimated waveform and the synthesized waveform. As mentioned, the dc error was subtracted in short time frames. The MSE achieved by the PSIAIF method was compared to that of the fuzzy clustering-based method, using the one-tail *t*-test.

Table I summarizes the numberical results of the abovementioned criteria and tests. The following findings can be discerned:

1. *Bias*—The closing event is estimated with no bias using the fuzzy clustering-based method, and with a very small bias using Wong's closed-phase algorithm. The timing of the opening event is estimated by the present algorithm with a small constant bias, whereas the closed-phase method fails to identify this event and identifies instead the closing event (some 37 samples away).
2. *Success proportion*—The fuzzy clustering method identifies the opening and closing events with 100% and more than 90% success, respectively. Wong's algorithm identifies the closing event, but totally fails in the opening events.
3. *Dispersion*—The closing event is estimated by both methods with a very low dispersion. For some phones the timings are extremely accurate and no dispersion is witnessed. Events in other phones are estimated by the fuzzy clustering method with a significantly smaller dispersion. The dispersion in the opening event, estimated by the present method, is much larger, but still satisfactory.
4. *MSE*—The fuzzy clustering-based algorithm estimates the waveform significantly more accurately than the PSIAIF algorithm. Errors in the fuzzy estimation rarely occur, and are very small. No ripple is observed. The PSIAIF gener-

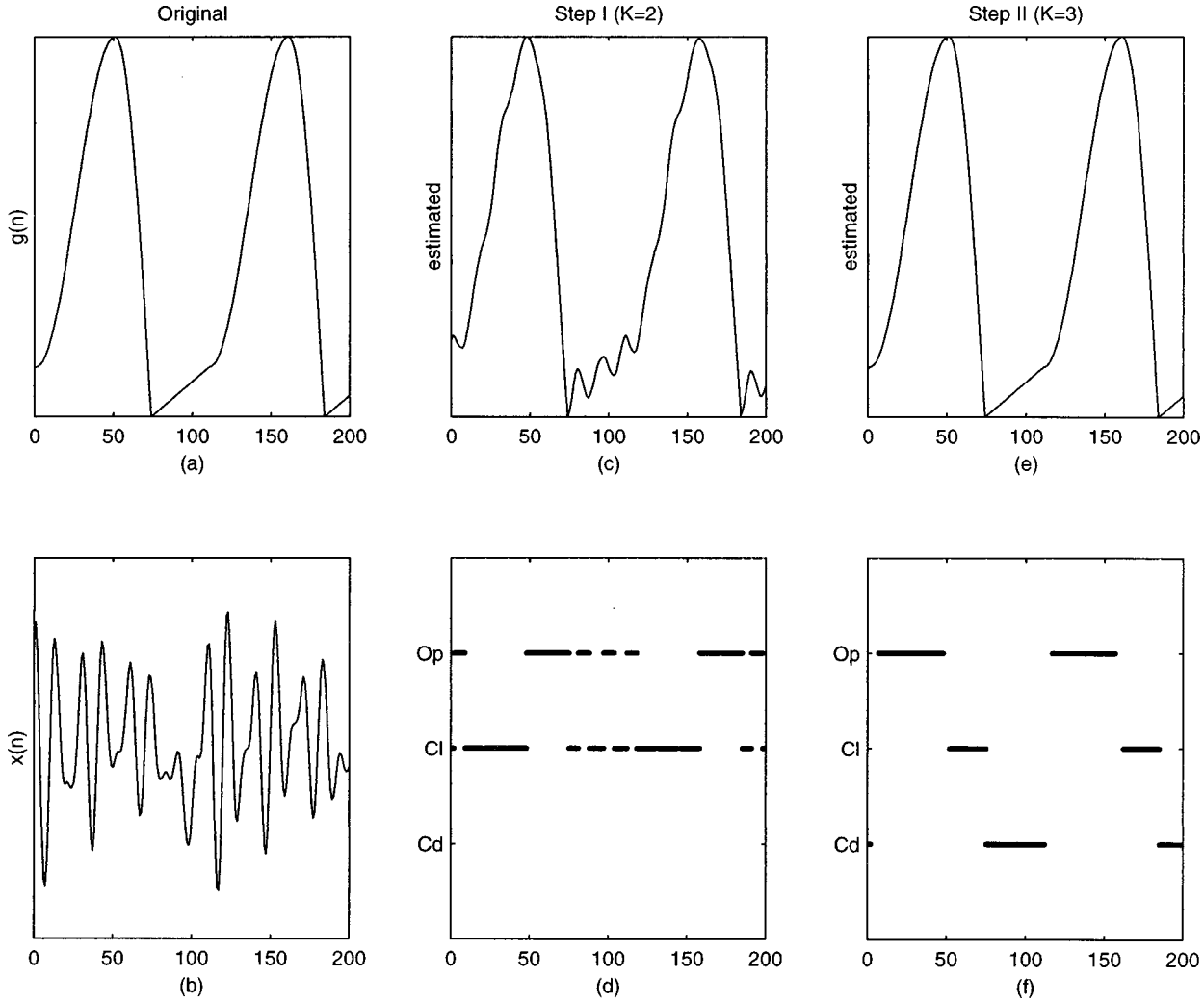

FIG. 3. Estimation of the GW employing the two steps fuzzy clustering algorithm. (a) A synthetic GW. (b) The synthesized vowel, /a/, obtained by passing the driving function in (a) through a six order AR filter (three formants). (c) Processing of the synthesized vowel in (b) by the two steps algorithm. The first step with $K=2$ clusters yields a rippled estimation. (d) The membership functions are crisped in order to segment the signal into the opening (op) and closing (cl) phases. (e) A second step with $K=3$ clusters yields a smoother GW. (f) Accurate segmentation of the signal into opening (op), closing (cl), and closed (cd) phases is obtained by the second step, after crisping the membership functions.

ates a very mild ripple, due to nonaccurate estimation of the vocal tract filter. The PSIAIF also suffers from a mild distortion due to a lack of initial conditions at the start of the signal.

B. Real data

Speech and electrolaryngographic (ELG) signals were recorded simultaneously using an ACO4165 microphone for the speech and Laryngograph's portable laryngograph for the ELG. The signals were sampled at 11 kHz, 16 bps, using a Turtle-Beach Tahiti A/D card.

A male speaker was asked to pronounce the phones /a/, /e/, /o/, /l/, /m/, /n/, /r/ for at least 5 s. The speaker was asked to try and retain a constant pitch and amplitude, and not to move his head.

The signals were processed using the fuzzy hyperplanes approach, with $K=2$ for event tracking, and with the two step approach for waveform estimation. The membership function was crisped using 0.7 as crisping threshold. Sequences of 16 samples or more in 1 cluster were detected, and the GW events estimated. The GW events were also estimated by Wong's closed-phase method.

The ELG served as a reference signal for the event timings. The timings of the closing and opening events were computed from the maximum derivative of the ELG signal. The events, estimated by both methods, were compared with the ELG reference. Errors were measured between an estimated event and the closest corresponding ELG event. Error vectors were calculated for the opening and closing events separately.

The error vectors were found to be non-Gaussian for most recordings, and therefore, nonparametric statistics was used for statistical testing. Success rate for both GW estimation methods was computed and statistically compared, using the Welch test. The bias was calculated from the errors median. A constant bias (12 samples≡1 ms≡30 cm) was subtracted, to compensate for the acoustic delay from the glottal generator to the microphone. The 30-cm acoustic distance is only a rough estimation, and a further constant delay may be

TABLE I. Comparison of the performance of the three methods of glottal waveform and event estimation, Fuzzy clustering, PSIAIF, and Wong's closed phase. Simulated data. ''+'' and ''−'' indicate statistically significant, and not significant, respectively.

Phone		/a/		/o/		/m/		/n/		/r/	
Event		Cl.	Op.	Cl.	Op.	Cl.	Op.	Cl.	Op.	Cl.	Op.
Bias [samples]	Fuzzy	0	4	0	3	0	0	0	0	0	4
	Wong	0	−37	−1	−37	−1	−33	0	−37	−1	−37
Success rate [%]	Fuzzy	92	100	86	100	92	100	100	100	99	100
	Wong	67	0	91	0	79	0	100	0	100	0
	Sig.	+	+	−	+	+	+		+	−	+
Dispersion [Std] [samples]	Fuzzy	0	2.7	0	4.1	0	2.2	0	1.9	0.2	1.4
	Wong	0	−	0.4	−	0	−	0	−	0.5	−
	Sig.			+						+	
MSE	Fuzzy	3.3×10^{-8}		2.4×10^{-8}		4.1×10^{-6}		7.5×10^{-8}		5.0×10^{-8}	
	PSIAIF	2.5×10^{-3}		1.4×10^{-2}		7.6×10^{-2}		5.0×10^{-3}		2.3×10^{-2}	
	Sig.	+		+		+		+		+	

found. Standard deviations were calculated, and the dispersions were compared using the nonparametric Siegel–Tuckey test. The numerical results are summarized in Table II.

The opening event estimate is often biased in both methods. The closing event is usually estimated almost unbiased. The success rate exhibited by the fuzzy clustering-based method is usually higher than Wong's. The success in estimating the closing event is higher, in both methods, than estimating the opening event. Dispersion is usually of the same order of magnitude in both algorithms and is satisfactory for most phones. According to dispersion as well, the closing event is estimated better than the opening event.

Figure 4 shows an example of a recorded /l/ [Fig. 4(a)], with its corresponding ELG. The GW and its events, estimated by the fuzzy clustering-based method, are compared to results obtained from Wong and the PSIAIF algorithms. The closed-phase method of Wong fails in detecting two of the opening events [Fig. 4(b)]. The fuzzy clustering-based method, on the other hand, accurately detects *all* opening and closing events with reference to the ELG signal [Fig. 4(c)]. The PSIAIF algorithm suffers from excessive ripple [Fig. 4(d)] compared to the fuzzy clustering-based method, and detection of GW events cannot be achieved.

C. Computational complexity

The computational complexity of the current method is a function of M, the length of the analysis window. The algorithm's bottleneck is stage 6 in algorithm 1 [Eq. (6)]. The multiplication of the matrix $\mathbf{X}$, which is an $M\times M$ matrix, is an order $O(M^3)$ computation. So is also the inversion of the matrix $(\mathbf{X}\mathbf{U}_k\mathbf{X}^T)$.

The one-frame algorithm is repeated N/M times. The algorithm's complexity is, therefore, linear in N, the total signal length. The total complexity order is $O(M^2N)$. The estimation of the GW in low pitch voices, where a long analysis window is indicated, suffers, therefore, from relatively high computational resource consumption.

A simulation experiment was executed to compare the computational complexity between the three algorithms, as well as to check the analytic complexity. The results are summarized in Table III.

III. CONCLUSIONS

Estimating the glottal waveform and event timing from the speech signal is a difficult task, solved only partially under assumptions, such as the existence of a closed phase, a low order AR driving function, or a parametric GW. These assumptions are often not met, with the consequence of a poor estimated GW.

TABLE II. Comparison of the performance of the two methods of GW event estimation, Fuzzy clustering, and Wong's closed phase. Real data. ''+'' and ''−'' indicate statistically significant, and not significant, respectively.

		Bias [samples]		Success rate [%]		Dispersion [samples]	
Phone	Method	Op.	Cl.	Op.	Cl.	Op.	Cl.
/a/	Fuzzy	−2	2	67%	74%	2.8	0.8
	Wong	10	1	62%	71%	4.9	0.3
	Sig.			+	+	+	−
/o/	Fuzzy	2	2	16%	90%	1.8	0.8
	Wong	10	1	62%	71%	2.7	1.5
	Sig.			−	+		
/e/	Fuzzy	−14	7	45%	86%	2.2	1.3
	Wong	2	0	59%	61%	2.9	1.1
	Sig.			−	+	−	+
/l/	Fuzzy	−7	6	73%	88%	4.8	2.3
	Wong	2	6	47%	89%	5.4	1.5
	Sig.			+	−		−
/m/	Fuzzy	−14	6	100%	87%	4.0	2.2
	Wong	−15	−13	100%	86%	4.0	3.8
	Sig.				+	−	+
/n/	Fuzzy	−4	8	48%	86%	4.4	2.2
	Wong	−11	6	48%	37%	4.0	3.7
	Sig.			−	+	−	
/r/	Fuzzy	1	3	31%	70%	6.1	5.0
	Wong	5	3	30%	43%	5.1	2.0
	Sig.			+	+	−	

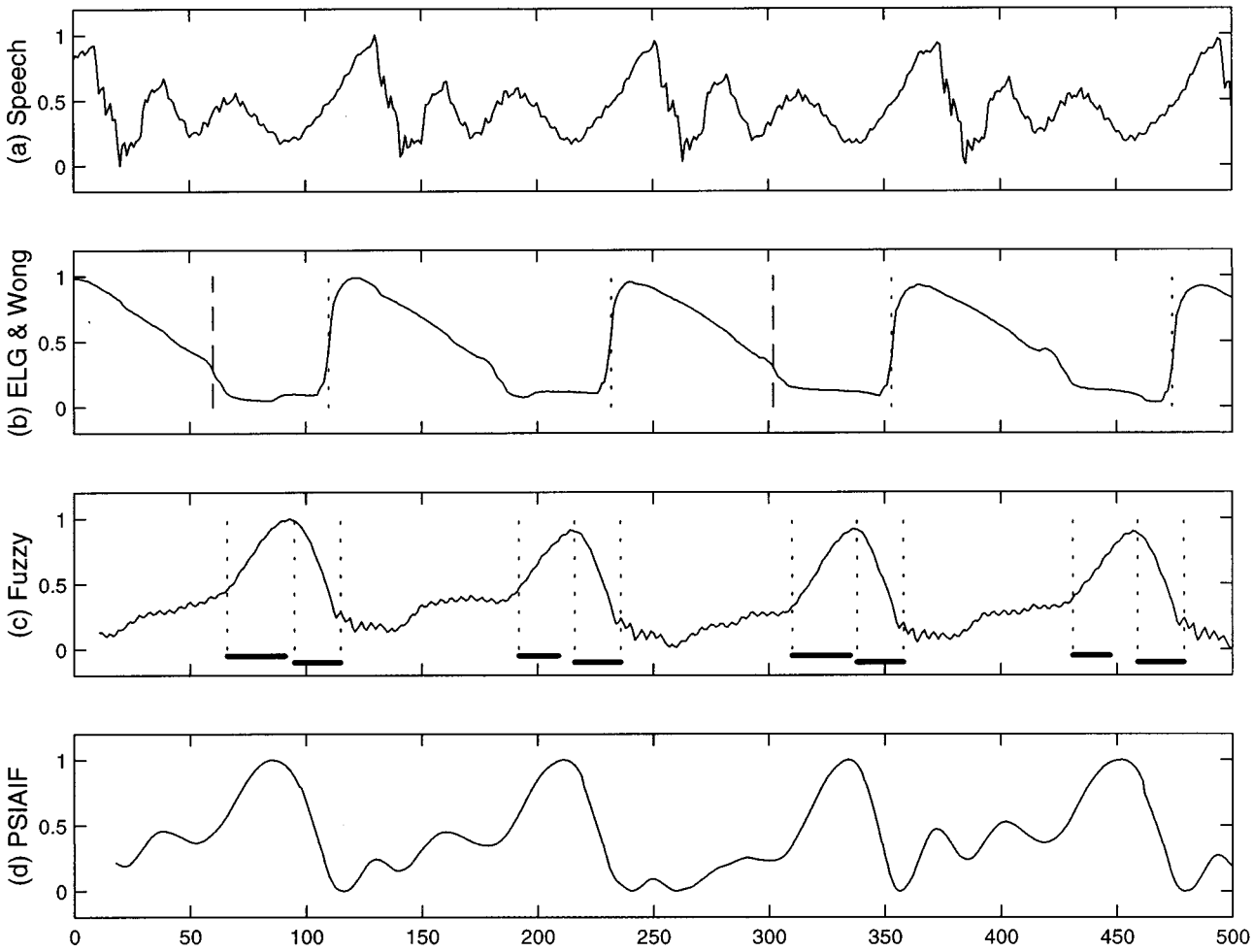

FIG. 4. Example of GW estimation from real data by the fuzzy clustering-based algorithm. (a) The time signal of the consonant /l/. (b) Its corresponding ELG. The GW time events, obtained by utilizing the closed-phase method of Wong, are displayed by vertical dashed line. (c) The glottal waveform and its events, estimated by the fuzzy clustering-based method. The opening, peak, and closing time instants are marked with dotted lines. Cluster affinity for the opening and closing phases is displayed by horizontal bars. (d) Glottal waveform estimation by the PSIAIF algorithm. The estimated waveform is corrupted by excessive ripple.

Regarding the speech signal in its shifts hyperspace, a typical three hyperplanes structure is displayed, and each hyperplane corresponds to a specific phase in the driving function. The sequence of distances from the shift vectors to the hyperplane is equivalent to inverse filtering the signal through an AR filter, the coefficients of which are the hyperplane's normal vector coefficients.

The hyperplanes are detected using a new fuzzy linear regression approach, where the distances from the hyperplanes determine the corresponding membership function. The membership function can then be regarded as the weight of an AR estimator, and used for event tracking.

The GW estimation method obtained utilizes a flexible and sometimes also noncontinuous analysis window. There is no need to segment the signal into phases, nor to use all data samples. The unsupervised clustering serves as a segmenting, weighting, and filtering engine, and a joint optimization of the analysis window and filter is accomplished.

The suggested method was tested on simulated and real data. In simulations, the fuzzy clustering approach exhibited an extraordinary performance, both on vowels and on voiced consonants. The glottal waveform and event timing were estimated with a very high precision.

On real data, GW events were compared to those derived from an ELG reference. The fuzzy clustering approach was usually superior to the closed-phase algorithm in event pointing, in particular for voiced consonants. The real acoustic glottal waveform could not be measured, as no reference signal exists. However, the glottal waveform estimated by the present algorithm was very similar to that obtained by the PSIAIF algorithm, although much smoother.

TABLE III. Comparison between the computational resource consumption of the three algorithms, measured in Matlab mega-flops.

N	M	Fuzzy	PSIAIF	Wong
1000	60	16	5	20
	120	33		
	240	143		
2000	60	29	11	42
	120	83		
	240	196		

The suggested algorithm was found to be very robust and accurate. The computational resources needed are relatively high, but can be reduced using nonrandom initial conditions.

Alku, P. (**1992**). ''Glottal wave analysis with pitch synchronous iterative adaptive inverse filtering,'' Speech Commun. **11**, 109–118.

Alku, P., Vilkannan, E., and Laine, U. K. (**1990**). ''A comparison of EGG and a new inverse filtering method in phonation change from breathy to normal,'' Proceedings of the 1st International Conference Spoken Language Processing (Kobe), pp. 197–200.

Bezdek, J. C. (**1981**). *Pattern Recognition with Fuzzy Objective Function Algorithms* (Plenum, New York), p. 68.

Bezdek, J. C., Coray, C., Gunderson, R., and Watson, J. (**1981a**). ''Detection and characterization of cluster substructure, I: Linear structure: fuzzy *c*-lines,'' SIAM (Soc. Ind. Appl. Math.) J. Appl. Math. **40**, 339–357.

Bezdek, J. C., Coray, C., Gunderson, R., and Watson, J. (**1981b**). ''Detection and characterization of cluster substructure, II: Fuzzy *c*-varieties and convex combinations thereof,'' SIAM (Soc. Ind. Appl. Math.) J. Appl. Math. **40**, 358–372.

Fant, G., Liljencrants, J., and Lin, Q. (**1985**). ''A four parameter model for glottal flow,'' Speech Transmiss. Lab. Q. Prog. Status Rep. (STL-QPSR) **4**, 1–13.

Hedelin, P. (**1986**). ''High quality glottal LPC-vocoding,'' ICASSP (Tokyo), pp. 465–468.

Miller, R. L. (**1959**). ''Nature of the vocal cord wave,'' J. Acoust. Soc. Am. **31**, 667–677.

Siegel, S., and Castellan, N. J., Jr. (**1988**). *Nonparametric Statistics for the Behavioral Sciences* (McGraw-Hill, New York), pp. 156–160.

Sondhi, M. M. (**1975**). ''Measurement of the glottal waveform,'' J. Acoust. Soc. Am. **57**, 228–232.

Witten, H. I. (**1987**). *Principles of Computer Speech* (Academic, London), p. 175.

Wong, D. Y., Markel, J. D., and Gray, A. H. (**1979**). ''Least squares glottal inverse filtering from the acoustic speech waveform,'' IEEE Trans. Acoust., Speech, Signal Process. **27**, 350–355.

Modeling global and focal hyperarticulation during human–computer error resolution

Sharon Oviatt,[a] Gina-Anne Levow,[b] Elliott Moreton,[c] and Margaret MacEachern[d]
Center for Human-Computer Communication, Department of Computer Science, Oregon Graduate Institute of Science and Technology, P.O. Box 91000, Portland, Oregon 97291

(Received 18 July 1997; accepted for publication 11 August 1998)

When resolving errors with interactive systems, people sometimes *hyperarticulate*—or adopt a clarified style of speech that has been associated with increased recognition errors. The primary goals of the present study were: (1) to provide a comprehensive analysis of acoustic, prosodic, and phonological adaptations to speech during human–computer error resolution after different types of recognition error; and (2) to examine changes in speech during both *global* and *focal* utterance repairs. A semi-automatic simulation method with a novel error-generation capability was used to compare speech immediately before and after system recognition errors. Matched original-repeat utterance pairs then were analyzed for type and magnitude of linguistic adaptation during global and focal repairs. Results indicated that the primary hyperarticulate changes in speech following all error types were durational, with increases in number and length of pauses most noteworthy. Speech also was adapted toward a more deliberate and hyperclear articulatory style. During focal error repairs, large durational effects functioned together with pitch and amplitude to provide selective prominence marking of the repair region. These results corroborate and generalize the computer-elicited hyperarticulate adaptation model (CHAM). Implications are discussed for improved error handling in next-generation spoken language and multimodal systems. © *1998 Acoustical Society of America.* [S0001-4966(98)04511-1]

PACS numbers: 43.72.Kb, 43.70.Fq [JLH]

INTRODUCTION

User acceptance of speech technology is influenced strongly by the error rate, the ease of error resolution, the cost of errors, and their relation to users' ability to complete a task (Kamm, 1994; Frankish *et al.*, 1995; Rhyne and Wolf, 1993). As a result, future spoken language systems will need to be designed to handle recognition errors effectively if they are to perform in a reliable manner and succeed commercially. Although ''designing for error'' has been advocated widely for conventional interfaces (Lewis and Norman, 1986), to date this concept has not been applied effectively to the design of recognition-based technology.

A. Hyperarticulation and the cycle of recognition failure

When speaking to interactive systems, recent research has demonstrated that people typically adapt their language during attempts to resolve system recognition errors (Oviatt *et al.*, 1996, 1998). This change in speaking style toward *hyperarticulate speech* involves a stylized and clarified form of pronunciation that speakers routinely use when accommodating what they perceive to be ''at risk'' listeners, adverse communication environments, or interactions involving miscommunication (Lindblom *et al.*, 1992; Oviatt *et al.*, 1998). Unfortunately, hyperarticulate speech introduces difficult sources of variability into the task of spoken language processing, which has been associated with elevated rates of system recognition failure (Shriberg *et al.*, 1992).

When people hyperarticulate to spoken language systems in an effort to correct recognition errors, recognition rates would be expected to degrade as hyperarticulated speech departs from the training data upon which a recognizer was developed. This problem arises because the basic principle of automatic speech recognition is pattern matching of human speech with relatively static stored representations of subword units. Although current recognition algorithms typically model phonemes and coarticulation effects, they do not tend to model dynamic stylistic changes in the speech signal that are elicited by environmental factors, such as the hyperarticulate speech adaptations that speakers make during miscommunication, or the ''Lombard speech'' adaptations that occur in a noisy environment (Lombard, 1911). With respect to training, current speech recognizers tend to be trained on original error-free input, typically collected under unnatural and constrained task conditions. Realistic interactive speech usually is not collected or used for training purposes, which means that training is omitted on hyperarticulate speech during system error handling. As a result, the signal variability posed by hyperarticulate speech represents a hard-to-process source of variability that threatens to degrade recognizer performance. Since hyperarticulate speech can be both a *reaction* to system recognition failure, and a potential *fuel* for precipitating a higher error rate, the net effect is that it has the potential to generate a *cycle of recognition failure*.

[a]Electronic mail: oviatt@cse.ogi.edu;http://www.cse.ogi.edu/~oviatt/
[b]Currently at Artificial Intelligence Laboratory, MIT, Boston, MA.
[c]Currently at Linguistics Department, University of Massachusetts, Amherst, MA.
[d]Currently at Linguistics Department, University of Pittsburgh, Pittsburgh, PA.

The design of recognition technology also can contribute to this cycle of recognition failure, and to *clustering* of recognition errors. For example, the design of Hidden Markov Models can propagate recognition errors, since a misrecognized word can cause others in its vicinity to be misrecognized (Rhyne and Wolf, 1993). Language models based on conditional probabilities also can propagate recognition errors, because an error can force the language model into an incorrect state and increase the likelihood of an error on subsequent words (Jelinek, 1985). In short, once a recognition error has occurred, both the properties of spoken language technology and users' reactive hyperarticulation can lead to perpetuation of the error in a way that complicates graceful recovery.

To design for both avoidance and resolution of errors, one research strategy is to analyze human–computer interaction specifically during system recognition errors. Such work could include modeling of users' hyperarticulated speech during interactive error handling, and the design of spoken language interfaces that aim to manage these strongly engrained speech patterns.

B. The CHAM model

Human speech to computers varies along a spectrum of hyperarticulation, such that its basic signal properties change dynamically and sometimes abruptly (Oviatt *et al.,* 1996, 1998). When a system makes a recognition error, the miscommunication that occurs can be a particularly forceful elicitor of hyperarticulate speech from users. Furthermore, the presence, form, and degree of hyperarticulation in users' speech to computers is a predictable phenomenon, which is transformed in principled ways during human–computer interaction. Compared with speech to a human partner during expected or actual miscommunication, users' hyperarticulate speech to a computer is in some ways unique, and the pattern of adaptation is consistent with their perception of the computer as a kind of ''at risk'' listener (Oviatt *et al.*, 1998).

During system error resolution, speech primarily shifts to become lengthier and more clearly articulated. In recent research, uniform increases in utterance duration were demonstrated during both low and high error-rate conditions (i.e., 6.5% versus 20% rate of utterances containing an error), with no significant difference in elongation between conditions. On average, a +12% relative increase was found in clongation of speech during error repair, whereas +92% more pauses were interjected, and the relative increase in pause duration was +75% (Oviatt *et al.*, 1996, 1998). That is, the most salient change in speech during error handling was alteration of pause structure.

During a high error rate, the phonological features of repeated speech also adapt toward an audibly clearer articulation pattern, with frequent changes including fortition of alveolar flaps to coronal plosives, such as ɛɪɾɛɪt changing to ɛɪt˺ɛɪt, and shifts to unreduced **nt** sequences, such as twɛ̃i changing to twɛnti (Oviatt *et al.*, 1996, 1998). Users' speech basically becomes more deliberate and well specified in its signal cues to phonetic identity. This shift toward hyperclear speech has also been shown to correspond with a drop in spoken disfluencies during a high error rate (Oviatt *et al.*, 1996, 1998). In contrast, during a low system error rate neither of these articulatory phenomena were observed to change significantly.

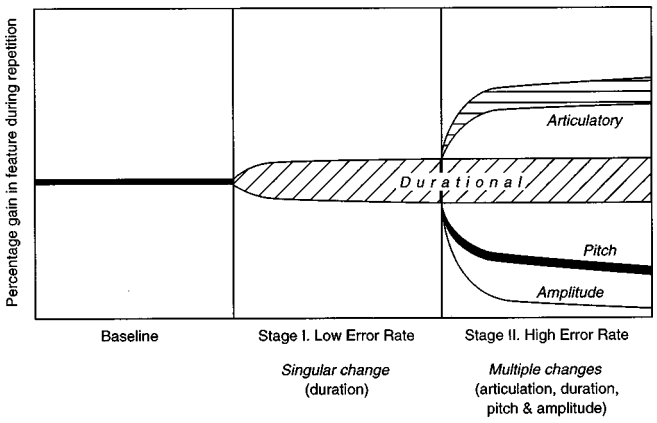

FIG. 1. Computer-elicited hyperarticulate adaptation model (CHAM).

With respect to intonation and fundamental frequency, during a high error rate, speakers also adopt a final falling intonation contour when repairing error subdialogues. This shift in intonation is also related to a slight decrease in fundamental frequency, which is reflected as a −2% average drop in minimum pitch (Oviatt *et al.*, 1998). Basically, speakers use final falling tones and a drop in pitch as cues to mark their repair subdialogues during human–computer dialogue interaction. However, neither of these changes are evident during a low system error rate, nor have reliable increases been reported in previous work in maximum pitch, pitch range, or amplitude (Oviatt *et al.*, 1996, 1998).

The two-stage branching computer-elicited hyperarticulate adaptation model (CHAM), illustrated in Fig. 1 and originally introduced in Oviatt *et al.* (1998), has been proposed as a unifying framework to account for these systematic changes in users' speech during interactive error handling. According to the empirically derived CHAM model, *Stage I* adaptations entail a singular change in durational characteristics. This stage is associated with a moderate degree of hyperarticulation during a low rate of system errors. *Stage II* entails multiple changes in durational, articulatory, and fundamental frequency characteristics. This stage is associated with a more extreme degree of hyperarticulation during a high rate of system errors. The two-stage CHAM model basically summarizes an unfolding of hyperarticulate speech adaptations that is consistent with the literature outlined above. In brief, it predicts that: (1) users' speech will adapt toward the linguistically specified hyperarticulation profile discussed above, including the type and magnitude of changes in articulatory, durational, and fundamental frequency features that has been outlined in previous empirical findings; (2) systems characterized by a low versus high error rate will elicit different types of hyperarticulate linguistic features, as illustrated in Stage I and II of the model shown in Fig. 1; and (3) abrupt rather than gradual transitions will occur in the signal profile of users' speech from one moment to the next as they begin and end episodes of error handling. Implications of the CHAM model for designing interactive

systems with improved error handling have been discussed elsewhere (Oviatt *et al.*, 1998).

C. The hyperarticulation spectrum: When and why speech is adapted

Based on experimental phonetics data involving interpersonal speech, Lindblom and colleagues have argued that speakers make a moment-by-moment assessment of their listener's need for explicit signal information, and they adapt their speech production to the perceived needs of their listener in a given communicative context (Lindblom, 1990, 1996; Lindblom *et al.*, 1992). According to Lindblom's H & H theory, this adaptation varies actively along a continuum from *hypo- to hyperclear speech*. Hypoclear speech is relatively relaxed, and contains phonological reductions. A hypoclear speech style involves minimal expenditure of articulatory effort by the speaker, and instead relies more on the listener's ability to fill in missing signal information from knowledge. In contrast, hyperclear articulation is a clarified style that requires more speaker effort in order to achieve ideal target values for the acoustic form of vowels and consonants, thereby relying less on listener knowledge. Essentially, Lindblom and colleagues maintain that the relation between the speech signal and intended phonemes is a highly variable one, which is neither captured entirely by mapping phonemes to physical acoustic or phonetic characterizations, nor by factoring in local coarticulation effects (Lindblom, 1996). During human interaction, speaking style also can range from hypo- to hyperclear in a way that contributes substantial variability to the speech signal.

Lindblom and colleagues believe that speakers operate on the principle of supplying *sufficient discriminatory information* for a listener to comprehend their intended meaning, while at the same time striving for articulatory economy. When a speaker perceives no particular threat to their listener's ability to comprehend them, articulatory effort typically is relaxed (Lindblom, 1996). The result is hypoclear speech, which represents the default speaking style. When a threat to comprehension is anticipated, as in a noisy environment or when a listener's hearing is impaired, the speaker will adapt their speech toward hyperclear to deliver more explicit signal information. In this sense, phonetic signals are dynamically modulated by the speaker to complement their listener's perceived speech processing ability and world knowledge. The effect of these speaker adaptations is to assist the listener in identifying a signal's intended lexical content.

In accord with these theoretical notions, there is evidence from a variety of studies that adaptation toward hyperarticulate speech does improve intelligibility by both normal and impaired listeners (Bond and Moore, 1994; Chen, 1980; Cutler and Buttertield, 1990; Gordon-Salant, 1987; Lively *et al.*, 1993; Moon, 1991; Payton *et al.*, 1994; Picheny *et al.*, 1985; Uchanski *et al.*, 1996). There is also linguistic and psychological literature indicating that people routinely adapt their speech during interpersonal exchanges when they expect or experience a comprehension failure from their listener. For example, modifications have been documented in parents' speech to infants and young children (Ferguson, 1977; Fernald *et al.*, 1989; Garnica, 1977), in speech to the hearing impaired (Picheny *et al.*, 1986), and in speech to nonnative speakers (Ferguson, 1975; Freed, 1978). Systematic changes also have been observed in speech during noise (Hanley and Steer, 1949; Junqua, 1993; Schulman, 1989; Summers *et al.*, 1988), during heavy workload or in stressful environments (Brenner *et al.*, 1985; Lively *et al.*, 1993; Tolkmitt and Scherer, 1986; Williams and Stevens, 1969), and when speakers are asked to ''speak clearly'' in laboratory settings (Cutler and Butterfield, 1990, 1991; Moon, 1991; Moon and Lindblom, 1994).

The specific hyperarticulate adaptations observed in these cases have differed depending on the target population and communicative context. For example, speech adaptations to infants often include elevated pitch, expanded pitch range, and stress on new vocabulary content—features that assist in gaining and maintaining infants' attention and in subserving teaching functions (Ferguson, 1977; Fernald *et al.*, 1989; Garnica, 1977). With hearing-impaired individuals, speech reportedly is higher in amplitude and fundamental frequency, longer in duration, and contains hyperclear phonological features (Picheny *et al.*, 1986). Speech adaptation in a noisy environment, characterized by the ''Lombard effect'' (Lombard, 1911), involves an increase in vocal effort that manifests itself as more than simple amplification of the speech signal. Among other features, it includes change in articulation of consonants, and increased duration and pitch of vowels (Junqua, 1993; Schulman, 1989). Lombard speech is analogous to hyperarticulate speech in the abruptness of signal change that often occurs. That is, Lombard and hyperarticulate speech both are characterized by episodic signal variability, which is a more challenging form of variability for recognizers to process than continuous signal deformation, as in the accented speech of a nonnative speaker.

To summarize, the interpersonal dynamics associated with different populations and circumstances clearly vary, even though all of them can be viewed as high risk communications. While they share features in common, the acoustic-prosodic and phonological features observed in these different cases nonetheless are defined by distinct hyperarticulation profiles. Recent research has begun to outline users' beliefs about the cause of communication failure as well as effective repair strategies when interacting with a computer (Oviatt *et al.*, 1998). Due to the error-prone nature of current recognition systems, speakers likewise may view the computer as a kind of ''at risk'' listener.

D. The concept of focal hyperarticulation

Recent research on hyperarticulate speech during human–computer error resolution has presented an analysis based on failure-to-understand errors, in which the system indicates its inability to recognize what the speaker said (Oviatt *et al.*, 1996, 1998). However, substitution errors constitute the majority of speech recognition errors (Brown and Vosburgh, 1989). During substitution errors, the system misrecognizes the user's speech and substitutes wrong lexical content. During some substitution errors, the speaker may not need to make a global repair of the entire utterance, but rather may selectively repair one focal part it—as in ''July

twenty-**first**, nineteen ninety-seven.'' There currently is a lack of research on how speakers adapt their speech to a computer when making focal repairs, or whether these adaptations share hyperarticulate features in common with those observed during global repairs. If both focal and global utterance repairs involve similar hyperarticulate change to the speech signal, then focal repairs may be viewed as a brief and highly selective form of hyperarticulate adaptation, one in which signal transition is particularly abrupt.

Although speech adaptations during focal error repairs with a computer are poorly understood, in linguistic theory the concept of stress is relevant. *Stress* involves assignment of prosodic prominence to one element or part of an utterance, and it can occur during interpersonal communication when an error is repaired in part of an utterance. Stress has several known acoustic and phonological correlates, including increased pitch, increased amplitude, longer duration, and greater differentiation of vowel formant structure (de Jong, 1995; Fry, 1955, 1958). The acoustic-phonetic features of linguistic stress are believed to enhance the overall prominence and perceptual clarity of the stressed region, which in the case of an error must serve as the critical repair region. Stress sometimes has been described as involving assignment of a pitch accent (Bolinger, 1958; Fry, 1958), or as a local shift toward hyperarticulate speech with greater phonemic contrast (de Jong, 1995).

Empirical research has analyzed cases in which people were disfluent and then spontaneously self-corrected. For example, a person might say ''Her name is Sara, no... uh, **Susan** Collins.'' In the literature on spontaneous self-corrections, acoustic-prosodic changes have been reported between error and repair segments, which indicate that the self-repair tends to be accented, or rendered more prominent intonationally (Levelt and Cutler, 1983). However, prominence marking on content self-repairs occurs only intermittently—usually in less than half of the self-repairs observed (Levelt and Cutler, 1983; Howell and Young, 1991). Furthermore, self-repairs that do not involve the replacement of wrong content (e.g., disfluent repetitions) usually do not receive prominence marking, or else receive negligible marking (Howell and Young, 1991; Levelt and Cutler, 1983; O'Shaughnessy, 1992).

During human–computer interaction, there also is prominence marking when a speaker spontaneously corrects a disfluency. This marking involves longer duration, increased pitch, and increased amplitude of the repair segment (Nakatani and Hirschberg, 1994; O'Shaughnessy, 1992), although the reported increases in pitch and amplitude have been extremely small (Nakatani and Hirschberg, 1994). It currently is not known whether these changes during self-corrected disfluencies bear any similarity to hyperarticulate change elicited by system recognition errors. Among other differences, the latter type of repair occurs in the context of a highly interactive spoken exchange, and in direct response to a computer partner's failure. Another difference is that analyses of repairs following system error have compared identical lexical content before and after system failure, whereas analyses of self-corrected disfluencies have involved comparison of different lexical content before and during the repair.

E. Goals and predictions of the study

The general goal of the present study was to examine the type and magnitude of linguistic adaptations that occur during human–computer error resolution. A further general aim was to develop a user-centered predictive model of hyperarticulate change during system error handling. The specific goals of this study were: (1) to provide a comprehensive analysis of acoustic, prosodic, amd phonological adaptations in speech during error resolution; (2) to test the generality of the CHAM model (computer-elicited hyperarticulate adaptation model) in response to qualitatively different types of system recognition error; (3) to examine changes in the speech signal during both *global* repair of an entire utterance and during *focal* repair of a syllable or word within an utterance; (4) to assess the relation between users' nonverbal reaction to system errors and change in the acoustic-prosodic features of their speech signal; and (5) to summarize implications of these findings for the development of improved error handling in next-generation spoken language and multimodal systems.

It was hypothesized that users' repetitions following system error would be adapted toward hyperclear acoustic-phonetic features, including higher amplitude, higher maximum pitch, lower minimum pitch, greater pitch range, longer duration of speech and pauses, more hyperclear phonological features, and fewer disfluencies. To make these assessments, within-subject data were examined for matched utterance pairs in which speakers repeated the same lexical content immediately before and after a simulated recognition error. Speech data were analyzed following qualitatively different types of error, including failures-to-understand, related substitutions, and unrelated substitutions.[1] Results for these different error types were compared to evaluate whether the magnitude of hyperarticulate change would be greater when the computer substituted wrong lexical content, rather than simply failing to guess it, or when users responded to unintuitive system errors with visible emotional reactivity.

In addition to investigating hyperarticulation during global utterance repairs, it was hypothesized that speakers would mark focal repairs as more prominent acoustically than neighboring speech within an utterance. Increased amplitude, fundamental frequency, and durational effects were all explored as potential markers of prominence during focal repairs. Although pitch and amplitude are relatively inactive during error resolution involving global utterance repairs, it was predicted that they would exhibit more change during prominence marking in focal repairs. To calibrate durational effects and the selectivity of their placement, the magnitude of change for speech segments and pauses in the immediate focal repair region was compared with that in surrounding nonfocal areas.

A further aim of this study was to explore users' nonverbal reactivity to different types of recognition error. In particular, an assessment was made of whether users react more strongly when wrong content is introduced, especially during substitution errors perceived to be unrelated semanti-

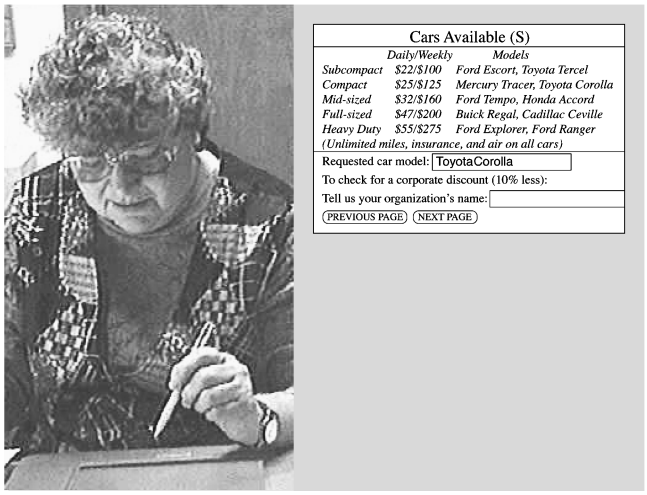

FIG. 2. A user speaks her organization's name as ''National Oceanographic'' but it is misrecognized as ''International Graphics'' during a related substitution error.

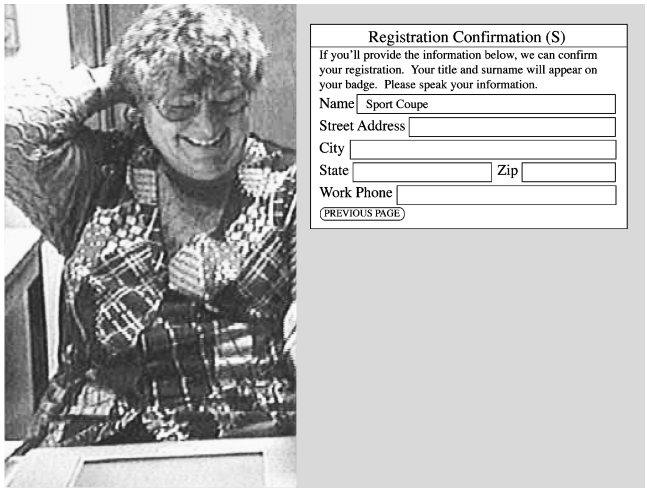

FIG. 3. A user speaks her name as ''Nancy Green'' and laughs when it is misrecognized as ''Sport Coupe'' during an unrelated substitution error.

cally and acoustically to their original input (e.g., ''Nancy Green'' misrecognized as ''Sport coupe''). If users are visibly more reactive to substitution errors, or to unrelated substitutions involving uninterpretable misrecognitions, then this greater degree of arousal may influence the signal characteristics of their repair speech. For example, volume and fundamental frequency may increase as a by-product of greater arousal.

I. METHOD

A. Subjects, tasks, and procedure

Twenty native English speakers, half male and half female, participated as paid volunteers. Their occupational backgrounds were varied, but excluded computer scientists.

A ''Service Transaction System'' was simulated that could assist users with conference registration and car rental transactions. Compared with an earlier study reported by Oviatt and colleagues (Oviatt *et al.*, 1996, 1998), in this study the corpus was designed to permit collection of a wider variety of articulated phonemes and three-fold more data than previously, in order to probe the generality of the CHAM Model. After a general orientation, people were shown how to enter information using a stylus to click-to-speak on active areas of a form displayed on a Wacom LCD tablet.

As input was received, the system interactively confirmed the propositional content of requests by displaying typed feedback in the appropriate input slot. For example, if the system prompted with **Car pickup location:_____** and a person spoke ''**San Francisco airport**,'' then ''**SFO**'' was displayed immediately after the utterance was completed. In the case of simulated *failure-to-understand* errors, the system responded with ''**????**'' feedback to indicate its failure to recognize lexical content. During these errors, the system basically informed the user of its inability to recognize what the user's input meant, so it was not necessary for the user to detect the error. In the case of *substitution* errors, illustrated in Figs. 2 and 3, the system instead responded with misrecognized or wrong content, such as ''**International Graphics**'' instead of ''**National Oceanographic**'' (i.e., acoustically and semantically *related* substitution), or with ''**Sport Coupe**'' instead of ''**Nancy Green**'' (i.e., *unrelated* substitution).

Following all errors, participants were instructed to try again by re-entering their information in the same slot until system feedback was correct. A form-based interface was used during data collection so that the locus of system errors would be clear to users. To successfully resolve a simulated error, the simulation was programmed so that the participant had to repeat their input once or twice, although analyses focused on the users' original input and first repetition.

Users were told that the system was a well-developed one with an extensive vocabulary and processing capabilities, so they could express things as they liked and not worry about what they could and could not say. They were advised that they could speak normally, work at their own pace, and just concentrate on completing their transaction. They also were told that if for any reason the computer did not understand them, they always would have the opportunity to re-enter their input. Following their session, all users were interviewed and then debriefed about the nature of the research. All participants reported that they had believed they were interacting with a fully functional system.

B. Semi-automatic simulation method

A flexible simulation method was devised for supporting varied studies on user responding during system recognition errors. The simulation developed for this purpose was an adapted version of a method previously outlined by Oviatt and colleagues (1992). Using this technique, people's spoken input was received by an informed assistant, who performed the role of responding as a fully functional system. The simulation software provided support for rapid subject-paced interactions, which averaged a 0.4-s delay between a subject's input and system response. Rapid simulation response was emphasized during software design, since it was judged to be an important prerequisite for collecting high quality data on human speech to computers.

To support research specifically on errors, a random error generation capability was developed that could simulate different types of system recognition error, different error baserates, and different realistic properties of speech recognition errors. This error generation capability was designed to be preprogrammed and controlled automatically so that, for example, errors could be distributed randomly across all task content. For the present study, the error-generation software was adapted to deliver qualitatively different types of system recognition errors, including: (1) failures to understand; (2) related substitutions; and (3) unrelated substitutions.[2] The simulated word error rate was held constant at 15%, and approximately one error occurred every five input slots.

C. Research design

The research design was a within-subject factorial that included the following independent variables: (1) Error status of speech (Original input; Repeat input); (2) Type of simulated error (Failure to understand; Related substitution; Unrelated substitution). All 20 subjects completed 6 tasks. Within each task, six simulated errors were delivered—two failures to understand, two related substitutions, and two unrelated substitutions. This represents a 20% rate of utterances containing an error, which is comparable to that associated with the CHAM model's Stage II changes in previous reports. In total, data were collected on 36 simulated errors per subject, or 720 simulated errors in the study. For all matched utterance pairs in which the lexical content was the same, original input provided a baseline for quantifying change during the first repetition. In total, this included approximately 638 utterance pairs, with over 200 representing each error type.

D. Data coding and analysis

Speech input was collected using a Crown microphone, and all human–computer interaction was videotaped and transcribed. The speech segments of matched utterance pairs involving original input and first repetitions were digitized, and software was used to align word boundaries automatically and label each utterance. Most automatic alignments then were hand-adjusted further by an expert phonetic transcriber. The ESPS Waves+ signal analysis package was used to analyze amplitude and frequency, and the OGI Speech Tools were used for duration.

1. Global linguistic adaptations

In these analyses, global spoken adaptations that occurred within the entire utterance were assessed.

a. Duration. The following were summarized: (1) total utterance duration; (2) total speech segment duration (i.e., total duration minus pause duration); (3) total pause duration for multi-word utterances in which at least one pause was present; and (4) average number of pauses per subject for multi-word utterances. No attempt was made to code pauses less than 10 ms in duration. Due to difficulty locating their onset, utterance-initial voiceless stops and affricates were arbitrarily assigned a 20-ms closure, and no pauses were coded as occurring immediately before utterance-medial voiceless stops and affricates. Further details of durational scoring conventions are outlined elsewhere (Moreton, 1996).

b. Amplitude. Maximum intensity was computed at the loudest point of each utterance using ESPS Waves+, and then was converted to decibels (dBs). Values judged to be extraneous nonspeech sounds were excluded.

c. Fundamental frequency. Spoken input was coded for maximum $F0$, minimum $F0$, and $F0$ range. A pitch-smoothing filter was applied to the data to remove or minimize: (1) glottalized regions; (2) spurious doubling and halving; (3) points below an amplitude threshold of 400 rms; and (4) 1- to 2-point pitch value outliers (e.g., due to hissing sound in ''s''). The fundamental frequency tracking software in ESPS Waves+ was used to calculate values for voiced regions of the digitized speech signal. Pitch minima and maxima were calculated automatically by program software, and then adjusted further to correct for pitch tracker errors such as spurious doubling and halving, interjected nonspeech sounds, and extreme glottalization affecting $\leqslant 5$ tracking points.

d. Intonation contour. The final rise/fall intonation contour of subjects' input was judged to involve a rise, fall, or no clear change. Each matched original-repeat utterance pair then was classified as: (1) rise/rise; (2) rise/fall; (3) fall/fall; (4) fall/rise; or (5) unscorable. The likelihood of switching final intonation contour from original input to first repetition (categories 2 and 4) versus holding it the same (categories 1 and 3) then was analyzed. In the case of a shifting contour from original to repeated input, the likelihood of changing from a rising to falling contour versus a falling to rising one also was evaluated. Finally, the percentage of all original versus repeated utterances that contained a final falling contour was compared.

e. Phonological alternations. Phonological changes within original-repeat utterance pairs that could be coded reliably by ear without a spectrogram were categorized as either representing a shift from conversational-to-clear speech style, or vice versa. The following contrasting categories were coded: (1) released and unreleased plosives; (2) unlenited coronal plosives and alveolar flaps; and (3) presence versus absence of segments. Alveolar flaps, deleted segments, and unreleased stops were considered characteristic of conversational speech, whereas unlenited coronal plosives, undeleted segments, and audibly released stops were indices of clear speech. A focus was placed on identifying uncontroversial phonological changes with respect to the conversational-to-clear speech continuum, and those that could be coded reliably by ear without access to a spectrogram. For example, cases of glottalization and glottal stop insertion were not included due to known difficulty with reliable coding (Eisen *et al.*, 1992).

f. Disfluencies. Spoken disfluencies were totaled for each subject and condition during original spoken input as well as repeats during errors, and then were converted to a rate per 100 words. The following types of disfluencies were coded: (1) content self-corrections; (2) false starts; (3) repetitions; and (4) filled pauses. For further classification and coding details, see Oviatt (1995).

g. Nonverbal responding. To assess users' subjective reaction to different types of recognition error, the following categories of nonverbal responding were coded from videotapes for each subject and error condition: (1) smiling—lips fully retracted upward in an unambiguous smile; (2) laughter—open-mouth smile accompanied by one or more breathy nonarticulated bursts of noise; (3) raised brows—eyebrows lifted upward, as if in surprise; and (4) knit brows—eyebrows moved together, with forehead wrinkled as muscles contract. These nonverbal facial changes, which were considered indices of emotional reactivity and heightened arousal, were assessed for possible correspondence with speech signal changes.

h. Self-reported perception of recognition errors. The percentage of subjects reporting specific beliefs about the causal basis of errors, as well as effective ways to resolve errors, was summarized from post-experimental interviews.

2. Focal linguistic adaptations

These analyses concentrated on focal error repairs involving one syllable or word within a longer multi-word utterance. In total, 96 original-repeat utterance pairs were available for analysis of focal error repairs, which constituted a subset of the related substitution errors. Examples of focal repairs during related substitution errors were *two seven seven Frill Street*→''two seven seven **Hill** Street,'' *September seven, 1996*→''September **eleven**, 1996.'' The goal of these analyses was to assess whether and to what extent the focal repair region received selective emphasis via acoustic cues during system error resolution.

a. Duration. (1) *Focal Speech Duration*—The total duration of the focal speech segment [FOC], which represented the repair region, was evaluated for original and repeat input.

(2) *Nonfocal Speech Duration*—The total duration of the surrounding nonfocal speech segments [NFOC] (i.e., total utterance duration minus focal speech duration minus total pause duration) was computed.

(3) *FOC/NFOC Speech Duration Ratio*—The ratio of focal to surrounding speech segment durations was computed to assess whether the focal region was relatively more elongated during repetition than surrounding speech.

(4) *Pause Duration Adjacent to Repair*—For all utterances with one or more pauses, total pause duration was computed both immediately before and after the repair region in original and repeated input.

(5) *Pause Duration Nonadjacent to Repair*—Total pause duration also was assessed for pauses not adjacent to a focal repair region in original and repeat utterances.

(6) *Number of Pauses Adjacent to Repair*—For all multiword utterances, the total number of pauses immediately before and after a focal repair region were scored for original and repeat utterances.

b. Amplitude. (1) *Focal Maximum Amplitude*—Maximum amplitude was computed from the loudest point during the focal repair region, and was summarized for both original and repeat utterances.

(2) *Nonfocal Maximum Amplitude*—The average maximum amplitude of spoken words not in the focal repair region also was calculated.

(3) *FOC/NFOC Amplitude Ratio*—The ratio of focal to nonfocal speech segment amplitudes was computed to assess whether the focal repair region had a relatively higher amplitude during repetition.

c. Fundamental frequency. (1) *Focal Pitch Maximum*—Maximum $F0$ during the focal repair was scored for original and repeat utterances, and analyzed separately when the repair was in sentence-final versus initial or medial position.

(2) *Nonfocal Pitch Maximum*—The average maximum $F0$ of nonfocal spoken words also was calculated, excluding words in sentence-final position.

(3) *Focal Pitch Minimum*—Minimum $F0$ during the focal repair was scored for original and repeat utterances, and analyzed separately when the repair was in sentence-final versus initial or medial position.

(4) *Nonfocal Pitch Minimum*—The average minimum $F0$ of nonfocal spoken words also was calculated, excluding words in sentence-final position.

(5) *Focal Pitch Range*—The $F0$ range ($F0$ maximum minus $F0$ minimum) was scored for focal repair segments occurring in all sentence positions, and then compared for original and repeat utterances.

(6) *Nonfocal Pitch Range*—The average $F0$ range of nonfocal spoken words also was scored, and compared for original and repeat input.

d. Reliability. For all measures reported except amplitude, 10%–100% of the data were second scored. For discrete classifications, such as number of pauses, disfluencies, phonological alternations, nonverbal responding, and intonation contour, all inter-rater reliabilities exceeded 88%. For phonological alternations, only cases agreed upon by both scorers were analyzed. For fundamental frequency, the inter-rater reliability for minimum $F0$ was an 80% match with less than 3-Hz departure, and for maximum $F0$ an 80% match with less than 9-Hz departure. For duration, pause length was an 80% match with less than 65-ms departure, and total utterance duration an 80% match with less than 59-ms departure.

II. RESULTS

Speech data were available for analysis on approximately 638 scorable utterance pairs for which the lexical content was identical during original and repeated input. Of these, over 200 utterance pairs representing each of the three error types were analysed. Spoken utterances in this corpus tended to be brief fragments averaging two to three words, and ranging from 1 to 13 words in length.

A. Overview of global linguistic adaptations

Table I presents a summary of all the significant global linguistic changes identified during human–computer error resolution. The magnitude of relative change shown for each linguistic dimension is an average across the three different error types. Specific results on each type of linguistic change are detailed in the following sections.

TABLE I. Overview of relative change in linguistic dimensions of hyperarticulation during global utterance repairs.

Type of change	Percentage change during repetition
Pause interjection	+44.0%
Pause elongation	+40.0%
Disfluencies	−38.5%
Intonation—final fall	+20.0%
Speech elongation	+8.5%
Hyperclear phonology	+6.0%
Pitch minimum	−2.0%
Amplitude	+0.5%

Table I clarifies that change in pause structure dominated hyperarticulate adaptation during error resolution, with durational increase in the speech segment also noteworthy but smaller in magnitude. Articulatory changes were a second prominent characteristic of global hyperarticulate adaptation, including both a drop in spoken disfluencies and an increase in hyperclear phonological features. With respect to prosody, speakers shifted to a final falling intonation contour during repetitions, which was associated with small decreases in fundamental frequency measures. While amplitude increases were reliably present, they were negligible. (Figure 7 illustrates that the overall profile of hyperarticulate adaptations was replicated across all three of the different error types.)

1. Duration

Total utterance duration averaged 1567 ms and 1786 ms in original and repeat input during failure-to-understand errors, 1677 ms and 1845 ms during related substitutions, and 1659 ms and 1815 ms during unrelated substitutions. The average gain in total utterance duration from original to repeated speech across all error types was +11%. A repeated measures ANOVA on log transformed data revealed that the main effect of original versus repeat speech was a significant one, $F=166.05$ (df=1, 165), $p<0.001$, although the main effect of type of recognition error was not significant, $F<1$, nor was the interaction between error type and original-repeat speech, $F=2.30$ (df=2, 330), N.S. Having ruled out significant variation in utterance duration due to type of recognition error, *a priori* paired *t* tests then were conducted on the prediction that duration would be elongated during repetition following all three types of error. These analyses confirmed a significant increase in utterance length for failure-to-understand errors, paired $t=4.58$ (df=197), $p<0.001$, one-tailed, for related substitution errors, paired $t=8.93$ (df=205), $p<0.001$, one-tailed, and for unrelated substitution errors, paired $t=6.63$ (df=219), $p<0.001$, one-tailed.

a. Speech segment duration. Analyses revealed an increase in the total speech segment from an average of 1446 ms during original input to 1591 ms during repetitions following failure-to-understand errors, 1525 ms and 1662 ms following related substitutions, and 1513 ms and 1613 ms following unrelated substitutions, as illustrated in Fig. 4. The average relative gain in speech segment duration from original to repeated speech across all error types was +8.5%. A repeated measures ANOVA on log transformed data revealed that the main effect of original versus repeat speech was significant, $F=142.46$ (df=1, 165), $p<0.001$, although error type was not, $F<1$, nor was the interaction between error type and original-repeat speech, $F=2.85$ (df=2, 330), N.S. Having ruled out significant variation due to type of recognition error, *a priori* paired *t*-tests were conducted on the prediction that repeated speech segments would be significantly elongated following all three types of recognition error. These analyses confirmed a significant increase in speech segment duration following failure-to-understand errors, paired $t=6.88$ (df=197), $p<0.001$, one-tailed, related substitutions, paired $t=8.95$ (df=205), $p<0.001$, one-tailed, and unrelated substitutions, paired $t=5.69$ (df=219), $p<0.001$, one-tailed.

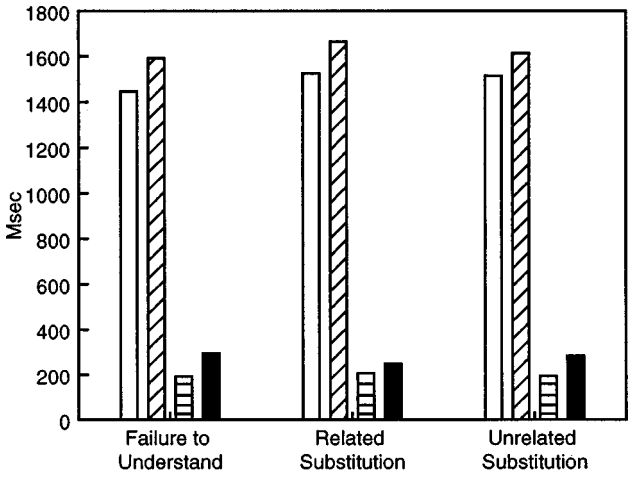

FIG. 4. Elongation of the speech segment and pauses in repeated utterances for three types of recognition error. Original speech □; repeat speech ◪; original pause ⊟; repeat pause ■.

b. Pause duration. The total pause duration of multiword utterances also increased from an average of 192–295 ms between original and repeat input after failure to understand errors, from 207 ms to 248 ms after related substitutions, and 193 ms to 283 ms after unrelated substitutions. The average gain in total pause duration from original to repeated speech across all error types was +40%. A repeated measures ANOVA on log transformed data revealed that the main effect of original versus repeat speech significantly influenced total pause duration, $F=57.68$ (df=1, 56), $p<0.001$, although type of error did not, $F<1$, nor did the interaction between error type and original-repeat speech, $F=1.93$ (df=2, 112), N.S. Having ruled out significant variation due to type of error, *a priori* paired *t*-tests were conducted on the prediction that pause duration would be elongated significantly in response to all three types of recognition error. These analyses confirmed a significant increase in pause duration following failure-to-understand errors, paired $t=5.59$ (df=77), $p<0.001$, one-tailed, related substitutions, paired $t=5.74$ (df=93), $p<0.001$, one-tailed, and unrelated substitutions, paired $t=4.59$ (df=84), $p<0.001$, one-tailed.

Figure 4 illustrates the average increase in pause duration for all three types of error, and its relation to increases in speech segment duration. Figure 5 also shows the increasing

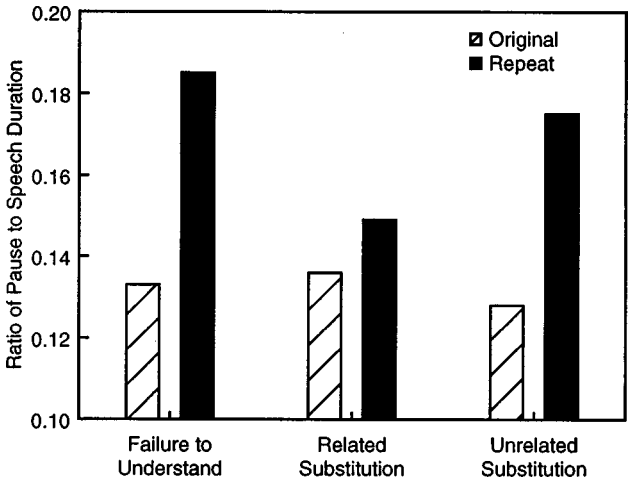

FIG. 5. Increasing ratio of pause to speech duration in repeated utterances for three types of recognition error.

ratio of pause to speech duration in repeated speech for all three types of error, which averaged +13% during original input but increased to +17% during repetitions. That is, the gain in pause duration during repetitions was relatively greater than for speech, a comparison that was statistically reliable across subjects by Wilcoxon Signed Ranks test, $z=3.24$ ($N=19$), $p<0.001$, two-tailed.

To test for elongation of individual matched pauses (i.e., independent of interjecting new ones that may have been brief), original and repeat utterance pairs matched on total number of pauses were compared for total pause length. This analysis confirmed that pauses were elongated significantly more in repeat utterances following all three types of errors, including failure-to-understand errors, paired $t=2.37$ (df $=34$), $p<0.02$, one-tailed, related substitutions, paired $t=2.02$ (df$=49$), $p<0.025$, one-tailed, and unrelated substitutions, paired $t=3.60$ (df$=45$), $p<0.001$, one-tailed.

c. Number of pauses. Approximately 63% of multi-word utterances contained one or more pauses during error resolution, even though utterances in the corpus tended to be brief. Figure 6 reveals that the average number of pauses per subject for multi-word utterances increased during repeat

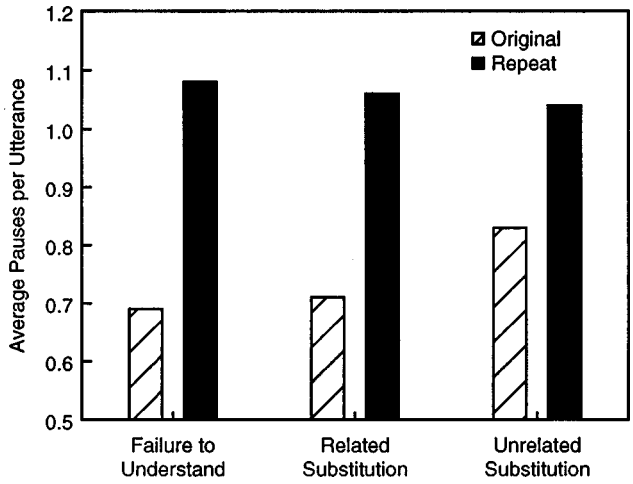

FIG. 6. Increase in number of pauses in repeated utterances for three types of recognition error.

speech for all three error types. For failure-to-understand errors, the number of pauses increased from an average of 0.69 to 1.08 between original and repeated utterances, significant by Wilcoxon Signed Ranks test, $z=3.32$ ($N=17$), $p<0.001$, one-tailed. For related substitutions, the number of pauses increased from 0.71 to 1.06 during repeat utterances, again significant by Wilcoxon, $z=3.62$ ($N=17$), $p<0.001$, one-tailed. Finally, for unrelated substitutions, pauses increased from 0.83 to 1.04 during repeat utterances, significant by Wilcoxon, $z=2.12$ ($N=16$), $p<0.02$, one-tailed. Overall, the net increase in average number of pauses during repeated speech was +44%.

2. Amplitude

The maximum amplitude averaged 70.3 dB and 70.6 dB in original and repeat utterances during failures to understand, 70.8 dB and 71.1 dB during related substitutions, and 70.6 dB and 71.0 dB during unrelated substitutions. A repeated measures ANOVA revealed that the main effect of original-repeat speech had a significant impact on amplitude, $F=23.76$ (df$=1, 163$), $p<0.001$, but there was no difference between error types, $F=1.45$ (df$=2, 326$), N.S., and no significant interaction, $F=1.40$ (df$=2, 326$), N.S. Having ruled out significant variation due to type of error, the prediction was tested that repeated speech would be increased in amplitude. Analyses using planned t tests confirmed a significant increase in amplitude on repeat speech for failures to understand, $t=2.45$ (df$=204$), $p<0.01$, one-tailed, for related substitutions, $t=3.00$ (df$=208$), $p<0.0015$, one-tailed, and for unrelated substitutions, $t=3.57$ (df$=223$), $p<0.001$, one-tailed. However, these increases were very neglible, averaging less than +0.5%.

3. Fundamental frequency

a. Pitch maximum. Maximum $F0$ averaged 190.8 and 190.2 for original and repeat speech during failures to understand, 188.8 and 189.6 for original and repeat speech during related substitutions, and 193.0 and 192.9 for original and repeat speech during unrelated substitutions. Repeated measure ANOVAs conducted on the whole sample and then reanalyzed separately by gender all revealed no significant effect of original versus repeat speech, error type, or their interaction on pitch maximum values (Fs<1).

b. Pitch minimum. Minimum $F0$ averaged 129.5 and 126.8 on original and repeat speech during failures to understand, 129.9 and 127.4 during related substitutions, and 129.1 and 127.6 during unrelated substitutions. A repeated measures ANOVA conducted on the whole sample revealed a significant main effect of original versus repeat speech, $F=4.68$ (df$=1, 158$), $p<0.035$, but no difference due to error type, $F<1$, or their interaction, $F=1.90$ (df$=2, 316$), $p>0.15$. Since a decrease was predicted in minimum $F0$ during repetitions, *a priori* paired t-tests were conducted to assess predicted drops during different error types. Significant decreases were confirmed for failure to understand errors, $t=2.42$ (df$=189$), $p<0.01$, one-tailed, for related substitution errors, $t=2.16$ (df$=190$), $p<0.02$, one-tailed, and for unre-

lated substitution errors, $t=1.76$ (df=216), $p<0.04$, one-tailed. These decreases in minimum $F0$ averaged less than -2%.

c. Pitch range. $F0$ range averaged 61.9 and 63.2 for original and repeat speech during failures to understand, 62.7 and 62.8 during related substitutions, and 63.9 and 65.4 during unrelated substitutions. Repeated measures ANOVAs conducted on the whole sample and then reanalyzed separately by gender all revealed no significant main effect of original versus repeat speech, error type, or their interaction on overall pitch range values for the utterance (Fs<1).

4. Intonation contour

The probability of *shifting* final intonation contour from rise to fall, or vice versa, averaged only 11.5% between original and repeated input. More specifically, speakers maintained the same final contour 89% of the time during failure to understand errors, 87% of the time during related substitutions, and 89% during unrelated substitutions, with no significant differences apparent between error types. Wilcoxon Signed Ranks analysis confirmed that speakers were significantly more likely to hold their intonation the same between original input and first repetition than to change it, $z=3.88$ ($N=20$), $p<0.001$, one-tailed. In this sense, it appears that whatever intonation contour originally is applied to the utterance tends to persist during verbatim correction.

Of the cases in which a change was evident in final intonation contour during repetition, 88% of the time the shift was from rising to falling, rather than the reverse. This difference was significant by Wilcoxon test, $T+=110$ ($N=15$), $p<0.003$, two-tailed. Analyses of all three error types reconfirmed this pattern of significantly more final falls than rises during repetitions. Overall, the likelihood of a final falling contour was 45% during original input, increasing to 54% during repetitions—for a net relative increase in final falling contours of $+20\%$.

5. Phonological Alternations

Approximately 6% of repetitions in this corpus contained a phonological alternation that could be classified along the hyperarticulation spectrum. Table II summarizes the number and type of alternations observed for each subject by the direction of shift toward conversational versus hyperclear speech.

The majority of subjects, or 79% of those who had at least one spoken adaptation classifiable according to hyperarticulation, shifted more often from a conversational to clear speech style, rather than the reverse, a significant difference by Wilcoxon Signed Ranks test, $T+=80$ ($N=13$), $p<0.007$, one-tailed. The rate of hyperclear alternations averaged 6% of repetitions during failures to understand, 4% of repetitions during related substitutions, and 5% during unrelated substitutions, with no significant difference among error types (see Fig. 7).

When one or more clear-speech phonological changes were present during repetitions, the number of pauses correspondingly increased $+67\%$ from baseline input (i.e., from 0.90 to 1.50 pauses between original and repeat input), compared with a gain of only $+44\%$ for the whole corpus. Likewise, total pause length increased $+61\%$ from baseline input to repetitions when a phonological change was present (i.e., from 191 ms to 307 ms), although the gain only averaged $+40\%$ for the whole corpus. Total speech duration averaged 1891 ms and 2126 ms during utterances with a phonological alteration, a $+12\%$ increase over baseline input, compared with $+8.5\%$ increase for the whole corpus. In short, durational change averaged about 49% greater during repetitions involving a phonological alternation than during those without one. When original-repeat utterance pairs containing a conversational-to-clear-speech phonological change were

TABLE II. Number and type of phonological alternations involving a shift toward clear speech (a–f) versus toward conversational speech (g–h), listed by subject.

Clear to conversational	Conversational to Clear	Phonological alternations
0	3	c, d, d
0	6	a, a, a, c, e, e
2	2	g, g / a, d
0	1	a
0	0	…
0	0	…
0	5	a, a, a, c, c
0	3	a, c, d
0	1	f
0	0	…
0	3	a, b, c
0	1	a
2	0	g, h
0	0	…
0	1	d
0	3	a, a, c
0	3	a, a, c
0	0	…
1	0	g
0	0	…
Total—5	32	

[a]Unreleased *t*>released *t*.
[b]Alveolar flap>coronal plosive.
[c]*n*/alveolar nasal flap>*nt* sequence.
[d]Segment insertion.
[e]Nasal flap>*n*.
[f]schwa>*I* altered vowel quality.
[g]Segment deletion.
[h]*nt* sequence>nasal flap.

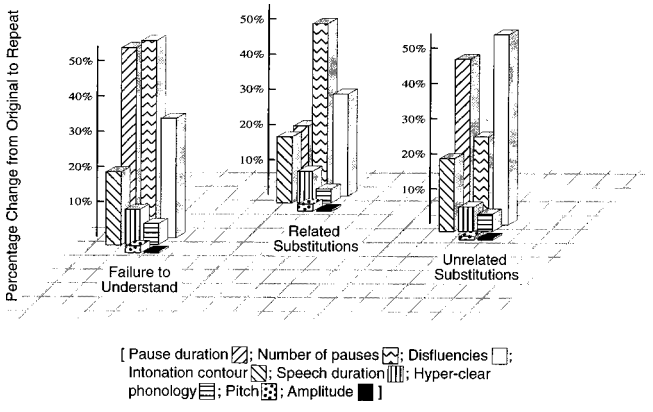

FIG. 7. Similarity of hyperarticulation profile for different error types.

compared with utterances from the corpus at large that did not contain any phonological change (i.e., that were matched on speaker and lexical content), it was confirmed that utterances with phonological change contained significantly more pauses than those in the corpus at large, $T+=55$ ($N=10$), $p<0.001$ one-tailed, and also significantly longer pauses, $T+=79$ ($N=13$), $p<0.01$, one-tailed. These data clarify that the degree of hyperarticulate adaptation varied along a spectrum, and also that durational and phonological changes during hyperarticulation were correlated within individual utterances.

6. Disfluencies

The disfluency rate during baseline speech (i.e., throughout the interaction when no errors were occurring) averaged 0.65 disfluencies per 100 words. However, this rate dropped to 0.40 during repeated input following system errors, a significant decrease by Wilcoxon Signed Ranks test, $T+=103$ ($N=15$), $p<0.01$, one-tailed. The rate of disfluencies per 100 words averaged 0.43 during failures to understand, 0.46 during related substitutions, and 0.30 during unrelated substitutions, which did not differ significantly.

7. Nonverbal responding

Users frequently reacted emotionally to system recognition failures. They smiled in response to 9% of errors, laughed after another 6%, raised their eyebrows after 4%, and knit their brows after 3% of errors. In total, 22% of system errors elicited a nonverbal response.

Participants were significantly more likely to smile after an unrelated substitution than after a failure to understand error, $z=2.73$ ($N=11$), $p<0.003$, one-tailed, or after a related substitution error, $z=1.69$ ($N=11$), $p<0.05$, one-tailed. Users also were significantly more likely to laugh after unrelated substitutions than after a failure to understand error, $z=2.40$ ($N=9$), $p<0.01$, one-tailed, or after a related substitution, $z=2.45$ ($N=9$), $p<0.007$, one-tailed. Finally, although raised eyebrows were not expressed more often after any particular error type, users also knit their brows significantly more often after unrelated substitutions than failure to understand errors, $z=1.81$ ($N=7$), $p<0.04$, one-tailed, and related substitutions, $z=1.62$ ($N=7$), $p<0.053$, one-tailed. In summary, participants were most reactive to the unrelated substitution errors.

8. Self-reported perception of recognition errors

Post-experimental interviews revealed that users typically posited a cause for errors that involved self-attribution of blame and a linguistically based cause of system failure (e.g., ''I just needed to speak more slowly and clearly''). Although the delivery of simulated recognition errors was not contingent at all on users' input, 70% of interviewees stated that altering the linguistic characteristics of their own language was effective in repairing system errors successfully. Another 15% said they had no idea why system errors occurred, and the remaining 15% cited mechanical reasons for recognition failure (e.g., ''My pen wasn't inside the input box, so it didn't get the last few digits'').

TABLE III. Overview of relative change in linguistic dimensions of hyperarticulation during focal repairs.

Type of change	Percentage change during repetition
Focal repair region:	
Pause duration next to repair	+149%
Number of pauses next to repair	+113%
Duration of speech repair	+18%
Pitch range of speech repair	+11%
Pitch maximum of speech repair[a]	+3%
Pitch minimum of speech repair[b]	−3%
Amplitude of speech repair	+1%
Nonfocal region:	
Pause duration nonadjacent to repair	+9%
Duration of nonfocal speech	+9%

[a]Change for all focal repairs, except those in sentence-final position.
[b]Change for focal repairs in sentence-final position only.

With respect to linguistic repair mechanisms, the following specific ones were cited most frequently as being effective: (a) speaking more clearly—mentioned by 45% of participants who maintained a linguistic theory; and (b) speaking more slowly—40% of participants. A small minority of people said they believed that speaking more loudly to the computer was effective in resolving errors (10%), or changing voice inflection (5%). In short, participants' self-reports regarding error repair strategies were consistent with the major changes observed in hyperarticulate speech.

B. Overview of focal linguistic adaptations

Table III presents a summary of all the significant focal linguistic adaptations that were identified during human–computer error resolution. It summarizes changes that occurred when users selectively emphasized a focal repair region in a related substitution error. Specific results on each type of linguistic adaptation are detailed in the following sections.

Table III clarifies that change in pause structure still dominated focal hyperarticulate adaptation, although it was three- to four-fold greater than that observed during global utterance repair. Changes in pause interjection and elongation also were selectively placed adjacent to the focal repair region. In fact, these pause changes were twelve-to sixteen-fold more pronounced immediately before and after the repair region than in other sentence positions. The focal speech region also was substantially elongated, approximately two-fold more than speech in surrounding nonfocal regions or during global utterance repairs.

Although relatively smaller in magnitude of change, the focal repair region also was selectively marked with a moderate increase in pitch range that was derived from an increase in maximum pitch in sentence-initial and medial positions and a decrease in minimum pitch in sentence-final position. Finally, the focal repair region was selectively marked with a small increase in amplitude. These data clarify how duration, fundamental frequency, and amplitude work together in a finely tuned manner to mark a highly specific repair region as acoustically more prominent than surrounding ones during human–computer error resolution.

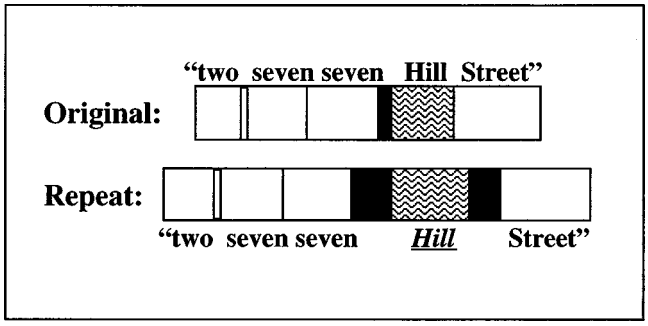

FIG. 8. During repair of a related substitution error, elongation of the focal speech region (box with wavy lines) and selective pause interjection and elongation next to the focal repair (■), compared with nonfocal utterance regions (□).

1. Duration

a. Focal speech duration. The total duration of the focal speech segment increased from an average of 400 ms during original input to 473 ms during repetition, a gain of +18%. This increase was significant by paired t test on log transformed data, $t=6.02$ (df=95), $p<0.001$, one-tailed.

b. Nonfocal speech duration. The total duration of the surrounding speech segments also increased from an average of 745 ms during original input to 811 ms during repetition, a gain of +9%. This increase also was significant by paired t-test on log transformed data, $t=5.11$ (df=95), $p<0.001$, one-tailed.

c. FOC/NFOC speech duration ratio. The ratio of focal to nonfocal speech duration increased significantly during repetition, paired $t=2.13$ (df=95), $p<0.02$, one-tailed. That is, the focal speech region was demonstrated to increase significantly more than other surrounding speech segments.

d. Pause duration adjacent to repair. Approximately 47% of all multi-word utterances contained one or two pauses adjacent to the focal speech repair during error resolution. The total duration of such pauses averaged 72 ms during original input, increasing to 179 ms during repetition, which was significant by paired t test on log transformed data, $t=5.60$ (df=35), $p<0.001$, one-tailed. That is, a substantial +149% increase was discovered in average pause duration immediately next to the focal repair region during repetitions. This increase in total pause duration was comparable in size for pauses positioned immediately before versus after the repair region (i.e., averaging 178.5 vs, 180.0 ms, respectively).

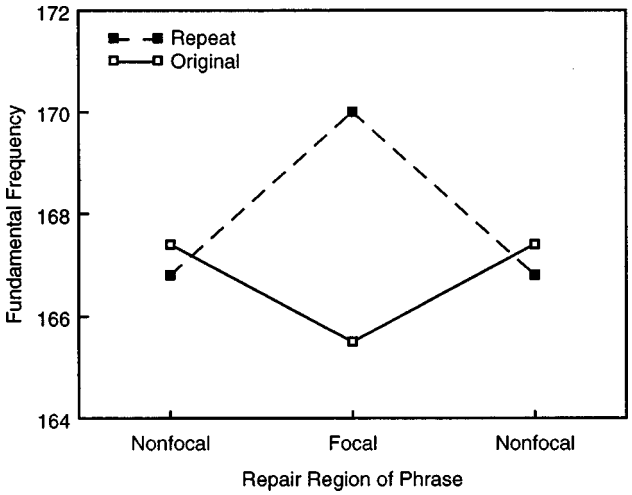

FIG. 10. Change in pitch maximum on focal repair region versus nonfocal segments, for focal repairs in sentence initial and medial position.

Further analysis confirmed that both interjection of new pauses and elongation of existing ones contributed independently to observed increases in total pause duration immediately around the focal region. In original-repeat utterance pairs for which the number of pauses was matched, pause elongation still was significant by paired t test, $t=2.96$ (df=13), $p<0.01$, one-tailed.

e. Pause duration nonadjacent to repair. Pause duration for positions nonadjacent to the repair region averaged 128 ms during original input and 140 ms during repetitions, a +9% increase. This increase also was significant by paired t test, $t=2.02$ (df=13), $p<0.04$.

f. Number of pauses adjacent to repair. The number of pauses immediately adjacent to a repair region averaged 0.80 during original input, increasing to 1.70 during repetitions, a

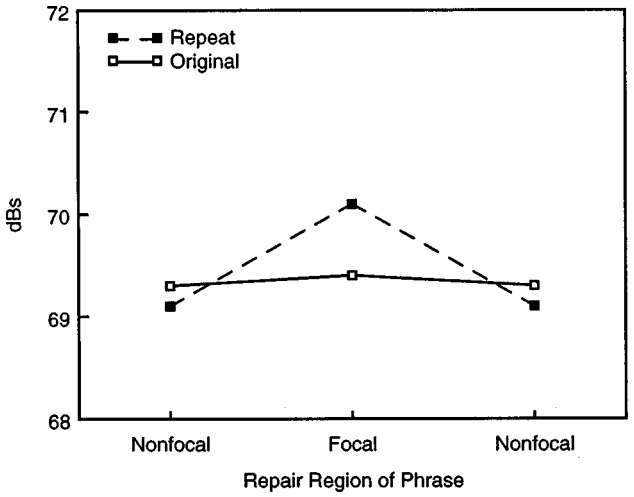

FIG. 9. Amplitude change on focal repair region versus nonfocal segments during related substitutions.

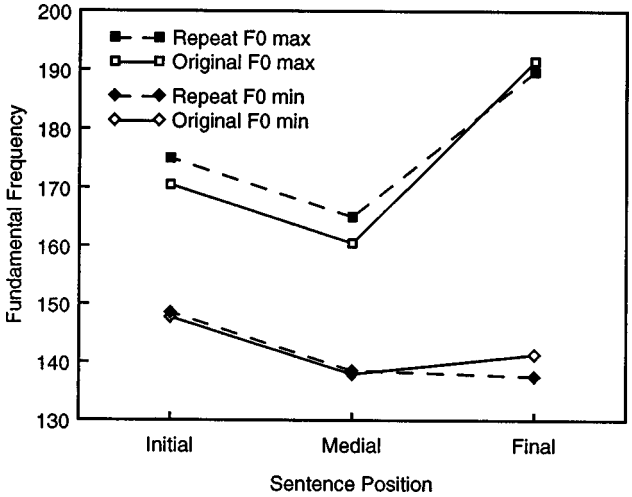

FIG. 11. Change in pitch maximum and minimum on focal repairs as a function of sentence position.

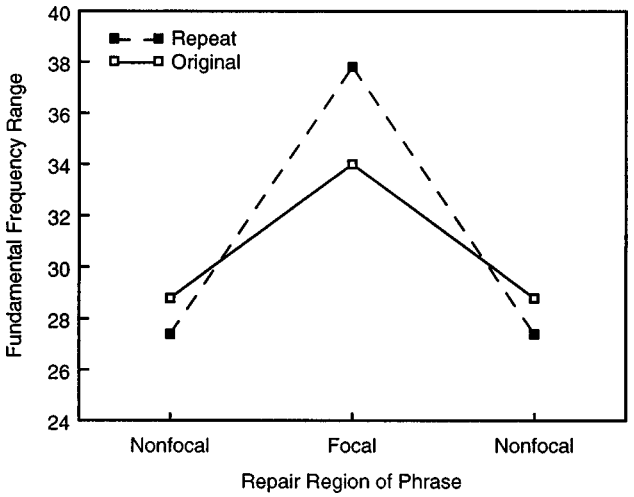

FIG. 12. Change in pitch range on focal repair region versus nonfocal segments during related substitutions.

+113% gain. This increase in average number of pauses was significant by Wilcoxon Signed Ranks test, $z=2.49$ ($N=12$), $p<0.01$, one-tailed. Analysis of the position of these pauses indicated an equal split between those located immediately before versus after the repair.

Figure 8 illustrates selective pause interjection and elongation immediately around the focal repair region, as well as elongation of the spoken repair region itself, during focal repair of a typical related substitution error from the present corpus.

2. Amplitude

a. Focal maximum amplitude. Maximum amplitude of the focal region averaged 69.4 dB during original input, increasing to 70.1 dB during repetition, which represented a +1% gain. This increase on the focal segment was significant by paired t test, $t=3.15$ (df=95), $p<0.001$, one-tailed.

b. Nonfocal maximum amplitude. Average maximum amplitude of the nonfocal repair region was 69.3 dB during original input and 69.1 dB during repetitions, which was not a significant change, $t<1$.

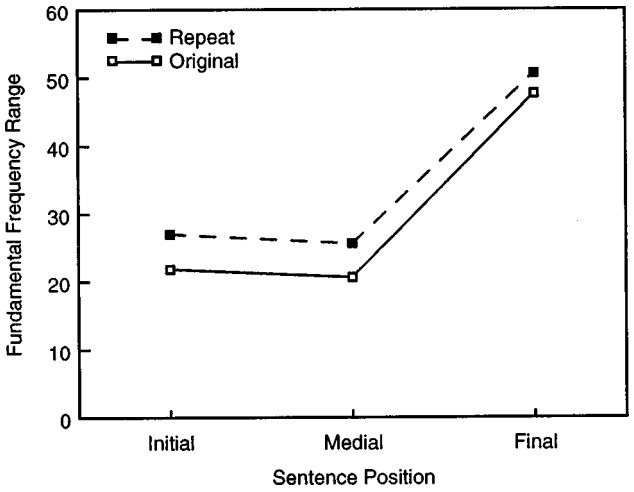

FIG. 13. Change in pitch range on focal repairs as a function of sentence position.

c. FOC/NFOC amplitude ratio. The ratio of maximum amplitude gain on focal versus nonfocal regions increased from 1.00 during original input to 1.01 during repetition, a significant relative change by paired t test, $t=2.71$ (df=95), $p<0.004$, one-tailed. Figure 9 illustrates the amplitude increase on focal repair regions during repeated utterances, compared with nonfocal segments.

3. Fundamental frequency

a. Focal pitch maximum. Maximum $F0$ on focal speech segments averaged 165.5 during original input and increased to 170.0 during repetition of the focal repair when it occurred in sentence initial and medial positions. This change represented a +2.7% increase in maximum $F0$ on the target repair region, which was significant by paired t test, $t=2.86$ (df=50), $p<0.003$, one-tailed. However, when the focal repair was in sentence-final position maximum $F0$ averaged 191.5 and 189.7 during original and repeated input, which did not represent a significant change, $t<1$.

b. Nonfocal pitch maximum. The average maximum $F0$ on nonfocal speech segments (i.e., excluding those occurring in sentence-final position) was 167.4 and 166.8 during original and repeated input, which was not a significant increase, $t<1$.

Figure 10 illustrates the increase in maximum $F0$ during repetition of a focal repair segment, compared with surrounding nonfocal ones. Figure 11 (top) illustrates that this increase occurred when the repair region was in any position except final.

c. Focal pitch minimum. Minimum $F0$ on focal speech segments averaged 143.6 and 143.5 on original input and repetitions when the focal repair was in sentence-initial or medial position, which did not represent a significant change, $t<1$. However, when the focal repair was in sentence-final position, minimum $F0$ averaged 141.3 on original input and dropped to 137.5 during repetitions, which was a −2.7% decrease and significant by paired t test, $t=1.72$ (df=41), $p<0.05$. Figure 11 (bottom) illustrates that this decrease in minimum pitch only occurred in sentence-final position.

d. Nonfocal pitch minimum. The minimum $F0$ on nonfocal speech segments occurring in sentence-final position averaged 135.6 and 133.3 during original input and repetition, which did not represent a significant difference, $t<1$. That is, sentence-final speech segments that were not the focus of repair showed no reliable drop in minimum $F0$ during repetitions.

e. Focal pitch range. The $F0$ range on focal repair segments occurring in all sentence positions averaged 34.0 for original input, increasing to 37.8 for repetitions. This was an +11.2% gain, and a significant expansion of pitch range, $t=2.11$ (df=95), $p<0.02$, one-tailed.

f. Nonfocal pitch range. The $F0$ range averaged a lower 28.8 and 27.4 for original and repeated input for speech segments throughout the sentence that were not the focus of repair, which did not represent a significant difference, $t=1.09$ (df=92), N.S.

Figure 12 illustrates the increase in pitch range during repetition of focal repair segments, compared with surrounding nonfocal ones. Figure 13 illustrates that this pitch range

expansion on focal repairs occurred uniformly in all sentence positions.

III. DISCUSSION

Human speech to computers varies along a spectrum of hyperarticulation, such that its basic signal properties change dynamically and sometimes abruptly. The present data demonstrate that system recognition errors can be a forceful elicitor of hyperarticulate speech from users. Furthermore, the presence, form, and degree of hyperarticulation in users' speech to computers is a highly predictable phenomenon. It has a specific constellation of linguistic features, and it occurs as a generalized response to different types of system recognition error. In addition, hyperarticulate adaptation can occur during global utterance repairs, and also during focal repairs involving one isolated region within a longer utterance. These research findings raise concerns with current algorithmic approaches to recognizing spoken language, which generally fail to model dynamic stylistic changes in the speech signal that are elicited during natural interactions, such as hyperarticulation during miscommunication, or Lombard speech during noise.

A. Global hyperarticulation to computers

During global utterance repairs, speech predominantly shifted to become lengthier and more clearly articulated, as summarized in Table I. Comparable durational changes were observed following all three types of system error, including +8.5% average elongation of the speech segment, +40% elongation of pause duration, and interjection of +44% more pauses. The most salient relative changes in repeated speech involved altered pause structure. Perhaps ironically, users' speech became somewhat more discrete during hyperarticulation, departing from the pattern of continuous speech upon which most current recognizers typically are trained. However, the changes observed in pause structure in no sense approached regularized discrete pausing between every word, as would be required by a discrete word recognizer. Instead, it often was highly targeted, as in selective pause interjection and elongation around focal repair regions.

The large durational increases obtained in this study are similar to those documented in hyperclear speech to the hearing impaired (Uchanski *et al.*, 1996). Previous literature on interpersonal speech also has reported increases in the number and length of pauses in hyperclear speech between people without hearing impairments (Cutler and Butterfield, 1990, 1991). In general, such changes in pause structure appear to play an important role in assisting listeners with marking word boundaries and segmenting a continuous stream of speech (Cutler and Butterfield, 1990, 1991; Maasen, 1986).

Articulatory changes also were a prominent characteristic of global hyperarticulate adaptation. The phonological features of repeat speech adapted toward an audibly clearer articulation pattern on 6% of repetitions, with frequently observed changes including the insertion of previously deleted segments (e.g., *'leven* changing to *eleven*), fortition of alveolar flaps to coronal plosives (e.g., ɛɪɾɛɪt changing to *eIt˜eIt), and shifts to unreduced* **nt** sequences (e.g., twɛ̃ɾi to twɛnti). This shift also corresponded with a 38.5% decrease in spoken disfluencies, which may have occurred in part because rearticulated utterances involve a reduced planning load (Oviatt, 1995). Essentially, users' speech became more deliberate and better specified in its signal cues to phonetic identity. These findings are consistent with the linguistic literature on hyperclear speech between people, which has reported change in both vowel and consonant quality including, for example, more audibly released word-final stops (Chen, 1980; Cutler and Butterfield, 1991; Moon, 1991; Picheny *et al.*, 1986). In future research, more detailed quantitative modeling will be needed on the major durational and articulatory changes observed during hyperarticulation to computers, as well as on their interrelation.

During global utterance repairs, an error correction subdialogue was initiated that also led to prosodic changes. Repeat utterances were 9% more likely to be closed with a final falling contour than were original utterances. Pitch minima also decreased significantly during global utterance repairs, although only by −2% overall. Both this increased rate of final falling tones on error correction subdialogues, and the small decline in pitch, apparently were used by speakers as cues to mark the close of a repair with their computer partner. These findings are consistent with previous research demonstrating that a final falling contour and reduction in pitch are the strongest cues used during interpersonal speech to produce finality judgements (Swerts *et al.*, 1994).

While amplitude increases were present during global utterance repairs, they nonetheless were negligible—averaging just +0.5%. In a previous study, no amplitude increases were found at all in speech during error resolution (Oviatt *et al.*, 1996, 1998). The statistically reliable amplitude effect in this study most likely was discernable because the data set was three fold larger, and the present experimental design afforded greater precision. In any event, the amplitude change observed in speech to computers was extremely small. This stands in contrast to the sizable increases often found in hyperarticulated speech between humans—for example, in speech to the hearing impaired and in a noisy environment. In summary, adaptation in both amplitude and fundamental frequency were relatively attenuated during error resolution with a computer partner, compared with the effects typically observed between humans during miscommunication.

The hyperarticulation profile described above was strikingly similar following all three types of system recognition error. Irrespective of the fact that users view substitution errors as interjecting *wrong* content, hyperarticulate change following both types of substitution error replicated the pattern found for failure to understand errors. Likewise, unrelated substitution errors were unintuitive, comical, and unique in their ability to evoke emotional reactions 22% of the time (e.g., ''Nancy Alston'' recognized as ''Dodge City''). Although one might assume that this emotional arousal would be associated with a larger magnitude of hyperarticulate change, including heightened pitch and amplitude changes, this was not the case. In spite of their evocative nature, the speech signal adapted nearly identically for unrelated substitution errors as the other two types. This

striking similarity in the hyperarticulation profile for different types of system error is illustrated in Fig. 7.

Compared with interpersonal speech during expected or actual miscommunication, the overall pattern of hyperarticulation to a computer is somewhat unique. This partly was evident in users' minimal amplitude and pitch changes, which was consistent with self-reports indicating that speakers generally did not believe that volume or pitch were key factors in eliminating recognition errors. Instead, users reported that controlling rate and articulatory clarity caused computer errors to resolve—comments that corresponded with dominant changes observed in their speech at the signal level. In this sense, speakers' beliefs about rate and articulatory clarity appear to apply more broadly to resolving miscommunications with both computers and varied human listeners. The present evidence supports the view that speakers view error-prone computers as a unique kind of ''at risk'' listener—one involving communication dynamics and sources of fallibility distinct from other at risk groups such as children, the hearing impaired, or nonnative speakers.

The hyperarticulate signal changes reported in this study represent a strong and persistent predilection by speakers. They may underestimate changes during interaction with some challenging application domains that are known to have high word error rates, such as the DARPA Switchboard corpus (Martin *et al.,* 1997). The Switchboard corpus contains speech from spontaneous telephone dialogues, and the best systems currently are generating word error rates two- to three fold higher on this corpus than that in the present study. For systems or application domains known to have such high error rates, previous research indicates that speech is likely to involve a substantial intensification of hyperarticulate effects (Oviatt *et al.,* 1998).

B. Focal hyperarticulation to computers

Since the majority of speech recognition errors are substitutions, sometimes cases arise in which the user selectively repairs one focal part of an utterance, as in ''July twenty-**first** nineteen ninety-seven.'' There is a sense in which these focal repairs may be viewed as a highly targeted, brief, and fine-tuned form of hyperarticulate adaptation in which durational, fundamental frequency, and amplitude cues function together to demarcate and highlight the repair region. Results from the present study clarify the nature and orchestration of hyperarticulate change during error resolution involving focal repairs.

Changes in pause structure still were dominant during focal hyperarticulate adaptation, as summarized in Table III—with a +149% increase in pause duration, and a +113% increase in pause interjection next to the repair region. However, the magnitude of these changes was three- to fourfold larger than during global utterance repair. Changes in pause interjection and elongation also were highly selective in their placement immediately before and after the focal repair region. In fact, these pause changes were twelve- to sixteen-fold greater next to the repair region than in other sentence positions. The function of this selective interjection and lengthening of pauses was most plausibly to demarcate the repair region clearly. However, there was no evidence that such pauses were placed in advance of the repair region more often than after it, for example as a way to signal upcoming repair. The focal speech region also was elongated by 18%, which was twofold more than speech elongation in surrounding nonfocal regions or speech elongation during global utterance repairs.

Although relatively smaller in magnitude of change, the focal repair region also was selectively marked with an +11% increase in pitch range, which derived from increases in maximum pitch in sentence-initial and medial positions, and decreases in minimum pitch in sentence-final position. Variation in absolute pitch levels were revealed to be highly sensitive to the location of a repair in the sentence. However, the net effect of this orchestration of maximum and minimum pitch changes was a uniform expansion of pitch range on focal repairs occurring anywhere in a sentence. As in the case of durational effects, pitch changes observed during focal repairs were highly targeted at the repair region. On average, there was a +38% greater expansion of pitch range on the focal speech repair than on surrounding nonfocal speech segments.

Expanded pitch range is known to mark linguistic segments as salient (Pierrehumbert, 1980), or as content that the listener should pay particular attention to in the moment-by-moment delivery of spoken information. Pitch range also is known to play an important role in conveying the hierarchical segmentation of discourse, generally being expanded at the beginning of new topics (Brown, 1983; Hirschberg and Grosz, 1992; Lehiste, 1975). In spontaneous conversations, pitch range expansion generally has been shown to mark the start of a new unit, whether a new topic, a new speaker turn, or a self-correction of disfluencies or content errors (Ayers, 1994; French and Local, 1986). During focal error repairs with a computer partner, both elevated pitch and expanded pitch range provided cues for identifying the precise boundaries of the correction region within a longer continuous utterance, which could facilitate linguistic processing of its lexical content. As a tool for demarcating focal repair regions, pitch clearly functioned more actively than during global utterance repairs.

The focal repair region also was selectively marked with small increases in amplitude, averaging less than a 1% gain. Although change in amplitude co-occurred with durational effects, increases in duration far exceeded the relative gains for amplitude. This finding is consistent with Turk and Sawusch's (1996) demonstration that, while duration and amplitude generally interact to yield judgements of prominence (Fry, 1955), the primary factor that gives rise to perceived prominence is increased duration. Their research demonstrates that the impact of durational and amplitude increases on the perceived salience of a speech segment are not equivalent or symmetric. At some level, speakers may be aware of this greater impact of durational increase on the intelligibility of speech, which may account for their similarly strong reliance on durational cues when resolving system recognition errors.

TABLE IV. Summary of absolute change in linguistic features of Stage I and II hyperarticulation,[a] based on past and present research.[b]

Linguistic feature	Stage I change[c]	Stage II change
Duration:		
Pause interjection	+0.57 pauses	+0.32 — +0.38 pauses[d]
Pause elongation	+97 ms	+78 — +102 ms
Speech elongation	+190 ms	+127 — +171 ms
Articulation:		
Hyper-clear phonology	N.S.	+6 — +9%[e]
Disfluencies	N.S.	−0.25 — −0.25[f]
Pitch:		
Intonation—final fall	N.S.	+9 — +9%[g]
Pitch minmum	N.S.	−2.2 — −2.7 Hz
Amplitude:		
Amplitude maximum	N.S.	N.S./+0.3 dB

[a]Values listed represent absolute change from original to repeat input for statistically significant changes (N.S.=not significant).

[b]Cumulative data included from past and present research are indicated in regular and bold font, respectively. Values based on the present research are averages across all error types. Values based on past findings are taken from Oviatt *et al.* (1998).

[c]Stage I changes were associated with a 6.5% overall error rate per utterances input, and Stage II changes with a 20% rate (upper bounds of the Stage II range based on spiral errors that repeated 1–6 times).

[d]Data represent change in average number of pauses per utterance in multiword utterances.

[e]Data represent change in percent of utterances with a phonological alternation involving a hyperarticulate shift.

[f]Data represent change in rate of disfluencies per 100 words.

[g]Data represent change in percent of utterances with a final falling intonation contour.

C. The CHAM model

These results corroborate and generalize the computer-elicited hyperarticulate adaptation model (CHAM), which is summarized schematically in Fig. 1 and elaborated quantitatively in the accompanying Table IV. The CHAM model predicts that specific features in users' speech will adapt during human–computer error resolution, and that the type and magnitude of adaptation will depend on a system's overall error rate (Oviatt *et al.*, 1998). In the present study, the hyperarticulate changes that were replicated across all three error types would be considered Stage II adaptations, and in fact the predicted multiple effects involving durational, articulatory, fundamental frequency, and amplitude changes all were evident (i.e., see Table IV values in bold font). Although no change in amplitude was reported in earlier findings by Oviatt *et al.* (1998), in the present study which was threefold larger and more carefully controlled, a significant but very small amplitude effect did emerge. As clarified by Table IV, the magnitude of adaptations for specific linguistic features in the present study was extremely close to previous reports. In addition to the above, the CHAM model predicts abrupt transitions in the signal profile from one moment to the next, which was observed continually in this study when brief episodes of hyperarticulation punctuated repetitions in juxtaposed original-repeat utterances.

Table IV summarizes the type and magnitude of absolute hyperarticulate changes during Stage I and II based on cumulative evidence from past research reported in Oviatt *et al.* (1998) (i.e., shown in plain font) and from the present findings (i.e., shown in bold font). Results from the earlier study by Oviatt *et al.* (1998) included data on Stage I and II hyperarticulation elicited by rejections errors. In contrast, the larger and more extensive present study included data on three common types of system recognition error, as well as on focal and global utterance repairs, although these latter comparative data all assessed Stage II hyperarticulation. The Stage I hyperarticulation data listed in Table IV were precipitated by a low error rate (i.e., 6.5%), whereas Stage II data were associated with a high error rate (i.e., 20%). The hyperarticulation values from the present study that are listed in Table IV tend to mark the lower bound on Stage II estimates, with Stage II values based on previous research ranging slightly but consistently higher because they involved spiral errors that could recur between one and six times. These spiral errors effectively would have compounded the error rate, which could account for the correspondingly greater changes in hyperarticulate features and would be consistent with the CHAM model.

With respect to hyperarticulate change during focal repairs, the acoustic dimensions that were examined—including duration, pitch, and amplitude—all adapted as predicted by the CHAM model. Furthermore, the relative degree of change in these three dimensions (i.e., large changes in duration, moderate ones in pitch, and minimal ones in amplitude) are similar to those observed during global error repairs. However, the absolute magnitude of durational and pitch range changes during focal repairs was larger than that found during global repairs. In addition, shifting to and from a hyperarticulate speech style was more abrupt and highly targeted than that during global utterance repairs. While consistent with the CHAM model, these characteristics of hyperarticulation during focal repairs may prove more difficult to accommodate in the design of future systems, as will be discussed further in the next section.

In brief, the present results confirm and further generalize the two-stage CHAM model, which was motivated by linguistic theory (Lindblom, 1990) and the specifics of which were derived from recent empirical research (Oviatt *et al.*, 1998). From cumulative research conducted to date, it is clear that Stage I and II of the CHAM model accurately predict the type and magnitude of hyperarticulate adaptations for a variety of linguistic features during human–computer error resolution, which vary according to a system's overall error rate. As demonstrated in the present study, the CHAM model's basic predictions apply to qualitatively different types of recognition error, and to both global and focal utterance repairs.

D. Designing interactive systems to handle hyperarticulation

The hyperarticulate speech documented in this research presents a potentially difficult source of variability that can degrade the performance of current speech recognizers and complicate their ability to resolve errors gracefully. One question raised by viewing the CHAM model in Fig. 1 is whether an utterance spoken during baseline conditions can be recognized as identical to its counterpart during Stage II

conditions. Like Lombard speech, hyperarticulate speech involves episodic and often abrupt signal variability that may pose a more substantial challenge to current recognition technology than chronic forms of variability, such as accented speech. The relatively static algorithmic approaches that currently dominate the field of speech recognition, including techniques like hidden Markov modeling, appear particularly ill suited to processing the dynamic stylistic variability typical of hyperarticulate speech. The present research therefore should provide a stimulus for developing fundamentally more dynamic, adaptive, and user-centered approaches to speech recognition.

There are several possible avenues for improving the performance of current spoken language systems on hyperarticulate speech. One is to train recognizers on more natural samples of users' interactive speech to systems, including error resolution with the type and baserate of errors expected in the target system. However, this alternative may be associated with trade-offs in accuracy, and it does not address the problematic issue of abrupt signal transitions in hyperarticulate speech.

Another approach is to design a recognizer specialized for error handling, which could function as part of a coordinated suite of multiple recognizers that are swapped in and out at appropriate points during system interaction. Such an alternative would be viable within a form-based interface with input slots, as was used in the present simulation, since in such an arrangement it is reasonable to assume that reentry into the same slot involves a correction. This approach would require data collection and recognizer training on a corpus of hyperarticulate speech. One advantage of this approach is that it is capable of handling abrupt shifts in hyperarticulation. However, not all applications may be amenable to identifying the start and end of error correction, which would be necessary to swap in the appropriate recognizer reliably.

Although hyperarticulate changes during focal error repairs were similar to those during global repair, in some respects they may be more difficult for systems to accommodate. For example, the durational and pitch range changes during focal repairs were more pronounced in magnitude, and shifts to and from hyperarticulate speech were more abrupt than during global repairs. One difficult problem raised by these data on focal repairs is how to identify their precise boundaries in a continuous utterance. This problem complicates the prospect of designing systems with specialized recognizers, as suggested above. In particular, it may be implausible in future systems to mark focal repair regions clearly via simple interface design techniques, for example, using a form-based interface to swap in a specialized recognizer at appropriate times. However, since strong acoustic cues naturally demarcate focal repairs, in the future it may be possible to develop methods for identifying focal repair regions automatically as an aid to advanced interface design.

The development of more adaptive systems likewise may improve current recognizer's performance, and is an option that has been advocated for processing Lombard speech (Applebaum and Hanson, 1990; Junqua, 1993). Since signal adaptations occur abruptly when users enter an error correction subdialogue, such a system should *not* be designed to adapt continuously to users' speech throughout an interaction. Rather, system adaptation specifically should avoid adapting across sharp boundaries that divide original input from error correction speech—instead adapting within error-correction subdialogues to the specific form and magnitude of a given user's hyperarticulation. The goal of such an approach would be to improve recognizer performance on a user's hyperarticulation during future correction episodes. To better assess the prospects and benefits of an adaptive approach, future research should explore individual differences in hyperarticulate speech, especially for durational effects (for discussion, see Oviatt *et al.*, 1998).

Perhaps the most promising long-term solution to improving current recognizers' performance is to avoid hyperarticulate speech by designing a multimodal rather than unimodal interface. This option has been discussed in detail elsewhere (Oviatt and vanGent, 1996; Oviatt *et al.*, in press), so will only be summarized here. First, when people are free to interact multimodally and can switch to an alternate input mode, the likelihood of both avoiding and rapidly resolving errors is facilitated. In part, this is because users have good intuitions about when to deploy a given input mode such that they avoid errors (Oviatt and Olsen, 1994). In addition, users naturally increase their alternation of input modes after a recognition error occurs. Since input modes such as speech and pen have different confusion matrices associated with the same propositional content, this switching of input modes in a multimodal interface can eliminate stubborn spiral errors effectively. In addition, multimodal system architectures that unify the propositional content carried in parallel input modes can result in mutual disambiguation during semantic interpretation, which then reduces the overall system's error rate (Johnston *et al.*, 1997; Oviatt, in press; Oviatt, in submission).

In the near future, it will become increasingly important to model speech in natural field environments and while users are mobile. Due to variable noise levels, movement, collaborating groups of users, interruptions, multi-tasking, stress, and other factors, acoustic-phonetic variability in the speech signal may be different and substantially magnified under such conditions. Rates of miscommunication also are likely to be elevated, in some cases beyond those currently reported for spontaneous telephone dialogues. Unlike the laboratory, speech in these settings can be expected to include a combination of hyperarticulate, Lombard, and other difficult forms of abrupt signal variation. The present research on user-centered modeling of speech adaptations during error begins to provide an empirical foundation for the design of these more challenging next-generation systems.

ACKNOWLEDGMENTS

This research was supported by Grant No. IRI-9530666 from the National Science Foundation, and by grants, contracts, and equipment donations from Apple, GTE Labs, Intel, Microsoft, NTT Data, Southwestern Bell, and US West. We especially thank Robert VanGent, Jon Lindsay, and Eric Iverson for adapting the simulation software to support this study, and Eric Iverson for acting as simulation assistant dur-

ing data collection. Thanks to Karen Kuhn for preparing detailed hard-copy transcripts, and to Karen Kuhn and David Fencsik for scoring assistance. Finally, we are grateful to the people who generously volunteered their time to participate in this research.

[1]The distinction between related and unrelated substitution errors refers to whether the system's substitution is related acoustically and semantically to the user's original input.

[2]In current systems, the percentage of substitution errors that would be classified as related versus unrelated varies considerably. As recognition technology develops algorithms that more closely model human perceptual and linguistic capabilities, an increasingly greater percentage should become related acoustically and semantically to users' input.

Applebaum, T. H., and Hanson, B. A. (**1990**). ''Robust speaker-independent word recognition using spectral smoothing and temporal derivatives,'' Proc. of EUSIPCO-90, 1183–1186.

Ayers, G. (**1994**). ''Discourse functions of pitch range in spontaneous and read speech,'' in *Working Papers in Linguistics* (Ohio State University, Columbus, OH), Vol. 44, pp. 1–49.

Bolinger, D. (**1958**). ''A theory of pitch accent in English,'' Word **7**, 199–210.

Bond, Z. S., and Moore, T. J. (**1994**). ''A note on the acoustic-phonetic characteristics of inadvertently clear speech,'' Speech Commun. **14**, 325–337.

Brenner, M., Shipp, T., Doherty, E., and Morrissey, P. (**1985**). ''Voice measures of psychological stress: Laboratory and field data,'' in *Vocal Fold Physiology, Biomechanics, Acoustics, and Phonatory Control*, edited by I. Titze and R. Scherer (Denver Center for the Performing Arts, Denver, CO), pp. 239–248.

Brown, G. (**1983**). ''Prosodic structure and the given/new distinction,'' in *Prosody: Models and Measurements*, edited by D. R. Ladd and A. Cutler (Springer-Verlag, Berlin), pp. 67–68.

Brown, N. R., and Vosburgh, A. M. (**1989**). ''Evaluating the accuracy of a large vocabulary speech recognition system,'' Proc. of the 33rd Annual Meeting of the Human Factors Society, pp. 296–300.

Chen, F. R. (**1980**). ''Acoustic characteristics and intelligibility of clear and conversational speech at the segmental level,'' Master's thesis, Massachusetts Institute of Technology, Cambridge, MA.

Cutler, A., and Butterfield, S. (**1990**). ''Durational cues to word boundaries in clear speech,'' Speech Commun. **9**, 485–495.

Cutler, A., and Butterfield, S. (**1991**). ''Word boundary cues in clear speech: A supplementary report,'' Speech Commun. **10**, 335–353.

de Jong, K. (**1995**). ''The supraglottal articulation of prominence in English: Linguistic stress as localized hyperarticulation,'' J. Acoust. Soc. Am. **97**, 491–504.

Eisen, B., Tillmann, H. G., and Draxler, C. (**1992**). ''Consistency of judgements in manual labelling of phonetic segments: The distinction between clear and unclear cases,'' Proc. of the Int. Conf. on Spoken Language Processing **2**, 871–874.

Ferguson, C. A. (**1975**). ''Toward a characterization of English foreigner talk,'' Anthropological Linguistics **17**, 1–14.

Ferguson, C. A. (**1977**). ''Baby talk as a simplified register,'' in *Talking to Children: Language Input and Acquisition*, edited by C. E. Snow and C. A. Ferguson (Cambridge U.P., Cambridge, MA), pp. 219–36.

Fernald, A., Taeschner, T., Dunn, J., Papousek, M., De Boysson-Bardies, B., and Fukui, I. (**1989**). ''A cross-language study of prosodic modifications in mothers' and fathers' speech to preverbal infants,'' J. Child Language, 477–501.

Frankish, C., Hull R., and Morgan, P. (**1995**). ''Recognition accuracy and user acceptance of pen interfaces'' Proc. of the Conf. on Human Factors in Computing Systems—CHI'95, pp. 503–510.

Freed, B. F. (**1978**). ''Foreign talk: A study of speech adjustments made by native speakers of english in conversation with nonnative speakers,'' Doctoral dissertation, Linguistics Department, University of Pennsylvania.

French, P., and Local, J. (**1986**). ''Prosodic features and the management of interruptions,'' in *Intonation in Discourse*, edited by C. Johns-Lewis (College-Hill, San Diego, CA), pp. 157–180.

Fry, D. B. (**1955**). ''Duration and intensity as physical correlates of linguistic stress,'' J. Acoust. Soc. Am. **27**, 765–769.

Fry, D. B. (**1958**). ''Experiments in the perception of stress,'' Language and Speech **1**, 126–152.

Garnica, O. K. (**1977**). ''Some prosodic and paralinguistic features of speech to young children,'' in *Talking to Children*, edited by C. E. Snow and C. A. Ferguson (Cambridge U.P., Cambridge, MA), pp. 63–88.

Gordon-Salant, S. (**1987**). ''Effects of acoustic modification on consonant recognition by elderly hearing-impaired subjects,'' J. Acoust. Soc. Am. **81**, 1199–1202.

Hanley, T. D., and Steer, M. D. (**1949**). ''Effect of level of distracting noise upon speaking rate, duration and intensity,'' J. Speech Hear. Disord. **14**, 363–368.

Hirschberg, J., and Grosz, B. (**1992**). ''Intonational features of local and global discourse structure,'' Proc. of the 5th DARPA Speech and Natural Language Processing Workshop, 441–446.

Howell, P., and Young, K. (**1991**). ''The use of prosody in highlighting alterations in repairs from unrestricted speech,'' The Quarterly J. of Experimental Psychology **43A**, 733–758.

Jelinek, F. (**1985**). ''The development of an experimental discrete dictation recognizer,'' Proc. IEEE **73**, 1616–1624.

Johnston, M., Cohen, P., McGee, D., Oviatt, S., Pittman, J., and Smith, I. (**1997**). ''Unification-based multimodal integration,'' Proc. of the 35th Annual Meeting of the Association for Computational Linguistics, 281–288.

Junqua, J. C. (**1993**). ''The lombard reflex and its role on human listeners and automatic speech recognizers,'' J. Acoust. Soc. Am. **93**, 510–524.

Kamm, C. A. (**1994**). ''User interfaces for voice applications,'' in *Voice Communication Between Humans and Machines*, edited by D. B. Roe and J. Wilpon (National Academy, Washington, DC), pp. 422–442.

Lehiste, I. (**1975**). ''The phonetic structure of paragraphs,'' in *Structure and Processes in Speech Perception*, edited by A. Cohen and S. G. Nooteboom (Springer-Verlag, Berlin), pp. 195–203.

Levelt, W. J., and Cutler, A. (**1983**). ''Prosodic marking in speech repair,'' J. Semantics. **2**, 205–217.

Lewis, C., and Norman, D. A. (**1986**). ''Designing for error,'' in *User-Centered System Design*, edited by D. A. Norman and S. W. Draper (Erlbaum, Hillsdale, NJ), pp. 411–432.

Lindblom, B. (**1990**). ''Explaining phonetic variation: A sketch of the H and H theory,'' in *Speech Production and Speech Modeling*, edited by W. Hardcastle and A. Marchal (Kluwer, Dordrecht), pp. 403–439.

Lindblom, B. (**1996**). ''Role of articulation in speech perception: Clues from production,'' J. Acoust. Soc. Am. **99**, 1683–1692.

Lindblom, B., Brownlee, S., Davis, B., and Moon, S. J. (**1992**). ''Speech transforms,'' Speech Commun. **11**, 357–368.

Lively, E., Pisoni, D. B., Van Summers, W., and Bernacki, R. (**1993**). ''Effects of cognitive workload on speech production: Acoustic analyses and perceptual consequences,'' J. Acoust. Soc. Am. **93**, 2962–2973.

Lombard, E. (**1911**). ''Le signe de l'elevation de la voix,'' Annals Maladiers Oreille, Larynx, Nez, Pharynx **37**, 101–119.

Maasen, B. (**1986**). ''Marking word boundaries to improve the intelligibility of the speech of the deaf,'' J. Speech Hear. Res. **29**, 227–230.

Martin, A., Fiscus, J., Fisher, B., Pallett, D., and Przybocki, M. (**1997**). ''System descriptions and performance summary,'' Proc. of the Conversational Speech Recognition Workshop/DARPA Hub-5E Evaluation.

Moon, S. J. (**1991**). ''An acoustic and perceptual study of undershoot in clear and citation-form speech,'' Doctoral dissertation, Linguistics Department, University of Texas at Austin.

Moon, S. J., and Lindblom, B. (**1994**). ''Interaction between duration, context, and speaking style in English stressed vowels,'' J. Acoust. Soc. Am. **96**, 40–55.

Moreton, E. (**1996**). ''Scoring procedure for duration,'' Oregon Graduate Institute of Science & Technology, unpublished manuscript.

Nakatani, C. H., and Hirschberg, J. (**1994**). ''A corpus-based study of repair cues in spontaneous speech,'' J. Acoust. Soc. Am. **95**, 1603–1616.

O'Shaughnessy, D. (**1992**). ''Analysis of false starts in spontaneous speech,'' Proc. of the Int. Conf. on Spoken Language Processing **1**, 931–934.

Oviatt, S. L. (**1995**). ''Predicting spoken disfluencies during human-computer interaction,'' Comput. Speech Lang. **9**, 19–35.

Oviatt, S. L. (**in press**). ''Ten myths of multimodal interaction,'' in *Communications of the ACM*.

Oviatt, S. L. (**in submission**). ''Mutual disambiguation of recognition errors in a multimodal architecture.''

Oviatt, S. L., and Olsen, E. (**1994**). ''Integration themes in multimodal

human–computer interaction,'' Proc. of the Int. Conf. on Spoken Language Processing **2**, 551–554.
Oviatt, S. L., and VanGent, R. (**1996**). ''Error resolution during multimodal human–computer interaction,'' Proc. of the Int. Conf. on Spoken Language Processing **1**, 204–207.
Oviatt, S. L., Bernard, J. and Levow, G. (**in press**). ''Linguistic adaptations during error resolution with spoken and multimodal systems,'' Language and Speech (in press).
Oviatt, S. L., Cohen, P. R., Fong, M. W., and Frank, M. P. (**1992**). ''A rapid semi-automatic simulation technique for investigating interactive speech and handwriting,'' Proc. of the Int. Conf. on Spoken Language Processing **2**, 1351–1354.
Oviatt, S. L., Levow, G., MacEachern, M., and Kuhn, K. (**1996**). ''Modeling hyperarticulate speech during human-computer error resolution,'' Proc. of the Int. Conf. on Spoken Language Processing, **2**, 801–804.
Oviatt, S. L., MacEachern, M., and Levow, G. (**1998**). ''Predicting hyperarticulate speech during human-computer error resolution,'' Speech Commun. **24**, 1–23.
Payton, K. L., Uchanski, R. M., and Braida, L. D. (**1994**). ''Intelligibility of conversational and clear speech in noise and reverberation for listeners with normal and impaired hearing,'' J. Acoust. Soc. Am. **95**, 1581–1592.
Picheny, M. A., Durlach, N. I., and Braida, L. D. (**1985**). ''Speaking clearly for the hard of hearing I: Intelligibility differences between clear and conversational speech,'' J. Speech Hear. Res. **28**, 96–103.
Picheny, M. A., Durlach, N. I., and Braida, L. D. (**1986**). ''Speaking clearly for the hard of hearing II: Acoustic characteristics of clear and conversational speech,'' J. Speech Hear. Res. **29**, 434–446.
Pierrehumbert, J. (**1980**). ''The phonology and phonetics of English intonation,'' Doctoral dissertation, Massachusetts Institute of Technology, Cambridge, MA.
Rhyne, J. R., and Wolf, C. G. (**1993**). ''Recognition-based user interfaces,'' in *Advances in Human–Computer Interaction*, Vol. 4, edited by H. R. Hartson and D. Hix (Ablex Publishing, Norwood, NJ), pp. 191–250.
Schulman, R. (**1989**). ''Articulatory dynamics of loud and normal speech,'' J. Acoust. Soc. Am. **85**, 295–312.
Shriberg, E., Wade, E. and Price, P. (**1992**). ''Human-machine problem solving using spoken language systems (SLS): Factors affecting performance and user satisfaction,'' Proc. of the DARPA Speech and Natural Language Workshop, 49–54.
Summers, W. V., Pisoni, D. B., Bernacki, R. H., Pedlow, R. I., and Stokes, M. A. (**1988**). ''Effects of noise on speech production: Acoustic and perceptual analyses,'' J. Acoust. Soc. Am. **84**, 917–28.
Swerts, M., Bouwhuis, D. G., and Collier, R. (**1994**). ''Melodic cues to the perceived finality of utterances,'' J. Acoust. Soc. Am. **96**, 2064–2075.
Tolkmitt, E. J., and Scherer, K. R. (**1986**). ''Effect of experimentally induced stress on vocal parameters,'' J. Exp. Psychol. **12**, 302–312.
Turk, A. E., and Sawusch, J. R. (**1996**). ''The processing of duration and intensity cues to prominence,'' J. Acoust. Soc. Am. **99**, 3782–3790.
Uchanski, R. M., Choi, S. S., Braida, L. D., Reed, C. M., and Durlach, N. I. (**1996**). ''Speaking clearly for the hard of hearing IV: Further studies of the role of speaking rate,'' J. Speech Hear. Res. **39**, 494–509.
Williams, C. E., and Stevens, K. N. (**1969**). ''On determining the emotional state of pilots during flight: An exploratory study,'' Aerosp. Med. **40**, 1369–1372.

The direct estimation of sound speed using pulse–echo ultrasound

Martin E. Anderson and Gregg E. Trahey
Department of Biomedical Engineering, Duke University, Durham, North Carolina 27708

(Received 8 May 1998; revised 8 July 1998; accepted 8 August 1998)

A method for the direct estimation of the longitudinal speed of sound in a medium is presented. This estimator derives the speed of sound through analysis of pulse–echo data received across a single transducer array following a single transmission, and is analogous to methods used in exploration seismology. A potential application of this estimator is the dynamic correction of beamforming errors in medical imaging that result from discrepancy between the assumed and actual biological tissue velocities. The theoretical basis of this estimator is described and its function demonstrated in phantom experiments. Using a wire target, sound-speed estimates in water, methanol, ethanol, and *n*-butanol are compared to published values. Sound-speed estimates in two speckle-generating phantoms are also compared to expected values. The mean relative errors of these estimates are all less than 0.4%, and under the most ideal experimental conditions are less than 0.1%. The relative errors of estimates based on independent regions of speckle-generating phantoms have a standard deviation on the order of 0.5%. Simulation results showing the relative significance of potential sources of estimate error are presented. The impact of sound-speed errors on imaging and the potential of this estimator for phase aberration correction and tissue characterization are also discussed. © *1998 Acoustical Society of America.* [S0001-4966(98)03711-4]

PACS numbers: 43.80.Ev, 43.80.Vj, 43.58.Dj [FD]

INTRODUCTION

In medical ultrasound imaging, ultrasound scanner performance depends greatly on the scanner's precision and accuracy in performing beamforming. Two fundamental assumptions underlying the beamforming process as it is currently practiced are (a) that the medium through which the sound propagates is homogeneous, and (b) that the speed of sound through this medium is known. These assumptions do not reflect the true nature of the tissues of the human body. While actual tissue velocities can range from 1400 to 1650 m/s,[1–3] the speed of sound *in vivo* is typically assumed to be 1540 m/s, potentially producing gross sound-speed errors on the order of $\pm 5\%$. Intra- and inter-patient variations in tissue sound speed produce steering and focusing errors that degrade the spatial and contrast resolutions as well as the flow velocity estimation performance of the ultrasound system. (Note that all references to sound speed in this paper refer to the longitudinal wave speed, as opposed to the transverse, or shear, wave speed.)

A number of techniques for estimating sound speed with pulse–echo ultrasound have been proposed in the literature and have been recently reviewed.[4] In addition, a number of techniques for correcting phase aberration errors, of which gross sound-speed errors are a subset, have been proposed and evaluated.[5–12] The impact of sound-speed error on blood flow velocity measurements has also been investigated and reviewed.[13] Creating tissue sound-speed maps is of interest in the tissue characterization research community, as certain variations in sound speed are correlated with pathological conditions of interest.[14,15,3,16] In this paper we describe a technique for the estimation of sound speed with pulse–echo ultrasound. Although we developed this technique independently, we have since found it to be related to techniques applied in exploration seismology. To our knowledge, the application in medical ultrasound of the various methods of sound-speed estimation commonly used in seismology has not been investigated.

I. THE SOUND-SPEED ESTIMATOR

In a homogeneous medium, the geometric delay pattern of echoes returning to an array of transducer elements from a target or region of interest is unique given the geometry of the array and target and the longitudinal sound speed of the medium. It is possible to estimate this speed solely from the delays in the radio frequency (rf) echo data recorded on individual elements of the array following a single transmittal. This technique is based on calculating the best-fit one-way geometric delay profile for this data set. The origin of the one-way geometric delay profile is shown schematically in Fig. 1. The medium sound speed and target coordinates are expressed in the coefficients in the function of this best-fit curve, and given reasonable assumptions, all but the target coordinate in elevation can be unambiguously estimated from them. Note that in this discussion, ''target'' can refer to either a point target or a region of interest in a speckle-generating medium.

We refer to this approach as a ''direct'' technique because the best-fit sound speed is calculated directly, as opposed to being inferred through the optimization of some other quality factor. This distinction may have significance in gaining regulatory approval of the application of this method in medical imaging. Ultrasound scanner manufacturers must demonstrate that their devices are rigorously calibrated to display geometrically correct images in 1540 m/s media. This calibration is jeopardized by adaptive imaging techniques based on the manipulation of the beamformer sound-speed variable either by an algorithm on the basis of signal

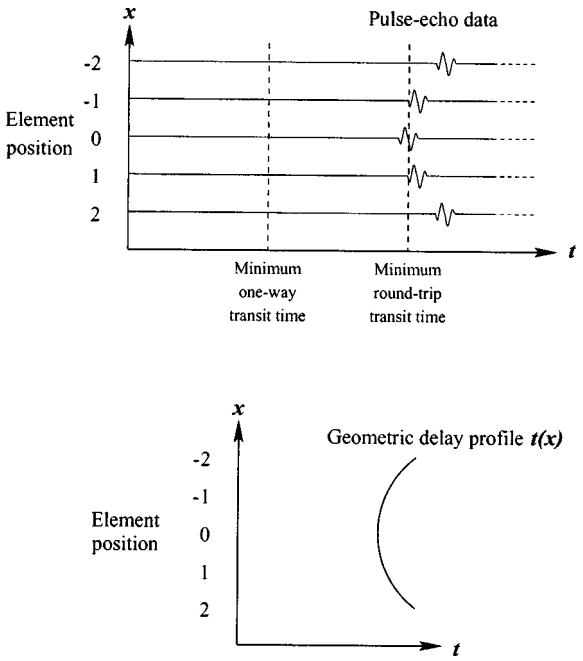

FIG. 1. Conceptual diagram of the determination of the one-way geometric delay profile from pulse–echo data. (Top) The minimum arrival time, relative to transmittal, of echoes returning from a target corresponds to the round-trip transit time. One-half of this time is the one-way transit time. (Bottom) The curve fit to the arrival times of echoes on all elements minus the one-way transit time is the one-way geometric delay profile. In a homogeneous medium, this profile, which is expressed solely in units of time, is a unique function of the target and array geometry and sound speed. The sound-speed estimator described in the text estimates this profile to derive the best-fit sound speed of the medium.

processing or by the clinician on subjective grounds. A method capable of reliably estimating the sound speed *in vivo* could improve image quality while maintaining geometric calibration.

Consider a Cartesian coordinate space defined relative to a transducer aperture such that x, y, and z coordinate axes correspond to the lateral, elevation, and axial dimensions. For an array of transducer elements oriented along the x axis, the observed one-way geometric delay profile $t(x)$ of echoes from a target located at (x_t, y_t, z_t) in a medium with sound speed c is

$$t(x)=\frac{\sqrt{(x-x_t)^2+y_t^2+z_t^2}}{c}. \tag{1}$$

Initially, only the profile $t(x)$ and the element positions in x are known. The values of x_t, y_t, z_t, and c are unknown but are constant. To fit a polynomial-based curve to the profile, we take the square of each side:

$$t^2(x)=\frac{(x-x_t)^2+y_t^2+z_t^2}{c^2}. \tag{2}$$

Equation (2) can be expanded and rearranged:

$$t^2(x)=\frac{x^2-2x_tx+x_t^2+y_t^2+z_t^2}{c^2}$$

$$=\frac{1}{c^2}x^2-\frac{2x_t}{c^2}x+\frac{x_t^2+y_t^2+z_t^2}{c^2}. \tag{3}$$

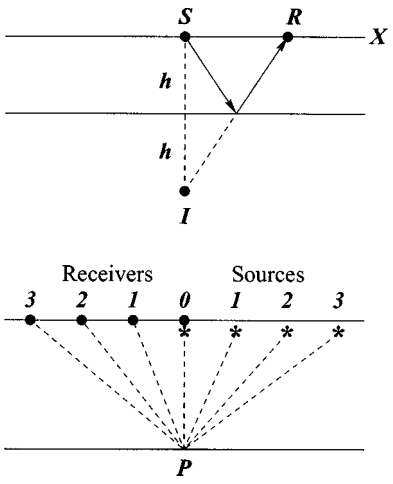

FIG. 2. (Top) The geometry used to describe the X^2-T^2 technique for seismological sound-speed estimation. The source S transmits sound that is reflected off the interface at depth h to a receiver at location R along the x axis. The interface echoes appear to emanate from a source at image point I. (Bottom) The source and receiver locations in a common midpoint (CMP) seismic mapping, in which sources and receivers are placed symmetrically about a midpoint to permit coherent summation on receive at a common reflection point P.

Equation (3) is of the form $f(x)=p_1x^2+p_2x+p_3$ where

$$p_1=\frac{1}{c^2},\quad p_2=-\frac{2x_t}{c^2},\quad p_3=\frac{x_t^2+y_t^2+z_t^2}{c^2}. \tag{4}$$

Given the one-way geometric delay profile $t(x)$, a second-order polynomial fit to $t^2(x)$ in the least-squares sense can therefore be used to determine p_1, p_2, and p_3. Observe that the medium sound-speed c can be determined from p_1. One can then solve for x_t using p_2, and estimate z_t using p_3 with the assumption that $y_t \ll z_t$. Explicitly,

$$c=\frac{1}{\sqrt{p_1}},\quad x_t=-\frac{c^2p_2}{2},\quad z_t\approx\sqrt{c^2p_3-x_t^2}. \tag{5}$$

Note that this method is based on the best-fit of a quadratic. In this light, the method can be applied with as few as three transducers, or even two transducers through the assumption of axial symmetry. For such cases in which the estimate is based on only a few arrival time estimates, knowledge of the exact position of each transducer would be more critical. However, a fixed arrangement of transducers could easily be calibrated in a reference medium.

A. Seismological sound-speed estimation

The estimator described above is seen to be closely related to several classes of seismological sound-speed estimators. The two most obvious analogues are the classical X^2-T^2 technique and *velocity analysis* based on data acquisition using the common-midpoint approach (CMP, sometimes referred to as common-depth-point, or CDP).[17] The source–receiver geometries of these two methods are shown in Fig. 2.

Rather than a point target or region of diffuse scatterers, the targets of interest in exploration seismology are typically interfaces between strata. These are essentially specular reflectors, although some geologic structures can produce diffractive effects.[18] As shown in Fig. 2 (top), in X^2-T^2 estimation, a horizontal interface at depth h reflects waves from

a seismic source at surface location $x=0$ to acoustic receivers spaced along the x axis.[19,20] The acoustic propagation path and reflection point between the source S and a receiver R are easily defined geometrically by placing an image point I at depth $2h$. The arrival time profile $t(x)$ of echoes recorded at the receivers is $t(x)=\sqrt{x^2+(2h)^2}/c$, which is squared to form the relation $t^2(x)=x^2/c^2+4h^2/c^2$. When $t^2(x)$ is plotted versus x^2, a line is defined with slope $1/c^2$, ideally indicating the velocity. The technique described in Sec. I is seen to be equivalent to this method once the horizontal reflector is replaced with an actual target at the image point. The coordinates of this target must also be confined to the z axis.

The CMP technique in seismology is conceptually related to coherent focusing in ultrasound.[21] In this method a series of source–receiver pairs are placed symmetrically about a common midpoint, as shown in Fig. 2 (bottom). Once appropriate delays are applied (known as *normal moveout correction*), the echoes recorded at these receivers can be coherently summed, or *horizontally stacked*, to focus the echoes from a single reflection point at depth h. This focusing implies knowledge of the best-fit sound speed, or *stacking velocity*. *Velocity analysis* refers to a class of methods of estimating the sound speed through some best-fit data processing approach in which the optimum alignment of echoes is chosen using some index of coherence.[22–25] To our knowledge, the direct calculation of sound speed from echo data aligned using cross correlation was first proposed and applied by Schneider and Backus.[23] The differences in the signal processing approach used by Schneider and Backus and that described in Sec. I can be attributed to the radically different data acquisition methods, array geometries, and target characteristics encountered in seismology versus ultrasound.

II. EXPERIMENTAL METHODS AND DATA ANALYSIS

We applied this sound-speed estimator to pulse–echo data from a wire target in four different fluids and from two separate speckle-generating phantoms. These experiments include media having sound speeds ranging from 1138 to 1547 m/s. All measurements were made with a commercial 7.5-MHz, 60% relative bandwidth linear array of a Siemens Elegra ultrasound scanner. This array has an active aperture 28.2 mm wide, comprising 128 elements. An ultrasound acoustic field simulation program indicated that this transducer has spatial resolutions at the focus of approximately 300 μm laterally, 160 μm axially, and 2.6 mm in elevation.[26] The medium temperature at the time of each trial was also automatically recorded using a digital thermometer with 0.015 °C accuracy (model HH42 with ON-402-PP probe, NIST traceable calibration, Omega Engineering, Stamford, CT). The atmospheric pressure was assumed to be equal to the current value as reported hourly by the National Weather Service (station KRDU, located 13 miles from our facility).

A. Wire target experiments

We first placed a 94-μm steel wire perpendicular to the image plane at the apparent transmit focus, set at 30 mm. Here the term ''apparent'' reflects that target placement was guided by the scanner display, which was based on a 1540 m/s sound speed and obviously not correctly calibrated geometrically for most of the media in this study. The radio frequency echoes returning from 25 pulse–echo acquisitions of the image line passing through the wire target were captured and recorded on each of 128 array elements. These echo data were digitized to 10-bit resolution at a sampling rate of 36 MHz and were then stored in a computer for subsequent processing.

We performed this procedure in deionized water, methanol (Mallinkrodt Baker, Paris, KY), ethanol (EM Science, Gibbstown, NJ), and *n*-butanol (Mallinkrodt Baker, Paris, KY). The alcohols were all anhydrous and reagent grade. All measurements were made within a short time interval of decanting the alcohol to minimize absorption of water vapor. Although the transducer used is specified by the manufacturer to withstand alcohol solutions such as those used for clinical disinfection, we were uncertain whether the transducer could be damaged by extended immersion in these pure alcohols. For this reason we protected the transducer with a polyethylene transducer cover (25 μm thick, CIVCO Medical Instruments, Kalona, IA) during measurements in all the fluids. We coupled the cover to the transducer with aqueous coupling gel (Aquasonic 100, Parker Labs, Orange, NJ) and were careful to minimize the thickness of the gel layer and to remove air bubbles in the gel from the region of the transducer aperture. We also performed one set of measurements in deionized water with no transducer cover.

All wire target measurements were made in a small tank lined with $\rho-c$ rubber, an absorbing material acoustically matched to water. We placed the temperature probe in the tank at the depth of the wire, away from the region of insonification.

Before applying the estimator to the wire target data, we applied a range gate to the data followed by axial interpolation by a factor of 8, giving an effective sampling rate of 144 MHz. The round-trip transit time was estimated by finding the arrival time of the peak amplitude of the echo envelope on the geometrically central element. The envelope of the rf echo data was calculated using the Hilbert transform.[27]

After this pre-processing, the geometric delay profiles of each data set were determined by first estimating the interelement delays using a normalized cross-correlation search.[6] These interelement delays were cumulatively summed across the array to form delay profiles relative to the first array element. These relative delay profiles were then offset in time to set the delay on the geometrically central element equal to the one-way transit time, or one-half of the round-trip transit time. The resulting geometric delay profiles were of the form of Eq. (1), from which we derived the corresponding estimates of c.

B. Speckle-generating target experiments

We also made sound-speed estimates in two speckle-generating materials. The first of these was a degassed small-celled sponge in a tank of deionized water, with the transducer coupled directly through the water. The temperature probe was placed in the water tank just above the surface of

TABLE I. The mean longitudinal sound-speed c compared to predicted published values for a wire target in four fluids and for two speckle-generating phantoms.

Medium	Mean estimate of c	Mean predicted value of c	Mean temperature	Pressure	Mean relative error	Standard deviation of relative error
	[m/s]	[m/s]	[°C]	[bar]	[%]	[%]
Wire target, without transducer cover						
$d\mathrm{H_2O}$	1480.72	1479.48	19.021	0.9993	0.08	0.07
Wire target, with transducer cover						
$d\mathrm{H_2O}$	1484.06	1480.00	19.186	0.9993	0.27	0.05
Methanol	1134.71	1138.33	14.889	1.001	−0.32	0.07
Ethanol	1167.71	1171.87	17.086	1.001	−0.36	0.06
n-Butanol	1259.65	1262.23	18.674	0.9993	−0.20	0.07
Phantom materials, without transducer cover						
Sponge	1477.41	1478.08	18.581	0.9959	−0.05	0.44
Agar–graphite	1544.03	1546.8	18.295	0.9953	−0.18	0.52

the sponge and away from the region of insonification. The second phantom was composed of agar and graphite in a 10% V/V *n*-propanol aqueous solution with an acoustic window composed of 13-μm polyvinylidene chloride film (Saran Wrap). Calibrated measurements of the sound speed and attenuation of this phantom (performed by Dr. Timothy Hall, Kansas University Medical Center) indicated a sound speed of 1546.8 m/s and an attenuation of 0.548 dB/cm MHz with an $f^{1.04}$ frequency dependence, where f is in MHz. The transducer was coupled to this phantom through a thin layer of a 10% V/V *n*-propanol aqueous solution with no transducer cover in place. For this experiment we placed the temperature probe in this coupling layer, away from the region of insonification. Between trials, the transducer was translated laterally relative to the phantoms using a computer-controlled linear translation stage (Parker Daedal 800000 series table, Parker Compumotor model SX6 microstep drive).

For estimator trials in speckle-generating media, it was necessary to ensure that the speckle regions sampled were completely independent between trials. For 50 preliminary acquisitions we used a lateral translation step size of 40 μm between rf acquisitions. We used these data to determine the transmit-only lateral spatial correlation length of the phantom speckle patterns. Using the rf data on the geometrically central element, we calculated the correlation coefficient ρ between the data from the first acquisition and that of all the following acquisitions, thus determining the correlation as a function of lateral translation. For each phantom material this analysis indicated that a step size of greater than 1.2 mm between acquisitions would guarantee no correlation ($\rho = 0$) between subsequent trials. For sound-speed estimation we captured 25 trials of pulse–echo rf data separated by 2-mm lateral translations in each phantom. On this basis we expect the trials within these data sets and the sound-speed estimates derived from them to be statistically independent.

Compared to the wire target data, the speckle-generating target data required more pre-processing before applying the estimator. In these cases we applied a 2.81-μs Hanning window to the rf data from each element, centered at the range of interest (30 mm) assuming $c = 1540$ m/s. Windowing was necessary to select speckle data at a particular range, and a Hanning window was used to reduce any bias in the subsequent cross-correlation operation due to window edge-effects. The location of this Hanning window was adjusted on each channel to follow the conventional receive focusing delay profile for this range, also assuming $c = 1540$ m/s. We based this windowing of the speckle data on an assumed sound speed of $c = 1540$ m/s to deny the sound-speed estimator any *a priori* information regarding the true sound speed. For rf speckle data, the round-trip transit time was simply the time corresponding to the center of the Hanning window on the geometrically central element. Like the wire target data, we axially interpolated the windowed speckle data by a factor of 8. Further processing was the same as for the wire target data as described in Sec. II A.

III. EXPERIMENTAL RESULTS

Results for all experiments are shown in Table I. These results were calculated by adjusting the sound-speed estimator output to compensate for the transducer's acoustic lens. Our analysis treated this lens as an overlying layer of a medium with known thickness and sound speed, using values specified by the manufacturer. The extent and curvature of the lens in the elevation dimension was disregarded. For each of 25 trials in each medium, the lens-compensated estimator output was compared to the value of a published polynomial expression for sound speed in each medium, taking into account the fluid temperature and atmospheric pressure at the time of each trial.[28,29] In Table I the mean output of the estimator for each target is compared to the mean literature-based value. The ''mean relative error of estimate'' results in Table I are the averages of the trial-by-trial relative errors in each medium.

The mean relative error was less than $\pm$ 0.4% for all experiments. For the wire and sponge experiments in water with no transducer cover in place, the mean relative error was less than 0.1%. The results for water with and without the transducer cover suggest that the cover and the associated layer of coupling gel introduced some estimation bias. The standard deviation of relative errors was on the order of 0.1% in all fluids using the wire target and 0.5% for the speckle-

generating phantoms. Because the target-array geometry was constant throughout the wire target experiment in each fluid, we attribute the variance of these estimates to electronic noise, which introduces jitter in the cross-correlation preprocessing. This type of estimate error is discussed further in Sec. IV. We do not know the temperature dependence of sound velocity in the agar–graphite phantom, and thus some error in this experiment may be due to a difference in the phantom temperature between this experiment and the phantom calibration.

The comparatively greater standard deviation in the speckle-generating phantom experiments is to be expected. We believe this reflects the characteristics of speckle signals, in that (a) the echo-returning volume is larger in spatial extent than that of a point or wire target, and (b) the spatial coherence length of these echoes at the array is shorter. Given the limited spatial coherence of speckle echoes across the array aperture, the cross-correlation based alignment of rf segments captured on spatially independent subsections of the array will be dominated by different bright speckles located at slightly different axial positions within the range gate. We believe that this apparent variation in target range across the array introduces error into the geometric curve fit. Further study is required to determine the optimum range gate window length for sound-speed estimation using speckle-generating targets.

IV. SOURCES OF ESTIMATE ERROR

The performance of this estimation method will depend on a number of factors, including the echo data signal-to-noise ratio, the transducer array geometry, the precision of transducer positioning, and phase errors introduced by inhomogeneities in the medium, as are found in the human body. We are able to assess the relative significance of these confounding factors using simulations in which we provide the estimator with intentionally degraded geometric delay profiles.

Given that the estimator operates on arrival time and element position data, errors in these quantities will degrade the estimates. We expect arrival time profiles to be degraded by jitter errors in the cross-correlation operation and phase aberration introduced by inhomogeneities in the tissue. Element position data will be degraded by manufacturing errors that reduce the accuracy of element registration. Table II lists the results of 10 000 simulation trials for examples of each of these confounding factors for the transducer described in Sec. II. The table shows the mean sound-speed estimate $\mu_{\hat{c}}$ and its standard deviation $\sigma_{\hat{c}}$, as well as the standard deviation expressed as a relative percent error $(100\cdot\sigma_{\hat{c}}/c)$. The methods applied in these simulations are described in the Appendix. It is important to note that while these factors were studied separately in these simulations, they are all present to a greater or lesser degree during real data acquisition.

Jitter error refers to the variance introduced into the estimate of the time delay between two signals by the decorrelation of those signals. This decorrelation may be due to electronic noise, window effects, and/or through some other process(es), such as the decorrelation of echoes across the array due to geometric effects or phase aberration. The impact of jitter on sound-speed estimation is shown in Table II for three signal-to-noise ratios for both point and speckle targets. The point target echoes were assumed to have perfect spatial correlation across the array, while the speckle target echoes were assumed to have spatial correlation predicted by the Van Cittert–Zernicke theorem. The infinite signal-to-noise ratio (SNR) case represents a negative control for electronic noise. Here the point target estimates have insignificant variance, while some jitter-induced error is present in the speckle target case due to spatial decorrelation. The 40-dB case is a more typical SNR for ultrasound imaging several centimeters within the body. It is seen that spatial decorrelation is still the dominant factor determining the jitter-induced estimate error. At 0 dB, the electronic noise is sufficient to raise the estimate error to $\approx$1% for both types of targets. It is important to note that the jitter magnitudes used were based on the Cramér–Rao lower bound, which implies that these results reflect the upper performance bound for the estimator.[30]

TABLE II. Simulation results showing the impact of various confounding factors on sound-speed estimate variance (see Sec. IV). The table shows the mean sound-speed estimate $\mu_{\hat{c}}$, and its standard deviation $\sigma_{\hat{c}}$, as well as the standard deviation expressed as a relative percent error $(100\cdot\sigma_{\hat{c}}/c)$.

Confounding factor	$\mu_{\hat{c}}$ [m/s]	$\sigma_{\hat{c}}$ [m/s]	$100\cdot\sigma_{\hat{c}}/c$ [%]
Jitter-induced error for point target:			
∞ SNR	1540.00	0.00	0.00
40 dB SNR	1540.00	0.13	0.01
0 dB SNR	1539.96	15.86	1.03
Jitter-induced error for speckle target:			
∞ SNR	1540.00	1.15	0.07
40 dB SNR	1540.00	1.16	0.08
0 dB SNR	1540.02	15.91	1.03
$\pm$5% element position deviation:			
	1540.00	0.26	0.02
Point target, 20 ms rms aberrator			
3 mm FWHM	1539.96	7.77	0.50
6 mm FWHM	1540.17	9.83	0.64
Point target, 50 ns rms aberrator			
3 mm FWHM	1539.59	19.71	1.28
6 mm FWHM	1540.35	24.59	1.60

To simulate severe element position uncertainty, over many trials the actual lateral coordinates of the array elements were allowed to randomly vary about their assumed positions. These position errors were normally distributed with a standard deviation of 5% of the element pitch. These errors are seen to have relatively small impact on the estimate variance. We expect this type of error to be of greater significance for transducer arrays having fewer elements than the array considered here.

The characterization of the severity and spatial structure of *in vivo* phase aberrators is the object of on-going research.[31–41] Currently there is no consensus on how these types of errors can be realistically modeled. In the simple analysis presented here, we draw a distinction between two components of aberration. These are (a) focal errors due to gross sound-speed error during beamforming, and (b) the

remaining random phase errors due to tissue nonuniformity. As the measurement of the first type of error is the object of sound-speed estimation, we wish to analyze the impact of the second type of error on such estimation. We model this component of aberration as a normally distributed, random phase error that varies across the array with a particular magnitude and spatial correlation length. As typical values for these parameters are subject to debate, we present results for several combinations of root-mean-squared (rms) phase error and correlation length, expressed as the full width at half maximum (FWHM) of the aberrator's lateral spatial autocovariance function. We consider the 20-ns rms case to represent mild aberration, and it is on the order of phase errors that we have observed in echoes from shallow targets in the breast.[41] The 50-ns rms case represents aberration on the order of that observed in through-transmission measurements in both the breast[36] and breast tissue specimens.[39] These results are presented for a point target, such that the aberration is reflected only as a phase error on receive and has no impact on the spatial coherence of the target's echoes. For a speckle target, phase aberration would also reduce the spatial coherence of echoes from the region of interest. Thus we expect that jitter error in the alignment of speckle signals will increase in the presence of phase aberration. Among the factors considered and listed in Table II, the 50-ns rms aberration has the greatest impact on estimate variance.

V. SOUND-SPEED ERRORS IN THE CONTEXT OF PHASE ABERRATION CORRECTION

The range of velocities encountered in the body can produce significant phase errors across a transducer array, particularly in low *f*-number systems. For example, for the array described in Sec. II, the rms phase error at the focus corresponding to a gross sound-speed error is shown as a function of relative error and target range in Fig. 3 for both fixed- and dynamic-receive-focused cases. As this figure reveals, the impact of sound-speed errors is much more significant in systems with dynamic receive processing, which includes most state-of-the-art commercial scanners. Because the receive beamforming delays applied in a dynamic-receive-focus system evolve over the receive interval, both the focal delays for a particular range *and* the time during the receive interval when these delays are applied are determined by the assumed sound speed, hence both are in error when a gross sound-speed error is present. The magnitude of this error is inversely proportional to the focal range, becoming more severe as the region of interest is moved closer to the transducer. When gross sound-speed error is the predominant source of phase error, correction on the basis of a sound-speed estimate conducted at a single region of interest could improve not only that region, but the entire ultrasound image as well, particularly in a dynamic-receive-focus system.

VI. DISCUSSION AND FUTURE WORK

Given that the sound-speed estimator described in this paper operates on conventional B-modes data, it is possible to calculate estimates throughout the acquired field of view.

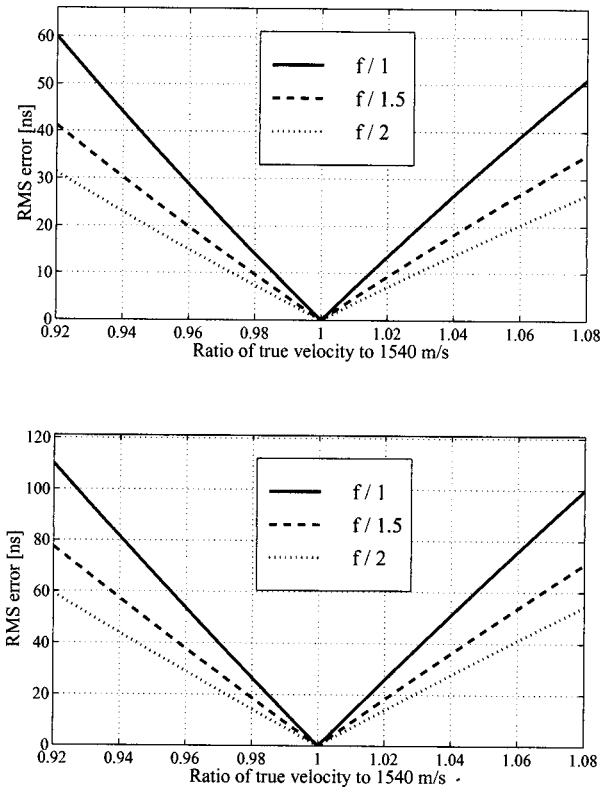

FIG. 3. (Top) The rms phase error resulting from gross sound-speed error as a function of the relative sound-speed error and the *f*-number for a fixed-focus system. (Bottom) The corresponding phase error in a dynamically focused system. At the focus, sound-speed errors have a greater negative impact in the dynamically focused system.

By estimating the sound speed at several ranges along a line, it may be possible in some tissue geometries to map the local, or ''interval,'' sound speed as a function of depth. The sound-speed estimate could be calculated at several ranges using data from a single transmit–receive cycle, or over several cycles with transmit foci spaced in range, such that on each cycle the estimate is calculated using a region of interest that coincides with the transmit focus. The accuracy of this method will depend on the geometry of the layers of tissue between the transducer and the region of interest. Measuring the local sound speed at a particular range would require comparing estimates at depths proximal and distal to that range and solving for the local sound speed that accounts for the difference between them.

Multiple sound-speed maps of this kind could be made as a function of position over two- or three-dimensional regions of interest. This information could be used for tissue characterization. In this application the sound-speed map for a line or region of interest, such as through or around a suspicious lesion, would be calculated and displayed to demonstrate pathologically correlated sound-speed variation. Sound-speed maps could also be used to perform higher-order phase aberration correction, in which the ultrasound beamforming would be adjusted to compensate for the refractive effects of estimated variations in sound speed throughout the imaging volume.

Finally, the technique described in this paper is an alternative to sound-speed measurements based on through-

transmission under circumstances in which through-transmission is inconvenient or impossible. Naturally this technique could be applied to sound-speed measurements in contexts other than medical imaging, such as the nondestructive evaluation of fluids or solids. It could also be implemented with an arbitrary array geometry through a straightforward extension of the geometry used in Sec. I.

VII. CONCLUSION

A method capable of making reliable measurements of sound speed *in vivo* has many potential applications, most notably the dynamic reduction of sound-speed errors in medical imaging and the mapping of tissue sound speed in one or more dimensions. We have described a technique for the direct estimation of the longitudinal speed of sound in a medium using pulse–echo ultrasound and have demonstrated this technique in basic experiments. Under the best experimental conditions, the estimator is capable of at least 0.1% mean accuracy for a point target and 0.5% mean accuracy for a speckle-generating target. In simulations we found the type of random phase error we expect to be induced by tissue inhomogeneities to have the greatest impact on estimator performance among the confounding factors considered.

ACKNOWLEDGMENTS

This work was supported by NIH Grants No. R01-CA43334 and No. R01-CA76059. Technical support was provided by the Siemens Medical Systems Ultrasound Group. We thank Dr. Timothy Hall for his technical assistance.

APPENDIX

All of the error analyses described in Sec. IV had a number of conditions in common. They were all based on the transducer described in Sec. II, which had a 128-element active aperture with 0.22-mm pitch, 7.5-MHz center frequency, and 60% relative bandwidth. The cross-correlation alignment window used was 2.81 μs long. The ideal two-way geometric delay profile was calculated for this array for a target located on the z axis at 30-mm range. This profile was degraded by the methods described below for each confounding factor. Sound-speed estimation was then performed on these corrupted arrival time profiles over 10 000 trials to produce the results listed in Table II.

The jitter-induced error simulations are based on an expression for jitter magnitude developed by Walker and Trahey, derived from the Cramér–Rao lower bound:[30]

$$\sigma(\Delta t-\Delta\hat{t})\geqslant\left[\frac{3}{2\,f_0^3\pi^2T(B^3+12B)}\times\left(\frac{1}{\rho^2}\left(1+\frac{1}{\mathrm{SNR}^2}\right)^2-1\right)\right]^{1/2}. \tag{A1}$$

Here $\sigma(\Delta t-\Delta\hat{t})$ represents the standard deviation of normally distributed errors in the cross-correlation-based estimate $\Delta\hat{t}$ of the time shift Δt between two signals. These two signals have center frequency f_0, fractional bandwidth B, signal-to-noise ratio SNR, cross-correlation coefficient ρ, and window length T. To develop this closed-form expression these signals are assumed to be bandlimited with flat power spectra. This expression was evaluated for the three signal-to-noise ratios investigated. The value of ρ was 1 for a point target and 0.992 for a speckle-generating target. The speckle target ρ value was based on the lateral spatial transmit–receive covariance function predicted by the Van Cittert–Zernicke theorem assuming rectangular transmit and receive apertures.[42] This covariance function is triangular, and for a lag of one element in an aperture of 128 has a value of $1-(1/128)$.

To simulate the impact of jitter error on the sound-speed estimator described in Sec. I, for each trial we generated a vector of 127 uncorrelated, normally distributed numbers with standard deviation determined by (A1). These represent the jitter errors for the 127 neighbor-to-neighbor cross-correlation operations performed across a 128-element array. These numbers were cumulatively summed and added to the ideal geometric delay profile values for elements 2–128. We then performed sound-speed estimation on this modified geometric delay profile. The cumulative summation of jitter errors reflects the fact that after finding the interelement time delays indicated by cross correlation, we estimate the delay profile relative to the first element by summing these time shifts across the array (described in Sec. II). In this operation the jitter errors from neighbor-to-neighbor cross correlation accumulate across the array.

To simulate the impact of element position variance, for each trial we generated a vector of uncorrelated, normally distributed numbers with standard deviation equal to 5% of the element pitch. We added these errors to the assumed element positions and calculated the resulting geometric delay profile for each trial. We then performed sound-speed estimation on each profile assuming that the element positioning was ideal.

To simulate the impact of aberration as defined in Sec. IV, for each trial we generated a random aberrator of the specified magnitude and spatial correlation length. We then performed sound-speed estimation on the sum of these simulated aberrators and the ideal geometric delay profile. These aberrators were created through the linear combination of random Gaussian variables that were scaled to the desired variance, and then weighted and summed to form the delay profile with the desired autocovariance FWHM.[43] The coefficients used in this weighted sum were determined by the Cholesky factorization of the desired aberrator spatial autocovariance matrix. For an even spatial autocovariance function represented by $a_{xx}(\chi)$ we found the Cholesky factorization of the Toeplitz matrix formed from N samples of $a_{xx}(t_i)$:

$$C^*C=\begin{bmatrix} a_{xx}(0) & a_{xx}(1) & \cdots & a_{xx}(N) \\ a_{xx}(1) & a_{xx}(0) & \cdots & a_{xx}(N-1) \\ \vdots & \vdots & \vdots & \vdots \\ a_{xx}(N) & a_{xx}(N-1) & \cdots & a_{xx}(0) \end{bmatrix}, \tag{A2}$$

where the asterisk represents the matrix transpose and N is the number of elements for which the delay profile is to be defined, in this case 128. The function $a_{xx}(\chi)$ was assumed

to be Gaussian and normalized such that $a_{xx}(0)$ equaled the desired aberrator variance. For each simulated aberrator created, one realization of a column vector X of N independent unit variance, zero-mean Gaussian variables was generated and multiplied by the Cholesky matrix transpose:

$$\text{aberrator} = C^{*}X. \tag{A3}$$

[1] P. N. T. Wells, ''Biomedical ultrasonics,'' in *Medical Physics Series* (Academic, London, 1977).
[2] S. A. Goss, R. L. Johnston, and F. Dunn, ''Compilation of empirical properties of mammalian tissues. II,'' J. Acoust. Soc. Am. **68**, 93–108 (1980).
[3] P. D. Edmonds, C. L. Mortensen, J. R. Hill, S. K. Holland, J. F. Jensen, P. Schattner, and A. D. Valdes, ''Ultrasound tissue characterization of breast biopsy specimens,'' Ultrason. Imaging **13**, 162–185 (1991).
[4] D. E. Robinson, J. Ophir, L. S. Wilson, and C. F. Chen, ''Pulse-echo ultrasound speed measurements: progress and prospects,'' Ultrasound Med. Biol. **17**, 633–646 (1991).
[5] M. Hirama, O. Ikeda, and T. Sato, ''Adaptive ultrasonic array imaging system through an inhomogeneous layer,'' J. Acoust. Soc. Am. **71**, 100–109 (1982).
[6] S. W. Flax and M. O'Donnell, ''Phase aberration correction using signals from point reflectors and diffuse scatters: basic principles,'' IEEE Trans. Ultrason. Ferroelectr. Freq. Control **35**, 758–767 (1988).
[7] L. Nock, G. E. Trahey, and S. W. Smith, ''Phase aberration correction in medical ultrasound using speckle brightness as a quality factor,'' J. Acoust. Soc. Am. **85**, 1819–1833 (1989).
[8] D. Rachlin, ''Direct estimation of aberrating delays in pulse-echo imaging systems,'' J. Acoust. Soc. Am. **88**, 191–198 (1990).
[9] R. Kanda, Y. Sumino, and K. Takamizawa, ''An investigation of wavefront distortion correction: correction using averaged phase information and the effect of correction in one and two dimensions,'' IEEE Ultrason. Symp. 2, 1201–1206 (1991).
[10] Dong-Lai Liu and R. C. Waag, ''Time-shift compensation of ultrasonic pulse focus degradation using least mean square error estimates of arrival time,'' J. Acoust. Soc. Am. **95**, 542–555 (1994).
[11] G. C. Ng, P. D. Freiburger, W. F. Walker, and G. E. Trahey, ''A speckle target adaptive imaging technique in the presence of distributed aberrations,'' IEEE Trans. Ultrason. Ferroelectr. Freq. Control **44**, 140–151 (1997).
[12] S. Krishnan, K. W. Rigby, and M. O'Donnell, ''Adaptive aberration correction of abdominal images using PARCA,'' Ultrason. Imaging **19**, 169–179 (1997).
[13] D. A. Christopher, P. N. Burns, J. W. Hunt, and F. S. Foster, ''The effect of refraction and assumed speeds of sound in tissue and blood on doppler ultrasound velocity measurements,'' Ultrasound Med. Biol. **21**, 187–201 (1995).
[14] J. C. Bamber and C. R. Hill, ''Acoustic properties of normal and cancerous human liver-I. dependence on pathological condition,'' Ultrasound Med. Biol. **7**, 121–133 (1981).
[15] F. S. Foster, M. Strban, and G. Austin, ''The ultrasound macroscope: initial studies of breast tissue,'' Ultrason. Imaging **6**, 243–261 (1984).
[16] K. Richter and S. H. Heywang-Kobrunner, ''Sonographic differentiation of benign from malignant breast lesions: value of indirect measurement of ultrasound velocity,'' Am. J. Roentgenol., Radium Ther. Nucl. Med. **165**, 825–833 (1995).
[17] R. E. Sheriff and L. P. Geldart, *Exploration Seismology* (Cambridge U.P., New York, 1995).
[18] A. W. Trorey, ''A simple theory for seismic diffractions,'' Geophysics **35**, 762–784 (1970).
[19] C. H. Green, ''Velocity determination by means of reflection profiles,'' Geophysics **3**, 295–305 (1938).
[20] C. H. Dix, ''Seismic velocities from surface measurements,'' Geophysics **20**, 68–86 (1955).
[21] W. H. Mayne, ''Common reflection point horizontal data stacking techniques,'' Geophysics **27**, 927–938 (1962).
[22] R. Garotta and D. Michon, ''Continuous analysis of the velocity function and of the move out corrections,'' Geophys. Prospecting **15**, 584–597 (1967).
[23] W. A. Schneider and M. M. Backus, ''Dynamic correlation analysis,'' Geophysics **33**, 105–126 (1968).
[24] E. E. Cook and M. T. Taner, ''Velocity spectra and their use in stratigraphic and lithographic differentiation,'' Geophys. Prospecting **17**, 433–448 (1969).
[25] M. T. Taner and F. Keohler, ''Velocity spectra-digital computer derivation and applications of velocity functions,'' Geophysics **34**, 859–881 (1969).
[26] J. A. Jensen and N. B. Svendsen, ''Calculation of pressure fields from arbitrarily shaped, apodized, and excited ultrasound transducers,'' IEEE Trans. Ultrason. Ferroelectr. Freq. Control **39**, 262–267 (1992).
[27] R. N. Bracewell, *The Fourier Transform and Its Applications* (McGraw-Hill, New York, 1986).
[28] G. S. K. Wong and S. Zhu, ''Speed of sound in seawater as a function of salinity, temperature, and pressure,'' J. Acoust. Soc. Am. **97**, 1732–1736 (1995).
[29] W. Wilson and D. Bradley, ''Speed of sound in four primary alcohols as a function of temperature and pressure,'' J. Acoust. Soc. Am. **36**, 333–337 (1964).
[30] W. F. Walker and G. E. Trahey, ''A fundamental limit on delay estimation using partially correlated speckle signals,'' IEEE Trans. Ultrason. Ferroelectr. Freq. Control **42**, 301–308 (1995).
[31] M. Moshfeghi and R. C. Waag, ''In-vivo and in-vitro ultrasound beam distortion measurements of a large aperture and a conventional aperture focused transducer,'' Ultrasound Med. Biol. **14**, 415–428 (1988).
[32] M. O'Donnell and S. W. Flax, ''Phase aberration measurements in medical ultrasound: human studies,'' Ultrason. Imaging **10**, 1–11 (1988).
[33] Y. Sumino and R. C. Waag, ''Measurements of ultrasonic pulse arrival time differences produced by abdominal wall specimens,'' J. Acoust. Soc. Am. **90**, 2924–2930 (1991).
[34] G. E. Trahey, P. D. Freiburger, L. F. Nock, and D. C. Sullivan, ''In vivo measurements of ultrasonic beam distortion in the breast,'' Ultrason. Imaging **13**, 71–90 (1991).
[35] Q. Zhu and B. D. Steinberg, ''Large-transducer measurements of wavefront distortion in the female breast,'' Ultrason. Imaging **14**, 276–299 (1992).
[36] P. D. Freiburger, D. C. Sullivan, B. H. LeBlanc, S. W. Smith, and G. E. Trahey, ''Two-dimensional ultrasonic beam distortion in the breast: in vivo measurements and effects,'' Ultrason. Imaging **14**, 398–414 (1992).
[37] Q. Zhu and B. D. Steinberg, ''Wavefront amplitude distribution in the female breast,'' J. Acoust. Soc. Am. **96**, 1–9 (1994).
[38] L. M. Hinkelman, D. L. Liu, L. A. Metlay, and R. C. Waag, ''Measurements of ultrasonic pulse arrival time and energy level variations produced by propagation through abdominal wall,'' J. Acoust. Soc. Am. **95**, 530–541 (1994).
[39] L. M. Hinkelman, D-L. Liu, R. C. Waag, Q. Zhu, and B. D. Steinberg, ''Measurement and correction of ultrasonic pulse distortion produced by the human breast,'' J. Acoust. Soc. Am. **97**, 1958–1969 (1995).
[40] Q. Zhu, B. D. Steinberg, and R. Arenson, ''Correlation distance measurements of the female breast,'' J. Acoust. Soc. Am. **98**, 694–705 (1995).
[41] M. E. Anderson, M. S. C. Soo, and G. E. Trahey, ''Microcalcifications as elastic scatterers under ultrasound,'' IEEE Trans. Ultrason. Ferroelectr. Freq. Control **45**, 925–934 (1998).
[42] R. Mallart and M. Fink, ''The Van Cittert-Zernike theorem in pulse echo measurements,'' J. Acoust. Soc. Am. **90**, 2718–2727 (1991).
[43] R. S. Walker, D. V. Crowe, and W. R. Mayo, ''Synthetic multichannel time series for simulating underwater acoustic noise,'' in *IEEE International Conference on Acoustics, Speech, and Signal Processing, 1981* (IEEE, New York, 1981), pp. 1042–1045.

LETTERS TO THE EDITOR

This Letters section is for publishing (a) brief acoustical research or applied acoustical reports, (b) comments on articles or letters previously published in this Journal, and (c) a reply by the article author to criticism by the Letter author in (b). Extensive reports should be submitted as articles, not in a letter series. Letters are peer-reviewed on the same basis as articles, but usually require less review time before acceptance. Letters cannot exceed four printed pages (approximately 3000–4000 words) including figures, tables, references, and a required abstract of about 100 words.

Simplified expressions for the displacements and stresses produced by the Rayleigh wave

Waled Hassan[a] and Peter B. Nagy[b]
Department of Aerospace Engineering and Engineering Mechanics, University of Cincinnati, Cincinnati, Ohio 45221-0070

(Received 28 May 1998; accepted for publication 20 August 1998)

In many cases involving Rayleigh wave propagation along the free surface of a solid, the ratio between the normal and transverse displacement components, i.e., the aspect ratio of the elliptical particle trajectory on the surface, is of great importance. Surprisingly, this aspect ratio is exactly the same as the ratio between the vector and scalar displacement potential amplitudes. More importantly, the aspect ratio is also identically the same as the ratio between the shear and normal stresses in any plane parallel to the surface at any depth, i.e., exactly the same ratio also shows up between two fundamental physical quantities. It is shown that the identical amplitude ratio, which apparently has not been pointed out in the otherwise very comprehensive literature on Rayleigh wave propagation, is a direct result of the requirement that just below the surface even the oscillating power, i.e., the imaginary component of the Poynting vector, be parallel to the surface (of course, the average power, i.e., the real component of the Poynting vector is everywhere parallel to the surface). [S0001-4966(98)06211-0]

PACS numbers: 43.20.Jr, 43.20.Mv, 43.20.Bi [DEC]

INTRODUCTION

The classical Rayleigh wave propagating on the free surface of an infinite isotropic, perfectly elastic half-space is undoubtedly one of the best known canonical problems in acoustics of solids and it is a familiar example discussed in great detail in every textbook on the subject. It is very well known that such a wave causes the particles on the surface of the infinite half-space to undergo a counterclockwise, elliptically polarized motion, as shown in Fig. 1, with the normal displacement component being larger that the transverse one.[1–10] The ratio between the two displacement components, i.e., the aspect ratio of the elliptical trajectory of the particle on the surface, is of great practical importance in many situations. For example, when the solid is immersed in fluid, the phase velocity slightly increases and the surface wave becomes strongly attenuated by leaking into the fluid. The sole source of acoustic loading by an inviscid fluid is the normal component of the surface vibration. It was recently shown that the aspect ratio of the elliptical particle trajectory produced by the dispersive Rayleigh-type surface wave on a curved surface is lower than that of the nondispersive wave on a flat surface, which results in a perceivably lower leaky attenuation.[11] Nagy and Kent used the leakage-induced attenuation, which is determined by the ratio between the normal and transverse vibration amplitudes at the surface of a rod, to assess its Poisson's ratio.[12] In the case of acoustic loading by a viscous fluid the tangential surface vibration causes additional coupling between the solid and the fluid. The aspect ratio of the surface displacement plays an important role in the acoustic loading of both rods and plates immersed in a viscous fluid and can be used to explain the sharp minimum observed in the viscosity-induced attenuation curves for such configurations.[13,14] Another area where the ratio between the tangential and normal surface displacements plays a significant role is the generation and detection of Rayleigh waves. Some excitation techniques, e.g., the so-called ''edge'' technique,[3] take advantage of the stronger normal displacement component to excite the Rayleigh wave. Laser interferometric detection is, in general, much more sensitive to the normal displacement of the surface than to the tangential component.[15–17] This implies that the displacement ratio has a crucial role in the detection of Rayleigh waves using laser based ultrasonic techniques.

In the following we briefly review the well-known analytical results for the relative amplitude of the displacements and stresses produced by the Rayleigh wave propagating on

[a]Current address: Metals, Ceramics, and NDE Division, Wright Laboratory, Wright-Patterson Air Force Base, Dayton, OH 45432-6533.
[b]Contact author: Electronic mail: pnagy@uceng.uc.edu

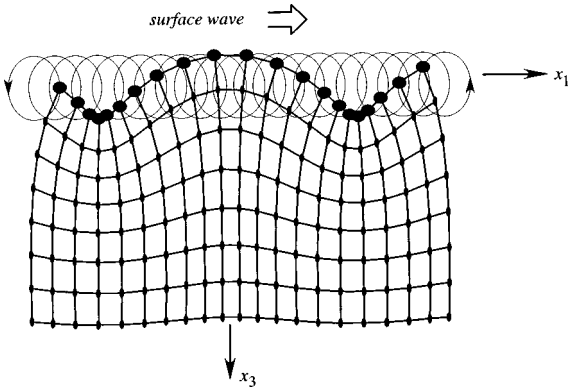

FIG. 1. Schematic diagram illustrating the particle's motion in a Rayleigh wave propagating on the free surface of an infinite half-space.

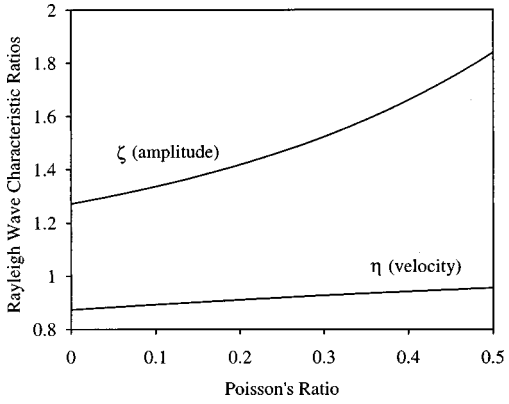

FIG. 2. Rayleigh wave characteristic ratios versus Poisson's ratio.

the free surface of an infinite half-space. By comparing these ratios, we observed an unexpected coincidence which, to the best of our knowledge, has not been pointed out in the literature yet and prompted us to write this Letter. These ratios are routinely presented in textbooks on this subject as unrelated parameters so that their identical nature remains hidden by their different algebraic forms.[1–10] We felt that the uniform presentation of these ratios could better elucidate the relationship between potentials, displacements, and stresses and, in a very modest way, might contribute to the better understanding of Rayleigh wave propagation.

I. REVIEW OF THE ANALYTICAL RESULTS

Let us consider a harmonic Rayleigh wave propagating on the free surface of an isotropic, elastic half-space. The schematic diagram illustrating the deformation in the near-surface region of the solid as well as the elliptical particle trajectory at the surface was shown in Fig. 1. The solid half-space occupies the region $x_3 \geqslant 0$ and the Rayleigh wave propagates along the x_1 axis. A common technique is to write the particle displacement vector $\mathbf{u}$ in terms of a scalar ϕ and a vector $\boldsymbol{\psi}$ potentials as follows:

$$\mathbf{u} = \nabla\phi + \nabla \times \boldsymbol{\psi}. \tag{1}$$

In an infinite isotropic solid, this representation of the displacement vector separates the wave equation into uncoupled shear and dilatational components. In contrast, at the free surface of a solid half-space the scalar and vector potentials are coupled by the requirement that together they satisfy the stress-free boundary conditions:

$$\phi = Ae^{-\kappa_d x_3} e^{i(k_R x_1 - \omega t)} \tag{2}$$

and

$$\psi = -i\zeta A e^{-\kappa_s x_3} e^{i(k_R x_1 - \omega t)}, \tag{3}$$

where A is the arbitrary potential amplitude, t denotes time, ω denotes the angular frequency, k_R is the wave number of the Rayleigh wave, and $\kappa_s = \sqrt{k_R^2 - k_s^2}$ and $\kappa_d = \sqrt{k_R^2 - k_d^2}$ are decay factors related to the shear k_s and longitudinal k_d wave numbers, respectively. Finally, $\zeta = \sqrt{\kappa_d / \kappa_s}$ denotes the magnitude of the amplitude ratio between the vector and scalar potentials, which is a negative pure imaginary number. Like the characteristic velocity ratio $\eta = c_R/c_s = k_s/k_R$ between the Rayleigh and shear waves, which can be calculated by solving the well-known dispersion equation

$$(\kappa_s^2 + k_R^2)^2 - 4\kappa_s \kappa_d k_R^2 = 0, \tag{4}$$

and is always cited in textbooks, the amplitude ratio ζ is also a function of Poisson's ratio only. Figure 2 shows the familiar curve for the normalized Rayleigh wave velocity, which ranges between 0.87 and 0.95, along with the less familiar amplitude ratio, which ranges between 1.3 and 1.8. For typical solids of Poisson's ratio around 0.3, the amplitude ratio is approximately 1.5.

Of course all this is well known and hardly new to anybody interested in acoustics. However, the authors were sincerely surprised to find out upon closer inspection that the amplitude ratio ζ is identically the same as (i) the ratio between the normal u_3 and tangential u_1 particle displacements, i.e., the aspect ratio of the elliptical particle trajectory, on the surface as well as (ii) the ratio between the shear τ_{13} and normal τ_{33} stresses at any depth.

Without the common $e^{i(k_R x_1 - \omega t)}$ term, the normal and tangential displacement components can be written as follows:

$$u_1 = \frac{\partial\phi}{\partial x_1} - \frac{\partial\psi}{\partial x_3} = iA(k_R e^{-\kappa_d x_3} - \zeta\kappa_s e^{-\kappa_s x_3}) \tag{5}$$

and

$$u_3 = \frac{\partial\phi}{\partial x_3} + \frac{\partial\psi}{\partial x_1} = -A(\kappa_d e^{-\kappa_d x_3} - \zeta k_R e^{-\kappa_s x_3}). \tag{6}$$

By specializing Eqs. (5) and (6) to the surface ($x_3 = 0$) and utilizing the dispersion equation given in Eq. (4) to simplify the result, we obtain

$$\left.\frac{u_3}{u_1}\right|_{x_3=0} = i\,\frac{\kappa_d - \zeta k_R}{k_R - \zeta\kappa_s} = -i\zeta. \tag{7}$$

Unexpectedly, the ratio of the normal and transverse displacement components on the surface turns out to be the same as the amplitude ratio between the vector and scalar potentials. Even more surprisingly, the same ratio also shows up between the shear τ_{13} and normal τ_3 stresses that can be written as follows:

$$\tau_{13} = -iA\mu 2k_R\kappa_d(e^{-\kappa_d x_3} - e^{-\kappa_s x_3}) \tag{8}$$

and

$$\tau_{33}=A\mu(k_R^2+\kappa_s^2)(e^{-\kappa_d x_3}-e^{-\kappa_s x_3}). \tag{9}$$

Both τ_{13} and τ_{33} have contributions from both longitudinal and shear partial wave components decaying with different rates according to $e^{-\kappa_d x_3}$ and $e^{-\kappa_s x_3}$, respectively. For both stresses the amplitudes of the longitudinal and shear components must be equal so that the combined stress could be zero on the free surface. As a result, they must have identical functional dependence on x_3, i.e., in any plane parallel to the surface the ratio between the shear and normal stresses is constant.[6] What is more surprising that this ratio turns out to be again the same as the amplitude ratio between the vector and scalar potentials:

$$\frac{\tau_{13}}{\tau_{33}}=-\frac{i2k_R\kappa_d}{k_R^2+\kappa_s^2}=-i\zeta. \tag{10}$$

It should be mentioned here that a similar but more limited relationship exists for both symmetric and asymmetric Lamb waves propagating in a free plate.[18] The ratio between the normal and tangential surface displacements, which is this time also a function of frequency, is identical to the amplitude ratio between the vector and scalar potentials on the surface. However, in the case of a free plate, the stress ratio is depth dependent and distinctly different from the displacement ratio on the surface. It is interesting to consider whether a similar relationship exists in the case of the corresponding Rayleigh-type surface wave propagating on the free surface of an anisotropic half-space. Generally, three partial waves are required to satisfy the stress-free boundary conditions and the particle motion no longer lies in the sagittal plane. Since the stress ratios (τ_{23}/τ_{33} and τ_{13}/τ_{33}) in a given plane parallel to the surface are depth dependent, they cannot be related to the displacement ratios (u_2/u_3 and u_1/u_3) on the surface. It was also found that the aspect ratio of the elliptical particle trajectory produced by the dispersive Rayleigh-type surface wave on a curved surface is different from that of the nondispersive wave on a flat surface and does not possess a direct correlation to either the potential ratio or the stress ratio.[11] In other words, the above described uniform nature of the amplitude ratio appears to be limited to the classical Rayleigh wave propagating on the free surface of an isotropic elastic half-space only.

II. DISCUSSION AND CONCLUSION

Although the theory of Rayleigh wave propagation has been widely investigated and is very well understood, its behavior still holds some surprises. We showed that the ratio of the vector potential to the scalar potential is equal to the ratio of the normal to transverse displacement components on the surface. Since the vector and scalar potentials are essentially theoretical abstractions introduced to facilitate the analysis of the problem but do not directly correspond to any real physical quantity, this observation by itself is not particularly important, although it is rather unexpected if we take into consideration the differentiation process necessary to calculate the displacement field from its potentials and that both displacement components depend on both potentials. Much more important is the observation that the aspect ratio of the elliptical particle trajectory on the surface is identically the same as the ratio between the shear and normal stresses in any plane parallel to the surface at any depth, i.e., exactly the same amplitude ratio also shows up between two fundamental physical quantities.

Of course the identity of the amplitude ratios for displacements at the surface on one side and stresses at any depth on the other side, which apparently has not been pointed out in the otherwise very comprehensive literature on Rayleigh wave propagation, cannot be very well attributed to pure coincidence only. It is a direct result of the requirement that just below the surface the energy flow be parallel to the surface. The acoustic Poynting vector is defined as[19]

$$\mathbf{P}=-\frac{\mathbf{v}^*\tau}{2}, \tag{11}$$

where $\mathbf{v}=-i\omega\mathbf{u}$ is the complex particle velocity vector, τ is the complex stress tensor, and $*$ indicates complex conjugation. The normal component of the Poynting vector can be written as follows

$$P_3=\tfrac{1}{2}i\omega(u_1^*\tau_{13}+u_3^*\tau_{33}). \tag{12}$$

Since u_3 and τ_{33} are pure real while u_1 and τ_{13} are pure imaginary, P_3 is always pure imaginary, i.e., the average acoustic power transmission is always parallel to the surface. On the surface P_3 is identically zero since both τ_{13} and τ_{33} vanish. However, just under the surface even the oscillating part of the normal acoustic power, i.e., the imaginary part of P_3 must vanish therefore $\tau_{13}/\tau_{33}=-u_3^*/u_1^*$. As we mentioned above, u_3 is pure real, therefore $u_3^*=u_3$, but u_1 is pure imaginary, therefore $u_1^*=-u_1$. Consequently, $\tau_{13}/\tau_{33}=u_3/u_1$, as we have found by simple inspection of the displacement and stress fields. Further below the surface, the oscillating part of the normal acoustic power is not necessarily zero therefore the amplitude ratio u_3/u_1, which varies with depth, is not necessarily equal to the stress ratio τ_{13}/τ_{33}, which does not vary with depth.

The same argument also explains why the common amplitude ratio does not apply to either dispersive Rayleigh-type surface waves propagating on a cylindrical surface, nondispersive Rayleigh-type surface waves propagating on an anisotropic substrate in nonsymmetry directions, or to Lamb waves propagating in flat plates. The main reason is that the stress ratio in all these cases is depth dependent therefore we cannot relate the displacement ratio at the surface to the stress ratio somewhere else. In addition, on a concave cylindrical surface, the Rayleigh wave becomes leaky into the bulk of the solid so that the Poynting vector is definitely not parallel to the surface.

[1] M. Redwood, *Mechanical Waveguides* (Pergamon, New York, 1960), pp. 50–51.
[2] H. Kolsky, *Stress Waves in Solids* (Dover, New York, 1963), pp. 16–23.
[3] I. A. Viktorov, *Rayleigh and Lamb Waves* (Plenum, New York, 1967), pp. 1–29.
[4] I. Tolstoy, *Wave Propagation* (McGraw-Hill, New York, 1973), pp. 206–212.

[5] J. Achenbach, *Wave Propagation in Elastic Solids* (North-Holland, Amsterdam, 1973), pp. 187–194.
[6] G. S. Kino, *Acoustic Waves* (Prentice-Hall, Englewood Cliffs, NJ, 1987), pp. 110–114.
[7] A. I. Beltzer, *Acoustic of Solids* (Springer-Verlag, Berlin, 1988), pp. 131–134.
[8] L. M. Brekhovskikh and O. A. Godin, *Acoustics of Layered Media I* (Springer-Verlag, Berlin, 1990), pp. 106–109.
[9] B. Auld, *Acoustic Fields and Waves in Solids* (Krieger, Malabar, FL, 1990), Vol. II, pp. 88–93.
[10] K. F. Graff, *Wave Motion in Elastic Solids* (Dover, New York, 1991), pp. 323–328.
[11] W. Hassan and P. B. Nagy, ''On the anomalously low attenuation of the leaky Rayleigh Wave in a fluid-filled cylindrical cavity,'' J. Acoust. Soc. Am. **104**, 1246–1255 (1998).
[12] P. B. Nagy and R. M. Kent, ''Ultrasonic assessment of Poisson's ratio in thin rods,'' J. Acoust. Soc. Am. **98**, 2694–2701 (1995).
[13] P. B. Nagy and A. H. Nayfeh, ''Viscosity-induced attenuation of longitudinal guided waves in fluid-loaded rods,'' J. Acoust. Soc. Am. **100**, 1501–1508 (1996).
[14] P. B. Nagy and A. H. Nayfeh, ''Excess attenuation of leaky Lamb waves due to viscous fluid loading,'' J. Acoust. Soc. Am. **101**, 2649–2658 (1997).
[15] C. B. Scruby, R. J. Dewurst, D. A. Hutchins, and S. B. Palmer, ''Laser generation of ultrasound in metals,'' in *Research Techniques in Nondestructive Testing* (Academic, New York, 1982), pp. 282–327.
[16] J. W. Wagner, ''Optical detection of ultrasound,'' in *Physical Acoustics* (Academic, New York, 1990), Vol. XIX, pp. 201–265.
[17] C. B. Scruby and L. E. Drain, *Laser Ultrasonics, Techniques and Applications* (Adam Hilger, Philadelphia, 1990).
[18] Private communication with S. I. Rokhlin.
[19] See, for example, p. 15 in Ref. 9.

A least-squares spectral element method for sound propagation in acoustic ducts

Wen H. Lin
Rocketdyne Propulsion and Power, The Boeing Company, Canoga Park, California 91309-7922

(Received 30 December 1997, accepted for publication 29 July 1998)

This letter presents a novel numerical method and results for sound waves propagating in two-dimensional acoustic ducts without a flow. The method is based on a least-squares finite-element formulation to solve the two-dimensional Helmholtz equation with acoustic boundary conditions. Numerical calculations were obtained for sound waves propagating in an acoustically lined duct and in a rigid duct with a 90-deg bend. The exact solution and the boundary element solution of the acoustically lined duct were also obtained to validate the proposed numerical algorithm. Sound pressures computed by the present method agree very well with the exact and BEM solutions. © *1998 Acoustical Society of America.* [S0001-4966(98)05511-8]

PACS numbers: 43.20.Mv, 43.55.Rg [DEC]

INTRODUCTION

Sound propagation in an acoustically lined duct is of theoretical interest and of practical importance for industrial applications. For instance, determinations of acoustic modes propagating in a duct with complex wall impedance are very involved from a theoretical point of view but have lots of applications in understanding noise characteristics and control in the duct systems of a jet engine, an internal combustion device, or a gas-cooled reactor. An analytical solution to the problem of sound propagation in an acoustically treated duct is difficult because many complicated factors, such as the flow and its gradients, the duct geometry, and the wall impedance, involved in governing the interaction of the sound waves and the medium. In most cases solutions to the duct acoustic problems are determined by numerical methods, such as finite difference, finite element, weighted residual, and boundary element methods. A fairly extensive list of references of numerical methods for solving duct acoustic problems can be found in Refs. 1–4.

In this paper a least-squares spectral element method is investigated for its applicability to calculate the numerical solutions of sound waves propagating in two-dimensional acoustic ducts without the effect of a mean flow. An incident sound wave is prescribed at the entrances of the ducts and the propagation of this sound wave in these ducts is numerically solved by the proposed method. The aims of this study are (1) to investigate the validity and accuracy of the method in solving the problems of duct acoustic propagation, and (2) to study the effects of acoustic parameters on the performance of the method. Sound propagation in both straight and curved ducts was treated, and the exit plane of the straight duct was considered as acoustically reacting with varied impedance. For the straight duct, the exact solution and the boundary element solution were also obtained for comparisons. All numerical results of sound pressures are in excellent agreement with the exact values. This demonstrates that the proposed algorithm is accurate to treat sound waves propagating in an acoustically treated duct.

I. SOUND PROPAGATION IN A DUCT

Consider a two-dimensional acoustic duct as shown in Fig. 1 for sound wave propagation. This duct is L units long and H units high with the inlet plane at $x=0$, and the exit plane at $x=L$. For simple-harmonic pressure waves, the motion of sound waves in the duct can be described by a Helmholtz equation as

$$\left[\frac{\partial^2}{\partial x^2}+\frac{\partial^2}{\partial y^2}+k^2\right]p(x,y)=s(x,y) \tag{1}$$

and boundary conditions. In the equation, k is the free-space wave number, and $s(x,y)$ represents an internal source function.

At the inlet plane of the duct the acoustic pressure is assumed known as $p_s(y)$, and along the exit plane it is assumed to be locally reacting with acoustic impedance $\zeta_{\text{exit}}(y)$. Therefore, the boundary conditions in the x direction are

$$p(0,y)=p_s(y) \tag{2}$$

and

$$\frac{\partial p(L,y)}{\partial x}=\frac{-ikp(L,y)}{\zeta_{\text{exit}}(y)}, \tag{3}$$

where $i=\sqrt{-1}$. In the y direction the boundary condition is

$$\frac{\partial p(x,H)}{\partial y}=0 \tag{4}$$

for the acoustically rigid wall, and

$$\frac{\partial p(x,0)}{\partial y}=\frac{ikp(x,0)}{\zeta(x)}, \tag{5}$$

for the locally reacting wall with acoustic impedance $\zeta(x)$. With these boundary conditions the solution for sound wave propagation in the duct can be uniquely determined.

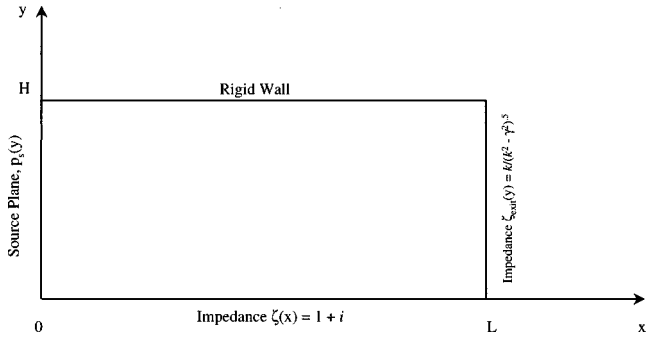

FIG. 1. A two-dimensional acoustic duct for sound wave propagation.

II. LEAST-SQUARES SPECTRAL ELEMENT METHOD

To apply the least-squares spectral element method to solving Eq. (1) with the boundary conditions, we first transfer Eq. (1) into a set of first-order partial-differential equations as

$$\mathbf{L}(x,y)\{\mathbf{u}\}=\{\mathbf{f}\}, \tag{6}$$

where

$$\mathbf{L}(x,y)=\begin{bmatrix} k^2 & \dfrac{\partial}{\partial x} & \dfrac{\partial}{\partial y} \\ \dfrac{\partial}{\partial x} & -1 & 0 \\ \dfrac{\partial}{\partial y} & 0 & -1 \end{bmatrix}, \quad \{\mathbf{u}\}=\begin{Bmatrix} p \\ F \\ G \end{Bmatrix},$$

$$\{\mathbf{f}\}=\begin{Bmatrix} s \\ 0 \\ 0 \end{Bmatrix}, \quad F=\frac{\partial p}{\partial x}, \quad G=\frac{\partial p}{\partial y}.$$

The aim of working with the first-order derivatives is to utilize C^0 continuity in field variables at the element interfaces. Next, we partition the acoustic duct into a finite number of elements and assume an approximate solution to Eq. (6) for a typical element can be written as

$$\{\mathbf{u}^{(e)}(x,y)\}=\sum_{i=1}^{M}\sum_{j=1}^{M}\{\mathbf{a}_{ij}\}\phi_i(x)\phi_j(y). \tag{7}$$

In this expression $\phi_i(x)$ and $\phi_j(y)$ are the one-dimensional, linearly independent basis functions; $\{\mathbf{a}_{ij}\}$ are the unknown expansion coefficients for p, F, and G, and M is the total number of basis functions in each direction of an element. The basis functions used in the present study are the Lagrangian interpolant based on Legendre polynomials of the independent variables.

Substituting Eq. (7) into Eq. (6), forming the residual, and then applying the *least-squares* method [e.g., Refs. 5 and 6] with respect to the expansion coefficients, one obtains the least-squares finite element equation as

$$\sum_{i=1}^{M}\sum_{j=1}^{M}\mathbf{K}_{mnij}\mathbf{a}_{ij}=\mathbf{F}_{mn}, \tag{8}$$

for each element, where

$$\mathbf{K}_{mnij}=\int^{(e)}(\mathbf{L}(x,y)\phi_m(x)\phi_n(y))^T \times(\mathbf{L}(x,y)\phi_i(x)\phi_j(y))dx\ dy, \tag{9}$$

$$\mathbf{F}_{mn}=\int^{(e)}(\mathbf{L}(x,y)\phi_m(x)\phi_n(y))^T\mathbf{f}(x,y)dx\ dy, \tag{10}$$

T indicating the transpose of a matrix. To evaluate the above integrals via the Gauss quadrature rules, we use the following relations to transform the coordinates (ξ,η) of a computational element onto the coordinates (x,y) of a physical element:

$$x=\sum_{m=1}^{l}x_m^{(e)}\phi_m(\xi), \qquad y=\sum_{m=1}^{l}y_m^{(e)}\phi_m(\eta), \tag{11}$$

where $x_m^{(e)}$ and $y_m^{(e)}$ are the coordinates of the lth node in the physical element, and ξ and η range from -1 to 1. The integrals in Eqs. (9) and (10) then become

$$\mathbf{K}_{mnij}=\int_{-1}^{1}\int_{-1}^{1}(\mathbf{L}(\xi,\eta)\phi_m(\xi)\phi_n(\eta))^T \times(\mathbf{L}(\xi,\eta)\phi_i(\xi)\phi_j(\eta))J\ d\xi\ d\eta, \tag{12}$$

$$\mathbf{F}_{mn}=\int_{-1}^{1}\int_{-1}^{1}(\mathbf{L}(\xi,\eta)\phi_m(\xi)\phi_n(\eta))^T\mathbf{f}(\xi,\eta)J\ d\xi\ d\eta, \tag{13}$$

where J is the Jacobian of the coordinate transformation. Up to this point, the choices of computational nodes along the ξ and η axes are quite arbitrary, and the determinations of these nodes are the essence of the proposed method.

The nodes along the ξ and η axes are chosen as the Legendre–Gauss–Lobatto collocation points[7–9] which are the roots of $(1-\xi^2)L_N'(\xi)$ and $(1-\eta^2)L_N'(\eta)$, respectively, where the prime indicates the derivative, and L_N is the Nth Legendre polynomial. With the collocation points defined in this way, the Lagrange interpolation functions in the computational element can be expressed in terms of Legendre polynomials and the above two integrals can be integrated exactly via the Gauss–Legendre quadrature rules[10] as

$$\mathbf{K}_{mnij}=\sum_{\alpha=1}^{N}\sum_{\beta=1}^{N}W(\xi_\alpha)W(\eta_\beta) \times[\mathbf{L}(\xi_\alpha,\eta_\beta)\phi_m(\xi_\alpha)\phi_n(\eta_\beta)]^T \times[\mathbf{L}(\xi_\alpha,\eta_\beta)\phi_i(\xi_\alpha)\phi_j(\eta_\beta)]J(\xi_\alpha,\eta_\beta), \tag{14}$$

$$\mathbf{F}_{mn}=\sum_{\alpha=1}^{N}\sum_{\beta=1}^{N}W(\xi_\alpha)W(\eta_\beta) \times[\mathbf{L}(\xi_\alpha,\eta_\beta)\phi_m(\xi_\alpha)\phi_n(\eta_\beta)]^T \times\mathbf{f}(\xi_\alpha,\eta_\beta)J(\xi_\alpha,\eta_\beta), \tag{15}$$

where N is the number of Legendre–Gauss–Lobatto points in each integration direction, and W is the weighting factor for the Gauss–Legendre quadrature.[8,9] With the aid of Eqs.

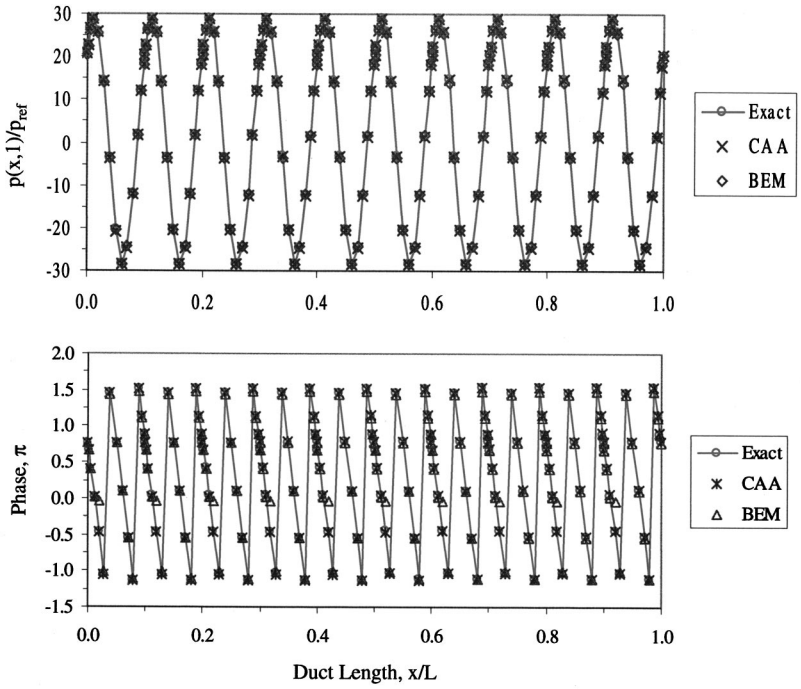

FIG. 2. Waveform and phase of sound pressure at $kL=20\pi$, $p_{\text{ref}}=1$ μPa.

(11), (14), and (15), we have cast the least-squares finite element equation [i.e., Eq. (8)] into a least-squares spectral element equation. This equation can be solved with the boundary conditions for the unknown coefficients, $\{\mathbf{a}_{ij}\}$, and for the pressure field and its derivatives at every node.

III. NUMERICAL EXAMPLES AND DISCUSSION

Using the algorithm presented above, we developed a code named CAA (computational acoustic analysis) and calculated sound pressures in an acoustically treated duct at $kL=20\pi$ and in an SSME (space shuttle main engine) duct with a 90-deg bend at $kh=5.97$ without the effects of flow and source function. The exact solution of the acoustically lined duct was also obtained to compute sound pressures for verifying the accuracy of the proposed method. The boundary element method in Ref. 4 was also used with spectral elements to compute sound pressures in the acoustically treated duct.

For the boundary conditions shown in Fig. 1 and an input wave of

$$p_s(y)=\cos\ \gamma y+\frac{ik\ \sin\ \gamma y}{\zeta(x)\gamma},$$

the exact solution is

$$p_{\text{exact}}(x,y)=[\cos\ \sigma x-i\ \sin\ \sigma x]p_s(y), \tag{16}$$

with $\sigma=\sqrt{k^2-\gamma^2}$, $\gamma\ \tan\ \gamma=0.5k(1+i)$, and $i=\sqrt{-1}$.

Figure 2 shows the waveforms and phases of the computed and exact sound pressures at $y=1$ in the acoustically treated duct. The computed results agree very well with the exact solutions. This indicates that the proposed method is accurate in predicting the propagation of general sound waves at these frequencies in an acoustically lined duct. At $kL=20\pi$ there are 10 waves in the duct. To resolve the detail of these waves, we used 10 elements in the x direction and one element in the y direction, each having 15 collocation points, to represent the duct to compute $\{\mathbf{a}_{ij}\}$ and sound pressures.

Figure 3 shows the detailed pressure contours of sound waves propagating at 1900 Hz in an SSME Lox (liquid oxygen) duct. The aim of this study is to determine the acoustic modes propagating in the duct for data analysis of SSME Lox acoustic tests. The computed results clearly resolve the allowable acoustic modes in this duct. At this frequency there are two propagating modes in the duct, namely, a plane wave and a cosine wave. This result again indicates that the proposed algorithm is indeed very accurate in predicting the propagation phenomenon of sound waves in a curved duct at a moderately high frequency.

IV. CONCLUDING REMARKS

A least-squares spectral element method has been demonstrated to accurately compute the solutions for sound waves propagating in two-dimensional acoustic ducts without a mean flow. The method employs Legendre polynomial for spatial discretization. Theoretically, the method is free of spatial numerical dispersion and can be accurate to any order of magnitude depending on the degree of the Legendre polynomial used. In real computations only a finite number of degrees of the polynomial is needed to achieve the desired accuracy. From the experience gained in this study, the rule of thumb is that there must be at least 12 grid points to represent a whole wave. The combination of elements and collocation points can be arbitrary as long as there are 12 grid points to represent a complete wave. That is, one can use the lower-order polynomial with large number of elements or the higher-order polynomial with less number of elements to resolve the wave motion.

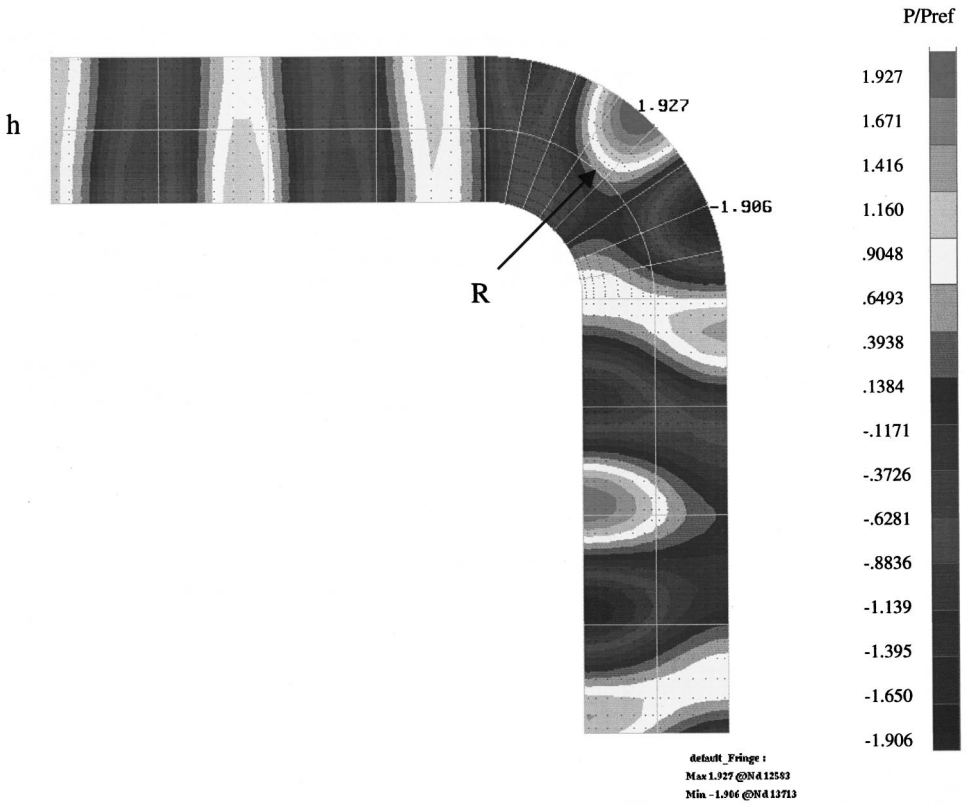

FIG. 3. Acoustic wave propagation around a 90-deg bend in a 2-D SSME Lox duct: $R/h=1$, $\lambda/h=1.05$, $f=1900$ Hz; $P_{\text{ref}}=1$ Pa.

Also, it is noted that more elements are needed for high-frequency waves than for low-frequency waves. With a reasonable grid (i.e., 12 points per wave), the method produces very good results compared with the exact and BEM solutions. The main advantage of the present method as compared with the boundary element method (BEM) is that no fundamental solution to the governing equation is needed *a priori* for minimizing the residuals. Besides, the influence coefficients used in BEM must be recalculated for every internal point, which are not needed in the present method. For the duct acoustic problems considered in this study both least-square spectral element method and BEM with spectral elements predict very close results and consume similar computing resources for a solution.

ACKNOWLEDGMENTS

I would like to thank Dr. D. C. Chan for introducing me to the finite-element and spectral-element methods for computational fluid dynamics, and for his helpful discussion and comments on the subject matter. I would also like to acknowledge Dr. Willie Watson of NASA Langley Research Center for suggesting to me the test problems and providing me with the eigenvalues of the straight duct in this study. This work was supported by NASA Aerospace Industry Technology Program Office.

[1] W. Watson and D. L. Lansing, ''A Comparison of Matrix Methods for Calculating Eigenvalues in Acoustically Lined Ducts,'' NASA TN D-8186, NASA Langley Research Center, 1976.
[2] K. J. Baumeister, ''Numerical Techniques in Linear Duct Acoustics: A Status Report,'' Trans. ASME J. Eng. Ind. **103(3)**, 270–281 (1981).
[3] W. Eversman, ''Theoretical Models for Duct Acoustic Propagation and Radiation,'' in *Aeroacoustics of Flight Vehicles: Theory and Practice, Vol. 2: Noise Control* (Acoustical Society of America, Woodbury, NY, 1995).
[4] C. A. Brebbia, J. J. R. Silva, and P. W. Partridge, ''Computational Formulation,'' in *Boundary Element Methods in Acoustics*, edited by R. D. Ciskowski and C. A. Brebbia (Comp. Mech. Pub., Boston, 1991), pp. 38–41.
[5] O. C. Zienkiewicz, *The Finite Element Method* (McGraw-Hill, London, 1977), p. 87.
[6] D. S. Burnett, *Finite Element Analysis: From Concepts to Applications* (Addison-Wesley, Reading, MA, 1987), p. 68.
[7] E. M. Ronquist and A. T. Patera, ''A Legendre Spectral Element Method for the Stefan Problem,'' Int. J. Numer. Methods Eng. **24**, 2273–2299 (1987).
[8] M. R. Schumack, W. W. Schultz, and J. P. Boyd, ''Spectral Method Solution of the Stokes Equations on Nonstaggered Grids,'' J. Comput. Phys. **94**, 30–58 (1991).
[9] C. Canuto, M. Y. Hussaini, A. Quarteroni, and T. A. Zang, *Spectral Method in Fluid Dynamics* (Springer-Verlag, Berlin, 1988), pp. 60–65.
[10] K. H. Huebner and E. A. Thornton, *The Finite Element Method for Engineers* (Wiley, New York, 1982), pp. 421–422.

Observation of acoustic streaming near Albunex® spheres

Gerard Gormley and Junru Wu
Department of Physics, University of Vermont, Burlington, Vermont 05405

(Received 7 October 1997; revised 12 August 1998; accepted 13 August 1998)

Using Albunex® spheres (a contrast agent for ultrasonic imaging), a specially designed microscopic device, a video peak storage technique and micron-size Latex spheres as tracers, acoustic streaming patterns around a single and a pair of Albunex® spheres of a few tens micrometer radius in a 160-kHz ultrasonic standing wave field have been recorded. The spatial peak pressure amplitude of the standing wave was estimated to be of the order of 0.5 MPa with optical interferometry. The acoustic streaming velocity was in the range of 50–100 μm/s. © *1998 Acoustical Society of America.* [S0001-4966(98)05611-2]

PACS numbers: 43.25.Nm [MAB]

INTRODUCTION

In this letter, our recent experimental observation of microstreaming near a single and a pair of Albunex® spherical bubbles trapped at acoustic pressure antinodes of an ultrasound standing wave of 160 kHz is reported. Albunex® is a commercial ultrasonic imaging contrast agent. It consists of air-filled human albumin microspheres (Mallinckrodt Medical, Inc., St. Louis, MO), and has been approved by the FDA for clinical use in the USA. The radius of the microspheres is roughly in the range of 1–10 μm (Bleeker and Shung, 1990; Marsh *et al.*, 1997).

Acoustic streaming is a bulk nonperiodic motion of a fluid, in which ultrasound propagates. When it is of small scale, it is often called microstreaming (Nyborg, 1996). Acoustic streaming has been used to pump fluids, transport solids (Moroney, 1991), and cool samples (Wu *et al.*, 1994). Microstreaming of bubbles in an ultrasonic field has also been considered to be one of physical mechanisms of nonthermal bioeffects generated by ultrasound (Nyborg, 1996); the shear stress associated with high-streaming velocity gradient within a boundary layer of a bubble may disturb the cells (Williams *et al.*, 1970; Rooney, 1970; Miller, 1987).

Elder (1959) observed the microstreaming in water near a vibrating bubble that was resting on a solid boundary; the bubble's vertical and horizontal dimensions were 400 and 480 μm, respectively; the ultrasound frequency used was 10 kHz. Theories (Davidson and Riley, 1971; Wu and Du, 1997) have been developed to calculate microstreaming velocity inside and outside an isolated air bubble in a liquid produced by a bubble-scattered sound field, taking into account two predominant modes of the bubble's motion: a monopole (pulsation), and a dipole (translational harmonic vibrations). It has been shown that the microstreaming is most pronounced for a bubble undergoing the volume resonance (monopole resonance).

In our experiments, streaming patterns of Albunex® bubbles in a 160-kHz ultrasonic field have been observed. A rigorous theory of most observed phenomena is still lacking. We hope that our experimental work may lead to useful discussions. Furthermore, since Albunex® bubbles are being used *in vivo*, the possible bioeffects related to acoustic streaming are worth investigating.

I. MATERIALS AND METHODS

A specially designed instrument—a modified upright microscope (NIKON LABPHOT 2)—was used to observe real time activities of bubbles under insonification; the detail was described in our previous publication (Wu and Tong, 1998). In brief, an objective lens (16x), a pair of eye pieces (10x), and a CCD camera were used in the instrument. The original stage of the microscope was replaced by a specially designed stage. An optically transparent circular disk made of fused silica (thickness=2 mm and diameter =11 mm) was used as a substitute for a regular microscope slide. The disk was glued on the top of a hollow cylindrical PZT transducer (thickness=6 mm, i.d.=6 mm, and o.d.=12 mm) concentrically. The radio frequency (rf) voltage was applied to the transducer via two electrodes across the wall of the radial direction; the concept of Poisson ratio of solid can be used to explain how the longitudinal vibration of the transducer along the axial direction of the hollow disk may be excited via the rf voltage applied across the wall thickness direction of the transducer. A sample solution which will be described later was sandwiched between the fused silica disk and a cover glass (diameter was 2.5 cm, thickness was 160 μm); caution was taken to make sure the space was fully filled with water and there was no trapped air pocket. Ultrasound was, then, generated in the sample solution by the PZT transducer. Light from the condenser lens at the bottom of the microscope could pass the hollow PZT transducer, fused silica disk, sample solution, cover glass, objective, and finally reaches the CCD camera or eye pieces located at the top of the microscope. Thus, bubbles' activities under insonification could be observed or recorded by a VCR connected to the CCD camera.

About 30-μl Albunex® was mixed with 10-ml distilled water in a test tube and then a small drop of 1-μm radius Latex particle suspension was added into the solution of the test tube. The solution was mixed well before a drop of specimen was taken out of the test tube by using a pipette and placed on the microscope stage for insonification. The drop of specimen sandwiched between the fused silica disk and the cover glass usually had approximately a cylindrical shape and of about 6 mm in diameter and less than 2 mm in height.

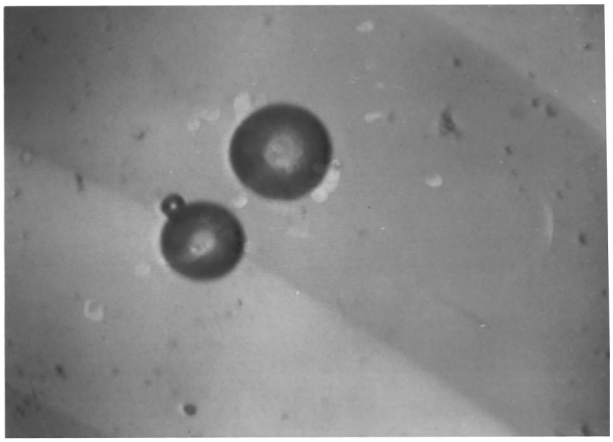

(a)

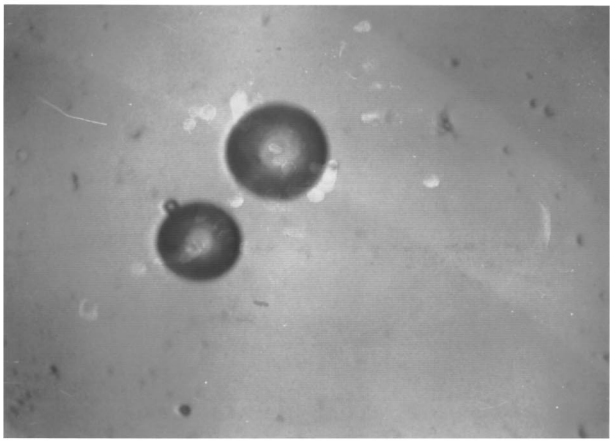

(b)

FIG. 1. Three Albunex® spheres were in a 160-kHz ultrasonic standing wave field; their radii were 4, 20, and 25 μm, respectively. They were all trapped at one of the pressure antinodes and pulsating. The 4-μm sphere coalesced with the 20-μm sphere. The picture shown in (b) was taken a minute later and the 4-μm sphere was significantly smaller than it was in Fig. 1(a) and finally was combined into the 20-μm sphere (not shown).

II. EXPERIMENTAL RESULTS

Since the shape of the water drop is nearly cylindrical, it is appropriate to use cylindrical coordinates (r,θ,z) to describe the standing wave sound field in the water drop. Physically, there are modes along r, θ, and z directions, and they are, respectively, described by the mth-order Bessel, trigonometry, and exponential functions (see the Appendix). In usual experimental situations, due to the complexity of the system, the modes which involve all r, θ, and z appeared. The dimensions of the water drop used were 6 mm of diameter and 2 mm of height and the frequency used was 160 kHz; it was observed that the trapping force was primarily along the radial direction. While along the axial direction, the buoyant force seemed to push the spheres close to the top cover glass. Albunex® spheres in an external ultrasonic standing wave field of 160 kHz were observed to migrate to pressure amplitude antinodes. The resonance size of air bubbles can be estimated by using a simple equation:

$$f_0 r_0 = 330, \tag{1}$$

where f_0 is the resonance frequency and r_0 is the radius of the bubble; both are in cgs units (Coakley and Nyborg, 1978). Letting $f_0 = 160$ kHz, we can calculate $r_0 = 22$ μm.

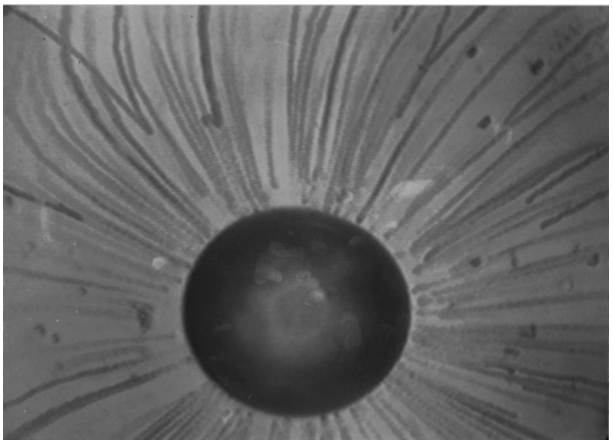

FIG. 2. Acoustic streaming pattern near a 55-μm radius Albunex® sphere trapped at a pressure antinode of a 160-kHz standing wave field along the radial direction of the cylindrical transducer and also located close to (about 0.15 mm away from) the top cover glass. The streaming velocity was estimated to be 50 μm/s near the bubble.

It was found that the shell stiffness of Albunex® spheres make the resonance frequency of the sphere much higher than Eq. (1) predicts (de Jong *et al.*, 1991). If the shell parameter is defined as

$$S = Et/(1-\nu), \tag{2}$$

where E is Young's modules, t is the thickness of the shell, and ν is the Poisson ratio. de Jong *et al.* found that the resonance frequency depends strongly on the shell parameter. For example, if the shell parameter is 10, the resonance frequency of 10-μm radius bubble would increase from about 300 kHz predicted by Eq. (1) to 800 kHz. Therefore, even for the biggest (radius is 55 μm) sphere tested by us, it is probably still smaller than the resonance size of the 160-kHz ultrasound. Thus, they all should be trapped to the pressure antinode (see the Appendix).

In addition to the migration, Albunex® spheres often moved close to each other and might finally coalesce to become bigger spheres. Figure 1 illustrates this process. In Fig. 1(a), there were three Albunex® spheres in a 160-kHz ultrasonic field; their radii were 4, 20, and 25 μm, respectively. They appeared to be spatially stable; presumably, they were all trapped at one of the pressure antinodes and pulsating. The picture shown in Fig. 1(b) was taken a minute later than that shown in Fig. 1(a). The 4-μm sphere in Fig. 1(b) was significantly smaller than it was in Fig. 1(a) and, finally, was combined into the 20-μm sphere (not shown). Further, it was observed that the number of big spheres in the sample solution seemed to increase with time of insonification.

In Fig. 2, a 55-μm radius Albunex® sphere was trapped at a pressure antinode of a 160-kHz standing wave field along the radial direction of the cylindrical transducer and also located close to (about 0.15 mm away from) the top cover glass. The sphere was pulsating. The trajectories of 1-μm latex particles shown in the figure demonstrated the acoustic streaming pattern near the sphere. This photograph and other photographs showing acoustic streaming, which

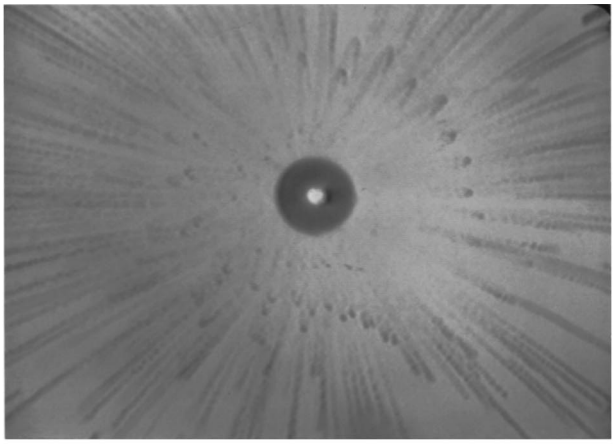

(a)

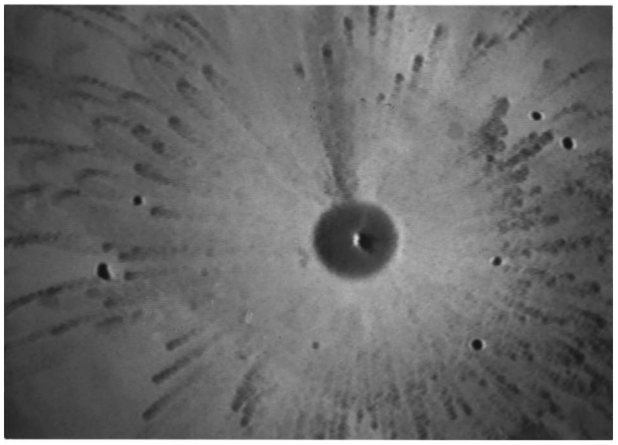

(b)

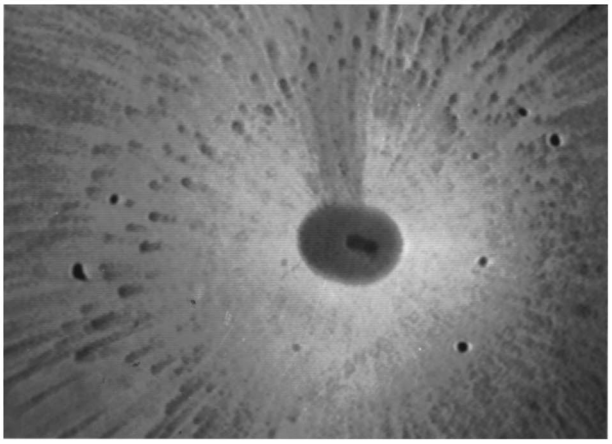

(c)

FIG. 3. Acoustic streaming pattern near an Albunex® sphere of 20-μm diameter in a 160-kHz standing wave field. (a) Acoustic streaming pattern generated by the sphere which was pulsating (monopole motions). As acoustic pressure amplitude of the standing wave was increased, the sphere was experiencing both monopole and dipole oscillations as shown in (b) and (c). The acoustic pressure amplitude of the standing wave was higher in (c) than in (b). It seemed that there were two jets leaving from the bubble in both (b) and (c); the spacing between the two jets were greater in (c) than in (b). This is the indication that the amplitude of translational (dipole) oscillation in (c) is greater than in (b). The streaming velocity was estimated to be 50–100 μm/s near the sphere.

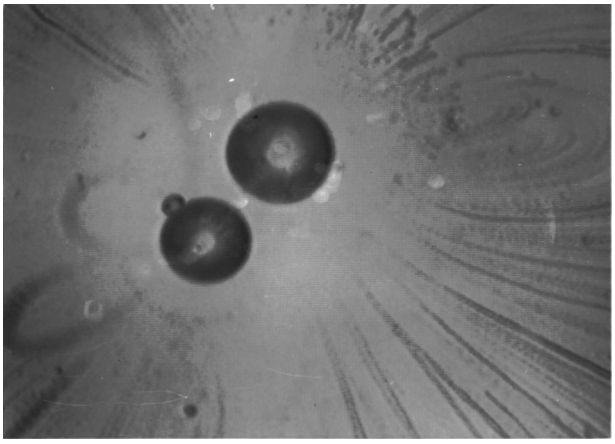

FIG. 4. Acoustic streaming pattern near a pair of Albunex® spheres trapped at a pressure antinode of a 160-kHz standing wave field.

will be discussed later, were taken using a video peak storage device (VPS) (Colorado Video, Inc., Boulder, CO). The VPS digitizes and stores a single video frame and also has the capability of comparing the stored image with later images and updating the stored image. A pixel in the stored image can be updated whenever that pixel is darker in a later image. Thus, each pixel in the stored image represents the maximum darkness value that occurred for that pixel during the time that the device was processing data. Thus, the VPS produces an image that is similar in many respects to that obtained by stroboscopic multiple-exposure photography. In our application, it was set that the image was updated every 0.1 s. Therefore, the time spacing between the two nearest dark dots is 0.1 s. The streaming speed (approaching/leaving the sphere) could be estimated by measuring the distance between the 10 dots near the sphere; in this case it turned out to be 50 μm/s. Due to the fact that the scale of the test solution was rather small, a direct measurement of the sound pressure amplitude was very difficult. Spatial peak pressure amplitude was estimated to be in the order of 0.5 MPa by using optical interferometry (Miller, 1976). Specifically, the spatial peak vibrational displacement amplitude at the front surface of the fused silica was measured using a Michelson interferometer. To get the spatial peak pressure amplitude, the measured value then was multiplied by the acoustic characteristic impedance of water and the angular frequency. Noting that Fig. 2 was a projection of the acoustic streaming pattern on the optical focal plane perpendicular to the propagation direction of the ultrasound, the actual individual trajectory looked under the microscope more like a parabola; it moved closer to the sphere and then returned. The pattern looked similar to the acoustic streaming around a solid sphere described by Lee and Wang (1990).

When the ultrasound amplitude was increased, the pulsation became unstable; the translational (dipole) vibration was introduced and superimposed to the pulsation. Photographs in Fig. 3 registered a typical example of such cases. Figure 3(a) was a picture of a pulsating Albunex® sphere of 20-μm radius in a 160-kHz standing wave field. Figure 3(b) and (c) were pictures of the same sphere when the amplitude of the standing wave field was increased gradually. It is quite evident that the translational vibrations were introduced in

Fig. 3(b) and (c). The amplitude of the dipole motion was higher in Fig. 3(c) than in Fig. 3(b) as the amplitude of the standing wave field was higher for the former than the latter. Meanwhile, the streaming pattern became more complex; a jet-flow seemed to be generated from the sphere.

Acoustic streaming was also observed for a pair of Albunex® spheres in a 160-kHz standing wave field. Figure 4 is a picture which was taken for the same spheres as shown in Fig. 1. The streaming pattern shown here can be considered to be that for a pair of spheres as the effect of the small sphere may be neglected. In addition to the similar streaming pattern of a single sphere as shown in Fig. 2, there were some vortex-ring type streaming patterns.

APPENDIX

The sound pressure field, p, within the drop should obey the Helmholtz equation in cylindrical coordinates (r,θ,z) as (Miller, 1976)

$$\frac{1}{r}\frac{\partial}{\partial r}\left(r\frac{\partial p}{\partial r}\right)+\frac{1}{r^2}\frac{\partial^2 p}{\partial \theta^2}+\frac{\partial^2 p}{\partial z^2}+k^2 p=0, \tag{A1}$$

where the positive z direction points upward vertically and k is the wave number. The solutions of Eq. (A1) satisfying the boundary condition $p=0$ when $r=a$ (the sound pressure should be equal to zero at the air–water interface) are

$$\begin{aligned} p=&\sum_{n=1}^{\infty}\sum_{m=1}^{\infty}[(A_{nm}e^{i\beta_{nm}z} \\ &+B_{nm}e^{-i\beta_{nm}z})\sin m\theta J_m(\alpha_{nm}r/a)] \\ &+\sum_{n=1}^{\infty}\sum_{m=0}^{\infty}[(C_{nm}e^{i\beta_{nm}z} \\ &+D_{nm}e^{-i\beta_{nm}z})\cos m\theta J_m(\alpha_{nm}r/a)], \end{aligned} \tag{A2}$$

where

$$\beta_{nm}=\sqrt{k^2-\alpha_{nm}^2/a^2}. \tag{A3}$$

Here α_{nm} denotes the nth root of the mth-order Bessel function, i.e.,

$$J_m(\alpha_{nm})=0. \tag{A4}$$

The constants of $A_{nm},B_{nm},C_{nm},D_{nm}$ are determined from the boundary conditions along z direction, namely, by how the fused silica and the cover glass oscillate.

The trapping force of ultrasonic standing waves can be explained using a simple one-dimensional model (Coakley and Nyborg, 1978). Let us assume $p(x,t)$ and $v(x,t)$ are, respectively, the instantaneous acoustic pressure in the neighborhood of a small bubble and its instantaneous volume fluctuation. Since the former is of a standing wave, its spatial and time part should be written as

$$p(x,t)=f(x)\cos(2\pi t), \tag{A5}$$

where $f(x)$ is an arbitrary function of x. The bubble responses to the acoustic pressure and thus

$$v(x,t)=bf(x)\cos(2\pi t+\beta), \tag{A6}$$

where b and β are constants. Due to the variation of acoustic pressure across the surface of the bubble, a net force is generated and applied on it. The instantaneous force F_x directed along x direction is given by

$$F_x=-v(x,t)[\partial p(x,t)/\partial x]. \tag{A7}$$

The time-average of F_x can be calculated from Eqs. (A5), (A6), and (A7) and given by

$$\langle F_x\rangle=-\frac{b}{4}\frac{df^2(x)}{dx}\cos\beta. \tag{A8}$$

For bubbles well below resonance size $\cos b\approx -1$ and the net force is in the direction of increasing pressure amplitude. Conversely, for the bubbles well above resonance size $\cos b\approx 1$ and the net force points to the pressure node direction.

Bleeker, H. J., and Shung, K. (**1990**). ''Ultrasonic characterization of Albunex, a new contrast agent,'' J. Acoust. Soc. Am. **87**, 1792–1797.

Coakley, W. T., and Nyborg, W. L. (**1978**). ''Cavitation: Dynamics of gas bubbles; Application,'' in *Ultrasound: Its Application in Medicine and Biology*, edited by F. J. Fry (Elsevier, New York), pp. 77–153.

Davidson, B. J., and Riley, N. (**1971**). ''Cavitation microstreaming,'' J. Sound Vib. **15**, 217–233.

de Jong, N., Hoff, L., Skotland, T., and Bom, N. (**1991**). ''Absorption and scatter of encapsulated gas filled microsphere: theoretical considerations and some measurements,'' Ultrasonics **30**, 95–103.

Elder, S. A. (**1959**). ''Cavitation microstreaming,'' J. Acoust. Soc. Am. **31**, 54–64.

Lee, C. P., and Wang, T. G. (**1990**). ''Outer acoustic streaming,'' J. Acoust. Soc. Am. **88**, 2367–2375.

Marsh, J. N., Hall, C. S., Hughes, M. S., Mobley, J., Miller, J. G., Brandenburger, G. H. (**1997**). ''Broadband through-transmission signal loss measurements of Albunex suspensions at concentrations approaching *in vivo* doses,'' J. Acoust. Soc. Am. **101**, 1155–1161.

Miller, D. L. (**1976**). ''Instrument for microscopical observation of the biophysical effects of ultrasound,'' J. Acoust. Soc. Am. **60**, 1203–1212.

Miller, D. L. (**1987**). ''A review of the ultrasonic bioeffects of microsonation, gas-body activation, and related cavitation-like phenomena,'' Ultrasound Med. Biol. **13**, 443–470.

Moroney, R. M., White, R. M., and Howe, R. T. (**1991**). ''Microtransport induced by ultrasonic Lamb waves,'' Appl. Phys. Lett. **59**, 774–776.

Nyborg, W. L. (**1996**). ''Basic physics of low frequency therapeutic ultrasound,'' in *Ultrasound Angioplasty*, edited by R. J. Siegel (Kluwer Academic, Boston).

Rooney, J. A. (**1970**). ''Hemolysis near an ultrasonically pulsating gas bubble,'' Science **169**, 869–871.

Williams, A. R., Hughes, D. E., and Nyborg, W. L. (**1970**). ''Hemolysis near a transversely oscillating wire,'' Science **169**, 871–873.

Wu, J., and Du, G. (**1997**). ''Streaming generated by a bubble in an ultrasound field,'' J. Acoust. Soc. Am. **101**, 1899–1907.

Wu, J., Winkler, A. J., and O'Neill, T. P. (**1994**). ''Effect of acoustic streaming on ultrasonic heating,'' Ultrasound Med. Biol. **20**, 195–201.

Wu, J., and Tong, J. (**1998**). ''Experimental study of stability of contrast agents in an ultrasound field,'' Ultrasound Med. Biol. **24**, 257–265.

A modified modal frequency spacing method for coating characterization

Z. Wang, X. Li, and J. David N. Cheeke[a)]
Department of Physics, Concordia University, Montreal, Quebec H3G 1M8, Canada

(Received 24 October 1997; accepted for publication 24 July 1998)

A modified modal frequency spacing (MMFS) method is developed, which can be used to directly evaluate the coating density ρ^c and the longitudinal velocities of the substrate and of the coating, V_L^S and V_L^c, based on the measured cutoff frequency data. Numerical simulation results showed that the error in evaluating V_L^S and V_L^c is less than 0.4% and is less than 4% in ρ^c compared with the input data. © *1998 Acoustical Society of America.* [S0001-4966(98)01811-6]

PACS numbers: 43.35.Cg [HEB]

INTRODUCTION

Ultrasonic techniques are among the most promising nondestructive testing methods for characterization of coatings. A number of coating properties vital to service performance are directly related to the elastic properties of the coatings. Leaky Lamb wave (LLW) modes carry more information and are now widely used in coating characterization. For obtaining quantitative assessment of the thickness, density and elasticity of coatings, an inversion procedure of the measured data to determine these parameters is necessary. Various inversion schemes for LLW mode problems have been proposed.[1–4] In principle, these mathematical inversion methods are capable of recovering unknown parameters of the sample from measured data. In practice, however, there are abundant problems in the real application of the inversion methods. The more parameters to be recovered in an inversion, the worse the accuracy, the stability and the reliability. It is desirable to decrease the number of parameters to be recovered in each inversion by decoupling the procedure into several steps. Another important topic is how to assign accurate initial values to the parameters to be recovered. P-C. Xu *et al.*[1] introduced the modal frequency spacing (MFS) as a global characteristic parameter of the Lamb wave, when the two elastic constants are separated at normal incidence and at oblique incidence. The inversion procedure was then carried out efficiently and in a straightforward manner. We present a method to directly evaluate two or three parameters of the two layers based on the MFS distribution. Three characteristic MFS values were derived based on the cutoff frequency relationships for the longitudinal wave components at normal incidence. Three parameters, the density of the coating and the longitudinal velocities of the two layers, for example, can be independently evaluated based on the measured cut-off frequency data. The procedure is forward rather than inversive.

I. CUTOFF FREQUENCY EQUATIONS OF A TWO-LAYER COMPOSITE AT NORMAL INCIDENCE

The configuration of a two-layer composite and its coordinates are shown in Fig. 1. Both the coating and the substrate are isotropic. The Lamb waves propagate along the x direction and all field quantities are independent of y. As discussed in Ref. 1, free traction can be assumed on both surfaces of the coated plate, because the minima of the amplitude spectrum of the reflected wave for a plate immersed in water coincide closely with the dispersion curves for the same plate in a vacuum to a very satisfactory extent. For a longitudinal wave coming in from the liquid at normal incidence only the transverse components of the Lamb wave are excited. The first cutoff frequency equation is then given by

$$\frac{\rho^c V_L^c}{\rho^S V_L^S}\cdot\tan(\alpha_2 h)+\tan(\alpha_1 b)=0, \tag{1}$$

with

$$\alpha_1=\omega/V_L^S,\quad \alpha_2=\omega/V_L^c, \tag{2}$$

where V_L^c and V_L^S are the longitudinal wave velocities in infinitive media of the coating and substrate, given by

$$V_L^c=\sqrt{\frac{\lambda^c+2\mu^c}{\rho^c}}=\sqrt{\frac{C_{11}^c}{\rho^c}},$$
$$V_L^S=\sqrt{\frac{\lambda^S+2\mu^S}{\rho^S}}=\sqrt{\frac{C_{11}^S}{\rho^S}}, \tag{3}$$

where ρ^c, ρ^S; λ^c, λ^S; μ^c, μ^S are the densities and Lame constants of the coating and substrate, respectively, h and b are the thickness of the coating and substrate, respectively, and $\omega=2\pi f$, where f is the frequency.

The second cutoff frequency equation, which corresponds to the transverse vibration in the z direction, is given by

$$\frac{\rho^c V_S^c}{\rho^S V_S^S}\cdot\tan(\beta_2 h)+\tan(\beta_1 b)=0 \tag{4}$$

with

$$\beta_1=\omega/V_S^S,\quad \beta_2=\omega/V_S^c, \tag{5}$$

where

$$V_S^c=\sqrt{\mu^c/\rho^c},\quad V_S^S=\sqrt{\mu^S/\rho^S} \tag{6}$$

are the transverse wave velocities of the coating and substrate medium, respectively. Experimentally, only the longi-

a)Electronic mail: cheeke@alcor.concordia.ca

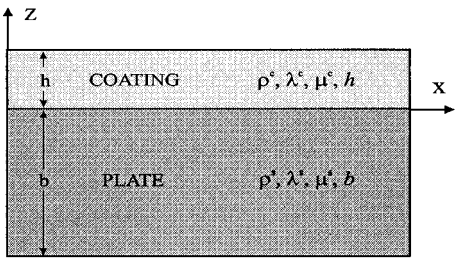

FIG. 1. Configuration and coordinates of the samples.

tudinal branch cutoff frequency data can be obtained at normal incidence, and in the following sections we will discuss this branch only. Accordingly, in the following we delete the subscript L for the MFS parameters. The method can be used for the transverse branch, as well, provided the experimental data can be acquired.

II. MODAL FREQUENCY SPACING (MFS) DISTRIBUTION AND ITS UNIQUE VALUES

The values of the cutoff frequencies, f_n, are determined by Eq. (1). The spacing between the adjacent modes, $\Delta f_n = f_n - f_{n-1}$, is known as the modal frequency spacing (MFS). The MFS distribution versus frequency, as shown in Fig. 2, is periodic and there are four unique values in the distribution: (1) the periodicity, Δf^C; (2) the maximum MFS value at the center of the regular regions, $\Delta f^{\max}$; (3) the minimum MFS value at the center of the transition regions, $\Delta f^{\min}$; and (4) the MFS value of the bare plate, Δf^S. The key point is that the four unique MFS values have definite relationships with the composite parameters, which are given by explicit formulas.

For the bare plate, the second term in (1) goes to zero. The cutoff frequencies are given by

$$f_n = n \cdot V_L^S / 2b. \tag{7}$$

The MFS of the longitudinal wave in the bare plate is a constant, given by

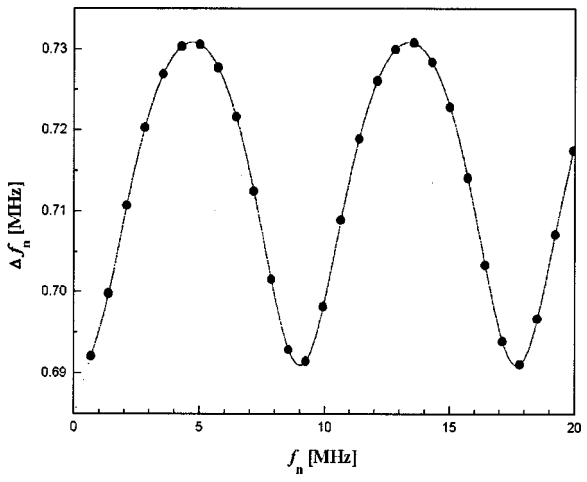

FIG. 2. Modal frequency spacing (MFS) distribution versus frequency (dots), and the interpolated curve, by which the three unique values are evaluated.

$$\Delta f^S = V_L^S / 2b. \tag{8}$$

The MFS distribution is changed due to the coating layer on the plate. Three unique values of the MFS distribution can be derived and are given as follows.

(1) At the center of the regular regions, where $\alpha_2 h \approx n\pi$ $(n=0,1,2,\ldots)$, the MFS value can be derived from (1). It is the maximum value in the distribution for the case of the acoustic impedance ratio $\rho^c V_L^c / \rho^S V_L^S < 1$ and is given approximately by

$$\Delta f^{\max} \approx \frac{V_L^S}{2b} \cdot \left(1 + \frac{2 \cdot (\rho^c h)}{\rho^S b} \right)^{-1/2}. \tag{9}$$

(2) At the center of the transition regions, where $\alpha_2 h \approx (n + \frac{1}{2})\pi$, the MFS value can be derived from (1) and it is the minimum value. The formula is given by

$$\Delta f^{\min} \approx \frac{V_L^S}{2b} \cdot \left(1 + \frac{C_{11}^S}{b} \cdot \frac{h}{C_{11}^c} \right)^{-1} = \frac{V_L^S}{2b} \cdot \left(1 + \frac{\rho^S \cdot (V_L^S)^2}{\rho^c \cdot (V_L^c)^2} \cdot \frac{h}{b} \right)^{-1}. \tag{10}$$

(3) The period of the cutoff frequency distribution derived from (1) is given by

$$\Delta f^C = \frac{V_L^c}{2h} = \frac{1}{2h} \cdot \sqrt{\frac{C_{11}^c}{\rho^c}}. \tag{11}$$

The value of the period of the cutoff frequency Δf^C depends only on the thickness and the longitudinal wave velocity of the coating. This formula could be very useful in coating characterization if wide frequency range cutoff frequency data can be experimentally acquired.

III. APPLICATION OF THE EXPLICIT FORMULAS—THE MMFS METHOD

In practice, the thickness of both the substrate and the coating, b and h, and the mass density of the substrate, ρ^S, are given, or determined by other approaches, as discussed in Ref. 1. Therefore, only three parameters, i.e., the density of the coating, ρ^c, and the longitudinal velocities of the substrate and of the coating, V_L^S and V_L^c, are to be recovered, based on the cutoff frequency distribution described in Eq. (1). Their initial values can be evaluated by using the three formulas based on the cutoff frequency data. In Eqs. (9), (10) and (11), just the three variables ρ^c, V_L^S, and V_L^c are involved, and thus they can be determined by knowing the three unique MFS values $\Delta f^{\max}$, $\Delta f^{\min}$, and Δf^C. We will see that the initial values evaluated from the above three formulas are sufficiently accurate compared with the input parameters. It is therefore unnecessary to carry out the inversion based on the cutoff frequency data using Eq. (1). We refer to this as the ''modified modal frequency spacing'' (MMFS) method.

To investigate the validity of the method, a simulation method is used numerically. The samples used in numerical calculations are the same as in Ref. 1 and are listed in Table I. Samples 1 and 2 are comprised of a Cu–Ni–In coating on Ti6Al–4V substrate plate, and sample 3 is an aluminum

TABLE I. Parameters of the three samples used in the simulation.

No.	ρ^S	V_L^S	V_S^S	b	ρ^c	V_L^c	V_S^c	h
1	4.43	6.23	3.35	6.00	3.00	3.20	1.25	0.20
2	4.43	6.23	3.13	6.00	3.00	2.85	1.33	0.28
3	2.80	6.35	3.10	4.00	2.00	4.20	2.15	0.25

plate coated with a NiAl alloy layer. All samples are plasma-sprayed and the dispersion data were acquired by LLW measurement.[1]

The cutoff frequencies were calculated using Eq. (1) and parameters listed in Table I, and the MFS values, defined by $\Delta f_n = f_n - f_{n-1}$, were obtained. In normal applications the MFS data are acquired from experiments. Here the calculated values are used. These data can be considered as acquired data from experiments **with absolute accuracy**. Taking the MFS values as a function of the frequency, we can obtain the three unique values, $\Delta f^{\max}$, $\Delta f^{\min}$, and Δf^C, for each sample. Substituting them into Eqs. (9)–(11), the three parameters, ρ^c, V_L^S, and V_L^c, can be evaluated. Comparing the three parameters evaluated based on the MFS data with those input data, we can estimate the intrinsic errors of the method, i.e., those which are independent of the experimental accuracy.

The distributions of the MFS versus frequency are typically shown in Fig. 2. The maxima and minima of the MFS and the corresponding positions of the frequency were determined by interpolating the curve with a simple program. The curve in Fig. 2 shows the smooth distribution of MFS after 200 points were interpolated. For the three samples discussed, the condition of $\rho^c \cdot V_L^c / \rho^S \cdot V_L^S < 1$ is satisfied, the maximum and minimum MFS values and the periodicity of the MFS are the $\Delta f^{\max}$, $\Delta f^{\min}$, and Δf^C, correspondingly. Substituting the three unique MFS values into Eqs. (9), (10) and (11), we obtained the initial values of the parameters. All the values are listed in Table II. The corresponding errors compared with the input data are given in brackets.

It is seen that the intrinsic errors in evaluating the V_L^S and V_L^c are less than 0.4%, and the errors in evaluating ρ^c are less than 4%. This suggests that the MMFS method can be used to determine the three parameters directly based on the cutoff frequency data. The final results of an inversion will not improve the accuracy of ρ^c, because the error shown above is caused by the insensitiveness of ρ^c on the dispersion property rather than by the MMFS method itself. It was shown in Ref. 1 that the effect of ρ^c on the dispersion curves is not sensitive and this parameter therefore cannot be accurately recovered by an inversion. The accuracy is not significantly changed when different interpolating functions are used.

It was found that the acoustic impedance ratio (AIR), $\rho^c \cdot V_L^c / \rho^S \cdot V_L^S$, has a sensitive effect on the MFS distribution. For the case discussed above, where $\rho^c \cdot V_L^c / \rho^S \cdot V_L^S < 1$, as the AIR becomes smaller, the change at the regular regions becomes more and more smooth, whereas the change at the transition regions becomes more and more violent. For the case where the AIR $\rho^c \cdot V_L^c / \rho^S \cdot V_L^S > 1$, the formulas of the maximum and the minimum MFS values are just the opposite. In this case, when the AIR value becomes larger, the change at the regular regions becomes more violent, whereas the change at the transition regions becomes more smooth. The physical significance of this behavior can be described more clearly by rewriting the formulas (9) and (10) in the following forms:

$$\Delta f^{\max} \approx \left[\frac{1}{\Delta f_S} + \left(\frac{\rho^c V_L^c}{\rho^S V_L^S} \right) \cdot \frac{1}{\Delta f_C} \right]^{-1}, \tag{12}$$

$$\Delta f^{\min} \approx \left[\frac{1}{\Delta f_S} + \left(\frac{\rho^S V_L^S}{\rho^c V_L^c} \right) \cdot \frac{1}{\Delta f_C} \right]^{-1}. \tag{13}$$

The factor preceding the second term in (12) is the acoustic impedance ratio and that in (13) is its reciprocal.

Another important factor which affects the accuracy significantly is the number of modal frequencies within a period, i.e., $N = \Delta f^C / \Delta f^S + 1$. It was found from numerical examples that the value should be larger than 10 in order to obtain acceptable accuracy.

IV. CONCLUSIONS AND DISCUSSIONS

In this paper, we report a modified modal frequency spacing (MMFS) method which can be used to directly determine the density of a coating layer, ρ^c, and the longitudinal wave velocities of the substrate and of the coating layer, V_L^S and V_L^c, based on the cutoff frequency data. Numerical simulation results showed that the accuracy in evaluating V_L^S and V_L^c is better than 0.4% and the accuracy in evaluating ρ^c is better than 4% for the three samples given in Ref. 1. This means that the MMFS method will not introduce significant errors compared with the results obtained by inversion based on the cutoff frequency data.

The simulation results showed that the acoustic impedance ratio, $\rho^c \cdot V_L^c / \rho^S \cdot V_L^S$, has a sensitive effect on the MFS

TABLE II. Unique values for the longitudinal branch evaluated from MFS distribution and the parameters evaluated by the MMFS method.

No.	Δf^c	$\Delta f^{\max}$	$\Delta f^{\min}$	ρ^c	V_L^c	V_L^S
1	7.98	0.5077	0.4387	3.064 (2.1%)	3.192 (−0.25%)	6.2313 (0.02%)
2	5.10	0.5031	0.3947	3.117 (3.9%)	2.856 (0.2%)	6.2323 (0.04%)
3	8.43	0.7597	0.6635	2.027 (1.4%)	4.215 (0.35%)	6.3467 (−0.05%)

distribution. Some suggestions for improving the accuracy in different $\rho^c \cdot V_L^c / \rho^S \cdot V_L^S$ value cases were given. Another important factor which affects the accuracy significantly is the number of modal frequencies within a period. It was found that the value should be larger than 10 for obtaining acceptable accuracy.

The topic discussed in this paper is limited to a theoretical analysis frame work. The cutoff frequency data by simulation were assumed to be accurate, but in practice the measurement errors of cutoff frequency cannot be much better than 1%. Therefore, the actual errors in determining the parameters will be larger than those shown above. This is not only caused by the insensitiveness in determining ρ^c, but also by the irregularity of the experimental data at the transition regions where the minima have to be determined by interpolating. These problems, however, are not introduced additionally by the MMFS method and they exist in the inversion procedure as well.

ACKNOWLEDGMENTS

This work was supported by the Natural Sciences and Engineering Research Council of Canada.

[1] P-C. Xu, K-E. Lindenschmidt, and S. A. Meguid, ''A new high frequency analysis of coatings using leaky Lamb-waves,'' J. Acoust. Soc. Am. **94**, 2954–2962 (1993).

[2] P-C. Xu, K-E. Lindenschmidt, and S. A. Meguid, ''High frequency leaky Lamb-wave measurement of elastic properties of coatings,'' Proceedings of the 1993 National Thermal Spray Conference, Anaheim, CA, 1993, pp. 499–503.

[3] M. R. Karim and A. K. Mal, ''Inversion of leaky Lamb-wave data by simplex algorithm,'' J. Acoust. Soc. Am. **88**, 482–491 (1990).

[4] O. Behrend, A. Kulik, and G. Gremaud, ''Characterization of thin films using numerical inversion of the generalized Lamb-wave dispersion relation,'' Appl. Phys. Lett. **62**, 2787–2789 (1993).

The perfect fifths tempered scale, a proposal or already a practice?

Klaus Gillessen
Virchowstrasse 10, D-74074 Heilbronn, Germany

(Received 20 April 1998; accepted for publication 21 July 1998)

An alternative tempered scale is proposed, the perfect fifths tempered scale (PFTS), which is stretched by an amount of 3.4 cents per octave in comparison to the common (perfect octaves) tempered scale (POTS). The PFTS is a better approximation to the musical practice of stretched intonation than the POTS. © *1998 Acoustical Society of America.* [S0001-4966(98)00411-1]

PACS numbers: 43.75.Bc [WJS]

INTRODUCTION

Our common musical scales, the just and the tempered scale, are based upon the octave, i.e., a frequency ratio of 2:1. The intervals of the just scale correspond with fractions of small integer numbers, for example, 3:2 (fifth), 4:3 (fourth). These ratios yield optimally consonant sounds, because many partials coincide exactly. The just scale is, however, not well suited for modulations, because the sizes of intervals are different in other keys. This problem was solved with the compromise of the tempered scale which divides the octave into 12 equal semitones of $2^{(1/12)}=1.05\,946$ and into 1200 cents of $2^{(1/1200)}=1.0\,005\,778$. (In the following the sign ''='' is used throughout, also where it should read strictly ''approximately equal.'' Decimal numbers are generally rounded to six significant digits, cent numbers are rounded to an accuracy of 0.1 cents.) In the tempered scale the fifth is 7 semitones or $2^{(7/12)}=1.49\,831=700$ cents, whereas the perfect fifth is $3/2=1.5=702.0$ cents. In other words, the fifth of the tempered scale is contracted so that 12 fifths are equal to 7 octaves. Alternatively, a new tempered scale can be constructed with perfect fifths (1.5) and stretched octaves of $1.5^{(12/7)}=2.00\,388=1203.4$ cents. This scale is named here the perfect fifths tempered scale, PFTS.

I. COMPARISON OF THE PERFECT FIFTHS TEMPERED SCALE WITH COMMON SCALES

The PFTS is constructed starting with the perfect fifth (1.5). Its semitone is $1.5^{(1/7)}=1.05\,963=100.3$ cents. The complete scale covering one octave is obtained from $T_n=1.5^{(n/7)}$ for $n=0$ (prime) to 12 (octave). Table I shows the PFTS in comparison with the common (perfect octave) tempered scale (POTS) and the just scale. Both the PFTS and the POTS have the largest deviations from the just scale at $n=4$, 9, and 11. The third and sixth of the PFTS are sharp by +14.8 cents and +18.1 cents, respectively, slightly more than those of the POTS (13.7 cents and 15.6 cents, respectively). The seventh of the PFTS by is also sharp by +14.8 cents, compared with +11.7 cents of the POTS. Because in the PFTS the octave is at the same time raised by +3.4 cents, the interval from $n=11$ to $n=12$ remains practically the same as with the POTS. Considering the other tones there are only minor deviations from the just scale. In two cases ($n=2,7$) the PFTS is even closer to the just scale than the POTS; for $n=5$ the difference is slightly larger.

In connection with the PFTS, it seems also reasonable to redefine the ''cent'' as 1/700 of the fifth, i.e., $1.5^{(1/700)}=1.0\,005\,794$. To avoid confusion the new measure could be named ''pent,'' beginning with a ''*p*'' from ''perfect,'' and related to the Greek ''five.'' According to the definition of the pent, the semitone of the PFTS is equivalent to 100 pents and the stretched octave equals 1200 pents.

II. USE OF STRETCHED SCALES AND RELATED EXPERIMENTS

It is well known that pianos sound best if they are tuned not exactly to equal temperament (i.e., to the tempered scale), but with slightly stretched intervals. This is described by Martin and Ward.[1] Figure 1 of their paper is reproduced here (as our Fig. 1) with an additional line inserted characterizing the PFTS. One can see that the largest deviations of plus and minus 30 cents from the equally tempered scale occur at the highest and lowest tones of the range, respectively. These deviations can be explained by the inharmonic partials of the piano strings, caused by the considerable stiffness of the string wire (see Ref. 2). With stretched tuning the partials match the partials of other tones better. It can also be seen that even in the middle range of the piano a small stretching of a few cents per octave is applied. It is remarkable that at least the range from C2 to C7 can be approximated with good accuracy using the PFTS (thick line). Because the strings of violins, violas, and violoncellos are tuned in fifths, there is a tendency for these instruments to play with stretched octaves close to the PFTS, if the fifths are assumed to be perfect. Other instruments are forced to match their intonation to this stretched scale when they play together with a piano or in an orchestra where the strings dominate. There are many investigations demonstrating a clear tendency towards stretched intonation. This was described first by Ward,[3] and later on, for example, by Sundberg and Lindqvist.[4] The amount of stretching found in these investigations is generally considerably larger than that of the PFTS. Slaymaker[5] has conducted an experiment with stretched and compressed scales and partials. Single tones and chords from stretched and compressed scales were assessed subjectively. His most important results were the following.

TABLE I. Comparison of the perfect fifths tempered scale with common scales.

		PFTS		POTS		Just scale	
n	Note in C	Ratio	Cents	Ratio	Cents	Ratio	Cents
0	C	1	0	1	0	1	0
1	C#	1.05 963	100.3	1.05 946	100		
2	D	1.12 282	200.6	1.12 246	200	1.125	203.9
3	D#	1.18 978	300.8	1.18 921	300		
4	E	1.26 073	401.1	1.25 992	400	1.25	386.3
5	F	1.33 592	501.4	1.33 484	500	1.33333	498.0
6	F#	1.41 558	601.7	1.41 421	600		
7	G	1.5	702.0	1.49 831	700	1.5	702.0
8	G#	1.58 945	802.2	1.58 740	800		
9	A	1.68 424	902.5	1.68 179	900	1.66667	884.4
10	A#	1.78 467	1002.8	1.78 180	1000		
11	B	1.89 110	1103.1	1.88 775	1100	1.875	1088.3
12	C	2.00 388	1203.4	2	1200	2	1200

(i) For stretching of up to an additional quarter-step per octave, only subtle changes of the tones and chords were found.
(ii) For stretching of an additional half-step per octave, the tones and chords sounded bell- or chimelike.
(iii) For strongly stretched or compressed octaves, the tones and chords were changed drastically; they became either dissonant or at least very strange.

With regard to the PFTS, these results mean that the very small stretching of 3.4 cents per octave will have no detrimental effect.

Terhardt and Zick[6] had synthetic test sounds in normal, stretched, and contracted intonation subjectively compared by larger groups of test persons. The amounts of stretching respectively compressing were chosen according to the data of Martin and Ward,[1] i.e., up to minus or plus 30 cents at C1 and B7, respectively. The results of this study can be summarized as follows:

(i) Stretched intonation is preferred for sounds composed of widely separated tones.
(ii) Normal intonation is best for sounds of medium complexity.
(iii) Contracted intonation may be suitable for highly complex sounds.

III. CONCLUSION

Starting with perfect fifths, an alternative tempered scale (PFTS) can be constructed which is stretched by an amount of 3.4 cents per octave. This scale is a better approximation to musical practice than the common tempered scale with perfect octaves. In particular, it provides a good fit for typi-

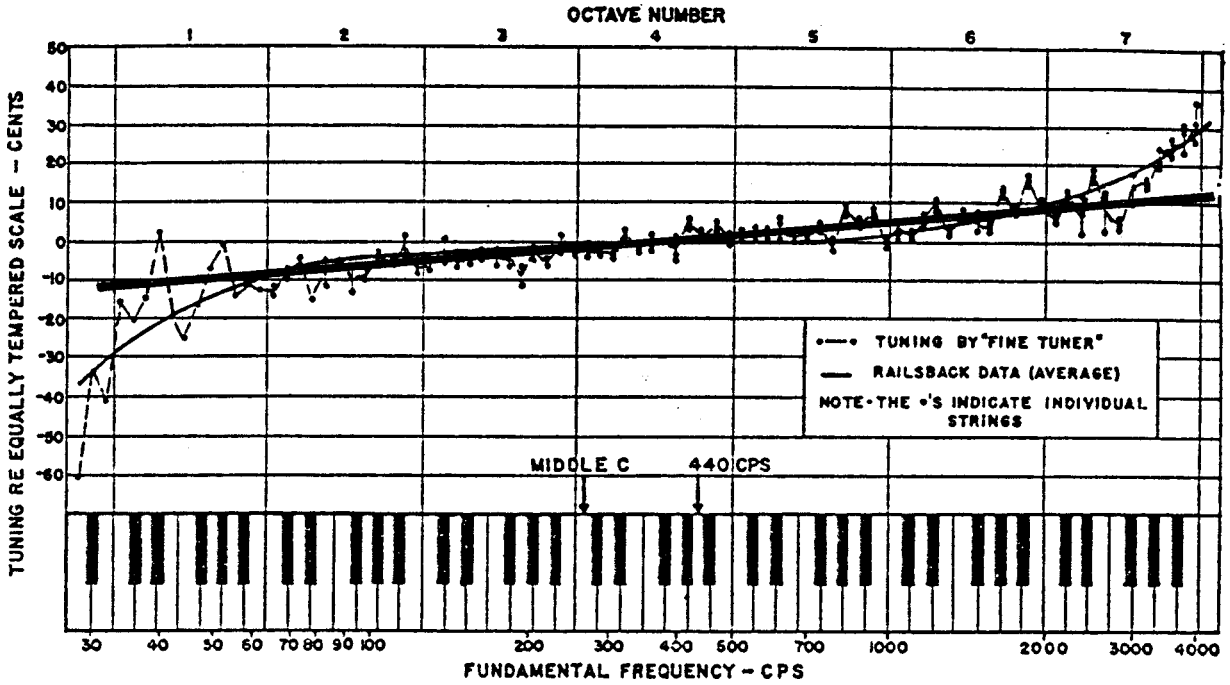

FIG. 1. Tuning of a piano (from Ref. 1), thick line: PFTS.

cal tuning of pianos in octaves 2 to 6. An additional justification for the use of the PFTS might be that perfect fifths are perhaps more important than perfect octaves, because the harmony in our music is mainly based on triads. However, the PFTS can at most partly explain the amount of stretching practiced which is more typically around 20 cents per octave.

[1] D. W. Martin and W. D. Ward, ''Subjective evaluation of musical scale temperament in pianos,'' J. Acoust. Soc. Am. **33**, 582 (1961).

[2] R. W. Young, ''Inharmonicity of plain wire piano strings,'' J. Acoust. Soc. Am. **24**, 267 (1952).

[3] W. D. Ward, ''Subjective musical pitch,'' J. Acoust. Soc. Am. **26**, 369 (1954).

[4] J. E. F. Sundberg and J. Lindqvist, ''Musical octaves and pitch,'' J. Acoust. Soc. Am. **54**, 922 (1973).

[5] F. H. Slaymaker, ''Chords from tones having stretched partials,'' J. Acoust. Soc. Am. **47**, 1569 (1970).

[6] E. Terhardt and M. Zick, ''Evaluation of the tempered tone scale in normal, stretched, and contracted intonation,'' Acustica **32**, 268 (1975).

Effects of tissue constraint on shock wave-induced bubble expansion *in vivo*

Pei Zhong[a)]
Department of Mechanical Engineering and Materials Science and Comprehensive Kidney Stone Center, Division of Urology/Department of Surgery, Duke University, Durham, North Carolina 27708

Iulian Cioanta, Songlin Zhu, and Franklin H. Cocks
Department of Mechanical Engineering and Materials Science, Duke University, Box 90300, Durham, North Carolina 27708-0300

Glenn M. Preminger
Comprehensive Kidney Stone Center, Division of Urology/Department of Surgery, Duke University, Durham, North Carolina 27708

(Received 2 April 1998; revised 8 July 1998; accepted 6 August 1998)

The collapse time of lithotripter shock wave-induced cavitation bubbles was found to be significantly reduced from *in vitro* (133–271 μs) to *in vivo* (34–99 μs), suggesting that bubble expansion *in vivo* could be severely constrained by the surrounding tissue. Calculations based on the Gilmore model for bubble dynamics suggest that inertial cavitation could be induced in blood, provided that appropriate nuclei are present. Without tissue constraint, the maximum bubble induced in blood by an HM-3 lithotripter was calculated in the range of 1.3 to 2.3 mm. These results suggest that intraluminal bubble expansion may cause the rupture of capillaries and small blood vessels during shock wave lithotripsy, especially when cavitation nuclei are introduced into the circulation. © *1998 Acoustical Society of America.* [S0001-4966(98)03811-9]

PACS numbers: 43.80.Ev, 43.80.Gx, 43.25.Yw [FD]

INTRODUCTION

During shock wave lithotripsy (SWL), the formation of cavitation bubbles *in vivo* is often observed by ultrasound B-scan imaging, which reveals a transient increase in echogenicity of tissues along the beam axis of the lithotripter. This characteristic hyperechogenicity has been observed in perinephric fat and the corticomedullary zone and parenchyma of the kidney, as well as in hepatic vessels and bladders.[1–3] Regions of hyperechogenicity in canine kidneys were also found to correlate with the areas of intrarenal hemorrhage, suggesting that cavitation is likely to be associated with the mechanism of tissue injury.[1] Using passive cavitation detectors, acoustic emission (AE) associated with SWL-induced bubble oscillations has been measured both *in vitro* and *in vivo*.[4,5] The collapse time (t_C) of the bubble cluster induced *in vivo* was found to be significantly reduced from that *in vitro*. Because SWL-induced cavitation bubbles *in vitro* can expand to a maximum size of 1–3 mm (which is larger than most of the fluid-filled space in tissue),[6] this finding suggests that bubble expansion *in vivo* is constrained by surrounding tissue.[5]

In this Letter, we report experimental data which demonstrate that the maximum expansion of cavitation bubbles *in vivo* is related to the size of the fluid-filled space where the bubbles are induced. This observation is important for understanding the mechanical interaction between an expanding cavitation bubble and the surrounding constraining tissue structure. In particular, recent studies have shown that intravenous injection of ultrasound contrast agents (well known as effective cavitation nuclei[7]) can significantly increase vascular injury during SWL.[7] Since intraluminal expansion of cavitation bubbles has been a concern for collateral damage of the vessels during laser angioplasty[8] and in electrohydraulic lithotripsy (EHL),[9] the possibility of vascular injury due to intraluminal bubble expansion in SWL is intriguing. To assess this possibility, we calculated bubble dynamics in blood without tissue constraint for various nucleus sizes. At clinical SWL pressure amplitudes, our results suggest that inertial cavitation could be induced in blood vessels, provided that nuclei greater than 10 nm in radius are present. Without tissue constraint, the maximum bubble diameters in blood were calculated in the range of 1.3 to 2.3 mm. The potential of such a large intraluminal bubble expansion suggests that capillaries and small blood vessels may be at much higher risks for mechanical rupture than large blood vessels. This prediction seems to be consistent with the observation of vascular injuries produced during SWL, especially when ultrasound contrast agents are introduced into the circulation.

I. EXPERIMENTAL METHODS AND RESULTS

To evaluate the influence of the size of the surrounding fluid-filled space on bubble expansion *in vivo*, we measured AE emanating from the lower pole and renal pelvis of three juvenile swine during SWL. Each swine (~27 kg in weight) was anesthetized with 5% Pentothal (10 mg/kg), placed on the motorized stretcher and lowered into the water tub (37 °C) of a Dornier HM-3 lithotripter. Between 15 and 25 kV, the peak compressive and peak tensile pressure of the shock wave produced by an HM-3 lithotripter in water vary in the range of 33–50, and −7.1−−9.5 MPa, respectively.[10]

a)Electronic mail: pz1@me1.egr.duke.edu

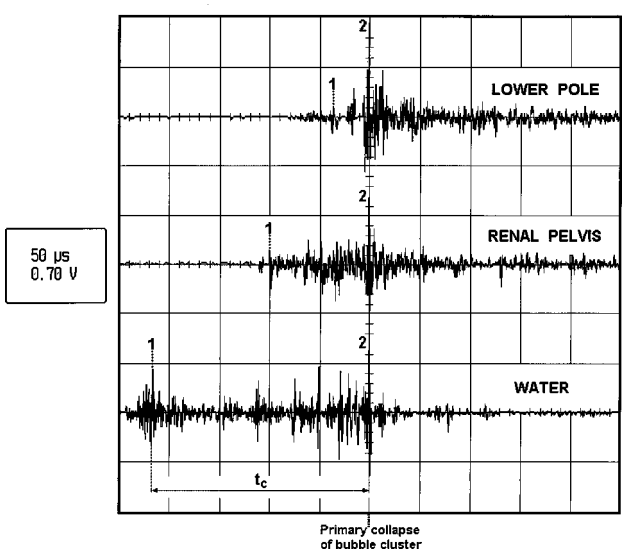

FIG. 1. Representative acoustic emission signals associated with cavitation bubble clusters produced by a Dornier HM-3 lithotripter at 20 kV in the lower pole, renal pelvis of a swine kidney, and in water, respectively. (See the text for further description.)

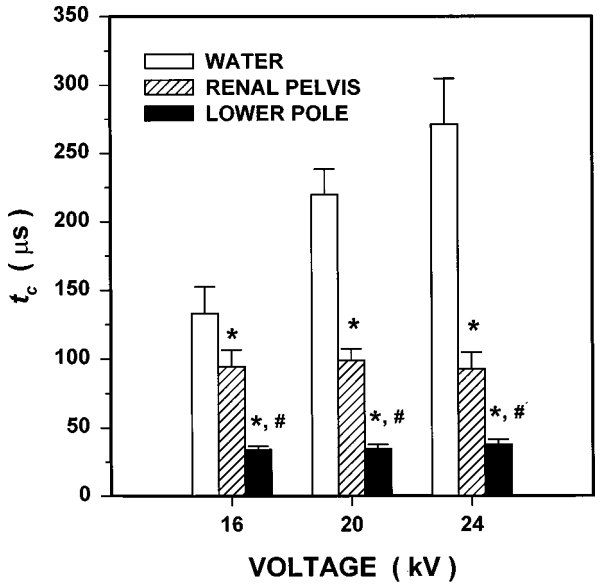

FIG. 2. Variations of collapse time, t_c, with lithotripter output voltage for cavitation bubbles produced in the lower pole and renal pelvis of a swine (#1) and in water. Paired *t*-test was used to determine statistically significant differences in the results. *Significant difference between water and renal pelvis or lower pole, $p<0.05$;#Significant difference between renal pelvis and lower pole, $p<0.05$.

At 20 kV, the −6-dB beam dimensions are 120 by 15 mm along and transverse to the lithotripter axis.[10] Using the motorized stretcher (0.1-mm precision), either the lower pole or renal pelvis of the swine could be aligned to coincide with the lithotripter focus under biplanar fluoroscopic guidance. Shock waves generated at 16, 20, and 24 kV, respectively, were then delivered to the lower pole and renal pelvis of the swine in random order at 1-Hz pulse repetition rate. Concomitantly, 20 AE signals associated with SWL-induced bubble oscillations around the beam focus were recorded using a 1-MHz focused hydrophone (Panametrics) with $f=101.6$ mm and a −6-dB reception zone of 20×9 mm ($L\times D$).[5] To provide a baseline comparison, AE signals produced in water under the same lithotripter output settings were also recorded.

Acoustic emission signals measured both *in vitro* and *in vivo* revealed a similar pattern of temporal variation (Fig. 1). Each AE signal consists of at least two distinct, temporally separated pressure bursts. Previously, comparison of AE signals with simultaneously acquired high-speed photographic sequence of bubble oscillation *in vitro* has shown that the first pressure burst correlates with the initial compression/expansion, while the second burst correlates with the subsequent primary collapse/rebound of the bubble cluster.[5] For each AE trace, the collapse time (t_c), defined as the time delay between the maximum pressure peaks of the first and second bursts (Fig. 1), was measured. Physically, t_c correlates with the maximum bubble expansion in an unconstrained medium.[6]

The most noticeable change in AE signals from *in vitro* to *in vivo* is the significant reduction in t_c (Fig. 2). At 20 kV, t_c (mean±s.d.) was found to decrease from 220 ± 19 μs in water, to 99 ± 8 μs in the renal pelvis, to 35 ± 3 μs in the lower pole. Although the value of t_c increases significantly with the lithotripter output voltage *in vitro*, the corresponding values *in vivo* remain almost unchanged. Considering that tissue attenuation may only reduce the tensile pressure of the lithotripter shock wave by less than 6%,[3] the significant reduction in t_c from *in vitro* to *in vivo* is most likely caused by the limited space for bubble expansion *in vivo*. This speculation is further supported by the fact that t_c decreases substantially from renal pelvis to lower pole, although in both cases tissue attenuation on the incident shock wave should be quite similar. This pattern of reduction in t_c from *in vitro* to *in vivo* and from renal pelvis to lower pole was observed consistently in all three animals (Table I). Anatomically, the lower pole of the kidney is comprised largely of renal parenchyma, and may also include some renal calyxes, whereas the renal pelvis is a funnel-shaped continua-

TABLE I. The collapse time (t_c) of cavitation bubble clusters induced in the lower pole and renal pelvis of three juvenile swine, and in water by a Dornier HM-3 lithotripter. (Mean ±standard deviation in microseconds, $n=20$.)

	Lower pole			Renal pelvis			Water
	Pig #1	Pig #2	Pig #3	Pig #1	Pig #2	Pig #3	
16 kV	33.95±2.46	38.73±4.26	42.28±9.30	94.47±11.93	69.70±6.56	78.30± 7.22	132.85±19.56
20 kV	34.50±3.30	39.00±4.57	43.20±7.75	98.87± 8.31	64.33±7.94	71.20±10.03	219.53±18.57
24 kV	37.48±3.78	39.33±3.23	47.65±8.06	92.63±12.14	63.50±8.01	69.70±10.75	271.00±33.62

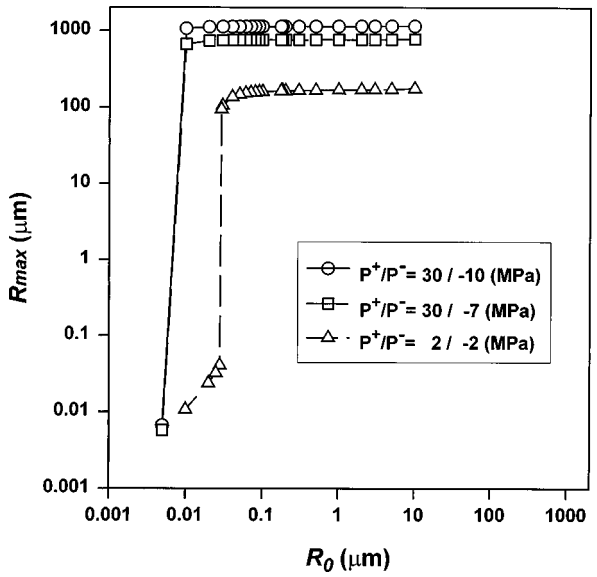

FIG. 3. Maximum bubble radius, $R_{\max}$, in blood induced by different lithotripter fields. Bubbles were assumed to expand and collapse spherically without tissue constraint. The following parameters of the blood were used for the Gilmore model calculation: equilibrium density, $\rho_0 = 1059$ kg/m^3; coefficient of shear viscosity, $\mu = 5 \times 10^{-3}$ kg/m·s; surface tension, $\sigma = 56 \times 10^{-3}$ N/m; infinitesimal sound speed, $C_0 = 1584$ m/s.

tion of the upper end of the ureter. The fluid-filled space in the lower pole, either in blood vessels or in calyceal spaces, is much smaller than the volume of the renal pelvis. Therefore, our results suggest that the size of the fluid-filled space in tissue has a significant influence on the maximum bubble expansion *in vivo*.

II. THEORETICAL CALCULATIONS OF BUBBLE DYNAMICS IN BLOOD

In laser angioplasty, it has been shown that the expansion and implosion of cavitation bubbles in the rabbit femoral and iliac arteries could produce rapid dilation and invagination of the arteries.[8] This intraluminal bubble oscillation was found to cause extensive rupture and abrasion of internal elastic lamina, and smooth muscle cell necrosis.[8] Similarly, the dilation and perforation of the ureteral wall has been observed during EHL, due to the rapid expansion of cavitation bubbles.[9] The maximum size of EHL-produced bubbles in water increases with pulse energy from 3 mm at 25 mJ to 15 mm at 1300 mJ.[9] When a large bubble expands inside the intact ureter, considerable distension or even disruption of the ureter could occur. The threshold for the perforation of the ureteral wall, measured by the ratio of maximum bubble diameter in water to the initial vessel diameter, was estimated to be approximately 3.[9]

In light of these observations, we have calculated the maximum bubble expansion in blood without tissue constraint using the Gilmore formulation for bubble dynamics.[6] The maximum bubble size, when compared with typical sizes of the vascular branches in the kidney, may provide a qualitative assessment of the potential for vascular injury due to intraluminal bubble expansion.

Figure 3 shows the variations of maximum bubble radius with the initial nucleus size in blood in response to different lithotripter shock waves. The top two traces correspond to the results produced by an HM-3 lithotripter. The peak positive/peak negative pressure (P^+/P^-) of the incident shock waves were 30/−10 MPa and 30/−7 MPa, respectively. The peak positive pressures were reduced by 25% from typical value measured in water (40 MPa at 20 kV[10]) to account for tissue attenuation. On the other hand, the peak negative pressures were selected from the minimum to the maximum values measured in water, since the effect of tissue attenuation on the tensile pressure is small.[3] The third trace at the bottom corresponds to the results produced in the lithotripter field used by Dalecki and associates to evaluate the influence of contrast agents on SWL-induced hemorrhage in mice.[7] The pulse is approximately 1.5 cycles of a sine wave with a peak pressure of ~2 MPa and with a fundamental frequency of 0.1 MHz.[7]

At each pressure level, inertial cavitation characterized by the explosive growth of the bubble was observed when the initial radius of cavitation nucleus, R_0, exceeds a critical value. This critical nucleus size corresponds to the transition from stable to inertial cavitation when the restraining effect of surface tension on bubble growth is overcome by the tensile stress of the incident pressure wave.[11] For the HM-3 lithotripter shock waves, the critical nucleus radius appears to be in the range of 5~10 nm. Across this critical value, the maximum bubble radius, $R_{\max}$, was found to increase dramatically by several orders of magnitude. In the inertial cavitation region, as R_0 varies from 10 nm to 10 μm, $R_{\max}$ increases slightly from 666 to 778 μm for P^+/P^- of 30/−7 MPa, and from 1066 to 1151 μm for P^+/P^- of 30/−10 MPa. For the 2-MPa sine wave, the critical nucleus radius was found to be around 28 nm. Above this critical value, $R_{\max}$ increases monotonically from 105 to 176 μm as R_0 varies from 30 nm to 10 μm.

III. DISCUSSION

Recently, Dalecki and associates showed that when mice were injected with the ultrasound contrast agent Albunex® (effective cavitation nuclei) and exposed to a lithotripter field of ~2-MPa pressure amplitude and fundamental frequency of 0.1 MHz, hemorrhage in the kidney was consistently observed.[7] Histologically, the primary damage in the kidney was rupture of glomerular capillaries. In comparison, mice exposed to the lithotripter field alone showed no kidney hemorrhage. Corresponding to the nuclei size of Albunex® (3–5 μm in diameter), our model calculation in this lithotripter field (bottom trace in Fig. 3) predicts a maximum bubble diameter of approximately 340 μm in blood without tissue constraint. This maximum bubble diameter is an order of magnitude larger than the size of capillaries and postcapillary venules (8–30 μm). Assuming that the criterion for ureteral wall rupture could be applied to vascular injury, the intraluminal expansion of these cavitation bubbles would cause a rupture of capillaries and postcapillary venules, but not of blood vessels larger than 120 μm. This prediction seems to agree with the histological observations of Dalecki and associates. On the other hand, the absence of hemorrhage in the kidney without Albunex® may indicate a rela-

tive lack of sufficiently large cavitation nuclei in normal renal tissue. This speculation is supported by the results from Coleman and associates, who reported that cavitation nuclei in the kidney and surrounding tissue may be less than 30 nm in radius.[3] For such small nuclei, our model calculation indicates that inertial cavitation may not be induced in the blood by the 2-MPa lithotripter field and thus no hemorrhage produced, as reported by Dalecki *et al.*[7]

In the clinical lithotripter field (top two traces in Fig. 3), inertial cavitation could be induced in the blood if nuclei with a radius larger than 10 nm exist. For these nuclei, the maximum bubble diameter predicted by the model calculation is in the range of 1.3 to 2.3 mm. Since inertial cavitation has been observed in hepatic vessels during SWL,[2] cavitation nuclei greater than 10 nm in radius apparently either preexist in the blood or are generated by the lithotripter shock waves. Although the exact size and distribution of cavitation nuclei in the vascular system is currently unknown, the potential for vascular injury due to intraluminal bubble expansion exists. Adapting the Vorreuther criterion for ureteral rupture, the results of our model calculations indicate that capillaries and small blood vessels (<400 μm) would be much more susceptible to rupture due to intraluminal bubble expansion than large blood vessels (>800 μm). This prediction appears to be consistent with the observation of vascular injuries in animals produced by SWL.[12]

ACKNOWLEDGMENTS

This work was supported by the Whitaker Foundation and by NIH grants No. PO1-DK20543 and RO1-DK52985.

[1] M. Kuwahara, N. Ioritani, K. Kamke, S. Shirai, K. Taguchi, T. Saitoh, S. Orikasa, K. Takayama, S. Aida, and N. Iwama, ''Hyperechoic region induced by focused shock waves *in vitro* and *in vivo*: Possibility of acoustic cavitation bubbles,'' Journal of Lithotripsy and Stone Disease **1**, 282–288 (1989).

[2] M. Delius, R. Denk, C. Berding, H. Liebich, M. Jordan, and W. Brendel, ''Biological effects of shock waves: cavitation by shock waves in piglet liver,'' Ultrasound Med. Biol. **16**, 467–472 (1990).

[3] A. J. Coleman, T. Kodama, M. J. Choi, T. Adams, and J. E. Saunders, ''The cavitation threshold of human tissue exposed to 0.2 MHz pulsed ultrasound: Preliminary measurements based on a study of clinical lithotripsy,'' Ultrasound Med. Biol. **21**, 405–417 (1995).

[4] A. J. Coleman, M. J. Choi, and J. E. Saunders, ''Detection of acoustic emission from cavitation in tissue during clinical extracorporeal lithotripsy,'' Ultrasound Med. Biol. **22**, 1079–1087 (1996).

[5] P. Zhong, I. Cioanta, F. H. Cocks, and G. M. Preminger, ''Inertial cavitation and associated acoustic emission produced during electrohydraulic shock wave lithotripsy,'' J. Acoust. Soc. Am. **101**, 2940–2950 (1997).

[6] C. C. Church, ''A theoretical study of cavitation generated by an extracorporeal shock wave lithotripter,'' J. Acoust. Soc. Am. **86**, 215–227 (1989).

[7] D. Dalecki, C. H. Raeman, S. Z. Child, D. P. Penney, R. Mayer, and E. L. Carstensen, ''The influence of contrast agents on hemorrhage produced by lithotripter fields,'' Ultrasound Med. Biol. **23**, 1435–1439 (1997).

[8] T. G. von Leeuwen, J. H. Meertens, E. Velema, M. J. Post, and C. Borst, ''Intraluminal vapor bubble induced by excimer laser pulse causes microsecond arterial dilation and invagination leading to extensive wall damage in the rabbit,'' Circulation **87**, 1258–1263 (1993).

[9] R. Vorreuther, R. Corleis, T. Klotz, P. Bernards, and U. Engelmann, ''Impact of shock wave pattern and cavitation bubble size on tissue damage during ureteroscopic electrohydraulic lithotripsy,'' J. Urol. (Baltimore) **153**, 849–853 (1995).

[10] A. J. Coleman and J. E. Saunders, ''A survey of the acoustic output of commercial extracorporeal shock wave lithotripters,'' Ultrasound Med. Biol. **15**, 213–227 (1989).

[11] T. G. Leighton, *The Acoustic Bubble* (Academic, London, 1994), pp. 312–335.

[12] M. Delius, ''Medical applications and bioeffects of extracorporeal shock waves,'' Shock Waves **4**, 55–72 (1994).

An acoustical frequency ratio technique for detection of a bifurcation hemiocclusion in a symmetrical branching structure

David T. Raphael[a)]
Department of Anesthesiology, University of Medicine and Dentistry of New Jersey—Robert Wood Johnson Medical School, New Brunswick, New Jersey 08901; and Department of Anesthesiology, Texas Tech University Health Sciences Center, El Paso, Texas 79905

Marshall H. Dean
Instructor in Electronics, El Paso Community College, El Paso, Texas 79998

(Received 7 April 1998; revised 19 July 1998; accepted 6 August 1998)

Within a symmetrical branching cylindrical structure open at one end and closed at the other, the ratio of the first overtone to the fundamental is either greater or less than 3, depending on the ratio of the distal branch length to the parent trunk length. For an unoccluded structure, the ratio is generally above 3. For an occluded structure, the ratio is generally below 3. This acoustical frequency ratio technique may be used to infer the extent of unilateral distal branch occlusion in a branching structure. © *1998 Acoustical Society of America.* [S0001-4966(98)03611-X]

PACS numbers: 43.80.Jz, 43.58.Bh [FD]

INTRODUCTION

When fluid in a branching duct is driven by a vibrating piston, waves are transmitted and reflected throughout the structure. The multiple reflections at the bifurcations generate waves traveling in the opposite direction which, upon interacting with the incident waves, lead to the production of standing waves. The resulting stationary oscillations are related to the phenomenon of resonance.[1]

I. ACOUSTIC RESONANCE CONDITIONS IN BRANCHING STRUCTURES

Resonance is defined as that frequency at which the reactive component of the input impedance vanishes.[1] The exact resonance conditions[2] associated with the propagation of a harmonic wave within a branching structure, open at one end and closed at the distal ends of the branches, have been determined for the general case of a rigid symmetrical branching network involving an arbitrary number, N, of nodal orders of bifurcation. Consider the Nth-order symmetrical branching network of Fig. 1. At any given level of bifurcation, the branches are characterized by a length l_i and area S_i, for $i=1,2,\cdots,N$. The end at z_0 is open, and the distal ends z_N of each terminal branch are closed. The complete Nth-order resonance condition is

$$l_1+k^{-1}\arctan[(2S_2/S_1)\tan k\{l_2 + k^{-1}\arctan[(2S_3/S_2)\tan k[l_3+\cdots+k^{-1} \times\arctan[(2S_{N-1}/S_N)\tan kl_N\}]=(2n-1)\pi/2k, \quad (1)$$

for modal number $n=1,2,3,...$ and where k is the wave number $k=\omega/c$ (ω is the angular frequency, and c is the sound speed in air).

Proceeding proximally from the most distal branch l_N, each successive branch is modified by an area-weighted operator of the form

$$P_i=k^{-1}\arctan[(2S_i/S_{i-1})\tan k, \quad i=2,3,...,N, \quad (2)$$

involving tangent and inverse tangent functions. The resulting equivalent length of this application of the operator, when added to the true length of the length of the immediately adjacent proximal branch, becomes the object length of the next application of the operator. It is evident that the degree to which a specific branch is successively embedded within the argument of the nested area-weighted trigonometric operators reflects its nodal order within the hierarchy of branches. In operator formalism, the general resonance condition becomes

$$l_1+P_2[l_2+P_3\{l_3+\cdots+P_Nl_N\}]=(2n-1)\pi/2k, \quad \text{for } n=1,2,3,... . \quad (3)$$

The resonance conditions associated with the propagation of a harmonic wave within rigid, lossless symmetrical[3] and asymmetrical[4] branching structures have been previously derived.

For a cylindrical straight tube open at one end and closed at the other, the ratio of the first overtone f_2 to the fundamental frequency f_1 is 3. In a bifurcating structure, an f_2/f_1 ratio of 3 is maintained only if the total area at any branch level is the same as that of the parent trunk area. Indeed, if the total area at all branch levels is constant and is equal to the area of the parent trunk, the observed modal pattern associated with this equi-areal branching structure will be indistinguishable at the open end from the pattern of modes observed with a nonbranching structure.

Consider a symmetrical first-order branching structure with two daughter branches. If the bifurcation is partially occluded (as in Fig. 2), such that sound waves are transmitted down one set of branches but not down the other, a heminodal occlusion occurs. This has the effect of halving the area distal to the first bifurcation.

[a)]Correspondence address: Dept. of Anesthesiology, University of Medicine and Dentistry of New Jersey, Clinical Academic Building, 125 Paterson St., New Brunswick, NJ 08901. Electronic mail:kfarnetter@aol.com

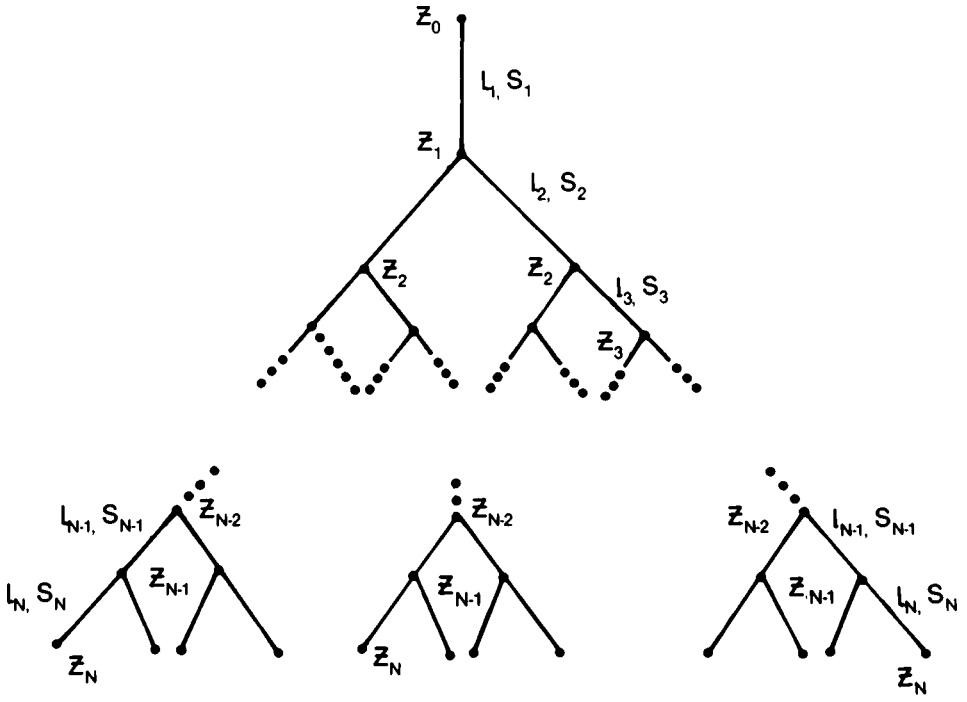

FIG. 1. An *N*th-order symmetrical branching network with branch lengths l_i and cross-sectional areas $S_i (i=1,2,3,...)$. The network is open at nodal point z_0 and closed at the distal ends z_N.

In the case of an idealized symmetric Weibel lung,[5,6] the diameters d_i of successive branches are related by $m = d_{i+1}/d_i = 2^{-1/3} = 0.794$ so that the area of a successive branch must be proportional to $m^2 = 0.63$ of the preceding branch, i.e., $S_2 = 0.63 S_1$, $S_3 = 0.63 S_2$, etc.

For a Weibel-like symmetrical first-order branching structure, the total area of the two daughter branches is $2S_1$, and the corresponding area ratio is $2S_2/S_1 = 1.26$. In the case of a heminodal occlusion, the postnodal area ratio is halved, i.e., $S_2/S_1 = 0.63$.

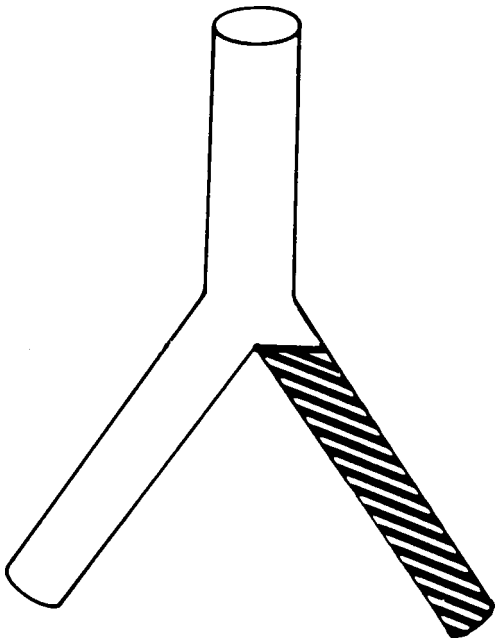

FIG. 2. A nodal hemiocclusion of the single bifurcation of a first-order symmetrical branching structure. One of the two distal branches is completely occluded (shaded area).

Applying the resonance conditions as described above, one obtains unoccluded:

$$l_1 + k^{-1} \arctan[1.26 \tan k l_2] = (2n - l)\pi/2k, \tag{4}$$

hemioccluded:

$$l_1 + k^{-1} \arctan[0.63 \tan k l_2] = (2n-1)\pi/2k \quad \text{for } n = 1,2,3,\ldots . \tag{5}$$

Theoretical calculations indicate that whenever the branch area S_T distal to the first node is greater than the parent trunk area S_1 in a symmetric unoccluded structure, then $f_2/f_1 > 3$. When one of the two branches is occluded at the single node, i.e., when a heminodal occlusion is present such that $S_T < S_1$, then $f_2/f_1 < 3$. It was decided to determine whether this occurs experimentally. When $S_T = S_1$, then $f_2/f_1 = 3$.

For a branching structure with *N* orders of bifurcation, the transcendental nature of Eq. (1) does not permit an explicit, closed-form analytical solution for the frequency ratio f_2/f_1. However, in the specific case of a branching structure where $l_1 = l_2$, it can be readily shown that, for the *unoccluded* case, the expected maximum value of the frequency ratio f_2/f_1 is

$$f_2/f_1 = [3\pi/2 - \arctan\{(2S_2/S_1)^{1/2}\}]/[\pi/2 - \arctan\{(2S_2/S_1)^{1/2}\}], \tag{6}$$

and, for the *occluded* case,

$$f_2/f_1 = [3\pi/2 - \arctan\{(S_2/S_1)^{1/2}\}]/[\pi/2 - \arctan\{(S_2/S_1)^{1/2}\}]. \tag{7}$$

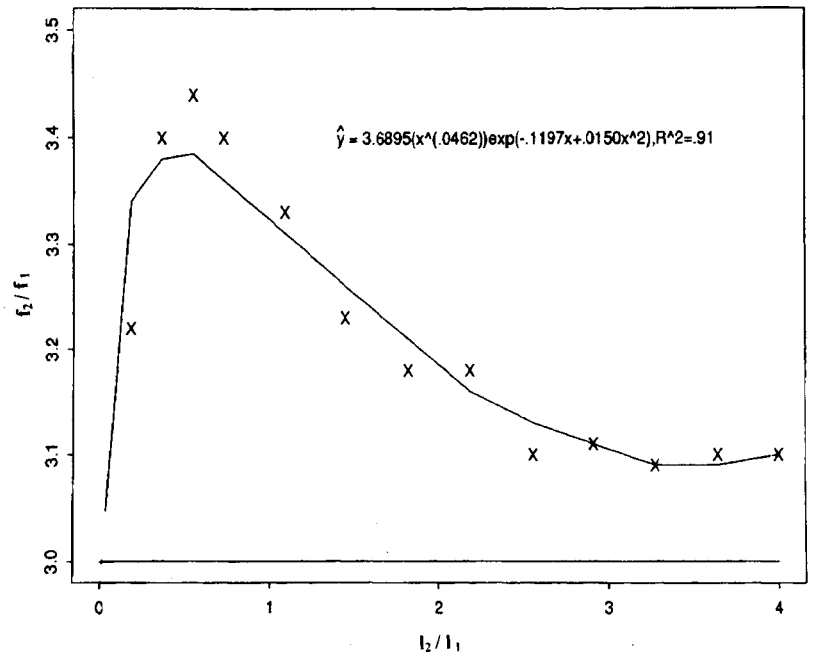

FIG. 3. For an unoccluded symmetrical branching structure, the frequency ratio (first-overtone-to-fundamental) is always three times greater than the branch-length ratio (distal branch length/parent trunk length).

Thus, the greater the ratio of the distal branch area to the parent trunk area, the greater the peak or trough of the corresponding maximum and minimum seen for the frequency ratios. It turns out, experimentally as well as theoretically, that the respective extrema occur when $l_1 = l_2$. Note that when either $2S_2/S_1$ or S_2/S_1, respectively, approach 1 in Eqs. (6) and (7), the corresponding frequency ratios both approach 3, as expected.

II. EXPERIMENTAL METHODS

A custom blown-glass rigid, symmetrical structure with a single bifurcation was placed in the upright position, open end up and distal closed ends down (Witeg Scientific, Anaheim, CA). The dimensions of the parent trunk were held constant for all measurements, namely, $l_1 = 11.0$ cm and inner diameter $d_1 = 2.16 \pm 0.3$ mm. The diameters of the distal branches were fixed and blown so as to exhibit a fractional decrease in area comparable to that expected in a Weibel[6] morphometric model of the lung. The inner diameter of each distal branch was 1.66 cm ± 0.2 mm. This resulted in the following: a diameter ratio $d_2/d_1 = 0.76$ (within 4% of the theoretical Weibel model ratio), and a corresponding calculated area ratio $2S_2/S_1 = 1.18$ (within 6% of the corresponding Weibel ratio).

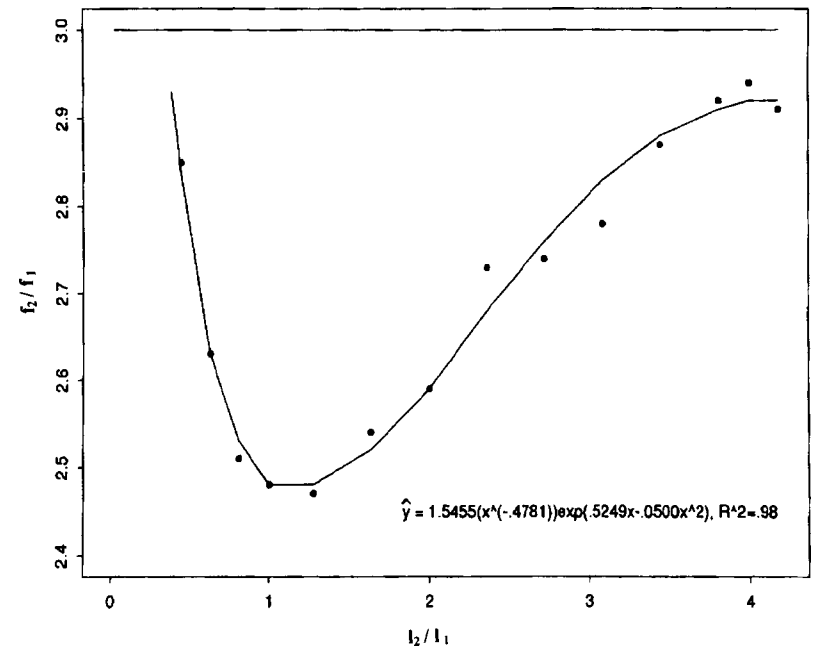

FIG. 4. For a symmetrical first-order branching structure with one of its two distal branches completely occluded, the frequency ratio is always less than three times the branch-length ratio.

Three distinct measurement sets were obtained for both unoccluded and occluded states. A heminodal occlusion was performed by filling one of the distal branches *completely* with water (up to the horizontal level allowed by the bifurcation, without spillage into the other branch), as illustrated in Fig. 2. The length of the other ''unoccluded'' branch was progressively filled with water, and the true distal length l_2 was taken to be the distance from the bifurcation to the water level in the unoccluded branch.

Random noise was generated using an Auditec random noise CD. The noise signal was amplified with a RadioShack MPA-46 PA amplifier with 35-watt capability, and transmitted through a 4 in. speaker mounted in a rectangular baffle into the open proximal end of the glass bifurcating structure. Clipping was avoided by observing the input noise signal on a type 654B storage oscilloscope. The speaker's random-noise output, directed toward the open end of the studied glass model, as well as any present resonance amplification, was detected by a subminiature Knowles Electret model EM-3046 microphone ($4\times6\times2.28$ mm) placed within the parent trunk at a distance of 2 cm from the open end. A computer-based data acquisition and analysis system was set up. Using a Gateway 2000 computer with a Pentium chip, the microphone analog output signal was amplified with a noninverting operational amplifier, and digitized by means of a Data Translation DAS-1801 a/d board at a sampling rate of 20 000 Hz. To minimize line separation in the frequency domain, a large sample size was used. Each final FFT determination was calculated with a LABVIEW real-time fast Fourier transform program based on a sample size of 8224 data points sampled, and ensemble-averaged over ten consecutive FFTs to give the resulting plot. To avoid aliasing, the input signal was band-limited to frequencies less than half of the sampling frequency.

Because the theoretical impedances are purely reactive, it is possible to infer that resonance occurs at those maxima associated with a spectral display of the moduli of the complex components of the FFT. For display purposes, an FFT display of the moduli was performed for the frequency rate of interest, and a manually controlled cursor was used to determine the frequencies at which distinct frequencies occurred. All observed frequency measurements were performed with a manually controlled cursor with a resolution no better than ±6 Hz.

III. RESULTS

The resulting plots of frequency ratios f_2/f_1 versus length ratios l_2/l_1 were in complete conformity with the theoretical predictions. For the unoccluded bifurcating structure shown in Fig. 3, the frequency ratio always exceeded 3. For the same structure hemioccluded at its single bifurcation, as shown in Fig. 4, the frequency ratio always was less than 3. As the l_2/l_1 ratio increases, i.e., as the relative length of the daughter branches increases, the f_2/f_1 ratio asymptotically approaches 3—in the case of the unoccluded case from above, in the case of the hemioccluded structure from below. When the distal branches are very short, i.e., as l_2/l_1 approaches zero such that only the parent trunk remains, the f_2/f_1 approaches 3, the known ratio for an unbranched structure open at one end and closed at the other.

IV. CONCLUSIONS AND DISCUSSION

In a branching structure like the lung, a variety of acoustical approaches has been used to obtain pulmonary characteristics, including the observation of resonance mode[2–4] and spectral band changes[7–9] in the presence of random noise, area-distance curves[10–13] using an acoustic pulse response technique, and inverse numerical methods.[14] The real-time frequency-ratio approach described above may have potential clinical utility in the diagnosis of an obstruction in a bronchial mucous plug close to the carina or a unilaterally developing lung infiltrate (both of which would encroach upon the available lung volume), as would be suggested by an f_2/f_1 ratio less than 3.

ACKNOWLEDGMENTS

This study was performed at Texas Tech University HSC—El Paso. The LABVIEW FFT processing program was developed by Joe Adam of Premise Development of Hartford, Connecticut. The nonlinear regression curves for Figs. 3 and 4 are due to Dr. Julia Bader of the UTEP Biostatistical Laboratory. We gratefully acknowledge their assistance with this research project.

[1] P. M. Morse and K. U. Ingard, *Theoretical Acoustics* (McGraw-Hill, New York, 1968), pp. 554–576.
[2] D. T. Raphael, ''An explicit resonance condition for a rigid symmetric *N*th-order branching network,'' J. Acoust. Soc. Am. **83**, 335–337 (1988).
[3] D. T. Raphael and M. A. F. Epstein, ''Volume estimation of symmetrical branching structures by resonance mode analysis,'' J. Acoust. Soc. Am. **82**, 800–806 (1987).
[4] D. T. Raphael and M. A. F. Epstein, ''Resonance mode analysis for volume estimation of asymmetric branching structures,'' Ann. Biomed. Eng. **17**, 361–375 (1989).
[5] K. Horsfield, G. Dart, D. Olson, G. Filley, and G. Cumming, ''Models of the human bronchial tree,'' J. Appl. Physiol. **31**, 207–217 (1971).
[6] E. R. Weibel, *Morphometry of the Human Lung* (Academic, New York, 1963).
[7] E. D. Michaelson, E. D. Grassman, and W. R. Peters, ''Pulmonary mechanics by spectral analysis of forced random noise,'' J. Clin. Invest. **56**, 1210–1230 (1975).
[8] M. A. F. Epstein, P. L. Conard, and A. B. Smith, ''Identification of changes in airway geometry *in vivo* using acoustic resonance tehniques,'' FASEB J. **8**, A687 (1994).
[9] K. Ishizaka, M. Matsudaira, and T. Kaneko, ''Input acoustic impedance measurement of the subglottal system,'' J. Acoust. Soc. Am. **60**, 190–197 (1976).
[10] A. C. Jackson, J. P. Butler, E. J. Millett, F. G. Hoppin, and S. V. Dawson, ''Airway geometry by analysis of acoustic pulse response measurements,'' J. Appl. Physiol. **43**, 523–536 (1977).
[11] A. C. Jackson, J. P. Butler, and R. W. Pyle, ''Input impedance of excised dog lungs,'' J. Acoust. Soc. Am. **64**, 1020–1026 (1978).
[12] J. J. Fredberg, ''Acoustic determinants of respiratory system properties,'' Ann. Biomed. Eng. **9**, 463–473 (1980).
[13] R. S. Sidell and J. J. Fredberg, ''Non-invasive inference of airway network geometry from broadband reflection data,'' Trans. ASME, Ser. K **100**, 131–138 (1978).
[14] M. M. Sondhi and B. Gopinath, ''The inverse problem for the vocal tract: numerical methods, acoustical experiments, and speech synthesis,'' J. Acoust. Soc. Am. **73**, 985–1002 (1983).